MC goes DIGITAL 2021

Microscopy Conference

Joint Meeting of Dreiländertagung &
Multinational Congress on Microscopy

22-26 AUGUST 2021

PROCEEDINGS

TU WIEN

www.mc2021.at

ÖMS

MCM

Content

Abstracts of plenary- and invited talks are shown in the proceedings, given they were submitted.

PL.001
Applications of Environmental SEM as In-Situ Surface-Science Tool with Atomic Layer Sensitivity

Marc Willinger[1]

[1] Scientific Center of Optical and Electron Microscopy, ETH Zürich, Switzerland

Methodological developments and the availability of commercial tools for in-situ electron microscopy have extended our abilities to observe materials beyond the thermodynamically isolated state of static atomic arrangements in vacuum.
Watching how (functional) materials react and interact with a defined (chemical) environment at high resolution and across various length and timescales is key for an atomistic understanding of processes that are relevant for material science, chemistry and biology.
Fascinated by the ability to resolve structures at the most fundamental, atomic scale, the electron microscopy community was largely focusing on in-situ TEM. As a very local method, it should be complemented by methods that are capable of delivering information about larger-scale dynamics, where processes that involve collective motion of many atoms and effects related to heat- and mass-transfer can be observed. Over the last years, we have thus complemented in-situ TEM with experiments performed inside the chamber of an environmental scanning electron microscope (ESEM). We thereby realized the fascinating potential of in-situ and operando SEM, which seems to have been partially overlooked by the growing in-situ TEM community.
The aim of my presentation is to highlight some of the capabilities of in-situ SEM, especially with regards to the high surface sensitivity that can be reached, and the important role in-situ SEM can play in bridging gaps between fundamental UHV-based surface science investigations of model systems on one hand, and studies on complex-structured functional materials under application relevant conditions on the other hand.
It will be shown that the combination of operando SEM and operando TEM enables context embedded observation of atomistic and collective processes [1,2]. Examples range from temperature induced phase transformations to chemical reactions and growth processes. Finally, I will also try to point out some limitations that should be easy to overcome once we convince microscope manufacturers to improve vacuum quality and base-pressure of instruments.

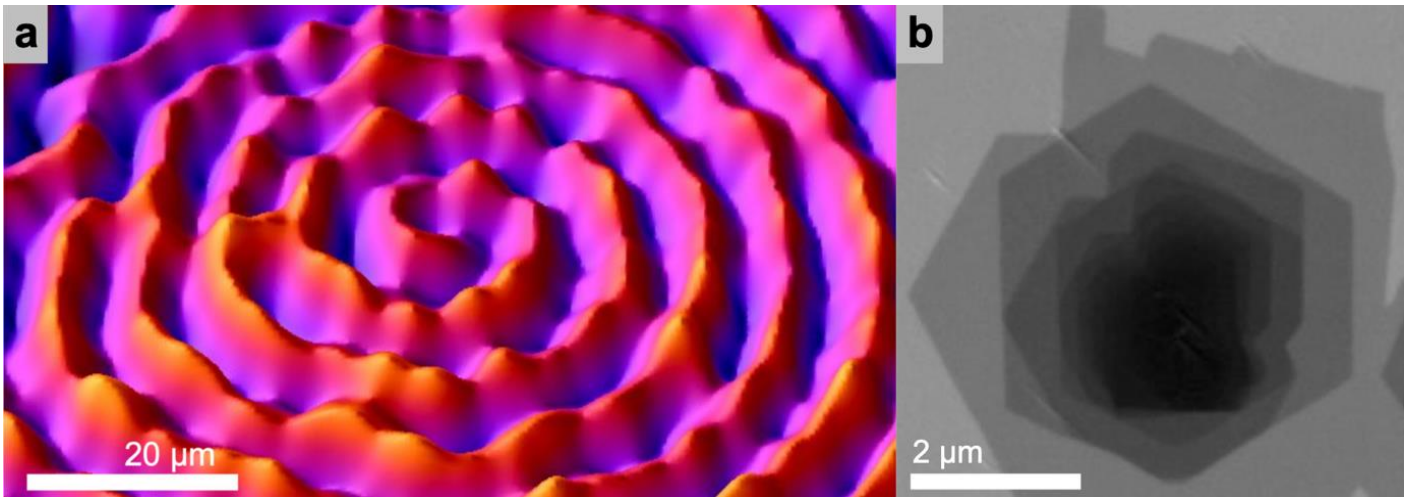

Figure 1 | Spirals: a) false-coloured image showing secondary electron intensity as height profile. The spiral pattern is caused by propagating reaction fronts on the surface of a platinum grain during NO2 hydrogenation [3]. b) Spiral growth of multi-layer graphene imaged during CVD growth on a platinum substrate inside the SEM chamber at ~ 1000 °C [4].

References:
[1] Cao J. et al. Nat Commun 11, 3554 (2020). https://doi.org/10.1038/s41467-020-17346-7
[2] Huang X. et al. Adv Mater., 2101772 (2021). https://doi.org/10.1002/adma.202101772
[3] Barroo C. et al. Nat Catal 3, 30–39 (2020). https://doi.org/10.1038/s41929-019-0395-3.
[4] Wang, Z.-J et al. Adv. Mater. Interfaces 5, 1800255 (2018). https://doi.org/10.1002/admi.201800255,
Wang, ZJ. et al. Nat Commun 7, 13256 (2016). https://doi.org/10.1038/ncomms13256

PL.004
Novel approaches to investigate the 3D atomic structure of nanomaterials and their dynamics from STEM images using statistical parameter estimation and deep convolutional neural networks

S. Van Aert[1], A. De wael[1], E. Arslan Irmak[1], A. De Backer[1], Z. Zhang[1], T. Friedrich[1], D.G. Sentürk[1], I. Lobato[1], P. Liu[1] T. Altantzis[1], L. Jones[2], P.D. Nellist[3], and S. Bals[1]

[1]EMAT & NANOlab Center of Excellence, University of Antwerp, Antwerp, Belgium
[2]CRANN & School of Physics, Trinity College Dublin, Dublin, Ireland
[3]Department of Materials, University of Oxford, Oxford, UK

Determining the 3D atomic structure of nanomaterials is critical to understand their unique properties. To overcome limitations related to conventional electron tomography, 3D characterization of beam-sensitive nanomaterials can be obtained from atom counts resulting from a single ADF STEM projection image [1]. For this purpose, the scattering cross-section (SCS), corresponding to the total intensity of electrons scattered by a single atomic column, has been shown to be a successful performance measure. In combination with energy dispersive X-ray spectroscopy, atom-counting can be extended from homogeneous to heterogeneous materials by using a deep convolutional neural network and an atomic lensing model to efficiently compute SCSs of mixed atomic columns.

Counting atoms with single-atom sensitivity requires a minimum electron dose, while on the other hand the risk of beam-induced damage puts an upper limit on the tolerable dose [2]. For beam-sensitive materials, where the optimal electron dose can be low, the maximum *a posteriori* (MAP) probability rule is introduced to reliably detect the presence or absence of atomic columns and even single atoms [3]. In addition, a deep convolutional neural network is proposed to restore low dose, scan noise distorted ADF STEM images. This network creates new opportunities to measure variations of the 3D atomic structure of nanoparticles under the flow of a selected gas (figure 1) [4].

Experiments performed under varying environmental conditions clearly demonstrate the need to quantify the material's dynamics from a series of sequentially recorded images. The standard approach for atom-counting, where each frame is analyzed individually, does not take advantage of the time aspect available in a series of ADF STEM images. We therefore extended the atom-counting method using the so-called factorial hidden Markov model. This new method is very promising for revealing dynamic structural changes resulting from adatom dynamics, surface diffusion, beam effects or during *in situ* experiments (figure 2) [5, 6].

Based on atom counts an initial atomic model can be created which serves as an input for an energy minimization to obtain a relaxed 3D reconstruction of a nanostructure. Recent developments using a Bayesian genetic algorithm is proposed including *a priori* information about the finite precision of the atom-counting results and neighbor-mass relations. This method shows excellent prospects for obtaining reliable reconstructions from images acquired at low incident electron doses. Finally, a methodology is proposed to characterize supported metallic nanoparticles at high temperature, which is of importance to understand their behavior during catalytic reactions [7].

References
[1] A De Backer et al., Nanoscale **9** (2017), p. 8791.
[2] S. Van Aert et al., Physical Review Letters **122** (2019), 066101.
[3] J. Fatermans et al., Physical Review Letters **121** (2018), 056101.
[4] T. Altantzis et al., Nano Letters **19** (2019), p. 477.
[5] A. De wael et al., Physical Review Letters **124** (2020), 106105.
[6] P. Liu et al., Nanoscale **13** (2021), p. 1770.
[7] This work was supported by the European Research Council (Grant 770887 PICOMETRICS to SVA and Grant 815128 REALNANO to SB). The authors acknowledge financial support from the Research Foundation Flanders (FWO, Belgium).

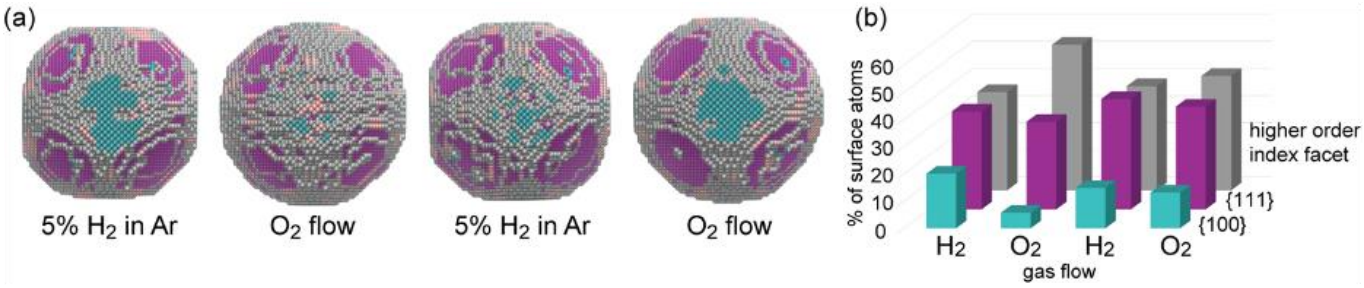

Figure 1. (a) Structural evolution of a Pt nanoparticle under different environmental conditions. (b) Occurrence of different surface facets as a function of the gas flow in time [4].

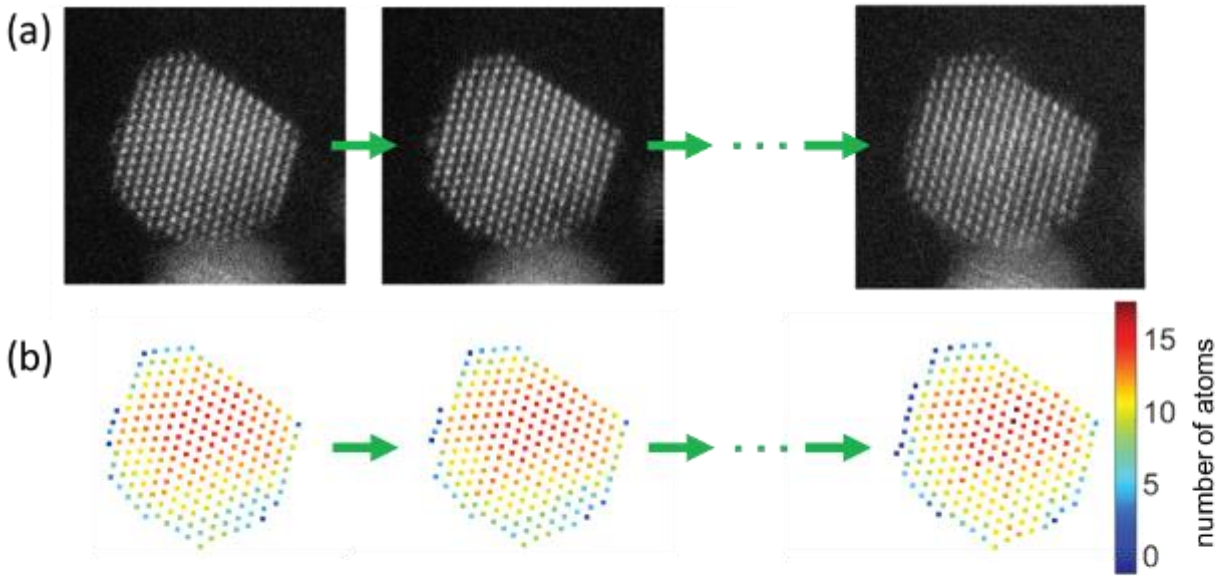

Figure 2 (a) Experimental ADF STEM time series of a Pt nanoparticle. (b) Estimated atom counts using a hidden Markov model [5].

PL.006
Understanding quantitative STEM – How far have we come?

A. Rosenauer[1,2]

[1]Universität Bremen, Institut für Festkörperphysik, Germany
[2]Universität Bremen, MAPEX Center for Materials and Processes, Germany

Scanning transmission electron microscopy (STEM) has developed into one of the most widely used imaging methods in electron microscopy. In the simplest case, a high-angle annular dark field (HAADF) detector collects electrons scattered at high angles. This results in STEM images that seem easy to interpret. The heavier an atom, the more electrons are scattered. Under this assumption, the brightness of an atom column in the image increases with its mean atomic number and with the number of atoms in the column (specimen thickness). However, GaN_xAs_{1-x} layers embedded in GaAs appear bright on a dark background, although N has a smaller atomic number than As. Image simulations revealed that strain fields around the N atoms cause diffuse scattering increasing the intensity on the detector. This example shows that a quantitative interpretation of STEM images requires a comparison with accurate image simulation.

One of the first applications of quantitative STEM was the measurement of composition in ternary semiconductor layers such as $In_xGa_{1-x}N$ [1]. This method is based on a segmentation of the image into Voronoi cells, averaging the intensities within the cells and comparing with a data set simulated as a function of specimen thickness and composition. As an image provides only one intensity value per scan point, specimen thickness and composition cannot be measured independently.

More than one intensity value per scan point can be obtained from angle resolved STEM. A precise setting of the upper limit of the angular range of detected electrons can be achieved with a motorized iris aperture installed in front of the HAADF detector. The difference between the image intensities for two openings of the aperture yields the intensity within a defined angular range. This allows the simultaneous measurement of thickness and composition [2] and enables a comparison of the intensity in intervals of the scattering angle with simulation. In this way, it was observed that the angle dependence of the scattered intensities at small angles close to the semiconvergence angle is significantly influenced by plasmon loss [3], phonon correlations and surface contamination [4].

The full information in the diffraction space can be exploited with a pixelated detector. Acquisition of a complete Ronchigram per scan point and computing the center of mass (COM) provide the average momentum transfer [5]. For specimens thinner than about 5 nm this yields projected and probe convolved values for electric field, charge density and Coulomb potential. Application examples of the COM approach include determination of the stacking sequence in bilayers of MoS_2 [6], evaluation of electrical polarization in AlN/GaN nanodisks (Fig. 1) [7,8] and characterization of p-n junctions [9].

Figure 1: (a) BF intensity of a part of a 110 nm thick nanowire with GaN/AlN layers, (b) evaluated momentum transfers, (c) projected electric field averaged within Voronoi cells, (d) line profile of the [000 -1] component of the electric field showing a difference of the polarization induced electric fields of 5.9 MV/cm between GaN and AlN, whereas a value of 12.5 MV/cm was expected for fully strained layers [7]. (e,f) Simulations reveal a similar reduction of the measured field difference [8].

[1] A. Rosenauer, T. Mehrtens, K. Müller, et al., Ultramicroscopy (2011), 111, 1316–1327
[2] K. Müller-Caspary et al., Scientific Reports, (2016), **6**, 37146
[3] A. Beyer, F.F. Krause, H.L. Robert, et al., Scientific Reports, (2020), 10, 17890
[4] T. Grieb, F.F. Krause, K. Müller-Caspary, et al. Ultramicroscopy (2021), 221, 1131
[5] K. Müller, F.F. Krause, A. Béché, et al., Nature comm. 5 (2014) 5653
[6] K. Müller-Caspary, M. Duchamp, M. Rösner, et al., Phys. Rev. B (2018), 98, 121408(R)
[7] K. Müller-Caspary, T. Grieb, J. Müßener, et al., Phys. Rev. Lett. (2019), 122, 106102
[8] T. Grieb, F.F. Krause, K. Müller-Caspary, et al., Ultramicroscopy (2021), 113321
[9] A. Beyer, M. S. Munde, S. Firoozabadi, et al., Nano Lett. (2021), 21, 2018-2025

Figure 1

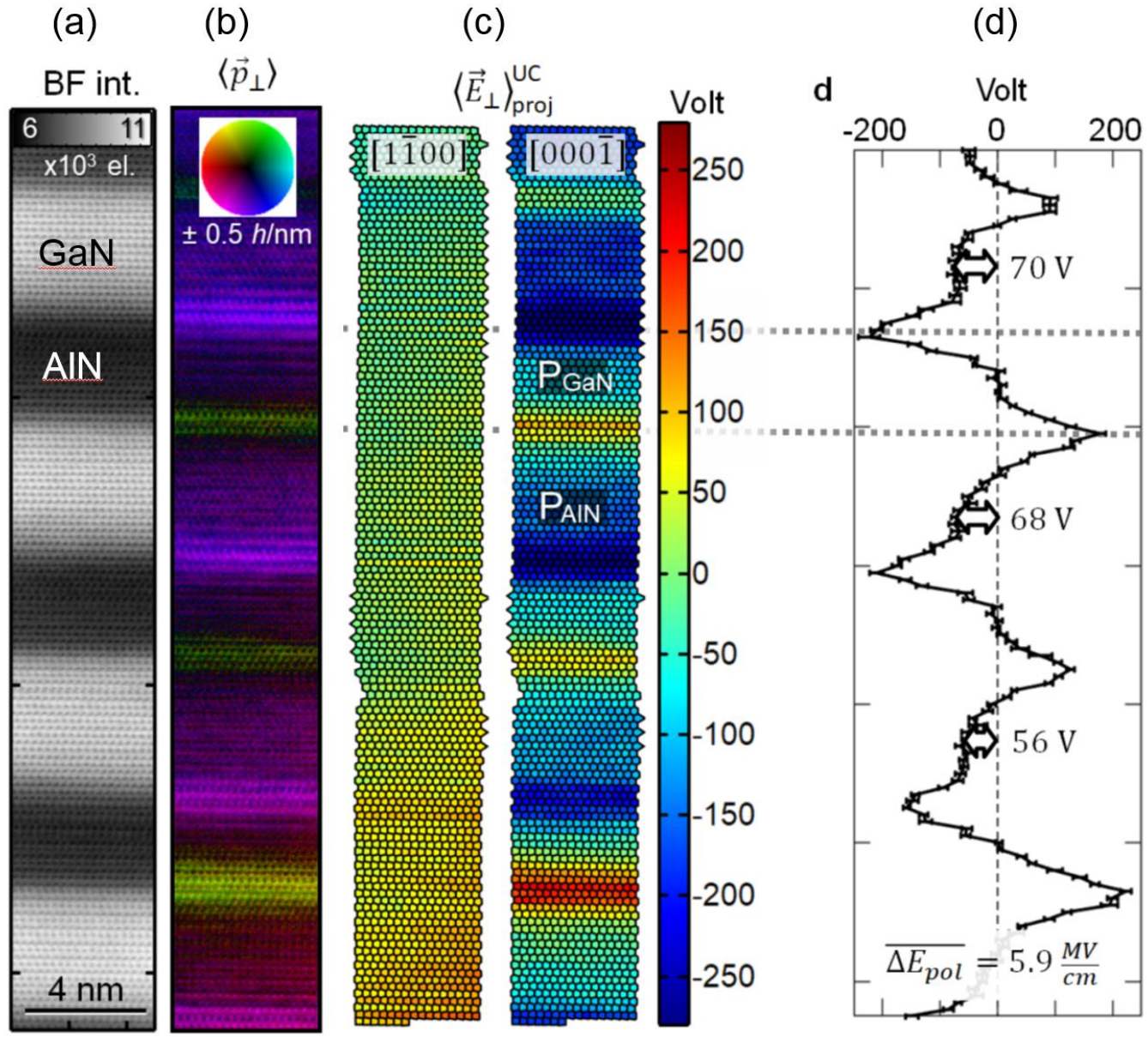
(a)
(b)
(c)
(d)
BF int.
6
11
x10³ el.
GaN
AlN
4 nm
± 0.5 h/nm
[1$\bar{1}$00]
[000$\bar{1}$]
P_GaN
P_AlN
Volt
250
200
150
100
50
0
-50
-100
-150
-200
-250
d
Volt
-200
0
200
70 V
68 V
56 V
$\overline{\Delta E_{pol}} = 5.9 \frac{MV}{cm}$

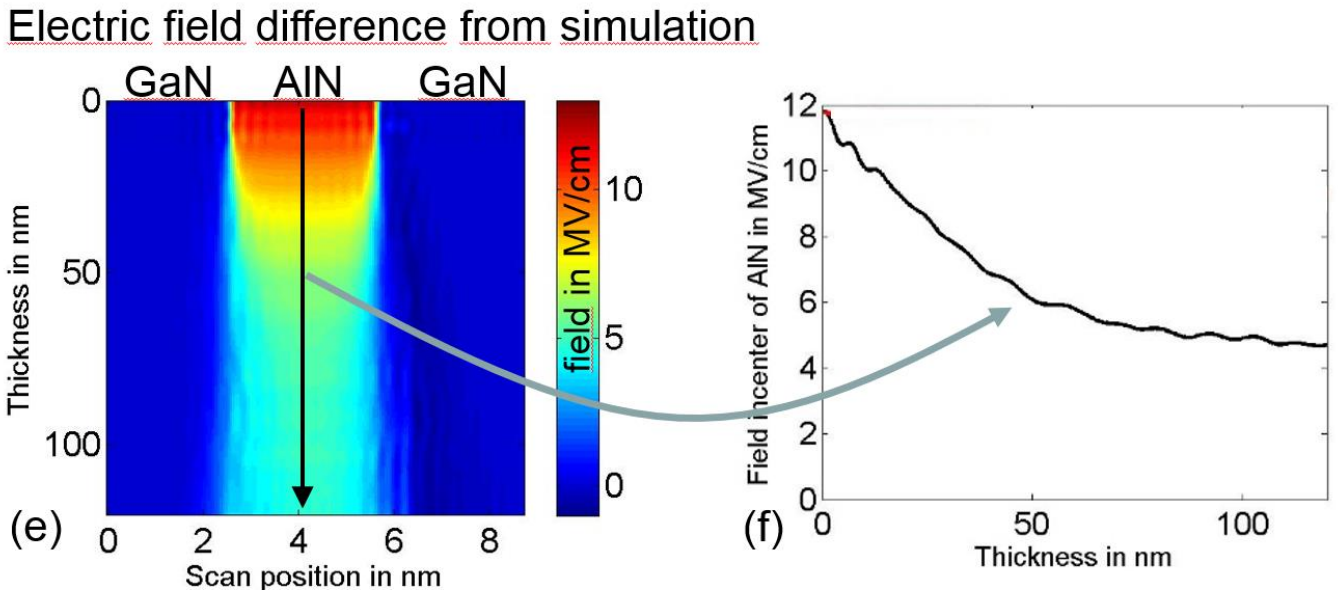
Electric field difference from simulation
GaN
AlN
GaN
Thickness in nm
0
50
100
Scan position in nm
0
2
4
6
8
field in MV/cm
10
5
0
(e)
(f)
Field in center of AlN in MV/cm
12
10
8
6
4
2
0
0
50
100
Thickness in nm

PL.007
Imaging Atoms and Fields by Electron Ptychography

D.. A. Muller[1,2]

[1]School of Applied and Engineering Physics, Cornell University, Ithaca, NY, USA
[2]Kavli Institute at Cornell for Nanoscale Science

Introduction: The past three decades have seen the rapid development and maturation of aberration-corrected electron lenses 1,2. With recent advances in detector technology and reconstruction algorithms, the resolution of the electron microscope is now limited by the dose to the sample, and thermal vibrations of the atoms themselves 3. By recording the full scattering distribution and using ptychographic algorithms to solve the multiple-scattering inverse problem in thick samples, we have been able to improve the dose efficiency of the imaging beyond all other electron microscopy methods, and equally important, obtain the highest resolution images ever recorded. The linearity of the recovered phase signal makes it possible to locate individual dopant atoms in 3D. These approaches have also allowed us to image strain in devices, magnetic fields in sub-nm thick layers, as well as the internal structures of both magnetic and ferroelectric vortices, skyrmions and merons, including their singular points that are critical for accurately describing the topological properties of these field textures.

Objectives: Ptychography uses scanning diffraction and 4D-STEM datasets to iteratively reconstruct the electrostatic potential4–6 and has reached a resolution of 39 pm in thin 2D materials7. However, the underlying strong-phase approximation usually fails for samples thicker than a few nanometers. For thick samples, attempts at phase retrieval from both multi-slice electron ptychography8,9 have been reported, but improvements were still needed in both resolution and denoising.

Materials & Methods: We have demonstrated a robust experimental realization of inversion of the multiple scattering using a regularized implementation of multislice electron ptychography3. This approach provides ultra-high-resolution reconstructions for samples hundreds of Angstroms thick (Figure 1(a)). More importantly, the contrast maintains a linear dependence on thickness over a wide thickness range. The linear phase-contrast also makes it possible to obtain three-dimensional structural information including the locations of single dopant and interstitial atoms (Figure 2).

Results: The potential reconstructed from multislice ptychography from an experimental dataset acquired from a 21-nm-thick PrScO3 sample (Figure 1a) shows only a slight additional blurring compared to the potential at 300 K (Figure 1c). The diffractogram of the phase image shows an isotropic information transfer up to 4.39 Å-1, corresponding to 23 pm in real space. Quantitative analysis reveals that the blurring from the instrument is smaller than 20 pm, smaller than the intrinsic broadening from thermal fluctuations.

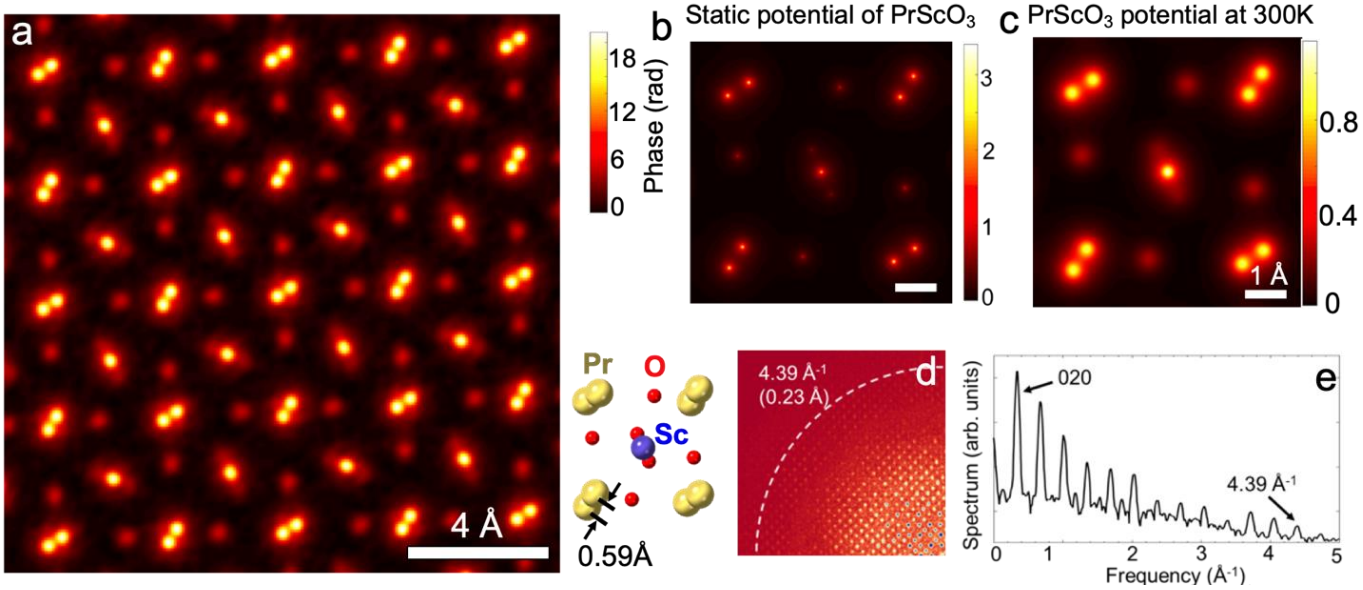

Figure 1: Lattice-vibration-limited resolution from multislice ptychography. (a). Multislice ptychographically-reconstructed phase image from an experimental dataset acquired from a 21 nm thick $PrScO_3$ sample. (b) static potential neglecting zero-point fluctuations, (c) Projected Potential calculated including thermal vibrations at 300 K. (d) Diffractogram of the phase image from experiment and (e) a line profile cut through d on a log scale.

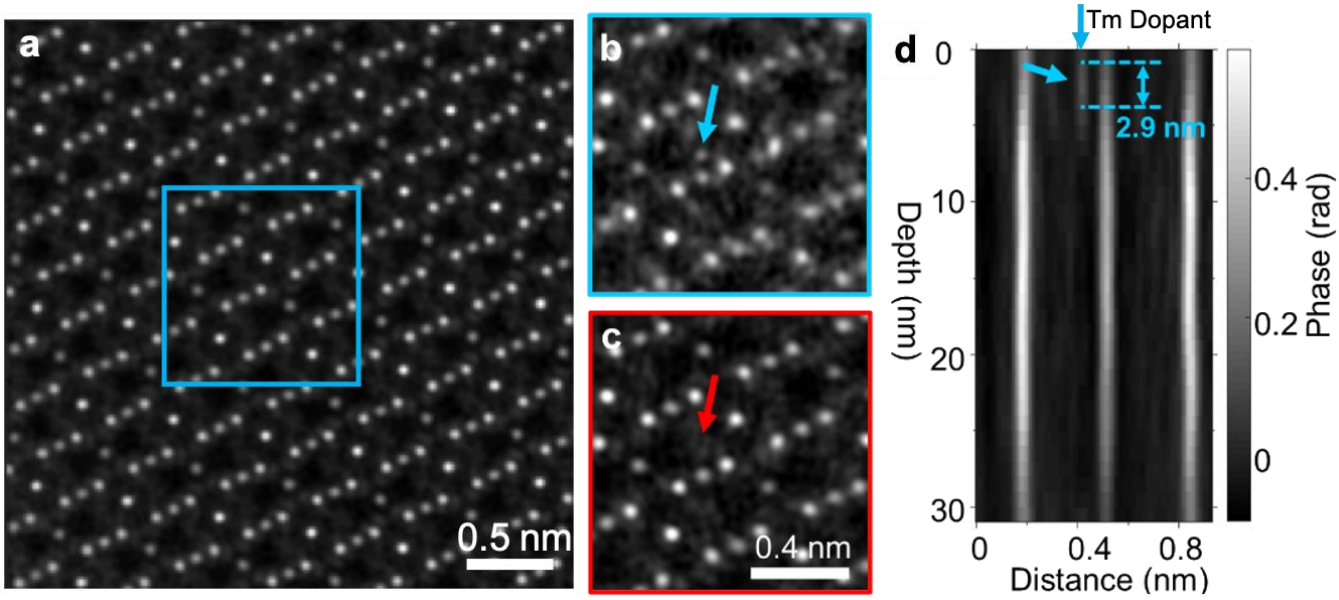

Figure 2: *(a) Multislice* ptychographic reconstruction of a Gd3Ga5O12 film near an interface with Tm3Fe5O12. Phase image at depths z=4 nm (b) and z=6 nm (c) within the blue box from (a). The red and blue arrows mark the location of an interstitial Tm atom 2nm apart in depth. (d) Depth variation of phase intensity across one dopant along a cut in the vertical direction.

References

[1] P. E. Batson, N. Dellby, and O.L. Krivanek, Nature 418, 617 (2002).
[2] M. Haider et al, Nature 392, 768 (1998).
[3] Z. Chen et al, Science 372, 826 (2021).
[4] A. M. Maiden et al, J. Opt. Soc. Am. A 28, 604 (2011).
[5] A. M. Maiden and J.M. Rodenburg, Ultramicroscopy 109, 1256 (2009).
[6] P. D. Nellist and J.M. Rodenburg, Ultramicroscopy 54, 61 (1994).
[7] Y. Jiang et al, Nature 559, 343 (2018).
[8] S. Gao et al, Nat. Commun. 8, 1 (2017).
[9] M. Schloz et al, Opt. Express 28, 28306 (2020).

PL.008
Molecular views into cellular functions by in-cell cryo-electron tomography

J. Mahamid[1]

[1]Structural and Computational Biology Unit, European Molecular Biology Laboratory (EMBL), 69117 Heidelberg, Germany

Most structural biology focuses on the structure and function of individual macromolecular complexes, but falls short of revealing how they come together to give rise to cellular functions. As a consequence, structural and cell biology have traditionally been separate disciplines and employed techniques that were well defined within the realm of either one or the other. Recent technology advances in cryo-electron tomography (cryo-ET) provide a unique opportunity for obtaining structural information to bridge the wide range across spatial scales - from whole cells to individual macromolecules embedded in their native environment at atomic-level detail. We develop and employ advanced sample preparation techniques for in-cell cryo-electron tomography, including cryo-focused ion beam thinning guided by 3D correlative fluorescence microscopy. Preparations of site-specific ‘electron-transparent windows’ in cellular model systems enable assignment of molecular structures directly from three-dimensional stills of intact cells and reveal their molecular sociology. Using the genome-reduced human pathogen Mycoplasma pneumoniae as a model system, we further demonstrate the synergistic application of whole-cell crosslinking mass spectrometry and cellular cryo-ET to determine an in-cell integrative model of actively transcribing RNA polymerases coupled to a translating ribosomes. Recent computational breakthroughs now allow resolving these molecular machines to residue-level and reveal small molecule antibiotics bound to their active site within the intact pathogen. These methodologies unlock an enormous potential for novel discovery enabled by label-free structural cell biology.

PL.009
Materials science or method development - turn left or right, or go straight ahead?

J. Mayer[1]

[1]Central Facility for Electron Microscopy, RWTH Aachen University, Aachen 52074, Germany and Ernst Ruska-Centre for Microscopy and Spectroscopy with Electrons, Forschungszentrum Jülich GmbH, Jülich 52425, Germany

Harald Rose has laid the foundations for many of the groundbreaking instrumental developments of the last three decades and has triggered a wealth of opportunities for young scientists developing new methods with the resulting electron optical components and instruments. Taking part in these electron optical developments and developing new methods based on the improved instruments has always been the most rewarding challenge for young researchers in the field. Up to the present day, excellence in these categories appears to be the most important prerequisite for successfully pursuing an academic career. However, this is also at the core of the fundamental uncertainty, which I encounter in many discussions with our young generation of electron microscopists. It is the feeling that a radical decision has to be taken, scientific excellence in the development of electron optical methods to take the next steps in an academic career, or experience in materials science applications in order to secure a job in other scientific fields or in industry (the same applies for life science, which is not my field). What feels like a bifurcation for the young scientists is actually reality in many disciplines and a career in electron optics does not make it easier to find recognition in the fields of physics or materials science (which Harald Rose encountered in many stages of his career).

However, it was Harald Rose himself who always pointed out that only applications with high relevance and visibility can make the developments sustainable, and who encouraged young materials scientists to become excellent in their application-oriented fields. Materials are technology drivers in many technological sectors, they are at the core of solving global challenges and they require interdisciplinary collaborations between experts in many scientific fields. Renewable energies, batteries, quantum or neuromorphic computing or the broad field of mobility are just a few of the most popular examples where materials science (as well as physics, chemistry and engineering which I do not always want to list to keep things simple) need characterisation down to the atomic level. For an electron microscopist, being active in these fields opens many doors to collaborate with other disciplines, to establish links to industry and to have access to large amounts of third party funding.

Should I turn left or should I turn right, method development or materials science, this decision is more frequently driven by the fear not to make a mistake: will I lose my chances for an academic career, will I be able to find a job, will I lose the recognition by my colleagues, will I lose the opportunity to publish in high impact papers? It is my strong belief that there are rewarding opportunities on either side and that one can only be successful if driven by confidence, competence and own interests, and not by the external pressure which is felt. At the same time, the effects of the existing bifurcation could certainly be reduced if young (and old) scientists develop visible activities on the other side, including the rewarding feeling to be able to succeed in areas which go beyond the personal comfort zone. The modern term would be a T-shaped scientist, who works with great confidence on the own disciplinary strength, yet is open to interdisciplinary collaborations in fields which extend far into other disciplines and communities.

MS1.003
Time- and atomic-resolution study of phase-transition and energy-storage pathway in antiferroelectric $PbZrO_3$

X. Wei[1], C. Jia[1], K. Roleder[2], R. E. Dunin-Borkowski[1], J. Mayer[1]

[1]Research Center Jülich, Ernst Ruska-Centre for Microscopy and Spectroscopy with Electrons, Jülich, Germany
[2]University of Silesia, Katowice, Germany

The ultrafast charging/discharging rates, high voltage endurance, superior reliability and broad operating temperature [1,2] of dielectric-based electrostatic capacitors make them promising for the design of electrical power systems such as portable/wearable electronics and collection of fluctuating energy sources. Aiming at further improving the recoverable energy density, *in situ* investigation of structure-property relationship provides an effective strategy for understanding the structural features that are responsible for the energy storage behavior. However, the ultrafast charging and discharging processes, completed in milliseconds or less in traditional parallel-plate capacitors, bring great challenges to capture the nature of the process, i.e., thetransient transition between different phase states [3,4].

Here, we report a time- and atomic-resolution transmission electron microscopy study of the energy storage process in $PbZrO_3$ by using electron beam irradiation as an external stimulus. Through imaging light oxygen and heavy atoms using negative spherical aberration imaging (NCSI) technique, our measurement shows that the unit-cell volume shrinks and then expands during the orthorhombic (AFE_O)-to-monoclinic (FE_M) and FE_M-to-rhombohedral (FE_R) phase transitions. Specifically, quantitative tracking of oxygen octahedral rotation reveals an unconventional FE-ferrodistortive transient phase [5], which is characteristic of Pb antiparallel displacements and a cycloidal polarization order (Figure 1A-C), and bridges the AFEO and FEM phases. In oxygen-and-Pb deficient $PbZrO_3$ [6], our *in situ* atomic-resolution study further reveals point-defect-induced unit-cell-wise energy storage pathway (Figure 1D-I). These findings unveil a new territory for exploring novel ferrodistortive phases in nonpolar dielectric materials and provide a straightforward approach for visualizing energy storage process in defect-engineered dielectric ceramics.

Figure 1: (A-C) Atomic-resolution TEM image of FE ferrodistortive phase recorded along [001] direction, image simulation and cycloidal polarization order in $PbZrO_3$. (D-I) Time- and atomic-resolution TEM images of point-defect-induced unit-cell-wise energy-storage pathway in $PbZrO_3$.

References:
[1] Hao Pan *et al.*, *Science* 365, 578 (2019).
[2] J. Li *et al.*, *Nat. Mater.* 19, 999 (2020).
[3] C. T. Blue, J. C. Hicks, S. E. Park, S. Yoshikawa, L. E. Cross, *Appl. Phys. Lett.* 68, 2942 (1996).
[4] H. He, X. Tan, *Phys. Rev. B* 72, 024102 (2005).
[5] X.-K. Wei, C. L. Jia, H. C. Du, K. Roleder, J. Mayer, R. E. Dunin-Borkowski, *Adv. Mater.* 32, 1907208 (2020).
[6] X.-K. Wei, C. L. Jia, K. Roleder, R. E. Dunin-Borkowski, J. Mayer, *Adv. Funct. Mater.* doi.org/10.1002/adfm.202008609 (2021).

Figure 1

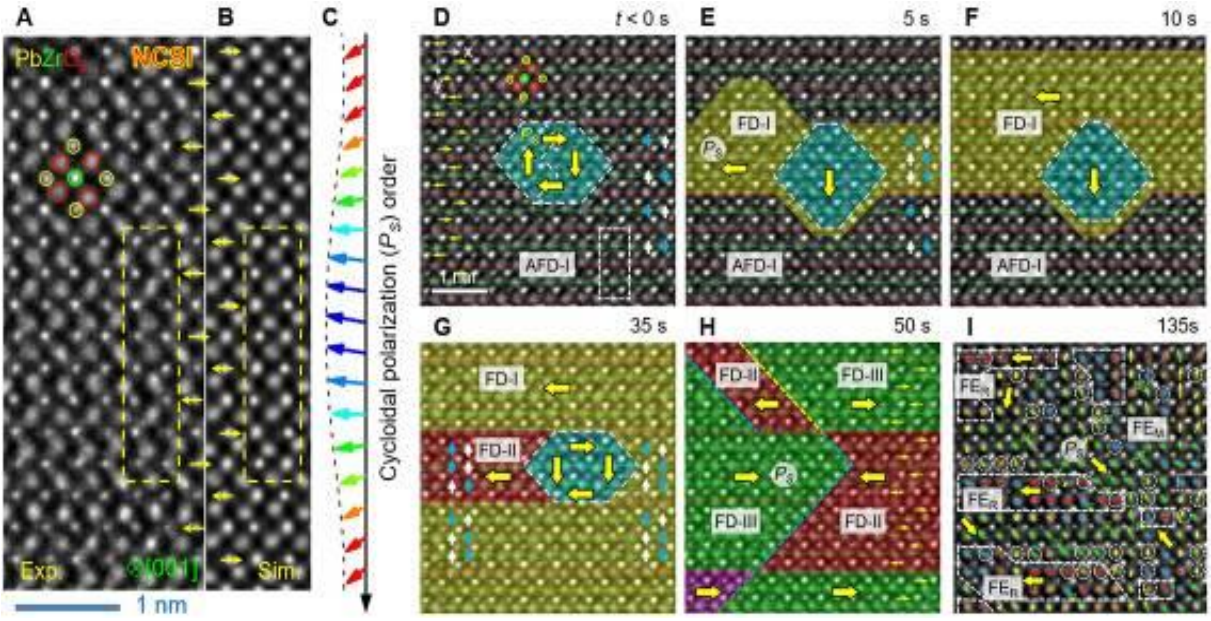

MS1.004
Comprehensive 3D-analysis of the Ga-Pd SCALMS catalyst system using correlative Nano-CT, Electron Tomography and analytical TEM

J. Wirth[1], S. Englisch[1], D. Drobek[1], B. Apeleo Zubiri[1], M. Wu[1], N. Taccardi[2], P. Wasserscheid[2], E. Spiecker[1]

[1]Institute for Micro- and Nanostructure Research (IMN), Materials Science, Erlangen, Germany
[2]Chair of Chemical Reaction Engineering, Erlangen, Germany

In this study, we present a comprehensive and in-depth structural and analytical characterization of the highly-promising Supported Catalytically Active Liquid Metal Solutions (SCALMS) system. This novel catalyst shows excellent performance for alkane dehydrogenation, especially in terms of resistance against coking [1]. SCALMS consists of a porous support containing catalytically active low-melting alloy particles (e.g. Ga-Pd) featuring a complex structure, which are liquid at reaction temperature. High-resolution three-dimensional (3D) characterization at various length scales is required to reveal the complex pore and droplet morphology and the location of the catalytically active sites on the droplets.

X-ray nanotomography (Nano-CT) enables non-destructive 3D materials research at multiple length scales. The Zeiss Xradia 810 Ultra at CENEM uses Fresnel optics to achieve a spatial resolution of down to (50 nm)³ and can be equipped with a Zernike phase ring that provides phase contrast in addition to the standard absorption contrast based on the Lambert-Beer law. The latter can be used to image materials containing regions of completely different densities (i.e., materials containing elements with highly different atomic numbers). In contrast, the former can be used to study materials with weak absorption (low Z) and similar density (similar Z). Its high resolution and flexible imaging modes (HRES Nano-CT with a pixel size of 16 nm and a field of view (FOV) of 16 µm; LFOV Nano-CT with a pixel size of 64 nm and a FOV of 65 µm) render Nano-CT ideal for correlative 3D studies on the micron-scale of functional materials in combination with scanning electron microscopy (SEM) and transmission electron microscopy (TEM) techniques [2,3].

We developed a correlative workflow by combining lab Nano-CT, electron tomography (ET), TEM, and energy-dispersive X-ray spectroscopy (EDXS) optimized to characterize the complex and hierarchical structure of this highly-promising catalyst material. Nano-CT enables a non-destructive 3D characterization of the SCALMS system and further a reliable acquisition of quantitative measures regarding droplet/particle size, pore size of the support material, as well as the exact position and distribution of particles inside the 3D volume (cf. Figure 1). ET and complementary STEM-EDXS and energy-filtered selected area electron diffraction analysis after site-specific focused ion beam (FIB) preparation allow for the investigation of single droplets regarding their chemical composition and crystal structure (cf. Figure 2). To complete the picture, SEM imaging reveals larger Ga-rich droplets on the surface of the porous silica support, and SEM-EDXS shows differences in chemical composition between the droplets on the surface compared to the droplets inside the 3D volume.

This comprehensive microscopic study considerably improves the understanding of this novel catalyst class and further helps to unravel and understand the underlying mechanisms and structural peculiarities leading to the reported superior catalytic performance.

[1] Taccardi et al., Nat. Chem. 2017, 9, 862-867.
[2] Apeleo Zubiri et al., Adv Mater Interfaces 2020, 8, 2001154
[3] Wirth et al., Microscopy and Microanalysis 2019, 25, 422-423
[4] We gratefully acknowledge financial support by the DFG within the frameworks of the GRK1896, the DFG project SP648/8 and the Collaborative Research Centre 1452.

Figure 1

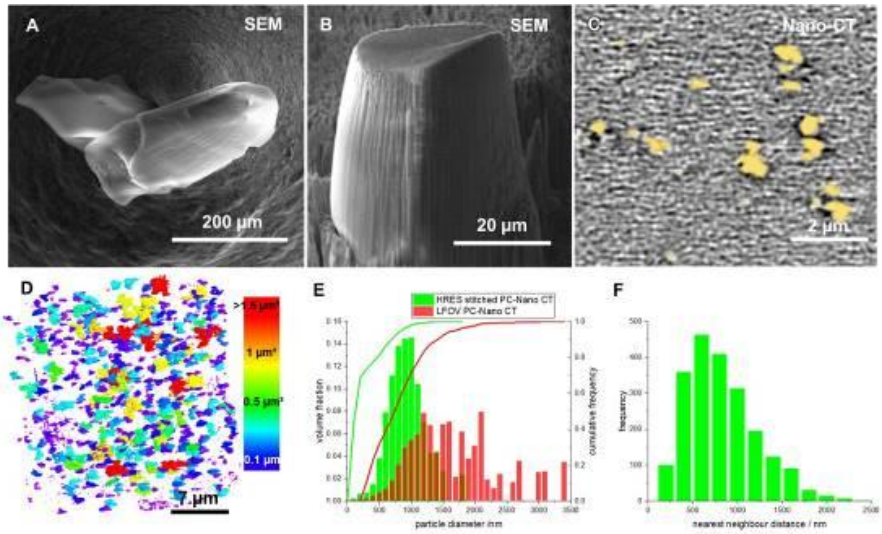

Figure 1. Evaluation of the 3D distribution of Ga-Pd droplets in a HRES Nano-CT reconstruction of a SCALMS sample. (a) Exemplary primary particles of the SCALMS system on a tomography tip. (b) FIB-prepared pillar suitable for Nano-CT imaging. (c)Virtual slice through the reconstructed stitched-HRES 3D volume. In the stitching approach several overlapping FOVs are processed into a combined tilt series and corresponding 3D reconstruction. The yellow areas indicate the segmented Ga-Pd droplets inside the porous glass network. (d) 3D rendering of the segmented stitched-HRES volume with the color bar indicating the size of the Ga-Pd droplets. (e) Particle size distribution of the Ga-Pd droplets (green: stitched-HRES Nano-CT, red: LFOV Nano-CT) indicating a larger mean diameter determined in LFOV mode. This can be attributed to the lower resolution and stronger phase contrast artifacts, and therefore renders the stitched-HRES analysis more reliable. The corresponding cumulative frequency curve describes the cumulative number of particles for each corresponding particle diameter. (f) Nearest neighbour (NN) analysis for each Ga-Pd structure with center of mass as center indicating an arbitrary distribution of the droplets inside the glass network.

Figure 2

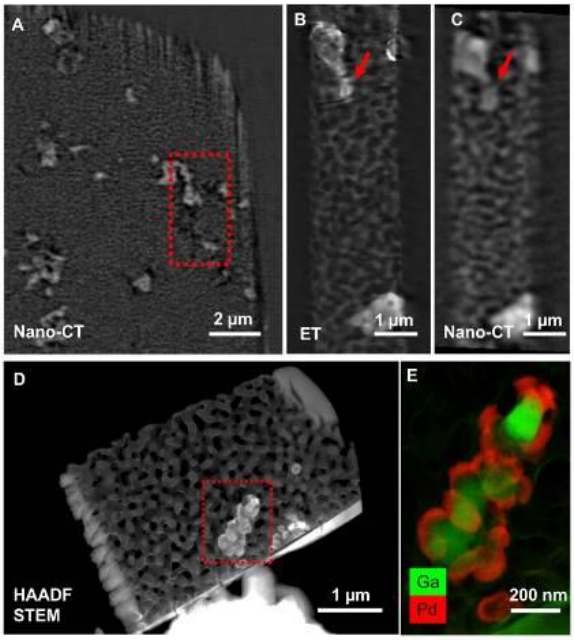

Figure 2. Correlative nanotomography and analytical TEM. (a) Virtual slice through a HRES Nano-CT reconstruction of a second FIB-prepared pillar with a diameter of ~12 µm revealing the structure of the porous glass network and the distributed Ga-Pd droplets. Matching virtual slices through (b) the ET reconstruction and (c) the HRES Nano-CT reconstruction of a smaller pillar with a diameter of ~2 µm site-specifically prepared out of the bigger pillar via FIB milling, which is indicated with a red rectangle in Fig. 2a. (d) FIB-prepared TEM lamella (thickness ~200 nm) enabling (e) STEM-EDXS analysis revealing the local elemental distribution of an exemplary Ga-Pd droplet inside the glass network. The droplets mostly exhibit a bimetallic structure with Pd-rich and Ga-rich parts occurring in direct contact with each other.

MS1.005
In situ TEM investigation of lithiation and delithiation inside graphene sheets

Y. Li[1], F. Börrnert[1], S. Fecher[2], M. Ghorbani-Asl[3], Z. Li[1], J. Biskupek[1], S. Yang[2], M. Kühne[2], A. V. Krasheninnikov[3] J. Smet[2], U. Kaiser[1]

[1]University of Ulm, Electron Microscopy Group of Materials Science, Ulm, Germany
[2]Max Planck Institute for Solid State Research, Stuttgart, Germany
[3]Helmholtz-Zentrum Dresden-Rossendorf e.V. (HZDR), Institute of Ion Beam Physics and Materials Research, Dresden, Germany

Lithium-ion batteries (LIBs) gained commercial success in recent years due to their high energy and power density. The use of graphite with high capacity as active material for anode is one of the major reasons. However, direct observing and understanding the dynamics of Li inside carbon host materials during cycling are still challenging. Superdense ordering of lithium as well as partial lithiation and delithiation process in an electrochemical cell architecture including bilayer graphene and polymer electrolyte placed on the Si_3N_4 membrane of a custom-made TEM sample carrier chip was observed by in-situ spherical and chromatic aberration-corrected low-voltage high-resolution transmission electron microscopy [1]. Here we concentrate on understanding the nucleation and step-by-step growth processes of Li crystals during lithiation and the melting process of Li during delithiation from low-mag overview TEM imaging with a large field of view, combined with C_C/C_S-corrected HRTEM. Figure 1 displays a series of TEM images of the first-cycle in the lithiation process between two graphene sheets. We see nucleation of Li (Figure 1b), growth of triangular Li crystal plates with random orientation (Figure 1c), rotation of the active Li crystal plates (Figure 1d and 1e marked by the arrows), and the merge of Li crystals (Figure 1f). A constant growth rate of Li crystals was measured according to the area of Li plates in each image, which may result from the linear Li diffusion reported by Kühne [2]. Figure 2 shows a delithiation process with an even larger field of view. Different from the lithiation process, here Li melts and we observe the correcponding amorphous/liquid characteristic instead of regular shaped crystals and facets observed during delithiation. From C_C/C_S-corrected HRTEM more details of the (de)lithiation process were discovered. Cubic close-packed (fcc) Li is now confirmed due to the loss of the first order reflection in the Fourier transform. The nucleation of Li was observed to start at C vacancy sites in graphene, which is energy favourable confirmed by our DFT calculations further. After a certain time of growth, the small Li crystals merge with rotation into the same orientation while the large Li crystals merge with formation of a grain boundary. Li grows vertically further after the bilayer graphene is completely filled, expanding the distance between graphene sheets. During delithiation, some additional impurity atoms were observed, which gather at the edge of Li, where a number of Li vacancies exist. As Si is always present in exfoliated graphene, it is most probable that these impurity atoms are Si. However, atoms such as N, O, F and S originating from the electrolyte cannot be fully excluded so far, as they can form strong ionic bond with Li. Our work gives a detailed insight of the existence and diffusion of Li inside graphene sheets, which may have relevance also in anodes of LIBs.

This work contributes to the research performed at CELEST (Center for Electrochemical Energy Storage Ulm-Karlsruhe) and was funded by the German Research Foundation (DFG) under Project ID 390874152 (POLiS Cluster of Excellence). We acknowledge financial support from the Baden-Württemberg Stiftung gGmbH (project CT 5) and from the Ministry of Science, Research and the Arts (MWK) of the federal state of Baden-Württemberg in the frame of the SALVE project.

Reference:
[1] Nature 564, 234-239 (2018)
[2] Nat. Nanotechnol. 12, 895–900 (2017)

Figure 1

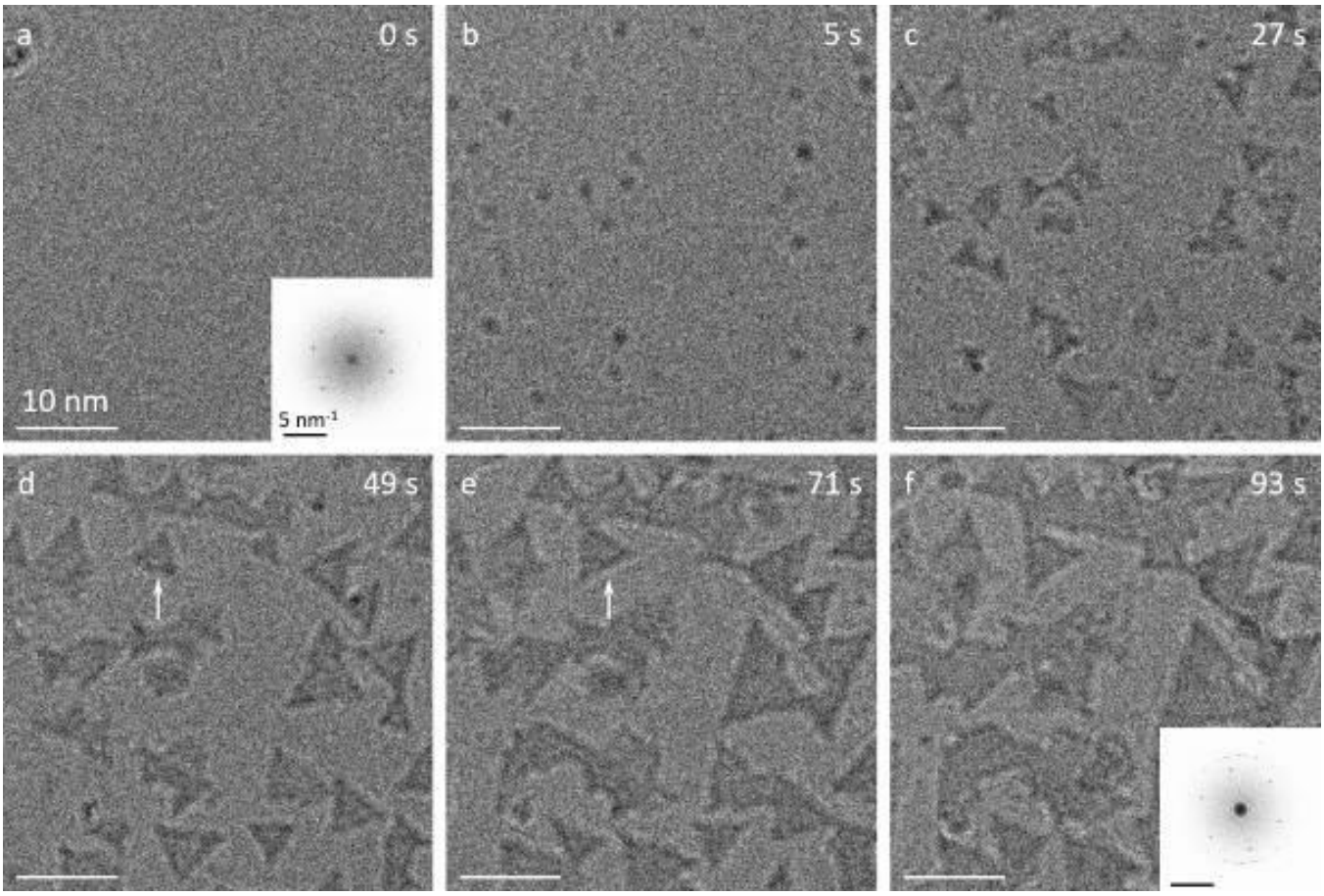

Figure 2

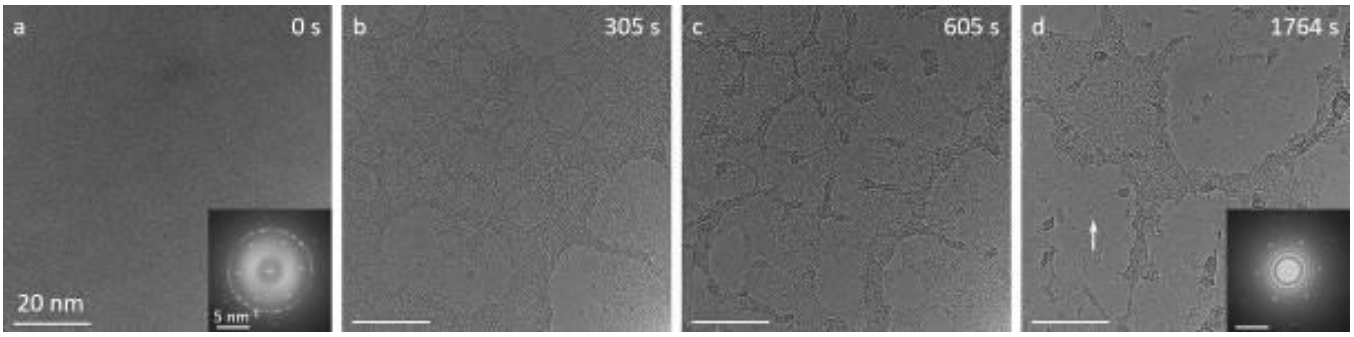

MS1.007
Atomic-scale microstructure of hybrid metal halide perovskite

M. Uller Rothmann[1], J. Kim[2,3], J. Borchert[1], K. Lohmann[1], C. O'Leary[4], A. Sheader[4], L. Clark[4], H. Snaith[1]
M. Johnston[1], L. Herz[1], P. D. Nellist[4]

[1]University of Oxford, Department of Physics, Oxford, United Kingdom
[2]Diamond Light Source, ePSIC, Didcot, United Kingdom
[3]Rosalind Franklin Institute, Didcot, United Kingdom
[4]University of Oxford, Department of Materials, Oxford, United Kingdom

Studying the crystallographic properties of photoactive hybrid organic-inorganic perovskites by transmission electron microscopy (TEM) has proved particularly challenging due to their electron beam sensitivity [1]. In particular, the very close structural relationship between a number of crystallographic orientations of the pristine perovskite and lead iodide has resulted in severe ambiguity in the interpretation of EM-derived information, severely impeding the advance of atomic resolution understanding of the materials.

Here, we successfully image the archetypal CH(NH2)2PbI3 (FAPbI3) and CH3NH3PbI3 (MAPbI3) hybrid perovskites in their thin-film form with atomic resolution using a carefully developed protocol of low-dose low-angle annular dark-field (LAADF) imaging in STEM [2]. Our images enable a wide range previously undescribed phenomena to be observed, including a remarkably highly ordered atomic arrangement of sharp grain boundaries and coherent perovskite/PbI2 interfaces, with a striking absence of long-range disorder in the crystal (Figure 1A). These findings explain why inter-grain interfaces are not necessarily detrimental to perovskite solar cell performance, in contrast to what is commonly observed for other polycrystalline semiconductors. Additionally, we observe aligned point defects and dislocations that we identify to be climb-dissociated (Figure 1B), and confirm the room-temperature phase of CH(NH2)2PbI3 to be cubic. We further demonstrate that degradation of the perovskite under electron irradiation leads to an initial loss of CH(NH2)2+ ions, leaving behind a partially unoccupied, but structurally intact, perovskite lattice, explaining the unusual regenerative properties of partly degraded perovskite films. Our findings thus provide a significant shift in our atomic-level understanding of this technologically important class of lead-halide perovskites.

[1] Adv. Mater. 2018, 30, 1800629
[2] Science 370, eabb5940 (2020)
[3] We thank the David Cockayne Centre for Electron Microscopy, University of Oxford, for access and support in the use of the JEO ARM200F instrument (proposal number EP/K040375/1) and additional instrument provision from the Henry Royce Institute (grant reference EP/R010145/1). We also thank Diamond Light Source for access and support in use of the electron Physical Science Imaging Centre (E02, MG21734) that contributed to the results presented here. L.M.H. and M.B.J. thank the Humboldt Foundation for research awards. This work was supported by the UK Engineering and Physical Sciences Research Council (EPSRC) through grant EP/P033229/1 and through the EPSRC CDT for New and Sustainable Photovoltaics.

Figure 1: A: Grain boundaries in a FAPbI3 thin film viewed using LAADF STEM. The sharpness of the grain boundaries are apparent and the dislocations forming the low-angle boundary in the top right can be clearly seen. Scale bar 10 nm. B: Isolated dislocations (highlighted in green) forming a low-angle grain boundary can be seen to have dissociated in the climb direction. Scale bar 10 nm.

Figure 1

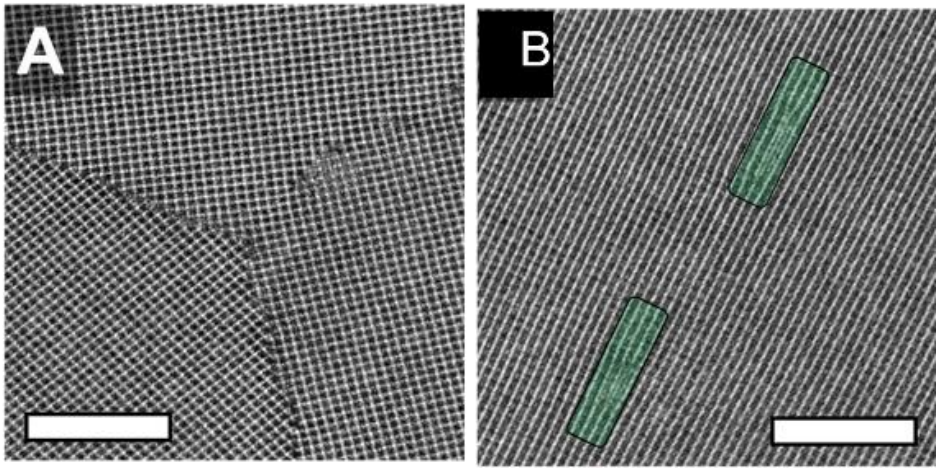

MS1.P001
Nanoscale analysis of battery materials using correlative ion & electron beam techniques

L. Cressa[1], Q. H. Hoang[1], T. Wirtz[1], S. Eswara[1]

[1]Luxembourg Institute of Science and Technology, MRT, Esch-sur-Alzette, Luxembourg

Battery research is gaining importance in a world where advanced energy storage is a major milestone to overcome future energy challenges. The complexity of novel composite materials often comes with major analytical challenges.

Here, we present an example of the correlative analysis of $LiCoO_2$-$LiNiCoAlO_2$ (LCO-NCA), a blend cathode being considered for future application in solid-state Li batteries. Its composition includes four major components being NCA, LCO, carbon black and pores. The pores are filled with Si based rubber for analysis purposes. The analysis is performed on a Thermo Fisher SCIOS DualBeam platform (focused ion beam – scanning electron microscopy) which is equipped with an in-house developed secondary ion mass spectrometry (SIMS) add-on system. Our SIMS enables the simultaneous detection and imaging of four atomic masses with highest sensitivity, allowing the user to differentiate components by chemical imaging [1].

Figure1b shows an SEM image of the LCO-NCA sample, which has been recorded under a primary energy of 10 keV and a current of 0.8 nA. Figure2a shows a secondary electron image taken by $^{69}Ga^+$ irradiation. From the same ROI Figure2b was obtained, corresponding to the four images of $^{7}Li^+$, $^{12}C^+$, $^{27}Al^+$ and $^{58}Ni^+$, which were simultaneously recorded by the SIMS add-on. The SIMS measurement was performed under a $^{69}Ga^+$ primary beam with an energy of 30 keV and a current of 50 pA over a field of view of 31.9 μm^2 and a dwell time of 1.3 ms per pixel. The sample was biased to +500 V, so that the primary ion impact energy was 29.5 keV. Figure2c shows an overlay of the SIMS data on the four detected elements. Carbon black takes the role of conductive additive and is being imaged by the $^{12}C^+$ signal. The distribution of $^{58}Ni^+$ reveals the presence of NCA-particles. The $^{27}Al^+$ signal is similarly distributed than the $^{58}Ni^+$ signal but additionally it shows a region with anomalously intense signal. Particles with significant $^{7}Li^+$ signal and no Al nor Ni can be attributed to LCO-particles.

The analysis could go beyond cathodes and cover of all parts constituting a full battery. The possibility in SIMS to detect all elements, including the light elements (e.g. H, Li, B) and its ability to distinguish isotopes (Figure1a) makes SIMS based correlative microscopy a powerful tool to analyse anodes, solid-state electrolytes, cathodes and all interfaces in between. These analyses can provide unique insights of the complex sample class of energy materials and provide powerful hints for the interpretations of electrochemical data and the development of new battery materials.

Acknowledgement: We thank Jochen Joos (KIT) for the sample and Jonas Fell (Uni Saarland) for fruitful discussions. This work was partially funded by FNR Luxembourg through the M-ERA.NET project INTERBATT.

Figure 1: a) SIMS mass spectrum showing both isotopes of Li with their matching SIMS-images, a SE image obtained by Ga^+ irradiation shows the same ROI; b) SEM-image of an NCA-LCO sample.

Figure 2: a) SE image obtained under Ga^+ irradiation; b) SIMS images detecting simultaneously $^{7}Li^+$, $^{12}C^+$, $^{27}Al^+$ and $^{58}Ni^+$; c) Composite image of the four elements, revealing the identity of different components by their chemical identity.

[1] Wirtz, T. et al. (2015): High-resolution high-sensitivity elemental imaging by secondary ion mass spectrometry: from traditional 2D and 3D imaging to correlative microscopy. In *Nanotechnology* 26 (43), p. 434001. DOI: 10.1088/0957-4484/26/43/434001

Figure 1

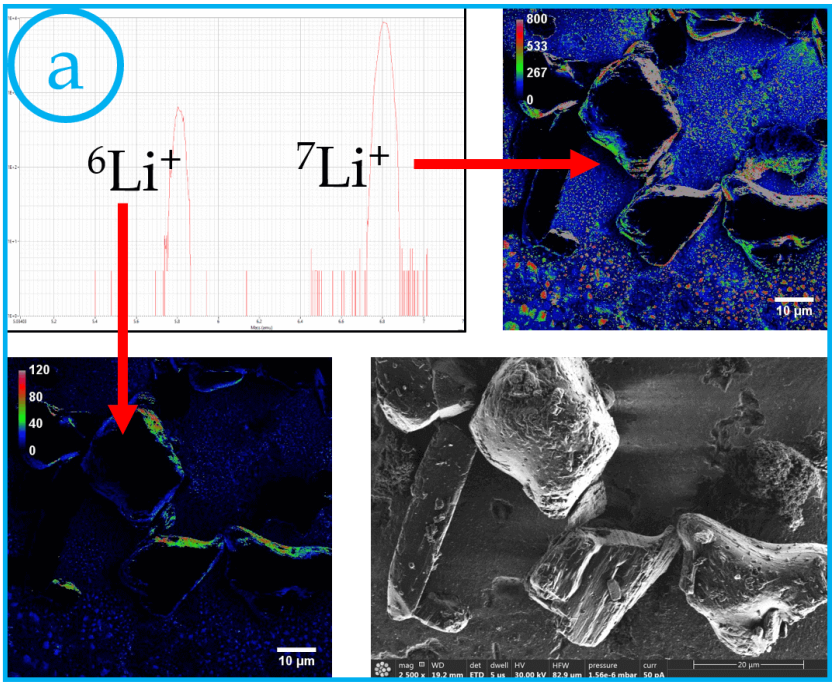

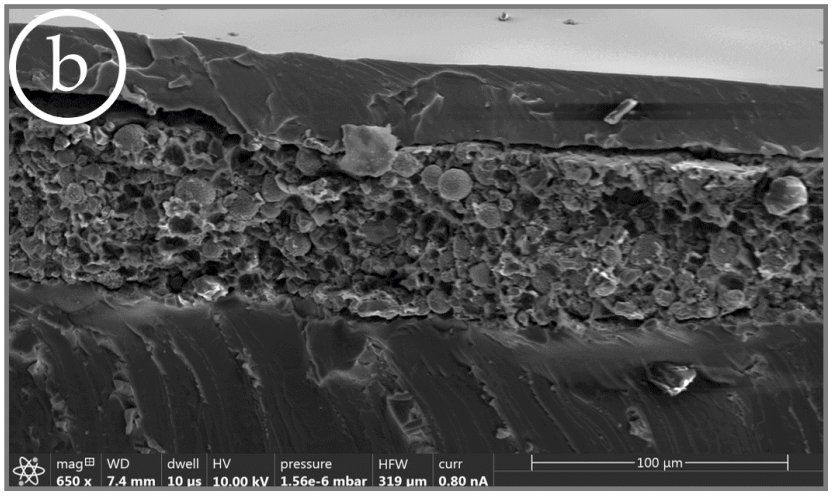

Figure 2

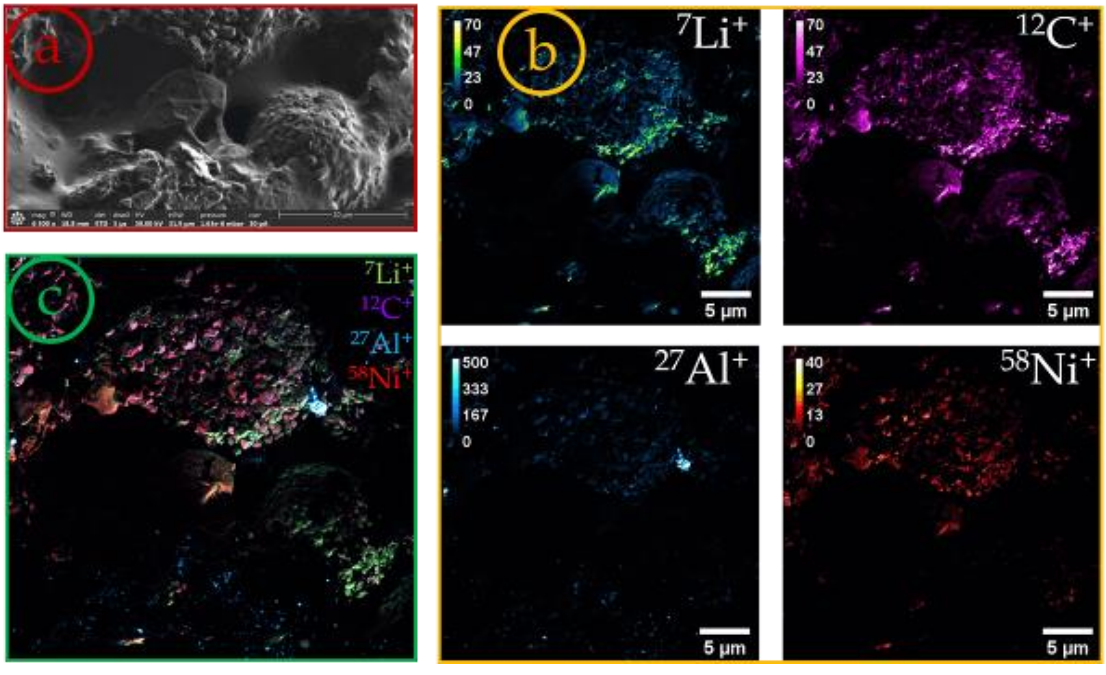

MS1.P002
Investigation of Al – SiN_x interactions for firing-through metallisation of passivating contacts solar cells

S. Libraro[1], M. Lehmann[1], J. J. Díaz León[2], C. Allebé[2], A. Descoeudres[2], S. Nicolay[2], C. Ballif[1,2], A. Ingenito[1,2]
F. J. Haug[1], A. Hessler-Wyser[1]

[1]Swiss Federal Institute of Technology Lausanne (EPFL), Photovoltaics and Thin-Film Electronics Laboratory (PV-lab), Neuchâtel, Switzerland
[2]CSEM, PV-center, Neuchâtel, Switzerland

Recombination at metal/semiconductor interfaces represents the main efficiency limitation in industrial c-Si solar cells[1]. The problem can be overcome by using full area passivating contacts (PCs), a concept based on a thin layer to passivate the Si surface and one or more doped layers in contact with the metal for carrier extraction. Usually, a hydrogenation step is used to improve the passivation, with a common approach being to release hydrogen from a silicon-nitride layer (SiN_x). The challenge for this technology is now its integration into industrial metallization schemes that are based on screen printing and firing through of a metal paste. Unfortunately, this method can strongly degrade the PCs due to deep metal penetration, which causes a passivation loss. While promising results have been shown with Ag pastes[2], no studies report successful metallization of PCs with Al, which is however of interest to reduce Ag consumption.

To contact PC solar cells with Al pastes, the reactions taking place between Al, SiN_x and PCs during firing need to be studied; in particular, the Al-SiN_x interactions play a crucial role in obtaining junctions with high passivation quality and low contact resistance.

The sample fabrication process is shown in Figure 1, with the PC formed by a thin oxide and a SiC_x(p) layer. Two types of SiN_x are used, one richer in Si ("Si-rich") and one closer to a stoichiometric composition ("N-rich"). Metallization is performed either via screen printing of a commercially available Al paste or by evaporating Al for more fundamental studies. Multiscale electron microscopy (SEM, EDX, STEM, TEM) is performed before and after firing for in-depth characterization of contact microstructure and contacting paths.

Figure 2 illustrates the interactions taking place during firing in a Si-rich nitride sample. SiN_x reacts with Al only partially, resulting in areas with different contrasts when observed after Al was etched (A). In the non-reacted area, SEM-EDX maps show that Al remains above the SiN_x, whereas, in the reacted area, Al has diffused into it. Al may also penetrate into the PC below the SiN_x, creating both large-scale (~µm) spikes (B) or smaller ones (< 200 nm), that can then form an Al layer below the SiN_x (C). In both cases, an electrical contact is established, but this also damages the PC. For samples with N-rich nitride, Al remains above the SiN_x, leaving the passivation unaltered, but the metal is confined above the insulating nitride layer, resulting in a bad electrical contact.

In this work, we will clarify some aspects of the interactions between Al and SiN_x. In particular, we demonstrate that the SiN_x properties are crucial in determining how reactions with the metal take place and that tuning them can provide ways of controlling the contacting mechanisms, enabling both good electrical contact and passivation.

References:
[1] Min *et al. IEEE J. Photovoltaics* 7,1541–1550 (2017)
[2] Chen *et al. Sol. Energy Mater. Sol. Cells* 206,1–8 (2020)

Figure 1: Sample preparation process (I–VI) and STEM–ADF micrograph of the finished structure (VII).

Figure 2: (A) SEM Top-view of the sample surface after Al etching, showing Al-SiN_x reacted areas (bright) and unreacted ones (dark). Cross-sectional SEM images with corresponding EDX mapping are shown for both areas. (B) Cross-sectional SEM image of the wafer/metal interface after firing. (C) STEM-BF micrograph of the interface resulting.from smaller scale interactions

Figure

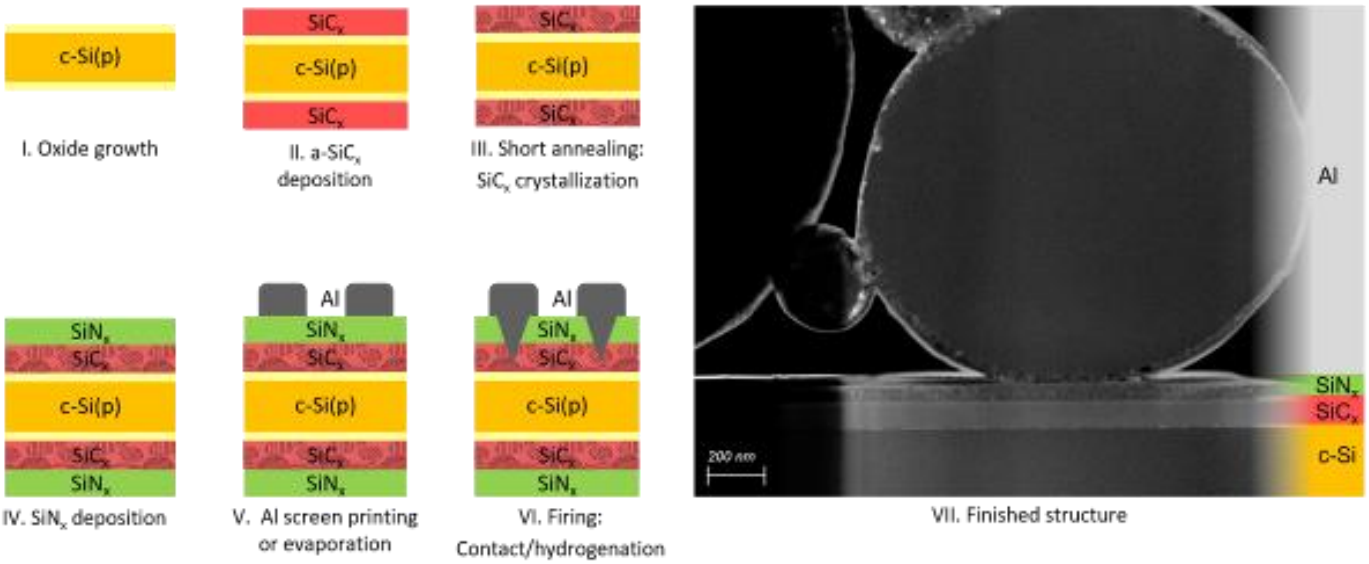

Figure **2**

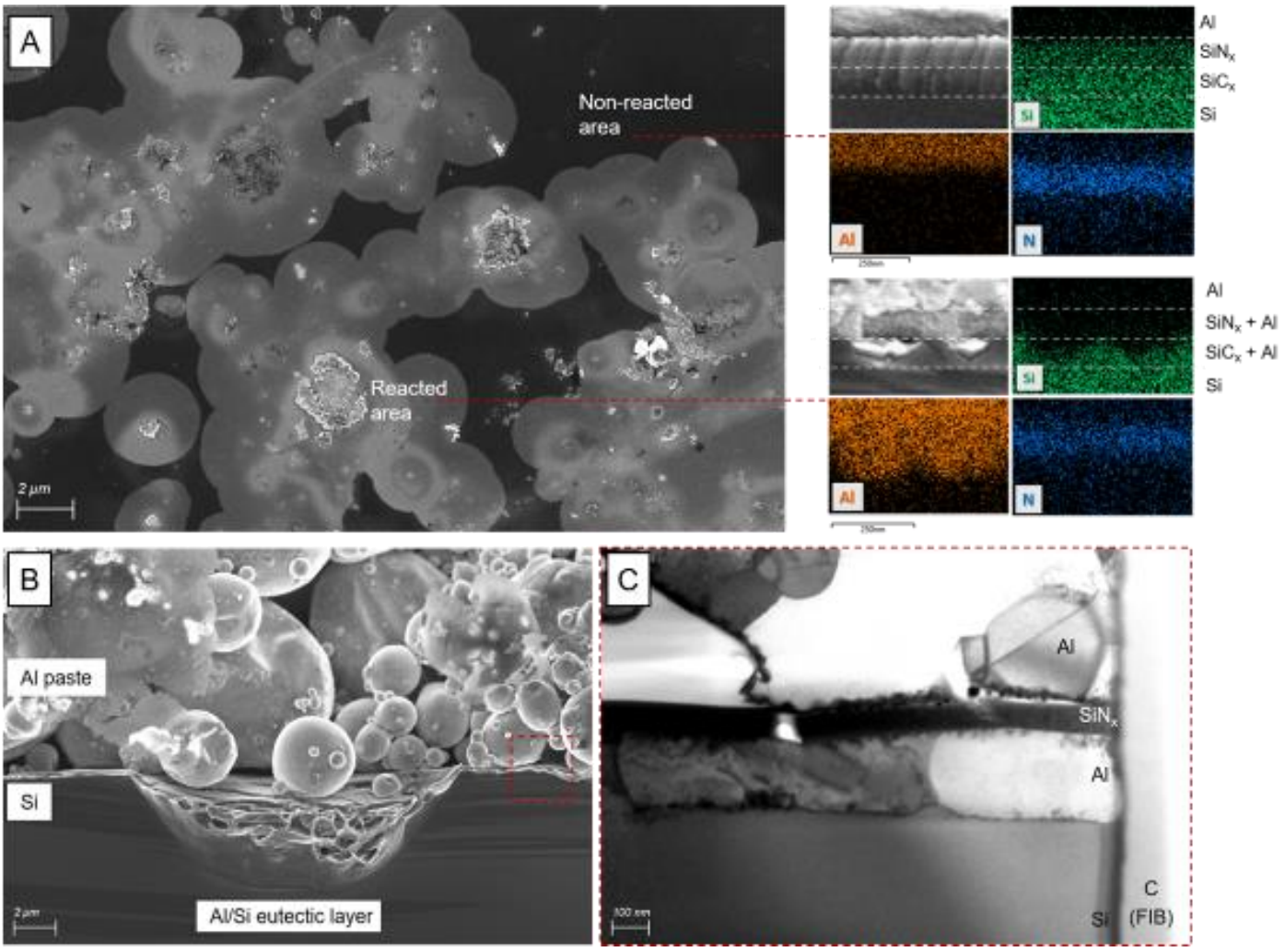

MS1.P003
Decoupling reaction from analysis by electrochemical *quasi in situ* TEM – the acidic and alkaline oxygen evolution reactions

T. Götsch[1], E. Stotz[1], R. Schlögl[1,2], T. Lunkenbein[1]

[1]Fritz Haber Institute of the Max Planck Society, Inorganic Chemistry, Berlin, Germany
[2]Max Planck Institute for Chemical Energy Conversion, Department of Heterogeneous Reactions, Mülheim an der Ruhr, Germany

Figure 1: A) A variety of species resulting from electron beam-water interactions. B) Using tweezers to contact the TEM grid as working electrode and C) resulting cyclic voltammograms (CVs) showing high background current. D) Identical location imaging of Co3O4 particles after 30 cycles of the CVs in C) using the tweezers. E) A dedicated cell for electrochemical measurements.

Renewable energy sources bring along the need for storage of excess energy to compensate for their intermittent power supply. Here, electrochemical pathways by, e.g., water splitting and subsequent hydrogen storage are promising technologies. However, the anodic oxygen evolution reaction (OER) is known to exhibit very sluggish kinetics. Thus, an in-depth understanding about the processes involved in this reaction is required to make water splitting more efficient, requiring investigations at the nanoscale; however, *in situ* liquid phase TEM suffers from drawbacks such as the strong interaction between beam and liquid water, leading to the formation of many radicals and oxidizing as well as reducing agents, as depicted in Figure 1A.[1] These can completely change the observed chemistry in unpredictable ways.

A good compromise between achieving analytics at the nanoscale and avoiding beam effects during the electrochemical reaction is the use of *quasi in situ* TEM, which has already been shown to be a viable technique for gas phase catalysis.[2] Here, the reaction is performed outside the TEM, and the sample is subsequently transferred to the microscope under inert conditions, where the analysis can be performed in vacuum, thereby minimizing the beam damage and improving resolution and signal-to-noise ratios. With identical location imaging, the same sample regions can be visualized before the reaction and after different steps by imaging and spectroscopy. This way, changes to morphology, structure and electronic states can be determined without the danger of altering the chemistry with the beam. Phases that are only stable at the electrified catalyst/water interface will be missed with this approach but irreversible transformations can be observed that could, for instance, lead to deactivation.

In this work, platinum- and cobalt-based electrocatalysts are used in the OER under acidic and alkaline conditions with H_2SO_4 and NaOH electrolytes (100 mM each). Microscopy is performed using a double-corrected JEOL JEM-ARM200F, equipped with a cold FEG and a GIF Quantum imaging filter. We compare an approach of simply submerging a TEM grid in the electrolyte with gold-plated tweezers (Figure 1B) to a more sophisticated, dedicated miniaturized electrochemical flow cell in three-electrode configuration (Figure 1E).

The cell was designed to allow reproducible cell geometry and potentials, while simultaneously minimize parasitic current contributions from other elements. This is in contrast to the tweezer approach, where strong signals resulting from the tweezers can be observed overlapping the electrocatalyst waves (see Figure 1C for cyclic voltammetry of Co_3O_4 particles on an UltrAuFoil TEM Grid). But already with this approach, morphological and structural changes can be observed in the bright-field images in Figure 1D as the particles become more rounded and additional nanoparticles, most likely reduced cobalt oxide species, are formed on the surface (marked by arrows).

[1] Wang et al. *Chem. Mater.* 2018, *30,* 7727
[2] Masliuk et al. *Ultramicroscopy* 2018, *195,* 121

Figure 1

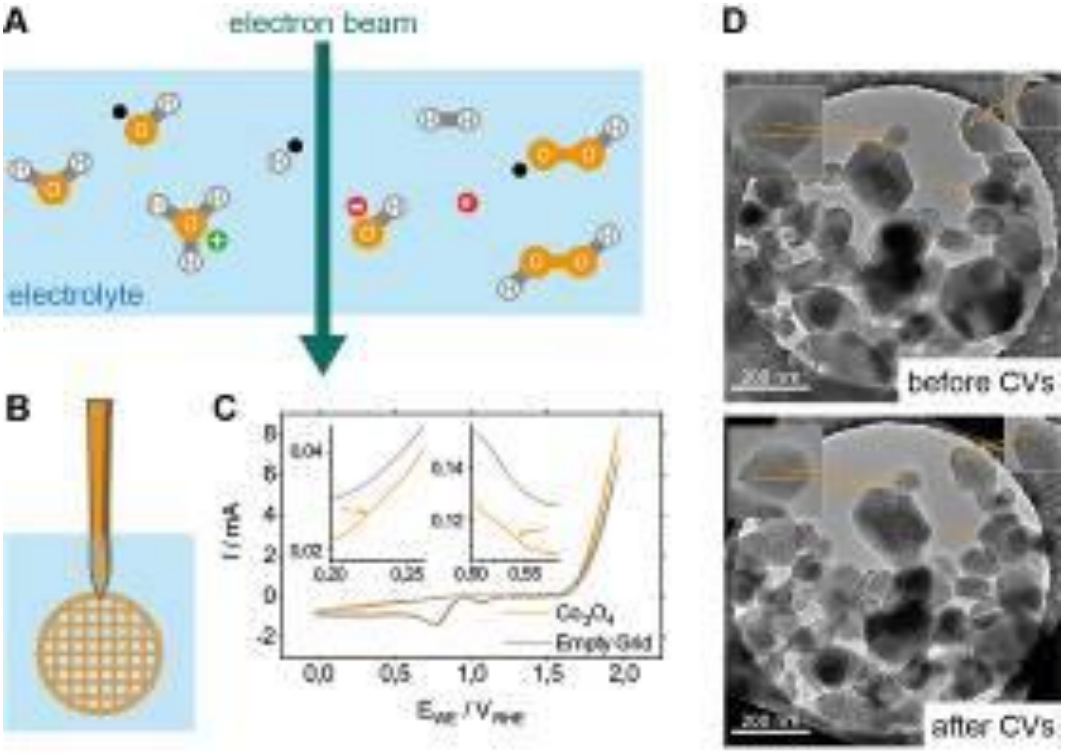
A
electron beam
electrolyte
B
C
I / mA
E_{WE} / V_{RHE}
Co_3O_4
Empty Grid
D
before CVs
after CVs

E

MS1.P004
Measuring dynamic structural changes of nanoparticles at the atomic scale using scanning transmission electron microscopy

A. De Wael[1,2], A. De Backer[1,2], L. Jones[3,4], A. Varambhia[5], P. D. Nellist[6], S. Van Aert[1,2]

[1]EMAT, University of Antwerp, Antwerp, Belgium
[2]NANOlab Center of Excellence, Antwerp, Belgium
[3]Advanced Microscopy Laboratory, CRANN, Dublin, Ireland
[4]School of Physics, Trinity College Dublin, Dublin, Ireland
[5]Johnson Matthey Technology Centre, Sonning Common, Reading, United Kingdom
[6]Department of Materials, University of Oxford, Oxford, United Kingdom

Quantitative analysis of any single atomic resolution electron microscopy image lacks insight in the structural dynamics. The atomic structure of nanomaterials can change over time, e.g. via surface diffusion, and so multiple observations are needed. Here, we propose an approach to reliably count the number of atoms in the atomic columns of a monatomic nanostructure in each frame of an ADF STEM time series using a hidden Markov model (HMM) [1-3].

A HMM consists of a "hidden" Markov chain state sequence (top row Figure1) and an observed sequence (bottom row Figure 1). Here, the hidden states are the number of atoms in each atomic column at each time, observed only via the ADF STEM images. Scattering cross sections (SCSs) result from the underlying number of atoms following a so-called emission probability. These SCSs - estimated from the ADF STEM images - measure the total intensity scattered towards the annular detector for each atomic column [4,5], and are used for atom-counting in monatomic nanomaterials [6-12]. Furthermore, the changing number of atoms through time is described by a transition probability. We find that the HMM far exceeds the atom-counting reliability of the existing methods [6-12], even at low electron dose [1,2].

We measure dynamic structural changes of an experimental ADF STEM time series of a catalyst Pt nanoparticle (Figure 2). This reveals a gradual loss of the facetted morphology due to electron beam-induced surface diffusion. We even determine an experimental value for the average cross section for surface diffusion, $\sigma=3.3 \times 10^{-6}$ Å^2, from the HMM analysis. This cross section for surface diffusion includes contributions of different migration mechanisms and from different types of surfaces. It can help to unravel dominant mechanisms and surfaces in the diffusion process and to gain new insights in surface related phenomena such as catalysis and nanoparticle growth.

In conclusion, the HMM for atom-counting is promising for a reliable quantification of dynamic structural changes by adatom dynamics, surface diffusion, beam effects, or during *in situ* experiments, and is implemented in the open source StatSTEM software [9].

[1] De wael et al., PRL 124 (2020), 106105
[2] De wael et al., UM 219 (2020), 113131
[3] Rabiner, Proc. IEEE 77 (1989), 257
[4] Van Aert et al., UM 109 (2009), 1236
[5] E et al., UM 133 (2013), 109
[6] Van Aert et al., Nature 470 (2011), 374
[7] De Backer et al., UM 134 (2013), 23
[8] Van Aert et al., PRB 87 (2013), 064107
[9] De Backer et al., UM 171 (2016), 104
[10] LeBeau et al., Nano Lett. 10 (2010), 4405
[11] Jones et al., Nano Lett. 14 (2014), 6336
[12] De wael et al., UM 177 (2017), 69
[13] This project received funding from the ERC under the European Union's Horizon 2020 research and innovation programme (770887 and 823717 ESTEEM3). The authors acknowledge financial support from the FWO through grants to ADw and ADB and projects G.0502.18N and EOS 30489208. LJ acknowledges SFI and the Royal Society (URF/RI/191637) for support. AV and PDN acknowledge the UK Engineering and Physical Sciences Council (EPSRC) for support (EP/K040375/1 and 1772738). AV also acknowledges Johnson-Matthey for support. We thank B. Theobald and J. Sharman from JMTC Sonning for provision of the Pt sample.

Figure 1: Schematic representation of the HMM for atom-counting.

Figure 2: (a) Experimental ADF STEM time series of a Pt nanoparticle. (b) From the estimated HMM, the hidden state sequence is retrieved.

Figure 1

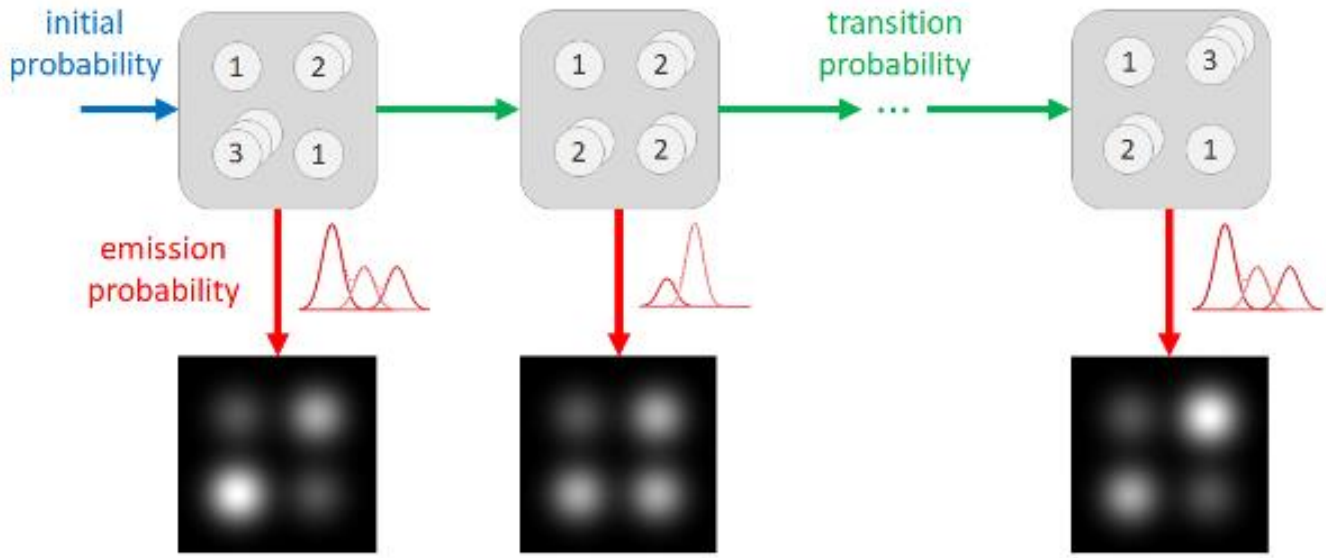

Figure 2

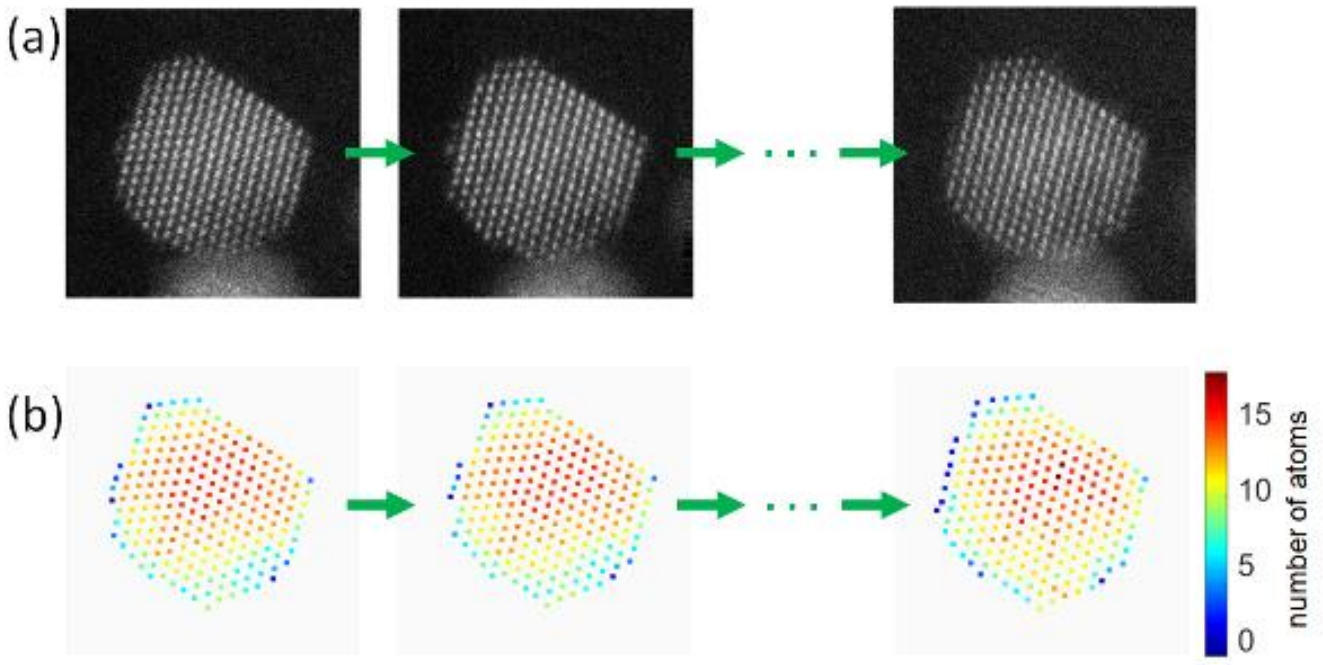

MS1.P005
Ageing phenomena of Lithium Ion Batteries investigated with Mass Spectrometry (MS) and Energy Dispersive X-Ray Spectroscopy (EDS)

G. Wilhelm[1], U. Golla-Schindler[1], G. Cooke[2], T. Bernthaler[1], G. Schneider[1]

[1]Aalen University, Materials Research Institute, Aalen, Germany
[2]Hiden Analytical GmbH, Düsseldorf, Germany

The combination of Secondary Ion Mass Spectrometry (SIMS) with Scanning Electron Microscopy (SEM) and Focused Ion Beam (FIB) technology enables high-resolution spatially resolved surface analysis. A qualitative evaluation method to interpret mass spectra using standard mass spectra of defined chemical compounds has been developed. The detection of light elements (e.g. lithium) provides new insights into ageing effects and mechanism of lithium ion batteries.

The following investigations were performed on a Zeiss Crossbeam 540 with Gemini II column and a Schottky field emission electron gun. The SEM is equipped with an Everhart-Thornley detector (ETD), two INLENS detectors and a X-Max 80 Energy Dispersive X-Ray detector (EDS). The Focused Ion Beam is used in combination with a new HIDEN Secondary Ion Mass Spectrometry (SIMS) detector and a ZEISS Time of Flight – Secondary Ion Mass Spectrometry (ToF-SIMS) detector. The study was performed on a new and a systematically aged (1024 cycles) lithium-ion cell [1,2]. The surface morphology change was visualized by Golla-Schindler et al. [3].

EDS can be used to identify the elemental changes between the cycled anode and the reference anode. The comparison of the mass spectra (Figure 1c, red – reference anode, yellow – cycled anode) reveals that additional elements (Si, Mn, Co and Ni) can be detected for the cycled sample (Figure 1c) and that the elements F, P and Cu are enriched at the cycled anode surface. The typical appearance of the aged SEI can be seen in the SEM image (Figure 1a). The elements with significant spatial distribution, namely C, Si, F, and O, are shown in Figure 1b. Silicon occurs in the round deposits and fluorine is part of a shapeless, superficial structure. The surface is enriched with oxygen. All other elements show a uniform distribution that requires a higher resolution.

Mass spectrometry overcomes the bottleneck of light elements (e.g. lithium, nitrogen). The mass spectrum of the cycled anode (Figure 2e) shows additional peaks which can be explained through additional elements (N, Si, Mn, Co, Ni) or fragmentation processes during measurement. In the SEM image (Figure 2a), the round (1) and fibrous (2) structures of the cyclized anode surface are clearly visible. An important part of the measurement is the spatially resolved elemental distribution of lithium and manganese. Lithium (Figure 2b) is present in all surface structures and manganese (Figure 2c) is enriched in the fibrous structures.

The elemental analysis of the ageing products reveals that cathode elements (e.g. Mn) can be measured at the anode surface. The elements must have been dissolved at the cathode during cycling and give an indication of cathode-dominated ageing.

References:
[1] J. Vazquez-Arenas et al., A rapid estimation and sensitivity analysis of parameters describing the behavior of commercial Li-ion batteries including thermal analysis, Energy Conversion and Management 87 (2014) 472–482.
[2] M. Bauer et al., Aging of Traction Batteries in Vehicle-to-grid Applications II: Light Commercial Vehicles Used for Home Delivery Services. Poster (2015).
[3] U. Golla-Schindler et al., Characterization of degeneration phenomena in lithium-ion batteries by combined microscopic techniques, Micron 113 (2018) 10–19.

Figure 1

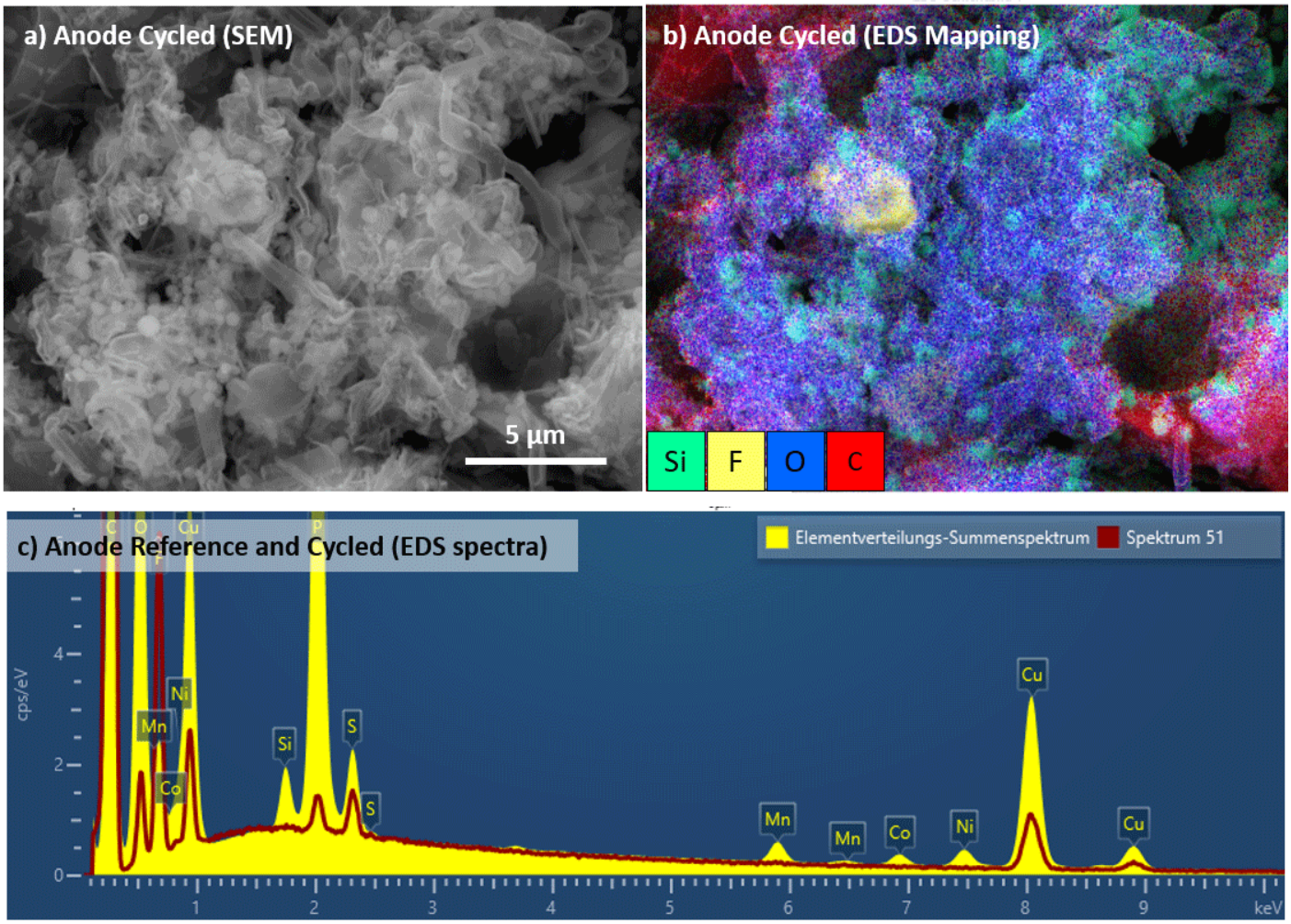

Fig. 1: Surface morphology of cycled anode foil (a); EDS elemental distribution for Si, C, F and O (b); EDS spectra comparison (c) of the reference anode (red) with the cycled anode (yellow);

Figure 2

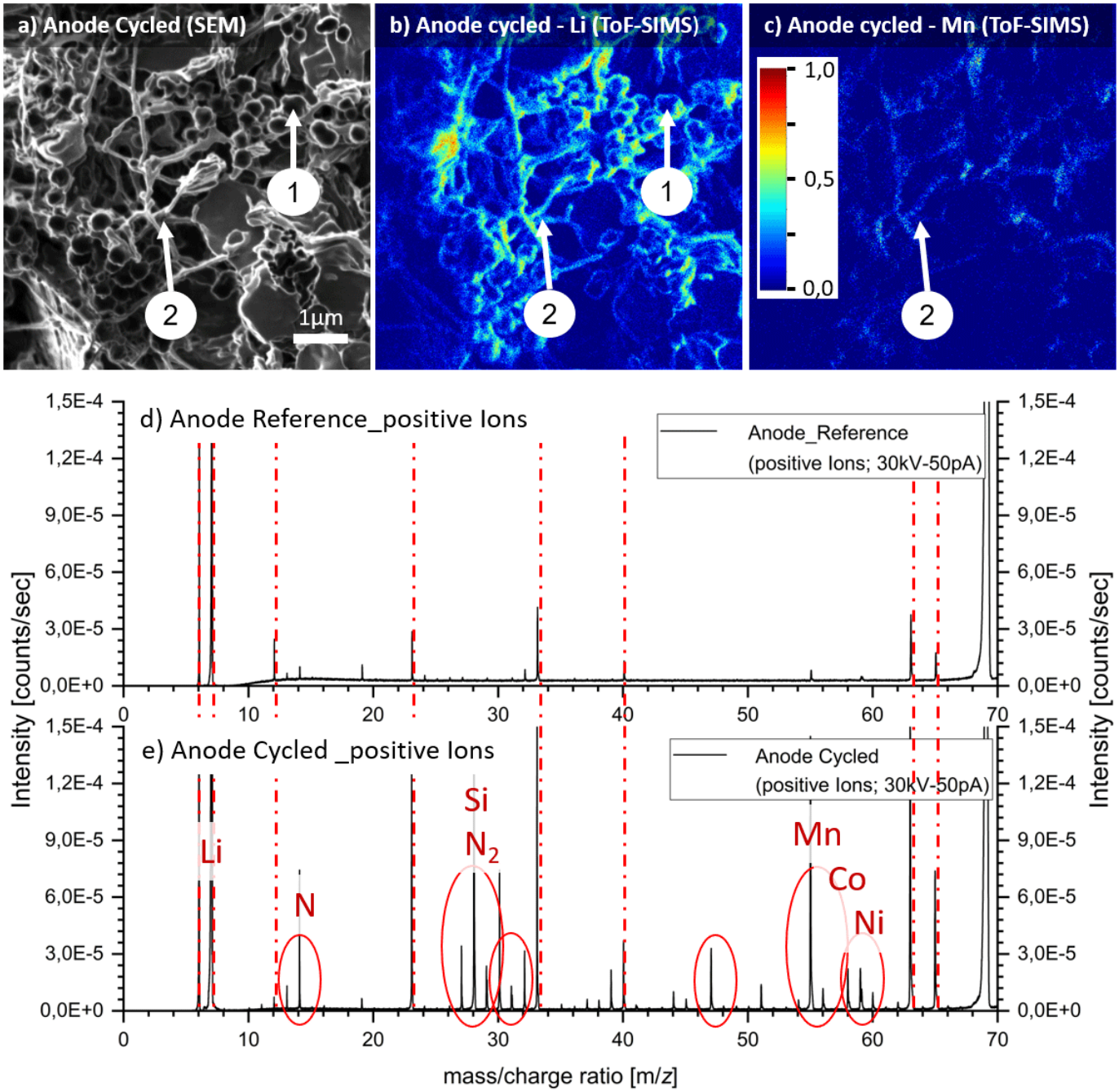

Fig. 2: Mass spectrometry applied to reference (d) and cycled (a,b,c,e) anode foil; anode foil morphology of the cycled cell (a) with element mapping of Li (b) and Mn (c) and mass spectra of anode reference (d) and anode cycled (e);

MS1.P006
Characterisation of Li-Ion battery aging by light, ion and electron microscopy combined with x-ray, raman and mass spectrometry

U. Golla-Schindler[1], P. Gnauck[2], T. Bernthaler[1], G. Schneider[1]

[1]Aalen University, Materials Research Institute (IMFAA), Aalen, Germany
[2]Carl Zeiss Microscopy GmbH, Oberkochen, Germany

The following investigations were performed on commercial available graphite/NMC (Li [Co1/3Ni1/3Mn1/3] O2) pouch cells, a reference (R), a cycled (C) and storage (S) one [1]. Non-destructive Computer Tomography (CT) yields a thickness increment of the treated cells. Light microscopy (LM) on cross sections enable the microscopic inspection. The figure shows SEM images of cathode and separator foils in top-view (a-d) and anode foils in cross-section (e, f). The cathode foils consist of NMC active material particles and conductive additives with binder material (Figure 1(a), marked as (1) and (2), respectively). The comparison of the reference with the aged films shows a surface coating on the aged NMC grains (Figure 1(b), marked as (3, 4)) also visible on the magnified inset of a single NMC particle with an atomic number of the precipitates above carbon and below (Li [Co1/3Ni1/3Mn1/3] O2) [2]. On top of the separator foils, Figure 1(c, d), arise spherical particles in the order of 10 nm to 1 micron (5, 6) and net-like structures (7). In the cross-sectional image of the anode foils Figure 1(e, f), a reaction rim with a thickness of a few µm formed by aging is visible. Analytic studies by EDS of the precipitates on top of the separator foil delivered an enriched content of F, Si O, C [3], where the information on the most important element Li is missing. The ORION NanoFab (ZEISS) is an instrument based on helium and neon ion beams, newly equipped with a Secondary Ion Mass Spectrometer (SIMS) producing element maps with lateral resolution down to 15 nm. This enables correlative SEM imaging and Li mapping. There the big spherical particles (1) and the flat like features (2) show an enriched Li content and the small particles (3) Si enrichment figure (g, h)). Correlative Raman-SEM applied on a treated anode foil delivers that the relative ratio of the D (characteristic for diamond, sp3 hybridization) and the G band (characteristic for sp2 hybridization graphite) shows differences. Where the increased D band contribution indicates a rise of border areas or implemented lattice distortions in the graphite particles [3]. Systematic study by CT, LM and SEM and the application of correlative LM-SEM, RAMAN-SEM and SEM-NanoFab SIMS delivered new unique insights in degeneration effects of Li-ion batteries. [4]

References:
[1] M. Bauer J. Power Sources 317 (2016), p. 93-102
[2] U. Golla-Schindler *et al*, micron 113 (2018) p. 10-19, DOI: 10.1016/j.micron.2018.06.013
[3] U. Golla-Schindler *et al*, Microscopy and Microanalysis*, 25*(S2) (2019), p. 1756-1757. doi:10.1017/S1431927619009516
[4] We thank C. Guenther and M.A. Danzer for the samples and Federal Ministry for Economic Affairs and Energy (BMWi) for financial support

Figure 1: Morphology studies with SEM on the reference- (a, c, e) and the treated- (b, d, f) battery foils (b, f, h cycled and d storaged). SEM top view (a-b) cathode, (c-d) separator, (e-f) anode, cross sectional view obtained with the FIB. (g, h) Correlative SEM NanoFab SIMS (g) SEM, (h) Li, Si distribution overlaid on top of SE (He) Orion Image.

Figure 1

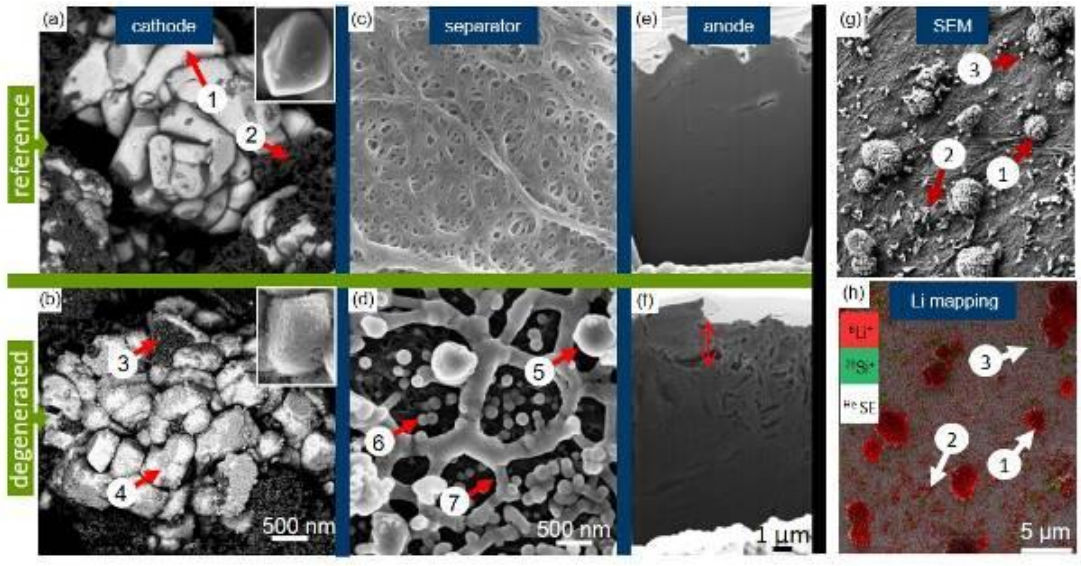

MS1.P007
Microstructure of garnet-based solid-state batteries – the LLZO|Li anode interface before and after cycling

J. Schmieg[1,2], M. Müller[2], S. Dierickx[2], J. Joos[2], A. Weber[2], E. Ivers-Tiffée[2], D. Gerthsen[1]

[1]Karlsruhe Institute of Technology (KIT), Laboratory for Electron Microscopy (LEM), Karlsruhe, Germany
[2]Karlsruhe Institute of Technology (KIT), Institute for Applied Materials (IAM-ET), Karlsruhe, Germany

Solid-state Li-ion batteries may overcome safety issues in future energy storage systems, if non-flammable solid electrolytes instead of liquid electrolytes are used. Garnet-type $Li_7La_3Zr_2O_{12}$ (LLZO) is a promising electrolyte material due to its high Li^+ conductivity and its chemical stability against Li metal used as battery anode. However, LLZO|Li interfaces are deteriorated by incomplete adhesion of Li on LLZO and by the morphological instability of the interface during cycling [1].

In this study, we aim towards a deeper understanding of microstructure formation of the LLZO|Li interface behavior during fabrication and cycling of symmetric anode model cells. Improved adhesion of metallic Li on the LLZO surface is achieved by introducing an In layer between Li anode and LLZO. The electrochemical properties are correlated with the interface structure by a suitable choice of preparation and imaging methods.

Ta-doped LLZO pellets ($Li_{6.6}La_3Zr_{1.6}Ta_{0.4}O_{12}$) are used to fabricate symmetric Li|LLZO|Li model cells. The In layer is deposited by magnetron sputtering after cleaning the LLZO surface by mechanical polishing. Li-metal foils are connected to LLZO in a heat-treatment step. Electrochemical impedance spectroscopy (EIS) is used to separate the impedance contributions of grain, grain boundaries (GBs) and interfaces.

The microstructure is investigated for pristine LLZO pellets, as-prepared cells and after cycling tests. Fast degradation in contact with ambient air and different mechanical properties of the brittle LLZO and soft Li complicate the access to the interfaces. Cutting a notch in cell samples with a wire saw and subsequent fracture in an Ar atmosphere (Figure 1(a, b)) yields clean interface cross-sections for scanning electron microscopy (SEM) imaging and energy dispersive x-ray spectroscopy (EDXS) analysis. In addition, structural analysis on a larger scale is performed by X-ray microtomography (µ-CT).

Optimized sample-fabrication parameters yield LLZO|Li interfaces without Li delamination from LLZO (Figure 1(c)). Indium is detected by EDXS only before annealing. Afterwards, In is below the detection limit at the interface and is assumed to be strongly diluted in the Li anode. Backscattered-electron SEM imaging shows dark contrast at GBs in LLZO (Figure 2(a)) indicating that Li or Li compounds are present. Cycling tests in combination with EIS demonstrate that the interface is stable up to current densities of 200 – 500 µA/cm². Higher current densities lead to changes at the interface and the formation of Li dendrites. The latter penetrate up to 70 µm into the LLZO electrolyte (Figure 2(b)). µ-CT imaging shows that the dendrites do not grow along the current direction, but mainly parallel to the interface along GBs, disconnecting larger LLZO regions from the bulk electrolyte. This could result from the mechanical properties and Li-containing weak GBs in LLZO.

To summarize, an In layer overcomes the lithiophobic surface properties of LLZO, resulting in a well-contacted LLZO|Li interface. The In layer acts as a non-permanent wetting aid that dissolves in the Li anode during heat treatment. Electrochemical failure of symmetrical cells is correlated with Li-dendrite formation and delamination of Li from LLZO observed by µ-CT and SEM.

[1] T. Krauskopf et al., *Chem. Rev. 120 (2020),* 7745–7794

We acknowledge funding by the German Federal Ministry for Education and Research within the FestBatt project (03XP0176A).

Figure 1

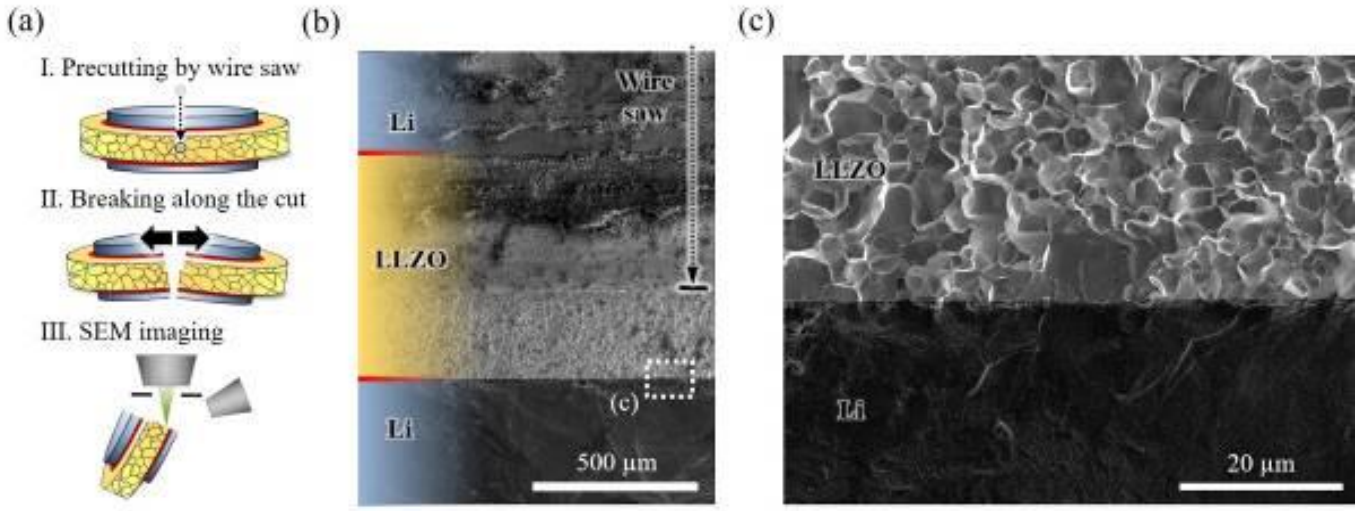

Figure 1. (a) Scheme of sample preparation, (b) 5keV cross-section secondary-electron SEM overview image of the Li|LLZO|Li model cell and (c) 5 keV secondary-electron SEM image of the LLZO|Li interface region

Figure 2

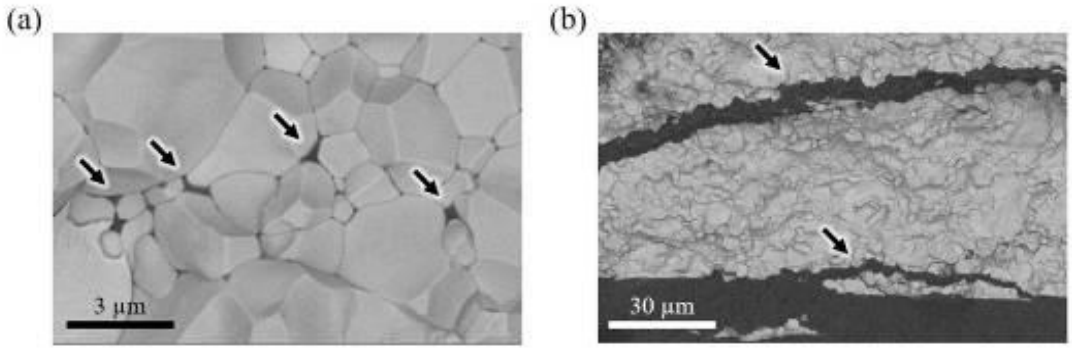

Figure 2. (a) 5 keV backscattered-electron SEM image of grain structure in the as-delivered LLZO sample. The dark grain-boundary contrast indicates the presence of a weakly scattering material such as Li or a Li compound. (b) 5 keV backscattered-electron SEM image of Li dendrites (see arrows) at the interface region of a cycled cell

MS1.P008
Electron microscopic investigation of post-annealed superconducting $GdBa_2Cu_3O_{7-\delta}$ thin films on MgO

L. Grünewald[1], R. Popov[2], J. Hänisch[2], B. Holzapfel[2], D. Gerthsen[1]

[1]Karlsruhe Institute of Technology (KIT), Laboratory for Electron Microscopy (LEM), Karlsruhe, Germany
[2]Karlsruhe Institute of Technology (KIT), Institute for Technical Physics (ITEP), Karlsruhe, Germany

$GdBa_2Cu_3O_{7-\delta}$ (GdBCO) is a promising high-temperature superconductor with potential application as coated conductor for power applications (e.g. transformers). However, further improvements in cost-effectiveness and superconducting properties are desired. The latter are influenced by O content [1], film texture, and film quality, where non-superconducting defects can effectively pin magnetic flux lines if they have favorable shape, size, and density [2]. The O content in GdBCO can be set in-situ after film deposition [3] or afterward by annealing in a different furnace (ex-situ) [4,5]. The correlation of oxygenation processes and defect formation/healing in GdBCO is not fully understood. In this work, we apply scanning transmission electron microscopy (STEM) to investigate the effect of different ex-situ oxygenation routes on the GdBCO microstructure.

GdBCO films with $\delta \approx 1$ are prepared by pulsed laser deposition (PLD) on MgO(001) substrates as described in [3]. One sample without any further annealing after PLD is used for reference. Other samples were oxygenated ex-situ using different heating routes. Cross-section samples for STEM are prepared by focused-ion-beam milling and in-situ lift-out in a FEI Strata 400S dual-beam instrument. A Titan^3 80-300 is used for high- and low-angle annular dark-field (HAADF/LAADF) STEM imaging and electron energy-loss spectroscopy (EELS).

A higher concentration of vertical defect structures is observed in LAADF-STEM images after oxygenation (cf. Figure 1(a, b)), which are threading dislocations, and antiphase and small-angle grain boundaries. An example of the latter is shown in Figure 1(d), where the loss of STEM resolution is caused by a slight in-plane rotation of the right grain. Stacking faults (SFs, dark lines) and smaller precipitates (bright regions) are visible in LAADF-STEM images (Figure 1(b, c)). Bright contrast around the dark SFs arises due to local strain resulting in de-channeling of the STEM probe. The precipitates are Gd-rich as determined by STEM-EELS (Figure 2) and identified as Gd_2CuO_4 by HAADF-STEM imaging (Figure 1(e)). Gd_2CuO_4 shows coherent, plate-like growth within the GdBCO matrix.

In conclusion, the oxygenation of GdBCO has a clear influence on the resulting microstructure. In an ongoing investigation, we are identifying and quantifying the concentration of the observed defects for different oxygenation routes.

References:
[1] R.J. Cava et al., *Phys. C Supercond.* 165 (1990) 419–433.
[2] J.P.F. Feighan et al., *Supercond. Sci. Technol.* 30 (2017) 123001.
[3] R. Popov et al., *J. Phys. Conf. Ser.* 1559 (2020) 012038.
[4] J. Lee et al., *IEEE Trans. Appl. Supercond.* 26 (2016) 1–6.
[5] W. Oh et al., *IEEE Trans. Appl. Supercond.* 28 (2018) 1–5.

Figure 1: Representative 300 keV LAADF-STEM cross-section images of films (a) directly after PLD and (b) after oxygenation. The latter shows a higher concentration of vertical defect structures and small, in-plane-oriented defects. (c) Higher magnification LAADF-STEM image of the sample in (b) with SFs marked by vertical arrows. (d) HAADF-STEM image of a small-angle grain boundary and stacking faults. (e) HAADF-STEM image of a Gd_2CuO_4 precipitate with overlaid structure model (O not shown).

Figure 2: (a) 300 keV ADF-STEM overview image with the marked STEM-EELS acquisition region of precipitates in the GdBCO film. (b) Extracted ADF-STEM, Ba M-, Cu L-, Gd M-, and O K-edge core-loss signals. The precipitates are Gd-rich.

Figure 1

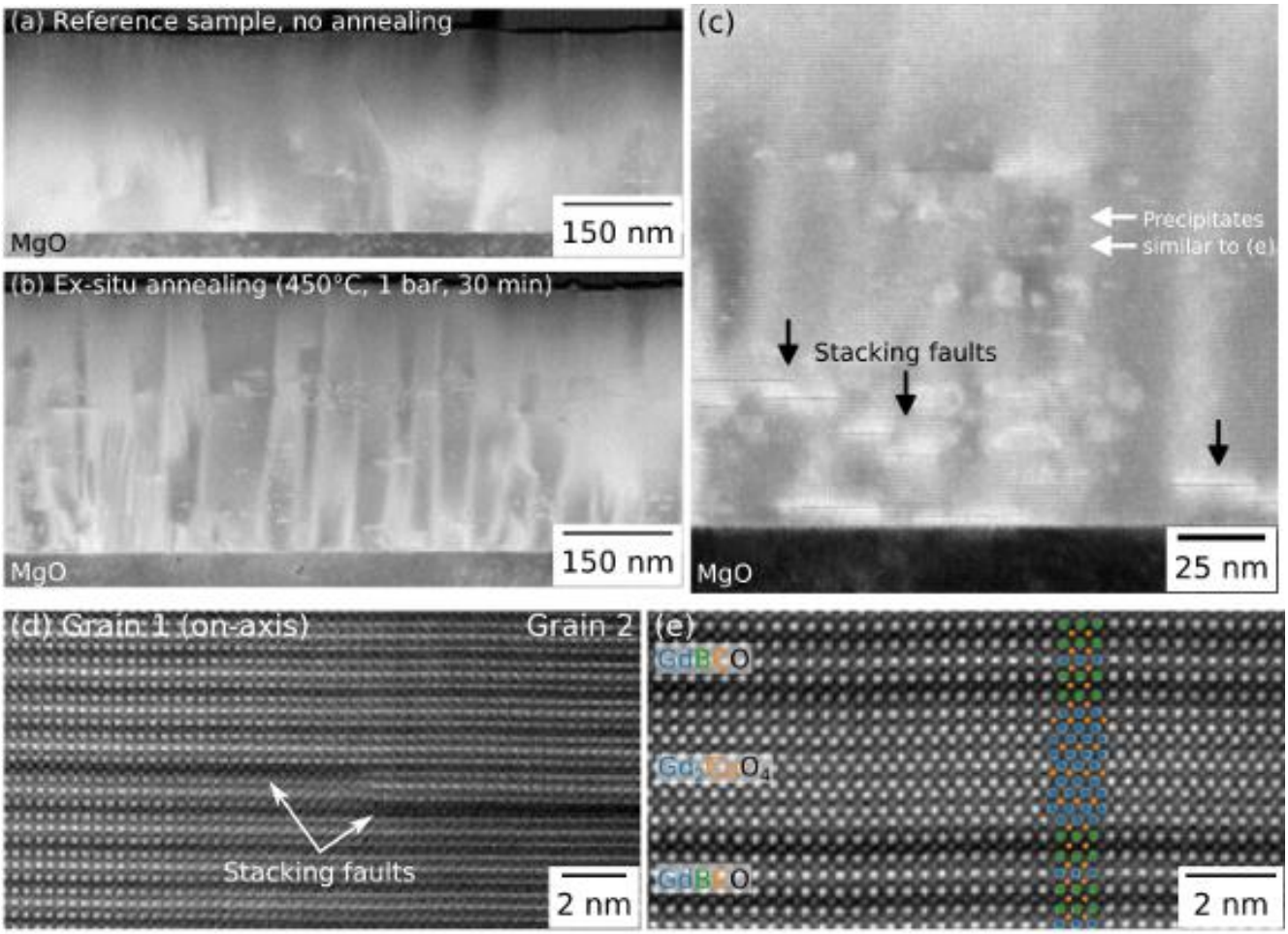

Figure 2

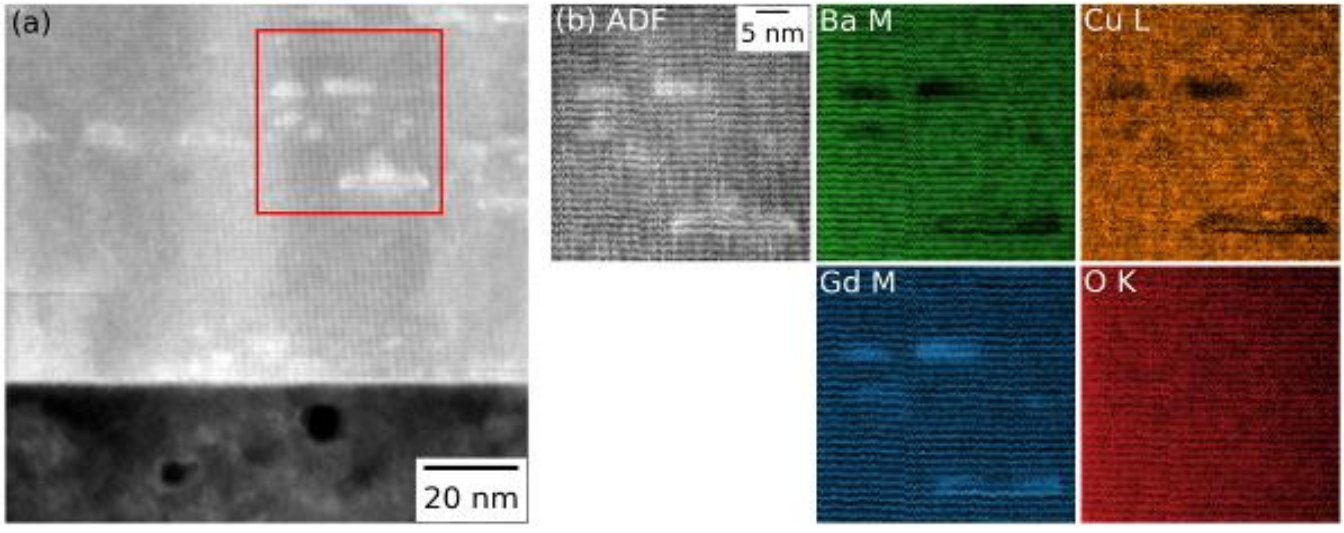

MS1.P009
Embedding of spheroidised graphite in indium and evaluation of the FIB/SEM data using machine learning

S. Sailer[1], M. Mundszinger[1], M. Mancini[2], J. Martin[2], U. Kaiser[1]

[1]Central Facility for Electron Microscopy, Electron Microscopy Group of Materials Science, Ulm Universtiy, Ulm, Germany
[2]Zentrum für Sonnenenergie- und Wasserstoff-Forschung (ZSW), Ulm, Germany

Introduction: Spheroidized graphite (provided by ZSW) is a widely used anode material in lithium ion batteries[1]. As its morphology influences the electrochemical properties[2], FIB/SEM tomography (Slice & View) data of graphite particles is recorded. By segmenting the serial 2D-images, a 3D-reconstruction of the particles is possible and morphological parameters, such as porosity, can be determined. An advanced investigation process including sample preparation and image segmentation is shown.

Objectives: A recording of multiple graphite particles within one Slice & View shall be achieved by embedding them into a stable and conductive matrix. A segmentation of the serial images will be accomplished by the usage of a convolutional neural network (CNN) with a U-Net[3] like structure. The CNN (a kind of machine learning) is used to overcome challenging segmentation tasks such as out-of-plane contrast or similar greyscales in different classes.

Materials and Methods: For the embedding, indium is chosen as a conductive matrix. The sample preparation is shown in figure 1. The graphite powder is mixed step by step into molten indium. After the sample has cured it is transferred on a pin-stub and the surface is polished.

Figure 1: Sketch of the sample preparation showing the different steps of embedding graphite in indium.

For the task of segmentation, a CNN is trained with a mixture of real and artificial images and their corresponding segmentation. The segmentations consist of three different classes: pore, graphite, and background (indium). After training, the CNN can assign each pixel of an experimental image to one of the different classes. The predictions of the CNN are further improved with automatic corrections. By comparing results of the automatic segmentation with a manual ground truth segmentation[3], the performance of the CNN can be determined.

Results**:** Figure 2 shows a cross-section of graphite particles embedded in indium (a), the corresponding ground truth segmentation (b), the prediction of the CNN (c) and its automatic correction (d). Challenging tasks in segmentation, such as voids in indium and a pore in graphite showing out-of-plane contrast, are marked white.

Figure 2: (a) Cross section of graphite particles embedded in indium and (b) the corresponding ground truth segmentation. The prediction of the CNN (c) and its automatic correction (d) are also illustrated.

As it can be seen in figure 2 there is a strong contrast between indium and graphite. Moreover, it provides the desired stable matrix for the graphite particles. The prediction of the CNN (and its automatic correction) are in good agreement with the ground truth segmentation.

Conclusion: We show that an embedding of graphite particles in indium is possible allowing the investigation of multiple graphite particles within one Slice & View recording. The segmentation with CNNs speeds up the segmentation process significantly.

This work is done in the RONDO project (BMBF, 03XP0112E).

[1] C. Pillot, *The rechargeable battery market and main trends 2014-2025*, in: AABC Europe 2016 - Advanced Automotive Battery Conference; Mainz, Germany, 2016.
[2] Y. Ishii et al., *Graphite particles and lithium secondary cell using them as cathode material*, (1998), WO9806679.
[3] O. Ronneberger et al., *U-net: Convolutional networks for biomedical image segmentation*. In: International Conference on Medical image computing and computer-assisted intervention. Springer, Cham, 2015.

Figure 1

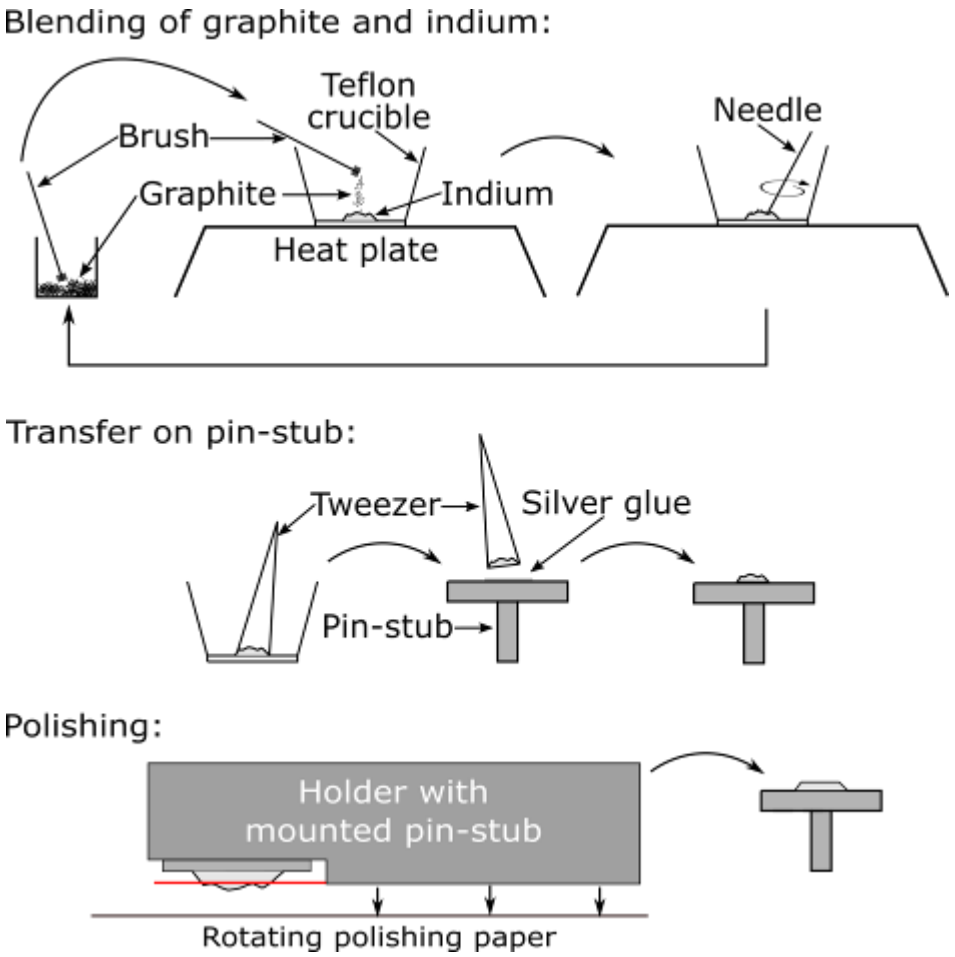

Figure 2

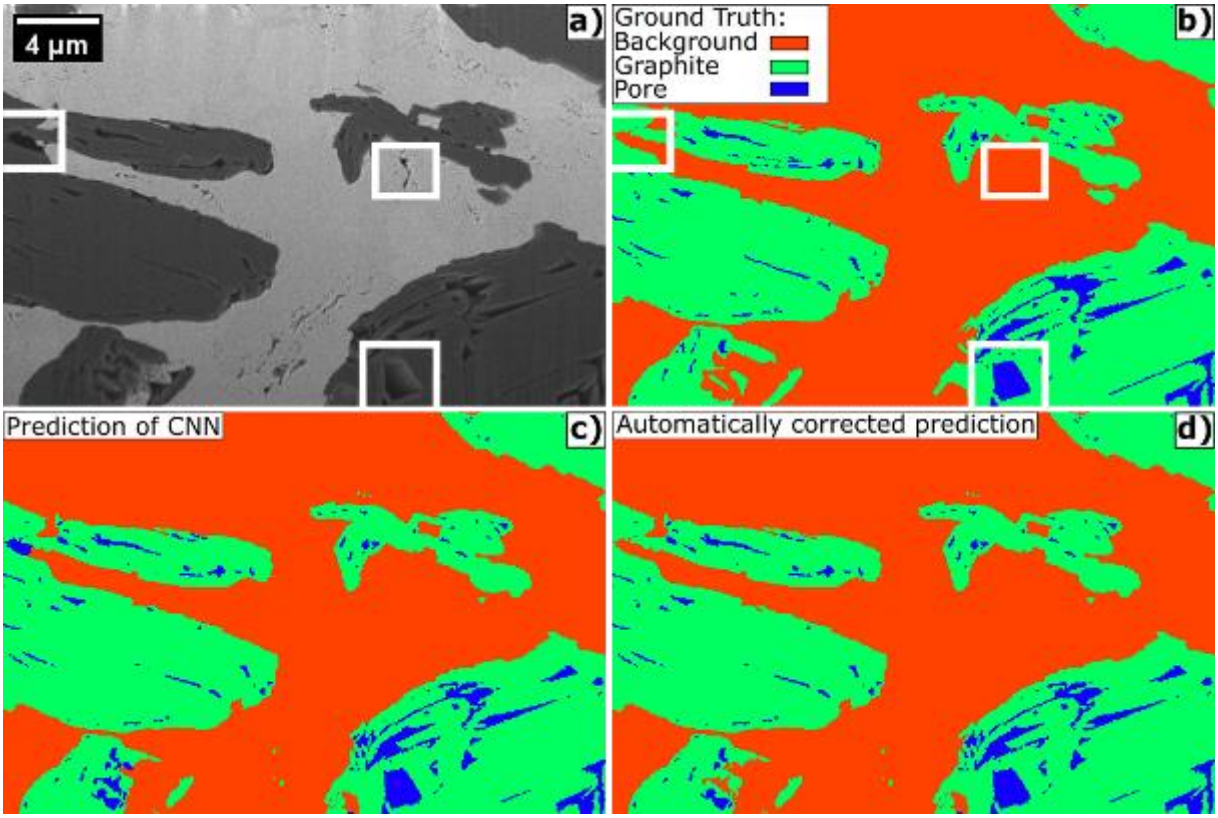

MS1.P011
In situ microscopy of deformation modes in flexible silver nanowire electrodes

N. J. Schrenker[1,2,3], Z. Xie[4], P. Schweizer[2,3], M. Moninger[2,3], F. Werner[2,3], N. Karpstein[2,3], M. Mačković[2,3]
G. D. Spyropoulos[5], M. Göbelt[6], S. Christiansen[6], C. J. Brabec[5], E. Bitzek[4], E. Spiecker[2,3]

[1]University of Antwerp, Electron Microscopy for Materials Science (EMAT), Antwerp, Belgium
[2]Friedrich-Alexander University Erlangen-Nuremberg (FAU), Institute of Micro- and Nanostructure Research, Erlangen, Germany
[3]Friedrich-Alexander University Erlangen-Nuremberg (FAU), Center for Nanoanalysis and Electron Microscopy, Erlangen, Germany
[4]Friedrich-Alexander University Erlangen-Nuremberg (FAU), Department of Materials Science & Engineering, WW1, Erlangen, Germany
[5]ZAE Bayern, Bavarian Center for Applied Energy Research, Erlangen, Germany
[6]Max Planck Institute for the Science of Light, Erlangen, Germany

Silver nanowire (AgNW) networks show excellent optical, electrical, and mechanical properties, which make them ideal candidates for transparent electrodes in flexible and stretchable devices.1 Indium tin oxide (ITO) is a commonly used material for transparent electrodes. However, new developments with ITO are hindered by its inherent brittleness, the low abundance of indium, and costly fabrication procedures based on various vacuum deposition techniques. Since AgNWs are the most promising alternative, several design and fabrication strategies have been developed in order to further increase the stretchability and flexibility. The objective of this study is to provide a comprehensive understanding of the mechanical deformation modes of fivefold twinned AgNWs and their electrical behavior.2 Therefore, we apply a scale-bridging approach by combining *in situ* nanomechanical testing of single NWs with large-scale SEM straining tests, which are directly correlated to the resistance response of the network. By exploiting capillary and shear forces during the coating process, we fabricate highly anisotropic AgNW network electrodes. A pronounced effect of the network anisotropy on the electrical performance is observed, which manifests itself in a one order of magnitude lower increase in resistance for networks strained perpendicular to the preferred wire orientation. This behavior can be explained by three microscopic deformation modes that we identified. (i) correlated tensile fracture of NWs, (ii) kink formation due to compression of NWs in transverse direction, and (iii) NW bending caused by the interaction of NWs in the strained network. It is noteworthy that the NWs show a high deformability under compression. Our HRTEM analysis and MD simulations revealed that specific defect processes in the fivefold twinned NW structure cause the formation of kinks with grain boundaries combined with V-shaped surface reconstructions, which presumably hamper crack initiation.

Moreover, in our current experiments we focus to extend *in situ* microscopy approaches to metal halide perovskites (MHPs) to analyze the role of defects and degradation mechanisms at a local scale as well as on the developments of low-dose STEM techniques due to the high beam sensitivity of MHPs. The insights gained on the deformation modes of AgNW electrodes as well as on the structure and stability of MHPs will enable to optimize design strategies and solar cells with increased efficiencies.

References:
[1] T. Sannicolo et al., Small, 12 (2016), DOI: 10.1002/smll.201602581
[2] Schrenker et al., ACS Nano 15 (2021), DOI:10.1021/acsnano.0c06480

Acknowledgement: Financial support from the German Research Foundation (DFG) via the Research Training Group GRK 1896 is gratefully acknowledged.

Figure 1: HRTEM analysis of triangular kinks. (a) TEM BF image of a AgNW network strained perpendicular to the coating direction (25% tensile strain, unloaded). (b) Close-up of the kinked wires in (a) illustrating GB formation. (c) HRTEM image of the wire in (b) marked with a green square depicting single dislocations at the GB. The scale bar of the FFTs is 10 nm−1. (d) BF TEM image of a kink with a V- defect at the NW top. (e) Close-up of the V-defect in panel d. The scale bars in the FFTs correspond to 10 nm−1. (f) Schematic of a kink illustrating the involved defect structures. Reprinted from Schrenker et al., ACS Nano 15, 2021. Copyright American Chemical Society (2020).

Figure 1

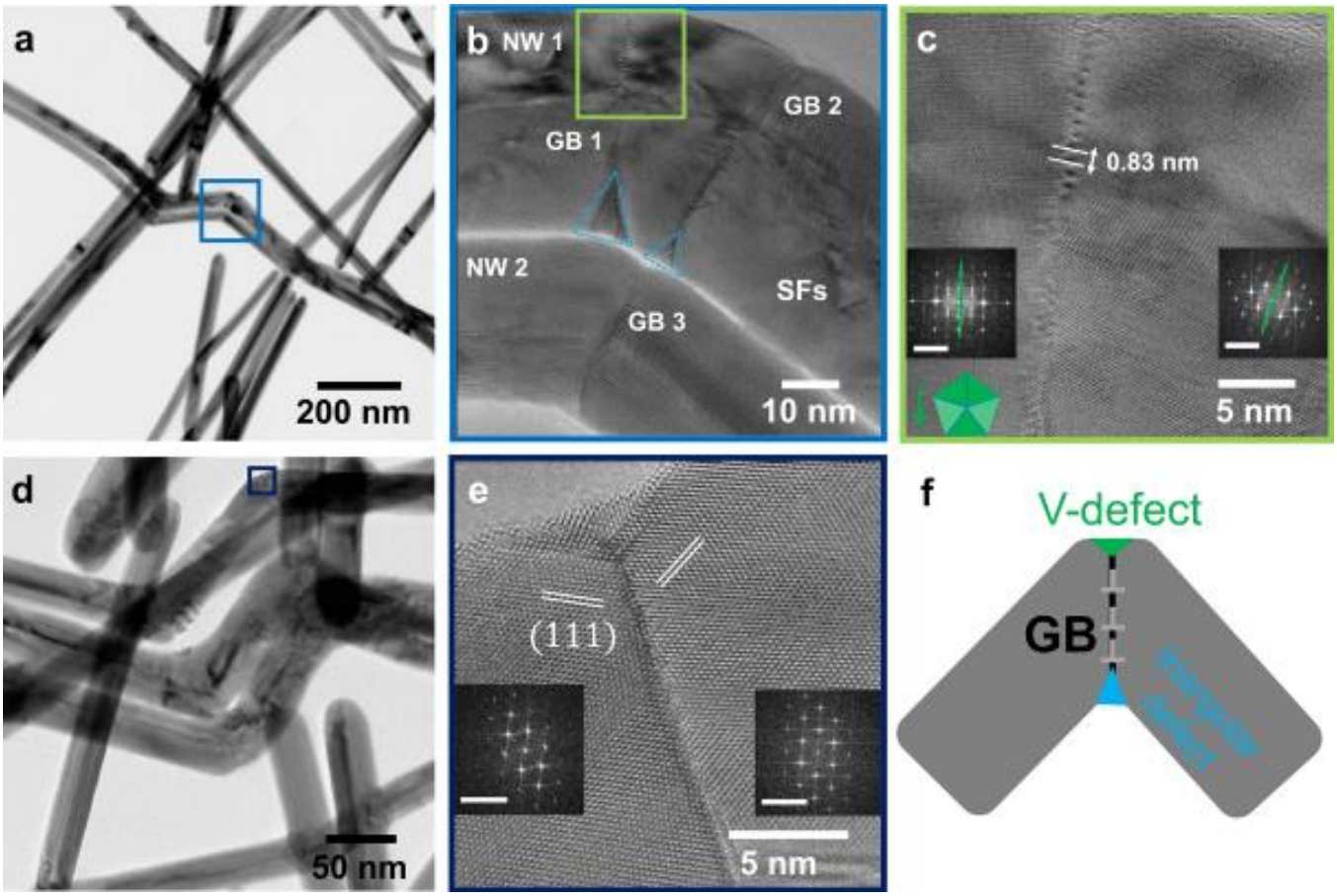

MS1.P012
Finding sub-µm descriptors for fuel cells gas diffusion layers by 3D FIB-SEM nanotomography

M. Bozzetti[1], A. Berger[2], H. A. Gasteiger[2], V. Tileli[1]

[1]Swiss Federal Institute of Technology Lausanne (EPFL), Materials Science, Lausanne, Switzerland
[2]Technical University of Munich, Munich, Germany

Proton exchange membrane fuel cells (PEMFC) are a promising technology for portable devices and automotive applications. Their advantages include theoretical high-power density, low system weight, clean by-products (water), and low emissions. One of the main unresolved issues in these devices is the mass transport limitation at the cathode, since by-product water from the catalyst can partially saturate the diffusion media, hindering gas diffusion and therefore lowering the performance. The key layer for water management is the microporous layer (MPL), which is traditionally made of carbon black and Teflon, having pores size in the range of tens to hundreds of nanometres. New designs of microporous layers have been developed, leading to a lower oxygen transport resistance and better performance at high current densities, but the mechanisms of water evacuation by the MPL is still poorly investigated. Better evacuation could come from the availability of larger pores, behaving as channels for water percolation [1]. To investigate the large pores, density and connectivity characterization techniques, that are able to probe the morphology with sub-µm resolution, are ideal. The goal of this work is to suggest a new approach taking advantage of focused ion beam (FIB) 3D tomography to look for new sub-µm scale descriptors for water management.

Two different designs of microporous layers have been investigated: a traditional acetylene black based MPL, named Li100, and a vapor grown carbon fiber (VGCF) based MPL. The latter MPL has shown to perform better in terms of water management [1][2]. The Li100 MPL has been embedded with ZnO by atomic layer deposition (ALD), and Ar-beam polished cross sections have been fabricated to avoid surface roughness artefacts. The sample preparation of the larger pores of VGCF proceeded with a combination of ALD and resin embedding to facilitate volume reconstruction. The volumes were acquired on a Zeiss CrossBeam 540 FIB, with 300 pA milling current at 30 kV. The voxel size was 8 nm. Image processing involved WEKA for segmentation and distance transform was used to evaluate the thickness distribution of the pores.

Figure 1a-b shows the reconstructions of the Li100 and VGCF. Their respective pore size distribution is depicted in **Figure 1c-d** Porosity and tortuosity have been characterized for both materials, showing good compatibility among them and their values were confirmed with other characterization techniques. In addition to the traditional diffusion descriptors, a new characterization approach involving the minimum size of the pores is proposed. This parameter was used to investigate the connections of larger pores and it provided information for all the pores of a certain size. The two MPL designs were also found to differ in the characteristic size of the constrictions between larger pores. For Li100 MPL, the constrictions are in the range of 100-120 nm whereas for the VGCF, they are in the range of 600-700 nm, meaning that in the traditional MPL design it is difficult to find percolating channels above 200 nm.

To conclude, this new approach to characterize the pore network provides a deeper knowledge on sub-µm scale morphology of the MPLs, and it represents a powerful tool to characterize their performance.

[1] C. Simon *et al.*, *J. Electrochem. Society,* vol. 164, n. 14, pp. F1697-F1711 , 2017.
[2] C. Simon *et al.*, *J. Electrochem. Society,* vol. 166, n. 13, pp. F1022-F1035, 2019.

Figure 1

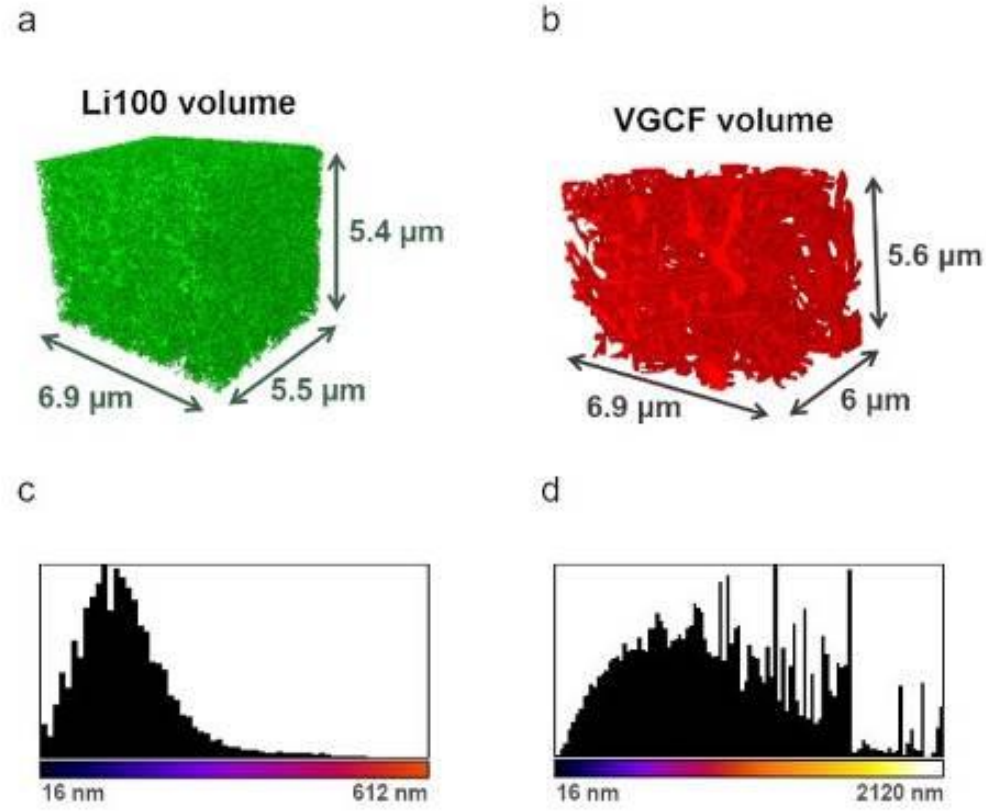
a
Li100 volume
5.4 µm
6.9 µm
5.5 µm
b
VGCF volume
5.6 µm
6.9 µm
6 µm
c
16 nm
612 nm
d
16 nm
2120 nm

MS1.P013
Matrix composition and fine-scale structure analysis of NMC Li-ion battery using atom probe tomography

Y. Chen[1], P. Clifton[1], R. Chemnitzer[1], T. Prosa[1]

[1]CAMECA Instruments Inc., Applications, Madison, United States

Introduction: Lithium-ion batteries are widely used for portable PCs, cellular phones and other portable electronics. A recent market forecast predicts a massive expansion in production driven by electric vehicles. An anode, a cathode and an electrolyte are the three main components in a Li-ion battery. Lithium-nickel-manganese-cobalt (NMC) is predicted to be the next generation cathode material [1]. Its market share is expected to increase to 48% in 2025 from the current 19%. Manufacturing R&D also shows a trend of shifting to high Ni content systems for enhanced capacity.

Objective: Structure transformation was reported exhibiting metal enrichment and Li depletion [2] near particle surface after cycling. In this work we investigate the composition and fine-scale microstructure of two types of NMC cathode materials. Ability of atom probe tomography will be demonstrated for assessing lithium to metal ratio and composition homogeneity from individual particles.

Materials and Methods: Cathode material with 90% active particles were obtained from NEI Corporation (EB-50E-622 and EB-50E-811). The nominal compositions are $Li(Ni_xMn_yCo_z)O_2$ X:Y:Z=6:2:2 and X:Y:Z=8:1:1. SEM and EDS analysis on these materials confirms the particles are ~10 µm in diameter and compositionally homogeneous at the sub-micron scale. Atom probe tomography [3, 4] was used for analysis of the sub surface region on various particles. On average each lift-out region extracts five atom probe specimens. Multiple particles from each sample were examined to better understand particle to particle variation. Analysis conditions for data collection were systematically studied and optimized to balance data quality and yield.

Results: A typical mass spectrum (Figure 1) includes both single element ions and molecular species formed with oxygen. The overall matrix/bulk compositions of three particles from NMC622 and two particles from NMC811 are reported in Figure 2. The compositional variation is well below the ±2 sigma statistic error calculated from each population indicating relatively good homogeneity from specimen to specimen and particle to particle.

Conclusions: In conclusion, atom probe tomography has been shown to provide high-quality results with an NMC cathode material for Lithium-ion batteries. It is capable of identifying the matrix composition and of investigation of nanoscale three-dimensional compositional variations. The two types of NMC may be quantitively and precisely differentiated using their metal-to-metal ratios.

Figure 1: Mass spectrum example of NMC cathode material acquired with LEAP 5000 XR.

Figure 2: Composition of NMC 622 particle A, B and C along with NMC811 particle D and E. The dashed lines indicate materials" nominal composition.

References:
[1] Worldwide Rechargeable Battery Market 2019-2030, Avicenne Energy, 28th edition.
[2] A. Devaraj, et al. Nature Communications 6.1 (2015): 1.
[3] D. J. Larson et al., "Local Electrode Atom Probe Tomography: A User"s Guide",
(Springer Scientific, New York, 2013).
[4] J.Y Lee, et al. Journal of Power Sources 379 (2018): 160.

Figure 1

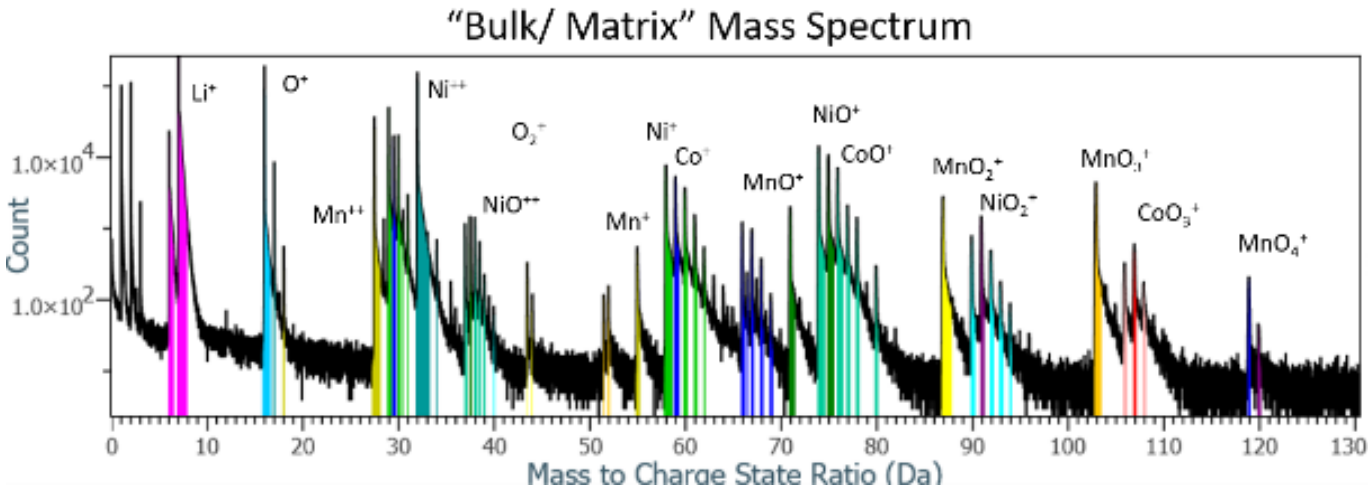

Figure 2

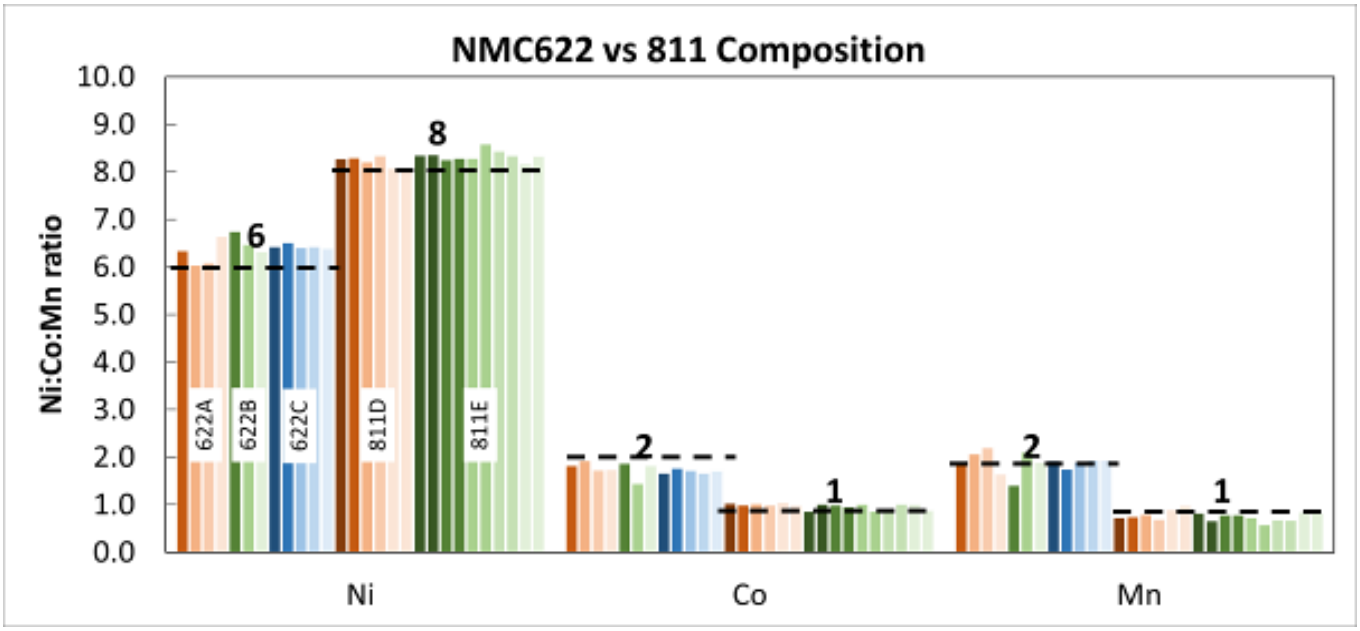

MS1.P014
Revealing dissolution and reprecipitation process of a copper catalyst for CO_2RR by electrochemical *in situ* TEM

J. Vavra[1], T. H. Shen[1], D. Stoian[1], R. Buonsanti[2], V. Tileli[1]

[1]Swiss Federal Institute of Technology Lausanne (EPFL), Institute of Materials, Lausanne, Switzerland
[2]Swiss Federal Institute of Technology Lausanne (EPFL), Institute of Chemical Sciences and Engineering, Sion, Switzerland

Electrochemical CO_2 reduction reaction (CO_2RR) could lessen the impact of human society on global climate by reusing waste CO_2 and turning it into fuels and chemical feedstock. Copper has been identified as the most promising catalyst for multi-carbon products. This work describes the mechanism responsible for reconstruction of a Cu-based catalysts during the initial stages of CO_2RR uncovered using liquid cell in-situ electrochemical transmission electron microscopy (in-situ LCTEM).

The electrochemical microcell consisted of in-house fabricated electrochemical LCTEM chip containing glassy carbon working electrode and auxiliary Pt electrodes operated within Hummingbird Scientific electrochemical LCTEM holder. 0.1M $KHCO_3$ saturated with CO_2 was used as an electrolyte. In-situ imaging experiments were performed on JEOL 2200FS at 200kV with zero-loss peak filtering by the in-column Omega filter and recorded on a Direct Electron DE-16 camera at a dose rate of 35 $e^-/nm^2/s$. In-situ selected area electron diffraction (SAED) experiments were performed on ThermoFischer Scientific Talos at 200 kV.

The mechanism responsible for the catalyst reconstruction was captured, where the initial Cu spheres evolve into larger particles selective for C2 products.[1] The as-synthesized catalyst consists of 7nm spheres of metallic Cu, but oxidizes to Cu_2O upon exposure to the cell environment at open circuit voltage (OCV) while releasing Cu ions into the electrolyte.[2] As the reductive potential is applied during the cell startup the dissolved Cu ions redeposit (Figure 1A) and the bulk of the catalyst is reduced back to metallic Cu (Figure 1B) both processes taking place simultaneously around 0.0 V vs RHE. Surprisingly, the catalyst dissolution and redeposition continues under cell operation, despite the absence of oxidized phases. (Figure 1 C, D) The observed process is analogous to Ostwald ripening and proceeds through an unknown soluble intermediate, rather then particle migration and coalescence. The mechanism

By monitoring the morphological and phase changes of the catalyst in real-time, we advance the understanding of the dynamic processes, responsible for the catalyst activation in the initial stages of CO_2RR and highlight the key role played by solution intermediates and surface oxides. While the process is certainly accelerated by the large number of undercoordinated atoms on the surface of the small Cu NPs, it remains valid for all Cu based CO_2RR catalysts. Understanding the underlying processes of the catalyst reconstruction will aid in the rational design of the next-generation of stable CO_2RR catalysts.

Figure 1: *Evolution of Cu catalyst monitored by in-situ LCTEM during the cell startup and operation.* ***(A)*** *Image series monitoring the catalyst morphology and* ***(B)*** *rotational average of SAED captured during the cell startup as a function of applied electrochemical potential (V vs RHE).* ***(C)*** *Image series monitoring the catalyst morphology under operation, where dissolving primary particles (blue box) and growing secondary particles (red box) are highlighted.* ***(D)*** *Corresponding area weighted particle size distribution as a function of time. Decrease in population of primary particles (I) is accompanied by growth of secondary particles (II).*

Figure 2: *Proposed reconstruction mechanism of a Cu catalyst during CO_2RR.*

[1] Kim, D. et al., *Proc. Natl. Acad. Sci.* **114**, 10560–10565 (2017).
[2] Vavra, J. et al., *Angew. Chem. Int. Ed.* **60**, 1347–1354 (2021).

Figure 1

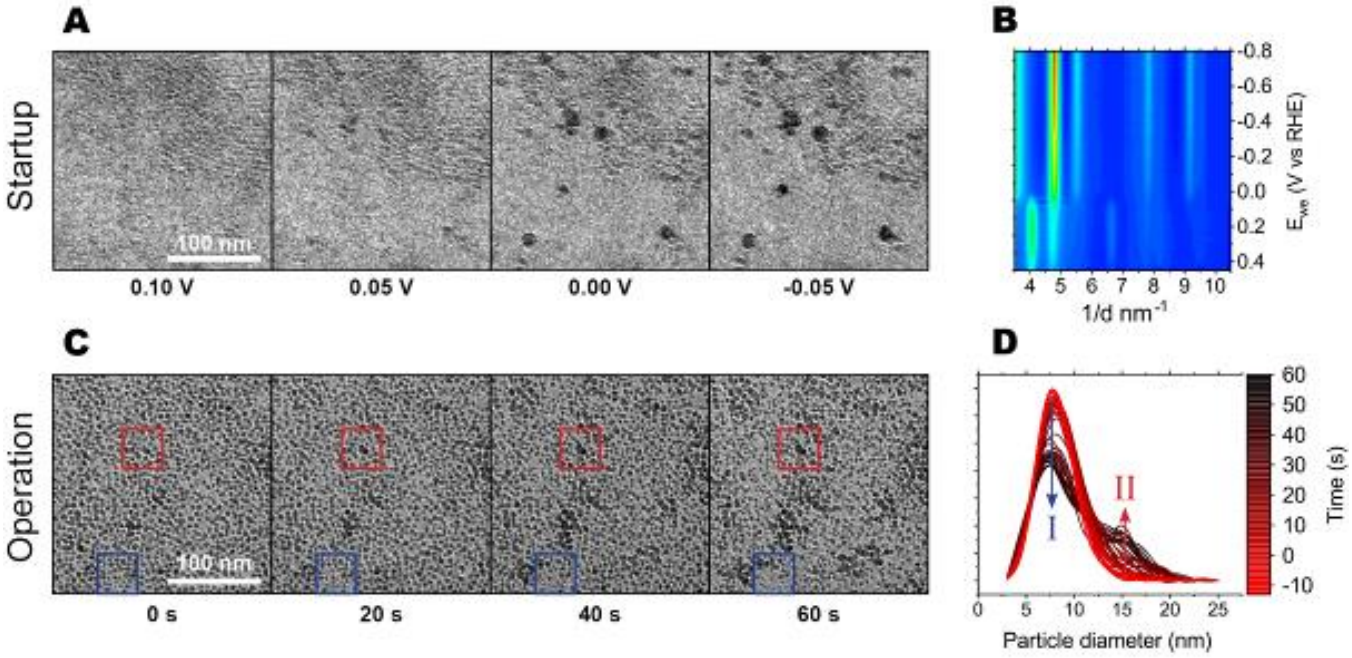

Figure 2

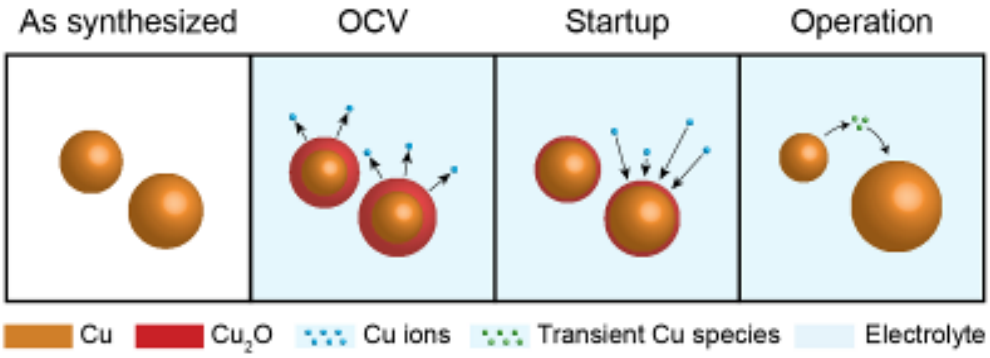

MS1.P015
STEM investigation of co-sintered cathode-solid electrolyte interfaces

M. Malaki[1], A. Pokle[1], J. P. Beaupain[2], J. Müller[3], A. Beyer-Leser[1], B. Butz[3], K. Wätzig[2], M. Kusnezoff[2], K. Volz[1]

[1]Philipps-University Marburg, Physics, Marburg, Germany
[2]Fraunhofer Institute for Ceramic Technologies and Systems IKTS, Dresden, Germany
[3]Institute of Materials Engineering, University of Siegen, Siegen, Germany

All-solid-state batteries (ASSBs) employing cathode-solid electrolyte (CSE) composites can circumvent the energy density and safety issues which hamper the performance of conventional Li-ion batteries (LIBs) resulting from the degradation of organic liquid electrolytes (LEs) at high redox voltages (>4 V)[1]. The demand for high Li-ion conductivity has led to the development of oxide solid electrolytes (SEs) such as the NASICON type $Li_{1.3}Al_{0.3}Ti_{1.7}(PO_4)_3$ (LATP)[2]. To promote Li-ion kinetics across interfaces and thus practically increase energy density, the SE is employed in combination with a Ni-rich cathode active material (CAM) such as the $LiNi_{0.6}Co_{0.2}Mn_{0.2}O_2$ (NCM622). To that effect, the CSE interface must be mechanically, chemically and electrochemically compatible. The SEs are initially synthesized in a sol-gel process as loosely packed particles[3], which are then pressed and sintered to obtain densely packed primary grains, forming a polycrystalline pellet. Although oxide SEs are chemically compatible with oxide cathodes, their rigid ceramic nature leads to poor interfacial contact resulting in high ionic impedance[2]. A simple and effective method to improve the interfacial contact is to directly co-sinter the electrode and electrolyte. Nonetheless, several combinations of SE and CAMs have been shown to undergo decomposition and intermediate transition layer formation during processing steps at the micron-scale[4]. A thorough transmission electron microscopy (TEM) investigation of these interfaces is challenging and hence, intimate knowledge on interfacial reactions and kinetics is lacking.

This study employs high-resolution scanning TEM (HR-STEM) and precession electron diffraction (PED) techniques to provide a comprehensive overview of phase decompositions/transformations at the interface. The CSE composites were synthesized by co-sintering NCM622 with LATP between 550-650 °C. Electron transparent lamellas were prepared from each CSE using the focused-ion beam (FIB) technique and by Ar-ion nanomilling, followed by HR-STEM imaging of the cathode interfaces. Phase analysis and chemical mapping of the bulk structure and interfaces were carried out with automated crystal orientation mapping (ACOM-TEM) and energy dispersive X-ray (EDX) analysis. In the CSE, we observe that the rise in sintering temperature leads to morphological degradation by pore formation and a steady widening of inter-granular cracks that were most severe at 650 °C. Elemental inter-diffusion and transition metal segregation steadily increase with temperature. The ACOM-TEM and EDX reveal the formation of secondary phases at the interphase, thus providing direct evidence of mixed conducting phases. The present study summarizes the evolution of chemical composition of NCM-LATP composite in relation to the sintering temperatures. These results help to directly visualize complex interfacial reactions when CSE composites are co-sintered, enabling us to better understand the temperature influence on interface stability to design reliable solid-state batteries.

References:
[1] Nanda, J., Wang, C and Liu, P., MRS Bull. 43 (10) (2018), pp. 740–745.
[2] Nie, K. et al. Frontiers in chemistry 6 (2018), p. 616.
[3] Waetzig, K. et al. Journal of Alloys and Compounds 818, (2020), 153237.
[4] Miara, L.et al. ACS applied materials & interfaces 8 (40) (2018), pp. 26842–26850.

MS1.P016
Probing ionomer coverage in proton exchange membrane fuel cell electrodes with cryo-electron tomography

R. Girod[1], T. Lazaridis[2], H. A. Gasteiger[2], V. Tileli[1]

[1]Swiss Federal Institute of Technology Lausanne (EPFL), Institute of Materials, Lausanne, Switzerland
[2]Technical University of Munich, Chair of Technical Electrochemistry, Department of Chemistry and Catalysis Research Center, Garching, Germany

Proton exchange membrane fuel cells (PEMFC) offer an attractive pathway towards decarbonized vehicle propulsion. Conventionally, they feature a porous catalyst layer whose structure is highly related to the cell performance and durability. This layer is composed of dispersed Pt nanocatalysts on carbon supports interconnected with a proton-conductive ionomer network. In particular, the ionomer network is thought to induce increased transport resistances at high current and low Pt loading due to inhomogeneities in coverage of the carbon supports, however direct evidence of its pristine morphology at the nanoscale is lacking[1]. Electron tomography (ET) offers access to volumetric data and spatial resolution required to probe these nanomaterials but is faced with important contrast and material sensitivity challenges that have led previous work to focus on model samples, or to be limited to qualitative results[2,3]. Here we present a method for quantitatively investigating the ionomer coverage in fuel cell samples using cryo-ET to mitigate beam-induced degradation and advanced image processing methods for analysis.

Samples from a rod-coated catalyst layer prepared with Pt/C catalysts (graphitized vulcan carbon black, 8.7wt% Pt) and Nafion D2021 ionomer (I/C = 0.7) were dry-dispersed onto a grid and analyzed in a ThermoFisher Scientific F20 transmission electron microscope (TEM) operated at 200 kV and equipped with a Falcon III direct electron camera.

First, the stability of the ionomer network under e-beam irradiation was evaluated. Figure 1a depicts the ionomer degradation as a function of the accumulated dose. At room temperature conditions, the degradation is immediate even at low electron dose of a few $e^-/Å^2$. Degradation is partially mitigated by working at cryogenic conditions, placing however stringent requirements on the electron dose for a complete tilt series. Optimization of the operating conditions involved working in phase contrast and defocused imaging mode, maintaining the total accumulated dose below 35 $e^-/Å^2$ at 95K. In this case, the TEM images exhibit a low signal-to-noise ratio as seen in Figure 1b. To improve the reconstruction quality and data interpretability, a denoising scheme using the cryo-CARE method was implemented[4]. Tomographic reconstruction was performed using the SIRT algorithm and shows limited artefacts and sufficient contrast after denoising for interpretation of the tomograms as seen in figure 1c. Figure 1d shows the result of a complete segmentation performed with YAPiC, a U-Net based pixel classifier[5], and reveals that the ionomer coverage on the carbon surface is partial at this I/C ratio.

To conclude, using cryo-TEM and state-of-the-art image processing tools, we were able to achieve three-dimensional reconstruction of PEM fuel cell catalyst layer samples and to accurately evaluate the ionomer coverage on the Pt/C system

[1] Ott, S. *et al. Nat. Mater.* 19, 77–85 (2020).
[2] Lopez-Haro, M. *et al. Nat. Commun.* 5, 5229 (2014).
[3] Cullen, D. A. *et al. J. Electrochem. Soc.* 161, F1111–F1117 (2014).
[4] Buchholz, T.-O., Jordan, M., Pigino, G. & Jug, F. *(ISBI 2019)* 502–506 (2019).
[5] YAPiC. available at https://yapic.github.io/yapic/

Figure 1: (a) Comparison of material shrinkage during TEM imaging at room and cryo temperature. Upper dose limit was set at 3500 e^-/nm^2 for the complete acquisition (image at 0° is shown in (b)) to limit degradation, allowing 3D reconstruction, tomogram inspection (c) and segmentation (d)

Figure 1

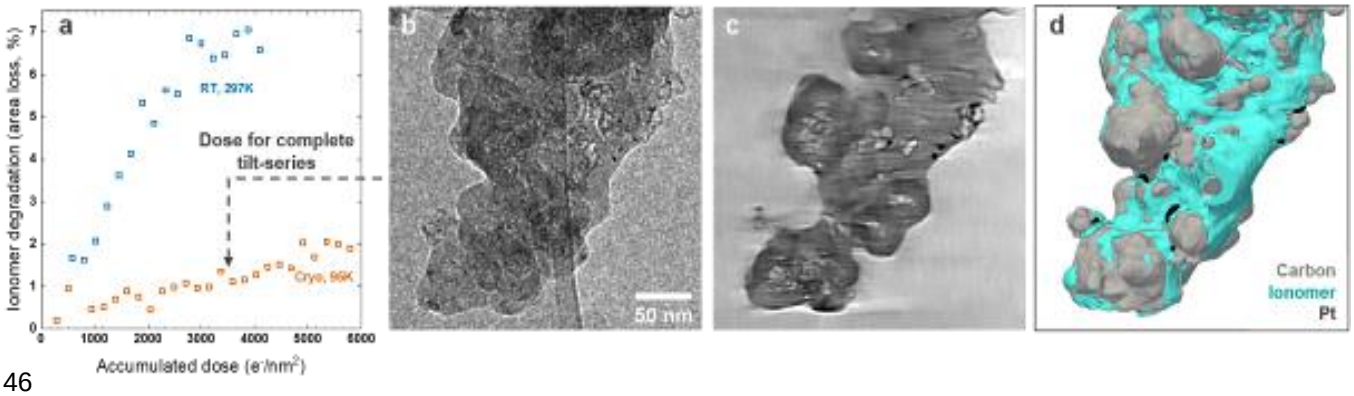

MS1.P017
TEM study of structural and chemical evolution of coated $LiNi_{0.33}Mn_{0.33}Co_{0.33}O_2$, $LiCoO_2$, and Si electrodes in Li-ion batteries

A. Makvandi[1], M. Peterlechner[1], S. Casino[2], M. Wolff[3], S. Lobe[3], J. Müller[4], C. Gammer[5], T. Gallasch[2], S. Uhlenbruck[3] B. Butz[4], M. Winter[2], G. Wilde[1]

[1]Institute of Materials Physics, University of Münster, Münster, Germany
[2]MEET Battery Research Center, University of Münster, Münster, Germany
[3]Institute of Energy and Climate Research, Materials Synthesis and Processing (IEK-1), Forschungszentrum Jülich GmbH, Jülich, Germany
[4]Department Maschinenbau, Micro - and Nano analysis - Tomography Research Group, University of Siegen, Siegen, Germany
[5]Erich Schmid Institute of Materials Science (ESI) of the Austrian Academy of Sciences , Leoben, Austria

The nanostructured coating of electrode materials is one of best approaches to optimize crucial parameters in Li-ion batteries. Interfaces (e.g. active material/coating; electrode surface/electrolyte) determine the local Li-ion transport kinetics and finally the electrochemical performance. Therefore, it is necessary to study the structure and chemistry of electrodes and electrode/electrolyte interfaces. In this work, the structural and chemical evolution of bulk and surface regions of uncoated and coated $LiNi_{0.33}Mn_{0.33}Co_{0.33}O_2$ (NMC-111), $LiCoO_2$ (LCO), and Si electrodes during electrochemical cycling were studied by transmission electron microscopy (TEM). The objective of this work is to understand the effect of the electrode/electrolyte interface on degradation mechanisms and also the impact of the coating layer on the stability of the electrode surface.

An Al-doped ZnO-coated NMC-111 powder electrode was prepared via a Microwave-assisted synthesis method. Carbon-coated silicon and Al-doped ZnO-coated LCO thin film electrodes were prepared via magnetron sputtering and physical vapor deposition (PVD), respectively. Cross-sectional TEM samples were prepared by FIB. High-resolution TEM (HR-TEM), Electron-energy-loss spectroscopy (EELS), energy dispersive X-ray spectroscopy (EDX), and nano-beam electron diffraction (NBD) were acquired using a FEI Titan Themis G3 60-300.

In Figure 1f, core-loss EELS spectra of an uncoated LCO film electrode after 40 charging / discharging cycles shows a Co-L_3 edge chemical shift to lower energies, confirming the reduction of Co valence state at the surface, which is compatible with the results of the intensity ratio (L_3/L_2) analysis. Moreover, the O-K edge pre-peak intensity decreases at the surface which also confirms Co valence state reduction due to direct electrolyte exposure (Figs. 1d, e). In case of C-coated Si film electrode after 1st lithiation, two intensity profiles, acquired by azimuthal integration of the intensity along NBD diffuse rings, show that there is a peak shift in the first peak of the intensity profile (Figs. 2b, d). A strain map, acquired by evaluating the peak shift, shows that lithiation-induced strain developed inside the electrode (Figure 2c). The results and possible conclusions about the effect of coating layers on the battery performance are discussed.

Figure 1: EELS analysis of an uncoated LCO film electrode after 40 cycles: (a) core-loss EELS spectrum image, (b, c) O and Co EELS mapping, (d) white lines intensity ratio (L_3/L_2) of the Co-edge at different distances from the surface, and (e, f) core-loss EELS spectra of O and Co acquired from the rectangular areas shown in (a).

Figure 2: NBD spectrum image of a C-coated Si film electrode after 1st lithiation: (a) reconstructed dark field image acquired using a virtual objective aperture, (b, d) Intensity profiles acquired from the two regions shown in (a); and (c) strain map.

Figure 1

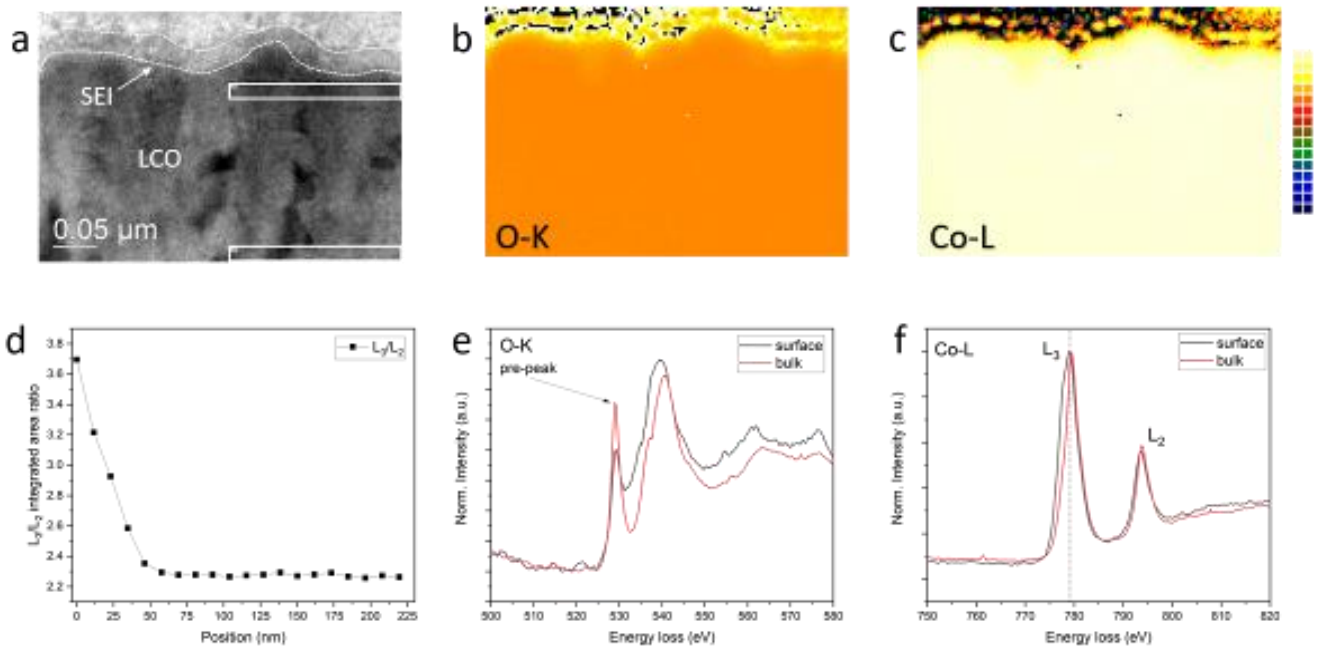

Figure 2

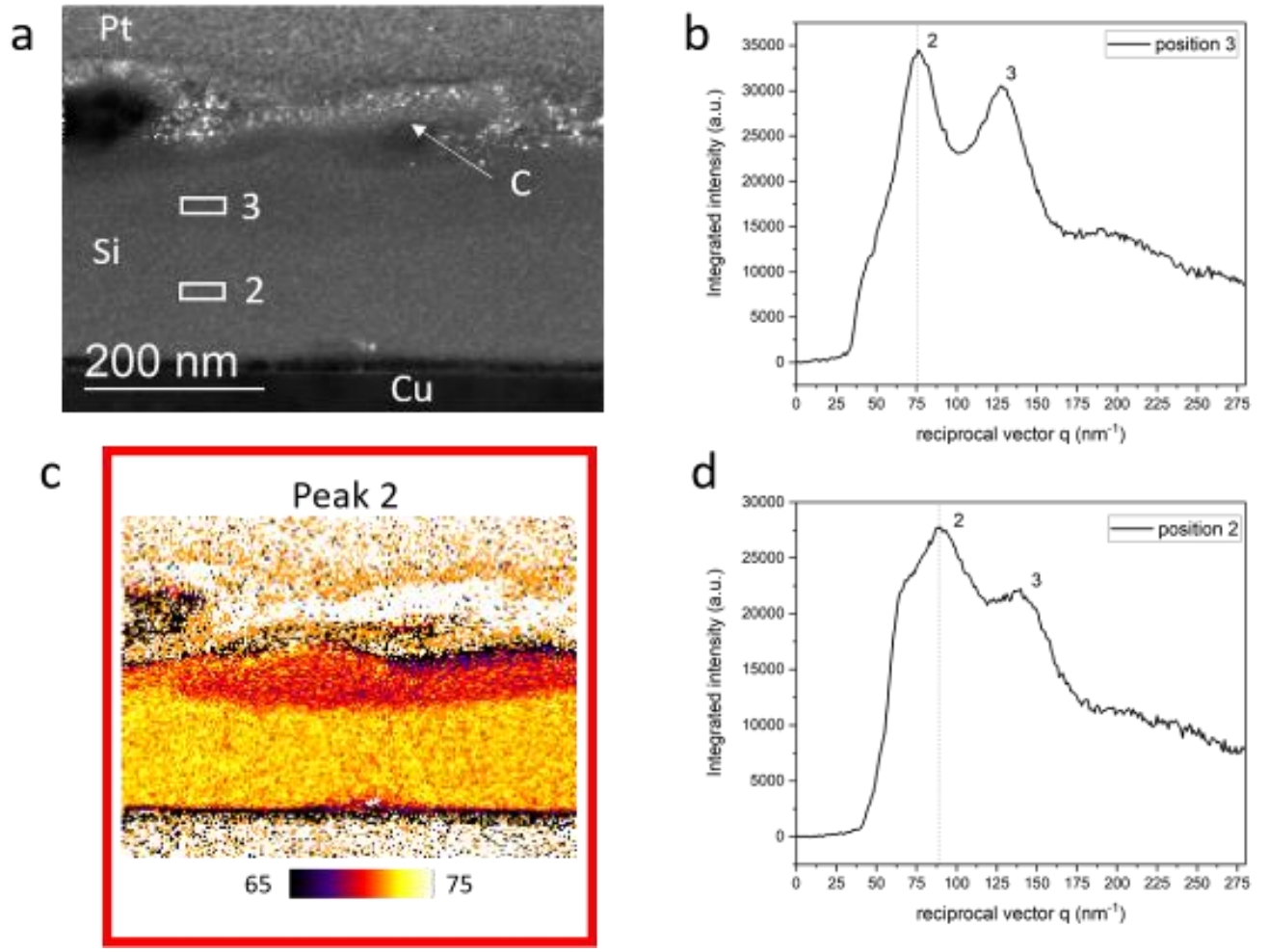

MS1.P018
High resolution imaging and spectroscopy of interfaces in solid-state Li-ion batteries

R. Zhang[1], W. Song[1,2], P. D. Nellist[1], P. G. Bruce[1,3,4,2]

[1]University of Oxford, Department of Materials, Oxford, United Kingdom
[2]The Faraday Institution, Didcot, United Kingdom
[3]University of Oxford, Department of Chemistry, Oxford, United Kingdom
[4]The Henry Royce Institute, Oxford, United Kingdom

Introduction: Solid-state lithium-ion batteries (SSLIBs) are promising candidates for next generation energy storage, owing to their improved safety while maintaining high energy density compared to conventional liquid electrolyte system lithium-ion batteries. [1] However, the commercialisation of SSLIBs are hindered by the capacity fading and voltage hysteresis which are closely related to side reactions at the solid-state electrolyte (SSE)/cathode interface [2].

Objective: To understand the origin of degradation and failure mechanisms in SSLIB, fundamental explanations of the electrochemical behaviour of SSLIB associated with the composition and structure change of SSE/cathode interphase will be discussed in this work.

Materials & Methods**:** Scanning transmission electron microscopy (STEM) has been extensively used as an atomic-scale characterisation technique. Together with annular dark field (ADF) detector, energy dispersive X-day spectroscopy (EDX) detector and electron energy loss spectroscopy (EELS) detector, the atomic position imaging, elemental mapping and electronic structure information can be simultaneously acquired. In this work, we applied ADF/EDX/EELS to study the interface between Ni-rich cathode material $LiNi_{0.6}Mn_{0.2}Co_{0.2}O$ (NMC622) and SSE Argyrodite Li_6PS_5Cl before/after cycling. Moreover, to distinguish the decomposition after cycling from beam damage, as they cause similar structural changes to the specimen, pristine argyrodite is examined in TEM for diffraction pattern evolution upon beam damage.

Results: Atomic-resolution HRTEM images of Argyrodite (Figure 1) has been successfully acquired and it shows the crystallite size is about 20-30nm while an amorphous phase is present. In the interface study, EDX elemental mapping (Figure 2) identifies an interface between NMC622 and Argyrodite. ADF images provide structural information, while EEL spectra reveal the oxidation state at high spatial resolution simultaneously. The oxidation state is determined by white-line intensity ratio L_3/L_2, the L_3/L_2 mapping will be discussed in the presentation.

Conclusion: It is observed in TEM that the primary effect of beam damage is amorphization. Compared to the pristine structure, NMC622 is slightly oxidised when in contact with Argyrodite due to the spontaneous reaction at SSE/cathode interface. With the comprehensive analysis of the microstructure and chemistry of SSE/cathode interphase by using ADF/EDX/EELS in STEM, our work can provide guide for future materials selection in Li-ion batteries by correlating the microstructure, composition with electrochemical performance.

References:
[1] N. Naoki *et al.* Mater. Today 18.5 (2015): 252-264
[2] A. Jeremie *et al.* Chem. Mater. 29.9 (2017): 3883-3890
[3] The authors acknowledge use of characterization facilities within the David Cockayne Centre for Electron Microscopy, Department of Materials, University of Oxford and in particular the Faraday Institution (FIRG007, FIRG008), the EPSRC (EP/K040375/1 "South of England Analytical Electron Microscope") and additional instrument provision from the Henry Royce Institute (Grant reference EP/R010145/1).

Figure 1

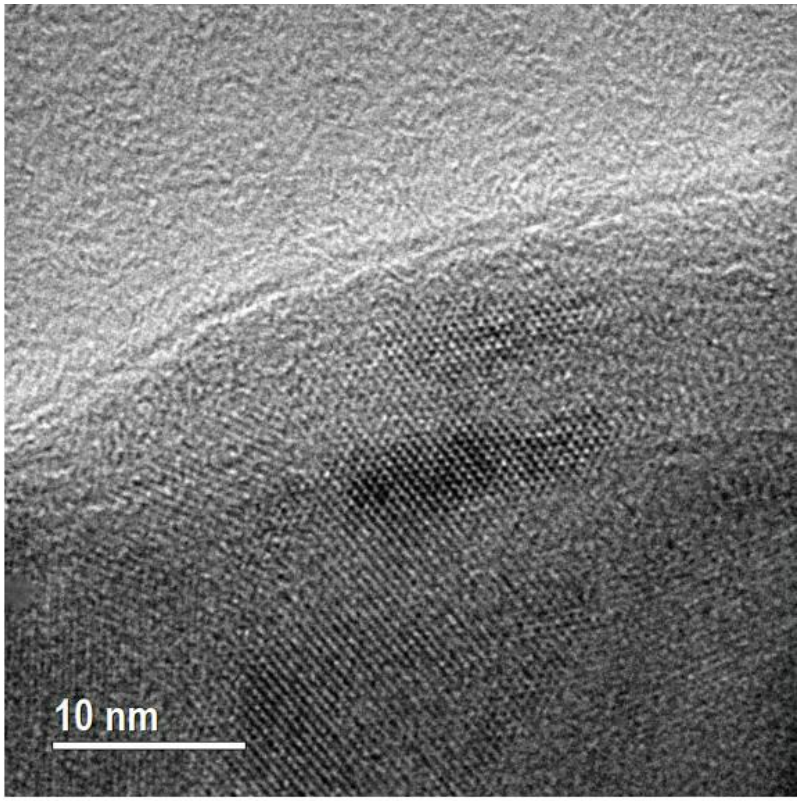

Figure1 HRTEM image of Argyrodite

Figure 2

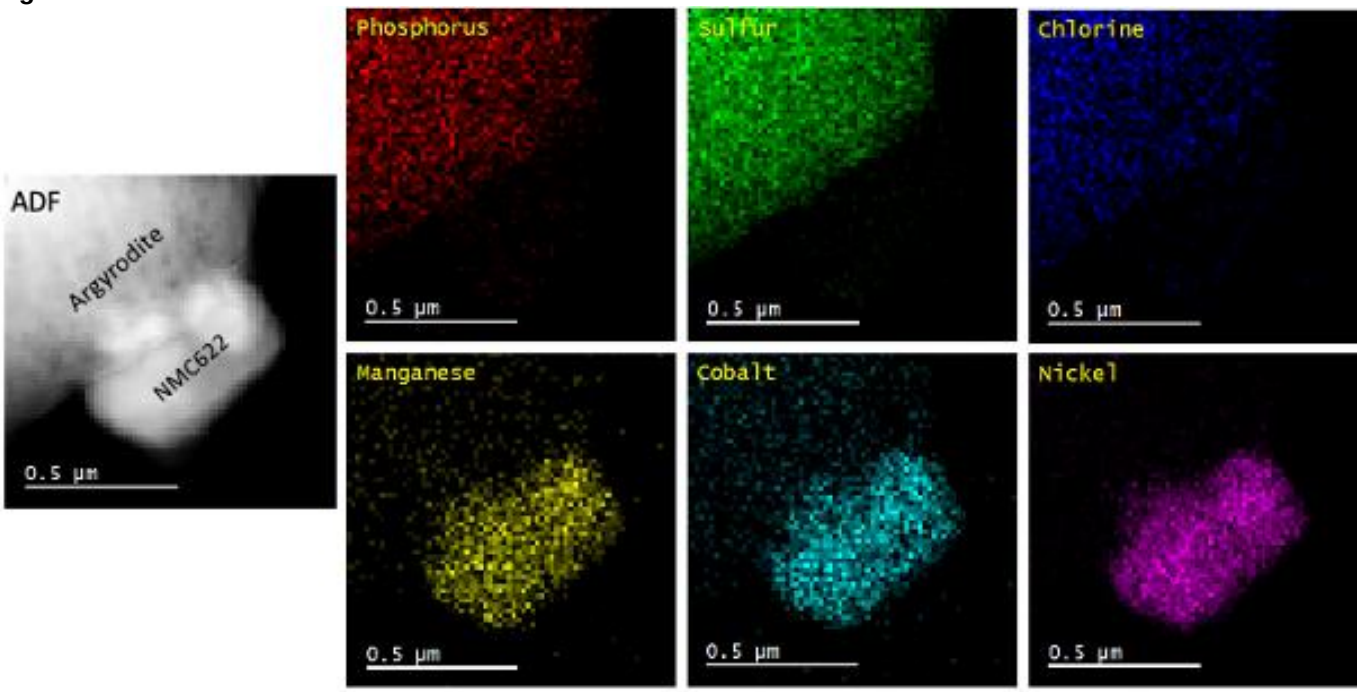

Figure 2 EDX elemental mapping of P, S, Cl, Mn, Co and Ni at Argyrodite/NMC622 interface

MS1.P020
Nature and origin of the spectral features observed in the valence energy loss of Li-Mn-Ni-O spinel oxides spectra with respect to Mn valency changes

M. K. Kinyanjui[1], P. Axmann[2], M. Mancini[2], G. Gabrielli[2], P. Balasubramanian[2], F. Boucher[3], U. Kaiser[4]

[1]University of Ulm, Electron Microscopy group of Materials Science, Ulm, Germany
[2]Centre for Solar Energy and Hydrogen Research (ZSW), Ulm, Germany
[3]Institut des Matériaux Jean Rouxel (IMN), Université de Nantes, Nantes, France
[4]University of Ulm, Electron Microscopy group of Materials Science, Ulm, Germany

Valence energy loss spectrum (VEELS) characterized by interband transitions, and plasmon excitations is rarely used in spectroscopy of Li ion battery materials. One reason being the large number of different excitations observed in this region as well as the difficulty in interpreting their nature and origin [1]. We have determined the spectral features observed in the VEELS spectra of Lithium-Manganese-Nickel spinel oxides (Li-Mn-Ni-O) with respect to Mn valency changes after insertion/extraction of lithium ion [2]. In Li-ion batteries, phase stability, voltage limits, and safety are closely related to the character of the transition metal ion in the cathode materials. This includes valency, spin state, co-ordination, and covalency [3].

We have determined the nature and origin of the spectral features observed in the VEELS spectra with respect to Mn valency changes during the lithiation of $LiNi_{0.5}Mn_{1.5}O_4$ to Lithium rich $Li_2Ni_{0.5}Mn_{1.5}O_4$ [1]. The lithiation process is characterized by a Mn valency change from Mn 4^+ in $LiNi_{0.5}Mn_{1.5}O_4$ to Mn $^{3+}$ in Lithium rich $Li_2Ni_{0.5}Mn_{1.5}O_4$. Figure 1 shows the VEELS spectra from $Li_2Ni_{0.5}Mn_{1.5}O_4$ (thin dotted curve) and $LiNi_{0.5}Mn_{1.5}O_4$ (thick solid curve). The VEELS spectra of $LiNi_{0.5}Mn_{1.5}O_4$ is characterized by sharp peaks around 7-10 eV whose intensity decrease with lithiation to $Li_2Ni_{0.5}Mn_{1.5}O_4$. Band-structure calculations and molecular orbital (MO) considerations show that the intense peaks in the VEELS spectra of $LiNi_{0.5}Mn_{1.5}O_4$ have a large contribution from ligand-metal-charge transfer (LMCT) transitions arising from states with mainly O-2p character to states with mainly Mn 3d character. Figure 2 displays a schematic MO diagram for a MnO_6^{9-} cluster with Mn valency of Mn 3^+ [4]. The figure shows hybridized molecular orbitals formed from Mn and O atomic orbitals. The dark squares represent filled states and the unfilled rectangles show the unfilled states. The solid arrows show the occupying spin of the electron, while dashed arrows show the possible interband transitions. LMCT transitions giving rise to sharp peaks observed in the VEELS spectra of $LiNi_{0.5}Mn_{1.5}O_4$ arise from the mainly O 2p non-bonding t2u and bonding t1u orbitals to the mainly Mn 3d anti-bonding t^*2g and e^*g orbitals.

In conclusion, we show that valence EELS spectra can be used to determine changes in the valency of the Mn ions in spinel oxide. The origins of the observed valence EELS spectra features is related to peaks shift, variations in occupancy, and variations in covalency as result of Mn valency changes occurring during lithiation.

Figure 1: Valence loss electron energy loss spectra (VEELS) obtained from lithium rich $Li_2Ni_{0.5}Mn_{1.5}O_4$ (thin dotted curve) and $LiNi_{0.5}Mn_{1.5}O_4$ (thick solid curve)

Figure 2: A schematic molecular orbital diagram from a MnO_6^{9-} cluster with Mn 3^+. The dark squares represent filled states and the unfilled rectangles show the unfilled states. The solid arrows show the occupying spin of the electron, while dashed arrows show the possible interband transitions.

References:
[1] M. K. Kinyanjui, P. Axmann, M. Mancini, G. Gabrielli, P. Balasubramanian, F. Boucher, M. Wohlfahrt-Mehrens, and U. Kaiser, Phys. Rev. Materials **1**, 074402(2017)
[2] J. M. Tarascon, E. Wang, F.K. Shokoohi, W.R. McKinnon, and S. Colson, J. Electrochem. Soc. 138, 2859 (1991)
[3] J. B. Goodenough, and Y. Kim, J. Solid State Chem. 182, 2904 (2009)
[4] D. M. Sherman, Am. Mineralogist 69, 788 (1984).

Figure 1

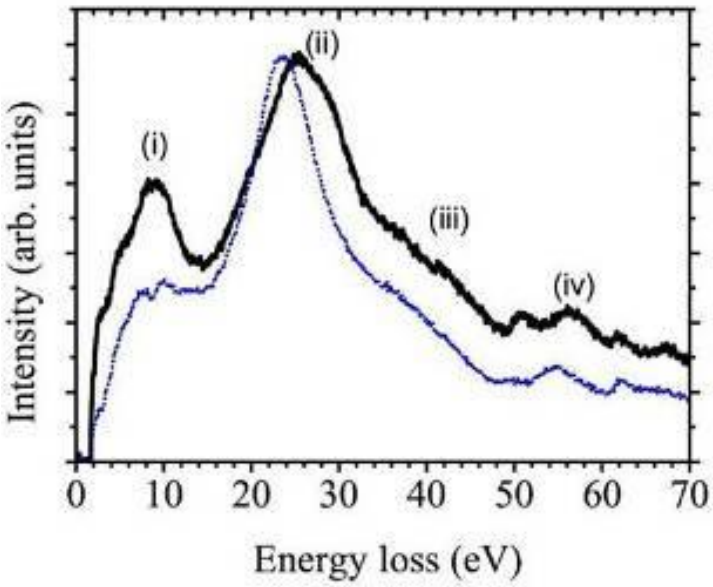

Figure 2

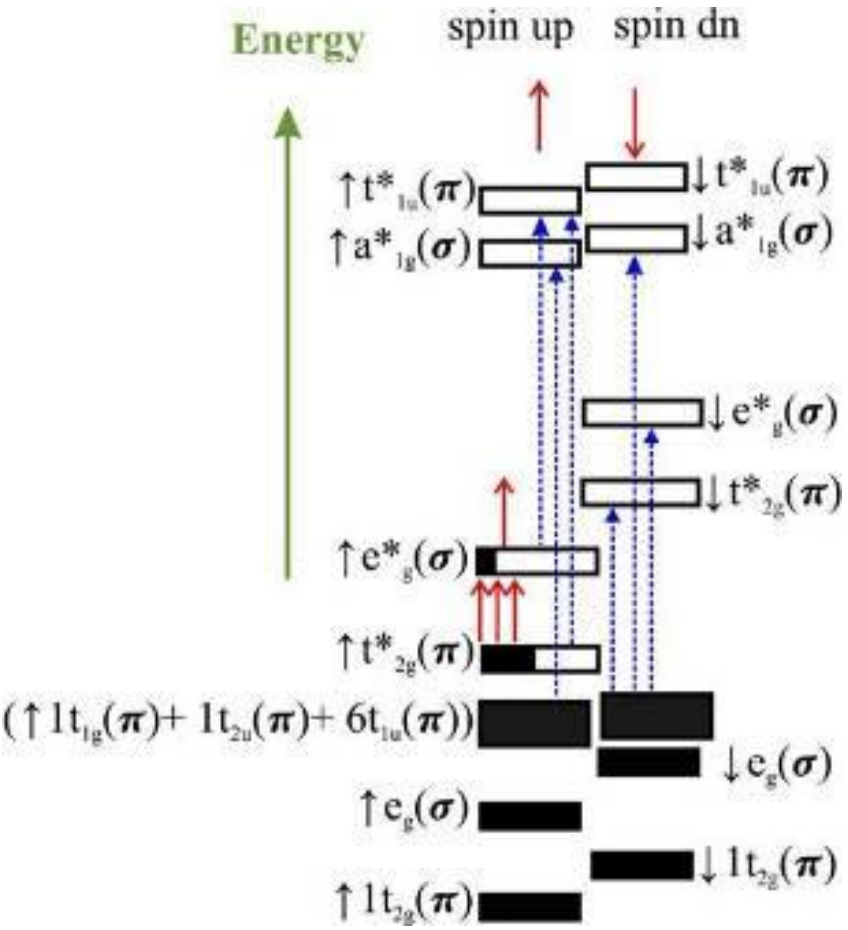

MS1.P021
Chemical state analysis of Silicon negative electrode material using SEM-SXES

Y. Yamamoto[1], T. Murano[1], S. Koshiya[1], Y. Hasebe[1], Y. Sasaki[1], H. Nishioka[1], R. Matsuda[2], K. Hikima[2], A. Matsuda[2]

[1]JEOL Ltd., Akishima, Tokyo, Japan
[2]Toyohashi university of technology, Toyohashi, Japan

Silicon (Si) has a large theoretical capacitance of 4200 mAh/g, and is attracting attention as a negative electrode material for Lithium (Li) ion secondary battery (LIB) to replace graphite. However, Si has problems such as volume expansion and decrease in charging efficiency during charging and discharging. Therefore, analysis for Si structure is being proceeded. In recent years, Soft X-ray emission spectrometer (SXES) that can be combined with an electron microscope has been developed (1). Chemical state analysis of sub-micron region on bulk materials can be successfully performed using a low voltage electron beam in the case of mounting SXES on a Field Emission-Scanning electron microscope (FE-SEM).

The purpose of this study is to perform elemental analysis using Energy dispersive spectrometry (EDS), chemical state analysis using SXES, and crystal structure analysis using Electron backscattered diffraction (EBSD) for the Si negative electrode of LIB, and attempting structural analysis of Si particles in charging state.

As a sample, a negative electrode prepared by mixing Li2S-P2S5-LiI solid electrolyte prepared by liquid-phase syntheses (2) and Si particles was used. A half-cell was prepared using this negative electrode and charged at 90% of the theoretical capacitance value of Si. After charging, it was cross-sectioned by an Ar ion beam using a CROSS SECTION POLISHERTM (JEOL, IB-19520CCP) under high vacuum and cooling conditions. A glove box filled with Ar gas and a transfer vessel were used in all processes to minimize the reaction of the sample with air.

Figure 1 shows the Backscattered electron (BSE) image by FE-SEM (JEOL, JSM-IT800) and elemental map by EDS (OXFORD, Extreme) for Si particle. Different contrast areas are observed inside the Si particles in the BSE image. As a result of elemental map, it was confirmed that the amount of Si count was larger in the brighter area of the BSE image, and Li is relatively more detected in the darker area.

Figure 2 shows the results of EBSD (OXFORD, Symmetry) and SXES (JEOL, SS-94000SXES) analysis of points (a) and (b) shown in the BSE image. The shape of Si L emission spectrum of (a) coincides with that of the spectrum of the crystalline Si as a reference. The EBSD pattern of (a) is also indexed with the EBSD pattern expected for crystalline Si. Therefore, uncharged crystalline Si remains in this part. On the other hand, the shapes of Si L and Li K emission spectra obtained at (b) suggest that Si and Li are alloyed. The EBSD pattern of (b) is indexed with the EBSD pattern expected for crystalline structure of Li15Si4 which is formed by charging (3). From these results, it can be confirmed that the alloys of Si and Li are mixed in several states inside the Si particle during the charging process.

In the analysis of the negative electrode Si, the Li content and the chemical state such as crystallinity can be detected at once using SEM-SXES. Furthermore, it is possible to deeply understand the data obtained by SXES-SEM analysis by combining with mutual complemental analysis methods such as BSE imaging by SEM, Li detectable EDS and EBSD. SEM-SXES is a very effective method for analysis of the sub-micron region of the Si negative electrode.

[1] Terauchi. M et al., *Journal of Electron Microscopy*, Vol. 61, (2012), P. 1–8
[2] Hikima. K et al., Solid State Ionics, Volume 354, (2020), 115403
[3] Obrovac. M. N et al., Electrochem. and Solid-State Lett., Vol.7, Num. 5, (2004), A93

Figure 1

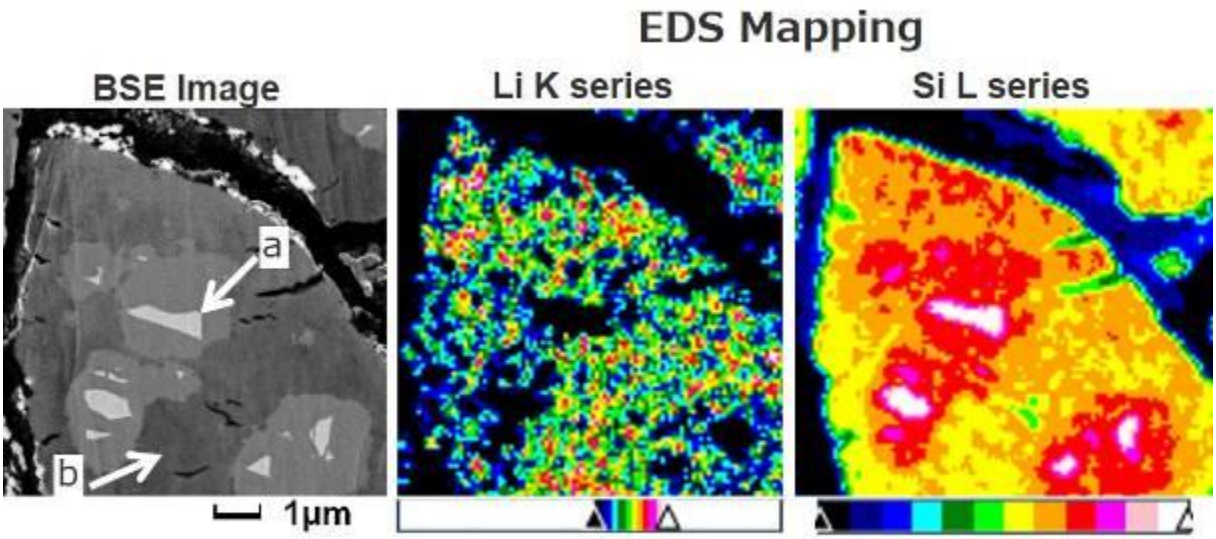

BSE image of Si cross-section and EDS Map results

Figure 2

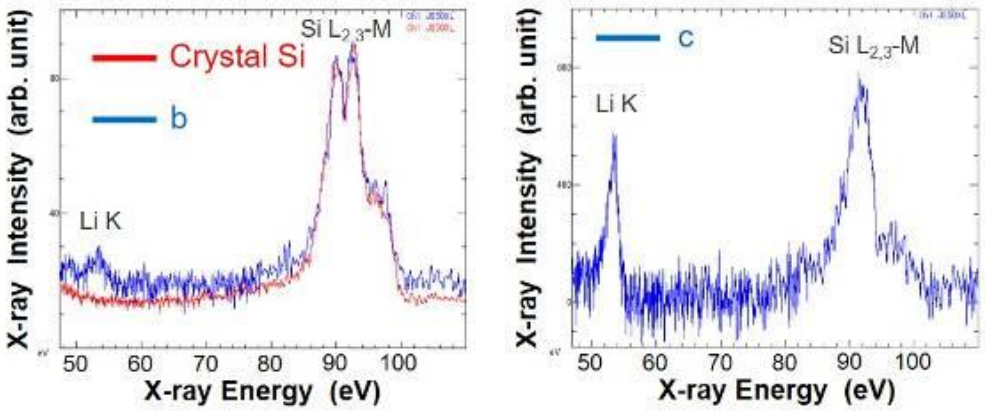

SXES spectrum (a)

SXES spectrum (b)

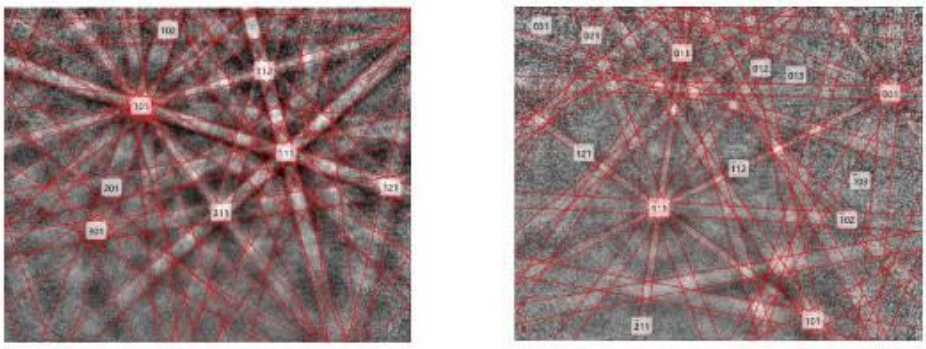

EBSD pattern (a): Indexed Si cubic

EBSD pattern (b): Indexed $Li_{15}Si_4$

SXES spectra and EBSD patterns of point a and point b

MS1.P023
Multi-method characterisations of the native oxide layer of Al Electrodes

D. Moser[1], S. Steiner[2], B. Gollas[2], A. Csik[3], M. Sterrer[4], G. Kothleitner[1,5]

[1]Institute of Electron Microscopy and Nanoanalysis, Graz University of Technology, Graz, Austria
[2]Institute for Chemistry and Technology of Materials, Graz University of Technology, Graz, Austria
[3]Institute of Nuclear Research, Hungarian Academy of Sciences, Debrecen, Hungary
[4]Institute of Physics, University of Graz, Graz, Austria
[5]Graz Centre for Electron Microscopy (ZFE), Graz, Austria

The aim of this work is to realize a new rechargeable Al-S battery, using an metallic aluminum anode in combination with a deep eutectic solvent (DES) consisting of AlCl3 and urea as electrolyte. [1, 2, 3] Starting with a natively passivated aluminum surface, the electrode performance is limited during discharge/charge cycling. Extending the contact between Al and electrolyte at open circuit potential (soaking) before subsequent low current cycling, can improve this issue (Figure 1.a).

Scanning electron microscopy (SEM) and transmission electron microscopy (TEM) in combination with spatially resolved energy dispersive x-ray spectroscopy (EDS mapping; Figure 1b and 1c) as well as x-ray photoelectron spectroscopy (XPS) and Secondary Neutral Mass Spectrometry (SNMS) revealed time-dependent modifications within the native oxide layer. A new type of thin film sample was developed to ensure a flatness in the nanometer range and the protection against oxygen and moisture during sample transfer. These methods are supplemented by optical in-situ studies to gain further insight on processes at and near the electrode surface.

Non-compact Al deposits are unwanted in batteries, because they can lead to short circuiting, capacity loss and a decrease in ion mobility. [4] Due to their high surface area, electrodes covered with these morphologies can have a low overpotential, which is generally an indicator for good electrochemical performance. This work shows that the results of electrochemical measurements can be misleading when encountering passivated surfaces and have to be interpreted alongside morphological studies.

Understanding the processes that occur during contact of the native oxide layer of Al with an AlCl3 and urea-based DES, paves the way to further advances in the field of secondary Al batteries with the ultimate goal of developing a low-cost, high-performance post-lithium technology.

Figure 1

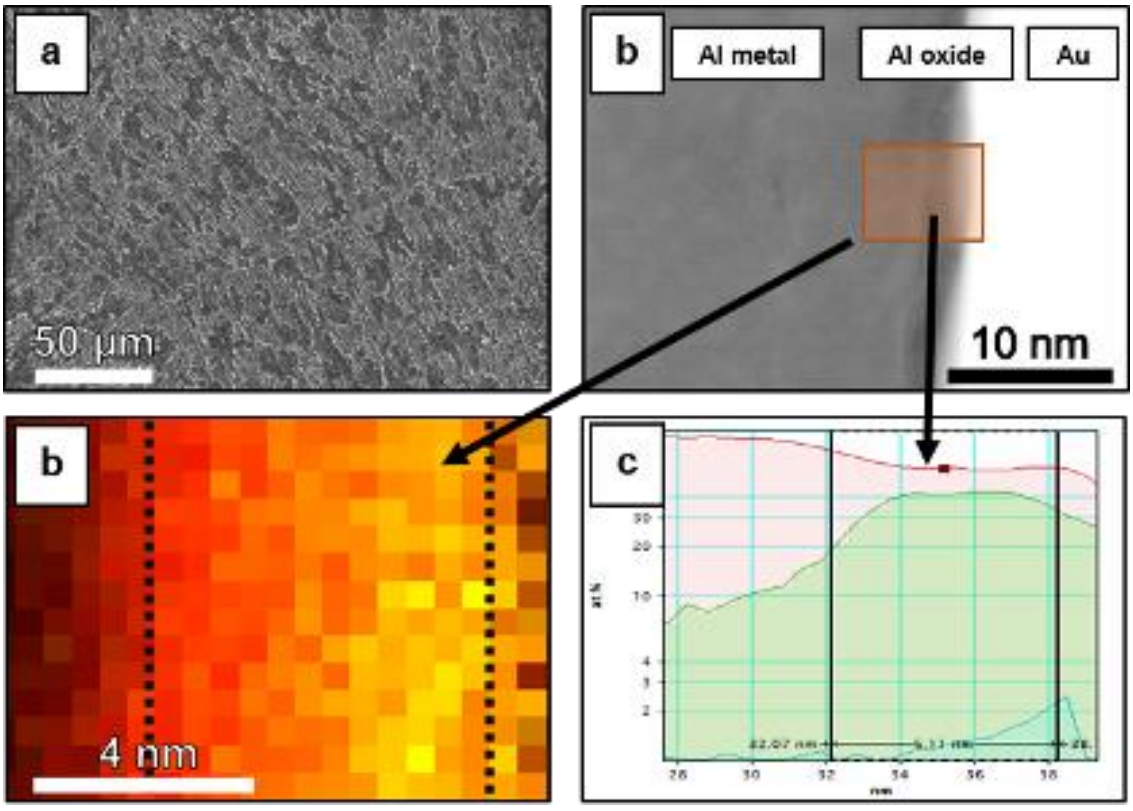

MS1.P024
Visualisation of the effects of grain boundaries in oxide electrolytes on Na-ion-migration

Z. Ding[1], G. Melinte[1,2], Y. Tang[1], C. Kübel[1,2,3]

[1]Karlsruhe Institute of Technology (KIT), Institute of Nanotechnology, Eggenstein-Leopoldshafen, Germany
[2]Helmholtz Institute Ulm, Ulm, Germany
[3]Institute of Nanotechnology & Karlsruhe Nano Micro Facility, Eggenstein-Leopoldshafen, Germany

Unlike popular sulfide or polymer based electrolytes serving in the all-solid-state batteries (ASSBs), oxide-based electrolytes presents a polycrystalline microstructure in which the grain boundaries (GB) are a non-negligible factor that decrease the overall ionic conductivity. However, while many reports discuss the influence of GBs on the ionic conductivity based on theoretical or spectroscopic data1,2, a comprehensive investigation at the atomic scale is still missing.

In order to understand the origin of low ionic conductivity of GBs of Na-β""-alumina, we are using high-resolution transmission electron microscopy (double corrected and monochromated Themis-Z(S)TEM) imaging and spectroscopy coupled to *in-situ* electrical probing. The crystallography of grain-boundaries and their influence on the anisotropic ion transport in Na-β""-alumina are investigated by 4DSTEM (Gatan one View IS camera) and high-resolution imaging. Electron energy loss spectroscopy (EELS)(K3 IS direct detection camera & GIF Continuum 970 HR) is probing the chemical and electronic properties of grain interior, GBs and potential phase impurities. In addition, differential phase contrast (DPC) (4-quandrant DF4 detector) imaging will be employed to analyze the space-charged layers (SCL) at GBs. Such a comprehensive approach offers invaluable insights into the properties of GBs and can help find new ways to mitigate their influence on the ionic conductivity of ASSBs.

For preparing selected GBs from a Na-β""-alumina ceramic electrolyte pellet (Ionotec Ltd) for TEM analysis, a Strata 400 S focus ion beam (FIB) (FEI company) system was used. The FIB based TEM preparation is following standard sample preparation approaches and attached to a Cu grid as counterelectrode. The Cu grid is assembled in a STM-TEM holder (ZepTools) with Au nano probe for in-situ bias experiment in the TEM.

Initial experiments focus on Na-β""-alumina as solid electrolyte under high *in-situ* biasing voltage up to ±30V. The initial high voltage helps to overcome the diffusion barrier at GBs and promotes the mobility of Na ions. Figure 1a shows an unindexed orientation map extracted from the 4DSTEM data showing the polycrystalline microstructure of the solid electrolyte. During biasing, Na segregation around certain GBs can be seen in real-time as the current increases due to the high Na ions mobility (Figure 1b and c). The final state of the segregated Na is shown in an EDX elemental map presented in Figure1d. The influence of the GB and the crystallography on the Na diffusion is very visible as the Na segregation appears to be promoted at certain GB geometries in agreement with the anisotropic 2D pathways for ion migration in Na-β""-alumina.

Present in-situ TEM measurements on Na-β""-alumina show that Na ion diffusion in polycrystalline materials and its behavior around GBs can be investigated by the means of electron microscopy. The initial results are used to create a characterization approach for the further TEM investigations not only on the single-phase electrolytes but also on the electrode-electrolyte interfaces.

Figure 1 a) RGB composite grain orientation mapping; **b)** Time series of HAADF-STEM images for different biasing periods which are corresponding to **c)** current to time curve (black) and voltage to time curve (green), respectively; **d)** HAADF-STEM EDS mapping after biasing period 6 in c.

[1] ACS Appl. Mater. Interfaces 2018, 10, 38151−38158
[2] Adv. Energy Mater. 2020, 10, 1902899

Figure 1

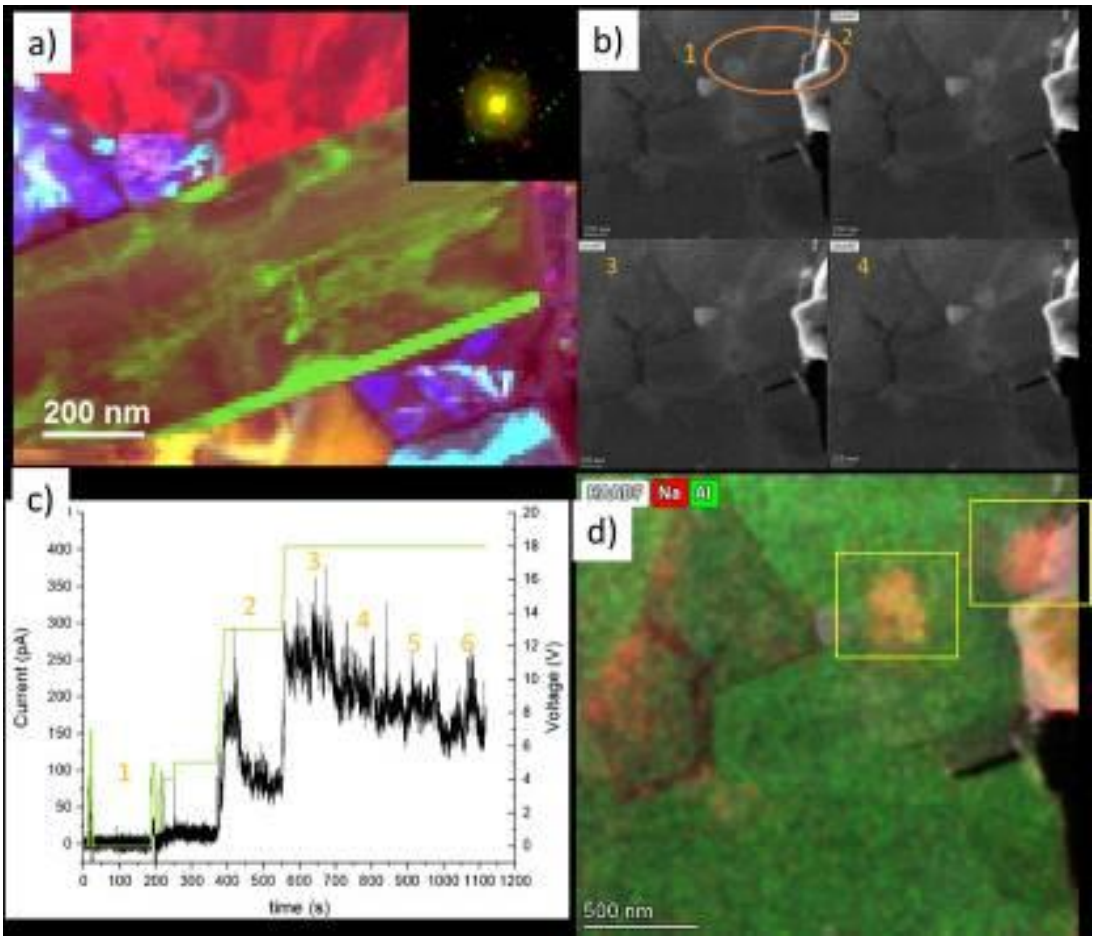
a)
200 nm
b)
1
2
3
4
c)
Current (pA)
Voltage (V)
time (s)
1
2
3
4
5
6
d)
Na
Al
500 nm

MS1.P025
Advanced identical location electron microscopy for the study of electrocatalytic effects of Pt-based nanoparticles

F. Ruiz-Zepeda[1,2], A. Hrnjić[1], A. Pavlišič[3], A. R. Kamšek[1], M. Gatalo[1], M. Bele[1], P. Jovanovič[1], G. Dražić[1]
N. Hodnik[1]

[1]National Institute of Chemistry, Department of Materials Chemistry, Ljubljana, Slovenia
[2]Institute of Metals and Technology, Department of Physics and Chemistry of Materials, Ljubljana, Slovenia
[3]National Institute of Chemistry, Department of Catalysis and Chemical Reaction Engineering, Ljubljana, Slovenia

In order to further understand the electrocatalytic performance of nanoparticles in fuel cells for the generation of clean energy, a close study on the changes happening at the surface and structure of the nanoparticles during electrochemical processes is necessary. The activity and stability of nanoparticles employed nowadays in the fuel cells industry are still below the desirable values to consider reaching a more wide application in electric vehicles [1]. When the electrocatalysts are submitted to electrochemical processes such as an activation protocol [2] or/and degradation cycling [3, 4], Pt-based metallic electrocatalysts typically suffer from dissolution or dealloying due to the harsh conditions occurring in a regular workload. Hence, identical location microscopy can shed some light by examining the same area (or spot) of the electrocalyst sample before and after an electrochemical process has taken place [5]. Current advances in electron microscopy methods and analysis can be incorporated and applied to retrieve important information regarding the effects on the structure and surface after degradation, and consequently try to improve their electrocatalytic properties. In this study, metallic Pt-based electrocatalysts were examined by identical location (IL) using aberration corrected scanning transmission electron microscopy (AC-STEM). Among other phenomena occurring during electrochemical degradation, recording individual nanoparticles at high resolution is highly valuable since then is feasible to discern whether they have experienced dissolution or redeposition on certain facets as well as analyzing precise information from the distribution of strain in the nanoparticle"s lattice. Different Pt-based systems were inspected under this methodology, and by being able to track these changes it was possible to gain a better overview of the different events involved in a single nanoparticle during the electrochemical cycling and on the existing relationship between nanostructure and the stability and activity of the electrocatalyst. Therefore the use of advanced IL-(S)TEM allowed us to go one step further and reach important observational structural and surface details that usually are hard to infer or interpret if the same nanoparticle is not followed during the steps of an electrochemical processes.

[1] K. Kodama, T. Nagai, A. Kuwaki, R. Jinnouchi, Y. Morimoto, Nat. Nanotech. 16 (2021) 140–147.
[2] A. Hrnjić, F. Ruiz-Zepeda, M. Gaberšček, M. Bele, L. Suhadolnik, N. Hodnik, P. Jovanovič, J. Electrochem. Soc. 167 (2020) 166501.
[3] F. Ruiz-Zepeda, M. Gatalo, A. Pavlišič, G. Dražić, P. Jovanovič, M. Bele, M. Gaberšček, N. Hodnik, Nano Lett. 19 (2019) 4919–4927.
[4] S. Rasouli, D. Myers, N. Kariuki, K. Higashida, N. Nakashima, P. Ferreira, Nano Lett. 19 (2019) 46–53.
[5] K. J. J. Mayrhofer, J. C. Meier, S. J. Ashton, G. K. H.Wiberg, F. Kraus, M. Hanzlik, M. Arenz, Electrochem. Comm. 10 (2008) 1144-1147.

MS1.P026
In-line detection of residual lens aberrations influencing differential phase contrast STEM images

J. Bürger[1], T. Riedl[1], J. K. Lindner[1]

[1]Paderborn University, Paderborn, Germany

Introduction: Differential phase contrast (DPC-)STEM imaging allows to analyse electric fields with sub-atomic resolution owing to state-of-the-art Cs-correction. Even though today, the optimisation of illumination conditions with e.g. a hexapole Cs-corrector minimising the lens aberrations up to the fifth geometrical order, residual lens aberrations have a considerable impact on the evaluation of measured electric fields.

Objectives**:** The present work evaluates the influence of residual lens aberrations and specimen tilt by analysing the deflection distribution in multislice simulated DPC images of SrTiO3 [001]. The deflection distribution is displayed as a scattergram showing the number of pixels within a small interval of deflection magnitude and direction. In addition, the scattergram is utilized as an "in-line"-tool during microscope operation. Its applicability to detect and subsequently correct residual lens aberrations is examined.

Materials and methods: DPC image simulations of SrTiO3 [001] and Si [110] are obtained using the multislice Dr. Probe software [1] in order to analyse the influence of specimen thickness, defocus, two-fold as well as three-fold astigmatism, coma, third-order spherical aberration and specimen tilt. Atomically resolved DPC images of Si [110] are acquired with a probe-side Cs-corrected JEOL JEM ARM200F equipped with a rotatable eight-fold segmented annular detector for the determination of beam deflection. A self-written Matlab-based program calculates and displays the scattergram directly after image acquisition.

Results and Discussion: SrTiO3 [001] image simulations show that increasing the specimen thickness above 9 nm reduces the measurable deflection per specimen thickness. This reduction arises from the presence of scattering, diffraction contrasts in the detection plane and the beam extension inside the specimen [2]. Furthermore, diffraction contrasts lead to line-like features at interatomic positions of the DPC images (Figure 1(a) marked with white lines) and are thus visible in the scattergram (Figure 1(b)). A defocus enhances these line-like features, reduces the overall measurable deflection magnitude, and thus compresses the scattergram deflection distribution. For higher order lens aberrations and specimen tilt, the scattergram changes characteristically. E.g., two-fold astigmatism gives rise to elongated DPC image features (Figure 1(c)) and a laterally compressed scattergram in the astigmatism direction (Figure 1(d)). Thus, an "in-line" scattergram analysis readily enables microscopists to detect residual lens aberrations and specimen misalignment. The applicability of scattergram analysis is confirmed by DPC measurements on Si [110] yielding good agreement with simulated images.

Conclusions: DPC imaging is highly sensitive to lens aberrations, specimen thickness and tilt. Lens aberrations have a characteristic influence on the beam deflection distribution. Thus, an "in-line" analysis of the deflection distribution enables microscopists to minimise residual lens aberrations.

[1] J. Barthel, Ultramicroscopy 193 (2018): 1-11.
[2] J. Bürger, T. Riedl, J.K.N. Lindner, Ultramicroscopy 219 (2020): 113118.

Figure 1: a) DPC image simulation of 3.51 nm SrTiO3 [001] without lens aberrations (defocus: -2 nm below the entrance slice), b) the corresponding scattergram, and c) with additional 4 nm of two-fold astigmatism exhibiting a laterally compressed scattergram in d).

Figure 1

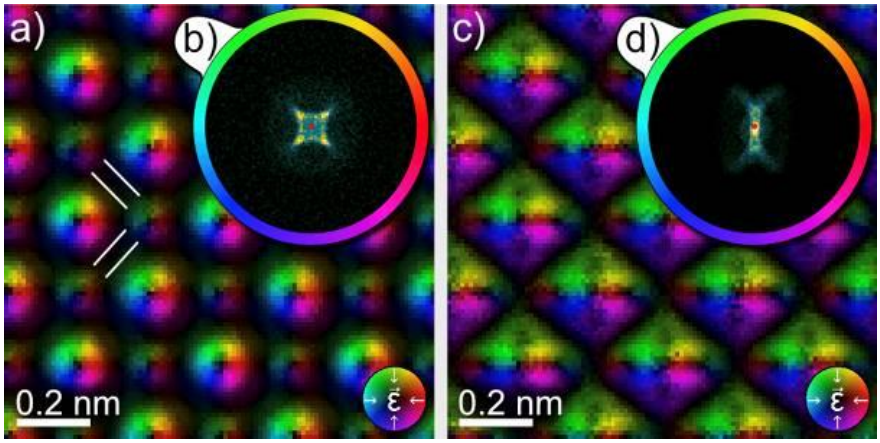

MS1.P027
HR(S)TEM analysis of phase changes and oxygen distortions in LiNixMnyCozO2 (NMC)

M. Boniface[1], S. Qian[2], T. Lunkenbein[1], H. A. Gasteiger[2]

[1]Fritz Haber Institute of the Max Planck Society , Department of Inorganic Chemistry, Berlin, Germany
[2]Technical University of Munich, Institute for Electrical Energy Storage Technology, Munich, Germany

Introduction: Layered lithium nickel manganese cobalt oxides (LiNixMnyCozO2, NMC) are one of the most promising class of cathode materials for Li-ion batteries thanks to their high specific capacity and energy density [1]. Given the sloped voltage profile of NMC, an even higher capacity and energy density can be achieved when the upper cutoff voltage is increased above the usual 4.3 V vs. Li+/Li limit [2]. Under such conditions, NMC electrodes age quicker with an increased formation of inactive spinel and rock-salt phases, which are accompanied by the release of lattice oxygen at high degrees of delithiation [2,3]. Understanding this ageing mechanism is critical to engineering more efficient NMC cathodes in the future.

Objectives: In this work, we aim to (i) gather a better understanding of the phase transitions happening during the oxygen release in NMC materials as well as (ii) study the oxygen sublattice itself, both in conventional NMC111 and Ni-rich NMC811.

(i) HRTEM analysis of the distribution of the spinel and/or rock-salt phases across aged primary NMC particles will reveal whether phase transitions are limited to particle surfaces or can be found in the bulk. NMC particles are too large (5-15µm) to be observed directly and FIB lamellae of complete cross-sections of particles can be prepared.

(ii) Measure oxygen-oxygen distances in TmO6 octahedra from high resolution annular bright field STEM (ABF-HRSTEM) images of the layered structure at different stages of ageing [4]. These O-O distances vary with the local Li occupancy i.e. the local state of charge (SoC), which can also be determined by counting Li atoms. Also of interest is the established relationship between SoC and lattice parameters for NMC materials [5], which can here be checked locally.

Materials and Methods: Samples were prepared by subjecting NMC111 and NMC811 particles to chemical delithiation (~60% SoC) and a thermal heat treatment (495°C) [6] in order to emulate harsh electrochemical cycling conditions [7] and yield extremely aged oxygen depleted materials that have undergone phase transition. Prior to TEM analysis, extensive characterization was carried out (TGA-MS, XPS, XRD) and revealed the presence of spinel and disordered layered phases.

Results: Preliminary experiments have shown unexpectedly large spinel domains in the heat-treated samples. Experiments on FIB lamellae are ongoing. ABF-HRSTEM allowed us to detect individual O and Li atoms and measure O-O distances of 400 pm (axial) and 270 pm (equatorial).

Figure 1: a) TEM observation of a NMC111 particle after chemical delithiation and heat-treatment. b) Fast Fourier transform (FFT) of a. c-d) Inverse FFT of b. after filtering for reflections specific to the layered and spinel phases. e) Filtered ABF-HRSTEM image obtained from stack averaging. The inset shows individual O (red), Tm (green) and Li (silver) atoms.

[1] K. G. Gallagher et al., Energy Environ. Sci., 7, 1555 (2014)
[2] Jung et al., *J. Electrochem. Soc.*, 2017, 164, 7, A1361-A1377
[3] Teufl et al., *J. Electrochem. Soc.*, 2018, 165, 11, A2718-A2731
[4] Liberti, E., et al., *Ultramicroscopy* 210 (2020): 112914.
[5] Buchberger et al, *J. Electrochem. Soc., 2015, 162 ,14, A2737-A2746*
[6] Qian et al., PRiME 2020 (ECS, ECSJ, & KECS Joint Meeting), 2020
[7] Bak et al., *ACS app. mat & int.,* 6.24 (2014): 22594-22601

Figure 1

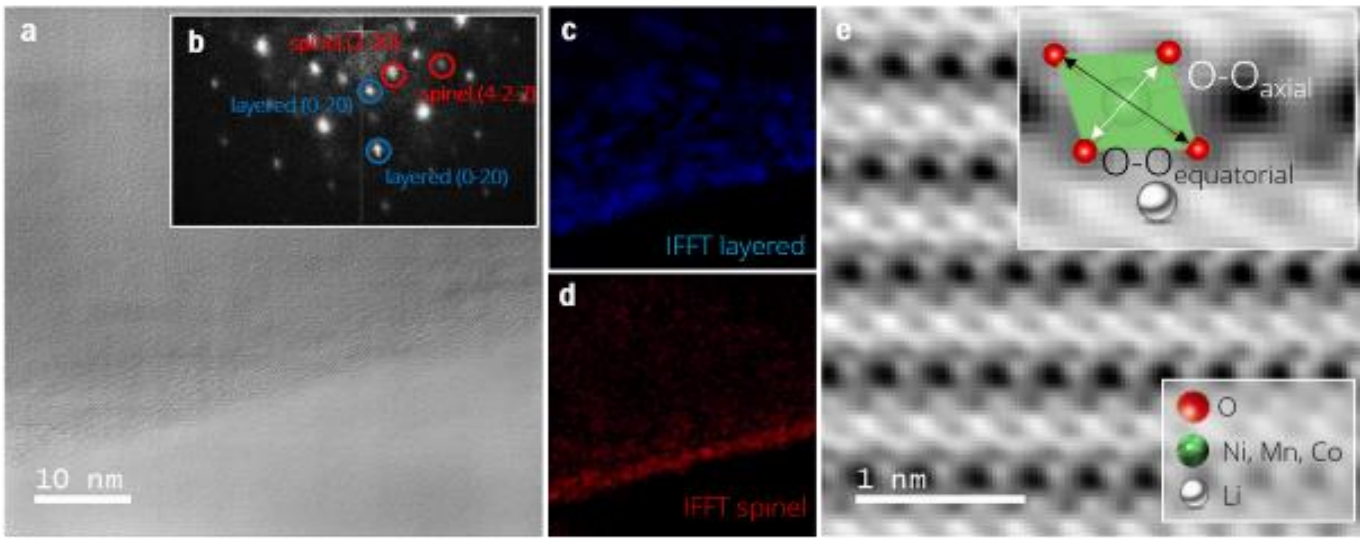
a
b
layered (0-20)
spinel (4-2-2)
layered (0-20)
10 nm
c
IFFT layered
d
IFFT spinel
e
O-O axial
O-O equatorial
1 nm
O
Ni, Mn, Co
Li

MS1.P028
Diffusion along defects in nitride multilayer thin films for energy applications as observed by state-of-the-art (S)/TEM and APT methods

M. Garbrecht[1], I. McCarroll[1], V. Bhatia[1], A. Indiradevi Kamalasanan Pillai[1], L. Yang[1], J. M. Cairney[1], B. Saha[2]

[1]The University of Sydney, Australian Centre for Microscopy and Microanalysis, Sydney, Australia
[2]Jawaharlal Nehru Centre for Advanced Scientific Research (JNCASR), Bangalore, India

Device failure from diffusion short circuits in microelectronic components occurs via thermally induced migration of atoms along high-diffusivity paths: dislocations, grain boundaries, and free surfaces [1-3]. Knowledge about the structural features along which diffusion paths in solids are formed is hence of great importance, since even well-annealed single-grain metallic films contain dislocation densities of about 10^{14} m^{-2}. While its theoretical concept was established already in the 1950s [4] and its contribution is commonly measured using indirect tracer, spectroscopy, or electrical methods [5], no direct observation of DPD at the atomic level has been reported until very recently [6]. Epitaxial metal/semiconductor nitride superlattices and multilayers are known to be promising candidates for applications as ultra-hard- and thermal- coatings, as well as for thermoelectric and plasmonic devices [7], and it was recently demonstrated that such superlattices can be grown epitaxially with low-defect densities by magnetron sputtering [8-10]. We present atomically resolved STEM images of the onset and progression of diffusion along threading dislocations in sequentially annealed nitride metal/semiconductor superlattices (Figure 1 a-c). The STEM micrographs showing the same region at different time-steps during annealing are accompanied by EDS maps and GPA analysis, and diffusivity coefficients are calculated directly from them. Most importantly, we show that this type of diffusion is independent of concentration gradients in the system but governed by the reduction of strain fields in the lattice [6]. The study of diffusion in this type of superlattice is important for the understanding of their potential applications at elevated temperatures [11-12].

Secondly, we present STEM imaging and EDS mapping in tandem with atom probe tomography (APT) of another metal/semiconductor superlattice thin film as a model system (Figure 1 d-f) to discuss the relative advantages of atomic resolution STEM and APT, by comparing results obtained from the same superlattice sample, and show that pitfalls of the individual techniques can be overcome by combining them [13]. Aberration-corrected STEM was employed using ACMMs (Australian Centre for Microscopy & Microanalysis) image- and probe-corrected and monochromated FEI Themis-Z 60-300 kV instrument equipped with a high-brightness XFEG source and Super-X EDS detector for ultra-high count rates.

Figure 1 (a-b): Heteroepitaxial metal/semiconductor nitride superlattice showing atomically flat interfaces [9]. (c): Pipe diffusion along a dislocation in HfN/ScN [6]. (d): APT needle shaped sample imaged by STEM-EDS mapping. (e-f): Oxygen rich voids decorate a defect throughout the superlattice stack, as imaged by STEM (e) and APT (f).

[1] R. S. Barnes, Nature 166, (1950)
[2] A. D. Le Claire, Philos. Mag. 42**,** (1951)
[3] N. A. Gjostein, In: Diffusion, (1973)
[4] R. Smoluchowski, Phys. Rev. 87**, (**1952)
[5] H. Mehrer, Diffusion in Solids, Berlin, 2007
[6] M. Garbrecht et al, Sci. Rep. **7,** (2017)
[7] T. D. Sands et al, Mater. Sci. Rep. 5, (1990)
[8] J. L. Schroeder et al, J. Mater. Sci. 50**,** (2015)
[9] B. Saha et al, Phys. Rev. B. 93**,** (2016)
[10] M. Garbrecht et al, J. Mater. Sci. 51**(**17), (2016)
[11] M. Garbrecht et al, Phys. Rev. Materials 01**,** (2017)
[12] M. Garbrecht et al, J. Mater Sci. 53(6) (2018)
[13] M. Garbrecht et al, J. Mater Sci. 55(4) (2020)

Figure 1

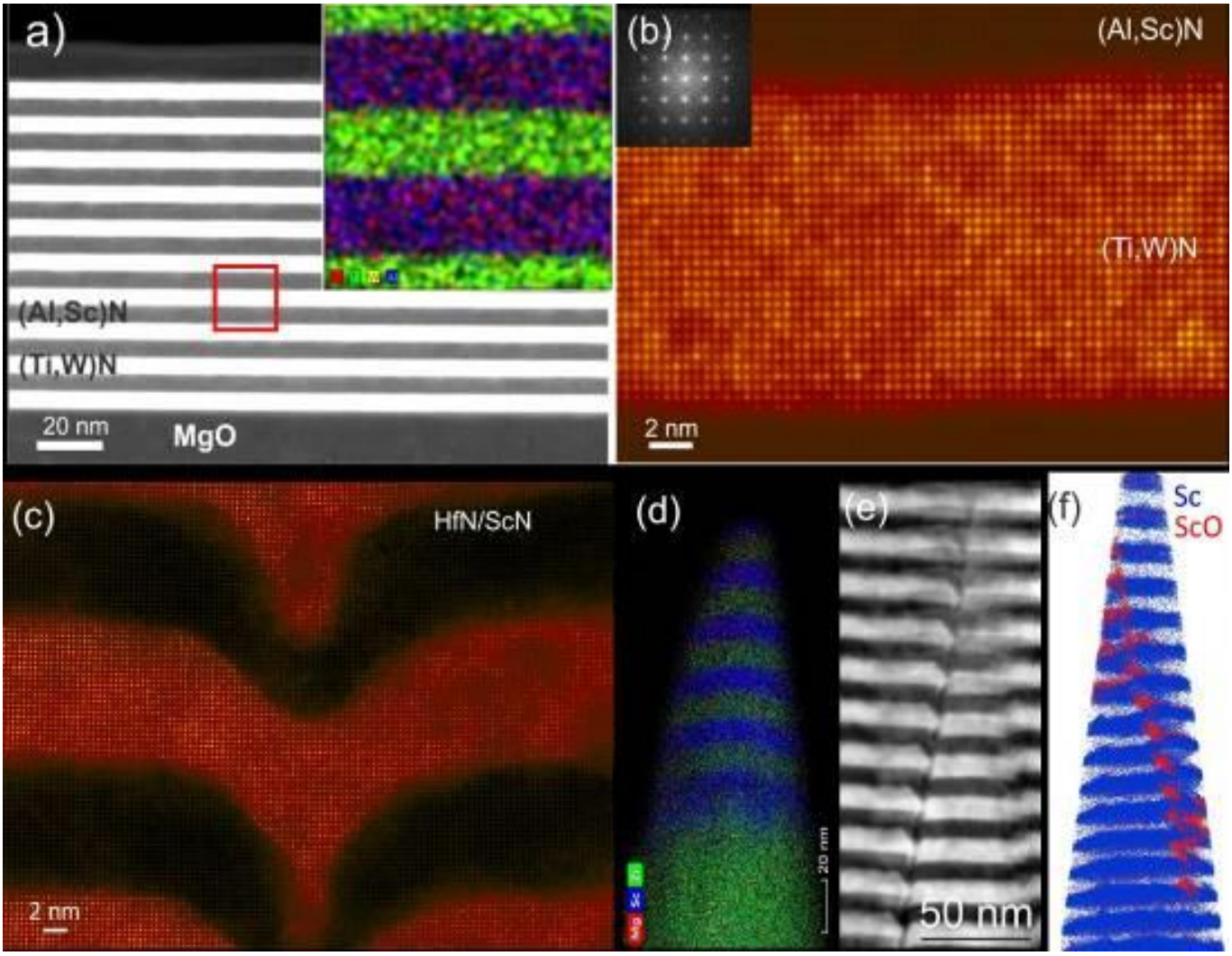
a)
(Al,Sc)N
(Ti,W)N
20 nm
MgO
(b)
(Al,Sc)N
(Ti,W)N
2 nm
(c)
HfN/ScN
2 nm
(d)
(e)
50 nm
(f)
Sc
ScO

MS1.P029
Investigations on sintering behavior of LLZTO/NCM composite cathodes for all-solid-state batteries

E. Reisacher[1], S. Kreißl[1], P. Kaya[1], V. Knoblauch[1]

[1]Material Research Institute (IMFAA), Aalen University, Aalen, Germany

LLZTO ($Li_{6.6}La_3Zr_{1.6}Ta_{0.4}O_{12}$) is a promising oxide solid electrolyte exhibiting a high chemical stability against Li metal, a wide electrochemical window and a high ionic conductivity reaching close to 10^{-3} S cm^{-1} at room temperature, while NCM ($Li_1Ni_{0.33}Co_{0.33}Mn_{0.33}O_2$) is a cathode active material providing high specific capacity [1] for solid state batteries. Despite their great potentials, there are still limitations to surmount, especially in manufacturing dense and thermodynamically stable composite electrodes [2] due that LLZTO and NCM are not stable at elevated temperatures in ambient atmosphere, presumably because of the presence of CO_2[3]. This emphasizes the need for advanced/alternative sintering methods or the usage of sintering additives to enable the manufacturing of high-performance composite cathodes [4,5] and further investigations of the sintering behavior in inert atmosphere.

In this study, the sintering behavior of LLZTO/NCM composite cathodes was investigated as a function of sintering temperature by X-ray-diffraction (XRD) and scanning electron microscopy (SEM). LLZTO powder was synthesized by solid-state reaction and the obtained LLZTO was mixed with NCM using Thinky mixer for 5 min at 300 rpm to prevent particle cracking. These composite powders were uniaxially pressed and sintered in air- and Ar-atmosphere at various temperatures. XRD results showed that decomposition of the NCM starts at 700°C and get more pronounced with increasing temperature until most of the NCM is decomposed at 1100°C (Figure 1a & 1b). At higher temperatures, decomposition products such as $La_2Zr_2O_7$, $La(Mn,Ni)O_3$ and Li-Co-oxides are formed through the reaction with the solid electrolyte (Figure 1a & 1b). At the same time, we observed hints of grain growth of NCM-primary particles above 900°C (Figure 2c). Increasing the temperature up to 1100 °C in order to get higher densification results in decomposition of the active material (Fig 1b & 2e).

Since 700°C was identified as a critical temperature where decompositions of NCM starts, we investigated sintering behavior at this temperature under Ar-atmosphere. At 700°C, we did not find any significant differences in SEM images compared to air-sintering (Figure 2b). However, XRD results demonstrate that sintering in inert Ar-atmosphere inhibits the decomposition of the NCM up to a temperature of 950°C (Figure 1c & 1d). Similar to air- sintering, hints of grain growth of NCM-primary particles are observed above 900°C, too (Figure 2d).

Figure 1: (a) XRD patterns of LLZTO/NCM composite cathodes sintered at different temperatures in ambient atmosphere. (b) Enlarged view of the pattern (31-38°) for the sample sintered at 1100°C in ambient atmosphere. (c) Comparison of XRD patterns of composites cathodes sintered in ambient and inert atmosphere. (d) Enlarged view of the XRD patterns (31.50-33.50°) of composite cathodes sintered in air and inert atmosphere at 900°C and 950°C.

Figure 2: SEM BSE images of LLZTO/NCM composite cathodes sintered at (a) 700°C/air, (b) 750°C/Ar, (c) 1000°C/air, (d) 950°C/Ar and (e) 1100°C/air.

References:
[1] Zhang, Zhizhen, et al., Energy & Environmental Science 11.8 (2018): 1945-1976.
[2] Ren, Yaoyu, et al., Journal of Materiomics 2.3 (2016): 256-264.
[3] Kim, Younggyu, et al., Chemistry of Materials 32.22 (2020): 9531-9541.
[4] Ihrig, Martin, et al., Journal of Power Sources 482 (2021): 228905.
[5] Shin, Ran-Hee, and Sung-Soo Ryu., Journal of Nanoscience and Nanotechnology 19.3 (2019): 1809-1813.

Figure 1

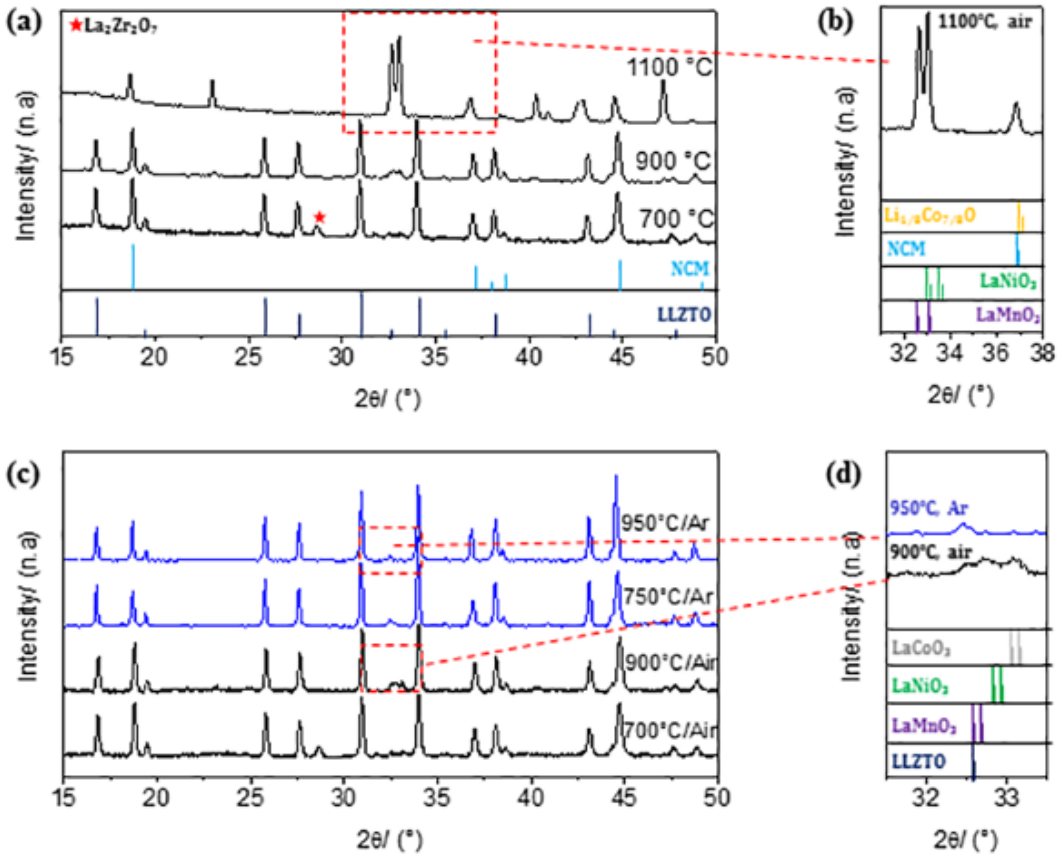

Figure 2

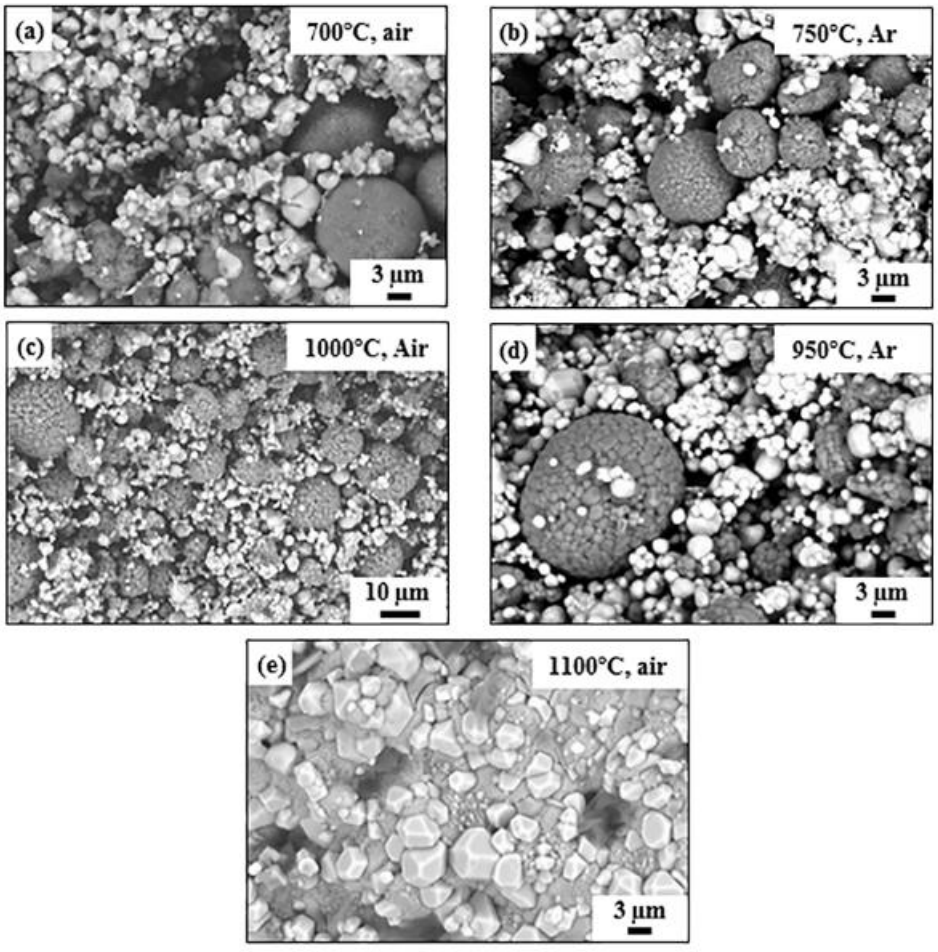

MS1.P030
Microstructural investigations on selectively laser treated LLZTO solid electrolyte

P. Kaya[1], S. Kreißl[1], D. Kolb[2], E. Reisacher[1], S. Ruck[2], H. Riegel[2], V. Knoblauch[1]

[1]Materials Research Institute (IMFAA) — Aalen University, Aalen, Germany
[2]Laser Application Center (LAZ) — Aalen University, Aalen, Germany

Energy conversion and storage applications are the key technologies for e-mobility. Besides the development of suitable materials, alternative approaches for microstructural design [1] and suitable manufacturing technologies [2,3] are of great importance in order to meet the requirements regarding performance as well as safety and durability. In this context, additive manufacturing (AM) techniques have gained significant attention to fabricate complex components with specified microstructures and almost unlimited freedom of design [4]. In the field of energy storage, the future potential is currently attributed to solid-state batteries as they are safer and more stable high-energy storage systems [5]. However, the manufacturing of solid-state batteries still remains a major challenge. Therefore, in this study, we investigated the laser-powder interaction using the selective laser sintering AM methods to optimize the sintering process of solid separators for solid-state batteries. $Li_{6.6}La_3Zr_{1.6}Ta_{0.4}O_{12}$ (LLZTO) was synthesized as an electrolyte powder by solid-state reaction and then a single layer of LLZTO powder on Al_2O_3 substrates, as well as pressed pellets of the electrolyte powder, were treated with different lasers in NIR and MIR spectrum range by varying the process parameters such as laser power, scan speed and track overlap. For comparison, a solid separator was produced by the conventional sintering method as well. Phase and microstructural analyses were performed by XRD and SEM (SE: secondary electron; BSE: backscattered electron) techniques, respectively. NIR laser radiation shows insufficient absorption into the LLZTO (Figure 1a & 1b). However, the MIR laser technology is promising for sintering LLZTO (Figure 2d) that is confirmed by large spectral-range FTIR-measurements. Moreover, no reaction product between LLZTO and the Al_2O_3 substrate was observed in the XRD pattern of the laser-treated samples (Figure 2a).

Figure 1: SEM SE image of (a) LLZTO pellet with NIR laser-treated regions. (b) Enlarged image of a NIR laser-treated region marked with green rectangular in "a".

Figure 2: (a) XRD pattern on the LLZTO powder, pristine substrate and MIR laser-treated region. (b) SEM BSE image of a MIR laser-treated region. (Bright regions: the laser-treated area, dark regions: substrate and loosen powder) (c) Enlarged image of the MIR laser-treated region marked in "b" (d) MIR laser sintered LLZTO region.

References:
[1] P. Kaya, G. Gregori, P. Yordanov, E. Ayas, H.-U. Habermeier, J. Maier, S. Turan, *Journal of the European Ceramic Society* 2017, *37*, 3367.
[2] J. Schnell, H. Knörzer, A. J. Imbsweiler, G. Reinhart, *Energy Technol.* 2020, *6*, 1901237.
[3] M. Bolsinger, M. Weller, S. Ruck, P. Kaya, H. Riegel, V. Knoblauch, *Electrochimica Acta* 2020**,** *330*, 135163.
[4] M. Cheng, R. Deivanayagam, R. Shahbazian-Yassar, *Batteries & Supercaps* 2020**,** *6*, 8.
[5] J. Janek, W. G. Zeier, *Nat Energy* 2016**,** *1*, 1167.

Figure 1

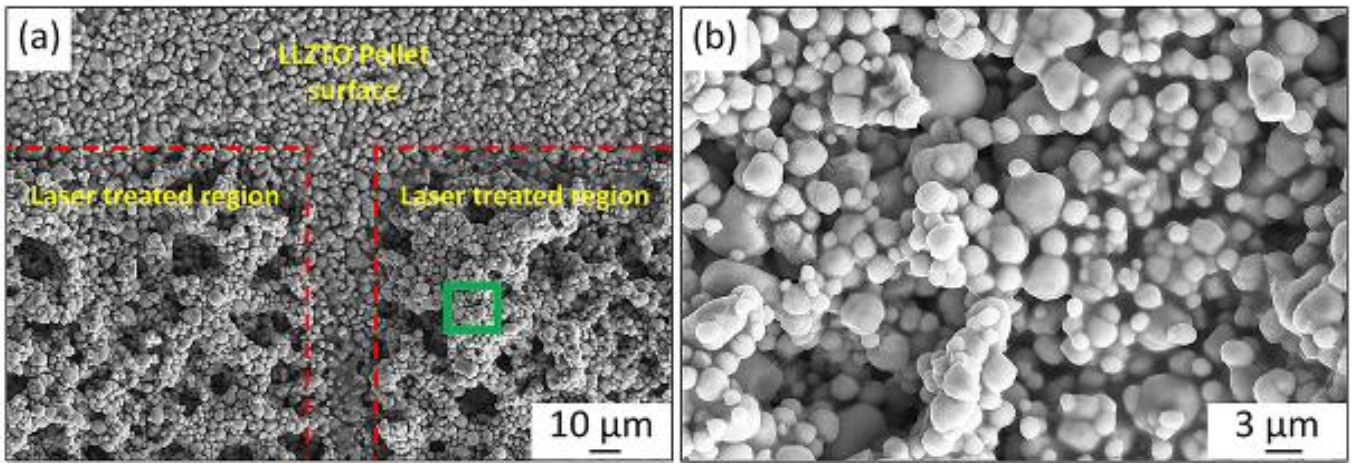

Figure 2

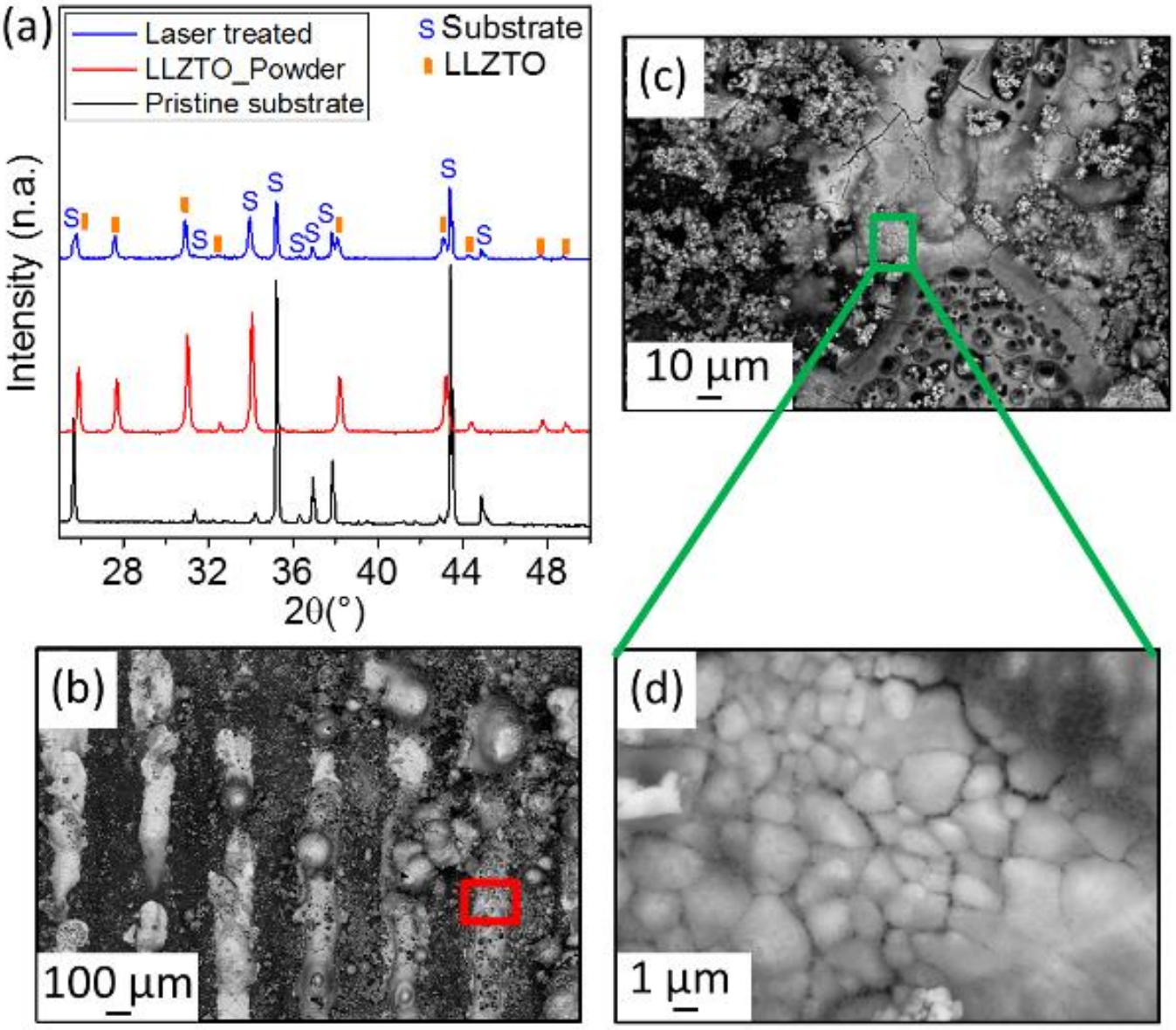

MS1.P031
Exploring low-dose EBSD acquisition using a direct electron detector

M. Nowell[1], R. De Kloe[1]

[1]EDAX LLC, Mahwah, NJ, United States

Electron Backscatter Diffraction (EBSD) has become an established microanalysis technique for the characterization of crystalline microstructures with a Scanning Electron Microscope (SEM). As the spatial scale of the microstructures of interest decreases, there is increasing interest in improving the EBSD spatial resolution through improved detector sensitivity and operation at lower beam currents and acceleration voltages. Traditional EBSD detectors use a phosphor screen optically coupled to a CMOS or CCD-based imaging sensor. The efficiency of these detectors can decrease at these lower beam dose conditions, and limit analytical performance.

With direct electron detection, the need for a phosphor screen and optical coupling system is eliminated. Electrons directly impinge onto the sensor surface, and the resulting charge is transferred directly to the thresholding, counting, and read-out circuitry. Direct detection technology has been successfully applied in the Transmission Electron Microscopy (TEM), and recent efforts to use this technology for EBSD pattern collection in an SEM have been reported [1-3]. In this work, a hybrid-pixel direct detector has been used to collect EBSD data. With this detector, there is no read-noise associated with detection. This allows for pattern acquisition at very low beam doses. Useable EBSD patterns have been collected with fewer than 10 electrons per pixel on average. This allows for the analysis of beam-sensitive samples that are traditionally difficult at more typical EBSD analytical conditions.

In this work, the application of this direct detection technology for the analysis of energy-related materials will be explored. One material system of interest is perovskite hybrid organic-inorganic photovoltaics. These materials are of interest for their performance and cost properties, but are electron beam sensitive and can be difficult to analyze under typical analytical conditions. Another system is Lithium Nickel Manganese Cobalt Oxide (NMC) cathode materials used in Lithium-Ion Batteries. The grain structure within these materials correlates with performance and the collection of EBSD data at lower voltages provides increased spatial resolution. Examples from both systems will be presented.

[1] K. P. Mingard, et. al, Practical Application of Direct Electron Detectors to EBSD Mapping in 2D and 3D, *Ultramicroscopy* (2017)
[2] S. Vespucci, et. al., Digital direct electron imaging of energy-filtered electron backscatter diffraction patterns, *Physical Review B* 92, 205301 (2015)
[3] A. J. Wilkinson, et. al., Direct Detection of Electron Backscatter Diffraction Patterns, *Physical Review Letters*, 111, 065506 (2013)

MS1.P032
Oxide film heterointerface induced phenomenon – segregation and vacancy ordering

Z. Zhang[1], U. Haselmann[1], Y. P. Ivan[1]

[1]Erich Schmid Institute of Materials Science (ESI) of the Austrian Academy of Sciences, Leoben, Austria

Introduction: Perovskite materials have a structure of 2 or more cations and oxygen in the arrangement ABO3 and provide a huge variety of physical phenomena and functional properties.[1] Oxide thin film heterostructure interfaces usually trigger novel physical phenomena due to the discontinuity of lattice, orbital as well as strain, etc. [1]

$BiFeO_3$ is among the few single-phase magnetoelectric multiferroics with Néel and Curie temperatures far above room temperature and is therefore a material of strong relevance to practical applications. The successful demonstration of the electrical control of antiferromagnetic domains further increased the interest in $BiFeO_3$ (BFO). Doping of BFO with cations such as Ca or Mn offers further possibilities for tuning the magnetic and electric properties. However, dopant segregation to heterointerface in such doped oxide films is neglected and less explored.

Another type of Perovskite oxide, such as mixed ionic electronic conducting (MIEC) oxides, which constitute an important materials class for solid oxide fuel cells (SOFCs), sensors, or permeation membranes. Mixed conducting $La_{0.6}Sr_{0.4}CoO_{3-\delta}$ (LSCO) for example is among the most promising SOFC cathode materials, particularly for reduced operation temperature. Due to the presence of oxygen vacancy, the oxygen transport property exhibits significant difference.

Objectives: Two objectives in this study are focused, 1) explore the dopant atom segregation to heterostructure interfaces at the atomic level; 2) to investigate in further detail the reasons of oxygen transport enhancement in $La_{0.}6Sr_{0.4}CoO_{3-\delta}$ or decline associated with strain on the atomic level.

Materials & methods: Bismuth Ferrite thin films were fabricated via pulsed laser deposition (PLD): A Ca and Mn co-doped $Bi_{0.98}Ca_{0.02}Fe_{0.95}Mn_{0.05}O_3$ (BCFMO) film and an only Mn doped $BiFe_{0.95}Mn_{0.05}O_3$ (BFMO) film. The thin films were deposited on single crystalline (100) oriented $SrTiO_3$ substrate by PLD technique using a KrF excimer laser (Lambda Physik COMPEX PRO 205F, λ = 248 nm) as the ablation source with a pulse repetition rate of 5 Hz, details are referred to [1]. For $La_{0.6}Sr_{0.4}CoO_{3-\delta}$ films, powder was prepared via the nitrate/citrate (Pechini) route. A pulsed laser deposition (PLD) target was produced by cold isostatic pressing (3.1 kbar, 1 min) and sintering (1250°C, 12 h). Epitaxial $La_{0.6}Sr_{0.4}CoO_{3-\delta}$ thin films with ~20 nm thickness were prepared on 10×10×0.5 mm^3 $LaAlO_3$ and $SrTiO_3$ (100) single crystals (Crystec, Germany) by pulsed laser deposition. Details are referred to publications [2]

The analytical STEM investigations were carried out on a FEI Titan^3 operated at 300 keV at a convergence angle of 19.7 mrad. For analytical data collection a GIF quantum^{35} energy filter (Gatan) and a super-X EDX detector^{36} (FEI) were used with simultaneous HAADF image acquisition with 38 mrad inner and 137 mrad outer detection angle on the Gatan 806 HAADF STEM detector.

Results: Firstly, we show on Ca segregation towards the interface of (Bi, Ca)FeO_3 thin film epitaxially grown on strontium titanate ($SrTiO_3$) substrate using atomic-resolution transmission electron microscopy. Consequently, Ca segregation triggers atomic and electronic structure changes at the interface (Figure 1). The phase contrast (HRTEM) image hardly changes while interface strain reduction, interplanar spacing variations and oxygen vacancies at the interface have experienced significant variations. Fe valence state at the interface has also been evaluated. The experimental observations are supported by density functional theory (DFT) calculations. [2]

Figure 1: Interface structure and chemical composition of the Ca doped film**.** (a) HAADF image of the interface along the [010]c zone axis. (b) Elemental map from the area of the HAADF image in (a) for the elements Ti (blue), Ca (green) and Fe (magenta) gained by processing the EELS spectrum image data. The grey dashed line indicates the exact position of the substrate film interface. The white dashed rectangles indicate the area considered for the Fe oxidation state analysis. (c) Profiles of elemental ratios from all sample elements including the dopants Ca and Mn (red) gained from EDS data by summing up along the image width ([100] orientation) of the area in the HAADF image in (a).

Secondly, different structures of the $La_{0.6}Sr_{0.4}CoO_{2.5}$ (LSCO) thin films grown in tensile (on $SrTiO_3$) and compressive strain ($LaAlO_3$) conditions were revealed using HRTEM/STEM (Figure 2). The pronounced domain structure of the Brownmillerite phase was found in tensile strained LCSO grown on the STO substrate. Oxygen vacancies ordering affected by strain from the substrate was observed. The structure peculiarity pertained to this oxide film strongly influences transport property as revealed by the oxygen isotope exchange experiments. [3-4]

Figure 2: HAADF images and corresponding EELS mapping of the LSCO64 thin films deposited on (a) LAO and (b) STO substrates.

Reference:
[1] Z. L. Zhang, S. Soltan, H-U. Habermeier, B. Keimer, Ute Kaiser, Atomic structure study of $SrTiO_3/LaNiO_3/SrTiO_3$ heterostructure interfaces by C_S-corrected HRTEM, *Journal of Applied Physics,* 115 (2014) 103519-10
[2] Ulrich Haselmann, Georg Haberfehlner, Weijie Pei, Maxim N. Popov, Lorenz Romaner, Daniel Knez, Jian Chen, Arsham Ghasemi, Yunbin He, Gerald Kothleitner, Zaoli Zhang, Study on Ca Segregation toward an Epitaxial Interface between Bismuth Ferrite and Strontium Titanate. *ACS Appl. Mater. Interfaces* 2020, 12, 12264-12274.
[3] Yurii P. Ivanov, Markus Kubicek, Jürgen Fleig, Matthäus Siebenhofer, Alexander Viernstein, Herbert Hutter, Andrey Chuvilin, Zaoli L. Zhang, Strain-induced structure and oxygen transport interactions in epitaxial $La_{0.6}Sr_{0.4}CoO_{3-6}$ thin films, *COMMUNICATIONS MATERIALS,* (2020) 1:25. https://doi.org/10.1038/s43246-020-0027-0.
[4] The authors would like to thank M. Kubicek and J. Fleig (from Vienna University of Technology), M.N. Popov and L. Romaner (Materials Center Leoben Forschung GmbH, Leoben), Y. He (Hubei University, China), G. Haberfehlner, and G. Kothleitner (Graz Centre for Electron Microscopy), and A. Chuvilin (CIC nanoGUNE Consolider, San Sebastian, Spain) for helps and successful cooperation. The financial support by the Austrian Science Fund (FWF): No. P29148-N36 is kindly acknowledged.

Figure 1

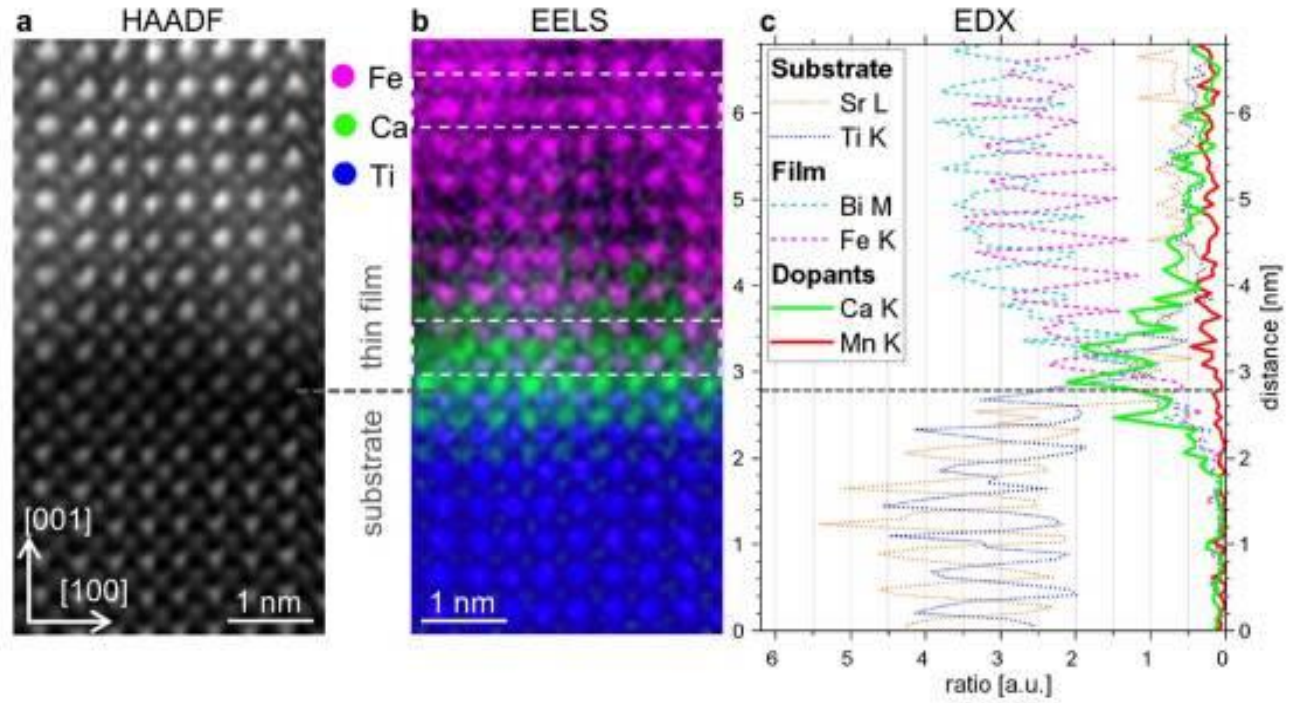

Figure 2

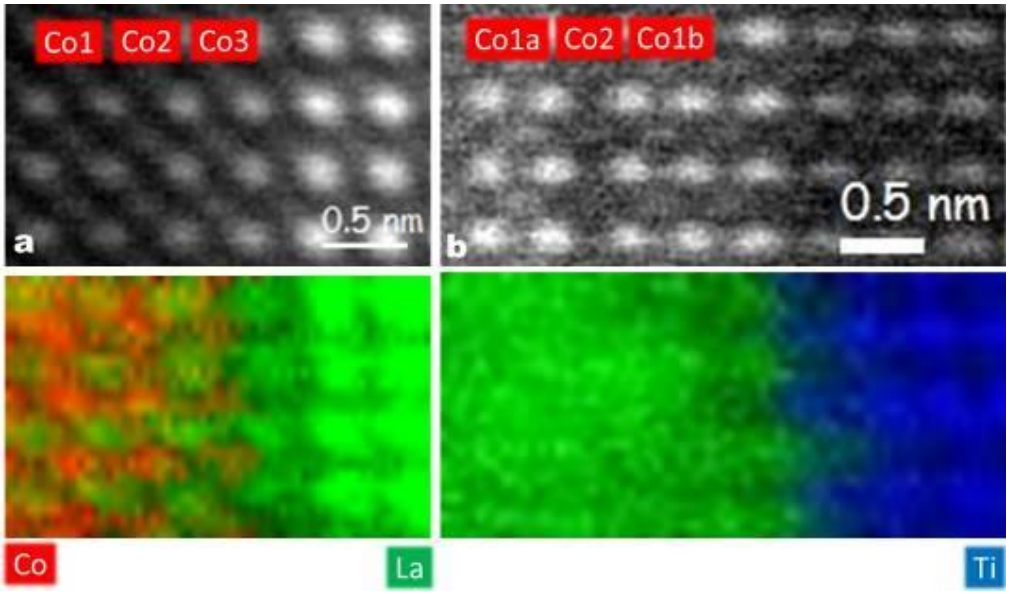

MS2.002-Invited
Multidimensional approach to study nanocatalyst in relevant reaction conditions by operando electron microscopy

M. Plodinec*[1,2], H.C. Nerl[3], T. Lunkenbein[2], M.-G. Willinger[1], R. Schlögl[2,4]

[1]ETH Zürich, ScopeM, Otto-Stern-Weg 3, 8093 Zürich, Switzerland
[2]Fritz-Haber Institute, Department of Inorganic Chemistry, Faradayweg, 14195 Berlin, Germany
[3]Humboldt University of Berlin, Department of Physics, Newtonstraße 15, 12489 Berlin, Germany
[4]Max Planck Institute for Chemical Energy Conversion, Stiftstrasse 34-36, 45470 Mülheim an der Ruhr, Germany

Facing the consequences of climate change, we are forced to find solutions towards a CO_2 neutral energy supply, and to develop industrial processes that are based on renewable resources. Chemistry and catalysis research will play an important role in enabling the urgent transition towards sustainability. It is therefore of crucial importance to improve our present knowledge in catalysis to ultimately lead to the rational design of better, more efficient catalysts for industrially relevant reactions such as CO oxidation, CO_2 reduction, propane dehydrogenation (DHP) and dry reforming of methane (DRM). Although catalysts have been studied for over a century, and regardless of our advances in synthesis and characterization methods, the empirical approach towards discovery of new catalysts still prevails. This is a very inefficient and time-consuming endeavour and a consequence of the complexity of catalytic processes. Indeed, some fundamental questions regarding the structure-activity correlation of active catalysts can only be answered by direct observation. To date, most electron microscopy (EM) studies of catalysts have been performed ex-situ, i.e., before and after catalytic testing. Observation of samples in vacuum and at room-temperature can, by principle, not reveal the working state of a catalyst. This approach has in the past contributed to a misleading picture of static catalysts.[1,2] However, recent developments in *operando* EM techniques have opened exciting horizons for studying catalysts during the different stages of industrial reactions in real time and under relevant conditions.[3-6]

In this presentation, it will be shown that the use of complementary operando EM techniques such as TEM and SEM allows to directly visualize structural and morphological transformations of catalysts induced by the reaction across length scales. This multi-scalar approach allows us to study collective dynamics at the µm scale in the SEM, and to relate them to atomistic processes that are observed by in-situ TEM. At the same time, we are able to bridge the pressure gap between surface-science model studies and real-world industrially relevant conditions.

Different active states of Pt and Ni catalysts and the influence of reaction conditions during CO oxidation, DHP and DRM will be presented.[4,5] It will be shown that the combination of real-time imaging with on-line mass spectroscopy and calorimetry enables correlative observation of local changes in structure, morphology and composition and changes in catalytic function. In-situ TEM results were obtained using a commercially available DENSsolutions ‘’Climate’’ gas-cell holder combined with a home-built gas-feeding system and an aberration-corrected TEM FEI Titan 80-300 kV. In situ SEM studies were obtained using a home-built gas-feeding system combined with of an environmental SEM FEI Quanta 200.[5,6]

In summary, using *operando* EM techniques we were able to gain meaningful insights into structural and morphological transformations of catalysts in a range of industrially relevant reactions. In the future, *operando* EM in combination with other macroscopic characterization techniques will provide crucial insights into the fundamentals underlying heterogeneous catalysis and at relevant reaction conditions, ultimately paving the way for design of better catalyst.

[1] Su, D.S. *et al*. *Chemical Reviews* 2015, *115(8)*, 2818-2882.
[2] Schlögl, R. Angewandte Chemie International Edition. 2015, *54(11)*, 3465-3520.
[3] Vendelbo, S. B. *et al. Nature Materials* 2014, *13*, 884-890.
[4] Plodinec, M. *et al. ACS Catalysis* 2020, *10 (5)*, 3183-3193.
[5] Plodinec, M. *et al. Microscopy and Microanalysis* 2020, *26(2)*, 220-228.
[6] Sandoval-Diaz, L. *et al. Journal of Energy Chemistry* 2020. *50*, 178-186.

MS2.003
Unraveling the structural transformation of gold nanorods upon femtosecond laser excitation with atomic resolution electron tomography and molecular dynamics simulations

E. Arslan Irmak[1], W. Albrecht[1,2], T. Altantzis[1], A. Pedrazo-Tardajos[1], A. Skorikov[1], T. S. Deng[3]
J. E. S. Van Der Hoeven[2], A. Van Blaaderen[2], S. Van Aert[1], S. Bals[1]

[1]University of Antwerp, EMAT and NANOlab Center of Excellence, Antwerp, Belgium
[2]Utrecht University, Debye Institute for Nanomaterials Science, Soft Condensed Matter, Utrecht, Netherlands
[3]Hangzhou Dianzi University, School of Electronics and Information Engineering, Hangzhou, China

There is a great scientific interest in gold nanorods (Au NRs) for a wide range of applications in optics, sensing, biomedicine and catalysis. Due to their anisotropic shape, Au NRs exhibit different or superior optical and catalytic properties compared to spherical nanoparticles. These properties can be further tuned by controlling the size, shape, and aspect ratio of the NRs [1]. In many applications, Au NRs are excited by pulsed laser irradiation. Unfortunately, Au NRs will hereby easily deform because electron-phonon scattering heats up the NR's crystal lattice. It is, therefore, crucial to understand the underlying deformation mechanism. Transmission electron microscopy (TEM) is a valuable tool for structural characterization with atomic resolution. Nonetheless, the 2D images provided by TEM are usually inadequate to analyse the structure-property relation of nanomaterials because they only provide a projected image of a 3D structure. Moreover, dynamic information, specifically on ultrafast time scales, cannot be accessed.

In this study, we performed atomic resolution electron tomography on the same mesoporous silica-coated Au NR before (Figure 1a) and after femtosecond laser irradiation to obtain 3D information of the structural transformation. To capture the fast dynamics of the structure deformation as observed in our experiments, molecular dynamics (MD) simulations were performed by creating an atomic input structure based on the electron tomography reconstruction (Figure 1b-c). This is highly important as it enables us to perform MD simulations based on the experimentally measured surface facets. For these simulations, a representative heating regime for the laser irradiation is crucial because the structural changes in the Au NR depend on the heating rates and the maximum temperature that is reached. Therefore, to mimic the experiments, a femtosecond heating profile was applied according to Baffou et al.[2] and heat dissipation was included by the Lumped capacitance method[3]. This combination of experiments and simulations enabled us to investigate the effect of surface morphology and the aspect ratio of the NRs, as well as the influence of the silica coating on the structural stability of the NRs. Our results give insight into the complex dynamics of the shape deformation and defect generation, driven by a combination of surface diffusion, facet restructuring and strain formation (Figure 1d).

Figure 1: a) Atomic resolution tomography of the Au NR before femtosecond laser excitation. b) Side view and internal structure of the created Au NR based on the tomography. c) The Au NR after simulated laser pulse excitation. d) Facets, strain, morphology and structure evolution during the simulated laser pulse excitation.

References:
[1] N. Li, P. Zhao, D. Astruc, Angew. Chem. Int. Ed, 53:1756-1789, 2014.
[2] G. Baffou, Thermoplasmonics: Heating Metal Nanoparticles Using Light, Cambridge University Press, 2017.
[3] F. P. Incropera, Fundamentals of Heat and Mass Transfer, John Wiley & Sons, Inc., 2011.
[4] The authors acknowledge funding from the European Research (ERC Consolidator Grants 815128-REALNANO and 770887-PICOMETRICS and ERC Advanced Grant291667-HierarSACol), European Commission (EUSMI) and financial support by the Research Foundation Flanders (FWO grant G.0267.18N). W.A. acknowledges an Individual Fellowship funded by the Marie Sklodowska-Curie Actions (MSCA) in Horizon 2020 program (grant 797153, SOPMEN).

Figure 1

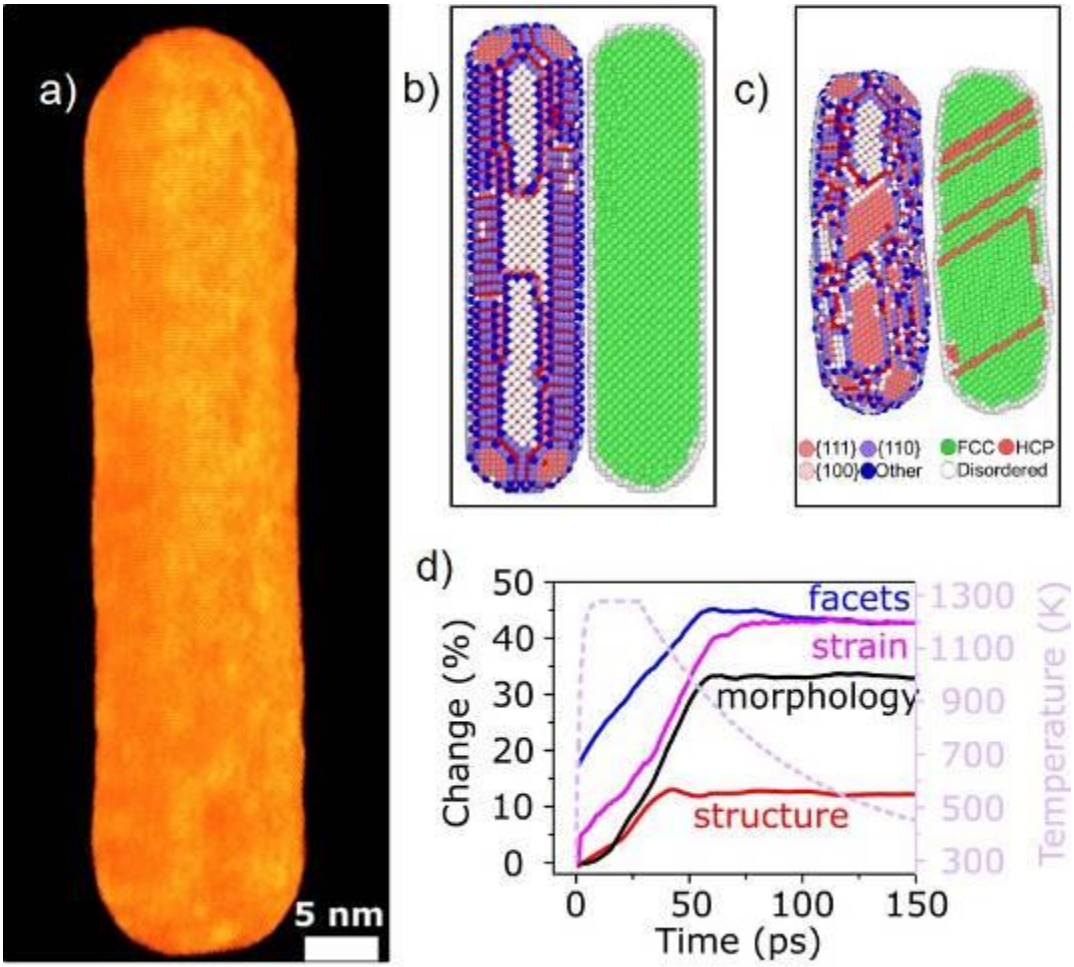
a)
5 nm
b)
c)
{111} {110} FCC HCP
{100} Other Disordered
d)
facets
strain
morphology
structure
Change (%)
Temperature (K)
Time (ps)
0
10
20
30
40
50
300
500
700
900
1100
1300
0
50
100
150

MS2.004
Three-dimensional magnetic field reconstruction of bloch skyrmion tubes at nanometer resolution

D. Wolf[1], S. Schneider[1,2], A. Kovacs[3], U. K. Rößler[1], R. E. Dunin-Borkowski[3], B. Rellinghaus[2], A. Lubk[1]

[1]Leibniz Institute for Solid State and Materials Research, Dresden, Germany
[2]Technische Universität, Dresden Center for Nanoanalysis, Dresden, Germany
[3]Research Center Jülich, Peter Grünberg Institute, Jülich, Germany

Three-dimensional (3D) nanomagnetism explores magnetic configurations in confined geometries [1]. Of particular interest are stable topologically non-trivial solitons referred to as skyrmions, which have been originally conceived as 2D magnetization patterns stabilized by antisymmetric exchange in chiral magnets [2]. In real 3D geometries they assume a tubular structure with their shape and structure playing an important role for skyrmion-skyrmion interactions and their coupling to surfaces and interfaces; and hence static and dynamic properties of skyrmion tubes (SkT) in spintronic applications. Until now crucial details of the 3D SkT structure, such as straightness and regularity remain elusive because of a lack of suitable 3D magnetic imaging techniques. Here, we fill that gap and report on the first 3D reconstruction of a SkT with ten nanometer resolution by adapting vector-field electron tomography (VFET) in the TEM.

Off-axis electron holography retrieves the phase shift that an electron wave experiences upon passing a sample containing information about the projected magnetic flux density $\boldsymbol{B}$. VFET combines EH with dual-axis tomography to reconstruct the full 3D $\boldsymbol{B}$-field [3]. The procedure involves a workflow of image acquisition, alignment, holographic-tomographic reconstruction, and 3D analysis.

We combined VFET with cryogenic TEM and in-situ application of a rotatable magnetic field to stabilize the skyrmionics magnetic texture in a FeGe needle, while recording the holographic tilt series (Figure 1) [4]. The 3D reconstruction (Figure 2) reveals SkTs that exhibit systematic local deviations from a homogeneous Bloch SkT character (e.g., local losses of axial symmetry, in-plane magnetic flux leaking among neighboring SkTs), a partial collapse of the skyrmion texture at the surface, and a correlated modulation of the SkT axes.

We anticipate that this novel experimental approach will pave the way to a better understanding of 3D spin textures in a variety of nanomagnets, benefitting the fields of both nanomagnetism and spintronics.

[1] A. Fernandez-Pacheco et *al.*, Nat Commun 8, 15756 (2017)
[2] U.K. Rößler et *al.*, Nature 442, 797 (2006)
[3] D. Wolf et *al.*, Comm Phys 2, 87 (2019)
[4] D. Wolf et *al.*, arXiv:2101.12630 (2021)
[5] D.W, A.L. and A.K. have received funding from the European Research Council (ERC) under the European Union"s Horizon 2020 research and innovation programme (grant agreement No 715620 and No 856538). D.W, A.L. S.S., and B.R. have received funding from the Deutsche Forschungsgemeinschaft (DFG) under the Schwerpunktprogramm SPP 2137.

Figure 1: Tomographic setup for holographic VFET. A FeGe needle-shaped FIB sample is placed above an out-of-plane magnetized Sm_2Co_{17} ring in a liquid nitrogen cooled TEM holder. A tilt series of 2D phase images is obtained from off-axis electron holographic tilt series around the *x* and *y* axes. Subsequently, *x* and *y* components of the *B*-field are reconstructed from the phase tilt series. Solving div$B$ = 0 yields the *z* component, the 3D vector of *B*.

Figure 2: 3D magnetic induction mapping of Bloch skyrmion tubes in FeGe. Volume rendering of the in-plane components *Bx, By* according to the colorwheel and iso-surface of the mean inner potential reconstruction highlighting the FeGe FIB-prepared specimen shape (grey, bottom half only). The magnified views visualize a single skyrmion tube (SkT) in which the three vectors slices plot the 3D spin texture inside the SkT at different *z*-heights.

Figure 1

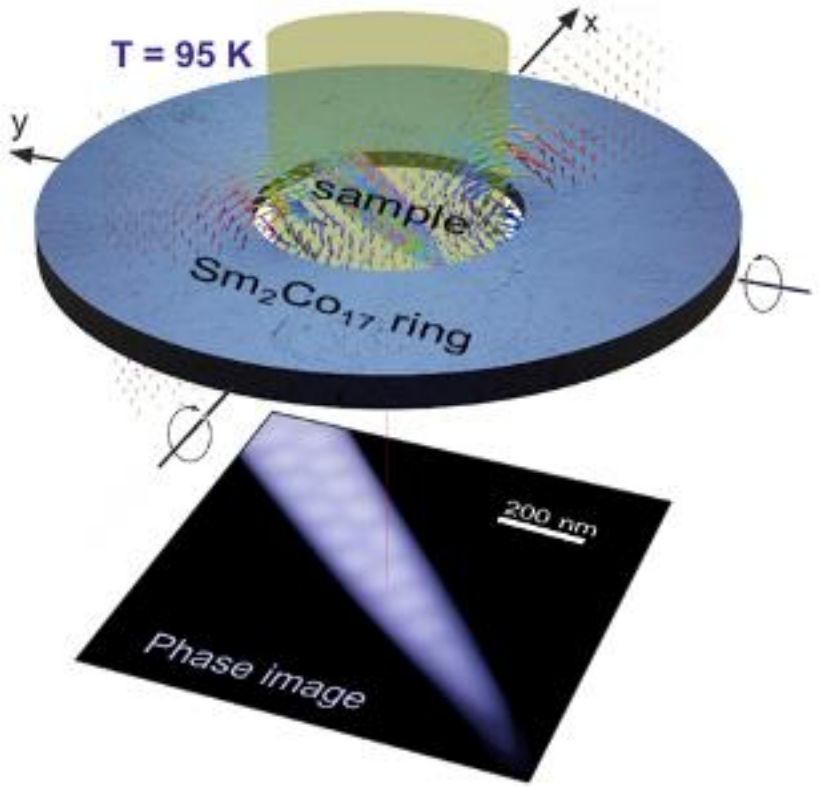

Figure 2

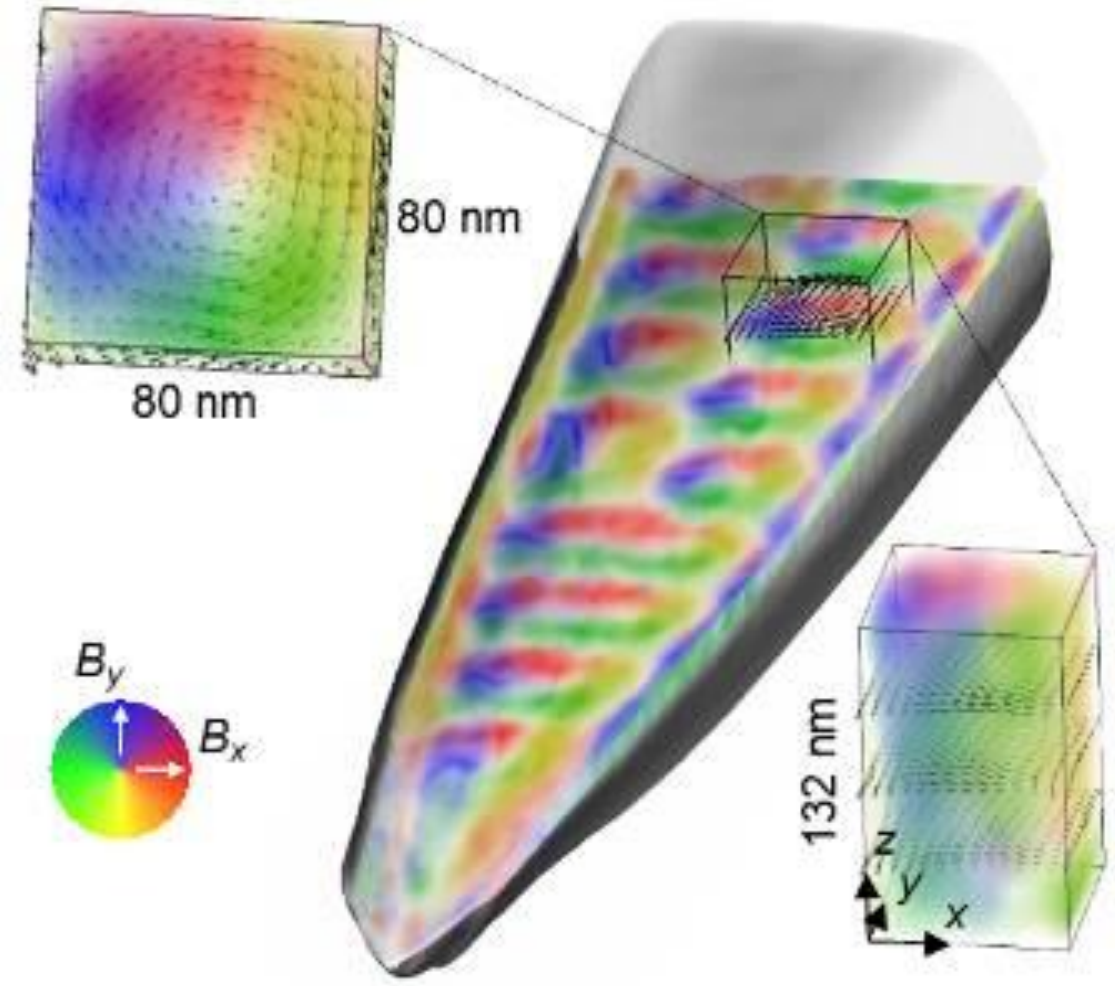

MS2.005
Structural evolution of a metal-organic framework upon heating imaged via atomic-resolution *in situ* HRTEM

H. Qi[1,2], B. Liang[1], D. Mücke[1], U. Kaiser[1]

[1]University of Ulm, Electron Microscopy Group of Materials Science, Ulm, Germany
[2]Technische Universität Dresden, Center for Advancing Electronics Dresden (cfaed) §Faculty of Chemistry and Food Chemistry, Dresden, Germany

Introduction: Due to the enormous structural and chemical variety, metal-organic frameworks (MOFs) are promising candidates for next-generation applications, such as filtration, gas adsorption, catalysis. However, the mechanism of MOF melting remains vague. Recently, Widmer *et al.* constructed a *p-T* phase diagram for ZIF-62 via in-situ PXRD and Raman microscopy[1]. It was found that pressure induced the lowering of the melting point, and this phenomenon can be very likely generalized to other MOFs. Despite their pioneering work, a microscopic view of the structural evolution upon heating is still lacking.

Objectives: In this work, we aim to unravel the dynamics of the crystalline-to-amorphous transition of a MOF under heating. The structural evolution will be demonstrated on the molecular or even atomic scale.

Materials & methods: 2D Cu-benzenehexathial (Cu-BHT) MOF (Figure 1) has been synthesized via the surfactant-monolayer-assisted interfacial synthesis (SMAIS)[2]. Due to the absence of hydrogen atoms[3] and good electrical conductivity[4], Cu-BHT MOF is expected to be highly resilient toward electron radiation, opening up the possibility of in-situ imaging down to atomic scale. The as-synthesized MOF particles were horizontally transferred to MEMs chips for subsequent heating experiments. We performed in-situ HRTEM imaging using the spherical-and-chromatic-aberration-corrected SALVE microscope operated at 80 kV (SALVE: sub-Angstrom low-voltage electron microscopy and spectroscopy, more details: www.salve-project.de)

Results and Conclusion: We found that, in contrast to the commonly observed crystalline-to-amorphous transition of MOFs upon heating[1], the Cu-BHT MOF transformed first to CuS crystal at c.a. 600 °C (Figure 2). Interestingly, the crystallographic orientation of the newly formed CuS is defined by the original Cu-BHT MOF orientation (Figure 2b and 2d). The formation of CuS was confirmed structurally (via electron diffraction) and chemically (via energy-dispersive X-ray spectroscopy). The interaction of the electron beam with the specimen was found to facilitate the structural evolution by lowering the MOF-CuS transition temperature. The CuS crystal evaporated when the temperature was raised above 800°C. In summary, we have successfully observed the structural evolution of a rather electron-resilient MOF upon heating and monitored in-situ the reaction dynamics on the molecular to atomic scale.

Figure 1: Structure of Cu-BHT MOF.

Figure 2: (a) 80kV Cc/Cs-corrected HRTEM image of the Cu-BHT MOF. (b) Fast Fourier transform (FFT) pattern of a. The pattern exhibits a hexagonal symmetry with first order reflections at 1.35 nm^{-1}, which agrees with the MOF structure. The red circle marks the spatial frequency of 10 nm^{-1} (i.e., 0.1 nm in real space) (c) Cc/Cs-corrected HRTEM image after heating up to 600 °C. (d) FFT pattern of c. The newly formed crystal has a hexagonal symmetry with first and second order reflections at 3.1 nm^{-1} and 5.0 nm^{-1}. The crystal structure well matches that of CuS.

Reference:
[1] *Nat. Mater.* 18, 370–376 (2019).
[2] *Nat. Chem.* 11, 994–1000 (2019).
[3] *Small* 11, 622–629 (2015).
[4] *Angew. Chemie Int. Ed.* 57, 146–150 (2018).

Figure 1

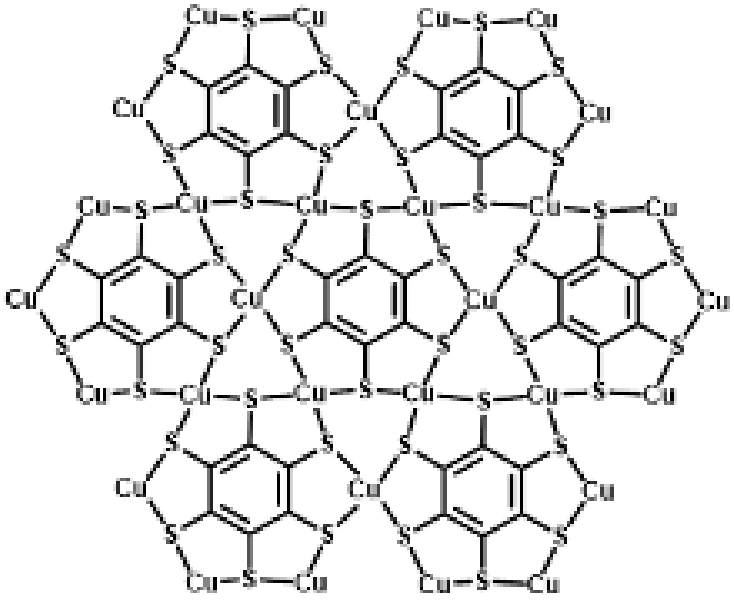

Figure 2

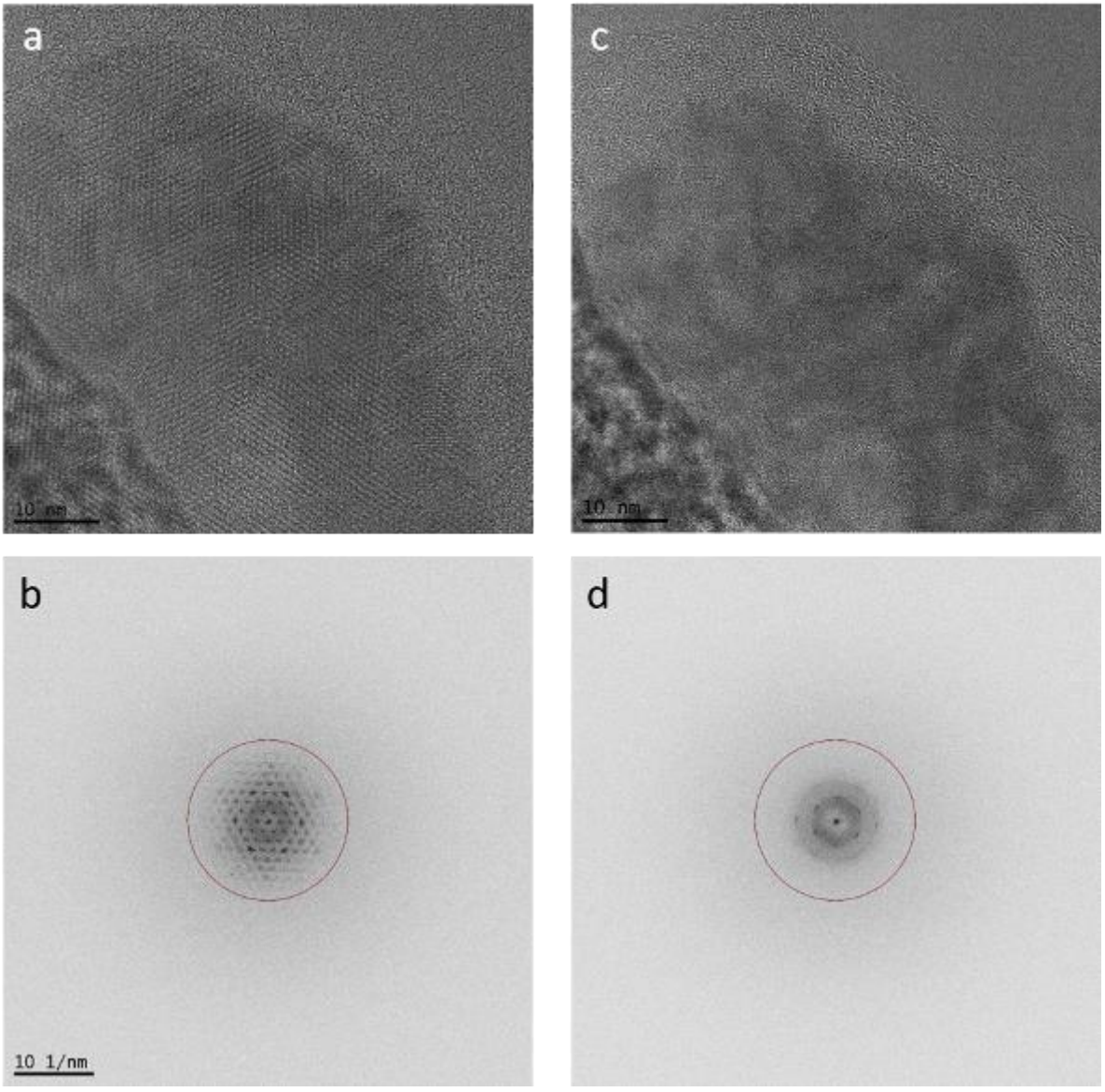

MS2.006
Hetero-phase interfaces induced CrN growth twins revealed by HRTEM

Z. Chen[1], Z. Zhang[1]

[1]Erich Schmid Institute of Materials Science (ESI) of the Austrian Academy of Sciences, Leoben, Austria

Twin boundaries with Σ3{111} and Σ3{112} are often observed in low stacking-fault energy (SFE) *fcc* (face-centered cubic) materials. Nano-twins with Σ3{111} coherent twin boundary (CTB) can improve strength, ductility, electrical conductivity and thermal stability. Σ3{112} incoherent twin boundaries (ITBs) have been found to play crucial roles in plastic deformation and de-twinning process in nano-twins metallic materials. However, in reality, it is not easy to generate numerous twins in transition-metal nitride films due to its high stacking fault energies (SFEs). Coming up with an effective route to introduce more twins into TMNs is of significance. Thus, this work is devoted to investigating the heterophase interface-facilitated twin nucleation mechanism, demonstrating a new method to synthesize high-density growth twins in TMNs.

The CrN/AlN gradient multilayer film [1] with a total thickness of ~2 μm is composed of 21 repeating blocks consisting of 10 bilayers with an alternative CrN and AlN layer. Since the AlN phase stability is thickness-dependent, two different phases can be readily detected in the gradient multilayer [1], i.e. metastable rock-salt AlN and stable wurtzite AlN. In this work [2], a high-density of rock-salt TMN twins with Σ3{112} incoherent twin boundaries (ITB) were found in the {111} rock-salt CrN ||{0002} wurtzite AlN hetero-phase interface (Figs.1). The extensive high-resolution transmission electron microscopy (HRTEM) observations reveal that rock-salt TMN twins with ITBs are frequently formed in wurtzite {0002} interface with a single-atomic-layer terrace (1×*d*{0002}*w*-AlN). However, twins with ITBs were hardly observed in the wurtzite {0002} interface with a double atomic-layer terrace (Figs.2). Combined with the experiment observation, DFT calculation and kinetics of, the formation of twins with ITBs can be interpreted by the *rs*-CrN/*w*-AlN interface structure (with a mirror-symmetry)-induced thermodynamically stable nucleation (Figs.3).In conclusion,the hetero-phase interface-facilitating nucleation process plays a dominant role in rock-salt growth-twins, which findings offer a new perspective on the formation mechanism of growth-twins in transition-metal nitride materials.

Figure 1 (a): TEM cross-sectional dark-field images from the 1st to 6th block area (dark-field images taken from the (0002)/(111) reflection). **(b)** is a corresponding selected area electron diffraction pattern. **(c)** HRTEM shows the CrN growth twins on w-AlN (0002).

Figure 2: HRTEM observation the terrace structure in the *rs*-CrN/*w*-AlN interface

Figure 3: Schematic illustration of the nucleation process on a single-layer terrace *w*-AlN.

Acknowledgments**:** The authors thank Dr. Matthias Bartosik and Prof. Paul H. Mayrhofer for the thin film synthesis at TU Wien for the sample preparation. Qinqin Shao (Hunan University) is gratefully acknowledged for helping with the DFT simulation.

Reference:
[1] Z. Chen, D. Holec, M. Bartosik, P.H. Mayrhofer, Z. Zhang, Crystallographic orientation dependent maximum layer thickness of cubic AlN in CrN/AlN multilayers, Acta Materialia 168 (2019) 190-202.
[2] Z. Chen, Q. Shao, M. Bartosik, P.H. Mayrhofer, H. Chen, Z. Zhang, Growth-twins in CrN/AlN multilayers induced by hetero-phase interfaces, Acta Materialia 185 (2020) 157-170.

Figure 1

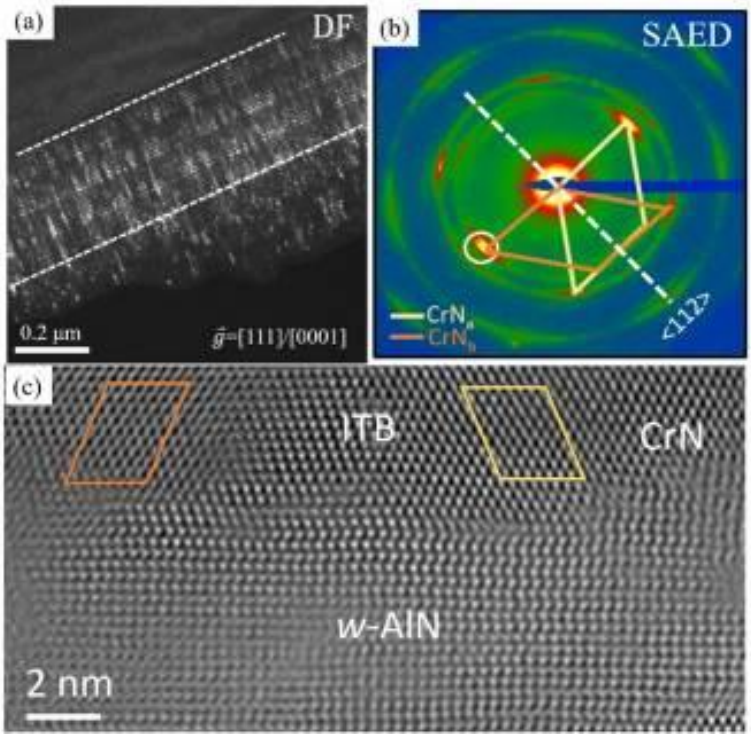

Figure 2

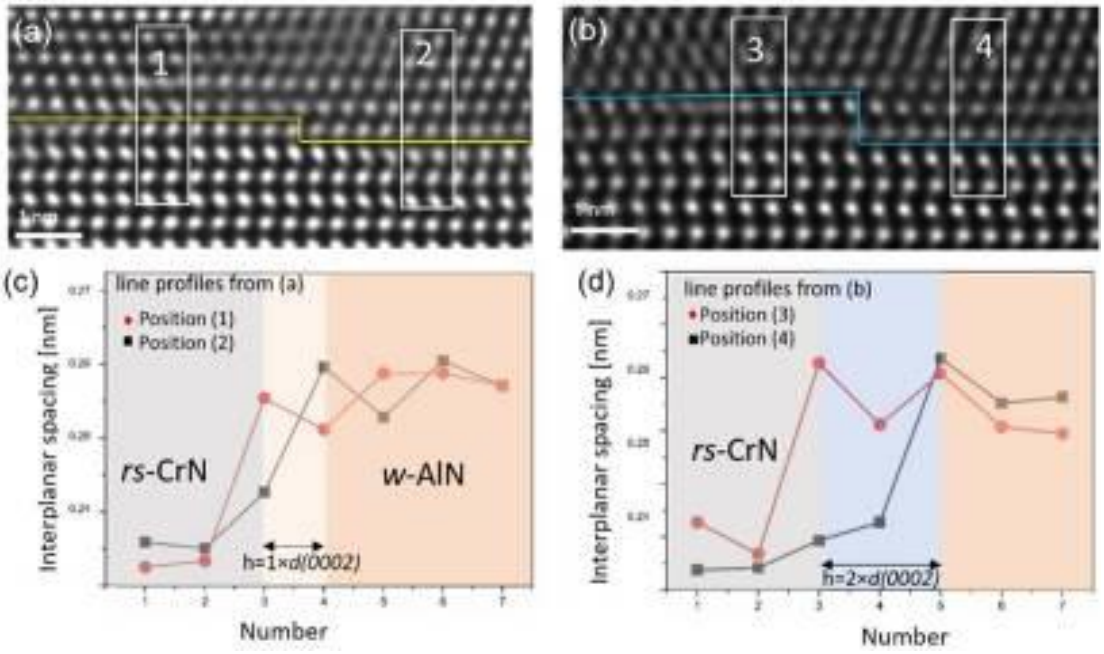

Figure 3

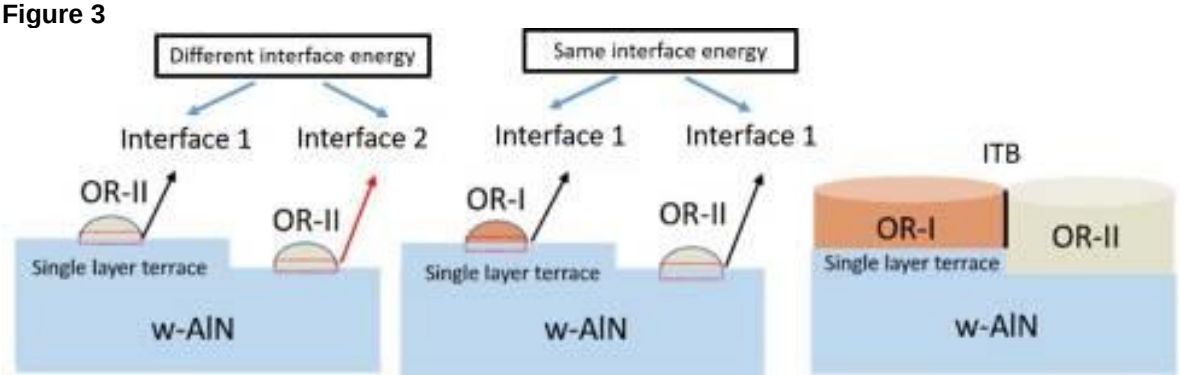

MS2.P001
Temperature-dependent displacement cross section of graphene and its impurities – Measuring the carbon adatom migration barrier

A. Postl[1], J. Madsen[2], P. P. P. Hilgert[2], J. Kotakoski[2], T. Susi[2]

[1]University of Vienna, Faculty of Physics & VDS Physics, Vienna, Austria
[2]University of Vienna, Faculty of Physics, Vienna, Austria

Surface diffusion is crucial for many physical and chemical processes, including epitaxial growth of crystals and heterogeneous catalysis. Although the phenomenon is common [1] and theoretically understood, measuring adatom migration barriers on 2D materials remains a daunting challenge. We are able to estimate the carbon adatom migration barrier on freestanding monolayer graphene, which has theoretically been predicted to be in the range of 350–500 meV [2,3], by quantifying the temperature dependence of its electron knock-on damage.

To measure damage and healing rates as accurately as possible, we use 90 keV electrons and choose the fastest possible time for image acquisition with our aberration-corrected scanning transmission electron microscope. Contrary to expectations, the damage rate decreases with increasing temperature, which is due to the fast healing of vacancies by recombination with diffusing adatoms. By comparing the predicted and observed damage rates at 300–1073 K we find a barrier of 140 meV, which is the first measurement reported to date.

We further measured the cross sections of electron-driven processes involving single silicon and phosphorus dopants in graphene at elevated temperatures. To aid in the analysis of our image series, we turned to automated structure recognition based on convolutional neural networks. By utilizing deep learning [4|, we quantified for the first time the direct exchange of carbon neighbors with the dopant in the lattice (so-called bond inversion) [5,6], the replacement of the dopants by carbon adatoms, which has emerged as a hindrance to their manipulation, and knock-on damage of a carbon neighbor, which transforms the sites from threefold to fourfold coordination, as a function of sample temperature.

We gratefully acknowledge funding from the European Research Council (ERC) under the European Unions Horizon 2020 research and innovation program (Grant agreement no. 756277-ATMEN) and the Vienna Doctoral School in Physics.

[1] R. Zan et al., Nano Letters 12 (2021) 3936–3940.
[2] A. V. Krasheninnikov et al., Physical Review B 69 (2004) 073402.
[3] P. O. Lehtinen et al., Physical Review Letters 91 (2003) 017202.
[4] Madsen, J. et al., Microscopy and Microanalysis 25(S2) (2019) 166-167.
[5] M. Tripathi et al., Nano Letters 18 (2018) 5319–5323.
[6] C. Su et al., Science Advances 5 (2019) eaav2252.

MS2.P002
TEM characterisation of laser-generated colloidal high-entropy alloy nanoparticles

M. Kamp[1], V. Duppel[2], F. Waag[3], Y. Li[3], A. R. Ziefuß[3], E. Bertin[3], G. Marzun[3], S. Barcikowski[3], B. Gökce[3], L. Kienle[1]

[1]Kiel University, Institute of Materials Science, Kiel, Germany
[2]Max Planck Institute for Solid State Research, Stuttgart, Germany
[3]University of Duisburg-Essen, Technical Chemistry I, Center for Nanointegration, Essen, Germany

A novel synthesis approach, called laser ablation in liquid (LAL), opens the field for a unique nanoparticulate material system to a wide range of applications. TEM characterization underlines the kinetically-controlled synthesis of high-entropy alloy (HEA) nanoparticles (NPs) by LAL. Defect-rich crystalline phases with complex metastable ultrastructures, e.g., core shell NPs are observed [1].

The unique mechanical, electromagnetic, and electrochemical properties of bulk HEAs are frequently studied [2]–[4]. The alloys are stabilized by a high-entropy effect, which is induced by a large number (≥5) of alloying elements. Due to limitations of state of the art synthesis methods, nanoparticulate HEAs are rarely reported, although the high surface to volume ratio of NPs offers applications in energy storage and enhanced catalytic properties [5], [6]. LAL is a suitable one-step synthesis method of colloidal high entropy NPs.

The establishment of a unique synthesis method needs to be supported by sample characterization with (scanning) transmission electron microscopy applying various methods, like high-resolution phase-contrast imaging, Z-contrast imaging, and selected area electron diffraction (Tecnai F30 STwin G^2 300 kV). Nanoprobe elemental mapping is performed with a Si(Li) detector (EDAX system). The Bps are generated in ethanol with a 10 ps pulsed Nd:YAG laser (Atlantic, Ekspla, Vilnius, Lithuania) at a wavelength of 1064 nm and are dispersed on carbon-coated copper grids for sample preparation.

Laser generated HEA NPs show two major size fractions. The highest frequency is observed for NPs <10 nm in diameter. Electron diffraction and high-resolution TEM investigations show a single crystal fcc lattice with a lattice constant of a = 3.62 Å. An equiatomic and homogeneous chemical composition CoCrFeMnNi is detected by STEM-EDX, which underlines the formation of HEA NPs. The heterogeneous catalysis of the alkaline oxidation reaction is demonstrated and dominated by NPs of this small size fraction. Interestingly, the stability of the NPs seems to be size-dependent. A size fraction with diameters >10 nm, shows segregated ultrastructures with high defect density. Elemental mapping illustrates a Mn- and Cr-rich oxide spinel formation that results in partial core shell NPs. The core represents an fcc crystal structure with a high defect density of Σ3-twins and domain sizes in the range of a few atomic layers [1]. In further experiments, we observed that variations in the liquid medium and the stoichiometry of Mn seem to control the size distribution and NPs ultrastructures.

In conclusion, we established LAL as a new kinetically-controlled synthesis method for HEA NPs with enhanced heterogeneous catalytic activity. The fcc single crystal structure is shown by XRD and SAED characterization. Furthermore, segregated ultrastructures with high defect concentrations and oxide spinel phases are analyzed for respective NPs size fractions. The results allow an application of the synthesis method to other unique material systems like high-entropy oxides, which are expected to be less sensitive to oxidation.

Funding by the German Research Foundation (Project KI 1263/15-1) is acknowledged.

[1] F. Waag *et al.*, *RSC Adv.* 9 (2019)
[2] D. B. Miracle and O. N. Senkov, *Acta Mater.* 122 (2017)
[3] A. Sarkar *et al.*, *Adv. Mater.* 31 (2019)
[4] Z. Li *et al.*, *Nature*, 534 (2016)
[5] A. Sarkar *et al.*, *Nat. Commun.* 9 (2018)
[6] P. Xie *et al.*, *Nat. Commun.*, 10 (2019)

MS2.P003
Multidimensional characterisation of differently shaped Au nanoparticles using transmission electron microscopy techniques

S. Neumann[1], A. Rezvani[2], M. Barasinski[3], G. Garnweitner[3], D. Segets[2,4], D. Rafaja[1]

[1]TU Bergakademie Freiberg, Institute of Materials Science, Freiberg, Germany
[2]University of Duisburg-Essen, Process Technology for Electrochemical Functional Materials, Duisburg, Germany
[3]Technische Universität Braunschweig, Institute for Particle Technology, Braunschweig, Germany
[4]University of Duisburg-Essen, Center for Nanointegration Duisburg-Essen (CENIDE), Duisburg, Germany

Au nanoparticles have been studied for decades, because they possess unique physical and chemical properties, which are required for high-technology applications, e.g., in photovoltaics, sensor technology, drug delivery, electronics and catalysis. As the properties of Au nanoparticles are very sensitive to their size and shape, the structural characteristics need to be adjusted during the synthesis and controlled very precisely afterwards. The structural properties of nanoparticles are frequently characterized using transmission electron microscopy (TEM). However, the capabilities of this analytical technique are frequently limited to the investigation of a single parameter, usually to the particle size, which is not always sufficient to explain observed materials properties. The aim of this work is to demonstrate the advantages of a multidimensional characterization of Au nanoparticles, which can contribute to a better understanding and explanation of their properties.

Spherical Au nanoparticles investigated in this study were synthesized by a rapid addition of an aqueous solution containing trisodium citrate and tannic acid to an aqueous solution of hydrogen tetrachloroaurate(III) trihydrate at 60 °C, followed by boiling the mixed solution [1]. Rod-shaped Au nanoparticles were synthesized via the seeded growth method in several steps with a cetyltrimethylammonium chloride (CTAC) double layer on the particle surface, followed by a ligand exchange resulting in Au nanoparticles stabilized with 11-mercaptoundecanoic acid [2]. During the TEM analysis, several low-magnification high-angle annular dark-field scanning transmission electron microscopy (HAADF-STEM) images were acquired and subjected to a semi-automatic segmentation routine, which was followed by the analysis of various size and shape parameters of individual particles such as circle equivalent diameter, circularity, aspect ratio and roundness. The application of a semi-automatic segmentation routine enabled the analysis of a considerably large number of particles and thus the acquisition of a statistically relevant data set. The analysis of the HAADF-STEM images revealed that the synthesized samples, which were expected to contain Au spheres or Au rods, contain particles with unwanted shapes and different sizes. The HAADF-STEM analysis was supported by the evaluation of the multivariate probability density, which was determined using multivariate kernel density estimators [3] and used for the identification of the correlations between structural features of individual particles, but with a high statistical reliability. In addition, high-resolution transmission electron microscopy (HRTEM) in combination with fast Fourier transformations (FFTs) of the HRTEM micrographs was applied in order to correlate the shapes of the Au nanoparticles with their atomic structure.

References:
[1] X. Han, J. Goebl, Z Lu, Y. Yin: *Role of Salt in the Spontaneous Assembly of Charged Gold Nanoparticles in Ethanol*, Langmuir 27 (2011), 5282–5289.
[2] X. Ye, Y. Gao, J. Chen, D. C. Reifsnyder, C. Zheng, C. B. Murray: *Seeded growth of monodisperse gold nanorods using bromide-free surfactant mixtures*, Nano letters 13 (2013), 2163–2171.
[3] D. W. Scott: *Multivariate Density Estimation: Theory, Practice, and Visualization*, John Wiley & Sons, New York, 2015.

MS2.P004
Quantitative imaging of trace and low-Z elements using correlative TEM, SIMS and APT analysis

S. Eswara[1], S. Pal[1], J. Barrirero[2], M. Lehmann[3], Q. Jeangros[3], N. Valle[1], F. J. Haug[3], A. Hessler-Wyser[3], C. N. Shyam Kumar[1], F. Mücklich[2], T. Wirtz[1]

[1]Luxembourg Institute of Science and Technology, Materials Research and Technology Department, Belvaux, Luxembourg
[2]Saarland University, Functional Materials, Department of Materials Science, Saarbrücken, Germany
[3]Swiss Federal Institute of Technology Lausanne (EPFL), Institute of Microengineering (IMT), Photovoltaics and Thin Film Electronics Laboratory, Neuchâtel, Switzerland

Transmission Electron Microscopy (TEM) is a well-known technique for high-resolution imaging and analysis of materials down to the atomic scale [1]. However, the analysis of elements in trace concentrations, low-Z elements and isotopic selectivity are very difficult or impossible using the conventional chemical analysis techniques available in a TEM such as Energy Dispersive X-ray Spectroscopy (EDX) or Electron Energy-Loss Spectroscopy (EELS). Atom Probe Tomography (APT) is a powerful method for 3D nanoscale chemical imaging and it is capable of distinguishing isotopes. However, the sample preparation is laborious, the analysed volume is small (~ 10^5 to 10^6 nm^3) and the data is susceptible to artefacts. Notably, a precise 3D APT reconstruction requires the local morphology of the sample tip at each instance in time which is often lacking. Furthermore, limited mass resolution and differences in the field evaporation of different elements can also introduce artefacts in the APT data. Secondary Ion Mass Spectrometry (SIMS) is a high-sensitivity technique to detect concentrations down to the ppm range. Moreover, all elements and isotopes in the periodic table can be analysed. However, SIMS suffers from matrix effects (i.e. ionization yield varies strongly as a function of matrix elements) and therefore a quantification of SIMS data requires reference samples. Relatively large volumes (~ 10^3 μm^3) are typically analysed in SIMS and the lateral resolution in SIMS imaging is fundamentally limited to ~ 10 nm by the ion-solid interaction volume. As individual techniques have their inherent strengths and weaknesses, a correlative approach is a powerful way to obtain complementary and comprehensive insights about the chemical composition in nanoscale structures in technological materials. In this presentation, we demonstrate a correlative TEM-APT-SIMS method for the quantification of hydrogen, deuterium and other trace elements (dopants) in passivating contact layers used in silicon photovoltaics [2]. The analysis and data treatment methodologies will be discussed in detail. In the same context, other new methods to quantify SIMS images will also be briefly discussed [3, 4].

This work was partially funded by the Luxembourg National Research Fund (FNR) by the grants C18/MS/12661114 (MEMPHIS) and INTER/SNF/16/11536628 (NACHOS).

References:
[1] D. B. Williams & C. B. Carter, Transmission Electron Microscopy, Springer, US 2009
[2] S. Pal et al, Appl. Surf. Sci, 2021
[3] S. Eswara et al, MRS Comm., 9, 916–923, 2019
[4] L. Yedra et al, J. Anal. Atom. Spectrom., 36, 56-63, 2021

Figure 1: STEM-HAADF, STEM-EDX and APT images of the nanostructured passivating contact in a silicon photovoltaic material. The APT line profiles across the sample tip are shown for masses 1 Dalton (H) and 2 Dalton (H2 or D) before and after background correction with insights drawn about D/H ratio from SIMS analysis. H and D concentrations are thus quantified within nanoscale layered structures. Adapted from our work in [2].

Figure 1

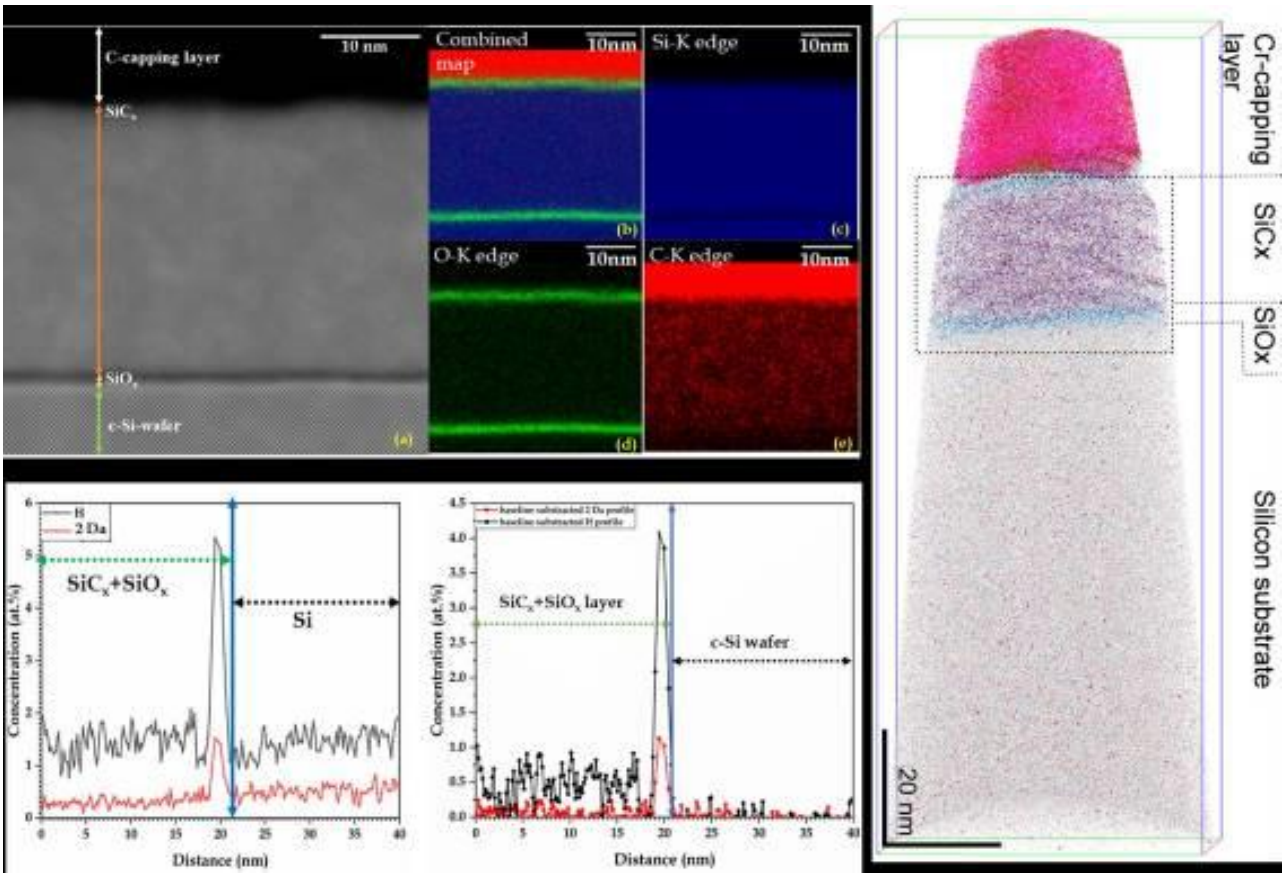
C-capping layer
10 nm
SiCx
SiOx
c-Si-wafer
(a)
Combined map
10nm
(b)
Si-K edge
10nm
(c)
O-K edge
10nm
(d)
C-K edge
10nm
(e)
H
2 Da
SiCx+SiOx
Si
Concentration (at.%)
Distance (nm)
SiCx+SiOx layer
c-Si wafer
Concentration (at.%)
Distance (nm)
Cr-capping layer
SiCx
SiOx
Silicon substrate
20 nm

MS2.P005
In situ Hall measurements in a transmission electron microscope

Y. Lee[1], D. Pohl[2], A. Thomas[1,3], B. Rellinghaus[2]

[1]IFW Dresden, Dresden, Germany
[2]TU Dresden, Dresden Center for Nanoanalysis, Dresden, Germany
[3]TU Dresden, Institute of Solid State and Materials Physics, Dresden, Germany

Introduction: Skyrmions are envisioned as nanoscale information carriers in future devices, since they can be electrically manipulated and detected. So far, topological Hall measurements on Skyrmion samples are conducted on separate samples with different thicknesses and confinements as compared to samples for magnetic imaging in a transmission electron microscope (TEM) [1,2]. Such TEM-based magnetic characterization has proven extremely valuable for unveiling the details of Skyrmionic spin textures [3]. Unfortunately, the occurrence and nature of Skyrmions depend strongly on thickness and confinements, and differences in the samples easily impede a correlation of magneto-transport data and TEM investigations. Unfortunately, in-situ Hall measurements in a TEM are not yet available.

Objective: We have devised an in-situ measurement platform to conduct in-situ magneto-transport measurements in the TEM and present first results.

Methods: A *Protochips Fusion Select* TEM holder with six electrical feedthroughs furnished with in-house made measurement chips is employed for in-situ Hall measurements in a TEM. Chips with Si3N4 membranes and Au leads are lithographically structured from Si3N4/Si/Si3N4 sandwiches. They can be used to contact FIB lamellae or thin films. A *JEOL F-200* TEM (200kV, cold FEG) equipped with a *Gatan Continuum* electron energy loss spectrometer and a fast *Gatan One View* camera and provides a variety of magnetic characterization techniques including Lorentz TEM (LTEM), electron holography, differential phase contrast imaging (DPC) and electron magnetic chiral dichroism (EMCD).

Results & Conclusion: A 20 nm Ni film was deposited, integrated in a measurement device by maskless lithography, and inserted in the *Fusion Select* holder. LTEM was then used to image the magnetic domain pattern during in-situ Hall effect measurements in the TEM. The results of these proof-of-principle experiments are shown in Figure 1. The magnetic field of the objective lens (OL) was controlled to continuously magnetize the Ni film towards saturation. In good agreement with ex-situ reference measurements in a dedicated cryostat for state-of-the-art magneto-transport experiments, the LTEM images reveal the coarsening of the magnetic domains upon increasing the field of the OL. As expected, the domain growth goes along with an increase of the Ni magnetization to saturation as probed by the simultaneously measured Hall voltage corresponding to the anomalous Hall effect. These successful first measurements pave the way to previously unreported in-situ and in-operando Hall measurements in combination with high-resolution magnetic imaging in the TEM. Details of the chip fabrication and technical limitations of the approach will be discussed.

B.R. gratefully acknowledges financial support by the DFG within SPP 2137.

[1] M.J. Stolt et al., Adv. Func. Mater. 2019 (2019) 1805418. DOI: 10.1002/adfm.201805418
[2] R. Schlitz et al., Nano Lett. 19 (2019) 2366. DOI: 10.1021/acs.nanolett.8b05042
[3] D. Wolf, et al., https://arxiv.org/abs/2101.12630

Figure 1: *Left to right*: Protochips Fusion Select holder with home-made measurement chip. Fourspring contacts are used for current supply and Hall voltage measurements. LTEM images recorded simultaneously with Hall measurements reveal the domain growth upon magnetizing a 20 nm Ni film in the field of the objective lens. The in-situ Hall data are in good agreement with ex-situ reference measurements.

Figure 1

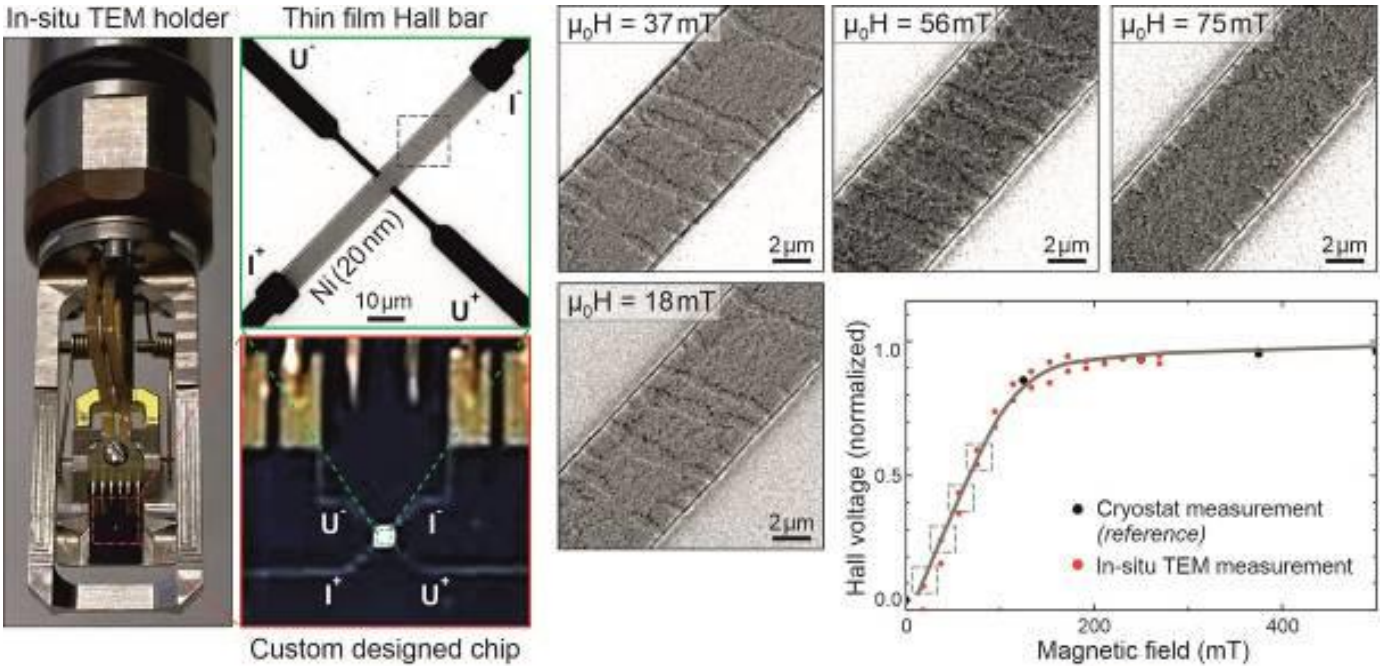
In-situ TEM holder
Thin film Hall bar
U-
I-
I+
Ni (20 nm)
10 µm
U+
U-
I-
I+
U+
Custom designed chip
µ0H = 37 mT
2 µm
µ0H = 56 mT
2 µm
µ0H = 75 mT
2 µm
µ0H = 18 mT
2 µm
Hall voltage (normalized)
1.0
0.5
0.0
0
200
400
Magnetic field (mT)
Cryostat measurement
(reference)
In-situ TEM measurement

MS2.P006
In situ observation of electron-beam-induced formation of nano-structures in PbTe

I. Zelenina[1], I. Veremchuk[1,2], Y. Grin[1], P. Simon[1]

[1]Max Planck Institute for Chemical Physics of Solids, Dresden, Germany
[2]Helmholtz-Zentrum Dresden-Rossendorf e.V. (HZDR), Dresden, Germany

Nanoparticles are the focus of substantial scientific interest due to their unusual chemical and physical properties. The current interest in PbTe nano-bars arises from their useful thermoelectric properties [**1**]. It is known that the presence of nano-bar-like formations in spark-plasma sintered (SPS) PbTe specimens increases the ZT value to approximately 0.45 at 300 K [2].

The PbTe single crystal was grown using the vertical Bridgman–Stockbarger method. The melt composition was chosen to be near stoichiometric, with a slight excess of Te (0.5%) [**3**]. To prepare the TEM specimens from the single crystal, the materials were ground by mortar and pestle for several minutes with a minimum applied force. Transmission electron microscopy investigations were performed using a FEI Tecnai F30-G2 at an acceleration voltage of 300 kV.

The fragmentation of PbTe micro-particles was clearly observed after electron-beam treatment beyond a certain threshold value of the current (**Figure 1** a, b). When the initial single-crystalline PbTe particle was exposed to electron irradiation, it partially evaporated. The evaporated material transferred to the colder part of the carbon substrate and produced rectangular-shaped particles (nano-bars) measuring 4–100 nm. The first step of the nano-bar formation is nucleation, which is subsequent to sublimation, where the formation of bars takes place at different times and is indicative of a stochastic process. The growth of isolated nanoparticles after reaching a certain cube size of 10–20 nm follows two possible patterns. The first possibility is that the particle predominantly increases in size along one direction while growing only gradually in the other two directions. The second growth pattern, in which all directions develop equally.

Commonly, coalescence events were observed between nanoparticles. Nano-bars, which nucleated at a short distance between them, may come into contact with each other while growing and coalesce. Larger particles incorporated smaller ones on the principle of gradual rebuilding of the crystal structure, i.e., smaller bars are used as a supplementary building material for larger particles. This behavior is known as the Ostwald ripening mechanism.

The decomposition of initial PbTe particles under well-defined electron-beam conditions may be understood by the crystal structure imperfections inherent to lead telluride at temperatures below 450°C. The atomistic depletion mechanism could be revealed at the atomic level by high-resolution TEM, proving that degradation occurs atom-by-atom. The recrystallized nanoparticles in turn exhibit an "ideal" crystal structure, which may explain their relative stability with respect to the beam in comparison with the initial particles. Direct formation of nano-bars and nano-layers of lead telluride using electron-beam treatment is a particularly interesting technique because it produces nanostructures free of synthesis-educts contamination.

[1] Heremans, Joseph P., et al. "Enhancement of thermoelectric efficiency in PbTe by distortion of the electronic density of states." *Science* 321.5888 (2008): 554-557.
[2] Khasimsaheb, Bayikadi, et al. "Thermoelectric properties of spark plasma sintered lead telluride nanocubes." *Journal of Materials Research* 30.17 (2015): 2638-2648.
[3] Gille, Peter, et al. "Crystal growth of PbTe and (Pb, Sn) Te by the Bridgman method and by THM." *Crystal Research and Technology* 19.7 (1984): 881-891.

Figure 1

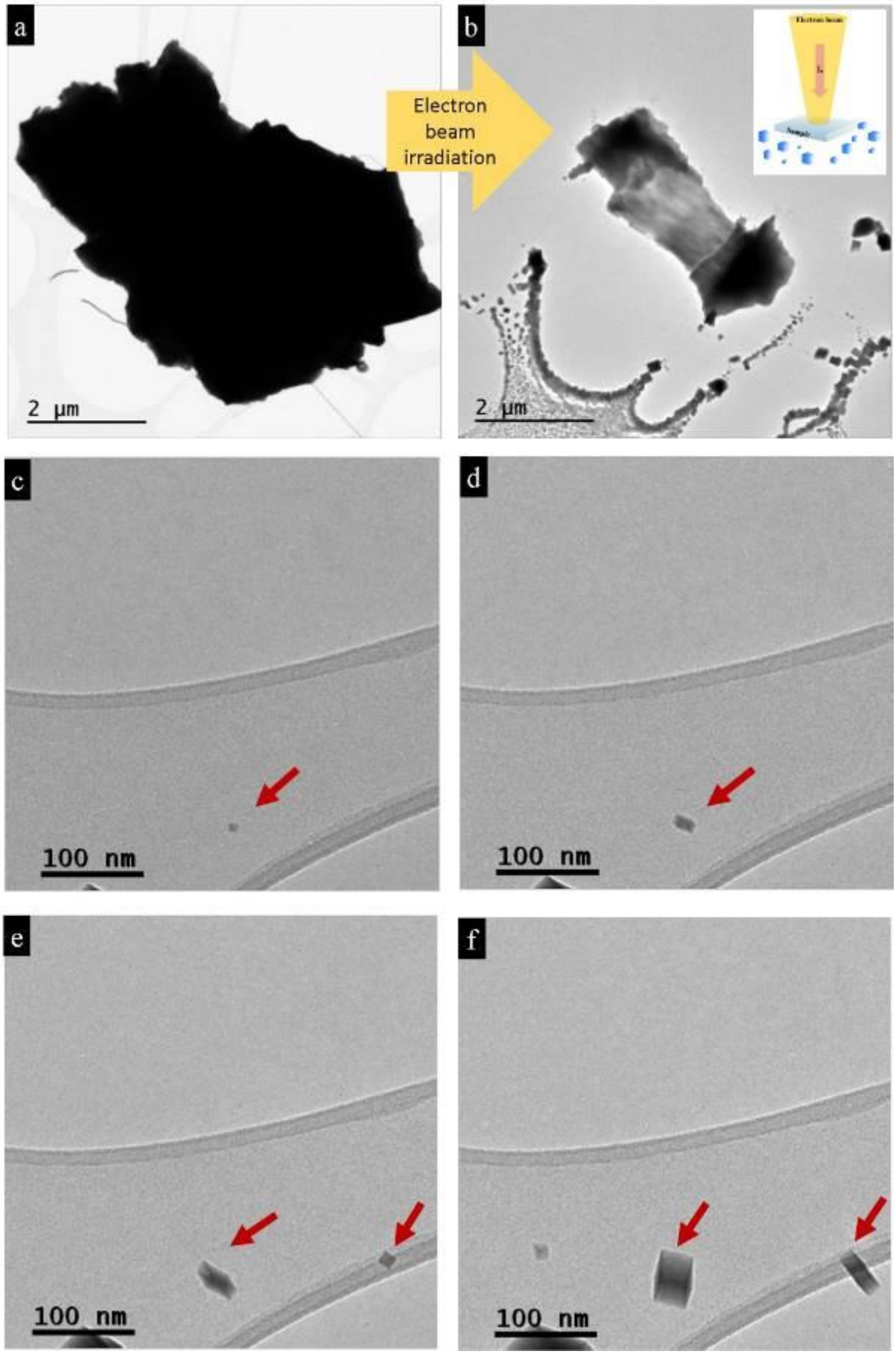
a
2 μm
Electron
beam
irradiation
b
2 μm
c
100 nm
d
100 nm
e
100 nm
f
100 nm

MS2.P007
TEM studies of phase boundary formation in one-dimensional $InRO_3(ZnO)_m$ nanostructures ($R \in$ {In, Fe})

G. Schaan[1,2], H. Schmid[3], W. Mader[2]

[1]Hamburg Institute of Technology, Electron Microscopy Unit, Hamburg, Germany
[2]Rheinische Friedrich-Wilhelms-Universität Bonn, Institute of Inorganic Chemistry, Bonn, Germany
[3]Max Planck Institute for Solid State Research, Stuttgart, Germany

Question: Structure, composition and properties of numerous compounds of the general formula $ARO_3(ZnO)_m$ with $A \in$ {In, Fe, $[Sn_{1/2}Zn_{1/2}]$, …}, $R \in$ {In, Fe, Ga, …} and $m \in$ integers have been studied for more than fifty years. [1-2] However, the mechanisms governing the formation of their most distinctive structural features have only recently become a focal point.[3] We present a comprehensive mechanism for the formation of inversion domain boundaries (IDBs) in nanowires of those compounds.

Methods: Nanostructures of $In_2O_3(ZnO)_m$ and $InFeO_3(ZnO)_m$ were synthesized via a two-step process. First, nanostructures of pure ZnO were grown on silica substrates using a thermal evaporation method. In the second step, these nanostructures were coated with a solution of various metal salts, e. g. indium nitrate and iron(III) acetylacetonate. The droplets decompose at elevated temperatures to yield nanoparticles of the corresponding sesquioxides, which then react with the surface of the nanostructure, leading to a local formation of IDBs.

Results: The onset of the formation of In-decorated b-IDBs is observable after only 2 min of annealing. Initially, b-IDB and p-IDB are parallel and directly adjoined to each other.EDS mapping reveals that each p-IDB is located on the same side relative to its associated b-IDB.

Subsequently, the p-IDB detaches from the b-IDB and takes the shape of a dome or triangle with a flat angle. In between the IDBs, an inversion domain forms, where the configuration of ZnO_4 tetrahedra is inverted with respect to those outside of the domain. Ultimately, the p-IDB will assume an equilibrium angle with respect to the b-IDB that is governed by the atomic species occupying the p-IDB, e. g. 38° to 40° in the case of Fe.

Figure 1: Experimental data (BF-TEM and EDS elemental maps) and atomic-scale models of b- and p-IDBs in the initial (left) and final stages (right) of their formation.

High-resolution HAADF-STEM imaging of $In_2O_3(ZnO)_m$ shows that b-IDBs preferentially form along the serrated edge of nanostructures. {0001}-type facets are not terminated by the b-IDB itself, but by at least two complete layers of Zn atoms. We conclude that, by forming a b-IDB and inverting the ZnO_4 tetrahedra close to the surface of the nanostructure, a reactive facet constituted by unsaturated Zn atoms is transformed into a close-packed inert facet.

{10-11}-type planes close to the surface show a visibly higher *Z* contrast than those further away from the surface and thus, a higher content of In instead of Zn. The atoms constituting them have a trigonal-bipyramidal coordination, which is more favorable for In3+. Atomic columns located directly at the surface have a tetrahedral coordination, although inverted with respect to the ones in the bulk of the material. {10-11}-type surface facets lie parallel to the side faces of the tetrahedra, which are close-packed with oxygen atoms and thus unreactive.

Figure 2: HAADF-STEM images of surface facets of an $In_2O_3(ZnO)_m$ nanowire.

Conclusions: Basal and pyramidal inversion domain boundaries initially form in a parallel arrangement and develop into their final zigzag shape over the course of the reaction. IDBs close to the surface facets of nanowires can reduce the overall reactivity of the nanostructure.

References:
[1] H. Kasper, *Z. Anorg. Allg. Chem.* 1967, *349*, 113-123
[2] S. Eichhorn *et al.*, *J. Solid State Chem.* 2017, *264*, 214-220
[3] A. Goldstein *et al.*, *ACS Nano* 2013, *7*, 10747-10751

Figure 1

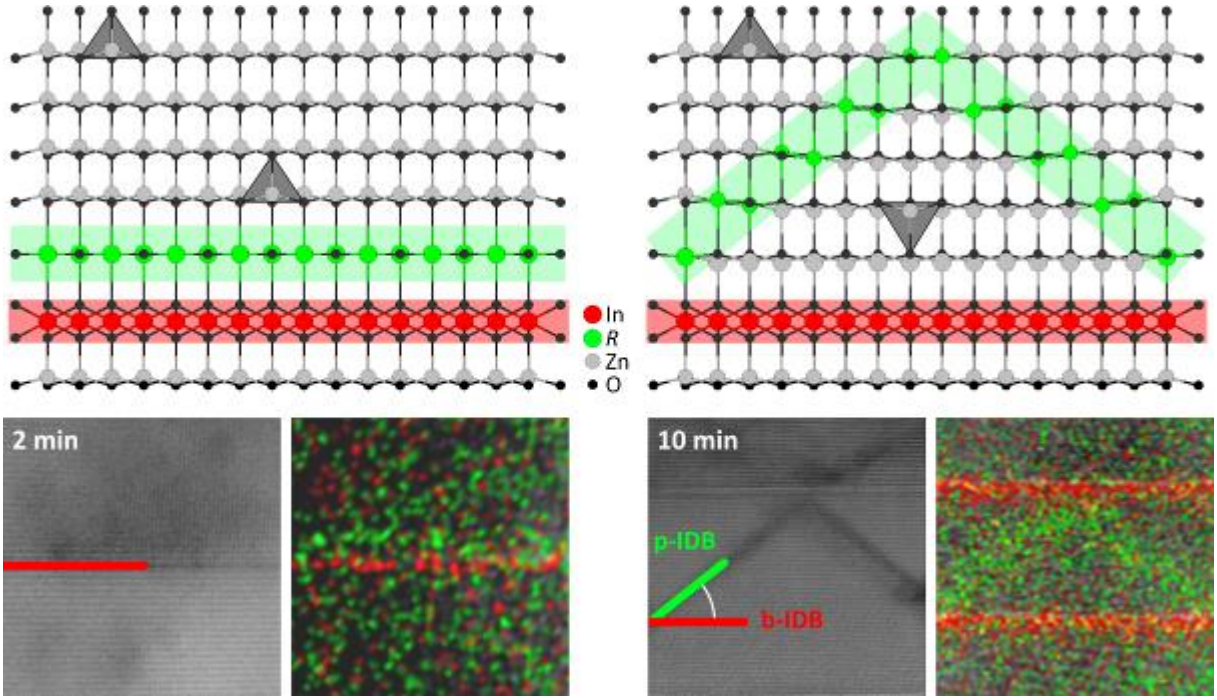

Figure 2

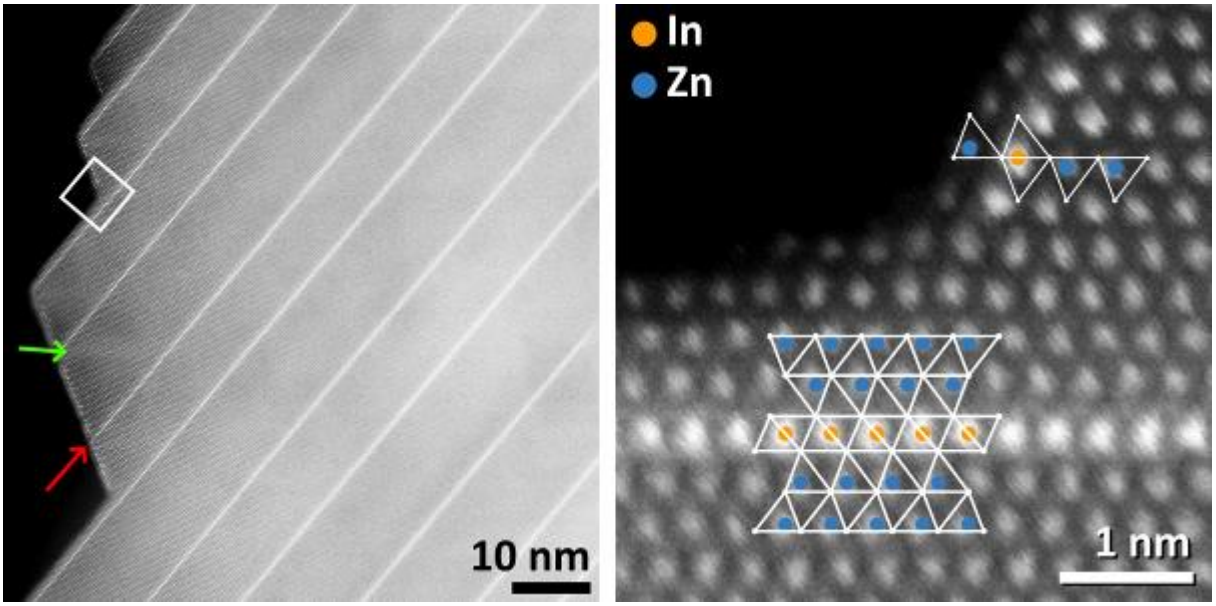

MS2.P008
Plasmonics of Ag nanoparticles embedded in thin silica shells

J. Schultz[1], F. Kirner[2], P. Potapov[1], E. Sturm[2], A. Lubk[1]

[1]Leibniz Institute for Solid State and Materials Research Dresden, Institute for Solid State Research, Dresden, Germany
[2]University of Konstanz, Department of Chemistry, Konstanz, Germany

Localized Surface Plasmons (LSPs) are collective charge oscillations that occur on closed interfaces between media of opposing sign in the dielectric function ε, hence are very sensitive to ε and the surface morphology. LSPs are characterized by strong electromagnetic field enhancement confined to the interfaces, which is exploited in, e.g., improved solar cells and SERS. In order to control the LSPs, non-noble metal nanoparticles (NPs) are frequently coated with a plasmonically inactive shell (ε>0). This provides stable protection against, e.g., oxidization, and a certain control of the dielectric surrounding of the NPs; and is therefore employed in a range of applications [1]. However, the latter degree of freedom may also allow tuning the LSPs in energy and shape by varying the thickness or the dielectric material, which can be used to increase efficiency in various applications. In order to explore this possibility, we studied Ag nanocubes of 60 nm edge lengths coated with SiO_2 shells of different thicknesses. To reveal the LSP mode structure, the NPs were characterized by Scanning Transmission Electron Microscopy (STEM) in combination with Electron Energy Loss Spectroscopy (EELS) [2]. Accordingly determined LSP cubic harmonic eigenmodes in dependence of the silica shell thickness are plotted in Figure 1. They exhibit exceptional agreement with simulation both in energy and spatial distribution due to the well-defined dielectric surrounding of the silica shell. In particular the dependency on the thickness follows a well-predictable trend that may be described by an adapted effective medium approach [3]. Most notably, however, we find a second field enhancement at the SiO_2-vacuum interface, besides the expected one at the silver-silica interface (see Figure 2). It is related to a whispering gallery like mode coupled coherently to the LSPs and effectively increases the long-range interaction of LSPs over few 10s of nanometers. In summary, we have demonstrated that dielectric shells do not only serve as protective layers but also allow to precisely tune and enhance plasmonic interactions of NPs. The latter opens new avenues for application in photonic crystals, amongst others.

[1] Hanske et al., Adv. Mater. 2018, 30 (27), 1707003.
[2] Nelayah et al., Nat. Phys. 2007, 3 (5), 1745-2481.
[3] Vernon et al., Nano Lett. 2010, 10 (6), 2080-2086.
[4] This project was funded by the European Research Council (ERC) under the Horizon 2020 research and innovation program of the European Union (grant agreement no. 715620). Furthermore is was funded by the Deutsche Forschungsgemeinschaft (DFG, German Research Foundation) under Germany's Excellence Strategy through Würzburg-Dresden Cluster of Excellence on Complexity and Topology in Quantum Matter - ct.qmat (EXC 2147, project-id 390858490).

Figure 1: *a) LSP resonance energy as a function of the silica shell thickness. The well-defined dielectric surrounding of the silica shell leads to a very good match between the simulated (solid lines) and experimental (diamonds) data. b) Spatial distribution of the loss probability corresponding to the different modes.*

Figure 2: *Simulated a) and experimental b) line profile of the loss probability for the p-mode on an Ag cube coated with a SiO_2 shell of 22 nm and 8 nm thickness, respectively. The line plot reveals a field enhancement at the Ag-SiO_2 interface. The enhancement increases the long-range coupling, which is of technological interest.*

Figure 1

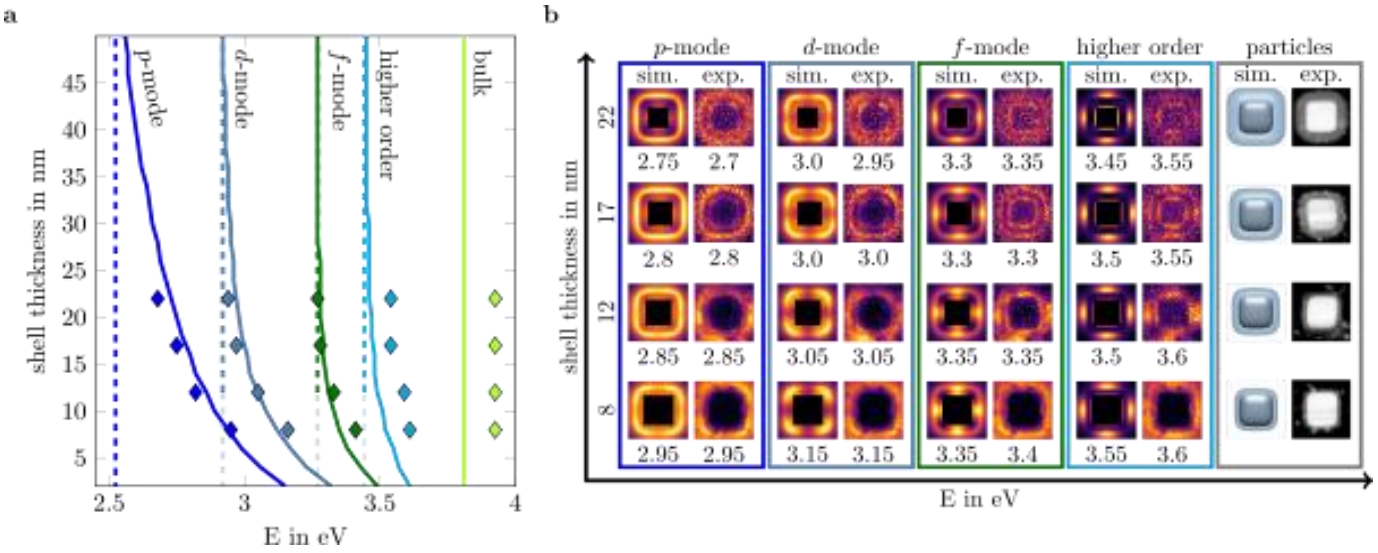

Figure 2

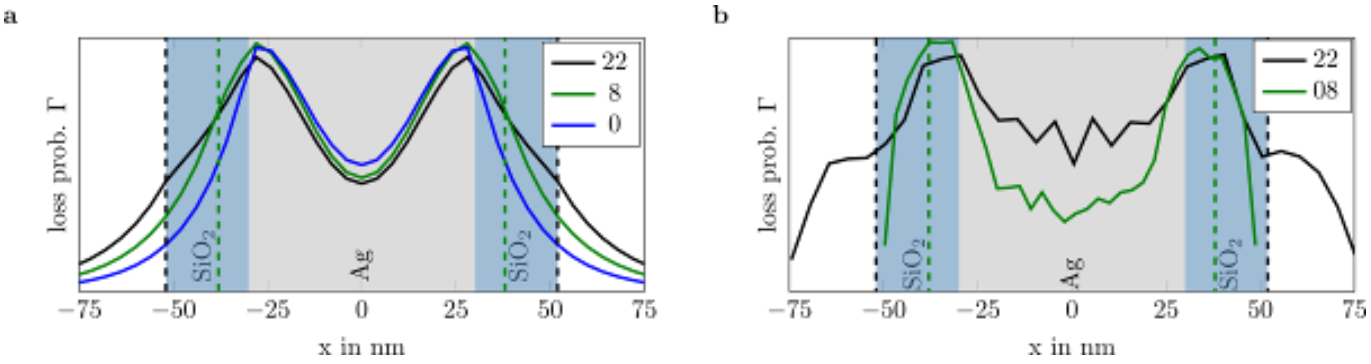

MS2.P009
Characterisation of selective layer and biomolecules fouling in polymeric membranes for microalgae filtration applications using 3D FIB/SEM, STEM and EDS

H. Roberge[1,2], P. Moreau[1], E. Couallier[2], P. Abellan[1]

[1]Institut des Matériaux Jean Rouxel (IMN), Université de Nantes, 44, Nantes, France
[2]GEPEA Laboratoire de Génie des Procédés, Environnement et Agroalimentaire, 44, Saint-Nazaire, France

Membrane filtration processes allow concentrating, separating and purifying the components from a complex mixture in a liquid phase. The two most important properties of a membrane are, thus, its permeability (ability to allow a fluid to pass through it under pressure gradient) and its selectivity (ability to retain a compound). Recently, they have been adapted for microalgae valorization, where filtration employing porous polymer membranes is used to separate and recover lipids and proteins from ground microalgae aqueous extracts. The biomolecules recovered can be used in pharmaceutical industry, cosmetics, food supplements or biofuel industry as biodiesel [1,2]. The permeability and selectivity of the membrane are related to the size and density of its pores, but also to the *selective layer* thickness (a thin layer placed directly in contact with the fluid to be filtered), as shown by Poiseuille"s law [3]. During filtration, the unwanted accumulation of biomolecules at the surface and in the membrane pores, termed *fouling*, hampers the membrane performances. A detailed characterization of the pore structure, as well as its interaction with the target biomolecules, is essential to understand and help minimize the fouling of the membrane.

Generally, porous polymer materials used as filtration membranes are characterized, based on large-scale indirect measurements and on simulation techniques [4]. Scanning electron microscopy (SEM) coupled with a focused ion beam (FIB) allows characterizing the 3D nanoporous structure of the material with a few nanometers resolution [5]. Data acquisition is particularly challenging with polymer membranes constituted of amorphous materials presenting little contrast and a strong sensitivity to the electron and ion beams [7]. Moreover, 3D reconstructions of porous media present a common issue: the shine through artefact, leading to a deformation of the reconstructed pores in the FIB-milling direction [8]. In order to observe lipids or proteins fouled hydrated membranes while maintaining their native structure, the FIB/SEM can be used in cryogenic conditions [9]. The use of spectroscopy (EDS and EELS) and of TEM/STEM microscopes allows for additional chemical and structural information with higher spatial resolution.

In this study, we tested two widely used polymer membranes: PAN (polyacrylonitrile, 30 nm, Orelis) and PES (0.1 µm polyethersulfone, Koch), with a pore size of their *selective layer* of respectively 30 and 100 nm. We developed a method to obtain quality 3D reconstructions with a 5 nm voxel size using 3D FIB/SEM on clean membranes and overcoming beam sensitivity and artefact difficulties. We used segmentation and quantification to obtain experimental properties of PES and PAN filtration membranes. Finally, we used cryogenic conditions with EDS, STEM-EELS spectroscopic analysis to observe lipids and proteins fouled membranes.

In this presentation, the sample preparation, the optimization of acquisition and the reconstruction parameters will be described. We will present a method for identifying the *selective layer* in polymer filtration membranes using FIB/SEM. The quantitative analysis of pore size distribution, porosity, connectivity and tortuosity (fig1) will be discussed. The properties-structure relationships will be analyzed, by linking these results with the theory of Hagen-Poiseuille on the porous media flow calculation. Our results on both: pristine and fouled membranes, will be presented.

Figure 1

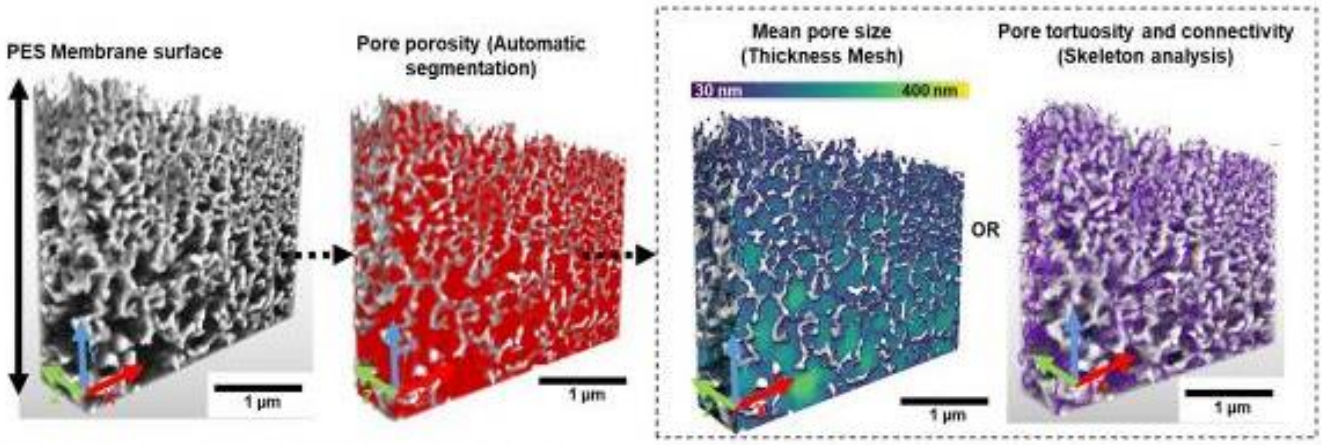

Figure 1 : Illustration of the main 3D analysis steps in the case of the PES membrane. Pores were segmented (DragonFly suite) to extract quantitative information on the volume porosity, the mean pore size (thickness mesh) and the pore tortuosity and connectivity (skeleton).

Figure 2

References :

[1] Rivera et al., *Process Biochemistry* 89 (2020) 199-207

[2] Villafaña-López et al., *Bioresource Technology* 288 (2019) , 121539.

[3] AIMAR et al., *Techniques de l'Ingénieur*, (2010).

[4] Kumar et al., *Desalination* 318 (2013): 1-8.

[5] Sundaramoorthi et al., *Industrial & Engineering Chemistry Research* 55 (2016).

[6] Shi et al., *Journal of Membrane Science* 487 (2015): 19-31.

[7] Huang et al., Journal of Membrane Science 573 (2019): 73 84

[8] Terao et al *Journal of Power Sources* 347 (2017): 108-13

[9] Mulder HG, GIT Imaging & Microscopy (2003)

MS2.P011
Microscopic investigation of selective-area MBE of cubic GaN in defect-trapping mask nanoholes on 3C-SiC/Si (001)

T. Riedl[1], J. Bürger[1], F. Meier[1], D. J. As[1], J. K. Lindner[1]

[1]Paderborn University, Physics, Paderborn, Germany

Introduction: Compared to their hexagonal wurtzite counterparts, metastable cubic zinc blende group III nitrides offer some benefits, e.g. the absence of built-in polarization fields due to higher crystal symmetry [1]. As for other III-V semiconductors, the lack of lattice matched substrates limits the crystal quality of heteroepitaxial cubic GaN (c-GaN) dramatically. Due to the lattice misfit of 3,7%, c-GaN growth on planar 3C-SiC/Si (001) leads to the formation of numerous stacking faults and a rough surface [2]. The regular growth temperature of such c-GaN thin films is in the range of 720 - 760°C.

It has been demonstrated that patterning the substrate with a dielectric mask having holes with sufficient height-to-diameter ratio (i.e. > 1) enables efficient trapping of threading defects at the mask sidewalls as well as a smooth film surface after mask overgrowth and film coalescence [3]. However, selective growth of c-GaN in mask nanoholes on 3C-SiC (001) has not yet been explored. Also, previous studies did not employ MBE for c-GaN selective-area growth (SAG).

Objectives: The aim is to study MBE SAG of c-GaN in SiO_2 mask holes prepared by nanosphere lithography on 3C-SiC/Si (001). The investigation focusses on the GaN nucleation behaviour, the evolution of growth fronts and the resulting spatial distributions of GaN phases as well as defects. The mechanisms of defect minimization are studied, in particular the defect trapping at the mask sidewalls.

Materials & methods: Arrays of nanoholes in the SiO_2 mask deposited on 3C-SiC/Si (001) pseudo-substrates are realized by means of nanosphere lithography, i.e. plasma-shrinking of polystyrene colloid monolayers, Ni hardmask deposition, polystyrene removal and reactive ion etching of SiO_2 (Figure 1). GaN heteroepitaxy is performed with a Riber plasma assisted MBE apparatus. Morphological characterization is carried out by means of imaging in a Raith-Pioneer FESEM. Atomic-scale structural-chemical characterization is achieved by HRTEM, aberration-corrected HRSTEM imaging and EELS in a Jeol ARM200F microscope operated at 200 kV equipped with a Gatan GIF Quantum ER. For strain mapping geometric phase analysis (GPA) is employed.

Results: In contrast to the expectations, it is found that GaN grows selectively in the cubic phase on 3C-SiC/Si (001) even at temperatures above the regular range. In macroscopic SiO_2 mask openings c-GaN SAG is observed for substrate temperatures around 930°C (Figure 2) [4]. For GaN SAG in nanoscale mask holes the resulting phases, defects and surface facets are analyzed by atomic-resolution TEM/STEM in dependence of growth temperature and time. The extent of misfit- and defect-related strain fields is mapped by GPA. In addition, the possible presence of surface oxides at the SiC/GaN heterointerface is evaluated by means of EELS.

Conclusion: Atomic-resolution TEM/STEM imaging and analytics enable profound insight into phase- and area-selective GaN heteroepitaxy in nanoscale mask holes on 3C-SiC (001).

References:
[1] S. Li et al.: Appl. Phys. Lett. 90 (2007) 071903.
[2] D. J. As, K. Lischka, in: M. Henini (Ed.), Molecular Beam Epitaxy (2nd Edition), Elsevier, 2018, pp. 95-114.
[3] C.-W. Hsu et al.: Nanotechnol. 23 (2012) 495306.
[4] F. Meier et al. (unpublished).

Figure 1: SEM tilted-view of a Si test sample patterned with a nanohole SiO_2/Ni mask.

Figure 2: SEM top-view of c-GaN selectively grown at 930°C in a SiO_2 mask opening on 3C-SiC (001).

Figure 1

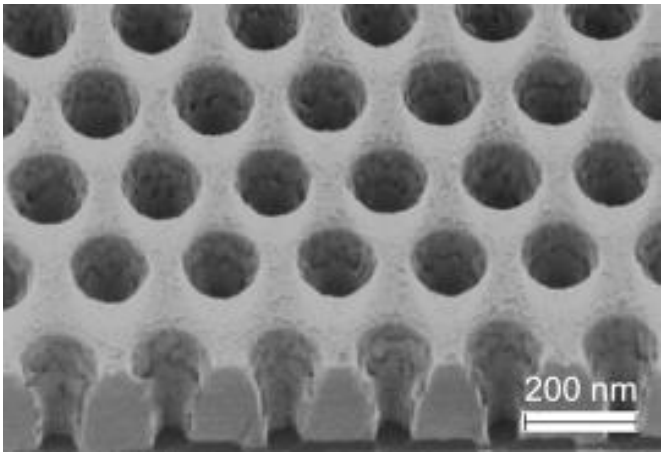

Figure 2

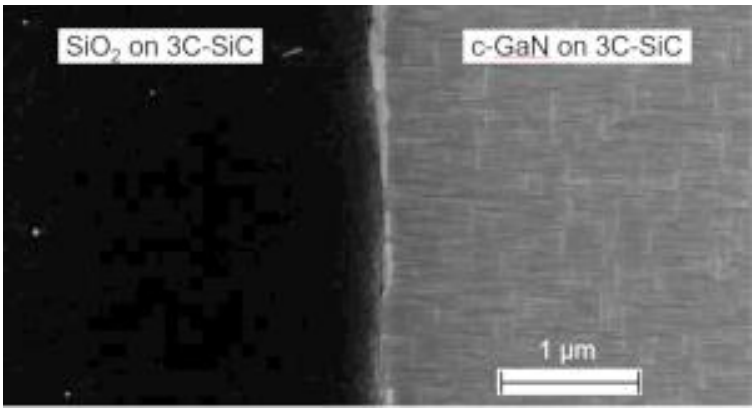

MS2.P012
Quantifying morphology of mesoporous materials by electron tomograph: a phantom simulation

X. Huang[1], D. Wang[1], C. Kübel[1]

[1]Karlsruhe Institute of Technology (KIT), Karlsruhe, Germany

Much attention has been paid to mesoporous materials because of their high surface area, variable pore structure and large pore volume, which is essential for various applications. Compared to bulk techniques such as physisorption and small angle X-ray diffraction, which provide an average measure of the pore structure and pore volume based on assumptions on the pore shape and connectivity, electron tomography has been demonstrated to provide high quality 3D structural information at the nanoscale. However, a quantitative interpretation of electron tomography results is still far from straightforward and an accurate quantification of the pore-space is challenging because of constraints during tilt-series acquisition (missing wedge, dose) and reconstruction artifacts introduced by reconstruction algorithms. Although many efforts have been tried to improve the fidelity of the segmented 3D reconstruction, an investigation of the effect of different algorithms, acquisition conditions and noise on the finial reconstruction and the corresponding quantification of properties such as diffusion is still limited.

In this work, phantom simulations were used to compare the difference of three reconstruction techniques SIRT, TVM and DART and the influence of imperfect tilt series and parameter selection for each algorithm to the final morphology and quantification for mesoporous materials. We first created a 3D phantom with disordered pore structure. Based on this phantom, forward projection was simulated representing the tilt series and some artificial disturbances like missing wedge, noise and misalignment were introduced to mimic realistic imaging conditions. The resulting projections were used as input for SIRT, TVM and DART reconstructions. For each reconstruction method, parameters are selected based on the criterion of minimizing the relative number of misclassified pixels (rNMP) and a median filter with radius of 2 was used for SIRT reconstruction prior to further segmentation. Figure 1 shows a 3D display of misclassified voxels from SIRT-, TVM-based segmentation and DART, comparing to the phantom truth. We found that the misclassified voxels of SIRT- and TVM-based segmentation are often distributed in large continues volumes, while the error voxels produced from DART are more separated and mostly existed on the boundaries around pores space. This has a significant impact on resulting properties of the porous structure.

Quantification of the pore network geometry and topology by skeleton analysis in Fig 2. showed smaller mean pore radius and average chord length are observed in the segmented SIRT reconstruction (Table 1) compared to the TVM and DART reconstruction. Such pore size distribution error for SIRT reconstruction should come from large amount of isolated small pores that caused by the noise artifacts and the misclassified narrow pores connectivity. TVM reconstruction provides slightly better quantification results than SIRT which may be attributed to the noise reduction by the gradient variation constraint. Nevertheless, the most reliable quantification results comes from DART. These results show that DART is a promising method for the quantifying analysis of porous materials compared with the other two algorithms. The differences between the reconstructions are evaluated in diffusion simulations to investigate the effect of reconstruction parameters and methods on the observed materials properties.

Figure 1

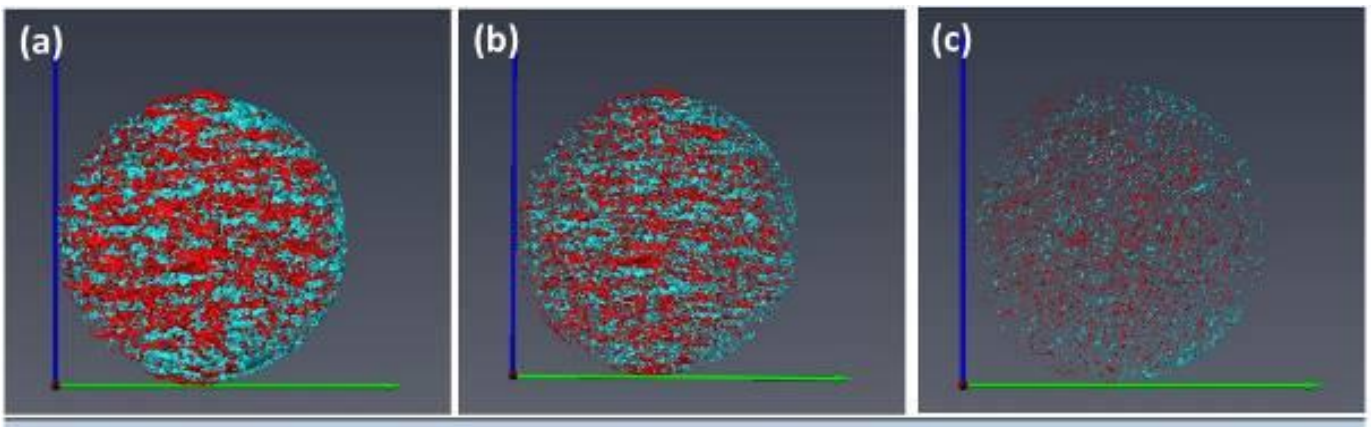

	SIRT	TVM	DART
rNMP (%)	14.75	9.14	6.42

Figure 2

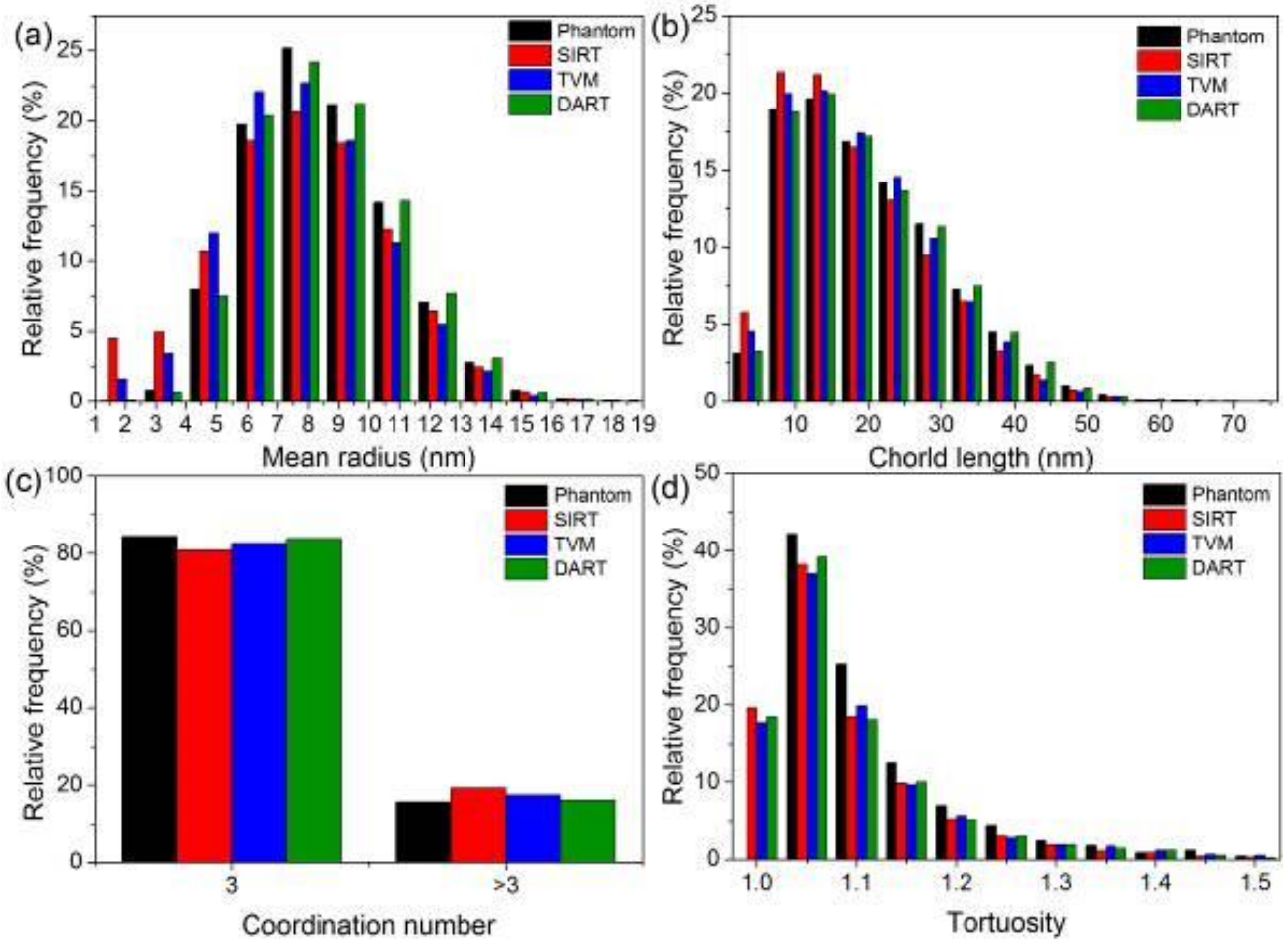

Figure 3

	Chord length (pixels)	Mean radius (pixels)	Tortuosity
Phantom	17.67±10.46	7.74±2.33	1.10±0.11
SIRT	16.00±10.12	7.06±2.87	1.12±0.28
TVM	16.58± 9.96	7.10±2.53	1.12±0.27
DART	17.61±10.40	7.77±2.34	1.10±0.12

MS2.P014
Neural-network-based investigation of defect-rich carbon monolayers

C. Leist[1], H. Qi[2,1], U. Kaiser[2]

[1]Universität Dresden, 2. Center for Advancing Electronics Dresden (cfaed) & Faculty of Chemistry and Food Chemistry, Dresden, Germany
[2]University of Ulm, 1. Central Facility for Electron Microscopy, of Electron Microscopy Group of Materials Science, Ulm, Germany

Introduction: Defect-rich and amorphous 2D carbon monolayers are becoming a rising star in the grand family of 2D materials due to their potential applications in, e.g., DNA sequencing and catalysis. Since aberration-corrected high-resolution transmission electron microscopy (AC-HRTEM) allows for unambiguous elucidation of atomic positions, revealing the atomic structure of defect-rich and even amorphous 2D materials can be readily achieved. However, due to the lack of long-range order, quantitative description (e.g., degree of disorder, defect density and distribution) of such materials is still challenging.

Conventional image analysis methods, e.g., handcrafted filter kernels, often require heavy user supervision and tremendous time cost, posing strong limitations on the data volume for statistical analysis and moreover the high risk of user-induced selection bias, which may lead to an overestimation of low-probability phenomena. Image analysis technique that could offer automation, precision, and extensive statistics, is thus highly desired.

Objectives: Here, we deploy a neural network of U-net architecture for automatic analysis of atomic positions in AC-HRTEM images of carbon monolayers. By determining the positions of every single atom, the distribution and local variation of bond lengths and angles can be evaluated statistically. In addition, the neural network is capable of polygon mapping, providing not only the occurrence frequency of n-membered carbon rings but also their real-space distribution.

Materials & methods: TEM image series where acquired from three different materials: CVD (chemical vapour deposition)-graphene, PDC (Pentagon defect rich carbon) and nanocrystalline graphene monolayer. TEM experiments were performed on the Cc/Cs-corrected SALVE instrument operated at 80kV (SALVE: Sub-Angstrom Low-Voltage Electron Microscopy and Spectroscopy). A combination of networks can be applied to automatically evaluate image series, including automatic exclusion of image regions unusable for evaluation. This method results in large statistics thus reducing the impact of individual errors, such as, image artefacts or misinterpreted spots in an image. The networks are trained with simulated data which reduces user bias and gives a time inexpensive way of generating the required training data.

Results: For validation the automatic evaluation is first applied to CVD graphene. The resulting statistics show excellent agreement with the literature. Evaluation of both PDC and nanocrystalline graphene exhibit substantially broader distributions when compared to CVD-graphene. Additionally the ratio of n-membered carbon rings deviates significantly between all the materials. Mapping of the different C-rings on the images facilitates better understanding of the origins of these different distributions (cf. Figure1).

Conclusion: Neural networks are successfully used to facilitate fully automatic evaluation of highly defective monolayers. Statistics over key parameters of a material were received with several thousand up to several hundred thousand data points each. The statistical analysis of bond length, bond angle as well as polygon mapping show clear differences between the three different carbon materials evaluated.

Figure 1: Left: 80kV SALVE image of CVD-graphene. Grayscale image with colour map. Right: result after automatic evaluation.

Figure 1

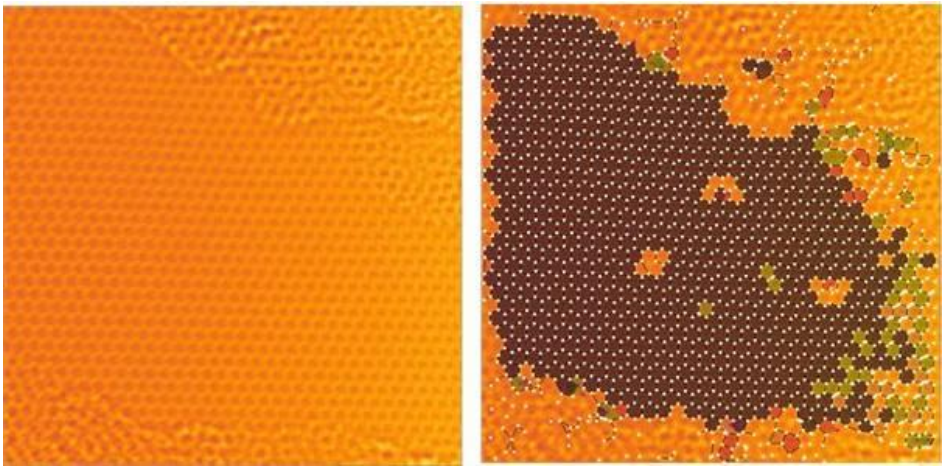

MS2.P015
Nanostructural study by TEM and spectroscopy techniques of Ag filaments in ZnO-based resistive switching devices

K. Bejtka[1,2], G. Milano[2], C. Ricciardi[2], C. F. Pirri[1,2], S. Porro[2]

[1]Italian Institute of Technology, Center for Sustainable Future Technologies, Turin, Italy
[2]Politecnico di Torino, Department of Applied Science and Technology, Turin, Italy

Introduction: Recently, great attention was devoted to memristive devices in the response to global demand of fast, low power and scalable memory technologies. This pushed researchers to study the physical mechanisms behind resistive switching, with particular focus on the creation, evolution, and dissolution of the conducting filament, which, even if improved over the time, are not yet fully understood. In particular, the microscopic nature of the filament and whether one or more filaments are created during the initial electroforming process remain themes of debate. The study of the changes within the storage media of the tested device is even more neglected. This is related to the fact that the random location of the switching filament creation in a macroscopic device makes it difficult to characterize. In situ biasing TEM studies shed some light on understanding the nucleation and growth processes of conducting filaments. It is important to notice that the structures realized for in situ studies are often not equivalent to those studied ex situ, as one dimension has to be drastically reduced.[1]

Objectives: Memristive devices based on polycrystalline ZnO with asymmetric electrodes made of Ag and Pt were prepared with the aim of analyzing the nano-structure of the conductive filaments after resistive switching operations. Focused ion beam (FIB) was used for creation of regular perturbation arrays by patterning the substrate before the deposition of top electrodes.[2] This resulted in confinement of the main conductive filament into a known region as the changes to the film morphology promoted the concentration of the electric field in proximity of the drilled features.[3] The fabricated devices were tested and lamellas were extracted. Nano-structural study have been performed to identify the atomic structure and components of both filament and surrounding region.

Methods: The morphologies of the grown structures and devices, including the characterization of filaments formed during the electrical measurements, were investigated by field emission scanning electron microscopy (FESEM), transmission electron microscopy, and energy dispersive X-ray spectroscopy. The I−V characteristics of the Ag/ZnO/Pt structures were performed in situ in the FESEM-FIB equipped with two Kleindiek manipulators using semiconductor parameter analyzer.

Results & Conclusion: Nano-structural study by TEM and spectroscopy techniques in cross-section helped to identify the atomic structure and components of both filament and surrounding region. It was revealed that multiple filaments can be created within single device, with main filament created at the perturbation and secondary filaments at another positions and/or grain boundaries. The filaments are formed mainly from monocrystalline Ag; which however remains polycrystalline in the zone where the switching occurs. The surrounding material shows that ZnO has a depredated quality in switching zone; however, its quality does not change in the rest of the device.

The morphological and structural characteristics of the devices will be compared with their functional properties, e.g. the switching behavior evaluated by electrical characterization.

Figure 1: TEM and EDX characterization of the filament: (a) at the perturbation,[2] (b) far from perturbation.

[1] W. Sun et al. *Nat. Commun*. 2019, 10, 3453
[2] K. Bejtka et al. *ACS Appl. Mater. Interf* 2020, 12, 29451
[3] K.-Y. Shin et al. *Adv. Electron. Mater.* 2016, 2, 1600233

Figure 1

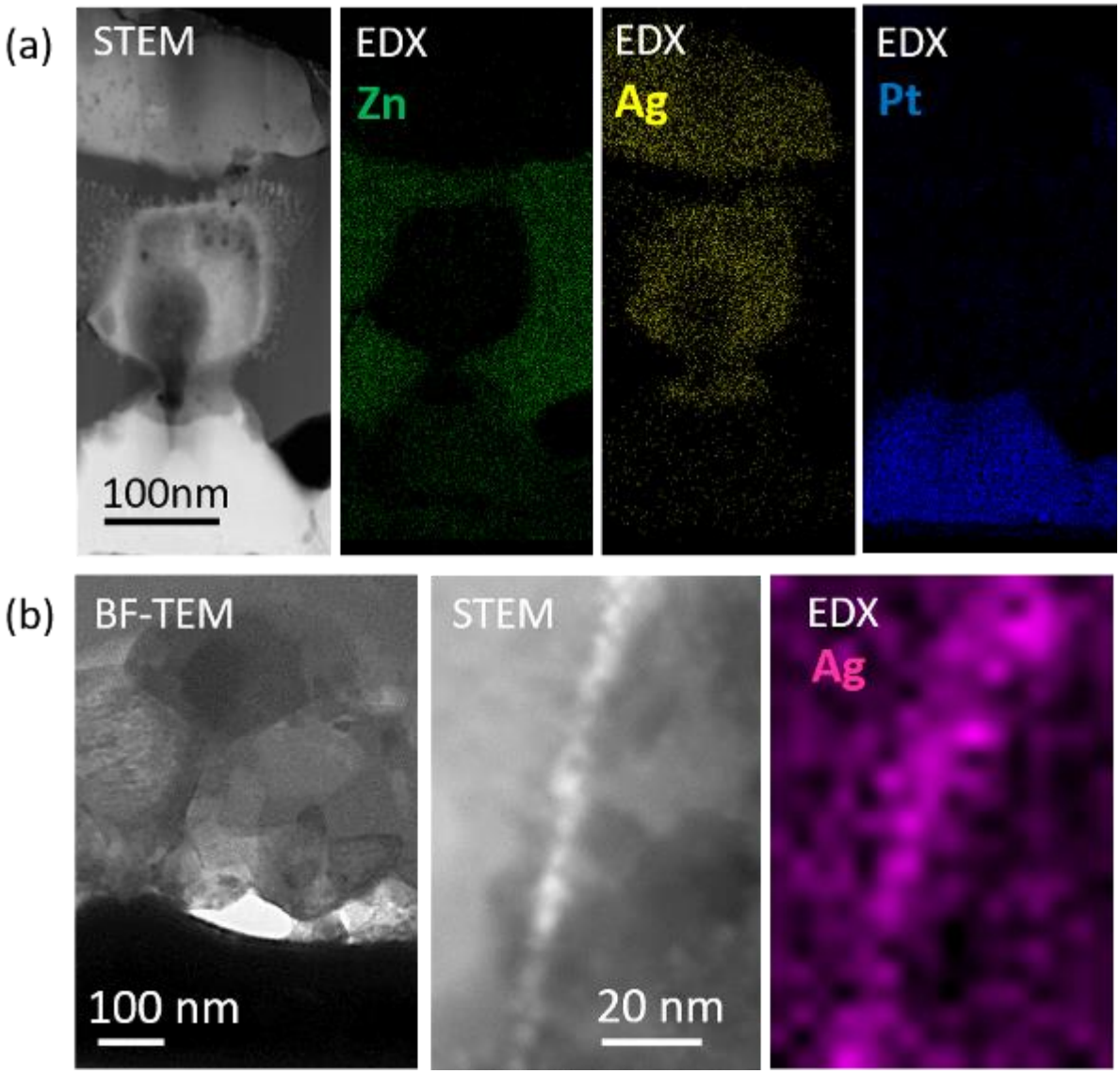

MS2.P016
Carbon-nanotube-based molecular motor and its application in revealing metal nucleation mechanism

K. Cao[1,2], J. Biskupek[2], S. T. Skowron[3], Y. Hu[1], C. T. Stoppiello[3], E. Besley[3], A. N. Khlobystov[3], U. Kaiser[2]

[1]ShanghaiTech University, School of Physical Science and Technology, Shanghai, China
[2]University of Ulm, Electron Microscopy of Materials Science, Central Facility for Electron Microscopy, Ulm, Germany
[3]University of Nottingham, School of Chemistry, Nottingham, United Kingdom

Introduction: Single-walled carbon nanotubes (SWNTs) is promising material to realize controllable transport of molecules owing to its narrow cylindrical cavity. Atomically-resolved, time-dependent in-situ transmission electron microscopy (TEM) imaging enables direct visualization of molecular motion in SWNTs. Forward and backward translations in SWNTs of carbon capsules, LaC_2 nanocrystal, and C_{60} molecules have been subsequently reported.[1-3] As predicted by theoretical simulation, the rifling-like helical orbits on SWNT are able to force the nanoparticle encapsulated in the SWNT to rotate when it moves linear[4].

Objectives: Although rotational motions have been observed in carbon-nanotube-based mass transfer systems[5-7], the interaction between the moving matter and the carbon nanotube has not been experimentally studied. In addition, the application of such kind of motion has not been developed yet.

Materials & methods: By applying the C_S-corrected FEI Titan 80-300 and C_C/C_S-corrected SALVE (Sub-Ångström Low-Voltage Electron microscopy) instrument, we directly observed and stimulated the helical motion of amorphous carbon nanostructures encapsulated in a SWNT. In addition, several kinds of metal atoms and clusters have been filled into the SWNT, which could interact with the amorphous carbon nanostructures and the host SWNT. Thus the interactions between the helically moving amorphous carbon nanostructures, the metal clusters and the SNWT have been observed with atomic resolution.

Results: Utilizing the electron beam both as stimulus and imaging probe, the amorphous carbon nanostructures encapsulated in a SWNT move along the helical track on the wall of the SWNT (Figure 1). This kind of helical motion can be controlled by a single metal atom brake. In addition, we applied this molecular motor for carrying metal atoms to a nucleation seed, realizing in situ observation of metal nucleation (Figure 2)[8].

Conclusion: In this study, we experimentally proved that the chiral structure of the SWNT can be utilized for assembling helical molecular motor. We also demonstrated that such molecular motor can be controlled by a single metal atom. Furthermore, this molecular motor is applied as atom carrier and proves that the nucleation of the metal confirms to two-step nucleation mechanism.

Figure 1: Cs-corrected HRTEM time-series showing the helical motion of an amorphous carbon nanostructure encapsulated in a SWNT stimulated by the electron beam irradiation. Scale bar, 1 nm.

Figure 2: In-situ HRTEM experiments demonstrating the metal nucleation mechanism revealed by applying carbon-nanotube-based molecular motors.

[1] Hiroshi Somada *et. al. Nano Lett.* 2009**,** *9*, 62-65
[2] Jamie H. Warner *et. al. ACS Nano.* 2009, 3, 3037-3044
[3] Ke Ran *et. al. ACS Nano.* 2011**,** 5, 3367-3372
[4] Philipp A. E. Schoen *et. al. Nano Lett.* 2006, 6, 1910-1917
[5] Masanori Koshino *et. al. Science* 2007*,* 316, 853
[7] Jamie H. Warner *et. al. Nano Lett.* 2008**,** 8, 2328-2335
[8] Kecheng Cao *et. al. Nat. Chem.* 2020, 12, 921–928

Figure 1

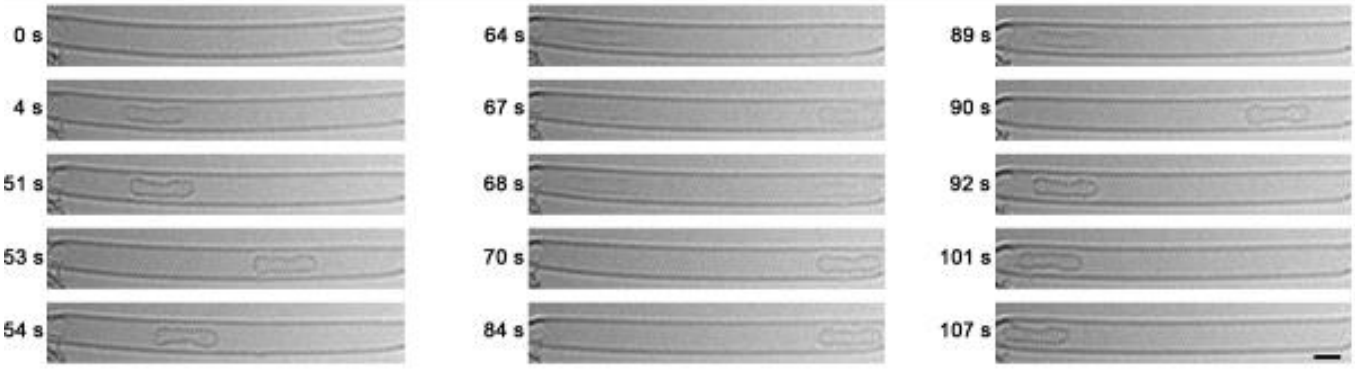

Figure 2

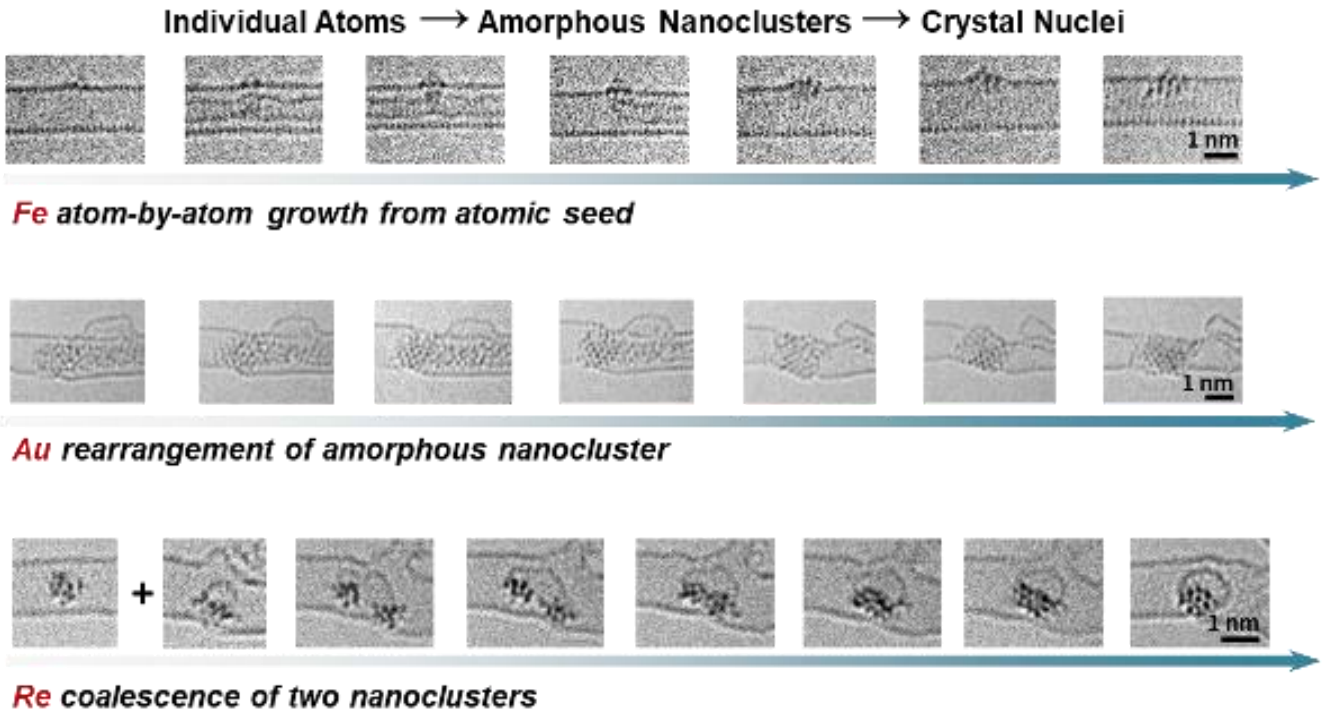

MS2.P017
Multimodal analysis of joint EELS and EDS data

R. Twesten[1], J. Rafaelsen[2], L. Spillane[1], P. Thomas[1]

[1]Gatan Inc., Pleasanton, CA, United States
[2]Ametek / EDAX LLC, Mahwah, NJ, United States

Introduction: Inelastic scattering of electrons leaves the sample in an excited state which can return to the ground state by the emission of a photon. This process has led the wide use of the complementary techniques of electron energy-loss spectroscopy (EELS) and energy dispersive [x-ray] spectroscopy (EDS) in the modern electron microscope. It is increasingly common to acquire joint EELS-EDS data for materials analysis, from large area mapping down to atomic scale analysis. However, these data sets are often analyzed in isolation negating the synergy of their complementary nature.

Objectives: To better take advantage of the complementary excitation/de-excitation process, we will review the strengths of each technique and show how analyzing data on a single platform opens new avenues for data analysis and interpretation. Table 1 shows several of the complementary aspects of the excitation (EELS) and de-excitation (EDS) process; by exploiting the strengths of each, a more complete analysis is possible.

Materials and methods: Data were acquired using a GIF Quantum EELS and SuperX EDS systems operating at 300 kV using Gatan Microscopy Suite (GMS) joint EELS/EDS acquisition software. A sample containing of Fe based magnetic nanoparticles embedded in a GaN matrix was used as an example specimen [1]. Data were analyzed off-line using GMS version 3.5 EELS/EDS analysis software.

Results: Figure 1 shows the analysis of a joint EELS and EDS data set from an Fe-nitride precipitate in a GaN matrix. Low-loss EELS is used to calculate the relative thickness and, when combined with core-loss EELS and EDS composition analysis, the absolute thickness is obtained. The composition in the bulk is close to GaN while the precipitate has over 55% Fe. Overlap with the bulk cannot be ruled out; however, the N K-edge (Figure 2) shows a clear ELNES change in the precipitate indicating compound formation. Using concurrent ELNES standards [2], the different chemical phases of nitrogen can be quantified. The defective region on the left of the precipitate shows a clear rise in the Fe L3 white line and nitrogen fine structure intermediate between the GaN bulk and the precipitate (Figure 2).

Conclusions: Combined EELS / EDS analysis has been used to analyze Fe based magnetic particle in GaN. We will present further analysis and detail the software tools used for this project.

References:
[1] Meingast, A., et al., (2015). Semiconductor science and technology, 30(3), 035002.
[2] Schaffer, B., et al., (2019). Microscopy and Microanalysis, 25(S2), 648-649.
[3] Special thanks G. Kothleitner and A. Meingast at FEMI/TU Graz for TEM samples and instrumentation access.

Table 1: Complementary information provided by multimodal EELS and EDS data analysis.

Figure 1: Joint analysis of an Fe-nitride precipitate in GaN. a) and b) chemical maps of N K edge using concurrent standards.; c) Fe L edge map; d) Ga L edge map; e) composition profiles (along the line in c) extracted from EDS data co-acquired with the EELS data; f) thickness map from EELS analysis.

Figure 2 (Upper) N-K edge fine structure from bulk GaN, the center of precipitate and the defective region on the left of the precipitate (dark green region in figure 1 c) (Lower) The chemical change in the defect can be seen in the Fe L23 edge where there is slight dip in the L3 white line possibly indication a change in spin state.

Figure 1

Property	Excitation (EELS)	De-excitation (EDS)
Beam current	Measure from ZLP	
	Calibrate dose / dose-rate	Use current for quantification
Absolute thickness	Measure from low-loss;	
	Correct quantification for diffraction	Correct quantification for absorption
Elemental identification	Exploit high localization to reject artefact and system peaks	Exploit high signal-to-background to find trace element
Compositional mapping	Exploit high sensitivity to map thin and dose sensitive regions	Exploit high signal-to-background to map thick regions
Quantification	Well defined instrumentation factors for light elements	Large energy range in every spectrum
	High sensitivity down to zero thickness	Rare to miss an element
	Able to separate most overlapping elements	Often multiple lines to for each element
Chemical state / physical properties	Use ELNES to quantify chemical bonding and oxidation state changes	
	Use plasmons to identify even subtle changes in composition and density	
	Probe phonon and electronic band structure with momentum resolved EELS	

Figure 2

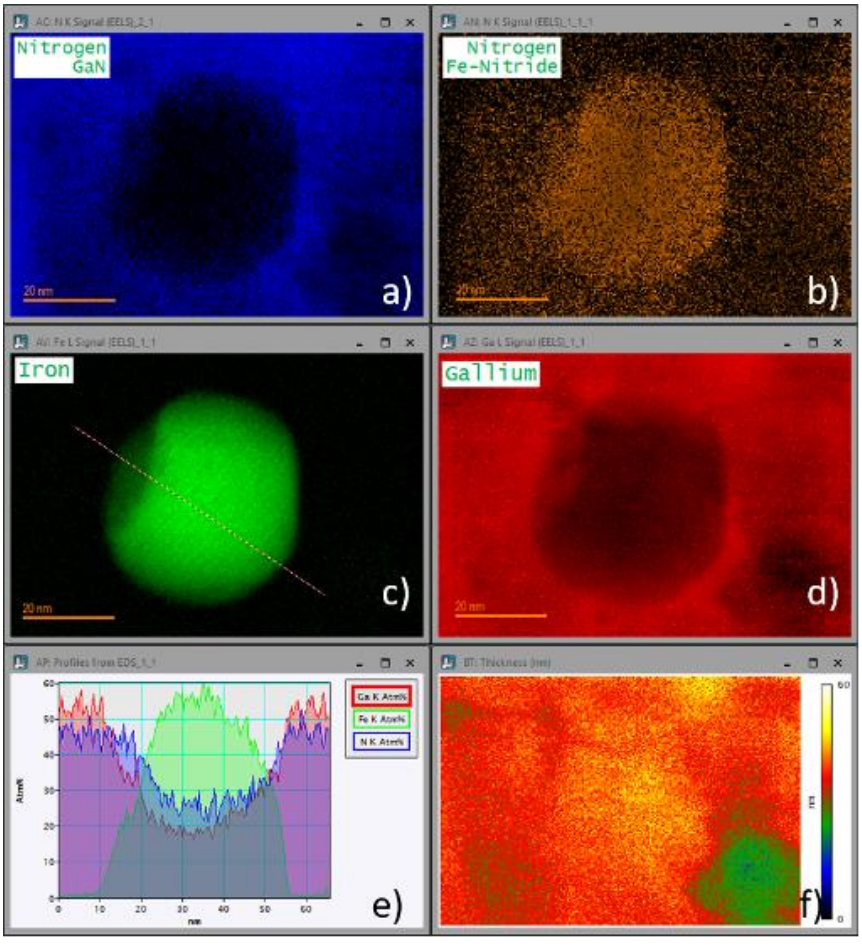

Figure 3

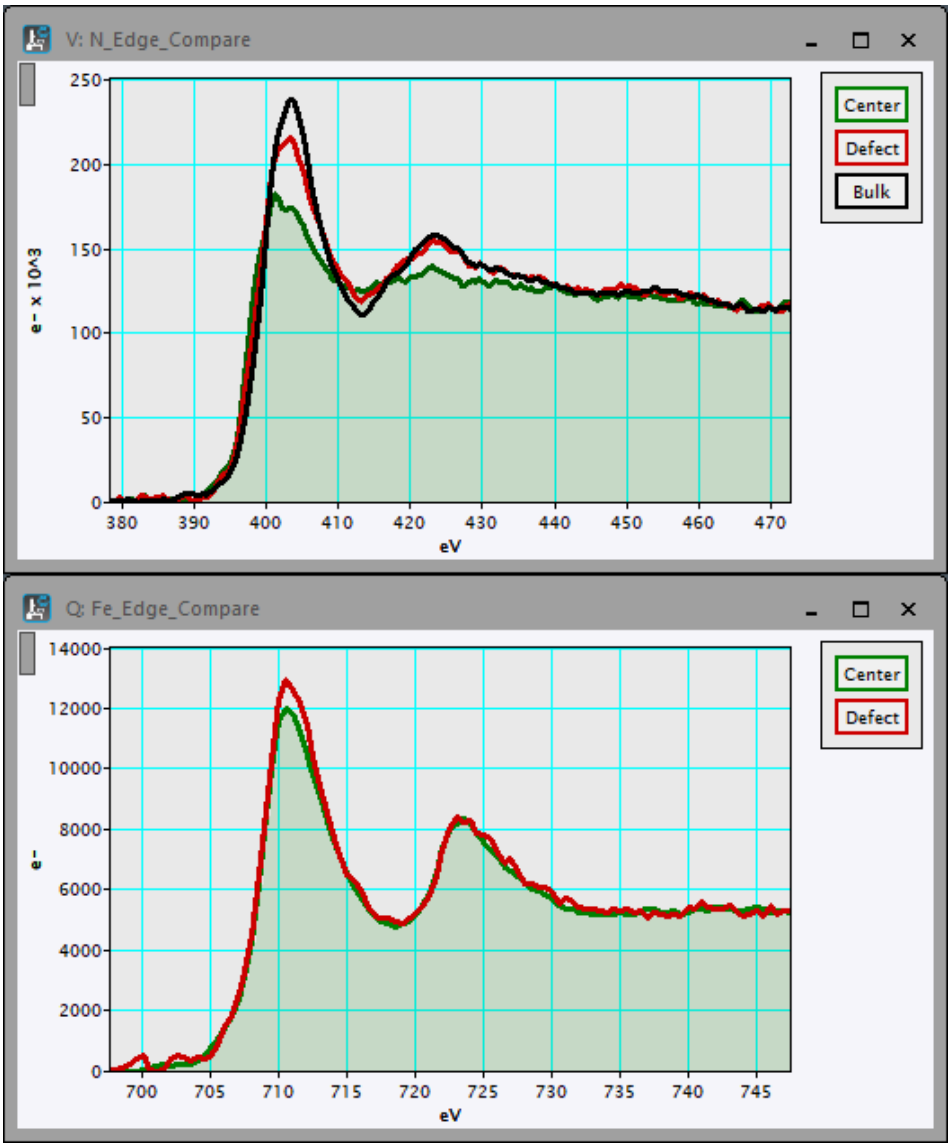
V: N_Edge_Compare
e- x 10^3
eV
Center
Defect
Bulk
Q: Fe_Edge_Compare
e-
eV
Center
Defect

MS2.P018
In situ pyrolysis of 3D nano printed metamaterials

Q. Sun[1], C. Dolle[1], C. Kurpiers[2], R. Schwaiger[3], P. Gumbsch[2,4], Y. M. Eggeler[1]

[1]Karlsruhe Institute of Technology (KIT), Laboratory for electron microscopy, Karlsruhe, Germany
[2]Karlsruhe Institute of Technology (KIT), Institute for Applied Materials, Karlsruhe, Germany
[3]Research Center Jülich, Institute of Energy and Climate Research, Jülich, Germany
[4]Fraunhofer Institute for Mechanics of Materials IWM, Freiburg, Germany

Keywords: mechanical metamaterials, pyrolysis, carbonization, electron microscopy

Mechanical metamaterials are micro-and nanostructural man-made materials. They can possess unusual properties such as negative elastic moduli, negative effective mass densities and non-linear behavior due to their structural design rather than their chemical character [1]. Polymeric mechanical metamaterials can for example be fabricated by three-dimensional direct laser writing (3D-DLW). By pyrolysis (thermochemical decomposition of organic materials at high temperature in vacuum or inert atmosphere), the polymer resin can be transformed into glassy carbon. This is accompanied by shrinkage and mechanical strengthening [2]. Both, miniaturization and strengthening have great potential for a variety of applications, such as carbon micro- and nanoelectromechanical systems (C-MEMS and NEMS) [3].

However, there is a lack of systematic and in-depth understanding of the pyrolytic conversion of polymeric metamaterials into glassy carbon structures. In this work, low-voltage *in situ* environmental SEM combined with *in situ* TEM are employed to investigate the evolution of the structural and mechanical properties during the pyrolysis process as well as the carbonization mechanism on the micro and nanoscale. The 3D polymer structures are directly printed on a MEMS-based heating chip and structural evolution processes are observed during *in situ* heating. Using this direct printing approach (vs. FIB lift out techniques), contamination and oxidization of the materials are avoided. In a first step, we printed scaffolding struts of a large metamaterial directly on the MEMS chip. The struts were printed inside and outside of the heating spiral, as shown in Figure 1a. Since a volume shrinkage of 80% is expected [2], the struts are printed on top of polymer-springs that account for this size change during heating, shown in more detail in Figure 1b. To understand the dynamic processes of polymerization we first conduct *in situ* heating experiments in an environmental SEM where temperatures up to 1300 °C can be reached (Figure 2). The kinetics of the shrinkage processes during polymerization is tracked on a micrometer scale. The complementary nanoscale study with information of structural details and changes will then be conducted using TEM to create a link between kinetics and the resulting properties.

A thorough scale-bridging understanding of the pyrolysis process will create a better understanding of the carbonization kinetics and how to link them to the mechanical properties as a function of temperature exposure towards tailoring desired functional materials.

Acknowledgements: All authors gratefully acknowledge funding by the Deutsche Forschungsgemeinschaft (DFG, German Research Foundation) under Germany"s Excellence Strategy 2082/1 390761711 and sincerely thank the Carl Zeiss Foundation for financial support.

References:
[1] Christensen, J. *et al. MRS Commun.* 5, 453–462 (2015)
[2] Bauer, J. *et al. Nat. Mater.* 15, 438–443 (2016)
[3] Jiang, S. *et al. J. Micromech. Microeng.* 25, 113001 (2015)

Figure 1: (a) SEM image of 3D printed polymeric struts on the MEMS-based heating chips. (b) SEM image of the polymeric bench printed with two springs, which were designed to tolerate the high expected shrinkage during carbonization.

Figure 2: (a) A series of SEM images of 3D printed polymeric struts during *in situ* heating process. (b) SEM image of one strut after heating to 740 °C.

Figure 1

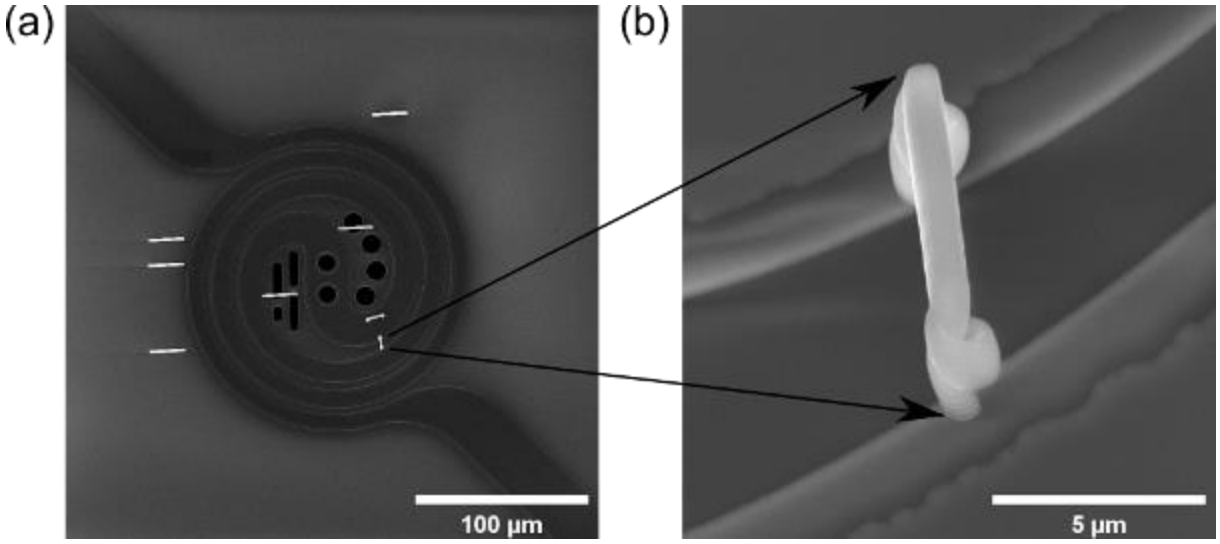

Figure 2

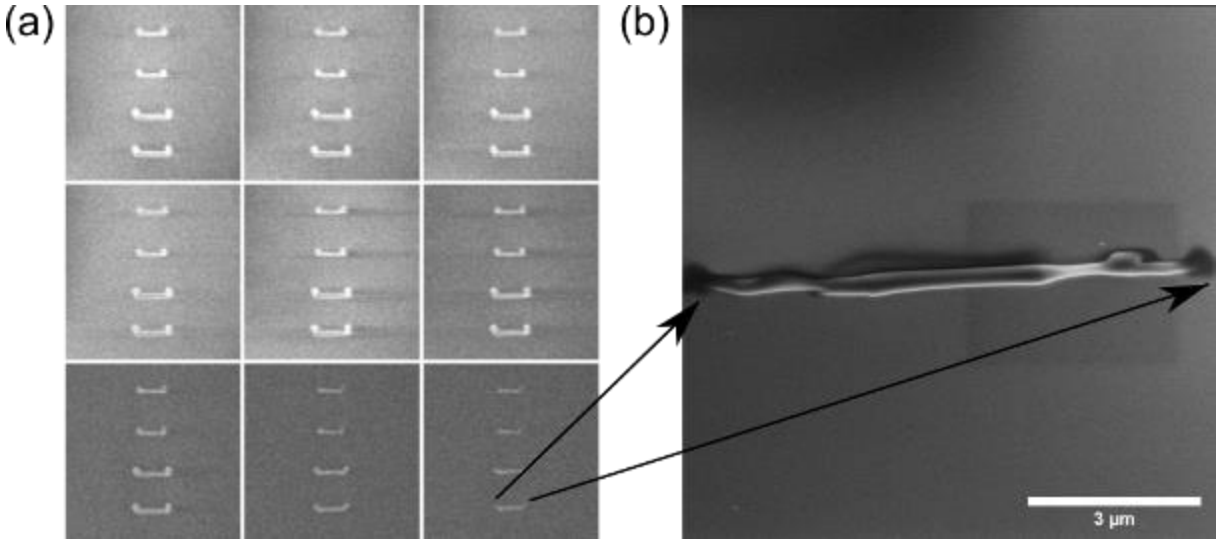

MS2.P019
Atomic-scale investigation of the structural and electronic couplings in rare-earth nickelate superlattices

B. Mundet[1,2], D. T. L. Alexander[2], C. Domínguez[1], A. B. Georgescu[3], J. Fowlie[1], Y. Zhang[4], A. Mercy[4], P. Ghosez[4], A. Georges[3,5,6], A. J. Millis[3,7], M. Gibert[8], J. M. Triscone[1]

[1]University of Geneva, Quantum Matter Physics, Geneva, Switzerland
[2]Swiss Federal Institute of Technology Lausanne (EPFL), Institute of Physics (IPHYS), Lausanne, Switzerland
[3]Flatiron Institute, Center for Computational Quantum Physics, New York, NY, United States
[4]University of Liège, Theoretical Materials Physics, CESAM, Liège, Belgium
[5]Collège de France, Paris, France
[6]Institut Polytechnique de Paris, Centre de Physique Théorique (CPHT), CNRS, Paris, France
[7]Columbia University, Department of Physics, New York, NY, United States
[8]University of Zurich, Physik-Institut, Zurich, Switzerland

Recent advances in thin film growth have enabled researchers to study the coupling of different order parameters by engineering epitaxial heterostructures where the interaction between two compounds can give rise to novel phenomena. The family of rare-earth nickelate oxide compounds (RENiO3), where RE stands for a rare-earth element, offers a wide playground for studying structural and electronic couplings. Most of these compounds display a sharp metal–insulator transition (MIT), whose transition temperature is governed by their characteristic Ni-O-Ni bond angle.[1] Although the structural and electronic properties of these materials have been widely studied, little is known about the characteristic length-scales over which the distinct electronic phases can be established.

In this work, we use a double-aberration-corrected FEI Titan Themis, operated in STEM mode, to determine the characteristic length-scales associated to the distinct structural and electronic couplings that are established in a series of $NdNiO_3$/$SmNiO_3$ superlattices (SLs). To this end, we progressively reduce the length of the SL periodic unit, keeping their overall film thickness constant. Transport measurements reveal that the SLs with a larger periodic length display two well-defined MITs, whereas the shorter ones display a single MIT.

First, we use monochromated electron-energy loss spectroscopy (EELS) to assess their chemical and electronic properties. The pixel size, dwell time and beam current are optimized to give a good compromise between output signal and material degradation. The resulting atomic-scale maps reveal that the interfaces are atomically sharp with a minimal degree of cationic intermixing. Then, we investigate the length-scale of their electronic couplings by assessing specific fingerprints of the Ni *L* edge fine structure, which are characteristic of the metallic and insulating state of these materials. The obtained near-atomic-scale electronic phase maps reveal that the metallic-insulating boundaries present a width of around 4 unit cells, and that all $SmNiO_3$ layers are metallic at room temperature in the short-period SLs.[2] Second, we investigate the structural couplings occurring at the nickelate interfaces by acquiring high-quality high-angle annular dark field (HAADF) and annular bright field (ABF). This is done by acquiring stacks of 24 images with low beam currents, iteratively clockwise rotated 90º, which are then cross-correlated and distortion corrected. From the resulting atomic coordinates, we determine that the structural couplings at the interfaces present a much shorter length-scale than that of the electronic one. Finally, we propose a theoretical model that describes well our experimental observations, which ascribes the emergence of a singular electronic coupling to the boundary energetics of the system.[3]

In summary, we have used aberration-corrected STEM-EELS to investigate in detail the structural and electronic couplings that are established in a series of $NdNiO_3$ / $SmNiO_3$ superlattices. Our results confirm that neither their chemical properties nor the structural ones can explain the singular electronic coupling that is established in this system, whose origin is ascribed instead to the interfacial energetics of the system.

[1] S. Catalano, et al., *Rep. Prog. Phys.* 81, 046501 (2018)
[2] B. Mundet et al., *Nano Letters*, In press
[3] C. Dominguez, A. Georgescu, B. Mundet et al., *Nature Materials* 19, 1182–1187 (2020)

MS2.P021
Low overvoltage application of standard customised coefficients in standard-less EDS analysis for improved spatial resolution

S. Mu[1], J. Rafaelsen[1]

[1]EDAX LLC, Mahwah, NJ, United States

When analyzing nanostructures with Energy Dispersive Spectroscopy (EDS) in a SEM, the excitation volume must be limited to provide enough spatial resolution and low acceleration voltages are used traditionally. Low overvoltage measurements can be used as an alternative to low kV analysis for improved spatial resolution. As can be seen in Figure 1a, the signal depth of the Fe K line with an ionization energy of 7.112 keV is lower than the Fe L line with an ionization energy of 0.846 keV up to an acceleration voltage of approximately 13 kV (overvoltage of roughly 1.82). However, low overvoltage measurements with standard-less quantification are exceedingly challenging since the ionization cross section changes dramatically as the acceleration voltage approaches the critical ionization energy (Figure 1b).

One way of improving the accuracy of low overvoltage measurements is by using Standard Customized Coefficients (SCC). Unlike quantification with standards, where the goal is to minimize model contributions to the quantification results, the goal of SCC factors is to optimize the model to a given experimental setup and set of conditions. The equation in Table 1 serves as a general example of quantification models. Most standard-less results are normalized to 100%, but by measuring a reference spectrum (typically single element standard) it is possible to determine the term of the equation and calculate non-normalized results. By measuring either compound or single element standards using the non-normalized results, it is now possible to determine any deviations between model output and certified values as well as compensate for the deviations by applying the SCC/scaling factor.

To examine the benefits of SCC for low overvoltage quantification, an iron silicide standard with two distinct phases was examined (see compositions in Table 2). A pure Si sample was used as a reference sample while a pure Fe sample was used to determine the Fe K SCC values. Spectra were collected in a range from 9 to 20 kV corresponding to an overvoltage range of 1.1 to 2.8. The quantification results in Figure 2 show a significant overestimation of Fe as the acceleration voltage approaches the Fe K ionization energy. By applying SCC measurements from a pure Fe sample, the deviations from implemented models can be compensated for and satisfactory quantification results can be achieved.

SCC measurements can be used to optimize standard-less models and provide high quality standard-less quantification results for low overvoltage analysis. This method serves as an alternative to low kV analysis for reducing excitation volumes to resolve nanostructures.

References:
[1] Ritchie, N.W.M. (2019). NIST DTSA-II software, including tutorials.
Available at https://cstl.nist.gov/div837/837.02/epq/dtsa2/
[2] Goldstein et al., Scanning Electron Microscopy and X-Ray Microanalysis (2018). ISBN: 978-1-4939-6674-5. 10.1007/978-1-4939-6676-9.
[3] J. Trincavelli et al, Spectrochimica Acta, Part B (101), pp. 76-85, 2014.

Figure 1: a) Simulation of signal depth as a function of acceleration voltage using NIST DTSA-II [1]. b) Calculated ioniza-tion cross section of Si K with an ionization energy of 1.839 keV and Fe K with an ionization energy of 7.112 keV [2].

Figure 2: Quantification results for the main matrix (a) and bright spots (b) of the iron silicide standard.

Table 1: An example of quantification models [1].

Table 2: Composition of iron silicide standard.

Figure 1

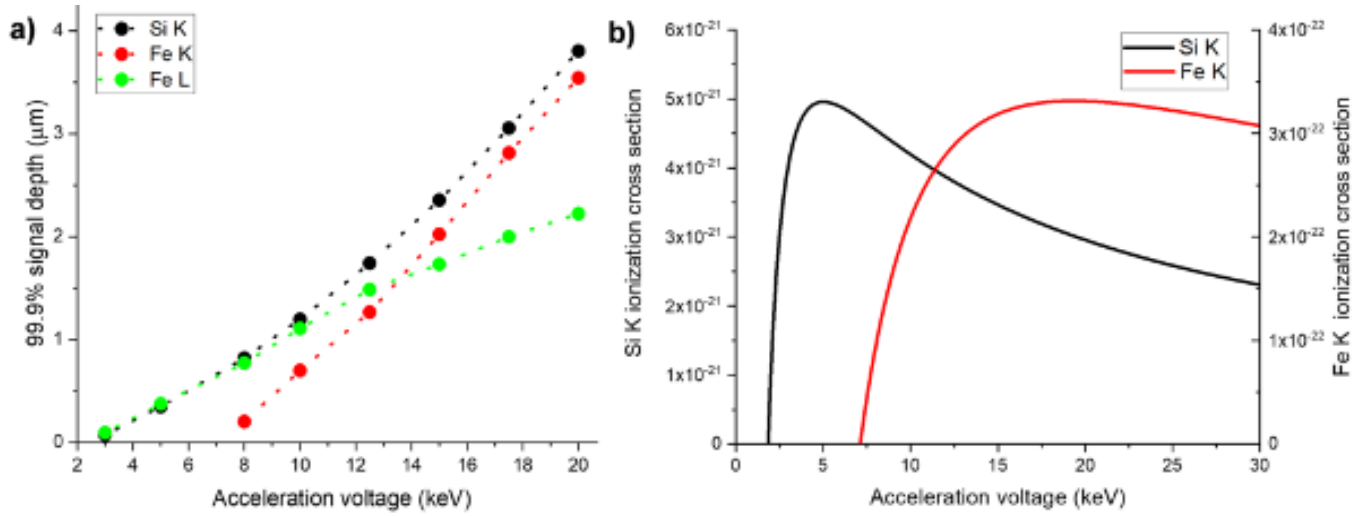

Figure 2

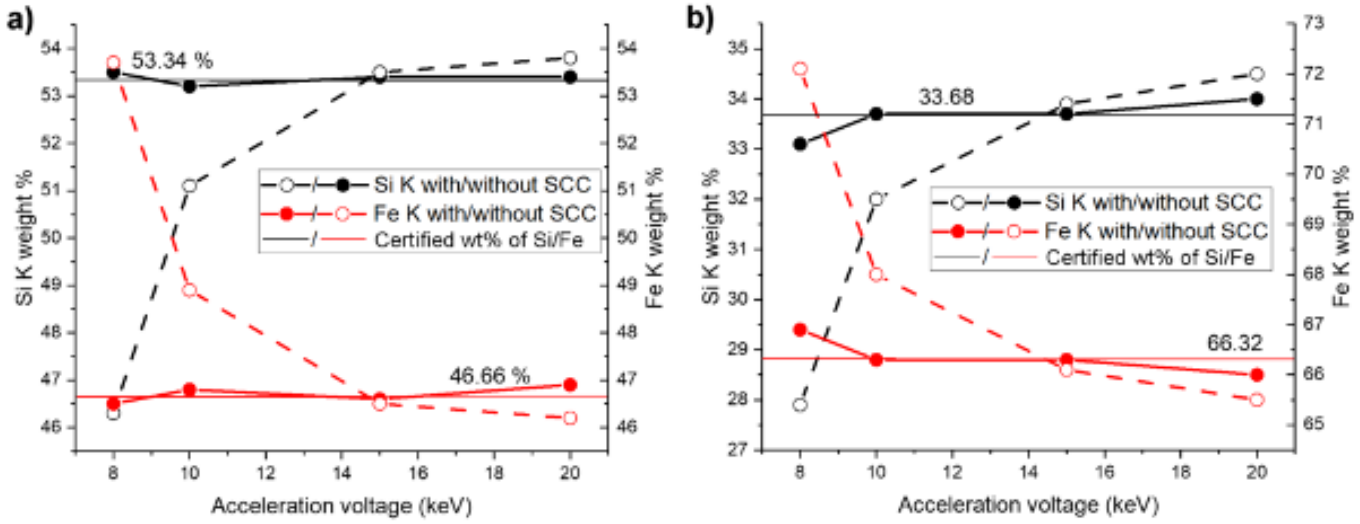

Figure 3

$$N_i = c_i \varepsilon_i i t \frac{d\Omega}{4\pi} \omega_i q_i S_i (RAF)_i$$

N_i	Net counts for element i	c_i	Concentration of element i
ε_i	Detector efficiency	i	Beam current
t	Measurement time	$\frac{d\Omega}{4\pi}$	Detector solid angle
ω_i	Fluorescence yield for element i	q_i	Line transition probability for element i
S_i	Number of excitations for element i	$(RAF)_i$	Matrix correction factors for element i

Figure 4

	Si	Fe
Main Matrix	53.34 wt%	46.66 wt%
Bright Spots	33.68 wt%	66.32 wt%

MS3.001-Invited
Investigation on the process and materials characteristic during laser metal deposition

S. Lotfian[1], G. AzimiRoeen[2], S. Tamimi[3]

[1]University of Strathclyde, Naval Architecture, Ocean & Marine Engineering, Glasgow, United Kingdom
[2]Isfahan University of Technology, Center of Educational Workshops, Isfahan, Iran
[3]University of Strathclyde, Advanced Forming Research Centre (AFRC), Glasgow, United Kingdom

Laser metal deposition as an additive manufacturing technique is used to fabricate functional metal parts in various industrial sectors (e.g. oil & gas, renewable energy, aerospace and automobile) due to its fabricating complex, intricate geometries and excellent material properties. Despite being a promising manufacturing technology, there is a lack of understanding about manufacturing process parameters and final product characteristic, which kept the product cost high and the technology readiness level (TRL) low. It is essential to understand and control the material"s behaviour to produce functional parts for critical industries. Accurate manufacture of such geometric features would require precise control over the material deposition process.

Process monitoring and analyses mechanisms are crucial in ascertaining the intended actions during deposition while also serving as practical learning tools. The current project involved incorporating an Infra-Red (IR) camera as a process-monitoring tool for laser metal deposition. The analysis helps plan ideal process parameters related to powder and manufacturing target using experiments. IR camera data used to track the regions of interest through the deposition and the final product characteristic through mechanical, microstructural analysis, and residual stress measurement will correlate LMD process parameters and manufactured components. It is essential to identify the qualitative and quantitative significance of process parameters and investigate the correlation between the robustness and sensitivity of the LMD process parameters over the geometric tolerances and mechanical properties. The main objective is to analyse the materials characterisation by varying a multitude of process parameters considering that the input parameters" changes during build-up significantly affect the output strength, microstructure, surface finish and tolerances of the fabricated part. In this study, the Inconel 718 (aerospace grade) is used to manufacture the 3D printed parts by LMD. The process parameters altered during the build-up. The materials characterisation was carried out by measuring the residual stress. The microstructural evolution was characterised by scanning electron microscopy (SEM) and electron backscatter diffraction (EBSD). The compositions of individual phases were analysed by energy- dispersive spectrometry (EDS).

MS3.002-Invited
Phase evolution clarification in Al-Ni-Co-RE amorphous alloys with varying Ni/Co ratio

P. Švec[1,2], M. Mihalkovič[2], B. Rusanov[3], D. Janičkovič[2], V. Sidorov[3,4,5], P. Švec Sr.[1,2]

[1]Centre of Excellence for Advanced Materials Application, Slovak Academy of Sciences, Bratislava, Slovakia
[2]Institute of Physics, Slovak Academy of Sciences, Bratislava, Slovakia
[3]Ural State Pedagogical University, Ekaterinburg, Russian Federation
[4]Ural Federal University, Ekaterinburg, Russian Federation
[5]Udmurt Federal Research Center, UB RAS, Izhevsk, Russian Federation

In this work, metallic ribbons of $Al_{86}Ni_yCo_xRE_6$ composition with different ratio of nickel and cobalt, (x/y=0, 1/3 and 1) and different rare earth (RE) element (Gd, Nd), were produced by standard planar flow casting method in amorphous state. The transformation sequence from amorphous state up to 750K is clarified by x-ray diffraction measurements and supported with scanning transmission microscopy and energy dispersive spectroscopy experiments (e.g. atomically resolved chemical mapping) for each relevant transformation stage.

Detailed microstructural characterizations (e.g. scanning electron diffraction experiments) were carried out to explain unusual phenomenon shown in x-ray diffraction data, calorimetric and complementary resistometry measurements bound to the second transformation stage. The observed phenomenon was proven to be solely connected with a newly observed structure forming nano-sized objects with high stacking disorder, Figure 1. The formation took place without previous chemical rearrangement forming from amorphous matrix surrounding fcc-Al(Ni) nanocrystals and is appearing as a second and single transformation step.

Figure 1: Typical XRD patterns of studied alloys ($Al_{86}Ni_yCo_xGd_6$) at indicated crystallization stages (left), HAADF STEM micrograph revealing nano fcc-Al (darker areas) surrounded with newly precipitated objects with stacking disorder after the second transformation stage, ($Al_{86}Ni_6Co_2Gd_6$).

Figure 1

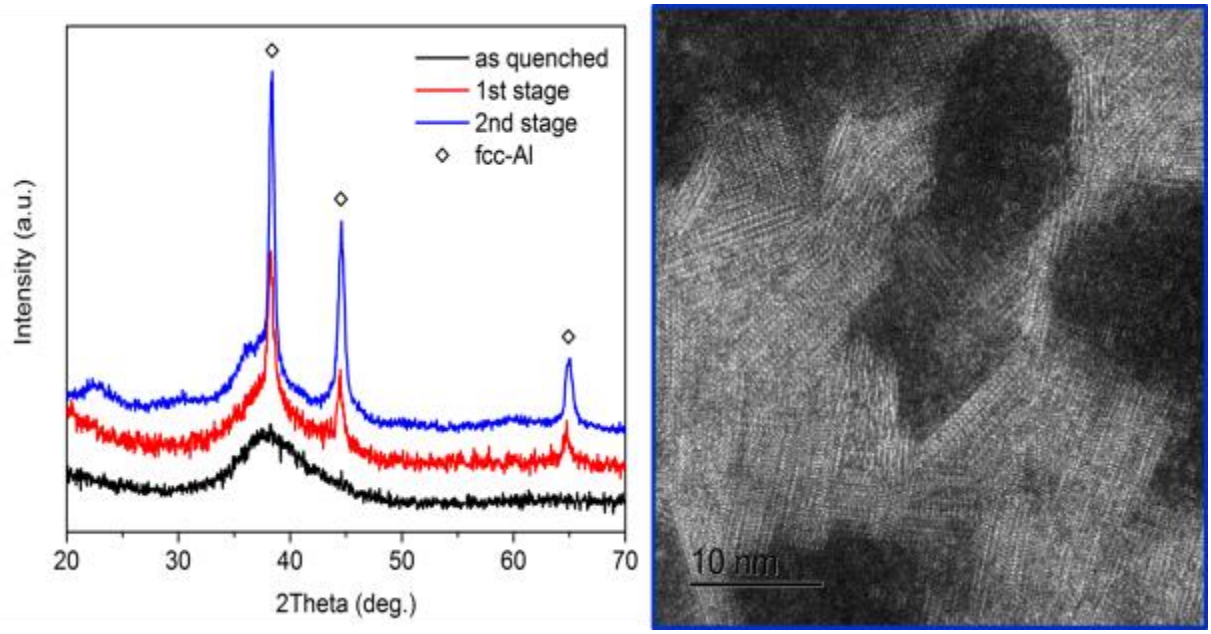

MS3.003
Correlative analytical tomography of metallic samples

G. Haberfehlner[1], C. Trummer[2], F. Mendez-Martin[3], M. Albu[2], G. Kothleitner[1,2]

[1]Graz University of Technology, Institute of Electron Microscopy and Nanoanalysis, Graz, Austria
[2]Graz Centre for Electron Microscopy (ZFE), Graz, Austria
[3]Montanuniversität Leoben, Department of Material Sciences, Leoben, Austria

Imaging of the three-dimensional elemental distribution within alloys at structural features, such as grain boundaries or precipitates is key to unraveling structure-property relationships. Two main techniques exist for elemental mapping at the nano- and atomic nano: atom probe tomography (APT) [1] and analytical transmission electron microscopy (TEM), using energy-dispersive X-ray spectroscopy (EDXS) or electron energy-loss spectroscopy (EELS), which can be extended to three dimensions by employing electron tomography (ET) [2]. Both have their advantages and drawbacks. APT provides high quality in elemental quantification, but can suffer from reconstruction artifacts, due to differences evaporation fields between different material in the sample. Analytical electron tomography (ET) is limited in terms of spatial resolution on accuracy of elemental quantification, but is generally reliable for sample morphology.

In this presentation, we will focus on the possibilities of analytical ET and show its application on different types of metallic sample. We will discuss the benefits of correlating different signals available in the TEM in the tomographic reconstruction process in order to improve reconstruction quality [3]. We apply these methods to 3D printed metals, such as an Al-Cu alloy. Within the alloy, we can image complex precipitates consisting of several phases, as well as grain boundary segregation (Figure 1). Second, we will also discuss the potential of correlating analytical ET to APT, for controlling, correcting and improving both techniques. We will focus on elemental quantification in analytical ET and show the impact of different factors, such as reconstruction parameters on quantification results and compare these to APT data.

[1] Gault, B., et al. Atom Probe Microscopy. Springer, New York, 2012.
[2] Leary, R.K. and Midgley, P.A. Analytical electron tomography. *MRS Bulletin* 41(7): 531–536, 2016.
[3] Huber, R., et al. Total generalized variation regularization for multi-modal electron tomography. *Nanoscale* 11(12): 5617–5632, 2019.

We thank Paola Bassani and Carlo Alberto Biffi, National Research Council of Italy CNR ICMATE Unit of Lecco for providing 3D printed samples. This project has received funding from the European Union"s Horizon 2020 research and innovation programme under Grant Agreement No. 823717 ESTEEM3.

Figure 1: Analytical tomography reconstruction of a 3D printed AlCu-alloy from EDXS data

Figure 1

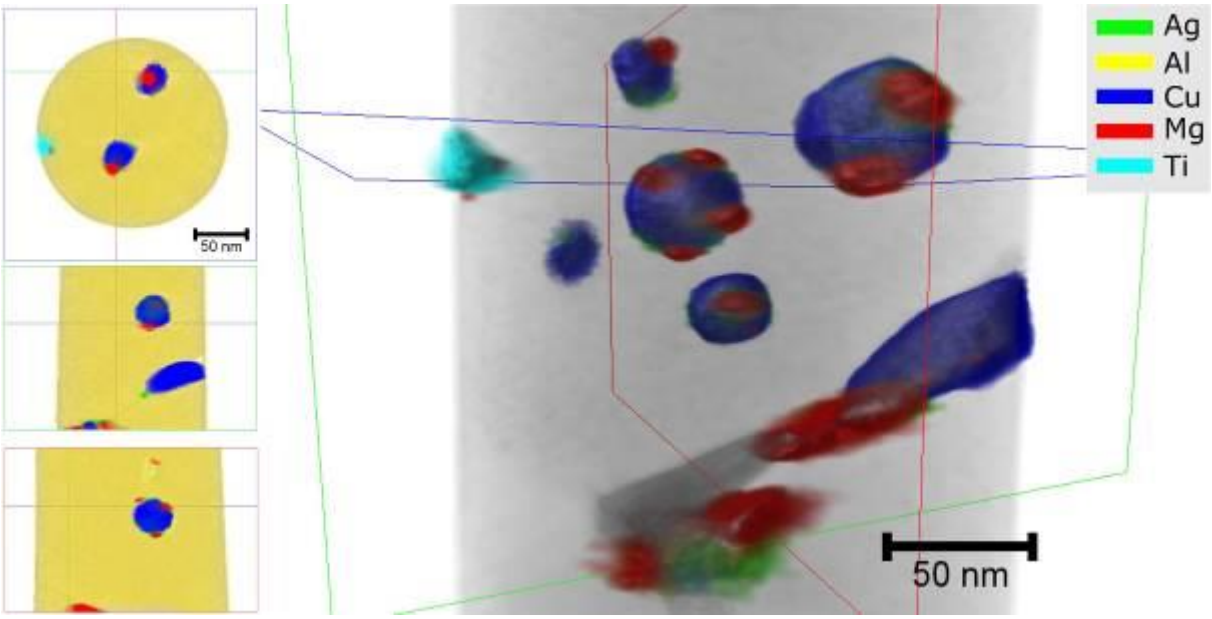

MS3.004
Grain boundary segregation induced precipitation in a non-equiatomic CoCuFeMnNi compositionally complex alloy

L. S. Mantha[1], B. E. MacDonald[2], A. Mazilkin[1], J. Ivanisenko[1], E. J. Lavernia[2], H. Hahn[1,2,3], S. Katnagallu[1]
C. Kübel[1,3,4]

[1]Karlsruhe Institute of Technology (KIT), Institute of Nanotechnology, Eggenstein-Leopoldshafen, Germany
[2]University of California, Department of Materials Science and Engineering, Irvine, United States
[3]Technical University of Darmstadt, Department of Material Sciences, Darmstadt, Germany
[4]Karlsruhe Institute of Technology (KIT), Karlsruhe Nano Micro Facility, Eggenstein-Leopoldshafen, Germany

Introduction: Compositionally complex alloys (CCA) are an emerging class of materials with distinct design approaches and diverse potential applications. Systems deviating from the traditional nearly equiatomic compositions1 and grain refinement to produce nanocrystalline (nc) alloys have been introduced to further develop CCAs. However, the complex composition and the high defect density in these nc alloys result in new challenges, e.g., to understand thermal stability and processing.

Objectives: The objective of the present work is to study the phase and structural transformations in nanocrystalline non-equiatomic $Co_{26}Cu_{10}Fe_{27}Mn_{10}Ni_{27}$ CCA focusing in particular on the role of grain boundaries for segregation and secondary phase evolution. We employed a combination of various *in-situ*/*ex-situ* transmission electron microscopy (TEM) heating experiments and atom probe tomography (APT) to understand the structural and chemical evolution.

Materials and Methods**:** The as-cast and homogenized single-phase CCA was subjected to high pressure torsion (HPT) to achieve a nc microstructure. TEM and APT specimens were carefully prepared by focused ion beam. In addition to *ex-situ* characterization using high-resolution and analytical TEM as well as APT techniques, we employed *in-situ* energy-filtered TEM spectrum imaging (EFTEM-SI) and automated crystal orientation mapping (ACOM) during heating to follow both the chemical and microstructural evolution at various temperatures.

Results and Discussions: While the alloy after HPT is a single phase fcc solid solution, heat treatment results in the formation of a new B2 phase (Figure 1a). *In-situ* heat treatment in the TEM reveals an increase in the B2 precipitate phase fraction with increasing temperatures up to 380 °C followed by the dissolution of the B2 phase at higher temperatures. The kinetics were analyzed. ACOM and HRTEM analysis further indicates that the B2 phase exhibits a preferential Kurdjumov-Sachs orientation relationship with the fcc matrix (Figure 1b). *In-situ* heating in combination with EFTEM-SI revealed a complex chemical evolution including co-segregation of Co, Ni, and Cu to grain boundaries followed by the formation of Fe-Co precipitates (Figure 2 a-c). APT of the *ex-situ* heat-treated sample showed 3 types of segregation phases (Figure 2 e,f). The observed behavior is discussed in terms of the enthalpy of mixing of different components.

Figure 1: ACOM maps of *in-situ* heat treatment at 420 ^{o}C. (a) shows the distribution of phases, orientation map (from left to right). (b) shows the HRTEM image of ex-situ heat-treated sample showing orientation relationship between fcc and B2 phase

Figure 2: Low loss EFTEM maps of *in-situ* heat-treated samples showing the segregation behavior of Fe, Co, Ni, Cu, Mn at a) 250 ^{o}C, b) 340 ^{o}C, c) 400 ^{o}C. (d) shows the APT 3D reconstructed volume of *ex-situ* HT sample e) and f) excerpts showing precipitation and segregation to triple junctions and grain boundaries.

Conclusions: The phase decomposition of nc $Co_{26}Cu_{10}Fe_{27}Mn_{10}Ni_{27}$ was investigated systematically using *in-situ* TEM heating and *ex-situ* heating experiments revealing different stages during the complex phase decomposition. Our analysis revealed both the chemical and the microstructural changes and how they are related.

References:
[1] Li, Z. & Raabe, D. Strong and Ductile Non-equiatomic High-Entropy Alloys: Design, Processing, Microstructure, and Mechanical Properties. *JOM* 69, 2099–2106 (2017).

Figure 1

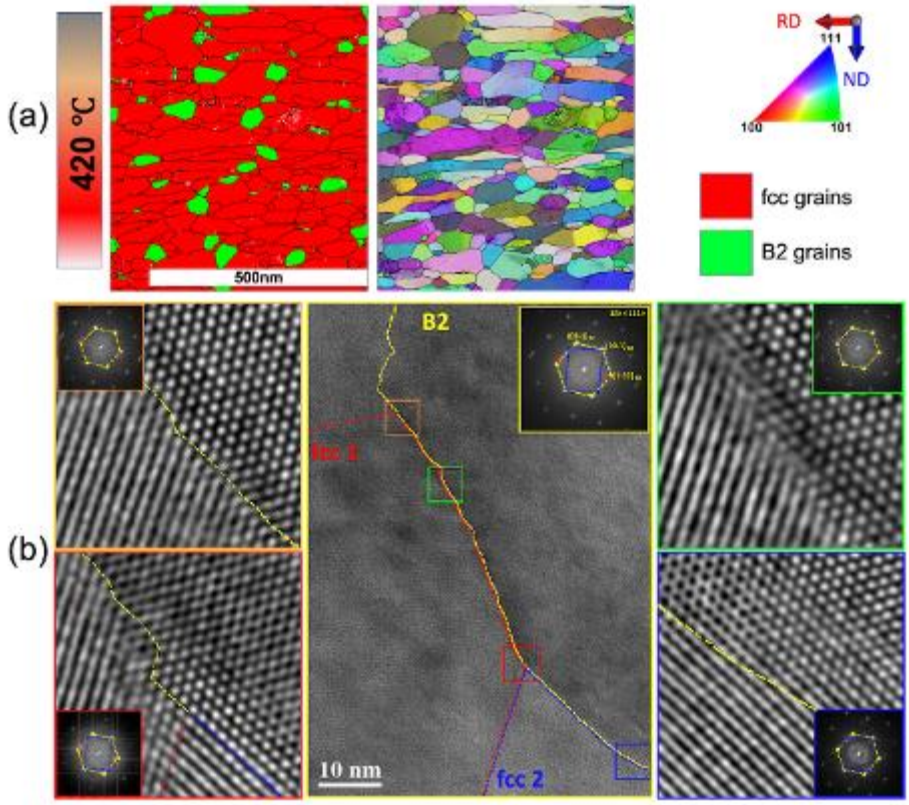

Figure 2

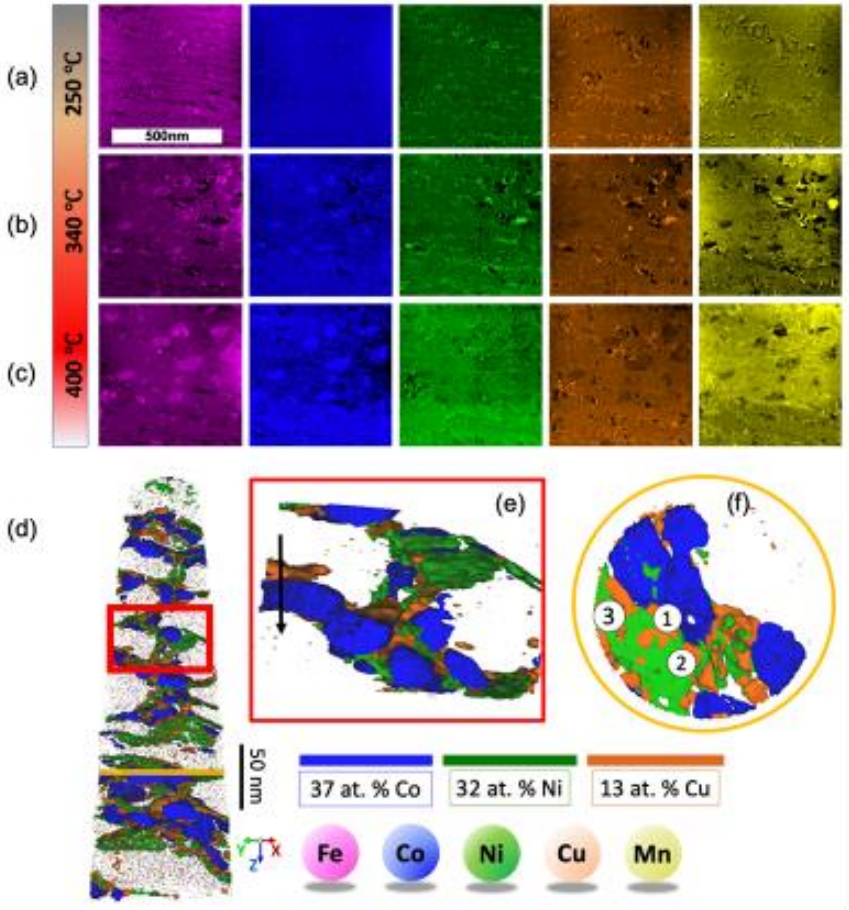

MS3.005
Congruent grain boundary phase transformations revealed by STEM in pure copper

L. Frommeyer[1], T. Brink[1], R. Freitas[2], T. Frolov[3], G. Dehm[1], C. H. Liebscher[1]

[1]Max Planck Institute for Iron Research, Düsseldorf , Structure and Nano-/Micromechanics of Materials, Düsseldorf, Germany
[2]Massachusetts Institute of Technology, Materials Science and Engineering, Cambridge, United States
[3]Lawrence Livermore National Laboratory, Livermore, United States

Grain boundaries (GBs), defined as the interfaces between two adjacent crystallites, influence electronic and mechanical properties of a material. Their atomic structure differs from the adjacent crystals and GBs themselves can exist in multiple phase states, termed "complexions". More than 50 years ago, it was proposed that even within one GB, several stable and metastable GB phases can exist [1]. They are distinct by their thermodynamic properties such as GB energy, excess volume or excess stress and typically also differ in atomic structure [2]. However, until now most studies have only been carried out by simulations and direct experimental evidence of phase co-existence at the atomic level is rare [3].

Using aberration-corrected HAADF-STEM, we observe two different GB phases, termed "pearl" and "domino", in a ∑37c symmetric tilt GB in copper, which are connected by a GB phase junction as visible in Figure 1. The "pearl" phase takes up segments with a length of 20 to 40 nm, whereas the "domino" phase has a higher fraction with segments of 30 nm to more than 100 nm. The atomic structure of the "pearl" phase consists of three subunits, a square shaped one and one looking like a pearl chain, which alternate, and a third subunit, similar to the letter "B", appearing after every second or third repetition of the other two subunits. The "domino" structure can be described by two alternating subunits that contain two squares each which are rotated by ±30° with respect to the GB plane. All of these subunits are indicated in Figure1. The GB phase transformation was modelled by molecular dynamics (MD) simulations and it is found that the domino phase is lower in energy at room temperature than the pearl phase. We investigated the Burgers vector of the GB phase junction and could reveal the components parallel and normal to the GB from the STEM images. Since the GB phase junction is correlated to differences in excess volume and excess shear of the GB phases, it may be responsible for the kinetics of the GB phase transformation, which will be discussed in detail [4]. Furthermore, we will show that such GB phase transformation are not only possible at symmetric GBs, but can be observed – both experimentally and in the model – when changing the GB plane inclination.

References:
[1] Hart, E.W., et al., Scripta Metallurgica, 2(3): p. 179-182 (1968).
[2] Frolov, T., et al., Nature Communications, 4:1899 (2013).
[3] Meiners, T., et al., Acta Materialia, 190: p. 93-104 (2020).
[4] Frolov, T., et al., arXiv preprint arXiv:2101.06574 (2021).

Figure 1

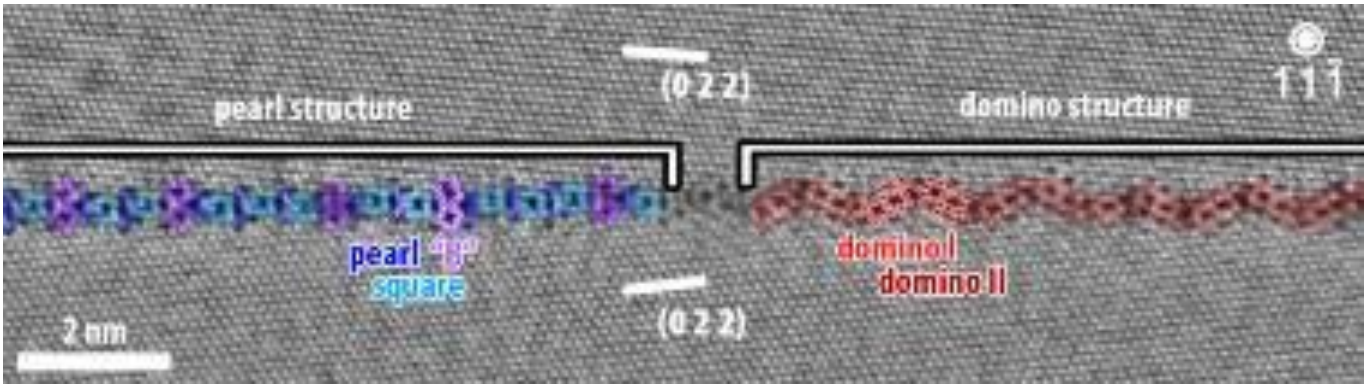

MS3.006
Observations of Alnico magnetic structure using non-Lorentz transmission electron microscopy

O. Kaczmarczyk[1], A. Pniakowska[2], A. Żak[1]

[1]Wroclaw University of Science and Technology, Electron Microscopy Laboratory, Faculty of Mechanical Engineering, Wrocław, Poland
[2]Wroclaw University of Science and Technology, Advanced Materials Engineering and Modelling Group, Faculty of Chemistry, Wrocław, Poland

Introduction: The formation of magnetic domains is characteristic of ferromagnetic materials such as iron, cobalt or special magnetic alloys. There are various domain observations techniques and one of them is Lorentz Transmission Electron Microscopy (LTEM). It applies to in situ studies of the magnetization process as well as multi-scale observations of domains in high resolution. The observations require either switching off the objective lens or the use of a dedicated lens to avoid sample magnetization. It has been previously discovered that the preparation method is of great importance in magnetic materials observations and there is a possibility to study magnetic structures in conventional TEM [1]. Inspired by the prior reports, the potentiality of domain observations in standard conditions has been extensively studied in this research.

Objectives: The main aims of the research were to study the effect of the preparation method on the ferromagnetic material and to investigate whether magnetic domain observations are possible in non-Lorentz TEM [2].

Materials & methods: Two microscopes were used in the research: Hitachi H-800 and JEOL JEM-F200. The observations of magnetic domains were performed on Alnico magnet in transverse view using the Fresnel method. The material was investigated in both magnetized and demagnetized state after electropolishing and ion polishing.

Results: The results showed, that ion polishing changed the material significantly and consequently the visibility of the magnetic domains. Despite the interaction of the objective lens with the sample, the magnetic contrast was visible in out-of-focus conventional TEM images. Both Lorentz and conventional TEM images of the magnetized sample showed a strong relation of the magnetic structure to the phase structure of the material. It was possible to observe the same magnetic contrast in the conventional mode as in Lorentz mode by increasing defocus value from ±10 nm up to ±1.5 µm. After measuring the magnetic field within the sample, it was found that the magnetization of the objective (0.88 T for H-800) was insufficient to saturate the specimen. Combined with increased defocus, this allowed for observations comparable to LTEM. The demagnetized sample was characterised by more complex structures which cannot be correlated directly to the material"s microstructure.

Conclusion: Argon ions could etch the area of the domain walls during polishing and consequently affect the contrast observed in TEM. Furthermore, the magnetic field of the objective lens was not strong enough to fully magnetize the material and as a result, the contrast originated from in-plane magnetization. Therefore it is possible to study magnetic domains in TEM with an active objective lens under specific observation conditions. However, the shape of the material hysteresis curve should be considered and, if possible, use low accelerating voltages, which mean weaker excitation of the lenses.

References:
[1] A. Żak, A. Łaszcz, M. Hasiak, G. Gerstein, H.J. Maier, W. Dudzinski, Ion polishing as a method of imaging the magnetic structures in CoNiGa monocrystal, Results Phys. 10 (2018) 277–280. https://doi.org/10.1016/j.rinp.2018.06.020.
[2] O. Kaczmarczyk, A. Pniakowska, A. Żak, Magnetic domains imaging with Lorentz and conventional transmission electron microscope in hard magnetics on the example of alnico magnets, Journal of Magnetism and Magnetic Materials, in review.

Figure1: The magnetized sample.

Figure 1

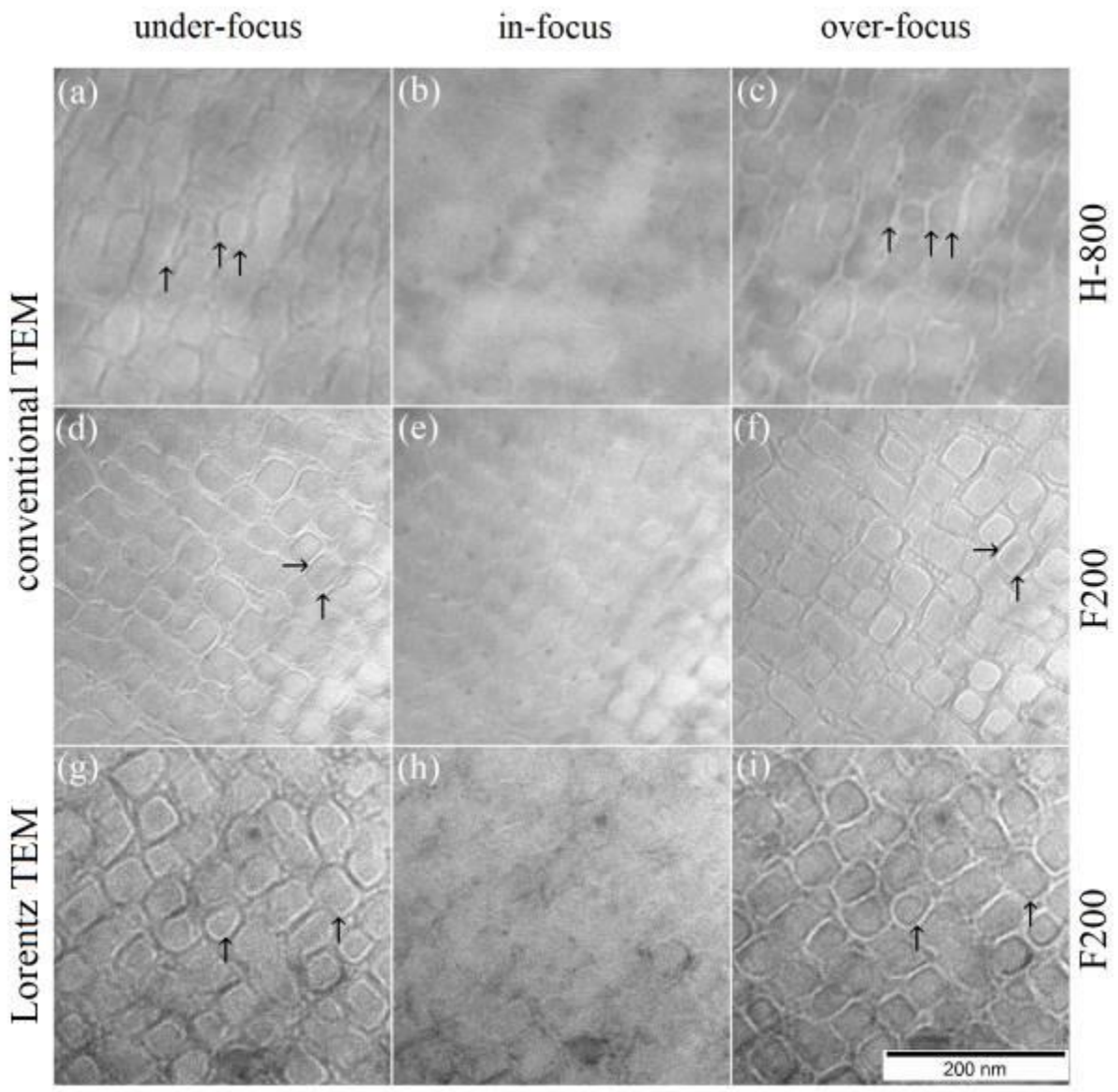

MS3.P001
Phase constitution in an intermetallic Ti-37Al-10Nb alloy: what we can learn about the phase equilibria?

B. Rashkova[1], M. Brabetz[1,2], F. Mendez-Martin[1], B. Distl[3], K. Hauschildt[4], F. Stein[3], H. Clemens[1]

[1]Montanuniversität Leoben, Department of Material Sciences, Leoben, Austria
[2]Forschungszentrum Seibersdorf, Seibersdorf, Austria
[3]Max Planck Institute for Iron Research, Düsseldorf , Düsseldorf, Germany
[4]Helmholtz-Zentrum Geesthacht, Institute of Materials Physics, Geesthacht, Germany

Intermetallic titanium aluminides are considered for high-temperature applications in the aviation and automotive industries due to their potential of significant component weight saving in combination with high-strength and good creep properties. In order to improve the existing alloys and their processing characteristics further alloy development is required. To achieve this goal, an exact knowledge of the phase equilibria and phase transformations at elevated temperatures is needed, as a pre-requisite for microstructure control to adjust the high-temperature mechanical properties.

The Ti-Al-Nb alloy system is one of the basic systems for the currently used alloys. However, there are few experimental results regarding the phase equilibria in this ternary alloy system below 1000 °C. This work presents the evolution of the microstructure in a TiAl-Nb alloy. A model alloy with the composition Ti-37Al-10Nb (in at.%) was synthesized in an advanced arc melter using high-purity elements and subsequently heat treated at 700 °C for 1500 hours followed by water quenching. The microstructure was analysed on different length scales by scanning electron microscopy (SEM), *in situ* high-energy synchrotron X-ray diffraction (HEXRD) and transmission electron microscopy (TEM). The specimens for TEM investigation were prepared by electropolishing and by employing a dual focused ion beam (FIB).

Figure 1: shows a SEM overview image of the microstructure (Figure 1a) and a BF TEM micrograph (Figure 1b), where only two phases are presented, namely ω_o and γ.

This work is part of a research collaboration with Helmholtz-Zentrum-Geesthacht (Germany), Max-Planck-Institut für Eisenforschung (Germany) and Thermo-Calc Software (Sweden) funded by the EU project ADVANCE (Clean Sky 2) – Horizon 2020 research and innovation programme under grant agreement No 820647.

Figure 1: Microstructure and distribution of the constituent phases. a) SEM image where the matrix (ω_o-phase) has a light contrast and the γ phase shows a dark to black contrast. b) BF TEM micrograph.

Figure 1

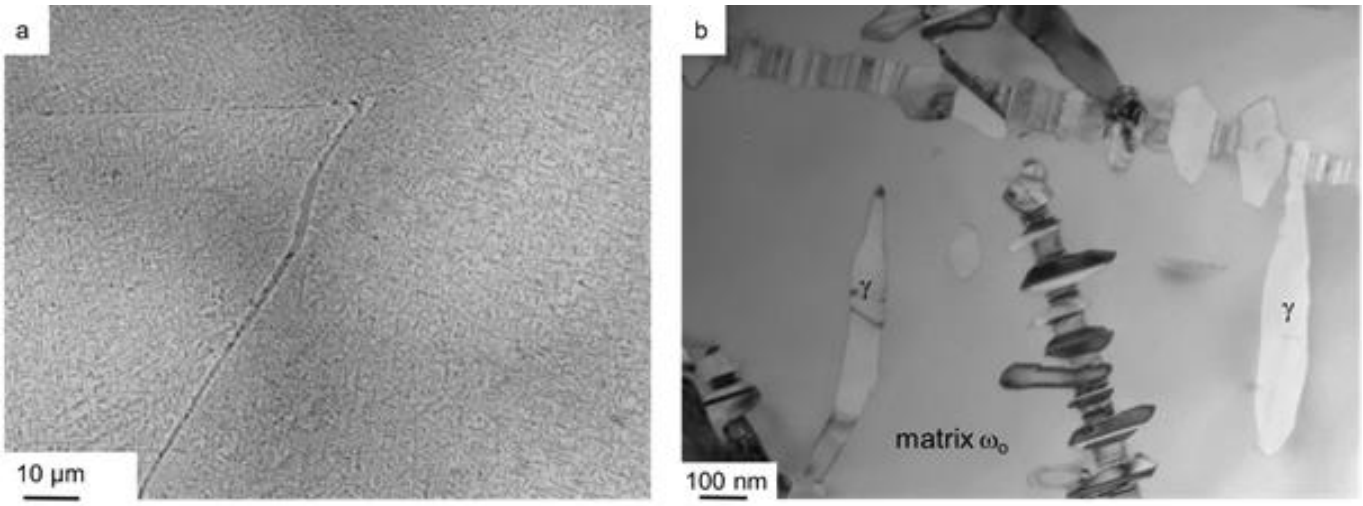

MS3.P002
Investigation of the ductile damage-dislocation interaction in case hardening steel using electron channeling contrast imaging

A. Dunlap[1], A. Aretz[1], A. Schwedt[1]

[1]RWTH Aachen University, Gemeinschaftslabor für Elektronenmikroskopie, Aachen, Germany

Introduction: The microstructural changes caused by metal forming result in various physical mechanisms that influence the macroscopic properties of the formed parts such as strain hardening or phase transformations. Ductile damage also accumulates in formed metal until a failure threshold is reached. Investigating the ductile damage may lead to an improved process route or material design that increases the efficiency and lifetime of formed parts and is the focus of a collaborative research center (TRR 188).

Objectives: Ductile damage appears as voids in the microstructure. The nucleation and evolution of these voids in metals are of interest. Dislocations have a significant influence on microstructural mechanisms. Therefore, this study focuses on the interaction between forming induced voids and dislocations in bent steel samples to obtain a full understanding of ductile damage.

Materials & Methods: A 16MnCrS5 ferritic-pearlitic case hardening steel, typically used in cold forming is used in this study. The material is formed using an in situ bending device in a large chamber SEM creating samples with varying strain rates ranging from tensile to compressive stress. The samples are afterwards cut and prepared for SEM investigation. Damage sites are located in panorama images recorded with a Zeiss Gemini SEM 300. Electron Backscatter Diffraction (EBSD) measurements are performed at the ductile damage sites to identify the crystal orientation of the neighboring matrix material. From these orientations the tilt and rotation parameters are calculated using the program TOCA (Tools for Orientation determination and Crystallographic Analysis) to perform controlled Electron Channeling Contrast Imaging (cECCI) and visualize the dislocation structure and its interaction with the ductile damage.

Results: The EBSD and cECCI investigation of damage sites revealed, that different types of damage occur in formed metals. As expected, more ductile damage is found in material that underlies tensile stresses. Grain boundaries within MnS inclusions are one prominent factor of void nucleation in the investigated material (Figure 1). In these cases, voids can be found with no direct dislocation interaction in the neighboring matrix material. Shear bands however, resulting from deformation of the material can also cause cracking of inclusions and subsequently creation of voids, indicating a direct correlation between dislocation and ductile damage (Figure 2). The investigations reveal that the cementite lamellae of the pearlite hinder dislocation progression but may also lead to delamination of the phases and hence new damage sites. The found damage mechanisms vary significantly and are dependent on the randomly oriented surrounding microstructure.

Figure 1: a) SE image of MnS inclusion in cross section of bent 16MnCrS5 Sample. b) Inverse Pole Figure Map of corresponding EBSD Measurement. The large void nucleates at grain boundary of MnS inclusion, the small crack on the right appears within MnS grain.

Figure 2: a) SE image with higher resolution. b) cECCI reveals a shear band, interacting with the MnS crack.

Figure 1

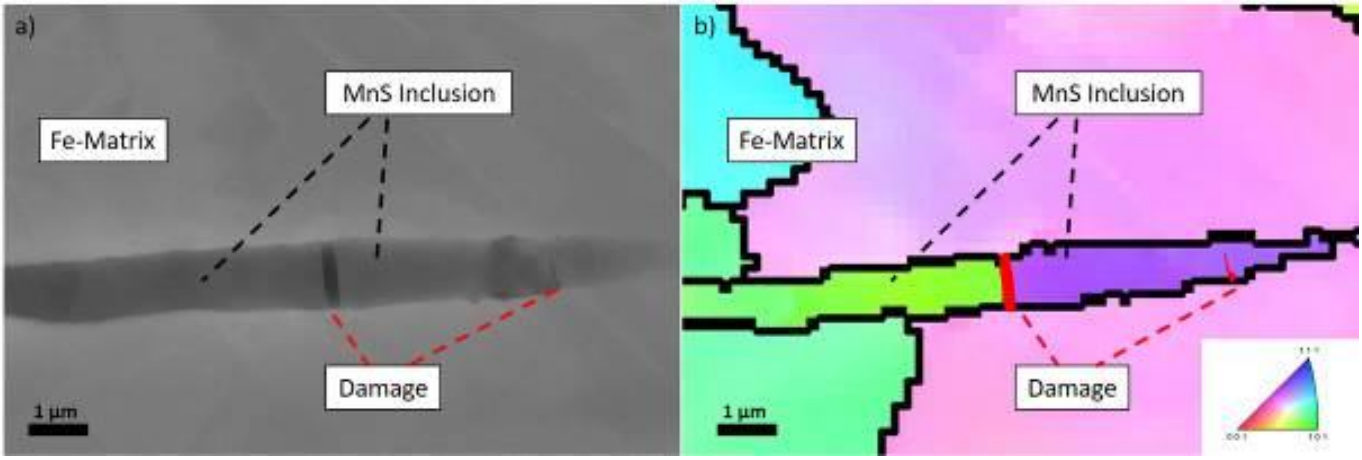

Figure 2

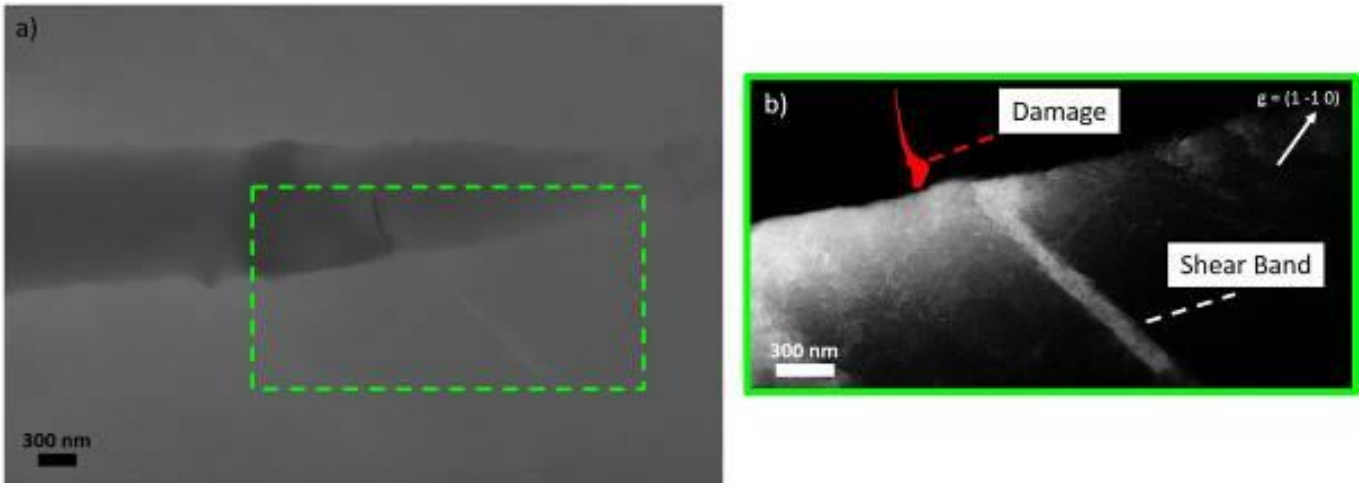

MS3.P003
Correlations between microstructural and magnetic properties of a spinodally decomposed $Cu_{52}Ni_{34}Fe_{14}$ alloy

T. Radlinger[1], F. Hofer[1,2], G. Kothleitner[1,2]

[1]TU Graz, Institute of Electron Microscopy and Nanoanalysis (FELMI - ZfE), Graz, Austria
[2]Austrian Centre for Electron Microscopy and Nanoanalysis (ZfE), Graz, Austria

CuNiFe alloys have shown to be promising materials in terms of manipulating magnetic properties by controlling their microstructure. Despite extensive research activities on such nano-scale magnetic materials for several decades now, the relationship between the evolution of the microstructure and its magnetic properties still remains to be fully explored. [1–4]. In this study, we investigate a spinodally decomposed CuNiFe alloy, using a wide variety of modern (S)TEM methods such as dark-field imaging, EDX spectroscopy and differential phase contrast (DPC) imaging. The specimen under investigation was solution treated and a subsequent heat treatment at 625°C for 10 hours leads to a spinodal decomposition of the alloy [3,5]. EDX elemental maps reveal the characteristic stripe/plate like Ni-rich phase embedded in a Cu-rich matrix [1,2]. Those plates are growing along the [100] directions of the crystal which is shown in figure 1 a). The EDX analysis reveals a chemical composition of 54 at% Ni, 27 at% Fe and 19 at% Cu for the Ni-rich phase which, is similar to the findings of Kobayashi et al [4]. To investigate the magnetic structure, LM-STEM DPC with a switched off objective lens was performed to ensure a nearly field-free environment. In DPC, the deflection of the electron beam due to the interaction with the magnetic field of the specimen is measured with a 4-quadrant annular detector. A magnetic field map is shown in figure 1 b), in which the colour represents a certain direction of the magnetic field. The DPC map shows a direct relationship between the magnetic field structure and the nanostructure along the [100] directions. The DPC map displays field vectors that point along the diagonals of the image, suggesting a [111] direction of the magnetic easy axis.

Figure 1: a) Color coded EDX elemental map along [001] zone-axis orientation using Ni K, Cu K and Fe K signals. Ni-rich plates (yellow) are embedded in a Cu-rich matrix (blue). **b)** Magnetic field map from 4-quadrant DPC signal. The colour of a certain position represents the direction the magnetic field is pointing. The colour-wheel relates to the direction of the field.

[1] Butler EP, Thomas G. Structure and properties of spinodally decomposed Cu-Ni-Fe alloys. Acta Metallurgica 1970;18.
[2] Li H, Hao X, Zhao G, Hao S. Characteristics of the continuous coarsening and discontinuous coarsening of spinodally decomposed Cu-Ni-Fe alloy. Journal of Materials Science 2001;36:779–84.
[3] Kang S, Bae D-S, Takeguchi M, Hong K-J, Chang C-H, Takeda M. Microstructural evolutions of a Cu75-Fe5-Ni20 alloy depending on the isothermal annealing temperatures. Met. Mater. Int. 2012;18(3):521–5.
[4] Kobayashi S, Yamaminami T, Sakakura H, Takeda M, Yamada T, Sakuma H, Trisnanto SB, Ota S, Takemura Y. Magnetization Characteristics of Oriented Single-Crystalline NiFe-Cu Nanocubes Precipitated in a Cu-Rich Matrix. Molecules 2020;25(14).
[5] Kim J-S, Takeda M, Bae D-S. Microstructural evolution and magnetic properties of ultrafine solute-atom particles formed in a Cu 75 –Ni 20 –Fe 5 alloy on isothermal annealing. Jpn. J. Appl. Phys. 2016;55(12):123002.

Figure 1

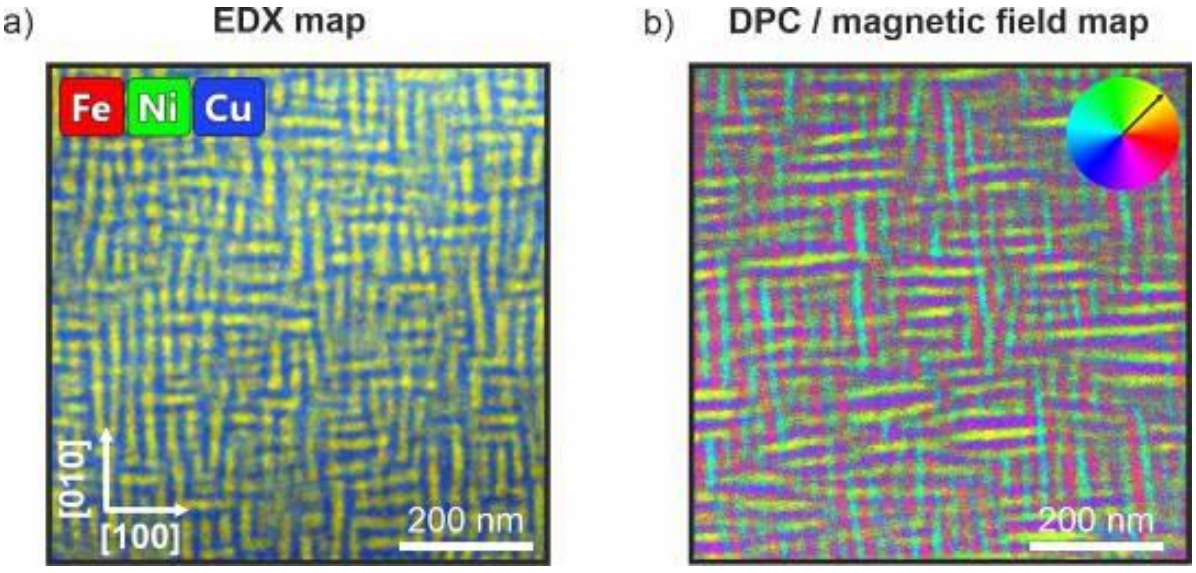

MS3.P004
Study of phase transformations in Ti-xNb-7Zr-0.8O alloy over wide range of compositions

J. Kozlik[1], D. Preisler[1], J. Strasky[1], J. Vesely[1], A. Veverkova[1], T. Chraska[2], M. Janecek[1]

[1]Charles University in Prague , Department of Physics of Materials, Prague, Czech Republic
[2]Czech Academy of Sciences, Institute of Plasma Physics, Prague, Czech Republic

Introduction & Objectives: Metastable biocompatible β titanium alloys can be used as a material for load-bearing implants. However, precise composition and microstructural tailoring is difficult, because of many degrees of freedom and a number of specific requirements on microstructure and phase composition, strength and elastic modulus. The aim of this study is to investigate a possibility of using a field-assisted sintering technique (FAST) to prepare such a heterogeneous alloy and to study the phase transformations during cooling in the wide range of composition.

Materials & Methods: Ti-xNb-7Zr-0.8O alloy was prepared from elemental powders by FAST. Nb is the main beta-stabilizing element, as well as being the element with the slowest diffusion. A compositional gradient of Nb was successfully produced in the alloy, allowing sample analysis over a wide range of compositions. SEM and TEM imaging and analytical methods were used for the material characterization.

Results: The investigations revealed that Nb-rich regions retained the metastable β phase, surrounded by transition region consisting of the β and ω phases and Nb-lean regions consisting of the α and β phases. The critical concentration of Nb determining whether α or ω will precipitate during cooling was determined to be 22 wt%. The observed as-sintered microstructure is discussed with respect to the Gibbs free energy curves and the phase diagram.

Figure: Graphical abstract

Conclusion: The viability of using FAST to prepare heterogeneous alloys was validated and the phase transformation sequence in Ti-Nb-Zr-O system was described for a range of Nb concentrations. The method can be also easily transferred to other alloy systems.

Kozlík, D. Preisler, J. Stráský, J. Veselý, A. Veverková, T. Chráska, M. Janeček, Phase transformations in a heterogeneous Ti-xNb-7Zr-0.8O alloy prepared by a field-assisted sintering technique, Materials & Design. 198 (2021) 109308. https://doi.org/10.1016/j.matdes.2020.109308.

Figure 1

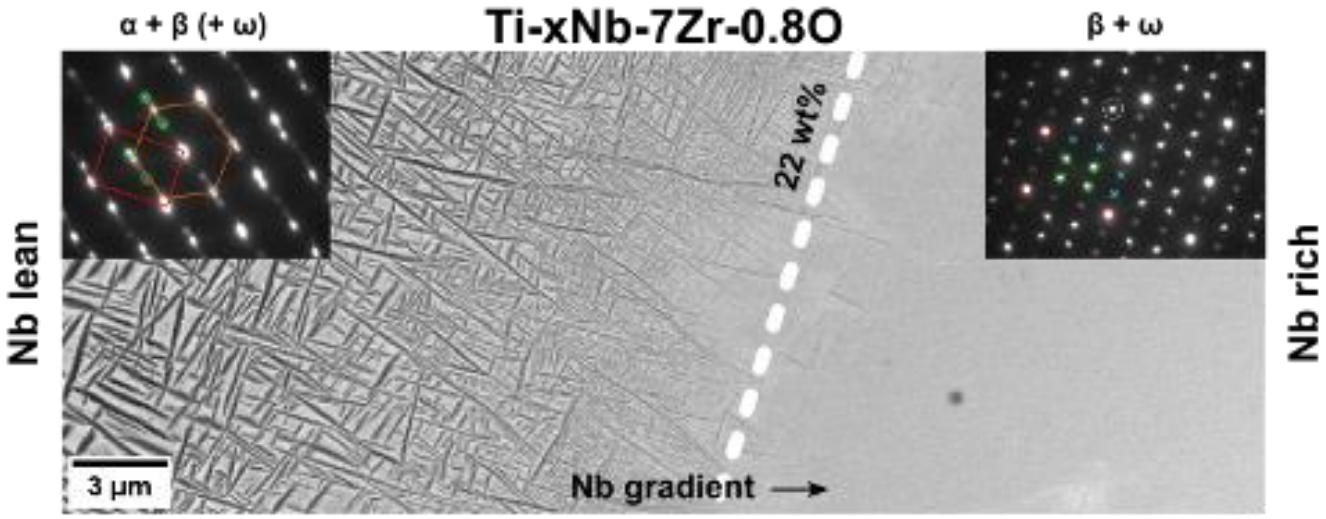

MS3.P005
Microstructural insights into Be/TiBe12 dual phase materials after high dose neutron irradiation

M. Dürrschnabel[1], R. Gaisin[1], N. Zimber[1], M. Rieth[1], P. Vladimirov[1]

[1]Karlsruhe Institute of Technology (KIT), Eggenstein-Leopoldshafen, Germany

Introduction: Beryllium-titanium compounds possess several outstanding properties, which make them attractive for various industrial applications. Their superior properties compared to pure beryllium such as high strength at elevated temperatures, excellent oxidation resistance and low density are key requirements for e.g. the aerospace industry. Furthermore, they can act as hydrogen storage materials as well as potential neutron multiplier for breeder blanket of the demonstration nuclear fusion power reactor (DEMO) and beyond. In the latter case, they have to withstand harsh conditions like intense neutron radiation and high temperatures and, thus, they should possess a high melting point, high oxidation resistance, low tritium retention and low swelling. However, microstructural analyses of such materials especially on the nanoscale are still rare, but significant for any industrial application.

Objectives: The objective was to assess the microstructural changes in beryllide and compare them to the pure Be part.

Materials & methods: Here we present analytical transmission electron microscopy (TEM) studies of a $TiBe_{12}$/Be composite material that was neutron irradiated up to 768°C within the high-dose irradiation program HIDOBE. The base material was manufactured by powder alloying with subsequent hot isostatic pressing (HIP). We prepared thin TEM lamellae using a FEI Helios Dual Beam focused ion beam (FIB) microscope. Afterwards, the lamellae were analyzed in a Thermofisher Talos F200X equipped with a Super-X energy-dispersive X-ray analysis (EDX) system and a Gatan Enfinium spectrometer for Electron Energy Loss Spectroscopy (EELS).

Results: **Figure 1:** TEM bright-field images and diffraction pattern of Be and $TiBe_{12}$ at two different irradiation temperatures. The presence of structural disorder in $TiBe_{12}$ is exemplary shown in the diffraction pattern on the lower right. The inset shows streaking and weak satellite reflections indicating the nanoscale structural disorder.

Figure 2: STEM-EELS mapping of a bubble in pure Be (left) and $TiBe_{12}$ (right) showing the distribution of tritium and helium within the bubble. The irradiation temperature was in both cases 768°C. STEM-EDX elemental mapping in a $TiBe_{12}$ grain acquired in the sample irradiated at 768°C. The Si-K map as well as the extracted line profile show that a thin layer of Si decorates the bubble edges.

Conclusion: The obtained results pave the way for a more thorough understanding of the material and its interactions with neutrons and it is of great interest for material recycling after the end-of-life of the reactor components. In particular, nanoscale structural disorder was induced into $TiBe_{12}$ along certain crystallographic directions during to neutron irradiation. The exact nature of this disorder still needs to be explained. Unlike in pure Be EDX did not reveal any precipitation of foreign elements like Fe, Al, U etc. in the composite samples. However, it was found by EDX mapping that bubbles in $TiBe_{12}$ are decorated by thin Si layer. Faceted 15 nm sized bubbles were observed in the $TiBe_{12}$ part, whereas in the Be part the bubble size exceeds 100 nm. EELS revealed that bubbles contain tritium and helium. The tritium retention in the beryllide material is much less than compared to pure Be, since the bubbles are much smaller in the beryllide part.

Figure 1

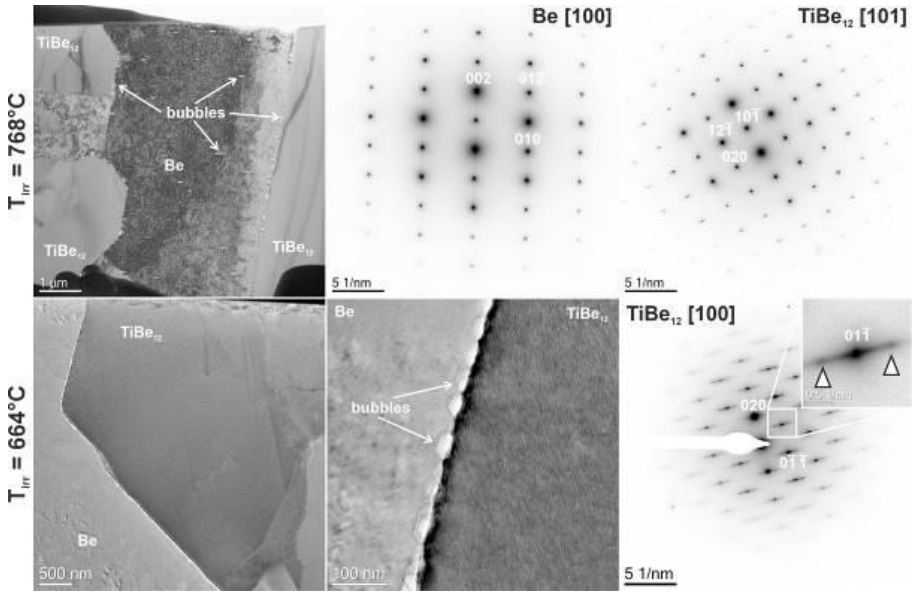

Figure 2

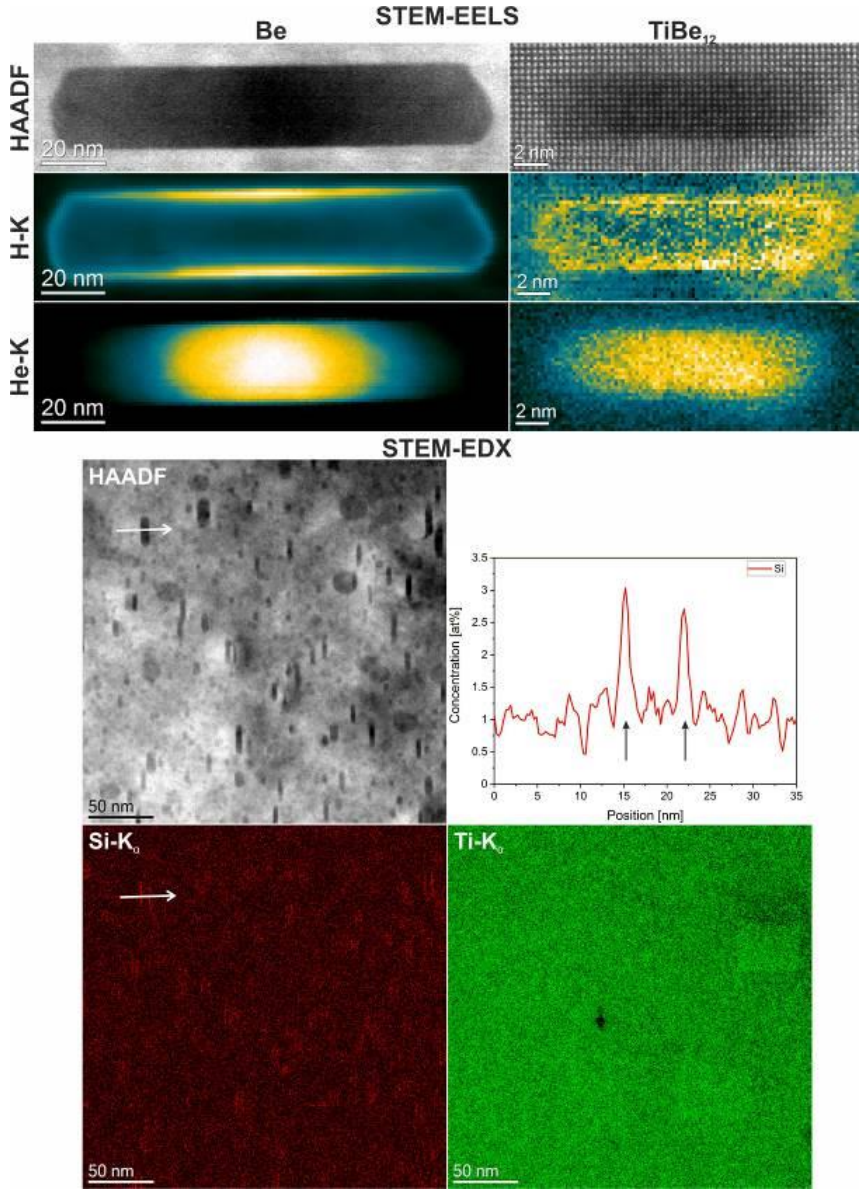

Structural resolution of severely deformed dual-phase high entropy alloys using nano-beam diffraction patterns in transmission electron microscopy

S. Taheriniya[a]*, C. Gadelmeier[b], H. Rösner[a], M. Peterlechner[a], C. Gammer[c], M. Tomut[a,d], S. V. Divinski[a], B. Butz[b]
U. Glatzel[b], G. Wilde[a]

[a]Institute of Materials Physics, University of Münster, Münster, Germany
[b]Metals and Alloys, University of Bayreuth, Bayreuth, Germany
[c]Erich Schmid Institute of Materials Science, Austrian Academy of Sciences, Leoben, Austria
[d]GSI Helmholtz Center for Heavy Ion Research, 64291 Darmstadt, Germany

s_tahe01@uni-muenster.de

In-depth understanding of the microstructure is crucial for the technological applications of metallic alloys and it becomes even more challenging with the increasing complexity of the metallic systems. The nanocomposite high entropy alloy (HEA) produced by high pressure torsion (HPT) in the present work is an example of such metallic systems. To explore how different HEAs respond to irradiation induced damage, nanocomposite HEA samples produced by HPT were exposed to Au swift heavy ion irradiation at room temperature (RT) and 50 K with $5 \times 10^{13}\ Au\ (\frac{ions}{cm^{-2}})$ and $5 \times 10^{12}\ Au\ (\frac{ions}{cm^{-2}})$ fluences respectively. The nanocomposite HEA samples were

prepared under quasi-hydrostatic conditions, during which separate disks of single-phase equiatomic FCC CoCrFeMnNi and single-phase BCC equiatomic BCC HfNbTaTiZr were stacked on top of each other, and then processed by HPT under 9 GPa pressure at ambient temperature. After the HPT process the samples were studied by scanning electron microscopy (SEM) and transmission electron microscopy (TEM) with respect to the chemical composition, local structure, and microstructure stability. According to our earlier report, a bulk nanocomposite HEA was found to develop after 15 revolutions. As a result, alternating nano-lamellae of elongated nanocrystalline CoCrFeMnNi and mixed amorphous-nanocrystalline HfNbTaTiZr appear, exhibiting complex microstructures with numerous vortex-like regions (1). After irradiation at RT and cryogenic temperatures, nano-beam diffraction mapping is used to obtain information with nanometer resolution about the different crystal structures and produce strain maps for each individual phase in the HEA nanocomposite. This in-depth study of the irradiation processed nanocomposite HEAs can help determine the effect of irradiation under different conditions on their microstructural evolution, and shed light on the possibility of altering the microstructure in such advanced materials for future applications.

[1] Shabnam Taheriniya, Farnaz A. Davani, Sven Hilke, Marco Hepp, Chris-tian Gadelmeier, Mohammed Reda Chellali, Torben Boll, Harald Rösner, Martin Peterlechner, Christoph Gammer, Sergiy V. Divinski, Benjamin Butz, Uwe Glatzel, Horst Hahn, Gerhard Wilde, High entropy alloy nano-composites produced by high pressure torsion,Acta Materialia,Volume 208, 116714, (2021)

MS3.P007
Radiation-induced formation of gas bubbles in beryllium after neutron irradiation

M. Klimenkov[1], N. Zimber[1], U. Jäntsch[1], P. Vladimirov[1], M. Rieth[1]

[1]Karlsruhe Institute of Technology (KIT), Institute for Applied Materials - Applied Materials Physics, Eggenstein-Leopoldshafen, Germany

The current interest in the mechanical properties and microstructure of neutron-irradiated beryllium relates to its planned application in the Helium-Cooled Pebble Bed (HCPB) European concept of a breeding blanket of DEMO of the European concept of a breeding blanket made of DEMO (Helium-Cooled Pebble Bed, HCPB).

Typical for beryllium irradiated at elevated temperatures intragrain microstructures containing gas bubbles are illustrated in Figure 1, 2 for all studied irradiation temperatures. The bubbles observed after irradiation at the lowest irradiation temperature of 643 K (370 °C) (Figure 1a) have a size of ca. 10 nm with a round or slightly faceted shape. Tilting of the lamellae does not reveal any anisotropy in the shape of bubbles inside grains, suggesting that their shape is close to spherical. The number density of bubbles decreases, correspondingly, by more than two orders of magnitude. In contrast to the lowest temperature, bubbles grown at higher temperatures have a pronounced hexagonal prismatic shape with their bases located on basal crystallographic planes {0001} (Figure 1c, d, Figure 2). Figure 2(a,b) or (c,d) shows the same areas tilted by the angle of ≈60° (from -29° to +30° inclination of the goniometer tilt). It is clearly seen that projection of the voids changes from hexagonal faceted void at +32° to the narrow strip at -29°.
EELS spectroscopy was used for detection and analysis of He and H2 gases trapped inside bubbles. The peaks at 13.0 eV and 22.4 eV detected in the low-loss EELS spectra suggest the presence of H2 molecules and He atoms. The number densities of both gases inside the bubbles were calculated using atomic scattering cross-section and the intensity of the zero-loss peak. The values He=(4.2±1) atoms/nm3 and nH2=(3.5±1.2) molecules/nm3 were determined for a bubble with a diameter of 160nm. The number densities of both gases increase with decreasing the bubble diameter.

Spherical second-phase precipitates formed at GBs and inside grains were observed at the two lowest (370°C and 440°C) irradiation temperatures only. EDX mapping reveal that precipitates inside grain and at the GB have increased iron and aluminum content suggesting formation of Fe-Al-Be phase. In the material irradiated at 440°C, most precipitates have also Fe-Al-Be composition, while several other single- and multi-phase precipitates were found. The Fe-Al-Be phase is observed as 10-15 nm precipitates inside grains and as 200 nm particle attached to a gas bubble at the GB. This suggests that stability of these precipitates decreases under irradiation and they dissolve at some temperature between 440-560°C.

In fact, dissolution due to the recoil atoms induced by neutron irradiation followed by reprecipitation of complex-phase precipitates was observed at 480 °C. Figure 3 shows two precipitates with sizes between 100-150 nm that are surrounded by numerous precipitates with sizes between 20-50 nm. The larger precipitates contain multiple phases of Al-Fe-Si-Cr-Ti-Mg-Mn-U elements, while the smaller precipitates contain a Fe-Al single phase.

Figure 1: Gas bubbles in beryllium pebbles irradiated at 643 K (a, b) and at 713 K (c, d).

Figure 2: Gas bubbles in beryllium pebbles irradiated at 833 K (a, b) and 923 K (c, d).

Figure 3 Radiation-induced dissolution of complex precipitates and subsequent re-precipitation.

Figure 1

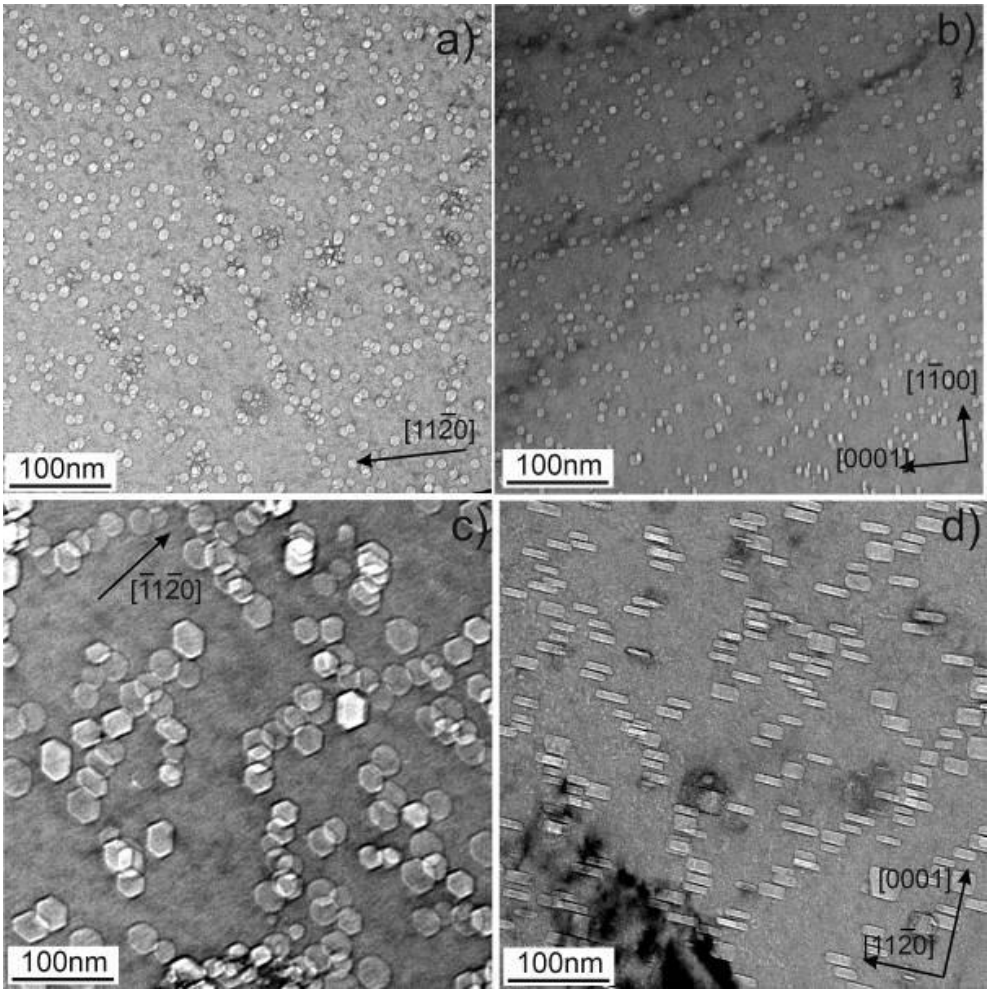

Figure 2

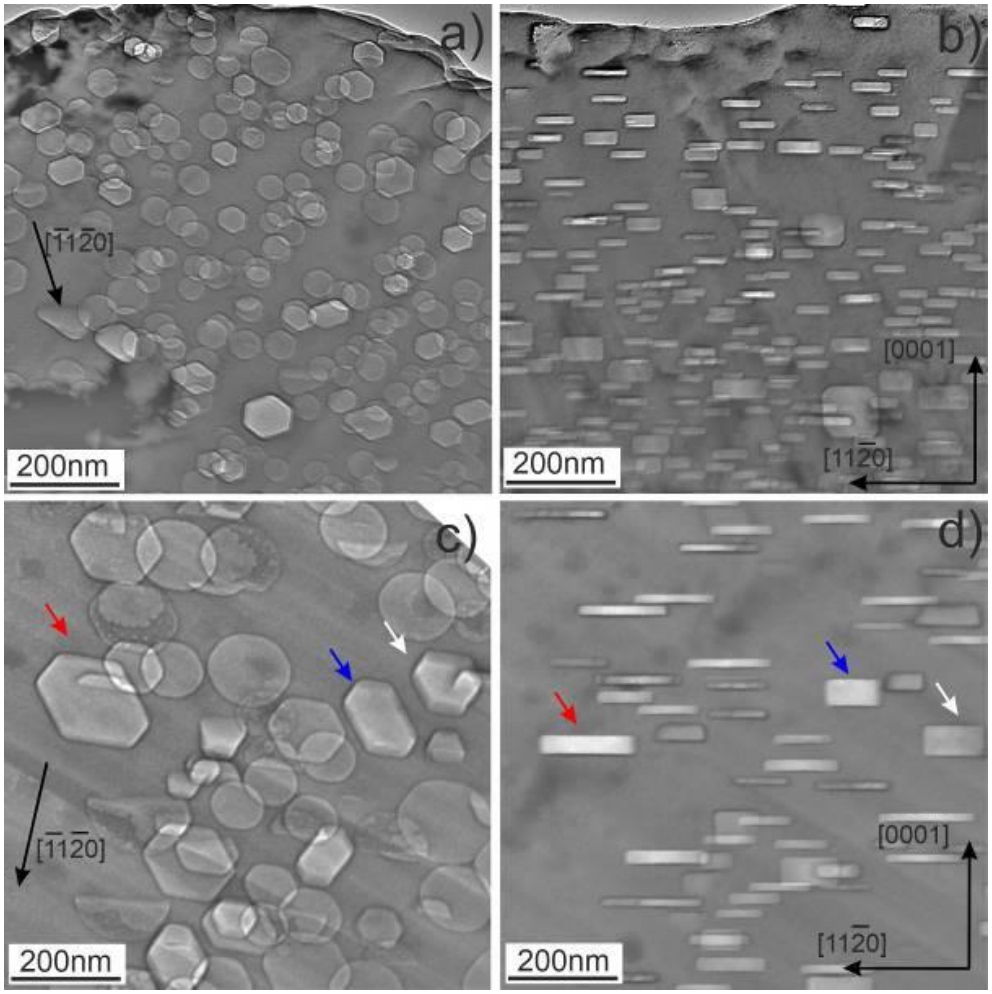

Figure 3

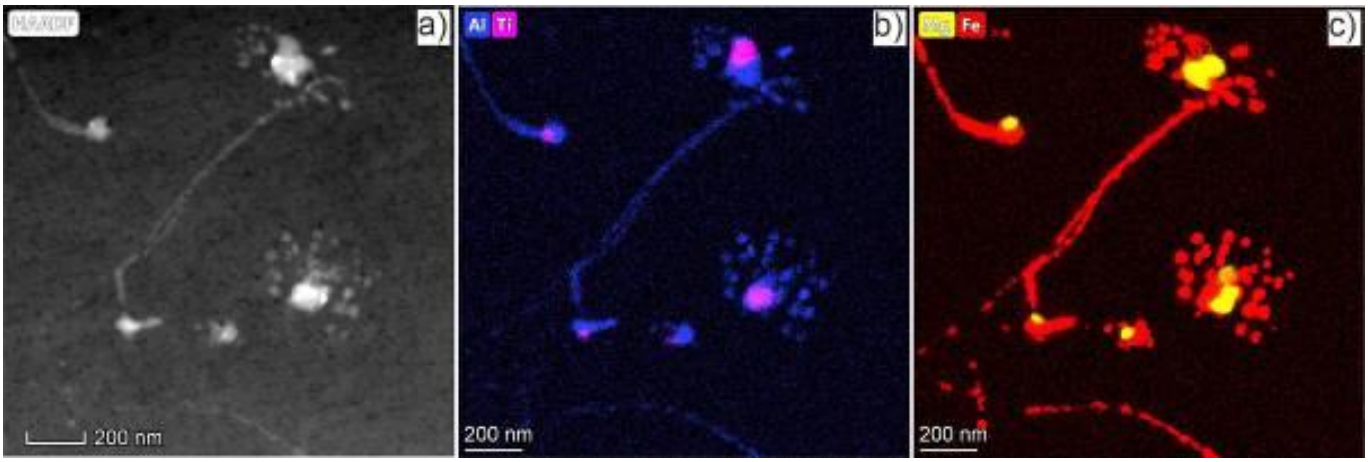

MS3.P009
Towards quantitative criteria for the assessment of the quality of automatic 3D reconstruction of dislocations by deep convolutional neural networks

G. Ganeeva[1], O. Altingövde[2], A. Mishchuk[1,2], A. Garin[3], E. Oveisi[4], P. Fua[2], K. Hess Bellwald[3], C. Hébert[1]

[1]Swiss Federal Institute of Technology Lausanne (EPFL), Electron Spectrometry and Microscopy Laboratory (LSME), Lausanne, Switzerland
[2]Swiss Federal Institute of Technology Lausanne (EPFL), Computer Vision Laboratory (CVLab), Lausanne, Switzerland
[3]Swiss Federal Institute of Technology Lausanne (EPFL), Laboratory for Topology and Neuroscience (UPHESS), Lausanne, Switzerland
[4]Swiss Federal Institute of Technology Lausanne (EPFL), Interdisciplinary Centre for Electron Microscopy (CIME), Lausanne, Switzerland

Three-dimensional (3D) distribution of curvilinear crystal defects known as dislocations are of particular interest in material science as structurally and opto-electronically important features.[i] 3D stereo reconstruction of dislocations in the field of electron microscopy proved itself as an acceptable alternative approach compared to laborious electron tomography, however existing algorithms require manual intervention and thus remain slow.[ii] We developed fully automatic approach to reconstruct dislocations in 3D volume of the sample by just acquiring two electron micrographs at different tilt angles (i.e. stereo-pairs)[iii]. In combination with scanning transmission electron microscopy (STEM) technique stereo 3D dislocation imaging brings many advantages to further reconstruction due to complex contrast formation.[iv].

We apply deep convolutional neural networks (CNN) allowing to detect curvilinear structures and match them on both views without any prior assumptions about their shape to finally build 3D reconstruction. Novel stereo contour matching deep CNN, we trained with various dislocation datasets from three different samples, demonstrates high performance even with noisy microscopy data and complicated dislocation structures and allows to obtain 3D reconstruction within a minute on a normal CPU (Figure1).

Quality of segmentation by detection network and visibility of dislocation structures at the images may vary for different imaging conditions (e.g. detector acceptance semi angle and deviation parameter, $\mathbf{s_g}$). For an optimum imaging and 3D reconstruction, it is crucial to have a quantitative assessment of the quality of the segmentation and ultimately of the 3D reconstruction. For this purpose, we develop tools from Topological Data Analysis (TDA) to analyze the topological correctness of the outputs and compare them to the ground truth. Using TDA methods in image processing helps to provide a global view of images, which considers intrinsic geometrical and topological properties of the images and complements very well with standard methods. We use the topological descriptors[v] to build topological distances between the outputs with different imaging conditions and the ground truth and choose the settings with the highest topological correctness.

Our global approach was also successfully applied to the "tilt-less" imaging technique[vi], which allows simultaneous acquisition of stereo-pairs in a single-shot. Figure2 represents the anaglyph obtained from superposition of simultaneously acquired stereo-pair STEM images with just 1.7 degrees tilt angle with a segmented detector on a Cs-corrected Themis Titan microscope. Further stereo 3D reconstruction with our approach reveals 3D distribution of dislocations precisely.

Figure 1: (a), (b) Stereo-pair of bright-field STEM images with 4 degrees tilt angle acquired in 2-beam condition g=(002), (c) corresponding reconstruction by 3D CNN.

Figure 2: (a), (b) Simultaneously-acquired stereo-pair of bright-field STEM images in 2-beam condition g=(002) with segmented detector, (c) corresponding anaglyph (best viewed with red-cyan 3D glasses)

[1] Amelinckx, "The Characterization of Defects in Crystals."
[2] Jácome et al., 2018, Ultramicroscopy, 195, 157–170
[3] Altingövde et al., 2021 – submitted to Ultramicroscopy
[4] Zhu et al., 2018, Ultramicroscopy, 193, 12–23
[5] A. Garin and G. Tauzin, 2019, https://doi.org/10.1109/ICMLA.2019.00256
[6] Oveisi et al., 2017, Scientific Reports, 7(1)

Figure 1

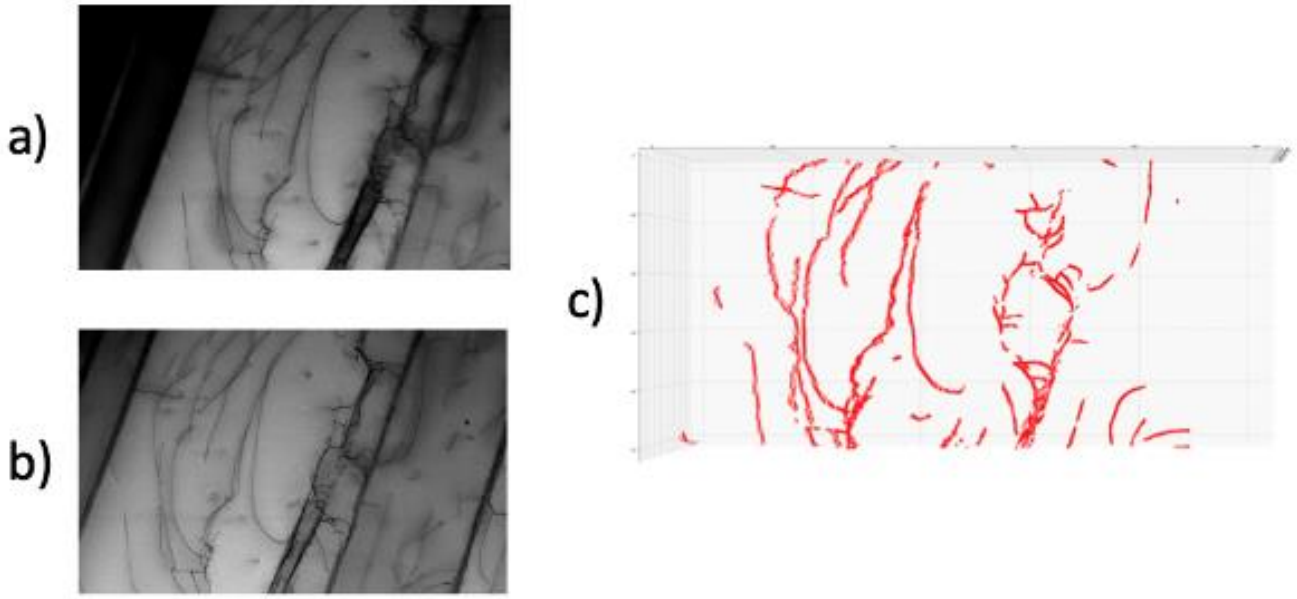

Figure 2

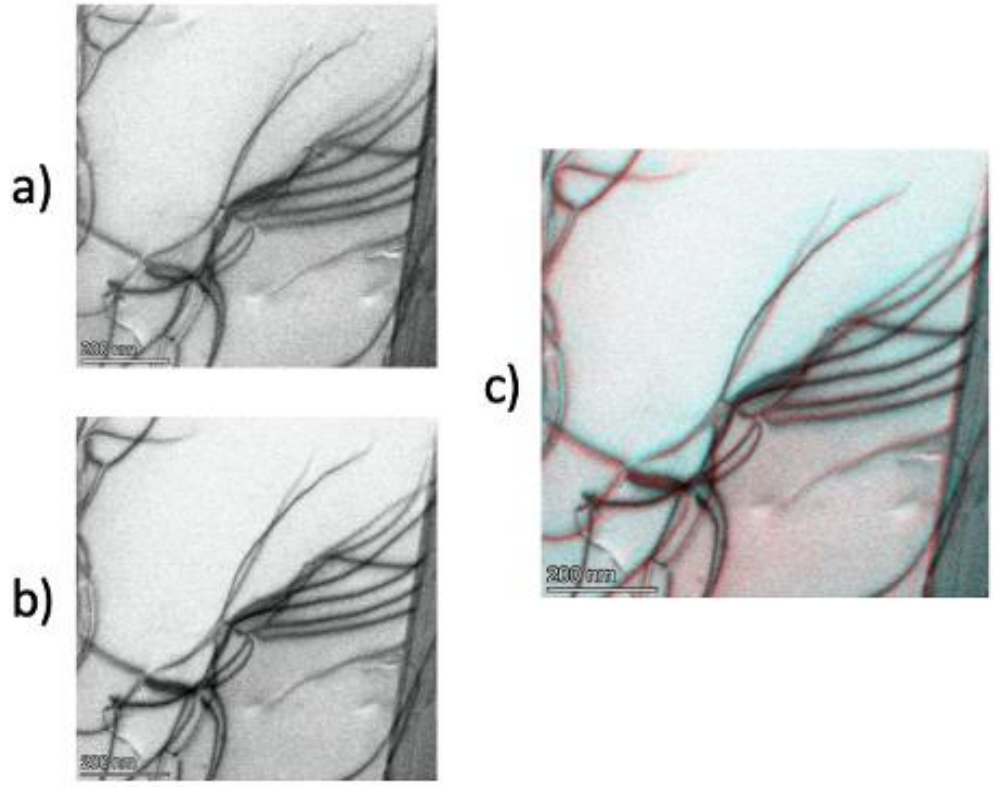

MS3.P010
Crystallisation of SLM-ed Fe-based metallic glass with low glass-forming ability

Ł. Szczepański[1], M. Bambach[2], F. Jensch[3], A. Ambroziak[1], T. Kurzynowski[1]

[1]Wroclaw University of Science and Technology, Wrocław, Poland
[2]Swiss Federal Institute of Technology Lausanne (EPFL), Zurich, Switzerland
[3]Brandenburg University of Technology Cottbus - Senftenberg, Cottbus, Germany

In recent years the Fe-based metallic glasses have become the subject of extensive research. They are characterized as advanced engineering materials having favorable and promising properties, such as high hardness, high elastic strain limit, and excellent magnetic properties. The application of metallic glasses in the Laser Powder Bed Fusion (L-PBF), also known as Selective Laser Melting (SLM), made possible the production of parts with any shape. The most important factor influencing the properties of final products is their microstructure.

The crystallization behavior of Fe-based metallic glass with low glass-forming ability ($Fe_{79}Zr_6Si_{14}Cu_1$ at.%) after selective laser melted samples was investigated in the field of structural X-ray diffraction (XRD), Scanning Electron Microscopy (SEM) and Transmission Electron Microscopy (TEM). Moreover, the conducted light microscopy studies allowed for the comparison of process parameters, such as laser scanning speed and laser power, and their influence on the porosity.

For samples with relative high energy density the fusion line is mainly composed of a solid solution α-Fe(Si) and low fraction of intermetallic $Fe_{23}Zr_6$ and $FeZr_2$ phases. The melt pool zone was characterized by nanometric α-Fe(Si) phases and an amorphous matrix. Besides, the α-Fe(Si) solid solution was also identified in the heat affected zone. Based on the conducted tests, it was found that the porosity fractions decreased by enhancing the laser power and by reducing the scanning speed.

The conducted structural studies will certainly contribute to a more complete understanding of the crystallization of Fe-based metallic glasses with low glass-forming ability produced in Additive Manufacturing technologies. On the other hand, the porosity studies will help to further parameter optimization of the Selective Laser Melting process and the production on near fully dense parts.

MS3.P011
Revealing heterogeneous structures on multiple length scales of metallic glass composites made by severe plastic deformation

S. Fellner[1], J. Eckert[1,2], C. Gammer[1]

[1]Erich Schmid Institute of Materials Science (ESI) of the Austrian Academy of Sciences, Austrian Academy of Sciences, Leoben, Austria
[2]Department Materials Physics, Montanuniversität Leoben, Leoben, Austria

Metallic glasses (MG) are of great research interest due to their superior mechanical and physical properties, such as large elastic limit, high strength, hardness, corrosion and wear resistance [1]. However, due to their amorphous structure, they lack tensile plasticity and thus fail catastrophically at room temperature. In recent years, several approaches were explored trying to improve plasticity by artificially introducing crystalline phases, pores or by bringing the material to a higher energy state by so-called rejuvenation [2, 3, 4]. The resulting material often show complex structural heterogeneities on different length scales, making it difficult to establish a structure-property relationship. Therefore, in the present work we demonstrate, that a multiscale characterization using scanning electron microscopy (SEM) and transmission electron microscopy (TEM) allows for an adequate representation of the generated composite structure and thus created a better understanding of the resulting properties.

CuZrAl was used as a model alloy. As a starting material we used either crystalline material or fully amorphous samples, manufactured by rapid melt quenching in a suction cast facility. Different combinations of processing routes such as controlled heat treatment and severe plastic deformation using high pressure torsion were used for tailoring structural heterogeneities. Crystallized phases and strain softened regions were examined using a combination of chemical and structural imaging. A combination of electron dispersive X-Ray spectroscopy and back scattered electrons in SEM and Z-contrast sensitive high-angle annular dark-field imaging in the scanning TEM was used to cover a wide range of length scales from the micro- to nanoscale. Similarly, the morphology of spatial distributed crystalline phases and multiscale soft-hard interfaces were examined using SEM, TEM and high-resolution TEM (HRTEM).

The results uncover the local structural heterogeneities on different length scales that are introduced by the different processing routes. A decrease in hardness with increasing number of revolutions indicates severely strained regions after HPT deformation. Only the combination of advanced SEM and TEM imaging along with mechanical hardness testing, allow to gain a deeper understanding of the changes in material properties caused by structural modifications.

References:
[1] A.L. Greer, Metallic glasses on the threshold, Mater. Today 12 (1-2) (2009);
[2] S. Pauly, G. Liu, G. Wang, U. Kühn, N. Mattern, J. Eckert, Microstructural heterogeneities governing the deformation of Cu47.5Zr47.5Al5 bulk metallic glass composites, Acta Materialia, 57(18) (2009) 5445-5453;
[3] D. Şopu, C. Soyarslan, B. Sarac, S. Bargmann, M. Stoica, J. Eckert, Structure-property relationships in nanoporous metallic glasses, Acta Materialia, 106, (2016) 199-207;
[4] W. Dmowski, Y. Yokoyama, A. Chuang, Y. Ren, M. Umemoto, K. Tsuchiya, A. Inoue, T. Egami, Structural rejuvenation in a bulk metallic glass induced by severe plastic deformation, Acta Mater. 58 (2) (2010) 429-438.

Figure 1: Elemental characterization of cross-sectional near-surface volume in HPT deformed metallic glass at micrometer scale

Figure 2: STEM HAADF image showing accumulated deformation in strain softened regions at nanometer scale

Figure 1

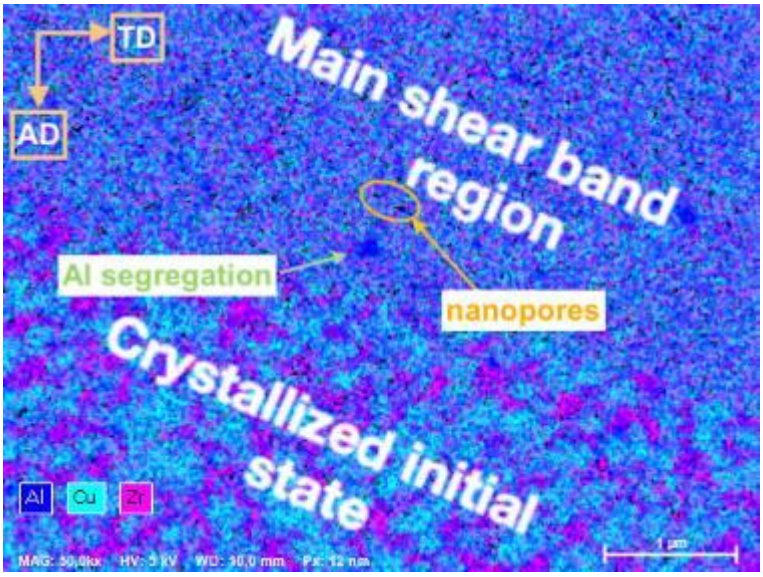

Figure 2

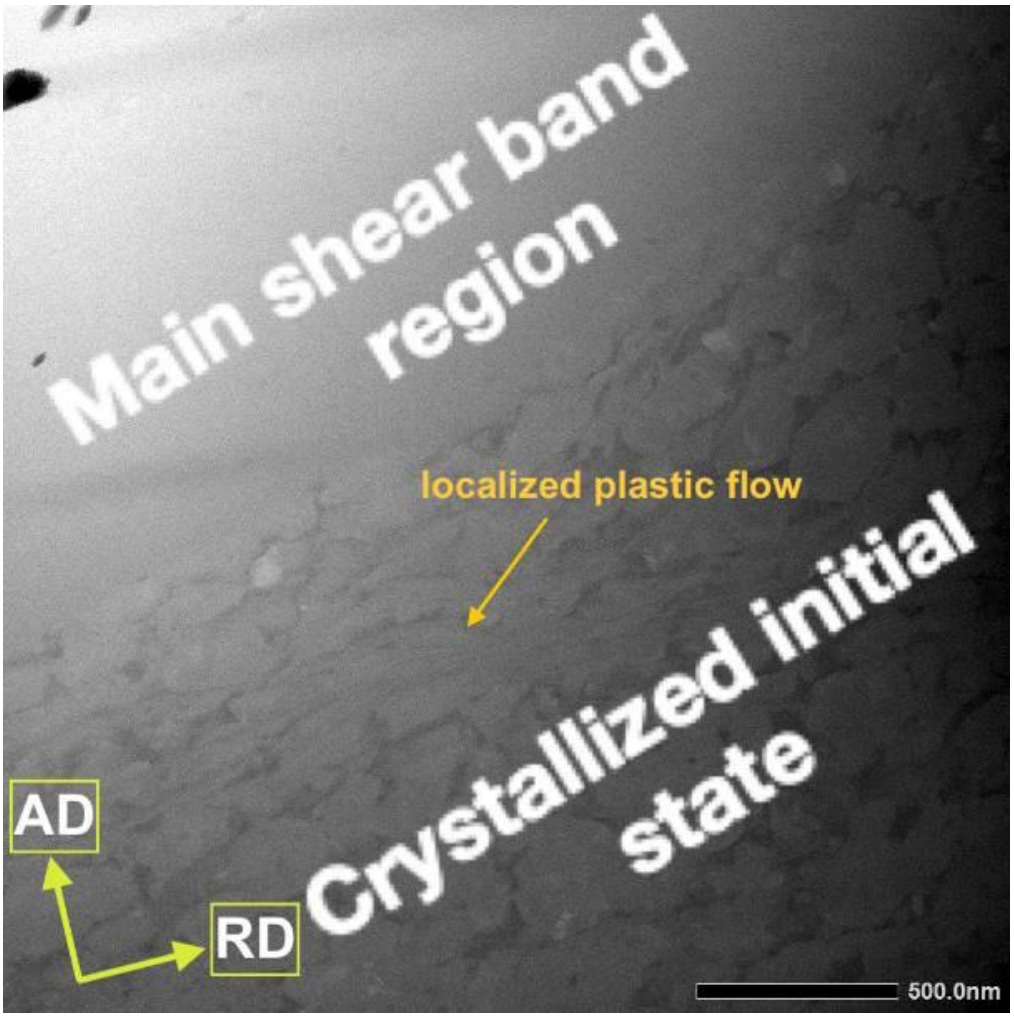

MS3.P012
Quantitative and qualitative insight into nanoscale bainite characterisations

A. Królicka[1], A. Janik[2], A. Żak[1], K. Radwański[2]

[1]Wrocław University of Science and Technology, Department of Metal Forming, Welding and Metrology, Wrocław, Poland
[2]Łukasiewicz Research Network – Institute for Ferrous Metallurgy, Gliwice, Poland

Introduction & Objectives: Over the past two decades, nanobainitic steels have been widely developed due to their high mechanical properties. The highest mechanical properties are obtained with a strong microstructure refinement[1]. The main research goal is to compare the possibilities of using the SEM, EBSD, and TEM techniques for qualitative and quantitative analysis of refined bainitic structures.

Methods: The research material was a commercial 9XC bearing steel (according to the GOST standard) characterized by a high concentration of C (0.94 wt.%) and Si (1.89 wt.%). The samples were austenitized at 1000 °C and then annealed at 300°C for 5 hours. The microstructure analysis was performed using an HR-SEM Joel JSM-7200F equipped with an EBSD detector, conventional TEM Hitachi H-800.

Results: These investigations present a proposal to use SEM, TEM, and EBSD techniques for microstructure characterization of high-carbon nanobainitic steel. It is particularly important to define both a qualitative and a quantitative approach. The method of identification of the microstructural constituents qualitatively (TEM/SAED) was used together with the quantitative analysis based on misorientation angle distributions (EBSD). Also, these distributions allow for the quantitative determination of crystallographic orientation and revealing the dominant orientation (mainly N-W or K-S) [3]. Despite the high concentration of silicon, the presence of partially coherent cementite was found, as confirmed in [4]. The microstructure of nanobainitic steels usually consists of austenite with film-like and blocky morphology, as well as bainitic ferrite, Figure 1. Besides, methods intended for the quantitative measurements of austenite with both film-like and blocky morphology were proposed. Hence, the method of measuring their thickness was demonstrated (TEM). Finally, the possibility of determining the prior austenite grain size by the EBSD method was also presented and compared to the conventional grain boundary etching method (by picric acid solution). The proposed methods of qualitative and quantitative analysis will be a complementary procedure for the microstructure characterization of bainitic steels characterized by a nanometric scale.

Figure 1: The microstructure of 9XC after isothermal heat treatment (bainitic ferrite, film-like and blocky austenite).

Conclusions: 1. The PAGS measurements can be performed by EBSD techniques by analyzing misorientation angles in the range of 20-40°. 2. The presence of partially coherent cementite precipitations was determined based on SAED/TEM, but they were not visible in bright field images. 3. Thickness measurements of bainitic ferrite and film-like austenite based on bright-field images (TEM) enabled the classification of 9XC steel after isothermal heat treatment as nanostructured steel. 4. The ratio of film-like austenite to blocky austenite can be determined by SEM and TEM images graphical editing, and EBSD.

References:
[1] Caballero, F.G.; Garcia-Mateo, C.; Miller, M.K. Design of novel bainitic steels: Moving from ultrafine to nanoscale structures. *Jom*2014, *66*, 747–755.
[2] Beladi, H.; Adachi, Y.; Timokhina, I.; Hodgson, P.D. Crystallographic analysis of nanobainitic steels. *Scr. Mater.*2009, *60*, 455–458.
[3] Timokhina, I.B.; Beladi, H.; Xiong, X.Y.; Adachi, Y.; Hodgson, P.D. Nanoscale microstructural characterization of a nanobainitic steel. *Acta Mater.* 2011, *59*, 5511–5522

Figure 1

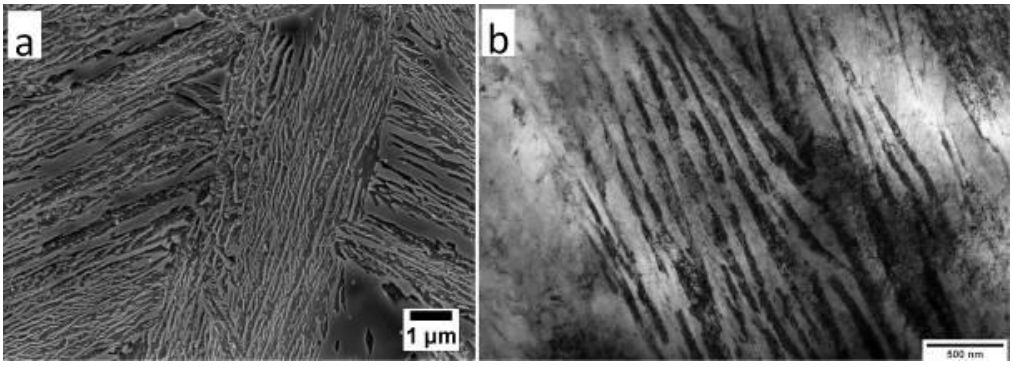

MS3.P013Reconstructing parent microstructures from EBSD based orientation measurements

S. Wright[1], R. De Kloe[2]

[1]EDAX LLC, Mahwah, NJ, United States
[2]Ametek BV, EDAX, Tilburg, Netherlands

When a material undergoes a transformation from one crystallographic phase to another, a grain in the original microstructure may transform into several different crystallographic variants. The transformed microstructure is generally quite different, but often traces of the original microstructure are recognizable. For example, in steels, austenite (face-centered cubic γ) is formed during high temperature processing and then transforms to ferrite (body-centered cubic α) as it cools to room temperature. It is difficult, if not impossible, to capture the microstructure of the high-temperature phase. It would be helpful to be able to characterize the microstructure (i.e., grain size, texture) of the high-temperature phase to optimize the full processing path of the material.

We have implemented the method by Ranger *et al.* [1] in conjunction with EBSD to allow reconstruction of the original high-temperature microstructures in a range of materials. The efficacy of the method was verified in the following metals:

•The observed high temperature grain structure in face-centered cubic β cobalt obtained by an in-situ phase transformation experiment was compared against the reconstruction of the final low temperature hexagonal close-packed α cobalt microstructure using the OR: {1 1 1}β ∥ {0 0 0 1}α and ⟨1 1-2⟩ β ∥ ⟨1-1 0 0⟩ α.

•The austenite parent microstructure in steel from EBSD measurements on ferrite was reconstructed using the Nishiyama-Wasserman OR: {1 1 1}γ ∥ {1 1 0}α and ⟨1 1 -2⟩ γ ∥ ⟨1 1 0⟩ α. The fidelity of the reconstruction algorithm was confirmed by comparison to other algorithms.

•The original high temperature body-centered cubic β Ti microstructure was obtained from EBSD measurements on a hexagonal close-packed α Ti microstructure in additively manufactured Ti6Al4V containing a small fraction (2%) of retained β Ti. The reconstruction was performed assuming an OR of {1 1 0}β ∥ {0 0 0 1}α and ⟨1-1 1⟩ β ∥ ⟨1 1 -2 0⟩ α. The retained original β Ti phase in the microstructure provided a marker confirming the results of the reconstruction.

The results of the algorithm in reconstructing the pre-transformation parent microstructures in all three cases are shown in Figures 1, 2 and 3. Because local misorientations between adjacent pixels instead of entire grains are used to identify the phase relationships, also orientation gradients like those displayed within several of the grains in Figure 3(b) may be present in the reconstruction and can provide an indication of residual strain in the material prior to the phase transformation.

The parent grain reconstruction algorithm performs well and allows quantitative aspects of the pre-transformation microstructure such as grain size, crystallographic texture, and even residual strain to be reliably characterized.

Figure 1: IPF Orientation maps from cobalt microstructures: (a) as-measured pre-transformation β Co, (b) as-measured post transformation α Co and (c) the as-reconstructed β Co.

Figure 2: IPF Orientation maps from steel microstructures: (a) as-measured post transformation α Fe and (b) the as-reconstructed γ Fe.

Figure 3: IPF Orientation maps from Ti6Al4V microstructures: (a) as-measured post-transformation α Ti, (b) reconstruc-ted pre-transformation β Ti and (c) the as-measured retained β Ti.

References:
[1] C. Ranger, V. Tari, S. Farjami, M.J. Merwin, L. Germain, A. Rollett, Metall. Mater. Trans. A 49 (2018) 4521-4535.

Figure 1

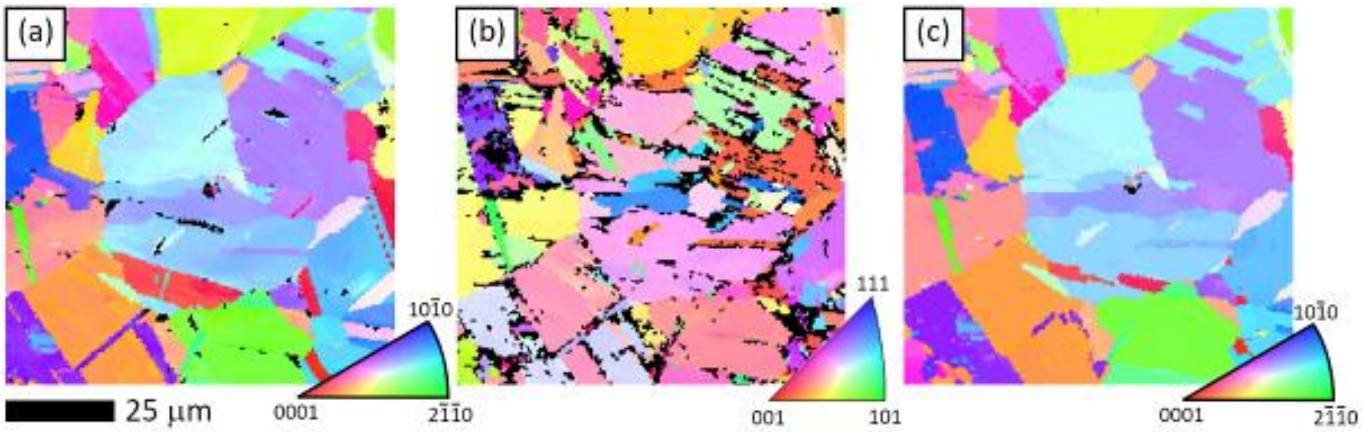

Figure 2

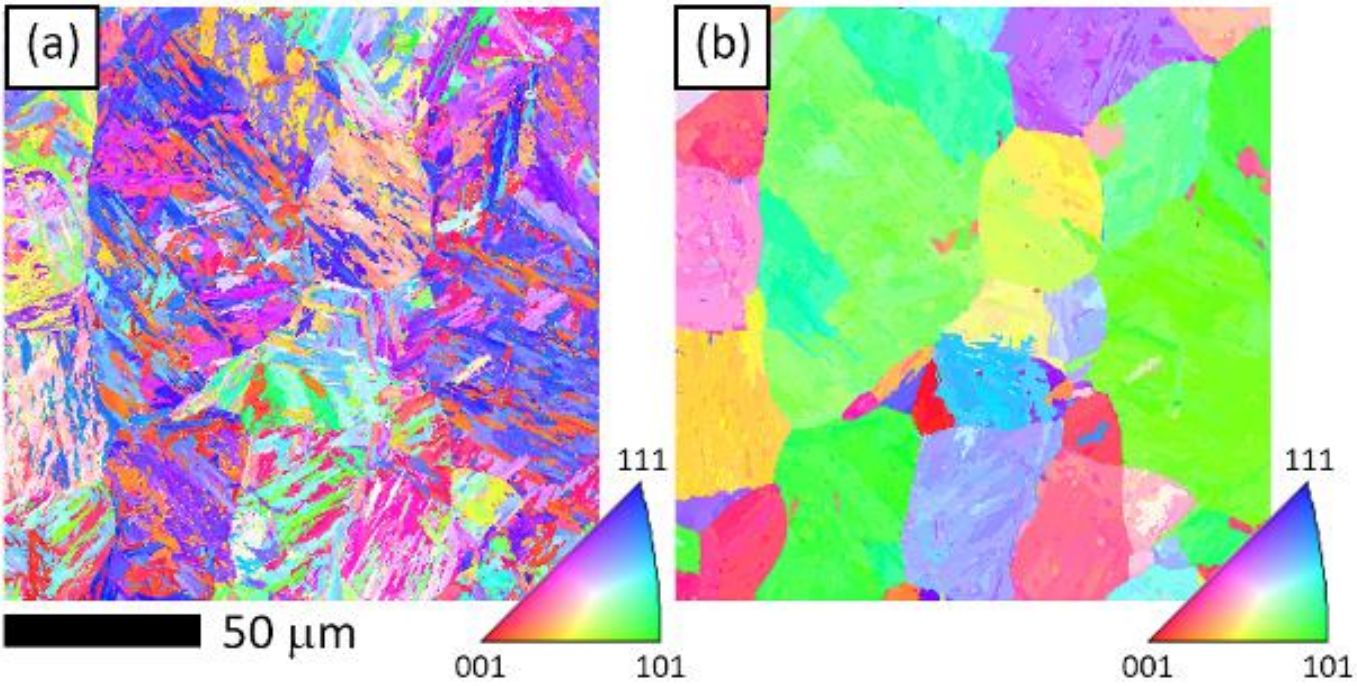

Figure 3

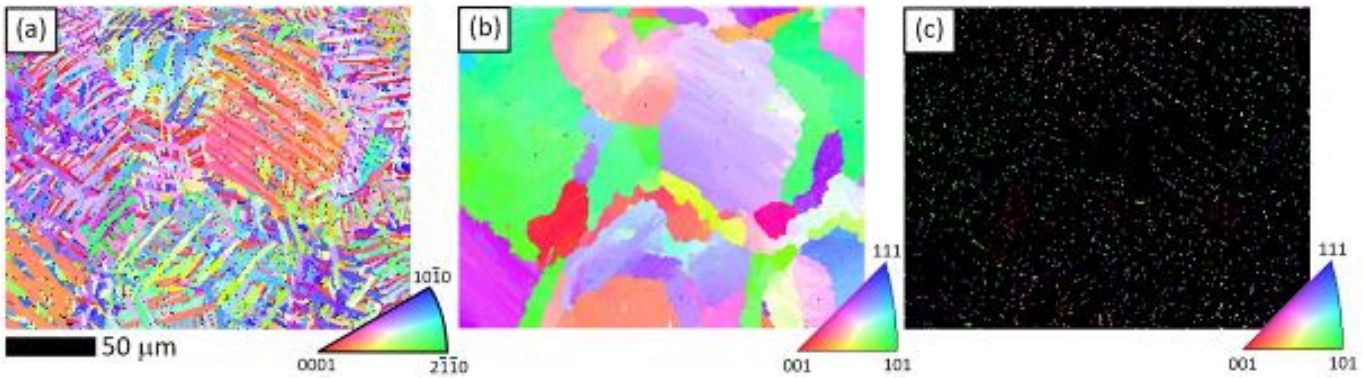

MS3.P014
The effect of water concentration on mechanical properties and fracture mode of austempered ductile iron

P. Janjatovic[1], D. Rajnović[1], O. Eric Cekic[2], S. Balos[1], M. Dramicanin[1], L. Sidjanin[1]

[1]Faculty of Technical Sciences, University of Novi Sad, Department of Production Engineering, Novi Sad, Serbia
[2]Faculty of Mechanical Engineering, University of Belgrade, Innovation Centre, Belgrade, Serbia

Austempered ductile iron (ADI) is an advanced cast iron material that is extensively used in the automotive and heavy machine industry due to excellent mechanical properties. However, in contact with fluids, especially water, ADI material becomes brittle [1]. For that reason, in this paper, the influence of different water concentrations in ethyl alcohol on the mechanical properties and fracture mode of ADI materials was studied.

The starting material was unalloyed ductile iron (3.5%C, 2.5%Si, 0.35%Mn, 0.031%Mg, 0.018%P, 0.015%S, Fe balance), with spheroidization >90%, graphite volume fraction 12±1.6%, nodule count 125÷175 mm−2, and nodule size 15÷30 μm. The samples were austenitized at 900 °C/1 h, and austempered in a salt bath at 400 °C/1 h. The tensile test was performed in dry conditions, distilled water, and 0.2, 4, and 10 vol.% mixtures of water and ethyl-alcohol (C_2H_5OH). The microstructure of ADI was examined by Leitz Orthoplan light microscope, while fractured surfaces were studied by a scanning electron microscope JEOL JSM 6460LV at 25 kV.

The fracture surface of samples tested in water reveals two areas: a flat bright fracture zone near the specimen free surface (which size decreases with the decrease of water concentration), and a larger dimpled zone, Figure 1ab. The water embrittled zone (bright zone) has characteristic striation lines and serrated facets, Figure 1cd. Furthermore, a small, isolated, brittle facets near sample free surface were noticed, Figure 2a. They have a fan-shaped form and exhibit a typical brittle fracture appearance with bright crystalline cleavage facets and river pattern strips, Figure 2b. The larger dimpled zone is identical to quasi-cleavage fracture mode of dry tested samples [2].

The results of mechanical testing are shown in Table 1. Values indicate the decrease in mechanical properties as the water content is increased in the environment. The statistically significant difference (ANOVA test) in relation to dry environment was not established for 0.2 vol.% water concentration, and for proof strength in 4 vol.% water, even though, the water embrittlement zone is present in all cases.

It can be concluded that as the water content in the environment increases, the tensile properties of ADI decrease, especially elongation. In all tested samples the crack propagation starts from the embrittlement zone, which originates from the free sample surface. The formation of the embrittlement zone acts as a primary weak spot for the crack nucleation and subsequent fracture. The origin of this phenomenon is the cyclic chemisorption of hydrogen atoms from water into the material surface [1,3].

Acknowledgment: The authors gratefully acknowledge research funding by the project " Innovative materials and joining technologies " on the Department of Production Engineering, Faculty of Technical Sciences, Novi Sad, Serbia.

References:
[1] D. Rajnovic, S. Balos, L. Sidjanin, O. Eric Cekic, J. Grbovic Novakovic, Mater. Charact. 2015, 101, 26–33
[2] R.A. Martinez, Eng. Fract. Mech. 2010, 77, 2749–62
[3] S. Komatsu, Y. Osafune, Y. Tanaka, K. Tanigawa, S. Shibutani, H. Kyogoku, Int. J. Cast Met. Res. 2003, 16, 209–214

Figure 1

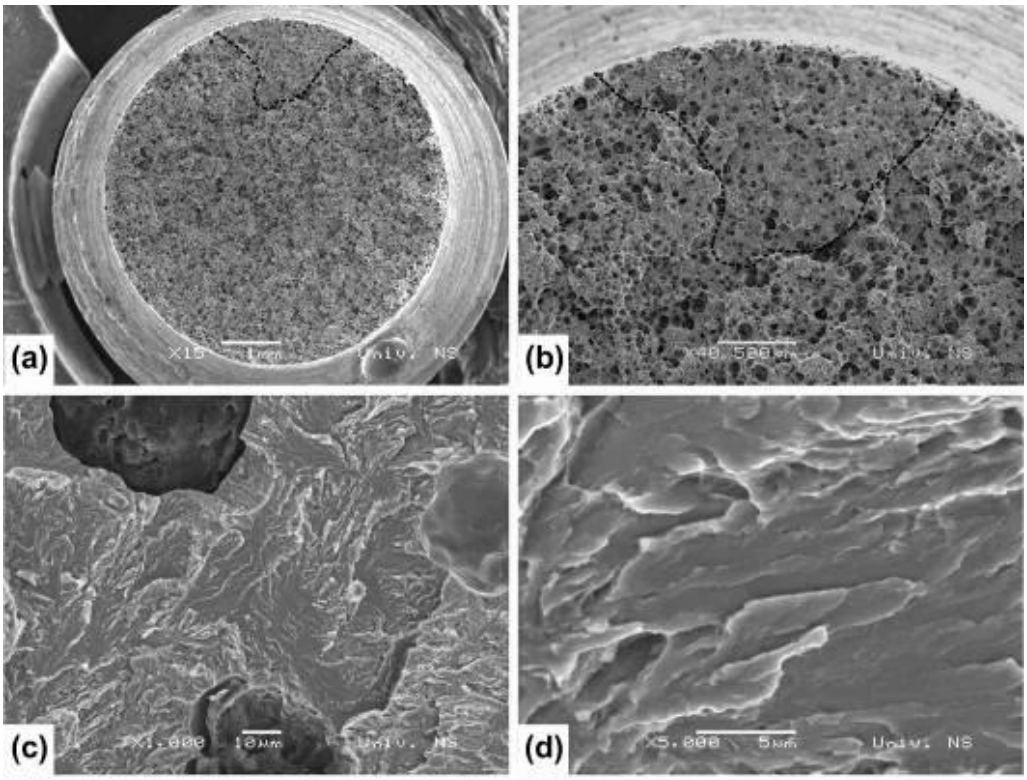

Figure 1. Fracture mode of the ADI tested in 100% water: a) and b) the embrittlement zone enclosed by dashed line; c) and d) striation lines in the embrittlement zone.

Figure 2

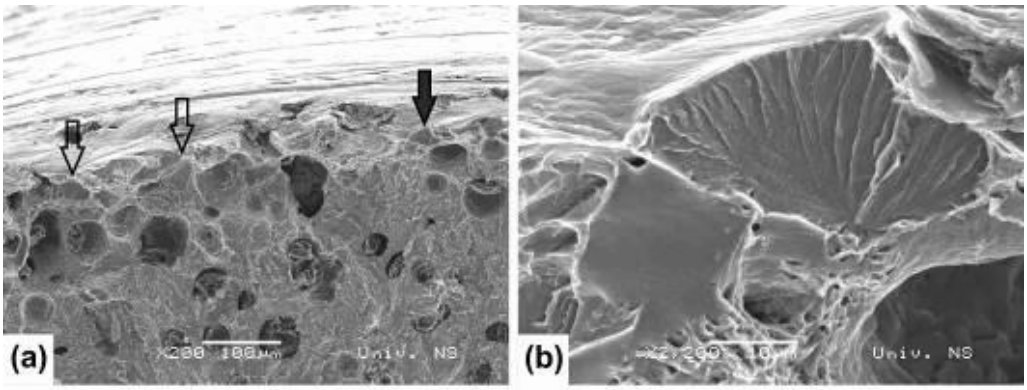

Figure 2. Surface detail of embrittlement zone of the ADI tested in 100% water: a) fan-shaped brittle facets indicated by arrows; b) higher magnification of the fan-shaped brittle facet marked with a black arrow.

Figure 3

Table 1. Mechanical properties (ISO 6892-1) of the ADI materials in dry and in different water concentrations environments.

Environment	Tensile Strength R_m [MPa]	Proof Strength $R_{p0.2}$ [MPa]	Elongation A [%]
Dry	959	722	11.5
0.2% Water	952	707	8.7
4% Water	901*	711	5.2*
10% Water	864*	678*	4.2*
Water	814*	675*	2.1*

* statistically significant difference in relation to dry environment, ANOVA test, $p < 0.05$.

MS3.P015
The effect of the flux based on TiO_2 nano and submicron particles in A-TIG welding

M. Dramicanin[1], S. Balos[1], P. Janjatovic[1], D. Rajnović[1], S. Adamovic[2]

[1]Faculty of Technical Sciences, University of Novi Sad, Department of Production Engineering, Novi Sad, Serbia
[2]Faculty of Technical Sciences, University of Novi Sad, Department of Graphic Engineering and Design, Novi Sad, Serbia

Tungsten Inert Gas (TIG) welding is a high-quality welding method for a wide range of materials, but it has a poor penetration, which contributes to low productivity [1]. The solution is a flux, developed to increase the penetration depth. This innovative process is called Activated TIG (A-TIG). Fluxes were produced as a mixture of metallic oxide powders and solvents in form of alcohol or acetone. Before welding, the flux is applyed over the surface [2].

In this paper, six different fluxes were made, with acetone as a solvent, and a mix of 20 nm TiO_2 nanoparticles (N) and 300 nm TiO_2 submicron particles (M). The resulting particle sizes were determined by zeta potential method. Each flux was applied on the base metal, around 20 mm wide. AISI 304 base metal plate had the dimensions of 50x50x10 mm. Welding - remelting was done on six plates with applied flux and one without the flux (control). A-TIG was done with 2 % thoriated tungsten electrodes with a conical shape and the tip angle of 90°. The welding direct current electrode negative was 200 A, the argon shielding gas was used, the arc length was 2 mm, and the welding speed was 100 mm/min. After welding, the samples were cut perpendicularly to welding and standard metallographic examination was done by light microscope. Etching was done by Aqua regia.

Figure 1: shows that the remelted specimen with the flux applied has a deeper penetration than the control specimen. A mixture of submicro and nanoparticles (3M2N) produced the highest penetration, since the highest amount of the smallest particles was obtained in the flux (Graph 1). This is because during mixing, nanoparticle agglomerates become crushed by submicron particles.

Micrograph of the weld metal and the fusion line near the surface of the selected samples is shown in **Figure 2**. In the base metal, near the fusion line in Figure 2a, a coarser grains can be observed than in sample remelted with the flux, Figure 2c. However, the microstructure near the fusion line under the weld metal of the sample welded with the flux is coarser (Figure 2d), compared to the control specimen (Figure 2b). The growth of austenite grains is caused by a high temperature in a specific region, caused by the direction of melt flow, as indicated in drawings in Figure 2. That means, in control specimen, the liquid metal flows from the center of the weld towards the edges, while in specimen welded with the flux, the liquid metal flow is reversed, it flows from the edges towards the center, increasing the penetration. This alteration of the liquid metal flow using activating flux is called the reversed Marangoni effect [3].

Acknowledgments: The authors gratefully acknowledge research funding by the project entitled "Innovative materials and joining technologies" on the Department of Production Engineering, Faculty of Technical Sciences Novi Sad, Serbia.

References:
[1] K. H. Tseng, P. Lin, Materials, 7 (2014) 4755-4772
[2] R. Vidyarthy, D. Dwivedi, J Manuf Process, 22 (2016) 211-228
[3] S. Balos, M. Dramicanin, P. Janjatovic, I. Zabunov, D. Klobcar, M. Busic, M. L. Grilli, Metals, 9 (2019) 567-578

Figure 1

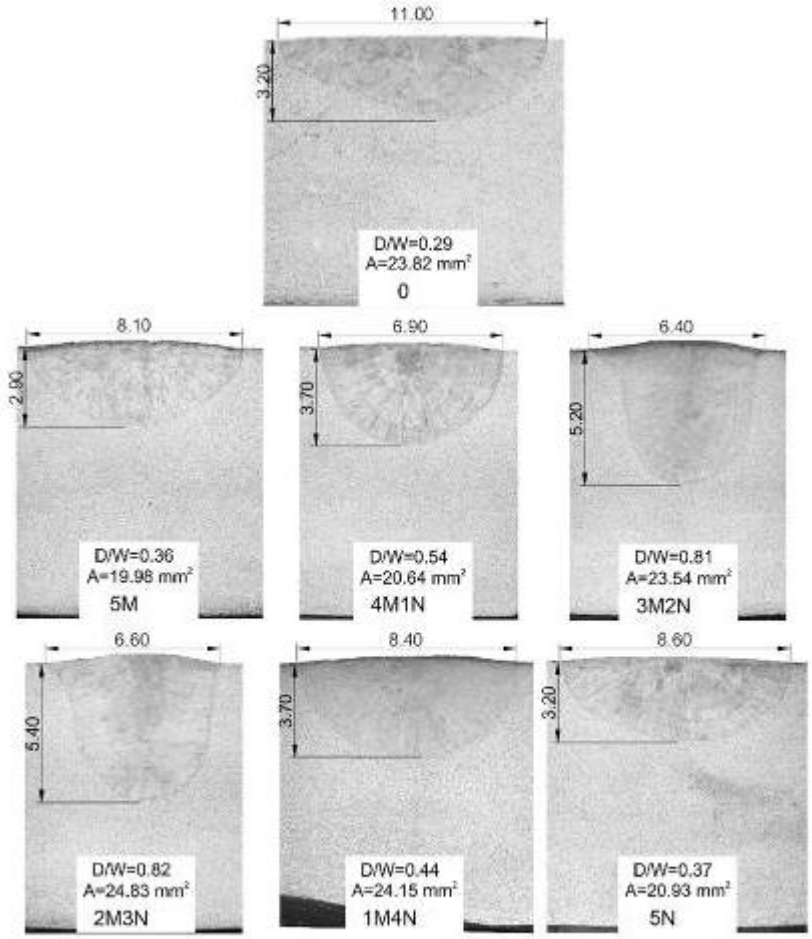

Figure 1. Macro images of specimens welded without and with flux, with indicated depths, widths, depth to width ratios, and weld surface areas

Figure 2

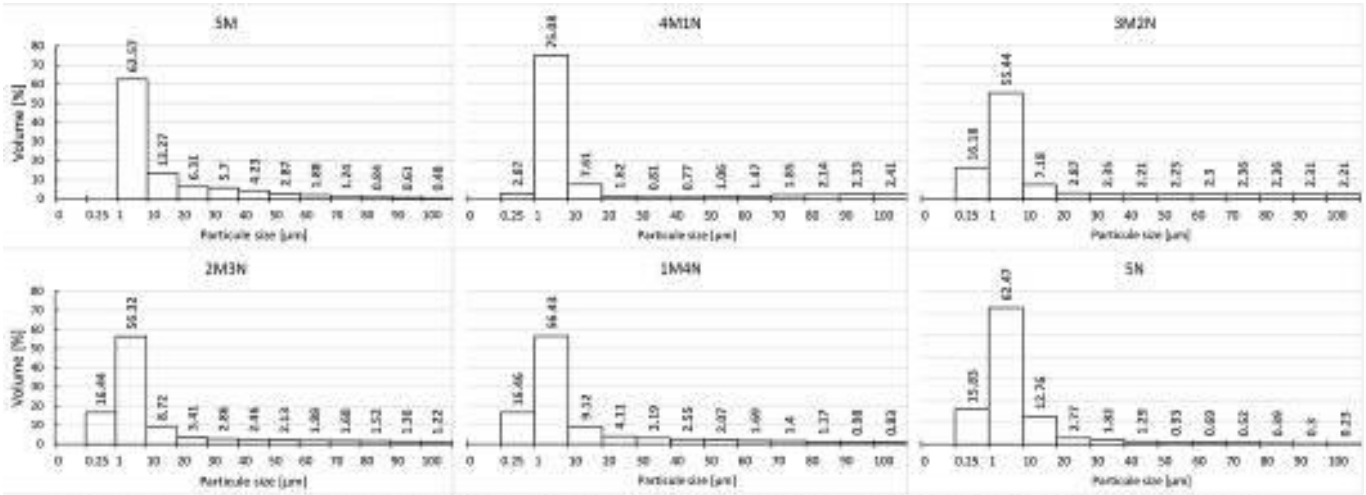

Graph 1. Zeta sizer results: volume of particle size in the fluxes used in the experiment

Figure 3

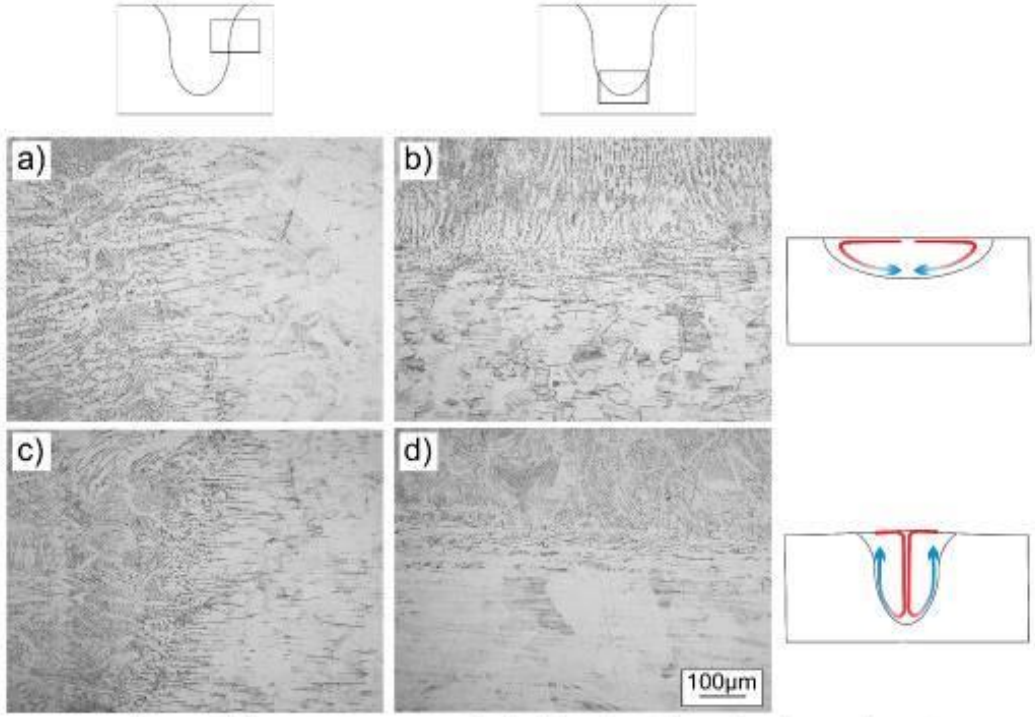

Figure 2. Microstructures near fusion line: a) under surface in specimen 0;
b) at the bottom of weld in specimen 0;
c) under surface in specimen 3M2N; d) at the bottom of weld in specimen 3M2N

MS3.P016
Microstructure evolution in 304L austenitic steel subjected to fatigue loading

I. Kubena[1], M. Jambor[1], S. Fintova[1], M. Smid[1]

[1]Institute of Physics of Material, Czech Academy of Sciences, Brno, Czech Republic

304L austenitic steel is frequently used as a structural material for components in power plants [1]. The steel, as well as other austenitic steels, is valued especially because of its excellent corrosion resistance, good strength and excellent work-hardening. The source of extended work-hardening can be attributed to the metastable nature of austenite (FCC lattice), which means that phase transformation known as transformation-induced plasticity (TRIP) usually takes place during plastic deformation. This phenomenon was thoroughly studied and modelled [2, 3]. Man et al. [4] showed that the distribution of the strain-induced martensite strongly depends on the chemical heterogeneity. Areas with lower content of nickel, aligned parallel to the rolling direction, exhibited distinctively higher sensitivity towards TRIP effect. The present work relates fatigue properties to the microstructural changes occurring in the material.

The 304L austenitic steel with a nominal composition (wt.%) of 8 % Ni, 18 % Cr, 1.8 % Mn, 0.17 % Si, 0.023 % C and Fe for balance was studied. Microstructure consisted of polyhedral grains with austenitic matrix with rare areas of delta ferrite. Cylindrical specimens were subjected to the symmetrical push-pull cycling (R = -1) in the total strain amplitude regime. Axial extensometer was attached to the gauge length of specimens in order to measure the applied strain precisely.

Regardless of the total strain amplitude applied, three stages of material cyclic hardening/softening response during the 304L steel fatigue life were identified. A very short cyclic hardening period at the cycling beginning was followed by the cyclic softening. The last stage of fatigue life was accompanied by rapid cyclic hardening. The magnitude of the described stages depends on the applied total strain amplitude. The higher total strain amplitude is, the more pronounced are the changes in material cyclic hardening/softening response. ECCI (electron channeling contrast imagining) and TEM (transmission electron microscopy) were adopted to explain these changes in relation to changes in the microstructure due to the cycling. The first two stages of material response to the loading are attributed to the new dislocation source creation (initial hardening) and to the localization of the cyclic plastic strain (following softening). In the last stage of fatigue life, pronounced cyclic hardening happens. Two main reasons responsible for the cyclic hardening were revealed in terms of microscopic analysis. Creation of thin deformation twins of a thickness of several nanometres was confirmed in the microstructure by SAED (selective area electron diffraction). The second mechanism which cyclically hardened the studied material is martensitic transformation. Thin martensitic laths in the interior of austenitic grains, as well as whole grains that transformed from the austenite to the martensite, were observed in the microstructure. The occurrence of the investigated microstructural evolution is closely relatedto the applied strain amplitude, namely its plastic part.

Acknowledgement: This research has been financially supported by Czech Science Foundation by the project 19-25571Y.

[1] K.H. Lo et al. Mat. Sci. Eng. R: Reports, 65 (2009) 39-104.
[2] R.G. Stringfellow et al. Acta Metall. et Mat., 40 (1992) 1703-1716.
[3] M. Bayerlein et al. Mat. Sci. Eng. A 114 (1989) L11-L16
[4] J. Man et al. Eng, Fract. Mech., 185 (2017) 139-159

MS4.002
Imaging the spatial distribution of π* states in graphene using aberration-corrected STEM-EELS – towards orbital mapping

M. Bugnet[1,2,3], M. Ederer[4], V. Lazarov[5], Q. Ramasse[1,2,6], S. Löffler[4], D. Kepaptsoglou[1,5]

[1]SuperSTEM Laboratory, SciTech Daresbury Science and Innovation Campus, Daresbury, United Kingdom
[2]University of Leeds, School of Chemical and Process Engineering, Leeds, United Kingdom
[3]Univ Lyon, CNRS, INSA Lyon, UCBL, MATEIS, Villeurbanne, France
[4]TU Wien, University Service Centre for Transmission Electron Microscopy, Vienna, Austria
[5]University of York, Department of Physics, York, United Kingdom
[6]University of Leeds, School of Physics & Astronomy, Leeds, United Kingdom

Electronic states are paramount to most physical and chemical properties of materials. For instance, electronic orbitals are responsible for chemical bonding between atoms of a crystal. Their experimental observation at defects and interfaces would help understanding material properties better and developing nanostructures with novel functionalities. Nevertheless, the visualization of orbitals in real space at the atomic scale is extremely elusive, and is mostly determined by surface microscopy tools, thus only with surface sensitivity. However, using electron energy-loss spectroscopy (EELS) in the scanning transmission electron microscope (STEM) allows to probe electronic transitions from core levels to momentum- and site-projected empty states, *i.e.,* orbitals, in the bulk of the crystal, as demonstrated in rutile [1].

Here, we focus on graphene, whose inherent 2-dimensionality presents surfaces as structural discontinuities. We determine the extent of the π* ($1s \rightarrow 2p_z$) state distribution in pristine graphene layers in side-view, and explore the mapping of π* orbitals in the aberration-corrected STEM. We interpret the experimental signals on the basis of inelastic channelling calculations (ICCs) [2].

Despite higher intensity of the π* fine structures relative to the σ* in between the graphene layers (Figure 1), the absolute π* intensity is higher on the C planes, and as a result π* states appear essentially localized on the graphene layers. However, the π*/σ* ratio map shows intensity maxima in between graphene layers, as highlighted by the π*/σ* and HAADF intensity profiles (Figure 2). All maps are well reproduced by ICCs, as shown by the overlap of experimental and calculated π*/σ* intensity profiles. ICCs also enable an evaluation of the effect of thickness on the orbital contrast. The π* map of an extremely (unrealistically) thin specimen (0.43 nm) displays lobes outside the C planes, and additional intensity is also expected on the C columns. For larger and more realistic thicknesses up to 25 nm, the π* intensity becomes progressively more important on the C planes than outside, in agreement with experiments.

This work highlights the successful mapping of π* states at high resolution in "free-standing" graphene multilayers. The thickness plays a significant role on the orbital contrast, and ICCs suggest that significant improvement will be expected only for specimens less than few nm thick [3].

[1] S. Löffler, M. Bugnet, *et al.*, Ultramicroscopy 177**,** 26 (2017).
[2] S. Löffler, *et al.*, Ultramicroscopy 131**,**39 (2013).
[3] The electron microscopy work was supported by the EPSRC (UK). SuperSTEM Laboratory is the EPSRC National Research Facility for Advanced Electron Microscopy. MB is grateful to the SuperSTEM Laboratory for microscope access, and to the School of Chemical and Process Engineering at the University of Leeds for a visiting associate professorship and financial support. ME and SL acknowledge funding from the Austrian Science Fund (FWF) under grant nr. I4309-N36.

Figure 1: (a) High resolution STEM-HAADF image of a six-graphene layer assembly. (b) C-K edge spectra – shifted vertically for visualization – corresponding to in (red) and out of (blue) atomic planes, as indicated in (a).

Figure 2: Experimental (a) and calculated (b) π*/σ* STEM-EELS maps. (c) π*/σ* profiles from (a, b), and HAADF intensity. Scale bars indicate 1 nm.

Figure 1

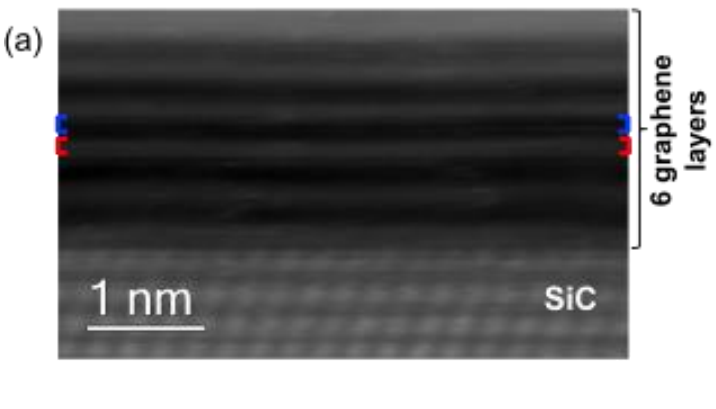

Figure 2

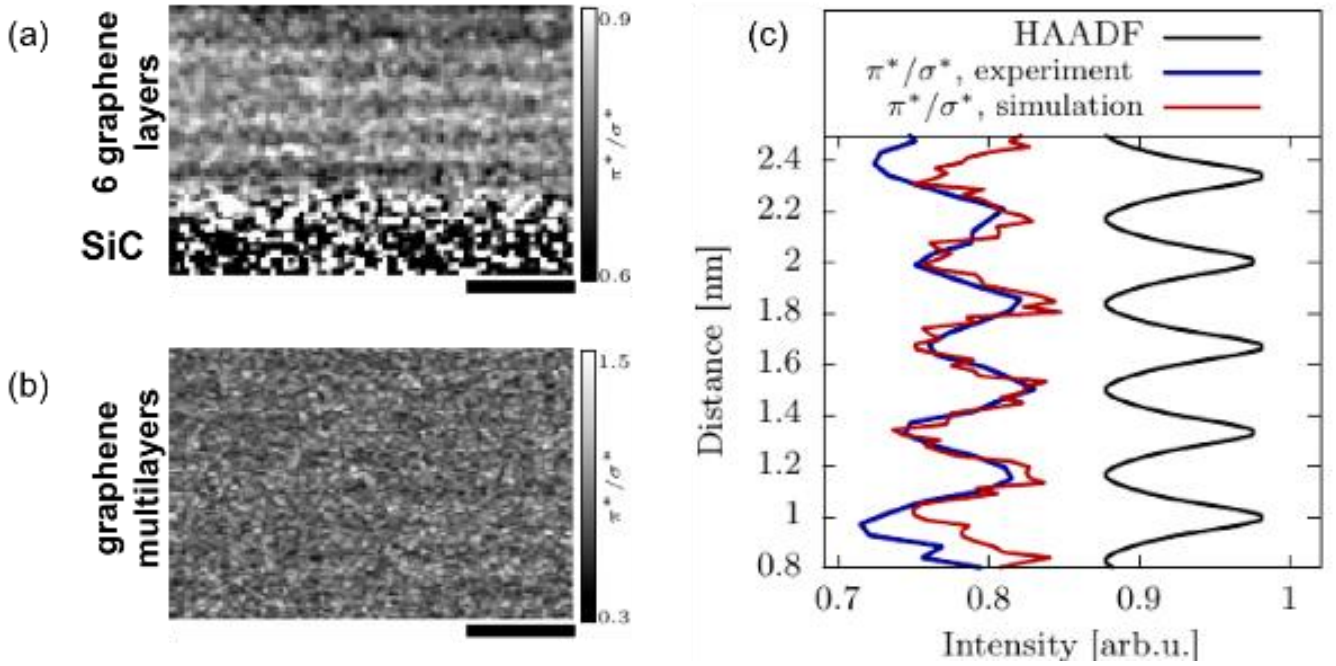

MS4.003
Comparison of electrostatic potentials recovered from energy filtered 4D-STEM via ptychography and centre-of-mass analysis

T. Pekin[1], M. Schloz[1], B. Haas[1], W. Van Den Broek[1], C. T. Koch[1]

[1]Humboldt University of Berlin, Physik, Berlin, Germany

Four dimensional scanning electron microscopy (4DSTEM) has been used to measure and map atomic potentials with high resolution and sensitivity to light elements in very thin materials [1-3], using either integrated center of mass measurements (iCOM) or ptychography.

Here we present an approach to remove the majority of inelastically scattered electrons from 4DSTEM experiments at atomic resolution and compare results obtained by iCOM and ptychography. By using the energy filter in the spectrometer on a Nion HERMES microscope operated at 60 kV, a cutoff at ~5 eV energy loss can be set, which removes the majority of electrons scattered from bulk plasmons.

Figure 1: shows a comparison between iCOM results of twisted bilayer graphene from a 4DSTEM dataset with and without energy filtering. The atomic Moiré pattern is clearly resolved in both, and there is no real improvement in the energy filtered iCOM results. In fact, that is to be expected, as only about 4% of the electrons that are scattered by the sample are removed.

Figure 2a) and **b):** show the same comparison but the atomic potentials have been recovered via ptychography, optimizing the object and probe. Figure 2c) is the central 3 nm of Figure 1c). In panels d-f), the spots corresponding to the misorientation angle between the bilayers are better resolved in the filtered data. This seems to hint at an improvement from energy filtering; a detailed comparison will be shown in person.

Following these initial results, we will show comparisons between results obtained with thick and thin samples as well, with up to 50% of the electrons removed. We expect that the results will show that energy filtration will be key to reconstructing the atomic potentials of thicker samples when larger percentages of electrons are removed.

Figure 1a): HAADF of twisted bilayer graphene corresponding to c). All scale bars are 1 nm. b) Atomic potentials as measured with iCOM, without energy filtering, and c) with energy filtering. d-f) FFTs of the images above, with a dotted circle marking 1 Å resolution. The results between b) and c), and e) and f) are roughly identical, with streaking in f) from a centering operation of the high resolution section of the image to the center before the FFT.

Figure 2a): Ptychographic reconstructions of the central 3 nm of Figure 1b, from unfiltered data, and b) of the central 3 nm of Figure 1c, from energy filtered data. c) The central 3 nm of Figure 1c, reproduced for comparison. The scale bars are 1 nm. d-f) The Fourier transforms of a), b) and c), respectively. The dotted circle marks 1 Å resolution. The reconstruction quality remains about the same, but the dumbbells (circled in green) corresponding to the misorientation of the bilayer in e) and f) are slightly higher resolved than in d).

Acknowledgements: T.C.P., M.S., and W.V.d.B. acknowledge financial support from the Deutsche Forschungs-gemeinschaft (DFG, German Research Foundation) Grant No. BR 5095/2-1.

References:
[1] Jiang, Yi, et al. "Electron ptychography of 2D materials to deep sub-ångström resolution." Nature 559.7714 (2018): 343-349.
[2] Hachtel, Jordan A., et al. "Sub-Ångstrom electric field measurements on a universal detector in a scanning transmission electron microscope." Advanced Structural and Chemical Imaging 4.1 (2018): 1-10.
[3] Schloz, Marcel, et al. "Overcoming information reduced data and experimentally uncertain parameters in ptychography with regularized optimization." Optics Express 28.19 (2020): 28306-28323.

Figure 1

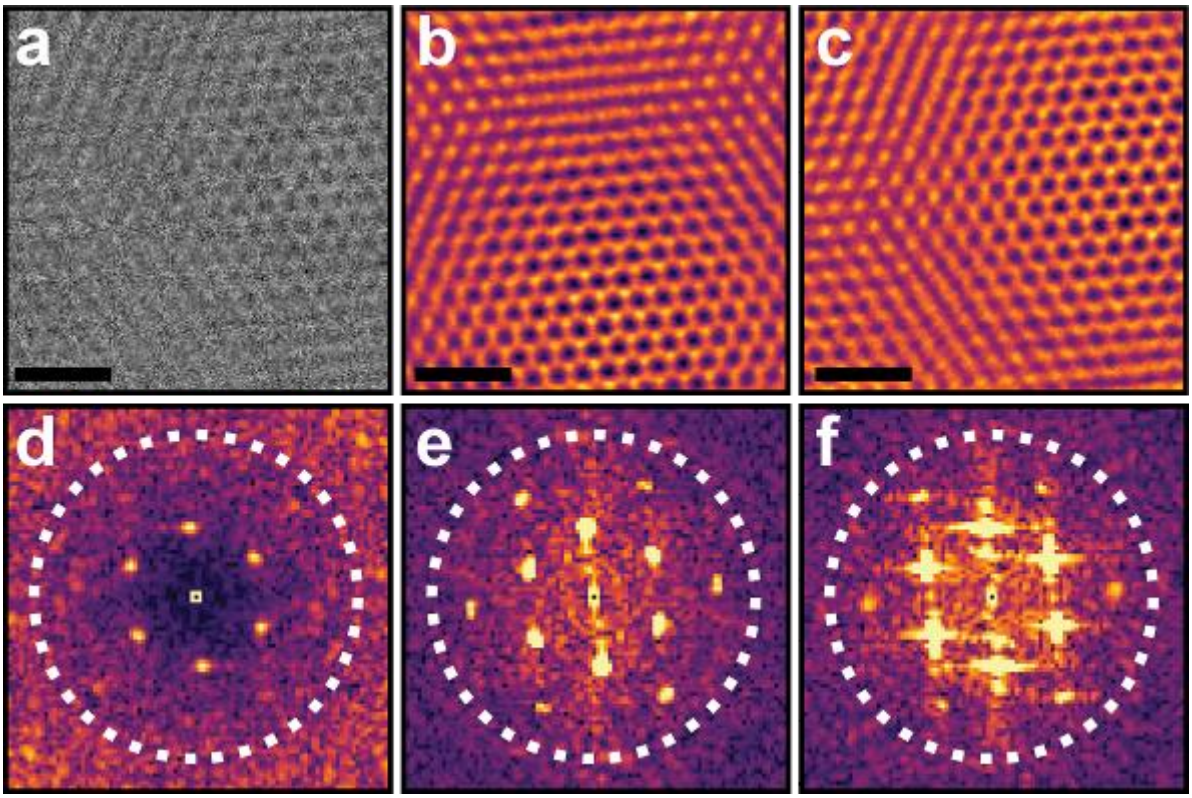

Figure 2

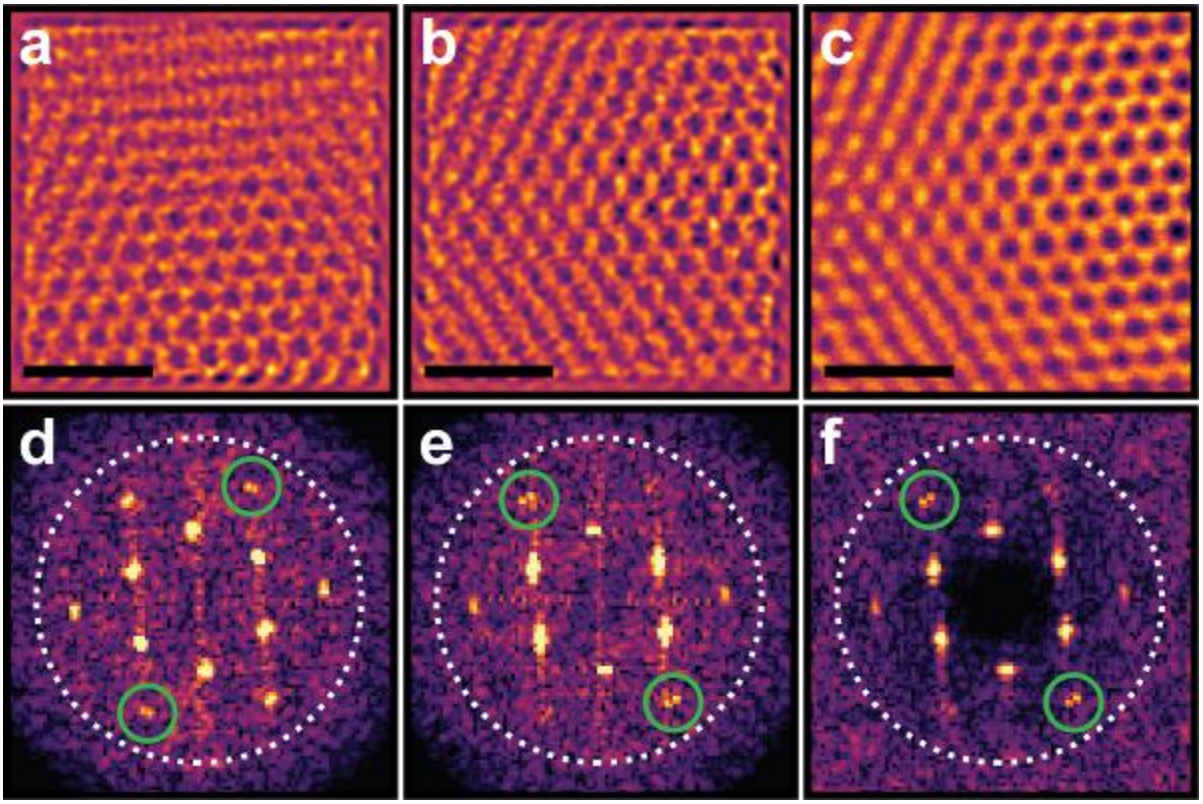

MS4.005
Ultrafast nanoimaging of the order parameter in a structural phase transition

T. Danz[1], T. Domröse[1], C. Ropers[1,2]

[1]University of Göttingen, 4th Institute of Physics – Solids and Nanostructures, Göttingen, Germany
[2]Max Planck Institute for Biophysical Chemistry, Göttingen, Germany

In this work, we demonstrate a new experimental approach enabling real-space phase imaging in a charge-density wave (CDW) model system with 5nm spatial and femtosecond temporal resolution. By means of a tailored dark-field (DF) technique, we obtain maps of the CDW order parameter in an ultrafast transmission electron microscope [1].

Ultrafast transmission electron microscopy (UTEM) is an emerging approach to study ultrafast processes in heterogeneous materials with nanometer spatial resolution using imaging, diffraction and spectroscopy contrast [2,3]. Some of the most interesting possibilities of UTEM are connected to the investigation of various kinds of structural and electronic phase transitions in correlated materials, such as the quasi-2D material 1*T*-TaS_2 [4]. Various ultrafast electron diffraction experiments have elucidated the optically induced dynamics of transitions between several CDW phases of this material [5-8].

In our experiments, a free-standing, single-crystalline 1*T*-TaS_2 thin film [9] is pumped out of the nearly commensurate CDW phase at room temperature towards the high-temperature incommensurate CDW phase using a spatially structured laser field distribution (see Figure 1A for a schematic of the experimental setup). We employ ultrafast DF imaging using a tailored DF aperture array to follow the formation, stabilization and relaxation of CDW domain patterns on their intrinsic timescales, yielding nanoscale access to the order parameter of the structural phase transition (Figure 1B).

Additionally, we obtain a precise thermal characterization of the specimen structure from a complementary steady-state heating experiment (Figure 1C). On this basis, we reproduce the most prominent features of the ultrafast experiment in a theoretical model using the time-dependent Ginzburg-Landau framework.

Taken together, our approach showcases that ultrafast DF imaging allows for intriguing insights into the interplay of order parameter dynamics and thermal transport on nanometer length and femtosecond timescales. Allowing for sensitivity to further degrees of freedom in complex materials, these results will hopefully pave the way for novel types of ultrafast investigation.

Figure 1: Dark-field imaging in the ultrafast transmission electron microscope. (**A**) Simplified schematic of the experimental setup, and scanning electron micrograph of the tailored DF aperture array. (**B**) Ultrafast electron micrographs of the specimen before and after time-zero, showing CDW domains of the room- (bright) and the high-temperature phase (dark). (**C**) Static electron micrographs of the steady-state heating experiment at two different continuous-wave laser heating intensities.

References:
[1] Th. Danz *et al.*, *Science* 371, 371-374 (2021).
[2] A. H. Zewail, *Science* 328, 187-193 (2010).
[3] A. Feist, Th. Danz *et al.*, *Ultramicroscopy* 176, 63-73 (2017).
[4] K. Rossnagel, *J. Phys. Condens. Matter* 23, 213001 (2011).
[5] M. Eichberger *et al.*, *Nature* 468, 799-802 (2010).
[6] K. Haupt *et al.*, *Phys. Rev. Lett.* 116, 016402 (2016).
[7] S. Vogelgesang *et al.*, *Nat. Phys.* 14, 184-190 (2018).
[8] A. Zong *et al.*, *Sci. Adv.* 4, eaau5501 (2018).
[9] Th. Danz *et al.*, *J. Phys. Condens. Matter* 28, 356002 (2016).

Figure 1

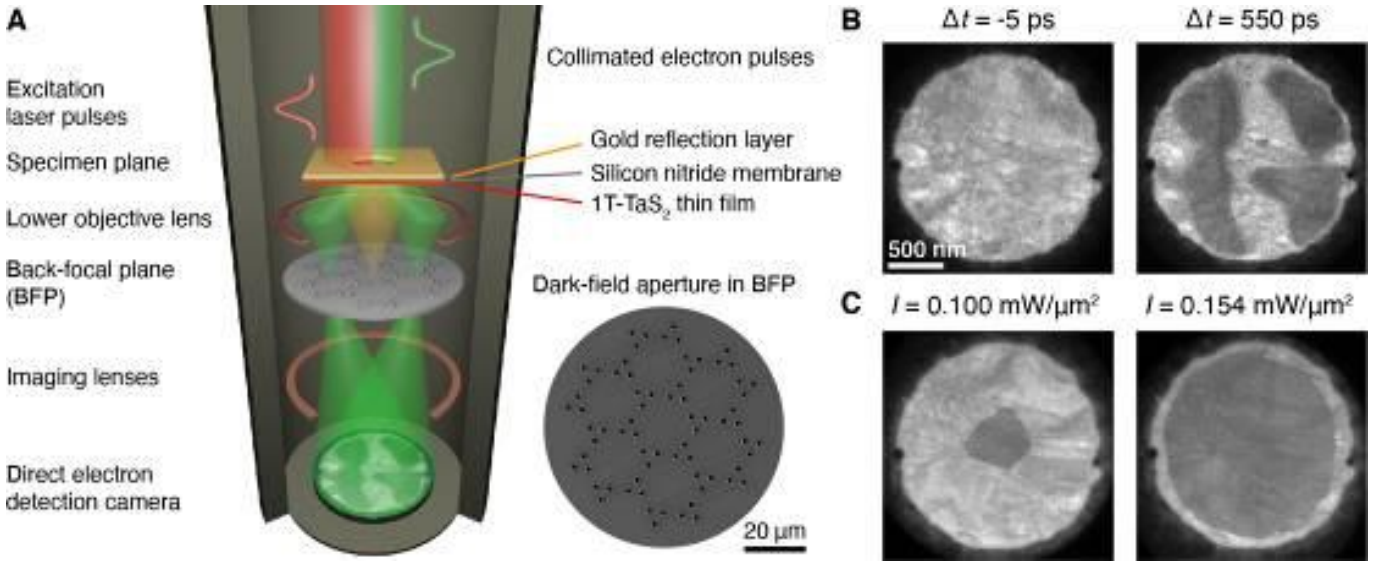
A
Excitation laser pulses
Specimen plane
Lower objective lens
Back-focal plane (BFP)
Imaging lenses
Direct electron detection camera
Collimated electron pulses
Gold reflection layer
Silicon nitride membrane
1T-TaS2 thin film
Dark-field aperture in BFP
20 µm
B
Δt = -5 ps
Δt = 550 ps
500 nm
C
I = 0.100 mW/µm²
I = 0.154 mW/µm²

MS4.006
The influence of size, shape, and defects on heat-induced alloying in individual Au@Ag core-shell nanoparticles

M. Mychinko[1], A. Skorikov[1], V. Kumar[2], W. Albrecht[1], X. Zhuo[2], A. Sánchez-Iglesias[2], L. Liz-Marzán[2], S. Bals[1]

[1]University of Antwerp, EMAT, Department of Physics, Antwerp, Belgium
[2]CIC biomaGUNE, Bionanoplasmonics laboratory, Donostia-San Sebastián, Spain

During the past decades, metal nanoparticles have attracted great attention in material sciences due to their specific optical properties based on surface plasmon resonances. Because of these phenomena, plasmonic nanoparticles are very promising for application in biosensing, medicine, solar energy conversion, etc. Currently, colloidal synthetic techniques enable scientists to routinely produce bimetallic core-shell nanoparticles of various shapes, sizes, and elemental distribution, with superior properties for plasmonic applications. However, operation in real conditions (e.g., at elevated temperatures) may cause redistribution of metals between the core and shell of the particle, which in turn gradually alter the properties of nanoplasmonics. Therefore, a thorough understanding of the influence of the size, shape, and presence of defects on the nature of such processes is crucial for the further development of nanoplasmonic-based technologies.

The recently developed combination of fast tomography based on High Angle Annular Dark Field Scanning Transmission Electron Microscopy with in situ heating holders has enabled the investigation of heat-induced processes at the single nanoparticle level with high spatial resolution in 3 dimensions (3D). Using this approach, we evaluated the influence of various parameters (size, shape, defect structure) on heat-induced elemental redistribution in Au@Ag core-shell nanoparticles qualitatively and quantitatively.

More specifically, the elemental redistribution at high temperature in single-crystalline (SC) Au@Ag nanocubes with similar size and composition, but with different shapes of the core (octahedra and sphere), was shown to be uniform along all directions (Figure 1c-d, upper rows). By performing 3D simulation of diffusion based on Fick"s law, similar diffusion constants were found (Figure 1a-b and Figure 1c-d, lower rows). Moreover, our investigation indicated significantly faster alloying kinetics for pentatwinned Au@Ag nanorods in comparison to single-crystalline nanorods of comparable sizes and composition. This may be related to the presence of twinning planes, which cause the formation of distortions and vacant sites in the crystal lattice, facilitating diffusion of atoms. Finally, the influence of the core shape was demonstrated to be negligible in the case of two pentatwinned nanorods with different Au cores (rod and bipyramid).

In conclusion, using our fast tomography approach we gained a fundamental insight into the nature of elemental diffusion at high temperature and its dependence on various factors, e.g., size, shape, and presence of twinning defects. We believe, that detailed knowledge of thermal stability of bimetallic nanoplasmonic materials will drastically improve the application of these materials in the future.

The project has received funding from European Research Council (ERC Consolidator Grant 815128, REALNANO) and European Commission (grant 731019, EUSMI).

Figure 1: (a) – (b) Comparison of the alloying progress of SC-nanocubes (with octahedral and spherical core, respectively) to diffusion simulations performed for different diffusion coefficients. (c) – (d) The upper rows show slices through the experimentally determined 3D elemental distribution at different stages of alloying of SC-nanocubes (with octahedral and spherical core, respectively). The lower rows display slices through the simulated 3D elemental distribution using the optimal diffusion coefficient.

Figure 1

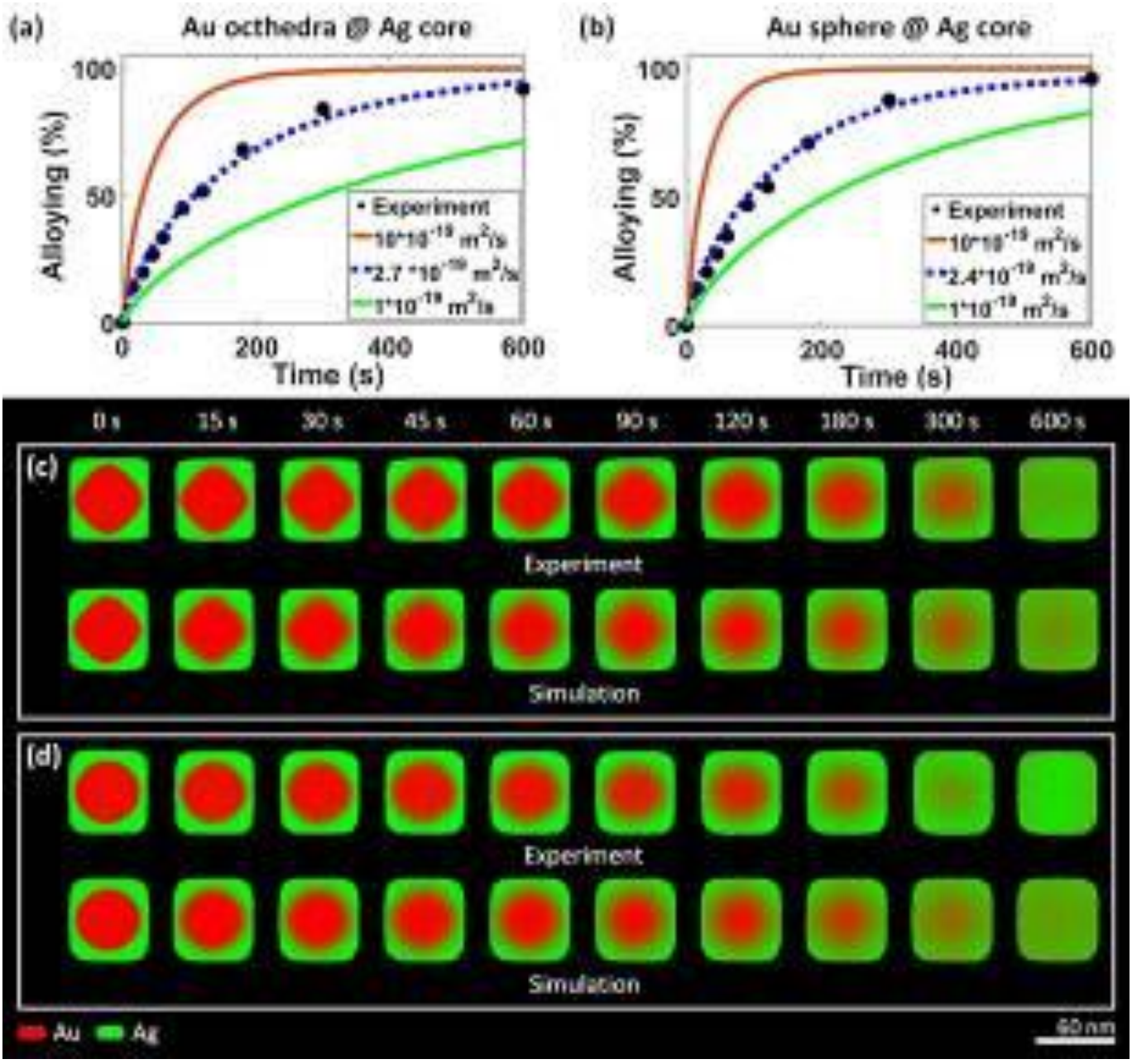

MS4.P001
Atomic-scale analysis on polymer-chain structures using scanning transmission electron microscopy

T. Miyata[1], R. Goseki[2], T. Ishizone[2], H. Jinnai[1]

[1]Tohoku University, Institute of Multidisciplinary Research for Advanced Materials, Sendai, Japan
[2]Tokyo Institute of Technology, Tokyo, Japan

Polymeric materials' properties originate from the primary structures (chemical structures and configuration), secondary structures (conformation), and higher-order structures, e.g., polymer crystals and self-assembled phase-separated structures. Although these hierarchical structures have been intensively studied with various approaches, including scattering, microscopy, spectroscopy, etc., atomic-scale observations of molecular configurations and conformations have rarely been performed. Thus, up to now, little is known about primary structures inside polymeric materials.

Transmission electron microscopy (TEM) is an atomic-resolution observation tool for the internal structures of materials. Although TEM being powerful, high-resolution TEM observation of polymer chains is still challenging because polymers are naturally low contrast for electrons. Annular dark-field scanning transmission electron microscopy (ADF-STEM), however, allows us to selectively observe the positions of heavy elements, which has been applied for direct observation of gold atoms inside organic materials [1]. In the present study, polymer chains labeled with heavy atoms are prepared, the positions of which are visualized by atomic resolution ADF-STEM. Furthermore, by analyzing the relative positions of bright spots observed in the ADF-STEM image, the local conformations and conformations of polymer chains are identified.

A labeled polymer, poly (4-iodostyrene) was synthesized by anionic polymerization of 4-iodostyrene (molecular weight Mn: 4,700) [2]. Because the atomic number of iodine (Z = 53) is much larger than those of the other constituent elements (H, C), the iodine atoms are imaged much brighter with ADF-STEM. Multilayer graphene was used for the substrate to reduce electron beam damage to the sample. Poly(4-iodostyrene) was cast from 1 wt% toluene solution and dispersed on the graphene, subjected to the ADF-STEM observations. An atomic-resolution scanning transmission electron microscope JEM-ARM200F (JEOL Ltd.) operated at 200 kV was used for the observation.

Figure 1 shows an ADF-STEM image of the poly(4-iodostyrene) sample dispersed on graphene. Many bright spots were observed in this image. The measured sizes of the bright spots were 0.08 ± 0.01 nm. In principle, a single atom is observed at the size of the electron beam in ADF-STEM images. Because the full width at half maximum of the electron beam used in this observation (0.08 nm) matches the sizes of the bright spots, the bright spots can be regarded as single atoms. Furthermore, an absorption edge of iodine (I-M4,5 edge) was detected by electron energy loss spectroscopy at the positions of bright spots. Therefore, we concluded these bright spots to be single iodine atoms.

Moreover, it was found that iodine atoms are arranged in chains, as shown by the blue lines in Figure 1. Because the distribution of the iodine atoms reflects the local structures (configurations and conformations) of polymer chains, by analyzing the arrangements of the bright spots in the ADF-STEM image, local configurations and conformations of poly(4-iodostyrene) were identified in three dimensions.

[1] T. Miyata, F. Uesugi, T. Mizoguchi, Science Advances 3, e1701546 (2017).
[2] R. Goseki, T. Koizumi, R. Kurakake, S. Uchida, T. Ishizone, Macromolecules 54, 1489 (2021).

Figure 1: ADF-STEM image of the poly(4-iodostyrene) sample. Bright spots are arranged in chains.

Figure 1

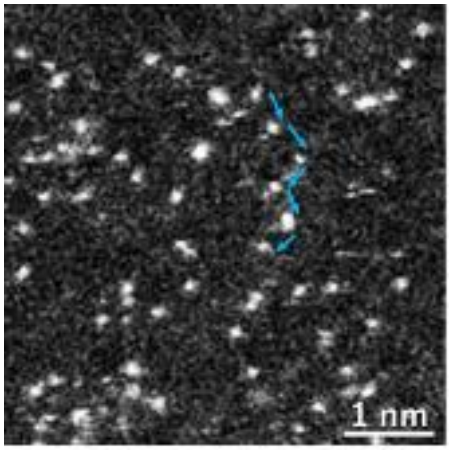

MS4.P002
Observation of chemical-vapor-transport-based processes utilising µReactor

L. Novák[1], K. Bukvišová[2], Z. J. Wang[3], V. Mahel[1,2], M. G. Willinger[3], T. Šikola[2], M. Kolíbal[2]

[1]Thermo Fisher Scientific, Brno, Czech Republic
[2]Brno University of Technology, Brno, Czech Republic
[3]ETH Zurich, ScopeM, Zurich, Switzerland

The real-time in-situ SEM imaging enables quantitative assessment of the mechanisms involved in the growth of 1D and 2D materials. In order to image nanoscale processes at high resolution in SEM, we have designed a µReactor device [1], which allows for safe injection of reactive gases into a small differentially pumped volume (7 µl) surrounding the processed sample (Figure 1). Sample heating is assured by a micro-heating plate [2].

As the first proof-of-concept experiment, we will show an oxidation reaction of tungsten disulfide nanotubes and platelets in a water vapor (up to 10 Pa) at elevated temperature (450-600°C). The oxidation process results in formation of tungsten oxide nanowires (Figure 2a) and continues until the whole nanotube gets consumed. The real-time imaging allows to track the kinetics of the process and together with additional characterization techniques allows to quantitatively describe the oxidation mechanism [3].

In the second example (Figure 2b) [4], the well-controlled conditions inside the µReactor (ethylene-hydrogen environment; sample temperature 900°C) was used to sustain chemical vapor deposition resulting in a controlled growth of graphene monolayers on platinum substrate [5] [6]. We will present our latest results on other material systems as well.

References:
[1] *Microsc. Microanal.* 2020 *26*(S2) 1144-1145, doi:10.1017/S1431927620017092
[2] *Microsc. Res. Tech.* 2016, 79, 4, 239-250
[3] *J. Phys. Chem. C* 2019, 123, 14, 9552-9559
[4] https://www.youtube.com/watch?v=GmIfGMcTsn0&list=PLhJ74CQiOr7bGhmkU2zOKMP-XXOhnLhOB
[5] *Nat Commun* 2016, 7, 13256
[6] *ACS Nano* 2020, 14 (2), 1902-1918

Figure 1: µReactor with a micro-heating plate (a). When µReactor is open (b), sample made from bulk by FIB can be placed on the heating plate using manipulator needle (c). Reaction volume is then closed by a retractable lid (d). Aperture in the lid (blue) assures overpressure up to 1 kPa in sample area, while the SEM chamber remains in high vacuum. Standard SEM detectors (including in-lens) can be used for high resolution SEM imaging of the heat & gas stimulated process (e).

Figure 2: a) A series of SEM micrographs showing a WS2 nanotube (time span between images: 3 minutes) oxidized in 10 Pa water vapour at temperatures 500-570°C. The experiment allowed for direct analysis of temperature-dependent reaction kinetics. Scale bar length is 100 nm. b) Graphene growth on platinum substrate imaged in-situ in the µReactor using TLD-SE detector in UHR mode of Helios FIB-SEM. Formation of graphene on a platinum surface, which was first cleaned in pure hydrogen at 900°C in the µReactor, was stimulated by sample temperature of 900°C and by hydrogen-ethylene environment (5 Pa C_2H_4 and 30 Pa H_2). Image sequence was acquired over 45 seconds. Scale bar length is 10 µm.

Figure 1

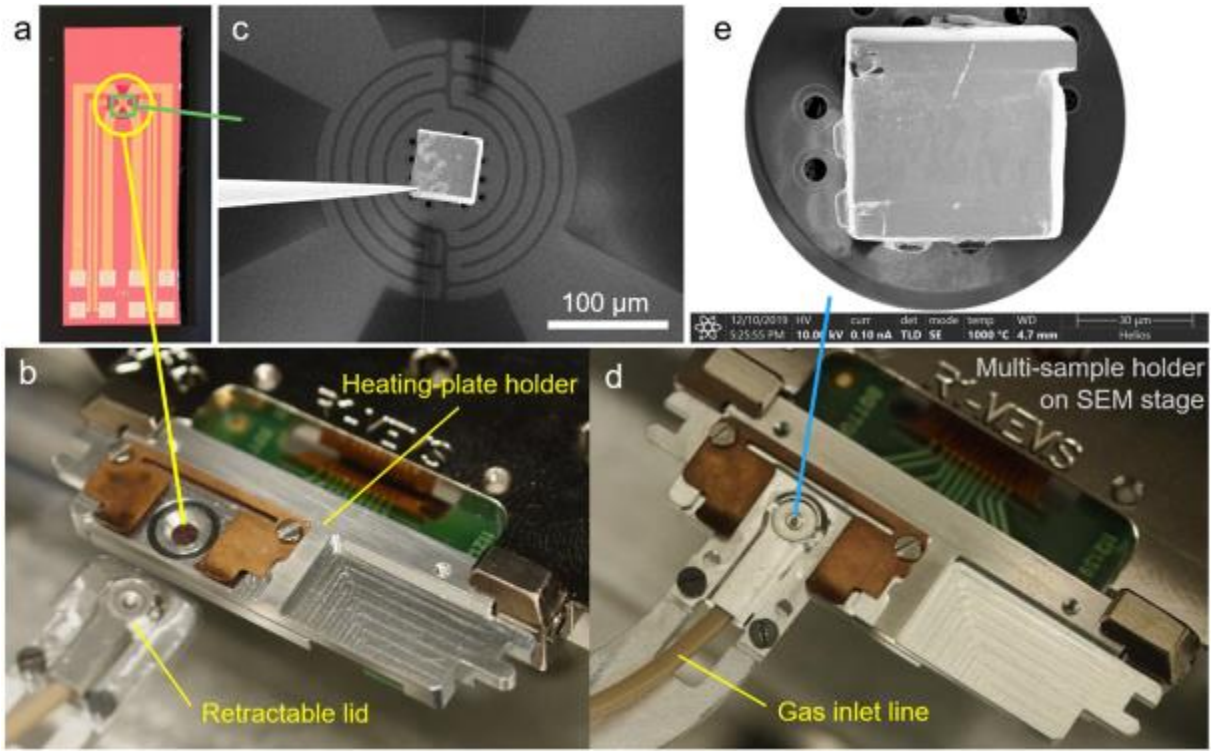

Figure 2

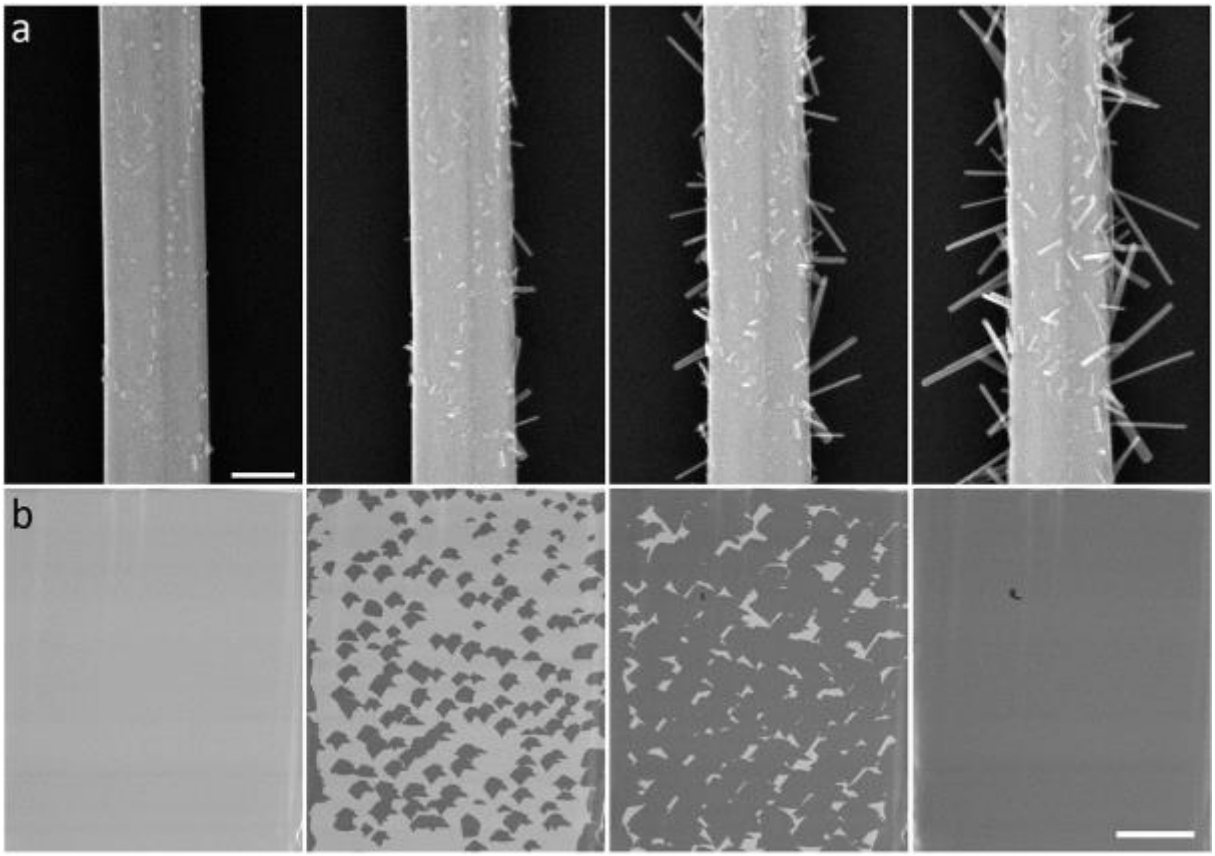

MS4.P003
Real time observation of vapor transport reactions in the scanning electron microscope

K. Bukvišová[1,2], L. Novák[2], A. Rothman[3], L. Kachtik[1], E. Joselevich[3], T. Šikola[1,4], M. Kolíbal[1,4]

[1]CEITEC BUT , Brno, Czech Republic
[2]Thermo Fisher Scientific, Brno, Czech Republic
[3]Weizmann Institute of Science, Rehovot, Israel
[4]Brno University of Technology, IPE, Brno, Czech Republic

Chemical vapor synthesis techniques are commonly used to synthesize a wide range of nanomaterials, especially 2D layers (graphene, perovskites, transition metal dichalcogenides), nanowires or bilayer crystals. However, ex-situ observation of the reaction products is not sufficient to truly understand the growth processes in detail which sometimes results in the difficulty to produce high quality nanomaterials. In our work, we present a methodology for real time SEM imaging of CVD reactions.

A simplified schematic showing the principle of the SEM reactor we have prototyped is in Figure 1. A carefully calibrated heater allows to vaporize precursor powder, which is carried by a carrier gas towards an independent substrate heater. The lid with an aperture for SEM imaging partly prevents contamination of the SEM chamber and protects the electron optics from heat as well.

As the first precursor chemistry, we have chosen zinc selenide (ZnSe), a semiconductor with a direct bandgap (2.7 eV) in visible range, which is interesting for applications in blue–UV photodetectors [1]. Guided growth of aligned in-plane nanowires catalyzed by gold nanoparticles has been reported on faceted sapphire in a two-zone tube furnace system [2], including modeling-based extraction of kinetic coefficients from the ex-situ data [3]. Our approach allows to observe the nanowire growth in-situ, and thus the experiments offer complementary data to create a more complete picture of the reaction mechanism. Figure 2 shows a part of the SEM sequence that has confirmed the nucleation times being independent on the catalyst's size. Our latest results on different material systems will be present as well.

[1] *Nanotechnology*, *17*(22), 5561-5564,
[2] *Advanced Materials*, *27*(27), 3999-4005,
[3] *Proceedings of the National Academy of Sciences of the United States of America*, 117(1), 152-160.

Figure 1: A schematic of the SEM-compatible CVD reactor. A carrier gas flows through an inlet (A) and carries precursor which is vaporized by the first heater (B). The vapor then condenses on a substrate kept at a different, lower temperature by the second heater (C). Bias can be applied to the sample to improve the secondary electrons signal. The protective lid has an aperture (E) for observation above the substrate and an outlet (D). The heaters allow to reach temperatures up to around 1000 °C.

Figure 2: Real-time SEM sequence showing growth of ZnSe nanowires catalyzed by drop-casted colloidal gold of average diameter 80 nm. The carrier gas was pure hydrogen (pressure $1.1 \cdot 10^{-2}$ Pa), precursor ZnSe powder was held at 990 °C and substrate, annealed R-plane sapphire, at 640 °C. Scale bar is 2 µm.

Figure 1

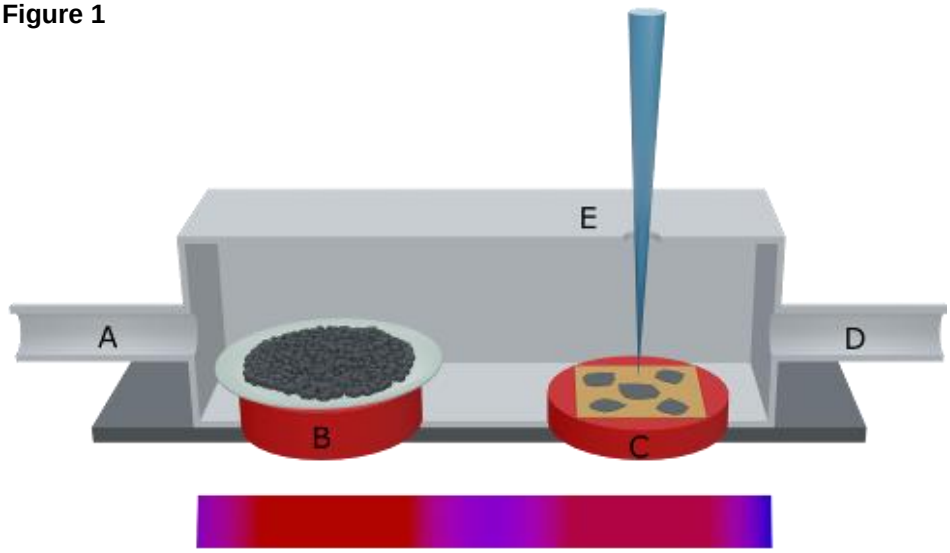

Figure 2

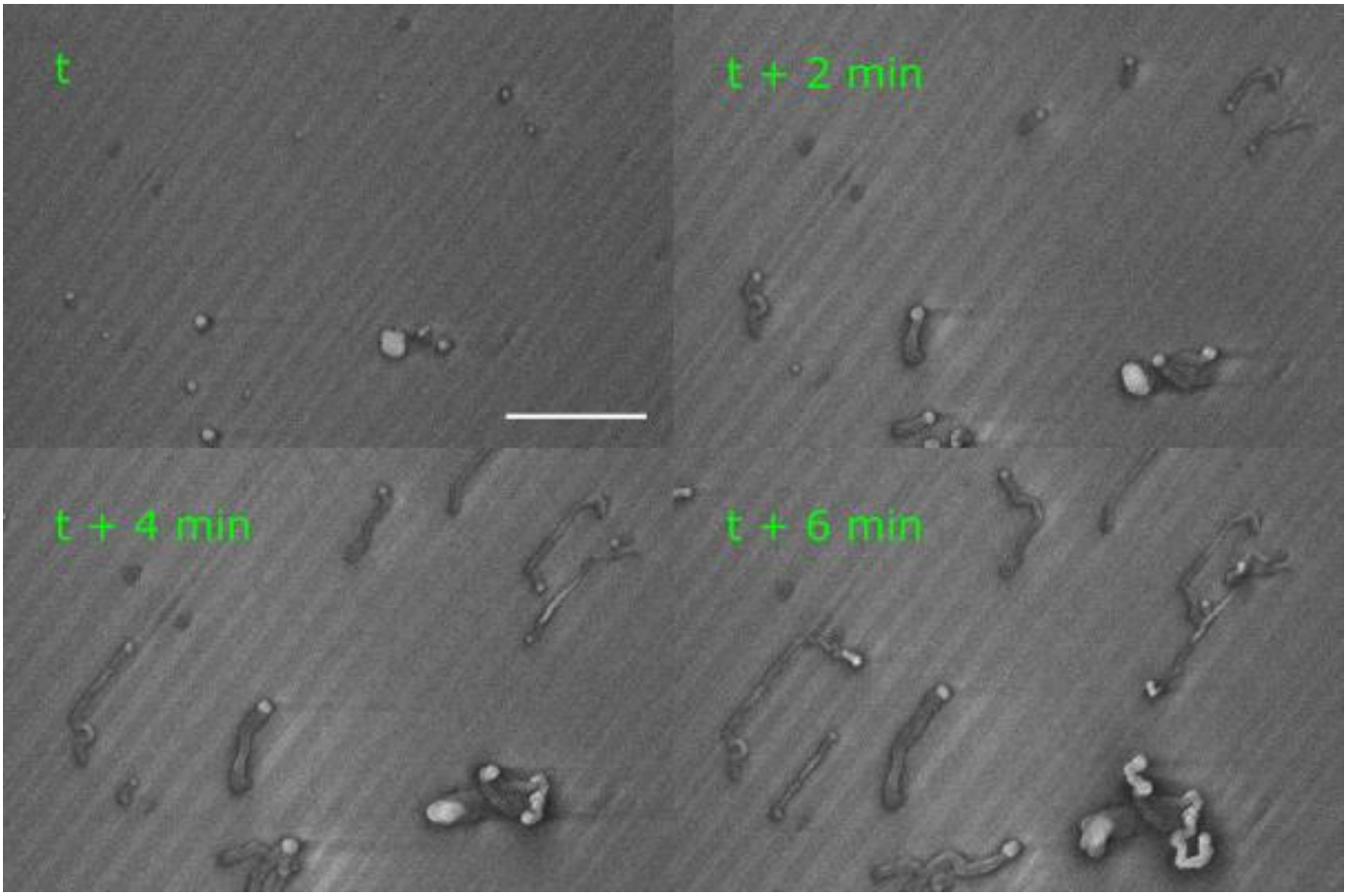

MS4.P004
Structural and chemical modifications of transition metal phosphorus trichalcogenides caused by electron beam irradiation

A. Storm[1], J. Köster[1], M. Asl-Gohrbani[2], S. Kretschmer[2], T. E. Gorelik[1], A. V. Krasheninnikov[2,3], U. Kaiser[1]

[1]University of Ulm, Electron Microscopy Group of Materials Science, Ulm, Germany
[2]Helmholtz-Zentrum Dresden-Rossendorf e.V. (HZDR), Institute of Ion Beam Physics and Materials Research, Dresden, Germany
[3]Aalto University, Department of Applied Physics, Aalto, Finland

Transition metal phosphorus trichalcogenides (TMPTs) are two-dimensional layered structures, which exhibit intriguing inherent properties as magnetic ordering down to a thickness of a single-layer as well as bandgaps in the 1.3 eV-3.5 eV range [1]. This makes them an ideal candidate for studying magnetism on a two-dimensional scale, and interesting candidates for device applications [2]. Yet, atomically resolved analysis of freestanding (without substrate) few-layer samples is difficult, and rarely reported due to susceptibility to oxidation for these materials [3].

In this study, we analyze structural and chemical modifications of three different freestanding TMPTs, namely $FePS_3$, $MnPS_3$, and $NiPS_3$, caused by electron irradiation in the transmission electron microscope (TEM). We predict the displacement thresholds, electronic properties, and the displacement cross-sections of single S and P vacancies in all materials by ab-initio calculations. In addition, we combine results obtained from spectroscopic, atomically resolved, and diffraction experiments to evaluate the modifications caused by electron irradiation at different stages of sample degradation.

All TEM samples were prepared with the help of our new polymer-assisted sample preparation method [3], which enables good TEM sample quality and strongly reduce oxidation in comparison to the commonly used KOH-based preparation technique. Energy dispersive X-ray spectroscopy (EDX) measurements were performed at a Talos F200X G2 STEM at (80 kV). 3D electron diffraction (ED), electron energy loss spectroscopy (EELS), and aberration corrected high resolution transmission electron microscopy (AC-HRTEM) experiments were conducted at the Cc/Cs-corrected Sub-Ångström Low Voltage Electron Microscope (SALVE) at 30 - 80 kV. The electronic properties and the displacement thresholds were predicted by DFT calculations, and subsequently the damage cross-sections were determined in the McKinley-Feshbach formalism for the static, as well as the dynamic case, which includes lattice vibrations [4].

Our theoretical calculations predict for all three TMPTs a higher damage cross section for S than P, which should allow a selective removal of S due to elastic damage at 80 kV. EDX and EELS experiments verify the removal of mainly S atoms due to interaction with the electron beam (80 kV) and show a valence change of the transition metal from 2+ to 3+ with progressing degradation of the sample. For $MnPS_3$, the growth of a new phase can be observed due to the removal of S and P atoms in the pristine material, which is shown in Figure 1 (a). With the help of 3D-ED and AC-HRTEM the new phase is identified as cubic MnP_xS_{1-x} (b). We show that the growth of the area of the new phase is linear with the total applied dose. Thus, we report on the understanding of a path to grow a new phase in a few-layer magnetic host material by electron irradiation.

Figure 1: HRTEM 80 kV image of an irradiated few-layer $MnPS_3$ sample. The growth of a new phase in the host material is observed (a). The new phase is identified as a cubic MnP_xS_{1-x} phase, and the growth direction in the host material is the [111] direction as presented in (b). A structural overlay of the new phase is given in (a).

[1] A. Hashemi et al. (2017). J. Phys. Chem. C 121, 27207
[2] X. Zhang et al. (2016). Adv. Sci. 3, 1600062
[3] J. Köster et al. (2021). Nanotechnology 32, 075704
[4] T. Susi et al. (2019). Nat. Rev. Phys. 1, 397-405

Figure 1

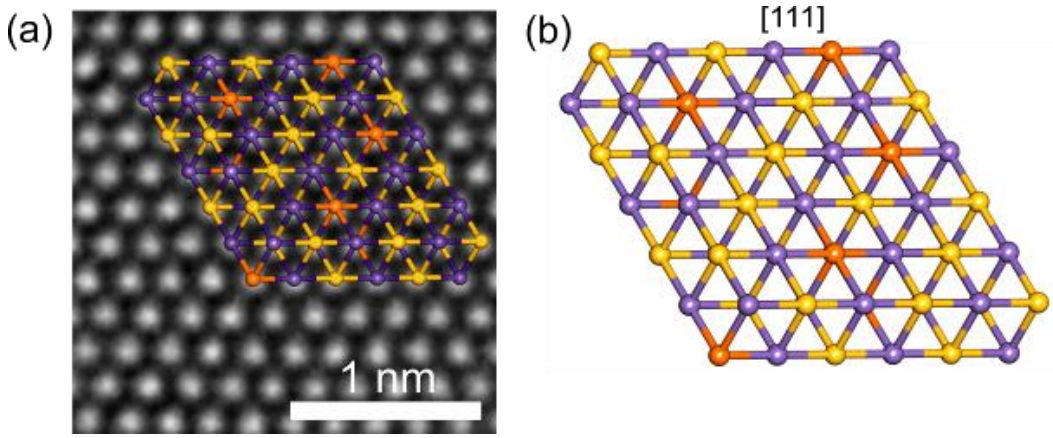

MS4.P005
3D electron diffraction of mono- and few-layer MoS_2

T. E. Gorelik[1], J. Köster[1], B. Nergis[2], U. Kaiser[1]

[1]University of Ulm, Ulm, Germany
[2]Karlsruhe Institute of Technology (KIT), Institute for Photon Science and Synchrotron Radiation, Eggenstein-Leopoldshafen, Germany

A variety of unprecedented physical properties originating from quantum confinement and surface effects were demonstrated for 2D crystalline materials [1, 2]. As an example, some bulk semiconducting transition metal di-chalcogenides (TMDs) with the trigonal prismatic metal coordination have an indirect band gap, while their corresponding monolayers show direct electronic and optical band gaps with enhanced photoluminescence at visible frequencies [3, 4], making them emerging materials for nanoelectronics based on photovoltaic and photoemission.

The dependence of properties on the number of layers in a crystal made the number of layers an important structural parameter. There are different ways to determine the number of layers experimentally, – optical contrast [5], EELS measurements, quantification of high-resolution images. Each of the methods has its own strengths and limitations. Here, we demonstrate the unambiguous determination of the number of layers in few-layer 2H MoS2 from 3D electron diffraction (3D ED) data.

A monolayer of 2H MoS2 has a mirror plane passing through the middle of the layer, as a result the layer group of the crystal is *pm2*, the symmetry of a bilayer is reduced due to the mutual layer shift down to the layer group *pm1*. With the increase in the number of layers the situation repeats, so that a structure with an odd number of layers has a higher symmetry - *pm2*, structures with an even number of layers - *pm1*. These different symmetries are clearly reflected in the symmetry of the reciprocal space. Additionally, with an increase in the number of layers, the widths of the peaks along the relrods decrease. The combination of symmetry with the width of the peaks allowed a clear discrimination between 2H MoS2 crystals containing 1, 2, 3, 4 and 5 individual layers. This method is general and can be used to assign unambiguously the number of layers for all 2H-TMDs.

[1] Xia et al., 2014. Nature Photonics. 8, 899.
[2] Nerl et al., 2017. npj 2D Materials and Applications 1, 2.
[3] Mak et al., 2010. PRL 105, 136805.
[4] Ugeda et al., 2014. Nature Materials, 13, 1091.
[5] Li et al., 2013. ACS Nano, 7, 11, 10344.

MS4.P006
Aberration-corrected TEM investigation and low-loss EELS of twisted TMD bilayers

R. Leiter[1], M. Federolf[1], T. E. Gorelik[1], M. J. Mohn[1], U. Kaiser[1]

[1]University of Ulm, Electron Microscopy Group of Materials Science, Ulm, Germany

Since the discovery of superconductivity in twisted bilayer graphene at a so-called magic angle [1], there has been an increasing interest in twisted bilayers of two-dimensional materials. Various interesting electronic and optical phenomena have been shown or predicted for these materials [2], and the pronounced moiré patterns occurring at certain twist angles [3,4] have led to the materials also being referred to as "moiré materials".

Here we investigate this moiré formation in twisted bilayers of graphene and two-dimensional transition metal dichalcogenides (TMDs) by means of theoretical predictions and TEM experiments. Firstly, by geometrical considerations, we identify potentially interesting twist angles with respect to their commensurable or incommensurable quasicrystal superstructures. As there are clear indications that the layers may partially relax in the lateral dimensions in order to obtain a lower energetic landscape [4,5], we also aim to describe the effects of relaxation in the layers. Secondly, we compare our theoretical predictions to high-resolution TEM experiments in the Cc/Cs-corrected SALVE low-voltage microscope. Lastly, we complement our structural characterization by low-loss electron energy-loss spectroscopy (EELS) experiments, in order to clarify if changes in the electronic structure and optical properties can be observed for varying twist angles.

The samples for our TEM investigations were prepared using mechanical exfoliation of graphene, MoS_2 and WSe_2 as a first step. Different twist angles were then introduced by a PMMA-based stamping technique, and subsequent transfer of the monolayers onto a holey carbon TEM grid. With the samples produced in this way, we were able to investigate various freestanding twisted bilayers in high-resolution TEM, electron diffraction and EELS. In order to reduce electron-beam-induced damage to the delicate samples, all of our TEM experiments were performed at a low acceleration voltage of 80 kV.

For the evaluation of our high-resolution TEM data, Fourier filtering was used to separate the signals from the two monolayers. Atom positions were then automatically detected in the filtered images by applying a maximum filter. From the comparison of simulated and experimental images reveals we determine whether twist-induced inhomogeneous stacking results in localized strain in the layers.

Figure 1: a) Simulated HRTEM image of a 15.1° twisted WSe_2 bilayer. Inset shows the atomic model overlaid with the atom positions from the top (red) and bottom layer (blue). b) shows the experimental Cc- and Cs corrected 80kV HRTEM image which is in good agreement with the calculated image. Scale Bar is 1nm. c) shows a corresponding low-loss EEL spectrum with background subtraction. A and B excitons are marked.

References:
[1] Cao *et al. Nature* 556 (2018)**,** 43–50
[2] Tran et al. Nature 567 (2019), 71–75
[3] Shallcross et al. Phys. Rev. B 81 (2010), 165105
[4] Campos-Delgado et al. Small 9 (2013), 3247-3251
[5] van Wijk *et al. 2D Mater.* 2 (2015), 034010
[6] Zhang and Tadmor *J Mech Phys Solids* 112 (2018), 225-238.

Figure 1

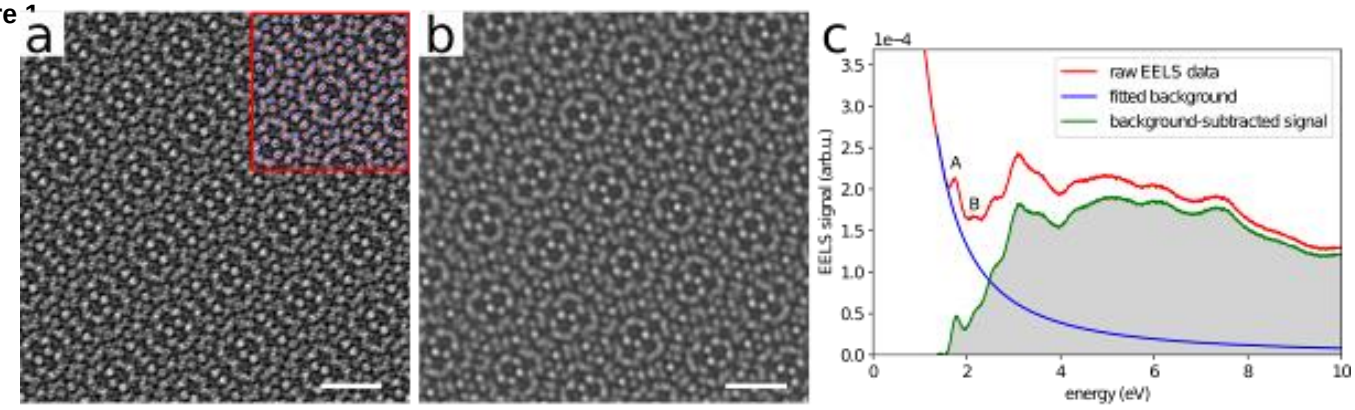

MS4.P007
Aberration-corrected STEM analysis of monolayer-thin InGaN/GaN quantum wells

I. G. Vasileiadis[1], A. Gkotinakos[1], V. Devulapalli[2], L. Lymperakis[2], C. H. Liebscher[2], E. Dimakis[3], A. Adikimenakis[4] A. Georgakilas[4,5], T. Karakostas[1], P. Komninou[1], G. P. Dimitrakopulos[1]

[1]Aristotle University of Thessaloniki, Department of Physics, Thessaloniki, Greece
[2]Max Planck Institute for Iron Research, Düsseldorf , Düsseldorf, Germany
[3]Institute of Ion Beam Physics & Materials Research, Helmholtz-Zentrum Dresden-Rossendorf, Dresden, Germany
[4]Microelectronics Research Group (MRG), IESL, FORTH, Heraklion, Greece
[5]University of Crete, Department of Physics, Heraklion, Greece

Short period superlattices (SPSs) of ultra-thin InGaN/GaN quantum wells (QWs) have concentrated significant interest for advanced optoelectronics and topological insulator applications. The QW thickness in such SPSs ranges between 1 and 2 atomic monolayers (MLs) and the direct determination of their composition poses a significant challenge. We present a methodological approach for extracting quantitative information from high resolution scanning transmission electron microscopy (HRSTEM) observations, by combining strain analysis with Z-contrast image simulations using reference models obtained by empirical potential and density functional theory calculations**.**

The properties of InGaN/GaN SPSs are sensitively dependent on unconventional growth conditions aiming for a high indium composition with concurrent pseudomoprhic growth, despite the large misfit. By controlling the indium and strain content, it can be possible to perform bandgap engineering for efficient optoelectronic devices, and to achieve topological insulator properties. Quantitative HRSTEM analysis of the ultra-thin QWs offers a direct way to obtain such critical information.[1]

InGaN/GaN SPSs grown by plasma-assisted molecular beam epitaxy on *c*-plane GaN templates were studied. QWs with thicknesses of 1 and 2 MLs were deposited under various growth conditions covering a wide range of growth temperatures. HRTEM and aberration-corrected HRSTEM observations were performed in order to systematically investigate the correlation between structural quality, strain state and composition in the heterostructures.

Quantitative Z-contrast and strain analysis was performed on high-angle annular dark field HRSTEM observations along the <-1-120> zone axis. A peak finding algorithm using 2D Gaussians was implemented in order to determine atomic column positions on HRSTEM images. The peak positions were then used for nanoscale strain mapping and for measuring atomic column intensities by delimiting Voronoi cells. Energetic calculations were performed to determine theoretically the strain behavior of the QWs. Energetically relaxed supercells of QWs were calculated considering both ordered and random InGaN alloy configurations, and composition dependent strain graphs were obtained. The relaxed supercells were used as input for extensive multislice image simulations of the Z-contrast under the frozen lattice approach. Graphs of InGaN/GaN column intensity ratios with respect to foil thickness were thus constructed in order to correlate the QW composition to the average column intensity.

The average composition of the QWs was determined directly by quantification of the Z-contrast as well as by comparing experimental strain measurements to the predicted values from energetical calculations. The combination of accurate quantification of elastic strain and column intensities in the heterostructure is critical for the determination of the composition in ultra-thin QWs, since the strain behavior of 1 ML QWs deviates from the prediction of anisotropic elasticity.

Figure 1: (a) Experimental HRSTEM image of a 1 ML InGaN QW (arrows). (b) Schematic illustration of the atomic model of an ordered 1 ML $In_{0.33}Ga_{0.67}N$/GaN QW heterostructure.

[1]G. P. Dimitrakopulos, et al., J. Appl. Phys. 123, 024304 (2018)
Supported by the IKY project "Strengthening Human Resources Research Potential via Doctorate Research" and the project "INNOVATION-EL" (MIS 5002772).

Figure 1

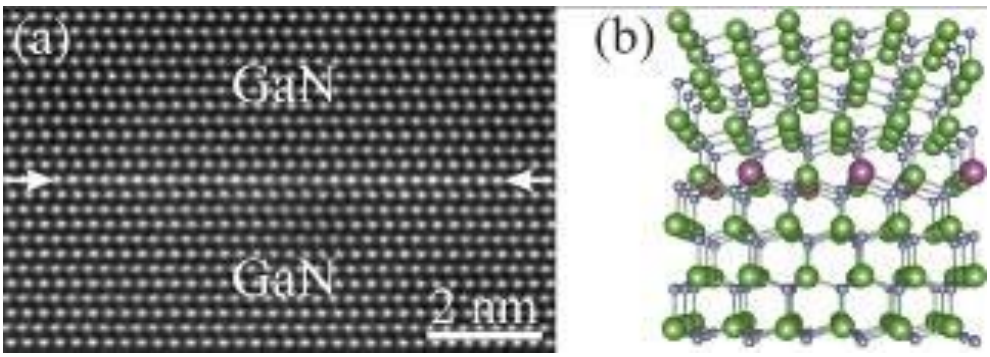

MS4.P008
Off-axis electron holography on 2D materials with small coherent and incoherent aberrations

A. Lubk[1], R. Imlau[2], S. Subakti[1], F. Kern[1], M. Linck[3], D. Wolf[1]

[1]IFW Dresden, Dresden, Germany
[2]Thermo Fisher Scientific, Einhoven, Netherlands
[3]CEOS GmbH, Heidelberg, Germany

The reduced dimensionality in two-dimensional materials (2DMs) leads to a wealth of unusual properties, which are currently explored for both fundamental and applied sciences. In order to study the crystal structure, edge states, the formation of defects and grain boundaries, high-resolution microscopy techniques, such as Transmission Electron Microscopy, adapted to the specifics of 2DMs (weak scatterer, radiation sensitivity), are indispensable.

Most 2DMs behave as weak phase objects (WPOs) in the TEM, i.e., they only slightly modulate the phase of the electron wave transmitting the sample. Therefore, conventional TEM (CTEM) and high resolution TEM (HRTEM) typically employ large defoci to generate sufficient phase contrast, which, however, has an unavoidable large transfer gap for low spatial frequencies (Figure 1) that can impede the quantitative evaluation of the recorded data (e.g., in terms of large-scale morphology changes).

Off-axis holography in principle resolves that problem by a reconstruction of amplitude and phase of the electron wave with a gap-free contrast transfer [1]. Reconstructing the whole wave also facilitates the *a posteriori* correction of residual aberrations [1] and a quantitative analysis of the electrostatic potentials with sub-nm resolution. Widespread exploitation of these advantages currently depends on a robust *a posteriori* aberration correction and high SNR of reconstructed phases, where the latter depends on brightness, aberrations and detector MTF and DQE.

Here, we tackle these critical points by combining electron holography with high-brightness cold field emission electron sources, spherical and chromatic aberration correction, low-noise CMOS detectors, and automatic a-posteriori residual aberration correction exploiting the WPO property and other Fourier space symmetries [2]. We use the technique to reconstruct potentials in multilayered hexagonal Boron Nitride (Figure 2), Graphene and several Dichalgogenides, such as WSe2. We reconstruct the average electrostatic potential as a function of layer thickness in these materials, delocalized edge states affected by edge reconstructions and defect potentials.

We conclude that off-axis electron holography adapted to specifics of 2DMs represents a powerful tool for multiscale potential analysis of 2DMs with no need for *a priori* knowledge about the sample or additional aberration assessment damaging the sample.

References:
[1] Winkler, F. et al., Phys. Rev. Lett. 120 156101 (2018)
[2] Kern, F.L. et al., Physical Review Research 2, 043360 (2020)
[3] We acknowledge funding from the European Research Council (ERC) under the Horizon 2020 research and innovation program of the European Union (grant agreement No 715620)

Figure 1: Signal-to-noise (SNR) transfer functions for HRTEM in negative Cs conditions and Electron Holography (EH) for two cases: Cc corrected with a Schottky FEG, residual linear Cc = 39 µm, energy spread = 0.7 eV (C1 = 6.7 nm, C3 = -8.1 µm) and without Cc correction and a Cold FEG, linear Cc = 1.3 mm, energy spread = 0.3 eV (C1 = 13.6 nm, C3 = -33.1 µm). Both transfer functions are given for an acceleration voltage of 80 kV, a semi convergence angle of 0.15 mrad and image spread envelope of 40 pm.

Figure 2: (a) High-resolution potential analysis in *h*-BN. Insets: Zig-zag steps comprising two atomic layers (b), (c), a monolayer region (d), and a BN void defect (d). Image adapted from [2

Figure 1

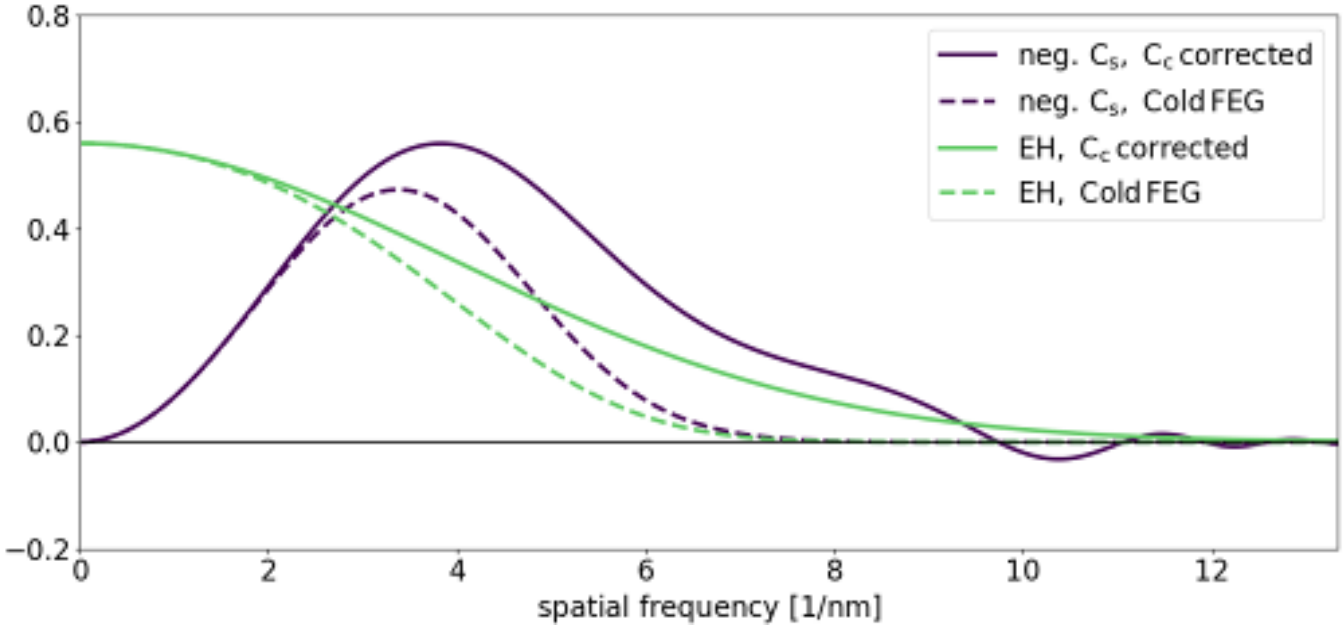

Figure 2

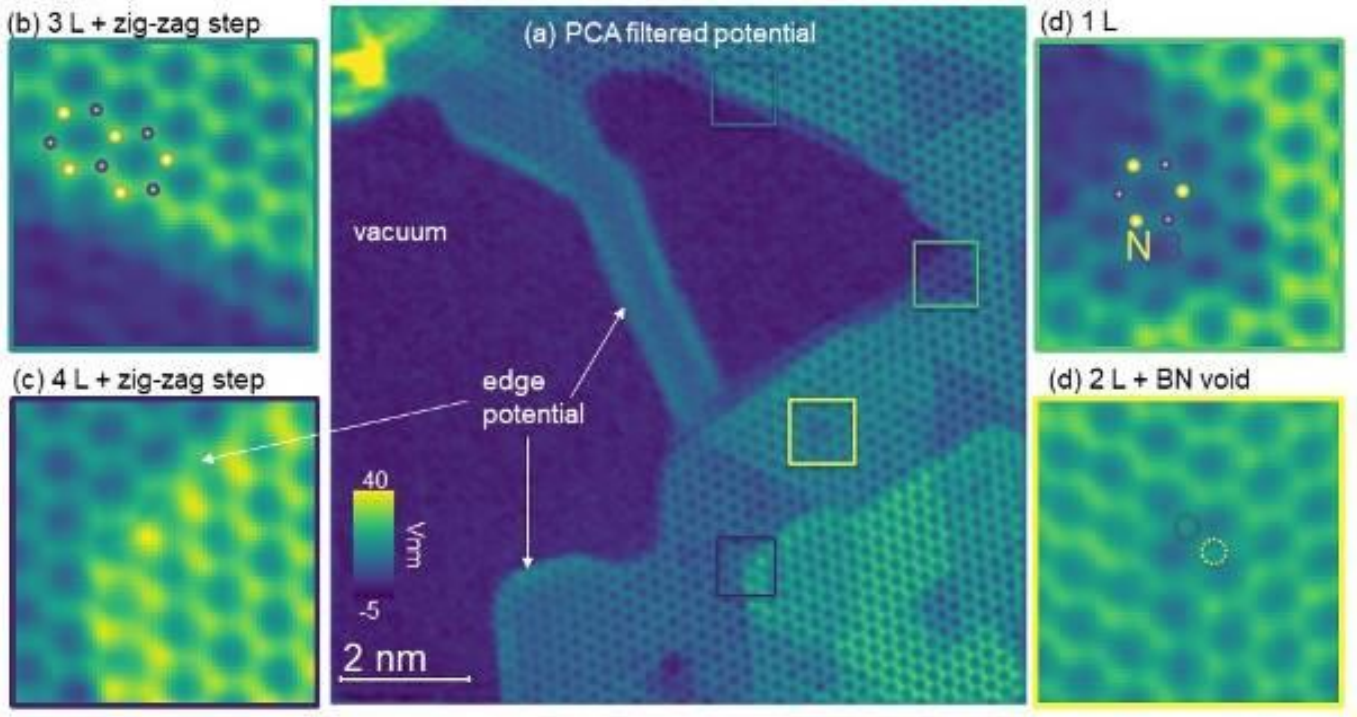

MS4.P009
The impact of specimen thickness on the accuracy of exit wave reconstruction in electron ptychography

B. März[1], C. Braun[2], A. Bangun[1], K. Müller-Caspary[1,2]

[1]Ernst Ruska-Centre for Microscopy and Spectroscopy with Electrons, Jülich, Germany
[2]RWTH Aachen University, Aachen, Germany

Introduction: Momentum-resolved scanning transmission electron microscopy (STEM) refers to the acquisition of two-dimensional diffraction patterns taken at each position of a specimen scanned by an electron probe. Since there are two dimensions involved in the specimen space and another two dimensions in diffraction (momentum) space, a 4D data set is generated.

One approach of evaluating momentum-resolved STEM data is to measure the angular deflection of the STEM probe, known as first moment (FM) STEM [1]. Electron ptychography is a different method of evaluation and makes use of the redundancy of information present in the 4D data. Both the Single side-band (SSB) and the Wigner distribution deconvolution (WDD) ptychography methods applied in this study allow for phase retrieval [2,3], while the WDD has the advantage of subsequent correction of probe aberrations due to its capability of recovering the complex illuminating STEM probe. It can therefore be used to improve spatial resolution after the actual experiment. Nevertheless, these methods are restricted to thin specimens considered as weak phase objects (SSB) or assume a single interaction via a complex object transmission function (OTF). Depending on the material, the thickness of the specimen, as well as the electron energy used, this can likely result in an incorrect reconstruction of the phase.

Objectives: We recorded 4D data of MoSe2 in [0001] orientation using a probe-correcetd ThermoFisher Titan Crewley at 80kV with an EMPAD camera and compared the phase information derived from FM-STEM with that of reconstructions using the WDD and the SSB ptychography methods as a function of the specimen thickness (i.e. number of MoSe2 monolayers). The obtained results from the experimental data were then validated using multislice simulations. We provide an estimate of the robustness of the methods used with respect to specimen thickness.

Methods: Multislice simulations of MoSe2 for a range of thicknesses were conducted using an in-house MATLAB implementation, FM-STEM and ptychographic reconstructions were done using our ImageEval MATLAB code.

Results: Figure 1 shows results obtained from simulated data. Linescans (A) across the charge density obtained by FM-STEM, (B) annular dark field (ADF) STEM intensity and (C) the phase recovered using the SSB method are presented. SSB and FM-STEM show different linearity with increasing sample thickness. While the intensity from FM remains linear across several bilayers, the SSB method fails already after one. The trend of WDD is currently discussed for comparison.

Figure 2 shows phase reconstructions using the (A) FM-STEM, (B) SSB and (C) WDD methods. The analysed region covers two thicknesses, 2 monolayers and 4 monolayers, respectively, as confirmed by quantitative STEM. Generally, similar structural characteristics are represented in all 3 cases. Enhanced resolution was achieved using SSB and WDD, while for WDD a -1nm defocus was applied during the reconstruction. Nevertheless, quantitative considerations remain still difficult.

Further iterative algorithms like ePIE will be evaluated with respect to present Poisson noise.

Acknowledgments: *Funding: Helmholtz IVF, contracts VH-NG 1317 (moreSTEM) and ZT-I-0025 (Ptychography 4.0)*

References:
[1] Müller, K. et al., Nature Comm., 2014, 5, 5653:1-8
[2] Rodenburg et al., Ultramicroscopy, 1993, 48, 304-314
[3] Rodenburg et al., Philosophical Transactions Section A, 1992, 339, 521-553

Figure 1

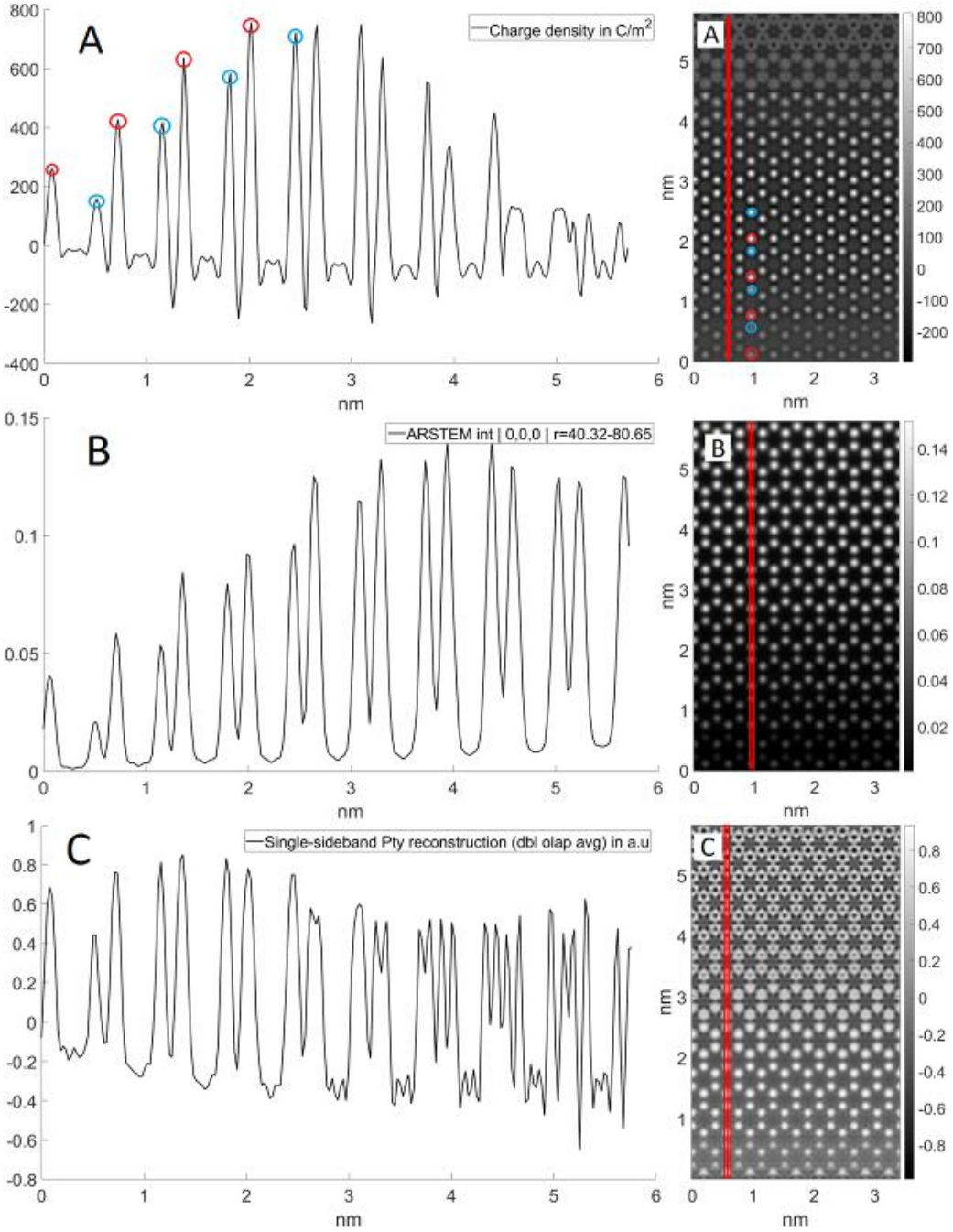

Figure 2

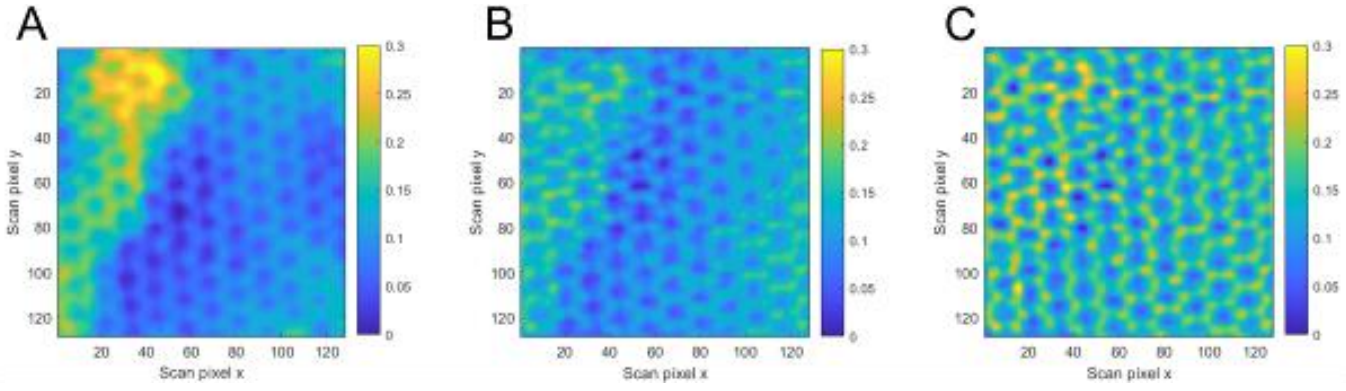

MS4.P011
The coalescence behavior of two-dimensional materials revealed by multiscale *in situ* imaging during chemical vapor deposition growth

Z. J. Wang[1,2], M. G. Willinger[1,2]

[1]ShanghaiTech University, School of Physical Science and Technology, Shanghai, China
[2]ETH Zurich, ScopeM, Zurich, Switzerland

Wafer-scale monocrystalline two-dimensional (2D) materials can theoretically be grown by seamless coalescence of individual domains into a large single crystal. Here we present a concise study of the coalescence behavior of crystalline 2D films using a combination of complementary *in situ* methods. Direct observation of overlayer growth from the atomic to the millimeter scale and under model- and industrially relevant growth conditions reveals the influence of the film–substrate interaction on the crystallinity of the 2D film. In the case of weakly interacting substrates, the coalescence behavior is dictated by the inherent growth kinetics of the 2D film. It is shown that the merging of coaligned domains leads to a distinct modification of the growth dynamics through the formation of fast-growing high-energy edges. The latter can be traced down to a reduced kink-creation energy at the interface between well-aligned domains. In the case of strongly interacting substrates, the lattice mismatch between film and substrate induces a pronounced moiré corrugation that determines the growth and coalescence behavior. It furthermore imposes additional criteria for seamless coalescence and determines the structure of grain boundaries. The experimental findings, obtained here for the case of graphene, are confirmed by theory-based growth simulations and can be generalized to other 2D materials that show 3- or 6-fold symmetry. Based on the gained understanding of the relation between film–substrate interaction, shape evolution, and coalescence behavior, conditions for seamless coalescence and, thus, for the optimization of large-scale production of monocrystalline 2D materials are established.

Figure 1

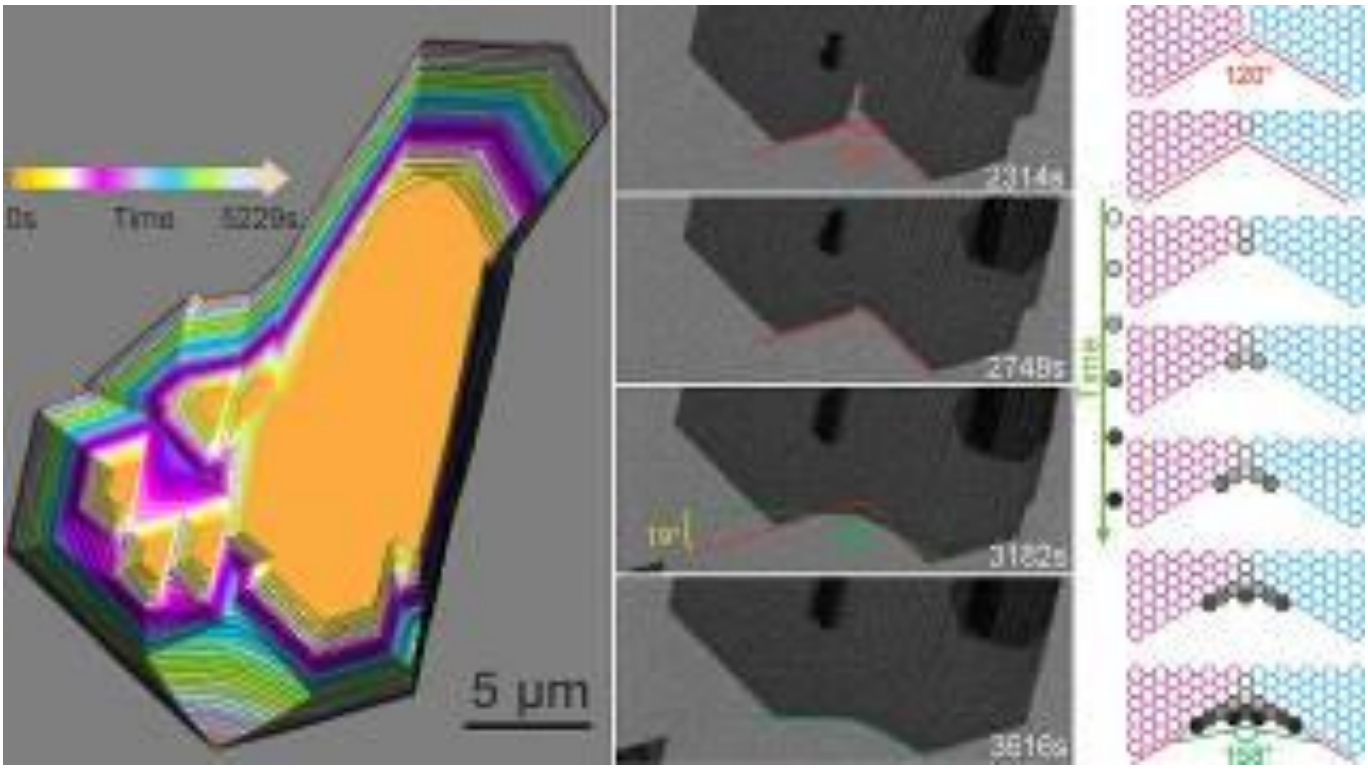

MS4.P012
Beyond elastic electron irradiation effects in two-dimensional materials

T. A. Bui[1], G. Leuthner[1], A. Chirita[1], T. Susi[1], J. Kotakoski[1]

[1]University of Vienna, Physics, Vienna, Austria

The highly energetic electron beam of a scanning transmission electron microscope (STEM) can cause damage to specimens. However, beam-induced effects may not always be detrimental and thus a fundamental understanding of the electron-irradiation response of two-dimensional (2D) materials such as graphene, MoS_2 or hexagonal boron nitride (h-BN) needs to be developed [1].

Knock-on damage and radiolysis are two dominant mechanisms of defect creation when electron beams interact with materials. Earlier studies have established that in a metallic specimen such as graphene, only the knock-on damage caused by elastically scattered electrons plays a role [2]. However, in semiconducting materials such as MoS_2 or insulators including h-BN, a purely elastic description fails and thus aspects of both damage mechanisms need to be considered [1]. In the case of MoS_2, very recent work has taken the first steps towards a quantitative theoretical understanding of its irradiation stability, proposing ionization-assisted knock-on damage as the dominant mechanism at electron energies below 80 keV [3].

In our work, aberration-corrected STEM was employed to study the damage mechanism in free-standing h-BN monolayers, where quantitative data exists only for larger defects [4]. The samples were prepared by transferring flakes grown with chemical vapor deposition directly onto TEM grids. Experiments were conducted using various electron energies (50–80 keV), and atomically resolved imaging was used to quantify the creation of single B or N vacancies. We compare the experimental cross section values with new theoretical modeling, showing that ionization-assisted knock-on appears to be responsible for defect creation also in h-BN.

Support from the European Research Council (grant 756277-ATMEN) and computational resources provided by the Vienna Scientific Cluster (VSC) are gratefully acknowledged.

[1] T. Susi, J.C. Meyer, J. Kotakoski, Nat. Rev. Phys. 1, 397 (2019)
[2] T. Susi *et al.*, Nature Commun. 7, 13040 (2016)
[3] S. Kretschmer *et al.*, Nano Lett. 20, 2865–2870 (2020)
[4] O. Cretu *et al.*, Micron 72, 21–27 (2015)

MS4.P013
Advanced electron microscopy characterisation of iron rich talc, a novel class of magnetic 2D materials

D. Knez[1], A. Matkovic[2], J. Genser[3], F. Hofer[1,4], C. Teichert[2], E. Fisslthaler[4]

[1]TU Graz, Institute of Electron Microscopy and Nanoanalysis, Graz, Austria
[2]Montanuniversität Leoben, Institute of Physics, Leoben, Austria
[3]TU Wien, Institute for Solid State Electronics, Vienna, Austria
[4]Graz Centre for Electron Microscopy (ZFE), Graz, Austria

Magnetic two-dimensional materials offer exceptional opportunities in the fields of 2D-spintronics, data storage, magnetoelectronics, and magnetooptics. However, most of the known representatives of this type of materials are unstable at environmental conditions or show their magnetic properties only at cryogenic temperatures, which poses large challenges to their actual application in devices [1]. As proposed recently, phyllosilicates satisfy these criteria [2]. This class of van-der-Waals materials consists of parallel double sheets of Si_4O_{10} silicate tetrahedra, comprising one important type of silicates. The complexity of the phyllosilicate structure enables a high degree of variability, and allows for instance the incorporation of iron, yielding 2D sheets with intrinsic magnetic properties. A prominent representative of this type of phyllosilicates is talc ($Mg_3[(OH)_2|Si_4O_{10}]$), where iron atoms occupy the Mg sites in the crystal.

We will present our in-depth transmission electron microscopy (TEM) investigations of free-standing iron-rich talc flakes, which were synthesized and pre-characterized by the scanning probe mcroscopy group of Christian Teichert at the Montanuniversität Leoben. Free standing flakes were prepared by micromechanical exfoliation [3], starting from a natural mineral aggregate and subsequent transfer to a SiN TEM substrate. The high beam sensitivity of these materials renders their characterization by means of TEM based techniques challenging and the achievable signal-to-noise ratio, especially with spectroscopy techniques, is rather limited.

By using low-dose aberration-corrected scanning transmission electron microscopy (STEM), combined with direct electron detection EELS and high-sensitivity EDX spectrometry, we were able to show that iron tends to form clusters within the Mg rich talc layers (Figure 1a-c). The thickness of the flake was approximately 5 layers, as confirmed by preceding AFM investigations. Moreover, the unparalleled performance of a Gatan K2 direct electron detection camera attached to our EELS spectrometer allowed to assess the oxidations state of the iron atoms within the crystal and revealed that iron is in its 2+ oxidation state, as predicted by DFT calculations [4].

Bibliography:
[1] Gong et al. (2019), Nature, 546 (7657), 265–269.
[2] Matkovic et al., under preparation.
[3] Novoselov et al. (2004) Science, 306 (5696), 666–669.
[4] Garvie et al., (1994) American Mineralogist, 79 (5-6), 411–425.

Figure 1: (a) Overview STEM HAADF image of a talc flake suspended over a hole in the SiN TEM support. (b) High resolution HAADF image showing a Fe cluster within the flake. Scale bar is 10 nm (c) EELS Fe L elemental map of the cluster shown in (b). (d) ELNES of the Fe L2/3 edge, showing the characteristic Fe2+ shape.

Figure 1

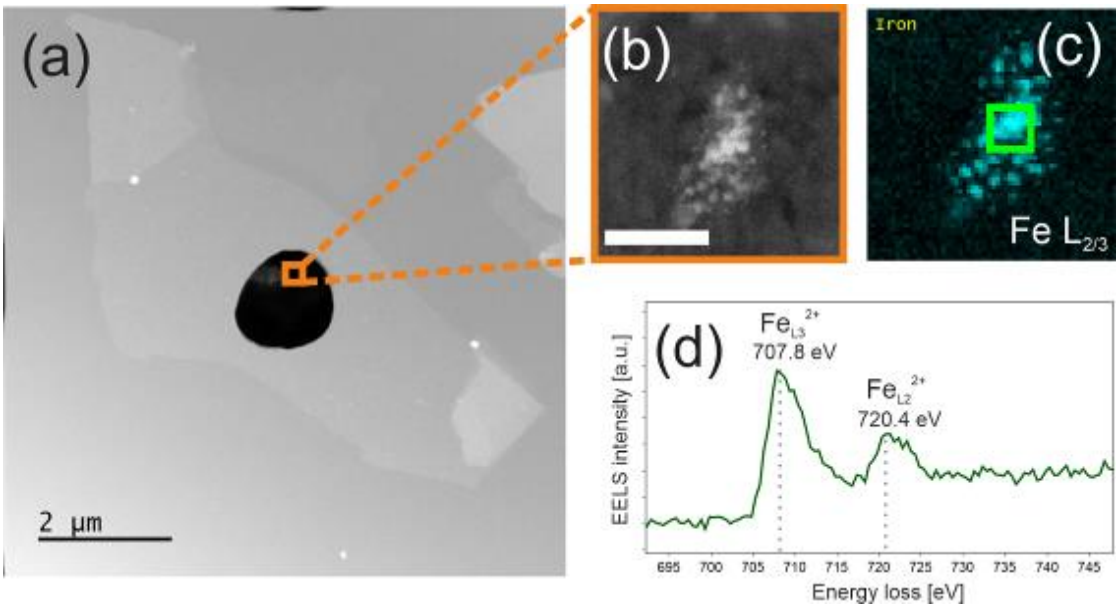

MS4.P014
Exploring defects of 2D materials in two- and three-dimensions

C. Hofer[1], V. Skákalová[2], J. Haas[3,4], J. C. Meyer[3,4], T. Pennycook[1]

[1]University of Antwerp, EMAT, Antwerp, Belgium
[2]University of Vienna, Faculty of Physics, Vienna, Austria
[3]University of Tübingen, Institute of Applied Physics, Tübingen, Germany
[4]Natural and Medical Sciences Institute at the University of Tübingen, Reutlingen, Germany

Introduction: Identifying the position and chemical identity of each atom in a specimen is the ultimate goal of structural characterization. With the rise of aberration correctors in scanning transmission electron microscopy (STEM) the Z-contrast based annular dark-field (ADF) imaging technique even allows to distinguish light elements in single layer materials [1]. However, residual aberrations are difficult to manually detect and correct under the low doses needed for beam sensitive materials hampering the analysis of ADF images. Moreover, a conventional tomographic approach for three-dimensional imaging is difficult due to the requirement of a large number of projections [2].

Objectives: I will introduce a novel approach to extract the atomic intensities of STEM images in the presence of residual aberrations and noise [3]. The method is based on an optimization process where the simulation of a model is iteratively matched to the experimental STEM image. In order to minimize artifacts arising from a non-perfectly shaped primary beam, the aberration coefficients are included in the optimization process. The reconstruction is based on an iterative optimization process where simulated images are matched to the experimental data set.

Furthermore, I will present results illustrating 3D imaging of 2D materials such as graphene [4] directly from as few as two tilt angles. We plan to show additional results extending the method to thicker 2D materials such as transmission metal dichalcogenides, utilizing ptychography to facilitate the simultaneous location of both heavy and light atoms.

Materials & methods: ADF STEM measurements were conducted using a Nion UltraSTEM100 operated at 60 kV and a JEOL JEM-ARM200F operated at 80 kV at a convergence angle of ~30 mrad, and tilts separated by ~20 deg. Ptychography data will be collected using a microsecond dwell time capable custom camera at EMAT.

Results: Our analysis reveals that our novel intensity method achieves more reliable results compared to other methods in the presence of small non-round aberrations, while still allowing us to extract atomic intensities even if the aberrations are strong. Our method allows us to extract the chemical elements reliably. The three-dimensional analysis reveals significant deformation of defect sites in 2D materials. Furthermore, we will present the extension to ptychographic few tilt tomography.

Conclusions: Our new methods provide reliable intensities from atomically resolved STEM images They allow one to decouple intensity variations arising from aberrations, beam tails and varying bond distances from those arising from sample variations. For light-element samples, they allow sharp intensity distributions around single elements to be obtained. They also allow the three-dimensional structure of a wide range of 2D materials to be obtained, and show that these materials are far from being flat, especially at defect sites.

[1] Krivanek, O. et al., Nature 464, 571–574 (2010).
[2] A. C. Kak et al., IEEE Engineering in Medicine and Biology Society, New York: IEEE Press (1988).
[3] Hofer C. et al., submitted
[4] Hofer C. et al., 2D materials 5, 045029 (2018)
[5] Research funded by the Ministry of Science, Research and Art Baden-Württemberg and by the European Research Council (ERC) under the European Union"s Horizon 2020 research and innovation programme via Grant agreement No. 802123-HDEM.

MS5.001-Invited
Combining microscopic techniques in the analysis of metamorphic rocks

B. Cesare[1]

[1]University of Padova, Department of Geosciences, Padova, Italy

I will summarise some outcomes in the analysis of geological materials, that emphasize the key role of research using both traditional and state-of-the-art microscopes. The focus will be on metamorphic rocks which have partially melted, i.e., migmatites.

In these rocks my research group has discovered the remnants of the magma produced during crustal melting, in the form of minuscule (5-20 µm) inclusions in minerals. These inclusions, named "*nanogranitoids*" (Cesare et al., 2015, *Lithos*) have become a key subject of research, as they provide on one hand a new microstructural criterion to infer the former presence of melt in a rock, on the other hand the unprecedented possibility to analyse the chemical composition of primary natural magmas.

The small size and the polyphase nature of nanogranitoids (Ferrero et al., 2012, *J Metamorph Geol*) are a challenge for their detailed microstructural and chemical characterization.

After preliminary phase recognition by micro-Raman spectroscopy, nanogranitoids are studied by FE-SEM and FE-EPMA on exposed inclusions. This allows textural and chemical characterisation on 2D sections of the entire inclusion. In order to reconstruct the 3D distribution of phases in the inclusion, and their relative volumes, FIB-SEM serial sectioning can be utilised. We applied serial slicing also to former fluid inclusions coexisting with nanogranitoids in garnet. These studies (Tacchetto et al, 2019, *Chem Geol*; Carvalho et al., 2020, *EPSL*) have demonstrated that primary CO_2-rich fluid inclusions do not survive in high-T rocks, as the fluid invariably reacts with the host garnet during cooling. The retrograde reaction produces step-daughter carbonates plus Al-bearing phases such as corundum, pyrophyllite or kaolinite depending on the presence and amount of H2O mixed with CO_2 in the fluid. FIB-SEM serial sectioning is very powerful, but destructive and time-consuming. In the future, microstructural analysis will take advantage of the rapid improvements in lateral resolution of non-destructive techniques like high-resolution 3D X-ray microscopy and computed tomography. With the current resolution, Synchrotron X-ray tomographic microscopy has been successfully applied to study the 3D distribution of melt and fluid inclusions in garnet crystals, and to demonstrate that a zonal arrangement of inclusions does not imply a two-stage garnet growth (Parisatto et al. 2018, *Am Min*).

The submicrometric size of crystals in nanogranitoids is still a major obstacle to quantitative chemical analysis, as contamination from neighbouring phases is unavoidable. Fortunately, we are more interested in the composition of the bulk former melt than in that of the single minerals that crystallised from it. Therefore, the analytical protocol provides for the experimental remelting of nanogranitoids to a homogeneous glass whose major element composition can be analysed by WDS techniques in a SEM or EPMA. Along with major elements, trace element contents of the former melt can be obtained by microscope-assisted LA-ICP-MS. As the fluid content of natural magmas is a key parameter affecting viscosity, behaviour upon cooling and explosivity, we have also studied the content of H_2O and CO_2 of remelted nanogranitoids by nanoSIMS (Bartoli et al. 2014, *EPSL*).

I will also highlight new developments in the use of the optical microscope in Geosciences, with the unexplored potentials of polychromatic polarised microscopy (Shribak, 2015, *Sci Reports*).

MS5.002-Invited
Developing a structural model of persistent luminescent strontium aluminate from multimodal microscopy analysis

C. W. Ow-Yang[1]

[1]Sabanci University

Although it is well known that the presence of boron (B) in europium (Eu) and dysprosium (Dy) co-doped strontium aluminate dramatically extends persistent luminescence from minutes to > 8 hours, the precise role of boron remains an open question. In this talk I am presenting our progress in applying a combination of multi-modal microscopy and spectral imaging techniques to construct a structural model of co-doped Sr4Al14O25 (4SrO-7Al2O3 or S4A7) that supports persistent luminescence. Using sintered pellets, we analyzed back-scattered electron images to determine the phase identity across the multi- phased microstructure, aided by cathodoluminescence (CL) spectroscopy, wavelength dispersive spectroscopy (WDS), and energy dispersive x-ray spectroscopy (EDS). While WDS and EDS revealed stoichiometry and elemental distribution, differences in the crystal field of divalent Eu induced changes to its electronic structure and enabled phase identification based on the wavelength of the CL emission peak. Moreover, WDS revealed that B2O3 enabled tuning of the Eu and Dy dopant concentrations to their solubility limit within equilibrium grains of S4A7, a necessary condition to suppress concentration quenching of photon emission. Within the S4A7 grains, Eu was divalent, but trivalent in the intergranular phase (IGP), as revealed by nano-CL in a dedicated scanning transmission electron microscope (STEM). Atomic resolution Z-contrast imaging in a spherical aberration-corrected STEM demonstrated that divalent Eu and trivalent Dy incorporated into adjacent Sr sites in S4A7. This arrangement enables the energy transfer between the optical emitter Eu and the auxiliary ion Dy that gives rise to persistent luminescence. Electron energy loss spectroscopy analysis in the STEM showed that B in the IGP is coordinated by 3 oxygens, but prefers 4-fold coordination in the S4A7 grains. Finally, Raman scattering analysis in a confocal microscope elucidated further the environment of B in the S4A7 grains, showing fingerprints of B-O vibrations in orthoborate and pyroborate configurations. The combined results these multi-modal analyses by imaging and spectroscopy yield a model that addresses how B modifies the atomic arrangements supporting persistent luminescence in B, Eu, and Dy co-doped S4A7.

MS5.003
Electron microscopy and X-ray diffraction as complementary methods for the structure determination of bronze-type niobium tungsten oxides

F. Krumeich[1], M. Wörle[1]

[1]ETH Zurich, D-CHAB, Zurich, Switzerland

The phases occurring in the pseudo-binary system Nb_2O5-WO_3 are all based on two-dimensional octahedral frameworks with the different compositions achieved either by forming different block sizes, by filling tunnels in the tetragonal tungsten bronze structures (TTB) or by crystallographic shear in the Magnéli phases [1]. Recently, these oxides have gained high attention because of their potential as high-rate Li-ion battery materials [2]. For the structural characterization of pure phases, X-ray diffraction (XRD) represents the suitable approach. However, all niobium tungsten oxides have an inclination to contain various defects and to form intergrowths for intermediate compositions. Starting with the pioneering HRTEM study on $Nb_8W_9O_{47}$ and $Nb_4W_7O_{31}$ [3], electron microscopy has been established as appropriate method for revealing the real structure of such oxides. In this contribution, possibilities and limits of Rietveld refinement of XRD powder data are probed and compared to the results of electron microscopy investigations.

$Nb_8W_9O_{47}$, which crystallizes in a threefold superstructure of the tetragonal tungsten bronzes (TTB), and $Nb_7W_{10}O_{47.5}$, with a slightly differing metal/oxygen ratio were investigated. Rietveld refinement of XRD powder data led to a good fit and confirmed the structure determination obtained with single crystal XRD data [4]. The sample $Nb_7W_{10}O_{47.5}$ was prepared by oxidation of $Nb_7W_{10}O_{47}$, which crystallizes isostructural to $Nb_8W_9O_{47}$ and contains not fully oxidized metal [5], and a separation into a mixture of $Nb_8W_9O_{47}$ and $Nb_4W_7O_{31}$ is expected at high temperature according to the phase diagram [1]. However, the XRD pattern can be fully described with the data of the $Nb_8W_9O_{47}$ phase [4]. A typical SAED pattern of this sample shows circular diffuse scattering besides sharp reflections of the threefold TTB superstructure (Figure 1a). HRTEM images reveal the presence of both phases intimately mixed and disordered at the 10 nm scale (Figure 1b, c). The predominance of the threefold superstructure is evident and confirmed by the corresponding peaks in the FT (Figure 1b). Grain boundaries appear between differently structured domains. In another area of the same crystal, $Nb_4W_7O_{31}$ is the main component (Figure 1c). Intergrowth of the two phases occurs frequently (Figure 2). Moreover, single blocks of 4x4 octahedra are often coherently embedded in the TTB structure. This investigation confirms that the mysteries underlying such an abundant structural variability can only be figured out by the direct visualization of the real structures by high-resolution TEM and STEM [6].

[1] Roth, Waring, *J. Res. Natl Bur. Stand.* 70A (1966) 281.
[2] Griffith et al., *Nature* 559 (2018) 556; Ma et al., *Electrochimica Acta* 332 (2020) 135380.
[3] Iijima, Allpress, *Acta Crystallogr. A* 30 (1974) 22.
[4] Wörle, Krumeich, *Z. anorg. allg. Chem.* 647 (2021) 98.
[5] Krumeich, *J. Solid State Chem.* 119 (1995) 420.
[6] Electron microscopy was performed on a double-corrected JEM-ARM300F at ScopeM (ETH Zürich). XRD was measured on a STADI P powder diffractometer (Stoe) with Cu $K_{\alpha 1}$ radiation at SMoCC (ETH Zürich).

Figure 1: $Nb_7W_{10}O_{47.5}$: SAED pattern (a) and HRTEM images (b, c) of two regions found in the same crystal. Fourier transforms (FT) are shown as insets.

Figure 2: HAADF-STEM image of an interface between $Nb_8W_9O_{47}$ (left) and $Nb_4W_7O_{31}$ (right) with the structural model shown as overlay. Frames mark the unit cells.

Figure 1

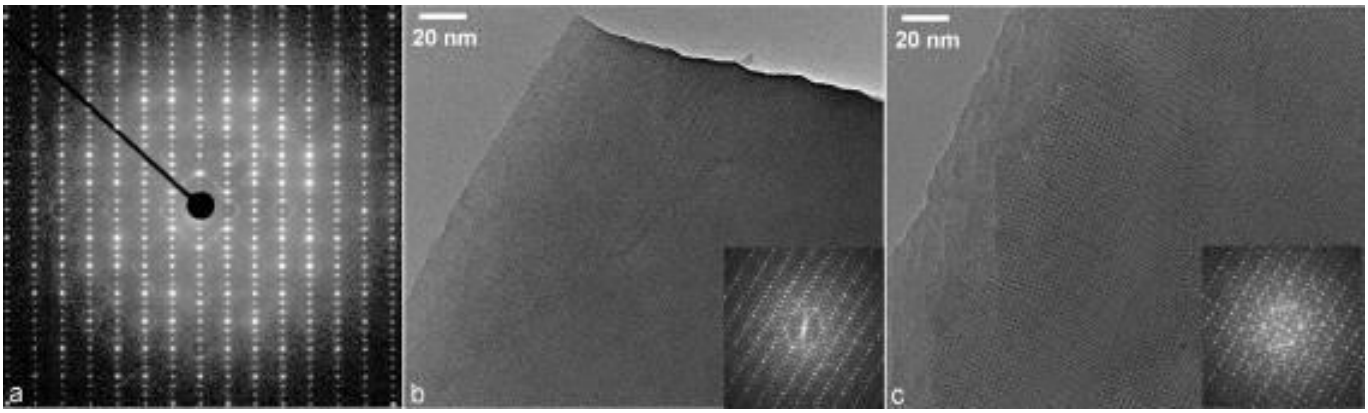

Figure 2

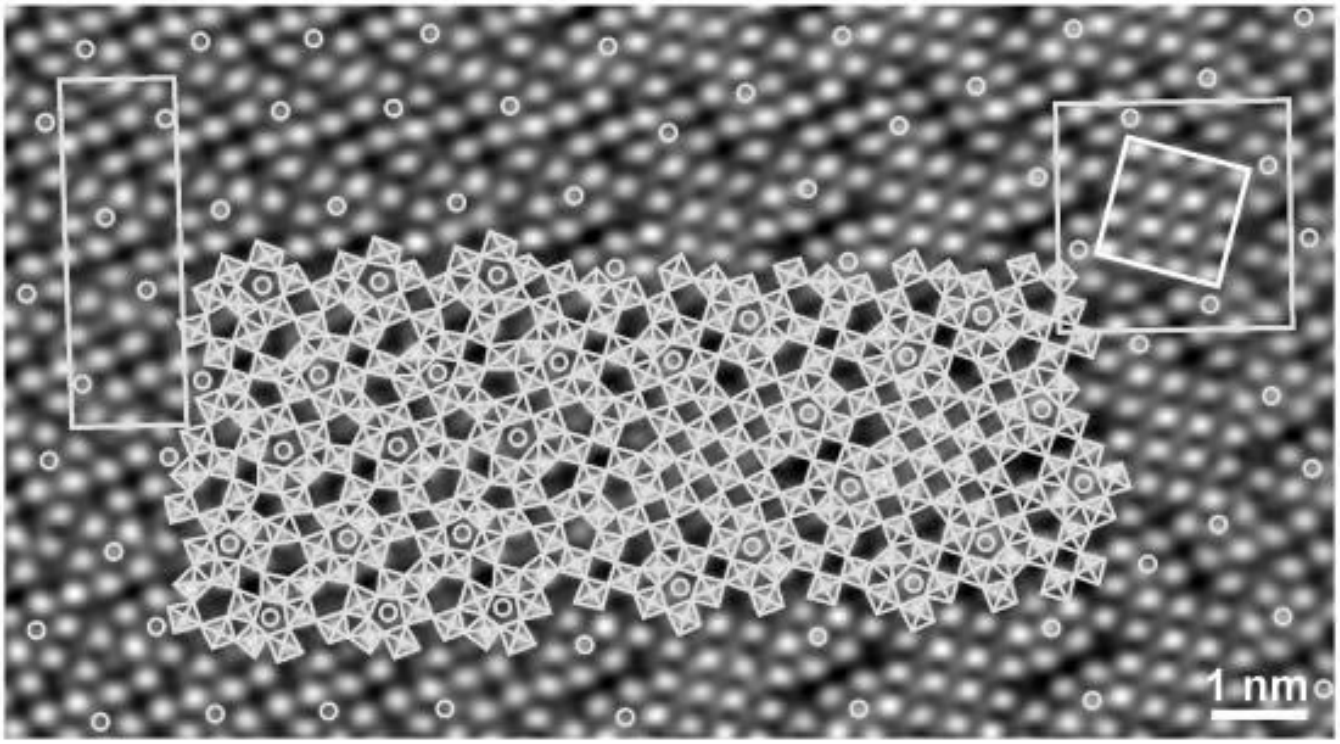

MS5.004
Formation of nanometer-scale water-filled cavities in ultra-high performance concrete due to mechanical fatigue

G. Schaan[1,2], S. Rybczynski[3,2], F. Schmidt-Döhl[2], M. Ritter[1]

[1]Hamburg Institute of Technology, Electron Microscopy Unit, Hamburg, Germany
[2]Hamburg University of Technology, Institute of Materials, Physics and Chemistry of Buildings, Hamburg, Germany
[3]Hamburg University of Technology, Institute of Solids Process Engineering and Particle Technology, Hamburg, Germany

Question: Since the first reports on ultra-high performance concrete (UHPC) in the early 1990s, a large amount of work has been published on the composition, properties and applications of UHPC. [1-3]. However, few if any reports so far have focused on the effects of mechanical fatigue on the microstructure of mineral building materials. [4] Our aim is to investigate these effects, down to their origins on a nanometer scale, using scanning transmission electron microscopy (STEM) and focused ion beam (FIB) sample preparation.

Methods: UHPC was fabricated with a formula of ordinary Portland cement (CEM I) with a water/cement (w/c) weight ratio of 0.24, quartz sand (maximum grain diameter ca. 500 µm) and quartz powder (20 µm) as aggregate, nanoscale silica fume and a polycarboxylate superplasticizer. After hardening in water for at least 56 days, cylindrical samples were subjected to cyclic uniaxial compressive loading between lower and upper limits of 5 and 80%, respectively, of the short-term compressive strength. This leads to failure of the sample after strongly varying load cycle numbers. From suitable fragments, TEM samples were extracted via mechanical as well as FIB methods and investigated using HAADF-STEM and EDS spectral imaging.

Results: The morphology of the calcium silicate hydrate (CSH) phases that make up the cement paste is originally finely fibrous. With increasing mechanical fatigue, a majority of this material is compacted, while numerous needle- or lath-shaped regions with a lower material contrast in HAADF imaging form concurrently. [4] These crack precursors do not significantly grow in size, retaining a length and width of ca. 200 and 30 nm, respectively. However, they increase in number and, become increasingle depleted with solid material, as indicated by their image contrast relative to the surrounding material.

Figure 1: Crack precursors formed in the cement paste of UHPC during mechanical fatigue.

Upon energy input from the electron beam during STEM investigation, the crack precursors quickly and irreversibly change in size, some growing while others shrink. We assume that these crack precursors are water-filled cavities. On a larger scale, water-filled interconnected voids have been shown to be an integral part of the failure mechanism of UHPC. [5]

Figure 2: Shrinking and growing cavities upon energy input from the STEM electron beam.

Using EDS spectral imaging, we detected increased amounts of aluminium and sulfur in regions of the cement paste containing multiple cavities. The presence of these elements indicates the presence of ettringite, a calcium aluminium sulfate hydroxide mineral that also contains 26 equivalents (up to 46 wt.%) of water. Ettringite is also known to readily undergo phase transformations.

Figure 3: EDS elemental distribution map of cavities in aluminium- and sulfur-rich sample regions.

Conclusions: During mechanical fatigue, nanoscale cavities form in the cement paste of UHPC. They shrink or grow upon energy input and are assumed to be cavities filled with water. They concentrate in sample regions rich in aluminium and sulfur, so a relation to residual ettringite is probable.

References:
[1] E. Ghafari et al., Mater. Design 2014, 59, 1-9.
[2] T. Oertel et al., Cem. Concr. Res. 2014, 58, 121-130.
[3] D. H. Wang et al., Const. Build. Mater. 2015, 96, 368-377.
[4] G. Schaan et al., Imaging & Microscopy 2020, 2, 25-27.
[5] C. Tomann, N. Oneschkow, Struct. Concr. 2019, 1204-1211.

Figure 1

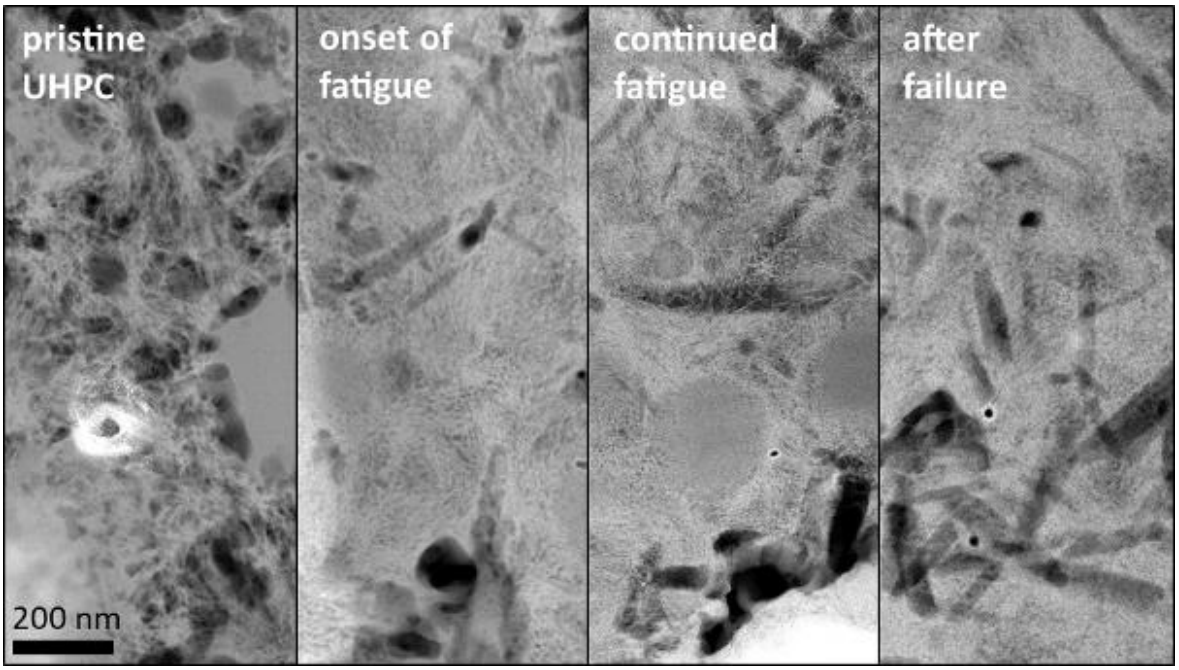

Figure 2

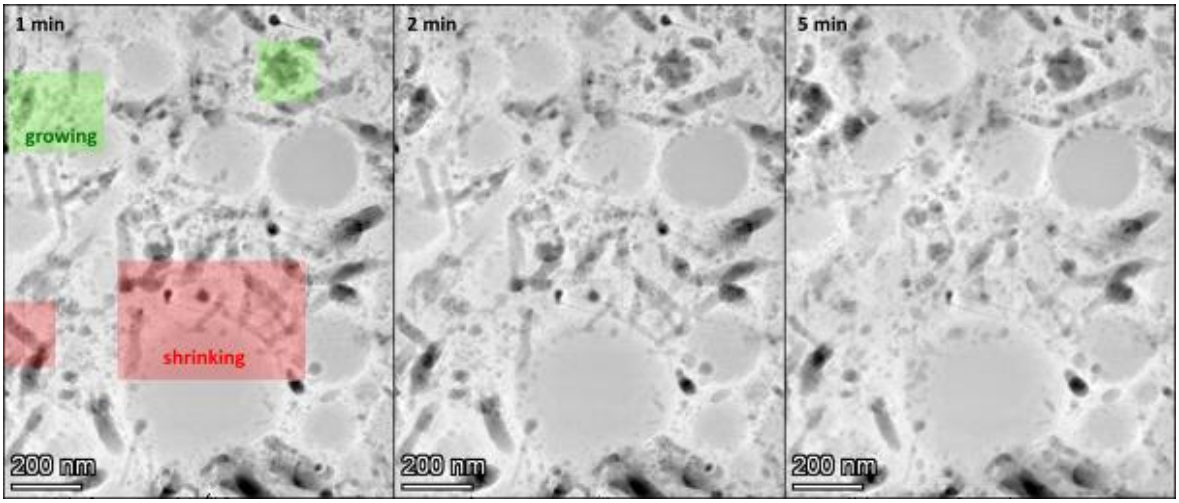

Figure 3

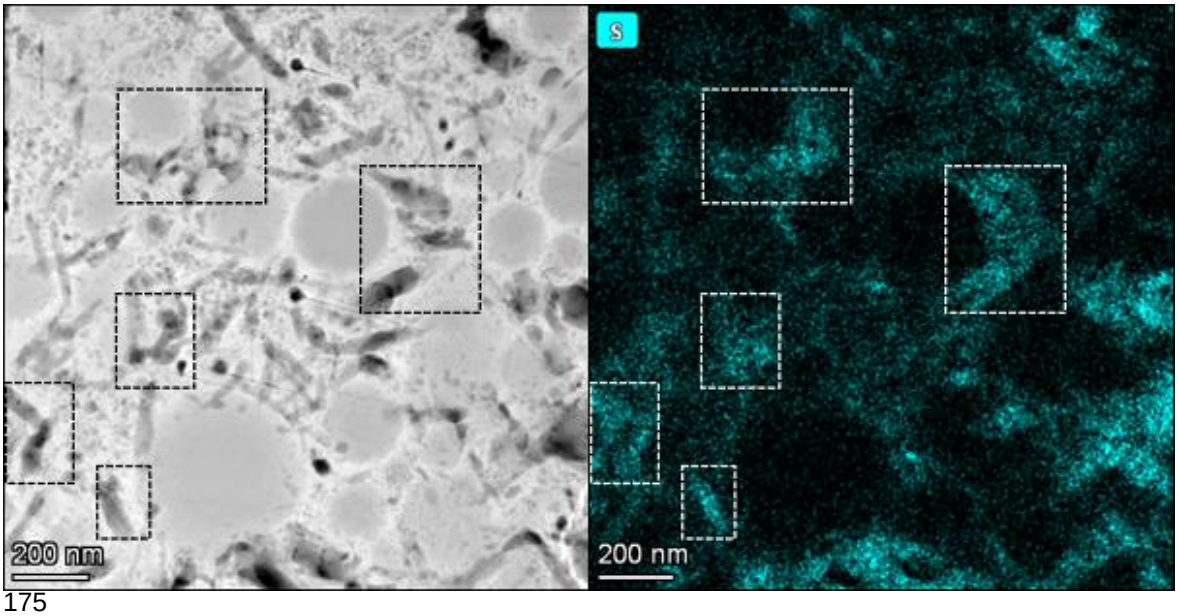

MS5.005
Machine learning on STEM-EDXS data for quantifying trace elements in bridgmanite

H. Chen[1], F. Nabiei[2], J. Badro[3], D. T. L. Alexander[1], C. Hébert[1]

[1]Swiss Federal Institute of Technology Lausanne (EPFL), IPHYS, Lausanne, Switzerland
[2]University of Cambridge, Department of Earth Sciences, Cambridge, United Kingdom
[3]Institute de Physique du Globe de Paris, Paris, France

The trace element characterization is important for geoscience, which allows probing numerous geological processes. For example, the trace element partitioning between silicate perovskites and silicate melts can be used to examine whether a proportion of lower mantle minerals could have fractionated in the magma ocean solidification [1]. Scanning transmission electron microscopy (STEM)-energy-dispersive X-ray spectroscopy (EDXS), a fast and easy-operated technique of superior spatial resolution, has been widely used for the chemical characterization of materials. While STEM-EDXS is not considered suitable for the detection and quantification of trace elements, we seek to address this challenging analytical problem by applying appropriate machine learning algorithms to the data processing of STEM-EDXS.

We have done a series of melting experiments in the laser-heated diamond anvil cell at 46 to 88 GPa on pyrolite composition including trace amount of Nd, Sm, Hf, Lu, and U (0.3 wt.% for each). The samples were molten, quenched, decompressed, and then prepared by the focused ion beam (FIB) lift-out technique. Figure 1(a) is a high-angle annular dark-field (HAADF) image of subsolidus mineral assemblages of the 71 GPa sample. The region contains three phases (Figure 1(b)), a bridgmanite (Brg) matrix, ferropericlase (Fp), and Ca-rich perovskite (CaPv) grains. An area—indicated by the green rectangle on Figure 1(a)—was selected to quantify Brg, and the integrated EDXS signals around U Mα, Nd Lα, and Sm Lα are depicted in Figure 1(c) and 1(d). The U Mα peak is hardly distinguishable, and the peaks of Nd Lα and Sm Lα are quite noisy.

We have considered two strategies to improve the quantification of the trace elements in Brg. One is to reduce noise for a certain signal, another is to integrate more signals. With the former, we utilized an algorithm, principal component analysis (PCA) [2], to filter noise out from the signals. The scree plot of PCA (Figure 1(c)) indicates that the first three components altogether could almost represent the original dataset. We compared the Brg spectrum reconstructed from the three significant components with the original one, the U Mα peak emerges (Figure 1(d)), and the Nd Lα and Sm Lα peaks stand out with improved signal-to-noise ratio (SNR) (Figure 1(e)). With the latter, we decomposed the dataset into three components using non-negative matrix factorization (NMF) [3] and found the 1st component, NMF#0, resembles the Brg phase, as indicated by the abundance map and the spectral curve (Figure 2(a)&(d)). The Brg, therefore, was masked and segmented apart from the Fp and CaPv (Figure 2(b)&(c)). The Brg spectrum integrated from all the available pure Brg area has markedly improved the SNR of trace elements (Figure 2(e)&(f)). Both methods presented here allow a more reliable quantification for trace elements in Brg, and further lead to a more accurate trace element partition analysis between Brg and the melt.

[1] MJ Walter et al., Geochimica et Cosmochimica Acta, 68 (2004).
[2] MR Keenan (2007), Multivariate Analysis of Spectral Images Composed of Count Data, HF Grahn & P Geladi (Ed).
[3] S Jia et al., IEEE Transactions on Geoscience and Remote Sensing, 47 (2009).

Figure 1: (a) The HAADF image of the subsolidus mineral assemblages of the 71 GPa sample; (b) overlaid Mg and Ca EDXS elemental maps to reveal the distribution of Brg, Fp and CaPv; (c) the scree plot of PCA decomposition; (d) U Mα, (e) Nd Lα and Sm Lα comparisons between the original EDXS spectrum and the PCA-denoised spectrum.

Figure 2: (a) The abundance map, and (d) the spectrum of the first component of NMF decomposition; (b) a binary mask covering the pure Brg area; (c) the pure Brg area; (e) U Mα, (f) Nd Lα and Sm Lα comparisons between the original EDXS spectrum and the NMF-masked spectrum.

Figure 1

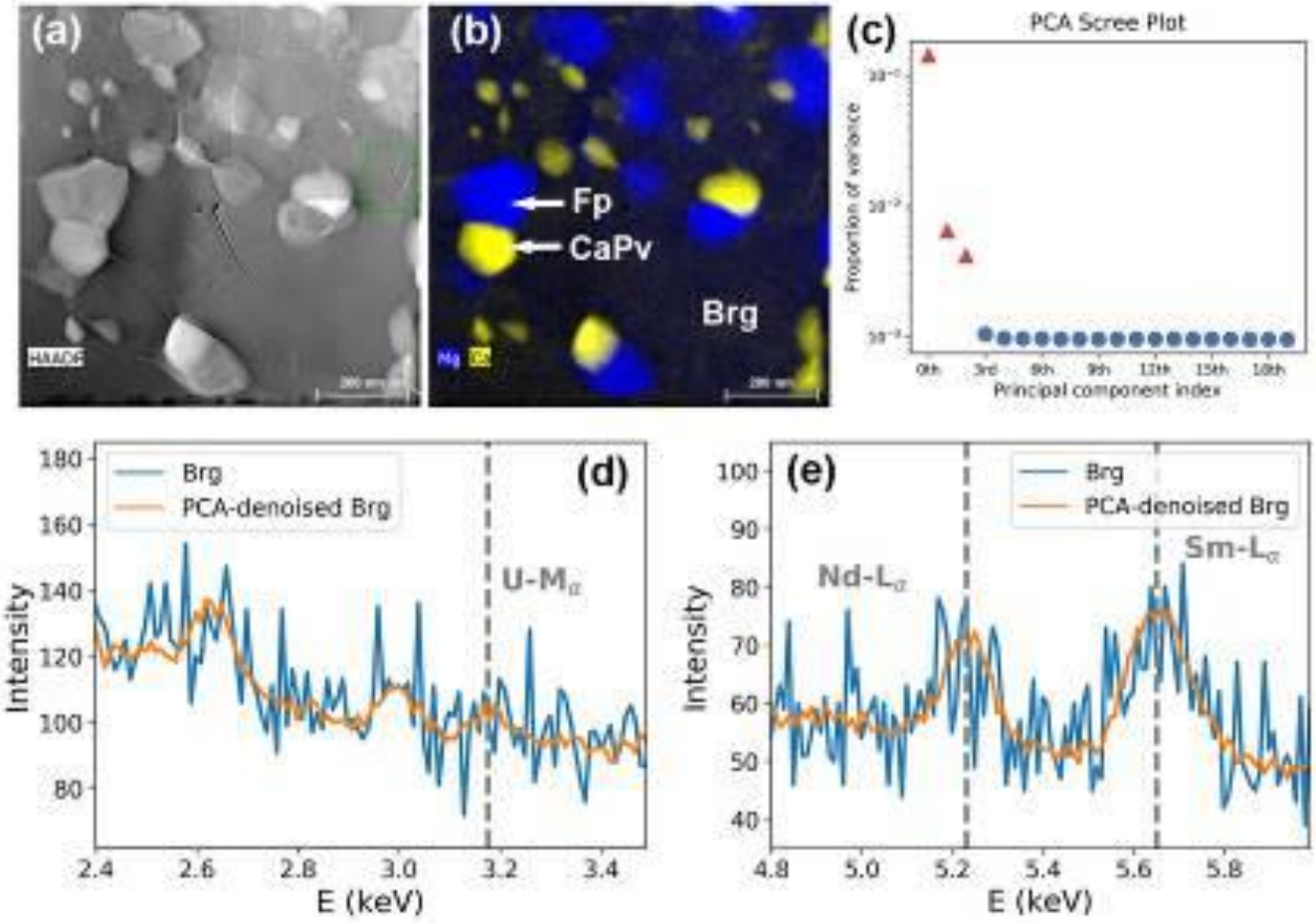

Figure 2

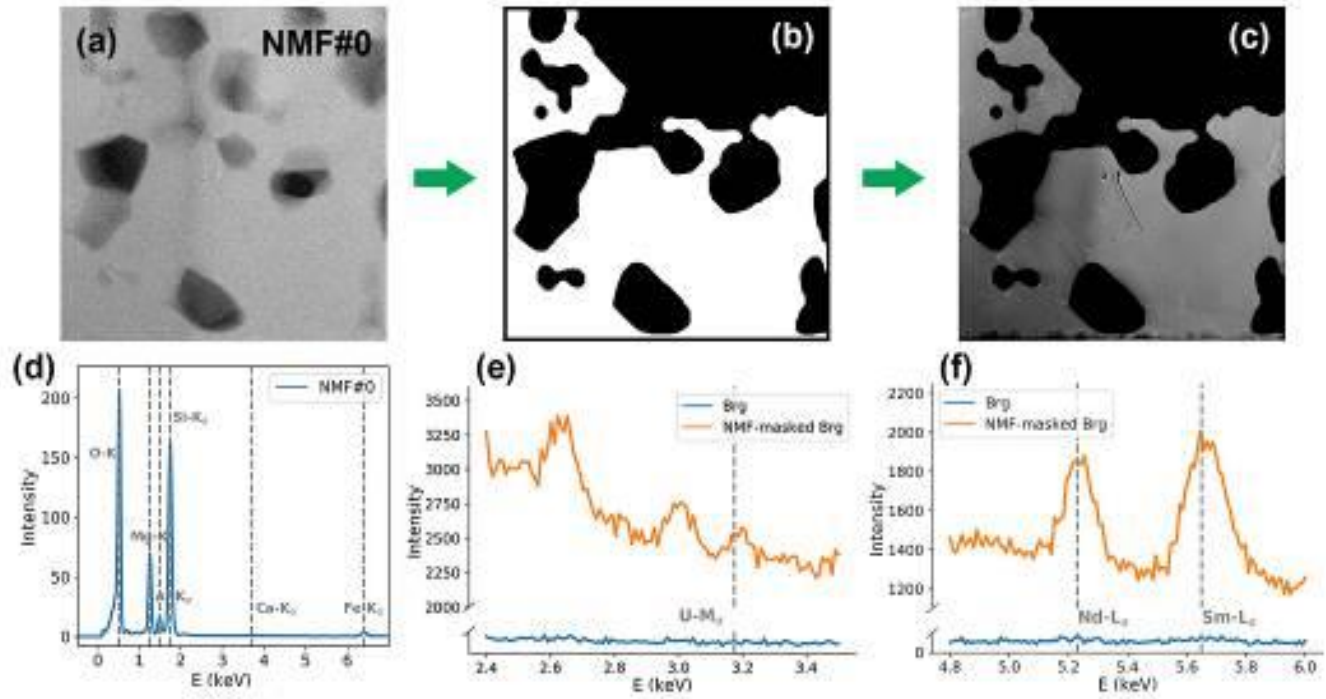

MS5.006
Transmission electron microscopy study on quenching induced domain structure and phase assemblage in $Na_{1/2}Bi_{1/2}TiO_3$-$BaTiO_3$ ceramics

A. K. Fetzer[1], A. Wohninsland[1], L. Kodumudi Venkataraman[1], H. J. Kleebe[1]

[1]Technical University of Darmstadt, Department of Materials and Earth Sciences, Darmstadt, Germany

Ceramic relaxor ferroelectric material systems find utilization in the area of energy storage and conversion. Their microstructural features comprise the presence of polarized units on the nanometer scale, so called polar nanoregions (PNRs), while conventional ferroelectrics are characterized by more long-range lamellar domain configurations. $Na_{1/2}Bi_{1/2}TiO_3$-based materials have gained considerable attention as lead-free alternative in order to replace lead-containing ferroelectrics due to environmental and health concerns [1]. Their dielectric and electromechanical properties render them a suitable alternative for high power ultrasonic applications [2].

Here, the relaxor ferroelectric (1-*x*)$(Na_{1/2}Bi_{1/2})TiO_3$-*x*$BaTiO_3$ (NBT-BT) system was studied by transmission electron microscopy (TEM) and high resolution X-ray diffraction [3]. Furnace cooled ceramics were compared to samples quenched in air from the sintering temperature. Quenching NBT-BT can be used as a tool to increase the depolarization temperature, where dielectric properties subside, and thus overcome the temperature limitations in the operational range.

The comparative TEM study demonstrates the change in domain structure and phase assemblage in NBT-BT (3, 6, 9 and 12 mol. % BT) using bright- and dark-field imaging techniques and selected area electron diffraction (SAED). The domain structure exhibits an increase in lamellar domain fraction upon quenching, which becomes in particular apparent for NBT-3BT and -6BT, where the domains in the furnace cooled state are characterized by an irregular structure or the absence of a lamellar domain contrast in the relaxor composition, respectively. For NBT-6BT, located at the morphotropic phase boundary (MPB), the average pseudocubic structure changes towards more pronounced rhombohedral and tetragonal phases. In NBT-3BT, a second rhombohedral phase emerges in addition to the *R*3*c* symmetry, exhibiting a herringbone domain configuration. In order to investigate the effect of quenching on poled specimens, quenched and furnace cooled NBT-6BT was poled prior to TEM sample preparation, where the quenched and poled composition features an increased tetragonal phase fraction and an even further pronounced lamellar domain contrast. In-situ TEM heating experiments show the development of the quenching induced structure with temperature. In summary, the structural changes featuring the development of a long-range ferroelectric domain morphology confirm the observed stabilization of ferroelectric order upon quenching NBT-BT.

[1] Bell, A. J. & Deubzer, O. Lead-free piezoelectrics - The environmental and regulatory issues. *MRS Bulletin* 43, 581–587 (2018).
[2] Tou, T., Hamaguti, Y., Maida, Y., Yamamori, H., Takahashi, K. & Terashima, Y. Properties of $(Bi_{0.5}Na_{0.5})TiO_3$-$BaTiO_3$-$(Bi_{0.5}Na_{0.5})(Mn_{1/3}Nb_{2/3})O_3$ Lead-Free Piezoelectric Ceramics and Its Application to Ultrasonic Cleaner. *Jpn. J. Appl. Phys.* 48, 07GM03 (2009).
[3] Fetzer, A.-K., Wohninsland, A., Hofmann, K., Clemens, O., Kodumudi Venkataraman, L. & Kleebe, H.-J. Domain structure and phase evolution in quenched and furnace cooled lead-free $Na_{1/2}Bi_{1/2}TiO_3$-$BaTiO_3$ ceramics. *Open Ceramics* 5, 100077 (2021).

MS5.P001
Combination of microscopic techniques for carbon analysis in Quartzite

M. Danneberg[1], K. J. Hünger[1]

[1]Brandenburg University of Technology Cottbus - Senftenberg, Building materials and construction chemistry, Cottbus, Germany

Introduction: The deposition of foreign matter is typical of natural structures. It can influence the chemical reactivity of solid materials. In addition to electrochemical changes, the microstructure can be deformed, leading to strained areas, for example. Most chemical reactions that can be affected by such changes are surface controlled. Therefore, a detailed knowledge of the surface state and possible changes is crucial. A combination of microscopic techniques is used to characterize the surface state of quartzite where carbon deposits are observed.

Objectives: Reflected light microscopy is used to obtain an initial overview of the sample. Grains can be differentiated and areas such as contact zones between grains or fracture zones can be classified. Combined with polarized light microscopy, grains can be categorized by getting an overview of potentially strained areas. This classification allows selection of specific areas for Raman and confocal analysis. Raman analysis is used to quantify the carbon content in the potentially strained areas, while confocal microscopy is performed to characterize the surface properties.

Materials and Methods: The used samples are thick and thin sections made of quartzite rock. The reflected and polarized light microscopy was made using a Zeiss LSM-700. For confocal analysis a 3D Optical Profiler PLμ NEOX from Sensofar was used. Raman analysis was performed with a Thermo Fisher DXR Raman microscope with a high-resolution grating (1800 lines/mm) and a 532 nm laser. The data presented are baseline corrected.

Results: There are several locations where carbon deposits and resulting strains can be expected. Strains can be released by cracks. It is possible that fractures are located next to undamaged quartz grains (Figure 1, position 1), indicating deposits in the surrounding grains. Contact zones (position 2) may also contain strains due to deformation that occurred during rock genesis. High pressure and temperature can cause lattice deformation and support the transport of carbon into the quartz structure. Different interference colors shown at position 3 may be caused by different crystal orientations or crystal defects.

Figure 1: Left hand reflected light micrograph, right hand polarized light micrograph

Figure 2: Left hand distribution of Raman intensity layered with the gray image from reflected light microscopy / right hand confocal micrograph of initial state

After the initial overview, Raman measurements are performed in selected areas of Quartz thin and thick sections. New unexpected signals at 1350 and 1600 cm^{-1} are found as it can be seen in the Diagram in Figure 2 left hand uper right corner. These Raman signals of carbon were found, distributed in solid quartz grains, as it is shown in the 2D-mapping in Figure 2 left hand. The initial state of the samples surface is recorded by confocal microscopy, as shown in Figure 2 right hand.

Conclusions: With the combination of the microscopic techniques used, the distribution of the deposited carbon in the quartzite grains could be better described. Such areas are possibly the origin for stress states and thus for a higher chemical potential. Accurate characterization of the surface state of quartzite is important for its reactivity. Dissolution experiments will show whether the carbon found has an influence on the dissolution behavior of quartzite and can be used as an indicator for strain states.

Figure 1

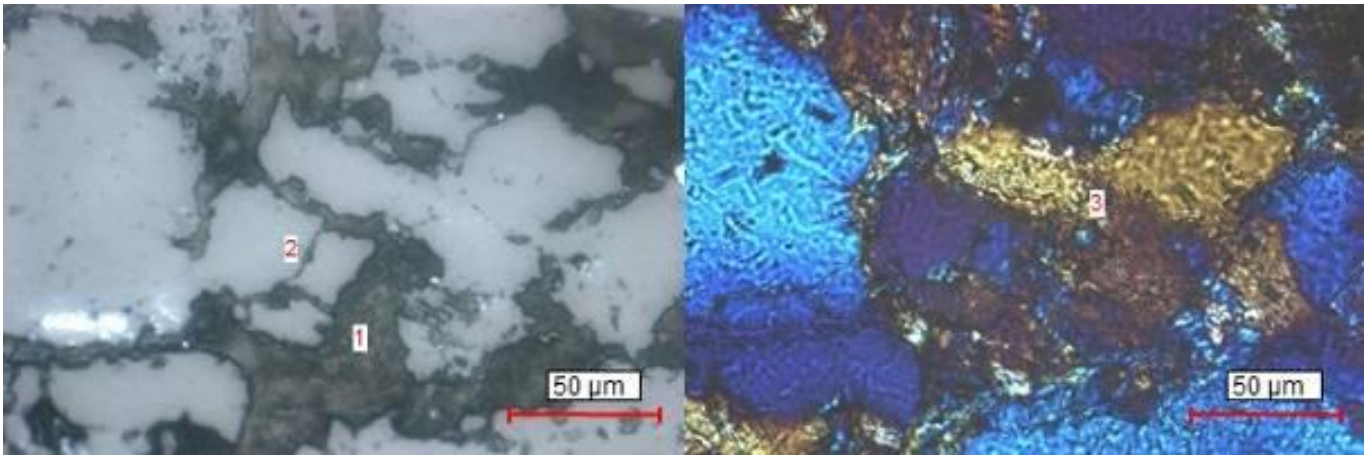

Figure 2

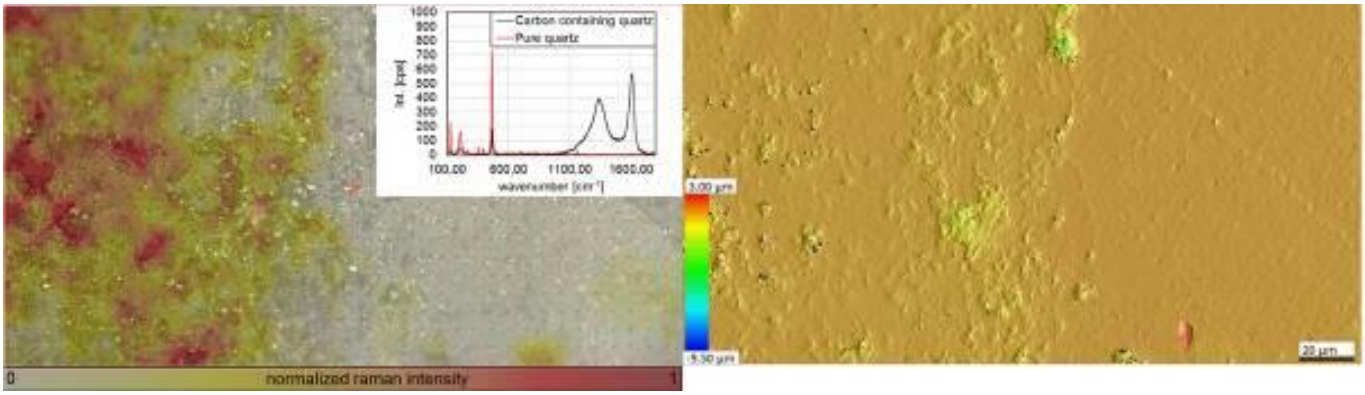

MS5.P003
REE enrichment and implications to REE mineralogy in the Tošići-Dujići bauxite deposit, Dalmatia Inland, Croatia

N. Tomašić[1], A. Čobić[1], M. Bedeković[1], S. Miko[2], N. Ilijanić[2], M. Matošević[3]

[1]University of Zagreb, Faculty of Science, Department of Geology, Zagreb, Croatia
[2]Croatian Geological Survey, Zagreb, Croatia
[3]INA-Industrija nafte d.d., Zagreb, Croatia

Introduction: Bauxite is a rock used primarily as raw material in production of aluminium. Along with major mineral constituents like gibbsite, boehmite, hematite, goethite, anatase and kaolinite, bauxite contains various metals like rare earth elements (REE), which are either associated with major mineral phases or are contained in accessory mineral phases. REE are typically enriched in the Mediterranean bauxites, sometimes reaching several thousand mg/kg in deeper horizons. This can trigger REE authigenic mineralization. An easy identification of REE minerals (minerals containing REE as major constituents) in bauxites is hampered by their low content, small size and dispersion throughout the samples.

Objectives: The bauxite deposit in Tošići-Dujići, Dalmatia Inland, Croatia, shows an enrichment of REE, reaching up to 3500 mg/kg in its deeper horizons. Such a REE content outreaches an average bauxite REE abundance of the area several times. Also, there is a significant enrichment of heavy REE (HREE), which is in contrast to usual prevalence of light REE (LREE) in the local bauxites. Thus, it is interesting to investigate origin of such a REE distribution and relate it to REE mineralogy in the rock. The research was funded by European Institute of Innovation and Technology (EU body supported from Horizon 2020 research and innovation programme) through KAVA 17089 REEBAUX.

Materials & methods: The bauxite samples were collected at six horizons of the former bauxite exploitation pit at the locality. All samples were analyzed for major and trace elements using ICP-MS after lithium borate sample decomposition. The samples were also treated by aqua regia and solute analyzed by ICP-MS, so that a fraction of REE in residual mineral phases could be determined. A correlation analysis of total and individual REE abundances with major chemical constituents was performed in order to determine REE preferences toward major or refractory mineral phases in the samples. Major minerals in the samples were determined by X-ray powder diffraction. The samples of two horizons with the highest REE concentrations were prepared for SEM-EDS analysis in order to identify occurrence of REE minerals. SEM analysis was performed by JEOL JSM-6510 LV and Oxford INCA X-act EDS system.

Results: REE abundances in the analyzed samples range from 959-3496 mg/kg. XRD yields boehmite, gibbsite, hematite, goethite, anatase and kaolinite as major mineral phases. Around 32-58% of REE are extracted from the samples by aqua regia (LREE 34-64%, HREE 44-67%). REE are positively correlated with P as well as HREE, while LREE are mostly correlated to Ca. LREE are most likely associated with carbonates, and HREE with phosphates, being also confirmed by the leaching data. SEM-EDS analysis confirms the occurrence of monazite-(Ce), xenotime-(Y) and florencite-(Ce). Occurrence of florencite-(Ce) is an indication of authigenic REE mineralization in the samples.

Conclusion: The SEM-EDS analysis provides an evidence on the occurrence of REE minerals in the Tošići-Dujići bauxite deposit. As supported by the correlation among REE and major constituents, the finding proves general criteria for occurrence of authigenic REE minerals in bauxites, although appearance and mineral morphology also suggest detrital origin of some REE minerals.

Figure 1: SEM images and related EDS spectra of monazite-(Ce) (left) and florencite-(Ce) (right).

Figure 1

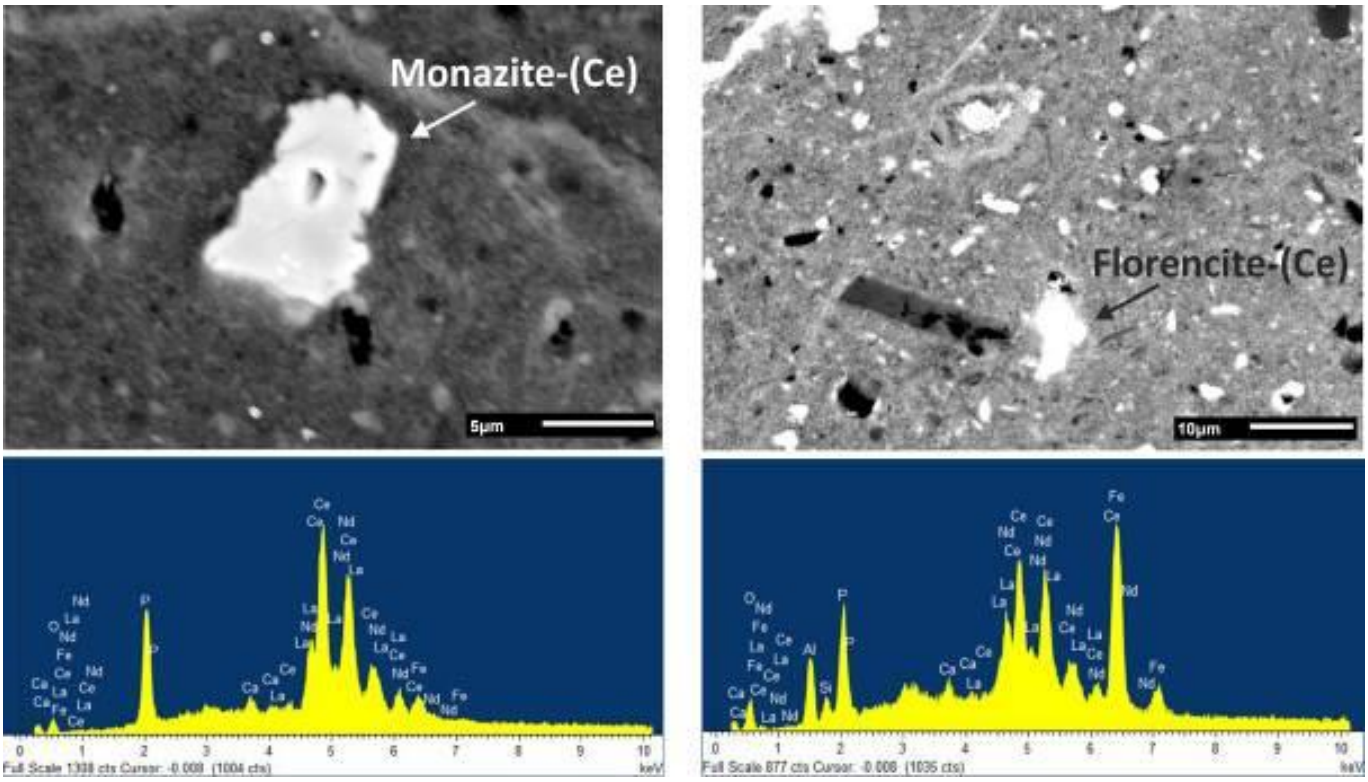

MS5.P004
Characterisation of hydrate phases composition of belite-calcium sulfoaluminate cements by SEM/EDS

M. Mrak[1], N. Daneu[2], F. Winnefeld[3], B. Lothenbach[3], S. Dolenec[1]

[1]Slovenian National Building and Civil Engineering Institute, Ljubljana, Slovenia
[2]Jožef Stefan Institute, Ljubljana, Slovenia
[3]Swiss Federal Laboratories for Materials Science and Technology, Dübendorf, Switzerland

Belite-calcium sulfoaluminate cements are promising low-energy and low-carbon cements, reducing CO_2 emissions up to 35 % compared to Portland cement and lowering the energy consumption during their production. The main phases of unhydrated belite-calcium sulfoaluminate cement are belite (C_2S) and calcium sulfoaluminate ($C_4A_3\$$), as well as ferrite (C_4AF) and calcium sulfate present as anhydrite, gypsum or bassanite [1,2]. One of the main factors influencing mechanical and physical properties and hydration of belite-calcium sulfoaluminate cements is temperature [3,4].

In this study, the influence of temperature on the composition of hydrate assemblage and microstructure of hydrated belite-calcium sulfoaluminate cement pastes was investigated by scanning electron microscopy.

Clinkers with two different belite-calcium sulfoaluminate-ferrite ratios were synthesized: i) phase composition of clinker KBA-1 with 65 wt. % C_2S, 20 wt. % $C_4A_3\$$, 10 wt. % C_4AF and ii) phase composition of clinker KBA-2 with 50 wt. % C_2S, 35 wt. % $C_4A_3\$$, 10 wt. % C_4AF. Clinkers were synthesized from limestone, flysch, bottom ash, titanogypsum, bauxite and mill scale. Furthermore, cements were prepared by adding gypsum to the clinkers, to reach a calcium sulfate to calcium sulfoaluminate molar ratio of 1.5. Water to cement ratio of 0.5 was used for cement pastes. Cement pastes were cured at the following temperatures: 5 °C, 20 °C, 40 °C and 60 °C and characterized after 150 days of hydration.

Cross sections of cement pastes were examined by scanning electron microscopy using backscattered electron mode (BSE). EDS analysis was carried out to identify the hydrate assemblage and chemical composition of hydration products. Over 100 points (EDS point analysis) per sample were analyzed (matrix of hydrated cement pastes). Graphs of different atomic ratios of elements (Al/Ca, S/Ca, Si/Ca and Ca/Si) were used to show trends in the composition of the hydrates and inclusion of minor elements. Cross sections of samples were studied in BSE mode to study the microstructure. Also, the morphology of hydrates was observed on freshly fractured surfaces of cement pastes using backscattered electrons.

The results showed that the chemical composition of hydrates varied with different temperatures, as well as with different phase compositions of cement clinker. The main identified hydrated phases were ettringite, monosulfate, C-S-H, strätlingite and hydrogarnet. The results revealed that temperature affected also the crystal size and shape of hydrates. At elevated temperatures (40 and 60 °C), the microstructure is less dense in comparison to lower temperatures.

Literature:
[1] E. Gartner, Cem. Concr. Res., 34 (2004) 1489-1498.
[2] F. Winnefeld, L.H.J. Martin, C.J. Müller, B. Lothenbach, B. Constr. Build. Mater. 2017, 155, 154–163.
[3] Y. Jeong, C. W. Hargis, S. C. Chun, J. Moon, Constr. Build. Mater., 166 (2018) 712-722.
[4] B. Lothenbach, T. Matschei, G. Möschner, F. Glasser. Cem. Concr. Res., 38 (2008) 1-18.

MS5.P005
Complex particle analysis of siliceous micro-milled sand powder using environmental scanning electron microscopy (ESEM)

M. Olbert[1], K. Závacká[1], V. Neděla[1], J. Jirák[1]

[1]Institute of Scientific Instruments, Czech Academy of Sciences, Environmental Electron Microscopy Group, Brno, Czech Republic

Micro-milled sands, also called quartz flours, are formed by modified silica sand with over 99% SiO2 content, what makes them an excellent raw material for wide spread of use (e.g. fillers in epoxy resin casting systems, glass fibers, ceramic enamels) [1, 2,].

Grain size and its distribution plays an important role in the micro-milled sands, since it defines an amount of used sand, for example, in epoxy system. Typically, laser diffraction is used for microparticles analysis. However, the environmental scanning electron microscopy (ESEM) has proven to be a suitable tool for combination of the size distribution evaluation and other morphological parameters of the grains. [2]

Siliceous sand samples dispersed onto carbon adhesive-coated aluminum mount [3] were observed in ESEM at low water vapor pressure (100 Pa), using scintillation and ionization detector. Images were subsequently analyzed in MountainsMap® SEM Topo software. First, contrast of image was increased. Then, using the "Binary thresholding" function, all particles in the image were detected. This function is based on contrast detection between bright particle and dark background. Finally, data were exported and analyzed. Detected grains are shown in Attachment 1.

From the graph analysis, we found that particles up to 2 μm in size made up almost 70% of the total number of analyzed sand particles. The amount of particles larger than 15 μm decreased rapidly and accounted for only 1.61% of the total number of particles. Images showing material contrast obtained by scintillation detector were used for particle distribution analysis. Images made by ionization detector were used for detailed topographic analysis (See Attachment 2, where image a) is made by scintillation detector and image b) is made by ionization detector).

This analysis technique provides new and complex information about microparticle structure, topography, morphology, material composition, shape, size, etc. A large number of these parameters can be statistically evaluated, what helps us to characterize the properties of the powder. The possibility to observe the samples with no additional coating, thus without unwanted charge artefacts, is an invaluable advantage provided by the ESEM. [4].

References:
[1] G. Wypych, Handbook of fillers (4th edition), (2016), p. 13-266.
[2] M. Linec, B. Mušič, Journal of Electronic Packaging, Transactions of the ASME, (2017), 11 p.
[3] O.P. Mills, W. I. Rose, Geosphere, (2010), p. 805-811.
[4] The project was supported by the Grant Agency of Czech Republic GA 19-08239S and GA 19-03909.

Figure 1

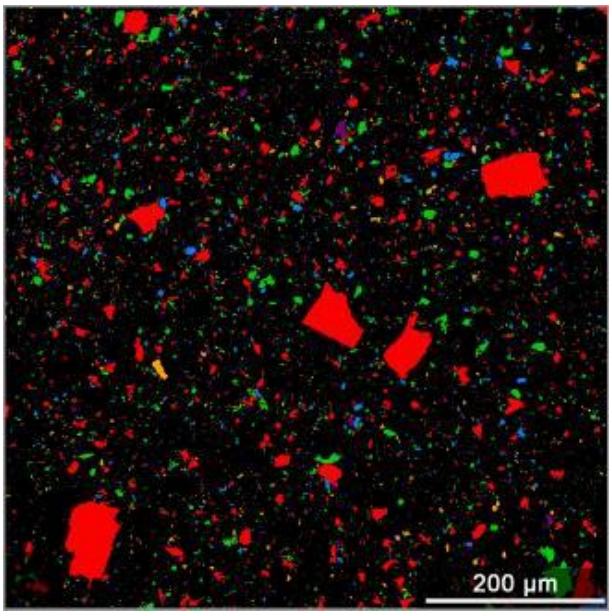

Figure 2

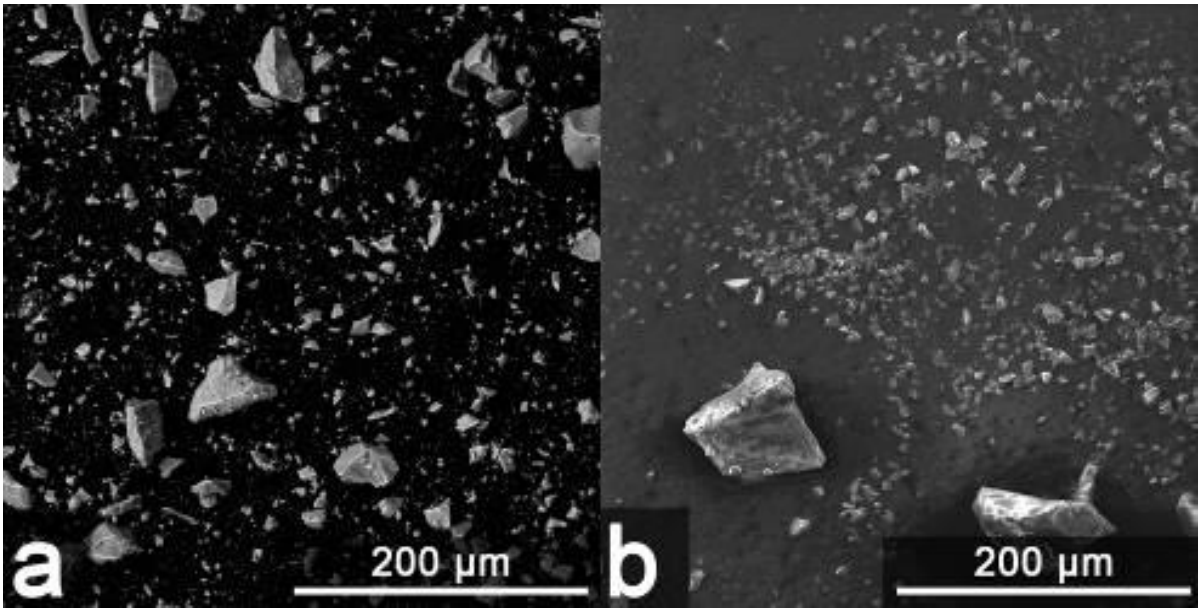

MS5.P006
Analysis of coating system using the scanning electron microscopy (SEM)

Z. Betáková[1], M. Mamoňová[1]

[1]Technical University in Zvolen, Department of Wood Science, Faculty of Wood Sciences and Technology, Zvolen, Slovakia

The life span of log houses is limited, but it mainly depends upon the appropriate construction solutions and design. The wood ageing is an irreversible change resulting from UV radiation, water and weather conditions. Wood can be also attacked by wood-destroying insects, wood-destroying fungi and molds are more common. Moreover, in specific situations, wood can be damaged by aggressive chemicals or fire. In order to minimize the timber weathering and damage by various biotic and abiotic factors, appropriate chemical treatment must be used.

The aim of the research was to analyze the quality of the naturally exposed surface adjustments of the log houses in Liptov area. The factors affecting the quality of the surface treatment and the coating systems used were theoretically analyzed. Subsequently, the quality of the surface treatment of log houses was analyzed using the SEM device TESCAN-VEGA TS 5130 (Tescan, Brno, Czech Republic). The effect of different surface treatments was microscopically evaluated and the coatings were microscopically analyzed.

The samples from the log houses in the Liptov region were used for electron microscopy (Figure 1). Each construction was unique in terms of material – tree species representation (spruce, fir larch, pine), in terms of decorative modification and the composition of the coating system. Electron microscopy was used to analyze the damaged surface of the samples. The surface morphology was monitored and the structures were highlighted using the secondary electrons to provide the best results. The backscattered electron (BSE) mode was used to highlight the fragile structures not located with the secondary electrons. The accelerating voltage used was 30.0 kV. The electron source was a tungsten filament.

The surface quality was analyzed at the beginning of the construction life and after several years (1-7 years) under outdoor conditions. Cracks, peeling of the coat, extrusion of the structure and bubbles on the sample surface were monitored (Figure 2). On the cross-sections, penetrating the coat and filling the lumens of spring tracheids in the surface layer (Figure 3, arrow A) was monitored as well as the difference between penetration into early and late wood, the interface of the coat system layers, contouring the surface and peeling off the coat over early and late wood (Figure 3, arrow B). The focus was given on the observation of sodium tetraborate crystals precipitating on the body of hyphae *Ophiostoma pini* on one of the samples (Figure 4).

As it was said in the introduction, the life span of the log houses is affected by chemical treatment and maintenance and it was also confirmed by our experiment. It is necessary to design and provide appropriate construction protection. Subsequently, chemical treatment must be provided correctly as well. It was found out that the best surface properties were achieved when applying the natural and ecological coatings based on oil and protective oil glazing as a top coat.

This work was supported by the Slovak Research and Development Agency under the contract No. APVV-16-0177.

Figure 2: Comparison of the surface with the coating system on the reference sample (Abies alba Mill.), using secondary (A) and backscattered electrons (B).

Figure 3: Detail on the cross-section, penetrating the coat and filling the lumens of early tracheids (*Pinus sylvestris L*) in the surface layer (arrow A) and peeling off the coat over early wood (arrow B).

Figure 4: Radial section of exposed sample (*Pinus sylvestris L*). The focus was given on the observation of borax salt crystals precipitating on the body of hyphae *Ophiostoma.*

Figure 1

Figure 2

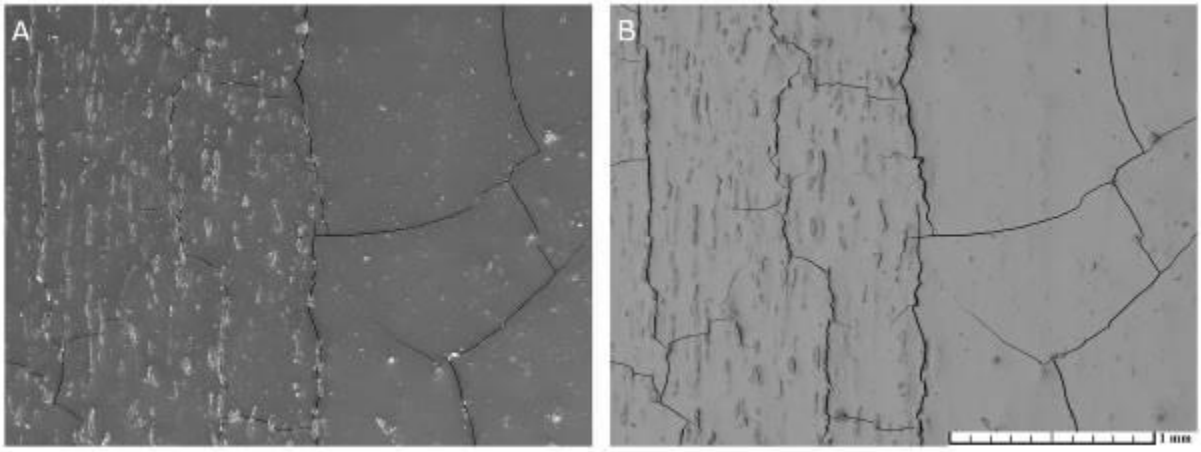

Figure 3

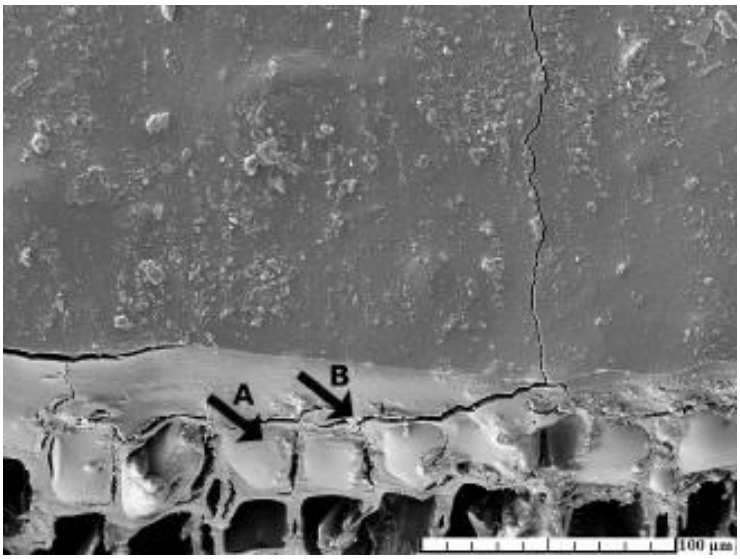

Figure 4

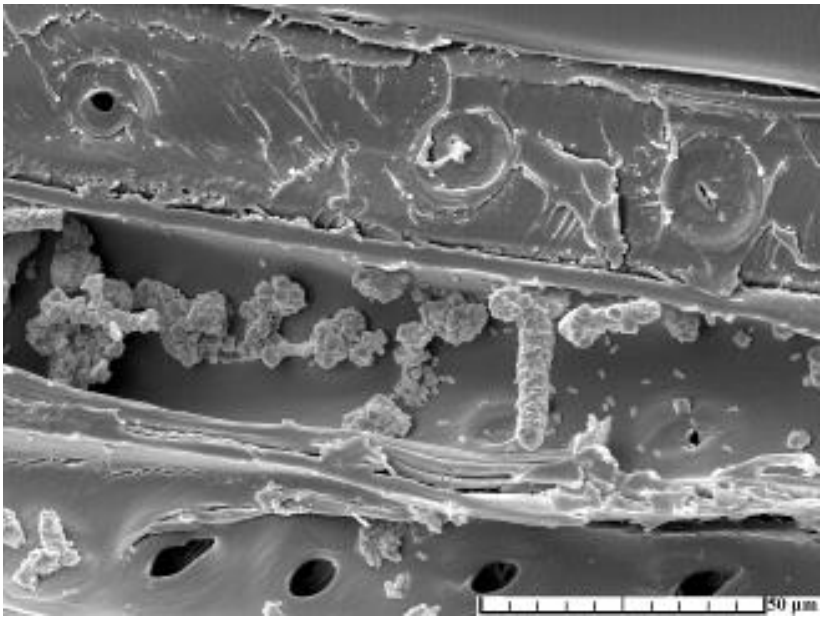

MS5.P007
TEM and SEM-comparative material analysis studies on vikings age brass ornaments from Ostriv and East Baltic Regions

K. Saleem[1], U. Schürmann[1], R. Shiroukhov[2], C. v. Bornheim[2], L. Kienle[1]

[1]Institute of materials science and engineering, technical Faculty, CAU Kiel, Kiel, Germany
[2]Zentrum für Baltische und Skandinavische Archäologie, Schleswig, Germany

Introduction: The material analysis techniques can affectively help understand the material culture in the past societies by analyzing typologically and chronologically synchronous artefacts. Development of advanced analytical methodology is leading to insights about the provenance of the artefacts and helps understand how people interacted with materials.

Objectives: In this study, analytical techniques namely Scanning Electron Microscopy (SEM) and Transmission Electron Microscopy (TEM) are used to analyze the elemental distribution on the surface and subsurface of the 11-12th century brass ornaments. These ornaments are compared with one another on basis of their chemical and structural compositions. This interdisciplinary research on archeological findings could help understand the difference between the intrinsic and extrinsic composition which, in turn, could highlight the true production mechanism of the artefacts.

Materials and Methods: The samples belong to the 11-12th centuries brass (copper alloys) such as fibulas and penannular brooches. The archaeological items were found by a group of Ukrainian scientists in Ostriv, Ukraine within the skeletal graves. These graves were often found at a depth of 0.5-1.0 m from the surface of the earth. Another set of samples were received from Berlin Museum for Pre- and Early History that belonged to the East Baltic regions. A comparative-material composition study was conducted between the artefacts excavated from the Ostriv cemetery and the samples belonging to East Baltic region. The surface of the ornaments was studied by means of Energy Dispersive X-Ray (EDX) Spectroscopy in a SEM (Zeiss Gemini Ultra55 Plus) and TEM was performed on lamellae prepared from the surface of the ornaments into a depth of ca. 10 µm via Focused Ion Beam (FIB). EDX point measurements and elemental maps were performed in STEM mode. TEM studies were performed in a Jeol JEM-2100 equipped with an EDX detector (Si/Li, EDAX).

Results: The SEM-EDX showed the presence of Copper rich brass with homogenous distributions of Copper and Zinc. Additional signals from Carbon, Iron, Lead, Chlorides, Sulphates, Oxides and Phosphates were also observed. Whereas, TEM-EDX on the FIB lamellae showed a difference in composition compared to the SEM-EDX with Cu and Zn as the major constituents with traces of organic compounds and oxidation. A varying trend of the elemental distribution was noticed between different surface layers of the ornaments. Higher contents of the Cu metal were observed with lesser zinc content in the regions presumably representing the original composition. The surface layer of the ornaments consisted of organic compounds along with Sulphates, Chlorides, Carbonates in a cloud-like pattern revealed by SEM-EDS elemental maps.

Conclusion: The advanced methodology for analyzing the archaeological artefacts is shown. The study demonstrated the comparison of chemical compositions between Vikings age brass artefacts from East Baltic and Ostriv. The authors further demonstrate the modification of surface and subsurface of the archaeological artefacts, that are buried under the soil since a thousand year. The EDS patterns marked differences in chemical compositions from outer to inner surface owing to the significantly modified outer surface, mainly at the interface with the geological environment.

Figure 1

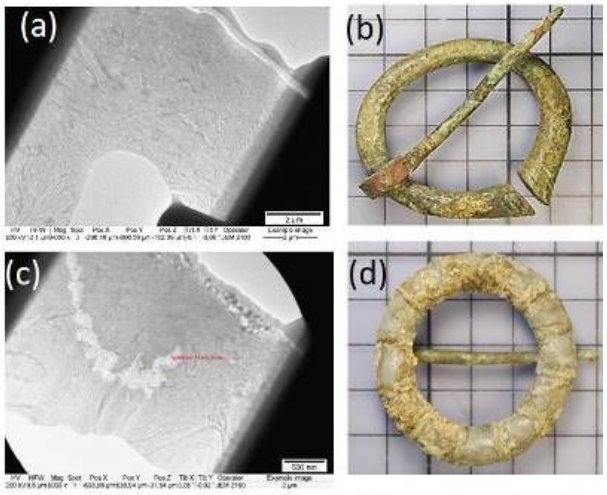

Fig.1 (a,c) FIB lamellae extracted from the (b,d) Round Brooches with ribbed bow from 11-12th century. Further analysis was conducted on the FIB lamellae using TEM-EDX and on the Brooches using SEM-EDX

MS5.P008
Microbiologically influenced corrosion (MIC) of steel – a study using correlative SEM, EDX and Raman microscopy

T. Planko[1], H. Fitzek[1], S. Eichinger[2], J. Rattenberger[1], G. Koraimann[3], H. Schröttner[1,4]

[1]Graz Centre for Electron Microscopy (ZFE), FELMI-ZFE, Graz, Austria
[2]Graz University of Technology, Institute of Applied Geosciences, Graz, Austria
[3]University of Graz, Institute of Molecular Biosciences, Graz, Austria
[4]Graz University of Technology, Institute of Electron Microscopy and Nanoanalysis, Graz, Austria

Direct costs due to corrosion worldwide amount to 3% and in some countries up to 5% of the GDP (gross domestic product) [1]. Microbiologically influenced corrosion (MIC) is responsible for 20% of all corrosion damage [2]. In this context, there is great interest in understanding MIC especially, since it has been shown that some microbes slow down the rate of corrosion [3], while others speed it up. The study of MIC is a challenge, as there is a wide range of potential microbes and mechanisms that make it difficult to find a generalized explanation of MIC.

During experiments in the Koralmtunnel iron oxidizing bacteria were found, to be part of a biofilm producing microbial community, dominated by a variety of eubacterial methanotrophs. Approximately 20% of the bacteria in the community are from the Gallionellaceae family. Typical exo-structures produced by these bacteria are shown in figure 1.

Figure 1: *Left:* SEM-image of typical microbial corrosion structures measured on a powder sample from the experimental setup in the Koralmtunnel (*Right*). The red mucus in the pipes is a biofilm, formed by the bacterial strain.

To study the effects of this strain, various steel samples, were placed in the experimental setup (figure 1, right). Both a macroscopic and microscopy analysis of the samples is performed. On the macroscopic side, the average corrosion rates and the pitting corrosion are determined. On the microscopic side a novel technique that combine Raman imaging with scanning electron microscopy (SEM) and energy dispersive X-Ray spectroscopy (EDX) (Zeiss Sigma 300 VP; Oxford X-Max 80; WITec RISE) is applied. The correlative Raman microscopy complements the established SEM-EDX combination with information about chemical bonds and oxidation states. An example of a correlative SEM-EDX-Raman measurement from the experimental setup with MIC is shown in figure 2 (Case- hardening steel 16MnCr5). The Raman spectra shows Graphite, hematite, amorphous maghemite, raw sienna, magnetite and sulfur oxide. The EDX-mappings shows the distribution of iron, carbon, chlorine, sulfur and silicon.

Figure 2: *Left (top):* SEM-image with Raman positions; *Right (top):* Raman spectrum: red à Graphite + hematite + amorphous maghemite; blue à Raw sienna + magnetite + graphite. On closer inspection, the band at 1000 1/cm does not turn out to be the band from the embedding agent (green spectrum), but rather a sulfur oxide. *Bottom:* EDX-mappings with the most important elements: iron, carbon, chlorine, sulfur and silicon.

In this contribution both the influence of MIC on the corrosion rates and the microscopic composition of the corrosion products as measured by correlative SEM-EDX-Raman will be discussed. A special focus will be on the specific benefits of the correlative SEM-EDX-Raman approach for the analysis of corrosion.

References:
[1] Biezma, M. V., and J. R. San Cristobal. "Methodology to study cost of corrosion." *Corrosion engineering, science and technology* 40.4 (2005): 344-352.
[2] Javaherdashti, Reza. "A review of some characteristics of MIC caused by sulfate-reducing bacteria: past, present and future." *Anti-corrosion methods and materials* 46.3 (1999): 173-180.
[3] Dubiel, M., et al. "Microbial iron respiration can protect steel from corrosion." Appl. Environ. Microbiol. 68.3 (2002): 1440-1445.

Figure 1

Figure 2

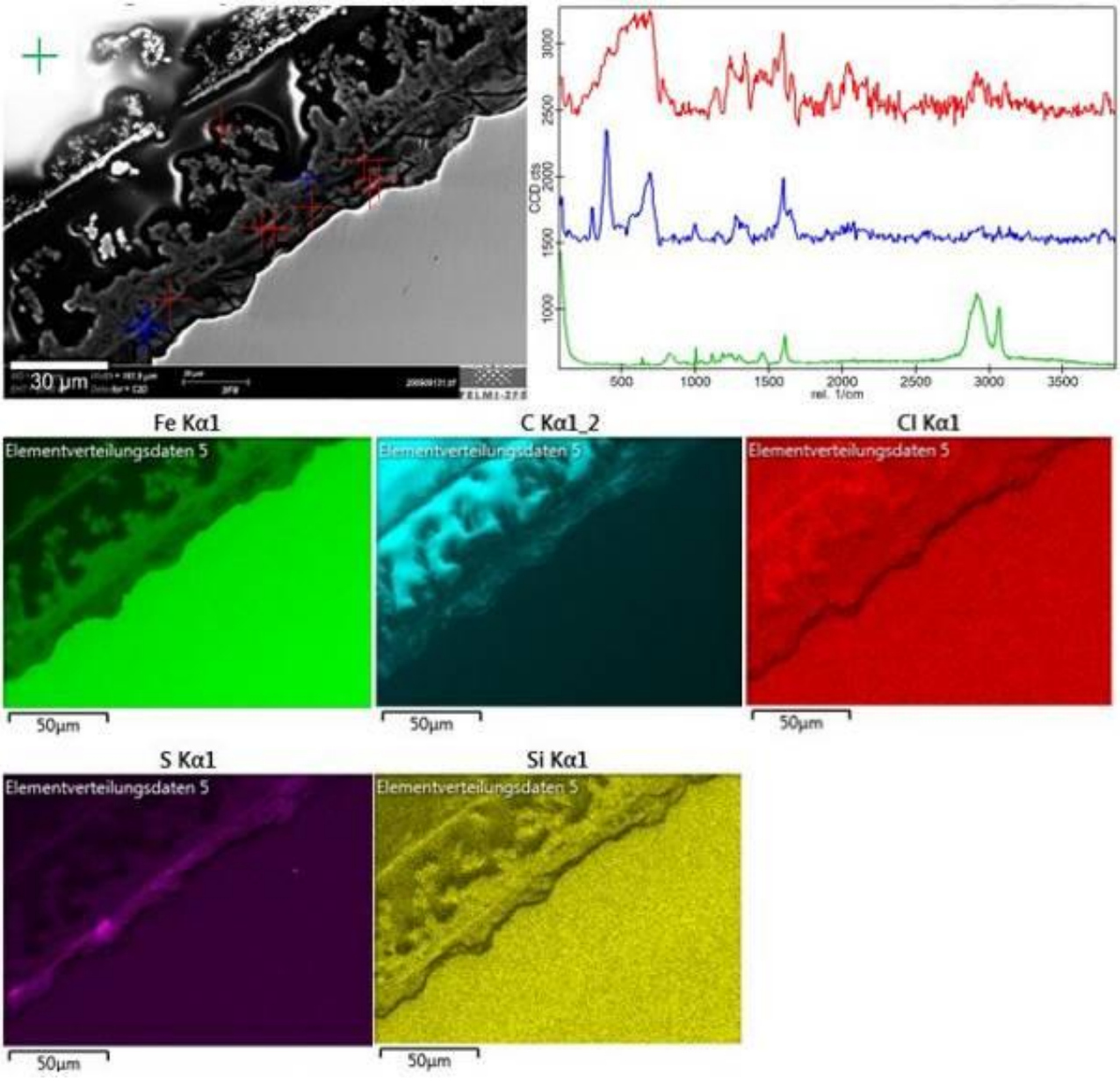

MS6.001-Invited
Grain boundary phases in pure and alloyed Cu –insights from advanced STEM

G. Dehm[1], N. J. Peter[1], T. Meiners[1], L. Frommeyer[1], T. Brink[1], T. Frolov[2], C. H. Liebscher[1]

[1]Max Planck Institute for Iron Research, Düsseldorf , Düsseldorf, Germany
[2]Lawrence Livermore National Laboratory, Livermore, United States

Grain boundaries belong to the most abundant imperfections in materials and impact material properties like strength, ductility, thermal or electrical conductivity. Their individual "fingerprint" on properties can vary and may even change by grain boundary (GB) phase transitions. The thermodynamic framework for GB phase transitions (sometimes called "complexion") has been derived in the last decades [1], but experimental evidence at the atomic structure level is scarce.

A prominent example for a GB phase transformation reported in literature is the symmetric ∑5 [100] GB in Cu(Ag). Molecular dynamics (MD) simulations revealed a structural change at 800K [2], a temperature where in experiments a change in GB diffusivity was observed [3]. In this talk we want to report on our recent experimental findings of GB phase transitions in pure Cu [4] and Cu alloyed with Ag [5, 6], Ta, and Zr [7] using atomic resolved scanning transmission electron microscopy (STEM).

We analyzed an asymmetric ∑5 [100] GB in pure Cu and with Ag as well as ∑19b [111] tilt grain boundaries in pure Cu and for the systems Cu(Ta) and Cu(Zr).

The STEM results revealed that in case of an asymmetric ∑5 [100] GB in bulk Cu, segregation of Ag leads to a faceting transition. Interestingly, the facets differ in chemical composition [6,7]. The ∑19b [111] tilt Cu GB was found to coexist with two different structural atomic motifs. MD simulations reveal similar energies for both GB phases, which require shear stresses for the phase transition [5]. The experimentally observed coexistence is metastable and may be caused by the low mobility of the line defect separating both GB phases. Upon alloying with Zr a very similar behavior is found as for pure Cu, while Ta nucleates as precipitates rather than decorating the GB by segregation [8].

The examples show that GB phase transitions can occur in a pure metal, which itself remains single phase fcc. Chemical induced GB phase transitions can deviate from a classical McLean type segregation behavior, possessing different elemental partitioning for different nano-facets. These findings call for deeper analyses of the local property changes imparted by individual grain boundaries on material properties.

Acknowledgement: GD acknowledges financial support from the European Research Council (ERC) through Grant No. 787446 – GB-CORRELATE

References:
[1] Cahn, J., W., J. Phys. Colloques, 1982. 43(C6): p. C6-199-C6-213.
[2] Frolov, T., et al., Nat Commun, 2013. 4: p. 1899.
[3] Divinski, S.V., et al., Physical Review B, 2012. 85(14): p. 144104.
[4] Meiners, T., et al., Nature, 2020. 579(7799): p. 375-378.
[5] Peter, N.J., et al., arXiv preprint arXiv:2009.00432, 2020.
[6] Peter, N.J., et al., Physical Review Letters, 2018. 121(25): p. 255502.
[7] Meiners, T., et al., Acta Materialia, 2020. 190: p. 93-104.

MS6.002
Complexion formation in solid oxide cells – inter-diffusion across the electrode/electrolyte interface

F. P. Schmidt[1,2], H. Tuerk[3,4], T. Götsch[2], F. Girgsdies[2], A. Hammud[2], D. Ivanov[2], I. C. Vinke[5], L. G. J. De Haart[5] R. Eichel[5,6], K. Reuter[3,4], R. Schlögl[1,2], A. Knop-Gericke[1], C. Scheurer[3,4], T. Lunkenbein[2]

[1]Max Planck Institute for Chemical Energy Conversion, Department of Heterogeneous Reactions, Mülheim an der Ruhr, Germany
[2]Fritz Haber Institute of the Max Planck Society , Department of Inorganic Chemistry, Berlin, Germany
[3]Technical University of Munich, Department of Chemistry, Munich, Germany
[4]Fritz Haber Institute of the Max Planck Society , Theory Department, Berlin, Germany
[5]Research Center Jülich, Institute of Energy and Climate Research, Fundamental Electrochemistry (IEK-9), Jülich, Germany
[6]RWTH Aachen University, Institute of Physical Chemistry, Aachen, Germany

Introduction: The intermittent output of renewable energy sources such as wind or solar power requires efficient and long-living technologies to store electrical energy and provide it at later point in time. Solid oxide cells (SOCs) fulfill both, they can store electrical energy operated as electrolysis cell (SOEC) and provide it in fuel cell mode (SOFC), reaching more than 80% efficiency and enabling mid-term chemical storage capacity. However, long-term use is not yet feasible predominantly due to degradation, which occurs at the oxygen electrode, therefore limiting the oxygen evolution reaction (OER).

Materials & Methods: Here we combine state-of-the-art electron microscopy (STEM-EDX, HR-STEM) and theoretical calculations (Monte Carlo, MC) to atomically resolve the interface between the solid electrolyte (yttria-stabilized zirconia with 8 mol% Y2O3, YSZ) and lanthanum strontium manganite (LSM, (La0.8Sr0.2)0.95MnO3) 3- δ.[1] In addition, the electronic structure of both materials is analyzed in detail using electron energy-loss (EELS) and X-ray absorption spectroscopy (NEXAFS), as well as density functional theory (DFT).

Results: STEM-EDX reveal the presence of a significant amount of inter-diffusion between YSZ and LSM. Only strontium does not show any diffusion into YSZ, resulting in a shift of its intensity profile of approximately 0.8 nm with respect to all other elements. All this is in agreement with MC-based simulations that were used to theoretically model the YSZ/LSM boundary including the ion and site-specific swapping probabilities for the diffusion process. According to these simulations, this diffusion region is slightly amorphous. By means of atomically resolved STEM, this reduction of long-range order was observed experimentally for an approximately 1.5 nm wide slab on the YSZ side of the boundary, clearly distinguishing it from the bulk fluorite structure. We identified this slab as a so-called complexion, i.e. a self-limiting interlayer that is stabilized by its confinement between the two adjacent bulk phases, rather than an infinitely sharp interface. These complexions have recently also been discovered in other energy-related systems such as battery materials [2] and might explain why the YSZ/LSM interface is not as prone to the formation of lanthanum or strontium zirconates as other perovskites. [3]

Conclusion: We found a 1.5 nm wide complexion layer between electrolyte (YSZ) and electrode (LSM), which may help to understand the origin of the function of SOFCs and SOECs in greater detail. This will guide how to fine tune the SOC performance and to increase the chemical stability of such SOCs.

References:
[1] H. Tuerk, F.-P. Schmidt, T. Götsch et al. in preparation
[2] J. Timmermann et al. Phys. Rev. Lett. 2020, 125, 206101
[3] W. Wang et al. *J. Electrochem. Soc.* 2006**,** *153,* A2066

Figure 1: (a) High-resolution BF-STEM image of the YSZ/LSM grain boundary with a superimposed cation density from the MC simulation (inset) in [110] zone axis (BF-STEM) and semi-reciprocal plot of the micrograph (FFT). The white dashed lines enclose the area of the complexion. (b) Monte Carlo simulation showing the formation of a complexion in between the bulk phases YSZ and LSM and its"s corresponding increase of amorphisation. (c) EDX maps of elements as indicated by the insets, with LSM on top of YSZ and (d) the corresponding elemental profiles for experiment and simulation. The dashed lines indicated again the complexion area.

Figure 1

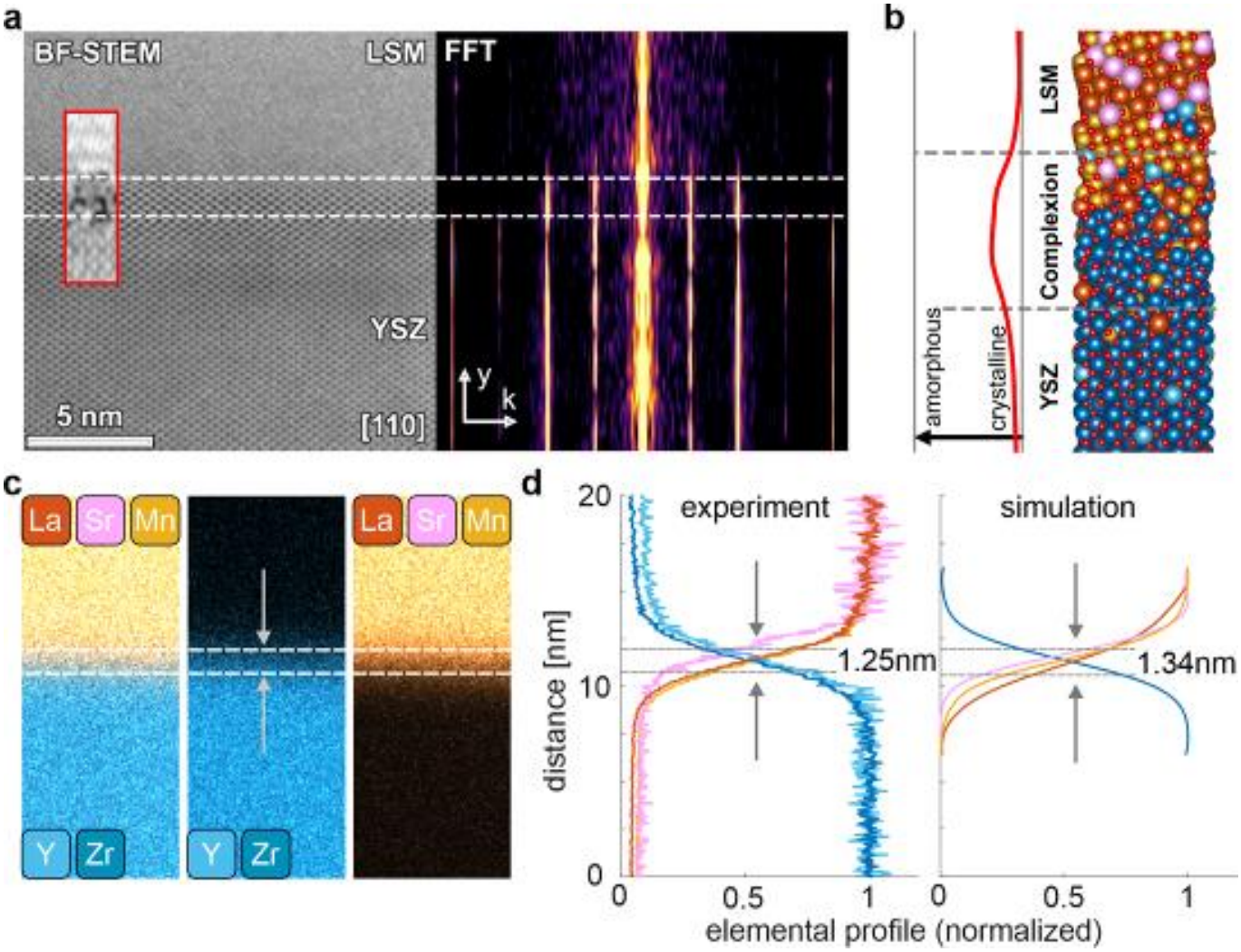

MS6.003
A quantitative analysis of *in situ* grain boundary sliding inside a transmission electron microscope

I. U. Haq[1], P. Cordier[2], H. Idrissi[3], D. Schryvers[1]

[1]University of Antwerp, Physics, Antwerp, Belgium
[2]Université de Lille, Lille, France
[3]Université Catholique de Louvain,, Louvain-la-Neuve, Belgium

The Earth's upper mantle is principally composed of olivine mineral (Mg,Fe)2 SiO4. In order to understand its dynamics, it is crucial to know the rheological properties of olivine. Various deformation mechanisms in olivine, such as diffusion creep, dislocation creep and dislocation accommodated grain boundary sliding are reported in the literature [1]. However, olivine does not have enough slip systems to satisfy the Von Mises criterion. Other intergranular deformation mechanisms could thus play a role to accommodate strains. Recently a stress induced grain boundary sliding mechanism in olivine based on grain boundary amorphization was proposed [2]. Still, quantitative investigation of the elementary processes involved in such mechanism is still missing. In this work, olivine samples synthesized from mixed, cold-pressed, and sintered SiO2 and Mg(OH)2 powders were used. A PI-95 TEM Pico-indenter holder with a Push-to-Pull (PTP) device (Bruker. Inc) was used to perform quantitative in-situ TEM tensile tests. To observe grain boundary mechanisms, bi-and tri-crystal nano tensile test olivine specimens were prepared from bulk pristine olivine by focused ion beam (FIB). We show that the specimens deform exclusively by grain boundary sliding while observing evidence of stress-induced amorphization in the sliding grain boundaries. Moreover, quantification of grain boundaries sliding is achieved using nano-digital image correlation (DIC) measurements using Pt nanoparticles deposited at the surface of the PTP specimens during FIB.

Figure 1: (a) HRTEM image of a grain boundary in bulk olivine before deformation. (b) HRTEM image of a sample deformed in a Paterson press, showing an amorphous grain boundary. Fast Fourier transforms are shown in the insets, confirming the olivine and amorphous structures.

Figure 2: In situ TEM nanomechanical testing (a) PTP device used for quantitative in situ TEM tensile experiments. The compression, with the diamond flat puncher indenter, of the semicircular end on the left opens the middle gap shown in (a). (b) The sample before fracture showing a grain boundary at the top right corner of the tensile sample, (c) showing the fractured and slided grain boundary after the deformation.

[1] Nishihara, Y. et al. "Rheology of fine-grained forsterite aggregate at deep upper mantle conditions" *J. Geophys. Res. Solid Earth*, vol. 120, pp. 1195–1209, 2014, doi: 10.1002/2014JB011376.
[2] Samaee, V. Cordier, P. Demouchy, S. Bollinger, C. and Gasc, J. Sylvie, D. Carline B. Julien, G. Sanae, K. Mussi, A. Schryvers, D. & Idrissi, H. "Stress-induced amorphization triggers deformation in the lithospheric mantle," *Nature*, vol. 591, 2021, doi: 10.1038/s41586-021-03238-3

Figure 1

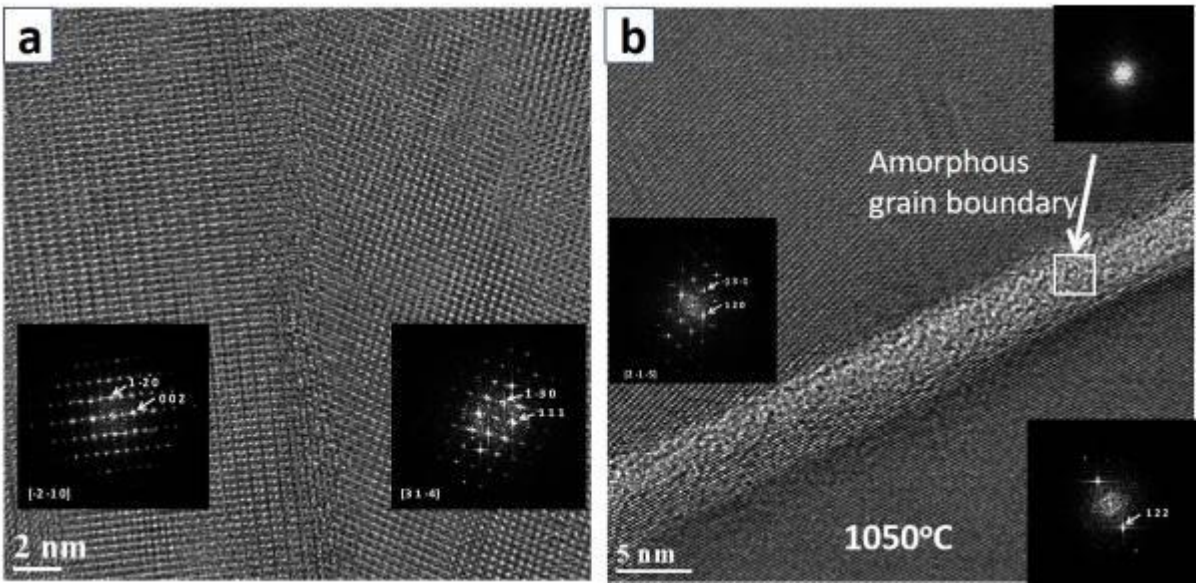

Figure 2

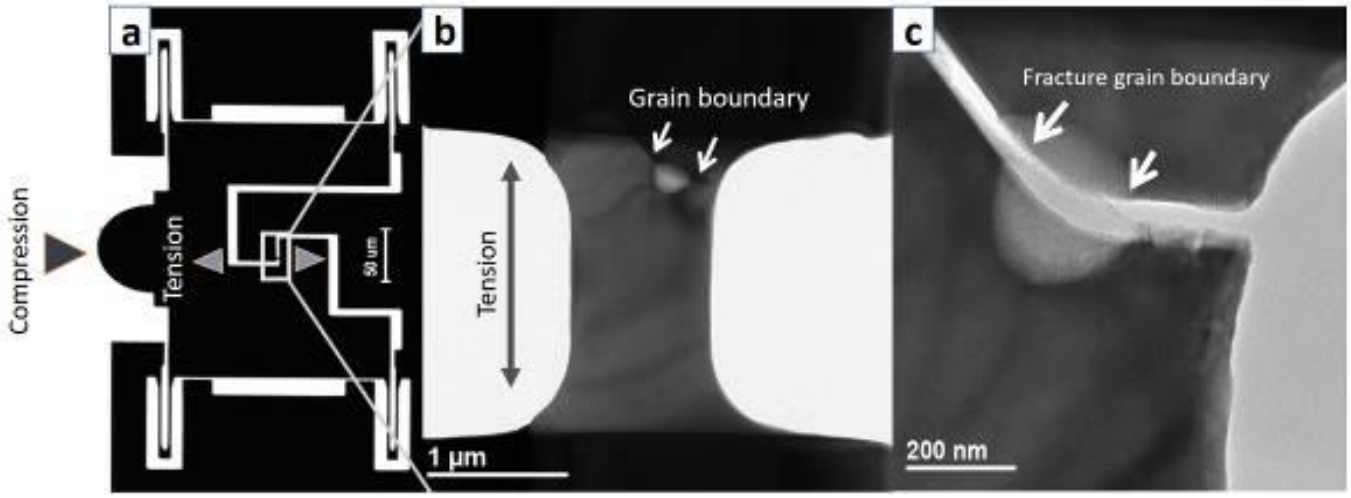

MS6.004-Invited
Twinning in minerals with the rutile-type structure: insights from TEM and EBSD

N. Daneu,[1] J. A. Padrón-Navarta,[2] F. Barou,[2] G. Dražić,[3] A. Rečnik[4]

[1]Advanced Materials, Jožef Stefan Institute, Jamova cesta 39, Ljubljana, Slovenia
[2]Géosciences Montpellier, Université de Montpellier and CNRS, UMR5243, Montpellier, France
[3]Inorganic Chemistry and Technology, National Institute of Chemistry, Hajdrihova 19, Ljubljana, Slovenia
[4]Nanostructured Materials, Jožef Stefan Institute, Jamova cesta 39, Ljubljana, Slovenia.

Minerals with the rutile-type structure, e.g. rutile, TiO_2 or cassiterite (Cst), SnO_2, are excellent model systems for studying twinning by growth because of the many morphologically different types of growth twins that occur in these compounds; from simple contact twins on (101) and (301) planes, to multiple polysynthetic (lamellar) twins and multiple cyclic twins with coplanar or alternating crystallographic setting [*see* Fig. 3.3.6.9 in Ref. 1]. Growth twins accelerate crystal growth in the direction of the twin boundary (TB) plane and also affect crystal morphology through the development of reentrant angles. Both effects have a potential of being exploited for the synthesis of materials with tailored properties, therefore, it is important to understand the formation mechanism of different types of growth twins. It has been shown that reticulated 2D structures composed of twinned rutile domains form by topotaxial replacement or by epitaxial growth on a structurally related precursor phase, e.g. ilmenite $FeTiO_3$ with the corundum-type structure [2]. In order to resolve the formation mechanism of a twin boundary, atomic-scale analyses of the twin interfaces are necessary. In this contribution we will present the results of our studies of growth-twins in synthesised polycrystalline SnO_2-based ceramics and natural cassiterite twins from Viloco mine in Bolivia.

Characteristic for SnO_2- based ceramics co-doped with Co- and Nb-oxides (Fig. 1a) is a significant fraction of twins in the form of contact and multiple cyclic twins [3]. We used EBSD to study the nature of cyclic twins and developed an automated procedure for identification of crystallographically different types of twins from the common zone axis [4]; the [010] for the coplanar and the [111] for the alternating twins (Fig. 1b). The twin boundaries were studied by HAADF-STEM, which revealed non-uniform segregation of Nb and Co along the twin boundaries (Fig. 1c). This can be interpreted by epitaxial growth of SnO_2 on preliminary formed nanosized grains of structurally related $CoNb_2O_6$ columbite-type and $Co_4Nb_2O_9$ corundum-type phases in the initial stages of crystal growth and their later local dissolution into the matrix SnO_2. On the other hand, detailed analysis of twin boundaries in natural magnetic cassiterite crystals from Viloco mine in Bolivia (Fig. 2a) revealed the presence of many oriented nanosized inclusions in the matrix and at the twin boundary (Fig. 2b). The results have shown that the inclusions are magnetite and hematite and indicate that the formation of twins is by oriented growth on preliminary hematite nanoparticles in the orientation relationship (OR) $(101)_{Cst}$ $[010]_{Cst}$ || $(101)_{Hm}$ $[001]_{Hm}$.

The hematite nanoparticles were later reduced to magnetite [5] yielding the following OR $(101)_{Cst}$ $[010]_{Cst}$ || $(2\overline{11})_{Mt}$ $[111]_{Mt}$ observed in SAED patterns shown Figure 2c. The analyses of growth-type twins in minerals with the rutile-type structure indicate that their formation is related to oriented growth on a structurally related precursor phase, however, interpretation of the process is not always straightforward.

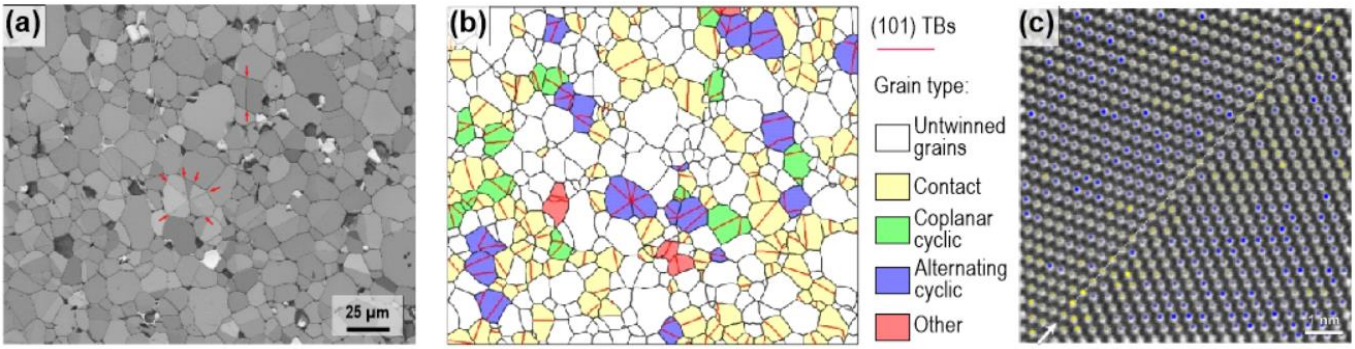

Figure 1: (a) Microstructure of SnO_2- based ceramics co-doped with CoO and Nb_2O_5 is composed of cassiterite grains with many (101) twin boundaries (red arrows). (b) The result of EDSD analysis revealed the presence of different types of twins in the sample. (c) HAADF-STEM analysis of a (100) TB (arrow) shows non-uniform distribution of Nb and Co near the interface.

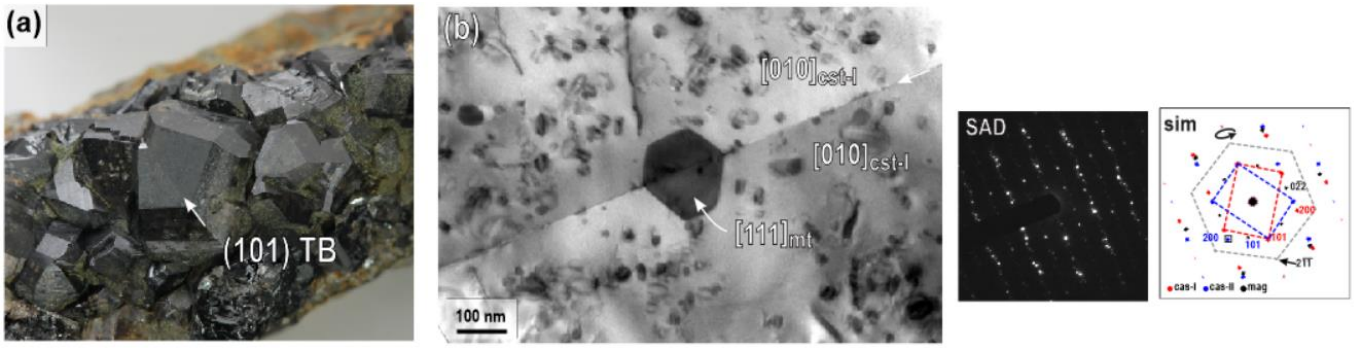

Figure 2: (a) Cassiterite crystals from Viloco mine in Bolivia are often twinned on (101) planes. (b) HRTEM/SAED analysis reveals the presence of oriented inclusions with large magnetite (Mt) particles along the interface.

References

[1] Hahn Th & Klapper H. *International Tables for Crystallography* 2006; D: 393–448.
[2] Rečnik A et al *Contrib Mineral Petrol* 2015; 169:19.
[3] Tominc S et al. *Ceram Int* 2018; 44:1603-1613.
[4] Padron Navarta et al. Acta Cryst. B 2020; B76:875-883.
[5] Kelly WmC & Turneaure FS. Economic Geology 1970; 65(6): 609-680.

MS6.005
Atomic structure and electron magnetic circular dichroism of individual rock salt structure antiphase boundaries in spinel ferrites

Z. Li[1,2,3], J. Lu[4,5], L. Jin[6], J. Rusz[7], V. Kocevski[7,8], H. Yanagihara[9,10], E. Kita[9], J. Mayer[6,11], R. E. Dunin-Borkowski[6] H. Xiang[4], X. Zhong[1,2,3]

[1]National Center for Electron Microscopy in Beijing, Key Laboratory of Advanced Materials (MOE), The State Key Laboratory of New Ceramics and Fine Processing, School of Materials Science and Engineering, Tsinghua University, Beijing 100084, China, Beijing, China
[2]Department of Materials Science and Engineering, City University of Hong Kong, Tat Chee Avenue, Kowloon, Hong Kong, China, Hong Kong, China
[3]Nanomanufacturing Laboratory (NML), Shenzhen Research Institute, City University of Hong Kong, Shenzhen 518057, People's Republic of China, Shenzhen, China
[4]Key Laboratory of Computational Physical Sciences (Ministry of Education), State Key Laboratory of Surface Physics, and Department of Physics, Fudan University, Shanghai 200433, China, Shanghai, China
[5]Department of Physics, Yancheng Institute of Technology, Yancheng, 224051, China, Yancheng, China
[6]Ernst Ruska-Centre for Microscopy and Spectroscopy with Electrons, Jülich, Germany
[7]Department of Physics and Astronomy, Uppsala University, P.O. Box 516, 75120 Uppsala, Sweden, Uppsala, Sweden
[8]Materials Science and Technology Division, Los Alamos National Laboratory, USA, Los Alamos, United States
[9]Department of Applied Physics, University of Tsukuba, Tsukuba, Ibaraki 305-8573, Japan, Ibaraki, Japan
[10]Tsukuba Research Center for Energy Materials Science (TREMS), University of Tsukuba, Tsukuba, Ibaraki 305-8573, Japan, Ibaraki, Japan
[11]Central Facility for Electron Microscopy, RWTH Aachen University, 52074 Aachen, Germany, Aachen, Germany

Introduction: Functional oxides are ubiquitous and exhibit a wide range of electric, magnetic, optical, and structural properties. Controlling of the defects and interfaces in thin-film devices are the new challenges in multifunctional oxides. Antiphase boundaries are the interfaces between two crystallographically identical regions with shifted phases. Based on previous studies, the correlation between existence of antiphase boundary and decreased saturation magnetization in oxides has been discussed [1, 2]. Due to the resolution limitation of magnetism measurement, it is difficult to investigate the structure-property relationship at high spatial resolution.

Objectives: Using electron magnetic circular dichroism (EMCD) technique with convergent probe size of 1.8 nm to reveal the localized magnetic property of antiphase boundary with a rock salt structure interlayer in inverse spinel NiFe2O4. Combing with atomic column resolution scanning transmission electron microscopy to achieve co-characterization of atomic structure and localized magnetic property.

Materials & Methods: EMCD, first experimentally verified by Schattchneider et al. [3], is a magnetism measurement method in a transmission electron microscope and is confirmed with the ability to reach spatial resolution better than 2 nm using convergent beam [4, 5]. This significant breakthrough enables us to study the magnetic properties of interfaces and boundaries on nanometer scale. In the meanwhile, our group have developed site-specific EMCD [6] and atomic plane resolved EMCD [7] in complex oxides such as spinel and double perovskite. Theoretical understanding of the magnetic degradation around APB is assessed by density function theory (DFT) calculations and dynamical diffraction simulation.

Results & Conclusion: Intensity analysis of antiphase boundary (APB) in HAADF (high angle annular dark-field imaging) STEM (scanning transmission electron microscopy) images suggests that only half of the octahedral interstices are occupied at the rock salt structure interlayer of a new type APB in NiFe2O4 with a relative translation of (1/4)*a*[011]. High-spatial-resolution EMCD have been used to experimentally demonstrate reductions of ~46.8%±8.2% and ~38.8%±14.5% in the EMCD strengths of Fe and Ni in APB, respectively, compared to perfectly ordered NiFe2O4 [8]. DFT calculations and dynamical diffraction calculations suggest that the reduced EMCD strengths result from the fact that Fe ions at the APB interlayer are antiferromagnetically coupled with each other, whereas Ni ions show a significant decrease in magnetic moment as a result of the formation of low-spin state Ni4+ (d6) ions. Our combined approach of using element specific EMCD under high-spatial-resolution and first-principles calculations to resolve and identify the atomic structure and magnetic coupling of an individual APB in spinel ferrite is applicable to studies of a broad spectrum of other defects in magnetic materials.

References:
[1] D. T. Margulies et al., Phys. Rev. Lett., 1997, 79, 5162
[2] K. P. McKenna et al., Nat. Commun. 2014, 5, 5740
[3] P. Schattschneider et al., Nature, 2006, 25, 441
[4] P. Schattschneider et al., Phys. Rev. B, 2008, 78, 104413
[5] L. Jin et al., Adv. Mater. Inter. 2016, 3(18), 1600414,
[6] Z. Q. Wang et al., Nat. Commun. 2013, 4, 1395
[7] Z. C. Wang et al., Nat. Mater. 2019, 18, 19-23
[8] Z. Li, et al., Adv. Funct. Mater., 2021, in press.

MS6.006
Plagioclase-Magnetite interface characterization at atomic scale

G. Bian[1], V. Roddatis[2], O. Ageeva[1,3], R. Abart[1]

[1]University of Vienna, Department of Lithospheric Research, Vienna, Austria
[2]Helmholtz Centre Potsdam, German Research Centre for Geosciences, Potsdam, Germany
[3]Institute of Geology of Ore Deposits, Petrography, Mineralogy, and Geochemistry, Russian Academy of Sciences, Moscow, Russian Federation

Magnetite (Mt) is the main carrier of natural remanent magnetization (NRM) in rocks. Needle and lath shaped, µm and sub-µm sized Mt micro-inclusions with systematic crystallographic- and shape orientation relationships (CORs, SORs) to their host often occur in plagioclase (Pl) from oceanic gabbro. The size effect leads to particularly stable NRM, but the CORs and SORs may cause bulk magnetic anisotropy of the Mt-Pl inclusion-host assemblage and bias its NRM. Understanding the Mt-Pl CORs and SORs is thus essential for paleomagnetic reconstructions.

The observed Mt-Pl CORs and SORs have been rationalized based on correlated optical- and scanning electron microscopy (SEM) including electron back scattered diffraction (EBSD) [1]. It was found that Mt is elongated perpendicular to the densely packed Mt{222} oxygen planes, which is, in turn, parallel to one of several Pl planes with high oxygen density and nearly identical d-spacing, including Pl(112), Pl(-312), Pl(150), Pl(1-50), etc. In addition, the Mt-Pl interfaces follow important oxygen layers in both Mt and Pl. Due to the beam sensitivity of Pl, direct imaging of the Mt-Pl interface is rarely reported. Here we present the microstructure of the Mt-Pl interface along the inclusion elongation direction using high angle annular dark field scanning transmission electron microscopy (HAADF-STEM) and integrated differential phase contrast (iDPC-STEM) techniques.

Two TEM foils were prepared from a needle shaped Pl(112)n_Mt and a lath shaped Pl(-312)n_Mt micro-inclusion using a focused Ga-ion beam (Ga-FIB). The inclusions are orientated in the foil with the elongation direction in the plane of the foil and the Mt-Pl interfaces edge on.

STEM showed that the Pl(112)n-Mt-Pl interface is perfectly straight and parallel to Pl(1-50)/Mt{110} with some local steps. Fast Fourier Transformation (FFT) revealed that its elongation is Mt<111>, which is aligned with the Pl(112) pole to within 1.5°. Edge dislocations at the Mt-Pl interface indicate that the 1.4% lattice misfit between Mt{222} and Pl(112) is at least in part accommodated by misfit dislocations.

The Mt-Pl interface of the Pl(-312)n-Mt-Pl inclusion is devoid of steps, perfectly straight and parallel to Mt{110}/Pl(150). FFT confirms a good fit of oxygen layers across the Pl-Mt interface along the elongation direction. The 2.4% difference in the d-spacings between Pl(-312) and Mt{222} is likely accommodated by edge dislocation every about 42'nd Mt{222} plane at the Mt-Pl interface. Moreover, lattice fringes in iDPC-STEM images reveal coherence between Pl(22-1) and Mt{111} planes without misfit dislocations. This additional coherence may explain the particularly strong alignment of Mt{111} and Pl(-312) reflected by the EBSD data.

We conclude that the elongation directions of the Mt inclusions correlate with the alignment of important oxygen layers of both Mt and Pl across the interfaces that are parallel to the elongation direction. The interfaces are parallel to low index lattice planes with high oxygen density in both phases. Minor lattice mismatch is likely accommodated by misfit dislocations at the interfaces. The well-organized interface structure ensures low interfacial energy and is a viable explanation for the observed Mt-Pl CORs and SORs.

Figure **a** Atomic structure of the straight Mt-Pl interface of Pl(112)n-Mt micro-inclusion; **b** iFFT of Mt-Pl interface with Mt{111} and Pl(112) lattice planes alignment denoted; c Atomic structure of the straight Mt-Pl interface of Pl(-312)n-Mt micro-inclusion; **d** iFFT of Mt-Pl interface with Mt{111} and Pl(-312) lattice planes alignment denoted.

Acknowledgement: Funding by FWF grant I 3998-N29 and RFBR grant 18-55-14003 is acknowledged.

Reference:
[1] Ageeva et al (2020) Contrib. Mineral. Petrol. 175(10), 1-16.

Figure 1

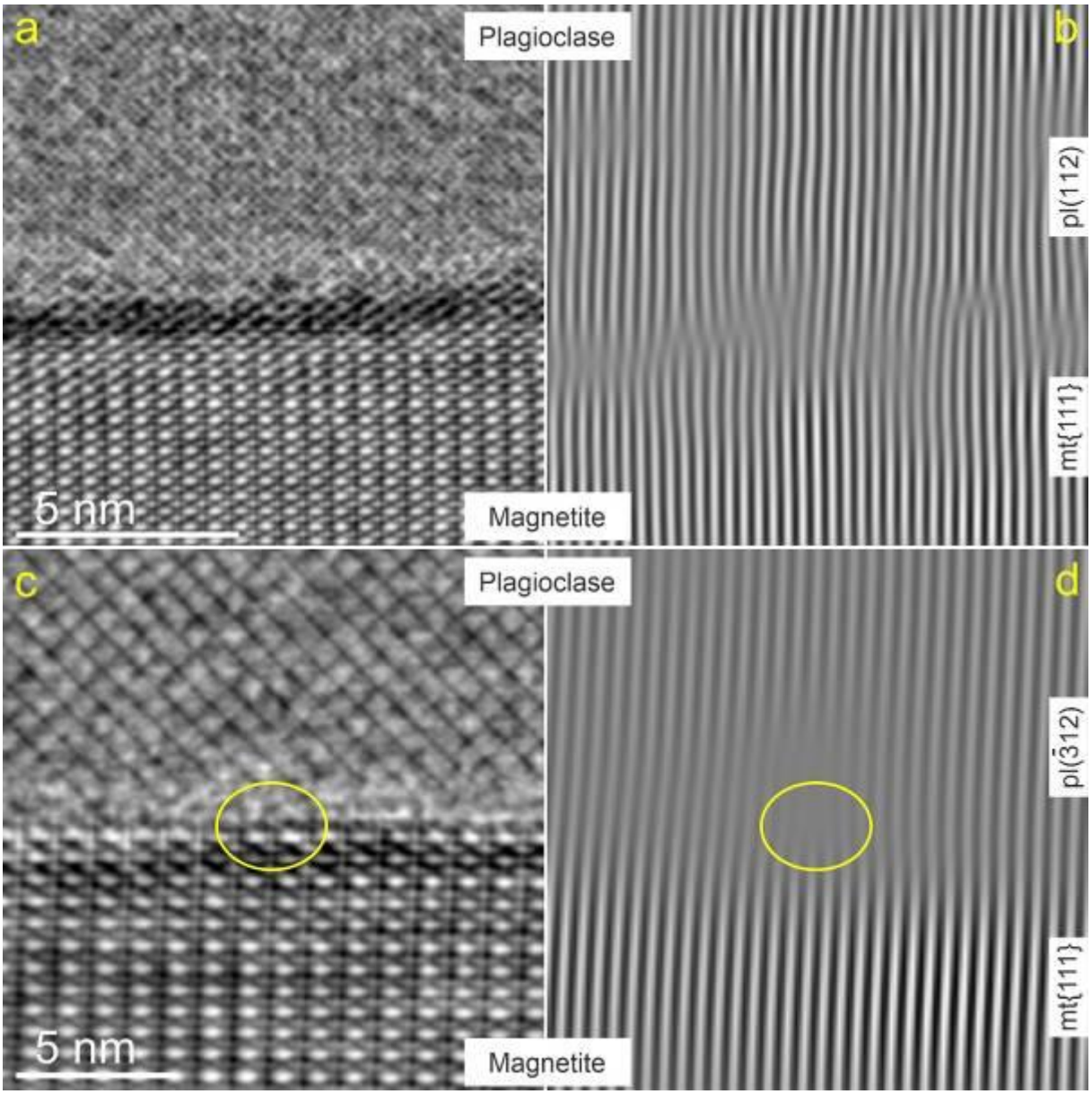
a
Plagioclase
b
pl(112)
mt{111}
5 nm
Magnetite
c
Plagioclase
d
pl(3̄12)
mt{111}
5 nm
Magnetite

MS6.P001
NiAu phase decomposition in twinned supersaturated thin films

M. Landes[1], J. Schubert[1], M. Dierner[1], T. Przybilla[1], J. Will[1], E. Spiecker[1]

[1]Friedrich-Alexander University Erlangen-Nuremberg (FAU), Chair of Micro- and Nanostructure Research, Erlangen, Germany

Because of the high atomic size mismatch, the miscibility gap in the Ni-Au system covers the whole concentration range reaching up to 810°C. During annealing inside the miscibility gap, high-angle grain boundaries (GBs) typically act as nucleation centers and will further induce discontinuous phase decomposition. In this context, fast material transport along the GBs enables migration of the GBs into one of the neighboring grains, leaving behind a characteristic decomposed lamellar structure [1]. A microstructure build of low energy GBs like twins could suppress this decomposition pathway. Here, crystalline substrates like c-plane sapphire can act as template for the growing microstructure of the deposited film. In this study, we utilize this concept, demonstrate the successful growth of supersaturated twinned NiAu thin films and further investigate the influence of twin boundaries on the decomposition behavior.

To tackle the problem 40 nm bilayer thin films with a composition of 30 at% Au (70 at% Ni) are fabricated by electron beam physical vapor deposition on a polished {0001} oriented α-Al2O3 substrate. First, the alloyed state is achieved by annealing the deposited films above the miscibility gap at 850°C for 30s and subsequently quenching to room temperature via a rapid thermal annealing furnace. Second, the phase-separation is monitored with sequential annealing steps at 600°C within the miscibility gap and subsequent site-specific ex situ characterization via Scanning Electron Microscopy after 2, 5, 15 and 30 minutes, respectively.

Figure 1 compares the initial state of phase decomposition after 2 min to that after 30 min. After 2 min a typical pattern of Ni and Au enriched areas is visible at the GBs, which is more established but similar after 30 min. This is in interesting since thin films with a random GB orientation exhibit already complete discontinuous phase separation within a few minutes. The origin of this difference in the phase decomposition behavior stems from the twinned microstructure as described above. Electron Back Scattered Diffraction (EBSD) confirms the type of proposed microstructure (Figure 2). A line cut perpendicular to the elongated grains reveals the typical 60° angles between the twinned grains. Further analysis yields a mean grain size of about 600 nm in width and several micrometers in length. The grains align along atomic terraces on the sapphire surface that result from a small miscut of <0.1° and annealing at 1000°C for several hours [2]. As twin boundaries have a lower energy, the necessary material transport is not as fast as for high-energy GBs, hence not supporting GB migration to form the characteristic lamellar structure. As a result no phase decomposition is visible in the area between the twins, spinodal decomposition, however, is likely to occur on the nanoscale [3].

Figure 1: Phase separation when annealing at 600 °C for a) 2 minutes and b) 30 minutes. The scale bar is valid for both images

Figure 2: a) EBSD Euler angle map of the sample heated for 30 sec at 850°C showing grains with only two different orientations. b) Linescan to extract the misorientation of the grains to each other (white arrow). The 60° misorientation confirming the formation of Twin boundaries.

[1] Manna, I., Pabi, S.K., Gust, W. *International Materials Reviews* 2001 *46/2* pp. 53-91
[2] Ryosuke Yamauchi *et al* 2012 *Jpn. J. Appl. Phys.* **51**
[3] Perovic, A., Garrett, J., Kirkaldy, J.S. *Scripta Materialia* 2009 60 pp. 1020-1022

Figure 1

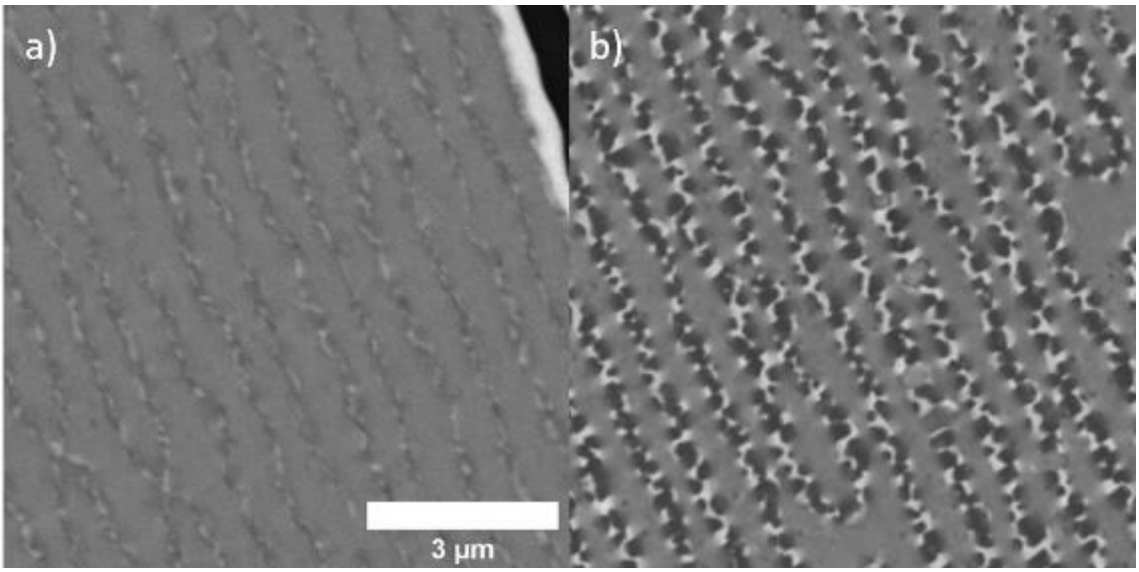

Figure 2

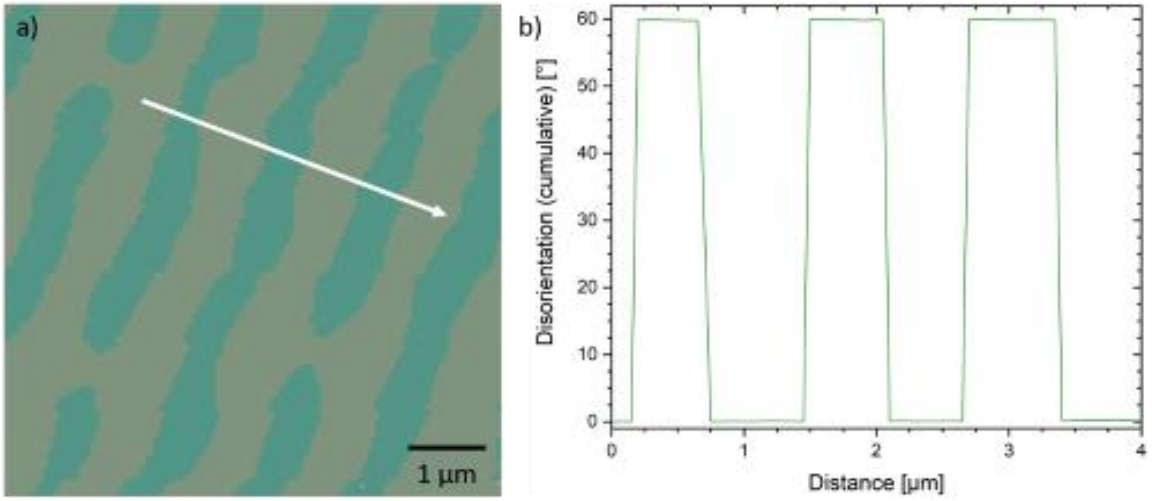

MS6.P002
Use of micro-cantilevers to evaluate dissimilar vitreloy 105 to grade 2 titanium laser welds

D. Sorensen[1], E. Hintsala[2], J. Pischlar[3], J. Stevick[4], B. Li[3], D. Kiener[5], D. Stauffer[2], J. Myers[6], H. Jin[3], J. Liu[3]
T. Keenan[3], A. Ramirez[7], R. Ritchie[8]

[1]Boston Scientific, Maple Grove, United States
[2]Bruker Nano Surfaces, Eden Prairie, United States
[3]Medtronic, Brooklyn Center, United States
[4]Hummingbird Scientific, Olympia, United States
[5]Montanuniversitat, Leoben, Austria
[6]University of Minnesota, Minneapolis, MN, United States
[7]Ohio State University, Columbus, United States
[8]University of California, Berkeley, Berkeley, CA, United States

Question: The medical device industry places unique demands upon materials, such as high fatigue resistance and biocomatability. One promising candidate material is bulk metallic glass like Vitreloy 105, which has several attractive properties including high strength, corrosion resistance, low density and near net shape molding. However, joining of this material to other common structural materials (grade 2 titanium being the most ubiquitous) is not well understood. A variety of techniques were utilized to optimize the welding schedule, but the focus is drawn here on micro-cantilever experiments to evaluate the ductility across the weld region, and in the base materials.

Methods: A series of welds which had different parameters such as laser peak power, pulse width, table speed, etc., were evaluated. A definitive screening design experiment [1] was utilized to determine which had significant effects and produce a final optimized weld. With the mixing of two alloys in a microscale weld, a variety of phases can be formed, including brittle intermetallics. To confirm the performance of the final optimzed weld schedule, microcantilevers were fabricated with focused ion beam machining and tested utilizing a Hysitron PI88 PicoIndenter in situ SEM.

Results: In the weld zone, a variety of responses were found from brittle to quas-brittle to ductile, which was correlated to the local chemistry and microstructure. We did not determine K_{Ic} fracture toughness values inside the weld zone, as the mixed metal after rapid solidification was unique and validity of K or J could not be established. However, it was discovered that Ziroconium-rich particles occurred in some regions of the weld, which appeared to toughen the material and provides a path towards further future improvements in weld quality. The results from the Vitreoly 105 base material was also interesting as the micro-scale fracture of bulk metallic glass has not been well-studied. Bulk metallic glasses are well known to have size-dependent and complex fracture behaviors [2]. We observed catastrophic shear banding in all our cantilever specimens. Using J-integral methods, we estimated the toughness of these cantilevers at approximately 9 MPa-$m^{1/2}$ and were able to determine that the J-dominance requirement was approximately met, which was further confirmed by finite element analysis. This is much lower than bulk values in comparable alloys, which can reach over 100 MPa-$m^{1/2}$. The difference in behavior was proposed to be due to a lack of extrinsic toughening mechanisms which were observed at the bulk scale, such as crack bridging or deflection.

Conclusions: The micro-cantilever experiments provided a unique and localized measure of the material toughness across a micro-scale laser weld and into the base materials, which would have been difficult to determine by any other method.

Figure 1: a) Dimensions of a cantilever used in this experiment; b) location of cantilevers across the weld zone; load-displacement responses grouped as (c) ductile (d) quasi-brittle (e) brittle and a representative SEM micrograph for each type, respectively (f-h).

[1] B. Jones, C. Nachtsheim, A class of three-level designs for definitive screening in thepresence of second-order effects, J. Qual. Technol. 43 (1) (2011) 1–15.
[2] B. Gludovatz, S.E. Naleway, R.O. Ritchie, J.J. Kruzic, Size-dependent fracture toughness of bulk metallic glasses, Acta Mater. 70 (2014) 198–207.

Figure 1

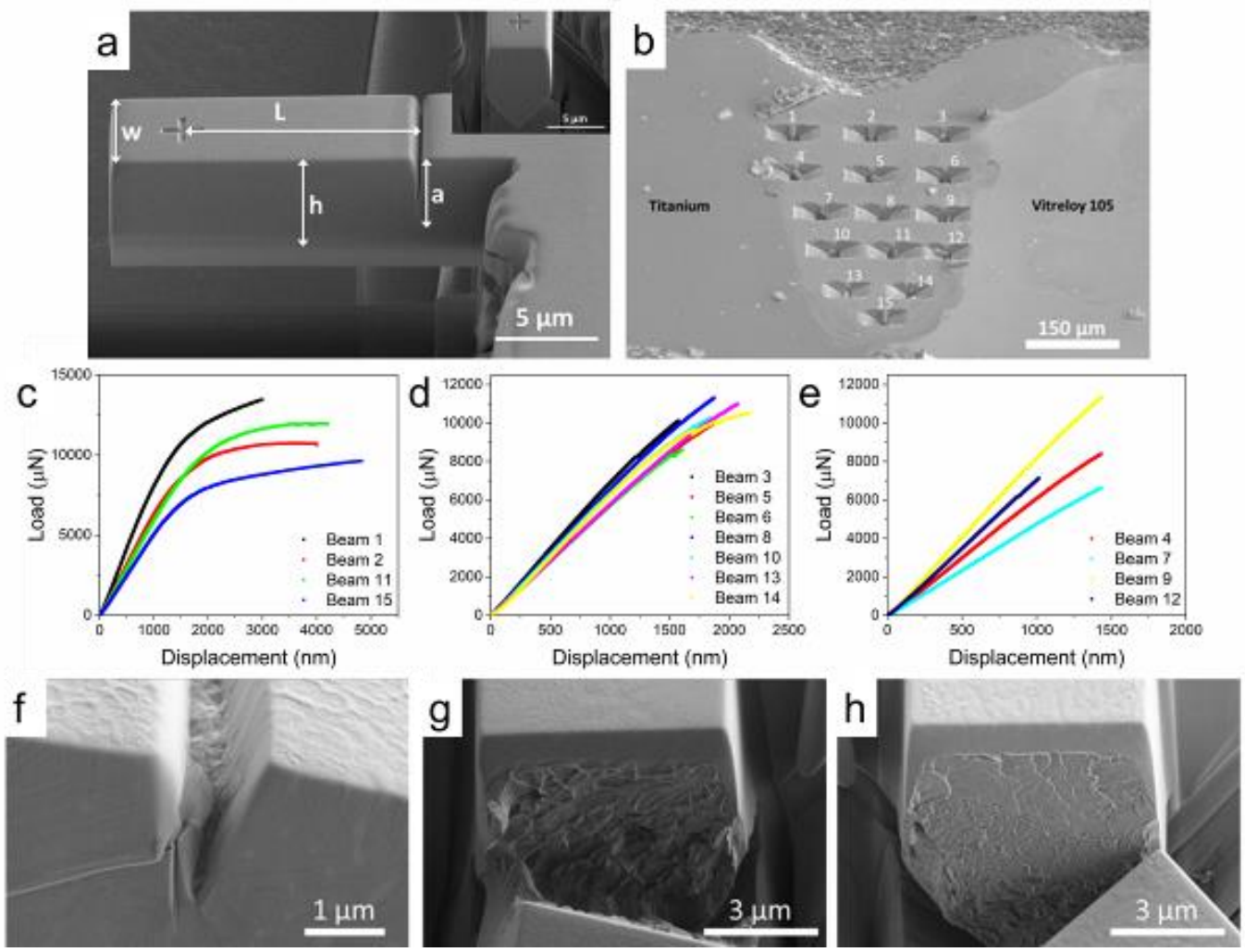
a
w
L
h
a
5 µm
b
Titanium
Vitreloy 105
150 µm
c
Load (µN)
Displacement (nm)
Beam 1
Beam 2
Beam 11
Beam 15
d
Load (µN)
Displacement (nm)
Beam 3
Beam 5
Beam 6
Beam 8
Beam 10
Beam 13
Beam 14
e
Load (µN)
Displacement (nm)
Beam 4
Beam 7
Beam 9
Beam 12
f
1 µm
g
3 µm
h
3 µm

MS6.P003
Design of lattice-matched $Au_xNi_{1-x}(111)/\alpha\text{-}Al_2O_3(0001)$ interfaces and their investigation by X-ray diffraction and electron microscopy

M. Dierner[1], J. Will[1], T. Yokosawa[1], T. Przybilla[1], T. Zech[2], P. Herre[3], T. Unruh[2], E. Spiecker[1]

[1]Friedrich-Alexander University Erlangen-Nuremberg (FAU), Institute of Micro- and Nanostructure Research & Center for Nanoanalysis and Electron Microscopy (CENEM), Erlangen, Germany
[2]Friedrich-Alexander University Erlangen-Nuremberg (FAU), Institute for Crystallography and Structural Physics (ICSP), Erlangen, Germany
[3]Institut für Nanotechnologie und korrelative Mikroskopie (INAM), Forchheim, Germany

Metal/ceramic interfaces are of great scientific and technological importance, with applications in electroceramic devices, structural composites and catalysis [1]. Due to different thermal expansion coefficients of metals and ceramics and, in many cases a high lattice mismatch applications suffer from mechanical stresses making the metal-ceramic interfaces the weak point in the device. The usage of a binary alloy system on the metal side offers the possibility to tailor the mismatch, leading to a less strained interface with improved mechanical stability.

In the present study, this concept is elaborated for the epitaxial interface between Au_xNi_{1-x} and $\alpha\text{-}Al_2O_3$. For this Au/Ni bilayers are e-beam evaporated on (0001) oriented $\alpha\text{-}Al_2O_3$. Rapid thermal annealing of the bilayers above the miscibility gap at 890 °C for 120 s in reducing atmosphere is used to fabricate Au_xNi_{1-x} alloy nanoparticles (NPs), which are subsequently quenched into a metastable supersaturated solid solution. Here, the Au concentration is utilized to tune the lattice parameter of the alloyed NPs towards lattice matching with the sapphire substrate. The influence of Au on the NP and the interface structure is monitored by X-ray and electrons.

XRD out-of-plane measurements confirmed the formation of AuNi alloy NPs and show that the lattice parameter follows the values for AuNi bulk alloys (Figure1). Furthermore, an influence of the lattice mismatch (e.g. at%Au) on the texturing of the NP can be seen. While all NPs show the typical 111-OOP texture, this texture is interestingly partially lost for samples close to lattice matching. (111)-XRD pole figures reveal i) a pronounced AuNi (111)[1-10] || $\alpha\text{-}Al_2O_3$ (0001)[10-10] orientation relationship and ii) the existence of two symmetric equivalent twin variants for all Au concentrations (Figure1). In XRD in-plane measurements as displayed in Figure2, the convergence of the NP lattice parameter towards lattice matching as well as the evolution of the diffuse background can be traced. For 59at% Au the in-plane NP and substrate peak match and the diffuse background, which stems from disorder at the interface, vanishes, both revealing the (semi-)coherent nature of the interface in contrast to an incoherent or delocalized coherent [2] interface for larger lattice mismatch.

To get a deeper understanding of the interface, cross-sectional EM-investigations on a <112> oriented lamella were carried out on the lattice-matched 59at% sample (Figure2). In the 220-DF image, a bright contrast on the interface can be detected, indicating a residual distortion of the lattice. The nature of this contrast is currently under further investigation. In agreement with the XRD data, the STEM-EDX maps confirm a successful formation of supersaturated AuNi particles, with a homogeneous distribution of Au and Ni through the whole particle including the interface and surface. In comparison Au segregation at the NP-substrate interface is observed for lower Au concentrations and consequently larger lattice mismatch [3].

Overall, we demonstrate an elegant route to produce lattice matched supersaturated metallic NPs on a ceramic substrate and provide insight into the structure and chemistry of the system by complementary scattering probes. In our contribution, the origin of the findings reported above will be discussed in light of existing literature and basic physical principles.

[1] Sinnott, Susan B., and Elizabeth C. Dickey. "Ceramic/metal interface structures and their relationship to atomic-and meso-scale properties." Materials Science and Engineering: R: Reports 43.1-2 (2003): 1-59. doi: 10.1016/j.mser.2003.09.001
[2] Meltzman, Hila, Dan Mordehai, and Wayne D. Kaplan. "Solid–solid interface reconstruction at equilibrated Ni–Al2O3 interfaces." Acta materialia 60.11 (2012): 4359-4369, doi: 10.1016/j.actamat.2012.04.037
[3] Herre et al. (in preparation)

Figure 1

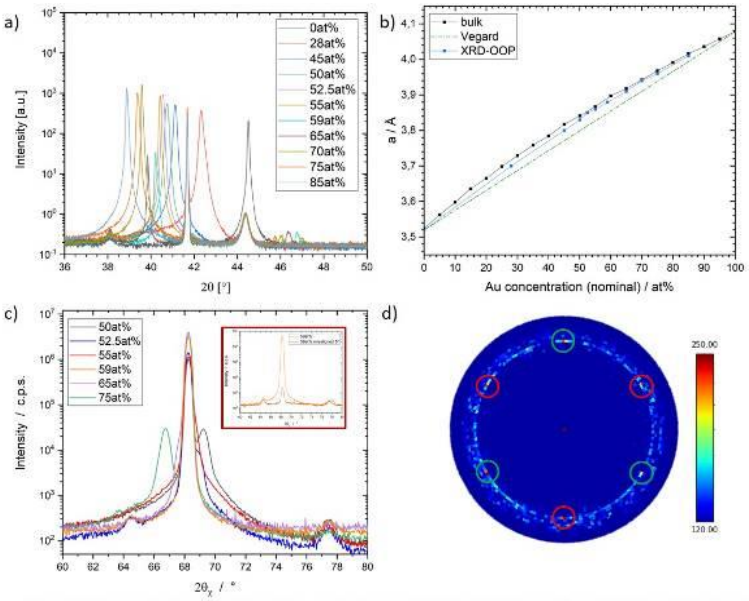

Fig. 1: a) XRD out-of-plane measurements, revealing a strong (111) texture and a partial loss of the texture for the samples close to lattice matching (59at% and 65at%). The left-shift of the peaks to smaller scattering angles as a function of the Au concentration indicates that alloying has taken place. b) Extracted evolution of the lattice parameter as a function of the Au concentration (blue), following the values for bulk alloys (black) reported from Crawley et al. [Crawley et al., Inst Metals J 94.1 (1966): 39-40]. c) In-plane XRD diffractogram showing the convergence of the NPs lattice parameters towards lattice matching and the development of a diffuse background. For the sample with 59at%, the diffuse background has completely disappeared. To determine the lattice mismatch of this sample, a measurement was made with a phi offset of 5° to capture only the scattering intensity from the NPs (see red box). The remaining lattice mismatch between the substrate and the NPs is determined to be 0.24%. d) (111)-XRD pole figures of the sample with 59at% Au showing a pronounced AuNi (111) [1-10] || α-Al2O3 (0001) [10-10] orientation relation (OR) and the presence of two symmetric equivalent twin variants rotated by 60° with respect to each other (red and green circles).

Figure 2

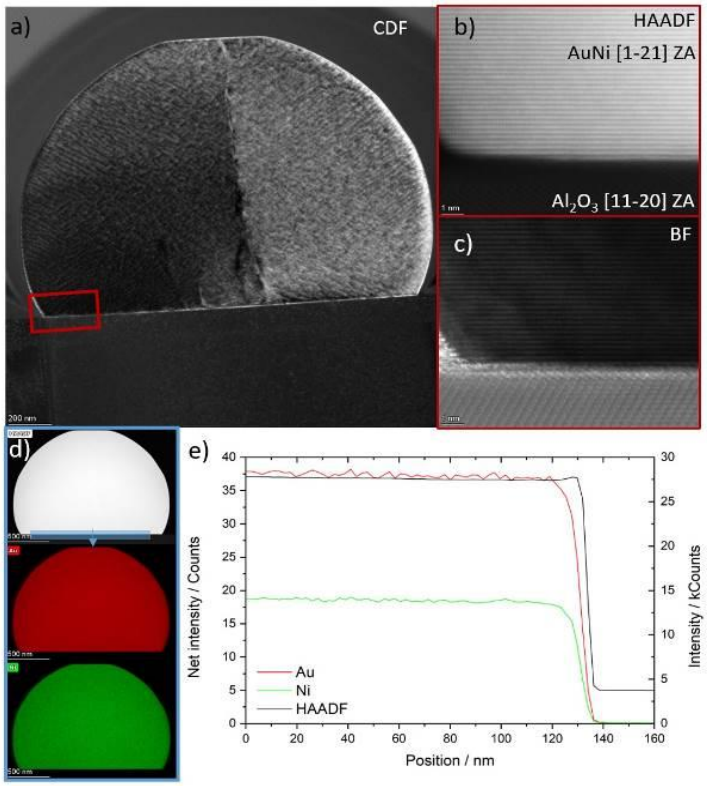

Fig. 2: a) Centered DF image of the Au59Ni41 particle. The bright contrast on the interface indicates a residual distortion of the lattice. b) HAADF and c) BF HR-STEM image of the interface. c) STEM EDX-maps confirming the formation of supersaturated AuNi particles. d) Linescan of the interface, showing that no interface segregation of Au is present.

MS6.P004
Strain-Induced Phase transition in Σ3 [111](211) tilt grain boundaries in Al

S. Ahmad[1], C. H. Liebscher[1], G. Dehm[1]

[1]Max Planck Institute for Iron Research, Düsseldorf, Structure and Nano-/Micromechanics of Materials, Düsseldorf, Germany

Grain boundaries are the interfaces separating differently oriented crystals and are one of the most important defects in polycrystalline materials. Advances in transmission electron microscopy and atomistic simulation techniques have provided strong evidence that grain boundaries are responsible for many material processes in polycrystalline materials, such as abnormal grain growth, stress-corrosion cracking, high temperature deformation and inter-granular fracture, where certain boundaries behave differently than the others under specific conditions [1,2]. One such example is the anisotropic grain growth in Al thin films on sapphire where Σ3 [111] tilt boundaries in domains with orientation relationship II (ORII) have higher mobility than that of ORI [3]. One possibility for such behavior is the existence of multiple stable and metastable states of the incoherent Σ3 twin boundaries for fixed macroscopic degrees of freedom. These different states of the grain boundary may lead to different interfacial properties, which ultimately affect grain boundary migration at high temperature. However, a direct correlation between the atomic structure of different structural states of Σ3 [111] tilt GBs and their effect on properties is still lacking.

In the present study, the microstructural features (grain size, grain orientation, CSL type and distribution) of the Al thin film on sapphire were characterized by electron backscatter diffraction as shown in below Figure 1. In-plane site specific TEM specimens from pre-examined thin films were extracted by plasma FIB to study the local atomic structure of Σ3 [111] (211) GBs from both ORs. The STEM results reveal that despite having the same macroscopic degrees of freedom, two different atomic structures of the symmetric incoherent Σ3 tilt boundary exist for two ORs. The atomic structure of both $\Sigma3_{ORI}$ and $\Sigma3_{ORII}$ comprises of two sub-units |EF| and |GF|, respectively. The E unit exhibits a square shape and the G unit adopts a hexagon shape. Both E and G sub units are followed by a sub unit F, which resembles a colon and comprises of two atomic planes. The asymmetric variant of $\Sigma3_{ORII}$ revealed a large number of facets and two different types of disconnections (Type A and Type B) along the boundary while $\Sigma3_{ORI}$ is comprised of a single disconnection (Type A) and no facets are observable. Furthermore, the cross sectional view of $\Sigma3_{ORII}$ along [011] direction shows two different translations along the boundary. The different structural states of incoherent Σ3 [111] twin boundaries will be explored in terms of their microscopic degrees of freedom and implications on interface properties will be discussed.

Acknowledgement: I gratefully acknowledge the financial support from the European Research Council (ERC) through Grant No. 787446 – GB-CORRELATE

References:
[1] Pan, Y., Adams, B.L., Olson, T. and Panayotou, N., 1996. Grain-boundary structure effects on intergranular stress corrosion cracking of alloy X-750. *Acta Materialia*, *44*(12), pp.4685-4695.
[2] Dennis, J., Bate, P.S. and Humphreys, F.J., 2009. Abnormal grain growth in Al–3.5 Cu. *Acta materialia*, *57*(15), pp.4539-4547.
[3] Hieke, S.W., Breitbach, B., Dehm, G. and Scheu, C., 2017. Microstructural evolution and solid state dewetting of epitaxial Al thin films on sapphire (α-Al2O3). *Acta Materialia*, *133*, pp.356-366.

Figure 1: EBSD map of Al thin film on (0001) sapphire substrate showing different types of CSL boundaries

Figure 1

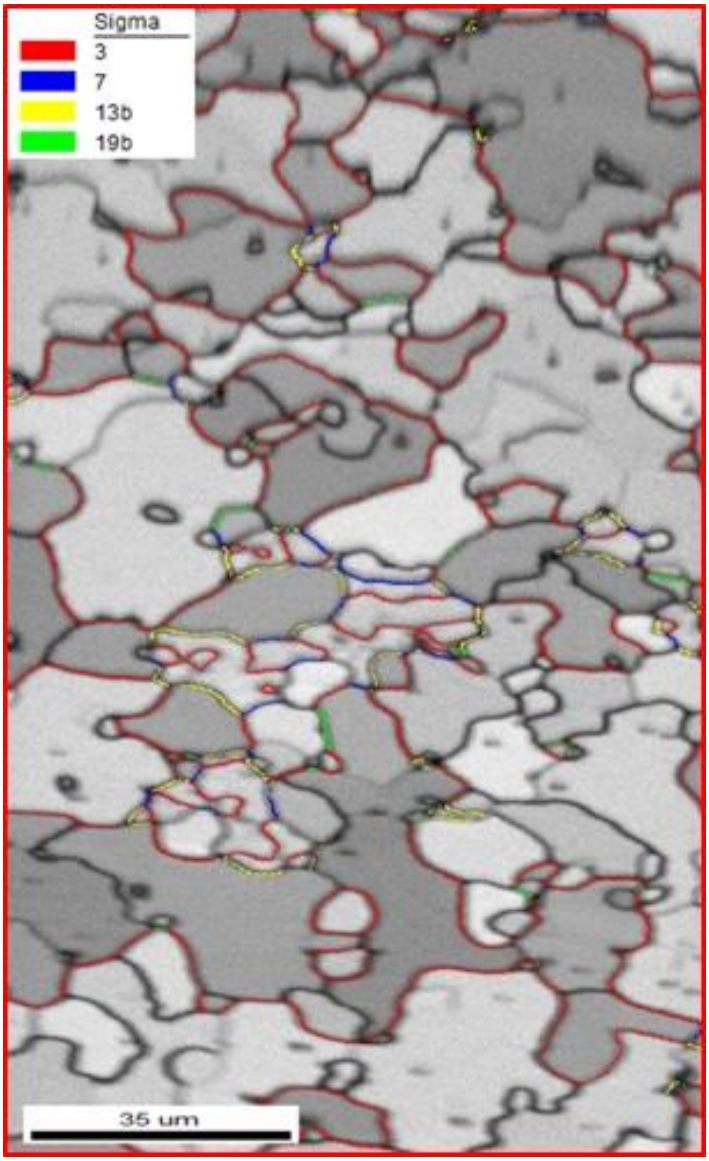

MS6.P005
Theoretically predicted inversion boundary structures in Sb2O3-doped ZnO confirmed by experimental and quantitative HRTEM analysis

V. Ribić[1], A. Rečnik[2], M. Komelj[2], A. Kokalj[3], G. Branković[1]

[1]Institute for Multidisciplinary Research, Belgrade, Serbia
[2]Jožef Stefan Institute, Department for Nanostructured Materials, Ljubljana, Slovenia
[3]Department of Physical and Organic Chemistry, Department of Physical and Organic Chemistry, Ljubljana, Slovenia

Inversion boundaries (IBs) in ZnO attract much attention as an essential 2D structural element in electron transport, phonon scattering, and most likely, also the unexplained p-type conductivity of ZnO [1]. With a wide range of dopants and the diversity of translations, IBs represent an excellent model system for studying the formation mechanisms and the thermodynamic stability of growth defects in crystals. Screening for the lowest energy IB configurations was based on density functional theory (DFT) calculations of IB models constructed from allowed stacking deviations in the wurtzite structure. Out of five crystallographically possible models, DFT optimization indicated that two of them have comparably low energies. Interestingly, as opposed to the previously accepted Aβ−Bα−AβC−γA−αC (IB2) model [2], DFT screening indicated a new model, with Aβ−Bα−AβC−γB−βC sequence (IB3), as the most stable translation of Sb-rich IB in ZnO. This was a very surprising result, that has not yet been identified for this system. Systematic HRTEM investigation of IBs in Sb2O3-doped ZnO samples had confirmed this new model; moreover we have shown, that it is even more frequent than the previously reported IB2 model. Quantitative HRTEM analysis of both stable IB structures have shown that the corresponding DFT optimized IB structures faithfully represent the real IB structures down to the HRTEM confidence limit of >5 pm. Combination of DFT calculations with quantitative HRTEM analysis of IBs is one of the first studies that links the experimental atomic-scale determined interface structures with optimized structures, giving impetus to trust predicted structures down to the limit of the DFT method down to 10-1 pm. Based on established confidence levels, newly determined sublattice expansions for the IB2 and IB3 models, ΔIB(Zn-Zn) are +81 pm and +77 pm, whereas the corresponding O-sublattice contractions ΔIB(O-O) are –53 pm and –57 pm, respectively [3]. Further, we have shown that stability of IB structures relates to the IB cationic stacking. IBs can thus be sequenced to cationic clusters, that contribute their characteristic energies to total energy of particular model (**Figure 1**). The energies of constituting stacking segments can be thus to predict the stability of any new IB structures without the need of further *ab-initio* calculations. The refined structures, on the other hand, will help to solve open questions related to their role in electron transport, phonon scattering, p-type conductivity, and underlying formation mechanisms, whereas the excellent match between the calculations and experiment demonstrated in our study opens new perspectives for prediction of such properties from first principles.

Figure 1: SF as a preparatory stage of IB formation (left). DFT analysis of stacking modes demonstrates that thermodynamically more stable structures involve less cubic bonds (above). The two stable IB structures in Sb2O3-doped ZnO: the old one (IB2) known from quantitative HRTEM study of IBs [2] and the new, more stable IB structure (IB3), predicted by DFT screening. Both IB structures coexist and are confirmed experimentally (courtesy of Ribić *et al*. Acta Materialia 199 (2020) 633-648; DOI: 10.1016/j.actamat.2020.08.035)

References**:**
[1] Yankovich et al, *Nano Letters*, 12 (2012) 1311−1316
[2] A. Rečnik et al, *J. Am. Ceram. Soc*., 84/11 (2001) 2657–2668
[3] V. Ribić et al, Acta Materialia 199 (2020) 633–648

Figure 1

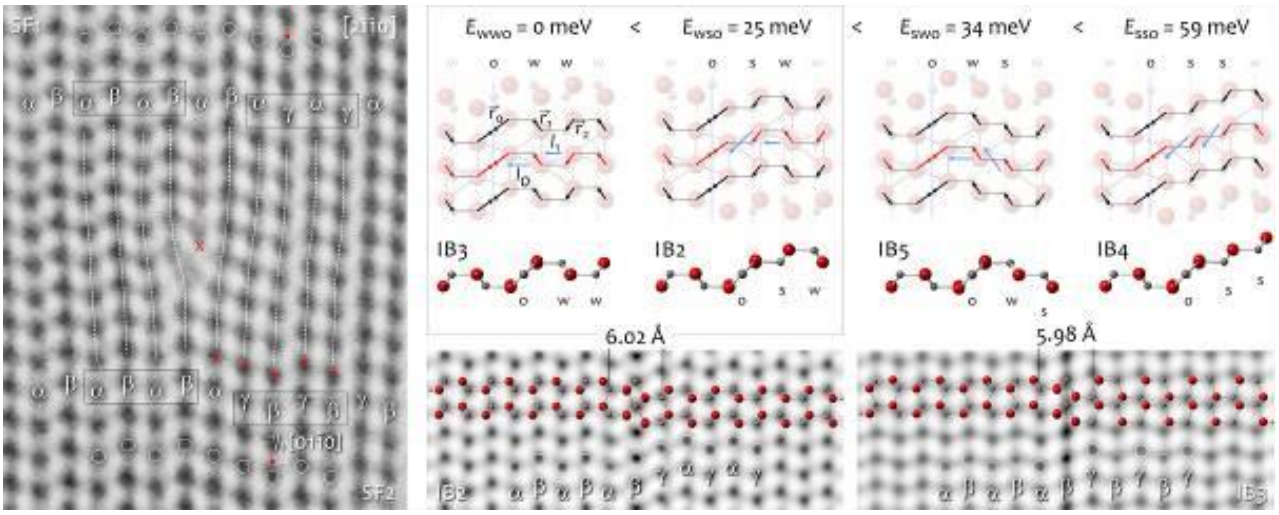

MS6.P006
Investigation of the microstructural and chemical heterogeneity in the as-cast and as-aged Ni-base superalloy ERBO/1

Z. Long[1], X. Jin[1], C. Dolle[1], D. Bürger[2], C. Lopes[1], Q. Sun[1], Y. M. Eggeler[1]

[1]Karlsruhe Institute of Technology (KIT), Laboratory for Electron Microscopy, Karlsruhe, Germany
[2]Ruhr-Universität Bochum, Institute for materials, Faculty of Mechanical engineering, Bochum, Germany

Keywords**:** Ni-based superalloys, γ/γ′ microstructure, as-cast and homogenized material states, dendrites.

Ni-base single-crystal superalloys (SX) are used as blade material in the combustion chamber of gas turbines in aero engines due to their capability of withstanding high temperatures and high stresses in harsh environments. The well-known γ/γ′ microstructure of SX superalloys, which exhibits γ′ precipitates coherently embedded in the γ-matrix, form the basis for excellent creep performance. The conventional Bridgman crystal-growth method is applied to produce SX superalloys that directionally solidify along [001][1]. The constituting elements have different partitioning preferences regarding their concentration in the dendritic or alternatively the interdendritic regions[2]. A subsequent homogenization heat treatment is necessary to improve the thermomechanical stability of SX superalloys. During the heat treatment, the macroscopic heterogeneity, such as residual microsegregation and eutectic mixtures within the dendritic and interdendritic regions are balanced and the creep performance is reinforced[3]. We aim to investigate chemical and microstructural heterogeneities of as-cast and as-aged ERBO/1 superalloy and its chemical evolution during isothermal high temperature exposure.

In this work, we will present a scale bridging microstructural analysis of the superalloy ERBO/1 directly after casting. On the macroscopic scale, the dendrites are apparent, with dendrite arms aligning along the [100] direction. The average dendrite arm spacing along the <100> direction is in the range of 362 µm, as shown in the backscattered electron micrographs of Figure 1a. Zooming in further onto the sub-10 µm scale, the γ′ precipitates embedded in the γ matrix become apparent within Figure 1b. Figure 1c shows that in the dendritic region in average four γ′ precipitates assemble in a butterfly shape filling 68% of the area fraction. Figure 1d presents the cuboidal γ′ precipitates within interdendritic regions, which in contrast to the dendritic region make up 76% of the area fraction. We expect the butterfly-shaped γ′ precipitates assemblies to separate after heat treatment. The γ′ area fractions of the as-cast material states and the homogenized samples are compared and their evolution as a function of heat treatment discussed.

Acknowledgment: The authors gratefully acknowledge the DFG priority program SFB-TR 103

Reference:
[1] RC Reed, *The superalloys fundamentals and applications* (2008).
[2] F Wang et al., *Sci. Technol. Adv. Mater.* **16**, 25004 (2015).
[3] K Demtröder et al., *Materwiss. Werksttech.* **46**, 563–576 (2015).

Figure 1: The as-cast ERBO/1 superalloys: (a) Dendrites embedded in interdendritic regions, exhibiting a mean dendrite arm spacing in <001> direction of 362 µm. (b)γ/γ′ phases within dendritic and interdendritic regions. (c) γ/γ′ phases in the dendritic core. (d) γ/γ′phases in an interdendritic region.

Figure 1

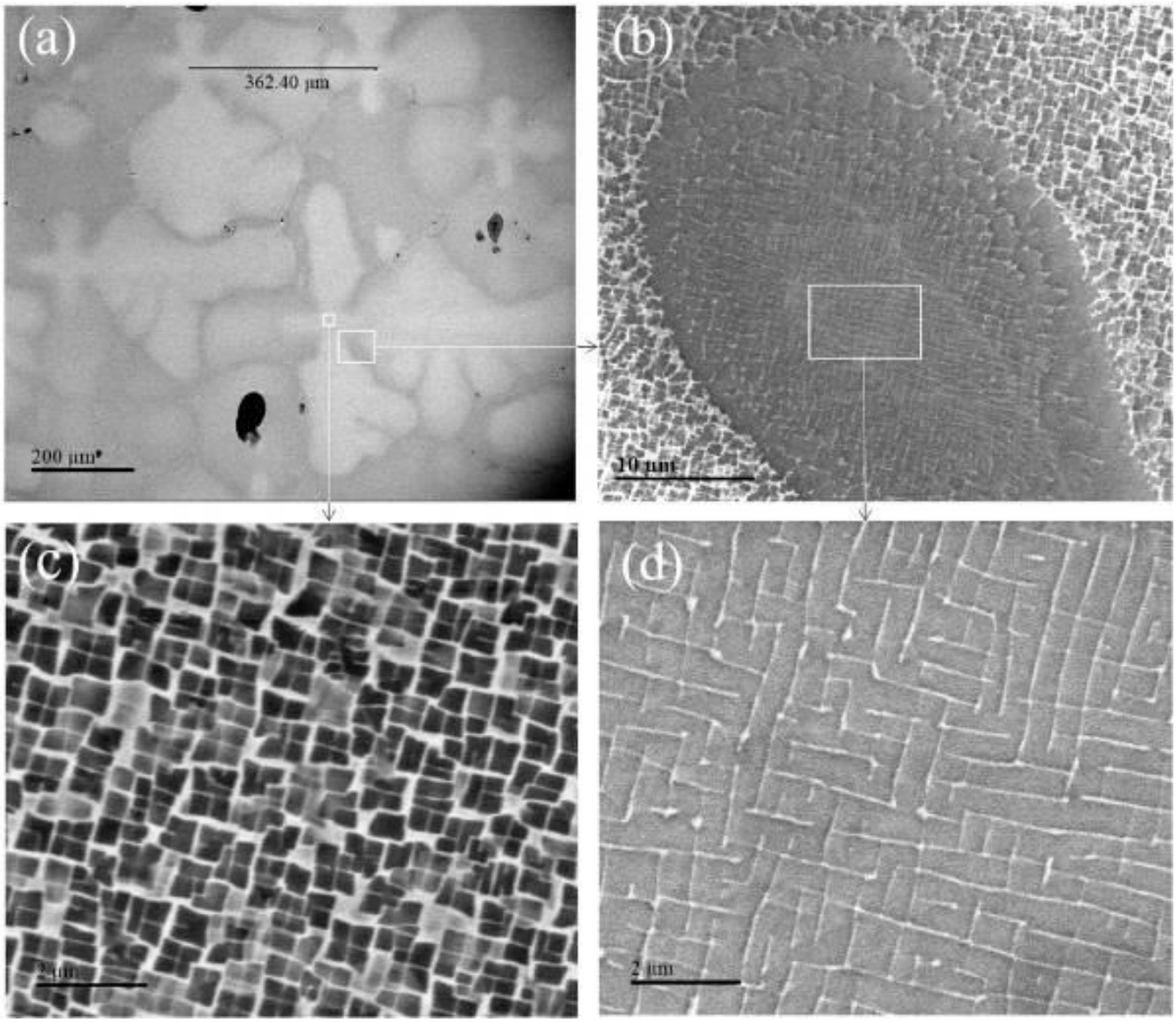

MS6.P007
STEM-EELS of $PbZr_xTi_{1-x}O_3/NdNiO_3$ interfaces

C. P. Su[1], G. Krieger[2], X. Li[1], N. Viart[2], D. Preziosi[2], A. Gloter[1]

[1]Laboratoire de Physique des Solides, Université Paris-Saclay, Orsay, France
[2]Institut de Physique et Chimie des Matériaux de Strasbourg, Université de Strasbourg, Strasbourg, France

The properties of epitaxial nickelates thin films are strongly related to the strains, oxygen octahedral distortions, bond and charge disproportionations [1]. The nickelates metal-insulator transition (MIT) can thus be tune by the substrate and, for instance, a slight difference in strain has the possibility to significantly changes the MIT temperature [2].

Here, we investigate the heterostructures $NdNiO_3/PbZr_xTi_{1-x}O_3$ (NNO/PZT) with $NdNiO_3$ and $LaMnO_3$ (LMO) buffer layer, grown on $SrTiO_3$ (STO) substrate. The Figure 1 shows the schematic diagram. The ferroelectric (FE) PZT has opposite polarization on each sample and changing the polarization direction at an interface between a correlated oxide and a ferroelectric is also known to control the physical properties such as the carrier density or the orbital polarisation [3].

Understanding the physical properties of such heterostructures requires to investigate the defects, the FE polarization, the strain, the Ni-O-Ni angle and the carriers distribution, with the challenging constrain of a nanometer scale resolution. For instance, X-ray and diffraction pattern can define the space groups [4], but they more hardly reveal the evolution of the octahedral distortions at interfaces that extended over only few unit cells. In this work, scanning transmission electron microscopy (STEM) combined with electron energy-loss spectrum (EELS) allow us to observe these structural parameters, and spectrum imaging with atomic resolution is able to quantify the chemical compositions and the transition metal valence on each layer.

The role of the buffers is made clear on the PZT structure, with a confirmed FE polarization reversal and the presence of more complicated domains, such as local a-type ferroelectric domains (Figure 1), for only one buffer. Furthermore, the EELS also shows carrier distributions across the buffer layers.

For the top NNO layers, we found that the first 5-6 u.c. exhibit a "defect-free" structure, with two epitaxial orientations, both displaying octahedral rotations (Figure 2 a and b), confirming that NNO can be interface with reversed FE polarization as controlled by the buffer. Above 5-6 u.c. the top NNO layers have more complex structures including structural and chemical defects, such as A-type Ruddlesden-Popper defects. In Figure 2 c-f, the top NNO layer shows such chemical heterogeneity with Ni-/ Nd-rich domains. Obviously, the results provide insights into this new heterostructure system that is a key to control the properties of NNO or the MIT temperature.

Figure 1: (a)-(c) the LMO buffered sample; (d)-(f) NNO buffered sample. (b), (e) HAADF images (collection angle: 80-200 mrad); (c), (f) MAADF images (collection angle: 30-60 mrad).

Figure 2: NNO/PZT/LMO//STO. (a) and (b) two kinds of the NNO oritations. (c) STEM image of the NNO/PZT and the corresponding chemical distributions of (d) Nd and (e) Ni. (f) color map of Nd (green) and Ni (red).

References:
[1] H. Kim et al., Strain-driven disproportionation at a correlated oxide metal-insulator transition, *Phys. Rev. B* **101**, 121105 (2020).
[2] F. Bruno et al., Rationalizing strain engineering effects in rare-earth nickelates, *Phys. Rev. B* **88**, 195108 (2013).
[3] D. Preziosi et al., Electric-field control of the orbital occupancy and magnetic moment of a transition-metal oxide, *Phys. Rev Lett.* **115**, 157401 (2015).
[4] Y. Zhang et al., Key role of lattice symmetry in the metal-insulator transition of $NdNiO_3$ films, *Sci Rep* **6**, 23652 (2016).

Figure 1

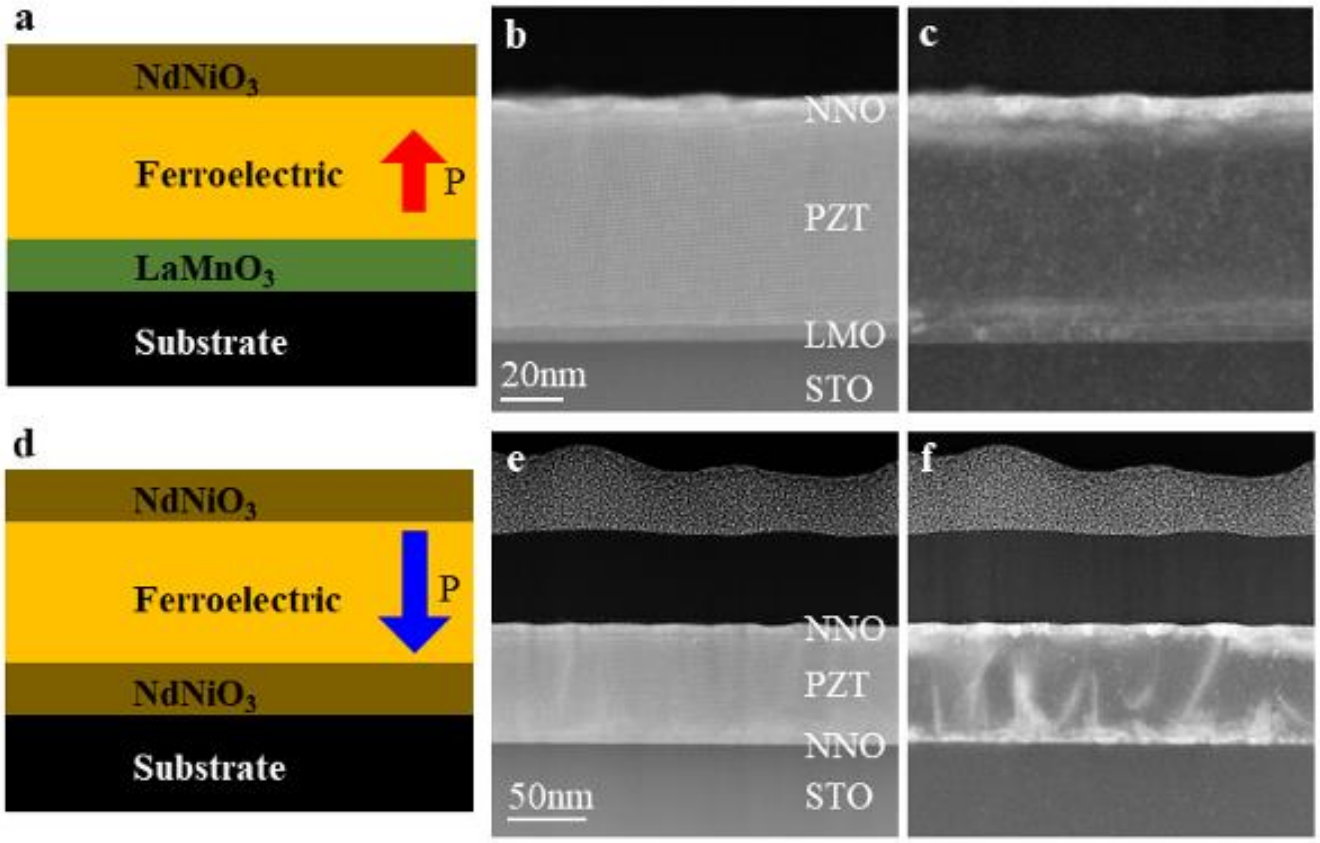

Figure 2

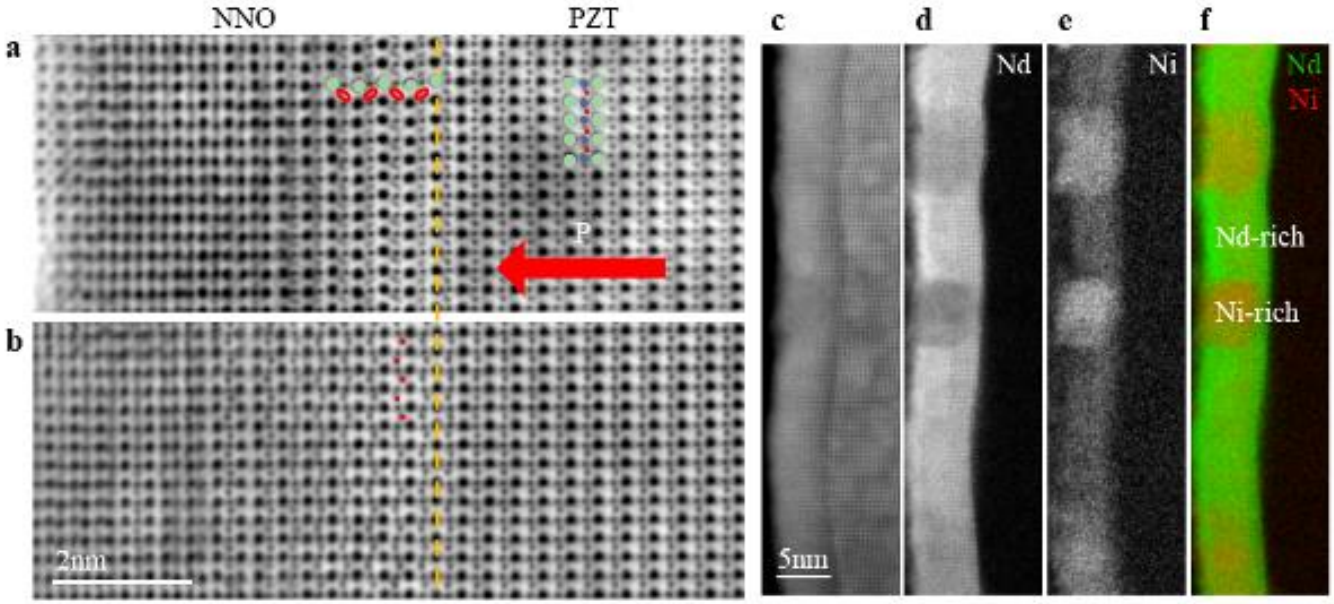

MS6.P008
Advances in correlative chemical analysis of grain and phase boundaries in conjunction with atom probe tomography

R. Ulfig[1], K. Rice[1], Y. Chen[1], R. Chemnitzer[1], D. Larson[1]

[1]CAMECA Instruments Inc., Madison, United States

Interfaces often dictate the limitations of the functional properties of materials and come in a myriad of phase and grain boundary chemistry and orientation. The segregation of solutes in steel grain boundaries for example varies strongly with the grain boundary character and can have dramatic effects on grain growth and bulk properties [1]. No technique alone can quantify all of the solute types and interfacial excess with the three-dimensional resolution desired while providing a complete characterization of the crystalline orientation of the grains.

Transmission Electron Microscopy (TEM) for example has an unmatched spatial resolution, but quantifying the composition with electron dispersion spectroscopy, (EDS) or electron energy loss spectroscopy (EELS) in three dimensions on nanoscale structures, especially when they are at high density, can be challenging [2]. Atom probe tomography has un-matched analytical compositional detection capability, reconstructing up to 80% atoms with nanoscale precision with respect to each other in 3D with a detection system that has the same response for elements from hydrogen to uranium and even heavy molecular ions, but it is known for its variable magnification across the field of view and limited ability to identify crystalline structure [3].

This work will review modern examples of crystalline orientation techniques that have been used correlatively with atom probe tomography enabling a comprehensive understanding to correlate materials properties with morphology and chemistry. Different diffraction techniques in SEM, TEM, FIB-SEM (See Figures 1&2) will be discussed and examples will be presented demonstrating cutting-edge interface analysis techniques including atom probe tomography (See Figures 2&3).

Figure 1: Left – Electron backscatter diffraction (EBSD) of a fine-grained steel with automatic identification of specific grain boundary types (center). Right scanning nanobeam diffraction with grain boundaries identified in red.

Figure 2: a) Secondary electron image showing grain boundary contrast that is lost as the volume is reduced to prepare the specimen for APT analysis. b) transmission kikuchi diffraction used to target the grain boundary for c) APT analysis, right Iron in green, carbon in black, boron in blue. d)Phase mapping of a Ti6Al4V specimen ready for APT analysis e) and f) a one-dimensional composition profile through the alpha/beta interface with the quantification of the oxygen level shown.

References:
[1] Herbig, M. et al. Atomic-Scale Quantification of Grain Boundary Segregation in Nanocrystalline Material. Phys. Rev. Lett. 112, 126103 (2014).
[2] Williams, D. B. & Carter, C. B. *Transmission Electron Microscopy*. (Springer, 2009).
[3] Larson, D. J., T. J. Prosa, R. M. Ulfig, B P. Geiser & T. F. Kelly. Local electrode atom probe tomography: a user"s guide. (Springer, 2013).

Figure 1

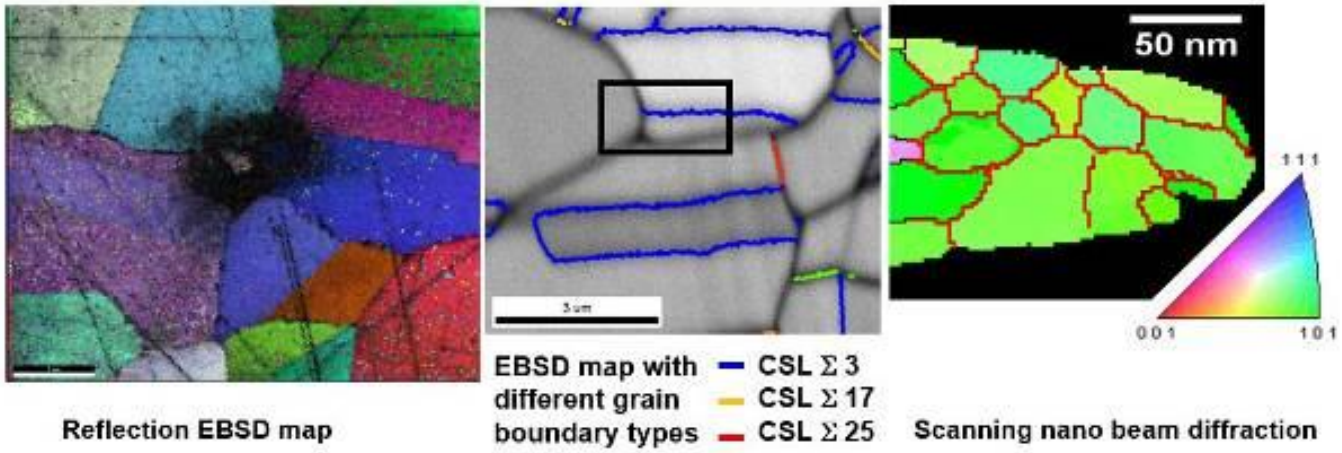

Figure 2

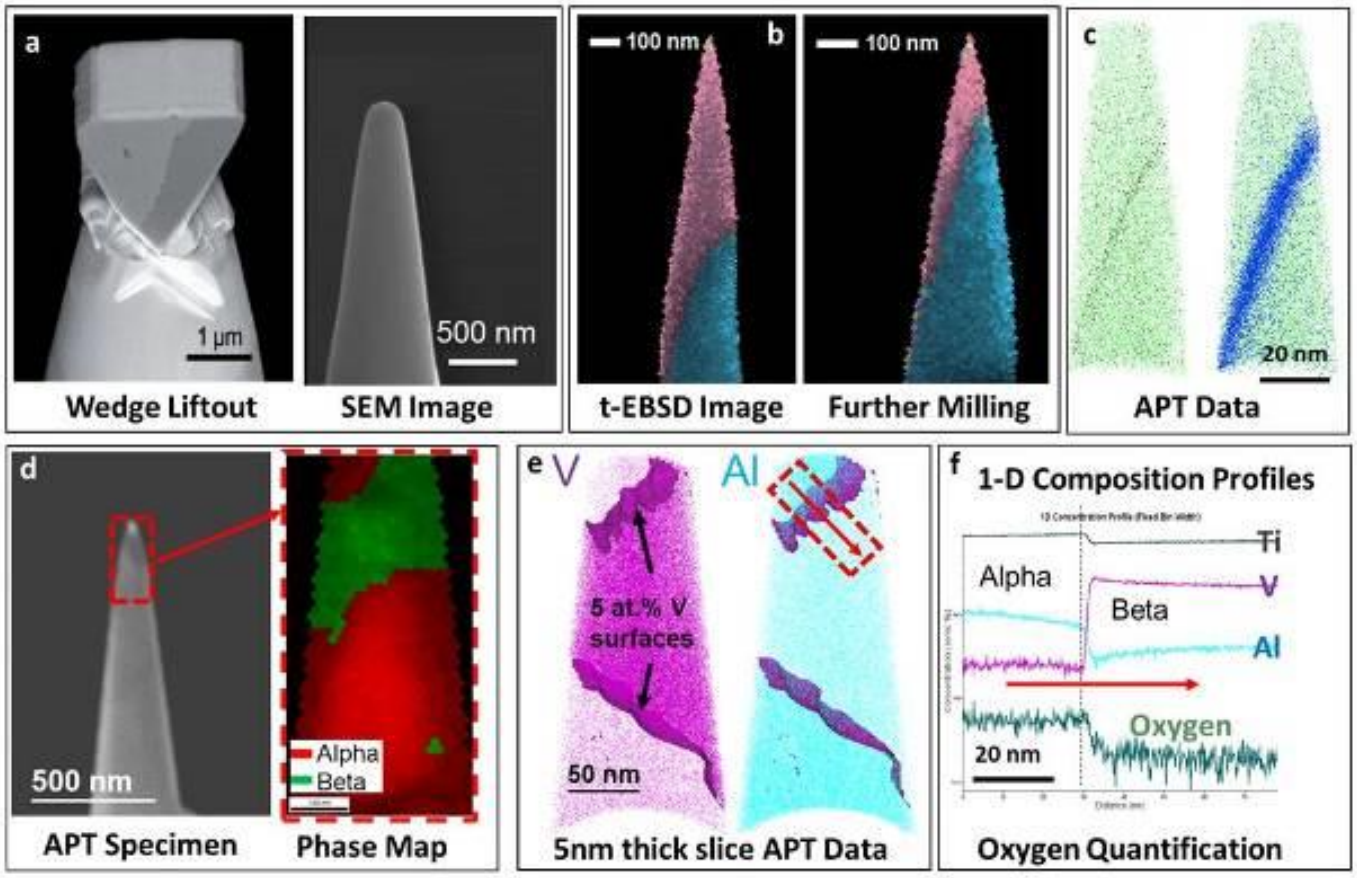

MS6.P009
Unravelling the atomic structure and segregation of Σ13 [0001] tilt grain boundaries in titanium by advanced STEM

V. Devulapalli[1], M. Hans[2], G. Dehm[3], C. H. Liebscher[1]

[1]Max Planck Institute for Iron Research, Düsseldorf, Advanced transmission electron microscopy group, Düsseldorf, Germany
[2]RWTH Aachen University, Materials Chemistry, Aachen, Germany
[3]Max Planck Institute for Iron Research, Düsseldorf , Düsseldorf, Germany

Titanium (Ti) is an important commercial material owing to its high strength to weight ratio, biocompatibility and excellent corrosion resistance. The hcp (α) to bcc (β) allotropic transition allows for great flexibility in microstructure and alloy design. A lot has been studied macroscopically about these interphase boundaries in polycrystalline α-β Ti alloys but corresponding work in α-Ti grain boundaries (GBs) is scarce. The GBs of α-Ti are interesting because they often act as nucleation sites for secondary phases during heat treatment. They also act as sinks for solute elements or impurities that can result in material failure by embrittlement. On the contrary, they can also strengthen the material by reducing GB energy and preventing coarsening during high temperature application. In either case, to establish a fundamental understanding of these interfacial processes it is necessary to understand the atomic structure of the GBs and segregation of solute elements in them.

In this study, we first developed a novel technique for obtaining hcp-Ti tilt GBs by depositing thin films using high power pulsed magnetron sputtering on MgO and SrTiO3 substrates. Electron backscatter diffraction in a scanning electron microscope was used to investigate the texture evolution and global GB character. Films deposited at 600ºC predominantly have (0001) basal plane texture and columnar grains. Interestingly, most GBs have Σ13 (27.8º / [0001]) coincidence site lattice (CSL) orientation with seemingly maze-like GB planes. Selected GBs were site specifically lifted out and thinned to electron transparency using a focused ion beam milling to explore their atomic structure in an aberration-corrected scanning transmission electron microscope (STEM). STEM imaging reveals the curved GBs to be faceted with typical segment length of 20-50 nm. Most of the GBs are symmetric Σ13 {25-70} with sporadic asymmetric {10-10}/{11-20} segments between them. Furthermore, atomic resolution STEM imaging was used to reveal the structural units, which are partly consistent with theoretical predictions [2]. They also resemble the *5-7-5 structural units* as was described for hexagonal 2D materials like graphene and MoS2 [3]. Additionally, energy dispersive spectroscopy (EDS) reveals preferential segregation of Fe to specific facets of {25-70} GBs. This can be explained using the CSL site density in the GB plane. The GB planes with low CSL lattice points have relatively higher energy and hence act as preferred site for solute segregation. To avoid knock-on damage at 300kV acceleration voltage, atomic resolution EDS at 120kV was used to observe the intrinsic segregation pattern of Fe at GBs. The influence of observed GB structures and segregation on GB mobility will be discussed.

KSB Stiftung is acknowledged for funding of the work.

References:
[1] D. Brandon, Acta Metall. 14 (1966) 1479–1484.
[2] Y. C. Wang, H.Q. Ye, Philos. Mag. A Phys. Condens. Matter, Struct. Defects Mech. Prop. 75 (1997) 261–272.
[3] E. Annevelink, E. Ertekin, H.T. Johnson, Acta Mater. 166 (2019) 67–74.

MS7.001-Invited
Using nanoindentation to study the mechanical properties of advanced functional polymer-based materials incorporating graphene

A. Flores[1]

[1]Instituto de Ciencia y Tecnología de Polímeros (ICTP-CSIC), Departamento de Física de Polímeros, Elastómeros y Aplicaciones Energéticas, Madrid, Spain

The development of graphene-based nanocomposites has significantly expanded the performance limits of traditional polymer composites. Graphene can enhance barrier, thermal, mechanical and electrical properties of the polymer matrix. The key aspect to achieve synergistic effects is an effective dispersion of the filler through *ad hoc* strategies.

The present work summarizes results obtained in the last few years in our research group on graphene/polymer-based materials. A large variety of matrices are considered ranging from commodity materials such as polypropylene (iPP) to thermoplastic elastomers such as poly(styrene-b-ethylene-co-butylene-b-styrene) (SEBS). In all cases, graphene is chemically modified with polymer brushes to enhance the interfacial interaction with the host matrix.

Nanoindentation is used to explore the mechanical properties of the nanocomposites and results are correlated with structural characteristics by X-ray diffraction studies and electron microscopic observations. It will be shown that instrumented indentation can provide a route to the evaluation of uniformity of mechanical properties at the micrometre scale as well as an assessment of property enhancement. Moreover, analysis of the indentation data allows the separation of the mechanical enhancement into two contributions, one attributed to the graphene reinforcement itself and a second one associated to changes induced in the polymer matrix due to the presence of the nanofiller. On the other hand, atomic force microscopy (AFM) nanoindentation can provide information on the local deformation mechanisms at the nanometre scale.

It will be shown that graphene can be successfully incorporated into polymer matrices to produce conductive lightweight materials. Indentation testing together with X-ray diffraction and microscopic techniques offer a thorough and comprehensive understanding of the material properties.

Acknowledgements: Financial support from MINECO (Ministerio de Economía y Competitividad), Spain, under grant MAT2017-88382-P is gratefully acknowledged.

References:
[1] S. Quiles-Díaz, P. Enrique-Jimenez, D.G. Papageorgiou, F. Ania, A. Flores, I. A. Kinloch, M. A. Gómez-Fatou, R. J. Young, H. J. (2017). Composites: Part A 100, 31-39.
[2] P. Enrique-Jiménez, S. Quiles-Díaz, H. J. Salavagione, D. Wesner, H. Schönherr, J. González-Casablanca, R. García Quismondo, G. Martínez, M. A. Gómez-Fatou, F. Ania, A. Flores, (2017). European Polymer Journal 97, 1-13.
[3] F. Ania, M. A. Gómez-Fatou, H. J. Salavagione, P. Enrique-Jimenez, S. Quiles-Díaz, A. Flores. (2020). Comp. Sci. Tech. 198, 108311.

MS7.002-Invited
Soft selective cell release interfaces – Detailed insight into stimulus-responsive polymer brushes by AFM nanoindentation

D. Wesner[1], J. Schumacher[1], E. Wassel[1], S. Jiang[1], H. Choi[1], A. Schulte[1], S.I. Druzhinin[1], M. Müller[1], H. Schönherr[1]

[1]Physical Chemistry I & Research Center of Micro and Nanochemistry and Engineering (Cμ), University of Siegen; Adolf-Reichwein-Str. 2; 57076 Siegen, Germany

Introduction: Polymer layers with stimulus-responsive functionality were shown to be attractive candidates for biointerfaces, which allow one to detach cells using a mild thermal trigger. Expanding on the pioneering work of Okano et al. we reported on the synthesis, characterization and application of thermoresponsive layers of end-grafted poly(di(ethylene glycol) methyl methacrylate) (PDEGMA) on gold. Depending on the brush thickness, PDEGMA brushes are passivating surfaces against protein adsorption or may introduce a selective cell release function [1-3].

Objectives: Since surface mechanical properties are important to control cell behavior nanomechanical characterization is an important target. To fully understand the performance of switchable PDEGMA interfaces [1-3] and to characterize such brushes on implants for triggered drug elution [4], their property changes were studied by atomic force microscopy (AFM) nanoindentation in water as a function of thickness below and above the lower critical solution temperature (LCST) of PDEGMA brushes of 32°C.

Materials and Methods: PDEGMA brushes on Au with dry ellipsometric thicknesses up to 30 nm were synthesized by conventional surface-initiated atom transfer radical polymerization (SI-ATRP) using self-assembled monolayers of ω-mercaptoundecyl bromoisobutyrate on gold. Thicker PDEGMA brushes (> 400 nm) were obtained on Ti implants via SI-ATRP with activators regenerated through the electron transfer technique, starting from a polydopamine layer functionalized with α-bromoisobutyryl bromide. AFM nanoindentation was carried out by means of AFM force-distance experiments using hydrophobized glass beads mounted to tipless cantilevers. Interaction forces were measured in Milli-Q water using a MFP-3D Bio (Asylum Research, Santa Barbara, USA) in a temperature range from 27°C to 60°C (Scheme 1).

Results: While the adhesion force showed a monotonic and reversible increase from 27°C to 60°C, the work of adhesion increased sigmoidally with increasing temperature. For brush thicknesses from 5 nm to 27 nm, the apparent transition temperature, determined from the corresponding inflection point, varied linearly. These transition temperatures match the transition temperatures determined by surface plasmon resonance (SPR). Additionally AFM force-displacement and indentation data show that the layers were swollen to 3 times their dry thickness below the LCST. For T > LCST, they collapsed and became progressively more adhesive and stiffer. Thicker brushes on titanium showed a marked decrease of the Young's modulus with increasing thickness, which reflects the unique swelling behavior and also complicated release pattern of incorporated antibiotics.

Conclusions: The apparent transition temperature of PDEGMA brushes as well as the mechanical properties in water depend on brush thickness. The interplay of polymer collapse and balanced interactions with the underlying substrate in very thin layers allows one to tune the efficient transition temperature to temperatures above the LCST, which is most useful to fabricate selective cell release surfaces.

References

[1] E. Wassel, D. Wesner, H. Schönherr *Europ. Polym. J.* 2017, 89, 440.
[2] S. Jiang, M. Müller, H. Schönherr, *ACS Appl. Biomater.* 2019, 2, 2557.
[3] S. Jiang, M. Müller, H. Schönherr, *Angew. Chem. Int. Ed. Engl*. 2019, 58, 10563.
[4] H. Choi, A. Schulte, M. Müller, M. Park, S. Jo, H. Schönherr *Adv. Healthcare Mater*. 2021, *in press*.

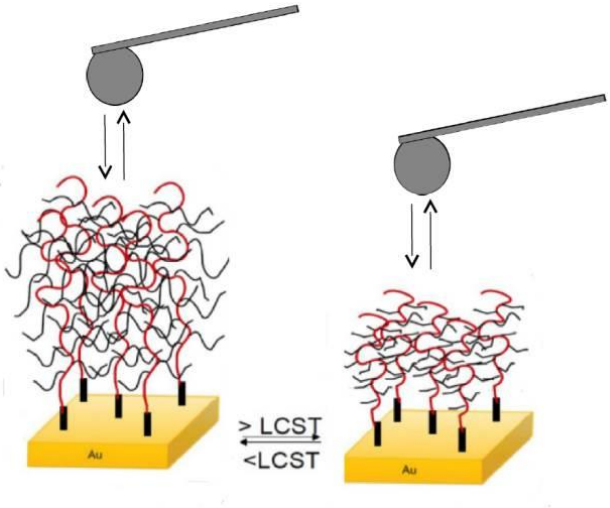
Au
> LCST
<LCST
Au

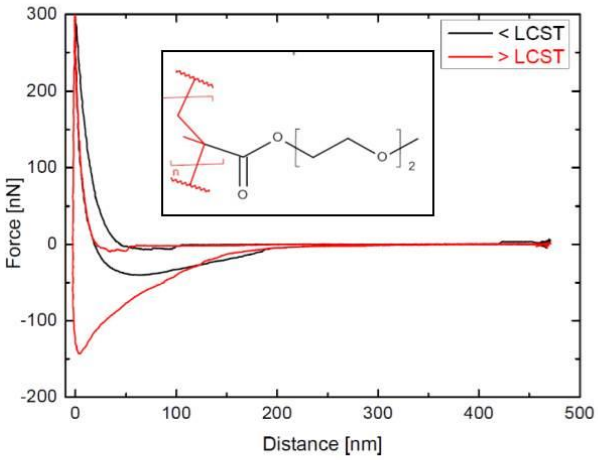
< LCST
> LCST
Force [nN]
Distance [nm]

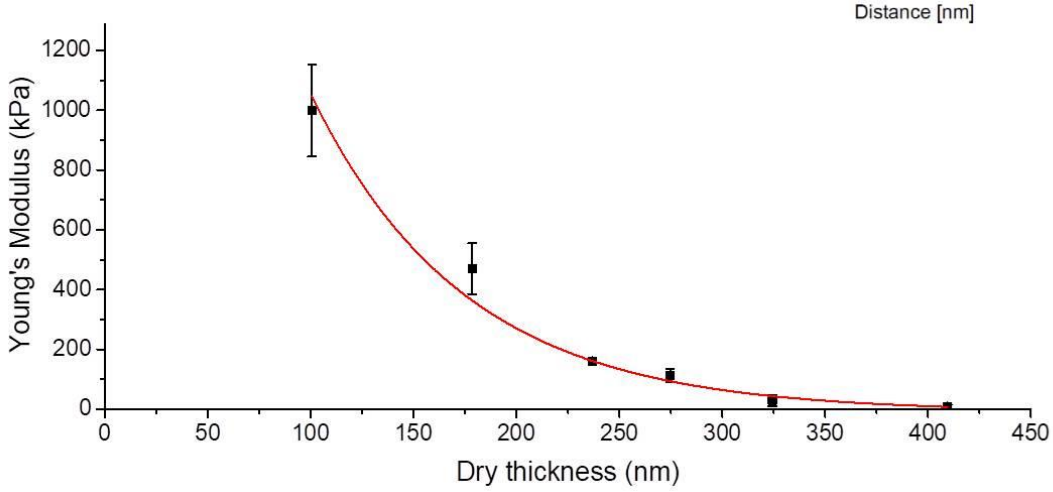
Young's Modulus (kPa)
Dry thickness (nm)

MS7.003
The challenge of digital image correlation in continuous micron scale mechanical tensile testing

M. Alfreider[1], M. Meindlhumer[2], V. Maier-Kiener[1], A. Hohenwarter[1], D. Kiener[1]

[1]Montanuniversität Leoben, Leoben, Austria
[2]Erich Schmid Institute of Materials Science (ESI) of the Austrian Academy of Sciences, Leoben, Austria

Introduction: In situ micromechanical testing techniques in scanning electron microscopes (SEMs) have become widely utilized in order to answering research questions with regards to very confined volumes, natively small structures, or localized phenomena in general. While the by far most common techniques involve nanoindentation [1] and micropillar compression [2], tensile loading, as is a standard in macroscopic materials testing, has been rarely conducted. This is owed to the more challenging experimental conditions and longer preparation times for an individual experiment [3]. Thus, it is desired to extract the most information from such a single experiment.

Approach: In the present study [4] continuous microtensile testing on a 6x6 µm2, dogbone-shaped specimen of a severely plastically deformed, nanocrystalline, equiatomic CoCrFeMnNi high entropy alloy was conducted in situ in an SEM. The load and displacement data was gathered by a nanoindentation device equipped with a negatively shaped tungsten gripper, while the images were acquired quasi-continuously with an acquisition time of 660 ms per frame and subsequently used for correlative measurement of a pre-processed point pattern. In conjunction with self-written point tracking algorithms and approaches from finite element analysis in the framework of finite strain theory, the true strain field on the specimen surface was evaluated and utilized to determine the accurate yield and flow behaviour as well as the Poisson"s ratio of the examined material.

Summary: The gathered true stress-strain data was validated with the novel, high throughput method of spherical nanoindentation and showed excellent agreement. Furthermore, the Poisson"s ratio, which is not directly obtainable from nanoindentation techniques, was compared to literature values from resonance excitation measurements on coarse grain bulk counterparts of the studied alloy. In comparison with commercial software solutions, it was found that the presented approach gives a better result for to the high image acquisition speed and thus noisy images during continuous testing. As such, this novel approach opens new possibilities to extract high fidelity strain field data from intrinsically noisy in situ images and in the future also allows for evaluation of even more complex strain fields, *e.g.* around notches or indents.

[1] C.A. Schuh, Nanoindentation studies of materials, Mater. Today. 9 (2006) 32–40. doi:10.1016/S1369-7021(06)71495-X.
[2] M.D. Uchic, Sample Dimensions Influence Strength and Crystal Plasticity, Science 305 (2004) 986–989. doi:10.1126/science.1098993.
[3] D. Kiener, W. Grosinger, G. Dehm, R. Pippan, A further step towards an understanding of size-dependent crystal plasticity: In situ tension experiments of miniaturized single-crystal copper samples, Acta Mater. 56 (2008) 580–592. doi:10.1016/j.actamat.2007.10.015.
[4] M. Alfreider, M. Meindlhumer, V. Maier-Kiener, A. Hohenwarter, D. Kiener, Extracting information from noisy data: strain mapping during dynamic in situ SEM experiments, J. Mater. Res. (2021). doi:10.1557/s43578-020-00041-0.

Figure 1: In situ SEM image of the dogbone-shaped tensile specimen, showing the pre-processed point pattern.

Figure 2: Calculated strain field for the direction along the specimen axis showing evident localization of plastic deformation with total strains exceeding 10% in the highly deformed region.

Figure 1

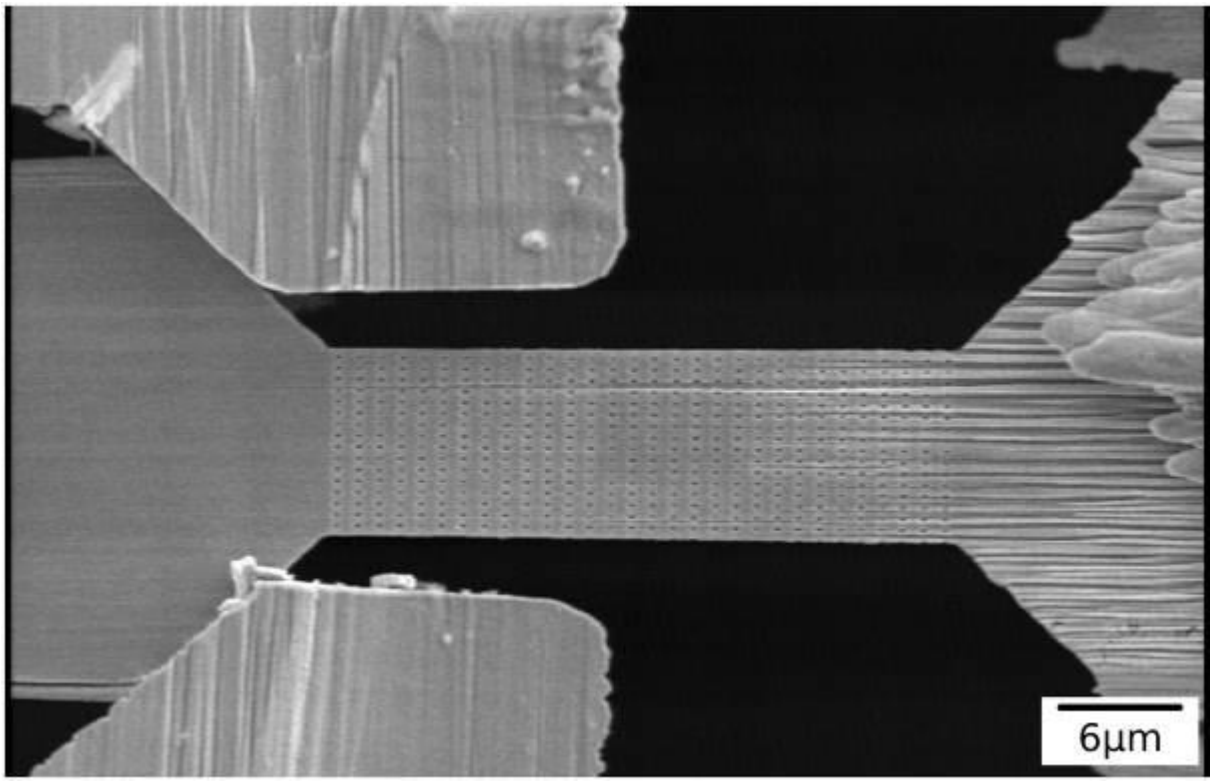

Figure 2

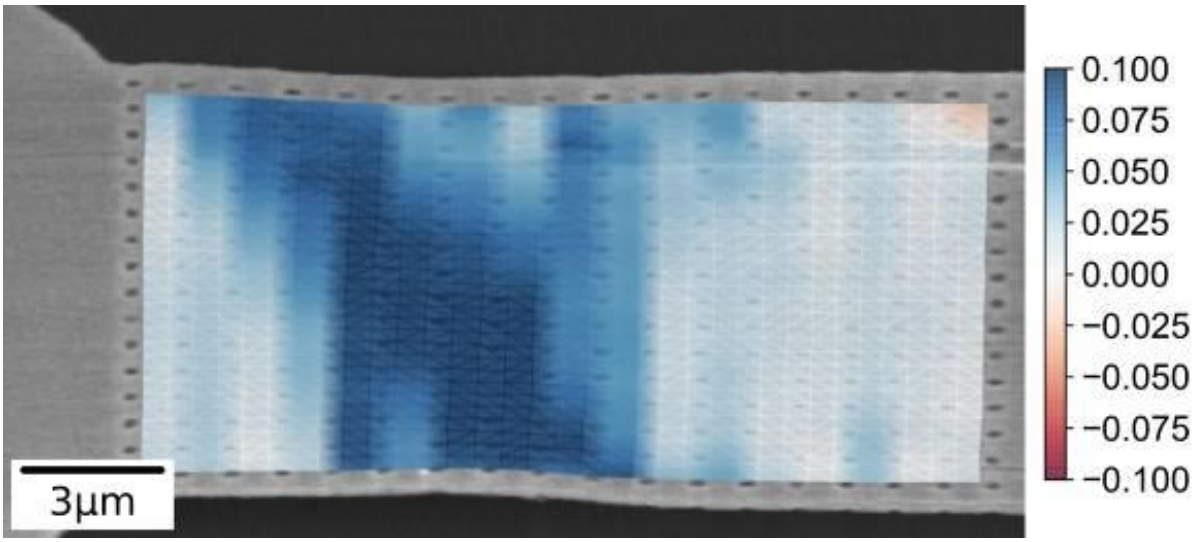

MS7.004
In situ study of the high-temperature phase of 2H-$MoTe_2$

J. Köster[1], M. K. Kinyanjui[1], U. Kaiser[1]

[1]University of Ulm, Ulm, Germany

The SALVE microscope operates at accelerating voltages between 20 – 80 kV and is equipped with a Cc/Cs-corrector [1,2,3], enables the investigation of electron-beam-induced structural transformations, properties and dynamics in two-dimensional (2D) materials on an atomic level. In single-layer $MoTe_2$ it was shown that local transformations from the semiconducting 2H to the metallic 1T" phase can be achieved by electron irradiation [4].

Here, we report about *in-situ* annealing of freestanding few-layer 2H-$MoTe_2$ in TEM. The samples are prepared by stamping few-layer $MoTe_2$ with the help of a PMMA layer onto a *ThermoFisher* MEMS-chip. A detailed depiction of the preparation process can be seen in Figure 1 (a) – (c). By slowly increasing the annealing temperature up to 1000°C under constant electron irradiation, the structural evolution of layered 2H-$MoTe_2$ to one-dimensional (1D) Mo_6Te_6 chains to isolated molybdenum can be observed and analysed [5]. Further, we can identify the 1D chains by HRTEM. An experimentally acquired freestanding chain at 80 kV is shown in (d) at a temperature of about 600°C, and in (e), a structural model of the 1D chain is shown.

Our results show the controlled step by step transformation of 2D freestanding 2H-$MoTe_2$ depending on the annealing temperature. Furthermore, we are able to show intermediate states of the transformation and to identify different atomic arrangements up to the high-temperature Mo_6Te_6 phase. These results provide a comprehensive picture of the responds of few-layer $MoTe_2$ crystals to heating. Furthermore, we compare the effect of electron irradiation to the found modifications of the atomically thin layers caused by annealing.

Figure 1: (a) – (c) illustrates the sample preparation of few-layer 2H-$MoTe_2$ onto a MEMS-chip. In (a), a Si/SiO_2 wafer is spin-coated with first PVA and second PMMA. The PMMA layer is removed from the underlying PVA layer and stamped in (b) onto the MEMS-chip. (c) shows the final setup in TEM with the $MoTe_2$ sitting on top of the heating coil (highlighted by an optical image in (f)). In (d), the formation of Mo_6Te_6 chains can be seen. A freestanding chain is highlighted by red arrows and a structure model of the 1D chain is shown in (e).

[1] U. Kaiser et al. Ultramicroscopy, 111, 8, 1239-1246 (2011)
[2] M. Linck et al., Phys. Rev. Lett. 2016, 117, 076101
[3] F. Börrnert and U. Kaiser, Physical Review A 98 (2) (2018) 023861-1–10
[4] T. Lehnert, et al., *ACS Applied Nano Materials* 2.5 (2019): 3262-3270.
[5] H. Kim, et al., *Small* 16.47 (2020): 2002849

Figure 1

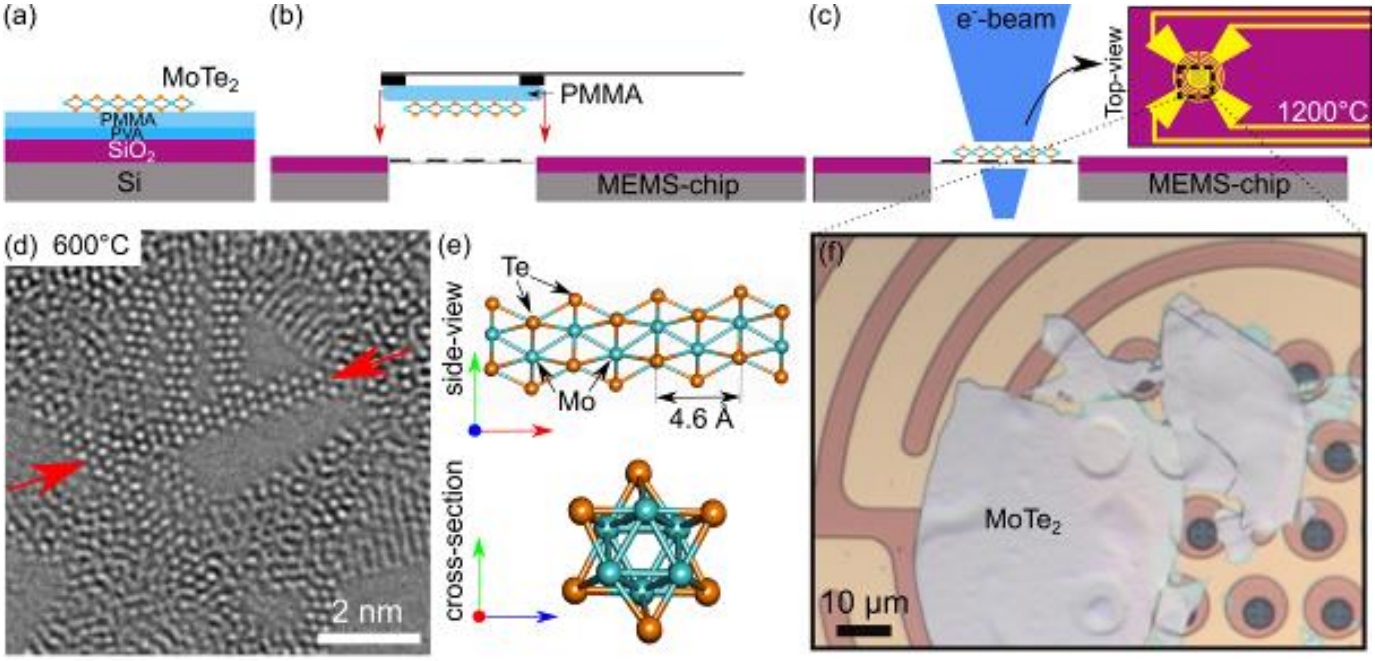

MS7.005
Dependence of micromechanical properties of synthetic polymers on loading force – explanation of the observed effects by means of 2D-SEM and 3D-LM microscopy

V. Gajdosova[1], J. Vanecek[2], M. Slouf[1]

[1]Institute of Molecular Genetics of the Czech Academy of Sciences, Polymer Morphology, Prague, Czech Republic
[2]Keyence International (Belgium) NV/SA, Prague, Czech Republic

Introduction: Microindentation hardness testing is a key method for the studying and characterization of materials in microscale. In a typical microindentation experiment, a square diamond pyramid is forced against a flat polymer surface. The mechanical properties are deduced either from the size of the imprint (non-instrumented microindentation, MH) or from the recorded *F*-*h* curves (instrumented microindentation, MHI) where *F* is the loading force and *h* is the penetration depth.

Objectives: Primary micromechanical property is microhardness ($H = F/A(h)$, where *A* is the area of the imprint on the polymer surface. For ideally plastic materials, *H* should be constant regardless of loading force (*F*) and penetration depth (*h*). For polymer materials that are elasto-visco-plastic, the value of *H* is changing as a function of *F*. The objective of this work was to elucidate the observed effects.

Materials & Methods: As testing material, ultra-high-density polyethylene (UHMWPE; GUR 1020, Ticona) was used. Micromechanical properties were measured by non-instrumented microindentation hardness tester (VMHT Auto Man; UHL, Germany) and instrumented microindentation hardness tester (MCT tester; CSM, Switzerland). Both MH and MHI measurements were carried out with Vickers indenter. 3D-LM measurements were performed by means of advanced digital microscope (VHX-6000; KEYENCE).

Results: In common MHI experiments on semicrystalline polymers, the indentation hardness (*H*IT), evaluated according to standard Oliver & Pharr theory decreases strongly (Figure 1a-b), whereas in MH experiments, the Vickers hardness (*H*V) increases slightly (Figure 1c). The seemingly contradictory changes of MHI/*H*IT and MH/*H*V could be explained by careful parallel microscopic measurements of the imprints on polymer surfaces. LM and SEM measurements provided an independent confirmation how the real size of imprints changed with *F* in MH and MHI (Figure 2a). 3D-LM measurements performed by means of advanced digital microscope (VHX-6000; KEYENCE) were able to prove pile-up effect (Figs. 2b-c). Apart from pile-up effect, the resulting properties are significantly affected by the exact determination of the contact point during the MHI measurements.

Conclusions: The combination MH, MHI, LM, SEM and 3D-LM measurements confirmed that the decrease in MHI/*H*IT with *F* was caused by creep (a time-dependent deformation) and strongly influenced by determination of contact point, while the increase in MH/*H*IT increase with F was caused by pile-up effect (a viscoelasticity-related phenomenon).

Acknowledgement: Technology Agency of the Czech Republic (TA CR; project TN01000008) and Czech Health Research Council (AZV CR; project NU21-06-00084).

Figure 1: Results of MH and MHI testing on UHMWPE polymer: (a) *F-t* curves showing the trapezoidal loading and unloading during MHI measurements, (b) microhardness from MHI experiments as a function of loading force, and (c) microhardness from MH experiments as a function of loading force.

Figure 2: Microscopic measurements, which supplemented the microindentation hardness testing results shown in Figure 1: (a) 2D-LM proving that the real sizes of imprints from non-instrumented and instrumented measurements are very similar, (b) 3D-LM measurement and (c) corresponding depth profile, which proved the pile-up effect.

Figure 1

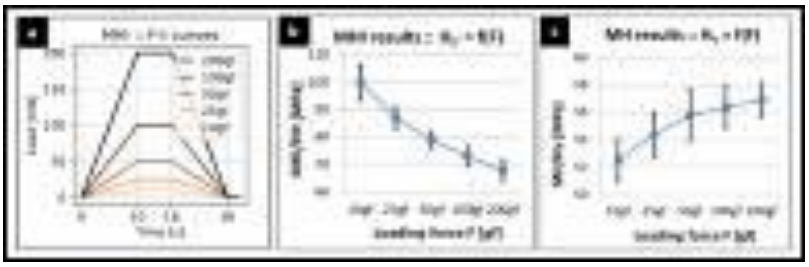

Figure 2

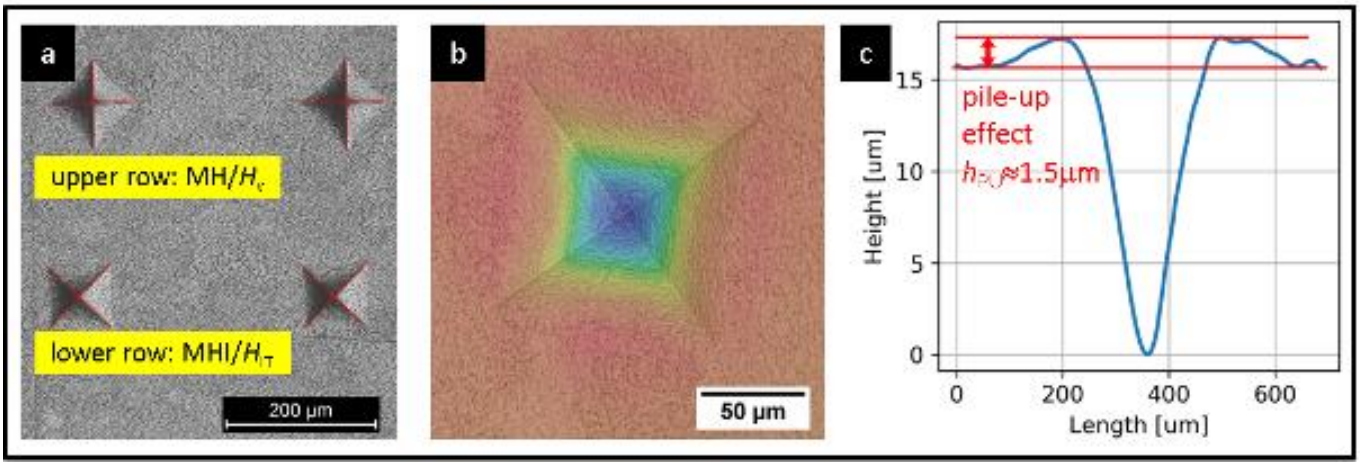

MS7.006
In situ observation of dislocation evolution in cerium oxide nanocubes in an environmental TEM

R. Zhang[1], L. Joly-Pottuz[1], T. Epicier[1], T. Albaret[2], G. Laurens[2], D. Stauffer[3], K. Masenelli-Varlot[1]

[1]INSA-Lyon, MATEIS CNRS UMR5510, Lyon, France
[2]UCB Lyon 1, ILM UMR5306, Lyon, France
[3]Bruker/Hysitron, Bruker Nano, Minneapolis, MN, United States

As one of the most important ceramic materials, cerium oxide is widely used in many applications, such as in solid oxide fuel cell electrodes, catalysis, and is also used as superior abrasive particles in chemical mechanical planarization [1]. Ceria may be difficult to be characterized by Transmission Electron Microscopy as it undergoes phase transformation under some conditions (irradiation [2], different oxygen partial pressure [3]). There are only few experimental experiments regarding its structural evolution when cerium oxides are tested under loading in different atmospheres. In this study, we will focus our study on the effects of irradiation under the electron beam and the influence of the gaseous environment on the mechanical behavior of cerium oxide nanocubes.

Two main phases of cerium oxides are investigated in this study: CeO2 has a fluorite structure (space group Fm-3m), while CeOx($1.5 \leq x < 2$) crystallizes in bixbyite (space group Ia-3). Cerium oxides nanocubes (20-50 nm in size) are compressed using a dedicated Hysitron PI 95 sample holder in an environmental transmission electron microscope (ETEM). Plastic deformation of the nanocubes is analyzed using live High-Resolution TEM imaging.

Oxygen-vacuum or on-off electron beam cycling may cause reversible changes from one phase to the other. First, CeO2 is compressed under oxygen, which helps to retain its original fluorite structure. No apparent defects are observed in the initial state. On the contrary, a cube irradiated using a high dose rate, completely reduced into CeO1.5, is compressed in vacuum along the same axis <110>. We find that many stacking faults have been produced during compression. We also evidence that a dislocation with Burgers vector [1-12] dissociated into a stacking fault. Finally, to better compare the yield stress of the two phases, a compression of the same cube with its two different phases has been performed. From the mechanical curve obtained, the yield stress is significantly reduced when the structure changes into CeO1.5.

In summary, we explore the effect of electron beam and oxygen atmosphere on cerium oxides' structure when compressed *in situ* in TEM. According to the evolution of defects and yield stress changes, the deformation mechanism in fluorite and bixbyite phases seems to be different and will be discussed.

[1] X. Feng *et al.*, "Converting ceria polyhedral nanoparticles into single-crystal nanospheres," *Science*, vol. 312, no. 5779, pp. 1504–1508, 2006.
[2] L. A. J. Garvie and P. R. Buseck, "Determination of Ce4+ / Ce3+ in electron-beam-damaged CeO2 by electron energy-loss spectroscopy," *J. Phys. Chem. Solids*, vol. 60, no. 1999, pp. 1943–1947, 1999.
[3] C. Sun, H. Li, and L. Chen, "Nanostructured ceria-based materials: Synthesis, properties, and applications," *Energy Environ. Sci.*, vol. 5, no. 9, pp. 8475–8505, 2012.

MS7.P001
Relation between morphology and micromechanical properties of alpha, beta and gamma phases of isotactic polypropylene

M. Slouf[1], E. Pavlova[1], S. Krejcikova[1], A. Zhigunov[1], V. Krzyžánek[2], E. Piorkowska[3]

[1]Institute of Molecular Genetics of the Czech Academy of Sciences, Prague, Czech Republic
[2]Institute of Scientific Instruments, Czech Academy of Sciences, Brno, Czech Republic
[3]CBMM Lodz, Polish Academy of Sciences, Lodz, Poland

Introduction: Isotactic polypropylene (PP) belongs to the four major thermoplastics (PE, PP, PS, and PVC), which together represent over 85% by volume of the world plastics consumption. The properties of PP are closely connected with its crystalline structure, which includes not only the overall crystallinity, average lamellar thickness and preferred orientation, but also the type of its crystalline modification (alpha, beta, and gamma). The alpha-PP is by far the most common, beta-PP can occur under specific preparation conditions, and gamma-PP is usually prepared at high temperatures and pressures.

Objectives: The objective of this work was to verify if gamma-PP exhibits better mechanical performance than more common alpha- and beta-PP, as indicated by some previous studies [1, 2].

Materials & methods**:** The PP samples with various crystalline phase compositions were prepared by a controlled high-pressure crystallization that enabled us to obtain not only alpha-PP and beta-PP modifications, but also a series of almost pure gamma-PP samples with gradually changing morphology, crystallinity and lamellar thickness [3]. Morphology and crystallinity were characterized by polarized light microscopy (PLM), scanning electron microscopy (SEM) and wide-angle X-ray diffraction (WAXS). The micromechanical properties were assessed by instrumented microindentation hardness testing (MHI), from which we determined indentation hardness (H_{IT}), indentation modulus (E_{IT}), indentation creep (C_{IT}) and elastic part of the indentation work (η_{IT}). The advantage of micromechanical characterization consisted in the fact that the pure gamma-PP samples were available in relatively small amounts, which were not sufficient for standard, macroscopic characterization. All experimental details have been described in our previous study [3].

Results and conclusions: The final properties of PP samples were strongly influenced by the phase composition (i.e. by the content of alpha-, beta- and gamma-phase), but the effect of overall crystallinity was equally important. Higher crystallinity resulted in higher stiffness-related micromechanical properties (H_{IT} and E_{IT}), slightly higher creep resistance (reciprocal value of C_{IT}) and higher elasticity (η_{IT}). This confirmed that the crystalline phase was not only stiffer, but also more elastic and more resistant to long-term deformation than the amorphous phase. Gamma-PP exhibited better mechanical performance than alpha- and beta-PP only if the gamma phase was well developed (as visualized by PLM and SEM) and if its crystallinity was high (as quantified by WAXS).

Acknowledgement: Technology Agency of the Czech Republic (TA CR; project TN01000008) and Czech Health Research Council (AZV CR; project NU21-06-00084).

References:
[1] E. Lezak, Z. Bartczak, A. Galeski, Plastic deformation behavior of beta phase isotactic polypropylene in plane–strain compression at room temperature, Polymer 47 (2006) 8562–8574.
[2] B. Lotz, S. Graff, C. Straupe, J.C. Wittmann, Single crystals of alpha phase isotactic polypropylene: combined diffraction and morphological support for a structure with non-parallel chains, Polymer 32 (1991) 2902–2910.
[3] Slouf M, Pavlova E, Krejcikova S, Ostafinska A, Zhigunov A, Krzyzanek V, Sowinski P, Piorkowska E: Relations between morphology and micromechanical properties of alpha, beta and gamma phases of iPP. Polymer Testing 67 (2018) 522–532.

MS7.P002
Bone damage driven by podosomes at senile osteoporosis captured at the nanometer scale

P. Simon[1], W. Pompe[2], M. Bobeth[2], H. Worch[2], R. Kniep[1], P. Formanek[3], A. Hild[4], S. Wenisch[4], E. Sturm[5]

[1]Max-Planck-Institut für Chemische Physik Fester Stoffe, Dresden, Germany
[2]Technische Universität Dresden, Dresden, Germany
[3]Leibniz-Institut für Polymerforschung Dresden e.V, Dresden, Germany
[4]University Giessen, Giessen, Germany
[5]University of Konstanz, Konstanz, Germany

The degradation mechanism of human trabecular bone harvested from the femoral head of a patient with a fragility fracture of the femoral neck under conditions of senile osteoporosis1 was investigated by high-resolution electron microscopy. As evidenced by light microscopy, there is a disturbance of bone metabolism leading to severe and irreparable damages to the bone structure. These defects are evoked by osteoclast and thus podosome activity where podosomes create typical pit marks and holes of about 200 nm in diameter on the bone surface. The platelets set free around the pit edges are considerable larger in size up to 120 x 80 nm2 in comparison with normal healthy bone showing 40 x 25 nm2. Detailed analysis of the stress field in the extracellular bone matrix was performed. The calculations yielded maximum stress in the range of few megapascals caused by forces in the actin-core module and the ventral actin-cable module of podosomes resulting in formation of microcracks around the podosomes. Disintegration of hydroxyapatite and free lying collagen fibrils were observed at the edges of the plywood structure of the bone lamella. At the ultimate state, the disintegration of the mineralized collagen fibrils to a gelatinous matrix comes along with a delamination of the apatite nanoplatelets resulting in a brittle, porous bone structure. The nanoplatelets aggregate to big hydroxyapatite plates with a size of up to 10 x 20 mm2. The age-related bone loss of elderly population can be explained by a competition of two mechanisms in the ruffled border zone: the accumulation of delaminated hydroxyapatite nanoplatelets near clusters of podosomes and the accelerated growth of big hydroxyapatite plates due to a higher percentage of undercarboxylated glutamic acid residues of osteocalcin2.

This work opens new insight into the interplay between inorganic and organic components resulting in malformation structures occurring at podosome driven disintegration of osteoporotic lamellar bone observed at high-resolution. The paper addresses an important topic of the modern and widespread disease osteoporosis. It sheds light on bone degradation mechanisms at the nanoscale and thus giving a new view on osteoporotic bone structure. For the first time, high-resolution images show the impact of osteoclast and podosome activity on the bone structure.

Figure 1: (a) Micron sized brittle apatite plates of osteoporotic bone. (b) Model of podosome.

SEM and TEM

SEM investigations were carried out by a Quanta 200 FEGi (FEI, Netherlands) at either 15kV and low vacuum conditions or at 1 kV and high vacuum by using a backscattered electron detector. For electron diffraction, a FEI Tecnai 10 electron microscope (FEI, Eindhoven, Netherlands) with a LaB6-source at 100 kV acceleration voltage was used. HRTEM was performed by a CM 200 FEG/ Lorentz at 200 kV (FEI, Eindhoven, Netherlands) at 200 kV acceleration voltage with a nominal point resolution of 0.24 nm and line resolution of 0.20 nm.

[1] B. Yu and C.-Y. Wang Osteoporosis: the result of an "aged" bone microenvironment. *Trends Mol. Med.*, **2016**, *22*, 641–644.
[2] Liu, G., Peacock, M. Age-Related Changes in Serum Undercarboxylated Osteocalcin and its Relationships with Bone Density, Bone Quality, and Hip Fracture. *Calcif. Tissue Int*. **1998**, *62***,** 286–289. https://doi.org/10.1007.

Figure 1

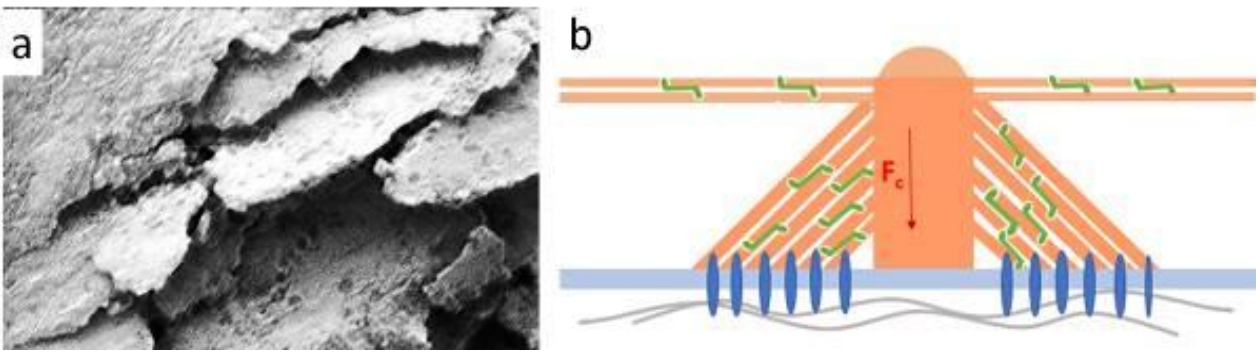

MS8.001-Invited
Enlightening the role of oxygen vacancies in structural properties of complex oxides thin films by atomic site HAADF-STEM and EELS

R. Ciancio[1]
[1]CNR-IOM Trieste, Istituto Officina dei Materiali, 34149 Trieste, Italy

Complex oxides are fascinating systems which host a vast array of unique phenomena, such as high temperature (and unconventional) superconductivity, 'colossal' magnetoresistance, all forms of magnetism and ferroelectricity, as well as (quantum) phase transitions and couplings between these states. In recent years, there have been considerable advancements in the ability to grow thin film heterostructures of these materials with atomic precision. With this level of control, the electrostatic boundary conditions at oxide surfaces and interfaces can be used to form new electronic phases or novel low-dimensional states at the interfaces inaccessible in bulk oxides. Oxygen vacancies play crucial roles in determining the physical properties of metal oxides and controlling and manipulating the defect structure provides a degree of freedom for harvesting and tailoring the functional properties of oxides. This is the case of anatase titanium dioxide TiO2, where the formation of oxygen vacancies in TiO2 has been proved to effectively tune the amount of Ti3+ ions [1-2]. As a result, localized defect states (DS) are stabilized within the band-gap of materials therefore extending the photoresponse of TiO2 from the UV towards the visible-light region. Unexpectively, at low Ti3+ concentration, DS are centered in the midinfrared (MIR) region at 1.6 eV while the increasing level of Ti3+ induced by a postannealing process, red-shifts the DS to the near-infrared region (NIR) at about 1.0eV [3].
The correlation between the functional and atomic scale properties can be obtained by local probe techniques with advanced capabilities, which allow the accurate determination of the atomic positions, the chemical composition and the electronic state with atomic resolution. In this regard, aberration-corrected STEM and the possibility to couple STEM imaging (in Z-contrast or Annular Bright Field) and EELS spectroscopy enables to determine the chemistry, crystal and electronic structure of new materials locally, with atomic resolution, and often in a quantitative way by the smart combination of imaging and spectroscopy.
This lecture will review the themendous impact in this field of having access to atomic resolution STEM, complemented by spectroscopic analysis, atomistic calculations and multislice simulation. As an example, we focus our attention on anatase TiO2 thin films, where the formation and distribution of oxygen vacancies as well as film/substrate lattice matching play an essential role in determining the electronic properties of this materials. Oxygen vacancies are indeed observed to form ordered superstructure [4] commonly attributed to the occurrence of shear-planes in anatase thin films. Elucidating the intrinsic structure of oxygen defects in oxide materials is therefore a crucial step for improving the functionalities of such material system and to engineer devices with targeted properties [4].

References

[1] Role of Oxygen Deposition Pressure in the Formation of Ti Defect States in TiO2(001) Anatase Thin Films, ACS Appl. Mater. Interfaces 2017, 9, 23099−23106
[2] Distinct behavior of localized and delocalized carriers in anatase TiO2 (001) during reaction with O2, Phys. Rev. Mater. 4, 025801 (2020)
[3] Tuning the Optical Absorption of Anatase Thin Films Across the Visible-To-Near-Infrared Spectral Region, Phys. Rev. Appl. 2020, 13, 044011
[4] Unveiling Oxygen Vacancy Superstructures in Reduced Anatase Thin Films, Nano Lett. 2020, 20, 6444−6451

MS8.002
Using Bayesian inference to improve three-dimensional atomic reconstructions from a single projection using Z-contrast imaging

A. De Backer[1,2], S. Van Aert[1,2], P. D. Nellist[3], L. Jones[4]

[1]EMAT, University of Antwerp, Antwerp, Belgium
[2]NANOlab Center of Excellence, University of Antwerp, Antwerp, Belgium
[3]Department of Materials, University of Oxford, Oxford, United Kingdom
[4]CRANN & School of Physics, Trinity College Dublin, Dublin, Ireland

In order to fully exploit structure-property relations of nanomaterials, a 3D characterization at high resolution is often required. However, many interesting materials are too beam-sensitive to handle the electron dose of the multiple projections required for tomography. Therefore, an alternative method was developed where 3D atomic models are reconstructed from atom counts obtained from a single ADF STEM projection image. These atom counts are used to create an initial atomic model which serves as an input for an energy minimization to obtain a relaxed 3D reconstruction [1-3].

Two possible approaches for the energy minimization are nowadays available. The energy is either minimized by shifting the atomic columns up and down while keeping the number of atoms in a column fixed to the outcome of the atom-counting procedure [2] or a a full molecular dynamics simulation is performed to relax the particle"s structure [3]. Where the first method is too strict by ignoring atom-counting imprecision especially at lower doses, the second method runs the risk of ending up in a global energy minimum and violating the physical constraints of the experimental observation. To overcome these limitations, we propose to include the atom-counting imprecision via a Bayesian inference scheme. Moreover, the incorporation of additional prior knowledge from neighbour-mass relations will be beneficial when reconstructing atomic models from low dose ADF STEM images. Genetic algorithms (GA) are powerful tools for solving large optimization problems [4,5]. Here, our prior knowledge is fused into a new Bayesian GA for reconstructing the 3D atomic structure.

In an extensive simulation study, the quality of the obtained reconstructions is quantitatively evaluated in terms of the coordination number of the surface atoms, which are of general interest for catalysis. Figure 1 shows the fraction of the surface atoms with the same coordination number as the ground truth Pt model. As a reference, the results for the reconstructions without prior knowledge are also included. Reconstructed models at different doses and the ground truth model are displayed in Figure 2. From Figs. 1 and 2, it is clear that a significant improvement is observed when including more relevant prior knowledge especially at lower doses. Therefore, the method is very promising for obtaining reliable reconstructions of beam-sensitive nanoparticles during dynamical processes from images acquired with lower incident electron doses [6].

[1] S. Bals et al., Nat. Comm. 3 (2012) p 897
[2] L. Jones et al., Nano Lett. 14 (2014) p 6336
[3] A. De Backer et al., Nanoscale 9 (2017) p 8791
[4] M. Yu et al., ACS Nano 10 (2016) p 4031
[5] Aarons et al., Nano Lett. 17 (2017) p 4003
[6] This work was supported by the European Research Council (Grant 770887 PICOMETRICS to SVA and Grant 823717 ESTEEM3). The authors acknowledge financial support from the Research Foundation Flanders (FWO Belgium) through project fundings and a postdoctoral grant to ADB. LJ acknowledges Science Foundation Ireland (SFI), the Royal Society, and the AMBER Centre.

Figure 1: Fraction of the correctly identified surface atoms with the same coordination number as the ground truth Pt model as a function of the incident electron dose.

Figure 2: Ground truth model and reconstructed models without and with prior knowledge at different doses. The colouring of the Pt atoms indicates the nearest-neighbour coordination from 1 in red to 12 in dark blue.

Figure 1

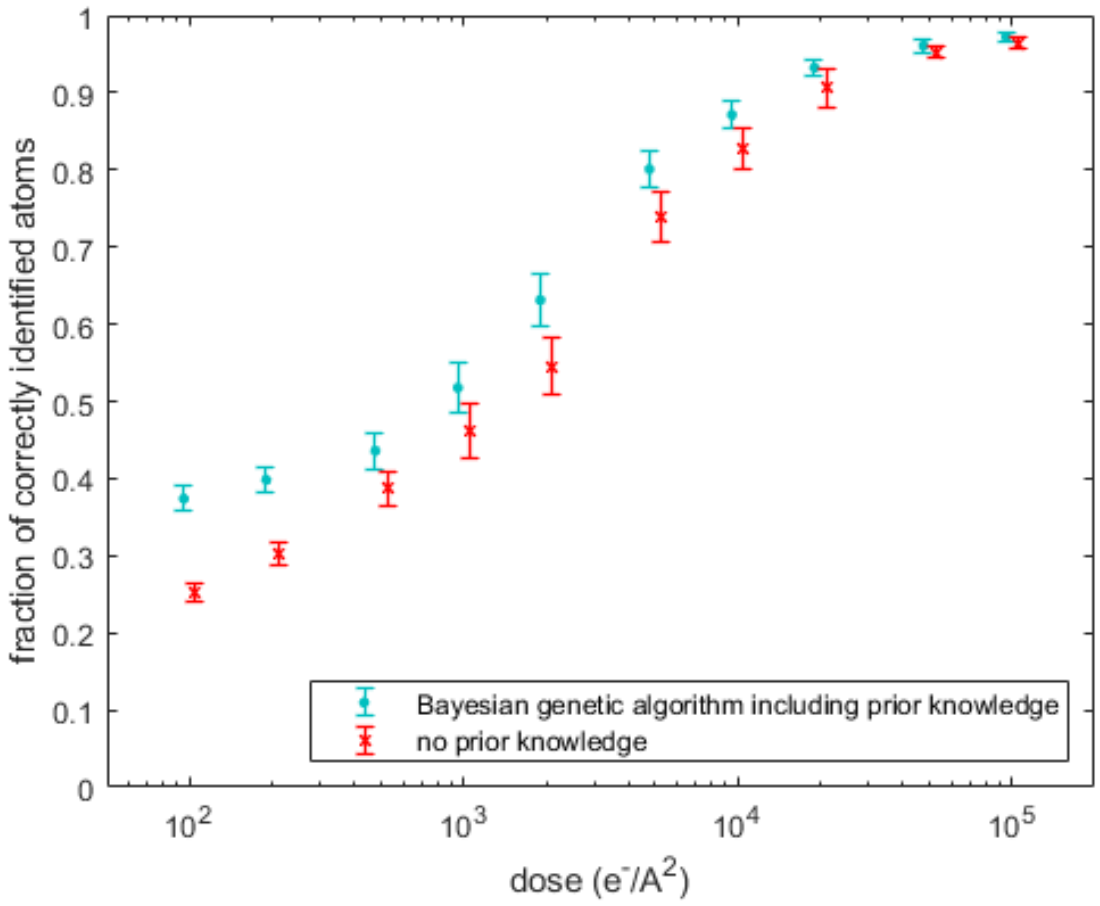

Figure 2

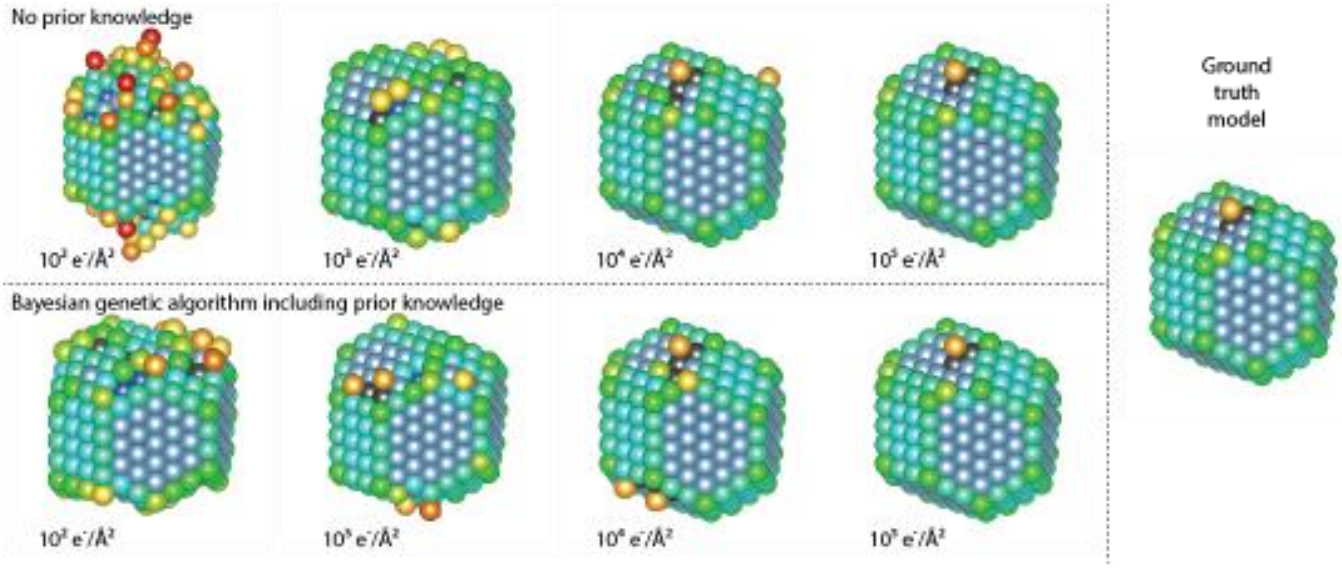

MS8.003
Atomic structure investigations on the III-N based Ferroelectric AlScN

N. Wolff[1], B. Haas[2], S. Fichtner[1,3], M. R. Islam[1], F. Niekiel[3], M. Kessel[4], O. Ambacher[4], C. T. Koch[2], F. Lofink[3]
L. Kienle[1]

[1]Kiel University, Institute for Materials Science, Kiel, Germany
[2]Humboldt University of Berlin, Institute of Physics & IRIS Adlershof, Berlin, Germany
[3]Fraunhofer Institute for Silicon Technology (ISIT), Itzehoe, Germany
[4]Fraunhofer Institute for Applied Solid State Physics (IAF), Freiburg, Germany

Introduction: A ferroelectric (FE) material inherits the ability to retain and reverse its spontaneous polarization vector along defined crystallographic directions in action to applied electric fields, which is particular suitable for microelectronic applications. In this respect, ferroelectric thin film devices require materials with superior FE properties as well as scalability and compatibility to thin film technology. In this regard, the recent advancements on AlScN in controlling thin film growth1 and the discovery of single-axis ferroelectricity2 along its preferred growth direction (inversion of polarity along c-axis of wurtzite-type unit cell) are promoting AlScN as new potential candidate for said applications.

Objectives: Thin film systems of AlScN can be grown onto various substrates and interlayers such as Pt or Mo by magnetron sputter deposition or pulsed laser deposition resulting in fiber-textured1,2 or epitaxial3 heterostructures. Especially, the analysis of the atomic structure at the interfaces and its related strain distribution are critical parameters for optimizing crystal growth and device functionality and give a first principal understanding of the ferroelectric behavior.
Materials & methods: In this work, we used the outstanding spatial resolution of high-resolution scanning transmission electron microscopy (HRSTEM, Nion HERMES, 200 kV) to study the atomic structure of N-polar and ferroelectrically switched m(etal)-polar epitaxial films of Al(1-x)ScxN (x = 0.27) and the large lateral resolution of 4D-STEM electron diffraction mapping for strain analysis. The atomic scale investigations of polarization inversion were supported by microscale anisotropic wet etching.

Results: First time atomic scale observations of AlScN in its ferroelectric stable N-polar and m-polar states unambiguously revealed the nanostructure mechanism of ferroelectric polarization switching (see Figure 1) described as the inversion of the wurtzite-type unit cell and is evidenced by anisotropic etching experiments. The investigation of the atomic interface structure at the Mo seedlayer points towards residual inversion domains which presence is discussed in relation to compressive interfacial strain revealed by strain mapping. However, further optimization of crystal growth and film quality is required for resolving this issue in detail.

Conclusion: The combination of HRSTEM imaging, 4D-STEM methods and anisotropic wet-etching experiments highly benefits the understanding of ferroelectric behavior and growth processes for optimization of AlScN-based thin film devices. This strategy will be translated in perspective also to improved AlScN-based thin film systems, especially to resolve its interface structures.

Figure 1: Annular brightfield HRSTEM images showing the N- and m-polar atomic structure in as-grown and ferroelectrically switched AlScN. (excerpt from [3], https://doi.org/10.1063/5.0033205)
[1] S. Fichtner, N. Wolff, G. Krishnamurthy, A. Petraru, S. Bohse, F. Lofink, S. Chemnitz, H. Kohlstedt, L. Kienle, and B. Wagner, Journal of Applied Physics **122**, 035301 (2017).
[2] S. Fichtner, N. Wolff, F. Lofink, L. Kienle, and B. Wagner, Journal of Applied Physics **125**, 114103 (2019).
[3] N. Wolff, S. Fichtner, B. Haas, M.R. Islam, F. Niekiel, M. Kessel, O. Ambacher, C. Koch, B. Wagner, F. Lofink, and L. Kienle, Journal of Applied Physics **129**, 034103 (2021).

Figure 1

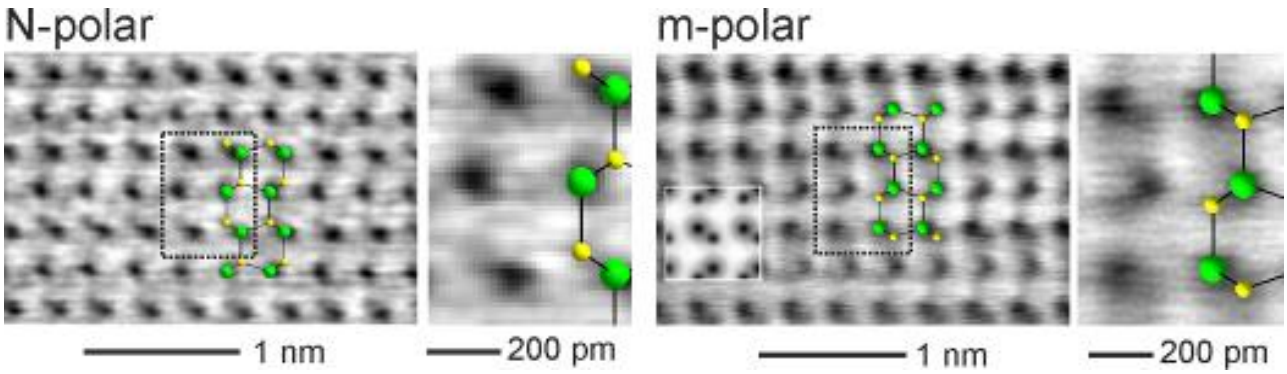

MS8.004
Application of an iris aperture to angle-resolved quantitative STEM of silicon

T. Grieb[1], F. F. Krause[1], A. Beyer-Leser[2], S. S. Firoozabadi[2], M. Schowalter[1], P. Kükelhan[2], H. L. Robert[3,4], C. Mahr[1] O. Oppermann[1], D. Heimes[2], K. Volz[2], K. Müller-Caspary[3,4], A. Rosenauer[1]

[1]IFP University of Bremen, Bremen, Germany
[2]Philipps-University Marburg, Marburg, Germany
[3]Research Center Jülich, Jülich, Germany
[4]RWTH Aachen University, Aachen, Germany

Quantitative comparison of annular-dark field (ADF) intensities in scanning-transmission electron microscopy (STEM) to reference simulations allows for the measurement of specimen thickness or composition with atomic-scale spatial resolution. Frequently, high-angle (HA) ADF data is exploited which simplifies respective simulations and quantitative analysis as it can be interpreted as Z-contrast [1]. Analysing medium-angle (MA) or even low-angle (LA) ADF data can provide additional information. For instance, it was shown that Huang scattering from static-atomic displacements predominantly scatters into medium and low angles [2]. Combining MAADF and HAADF allowed to determine simultaneously specimen thickness and chemical composition in GaNAs [2].

In this study we investigate various scattering effects on high, medium and low scattering angles in ADF STEM of silicon (100), which are: (i) inelastic (plasmon loss) scattering, (ii) scattering from amorphous surface layers, (iii) the influence of phonon-correlation and (iv) distortions in the diffraction plane as well as (v) experimental settings such as mistilt, defocus and others [3,4].

For the investigation of different angular ranges, we installed a motorized iris aperture (Figure 1a) above the ADF detector in an FEI Titan 80/300 microscope that allows to achieve ADF-STEM images with well-defined outer detector radii [2,3]. By recording detector scans for each iris-aperture position (Figure 1b), a quantitative comparison to frozen-lattice simulations calculated with the STEMsim code [5] is possible. Figure 1c shows the sensitivity of the ADF detector for the different iris positions.

We investigated for different thicknesses how the exploited angular range affects the determined thickness, where the thickness evaluated from PACBED [6] was used as a reference. Figure 1d shows the relative discrepancy between measured thickness and the thickness from PACBED for reference simulations in the Einstein approximation ignoring all additional scattering effects: the strong deviations occur especially for small angles. Figure 1e shows the strongly reduced discrepancy for the case of reference simulations taking inelastic scattering, phonon-correlation and amorphous surface covering into account.

Figure 1f and Figure 1g visualize the angle dependence of the inelastic scattering and the effect of phonon correlation. It shows that mainly low angles are influenced by these effects.

[1] S. Molina, et al., Ultramicroscopy **109** (2009) 172-176.
[2] K. Müller-Caspary et al., Sci. Rep. **6** (2016) 37146.
[3] T. Grieb et al., Ultramicroscopy **221** (2021) 113175.
[4] A. Beyer et al., Sci. Rep. **10** (2020) 17890.
[5] A. Rosenauer and M. Schowalter, Springer Proc. Phys. **120** (2007) 169-172.
[6] J.M. LeBeau et al., Ultramicroscopy 110 (2010) 118-125.
[7] TG and AR acknowledge the German Research Foundation (RO2057/8-3), KM-C the Helmholtz Network and Initiative Support (VH-NG 1317).

Figure 1: (a) Motorized iris aperture, (b) ADF detector scans and (c) radial detector sensitivities for different iris openings. (d,e) Discrepancy of the thickness measured from quantitative ADF STEM to the thickness evaluated from PACBED: (d) using standard reference simulations (Einstein approximation) and (e) considering additional scattering effects. (f) Ratio of experimental inelastic and elastic scattering. (g) Ratio of simulated intensity with/without consideration of phonon correlation. Figures from Refs.[3,4].

Figure 1

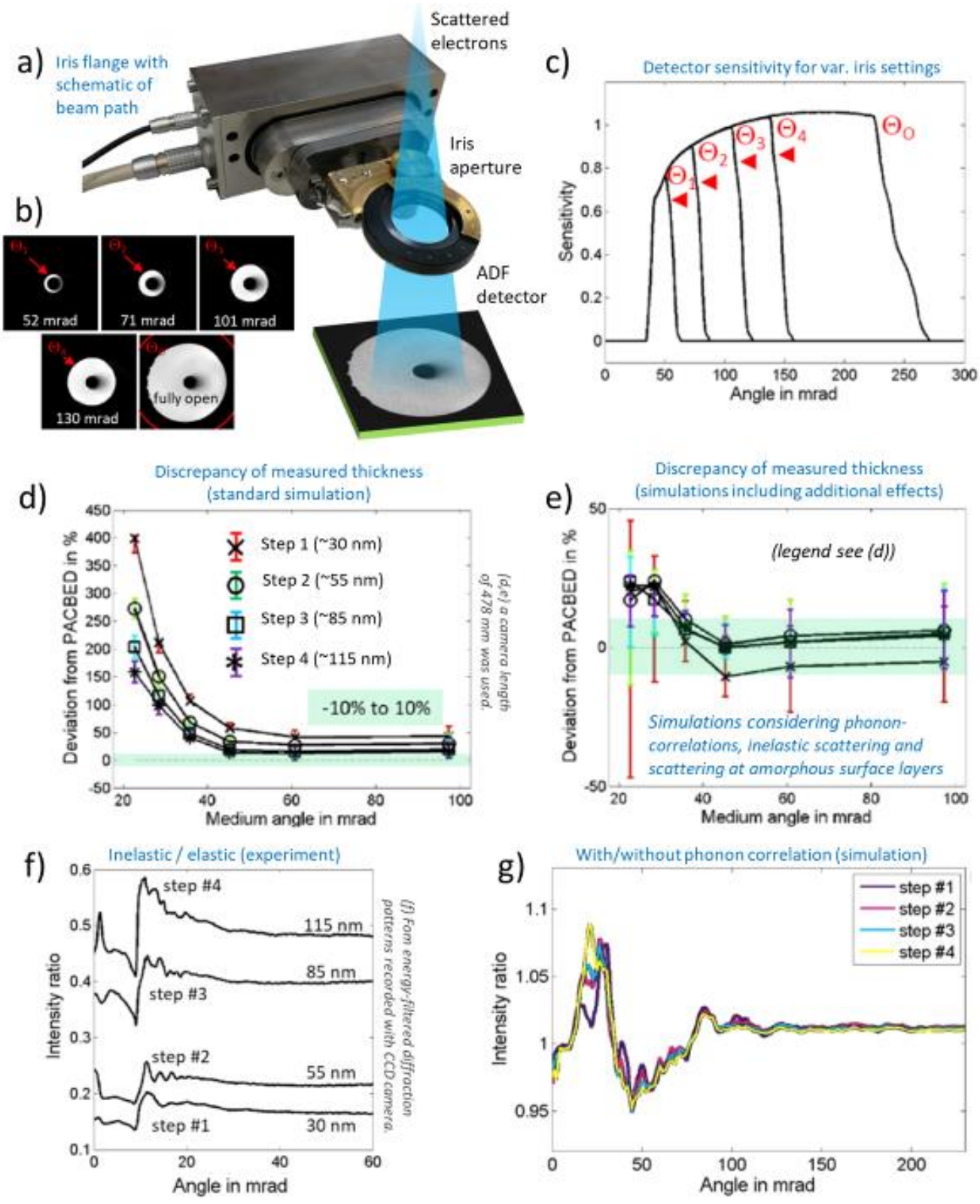

MS8.005
Real-space topological ferroelectricity and self-epitaxial hetero-nanolayers in nickel phosphides

X. Wei[1], G. Bihlmayer[2], Y. V. Kolen'ko[3], L. Liu[3], S. Blügel[2], J. Mayer[1], R. E. Dunin-Borkowski[1]

[1]Research Center Jülich, Ernst Ruska-Centre for Microscopy and Spectroscopy with Electrons, Jülich, Germany
[2]Research Center Jülich, Peter Grünberg Institute and Institute for Advanced Simulation, Jülich, Germany
[3]International Iberian Nanotechnology Laboratory (INL), Braga, Portugal

Surface compositional, atomic and electronic structures play key roles in controlling activity of catalysts during electrochemical reactions. As for the supporting matrix, factors such as conductivity, elemental valence state, polyhedral polarity and spin structure [1-3] are also important in influencing performance of the catalysts. However, for earth-abundant and efficient transition-metal phosphides used for water splitting, such atomic-scale structural information is largely missing, which hinders design and optimization of catalysts with superior electrochemical activity.

Here, we report the discovery of real-space topological ferroelectricity in non-centrosymmetric Ni_2P (space group P-62m). Focusing on polyhedral polarity [4], we establish symmetry equations of polarity and the solution yields that the polarity couples with elemental valence states through nickel atomic sites, which is verified by valence state measurement using electron energy-loss spectroscopy (EELS) and structural characterization. First principles calculations reveal that associated with center-convergent to center-divergent transition of topological geometry under in-plane compressive strain (winding number n = 1), the polyhedral polarity also couples to momentum-dependent spin polarization. The dual roles of nickel cations, i.e., their polar displacements and 3D bonding network, enables the coexisting topological polarity with metallicity [5]. In combination with electron-beam bombardment, our image-simulation-based scanning transmission electron microscopy (S/TEM) study reveals coverage of self-epitaxial Ni_2P and NiP_x ($0 < x < 0.5$) nanolayers on (001) surfaces of Ni_5P_4 nanosheets [6]. The discovery of topological ferroelectricity and core-shell scenario in nickel phosphides provide novel insights to understand the catalytic performance of transition-metal catalysts for electrochemical energy conversion.

Figure 1: (A-D) Polyhedral polarity, HAADF images, atomic-resolution EELS of nickel atoms in Ni_2P and transition of topological polarization (P_S) under in-plane compressive strain. (E-H) Sample morphology and self-epitaxial hetero-nanolayers on (001)-oriented Ni_5P_4 nanosheets probed by image simulations.

References:
[1] F. A. Garcés-Pineda *et al.*, *Nature Energy* 4, 519 (2019).
[2] R. B. Wexler, J. M. P. Martirez, A. M. Rappe, *Chem. Mater.* 28, 5365 (2016).
[3] W. Mtangi *et al.*, *J. Phys. Chem. Lett.* 6, 4916 (2015).
[4] X.-K. Wei *et al.*, *Phys. Rev. B* 98, 020102(R) (2018).
[5] X.-K. Wei, G. Bihlmayer, X. Zhou, W. Feng, Y. V. Kolen'ko, D. Xiong, L. Liu, S. Blugel, R. E. Dunin-Borkowski, *Adv. Mater.* 32, 2003479 (2020).
[6] X.-K. Wei, D. Xiong, L. Liu, R. E. Dunin-Borkowski, *ACS Appl. Mater. Interfaces* 12, 21616 (2020).

Figure 1

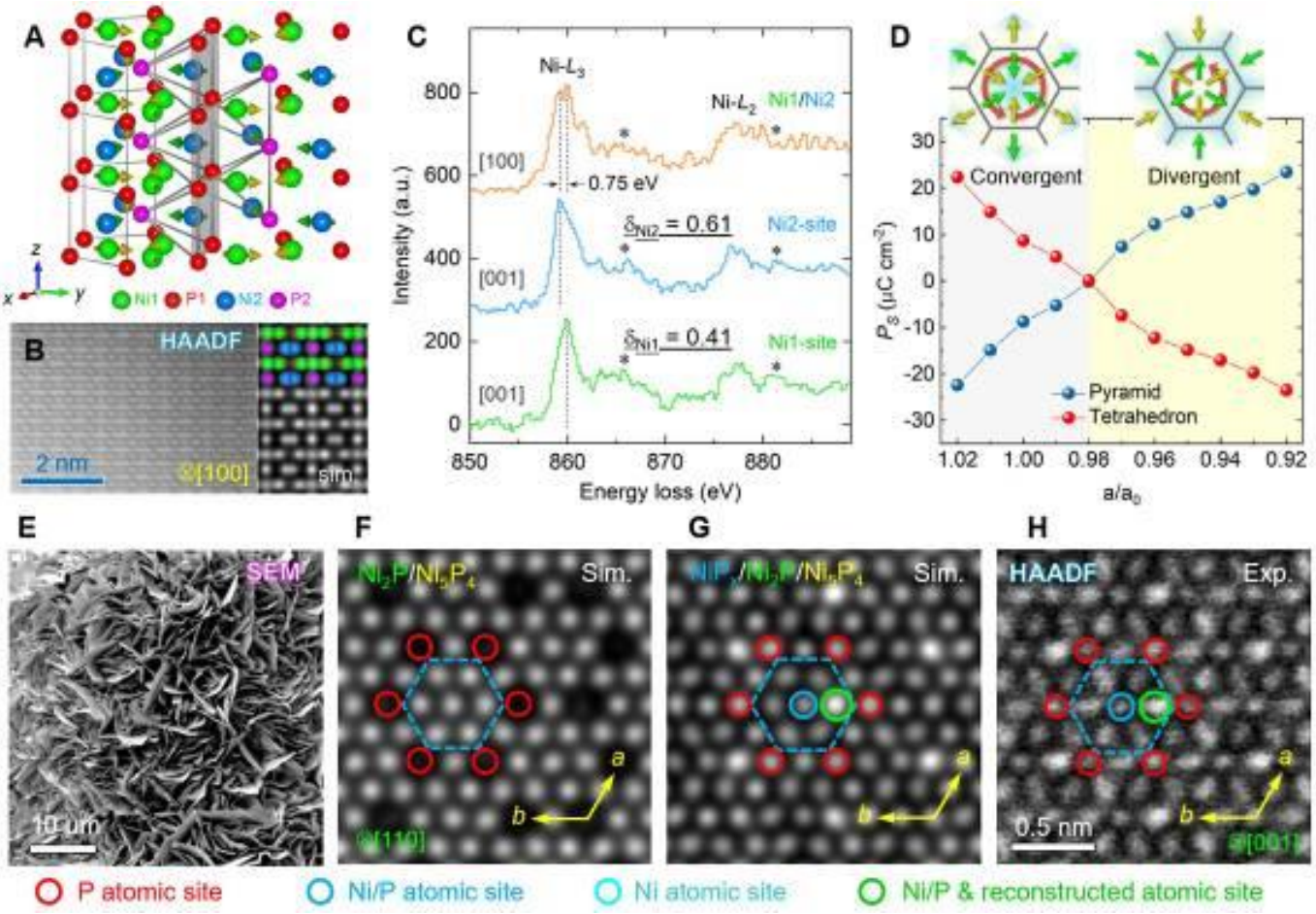
A
Ni1 P1 Ni2 P2
B
HAADF
2 nm
sim.
C
Ni-L_3
Ni-L_2 Ni1/Ni2
[100]
0.75 eV
δ_{Ni2} = 0.61
Ni2-site
[001]
δ_{Ni1} = 0.41
Ni1-site
[001]
Intensity (a.u.)
Energy loss (eV)
D
Convergent
Divergent
Pyramid
Tetrahedron
P_S (μC cm^{-2})
a/a$_0$
E
SEM
10 μm
F
Ni_2P/Ni_5P_4
Sim.
G
$Ni_2P_1/Ni_2P/Ni_5P_4$
Sim.
H
HAADF
Exp.
0.5 nm
P atomic site
Ni/P atomic site
Ni atomic site
Ni/P & reconstructed atomic site

MS8.006
Advances in 3D *in situ* characterisation of rapid nanoparticle dynamics during gas-phase catalysis

K. Jenkinson[1], I. Lobato[1], E. Arslan Irmak[1], A. De Backer[1], P. Liu[1], A. Pedrazo-Tardajos[1], S. Van Aert[1], T. Altantzis[1], S. Bals[1]

[1]EMAT, University of Antwerp, Antwerp, Belgium

The realisation of metal nanoparticle (MNP) transformations during heterogeneous catalysis has highlighted fundamental flaws within catalyst technologies, where surface faceting-activity relationships are principally derived from the structure of pristine unreacted catalysts. However, it is known that when MNPs interact with reactant molecules or elevated temperatures results in changes in relative free energies of surface facets which can lead to drastic changes within the MNP morphology, surface faceting and elemental distribution. Therefore, the identity and structure of the "active" MNP catalysts formed during a chemical reaction is still fiercely debated and poorly understood. The development of *in situ* characterisation techniques has therefore become a priority to identify the *real* catalyst in addition to understanding MNP *in situ* dynamics. For instance, the MNP catalysed CO oxidation reaction displays a periodic oscillation in performance that could not be explained until *in situ* gas-phase electron microscopy identified continuous surface refaceting upon the exposure of CO molecules. [1] Such studies have resulted in a better understanding of MNP behaviour to influence future MNP catalyst design.

This project strives to track high-temperature structural transformations to identify atom-level mechanisms with unprecedented detail and in three dimensions using state of the art *in situ* heating and gas-cell catalysis experiments. [2,3] Due to its global importance within transport emission control, the CO oxidation reaction using MNPs is an ideal benchmark gas-phase reaction to investigate as our model system. Furthermore, CO oxidation allows for the assessment of MNP performance in real time using a dedicated Gas Chromatography - Mass Spectrometry (GCMS) to identify how structural transformations within the catalyst influence performance. To capture rapid dynamics with atomic resolution we utilise ultra-fast STEM imaging conventionally applied to beam sensitive materials. Atomic resolution imaging of this nature was restored using bespoke convolutional neural networks to compensate for scanning distortions and significant image noise. Ideally, these *in situ* experiments would be combined with electron tomography to accurately quantify changes within MNPs to consider transformations within the entire structure rather than simply considering changes within their 2D shape. However, the rapid structural transformations require alternative techniques to visualise catalyst transformations in 3D with sub-second time resolution. Through the quantitative analysis of 2D atomic resolution imaging known as atom counting, we are able to generate 3D structures from a single calibrated image supported by molecular dynamics simulations. [4] Therefore, through atomic-resolution *in situ* gas cell experiments coupled with quantitative image processing, we are able to visualise atomic resolution mechanisms and answer fundamental questions relating to MNP dynamics during gas-phase catalysis in three dimensions.

References:
[1] S. B. Vendelbo *et al*, *Nat. Mater.*, 2014, **13**, 884–890.
[2] T. Altantzis *et al*, *Nano Lett.*, 2019, **19**, 477–481.
[3] P. Liu *et al*, *Nanoscale*, 2021, **13**, 1770–1776.
[4] S. Van Aert *et al, Nature*, 2011, **470**, 374–377.

Figure 1

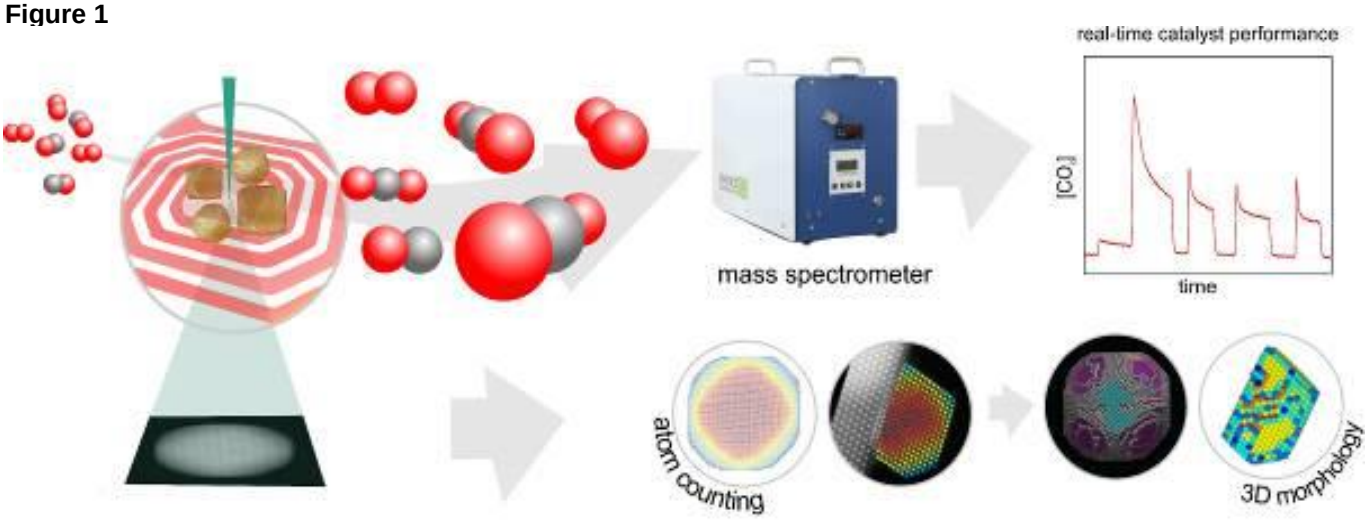

MS8.007
Dynamics of the metal-support interaction under catalytic reaction conditions as seen by *in situ* TEM

H. Frey[1,2], A. Beck[2], X. Wang[3], D. Palagin[3], X. Huang[1,4], J. Van Bokhoven[1,2], M. G. Willinger[1]

[1]ETH Zurich, ScopeM, Zurich, Switzerland
[2]ETH Zurich, Institute for Chemical and Bioengineering, Zurich, Switzerland
[3]PSI, Villingen, Switzerland
[4]Fuzhou University, College of Chemistry, Fuzhou, China

Introduction: The interface between noble metals and reducible metal oxide supports exhibits properties that make interfacial sites some of the most active and selective in heterogeneous catalysts. High-temperature reduction reveals the strong-metal-support-interaction, characterized by encapsulation of the noble metal nanoparticle by a thin layer of the support material[1]. However, little is known about the structure and dynamics of the metal-support interface under catalytic conditions. Here, we show by real-time imaging using in-situ transmission electron microscopy, that the overlayer is not stable and varies readily with changes in gas phase composition. Moreover, the interface between platinum and titania shows dynamic behavior when simultaneously exposed to both an oxidizing and a reducing reactant. The dynamic picture that is revealed by direct real-time and real-space imaging is forcing a reconsideration of the concept of active sites at the metal-support interface. The interaction between the noble metal particle, the reducible support and the gas-phase leads to dynamic redox processes at the interface.

Material and Methods: The Sample was a Pt-rTiO2 catalyst, Pt loading was 2 wt%. with an average platinum particle size is 12 nm. *In-situ* TEM studies were performed using an aberration-corrected 300 kV JEOL Grand-ARM300F. A modified DENSsolutions Climate+ System was used to study samples under controlled gas-flow, pressure and temperature conditions. The setup was coupled to a quadrupole mass spectrometer, enabling simultaneous imaging and detection of catalytic conversion.

Results and Discussion: An overlayer formed after high temperature reduction conditions (HTR, p_{H2} = 700 mbar, T = 600°C) and was stable after a subsequent switch to a purely oxidizing (p_{O2} = 700 mbar, T = 600 °C) gas atmosphere, as described in a previous work by our group[2]. When a small (60 mbar) amount of hydrogen was added to the atmosphere, the overlayer retracted from the platinum particles first from low energy platinum {111} facets, then from the entire particle (Figure 1). Subsequently, platinum particles engaged in dynamic restructuring and/or particle migration (Figure 2). Retracting hydrogen from the gas atmosphere quickly re-encapsulates platinum again by a TiO_x layer (shown by EELS), which effectively seizes the particle mobility (Figure 3). Reference experiments on unsupported platinum particles (i.e. supported on an inert SiN_x membrane) did not show such dynamical behavior under otherwise identical reaction conditions. This proofs that particle dynamics Pt/TiO_2 catalyst are a result of the redox processes observed at the metal - oxide interface: Hydrogen activated at the platinum surface readily reduces titania lattice oxygen at the strained particle – support interface, leading to a structural collapse of the titania lattice at the interface - which is periodically restored by excess oxygen in the atmosphere.

[1] Tauster SJ, Fung SC, Baker RTK, Horsley JA. Strong Interactions in Supported-Metal Catalysts. *Science (80-)*. 1981;211(4487):1121 LP - 1125. doi:10.1126/science.211.4487.1121
[2] Beck A, Huang X, Artiglia L, et al. The dynamics of overlayer formation on catalyst nanoparticles and strong metal-support interaction. *Nat Commun*. 2020;11(1):3220. doi:10.1038/s41467-020-17070-2

Figure 1

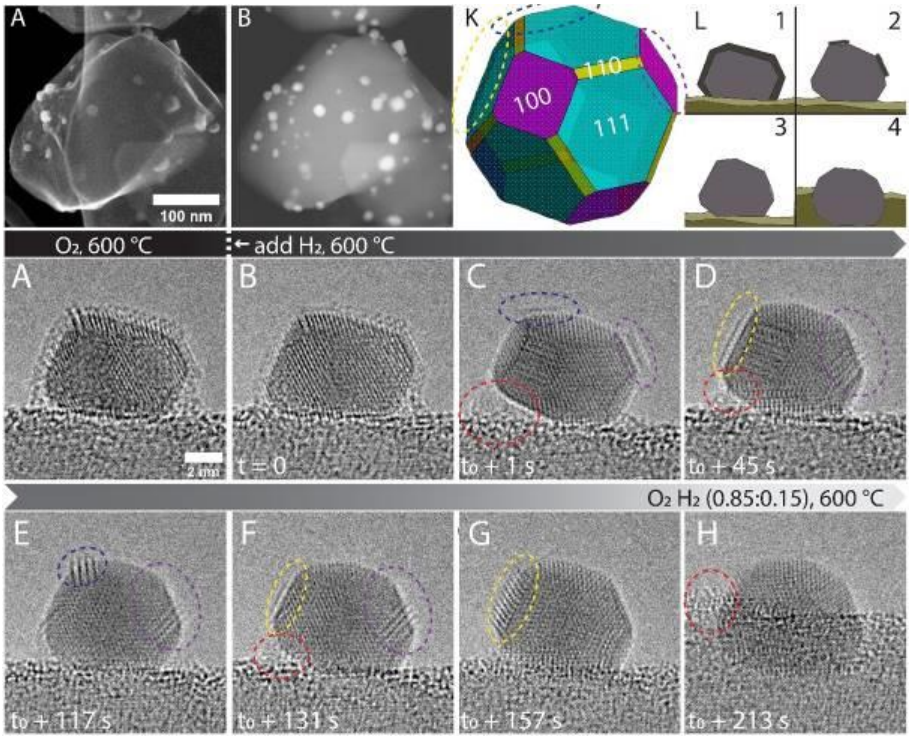

Figure 2

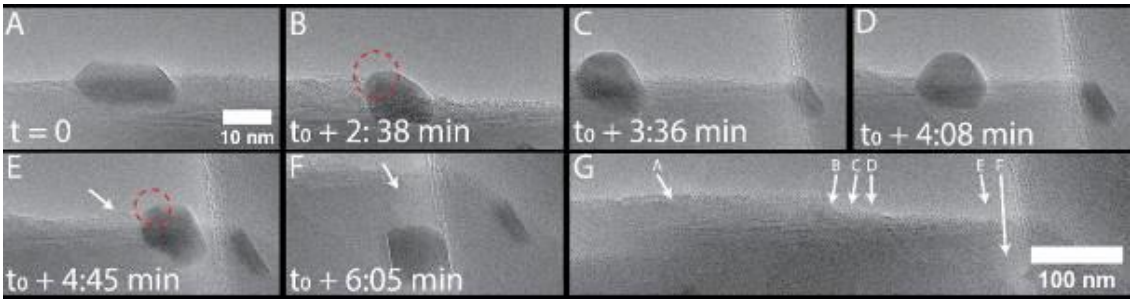

Figure 3

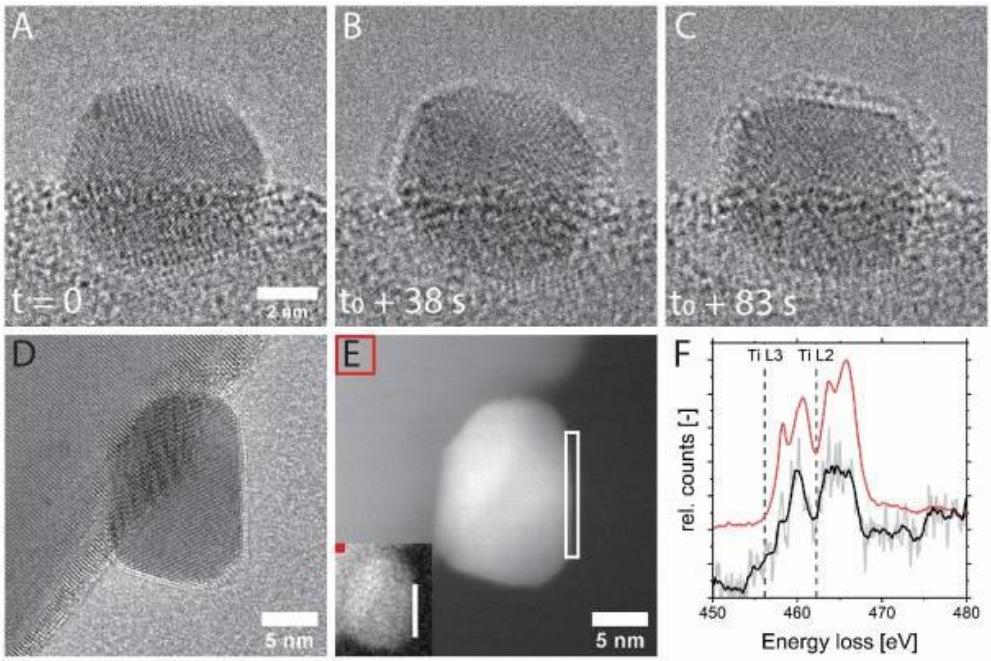

MS8.P001
Development and characterisation of nanopyramid arrays as substrates for surface enhanced Raman spectroscopy (SERS)

C. Burkhardt[1], M. Fleischer[2], C. Simo[2]

[1]NMI Natural and Medical Sciences Institute, Center for Nanoanalysis, Reutlingen, Germany
[2]Institute for Applied Physics and Center LISA+, University of Tübingen, Tübingen, Germany

Question: Raman spectroscopy is a versatile technique for characterization of biological and material samples by measuring their vibrational states. A critical drawback is the very low cross section for excitation of Raman scattered light. One option to increase the Raman signal is the enhancement by using metallic nanostructures. This work addresses the question how to prepare such surface enhanced Raman spectroscopy (SERS) platforms based on nanopyramids on flexible substrates to allow for detection of low abundance analytes.

Methods: The fabrication pathway by nanosphere lithography (NSL) is represented in Figure 1(left). NSL was performed with 520 nm diameter polystyrene nanospheres (PN) that were spin-coated onto a (100) silicon wafer. The PNs were then etched with an oxygen plasma to achieve diameters of 300-350 nm, and a chromium etch mask was evaporated. The PNs were removed through wafer tape stripping, leaving behind a silicon wafer with a chromium layer with nanocavities. A potassium hydroxide solution was used to etch the inverted pyramids, then the chromium etch mask was removed. The resulting structure served as the negative mold for the gold nanopyramid arrays. The mold was functionalized with a F13TCS anti-sticking layer, and a 50 nm thin film of gold was evaporated. The silicon mold with the functionalized gold film was pressed onto an elastomeric PDMS patch. The mold could then be stripped off, leaving behind the continuous gold film with the hollow nanopyramid arrays. This could then be used for SERS measurements with 4-Mercaptobenzoic acid (4-MBA). Three different concentrations (2 mM, 100 µM and 50 µM) were chosen to test the SERS sensitivity of the nanopyramid arrays.

Results: The template stripping of the continuous gold film with hexagonal nanopyramid arrays reproducibly yielded ≥90% area transfer to the PDMS while maintaining the pyramidal shape. SEM images (ZEISS Crossbeam 550 with Gemini 2) reveal that the nano pyramids showed base lengths of ~414 nm and tip radii of ~14 nm, with some neighboring pyramids being joined at the base (Figure 1(right)). Additional control of the pyramid shape was performed with Focused Ion Beam microscopy (Capella FIB within the Crossbeam) and Helium Ion Microscopy (ZEISS Orion NanoFab). Ion microscopy enables also a final local modification of the pyramide arrays. SERS data was acquired with a confocal Raman spectrometer (Renishaw inVia™) equipped with a HeNe Laser (633nm). Raman spectra of the 4-MBA were taken on the areas structured with nanopyramids and compared to spectra taken on a continuous gold film on the same sample. Raman maps were acquired over larger areas. The 4-MBA ring breathing mode signal from each grid point was collected and averaged to calculate the relative enhancement factor. The spectra and maps showed a clear relative enhancement of about two orders of magnitude on the structured nanopyramid areas compared to the flat gold (Figure 2).

Conclusion: Arrays of gold pyramids could be successfully fabricated using a template stripping process. SERS measurements with 4-MBA showed a relative enhancement factor of more than 100 in comparison to a bare gold surface. As the arrays are transferred to a flexible PDMS substrate, tuning of the SERS is envisaged for advanced applications.

[1] Langer et al. ACS Nano 2020, 14, 28
[2] N.C. Linn et al., Nanotechnology 2009, 20, 225303
[3] He et al., Int. J. Extrem. Manuf. 2021, 3, 01200

Figure 1

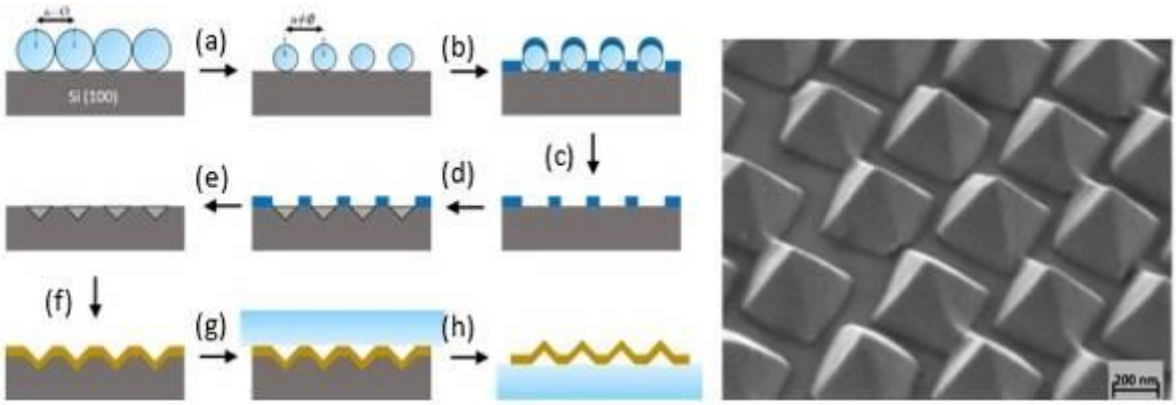

Figure 1: (left) Illustration of the fabrication procedure. After spin-coating the PN diameters were reduced through an oxygen plasma (a). A 40 nm chromium layer was deposited (b) and the PNs were stripped off with some wafer tape (c). The exposed silicon was then etched with KOH (d) and the chromium layer removed (d). After functionalizing the mold with F_{13}TCS a 50 nm thin film of gold was evaporated (f), which was functionalized with MPTS afterwards. By using a PDMS stamp (g) the continuous film of gold with the hollow pyramids was stripped off the silicon mold (h). (right) SEM image with tilt 54°.

Figure 2

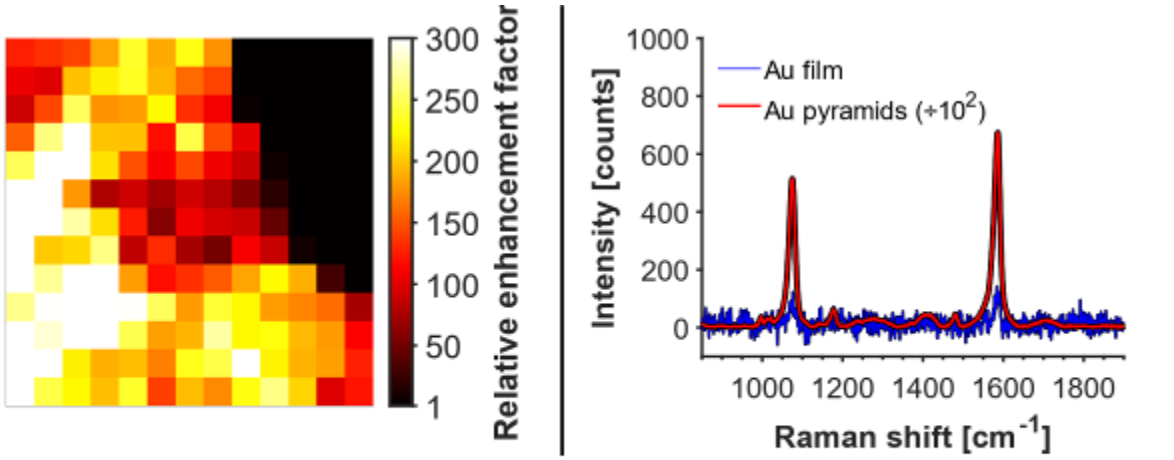

Figure 2: (left) Heatmap of the relative enhancement factor for 50 µM 4-MBA detection which included a film of unstructured gold in the top right corner. (right) Comparison of the 4-MBA signal on the gold film and nano pyramid array (reduced by a factor of 100).

MS8.P002
Plasma surface interaction and modification on the nanoscale – towards *in situ* TEM studies

N. Kohlmann[1], L. Hansen[2], O. Lupan[1,3], U. Schürmann[1], F. Schütt[1], F. Rasch[1], R. Adelung[1], H. Kersten[2], L. Kienle[1]

[1]Kiel University, Institute for Materials Science, Kiel, Germany
[2]Kiel University, Institute for Applied and Experimental Physics, Kiel, Germany
[3]Technical University of Moldova, Department of Microelectronics and Semiconductors Devices, Chisinau, Moldova

Summary: We present the current design state as well as preliminary results for an *in situ* microplasma cell for integration into a TEM holder. In addition, results of *ex situ* plasma treatment on 3D porous networks consisting of tetrapodal zinc oxide are reported. Effective etching and nanostructuring of ZnO was observed for acetylene-hydrogen plasma treatment.

Introduction: Fabrication or modification of nanostructured materials and surfaces often requires plasma processes. Dry etching of ZnO in hydrogen-hydrocarbon plasmas is thereby an established technique for device fabrication and material treatment [1].

Understanding of the interaction between plasma discharge and material itself is limited by treatment and analysis normally being separated processes. To overcome this separation a microplasma chamber based on proof-of-principle experiments [2] for *in situ* plasma treatment inside a TEM is in development; thus, enabling the direct study of plasma and material surface interaction.

Materials & Methods: TEM was carried out using a FEI Tecnai F30 G² STwin as well as with a JEOL JEM-2100. SEM analysis was performed using a Zeiss Supra 55 V.

Ex situ plasma treatment was carried out using a capacitively coupled low-pressure RF discharge with a hydrogen-acetylene (H2-C2H2) gas mixture. The ZnO tetrapod material is prepared onto Si wafers placed on top of the powered electrode.

The *in situ* microplasma cell design is optimized for vacuum-tightness and reproducibility, see Figure 1 a). Due to the single-shot design cells can be tested for function and being vacuum sealed before introduction into the TEM.

Results & Discussion: The influence of plasma treatment on 3D networks of tetrapodal ZnO [3] was studied *ex situ* to lay out the basis for *in situ* studies using the microcell. Self-patterned preferential etching leading to the formation of ZnO nanowire arrays was observed. SAED and HRTEM show that nanowires retain the crystallographic orientation of the pristine ZnO tetrapod arms. Brush-like nanostructures with greatly increased surface area (Figure1 b), c)) are created. Additionally, etch rates are determined and compared to previous studies with similar experimental conditions [1] finding good agreement.

Gas sensing measurements using a single etched tetrapod arm show good H2 sensitivity as well as selectivity. Comparison to untreated tetrapod arms show enhanced sensing properties.

Finally, we present an outlook for adapting the *ex situ* experiments to our *in situ* microplasma chamber as well as further experimental studies that will be enabled by the microcell.

Conclusion: Fabrication of highly porous nano on micro structure for sensing application was achieved. Thus, the impact of plasma treatment on ZnO material was shown. The current design state and potential impact of a plasma microcell for TEM integration is given. The authors further present an outlook for adaptation of experiments to the microcell environment.

Figure 1: a) Sketch of the in situ cell. b), c) SEM and STEM HAADF micrographs of etched ZnO tetrapod arms respectively.

The authors thank the Deutsche Forschungsgemeinschaft (DFG, german research foundation) for funding (KI 1263/17-1, KE 574/8-1).

References:
[1] Guo *et al*. Japanese Journal of Applied Physics, Vol 45, pp 8597–99, year 2006.
[2] K. Tai *et al*., Scientific Reports, Vol. 3, pp 1325, year 2013.
[3] Y. K. Mishra *et al*., ACS Appl. Mater. Interfaces, Vol. 7, pp 14303-14316, year 2015

Figure 1

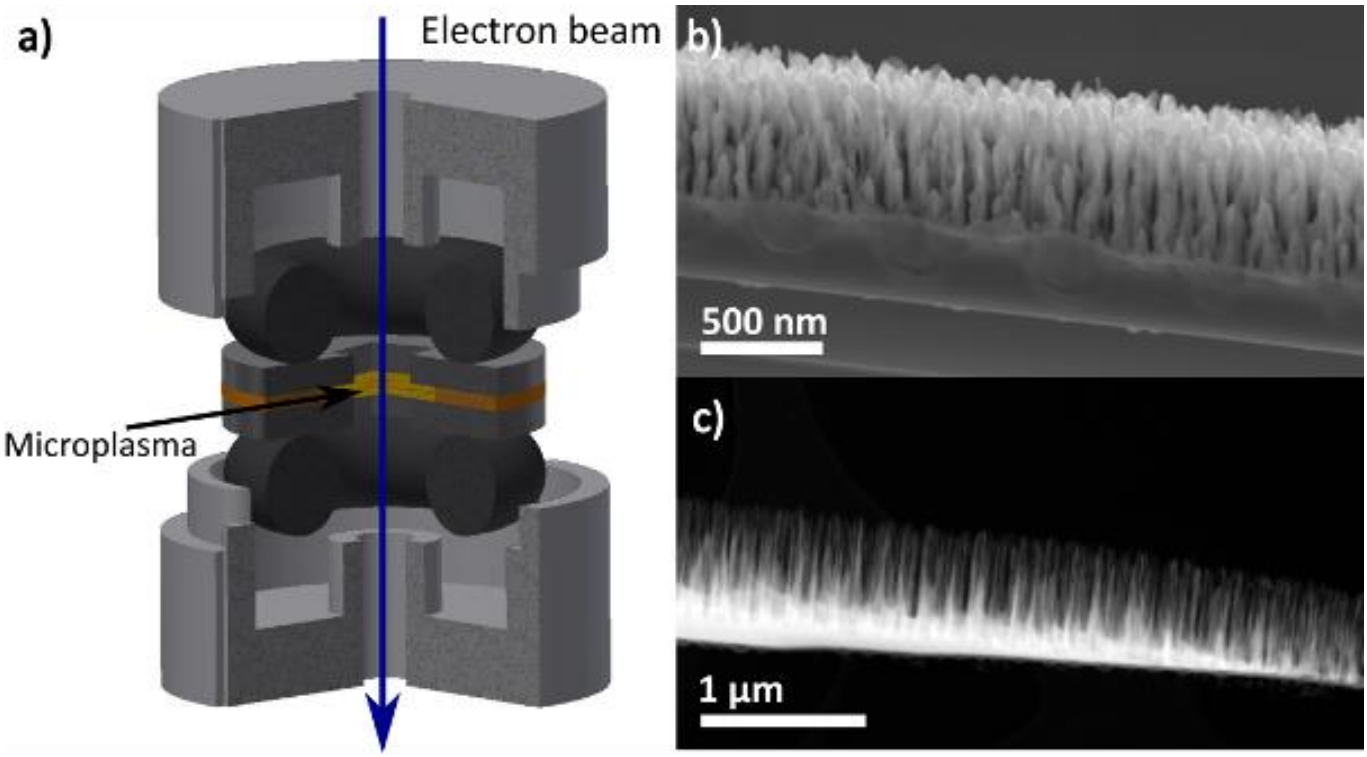

MS8.P003
A multi-modal and multi-scale *operando* investigation of the vapor-based selective oxidation of 2-propanol on cobalt

T. Götsch[1], L. Sandoval-Diaz[1], R. Schlögl[1,2], A. Knop-Gericke[1,2], T. Lunkenbein[1]

[1]Fritz Haber Institute of the Max Planck Society , Inorganic Chemistry, Berlin, Germany
[2]Max Planck Institute for Chemical Energy Conversion, Department of Heterogeneous Reactions, Mülheim an der Ruhr, Germany

Figure 1: ESEM images of a cobalt foil during selective 2-propanol oxidation after pre-reduction (top row) and after pre-oxidation (bottom row). The insets show X-ray absorption spectra fort he O-K and Co-L edge, and below the arrows, the product intensities are given for acetone (blue) and CO_2 (green).

Selective oxidation reactions of alcohols belong to the most important processes in the chemical industry, being employed in the synthesis of base chemicals such as formaldehyde or acetone.[1] In the field of heterogeneous catalysis, *operando* techniques have become increasingly important in the last few years. In contrast to *in situ* methods, *operando* requires not only the investigation under reaction conditions (e.g. gas phase and temperature), but also the simultaneous detection of activity and selectivity.

Here, we present a study of the vapor-based selective (aerobic) oxidation of 2-propanol on cobalt foils after different pre-treatments using a multi-modal and multi-scale approach. This multi-modal and multi-scale approach involves multiple microscopic and spectroscopic *operando* techniques, including environmental scanning electron microscopy (ESEM) and synchrotron-based surface-sensitive, integral X-ray photoelectron spectroscopy as well as X-ray absorption spectroscopy.

Operando SEM experiments were conducted in a modified ThermoFisher Scientific Quanta instrument, fitted with a Pfeiffer Prisma quadrupole mass spectrometer (QMS) for product detection and an infrared laser for sample heating.[2] *Operando* X-ray spectroscopy was performed at the CAT end station, using the soft X-ray branch of the EMIL beam line of BESSY II. Photoelectrons were detected using a Specs Phoibos 150 NAP analyzer and X-ray absorption was measured in total and Auger electron yields. In this setup, the same sample holder as in ESEM could be used, allowing for complementary experiments at the same total gas pressures of about 0.5 hPa. A Pfeiffer Prisma QMS was attached to the X-ray spectroscopy chamber as well for product detection.

In the top-left panel of Figure 1, the pre-reduced metallic state of the cobalt foil can be seen, with surface domain formation already underway. Upon reaction up to 300 °C, the metallic cobalt gets gradually oxidized by the 1:1 2-propanol/O_2 mixture to a CoO-like oxidation state (accompanied by a roughening of the surface). During the reaction, there is a pre-maximum in acetone formation at around 150 °C, which is clearly separated from the main reaction channel at high temperatures.

If the surface is instead pre-oxidized to a well facetted Co_3O_4 spinel, the reaction lacks this pre-maximum and only shows a high-temperature activity regime at 300 °C. This suggests that the surface states required for the low temperature activity are only formed by low-temperature *in situ* oxidation in the reaction mixture, but not during high-temperature pre-oxidation. To elucidate this mechanism in more detail, we have currently scheduled *operando* TEM experiments in order to prospectively be able to relate the crystallographic and electronic structure to these two reactivity pathways at the nanoscale, as well as *operando* transmission X-ray microscopy to obtain spatially resolved, high-energy-resolution electronic structure information.

[1] Mallat, Baiker In *Handbook of Heterogeneous Catalysis*, Wiley-VCH, 2008
[2] Sandoval-Diaz et al. *J. Energy Chem.* **2020,** *50,* 178

Figure 1

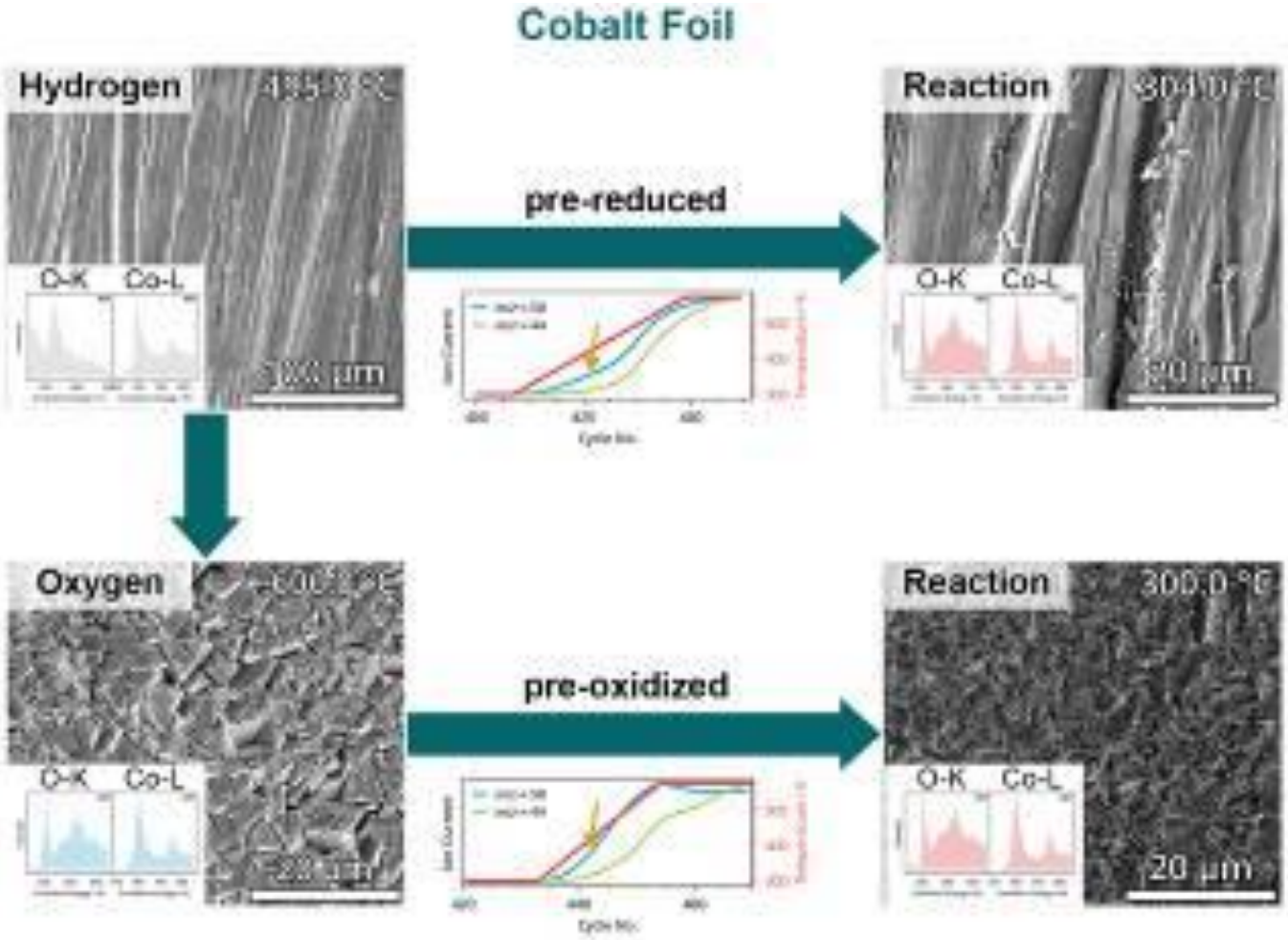
Cobalt Foil
Hydrogen
O-K
Co-L
pre-reduced
Reaction
20 µm
Oxygen
pre-oxidized
Reaction
20 µm

MS8.P004
Quantitative 3D characterisation of nanoporous gold nanoparticles by scanning transmission electron microscopy

C. Mahr[1,2], A. Dworzak[3,4], M. Schowalter[1,2], M. Oezaslan[3,4], A. Rosenauer[1,2]

[1]University of Bremen, Institute of Solid State Physics, Bremen, Germany
[2]University of Bremen, MAPEX Center for Materials and Processes, Bremen, Germany
[3]Technical University of Braunschweig, Institute of Technical Chemistry, Braunschweig, Germany
[4]Carl von Ossietzky University of Oldenburg, Institute of Chemistry, Oldenburg, Germany

Although regarded as inert for a very long time, gold (Au) in a nanostructured form can show a very high catalytic activity. This was demonstrated for Au nanoparticles [1] and dealloyed nanoporous gold (npAu) [2], which is obtained by corrosion of alloys of Au and a less noble metal such as e.g. silver (Ag). NpAu is a completely unsupported bulk material with an open porous structure, built-up of ligaments and pores, which is penetrable for gases and liquids, making it a designated catalyst.

Dealloying of alloy nanoparticles combines advantages of nanoparticles and npAu [3]. Besides applications in catalysis, dealloyed nanoparticles further have interesting applications in the field of surface-enhanced Raman spectroscopy [4]. In this contribution, we provide a first quantitative three-dimensional characterization of porous Au nanoparticles obtained by dealloying of initial $Ag_{77}Au_{23}$ alloy nanoparticles [5].

Figure1: Representative STEM images of porous Au-rich nanoparticles prepared by dealloying of $Ag_{77}Au_{23}$ nanoparticles with initial diameters of *(77 ± 26) nm.* (a) Nanoparticle of structure type A. (b) Nanoparticle of structure type B. (c) Three connected nanoparticles of types A and B.

Dealloyed nanoparticles have two different structure types. This is shown in Figure 1 by three representative scanning transmission electron microscopy (STEM) images. In these two-dimensional projections, nanoparticles of type A have a structure that seems to be more dense compared to that of type B nanoparticles. The latter resembles more the structure of dealloyed bulk nanoporous gold. We found that type A particles have a higher content of residual Ag than particles of structure type B.

To confirm different structures in 3D, particle shapes were reconstructed using STEM tomography [6]. Reconstructions were evaluated quantitatively using chord length distributions. We found that particles with a higher Ag content have larger ligaments resulting in a lower porosity compared to particles with a low Ag content. This is also reflected in a smaller specific surface area of particles with a higher Ag content.

Figure 2: 3D structure analysis of a dealloyed porous nanoparticle (structure type A). (a) STEM tomography reconstruction. (b) Skeleton representation of the material. (c) Skeleton representation of the pores. Red and green points in (b) and (c) represent branch and end points of the skeletons, respectively, the z-position of skeleton points is colour-coded.

Tortuosity describes an effective elongation of a path between two points through a porous medium compared to the direct connection between these points. Hence, it is an important property of a porous material. To complete our study we determined the tortuosities of different particles evaluating the material and pore skeletons shown in Figure 2. We found within error bars equal tortuosities of $\tau \approx 1.9$ for pore and material space.

Our results show significant differences compared to the structure of dealloyed bulk samples and can be used as input for simulations of diffusion or mass transport processes e.g. in catalytic applications.

[1] M. Haruta et al., Chem. Lett., **16** (1987), p.405.
[2] V. Zielasek et al., Angew. Chem. Int. Ed., **45** (2006), p.8241
[3] X. Li et al., Nano Lett. **14** (2014), p.2569.
[4] C. W. Huang et al., J. Nano. Res., **10** (2010), p.137.
[5] C. Mahr et al. submitted to Microsc. Microanal.
[6] P. Midgley et al., Ultramicroscopy, **96** (2003), p.413.

Figure 1

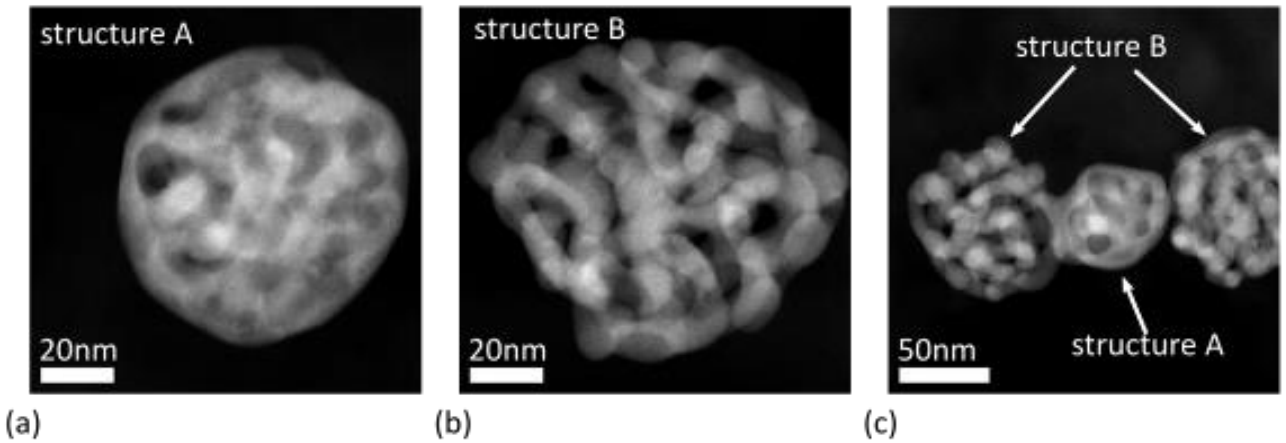

Figure 2

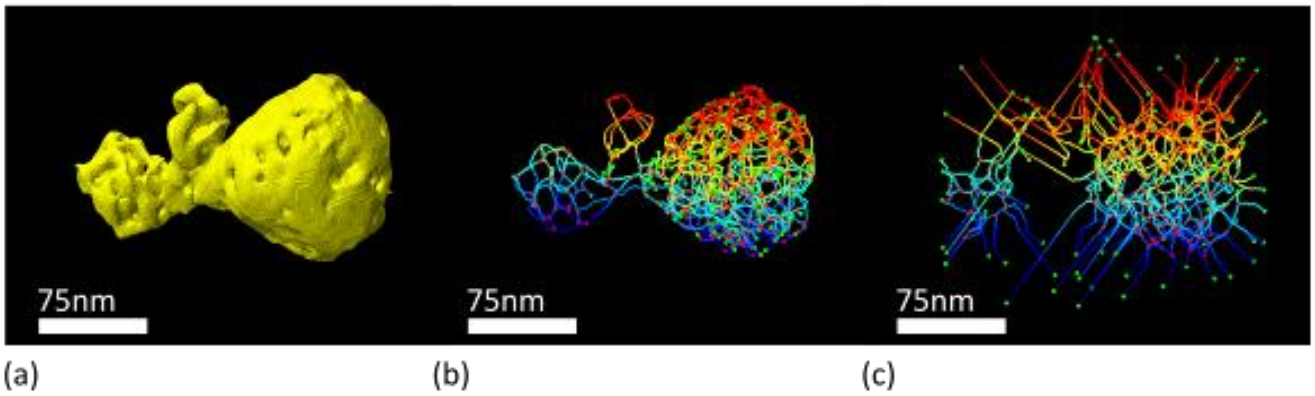

MS8.P005
Gas inclusions within a 7 nm Al2O3 thin film part of a Memristive Device

O. Gronenberg[1], F. Zahari[2], J. Strobel[1], G. Haberfehlner[3], H. Kohlstedt[2], L. Kienle[1]

[1]Institute for Materials Science, Synthesis and Real Structure, Kiel, Germany
[2]Institute for Electrical Engineering and Information Technology, Nanoelectronic, Kiel, Germany
[3]Institute of Electron Microscopy and Nanoanalysis, Graz University of Technology, Graz, Germany

Double barrier memristive devices are under investigation, which consist of a 2.5 nm thick NbOx (or HfOx) layer sandwiched between an Al2O3 tunnel barrier and a Schottky-like contact to an Au top electrode. These devices show bipolar interface-based analogue resistive switching which is most probably due to the migration of oxygen vacancies that change the interfacial properties [1]. Inside the tunnel barrier, argon and oxygen gas was found in pores of FIB lamellas which are vacuum-tightly encapsulated in the thin film. The formation and the influence of these pores on the devices are analyzed in this study.

Most probably, Ar stems from the sputtering process or the nanomilling of the FIB-lamella and O2 from the oxidation step. Under investigation is the origin of the pores and the influence on the functionality of the memristive devices.

Scanning transmission electron microscopy (STEM) investigations were performed on a FEI Titan3 60–300 operated at 300 kV.

Different oxidation methods for the two oxide thin films were tested, including reactive sputtering, thermal oxidation and anodic oxidation. Only reactive sputtering leads to functional devices. It is assumed that no pores exist in the unoxidized Al thin film because of its good wetting properties on the Nb-back-electrode. Additional, functional and non-functional devices from one and the same wafer were investigated with respect to the pores. For this purpose, FIB lamellas were prepared for STEM EELS and EDX analysis and atom probe tomography is scheduled for 3D morphological information of this system.

In HAADF STEM images dark contrast is observed in the middle of the Al2O3 thin film indicating pores up to 10 nm length and 2 nm thickness (cf. Figure 1). At the same position an oxygen pre-edge peak appears (cf. Figure 2) and further, an Ar-EDX-signal was found at the very same position (up to 5 at. %). The pre-edge feature most likely originates from the unoccupied π* orbitals of molecular oxygen (gas) [2]. These are strong indications for gas filled pores inside the Al2O3 thin film. Noteworthy, these pores are vacuum-tight in the cross-sectional FIB lamella.

Figure 1: STEM images of the thin film stack with gamma correction to improve the visibility of the pores (dark contrast)

Figure 2: Background subtracted and normalized oxygen K peak with pre-edge peak from the middle of the Al2O3 thin film.

Independent of the oxidation method gas filled pores are found inside the Al2O3 thin film. Three explanations for the pore-formation can be discussed. First, the pores could form due to stress formation during the oxidation Al thin film. Second, they could form due to ion implantation in the following reactive sputtering of NbOx or HfOx. And third, the TEM-preparation with the NanoMill might degrade the Al2O3 and implant Ar-ions. Further, the electron beam might reduce the Al2O3 and produce molecular oxygen. Functional and non-functional devices exhibit gas filled pores inside the Al2O3 thin film.

Within an amorphous Al2O3 thin film of max. 7 nm thickness of a memristive device planar pores filled with Ar and O2 gas were observed. The formation mechanism is discussed and it is assumed that they form during the oxidation due to stress.

[1] M. Hansen, M. Ziegler, L. Kolberg, R. Soni, S. Dirkmann, T. Mussenbrock, and H. Kohlstedt, Sci. Rep. **5** (2015)
[2] S. Fritz, A. Seiler, L. Radtke, R. Schneider, M. Weides, G. Weiß, und D. Gerthsen, *Sci Rep*, Bd. 8, Nr. 1, S. 7956, Dez. 2018.

Figure 1

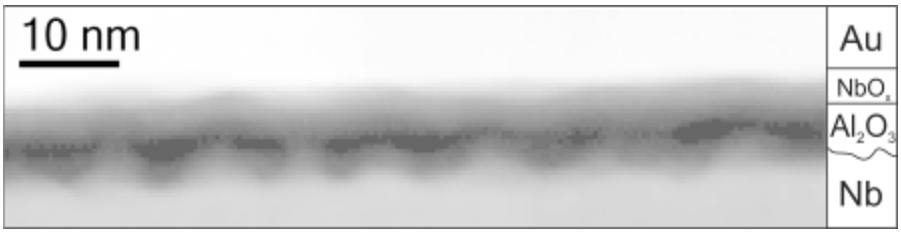

Figure 2

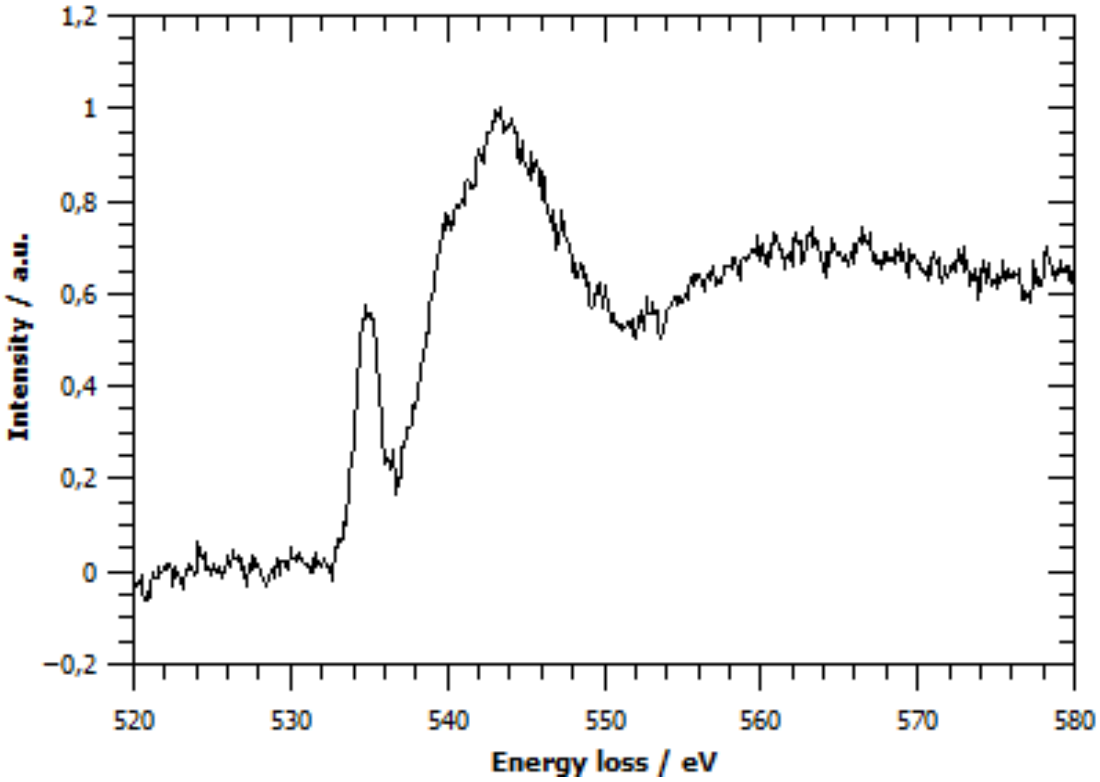

MS8.P006
Atomic-scale investigation of nickelate-based perovskite superlattice interfaces

F. Misjak[1], R. Ortiz[2], Q. Lan[3], R. E. Dunin-Borkowski[3], E. Benckiser[2], U. Kaiser[1]

[1]University of Ulm, Ulm, Germany
[2]Max Planck Institute for Solid State Research, Stuttgart, Germany
[3]ER-C Forschungszentrum Jülich GmbH, Jülich, Germany

Most of the interest in rare-earth nickelates ($RNiO_3$ where R= rear earth ion) is recently focused on thin films with the general objective of modulating their physical properties through strain control, confinement and interface effects. With respect to the bulk counterparts, the behavior of thin films is highly sensitive to the choice of substrate, dimensionality and the possibility to combining different compounds into a superlattice structure. The chosen materials combination will affect the interfacial mismatches in lattice parameter, oxygen octahedral distortions, chemistry, or valence state and the result is often an interfacial transition layer with novel physical properties different from the bulk material ones.

In this work, we investigated two different stacks of nickelate $LaNiO_3$//$LaGaO_3$ heterostructures grown by pulsed laser deposition on $SrTiO_3$ substrate. Cross-sectional transmission electron microscopy (TEM) specimens were prepared by focused ion beam. Negative-spherical-aberration (C_s) imaging was used to resolve the oxygen atomic columns and the interface structures using 300 kV aberration-corrected (AC)-HRTEM. 300 kV AC scanning (S)TEM equipped with an energy-dispersive X-ray spectrometer (EDX) was used to map the chemical composition across the heterointerfaces.

Figure 1 shows AC-HRTEM image of [4 uc. $LaNiO_3$//8 uc. $LaGaO_3$]x12 superlattice structure recorded under negative C_s condition. At the heterointerfaces of the superlattice, a short length scale interaction was observed, which gives rise to enhanced NiO_6 rotations as well as reduced GaO_6 rotations. The accommodation length scale over which the NiO_6 and GaO_6 interact is 1 - 2 unit cell both above and below the heterointerface. Quantitative evaluation of the octahedral distortions and comparison between different superlattice stacking were made.

We observed that the NiO_6 octahedral distortion and rotations about [100] and [010] axes can be tuned with the dimensionality of the superlattice. The magnetic and electronic states of rare-earth nickelates are strongly coupled to the octahedral rotations and distortions, therefore the results contribute to our understanding of how to manipulate the material properties in a controllable way.

Acknowledgements: We are grateful for financial support from DFG KA1295/26-1 and IQST project-between University of Ulm and University of Stuttgart. We gratefully acknowledge M Mundszinger and M Kruth for TEM sample preparation.

Figure 1: Example of $LaNiO_3/LaGaO_3$ superlattice thin film grown on $SrTiO_3$ substrate prepared in [110] projection. The HRTEM images were recorded under negative C_s of - 15 µm and overfocus, under which atoms were imaged white. Clearly resolved interfaces can be seen. (a) At the substrate the interface is coherent and composed of one terminated layer of TiO (labeled by red arrows) followed by a layer of LaO units. The heterointerfaces in the first set of bi-layer is labeled by green arrows. Mixing of NiO and GaO units exists at the interfaces. (b-c) Enlargement of the near substrate part of the superlattice, and the corresponding image simulation (C_s =−15 µm, defocus +5 nm, thickness 5 nm) together with the atomic model based on bulk $LaNiO_3$ and $LaGaO_3$ data. Red arrows show the interfacial layers, where mixed of (La,Ga)O layer seems to exist. The first GaO layers show consistently lower waviness compared to simulation based on bulk data (black arrows) indicating 1 unit cell accomodation layer at the interfaces.

Figure 1

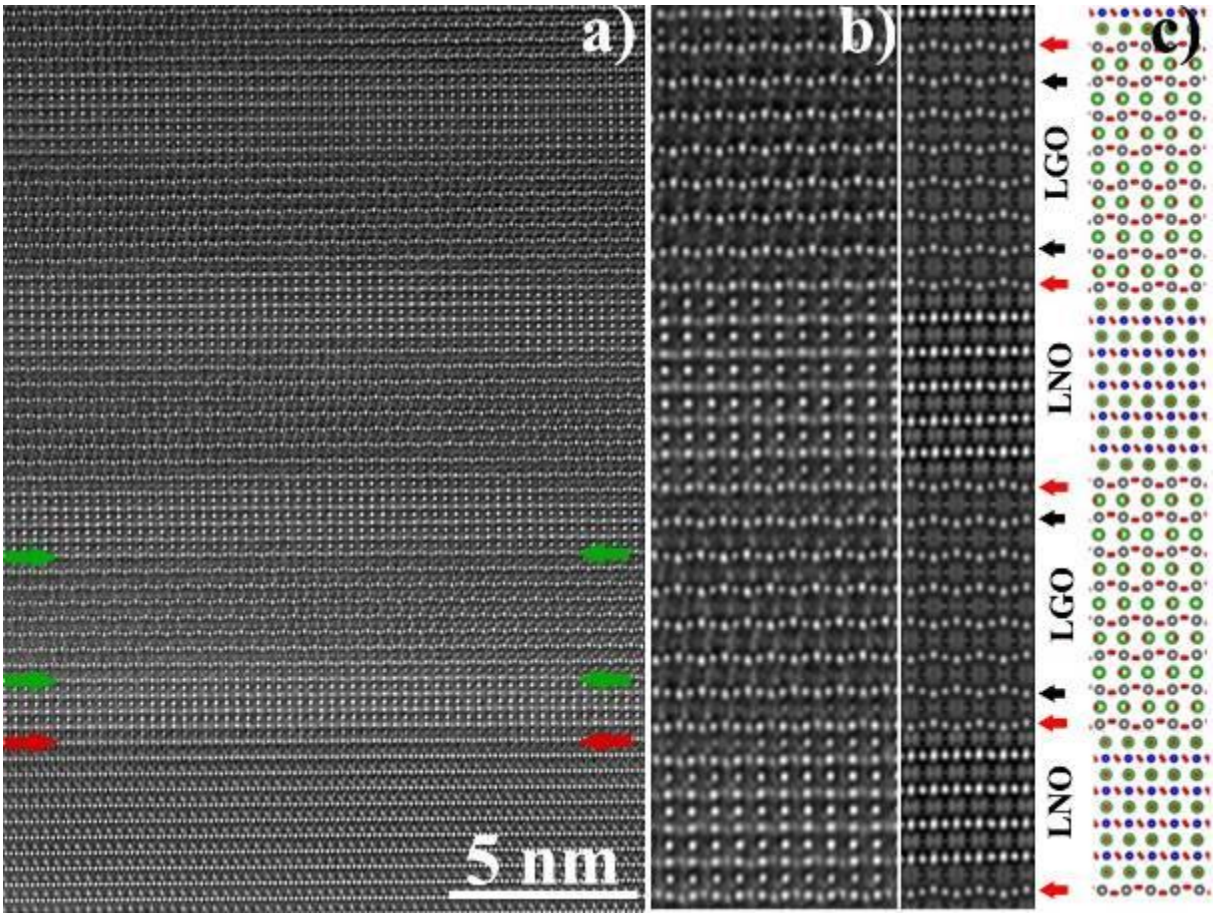

MS8.P007
In-situ imaging of hydrogen-induced surface reactions using a SEM-compatible atomic hydrogen source

K. Bukvišová[1], L. Novák[2], M. Dhankhar[1], J. Mach[1], T. Šikola[1], M. Kolíbal[1]

[1]Brno University of Technology, Brno, Czech Republic
[2]Thermo Fisher Scientific, Brno, Czech Republic

Reduction reactions are very important chemical processes taking part in many fields of technology. They are used for extracting pure metals from ores, which are usually oxides or sulfides. Hydrogen-induced reduction plays a significant role in nanotechnology as well, since molecular hydrogen is an important constituent of reaction atmosphere in chemical vapour deposition, either as a reactive or carrier gas. In this particular case, its role is usually underestimated or neglected, despite its significance. This could be due to a fact that molecular hydrogen is not very reactive and high temperature is necessary for the dissociation of the molecule into atomic hydrogen radicals, which are very reactive and responsible for most reactions. To study the hydrogen-induced reactions, it is thus advantageous to pre-crack the hydrogen molecule, which allows performing the processes at lower temperatures in a much more controlled way.

In order to monitor these reactions in-situ, we have designed a cracker source for generation of atomic hydrogen radicals. The dissociation is done at a tungsten capillary heated to a high temperature (> 2200 K) while the molecular hydrogen gas flows through it. The thermal energy delivered to the molecules during collisions with the capillary held at high temperature is enough to dissociate the diatomic molecule into two monoatomic radicals. The principle of the source is schematically depicted in Figure 1. The source is compatible with high-vacuum SEM operation. Thanks to the additional shielding optics, it is possible to mitigate parasitic signals generated by the heated capillary and thus, in-situ imaging is also possible.

As a proof-of-concept experiment, we demonstrate nickel oxide reduction at temperatures below 600 °C (Figure 2). Nickel is an important industrial catalyst, with applications in chemical looping combustion, solid state fuel cells etc. Reduction of nickel oxide to nickel is a model process as it comprises only one step reduction, compared to other oxides. The experiment involves a cleaning step (high temperature annealing in molecular hydrogen) as well as the controlling step (exposure to molecular hydrogen under the same conditions). The reaction cycle is repeatable (the sample can be re-oxidized in a low vacuum mode), so that a complete redox cycle on the sample can be repeated many times.

The proof-of-concept experiment demonstrates the feasibility of this approach to monitor the hydrogen-induced surface reactions in-situ in SEM. Going beyond the initial experimental demonstration, we will present our latest results on other material systems as well.

Figure 1: a) A schematic of the thermal hydrogen cracker. The molecular hydrogen is dissociated at a heated tungsten capillary and the beam of atomic hydrogen radicals is directed by the collimator onto a sample. b) The atomic hydrogen cracker attached to an SEM.

Figure 2: A Nickel sample is cleaned by annealing in molecular hydrogen under 2·10-2 Pa at 730 °C for 30 minutes which yields a well-defined surface. B The sample is oxidized by exposure to 30 Pa air in the low vacuum mode for 15 minutes at 580 °C. C In the control experiment, the sample is exposed to molecular hydrogen (8·10-4 Pa) at 540 °C for 1 hour. The contrast changes only slightly as almost no oxide was reduced. D Exposure to atomic hydrogen by applying 36W to the dissociation capillary for 1 hour at the same conditions yields a clean sample again.

Figure 1

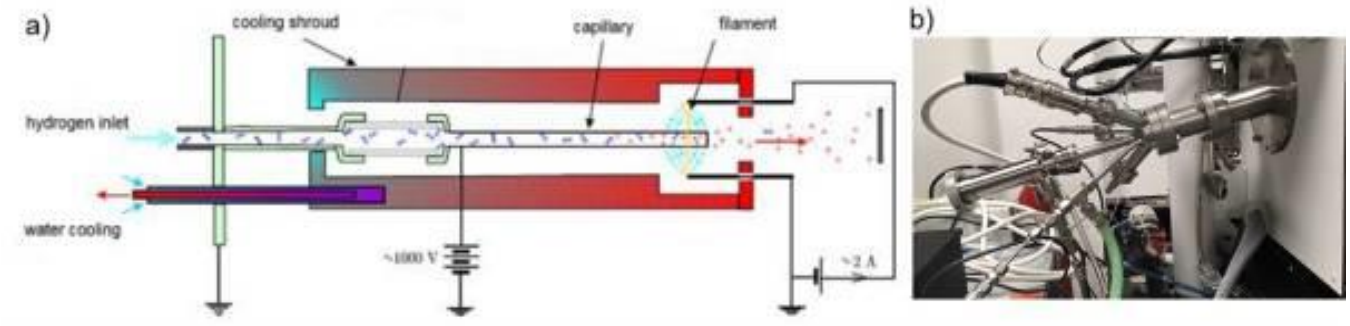

Figure 2

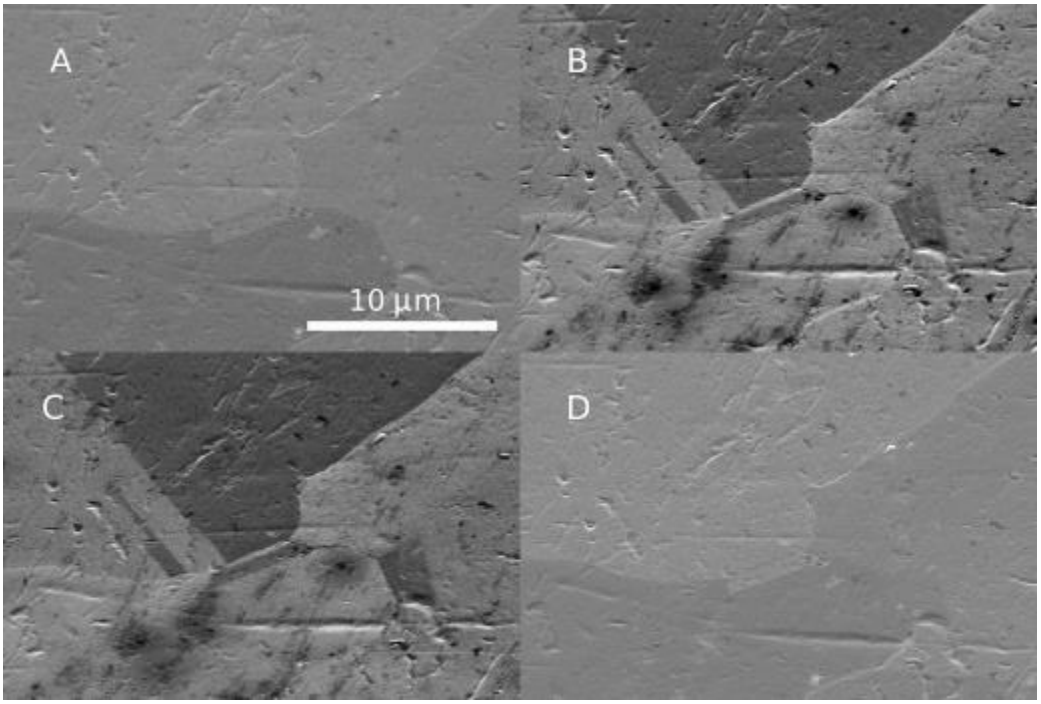

MS8.P008
Watching crystals grow – *in situ* TEM observation of the microstructure evolution in HfO_2 based memristive devices

R. Eilhardt[1], A. Zintler[1], O. Recalde[1], D. Nasiou[1], S. Petzold[2], L. Alff[2], L. Molina-Luna[1]

[1]Technical University of Darmstadt, Advanced Electron Microscopy, Darmstadt, Germany
[2]Technical University of Darmstadt, Advanced Thin Film Technology, Darmstadt, Germany

During heating in the TEM, local structural changes (crystallization and grain growth) were investigated *in situ* by Scanning Precession Electron Diffraction (SPED) (4D-STEM) using a MerlinEM Medipix3 (Quantum Detectors) direct electron detector.

Resistive random access memory (RRAM) devices are composed of a dielectric layer sandwiched between two metal layers. Using HfO_2 as the insulator material is appealing because of the back-end-of-line processes compatibility in the current semiconductor fabrication process and good chemical and thermal stability (*1*, *2*). In filament type resistive switching, grain boundaries in the dielectric layer provide predefined breakdown paths for filament formation, as shown by conductive atomic force microscopy (C-AFM) (*3*). Careful grain boundary engineering with grain boundaries threading through the dielectric (interconnecting the metals) is a promising way to significantly lower the electrical stress required for filament formation thus achieving electroforming free RRAM devices (*4*). To give insight into the grain growth mechanism and the development of a grain boundary we show a heating experiment of a RRAM device with amorphous hafnia in the TEM while *in situ* monitoring structural changes with SPED.

Stack combinations of Au/Pt/HfO_2/TiN/Al_2O_3 with amorphous hafnia were grown. A cross sectional lamella was prepared by using Focused Ion Beam (FIB) and transferred onto a Micro Electrical Mechanical System (MEMS) based heating chip. During *in situ* heating, laterally resolved structural information were acquired by SPED and TEM. Structural changes during *in situ* heating were further compared to an *ex situ* annealed stack combination to correlate very local structural changes observed in the TEM to a macroscopic scale.

The heating experiment in the TEM revealed, that grain growth in the hafnia layer started at 150°C and the developed grain boundaries thread the dielectric (interconnecting the metals). The observed microstructural changes in the TEM coincide with structural changes of the *ex situ* annealed stack. Further, crystallization of the dielectric layer lowered the electrical stress required for filament formation.

The development of grain boundaries in the hafnia layer was investigated *in situ* by monitoring grain growth during heating inside a TEM which yields a unique insight into the grain growth mechanism. The *ex situ* annealed stack complemented structural changes on a very local scale and showed improved electroforming voltages. The results of this study serve as a basis for a direct structure-property correlation in this system.

References:
[1] F. Pan, S. Gao, C. Chen, C. Song, F. Zeng, *Materials Science and Engineering: R: Reports*. **83**, 1–59 (2014).
[2] E. A. Miranda, C. Walczyk, C. Wenger, T. Schroeder, *IEEE Electron Device Letters*. **31**, 609–611 (2010).
[3] M. Lanza *et al.*, *Appl. Phys. Lett.* **100**, 123508 (2012).
[4] S. Petzold *et al.*, *Advanced Electronic Materials*. **5**, 1900484 (2019).

The authors acknowledge funding from the DFG under Grant No. 384682067 and the European Research Council (ERC) "Horizon 2020" Program under Grant No. 805359-FOXON.

MS8.P009
Structural study of stabilised $FAPbI_3$ films on ZnO nanorods for perovskite solar cells

V. Kojić[1], M. Bohač[1], L. Pavić[1], K. Salamon[1], T. Čižmar[1], K. Juraić[1], T. Brodar[1], M. Čeh[2], A. Gajović[1]

[1]Ruđer Bošković Institute, Division of Materials Physics, Zagreb, Croatia
[2]Institute Jožef Stefan, Ljubljana, Slovenia

Introduction: After the first report of a unique photoactive material based on lead halide [1] a whole new field of scientific research emerged related to inorganic – organic lead halide perovskites (LHP). LHP employ an ABX_3 crystal structure, where lead acts as a divalent cation with halide elements (I^-, Br^-) serving as anions, while methylamonium (MA^+), formamidinium (FA^+) and Cs^+ are often added as monovalent cations. In comparison to MA variant, $FAPbI_3$ perovskite bandgap (1.43 eV) is closer to the ideal value (Shockley-Queisser limit curve). However, FA based perovskites (cubic α- $FAPbI_3$) is unstable; under ambient and humid atmosphere transforms into the undesirable non-perovskite yellow δ- $FAPbI_3$ polymorph [2]. To improve the phase stability of the cubic α- $FAPbI_3$, researches attempted various approaches, from incorporation of different cations/anions in perovskite structures, to addition of inorganic/organic compounds.

Objectives: In this work we studied enhancement of perovskite α- $FAPbI_3$ films stability with addition of (unconducive) polymer-based additive. With the aim to understand the influence of additive on stability, the crystal structure and the morphology of stabilised and pure $FAPbI_3$ films, deposited on a nanostructured ZnO as electron transport layer (ETL), were investigated. The obtained structural properties were correlated with conductivity, photoconductivity, charge carriers activation energies (E_a) and charge carriers life-times.

Materials & methods: $FAPbI_3$ films with additive were deposited on a nanostructured ZnO ETL under various temperatures. The morphology of the $FAPbI_3$ films on ZnO and the penetration of the $FAPbI_3$ in ZnO nanostructures, depending on aditive, were studied in cross section using SEM and TEM techniques. The crystal structure and the stability of the $FAPbI_3$ films, depending on the polymer addition, were studied using grazing incidence X-ray diffraction (GI-XRD). The conductivity, E_a, and charge carriers life-times were measured using impedance spectroscopy (IS) and photoluminescence (PL), respectively.

Results: The polymer-based additives to $FAPbI_3$ increase the penetration of the $FAPbI_3$ in ZnO nanostructures in the form of nanorods in comparison with pure $FAPbI_3$ film (Figure 1). GI-XRD proved considerable increase in stability of the perovskite α- $FAPbI_3$ phase with addition of polymer to more than 3 months. On the other hand, pure $FAPbI_3$ film shows the degradation of α- $FAPbI_3$ phase into the δ- $FAPbI_3$ polymorph in less than 24 hours.

The IS results of stabilised and pure $FAPbI_3$ films were compared and it was shown that the stabiliser even increased the conductivity of $FAPbI_3$ films on ZnO, while the E_a of the charge carriers was decreased. The increase of conductivity and decrease of the E_a in the stabilised films on ZnO nanostructures will be discussed in the view of morphology and structure.

Conclusion: Stabilised $FAPbI_3$ films on nanostructured ZnO was shown to be a promising material for a long-lasting perovskite solar cells.

References:
[1] Kojima et al, J. Am. Chem. Soc., 2009, DOI: 10.1021/ja809598r [2] Ma et al., Chem. Sci., 2016, DOI: 10.1039/C6SC03542F
[3] This work has been supported by Croatian Science Foundation (IP-2018-01-5246), Centre of Excellence for Advanced Materials and Sensing Devices, RBI, KK.01.1.1.01.0001 and European Regional Development Fund, IRI project (KK.01.2.1.01.0115).

Figure 1: SEM cross section of $FAPbI_3$ films on ZnO: a) without and b) with additive.

Figure 1

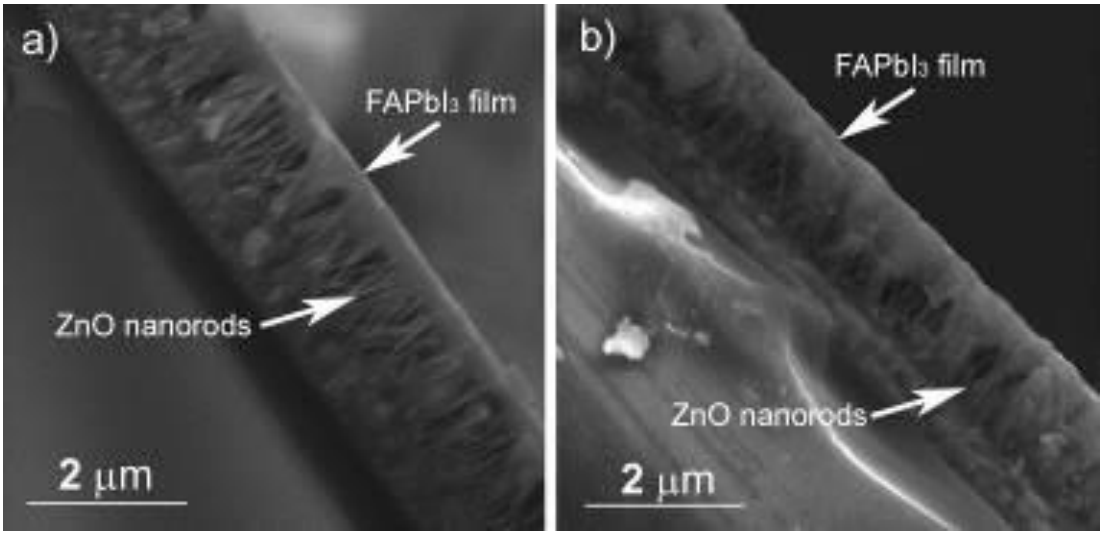

MS8.P010
EELS investigation of a V-CeFe-oxide catalyst for low-temperature NH_3-SCR

C. R. Kreyenschulte[1], N. Rockstroh[1], S. Keller[1], A. Brückner[1]

[1]Leibniz Institute for Catalysis e.V., Catalytic In Situ Studies, Rostock, Germany

The effect of varying iron content of a Ce1-xFex02-δ catalyst impregnated with V was investigated in the low-temperature selective catalytic reduction (SCR) of NOx by NH3 in a temperature regime between 150 and 300°C [1]. The catalysts were characterized by XRD, XPS, Raman spectroscopy and STEM as well as *in situ* XANES and *operando* DRIFTS and EPR measurements. It was found that the NOx conversion was raised with increasing iron content due to increased oxygen vacancies as well as the Fe3+/Fe2+ redox couple as possible active sites. Impregnation with V improved the SCR activity and the resilience to H2O of all supports, however, optimum iron contents in this case was 0.05.

Preparations of the catalysts were performed by a coprecipitation method with subsequent impregnation with VOy [1]. STEM-EELS characterization of the V impregnated catalysts with a content of x=0.05 and x=0.2 of Fe was used to determine the V distribution on the catalyst, but also to determine the potential Fe inclusion into the ceria. The specimen with the higher Fe content showed the formation of rather large iron oxide crystallites indicating the limited solubility of Fe in ceria.

Due to overlapping peaks in EDXS it was necessary to determine the V distribution by STEM-EELS which was done in our probe corrected JEOL JEM-ARM200F equipped with a Gatan Enfinium ER EELS. In order to keep acquisition times low, a rather high beam current was used, giving a fwhm of about 1.2 eV of the zeroloss peak. The microscope is not equipped with de-scan, therefore using the DualEELS mode was essential. Due to almost simultaneous acquisition of the zeroloss peak, it was possible to recalibrate the shift of the spectra for each pixel of the area used for spectrum imaging.

For the two investigated specimens, the V could be shown to form a quite even distribution on the catalyst surface, both on the Fe doped ceria and on the Fe oxide crystallites in the catalyst with the higher Fe content (Figure 1). As the Fe edge region was also acquired within the EEL spectra, it was also possible to investigate the fine structure of the Fe-L edge (Figure 2). While the form of the Fe fine structure of the Fe doped ceria in both samples was comparable, it differed from the form of the fine structure of the Fe oxide crystallites formed by the excess of Fe. This effect was also reflected by the XANES results in [1].

Using STEM-EELS with this catalyst system, it was possible to benefit from this additional spectroscopic method by providing information on the V distribution when EDXS would have been unsuitable due to overlapping peaks. Although in-situ XANES measurements provided a hint of modified chemical states, the differences in the EELS fine structure of the Fe-L edge presented here allow for localization of the signal sources.

[1] S. Keller, et al, *ChemCatChem* 10.1002/cctc.201902167

Figure 1: STEM-ADF image of V-Ce0.8Fe0.2O2-δ catalyst with marked regions used for the background subtracted EEL spectra depicted on the right side showing the difference in V content. Region 1 represents the Fe oxide crystallite phase, region 2 the V-CeFe oxide phase.

Figure 2: STEM-ADF image of V-Ce0.95Fe0.05O2-δ catalyst with the additional region marked. The accompanying EEL spectra compare the Fe edge region of the high Fe content catalyst (1&2) with the low Fe content catalyst (3). Here the EEL spectra were also deconvoluted based on the zeroloss peak.

Figure 1

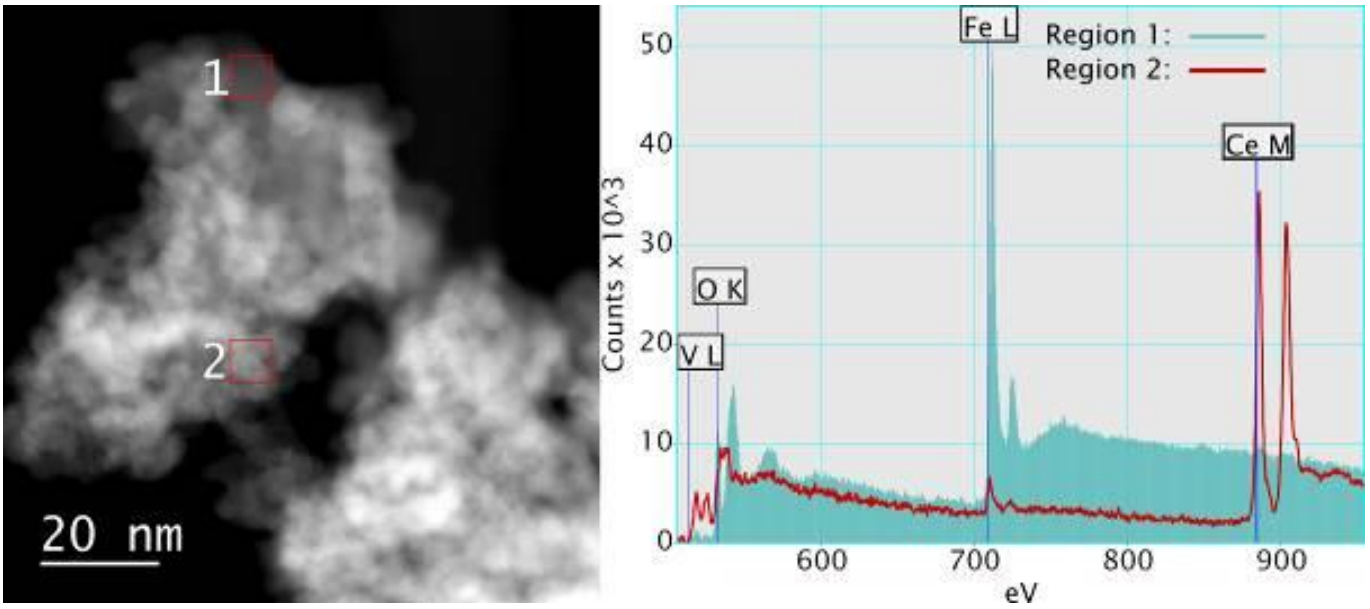

Figure 2

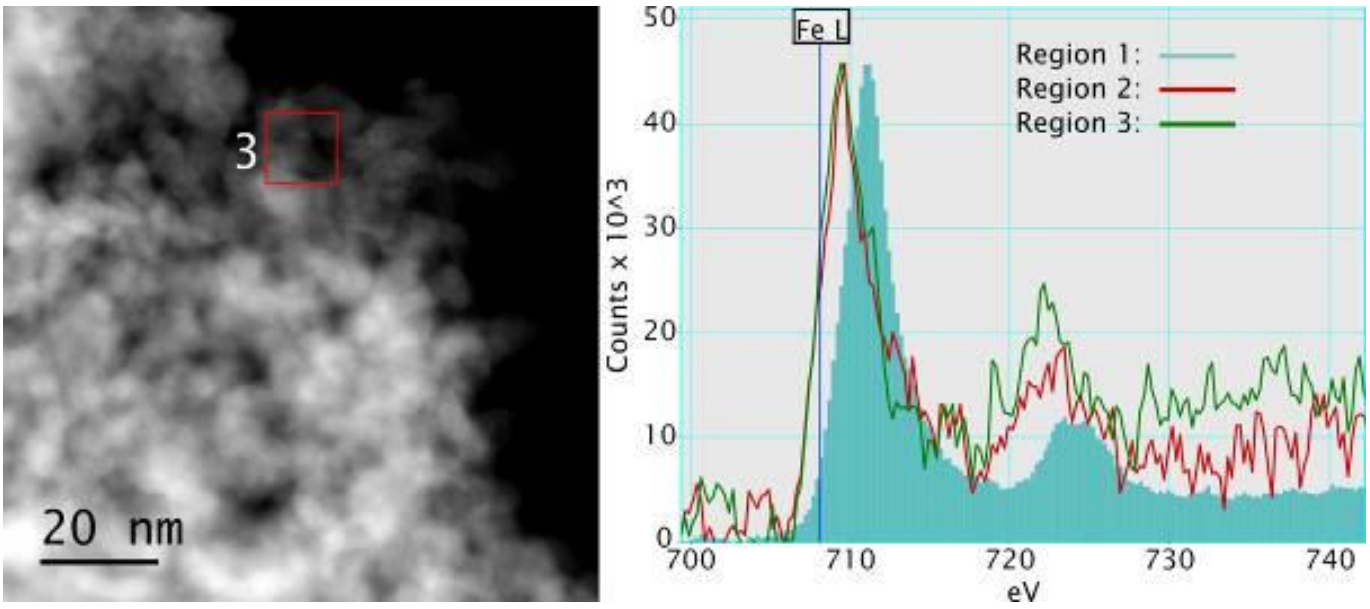

MS8.P011
Analysis of superconducting thin films in a modern FIB/SEM dual-beam instrument

L. Grünewald[1], D. Nerz[1], M. Langer[2], S. Meyer[2], N. Beisig[2], P. Cayado[2], R. Popov[2], J. Hänisch[2], B. Holzapfel[2], D. Gerthsen[1]

[1]Karlsruhe Institute of Technology (KIT), Laboratory for Electron Microscopy (LEM), Karlsruhe, Germany
[2]Karlsruhe Institute of Technology (KIT), Institute for Technical Physics (ITEP), Karlsruhe, Germany

Thin-film technology is used in many applications and often requires structural and chemical analyses on the nanoscale. (Scanning) transmission electron microscopy ((S)TEM) in a dedicated (S)TEM instrument is a powerful analysis tool for this purpose. However, the TEM sample preparation and consecutive (S)TEM measurement in different instruments limit high-throughput analysis. Modern combined focused-ion-beam (FIB)/SEM systems are routinely used for TEM sample preparation and can be equipped with a STEM- (for STEM-in-SEM imaging), energy-dispersive x-ray spectroscopy- (EDXS), and other detectors, resulting in a large versatility for material analysis [1].

In this work, we demonstrate how correlative SEM, EDXS, and STEM-in-SEM in a Thermo Fisher Helios G4 FX FIB/SEM instrument, equipped with a dedicated STEM holder and a Bruker XFlash 6|60 EDXS system, can be used for sample preparation and structural and chemical characterization within one instrument [1]. We have investigated $Ba(Fe_{0.92}Co_{0.08})_2As_2$ (Ba122) and $REBa_2Cu_3O_{7-\delta}$ (REBCO, RE: rare earth, e.g. Gd) thin films grown by pulsed laser deposition on different substrates.

Figure 1 shows results of an SEM-EDXS analysis of a 60 nm thin Ba122 film with precipitates at the surface (white spots in Figure 1(a)). A low beam energy of 2 keV was applied to maximize the spatial resolution while still exciting all necessary x-ray lines. Due to the low x-ray yield at 2 keV, principal component analysis (PCA) (Figure 1b) is used to increase the signal-to-noise ratio and yields PCA-filtered element maps (Figure 1(c)). The precipitates show a high Fe/Co content, in agreement with TEM results [2]. Non-negative matrix factorization (NMF) analysis [3] shows 3 chemical phases as determined from the scree plot, i.e. Ba122 film, contamination, and Fe/Co precipitates (Fig 1(d)). The O map reveals oxidation of Ba122 and the Fe/Co precipitates.

Examples for STEM-in-SEM imaging at 30 keV of in-situ FIB-prepared samples are presented in Figure 2. The bright-field (BF-)STEM cross-section image Figure 2(a) shows lattice fringes and an amorphous interface layer between Ba122 and the $LaAlO_3$ substrate. The latter may be caused by FIB preparation. Figure 2(b,c) present plan-view high-angle annular dark-field (HAADF) STEM images of a GdBCO film. Roundish precipitates, twin boundaries along the [110] direction (as in [4]), and threading dislocations are observed.

In conclusion, modern FIB/SEM instruments with STEM detectors combine sample preparation and structural and chemical analysis down to the nm-scale, which can be applied for efficient thin-film analysis. It also avoids exposure of reactive materials to ambient air.

References:
[1] C. Sun et al., *J. Mater. Sci.* **55** (2020) 13824–13835.
[2] L. Grünewald et al., *Supercond. Sci. Technol.* **34** (2021) 035005.
[3] B.R. Jany et al., *Nano Lett.* **17** (2017) 6520–6525.
[4] R. Guzman et al., *Phys. Rev. Mater.* **1** (2017) 24801.

Figure 1

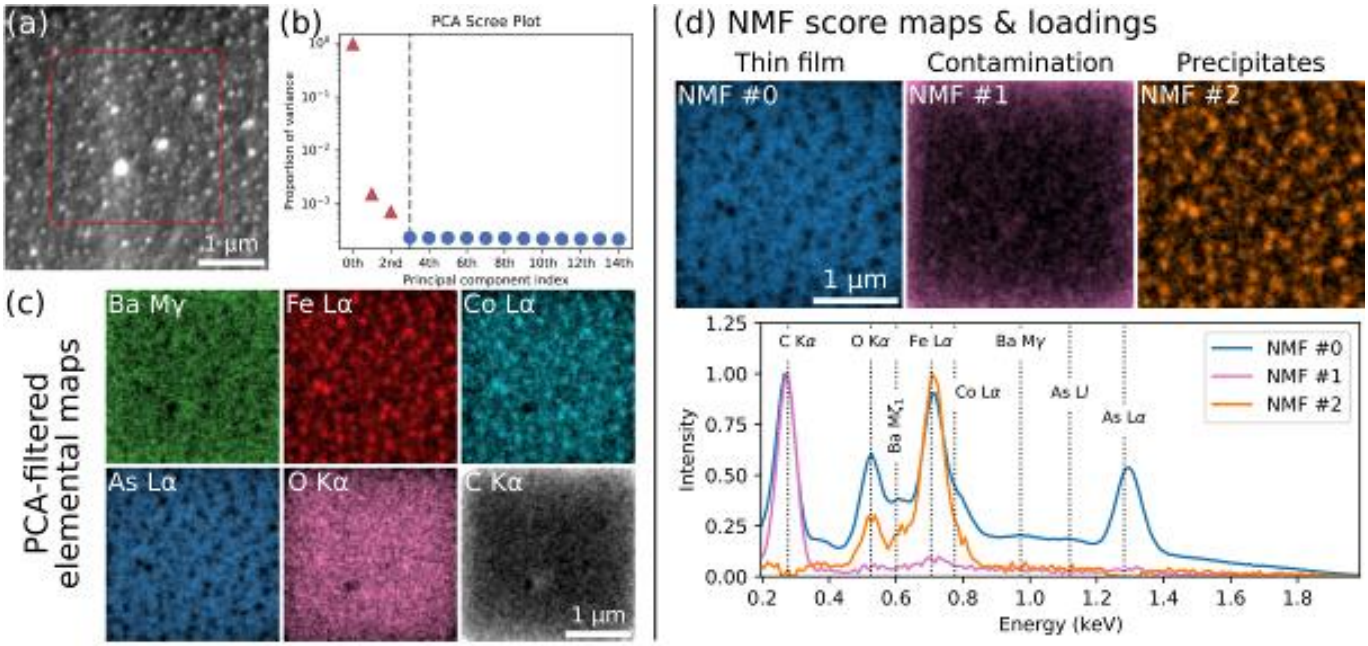

Figure 1: SEM-EDXS analysis of a ~60 nm thin Ba122 film. (a) Overview secondary-electron SEM image of the analyzed region showing precipitates (bright dots) on the surface. (b) The PCA scree plot shows 3 trends/components in the dataset, which are used for PCA reconstruction and as NMF output dimension. (c) Extracted elemental signals from the PCA-filtered dataset. (d) NMF score maps (top row) and extracted x-ray spectra of the three phases (bottom, normalized).

Figure 2

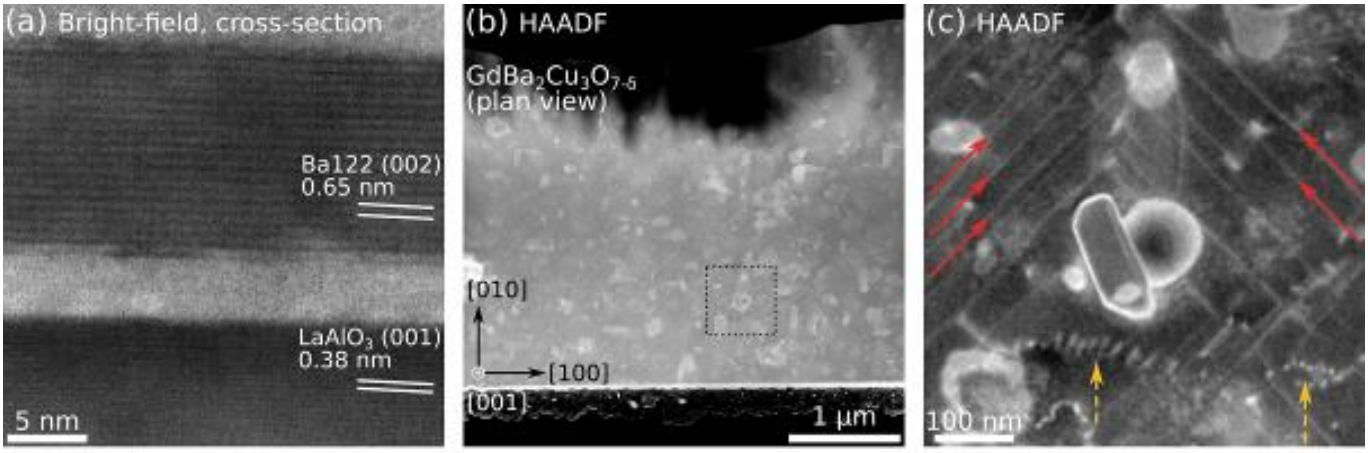

Figure 2: Examples for STEM-in-SEM imaging. (a) Cross-section BF-STEM image of a Ba122 film on $LaAlO_3$ showing lattice fringes and an amorphous interface layer. (b) Plan-view HAADF-STEM image of an in-situ prepared plan-view lamella of a GdBCO film. (c) Higher-magnification image of the region marked in (b). Twin boundaries (red arrows) and threading dislocations (yellow, dashed arrows) are visible besides precipitates.

MS8.P012
Observation of achievements in prevention of electrode passivation during monitoring of organic pollutants

A. Michalcova[1], B. Kratochvil[1]

[1]University of Chemistry and Technology in Prague, Department of Metals and Corrosion Engineering, Prague, Czech Republic

The immense potential of modern electroanalytical methods in the monitoring of environmental organic pollutants is generally recognized and appreciated. Their main advantage is their low costs, variability, selectivity and easy automatization. Nevertheless, the big problem connected with their use remains to be the passivation of working electrodes.

The electrodes in initial state, after exposure and after re-cleaning were observed by scanning (SEM) and transmission (TEM) electron microscopy. The TEM was used for characterization of the new materials, mainly on the carbon base. The SEM was used for surface observation. It was proved that the metal electrodes (Au, Ag and Pt) were successfully mechanically cleaned.

Acknowledgements: Authors thank for financial support by Czech Science Foundation, project No. 20-01417J.

MS8.P013
In situ chip-based heating studies of metal-induced layer exchange and Si crystallisation using multimodal STEM, LEND and SE imaging in SEM

T. Schwope[1], P. Denninger[1], P. Schweizer[2], C. Dolle[3], E. Spiecker[1]

[1]Friedrich-Alexander University Erlangen-Nuremberg (FAU), Institute of Micro- and Nanostructure Research, Erlangen, Germany
[2]EMPA, Thun, Switzerland
[3]KIT, Microscopy of Nanoscale Structures & Mechanisms, Karlsruhe, Germany

In situ experiments are an indispensable tool for the analysis of phase transitions and material behaviour at high temperatures. A broad range of instruments in material science are used for *in situ* experiments. SEMs offer great potential for *in situ* investigations due to their low acceleration voltages, large chamber size and field of view, and strong topographic contrast. However, combining *in situ* heating with transmission imaging is a novel approach. [1]

In this work, we introduce an update of our low-energy nanodiffraction (LEND) setup1, which enables combined *in situ* heating, imaging, and transmission diffraction in SEM (Figure 1b-c). Implementing a custom heating stage for heating chips allows precise and fast local heating and cooling of specimens. The setup has been implemented and successfully tested in solid-state dewetting experiments, where the simultaneous acquisition of real- and reciprocal space information *in situ* is needed to elucidate phenomena such as grain rotation.

To showcase the benefits of combining several imaging modes *in situ*, we present current results about the crystallisation of thin semiconductor (SC) layers via metal induced layer exchange (MILE). This process was intensively studied in the last two decades. A stack of metal, some native oxide, and an amorphous SC invert their stacking order while the SC crystallises (Figure 2a). Since induced crystallisation occurs at temperatures below that of the bulk crystallisation temperatures of the respective SCs, the MILE process was investigated for its applicability in the fabrication of thin crystalline SC films even on heat-sensitive substrates.

Annealing parameters for the Ag/Si system were previously determined with respect to suitable reaction rates and morphology by *in situ* light microscopy experiments (Figure 2b). Characteristic dendritic growth of Si grains can be observed, with the size and number of grains exhibiting strong temperature dependency. The sample thickness is also important for obtaining sufficient signal of the transmitted electrons.

During *in situ* heating experiments, all available signals were acquired to provide essential information about the phase transitions, crystal growth and orientation, change of grain structure, and topography. The phase transition from amorphous to polycrystalline Si caused formation of a typical Si (111) diffraction pattern, while crystal growth and layer exchange are observed through SE & STEM imaging. High Angle Annular Dark Field (HAADF) imaging facilitates the distinction between Ag and Si phase due to their pronounced Z contrast. While the experimental results largely confirmed the most recent layer exchange model, we proposed an expanded model for the AgILE process. [2]

In the future, simultaneous *in situ* diffraction and STEM imaging is planned, which expands the versatility of correlative *in situ* methods in the SEM. Additionally, EBSD/TKD measurements will be performed to further investigate grain orientation and morphology. [3]

[1] P. Schweizer, P. Denninger, C. Dolle, E. Spiecker, Ultramicroscopy 213 (2020) 112956
[2] Z. Wang, L.P.H. Jeurgens, E.J. Mittemeijer (Eds.), Metal-induced crystallization: Fundamentals and applications, Pan Stanford Publishing, [Singapore], 2015.
[3] The authors acknowledge funding by the German Research Foundation (DFG) via the Research Training Group GRK 1896 "*In situ* microscopy with electrons, X-rays and Scanning probes

Figure 1

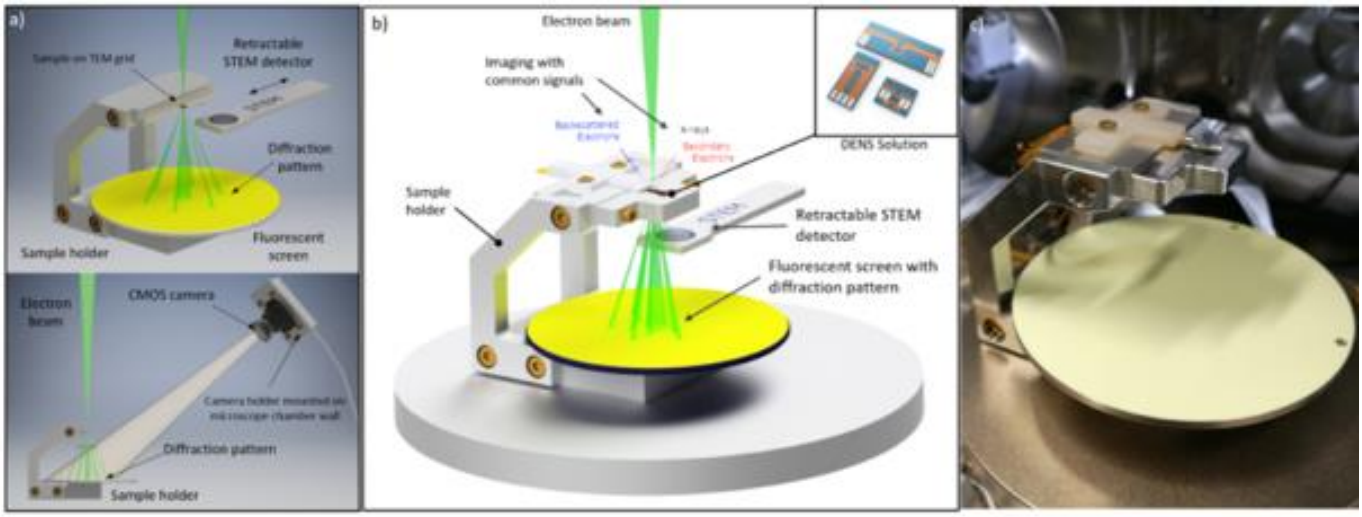

Figure 1: In situ heating and diffraction setup in the SEM. a) Setup of Low Energy Nano Diffraction (LEND). b) Illustration of the developed heating stage for DENSSolutions heating chips. c) Installed heating stage in the SEM.

Figure 2

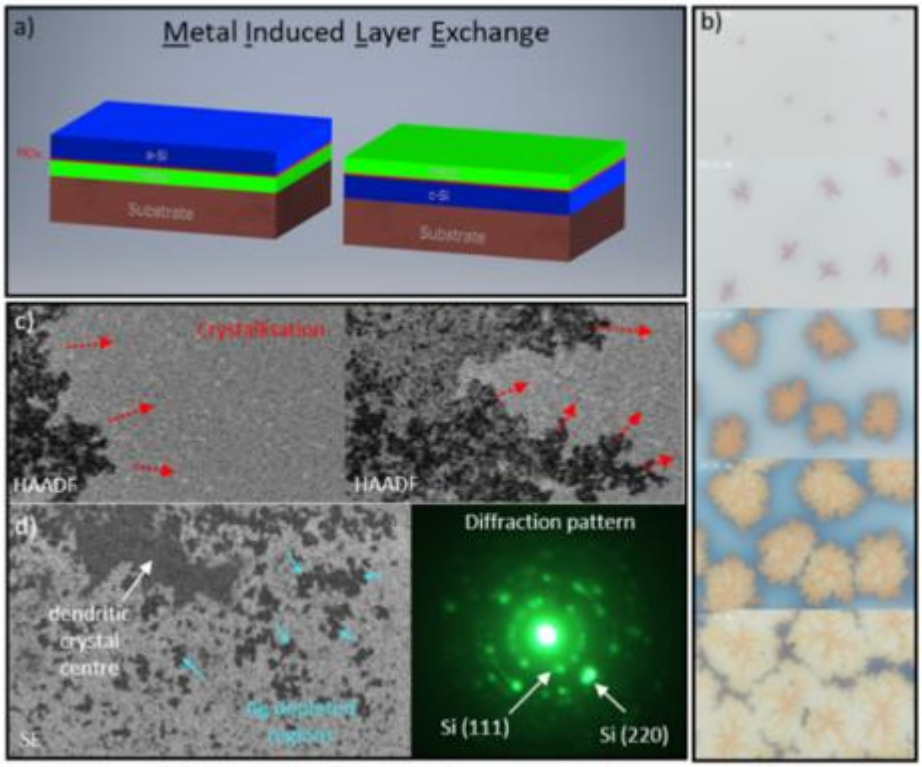

Figure 2: Investigation of the Metal Induced Layer Exchange process. a) Schematic of the MILE process. b) Pre-characterisation of the Ag/Si system via in situ light microscopy. c) Crystallisation of Si acquired by HAADF imaging. d) Overview of a reacted area (SE) with corresponding diffraction pattern, which reveals the structure of the grown grains.

MS8.P014
STEM tomographic study of three-dimensional ligand-linked porous Pt-nanoparticle networks for catalytic hydrogen sensing

M. Schowalter[1,2], D. Loof[3], C. Mahr[1,2], O. Thüringer[3], A. S. Pranti[4], W. Lang[4], V. Zielasek[3], M. Bäumer[3], S. Kunz[3]
A. Rosenauer[1,2]

[1]University Bremen, Institute of Solid State Physics, Bremen, Germany
[2]University Bremen, MAPEX Center for Materials and Processes, Bremen, Germany
[3]University Bremen, Institut für Angewandte und Physikalische Chemie, Bremen, Germany
[4]University Bremen, Institut für Mikrosensoren, -aktoren und -systeme, Bremen, Germany

Pt-nanoparticles (NPs) are a promising candidate as catalyst in hydrogen combustion gas sensors [1]. Bifunctionalized organic ligands can be used to link Pt-NPs to three-dimensional porous networks [2] exhibiting a higher mass fraction of Pt and a lower heat capacity compared to catalysts on inorganic support materials and are favourable for sensitivity and response time of sensors. The arrangement of the network and the particle distances are of great importance for the performance of the material as sensor and therefore three-dimensional analysis is required.

The ligand-linked Pt particle networks were prepared similar to Ref. [2] using cyclohexanone as solvent. Figure 1a) shows structure and theoretical distances between particles for the used ligands. Networks were dispersed on carbon coated grids. Tilt series were recorded in a non-probe corrected Titan80-300ST transmission electron microscope and reconstructed using the IMOD software [3].

Particle positions were found using an iterative procedure: First, the absolute maximum in the tomogram was searched and its position refined using the center of mass (COM) within a sphere of radius r_0=0.7 nm. Then, the density in a sphere with radius $2r_0$ was set to zero. Further particles were found by repeating the procedure until the maximum fell below a threshold. To identify the correct threshold a model of the network with spherical particles was set up. The model with minimum deviation between model and tomogram was selected for further analysis (Figure 1b)-d)).

For each particle we computed the distances to all other particles. Figure 1e) shows the average n.th nearest neighbor distance d_n as function of n. We found a clear trend for n larger than 2, whereas this trend is disturbed for NPs with smaller distance. A closer inspection of the NP distribution reveals that some NPs appear to have coalesced. The particle distances R_i from the COM of the network were computed and the inter-particle distances d_i were estimated by $d_i = (4/3\ \pi\ R_i^3/N_i)^{1/3} - r_0$, with N_i being the number of particles with distances smaller than R_i assuming an average coordination number of 6. Figure 1f) shows d_i as function of R_i. The curves are noisy for small R_i below 6 nm and are fairly constant between 6 nm and 10 nm. Depending on size of the network d_i starts to increase due to the border of the network, where the particle density strongly deviates from the central part of the cluster suggesting to determine the final inter-particle distance in this range yielding 0.7, 0.8, 1.0, 1.0 and 1.4 nm with an error of 0.1 nm for DACH, PDA, DAN, BEN and DATER, respectively. A denser packing of NPs which would yield a larger coordination number than 6 might explain the slight underestimation of the inter-particle distances compared to ligand lengths.

Figure 1: a) Chemical formulae of the ligands. b) Deviation of tomogram and model as a function of threshold. c) and d) Isosurface plots of data and model using the threshold value determined by the minimum of the curve in b). e) Average distance between a particle to its n-th nearest neighbor as a function of the nearest neighbor number n. f) Measured distance d_i between particles as function of the distance from the COM.

[1] E. Brauns, E. Morsbach, S. Kunz, M. Bäumer, W. Lang, Sensors and Actuators B (2014), **193**, 895
[2] E. Morsbach, S. Kunz and M. Bäumer, Catal. Sci. Technol. (2016), **6**, 339
[3] J. R. Kremer, D. N. Mastronarde and J. R. McIntosh, J. Struct. Biol. (1996), **116**, 71

Figure 1

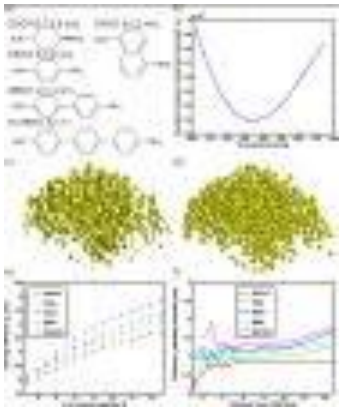

MS8.P015
New way of resistivity contrast imaging of semiconductor structures with ultra-low energy electrons

I. Jozwik[1,2], J. Jagielski[1,2], E. Dumiszewska[1], P. Caban[1], M. Kaminski[3,4], U. Kentsch[5]

[1]Lukasiewicz Research Network: Institute of Microelectronics and Photonics, Centre of Electronic Materials Technology, Warsaw, Poland
[2]National Centre for Nuclear Research, Swierk-Otwock, Poland
[3]Warsaw University of Technology, Institute of Microelectronics and Optoelectronics, Warsaw, Poland
[4]Lukasiewicz Research Network: Institute of Microelectronics and Photonics, Warsaw, Poland
[5]Helmholtz-Zentrum Dresden-Rossendorf e.V. (HZDR), Dresden, Germany

Introduction: The technique of implant isolation by ion irradiation with various energetic ions was found applicable in the microelectronic industry to create insulating regions in electronic semiconductor devices. To verify the extent of the modified area, usually the wet selective etching is used. However, it cannot be applied to materials, for which selective etchants do not exist (i.e. GaN). The low-voltage scanning electron microscopy (low-kV SEM) paves the way towards new applications in semiconductor technology to detect contrast originating from highly insulating channels produced by ion damaging of semiconductors.

Objectives: The purpose of the study was to directly visualize the resistive areas created by ion irradiation in various semiconductors by means of low kV SEM. The imaging of the cross-sections of the irradiated specimens were performed under ultra-high vacuum conditions with the samples loaded quickly after they were cleaved.

Materials & methods: The AlGaAs, GaAs, InAlP and GaN epitaxial layers grown by (MOCVD) technique were covered with the mask of gold stripes and irradiated with He+ ions of energy 600 keV with fluencies ranging from 8e12 to 5e14 cm-2. The SEM images of the freshly-cleaved cross sections of irradiated specimens were collected at low energy operation (E<0.5 keV) using high-resolution SEM SU8230 (Hitachi) and Auriga (Carl Zeiss), both equipped with the highly efficient in-lens SE detection systems.

Results: The Damage-Induced Voltage Alteration (DIVA) contrast mechanism [1,2] is based on the idea of local changes in the surface potential formed as the result of the primary beam interaction with the resistive (less conductive) areas of the samples, that affect the SE collection efficiency. In the studied cases, the resistive region of ion-generated damage is not homogenous, but the damage evolves along the ion irradiation direction, starting from the sample surface towards the bulk, along the initial ion beam direction. As observed, the image contrast resulting from the ion irradiation and subsequent damage formation within the irradiated layers expands along the irradiation direction and evolves with the increase of ion fluence.

Conclusion: The SEM imaging with DIVA contrast can serve as a tool to reveal qualitatively the information on the ion-irradiation damage level in semiconducting materials. It allows one for direct visualization in two dimensions of modified areas basing on changes in their resistivity even in the materials, which are not suitable to characterize by other methods (i.e. wet chemical etching), which is the main goal of isolating electronic devices by radiation defects. We conclude that the DIVA contrast technique is a unique, easy, fast and reliable method of verification of implant isolation profile, which is extremely important for the opto- and microelectronics technologies using gallium nitride technology and other compound semiconductors. The unrivalled advantage of the technique of low-kV SEM lies in its immediate SEM image generation without a need of complex sample preparation.

Acknowledgment: This work has been financed by the National Science Centre, Poland, under the grant number 2017/27/B/ST8/01158. I.J. acknowledge support by RADIATE project under the Grant Agreement 824096 from the EU Research and Innovation program HORIZON 2020.

References:
[1] I. Jóźwik et al., ECS J. Solid State Sci. Techn. 6(2017)415
[2] I. Jóźwik et al., Ultramicroscopy 204(2019)6

Figure1: SEM image of InAlP layer cross-section with visible ion-damaged regions.

Figure 1

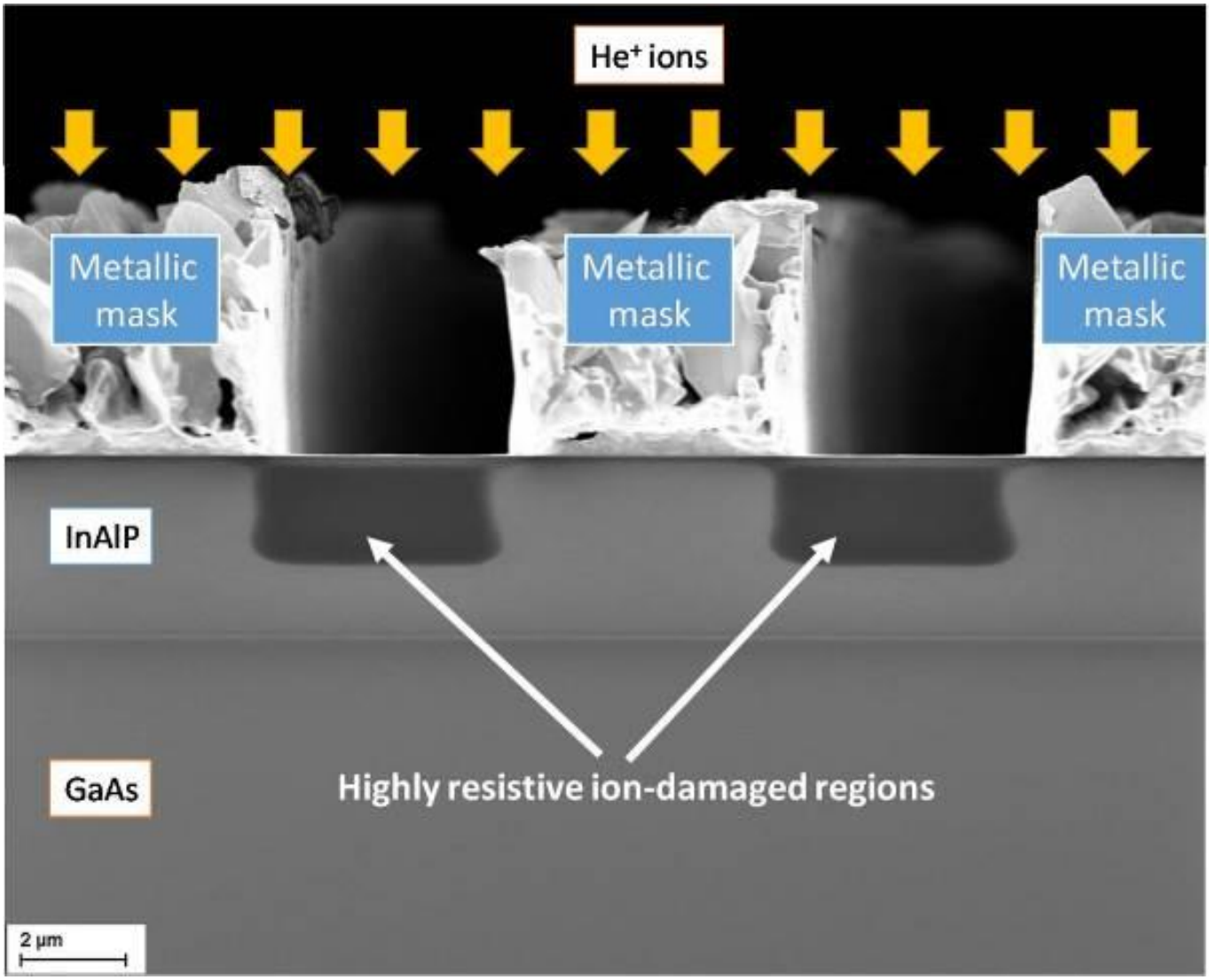

MS8.P016
Transmission electron microscopy of Ni-Cu bimetallic nanomaterial prepared by impregnation and coprecipitation – studying the activation process

L. Duarte Correa[1], M. Stredansky[1], L. He[1], M. Hashagen[1], F. Girgsdies[1], K. Skorupska[1], F. Rosowski[2,3]
T. Lunkenbein[1], R. Schlögl[1,4], W. Hetaba[4]

[1]Fritz Haber Institute of the Max Planck Society , Anorganische Chemie, Berlin, Germany
[2]Process Research and Chemical Engineering, BASF SE, Ludwigshafen, Germany
[3]BasCat UniCat BASF JointLab, Technische Universität Berlin, Berlin, Germany
[4]Max Planck Institute for Chemical Energy Conversion, Mülheim an der Ruhr, Germany

Nanoparticular systems are an important class of catalysts to achieve chemical transformations in industrial processes and their properties influence their performances. Compared to supported monometallic catalysts, bimetallic catalytic systems have been reported to enhance the activity and/or selectivity of several processes [1]. For instance, Ni-Cu supported nanoalloys are characterized by a synergistic effect that increases the performance in dehydrogenation of alcohols [2] and ethanol steam reforming [3]. However, the performance of the catalyst is highly dependent on the synthesis method, the oxidation state of the metal components and the particle sizes. Often, metallic species form part of the active phase of the catalysts and high temperatures are required to properly reduce Ni catalysts [4].

In this work we studied the activation process and properties of a supported bimetallic Ni-Cu system obtained from two different synthesis approaches: impregnation of Al_2O_3 support and coprecipitation. The materials were characterized by chemical electron microscopy [5], temperature programmed reduction and related complementary techniques. The impregnated Ni-Cu system was reduced under hydrogen atmosphere using different conditions. The coprecipitated material, consisted of layered double hydroxides (LDH) structures, was decomposed under oxygen atmosphere prior reduction. After reduction, the crystal and electronic structure of Ni-Cu systems were studied using X-ray diffraction (XRD) and electron energy-loss spectroscopy (EELS). Local information at the nano/atomic scale regarding morphology and particle sizes was obtained by high resolution (scanning) transmission electron microscopy (HR-(S)TEM).

Our results revealed on one hand, that the impregnated catalyst showed mainly agglomeration and sintering of nanoparticles after activation process, as is shown in Figure 1 left. On the other hand, when the catalyst is prepared by coprecipitation, i.e. ex-LDH structures, after the activation procedure the material evidenced well and highly dispersed metal nanoparticles (Figure 1 right). It is worth noting that in the Figure 1, the flake-morphology of the material is visible, similar to the LDH precursor but decorated with the nanoparticles (formed in during the reductive process). We also proved that the nanoparticle size of the activated material can be tuned with the activation process conditions. Furthermore, using EELS measurements we confirmed the presence of metal Ni species, but not Cu $L_{2,3}$-edge signal was observed probably due to the low Cu content. Our XRD analysis revealed the formation of Ni-Cu alloy after reduction and elemental studies with STEM-EDX evinced the coexistence of both elements.

In conclusion, the present work highlights the importance of the proper synthesis method to achieve desired structures. We systematically approached the activation parameters of Ni-Cu catalysts by comparatively assessing the change of structural and electronic properties of different catalysts. All in all, the present work contributes to an improved understanding on the activation processes involved in Ni-Cu supported nanomaterials.

Figure 1: TEM and STEM-HAADF image of activated Ni-Cu catalysts from impregnated and coprecipitated synthesis method.

References:
[1] Applied Catalysis A: General 222 (2001) 31–45
[2] Chinese Journal of Catalysis 35 (2014) 1911–1916
[3] Energy Fuels 31 (2017) 3091−3100
[4] ACS Catalysis (2019) 8534−8546

Figure 1

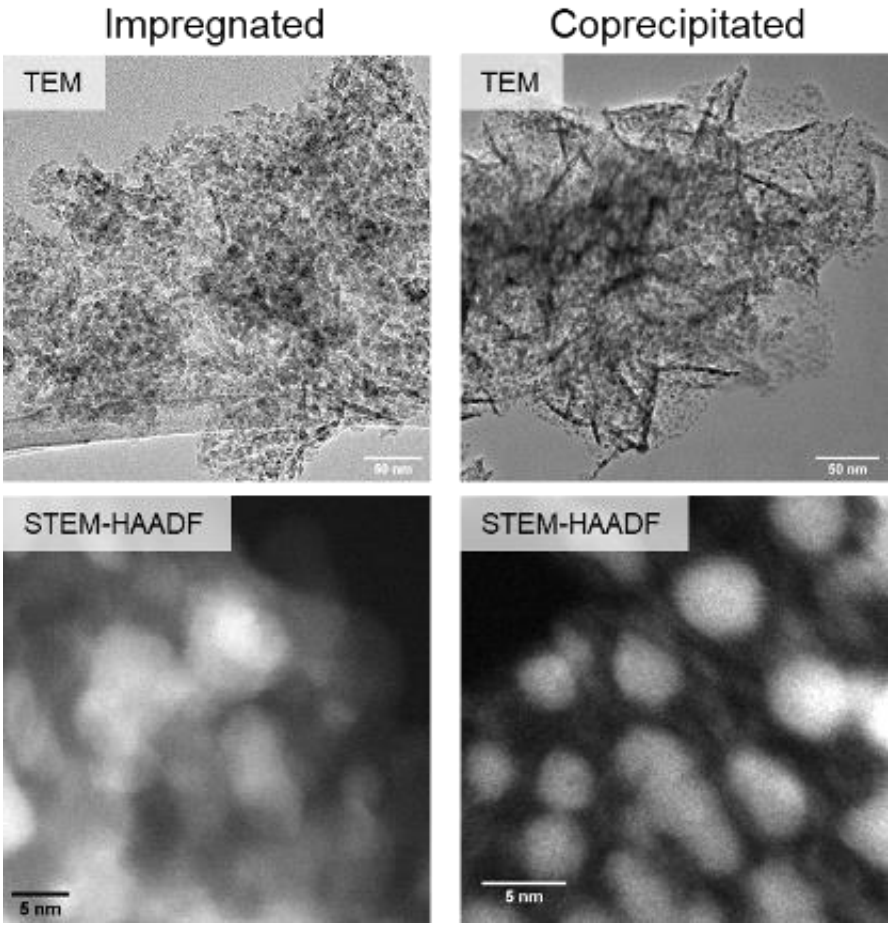
Impregnated
Coprecipitated
TEM
TEM
50 nm
50 nm
STEM-HAADF
STEM-HAADF
5 nm
5 nm

MS8.P017
Transmission electron microscopy of bimetallic tandem catalyst for coupling reactions

L. Duarte Correa[1], E. Gioria[2], N. Bashiri[2], R. Schomäcker[3], A. Thomas[2], T. Lunkenbein[1], R. Schlögl[1,4], W. Hetaba[4]

[1]Fritz Haber Institute of the Max Planck Society , Anorganische Chemie, Berlin, Germany
[2]Technische Universität Berlin, Fakultät II, Institut für Chemie: Funktionsmaterialen, Sekretariat BA2, Berlin, Germany
[3]Technische Universität Berlin, Fakultät II, Institut für Chemie, Sekretariat TC8, Berlin, Germany
[4]Max Planck Institute for Chemical Energy Conversion, Mülheim an der Ruhr, Germany

The active centers of bimetallic catalysts comprise two different metals which can form an alloy or separated nanoparticles (NPs). In order to achieve more efficient processes, in the last decades researchers focused on studying materials that allow coupled reactions in one-pot process using tandem catalysts [1,2]. Tandem catalysts consist of two different active sites to perform two consecutive reactions in one process. However, the fine tuning of the properties is challenging. Core-shell structures have become a promising arrangement to ensemble two different active centers with specific distance [3]. In this work, we present electron microscopy evidence from different synthesis stages of a material prepared with controlled ensembles of nanoparticles in a core-shell arrangement. The sophisticated material is evaluated as a tandem catalyst for CO_2 hydrogenation to olefins.

The catalysts synthesis was performed in several steps. The core of the ensemble is form by monodisperse silica particles prepared by Stöber process. Afterwards the silica spheres were decorated with platinum NPs obtaining SiO_2-Pt (Figure 1A). Consecutively, the core was encapsulated by the growth of a mesoporous silica shell (@m-SiO_2, Figure 1B). It is worth noting that synthesis of m-SiO_2 was tuned to have ca. 50 nm thickness; it is employed as a spacer and for allowing the diffusion of molecules between both active centers [4]. Finally, preformed cobalt NPs of 15 nm mean size were deposited on top of the shell (Figure 1C). The materials in the different synthesis steps were characterized by N_2-adsorption-desorption isotherms and chemical electron microscopy [5].

Figure 1 shows the Transmission Electron Microscopy (TEM) images of the material during the synthesis steps. It was observed that particle size of the PtNPs did not change after the formation of the mesoporous silica shell and the subsequent CoNPs deposition. Elemental analysis using Scanning TEM (STEM)-Energy Dispersive X-ray Spectroscopy (EDS) measurements of the core-shell material (SiO_2-Pt@m-SiO_2-Co) are shown in Figure 2. The intensity profiles of the elemental mapping confirmed the Co and Pt NPs sizes. The present results highlight the possibility to produce a core-shell arrangement of bimetallic tandem catalysts with specific conformation. The catalytic activity and selectivity's, evaluated in the CO_2 hydrogenation to C_2-C_4 olefins, proved the orthogonal tandem performance of the material.

In conclusion, the present work remarks the importance of electron microscopy as the main tool for verifying the synthesis protocol in material science. In our case, we observed the successful production of spatially controlled core-shell nanoparticles with two different types of active centers.

Figure 1: TEM images of the tandem core-shell catalyst during each synthesis step.

Figure 2: STEM image and EDS analysis of the core-Pt-shell-Co structures. (a) HAADF-STEM image and elemental maps of (b) O, (c) Pt, (d) Si, (e) Co, (f) mixed coloured mapping, and (g) line-scan profile of Si, Co, Pt and HAADF signals.

References:
[1] Coordination Chemistry Reviews 2004, 248, 2365–2379
[2] ACS Catalysis 2019, 9, 2639−2656.
[3] Nano Letters 2017, 17, 6, 3798–3802
[4] Nature Mater 2009, 8, 126–131.
[5] Chemical Reviews 2015, 115, 2818−2882
[6] The authors gratefully acknowledge funding from the Deutsche Forschungsgemeinschaft (DFG, German Research Foundation) under Germany's Excellence Strategy – EXC 2008 – 390540038 – UniSysCat

Figure 1

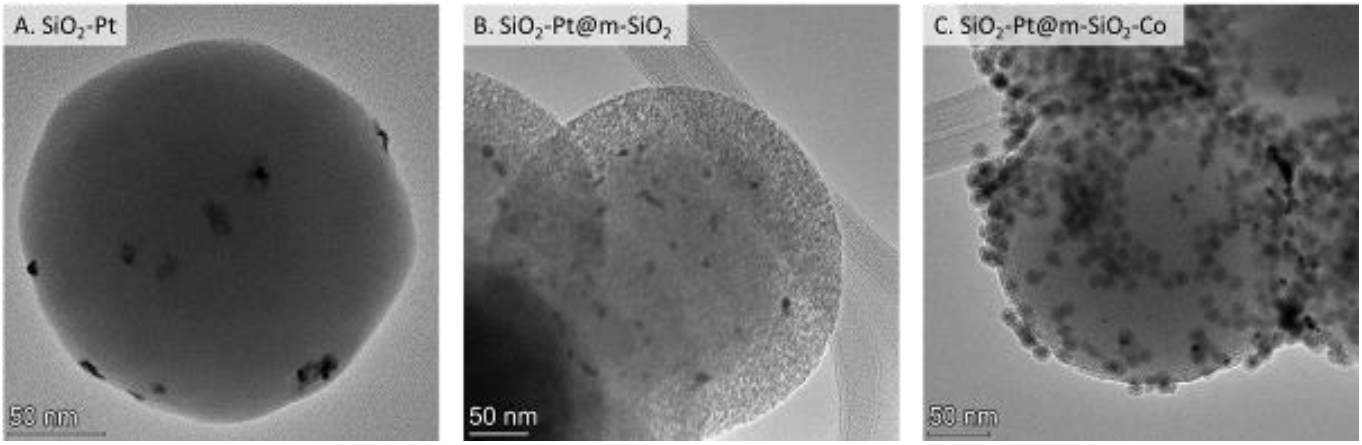

Figure 2

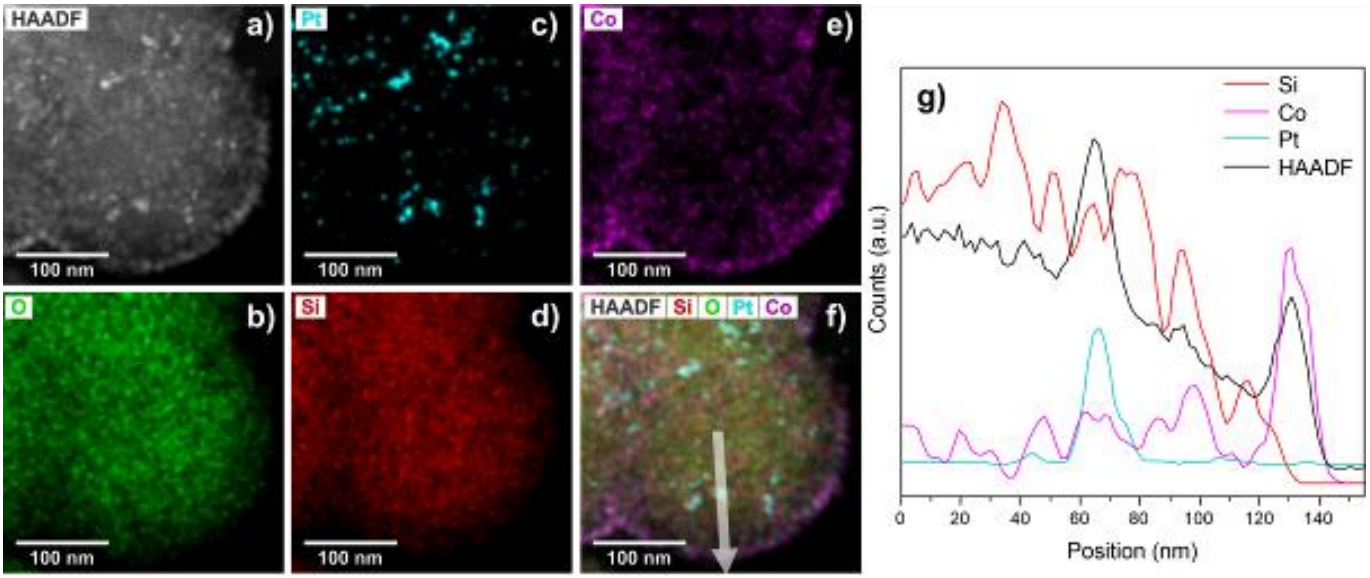

MS8.P018
In situ biasing and temperature dependence of electric fields across GaAs based p-n junctions measured by 4D STEM

A. Pokle[1], D. Heimes[1], A. Beyer-Leser[1], K. Volz[1]

[1]Philipps-University Marburg, Materials Science Centre and Department of Physics, Marburg, Germany

Keywords: *in-situ biasing, cryo, p-n junction, electric field measurements, FIB, 4D STEM and COM*

The ability to determine electric fields at the nanoscale quantitatively is critical for understanding semiconductor device properties. By employing transmission electron microscopy techniques like electron holography and differential phase contrast imaging (DPC), fundamental aspects of the electron interaction with the electric potential field have been investigated before [1,2]. By performing in situ biasing, the effect of external voltages on GaAs and Si p-n junctions have also been already investigated with electron holography [3,4]. However, this approach requires a specialized setup where the primary beam is split into two, wherein the reference wave later interacts with the second wave passing via the specimen.

Nevertheless, in recent times accessibility to direct electron detectors has enabled us to acquire four-dimensional datasets (diffraction patterns at each scan point), paving the way for new advanced developments. Here, we combine in-situ biasing and heating with four-dimensional scanning transmission electron microscopy (4DSTEM) technique to study for example the influence of applied voltage and temperature on the width of the depletion regions in the GaAs-based p-n junctions. The temperature dependence of the electric fields is investigated ranging from liquid nitrogen temperature (~ -183 °C) to above room temperature (~50 °C). The biasing and temperature-dependent studies are conducted by incorporating an in situ biasing and a cryo holder, respectively.

In this study, our sample preparation approach is based on the focused ion beam (FIB) method (JEOL JIB-4601F dual beam system), which is nontrivial from the perspective of placing the lamella on the biasing MEMS chip. This enables us to determine the electrical properties for a known sample thickness observed from both biased and unbiased junctions followed by temperature application. Moreover, the momentum transfer induced by internal electric fields is measured by the diffraction pattern's center-of-mass (COM) shift [5] (PNDetector Camera). Identical imaging conditions are employed, which are used for obtaining high-resolution STEM images (double Cs corrected JEOL JEM-220FS system). Here we will show the biasing and temperature influence's critical characteristic on the depletion region width.

References:
[1] Shibata, N. *et al.* Imaging of built-in electric field at a p-n junction by scanning transmission electron microscopy. *Sci Rep* **5**, (2015).
[2] McCartney, M. R., Dunin-Borkowski, R. E. & Smith, D. J. Quantitative measurement of nanoscale electrostatic potentials and charges using off-axis electron holography: Developments and opportunities. *Ultramicroscopy* **203**, 105–118 (2019).
[3] Twitchett, A. C., Dunin-Borkowski, R. E. & Midgley, P. A. Quantitative Electron Holography of Biased Semiconductor Devices. *PHYSICAL REVIEW LETTERS* **88**, 4 (2002).
[4] Anada, S. *et al.* Precise measurement of electric potential, field, and charge density profiles across a biased GaAs p-n tunnel junction by in situ phase-shifting electron holography. *Journal of Applied Physics* **122**, 225702 (2017).
[5] Beyer, A. *et al.* Quantitative Characterization of Nanometer-Scale Electric Fields via Momentum-Resolved STEM. *Nano Lett.* (2021) doi:10.1021/acs.nanolett.0c04544.

MS8.P019
Tuning strain in nanosheet devices

P. Favia[1], G. Eneman[1], A. Veloso[1], A. Hikavyy[1], A. De Keersgieter[1], N. Horiguchi[1], O. Richard[1], H. Bender[1]

[1]Imec, MCASA, Leuven, Belgium

Strain of the crystal lattice, compressive along the channel for p-metal–oxide–semiconductor (PMOS) and tensile for NMOS structures, is well known as a carrier mobility booster in transistors [1,2]. Strain is also a critical parameter for the next generation of nanodevices, such as nanowires (NW), nanosheets (NS) and complementary field emission transistors (CFETs) and needs to be optimized and tuned if these are to compete with the performances of the current architecture of FinFETs.

In this work, strain analysis by nano beam electron diffraction (NBD) is used to understand the strain mechanisms in NS structures during source/drain (S/D) epitaxial growth in the presence of inner spacers. In the 3D integration process of gate-all-around (GAA) stacked NS, inner spacers have been introduced in order to reduce gate-S/D capacitances [3][4]. The presence of inner spacers changes the way S/D are grown and it is, therefore, important to assess whether S/D stress generation in NS is comparable to inner spacers-free architectures [5]. In addition, we will try to understand if strain can be modulated by varying the shape and defectivity of S/D.

The epitaxial layers presented here have been grown in an ASM Intrepid XP™ reduced pressure chemical vapour deposition tool [6]. Samples consist of fin-shaped structures of Si/SiGe double-layers used to fabricate GAA Si NS. The SiGe layers are sacrificial layers that will be etched away later in the process in order to release the NS. These sacrificial layers are also indented after S/D recess to leave space for inner spacer deposition. The samples in this study are observed at different stages of the S/D epi growth. TEM specimens are prepared by FIB lift-out.

Inner spacers are formed after the partial lateral etching of the sacrificial SiGe layers from the Si/SiGe multi-layer fins. In these type of devices, the S/D SiGe:B epitaxial layer [6] growth is initiated from two sources as shown in Figure (1a):1) epi growing from the exposed sidewalls of the Si channels (with a triangular like shape in the HAADF-STEM 2D projected image); and 2) epi growing from the bottom Si surface, in the fins recessed in-between gates. NBD measurements reveal a tensile strain along the Si NS in presence of such incomplete S/D configuration (Figure 2a,c,e). By continuing the deposition, the three SiGe growth fronts will eventually merge as shown in Figure 1b. At this point, the tensile strain is reduced in intensity and should finally reverse from tensile to compressive. This is shown in Figure 2d,f for top and bottom wire respectively, where the top NS is relaxed while the bottom one is compressed at the edges.

In conclusion, preliminary studies show that the strain type can be reversed from tensile to compressive by controlling the defectivity of the S/D growth. This understanding is an important step towards tuning strain for mobility enhancement in CMOS GAA NS.

[1] Krishnamohan T et al. IEDM 2008 **4** 1–4
[2] Eneman G, et al. IEDM 2012 131-134
[3] Barraud et al. IEDM 2016
[4] Gaben L et al., ECS 2016
[5] Favia P. et al. MSMXXI
[6] Hikavyy A, et al., Thin Solid Films 602 2016 72–77
[7] Sentaurus Process Reference Manual M-2016, 12

Thanks to the Imec SEMTEM team for TEM specimen preparation

Figure 1: HAADF-STEM of incomplete triangular S/D (a) and complete S/D at the end of growth. (b)

Figure 2: DF-STEM of incomplete S/D (a); tensile longitudinal and compressive vertical strain along top (c) and bottom (e) NS. DF-STEM of re-grown S/D (b); longitudinal and vertical strain along top (d) and bottom (f) NS.

Figure 1

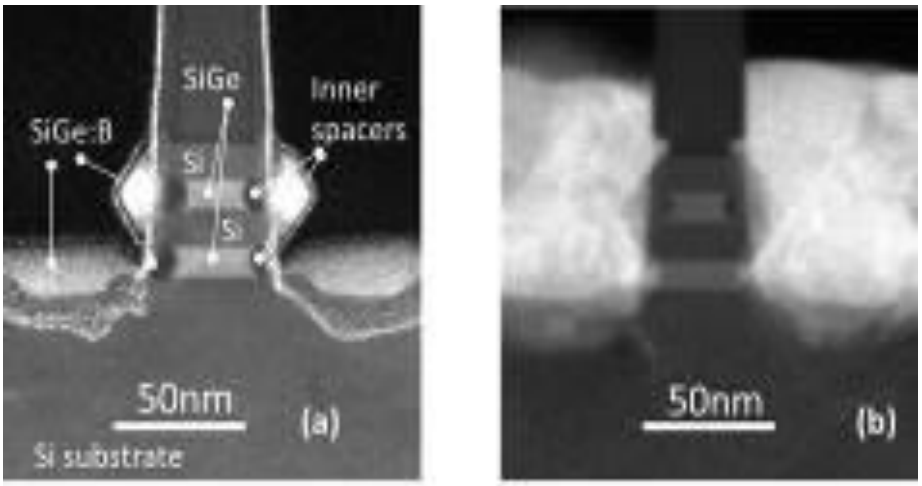

Figure 2

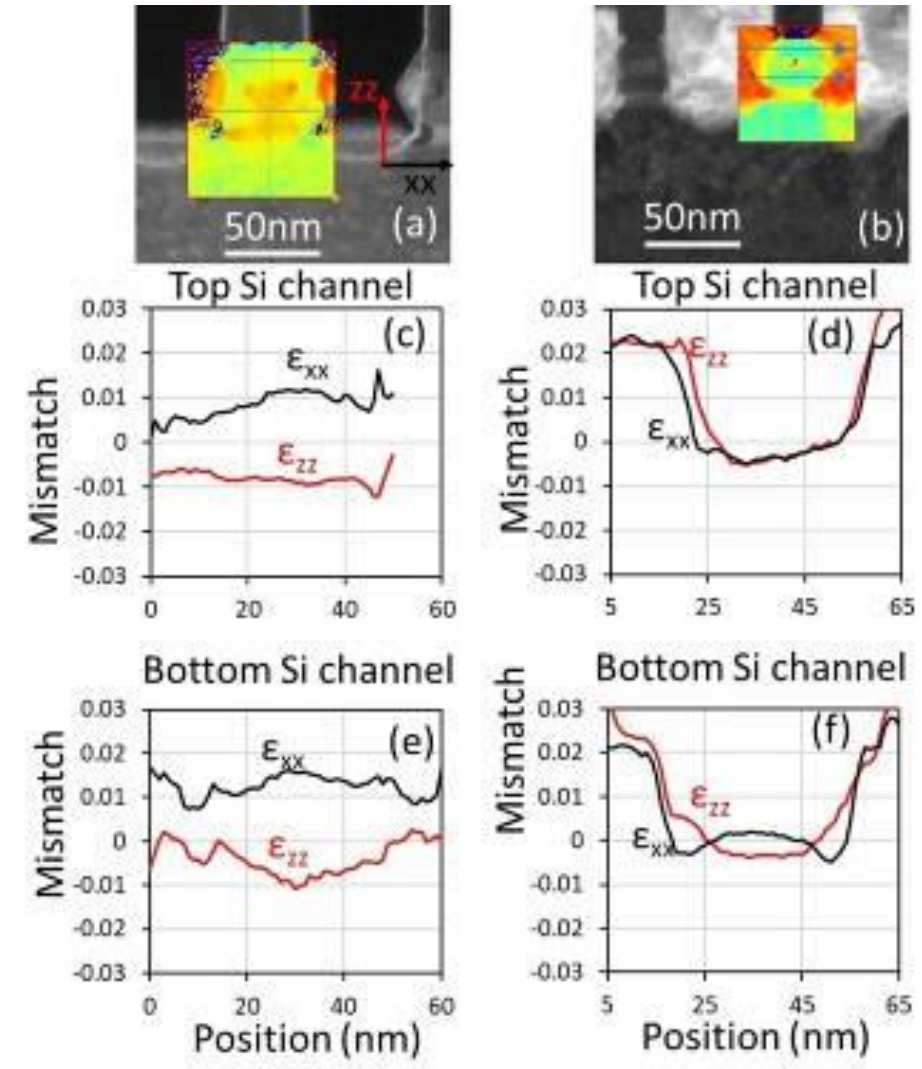

MS8.P020
Great impact of crystalline structure on photocatalytic properties of thin ZnO (PE)ALD films

D. Jardas[1,2], R. Peter[1,2], M. Podlogar[3], D. Vengust[3], K. Salamon[4], M. Petravić[1,2], A. Omerzu[1,2]

[1]University of Rijeka, Department of Physics, Rijeka, Croatia
[2]Centre for Micro- and Nanosciences and Technologies, Rijeka, Croatia
[3]Jožef Stefan Institute, Ljubljana, Slovenia
[4]Ruđer Bošković Institute, Zagreb, Croatia

The synthesis of thin ZnO films using atomic layer deposition (ALD) technique has many advantages over other techniques, such as good repeatability, accurate control of the film thickness, and great uniformity of the films [1,2]. Moreover, different structural and physical properties can be obtained using ALD or plasma-enhanced (PE)-ALD method and different synthesis parameters. The ALD and PE-ALD deposition temperatures for ZnO ranges from 60 °C to 250 °C and it has a huge impact on the photocatalytic activity of the deposited films. For ZnO films deposited by a conventional thermal ALD, it is known that the final photocatalytic activity of the films is greatly improved when the substrate deposition temperature is increased [2,3]. On the other hand, the photocatalytic activity of the films deposited by the PE - ALD method shows a maximum value for films deposited at 80 °C. In the present study, we have compared the surface morphology and crystallinity of the thin films deposited at 80 °C by the ALD and PE-ALD methods. For this purpose, scanning electron microscopy (SEM) and transmission electron microscopy (TEM) were used. From the SEM images and the particle size diagram, it can be seen that the ALD film consists of round grains with sizes between 10 and 20 nm (Figure 1.a) and the PE - ALD film consists of cylindrical grains with sizes between 5 and 10 nm (Figure 1.b). TEM images confirm the size distribution and provide additional information about crystal boundaries along the cross-section. Measurements of photocatalytic activity have shown that the PE-ALD thin ZnO film exhibits a *ten times* higher activity compared to those grown by the thermal ALD method. Thus, we conclude that surfaces of ZnO films with smaller crystal grains are much more effective in the photocatalytic processes.

References:
[1] A. Omerzu, R. Peter, D. Jardas, I. Turel, K. Salamon, M. Podlogar, D. Vengust, I. Jelovica Badovinac, I. Kavre Piltaver, M. Petravic (2021), Large enhancement of photocatalytic activity in ZnO thin films grown by plasma-enhanced atomic layer deposition, *Surfaces and Interfaces,* 23, 100984.
[2] R. Peter, K. Salamon, A. Omerzu, J. Grenzer, I. J. Badovinac, I. Saric, M. Petravic, (2020), Role of Hydrogen-Related Defects in Photocatalytic Activity of ZnO Films Grown by Atomic Layer Deposition, *J. Phys. Chem. C,* 124 (16), 8861-8868.
[3] V. Roge, N. Bahlawane, G. Lamblin, I. Fechete, F. Garin, A. Diniac, D. Lenoble, (2015), Improvement of the Photocatalytic Degradation Property of Atomic Layer Deposited ZnO Thin Films: The Interplay Between Film Properties and Functional Performances, *J. Mater. Chem. A*, *3*, 11453–11461.

Figure 1

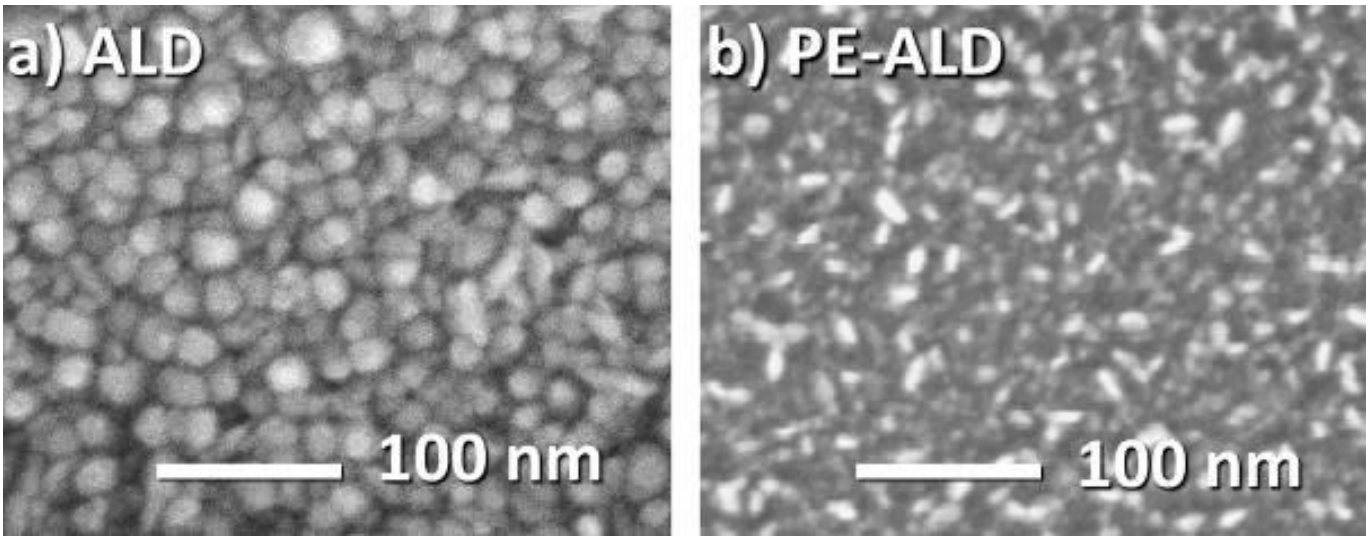

MS8.P021
Structure of vertically self-assembled ZnO nanowires epitaxial growth on sapphire and silicon in carbo-thermal process

W. Zajkowska[1], H. Teisseyre[1], K. Fronc[1], S. Kret[1], J. Turczyński[1], B. Kurowska[1], M. Bilska[1]

[1]Institute of Physics Polish Academy of Sciences, Warsaw, Poland

Zinc oxide nanostructures have been investigated for the last decades due its potential applications for various electronic devices such as laser diodes [1], optical switches [2] and photodetectors [3]. ZnO nanowires (NWs) have numerous physical advantages over other compounds like high exciton binding energy (60 meV), large piezoelectricity, low cost production and wide direct band gap (3.37 eV). Among the numerous methods of ZnO NW synthesis like vapor-liquid-solid growth, one of the simplest, fastest and cheapest is the carbo-thermal method [4]. The aim of this work is to conduct a full, systematic optimization of growth parameters vertically oriented ZnO NWs without usage of any additional catalyst or carrier gas flow. Influence of factors such as temperature or process time was observed during SEM (NWs topology) and HRTEM/STEM (NWs quality) imaging. The mixture of ZnO powder and graphite ground in a mortar in a molar ratio of 1:1 were transferred into an alumina crucible covered by silicon or sapphire wafer. The process was carried out in a tube furnace at temperatures of 880-940 °C in air, without gas flow. The crucible was heated with the furnace from room temperature. Consecutive stages of NWs growth were observed on SEM, both as "hedgehogs" (Fig 1b) and vertical, perpendicular to the substrate NWs (Fig 1a). The experiments were done for both Si (100) and sapphire (11-20) substrates. In addition to observing the NWs morphology by SEM, the Focused Ion Beam (FIB) was used to prepare thin cross-sections of NWs as well as interface between substrate and NWs. In order to conduct TEM studies, NWs were transferred mechanically onto standard TEM 3mm diameter copper grid covered by holey carbon film. Vertical NWs grown on sapphire (Fig 1a) have an average length of 4-7 µm and diameter of 50-500 nm. NWs with a length of tens of micrometers were obtained on silicon substrate oriented in any directional preferences (Fig 1b). The orientation, strains, the presence of defects, morphology and the smoothness of the nanowires walls were observed on the TEM in order to find the most favorable conditions for nanowires growth. The thin nanowires (diameter < 400 nm) have perfect crystal structure without any structural defect. The dislocations have been observed in the case of thick wires (diameter > 400 nm). HRTEM imaging of the cross-section of the nanowires is performed in Fig 1c, where it can be seen along the [0001] axis. Visible radiation defects are caused by FIB process by which gallium ions cut the specimen. Also, the details of the interface structure between sapphire substrate and ZnO NWs is presented in image Figure 1d. The presence of a spontaneously formed buffer layer between the sapphire substrate and NW was observed. This approximately 3 nm layer was identified as a $ZnAl_2O_4$ spinel as was reported in [5]. A low magnification example of 9.25 µm thick nanowire under study in TEM is visible in Fig 1e. What was proved is that it is possible to create high quality NWs with high length to diameter ratio, using the simple carbo-thermal method on Si and additionally sapphire.

[1] Zhi-Feng Shi et al., Phys. Chem. Chem. Phys., 17, 13813-13820 (2015)
[2] T. Smith, S. Haeuser, S. King, Proceedings of the Wisconsin Space Conference 1 (2020)
[3] J. Law, J. Thong, Appl. Phys. Lett., 88, 133114 (2006)
[4] W. Zaleszczyk, K. Fronc et al., Acta Physica Polonica A, Vol. 114, No. 5 (2008)
[5] C. Gorla et al., Journal of Applied Physics, 87, 3736 (2000)

Figure 1

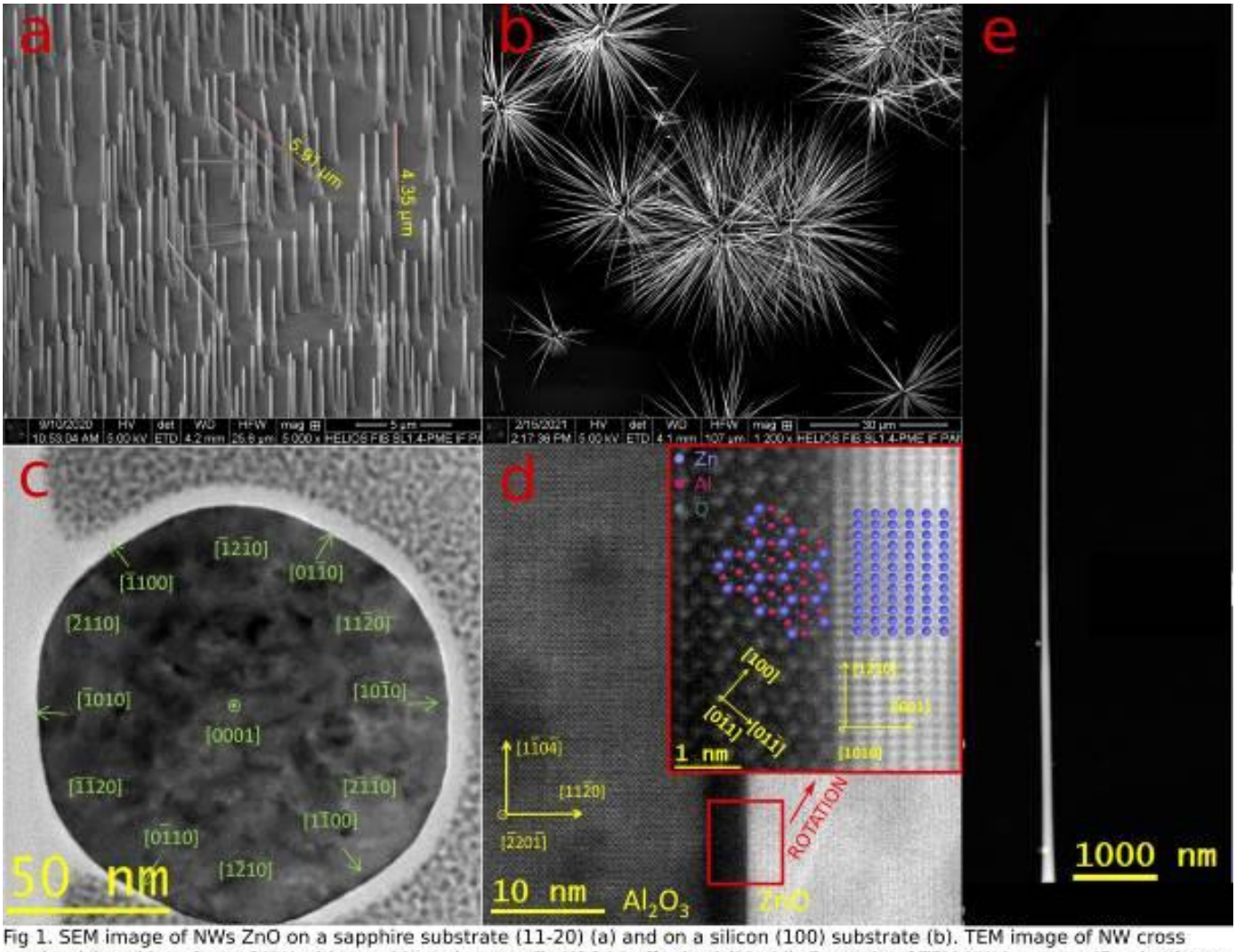

Fig 1. SEM image of NWs ZnO on a sapphire substrate (11-20) (a) and on a silicon (100) substrate (b). TEM image of NW cross section (c) and interface of NW with sapphire substrate, ZnAl2O4 buffer is visible (d). Example of TEM NW low magnification image (e).

MS8.P023
Investigation of electrocatalysts produced by a novel thermal spray deposition method

W. Hetaba[1,2], A. Y. Klyushin[2,3], L. J. Falling[2], D. Shin[1], A. K. Mechler[1], M. G. Willinger[2], R. Schlögl[1,2]

[1]Max-Planck-Institut für Chemische Energiekonversion in Mülheim an der Ruhr, Heterogene Reaktionen, Mülheim an der Ruhr, Germany
[2]Fritz Haber Institute of the Max Planck Society , Abteilung Anorganische Chemie, Berlin, Germany
[3]Helmholtz-Zentrum Berlin für Materialien und Energie GmbH, Division of Energy Materials, Berlin, Germany

Typical preparation methods for electrocatalysts include, but are not limited to, impregnation, precipitation and different spraying techniques [1,2]. In this work we investigated catalysts produced by a novel thermal spray deposition method which allows for a wide variety of metals used for deposition and support materials [3]. We used a combination of electron microscopy (EM), X-ray photoelectron spectroscopy (XPS) and cyclic voltammetry (CV) to analyse the structural properties and elemental composition of the catalysts and to perform a first assessment of the electrochemical performance.

The samples were produced using different combinations of steel and Ti substrates as well as combinations of Au, Pt and Ru catalyst particles. The production process yielded nanoparticles of different size, shape and different coverage on top of the substrate. Figure 1 shows an exemplary SEM overview and EDX map of one of the investigated samples from which the different sizes, shapes and compositions of the catalyst particles can be seen. FIB lamellae were prepared to investigate the interface between the particles and the substrate more closely. In Figure 2 a STEM EDX map and a corresponding elemental line profile acquired from such a lamella is shown. An oxide layer at the interface is well visible. Additional sample positions were examined to investigate the material diffusion. Cyclo-voltammetric measurements allowed a first assessment of the electrochemical activity of the samples. The amount of catalyst materials deposited on the substrate as well as the accessible electrochemical surface influences the activity of the investigated materials.

We found that the investigated thermal spray deposition method is able to generate a variety of electrochemically active materials. It allows to select different coverages of the catalyst material on the substrate. However, care has to be taken that a possible oxide layer on the substrate or material diffusion do not limit the desired functionality but facilitate a conductive connection to allow for electrochemical activity. All in all, the method provides a new and versatile approach for electrocatalyst synthesis, providing a useful addition to established methods.

Figure 1: a) SEM overview image of one of the investigated samples. Different shapes and sizes of the catalyst particles are visible. B) EDX map of several particles consisting of Ru and Zr on a Ti support. Figure adapted from [3].

Figure 2: a) EDX linescan of one of the investigated samples showing the Pt, Ti and O signal intensities. B) STEM-EDX map of the interface between Ti substrate, oxide layer and Pt particle. The marker indicates the region from which the linescan in a) was extracted. Figure taken from [3].

[1] Shao et al., Chem. Rev. 2016, 116, 3594-3657
[2] Herman et al., MRS Bull. 2000, 25, 17-25
[3] Hetaba et al., Materials 2020, 13(12), 2746
[4] The authors thank TreadStone Technologies, Inc. For providing the samples.

Figure 1

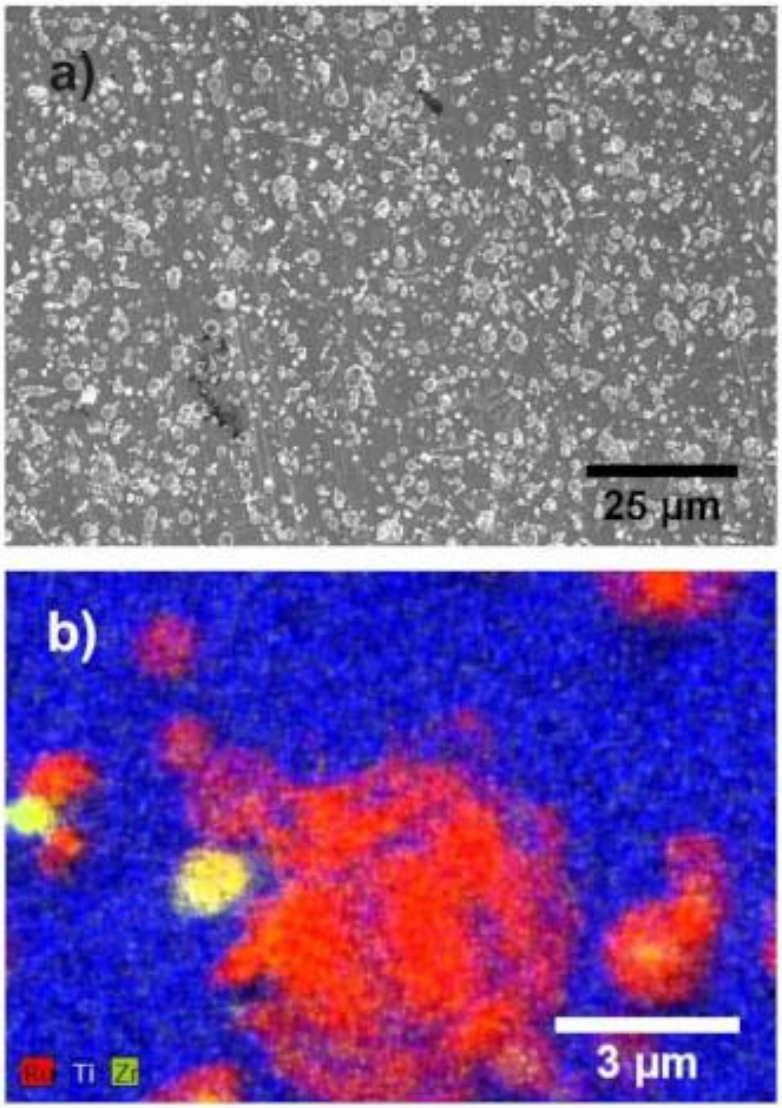

Figure 2

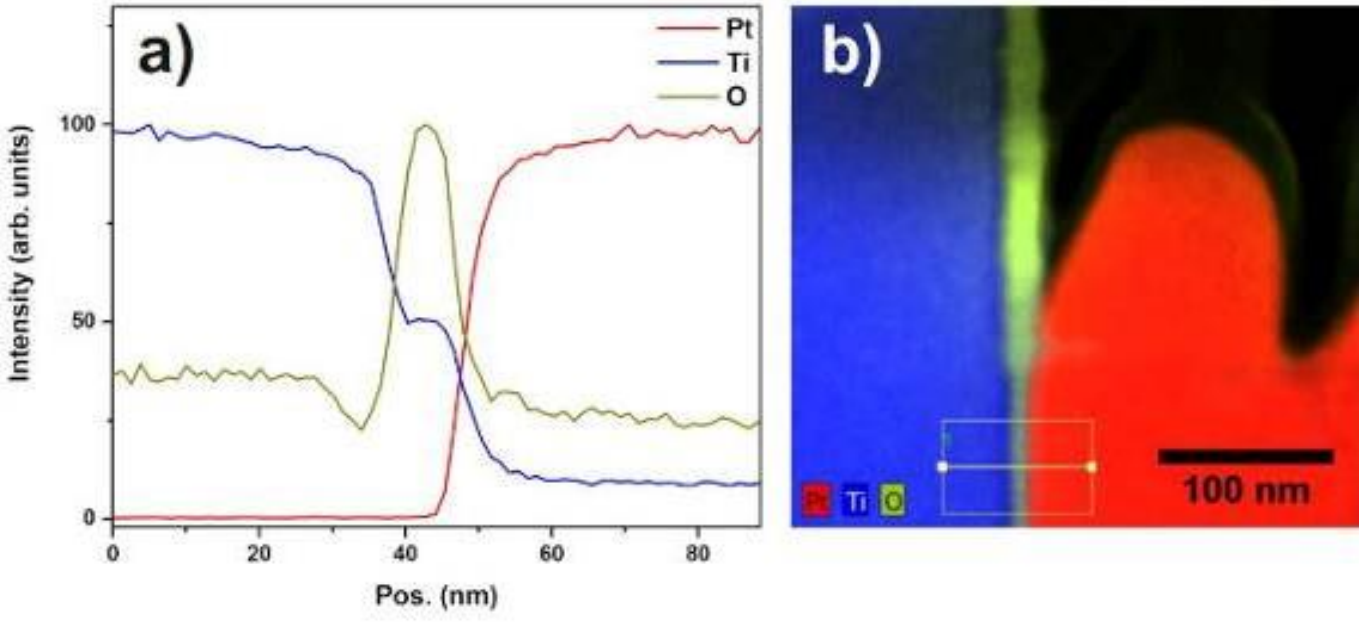

MS8.P024
Correction for artifacts of EDXS-based quantification of chemical composition of SiGeSn-based epitaxial structures

H. Kirmse[1], D. Schwarz[2], K. Elsner[1], H. Kropf[3], M. Wollgarten[3], J. Schulze[2], C. T. Koch[1]

[1]Humboldt University of Berlin, Physik, Berlin, Germany
[2]Universität Stuttgart, Institut für Halbleitertechnik, Stuttgart, Germany
[3]Helmholtz-Zentrum Berlin für Materialien und Energie GmbH, Institut Solare Brennstoffe, Corelab Correlative Microscopy and Spectroscopy, Berlin, Germany

Energy dispersive X-ray spectroscopy (EDXS) performed in a transmission electron microscope (TEM) provides access to the chemical composition of a material. The result of quantification strongly depends on the geometry of the TEM specimen. Parameters like specimen thickness at the position of analysis and its distance from adjacent material might systematically alter the result. In this work we present a compensation for artifacts of EDXS-based quantification of chemical composition by means of a calibration using artifact-minimized TEM specimen prepared by focused ion beam (FIB) thinning.

A series of 6 samples was grown by molecular beam epitaxy on Si(001) on which a 500 nm thick Ge layer and a 100 nm SiGeSn layer have been deposited. The Sn content of the SiGeSn was increased from x_{Sn} = 0.025 to 0.150 in steps of 0.025. For matching the lattice of the underlying Ge the Si/Ge ratio of the SiGeSn layer was adapted depending on the Sn content. Details of the growth process are described elsewhere [1]. For TEM investigation, all specimens were conventionally prepared in cross-section. FIB lamellae of selected samples were prepared in a Zeiss Crossbeam. EDXS was performed in scanning TEM (STEM) mode at a JEOL 2200FS operated at 200 kV using a Bruker silicon drift detector. The chemical composition was calculated using Cliff-Lorimer factors [2] calibrated using a $Si_{0.30}Ge_{0.70}$ standard.

The particular influence of the type of specimen, i. e. conventional or FIB prepared, on the EDX spectrum is summarized in Figure 1. The conventionally prepared specimen exhibits a wedge shape and provides a bulky Si substrate (Figure 1a) potentially causing secondary fluorescence of Si. Moreover, a both-sided Si cover layer has to be considered resulting from the final Ar+ ion milling. The FIB sample, in comparison (Figure 1b), contains only a small volume of remaining Si substrate and hence does not contribute significant Si signal to the EDX spectrum recorded in an area of pure Ge (Figure 1c).

In Figure 2 the quantified chemical composition of all SiGeSn layers is given. The Si and Ge content are presented as a function of the quantified Sn content. An almost perfect agreement is found for the chemical composition derived from FIB prepared specimen with the nominal composition (dotted lines). This proves the layers to be composed as intended. Against that, the composition derived from conventionally prepared specimens systematically deviates from the nominal values. In particular, the Si content is overestimated whereas the Ge content is underestimated. The deviation can be approximated as a linear function of the Sn content and can be used for compensation. The quantified Sn content agrees well with the nominal content.

Figure 3 represents the Si and Ge content after compensation. The error bars of the measurement and subsequent quantification are additionally given. The error bar for the Si and Ge content amounts to ±2 atom%.

This work shows that conventionally prepared SiGeSn layers can provide reliable insights into the chemical composition although raw data are falsified by a bulky Si substrate and Si cover layers.

Figure 1: Sources of artifacts of EDXS due to geometry of the TEM specimen.

Figure 2: Si and Ge content of the SiGeSn layer of conventionally prepared TEM specimens vs. measured Sn content.

Figure 3: Artifact-compensated composition of SiGeSn layer.

[1] D. Schwarz et al., in preparation.
[2] G. Cliff, G.W. Lorimer, J. Microsc. 103 (1975) 203.

Figure 1

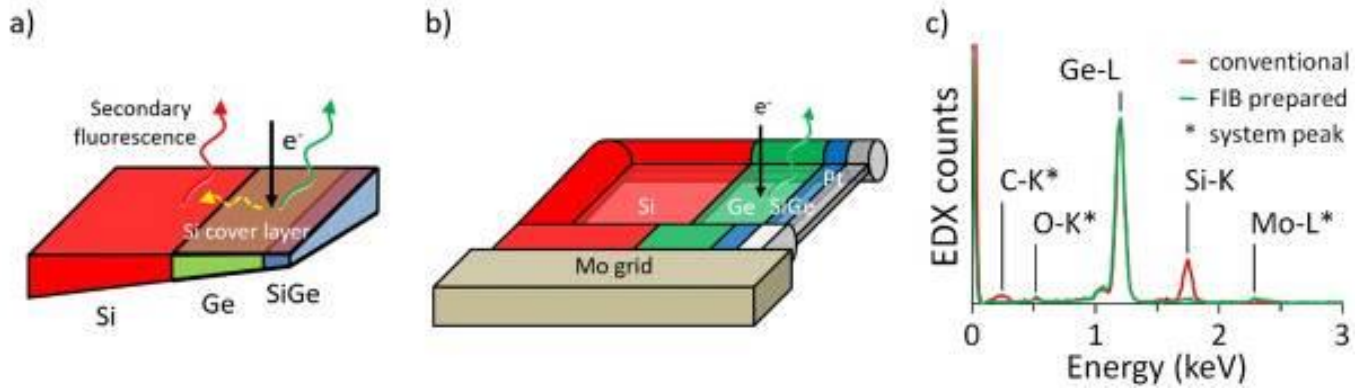

Figure 2

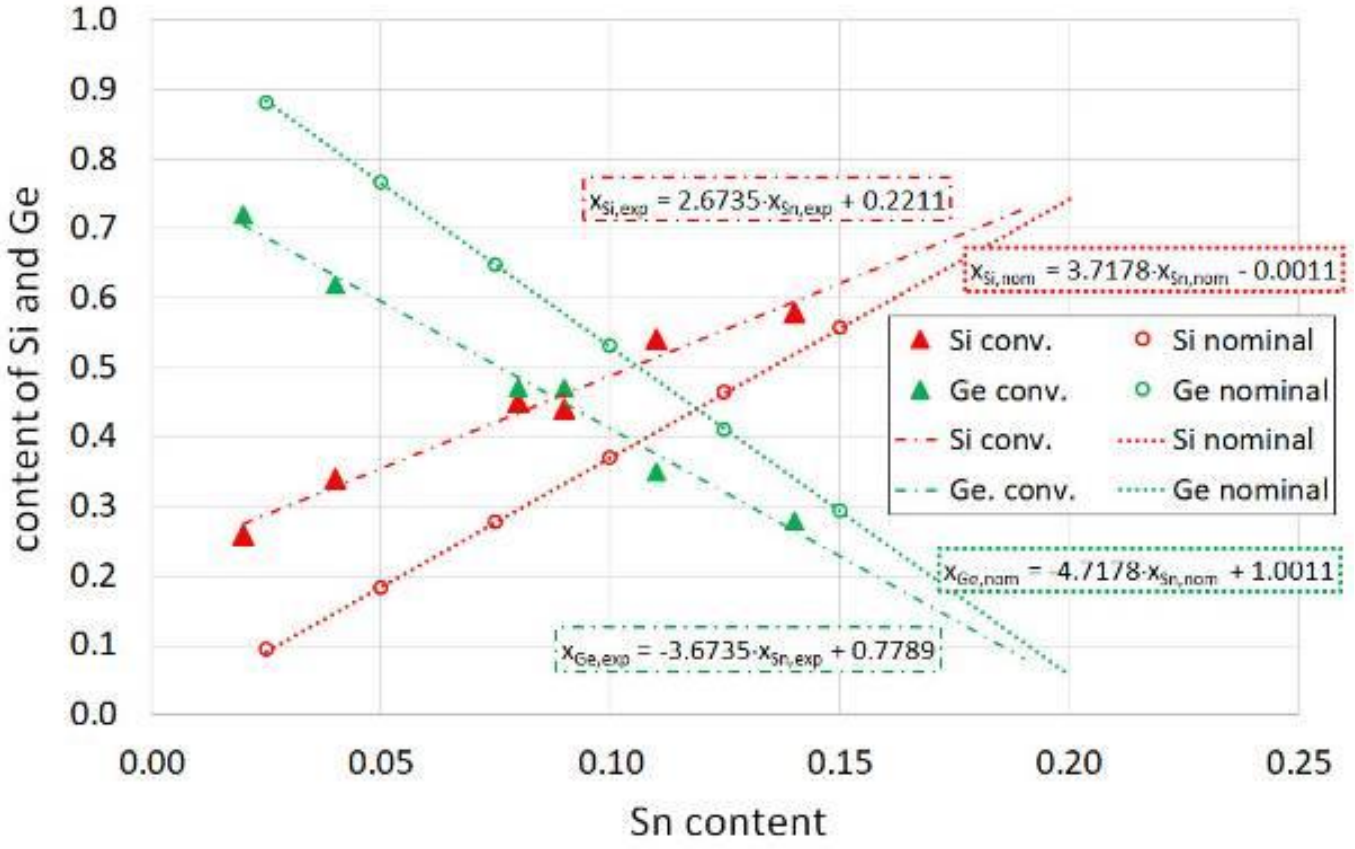

Figure 3

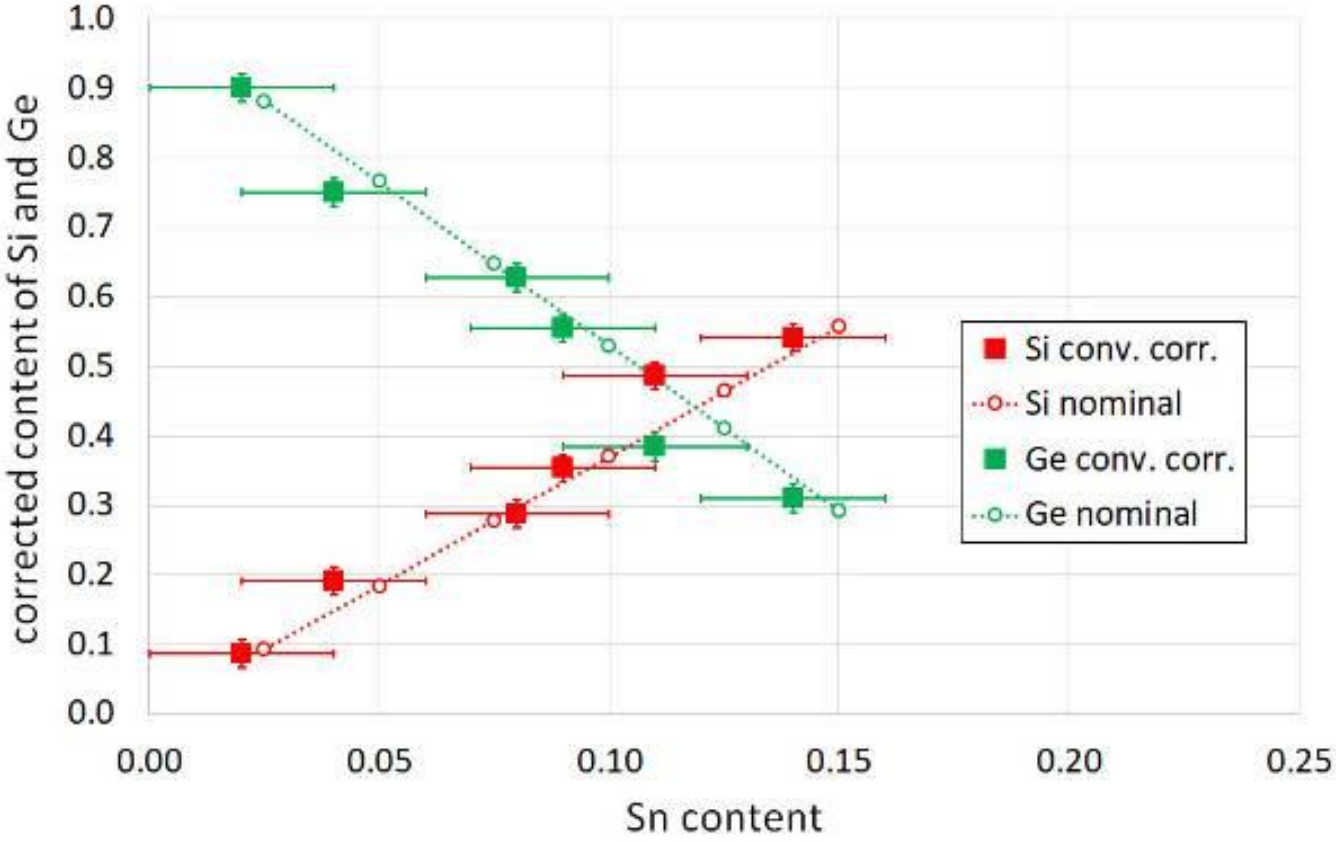
corrected content of Si and Ge
1.0
0.9
0.8
0.7
0.6
0.5
0.4
0.3
0.2
0.1
0.0
0.00
0.05
0.10
0.15
0.20
0.25
Sn content
Si conv. corr.
Si nominal
Ge conv. corr.
Ge nominal

MS8.P025
Phase transitions in a perovskite thin film studied by environmental *in situ* heating nano-beam electron diffraction

T. Meyer[1], B. Kressdorf[1], V. Roddatis[1,2], J. Hoffmann[1], C. Jooss[1], M. Seibt[3]

[1]Institute of Materials Physics, University of Göttingen, Göttingen, Germany
[2]German Research Centre for Geosciences GFZ, Potsdam, Germany
[3]4th Institute of Physics, University of Göttingen, Göttingen, Germany

Introduction: Compounds including volatile elements are subject to research activities in the context of many possible applications such as UV-LEDs [1], solid oxide fuel cells [2], solid state batteries [3], or neuromorphic computing [4]. Particularly in the three latter fields, transition metal oxide perovskites are a prominent example as their properties can be tuned by orbital, lattice, and spin degrees of freedom [5]. Due to their strong correlation, the materials" lattice parameters are typically a suitably indirect fingerprint to study underlying phase transitions making the transmission electron microscope (TEM), particularly nano-beam electron diffraction (NBED) [6], a highly suitable observation tool to study materials with nanoscale heterogeneities.

Objectives: The goal of this study is two-fold: Firstly, from the methodological point of view, the effect of ambient conditions in an environmental TEM on reaction paths upon in-situ heating is studied. Secondly, NBED is conducted to achieve spatial resolution sufficient to observe structural phase transitions in epitaxial thin films with nanotwinned domain structure.

Materials & methods: 400nm thick Pr0.9Ca0.1MnO3 films, epitaxially grown on single-crystalline SrTiO3 substrates by reactive ion beam sputtering, are studied with NBED to follow the quantitative lattice parameters upon in-situ heating in an environmental TEM (ETEM). Using the ETEM"s gas inlet capabilities, the oxygen partial pressure is varied during the experiments. The TEM results are furthermore compared to XRD data of macroscopic samples.

Results: Two fundamentally different reaction paths are found in ultra-high vacuum and oxygen environment, respectively. In the former case, an irreversible oxygen loss occurs during in-situ heating, which affects both the crystallographic extinction rules as well as the lattice parameters considerably. Using an oxygen environment, however, the irreversible changes due to oxygen vacancy formation can be suppressed and a reversible orthorhombic to pseudo-cubic phase transition is observed in combination with a spontaneous change in the strain state when approaching the pseudo-cubic phase (see Figure 1).

Conclusion: Controlling the ambient condition during in-situ heating of compounds containing volatile elements is a prerequisite to steer the reaction paths of phase transitions and can be realized by means of environmental transmission electron microscopy.

Figure 1: ADF-STEM overview of an epitaxial PCMO thin film on STO (top) showing a nanotwinned domain structure with two different orientations as revealed by NBED (middle). Upon heating in a 10 Pa oxygen environment, an orthorhombic to pseudo-cubic phase transition is observed in combination with a spontaneous change in the strain state when approaching the pseudo-cubic phase (bottom).

[1] O. Lupan, T. Pauporté, B. Viana, *Advanced Materials* **2010**, *22*, 30 3298.
[2] Y. Wang, H. Arandiyan, H. A. Tahini, J. Scott, X. Tan, H. Dai, J. D. Gale, A. L. Rohl, S. C. Smith, R. Amal, *Nature Communications* **2017**, *8*, 1 1.
[3] S. Luo, K. Wang, J. Wang, K. Jiang, Q. Li, S. Fan, *Advanced Materials* **2012**, *24*, 17 2294.
[4] D. S. Jeong, C. S. Hwang, *Advanced Materials* **2018**, *30*, 42 1704729.
[5] Y. Tokura, N. Nagaosa, *Science* **2000**, *288*, 5465 462.
[6] A. Béché, J. L. Rouvière, L. Clément, J. Hartmann, *Applied Physics Letters* **2009**, *95*, 12 123114.

Figure 1

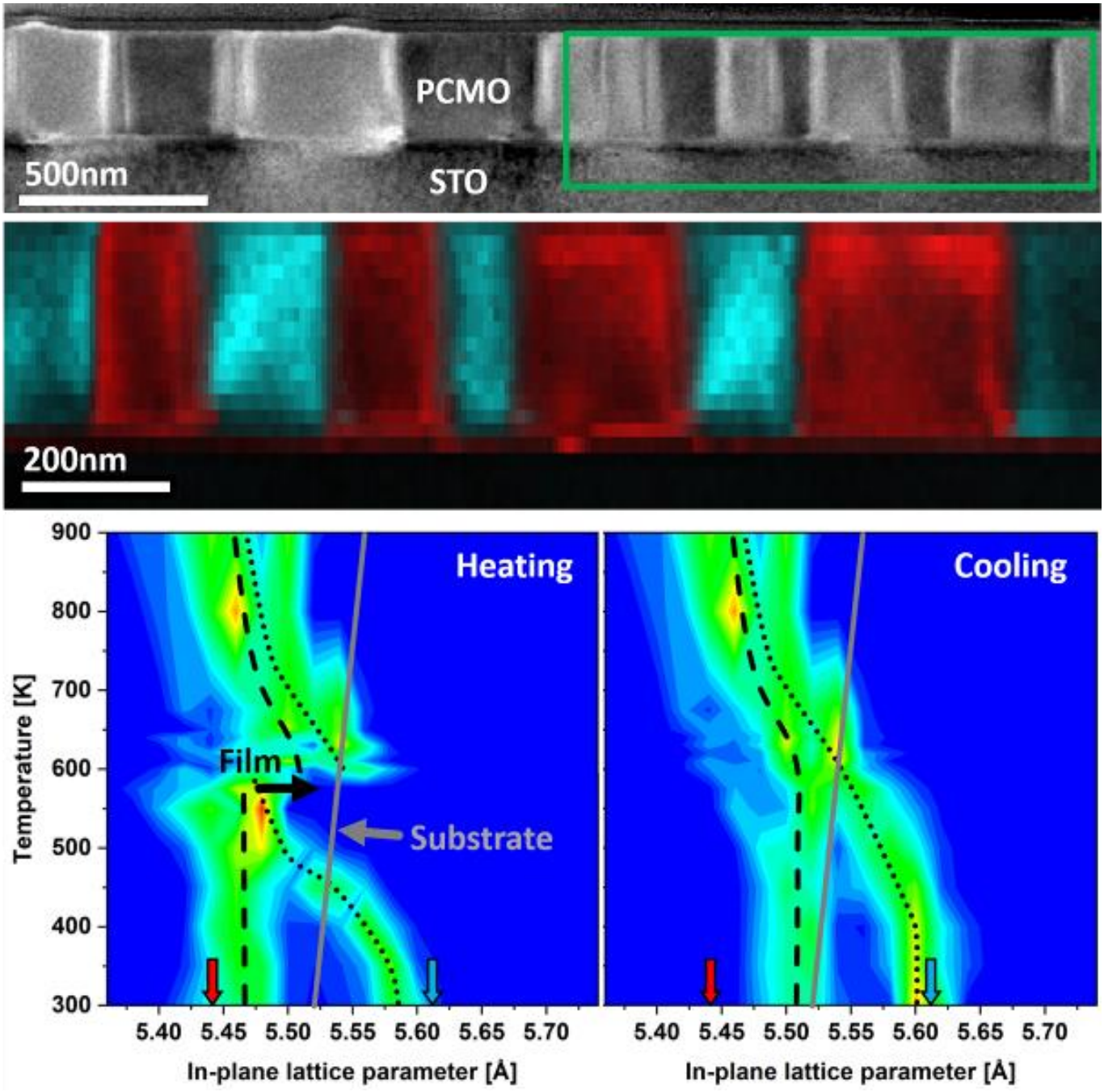
PCMO
STO
500nm
200nm
Heating
Cooling
Film
Substrate
Temperature [K]
900
800
700
600
500
400
300
5.40
5.45
5.50
5.55
5.60
5.65
5.70
In-plane lattice parameter [Å]
In-plane lattice parameter [Å]

MS8.P026
In situ study of manganese adatoms mobility/leaching at perovskite oxide catalyst-water interface in ETEM

G. Lole[1,2], V. Roddatis[1,3], U. Ross[1], M. Risch[1,4], T. Meyer[1,5], L. Rump[6,5], J. Geppert[1], G. Wartner[1,7], P. Blöchl[6,8] C. Jooss[1,2]

[1]Georg-August-Universität Göttingen, Institut für Materialphysik, Göttingen, Germany
[2]Georg-August-Universität Göttingen, International Center for Advanced Studies of Energy Conversion (ICASEC), Göttingen, Germany
[3]Helmholtz Centre Potsdam, German Research Centre for Geosciences, Potsdam, Germany
[4]Helmholtz-Zentrum Berlin für Materialien und Energie GmbH, Berlin, Germany
[5]Georg-August-Universität Göttingen, 4th Institute of Physics - Solids and Nanostructures, Göttingen, Germany
[6]Georg-August-Universität Göttingen, Institut für Theoretische Physik, Göttingen, Germany
[7]Helmholtz-Zentrum Berlin für Materialien und Energie GmbH, Young Investigator Group Operando Interface-Photochemistry, Berlin, Germany
[8]Clausthal University of Technology,, Institute for Theoretical Physics,, Clausthal-Zellerfeld, Germany

Understanding the dynamic catalyst - water interface in operando catalytic conditions such as oxygen evolution reaction (OER) is challenging. Therefore, in-situ characterization methods implemented under condition comparable to OER are required. Environmental transmission electron microscopy (ETEM) successfully contributed to this topic since it offers a comprehensive study of interactions of catalyst surfaces in controlled environments of water vapour and other reactive and non-reactive gases with atomic column resolution in electric potentials[1, 2]. Here, we report the reversible dynamics of highly mobile manganese (Mn) adatoms at single crystalline La/Sr terminated (001) surfaces of $La_{1-x}Sr_xMnO_3$ (x=0.4) (LSMO) and irreversible Mn leaching at mixed terminated (001) surface of $Pr_{1-x}Ca_xMnO_3$ (x=0.33) (PCMO) manganites at the interface to an absorbed H_2O layer[3]. The behaviour of the surfaces of both manganites is compared to high vacuum (HV) conditions as well as to O_2 and N_2. In addition to the surface dynamics of adatoms which is more than 20 time higher in contact to H_2O than for all other studies conditions, also the surface termination of the LSMO and PCMO (001) surfaces changes in different gases. To quantify the atomic dynamics we compared the experimental images to the images simulated using a Monte–Carlo-based least-squares optimization of simulated images based on the multislice method. The optimal electron optical parameters and thickness are obtained by contrast fitting. Figure 1 shows two experimental images of a times series with a Mn adatom hopping event on LSMO (001) on top of stable A-site cations (Figure 1a), the Mn adatom configurations used for image simulations (Figure 1b) and the simulated contrast for different Mn column occupancy, compared to measured contrast (Figure 1c). Our results are interpreted as an enhanced thermally activated Mn adatoms mobility due partial solvation of Mn adatoms in absorbed liquid H2O. Partially solvated surface Mn atoms thus have a different coordination than previously assumed. This result is essential for the understanding of the active state of Mn-O based catalysts and opens new perspectives in atomic scale design of efficient and stable electrode surfaces for OER.

Figure 1: (a) Two consecutive HRTEM images showing Mn-adatom hopping on a LSMO (001) surface in 0.5 Pa of H_2O with a stable La(Sr)O surface layer as indicated by white arrow. (b) Visualization of the used surface structure model for image simulation indicating the possible Mn adatoms hopping directions at LSMO-water interface. (c) Simulated HRTEM image with Mn-adatom column occupation of 3, 4, and 5 and line profiles of simulated (red) and experimental (black with symbols) images of B-columns with 3, 4, and 5 Mn atom occupation.

Reference:
[1] S. Raabe, D. Mierwaldt, J. Ciston, M. Uijttewaal, H. Stein, J. Hoffmann, Y. Zhu, P. Blöchl, and Ch. Jooss, Advanced Functional Materials, 22 (2012) 3378–3388.
[S] Mildner M. Beleggia, D. Mierwaldt Th. W. Hansen, J. B. Wagner, S. Yazdi, T. Kasama, J. Ciston, Y. Zhu, and Ch. Jooss, J. Phys. Chem. C, 119 (2015) 5301–5310.
[3] G. Lole, V. Roddatis, U. Ross, M. Risch, T. Meyer, L. Rump, J. Geppert, G. Wartner, P. Blöchl and Ch. Jooss, Communication Materials 1, 68 (2020).

Figure 1

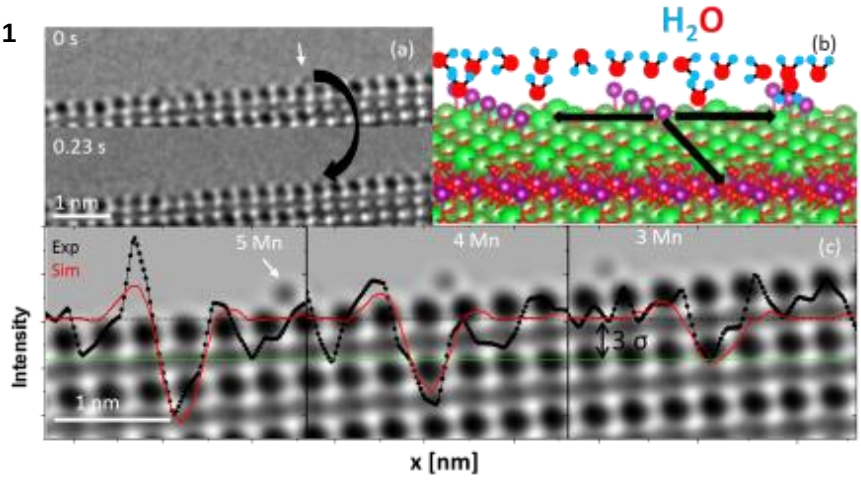

MS8.P027
Nano-structural characterisation of Zn- and Ti-doped SnO_2 catalyst for enhanced electroreduction of carbon dioxide

K. Bejtka[1,2], N. B. D. Monti[1,2], A. Sacco[1], M. Castellino[2], S. Porro[2], M. A. Farkhondehfal[1], J. Zeng[1], C. F. Pirri[1,2] A. Chiodoni[1]

[1]Italian Institute of Technology, Center for Sustainable Future Technologies, Turin, Italy
[2]Politecnico di Torino, Department of Applied Science and Technology, Turin, Italy

Introduction: The production of carbon-based chemicals and fuels by exploiting anthropogenic CO_2 is a topic of huge attention. CO_2 electrochemical reduction can result in value-added products, and among many products that can be obtained, which depend on the catalyst characteristics and reaction conditions, the CO_2 reduction reaction (CO_2RR) to CO or formic acid is up to now the economically most viable processes that can challenge conventional production routes.[1] Tin oxide-based materials are known to catalyze the CO_2RR to these two valuable products. These materials are environment-friendly and inexpensive. Their structure and morphology can play a decisive role in enhancing the catalytic properties.

Objectives: This work presents a strategy for the preparation of doped SnO_2 as an efficient electrocatalyst for the CO_2RR to formic acid and carbon monoxide. Zn or Ti doping was introduced into a mesoporous SnO_2 matrix via wet impregnation and atomic layer deposition. The interest in this material comes from the evidence that superior catalytic performances are observed in high-surface area materials like mesoporous structures, due to easier access of the electrolyte to the catalytic sites and efficient mass diffusion.[2] Doping was suggested to be an effective strategy to enhance catalytic activity by lowering the overpotential for CO_2 reduction with respect to un-doped SnO_2.[3]

Methods: The composition, morphology, and crystal structure, the pristine and doped SnO_2 nanocatalysts were characterized using transmission electron microscopy (TEM), X-ray diffraction (XRD), Raman, and X-ray photoelectron spectroscopy (XPS). Cyclic voltammetry, electrochemical impedance spectroscopy and chronoamperometric measurements were conducted in order to elucidate the catalytic performance of the electrodes for the CO_2RR.

Results & Conclusions: TEM showed formation of interconnected NPs with an irregular pore structure, which is typical of the SnO_x prepared by anodic oxidation,[2] and confirmed that the morphology of the undoped sample is preserved with no evidence of any other structures created. The presence of polycrystalline SnO_2 was confirmed by SAED and XRD in both undoped and doped catalysts. There is no detectable evidence of dopant in the diffraction pattern, attributed to metallic dopant or metal-based compounds. The structural properties of the catalysts were further investigated by Rietveld refinement. The presence of dopants was confirmed by EDX in the same samples, and mapping confirmed their uniform distribution. It was found that doping of SnO_2 generates an increased amount of oxygen vacancies, which are believed to contribute to the CO_2 conversion efficiency, and among others, Zn doping resulted the most efficient process, as confirmed by XPS. It is important to study the catalyst not only before, but also during the reaction with the in-situ methods, as this can help to optimize its properties including durability and catalytic capability. We discuss changes catalysts undergo during the reaction and show that the proposed preparation route results in a stable and durable material. The morphological and structural characteristics of the obtained catalysts will be compared with their electrochemical behavior. The introduction of doping results in enhanced performance for formic acid formation, in comparison to un-doped SnO_2. In addition, a threefold increase in current density was observed in the Zn doped sample. The enhancement of these characteristics relates to the improved charge transfer and conductivity with respect to bare SnO_2.

References:
[1] O.S. Bushuyev et al. Joule, 2018, 2, 825.
[2] K. Bejtka et al. ACS Appl. Energy Mater., 2019, 2, 3081.
[3] K. Saravanan et al. J. Mater. Chem. A, 2017, 5, 11756.

Fig 1. STEM characterisation of fresh and tested Zn doped SnO_2 catalyst.

Figure 1

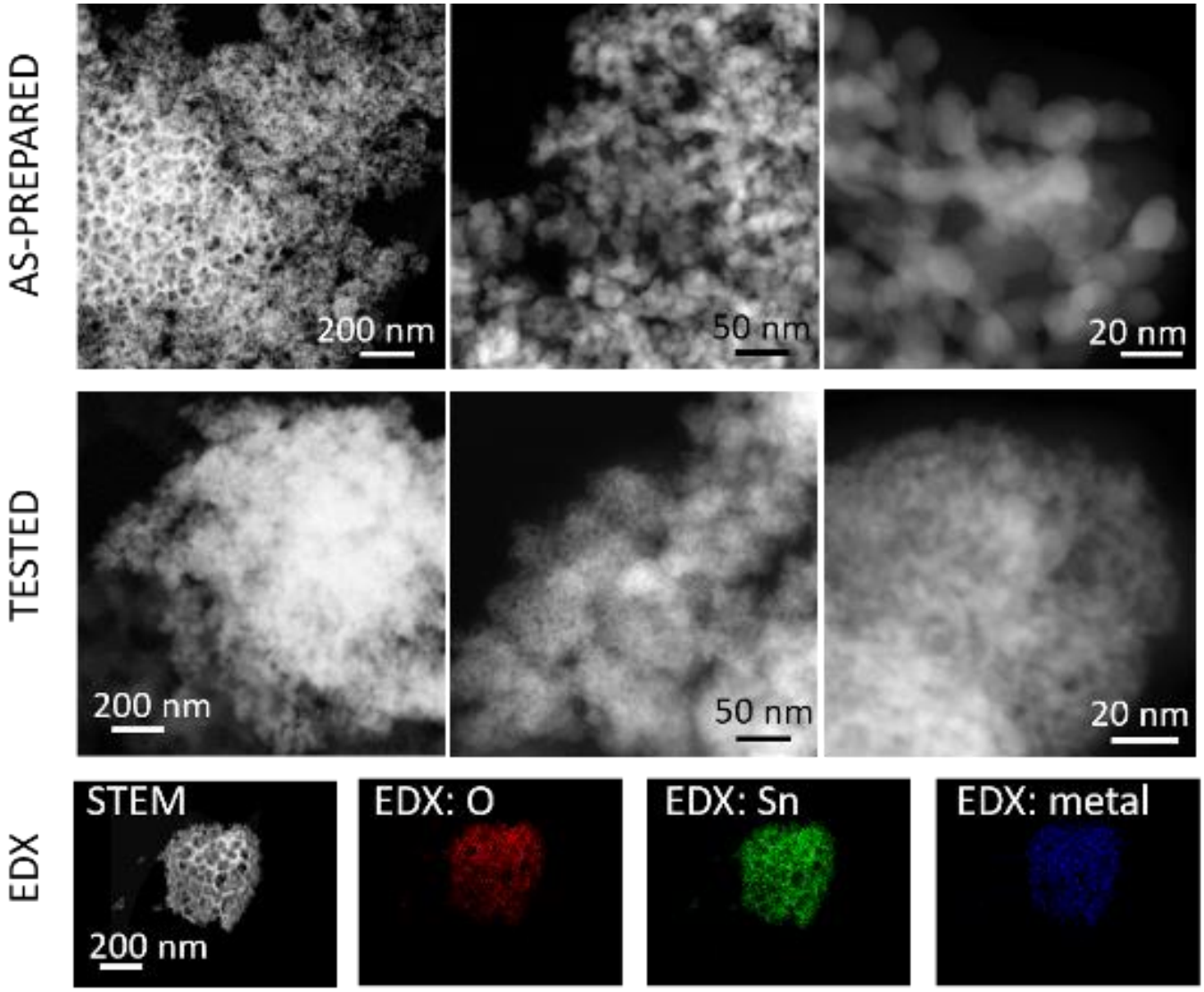

MS8.P028
Semblance of imaging zeolites implanted with single metal sites for catalysis

P. L. Ho[1,2], P. D. Nellist[2], S. C. E. Tsang[1]

[1]University of Oxford, Department of Chemistry, Oxford, United Kingdom
[2]University of Oxford, Department of Materials, Oxford, United Kingdom

Introduction: Considerable efforts have been made to develop atomically-dispersed supported metal catalysts in order to maximize the number of catalytically active sites at a reduced metal loading. Compared with conventional catalyst supports such as various metals and metal oxides, porous crystalline materials have designable topology, porosity and functionality. Many works have reported that identifying the atomic structures of porous materials in spatial dimension by scanning transmission electron microscopy (STEM) is significant for explaining their chemical reaction mechanism in catalysis [1,2]. In order to the diversification and rapid development of imaging technology, scientists should carefully investigate signals displaying high-contrast atomic images, the image has a high chance of containing artificially modulated signals. Our current work focuses on complex zeolite images, and providing a solution by using Electron Ptychography.

Objectives: There are two significant challenges associated with imaging metal in zeolite systems: the sensitivity of zeolites to radiation damage and the need to image elements over a wide range of atomic numbers. In addition to one more question in this work is that how to "efficiently" capture a single atom of metal within this radiosensitive framework, especially single atom information concealed in the high-frequency signal with amorphous and carbon deposition. The simultaneously recorded combination of annular dark-field (ADF) STEM and electron ptychography addresses both these problems, as has been demonstrated previously for similarly beam sensitive Li-ion battery cathode materials [3]

Materials & methods: Different loading amounts of Re-USY zeolite systems investigated as part of this work. The Merlin/Medipix system delivered the 4D-STEM imaging speeds necessary for low-dose STEM imaging and simultaneous ADF imaging is available on this instrument. The 300 kV beam energy reduced the rate of beam damage given that the likely damage mechanism of the zeolite is radiolysis. The experimental result will be verified through multilayers simulation, the Fourier filter and multi-characterisations.

Results: The work builds upon the quantitative ADF methods to accurately measure the number of atoms and to reduce the noise signal ratio of structure of nanoparticles through multi-frame. Importantly, the location of the nanoparticles or single atoms can be related to the zeolite framework through the simultaneous ptychography-ADF combination. Using to acquire a statistically meaningful quantity of image data over a range of nanoparticles demonstrated the strategic placement of defined metal catalytic active sites in the confined atom-dimensional pores of these materials, and to relate catalytic performance to the size and shape selectivity of zeolite pores and the synergy between different active sites in the confined space.

Conclusion**:** The impact of this work is in enabling a link between the detailed atomic configuration of the catalyst without the effect of high-frequency periodic signal, the synthesis method used, and the resulting catalytic activity, enabling understanding to drive the development of the synthesis methods.

Publications:
[1] L. Liu et al, *Angew. Chem. Int. Ed.* **2020** *59*, 819.
[2] B. Shen et al, *Adv. Mater.* **2020** 32, 1906103
[3] J. G. Lozano et al, *Nano Letters*, **2018** 18, 6850.

Figure 1

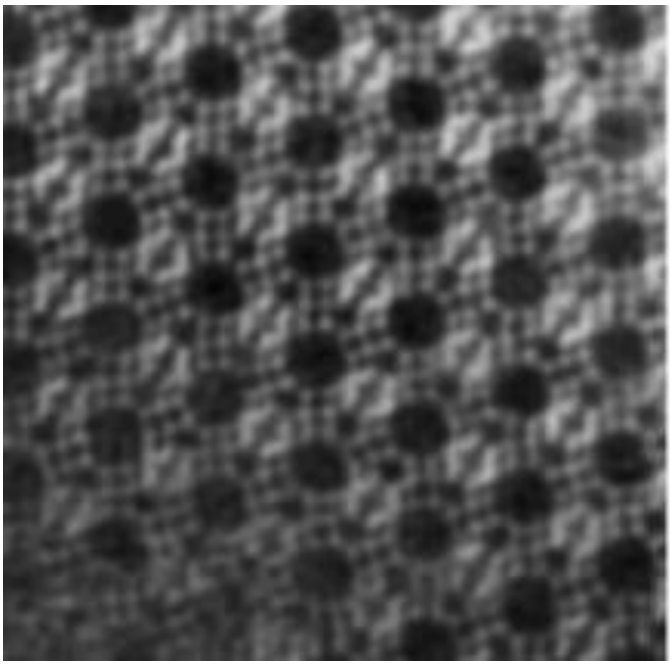

Figure 2

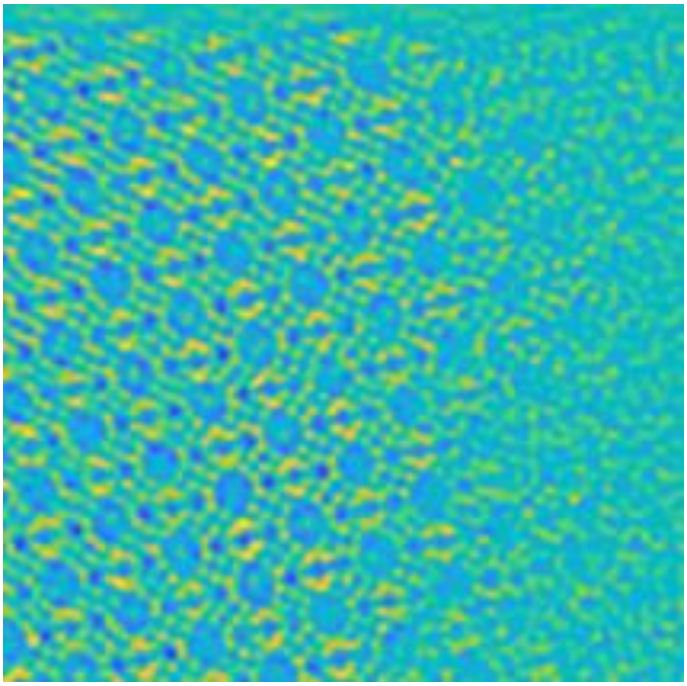

MS8.P029
Operando SEM studies on the catalytic behavior of Ni under dry reforming conditions

C. Claudiu[1], M. Wang[1]

[1]ETH Zurich, ScopeM, Zurich, Switzerland

Our generation is already facing the drastic consequences of climate change. As scientists, we have the responsibility to pave the way towards developing a sustainable economy that is based on renewable natural resources and to mitigate the emission of greenhouse gases. Concerning the second point, dry reforming of methane (DRM) has recently gained a lot of attention. The advantage of converting methane from natural gas to valuable products is twofold: first, it prevents carbon dioxide emissions from methane flaring, and second, it produces highly exploitable syngas mixtures. Amongst the most studied technologies for converting methane to syngas are the reforming techniques (steam, dry and autothermal) which differ in the oxidant used, final hydrogen to carbon monoxide ratio, and the kinetics and energetics of the reaction. In the case of dry reforming of methane (DRM), carbon dioxide is used as oxidant [1]. Although DRM is a highly endothermic reaction, it is attractive because of the high selectivity that can be achieved when operating at low pressure and high temperature. The main barrier that still prevents its industrial implementation is related to a fast deactivation of the catalyst through sintering and carbon coking [2]. Suitable model systems are essential for providing a fundamental understanding of the complex mechanisms of a working catalyst under relevant conditions. Therefore, poly-crystalline foils and nickel foams are employed for the detection and investigation of reaction-induced processes. While high-surface-area nickel foams are most suitable for the detection of catalytic conversion inside the SEM chamber, polycrystalline foils will provide insights into the relationship between surface structure and dynamics, which can then finally be studied in more detail on selected single crystal surfaces. A commercially available Thermo Fisher Scientific Quattro S SEM was modified to meet the prohibitive requirements for assessing the mechanisms of catalytic act. The specialty of this dedicated setup resides in the high precision and exceptional stability of the experimental parameters. We have discerned the active species of a Ni catalyst that are implied in the dry reforming of methane, as well as the spectator structures that exist alongside carbon forming species. We have studied the surface morphology as a function of operation parameters and encountered a stable active regime in non-stoichiometric environments. Our unique in-situ SEM set-up allows us to visually observe the state of the active catalyst under reaction conditions in real-time, at high spatial resolution using a combination of dedicated secondary electron, high-temperature 3D backscatter- and an electron-beam absorbed current detectors. Direct observation combined with on-line mass-spectroscopic analysis of the gas-phase and detection of catalytic conversion enables studies of the structure-reactivity correlation under relevant working conditions. The method is very surface sensitive, as has recently been demonstrated [3], and enables observations of the surface structure and collective non-equilibrium dynamics with relevant temporal resolution under controlled atmosphere at pressures between 10^{-4} to 10^{+3} Pa and temperatures of up to 1200°C.

[1] Palmer, Clarke, et al. *Nature Catalysis* 3.1 (2020): 83-89
[2] Sandoval-Diaz, Luis, et al. *Journal of Energy Chemistry* 50 (2020): 178-186
[3] Barroo, Cédric, et al. *Nature Catalysis* 3.1 (2020): 30-39

Figure 1

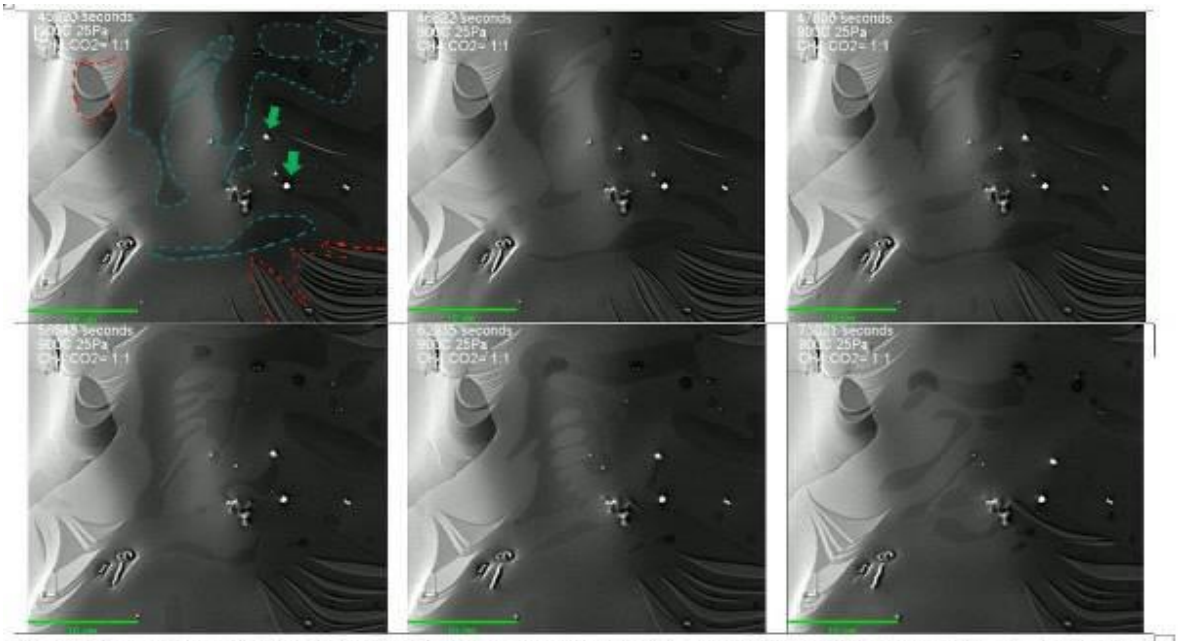

Figure S1: Surface of Ni catalyst in the active regime (900°C and 25Pa of CH_4:CO_2 mixture). In the first panel, green arrows indicate residual silica particles, red dotted enclosures indicate oxygen induced surface reconstructions, blue dotted enclosures indicate carbonaceous species

MS8.P030
Analytical TEM study of thin PLD-grown $LuFeO_3$ layers on Pt/sapphire substrates

X. Jin[1], B. Nergis[2], A. Rodrigues[2], S. Bauer[2], L. Horák[3], T. Baumbach[2], V. Holý[3,4], R. Schneider[1]

[1]Karlsruhe Institute of Technology (KIT), Laboratory for Electron Microscopy, Karlsruhe, Germany
[2]Karlsruhe Institute of Technology (KIT), Institute for Photon Science and Synchrotron Radiation, Eggenstein-Leopoldshafen, Germany
[3]Charles University in Prague , Department of Solid State Physics, Prague, Czech Republic
[4]Masaryk University, Faculty of Science, Brno, Czech Republic

Ferrites of rare earth metals with hexagonal crystal structure in form of *h*-$RFeO_3$ (R = Y, Dy-Lu) are promising candidates for many future applications in information processing and storage due to their multiferroic properties [1].

In this work, the structure and microchemistry of thin $LuFeO_3$ (LFO) layers produced by pulsed laser deposition (PLD) were studied by transmission electron microscopy (TEM), including high-resolution TEM (HRTEM) as well as scanning TEM (STEM) combined with energy-dispersive X-ray spectroscopy (EDXS). The crystal quality of LFO was investigated in dependence on the growth parameters and the substrate of either sapphire or a PLD-grown Pt layer. These studies aimed to find suited experimental conditions for epitaxial growth of high-quality *h*-LFO on different substrates.

LFO films were deposited on Pt layers with nominal thicknesses of 20 nm and 40 nm on top of Al_2O_3 (0001) or directly on this substrate by PLD via a Nd:YAG laser at a repetition rate of 5 Hz. Cross-section TEM lamellas were prepared from these samples by focused-ion-beam milling using an FEI dual beam Helios G4 FX microscope. For TEM investigations, a 200 kV FEI Tecnai Osiris and a 300 kV FEI Titan 80-300 transmission electron microscope was used, where the latter has a C_S image corrector. Combined STEM/EDXS analyses were performed on the Osiris microscope with an FEI Super-X detector.

Typical STEM HAADF images and X-ray maps of Lu and Fe of the three different samples are depicted in Figure 1. In the sample with the bare LFO (Figs. 1a-I – 1a-III), the layer thickness appears to be homogeneous, which is ~10 nm. For the sample with 20 nm thick Pt (Figs. 1b-I – 1b-III), no continuous Pt layer is present but rather island-like structures. The Pt islands have the shape of truncated pyramids with heights in the range between 70 nm and 100 nm. Evidently, in regions without Pt islands there is no Pt interlayer between LFO and Al_2O_3. An incomplete Pt interlayer is also observable in the sample with nominal 40 nm thick Pt, however, because of the thicker Pt layer, the islands" height is likewise much larger (~145 nm to 220 nm). In addition, there are also regions with layer-on-layer growth of LFO on Pt. For each sample, the hexagonal crystal structure of LFO was proved by HRTEM imaging (Figure 2). However, there are clear differences in the crystalline quality of the individual LFO layers, which can be attributed to the particular subjacent material, i.e. sapphire or Pt. For LFO on sapphire, the layer shows a partly strongly disturbed crystal structure, in particular many stacking faults, owing to the high misfit of 29% between the lattices of *h*-Al_2O_3 and *h*-LFO. For *h*-LFO grown on Pt, there is a good epitaxial relationship of the two crystal lattices due to the less misfit of ~6%. Digital image analysis revealed that, in the out-of-plane direction, there is an epitaxial match of the (0001) lattice planes of LFO and the (111) Pt planes. In in-plane direction, there is, e.g., (1210) *h*-LFO || (112) Pt (Figure 2b) or (0110) *h*-LFO || (110) Pt (Figure 2c).

The results clearly demonstrate that the crystalline quality of the LFO layers on Pt is better than on sapphire, and moreover, it seems to improve with increasing thickness of the Pt interlayer.

[1] H. Schmid, Ferroelectrics **162** (1994) 317.
[2] S. Bauer *et al.*, Materials **13** (2020) 61.
[3] The support of Czech Science Foundation (project 19-10799J) and German Research Foundation (projects SCHN 669/11 and BA 1642/8-1) is acknowledged.

Figure 1

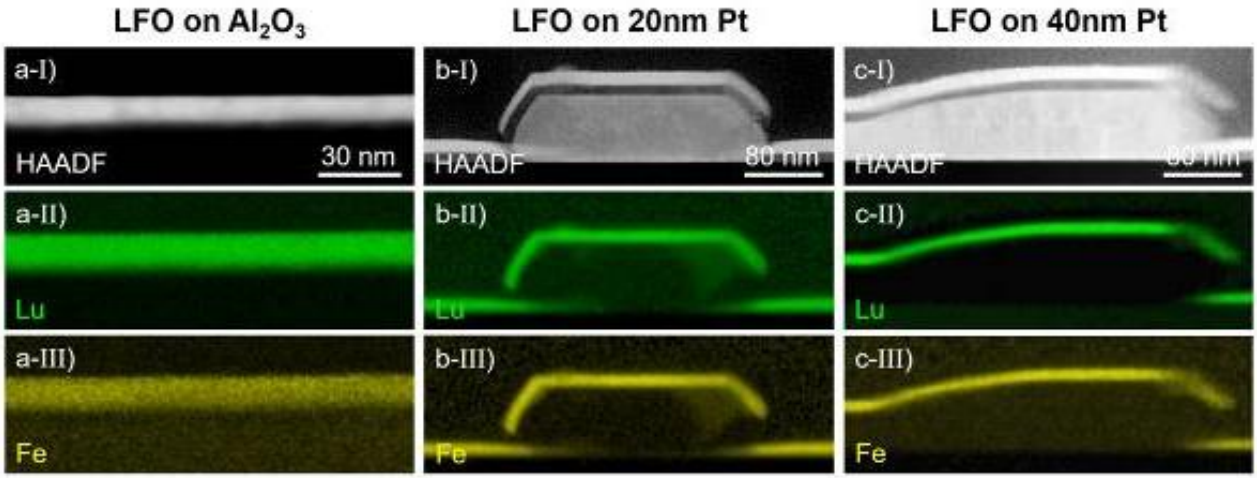

Figure 1. STEM HAADF images and X-ray maps of the distribution of the elements Lu and Fe for the LFO layer directly deposited on sapphire (panels a-I – a-III), on top of the 20 nm Pt layer (b-I – b-III), and on the 40 nm Pt layer (c-I – c-III).

Figure 2

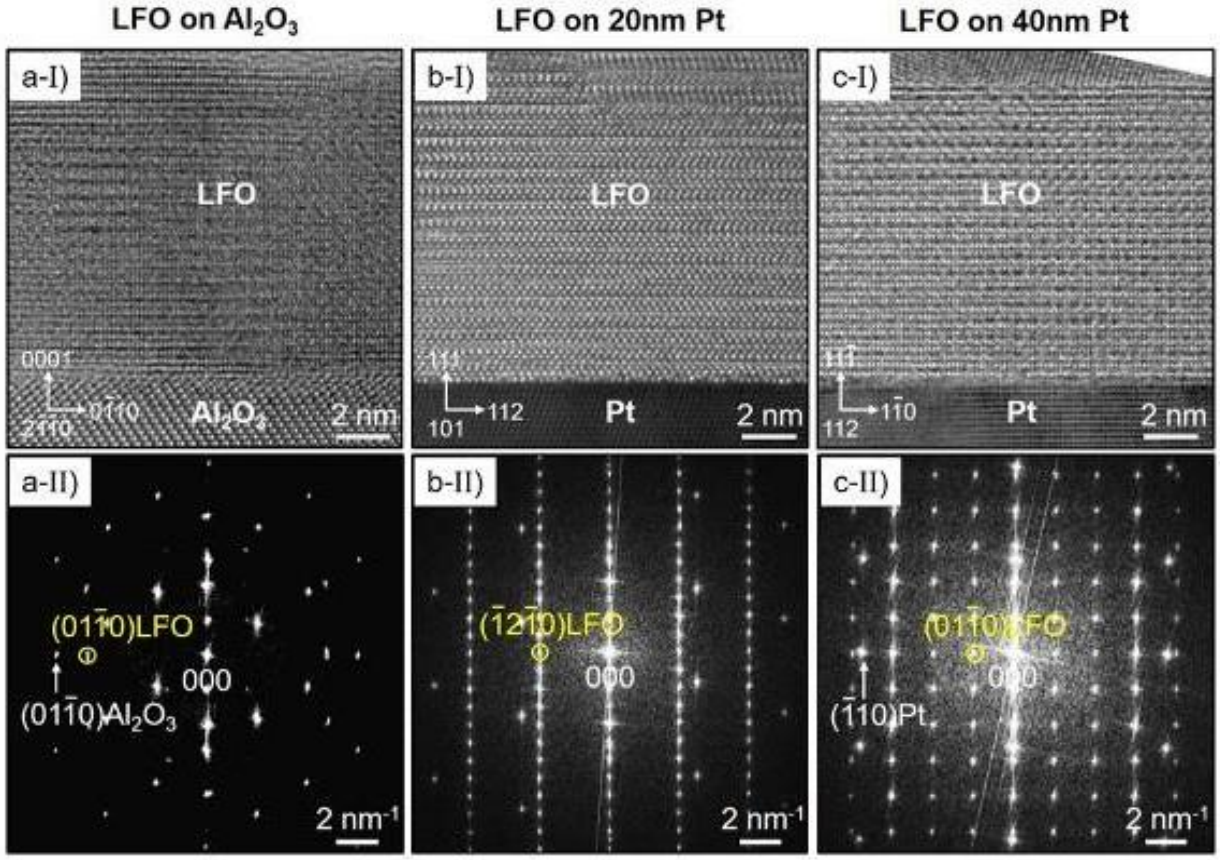

Figure 2. Structural characterization of the LFO layers and their orientation relationships with respect to the subjacent sapphire substrate or Pt layer, respectively, by HRTEM and fast Fourier transformation analysis: LFO layer deposited directly on sapphire (column (a)), on a nominally 20 nm thick Pt layer (b), and on a Pt layer of 40 nm nominal thickness (c).

MS8.P031
Mass spectrometry investigations on the decomposition behavior of III/V semiconductor precursor gases in a closed gas cell *in situ* TEM holder

M. Widemann[1], D. P. Krug[1], F. Gruber[1], A. Beyer-Leser[1], K. Volz[1]

[1]Philipps-University Marburg, Marburg, Germany

A widely used fabrication process for III/V semiconductor materials is metal organic vapor phase epitaxy (MOVPE). Mass spectrometry analysis of the gas phase in the MOVPE reactor gives detailed insights into the decomposition of the precursor gases, and thus into the growth process [1]. *In-situ* studies of the growth process promise an improvement of the performance of the fabricated materials, however direct observations of the crystal growth in conventional MOVPE reactors are challenging. *In-situ* (scanning) transmission electron microscopy ((S)TEM) allows the investigation of dynamic processes, which occur during growth of III/V semiconductors. Gas environmental cell and heating holders enable the supply of gases while heating the sample so that conditions comparable to those during the MOVPE process can be realized in any microscope [2] and semiconductor growth can be performed. The comparability of such a micro reactor with a conventional one, however, still needs to be proven.

To this end, a commercially available Protochips *in-situ* system, equipped with a quadrupole mass spectrometer working with 70 eV electron ionization, has been modified to investigate the processes occurring during semiconductor growth. In order to allow the usage of toxic and pyrophoric gases, like the precursor gases used in MOVPE growth, a gas mixing system, an appropriate gas monitoring system as well as a gas scrubbing system have been added to the setup [3]. A double CS-corrected JEOL JEM 2200FS operating at 200 kV was used for the TEM observations. Investigated precursor gases are tertiarybutylphosphine (TBP) and trimethylgallium (TMGa) at partial pressures between 10^{-1} and 10^{-3} hPa and a V/III ratio of around 10. Additionally, N_2 is used as carrier gas at pressures in the range of 10^2 hPa.

We observe the decomposition behavior of the precursor gases in the micrometer scaled TEM holder tip as well as the influence of the irradiating electron beam interacting with the gas volume. Figure 1 shows two mass spectra of the thermal decomposition species of TBP, measured at temperatures of 750 °C and 900 °C. The spectra were recorded with a mixture of 99% nitrogen and 1% TBP with a total pressure of 100 hPa. The contributions of the background, nitrogen and undecomposed TBP molecule signal were subtracted. Additionally, they were normalized to the phosphine peak intensity at 34 u. In this way, only the signal of TBP decomposition species are visible enabling a comparison of their ratio. The experiment was performed without an impinging electron beam to only see the effect of temperature. Increasing temperature especially reduces the intensity at 43 u, the base peak position of isobutane, whereas the 39 u, 41 u and 56 u peaks, pertaining to isobutene, increase. The results show, that isobutane and isobutene appear as decomposition products of TBP with an increasing fraction of isobutene with increasing temperature. Isobutane is produced by homolytic fission, whereas isobutene is a result of beta-hydrogen elimination of TBP, which becomes a more favorable as decomposition mechanism for TBP with increasing temperature.

Figure 1: Mass spectra of TBP decomposition species at 750 °C and 900 °C corrected with respect to the pure TBP and nitrogen intensities.

References:
[1] P. W. Lee, *et al., Journal of Crystal Growth* **85.1-2** (1987).
[2] L. F. Allard, *et al.*, *Microscopy and Microanalysis* **18.4** (2012).
[3] R. Straubinger, *et al.*, *Microscopy and Microanalysis* **23.4** (2017).

Figure 1

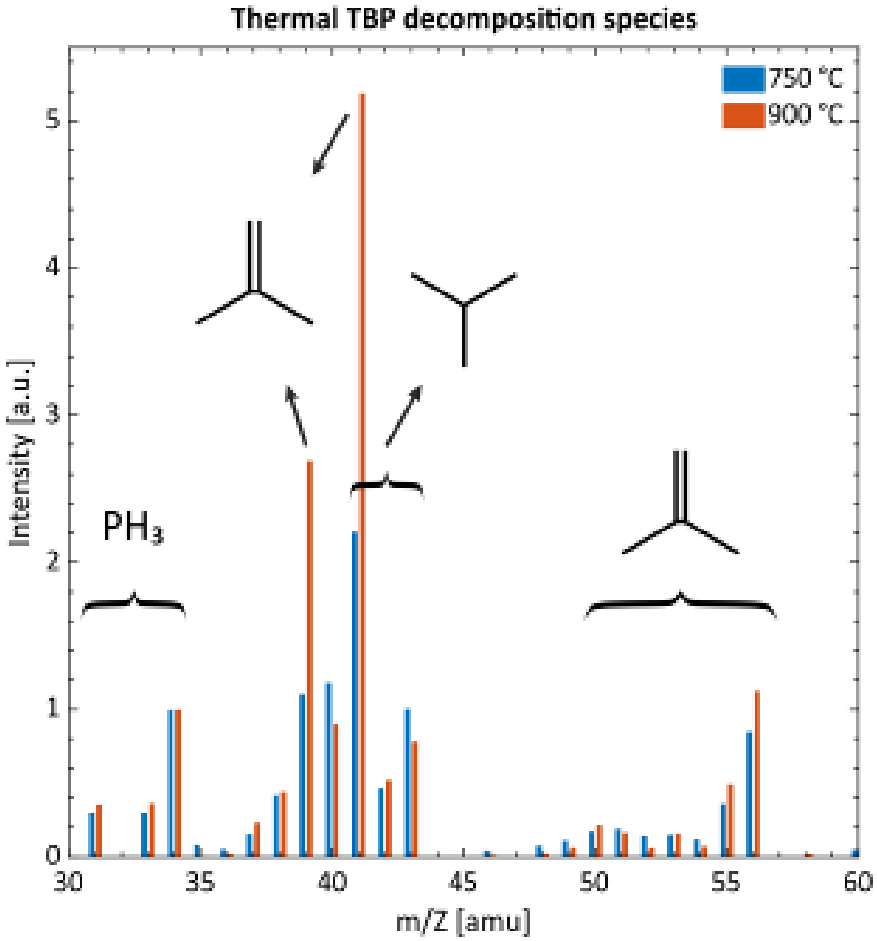
Thermal TBP decomposition species
750 °C
900 °C
Intensity [a.u.]
PH3
m/Z [amu]
0
1
2
3
4
5
30
35
40
45
50
55
60

MS8.P033
Magnetic imaging of thin film systems

I. Ennen[1], D. Ramermann[1], A. Becker[1], B. Büker[1], T. Almeida[2], R. Webster[2], S. McVitie[2], A. Hütten[1]

[1]Bielefeld University, Thin Films and Physics of Nanostructures, Bielefeld, Germany
[2]University of Glasgow, School of Physics & Astronomy, Glasgow, United Kingdom

Introduction: Since the implementation of segmented or pixelated detectors for differential phase contrast (DPC) [1,2] and electron energy loss magnetic chiral dichroism (EMCD) [3], is the high-resolution magnetic characterization of magnetic materials in the transmission electron microscope (TEM) accessible. Nevertheless, the magnetic imaging of thin film systems in cross-section remains still challenging not at least due to such issues as interdiffusion, interfacial roughness and surface corrugation [4].

Objectives: In this contribution, we aim to demonstrate the potential of the combined application of analytical TEM with DPC and/or EMCD utilizing a Fe/Co2FeSi/Fe thin film sample as a magnetic model system.

Materials & Methods: Thin film systems have been produced by magnetron co-sputter processes from elemental targets onto a (001)-oriented MgO substrates. The substrates have been rotated at 10 rpm to achieve uniform layer deposition and, in the case of Heusler compounds, heated to 450°C to obtain a homogeneously grown Co2FeSi-layer. The TEM cross-section lamellae has been prepared using a FEI Helios FIB including a second ion beam milling after thinning at 5 kV to reduce beam damage on the specimen. The magnetic multilayers have been investigated using a dedicated Lorentz JEOL ARM200cF microscope at University of Glasgow and the JEOL ARM200F of the OWL Analytic center.

Results: The TEM imaging of our multilayer model system showed a smooth bottom Fe layer, while the upper Fe layer reveals a corrugated surface. Micromagnetic simulations have shown that the wavy nature of the upper Fe layer can result in strong dipolar stray fields which can reduce the magnetic reversal field [5]. A chemical characterization of the cross-section sample identified an interdiffusion of Fe at the Fe/Co2FeSi interface, which can cause a complex magnetic interplay. The magnetic switching of the system has been monitored by DPC imaging. All possible magnetic conditions, i.e., a parallel orientation in both directions or an antiparallel configuration of the Fe layers have been achieved and confirmed by determination of the magnetic induction. Here, it seems that the observed asymmetry in the signal of the magnetic induction near the interface correlates with the interdiffusion depth of the Fe into the Heusler layer. Furthermore, a head-to-head domain configuration have been observed in the Fe-layer.

Additionally, first experimental results will demonstrate the great opportunities of a combination of DPC and EMCD for the investigation of proximity effects in multilayered magnetic systems.

Conclusion: Analytical HRTEM combined with DPC and EMCD opens great possibilities for in situ characterization of magnetic multilayers, as microstructure, chemical and magnetic properties can be correlated. Furthermore, this combination can be used to generate experimental support for micromagnetic simulations of magnetic configurations in thin films.

References:
[1] Chapman J.N. and Scheinfein M. R., Journal of Magnetism and Magnetic Materials 200 (1) 729 (1999)
[2] Chapman J.N., McFadyen I.R., and McVitie S, in 1990 IEEE International Magnetics Conference (INTERMAG), 1506, (1990)
[3] P. Schattschneider, S. Rubino, C. Hébert, J. Rusz, J. Kunes, P. Novák, E. Carlino, M. Fabrizioli, G. Panaccione, and G. Rossi, Nature 441, 486 (2006).
[5] D. Ramermann, A. Becker, B. Büker, T. Almeida, R. Webster, S. McVitie, I. Ennen, A. Hütten, Imaging & Microscopy 1 (2021)

LS1.001-Invited
The role of electron microscopy in characterisation of viral vectors for gene therapy

D. Dobnik[1], M. Janc[1], P. Kogovšek[1], M. Tušek Žnidarič[1]

[1]National Institute of Biology, Ljubljana, Slovenia

Introduction: Recent developments in the biomedical fields have enabled that viruses can also be used to help us fight against numerous diseases. Even though the production of recombinant viral vectors began 40 year ago, the established technologies still haven"t reached the optimal level. Different product and process related impurities affect the efficiency of the production. To improve the overall production process, advanced analytical techniques are needed to accurately follow presence of desired product and possible impurities in various production steps. For gene therapy products it is important that viral particles are filled with the desired vector genome (full particles), as they are responsible for therapeutic effect. But the production process yields empty particles as well, thus it is important to know their ratio.

Objectives: The role of electron microscopy (EM) in characterization of viral vectors for gene therapy is very specific as this is the only technique that enables direct observation of viral particles and all of other impurities present in the sample. Our objective was to use EM for determination of empty to full particle ratio, since those particles can be distinguished on the micrographs, as well as to determine presence of any other visible impurities.

Materials & Methods: We used Transmission EM (TEM) with uranyl acetate negative staining of the viral particles. Viral particles (viral vector samples) were applied on glow-discharged copper grids, stained and observed by two different microscopes. As full and empty viral particles appear differently on the micrographs, we were able to determine their ratios in different samples. Additionally we started implementing Cryo-EM approach, where samples can be observed in a native state.

Results: We were able to determine empty/full ratios with EM and also identified other impurities in the samples. To some extent we were able to correlate those results to the results of molecular analytical methods.

Conclusions: Although EM is a characterization method that is not so simple to implement as a routine analytical technique, especially in the pharmaceutical GMP environment, its role in the characterization of viral vectors is still important. The presentation will show how EM can help in providing additional information on viral vector samples that can help in optimization of production and purification of the viral vectors.

LS1.002-Invited
Detection and localisation of silver nanoparticles in roots cells of *A. thaliana* seedlings

P. Peharec Štefanić[1], B. Komazec[1], D. Vondrášek[2], I. Letofsky-Papst[3], B. Balen[1]

[1]Faculty of Science, University of Zagreb, Department of Biology, Zagreb, Croatia
[2]Institute of Physiology of the Czech Academy of Sciences, Laboratory of Biomathematics, Prague, Czech Republic
[3]Institute of Electron Microscopy and Nanoanalysis (FELMI), Graz University of Technology, Graz Centre for Electron Microscopy (ZFE), Austrian Cooperative Research (ACR), Graz, Austria

Nanoparticles (NPs) research is currently an area of intense scientific surveys due to a variety of their potential applications. Silver NPs (AgNPs) are of particular interest because of their well-known antibacterial and antifungal properties. Therefore, they can be found in various consumer products. Since plants play a significant role in accumulation and biodistribution of many environmentally released substances, they could be influenced by AgNPs, serving as a potential pathway for AgNP-transport and bioaccumulation into food chains. In this study, we aimed to detect the localisation and accumulation sites of AgNPs in root cells of wild type Arabidopsis seedlings, after exposure to AgNPs stabilised with polyvinylpyrrolidone (AgNP-PVP). Four days old seedlings grown *in vitro* on a solid MS medium were transferred to a modified solid 1/2 strength MS medium supplemented with 100 µM AgNP-PVP. Arabidopsis roots were analysed after the 1st and 11th day of treatment and for detection and localization of AgNP-PVP in root cells, multiphoton confocal microscopy (Leica TCS SP8 X) and monochromated TF20 (FEI Tecnai G2) transmission electron microscope with EDX detector were used. Roots were placed on the microscopic slide and acquisition of reflection and transmission images was done with the excitation light source 476 nm argon laser. The emission signal was filtered using a system of acusto-optical beam splitter, prism-based dispersion and mirrors before the desired emission light reached the internal HyD detectors. Multiphoton and FLIM images were acquired using the excitation light source of 740 nm from multiphoton pulsed laser (Chameleon Discovery TPC, tunable output, 80 MHz, 140 ± 10 fs). The emission signal was filtered using SP680, dichroic mirror 560, band-pass filters 525/50 and 610/70. Non-descanned Leica HyD detectors were used to acquire both multiphoton and FLIM images. FLIM images were acquired using Becker and Hickl SPC-150 using time correlated single photon counting method (TCSPC) from 300 sec. For TEM-EDX analyses, roots were fixed with 1% glutaraldehyde in 50 mM cacodylate buffer (pH 7.2) for 1 h at +4 °C, washed twice and post-fixed with 1% OsO4 in the same buffer for 1 h at +4 °C followed by 10 min wash in ice-cold water. After dehydration in a graded series of ethanol, the tissue was embedded in Spurr´s resin. The sections were examined using the TEM-EDX for confirmation of AgNPs localization in the tobacco cells. Multiphoton confocal images (Figure1.) revealed that the reflective (Figure1F, J) and luminescent particles (Figure1G, K) with short fluorescence lifetime (120 ps) (Figure1H, L) could be observed in the root cap of Arabidopsis seedlings grown on a solid nutrient medium supplemented with AgNPs already after the 1st day of treatment (Figure1E-H). After the 11th day of AgNP exposure, further accumulation of these particles could be seen in the root cap (Figure1I-L). TEM-EDX analyses (Figure2.) confirmed that small black dots (Figure2B, F) in the root cell wall contained silver (Figure2C, D, G, H), which proves that AgNPs have been directly uptaken by root cells, in which they accumulated after the 1st and 11th day of exposure. The obtained results show that the AgNPs are uptaken by the roots cells already after the 1st day of exposure and that they accumulated in the root cap. Furthermore, it is shown that the AgNPs could be seen with the confocal microscope as reflective and luminescent particles with short fluorescent lifetime.

Figure 1

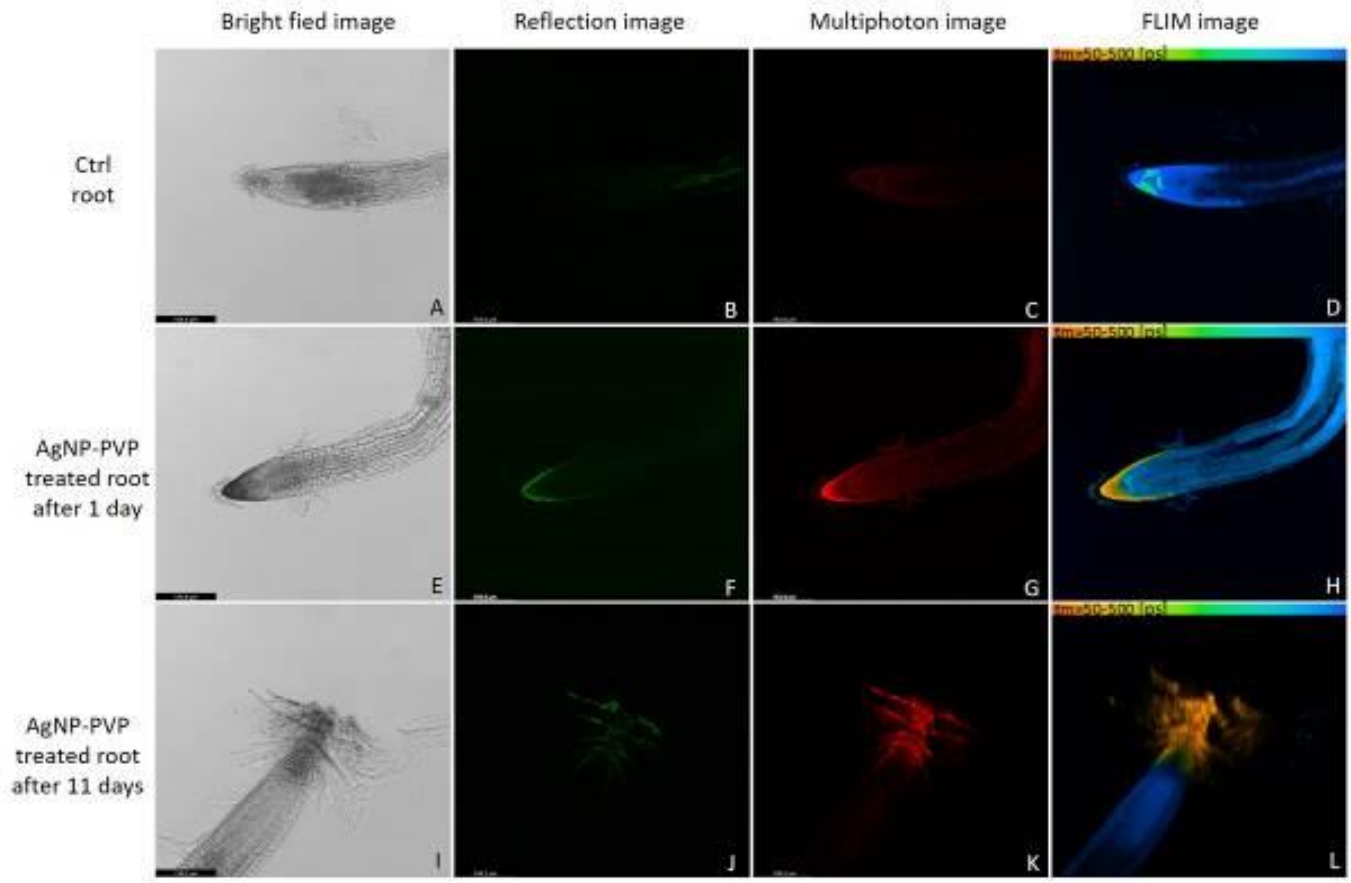

Figure 2

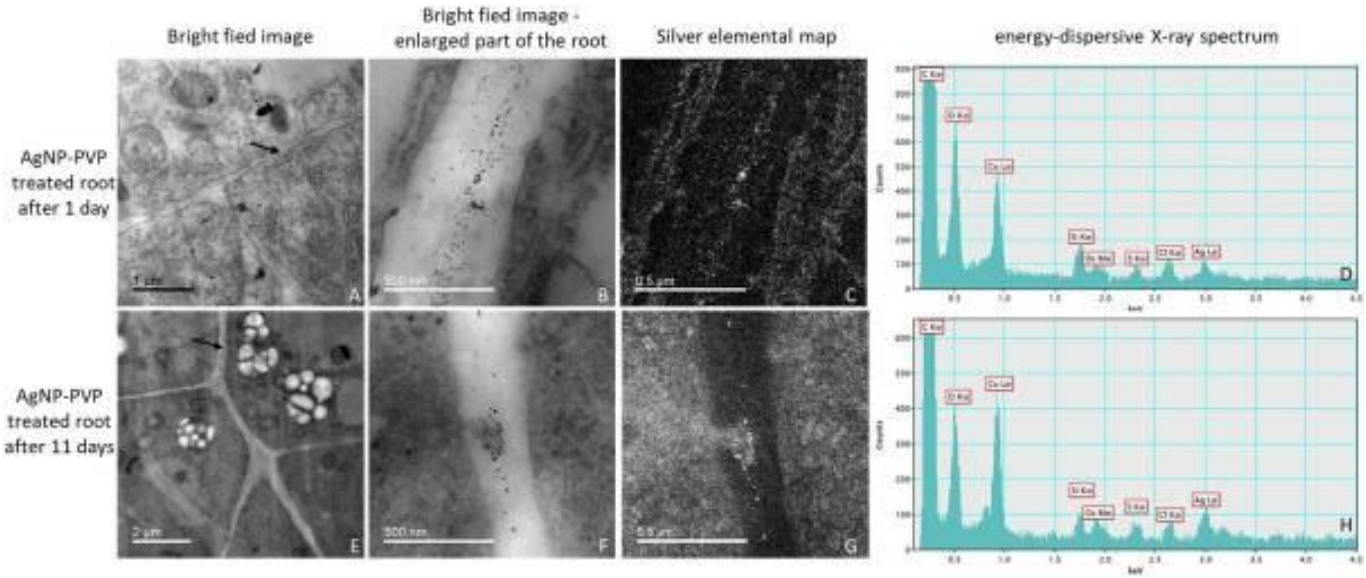

LS1.003
BiofilmQ, a software tool for quantitative image analysis of microbial biofilm communities

H. Jeckel[1,2], R. Hartmann[2], E. Jelli[1,2], K. Drescher[1,2]

[1]Philipps-University Marburg, Physics, Marburg, Germany
[2]Max-Planck-Institute for Terrestrial Microbiology, Marburg, Germany

Biofilms are now considered to be the most abundant form of microbial life on Earth, playing critical roles in biogeochemical cycles, agriculture, and health care. Phenotypic and genotypic variations in biofilms generally occur in three-dimensional space and time, and biofilms are therefore often investigated using microscopy. However, the quantitative analysis of microscopy images presents a key obstacle in phenotyping biofilm communities and single-cell heterogeneity inside biofilms. Here, we present BiofilmQ, a comprehensive image cytometry software tool for the automated high-throughput quantification and visualization of 3D and 2D community properties in space and time. Using BiofilmQ does not require prior knowledge of programming or image processing and provides a user-friendly graphical user interface, resulting in editable publication-quality Figures. BiofilmQ is designed for handling fluorescence images of any spatially structured microbial community and growth geometry, including microscopic, mesoscopic, macroscopic colonies and aggregates, as well as bacterial biofilms in the context of eukaryotic hosts.

Image modified from Hartmann, R., Jeckel, H., Jelli, E. *et al.* Quantitative image analysis of microbial communities with BiofilmQ. *Nat Microbiol* 6, 151–156 (2021).

Figure 1

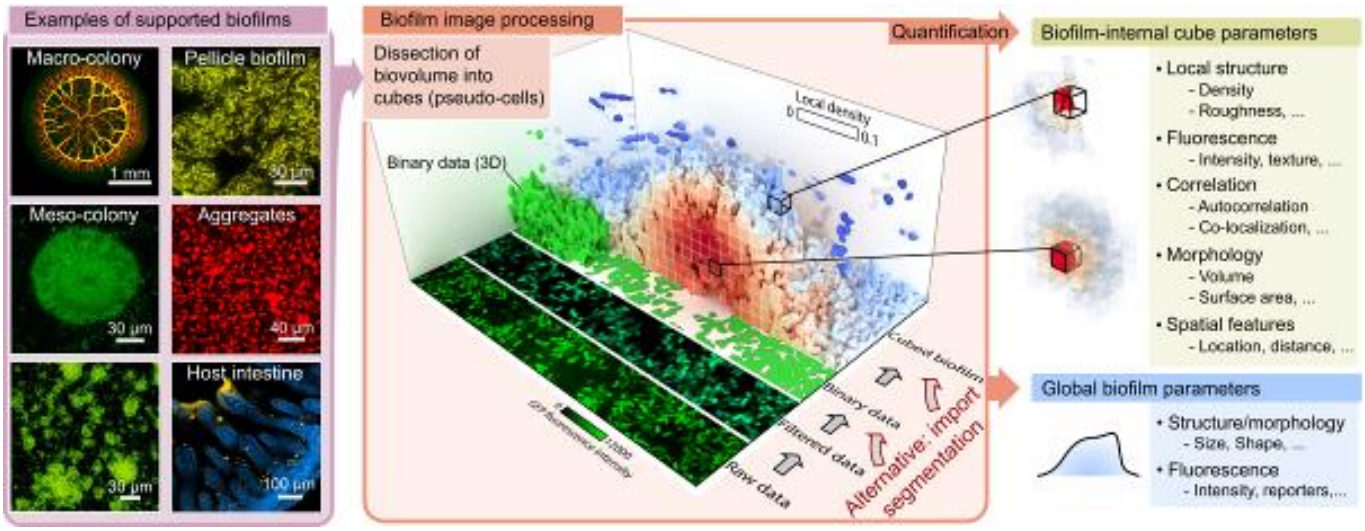

LS1.004
Exploring sample preparation for structural preservation of environmental archaeal biofilms for CLEM analyses

I. Monsees[1], V. Turzynski[1], M. Hasenberg[2], A. Klingl[3], A. Probst[1]

[1]University Duisburg-Essen, Chemistry, Essen, Germany
[2]University Duisburg-Essen, Imaging Center Essen, Essen, Germany
[3]LMU München, Biologie I- Botanik, Munich, Germany

Introduction: Sample preparation for correlative light and electron microscopy (CLEM) is a complex challenge particularly for natural samples. For instance, strong fixation preserves ultrastructure but hinders entering of probes into cells for detecting regions of interest in fluorescence microscopy[1]. GenomeFISH is a novel technique able to label small genomic entities like viruses or small symbiotic cells [2]. In the current body of literature, no technique is available for linking genomic information of metagenomic approaches (aimed at analyzing viral infections or symbiotic interactions) to morphological changes of target cells in environmental samples via electron microscopy.

Objectives: The aim of this study was to establish a protocol to conserve the ultrastructure of *Candidatus Altiarchaeum hamiconexum* biofilm during sample preparation for fluorescence microscopy (FM) and scanning electron microscopy (SEM). This structural conservation will be necessary to evaluate morphological changes of cells via SEM, which are suffering from viral infections.

Materials & methods: GenomeFISH was performed as described recently[2]. To correlate the results of genomeFISH with electron micrographs, glass slides with a coordinate system engraved on the surface were used. The biofilm flocks were examined for viral infections by FM. The shape and the coordinates of the flocks were documented. Sample preparation for SEM including critical point drying was varied by different storage attempts after FM, a change of the dehydration medium (acetone after osmium fixation and ethanol) and variation of the platin/palladium layer thickness.

Results: A storage outside of any buffer medium between FM and SEM sample preparation with ethanol dehydration resulted in a complete loss of expected surface structures. Without drying of the sample, the structure was conserved better than with drying and cell surface appendages became visible being indicative of a well-preserved ultrastructure. However, they were not conserved as a fine mesh but just as a layer on the slide surface. When treating the sample with osmium tetroxide and dehydration in acetone the cell surface appendages were observed as a 3-dimensional network between individual cells. The thickness reduction of the platin/palladium layer resulted in an additional improvement of the visibility of fine details. In any preparation, the position of the archaeal cells could still be correlated with the fluorescence signals. In areas where a viral infection was observed by FM, varying morphologies were identified by SEM.

Conclusion: The established protocol successfully conserved the ultrastructure of the targeted environmental biofilm flocks to study morphological changes during viral infection. This facilitates future research on the structural components involved in viral infections of ecosystems and will ultimately enable insights into the effect of viral infection on subsurface carbon cycling for this research endeavor.

[1] de Boer, P., Hoogenboom, J. P. & Giepmans, B. N. G. Correlated light and electron microscopy: ultrastructure lights up! *Nat. Methods* **12**, 503 (2015).
[2] Rahlff, J. *et al.* Genome-informed microscopy reveals infections of uncultivated carbon-fixing archaea by lytic viruses in Earth"s crust. *bioRxiv* 2020.07.22.215848 (2020) doi:10.1101/2020.07.22.215848.

LS1.005
Organelle specific localisation of glutathione in *Arabidopsis* grown under different light intensities and spectra

A. Gasperl[1], E. Balogh[2], Á. Boldizsar[2], G. Zellnig[1], G. Kocsy[2], M. Müller[1]

[1]University of Graz, Institute of Biology - Dept. of Plant Sciences, Graz, Austria
[2]Agricultural Institute, ELKH, Centre for Agricultural Research, Martonvásár, Hungary

Plant **glutathione metabolism** reacts upon oxidative stress [1]. **Immunocytochemistry and TEM imaging** allow the quantification of metabolites such as glutathione on the subcellular level [2]. We have shown previously that subcellular ascorbate and glutathione levels are affected by high light stress in ***Arabidopsis*** [1]. The use of **light emitting diodes (LEDs)** gains increasing importance in growing indoor crops and ornamental plants. A combination of different LED types allows custom-made combinations of wavelengths and prevents damages related to high photon flux rates. However, scientific studies exploiting these LEDs are scarce [3]. In the present study the effects of different light spectra and light intensities related to glutathione metabolism were investigated on **organelle level** in *Arabidopsis* leaves [4].

Arabidopsis thaliana L. plants (wildtype Col-0, ascorbate deficient mutant *vtc2-1* and glutathione deficient mutant *pad2-1*) were cultivated for two weeks in climate chambers under different light quality treatments (white 250 (NL) and 500 (HL) µmol m^{-2} s^{-1}, far red 250 (FRL) µmol m^{-2} s^{-1}) under controlled conditions [4]. Immunogold labeling of glutathione with computer supported transmission electron microscopy (TEM) was used to determine glutathione in different cell organelles of *Arabidopsis* leaves [2].

Light intensity had a more pronounced effect on subcellular glutathione concentration in Col-0 and *pad2-1*, whereas *vtc2-1* mainly responded to a change in light spectrum (**Figure 1**). Our results for Col-0 and *pad2-1* mitochondria and nuclei under LED light treatment correspond to the results of a previous study, where high light likewise caused an increase in glutathione compared to control conditions [1]. Interestingly, far-red light mainly affected glutathione levels in ascorbate (*vtc2-1*) and glutathione (*pad2-1*) deficient mutants [4]. The findings obtained in this study demonstrate that both **light intensity and quality** significantly affect **glutathione** metabolism thereby causing **genotype-specific reactions** in the investigated *Arabidopsis* lines.

Figure 1: Subcellular glutathione distribution in *Arabidopsis* grown under various light conditions. Compartment specific means of gold particles bound to glutathione (± SE) per µm² in in A: mitochondria, B: chloroplasts, C: nuclei of *Arabidopsis* (Col-0 black circles, *vtc2-1* black triangles, *pad2*-1 black inverted triangles) after 4 days treatment with different light quality and quantity (white 250 (normal light, NL) and 500 (high light, HL) µmol m^{-2} s^{-1} and far-red 250 (FRL) µmol m^{-2} s^{-1}) under controlled conditions. Values represent the mean of 60 cell compartments. Significant differences between control treatment (NL) and the other treatments (HL, FRL) were compared within the same line (Col-0, *vtc2-1*, *pad2-1*) via the Mann Whitney U-Test. Significance is indicated at the 0.01 (**) or 0.001 (***) level of confidence

[1] E Heyneke, N Luschin-Ebengreuth et al, BMC Plant Biology (13)104 (2013), p.19.
[2] B Zechmann and M Müller, Protoplasma 246 (2010), p.15.
[3] I Monostori et al, Frontiers in Plant Science (9)605 (2018), p.16.
[4] A Gasperl, E. Balogh et al, International Journal of Molecular Sciences 22 (2021), p.19.

The authors gratefully acknowledge funding from the Austrian Science Fund (FWF, I 2818 to M.M) and the OeAD (Österreich-Ungarn HU-0616 to M.M. and G.K.) and by the National Research, Development and Innovation Office (grants ANN117949, K131638, TéT_15-1-2016-0048 to G.K.).

Figure 1

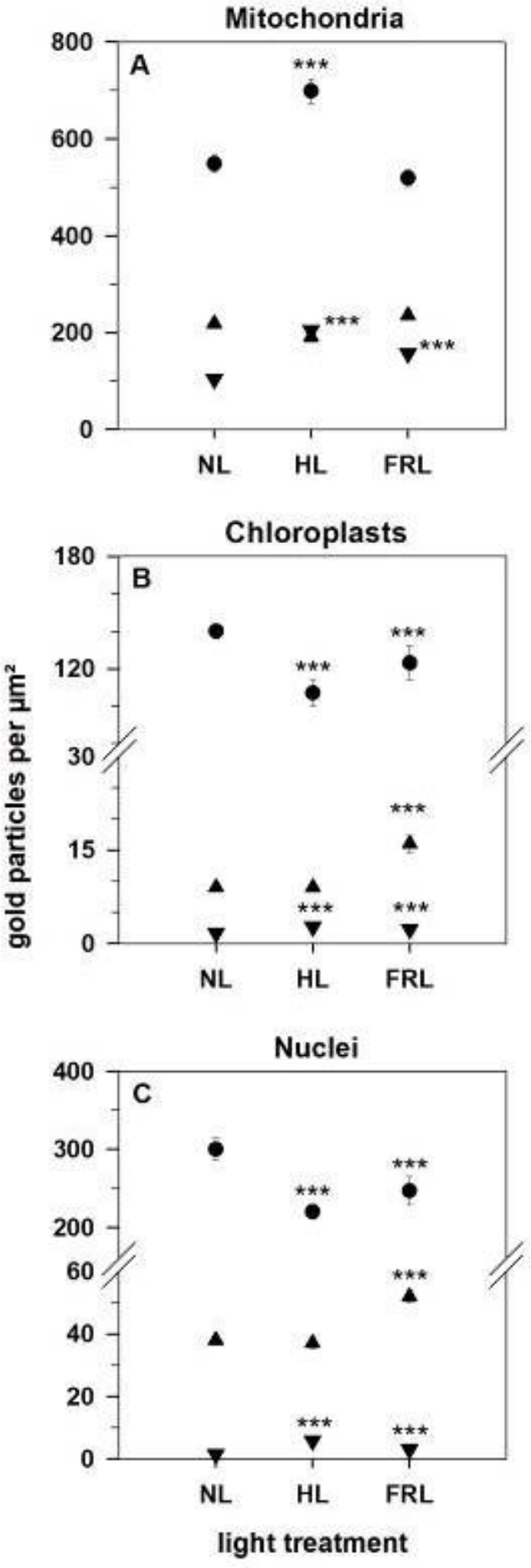
Mitochondria
A
800
600
400
200
0
***
***
***
NL
HL
FRL
Chloroplasts
B
180
120
30
15
0
gold particles per µm²
***
***
***
***
***
NL
HL
FRL
Nuclei
C
400
300
200
60
40
20
0
***
***
***
***
***
NL
HL
FRL
light treatment

LS1.006
SBEM analysis of *Trypanosoma brucei* life cycle progression from procyclic to metacyclic stages

J. Týč[1], F. Kitzberger[1], E. Doleželová[1], A. Zíková[1], J. Nebesářová[1], M. Vancová[1]

[1]Institute of Parasitology, Biological Centre, Czech Academy of Sciences, Ceske Budejovice, České Budějovice, Czech Republic

Trypanosoma brucei, the causative agent of Human and Animal Trypanosomiases, undergoes a striking cellular transformation during its digenetic life cycle. The transition between the insect forms found in various tse-tse tissues to the mammalian life cycle stages are accompanied by extensive organelles remodelling, including mitochondria regression and repositioning of mitochondrial DNA and flagellum. We aim to describe these changes in high quantifiable detail including the volume, number and spatial organization of the organelles and other ultrastructural features of the cells. We use serial block-face scanning electron microscopy (SBEM) to reconstruct three distinct insect life cycle forms generated in vitro, the procyclic trypomastigotes a the epimastigotes and the infective metacyclic trypomastigotes. Chemically fixed T. brucei cells were processed with "OTO" protocol and embedded in hard plus resin 812 (EMS). Images were acquired in 3D using Apreo SEM equipped with VolumeScope (Thermofisher Scientific) and variable pressure control. SBEM technology images regions of interest with dimensions up to several hundreds of µm yielding tens of whole cells for an analysis, therefore allowing for statistical evaluation of the obtained data. The final resolution at 6,5 nm (in X, Y axes) and 100nm (Z) or higher facilitated the distinction of fine ultrastructural features within the cell. Cells were segmented and visualized in 3D using Microscopy Image Browser and Amira software. This approach provided quantifiable results (volumes, lengths) and ultrastructural details of all cellular organelles and allowed us to compare the three insect forms to the published reconstruction of T. brucei mammalian bloodstream form (Hughes et al., J. Cell Sci. 2017). Our study provides a deeper understanding of how organelles are remodelled during the complex life cycle of these medically and veterinary important parasites.

Acknowledgement: This work was supported by TACR (TN01000008) and Czech BioImaging (LM2018129).

Figure 1

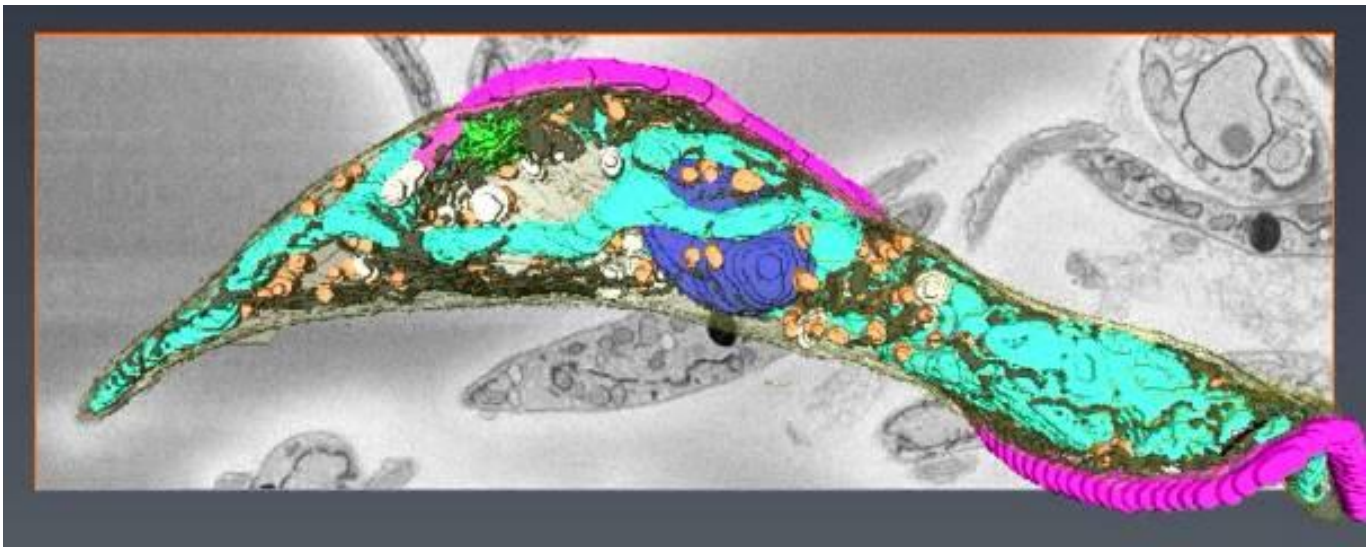

LS1.P001
Multi-modal spectroscopy and imaging of label-free cells and multicellular organisms for monitoring environmental pollution

A. Marcek Chorvatova[1,2], M. Uherek[1], D. Chorvát[1]

[1]Slovak Centre of Scientific and Technical Information, International Laser Center, Department of Biophotonics, Bratislava, Slovakia
[2]University of Ss Cyril and Methodius, Faculty of Natural Sciences, Department of Biophysics, Trnava, Slovakia

Introduction: Monitoring processes in living cells by detecting excited state dynamics and/or spectral characteristics of their endogenous fluorescence using latest time- and spectrally-resolved imaging techniques is becoming an important feature focused at monitoring environmental changes and particularly repercussion of the environmental pollution [1-5].

Objective: Our aim is to test time- and spectrally-resolved imaging as a potential method for detecting pollution in the sweet water environment by employing endogenous fluorophores, such as chlorophylls in algae and moss as potential indicators of environmental pollution.

Material and Methods: Fluorescence lifetime imaging microscopy (FLIM) and fluorescence spectroscopy imaging microscopy (FSIM) were used to study properties of endogenous fluorophores in the *Chlorella algae* and *Fontinalis antipyretica* moss leaves. To obtain the autofluorescence images by FLSI, combination of confocal microscopy and spectral detection was used. FLIM data were recorded using time-correlated single photon counting following pulsed laser excitation.

Results: We focus at the pollution induced by acidification, presence of heavy metal nanoparticles and/or by microplastics. FSIM and FLIM images uncovered changes following environmental pollution (an example of modification of fluorescence lifetimes following acidification in the sample of *Fontinalis antipyretica* is represented at Figure1). Analysis of the complex multi-dimensional datasets gathered by spectrally- and time-resolved fluorescence monitoring, aimed at precise understanding of the origin and behavior of the underlying autofluorescence components, is discussed. We describe various approaches to analyse multi-modal images, which is currently one of the bottlenecks in label-free imaging due to low intensity of autofluorescence and complex determination of individual molecular components generating the optical signal.

Conclusions: Multimodal optical imaging is shown as a promising method for environmental applications and gathered observations constitute the first step towards evaluation and proposal of methodological approaches for fast natural biosensing of the effects of environmental pollution directly in water environment.

Figure 1 FLIM image of leaf *Fontinalis antipyretica*. A - sample in distilled water with pH 7; B - sample in acidic environment with pH 2,4;

Acknowledgements: This publication received funding from the European Union's Horizon 2020 research and innovation programme under the grant agreement no 871124 Laserlab-Europe V, as well as from the Grant Agency of the Ministry of Education, Science, Research and Sports of the Slovak Republic VEGA 2/0070/21.

References:
[1] *Journal of Biotechnology X* 6: 1-10, doi 10.1016/j.btecx.2020.100018.
[2] *Methods and Applications in Fluorescence* **8:** 024007**,** doi 10.1088/2050-6120/ab77f4.
[3] *European Biophysics Journal* 48: 231-248. EBJO-D-18-00162, doi 10.1007/s00249-019-01347-6, https://doi.org/10.1007/s00249-019-01347-6.
[4] *Nova Biotechnologica et Chimica 17* (1): 38-47. DOI: 10.2478/nbec-2018-0004.
[5] *AEEE Journal 15* (2): 362-367. DOI: 10.15598/*aeee*.v15i2.2015.

Figure 1

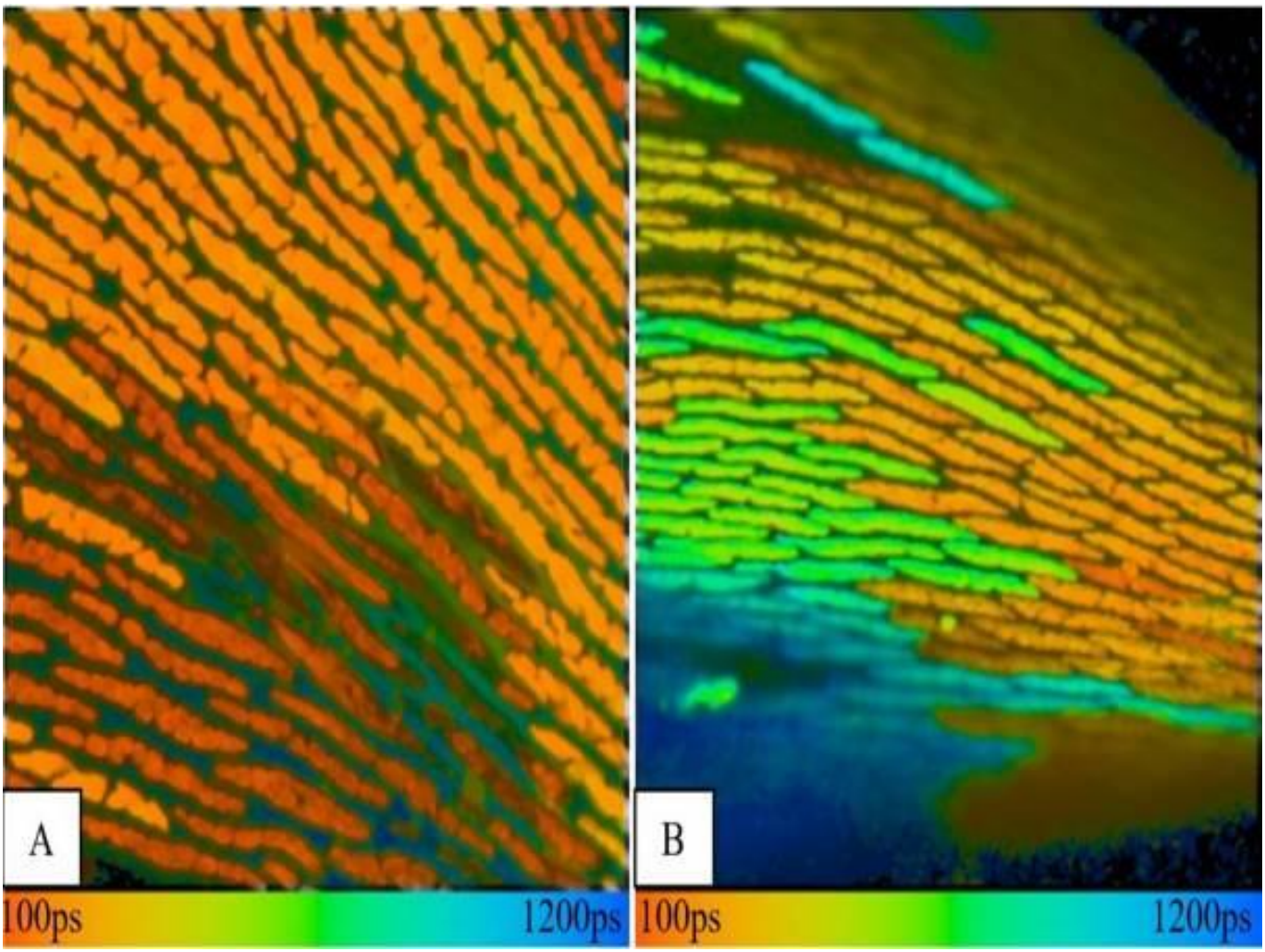

LS1.P002
Nanoplastics in the marine environment – Effect of microalgal extracellular polymers studied by AFM

T. Mišić Radić[1], P. Vukosav[1]

[1]Ruđer Bošković Institute, Department for Marine and Environmental Research, Zagreb, Croatia

The stability of plastic nanoparticles - nanoplastics in the marine environment plays an important role in determining their environmental implication and potential risk to marine biota and eventually to human health. In order to understand the behavior of nanoplastics in the marine environment, it is important to understand possible mechanisms involved in nanoplastics interaction with the naturally occurring seawater components, particularly natural organic matter including algal extracellular polymers (EPS). We studied the role of diatom extracellular polysaccharides in scavenging and stabilizing amine-modified polystyrene nanoparticles (PS-NH2) in the marine environment. Atomic force microscopy (AFM) revealed that EPS polymers displayed strong interaction with PS-NH2 and the incorporation of nanoparticles into the polymer network was visualized. PS-NH2 dispersed in seawater without the presence of EPS showed aggregation of nanoparticles that was visualized by AFM. Our results indicate that the presence of EPS biopolymers changes the fate of NPs in the marine environment. By scavenging nanoplastics, EPS could prolong their presence in the water column. Furthermore, EPS polymers are an important source of food for phytoplankton grazers and higher trophic levels and the incorporation of nanoplastics in EPS may have a significant impact on marine biota and make them available to higher organisms. This study shows that the presence of natural organic matter including microalgal extracellular polymers should be accounted for in future research evaluating the impact of nanoplastics in the marine environment.

LS1.P003
Establishment of the insect pathogenic fungus *Beauveria brongniartii* in the rhizosphere of apple tree roots (*Malus* sp.) for biological control of cockchafer grubs

R. G. Kleespies[1], C. I. Ullrich[1], D. Stephan[1], N. Heil[1], F. Rabenstein[1]

[1]Julius Kühn-Institut, Institut für Biologischen Pflanzenschutz, Darmstadt, Germany

Introduction: Entomopathogenic fungi are efficiently used in biological control of economically important herbivorous insects. The largely specific entomopathogenic fungus *Beauveria brongniartii* is particularly well suited for the biological control of root-damaging cockchafer grubs.

Objectives: Qualitative as well as quantitative spread and persistence of applied *B. brongniartii* inoculates are detected using various methods: Conventionally using selective culture media or using the specific *in situ* method developed at the JKI-Institute for Biological Control using immunofluorescent labeling of *Beauveria* spp. on young fine roots from various soils, without microtomy (Matek *et al.* 2019).

Materials & methods: Root samples are fixed in p-formaldehyde, incubated with polyclonal anti-*Beauveria* IgG, and then labeled with FITC-coupled secondary antibodies. In this way, the *Beauveria* species can be identified selectively on root samples either with the epifluorescence microscope or, preferably, with the confocal laser scanning microscope.

Results: *brongniartii* strains, inoculated in various formulations in an organically farmed apple orchard as well as in potted young trees in the greenhouse, can be detected in soil samples and on apple roots with the applied specific microscopic techniques. Possible differences in persistence and in relation to apple varieties are taken into account.

Conclusion: The present work shows that the aim of cultivating *B. brongniartii* with long persistence on apple roots, in order to protect them permanently from damage caused by grubs, seems to be a successful long-term strategy.

Figure 1: *Beauveria brongniartii* on fine roots of an apple tree (*Malus* sp.), detected with polyclonal antibodies (IgG)/FITC, three years after inoculation.

Reference:
Matek, M., Ullrich, C. I., Rabenstein, F., Koch, E., & Kleespies, R. G. (2019). *In situ* immunofluorescence localization: A method for rapid detection of *Beauveria* spp. in the rhizosphere of *Quercus robur* saplings. *Journal of Cultivated Plants*, *71*(7), 211-218.

Figure 1

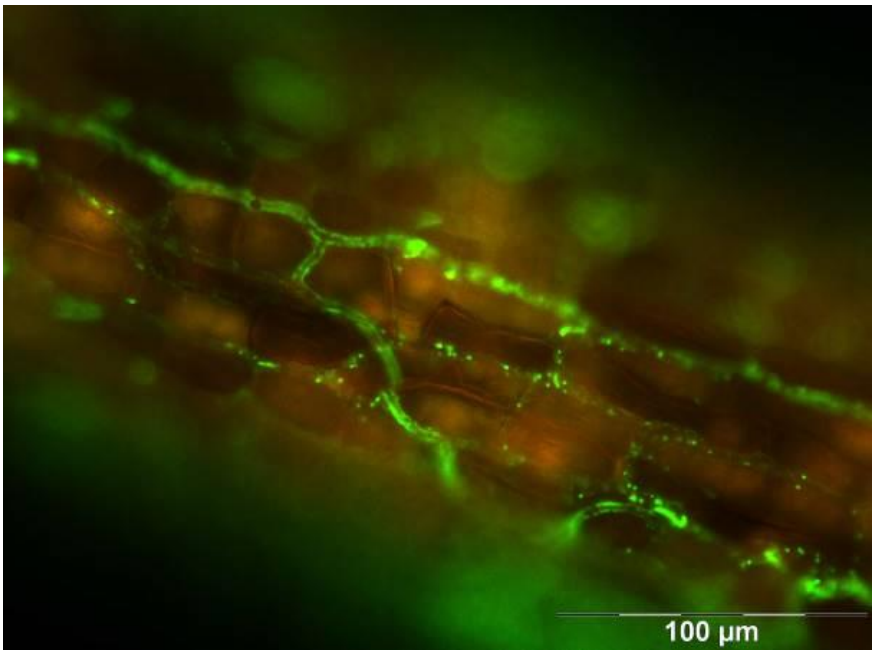

LS1.P004
Ultrastructural changes in *Chlorella vulgaris* induced by silver nanoparticles and silver ions

B. Komazec[1], P. Peharec Štefanić[1], B. Balen[1], D. M. Lyons[2]

[1]Faculty of Science, University of Zagreb, Department of Biology, Zagreb, Croatia
[2]Center for Marine Research, Ruđer Bošković Institute, Rovinj, Croatia

Silver nanoparticles (AgNPs) have been used in a variety of industries including the medical, textile and agriculture sectors. Due to their tendency to agglomerate in various media, they are stabilised with various surface coatings like polyvinylpyrrolidone (PVP). As the use of AgNPs increases, so does the potential for their release into the environment. Since *Chlorella vulgaris* is one of the most ubiquitous microalgae inhabiting aquatic ecosystems, it is widely used as a model organism for assessing the impact of materials of anthropogenic origin, e.g. AgNPs, on aquatic habitats. To better evaluate the impact of AgNP-PVP on *C. vulgaris*, algae cultures were grown in a modified liquid BBM nutrient medium with and without the addition of 1% glucose. Once the algae reached the exponential growth phase, they were treated with 1.5 mg L^{-1} of either AgNP-PVP or ionic silver ($AgNO_3$) (Figure1). To evaluate the effects of AgNP-PVP and $AgNO_3$, changes in the absorbance spectra (in the range 300-800 nm) of the algae cultures, and algae growth were analysed after 5 and 24 hours of exposure. Furthermore, to visualize ultrastructural changes after the treatments, algae cells were fixed with 1% glutaraldehyde in 50 mM cacodylate buffer (pH 7.2) for 1 h at +4 °C, washed twice and post-fixed with 1% osmium tetroxide in the same buffer for 1 h at +4 °C followed by 10 min wash in ice-cold water. After dehydration in a graded series of ethanol, the tissue was embedded in Spurr"s resin. Ultrathin sections were stained with 2% uranyl acetate and 2% lead citrate and examined using a FEI Morgagni 268D transmission electron microscope. After treatments with either AgNP-PVP or $AgNO_3$, a significant dose-dependent decrease in cell number was observed when compared to the control sample. A significantly greater decrease was observed in cultures without added glucose compared to the cultures with added glucose. Similarly, a significant decrease was observed in the characteristic chlorophyll *a* and *b* absorbance ranges after treatments which is an indicator of toxic effect of the treatments on the algae. Again, a greater decrease was noted in the cultures without added glucose. Results from the TEM analyses (Figure2.) showed that after 5 hours exposure in the nutrient medium without glucose, cells had undergone plasmolysis and had less starch, which can also be seen after 24 hours exposure (Figure 2B-E). Furthermore, cell integrity was disturbed compared to the control sample, with greater disruption after exposure to $AgNO_3$ (Figure 2C and E). In comparison, after 5 hours of both treatments in a nutrient medium with 1% glucose, cells showed better integrity and contained more starch (Figure 2G-J). However, after 5 hours of the same treatments supplemented with glucose, synthesis of lipid droplets had occurred, and which significantly progressed up to 24 hours (Figure 2G-J). In conclusion, AgNP-PVP and $AgNO_3$ showed toxic effects on the algae cultures, but with the addition of glucose to the nutrient medium, cells retained better integrity and suffered less ultrastructural damage. Decreased UV-vis absorbance and algae growth, combined with ultrastructural analyses, may indicate that AgNP-PVP and $AgNO_3$ disrupt photosynthetic activity of the algae since the overall toxicity of both treatments was much lower in cultures grown in the nutrient medium with addition of glucose compared to those in the medium devoid of glucose.

Figure 1

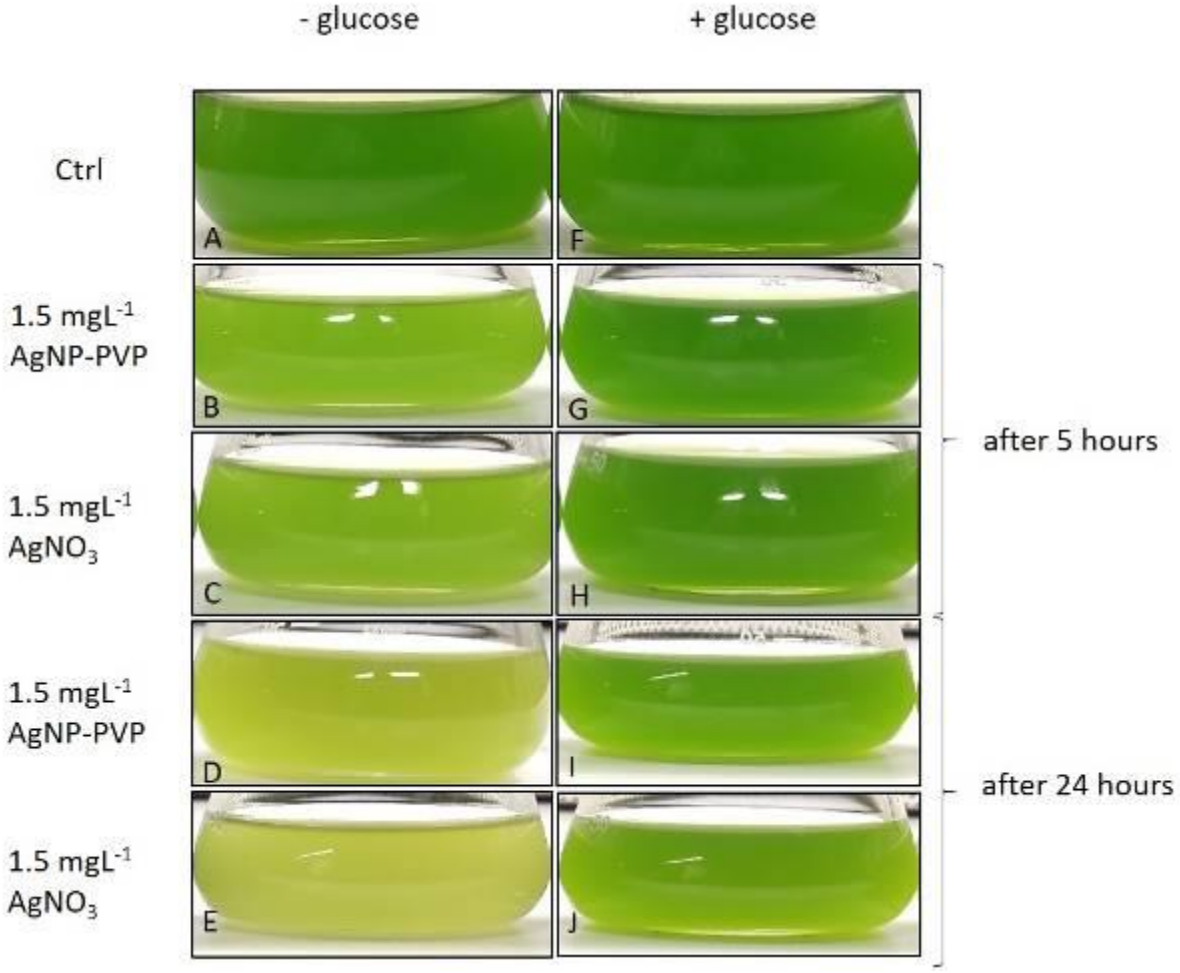
- glucose
+ glucose
Ctrl
1.5 mgL-1 AgNP-PVP
1.5 mgL-1 AgNO3
1.5 mgL-1 AgNP-PVP
1.5 mgL-1 AgNO3
A
F
B
G
C
H
D
I
E
J
after 5 hours
after 24 hours

Figure 2

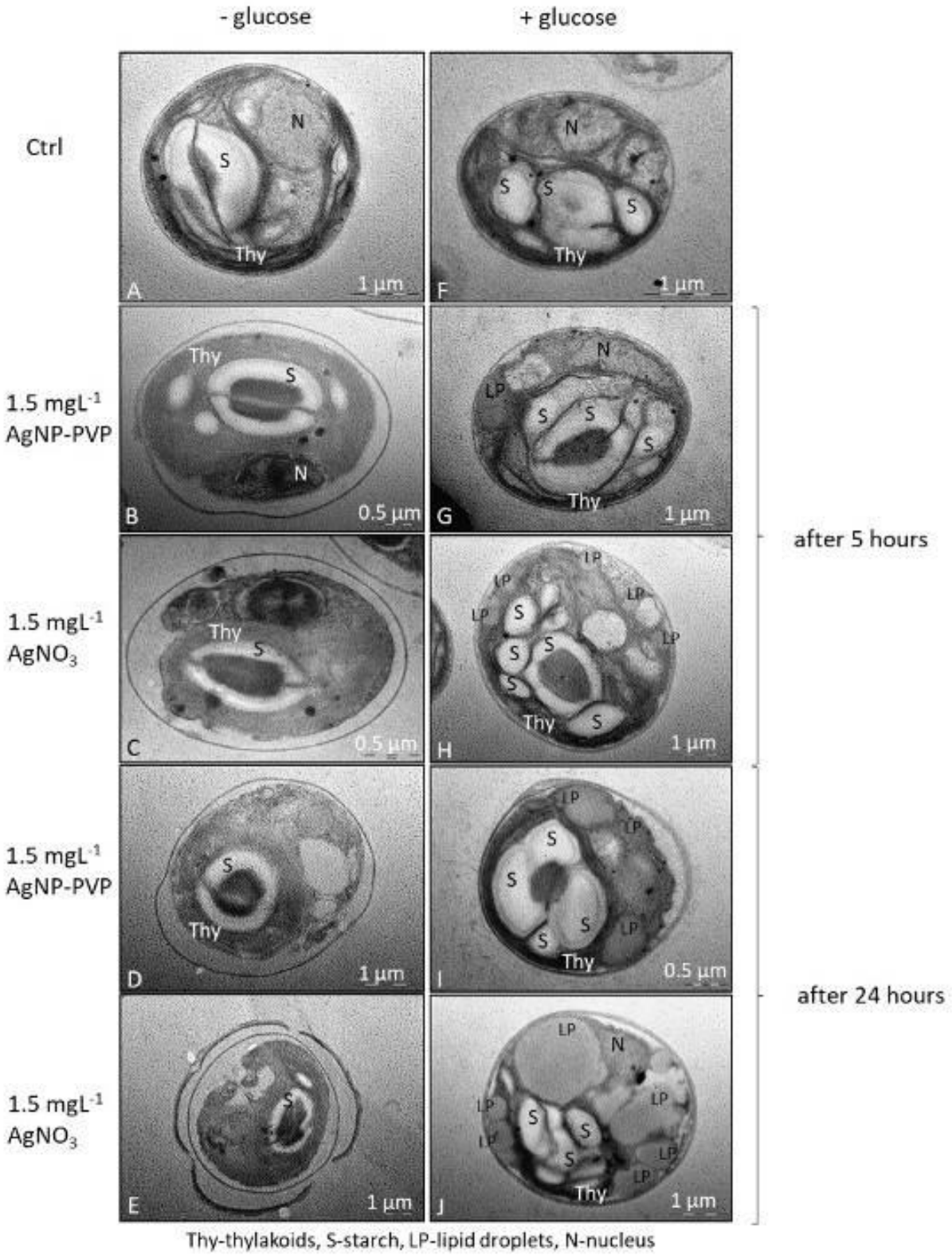

Thy-thylakoids, S-starch, LP-lipid droplets, N-nucleus

LS1.P005
Combined AFM-CLSM reveals morphological and mechanical changes in *Rhodococcus* cells exposed to nickel nanoparticles

G. Glebov[1], M. Kuyukina[2,1], I. Ivshina[2,1]

[1]Institute of Ecology and Genetics of Microorganisms, PFRC UB RAS, Perm, Russian Federation
[2]Perm State University, Perm, Russian Federation

Despite the growing industrial potential of metal nanoparticles due to their large specific surface area and high reactivity, there is a gap in our knowledge about their long-term effects on the environment and living organisms, including bacteria (1). Actinobacteria of the genus *Rhodococcus* are valuable bioremediation agents degrading a range of harmful and recalcitrant chemicals, such as petroleum hydrocarbons, phenols, solvents, pesticides and pharmaceutical pollutants (2). Rhodococci are also able to sequester heavy metal ions by biosorption and active accumulation, while the study of their interaction with metal nanoparticles is only at the very beginning, and further research is needed to restore water and soil contaminated with nanometals (3).

In this study, effects of nickel nanoparticles (Ni NPs) on the viability, surface topology and nanomechanical properties of *Rhodococcus* cells were examined using a combined atomic force microscopy and confocal laser scanning microscopy (AFM-CLSM) performed in the liquid medium. We used *R. ruber* IEGM 231, *R. pyridinivorans* IEGM 1227, and *R. rhodochrous* IEGM 1363 strains from the Regional Specialized Collection of Alkanotrophic Microorganisms (IEGM, www.iegmcol.ru). Ni nanoparticles were prepared in tenfold (0.0001–1.0 g/l) concentrations. A coupled AFM-CLSM system of the Asylum MFP-3D-BIO & Olympus FluoView 1000 was used to determine cell surface parameters, changes in their viability, morphology, and adhesive forces upon the exposure to increasing concentrations of Ni NPs.

The CLSM revealed a decline in the number of living bacteria as a result of Ni NPs concentration increase up to 98% death after 24 and 48 hours of exposure. However, individual viable *R. ruber* IEGM 231 and *R. pyridinivorans* IEGM 1227 cells were observed even at 1.0 g/l Ni NPs, suggesting high rhodococcal resistance to nanometals. Using combined 3D AFM-CLSM imaging, a toxic effect of Ni NPs on the ultrastructure of *Rhodococcus* cell envelopes was revealed, which was manifested in altered cell dimensions and increased surface roughness (Figure 1). Additionally, AFM spectroscopy results indicated a significant reduction of Young's modulus (from 49 to 6 MPa) correlated with the corresponding increase in cellular adhesion forces (from 0.04 to 1.4 nN) upon the exposure to 1.0 g/l Ni NPs. The adhesive ability is an important indicator of bacterial cells, which determines a primary attachment to the substrate and biofilm formations. The Ni NPs-induced higher surface roughness of the cell, combined with its lower elasticity, appears to facilitate the attachment of bacteria to the substrate due to the exposure of highly adhesive sites on the cell wall. These findings can be used for the functionalization of *Rhodococcus* cells with Ni nanoparticles to enhance their catalytic properties and potential use in bioremediation.

This work was supported by RFBR grants 18-29-05006 and 20-44-596001.

References:
[1] Slavin et al. (2017) J. Nanobiotechnology, 15:65.
[2] Kuyukina, Ivshina (2019) *In*: Biology of Rhodococcus, Springer Nature, 231-270.
[3] Pressentato et al. (2019) *In*: Biology of Rhodococcus, Springer Nature, 333-357.

Figure 1: Combined AFM-CLSM (*upper row*) and AFM (*middle row*) images and force maps (*lower row*) of *R. ruber* IEGM 231 cells in control (*on the left*) and after the exposure to 0.1 g/l Ni NPs (*on the right*).

Figure 1

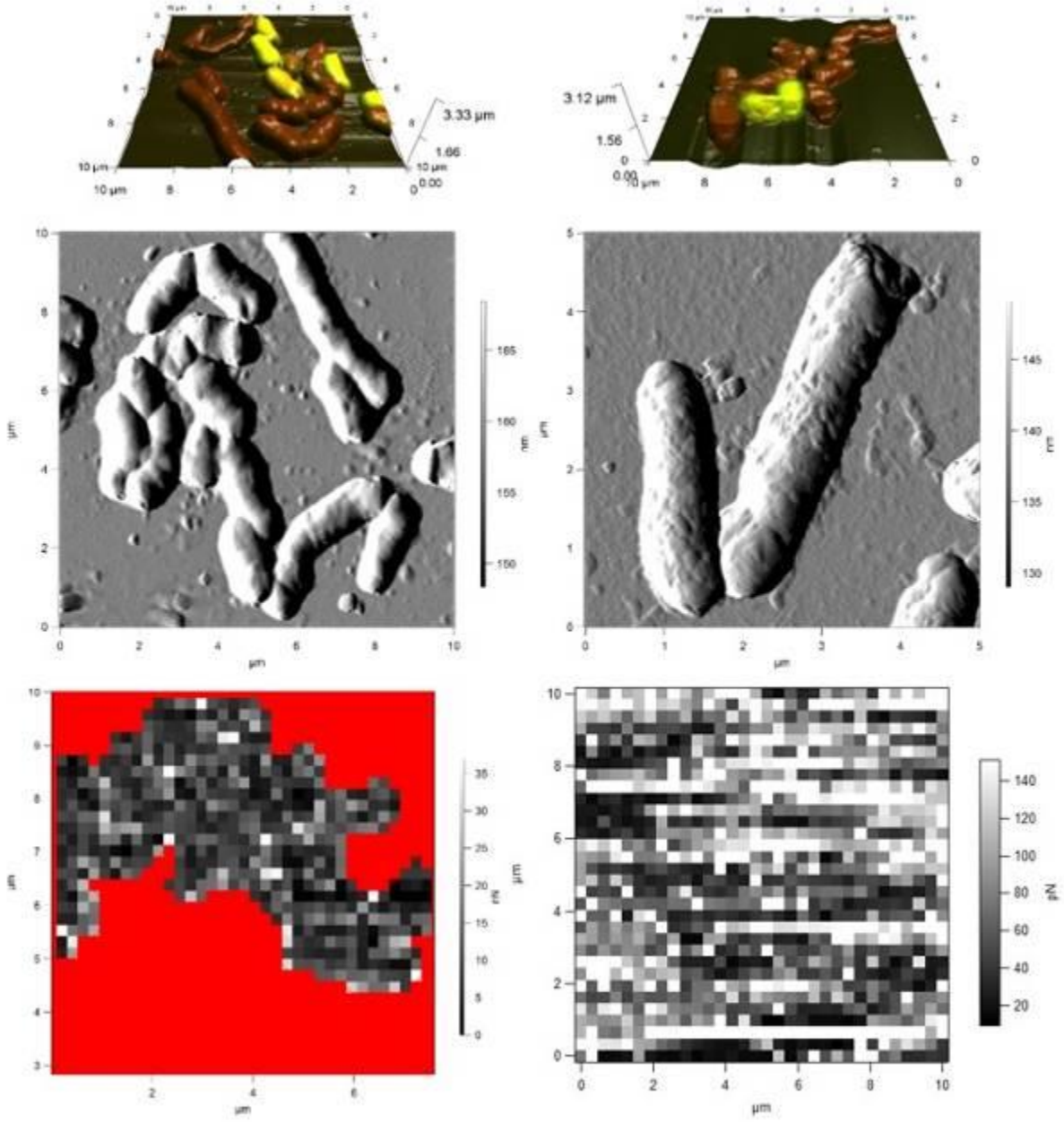

LS1.P006
Use of 3D subcellular imaging to study phytoplankton

S. Flori[1], C. Uwizeye[1], J. Decelle[1], D. Falconet[1], P. H. Jouneau[2], B. Gallet[3], J. B. Keck[4], D. Dal Bo[1], C. Moriscot[3,5]
C. Seydoux[1], F. Chevalier[1], N. Schieber[6], R. Templin[6], G. Allorent[1], F. Courtois[1], G. Curien[1], Y. Schwab[6,7]
G. Schoehn[4], S. Zeeman[8], G. Finazzi[1]

[1]UGA,CNRS,CEA,INRAE,IRIG, LPCV, Grenoble, France
[2]UGA, CEA, IRIG-MEM, Grenoble, France
[3]UGA, CNRS, CEA, IRIG-IBS,, Grenoble, France
[4]UGA, Laboratoire Jean Kuntzmann,, Grenoble, France
[5]UGA, CNRS, CEA, EMBL, Integrated Structural Biology Grenoble (ISBG), Grenoble, France
[6]Cell Biology and Biophysics Unit, European Molecular Biology Laboratory,, Heidelberg, Germany
[7]Electron Microscopy Core Facility, European Molecular Biology Laboratory,, Heidelberg, Germany
[8]Institute of Molecular Plant Biology, Department of Biology, ETH Zurich, Zurich, Switzerland

Introduction: Phytoplankton comprises microscopic phototrophs localized in the photic zone of oceans and fresh waters on Earth. While these organisms constitute a minor fraction of the photosynthetic biomass on earth, they contribute almost half of the oxygen released on Earth and are promising organisms for biotechnological applications (food, feed and biofuel). This photosynthetic performances likely reflects the existence of peculiar, but still largely unexplored features of phytoplankton cells. Their heterogeneous origin has led to a large biodiversity of phytoplankton, which comprises cells with different morphologies and sizes (from 0.8 to up to a few tens of microns). Although they are exposed to extremely variable environments, phytoplankton cells are on average fast growing, suggesting that their metabolism should be highly flexible. However, we still do not know if these original metabolic strategies are linked to singular cell topological arrangements, due to the lack of high resolution imaging studies.

Objectives: Use a FIB-SEM–based workflow to generate 3D reconstructions of different eukaryotic microalgae representing major oceanic phytoplankton lineages suitable for quantitative morphometric analysis (surfaces and volumes) of organelles and subcellular structures.

Materials & methods: Cells were cryo-fixed using high-pressure freezing (to maximize preservation of native structures) followed by slow freeze substitution and resin embedding. FIB-SEM datasets were processed to 3D models using open-access software (Figure 1).

Results: 3D morphometric analysis across seven distant phytoplankton taxa indicate preserved volumetric ratios between plastids and mitochondria (Figure 2), suggesting that phytoplankton subcellular topology is modulated by energy-management constraints. Consistent with this hypothesis, shifting the diatom Phaeodactylum from low to high light enhances photosynthesis and respiration, increasing cell-volume occupancy by mitochondria and the plastid CO2-fixing pyrenoid, and boosting plastid-mitochondria contacts (Figure 3).

Conclusion: By revealing evolutionarily-conserved topologies of energy-managing organelles, and their role in phytoplankton acclimation, this work deciphers phytoplankton responses at subcellular scales (1).

[1] Uwizeye, C., al. (2021) Morphological bases of phytoplankton energy management and physiological responses unveiled by 3D subcellular imaging. Nat Commun 12, 1049 (2021). https://doi.org/10.1038/s41467-021-21314-0.

Figure 1

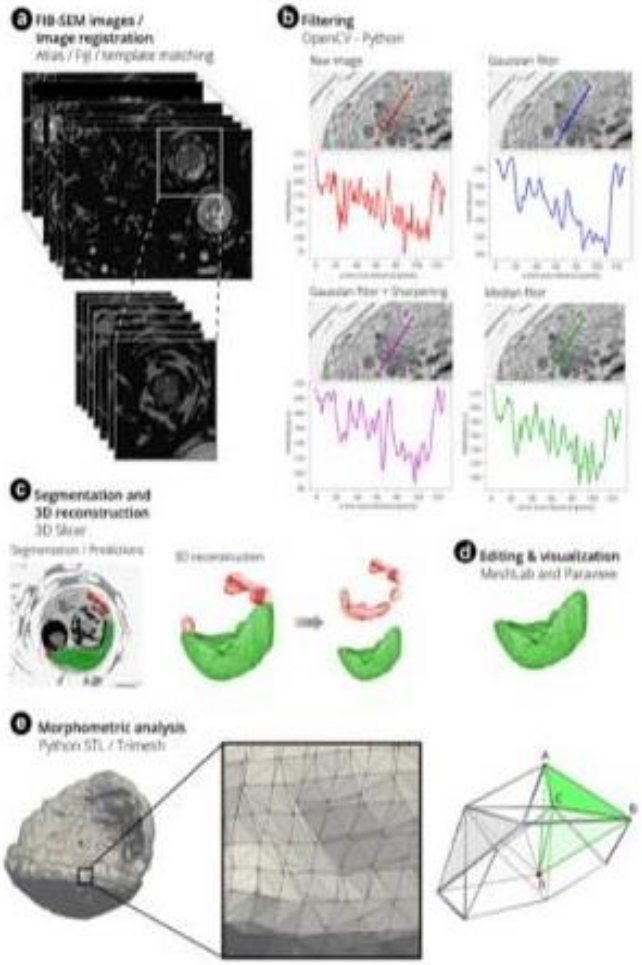

Figure 1. Flowchart of image processing from data acquisition to 3D reconstruction and morphometric analysis. a The pipeline includes data acquisition with FIB-SEM and registration with Fiji. **b** Single cells are selected from the whole FIB-SEM stacks, images are registered before inverting their contrast. Stacks are filtered in Python using the PyOpenCV module. Linear (Gaussian) filter followed by edge enhancement (sharpening) or non-linear filter (median filter) are suitable in different species based on their cellular features (see text). A scan line of the Golgi apparatus drawn with Fiji in Emiliania huxleyi shows the impact of different filters on the profile plot of the flattened membrane-enclosed disks (the cisternae). Red: original image. Blue: the Gaussian filter smooths the edges and some membranes disappear. Purple: sharpening after application of the Gaussian filter allows recovery of some image details after smoothing edges. Green: The median filter is less sensitive to edges. Sections are representatives micrographs of an experiment repeated three times with similar results. **c** Image processing was done with 3D Slicer for segmentation and **d** MeshLab and Paraview, for editing and visualisation, respectively. **e**: The STL and Trimesh python packages were used to quantify volumes, surfaces and distances. From a watertight mesh, surface is obtained by summing the surface of each individual triangle present in the mesh.

Figure 2

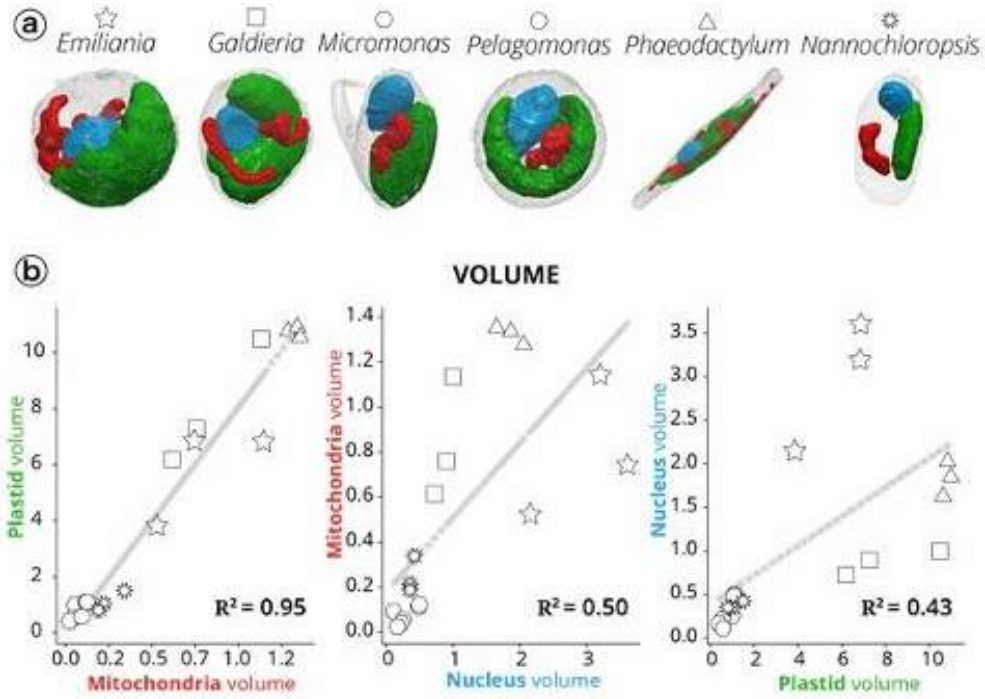

Figure 2. Morphometric analysis of phytoplankton members. a 3D topology of the main organelles (green: plastids; red: mitochondria; blue: nuclei) in the different cell types. **b** Volume relationships in different subcellular compartments, as derived from quantitative analysis of microalgal 3D models. Three cells were considered for every taxum. Stars: *Emiliania*; squares: *Galdieria*; hexagons: *Micromonas*; circles: *Pelagomonas*; triangles: *Phaeodactylum*; suns: *Nannochloropsis*.

Figure 3

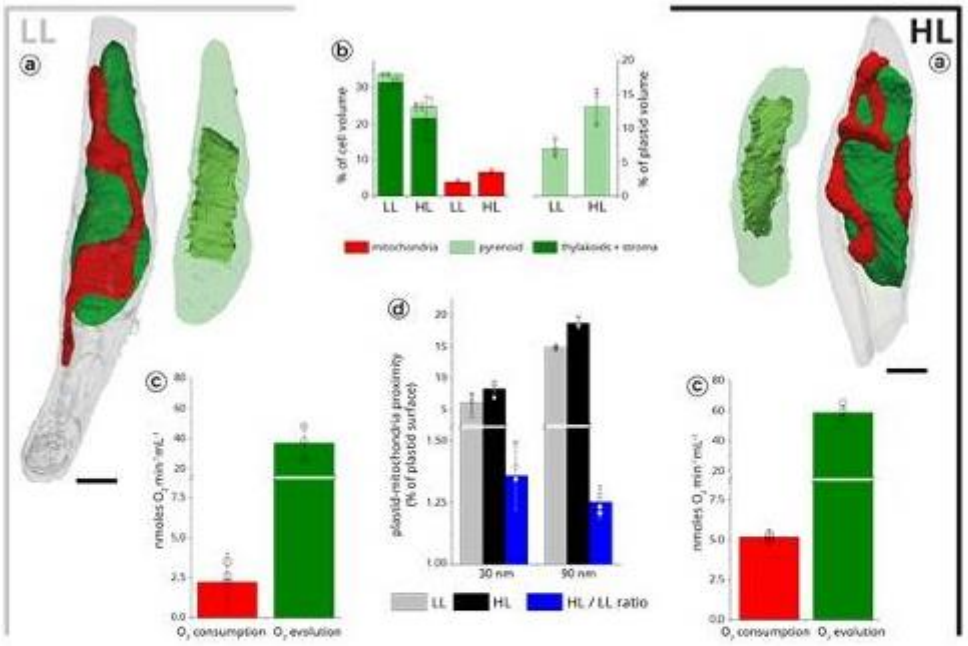

Figure 3. Structural analysis of light acclimation in *Phaeodactylum tricornutum*. a Cells were imaged at two different light regimes: LL (40 µmol photons m^{-2} s^{-1}, left) and HL (350 µmol photons m^{-2} s^{-1}, right). Scale bar: 1 µm. **b** Volume occupancy by the plastids (dark green), mitochondria (red) and pyrenoid (light green) in the two conditions. Data refer to three cells ± s.d. for each growth condition. **c** Respiratory activities (red) and photosynthetic capacities (green) are indicated for LL (left) and HL (right) cells. Data refer to three biological samples ± s.d. for each growth condition. **d** Plastid-mitochondria proximity surface points in LL and HL cells, measured at ≤30 nm (grey) and ≤90 nm (black). At both distances, proximity areas points are increased by around 25% (blue) upon HL transition. Data refer to three cells ± s.d. for each growth condition.

LS1.P007
Direct observation of settlement phenomena of individual diatom cells of four different species

R. Hamano[1], S. Shoumura[1], Y. Takeda[1], T. Yamazaki[1], K. Hirayama[1], Y. Hanada[2], S. Mayama[3], M. Takemura[4]
H. J. Lin[5], K. Umemura[1]

[1]Tokyo University of Science, Department of Physics, Tokyo, Japan
[2]Hirosaki University, Graduate School of Science and Technology, Aomori, Japan
[3]Tokyo Gakugei University, Advanced Support Center for Science Teachers, Tokyo, Japan
[4]Tokyo University of Science, Laboratory of Biology, Institute of Arts and Sciences, Tokyo, Japan
[5]National Taiwan Ocean University, Institute of Bioscience and Biotechnology, Keelung, Taiwan

Introduction: We have established a "tumbled" inverted optical microscope in order to directly observe floating or sinking phenomenon of microorganisms affected by gravity. It can be understood as a micro-size aquarium. In a macroscopic aquarium, we can watch swimming behaviors of fishes via a transparent window. In our microscopic aquarium, behaviors of micron-size cells can be well observed. We already published a paper which described settlement phenomenon of one species of diatom cells (shoumura et al, 2020). However, comparison of different types of diatom cells have not yet been reported.

Objectives: In this work, we demonstrated direct observation of sinking phenomena of four different types of diatom cells using the "tumbled" microscope in order to evaluate effects of size and shapes of diatom cells.

Materials & methods: Isolated four types of diatom cells, *Nitzschia* sp., *Pheodactylum tricornutum*, *Navicula* sp., and *Odontella aurita*, were prepared by subculture. Cell suspension was injected in a microchamber (1 mm3) and observed. The microchamber was used to minimize the effects of convection currents. Trajectories of sinking diatom cells were analyzed by automatic centroid analysis and manual two-point analysis. In the centroid analysis, centroids of each cell were automatically tracked by using a computer software (Move-tr/3D, Library Co., Japan). In the two-points analysis, coordinates of two longitudinal ends of each cell were manually tracked.

Results: We successfully observed settlement phenomena of individual diatom cells by our method. The effects of convection currents were negligible. Settlement speeds of the four types cells, *Nitzschia* sp., *Pheodactylum tricornutum*, *Navicula* sp., and *Odontella aurita*, were 0.81 ± 5.56, 3.03 ± 10.17, 3.29 ± 7.39 and 11.22 ± 21.42 mm/s, respectively. Some of the cells were rotated during the settlements. Analysis of rotation angles and angular velocities of rotating cells were well analyzed by the two-points trajectory analysis. As a result, there was no significant differences of rotation behaviors among the four types of diatoms although the size and shape were significantly different among the diatom cells. In addition, the effects of the cell shapes on settlement velocity could be explained by hydrodynamic simulation.

Conclusion: We demonstrated direct observation of four types of diatom cells by a "tumbled" microscope. Our knowledge is valuable to understand floating and sinking phenomena of diatom cells. Furthermore, our approach might be available for studying behaviors of various microorganisms in water.

LS1.P008
Thermophilic bacteria as a source of polyhydroxyalkanoates

K. Mrazova[1], K. Hrubanova[1], T. Ikrenyiova[2], E. Slaninova[2], S. Obruca[2], V. Krzyžánek[1]

[1]The Czech Academy of Sciences, Institute of Scientific Instruments, Brno, Czech Republic
[2]Faculty of Chemistry, Brno University of Technology, Brno, Czech Republic

Introduction, objectives: Thermophilic bacteria are microorganisms capable of growing in extreme conditions, they survive temperatures above 45 °C and can be found in various habitats. These organisms have been studied because of their unique abilities to survive in harsh conditions and they also stand as promising biotechnological producers of various metabolites from thermostable enzymes to biopolymers such as polyhydroxyalkanoates (PHAs). One of the advantages of using extremophilic organisms in biotechnological processes is the prevention of possible contamination by mesophilic microorganisms, which results in a reduced requirement for sterilization. Also, elevated temperatures can improve the solubility of substrate in the cultivation media (1–3).

As was previously mentioned, one of the metabolites produced by thermophiles is the group of PHAs. PHAs are polyesters of hydroxyalkanoic acids accumulated in various microbial cells in form of storage granules. Several reports indicated that the presence of PHA granules in cells enhances the ability to survive various stress conditions (4,5). PHAs are also interesting polymer material with properties similar to conventional plastics like polypropylene. However, unlike petrochemical plastics, PHAs are fully biodegradable and therefore could pose as an "ecology-friendlier" alternative to the conventional ones (3).

In our work, we focused on the morphological study of thermophilic bacteria *Schlegelella thermodepolymerans* and *Thermomonas hydrothermalis* using cryo-SEM and also on the evaluation of the amount of PHAs in microbial cells using gas chromatography (GC).

Materials, methods: For cryo-SEM analysis, bacterial cells were fixed using high pressure freezing method without using any cryo-protectants. Frozen samples were transferred into cryo-vacuum preparation chamber for freeze-fracturing followed by sublimation and then observed in SEM equipped with cryo-stage.

For GC analysis, bacterial cells were centrifuged, supernatant was discarded and cells were dried. Dry cells were then processed as previously described in (6) and analysed using GC with FID.

Results, conclusion: Cryo-SEM confirmed the presence of PHA granules in both strains and also revealed that the granules remain elastic at cryogenic temperatures and can be observed sticking out of fractured rod-shaped cells. The content of PHA in cells was analysed by GC and in *S. thermodepolymerans* the amount was determined to (77,13±6,39)% of dry cell mass and in *T. hydrothermalis* (30,18±1,68)%.

The results indicate that both of the studied organisms are promising PHA producers, however *S. thermodepolymerans* containing significantly higher amount of the polymer. Both organisms shall be further investigated with focus on the protective properties of PHA against various stress factors.

Figure 1: Cryo-SEM images of *S. thermodepolymerans*. PHA granules marked with arrows.

Figure 2: Cryo-SEM images of *T. hydrothermalis.* PHA granules marked with arrows.

References:
[1] Kourilova X. et al.: Bioresource Technology 315(2020), 1238852
[2] Pernicova I. et al.: Polymers 12(2020), 1235
[3] Obruca S. et al.: Biotechnology Advances 36(2018), 856-870
[4] Pernicova I. et al.: International Journal of Biological Macromolecules 144(2020), 698-704
[5] Obruca S. et al.: New Biotechnology 39(2017), 68-80
[6] Obruca S. et al.: Applied Microbiology and Biotechnology 98(2014), 5883-5890
[7] The authors gratefully acknowledge funding from the TACR (project TN01000008)

Figure 1

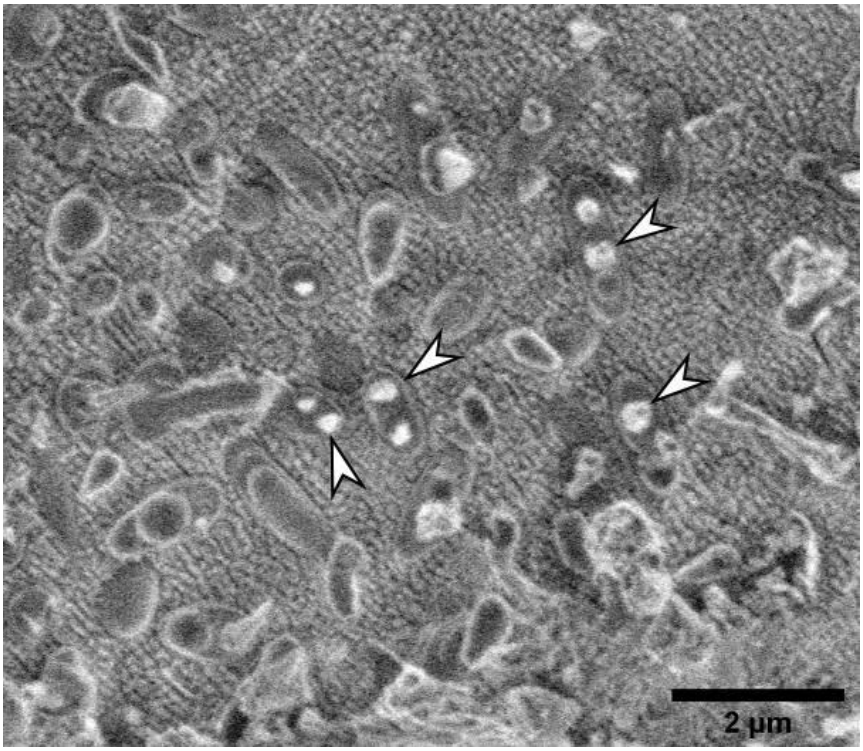

Figure 2

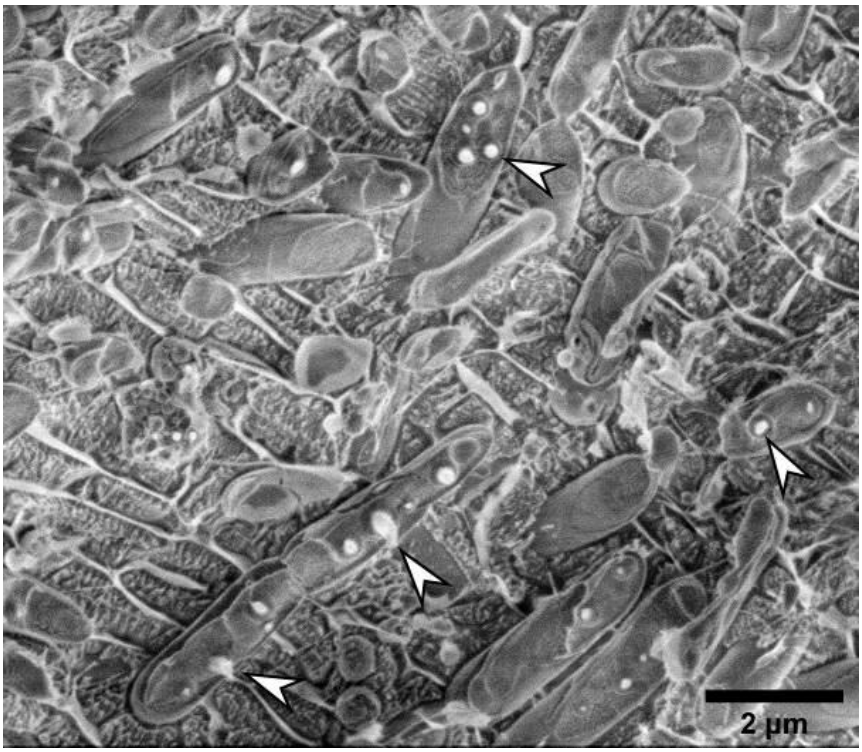

LS1.P009
A simple method to produce cyanobacterial biofilms appropriate for SEM studies

I. Domonkos[1], I. Mallick[1], P. Kirtania[1], P. B. Kós[1], I. Vass[1]

[1]Biological Research Centre, Eötvös Loránd Research Network, Institute of Plant Biology, Szeged, Hungary

Cyanobacteria are photoautotrophic prokaryotes played crucial role in the evolution of life and fundamental in ecosystems as primary producers. They exist in free-living form in the natural waters or form multicellular surface-attached communities, called biofilms. Cyanobacterial biofilms have a high potential for biotechnological applications as source of valuable compounds and fuel, tool in bioremediation or in wastewater treatment. Despite the importance of cyanobacterial biofilms, our knowledge about photoautotroph biofilms is very poor. For laboratory studies, it is advantageous to use well-characterized model organisms with known genetic background. The unicellular cyanobacterium *Synechocystis* sp. PCC6803 (*Synechocystis* from now) is a model organism for the study of oxygenic photosynthesis. Usually it is studied in liquid cultures and only in the last some years started to investigate *Synechocystis* biofilms.

Our aim was to develop a simple method for producing *Synechocystis* biofilm under laboratory conditions, which can be used directly for SEM studies and physiological measurements. We also wanted to investigate whether surface properties could affect biofilm formation.

Synechocystis cells were grown in BG11 medium under 40 µmol photons m^{-2} s^{-1} intensity white light, at 30˚C. The cells were grown till mid-log phase in liquid cultures and then small pieces of sterile membranes (Millipore Isopore Membrane Filter, and Whatman glass microfibre GF/C filters (GMF)) were inoculated by 5 µl culture. Biofilms were grown in an incubator at 30˚C for 7 days under 40 µmol photons m^{-2} s^{-1} white light intensity. For coating the GMFs, a single granule of polyhydroxybutyrate (PHB) was dissolved in hot chloroform (70˚C) and the membrane pieces were dipped into it and subsequently dried.

For SEM studies, the filters covered by biofilms were submitted to chemical fixation, dehydrated in a graded series of ethanol, critical point dried, covered with10 nm gold and observed in a JEOL JSM-7100F/LV scanning electron microscope.

After seven days of culturing, *Synechocystis* cells remained attached on the Millipore Isopore Membrane but they were not able to form biofilm because of the improper adherence to the smooth surface. In the next step, glass microfiber filters (GMFs) were tested, as they have a visible roughness. After seven days of incubation the cells formed biofilm on the GMFs, as SEM images displayed a well-built exopolysaccharide network along with pili among the cells. Although the roughness of the GMF filter surface provided proper support for adhering the cells, the GMF membrane was very fragile and it could not withstand harsh treatments during sample preparation for SEM, leading to damage of the biofilm structures. Therefore, we used a water-resistant polyhydroxybutyrate (PHB) coating on the membrane to increase the integrity of the surface. The SEM images show that if the GMFs were coated with PHB, *Synechocystis* was able to form biofilms, which remained intact during sample preparation.

We present an easy and fast method to establish *Synechocystis* biofilm models under standard laboratory conditions that can be used for both physiological and SEM investigations.

This work was supported by the Hungarian Ministry for National Economy (https://www.kormany.hu/en) GINOP-2.3.2-15-2016-00058 and GINOP-2.3.2-15-2016-00001.

LS1.P010
Comparative ultrastructural analyses of rhabdovirus replication in plants and animals

K. R. Richert-Pöggeler[1], K. Franzke[2]

[1]Julius Kühn-Institut, Federal Research Centre for Cultivated Plants, Institute for Epidemiology and Pathogen Diagnostics, Braunschweig, Germany
[2]Friedrich-Loeffler-Institut, Federal Research Institute for Animal Health, Institut für Infektionsmedizin, Greifswald -Insel Riems, Germany

Introduction: Virus evolution is assumed to start from precellular replicons that combined with escaped genes forming protocapsids from primitive cells. Enveloped viruses, like vertebrate, invertebrate and plant infecting rhabdoviridae originated later in evolution when modern cells entered the stage. This virus family encapsidating a negative sense ssRNA genome is quite successful in finding cellular niches for replication. Rhabdoviridae can be found in symbiosis with aquatic as well as teresstrial hosts. The observed emergence of rhabdoviruses is illustrated by a five fold increase in number of virus genera within the last decade.

Objectives: Comparative ultrastructural analyses of rhabdovirus replication in plants and animals to investigate rhabdovirus plasticity and evolution at the cellular level. Rhabdovirus developmental stages in naturally as well as artificially infected hosts are studied.

Materials and methods: For electron microscopy, small pieces of symptomatic leaves were directly homogenized in 2% ammonium molybdate, pH 6.5 with one drop of 0.5% bovine serum albumin (BSA) added. In addition, leaves of systemically infected plants were embedded in Epon 812 after consecutive fixation of samples with 2.5% glutaraldehyde and 0.5% osmium tetroxide. Grids were examined in a Tecnai G2 Spirit electron microscope at 80 kV. Images were taken with a 2K Veleta camera. Specificity of polyclonal antisera was tested in IEM.

Results: Despite distinct grades in symptom expression the ultrastructure of infected cells is similar in natural and artificial hosts. A polarity in bacilliform shaped virions is visible during disassembly. During assembly virions appear in parallel arrays within the nuclear matrix next to the nuclear envelope. In later stages of infection the heterochromatin is more and more replaced by viroplasmn and budding virons. Besides the nucleus, chloroplasts organization is disturbed and in one case, stromules were visible.

Conclusions: Both cytoplasmic and nuclear RNA interactome offer niches for rhabdovirus replication. Embodyment of the host nuclear membrane system for envelope production enables plant rhabdovirus replication in related (lamiales and solanales) as well as distinct (fabales and solanales) plant orders. We are currently applying a double stranded (ds)RNA binding antibody to identify rhabdovirus replication intermediates in the cell.

LS1.P011
Structural analyses of the brown *algae Ectocarpus*

J. Berger[1], I. Koch[1], B. Sailer[1], A. Henschen[2], S. M. Coelho[2], K. Hipp[1]

[1]Max Planck Institute for Developmental Biology, EM Facility, Tübingen, Germany
[2]Max Planck Institute for Developmental Biology, Department of Algal Development and Evolution, Tübingen, Germany

Brown algae belong to the stramenopiles and as such are phylogenetically distant from plants, animals and fungi. They have been evolving independently from plants and animals more than one billion years ago. Brown algae are one of only five eukaryotic lineages that have evolved independently to develop into complex multicellular organisms.

To contribute to the understanding of developmental processes that lead to the observed complex multicellularity in brown algae we have analysed *Ectocarpus siliculosus* both by scanning and transmission electron microscopy. Several sample preparation techniques were tested to find optimal conditions for structure preservation for this organism. In order to characterise the morphology and ultrastructure of Ectocarpus we have compared the wild-type and a mutant that shows defects in the first cell divisions of the developing organism.

LS1.P012
Insights into chloroplast ultrastructure under drought and osmotic stress

R. Hembrom[1], S. Horváth[1], F. Ágh[1], A. Sóti[1], E. Enkhbileg[1], R. Ounoki[1], K. Solymosi[1]

[1]Eötvös Loránd University, Department of Plant Anatomy, Budapest, Hungary

Introduction: Drought represents an important threat to mankind causing inhibition of crop growth, yield and development. It influences plant metabolism in a complex manner including impaired metabolism related to decreased water uptake, stomatal closure and thus maybe lack of carbon dioxide, nutritional imbalance, and all these phenomena are often also accompanied or aggravated by oxidative stress. The above factors evidently affect the development, structure and activity of the photosynthetic apparatus, but literature data about the effect of osmotic/drought stress on plastid structure are scarce and somewhat controversial. Some authors reported the swelling of the intrathylakoidal space in chloroplasts of stressed plants, while others did not observe it. The molecular background of the swelling is unclear, because one would rather expect the shrinkage of a water-containing compartment (the thylakoid lumen) under severe water loss. Literature data are also difficult to compare because plants have evolved highly diverse tolerance mechanisms towards drought stress and also the applied treatments and their lengths greatly vary. In this work, we are summarizing our ultrastructural data obtained in various crops in the last few years under various drought stress conditions.

Objectives: Our major aim was to study whether long and short term osmotic or drought stress induce swelling of the intrathylakoidal space of chloroplasts in various crops and if yes under which conditions.

Materials and Methods: Sections (1 mm × 1 mm) of the treated leaf segments of the studied plant species were fixed in 2.5% (v/v) glutaraldehyde for at least 3 h, then post-fixed in 1% OsO4 (w/v) for 2 h (buffer: 70 mM Na2HPO4–KH2PO4, pH 7.2). After washing with buffer and dehydration in ethanol, samples were embedded in Durcupan ACM resin, sectioned and analyzed by a JEOL JEM 1011 transmission electron microscope. ImageJ software was used to quantify ultrastructural parameters and GraphPad Prism for statistical analyses.

Results: Swelling of the intrathylakoidal space was only observed under severe drought stress conditions in drought-sensitive species (wheat and barley, 2 weeks of water withdrawal at 3-weeks-old stage), and was often accompanied by the disruption of the chloroplast envelope, and thus assosiated with serious damage of the chloroplast and cellular integrity. In species having drought tolerance mechanisms (e.g. the ability to somehow minimize water loss, or to retain photosynthetic activity intact, or to protect the intrathylakoidal space by the accumulation of some electron-dense luminal substance) a shrinkage of the grana was observed also under severe drought stress instead of swelling.

Conclusion: Based on our investigations of various crops under various severity of drought stress we can conclude that the swelling of the intrathylakoidal space is mostly occurring in case of very severe stress conditions, i.e. close to the level of plant death. Therefore, observations reporting it are valid, however, one has to be careful when interpreting these as they seem to indicate serious damage to cellular integrity.

LS1.P013
Automated EDX particle analysis on fine dust filters of extreme events – New Year´s Eve

M. Nachtnebel[1], T. Pongratz[2], H. Schröttner[1,3], J. Rattenberger[1]

[1]Graz Centre for Electron Microscopy (ZFE), Graz, Austria
[2]Amt der Steiermärkischen Landesregierung, A15 Referat Luftreinhaltung, Graz, Austria
[3]Institute of Electron Microscopy and Nanoanalysis (FELMI), TU Graz, Graz, Austria

Introduction: Every year thousand tons of fireworks are used to enlightening the sky in different colours. Investigations have shown, that the main environmental impact of fireworks is the production of fine dust, followed by sulphur compounds and traces of different metals [1]. To obtain information about the presence of the different elements in particulate matter (PM) in the air, various qualitative and quantitative methods are available. In this study scanning electron microscopy (SEM) combined with energy dispersive spectroscopy (EDX) was used to analyse PM at fine dust filters. Although quantifying the element concentration is not legitimate, the composition of each individual particle can still be revealed. This should give new insights into airborne particles during New Year´s Eve.

Materials & methods: Absolute filters tapes (AFT) are standardly used in air quality monitoring to measure the fine dust concentration at various sites. To obtain the fine dust concentration in the air, air is sucked with a specific flow rate thought the AFT at a pristine spot for one hour. Presiding EDX analysis of the pristine AFT have shown, that it is made out of O, Si, Na, Ba, Zn, Al, K and Ca (in wt% descending order). To obtain a good spatial resolution and contrast in the SEM (Zeiss, Sigma 300 VP), the electrically non-conductive filter was coated by carbon evaporation (appr. 40nm). For the automated EDX measurements, an Oxford X-Max^{N}80 system was used with Aztec 3.4 software.

Results: Three of the recorded samples are shown, while several thousand of particles are recorded each: New Year´s Eve 2017/18, New Year´s Eve 2020/21 and a measurement at the night 23th of December 2020. The weather propagation conditions of the three nights are comparable as always an atmospheric inversion and a comparable windspeed prevailed [2]. Figure 1 shows the comparison of the fine dust concentration at both New Year´s Eve nights. Here the maximum concentration in the Silvester night 2017/18 is about three times higher as in the Silvester night 2020/21. For a better comparison of the detected particle elements, all data are normalised to particle per analysed mm² of filter. The first column in Figure 2 shows the comparison of total detected particles, it can clearly be seen that the fine dust pollution of New Year´s Eve 2017/18 is about ten times higher than 2020/21. The comparison of a few selected elements shows, that some concentrations are significantly higher at the Silvester nights, e.g. Pb, Sr or Bi, while others like Fe can be counted to the background elements.

Conclusion: Unsurprisingly the annual New Year´s Eve firework leave traces of heavy elements as PM in the air. Further detailed analysis of the composition of individual particles should help understanding the toxicity of those airborne dust.

[1] Von Arx U. 2014: Feuerwerkskörper. Umweltauswirkungen und Sicherheitsaspekte. Bundesamt für Umwelt, Bern. Umwelt-Wissen Nr. 1423: 139 S.
[2] https://www.umwelt.steiermark.at/cms/ziel/2060750/DE/; Onlinedaten Kontinuierliches und mobiles Messnetz; Land Steiermark

Figure 1: Comparison of the PM_{10} concentration at both analyised Silvester nights at the investigated air quality monitoring site Graz south

Figure 2: Comparison of few selected elements (Fe, Pb, Sr, Bi) at all three nights, while first row column shows the total detected particle per mm² of investigated filter (note logarithmic scale)

Figure 1

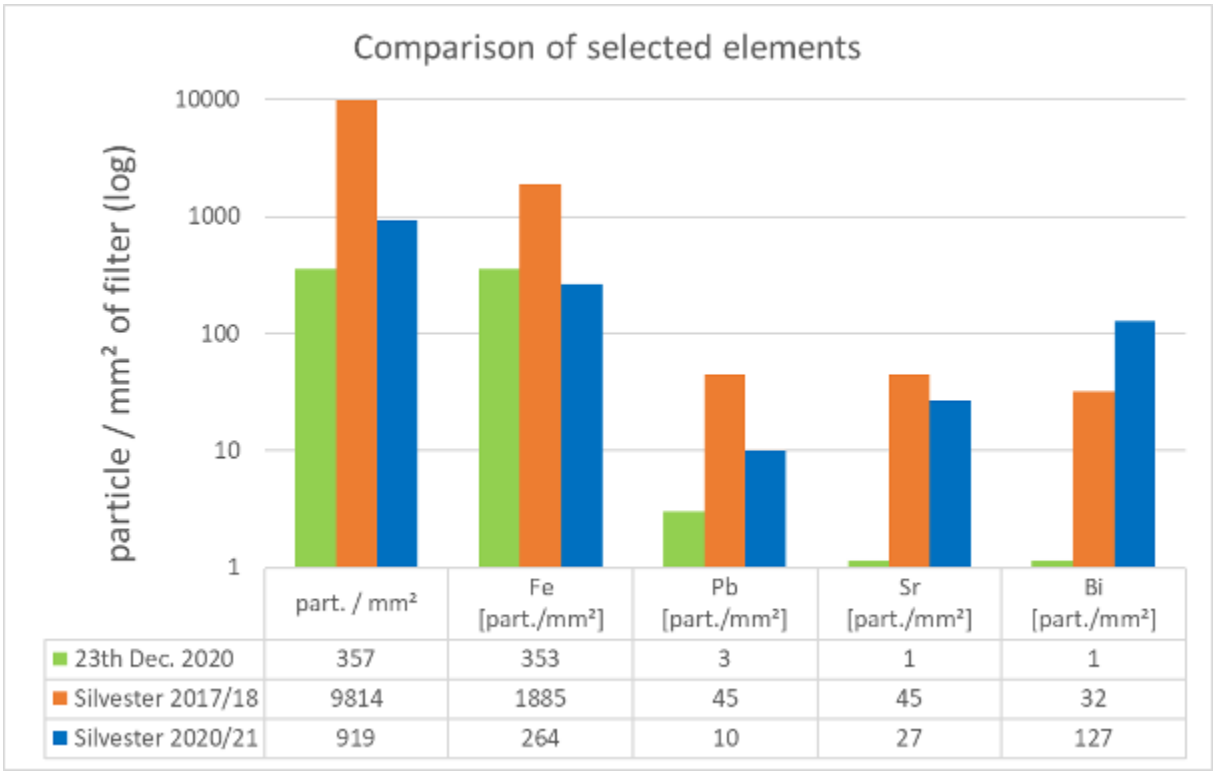

	part. / mm²	Fe [part./mm²]	Pb [part./mm²]	Sr [part./mm²]	Bi [part./mm²]
23th Dec. 2020	357	353	3	1	1
Silvester 2017/18	9814	1885	45	45	32
Silvester 2020/21	919	264	10	27	127

Figure 2

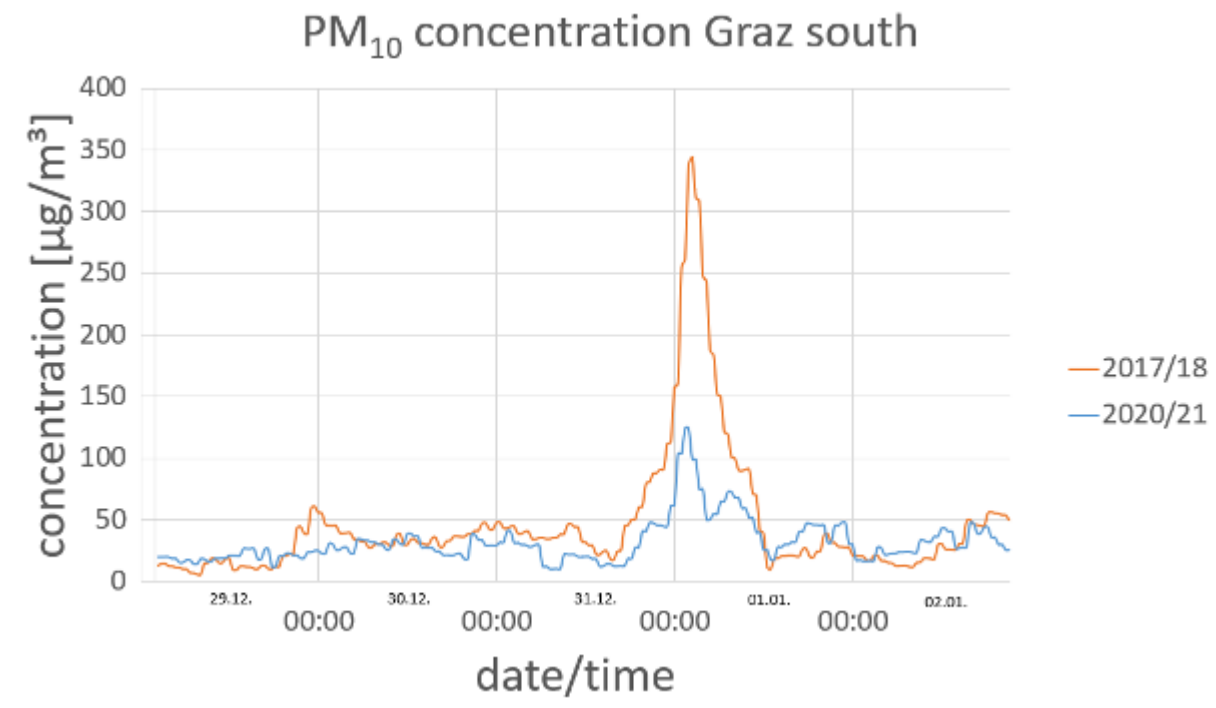

LS2.001-Invited_
Golgi apparatus – a complex organelle that determines the biology of urothelial cells in health and disease

M. E. Kreft[1], T. Višnjar[1], S. Hudoklin[1], N. Resnik[1], T. Ž. Ramuta[1], M. Ž. Mekuč[2], R. Polishchuk[3], G. V. Beznoussenko[4] M. Pavelka[5], H.Robenek[6], M. Kreft[7], K. Jezernik[1], P. Veranič[1], R. Romih[1], A. A. Mironov[4]

[1]University of Ljubljana, Faculty of Medicine, Institute of Cell Biology, Ljubljana, Slovenia
[2]University of Ljubljana, Faculty of Computer and Information Science, Ljubljana, Slovenia
[3]Telethon Institute of Genetics and Medicine (TIGEM), Pozzuoli (NA), Italy
[4]The FIRC Institute of Molecular Oncology, Milan, Italy
[5]Department of Cell Biology and Ultrastructure Research, Center for Anatomy and Cell Biology, Medical University of Vienna, Vienna, Austria
[6]Institute for experimental musculoskeletal medicine, University of Münster, Münster, Germany
[7]Laboratory of Neuroendocrinology – Molecular Cell Physiology, Institute of Pathophysiology, Faculty of Medicine, University of Ljubljana, Ljubljana, Slovenia, Laboratory of Cell Engineering, Celica Biomedical, Ljubljana, Slovenia, Department of Biology, Biotechnical Faculty, University of Ljubljana, Ljubljana, Slovenia

Introduction: The formation of effective blood–urine barrier is of fundamental importance for bladder function and metabolic homeostasis. It is known that in a healthy bladder, the barrier is provided by the urothelium, during its differentiation from the basal to the superficial cell layer. Differentiation of superficial urothelial cells (SUCs) follows the expression sequence of specific tight junctional proteins, surface glycans, apical membrane lipids, and integral plasma membrane proteins uroplakins (UPs). The latter are the most significant molecules in the apical plasma membrane (PM) of differentiated SUCs and besides well-developed tight junctions, they contribute to permeability barrier by their structural organization and by hindering endocytosis from the apical plasma membrane (1-3).

Objectives: Work in the past few years have shown that the Golgi apparatus (GA) undergoes major structural rearrangement during urothelial cell differentiation in vivo (4) and in vitro (5, 6). This lecture will review the currently known GA contribution to the formation of the blood-urine barrier in normal urothelial cells and how it might be involved in the loss of the blood-urine barrier in cancer.

Materials and Methods: We used different in vitro and in vivo models. With a generation of specific UP cDNA constructs, we examined the dynamics of UPIb/UPIIIa transport in living UCs. Using cell transfection, time-lapse microscopy, immunohistochemistry and freeze-fracture replica immunolabelling, we studied biosynthesis and transport of UPs in urothelial cells and also the cells, which do not synthesize UPs endogenously and have primarily a ribbon-like GA. By correlative light–electron microscopy, we examined the GA fragments in cells expressing UPs. We performed the ultrastructural studies by transmission electron microscopy; and to study three-dimensional (3D) ultrastructure of cellular compartments and their spatial and temporal distribution at nanometer resolution, methods of electron tomography and dual beam microscopy methods (i.e. FIB-SEM) (7) were used.

Results: By dissecting the trafficking of UPs we demonstrated its differentiation-dependent impact on GA architecture. Our findings showed the significant effect of the UPs expression on the GA fragmentation, which enables secretory Golgi-outpost to be distributed as close as possible to the sites of cargo delivery at the PM (6, 8). GA-units can also be seen in tunneling membrane nanotubes between normal and cancer urothelial cells. During urothelial carcinogenesis, the urothelial cells lose the expression of uroplakins, consequently also the fragmentation of GA is significantly hindered in the muscle-invasive bladder cancer cells.

Conclusion: Although GA fragmentation is well recognized in conjunction with mitosis and apoptosis, we propose that the process of GA fragmentation is needed for delivery of certain specific cargoes to PM. This process might also be needed in specific cell-to-cell communication structures like they are tunneling membrane nanotubes. In the future, it will be important to understand how the trafficking machinery of the urothelial cells drives GA fragmentation in response to the expression of such cargo proteins and which transcriptional program and epigenetic changes are required for GA reorganization.

References

[1] Kreft ME, Hudoklin S, Jezernik K, Romih R. Formation and maintenance of blood-urine barrier in urothelium. Protoplasma. 2010;246(1-4):3-14.
[2] Lasič E, Višnjar T, Kreft ME. Properties of the Urothelium that Establish the Blood-Urine Barrier and Their Implications for Drug Delivery. Rev Physiol Biochem Pharmacol. 2015;168:1-29.
[3] Kreft ME, Romih R, Kreft M, Jezernik K. Endocytotic activity of bladder superficial urothelial cells is inversely related to their differentiation stage. Differentiation; research in biological diversity. 2009;77(1):48-59.
[4] Hudoklin S, Jezernik K, Neumüller J, Pavelka M, Romih R. Urothelial plaque formation in post-Golgi compartments. PLoS One. 2011;6(8):e23636.
[5] Kreft ME, Di Giandomenico D, Beznoussenko GV, Resnik N, Mironov AA, Jezernik K. Golgi apparatus fragmentation as a mechanism responsible for uniform delivery of uroplakins to the apical plasma membrane of uroepithelial cells. Biol Cell. 2010;102(11):593-607.
[6] Višnjar T, Chesi G, Iacobacci S, Polishchuk E, Resnik N, Robenek H, et al. Uroplakin traffic through the Golgi apparatus induces its fragmentation: new insights from novel in vitro models. Scientific Reports. 2017;7(1):12842.
[7] Žerovnik Mekuč M, Bohak C, Hudoklin S, Kim BH, Romih R, Kim MY, et al. Automatic segmentation of mitochondria and endolysosomes in volumetric electron microscopy data. Comput Biol Med. 2020;119:103693.
[8] Kreft ME, Di Giandomenico D, Beznoussenko GV, Resnik N, Mironov AA, Jezernik K. Golgi apparatus fragmentation as a mechanism responsible for uniform delivery of uroplakins to the apical plasma membrane of uroepithelial cells. Biology of the cell / under the auspices of the European Cell Biology Organization. 2010;102(11):593-607.

LS2.003
GliaMorph – a data analysis toolkit to quantify glial cell morphology *in vivo*

E. Kugler[1], R. B. MacDonald[1]

[1]UCL, Institute of Ophthalmology, London, United Kingdom

Introduction: Microscopy techniques are continuously evolving towards increased resolution, speed, and information to acquire high quality images of cells and their morphologies. However, our abilities to process, quantify, and compare results across multiple datasets lags behind, leading to a data analysis bottleneck.

Cells in the central nervous system (CNS) have diverse morphologies patterned into circuits, required for CNS function. Glial cells, the CNS support cells, have complex morphologies to contact neurons and blood vessels, facilitating their function. This intricate relationship is known to be disrupted in many neurological and neurodegenerative diseases.

As a CNS part, the retina is a tractable and accessible model to analyse glial cell shape and elaborations during development (**Figure 1**). Müller Glia (MG) are the principal retinal glial cell type, similar to astrocytes in the brain, with a unique morphology to support several neuron types. However, it is difficult to accurately describe and quantify individual glial cells, particularly when comparing different tissue preparations, ages, or health states. As such, there is the need to accurately model glial morphologies to understand fundamental cellular mechanisms pertaining to CNS architecture, function and degeneration.

Here we use advanced confocal microscopy methods to image MG in the zebrafish retina *in vivo* and objectively process and analyse glial projections, dynamics, and interactions with other retinal components (e.g. neurons or blood vessels).

Objectives**:** To resolve and quantify retinal glia cell morphological subdomains and their interactions with neurons and blood vessels throughout retina development using AiryScan microscopy and novel computational image analysis methods.

Material and Methods**:** Imaging datasets of MG, neuronal synapses and blood vessels were visualised by transgene or immunohistochemistry in zebrafish retinas using Zeiss AiryScan microscopy throughout several stages of development. Open-source image analysis methods were developed using Fiji, with individual tools integrated into the GliaMorph toolkit (**Figure 2A**).

Results**:** As part of the GliaMorph toolkit box, the "*DeconvolutionTool*" allows for acquisition-specific (confocal vs AiryScan) image pre-processing, to improve image quality (*i.e.* contrast-to-noise ratio and glia morphology). The "*RotationTool*" (**Figure 2B**) allows semi-automatic region-of-interest selection, to allow comparability between samples/groups, and the "*ZonationTool*" builds on this by extracting glia-specific subregions, such as cell bodies and endfeet. To establish cell segmentation, the "*SegmentationTool*" is currently under development. This will be the foundation for the "*QuantificationTool*", which enables the extraction and analysis 18 different glial shape descriptors (e.g. volume, surface, interaction). Applying the GliaMorph toolkit, we show that at specific developmental time points, during neuronal neurite extension and synaptogenesis, MG elaborate, forming cell contacts and ultimately support retinal function.

Conclusion**:** The GliaMorph toolkit enables an in-depth understanding on MG development, functionality, and interactions with retinal neurons and blood vessels *in vivo* in the healthy retina, and eventually disease pathogenesis.

Figure 1

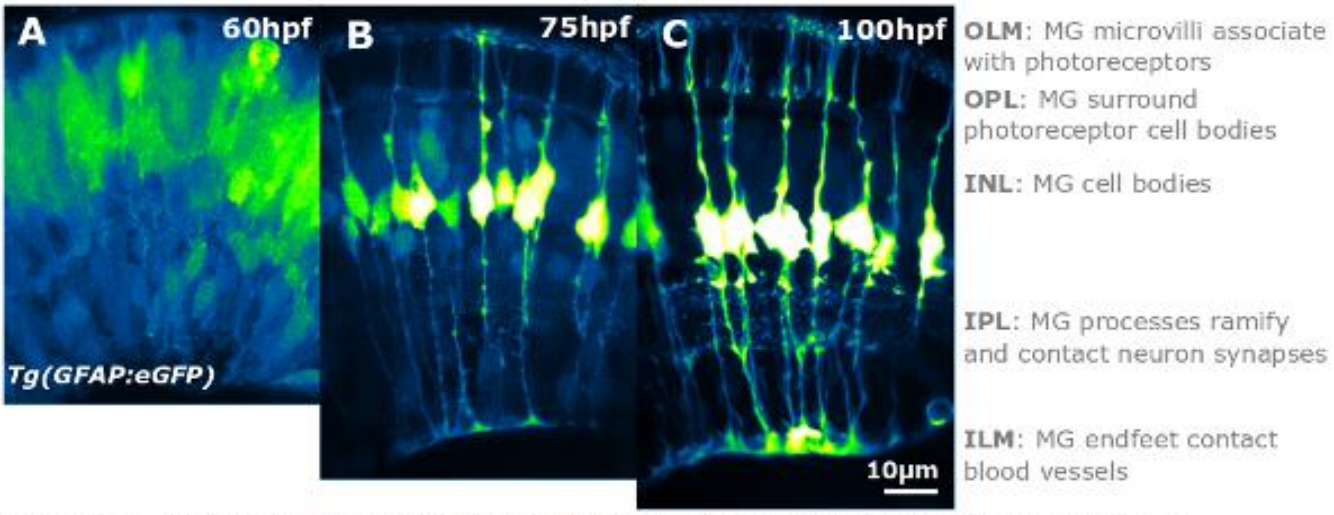

Figure 1. MG morphology is tightly linked to their maturity (A-C) and function.

Figure 2

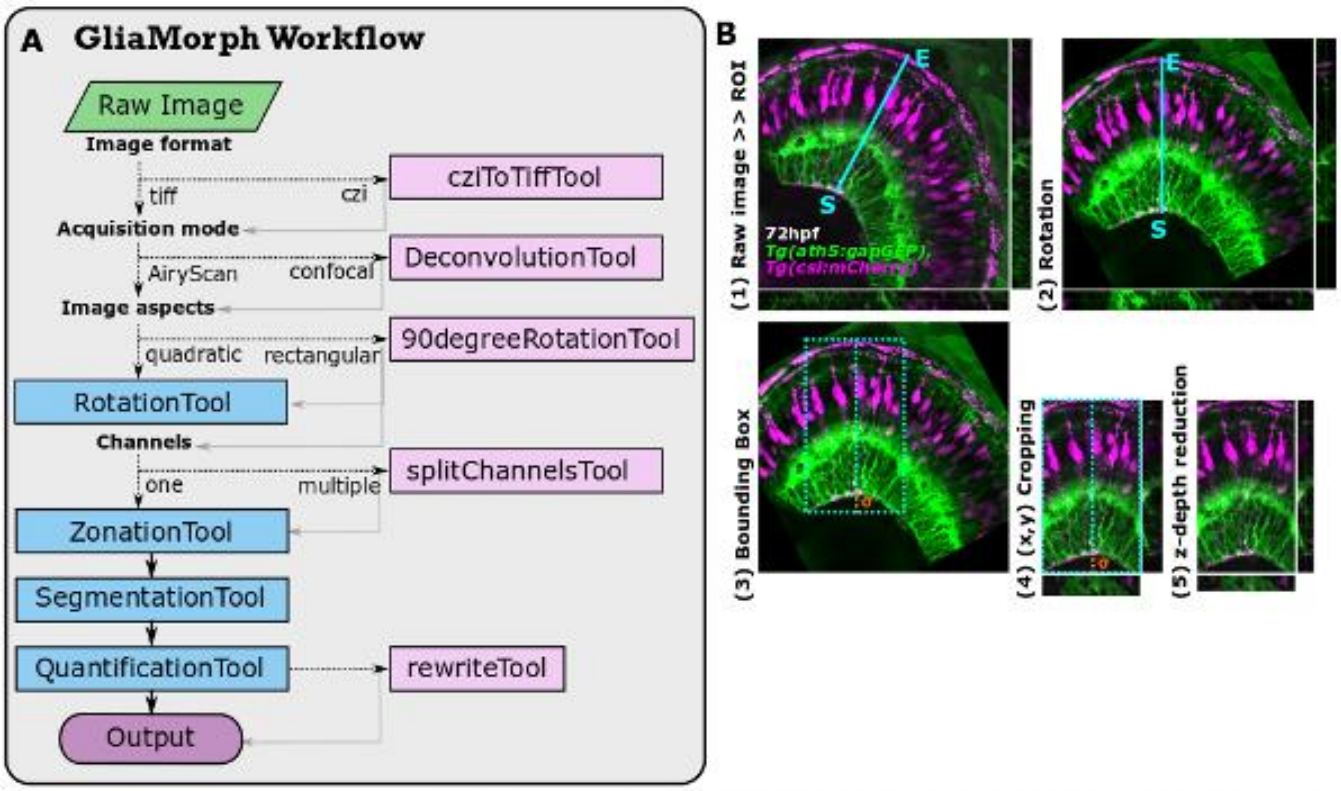

Figure 2. (A) GliaMorph is a modular data analysis workflow to analyse 3D glia morphology and interactions. **(B)** The RotationTool allows semi-automatic 3D ROI selection, reducing input images to user-defined image outputs. Example image input 3208 x 3208 x 53 vx (x,y,z) and output 1210 x 2010 x 40 vx.

LS2.004
Neuroanatomy and cellular structure of the *C. elegans dauer* nervous system investigated with 3D-EM techniques

S. Britz[1], S. M. Markert[1], D. Witvliet[2], A. Steyer[3], S. Tröger[1], B. Mulcahy[2], Y. Schwab[3], M. Zhen[2], C. Stigloher[1]

[1]Imaging Core Facility at the Theodor-Boveri-Institute of Bioscience, Würzburg, Germany
[2]Lunenfeld-Tanenbaum Research Institute, Mount Sinai Hospital, Toronto, Canada
[3]Electron Microscopy Core Facility, European Molecular Biology Laboratory, Heidelberg, Germany

Markert S.M. and Witvliet D. have contributed equally to this work and share second authorship.

In this study we focus on the *Caenorhabditis elegans dauer* larva, an alternative branch in the life cycle of the nematode when facing adverse environmental conditions (Golden & Riddle, 1982). The *dauer* larva shows specific behaviors, such as nictation, which is characterized by raising of the anterior body part and circular swing-like movement. This is thought to increase the chance of hitchhiking to better environmental conditions by transport vectors. Sensory IL2 neurons regulate nictation and show a *dauer*-specific dendritic branching, as previously shown by fluorescence microscopy (Lee *et al.*, 2011; Schroeder *et al.*, 2013). Furthermore, many sensilla with a diverse functional spectrum are located in the anterior end of the *C. elegans* body where IL2 neuron endings form characteristic branches in *dauer* (Albert & Riddle, 1983; Schroeder *et al.*, 2013; Doroquez *et al.*, 2014). We present a detailed description of the morphology of the anterior sensilla of *dauer* by reconstruction of Focused Ion Beam Scanning Electron Microscopy (FIB-SEM) image stacks of high-pressure frozen, freeze substituted and minimally embedded samples (Schieber *et al.*, 2017). For our investigation of sensilla structures we applied volumetric segmentation using the IMOD software package (Kremer *et al.*, 1996). In this high-3D resolution analysis we specifically focus on the branching of IL2 neurons. In addition, we investigated *dauer*-specific synaptic connectivity. Therefor we traced nerve rings where most of these connections are located. We performed this for several *dauer* larva individuals and analyzed plasticity by comparison with other stages. For cell tracing and labelling of synapses, we were taking advantage of the multi-user annotation versatility of the server based CATMAID tool (Saalfeld *et al.*, 2009). Our study completes further the list of almost fully mapped connectomes of other larval stages and adults as the *dauer* stage is still missing.

Figure 1: 3D analysis of the anterior *C. elegans dauer* nervous system by 3D-electron microscopy reconstruction. **A:** Volumetric reconstruction of the anterior sensilla of a *dauer* larva of a FIB-SEM image stack. **A':** Arrowhead points to a branch of a IL2 neuron at the sensilla region. **B:** Skeleton tracing from the anterior end up to the nerve ring of the data set in A. Scale: anterior-to-posterior 82µm and ventral-to-dorsal 15µm. **B':** Arrowheads point to dendritic branches of an IL2 neuron from B. **B'':** Part of the nerve ring from B where chemical synapses are labelled as cyan and red beads.

References:
[1] Albert & Riddle, 1983, doi: 10.1002/cne.902190407.
[2] Doroquez *et al.*, 2014, doi: 10.7554/eLife.01948.
[3] Golden & Riddle, 1982, doi: 10.1126/science.6896933.
[4] Kremer *et al.*, 1996, doi: 10.1006/jsbi.1996.0013.
[5] Lee *et al.*, 2011, doi: 10.1038/nn.2975.
[6] Saalfeld *et al.*, 2009, doi: 10.1093/bioinformatics/btp266.
[7] Schieber *et al.*, 2017, doi: 10.1016/bs.mcb.2017.03.005.
[8] Schroeder *et al.*, 2013, doi: 10.1016/j.cub.2013.06.058.

Figure 1

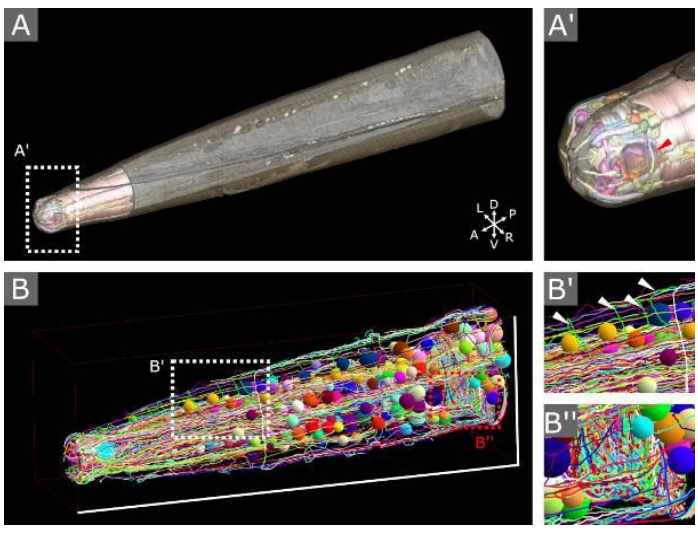

LS2.005
Nanoscale analysis of nuclear phosphatidylinositol phosphate distribution between nucleaoplasm and nuclear speckles

P. Hoboth[1,2], M. Sztacho[1], O. Šebesta[2], P. Hozák[1]

[1]Institute of Molecular Genetics of the Czech Academy of Sciences, Department of Biology of the Cell Nucleus, Prague, Czech Republic
[2]Charles University in Prague , Laboratory of Confocal and Fluorescence Microscopy, Prague, Czech Republic

Single-molecule localization microscopy (SMLM) provided an unprecedented insight into the sub-nuclear organization of proteins and nucleic acids. However, the role of the nuclear lipids in the establishment of the functional nuclear architecture, apart from the nuclear envelope, has been neglected. Nevertheless, the roles in gene expression of the nuclear lipids and phosphatidylinositol phosphates (PIPs) in particular started to emerge. Therefore, we implemented and optimized the SMLM-based approach for the quantitative evaluation of the nuclear PIP distribution while preserving the context of nuclear architecture. We have quantitatively characterized the spatial distribution of nuclear phosphatidylinositol 4,5- and 3,4-bisphosphate (PI(4,5)P2 and PI(3,4)P2, resp.) and showed that PI(4,5)P2 and PI(3,4)P2 localize within matrix of the nuclear speckle marker SON and in the nucleoplasmic foci. Moreover, we found PI(4,5)P2 and PI(3,4)P2 in the close proximity with the subset of RNA polymerase II (RNAPII) foci either in the nucleoplasm or at nuclear speckles. We started to investigate the cross-talk between nucleoplasmic and nuclear speckle-associated PI(4,5)P2 and PI(3,4)P2 pools and their possible roles in the regulation of RNAPII transcription. Our preliminary data suggest that upon transcription inhibition PI(4,5)P2 and PI(3,4)P2 accumulate within nuclear speckles. Therefore, nuclear speckles could play a role in the buffering of the nuclear PIP levels and thereby possibly regulate RNAPII transcription.

Figure graphically summarizes the experimental approach (A) where we visualized nuclear PIPs and nuclear speckle marker SON or RNAPII by dual-color dSTORM and analyzed by nearest-neighbor distance (NND) analysis using ThunderSTORM Fiji plug-in and developed an *in-cellulo* visualization tool based on NND analysis for the spatial relationship between PIPs and SON or RNAPII. This tool is applicable to any markers of interest. Schematic summary of main results (B). Nuclear PI(4,5)P2 and PI(3,4)P2 form foci that concentrate in nuclear speckles and distribute through the nucleoplasm, where they localize in the close proximity with the subset of RNAPII foci that also localize to the nuclear speckle periphery.

Figure 1

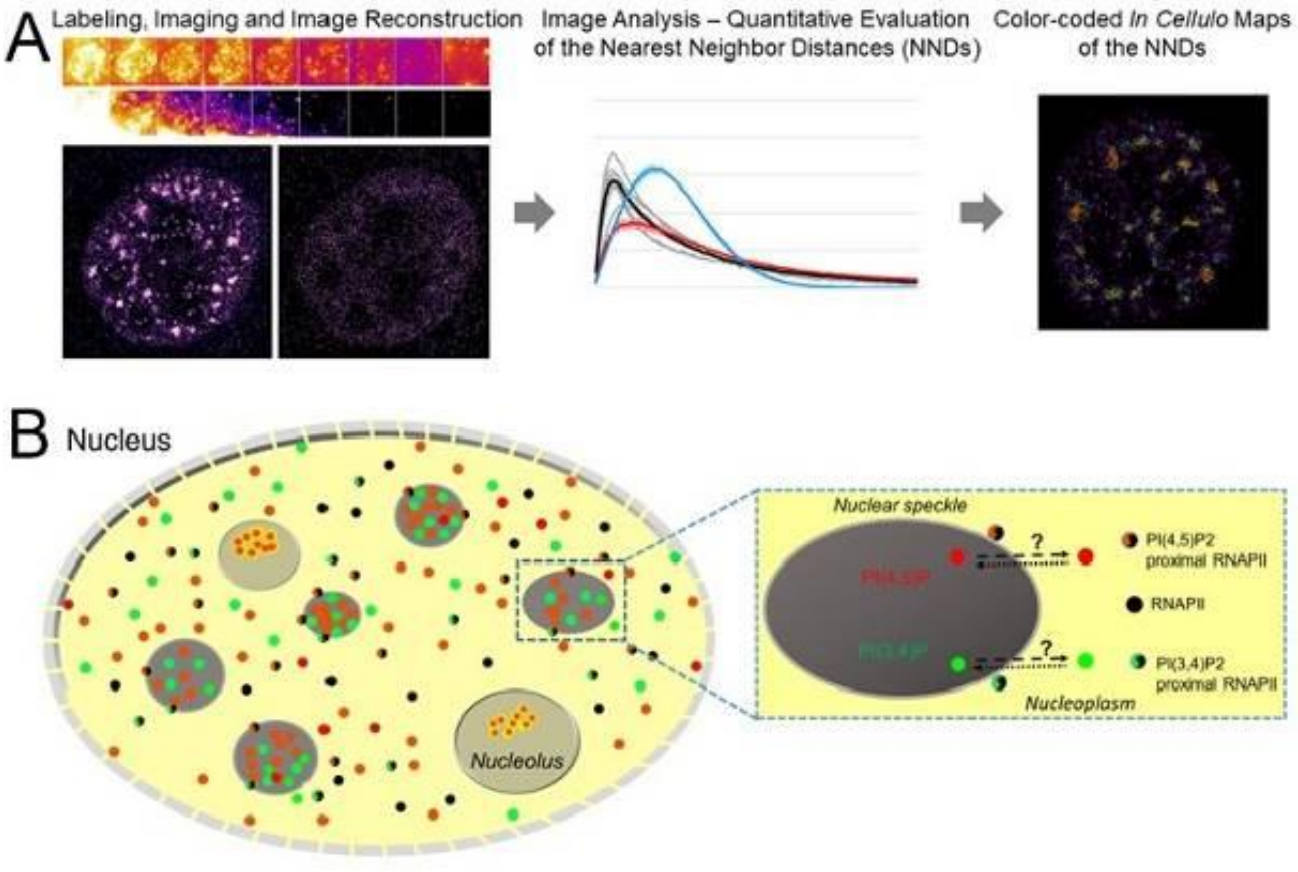

LS2.006
High-performance polarising microscopy reveals structural remodeling in rat calcaneal tendons during *in vitro* culture

E. H. M. Dos Anjos[1], M. L. S. Mello[1], B. D. C. Vidal[1]

[1]University of Campinas, Structural and Functional Biology, Campinas, Brazil

Optical anisotropic properties, as revealed using polarizing microscopy, have allowed for the determination of organizational and macromolecular characteristics of tendon collagen bundles [1-3]. These properties are modified during animal development, tissue repair and aging and in response to various biomechanical demands [4-10]. Because there are no data reporting how tendon collagen fibers behave under the experimental conditions used to obtain primary fibroblast cultures, we investigated the optical anisotropic characteristics of collagen fibers in tendons subjected to *in vitro* culture.

We isolated calcaneal tendons from male Wistar rats and cultured these tendons on glass slides (cov) and in direct contact with the surface of culture dishes (pla) for 8 and 12 days in DMEM/HAMF12 (v/v) medium supplemented with 10% bovine fetal serum and penicillin/streptomycin at 37 °C and 5% CO_2. Tendons that were not subjected to *in vitro* culture were used as controls. Tendon fragments were fixed in 4% paraformaldehyde, embedded in Histosec, cut at a thickness of 8 µm, and examined using an Olympus BMX-51 high-performance polarization microscope equipped with a Q-color 5 camera, differential interference contrast optics (DIC-PLM), and Sénarmont compensator. Images of the birefringence brilliance intensity were captured and analyzed using Image-Pro Plus 6.3 software. Optical retardations in pixels in the tendon sections were determined for image areas equal to 10^5 µm^2.

The DIC-PLM images shown in Figure 1 indicate a gradual swelling and unpacking of collagen bundles as the time that the tendons were maintained in the tissue culture medium increased. Decreased values of birefringence optical retardation were detected in tendons that were cultured *in vitro* compared with control tendons (Table 1).

These results demonstrate structural remodeling of calcaneal tendons during *in vitro* culture. The decreases in the aggregation state of collagen bundles and their macromolecular orientations were probably due to changes in the molecular orientation of the polypeptide chains that compose the collagen fibers and a reduction in the crystallinity degree of the tendon structure under present experimental conditions.

[1] B.C. Vidal, Micron 34 (2003), 423-32; Biotechn. Histochem. 85 (2010), 365-78.
[2] B.C. Vidal and M.L.S. Mello, Acta Histochem. 112 (2010), 53-61.
[3] M.L.S. Mello et al., Ann. Histochim. 20 (1975), 145-52; Gerontology 25 (1979), 2-8.
[4] R. Vilarta and B.C. Vidal, Matrix 9 (1989), 55-61.
[5] A. Cunha et al., Ultrasound Med. Biol. 27 (2001), 1691-6.
[6] A.A. de Aro et al., Life Sci. 1973 (2012), 885-93.
[7] Frauz, K. et al., Cells 8 (2019), 56.

We are indebted to Dr. José Luiz Módena and Dr. Cristina Vicente for facilities at their laboratories (Unicamp), to Mrs. Camila Oliveira for tissue culture technical support, and to FAPESP (Brazil) for the acquisition of the Olympus BMX-51 polarization microscope (grant no. 2007/58251-8).

Figure 1: DIC-PLM birefringence images of rat calcaneal tendon sections. Structural changes in the collagen bundles gradually occurred after the tendons were cultured on glass slides for 8 (B) and 12 (C) days. A, control. Bar, 50µm.

Table 1. Frequency distribution of birefringence OR in sections of tendons cultured *in vitro*.

Figure 1

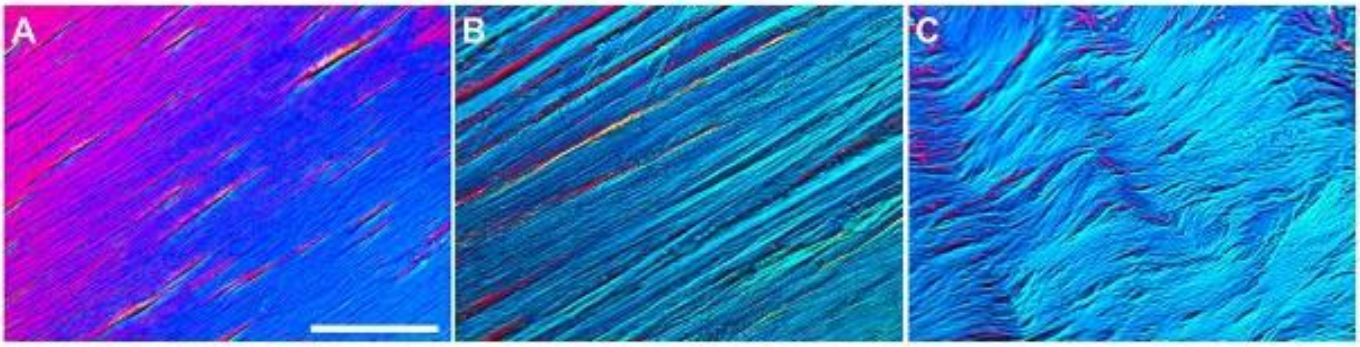

Figure 2

	OR (pixels)				
	Control	$8D_{cov}$	$8D_{pla}$	$12D_{cov}$	$12D_{pla}$
No. of measurements	206	206	251	206	207
Minimum	40.3	22.6	14.1	27.3	28.9
Maximum	247.9	247.9	199.5	247.0	218.4
Median	140.0	157.6	41.2	96.6	52.8
Mean	148.3	158.3	54.9	115.0	65.0
Standard Deviation	46.6	61.9	34.6	64.6	36.6

D, days; cov, culture on glass slides; pla, culture on culture dishes.

LS2.P001
Differences in renal microscopic morphology between wild-type and *Tff3* knock-out mice

N. Bijelić[1], E. Rođak[1], M. Firić[2], T. Belovari[1], K. Šešelja[3], I. Bazina[3], M. Baus Lončar[3]

[1]Faculty of Medicine Osijek, Department of Histology and Embryology, Osijek, Croatia
[2]Faculty of Medicine Osijek, University Graduate Study of Medical Laboratory Diagnostics, Osijek, Croatia
[3]Institute Ruđer Bošković, Zagreb, Croatia

Introduction: Tff3 protein is a mucosal protein involved in protection and restoration of the mucosal barrier, especially in the intestines. It is also found in the kidney and is believed to facilitate the repair of kidney tubular epithelium injury. Tff3 protein expression is also related to some renal pathological conditions, such as renal cancer and chronic kidney disease.

Objectives: The objectives of this study were to determine effect of Tff3 deficiency on histomorphometric properties of kidney tissue using wild-type mice and *Tff3* knock-out mice.

Materials & methods: Male mice (background C57Bl6/J//Sv129) deficient of Tff3 protein and appropriate wild type mice were used in the study (N=5 each group). Kidneys were harvested, fixed in 4% paraformaldehyde and paraffin-embedded. Blocks with kidney tissue were cut (6 um thick) and slides were stained using PAS method. Digital photographs were taken (5 images of cortex and 3 images of medulla for each animal) and measured using FIJI software. Arithmetic means were obtained for each sample and used for further analysis.

Results: Tff3 deficient mice have larger total diameter and lumen width of proximal convoluted tubules compared to wild-type mice. Significant difference was not found in other renal histomorphological properties of the examined groups (glomerular cross-sectional area, total diameter and lumen width of distal and collecting ducts, and epithelial height of proximal, distal and collecting ducts).

Conclusion: Increased diameter of the proximal tubules might point to proximal tubule hypertrophy in *Tff3* knock-out mice. In order to confirm this assumption additional studies are needed (possibly including total renal volume measurement, serial kidney sections, studies on mice of different age and studies after pharmacological challenge of kidney function, e.g. using furosemide).

Keywords: kidney; renal tubules; glomerulus; histology; Tff3 protein

This research was funded by Croatian Science Foundation grant IP-2016-06-2717. The work of doctoral student Iva Bazina has been fully supported by the "Young researchers career development project – training of doctoral students" of the Croatian Science Foundation funded by the European Union from the European Social Fund[m1]

LS2.P002
Morphological analysis of renal morphology in wild-type and *Tff3* knock-out mice subjected to tunicamycin-induced endoplasmic reticulum stress

N. Bijelić[1], Đ. Aliti[2], E. Rođak[1], T. Belovari[1], K. Šešelja[3], I. Bazina[3], M. Baus Lončar[3]

[1]Faculty of Medicine Osijek, Department of Histology and Embryology, Osijek, Croatia
[2]Faculty of Medicine Osijek, University Graduate Study of Medical Laboratory Diagnostics, Osijek, Croatia
[3]Institute Ruđer Bošković, Zagreb, Croatia

Introduction: Tff3 protein is secreted by different mucosal epithelial cells and is important for protection and restoration of mucosal integrity and function. It is expressed in normal kidney tissue, but also in some renal diseases, such as oxidative stress-induced renal carcinoma and chronic kidney disease. Accumulation of unfolded proteins within the endoplasmic reticulum (ER) is one of the early events in pathological changes of different organs including kidney. Tff3 deficiency has been linked to the function of ER.

Objectives: The aim of this study was to asses effect of Tff3 deficiency on microscopic morphology of renal cortex and medulla in case of induced acute ER stress.

Materials & methods: Five 7 weeks-old male Tff3−/−/C57BL6/NCrl mice (*Tff3* knock-out mice) and five male C57BL6/NCrl (wild-type) mice were used in the study. ER stress was induced with single dose of tunicamycin (Tm) (3 µg of Tm/g of body weight), a drug that blocks the initial step of *N*-glycosylation, leading to accumulation of misfolded proteins in the ER. Kidneys were collected after 24 h and prepared for histological analysis. The samples were stained using PAS method. Digital images were taken (5 images of the cortex and 3 images of the medulla for each animal) and on each image representative tubules were measured using FIJI software. Arithmetic means were obtained for each sample and used for further analysis.

Results: The analysis of renal morphometric parameters did not show significant differences in the glomerular area, tubular diameter, height of tubular epithelium and diameter of tubular lumen between wild-type mice and *Tff3* knock-out mice after ER stress.

Conclusion: Tff3 deficiency does not affect tubular and glomerular morphology in applied acute ER stress model. This may point to the conclusion that Tff3 protein deficiency does not affect the cellular mechanisms during 24 h after induction of ER stress. However, model of chronic ER stress occurring in course of normal aging could provide more valuable data of Tff3 deficiency role in kidney function.

Keywords. kidney; endoplasmic reticulum stress; Tff3 protein; glomerulus; tubular diameter

This research was funded by Croatian Science Foundation grant IP-2016-06-2717. The work of doctoral student Iva Bazina has been fully supported by the "Young researchers career development project – training of doctoral students" of the Croatian Science Foundation funded by the European Union from the European Social Fund

LS2.P003
Tropaeolum majus L. *altum* essential oil exhibits anticancer activity that manifests through cell morphology alterations

I. Vrca[1], L. Krce[2], V. Čikeš Čulić[3], I. Aviani[2], I. Blažević[4], T. Bilušić[1]

[1]Faculty of Chemistry and Technology, Department of Food Technology and Biotechnology, Split, Croatia
[2]Faculty of Science, Department of Physics, Split, Croatia
[3]School of Medicine, Department of Medical Chemistry and Biochemistry, Split, Croatia
[4]Faculty of Chemistry and Technology, Department of Organic Chemistry, Split, Croatia

Introduction: *Tropaeolum majus* L. *altum* is a plant that belongs to Tropaeolaceae family and is known for its ornamental and medicinal properties [1]. It contains benzyl glucosinolate (glucotropaeolin) whose degradation product benzyl isothiocyanate shows various biological activities such as anticancer, antimicrobial and anti-inflammatory [2,3,4].

Objectives: The aim of this study was to investigate the anticancer activity of *T. majus* essential oil against human bladder cancer cell line TCCSUP and to determine if membrane alterations are a part of the anticancer mechanism of *T. majus* essential oil.

Materials & methods: The essential oil of *T. majus* seeds was obtained by microwave-assisted distillation. Gas chromatograph equipped with mass spectrometer was used to identify volatile compounds. The half maximal inhibitory concentration (IC_{50}) of *T. majus* essential oil was determined against TCCSUP cell line *via* the MTT assay. Atomic force and optical microscopy were used to detect morphology and membrane changes of cells treated with sub-IC_{50} concentration.

Results: *T. majus* essential oil has shown anticancer activity against TCCSUP cell line due to high amount of benzyl isothiocyanate. Bright-field microscopy of sub-IC_{50} concentration treated cells reveals the change in cell morphology and possible membrane blebbing of some cells. Atomic force microscopy analysis suggests notable cell surface alterations/membrane bleb formation as a part of the anticancer mechanism.

Conclusion: The *T. majus* essential oil exhibits anticancer activity against TCCSUP cancer cells by altering cell morphology after exposure with sub-IC_{50} concentration.

References:
[1] Garzon, G.A., Wrolstad, R.E. (2009): Major anthocyanins and antioxidant activity of Nasturtium flowers (*Tropaeolum majus*). *Food Chem*. 114 (1), 44-49.
[2] Romeo, L., Iori, R., Rollin, P., Bramanti, P., Mazzon, E. (2018): Isothiocyanates: An overview of their antimicrobial activity against human infections. *Molecules,* 23 (3), 624, 1-18.
[3] Wu, X., Zhou, Q.H., Xu, K. (2009): Are isothiocyanates potential anti-cancer drugs? *Acta Pharmacol. Sin*. 30 (5), 501-512.
[4] Ko, M.O., Kim, M.B., Lim, S.B. (2016) Relationship between chemical structure and antimicrobial activities of isothiocyanates from cruciferous vegetables against oral pathogens. *J. Microbiol. Biotechnolog*., 26 (12), 2036-2042.

LS2.P005
Anatomical research on *Potentilla indica* (Rosaceae)

D. Rančić[1], M. Mačukanović-Jocić[1], S. Kilibarda[1], R. Radošević[1]

[1]Faculty of Agriculture University of Belgrade, Agrobotany, Belgrade, Serbia

Introduction: *Potentilla indica* (Jacks.) Th. Wolf commonly known as Indian Mock Strawberry or false strawberry, is native to eastern and southern Asia (Himalayas, China, and Japan), but has been introduced worldwide and commonly grown as ornamental. *P. indica* is very tolerant to different environmental conditions including high-altitude habitat, areas with low/high temperatures, sun/ shade or drought.

Objectives: The aim of the research is to contribute to the ecophysiological study of the plant by analyzing the anatomical characteristics that could be involved in response of plants to environmental stimuli and the adaptation to abiotic stress.

Materials & methods: For light microscopy fixed plant material (petiole, leaf blade, stem, stolons, rhizome and adventitious root) was dehydrated and embedded in paraffin. Sections were cut by sliding microtome and stained with Alcian Blue-Safranin. Observation and photographs were done using a light microscope (Leica DM2000).

Results: Leaves are dorsiventral and amphistomatic (Fig 1a). Two types of *trichomes* are identified, non-glandular and glandular present on both leaf surfaces. Non-glandular trichomes are unicellular, while glandular ones have uniseriate stalk and globular head, usually made up of four cells each (Fig 1b). Palisade parenchyma is composed of two or three layers of elongated cells while spongy parenchyma is composed of a few layers of cells with prominent intercellular spaces.

In stolons subepidermal collenchyma is followed by one or two chlorenchyma layers and large cortical parenchyma cells (Fig 1c). Pericycle is composed of continuous ring of sclerenchyma cells (Fig 1d). Vascular bundles are open collateral, separated by parenchyma rays between.

Peridermis, cortical parenchyma and collateral vascular bundles are observed in the cross section of the rhizome and pith parenchyma occupying the large area in the central part (Fig 2a, b, c).

In adventitious roots diarch, triarch, tetrarch or polyarch radial vascular bundles occur depending on the stage of development (Fig 2d, e). Older roots have typically developed secondary xylem and phloem, and in external parts of roots are visible rings of secondary meristem (Fig 2f).

Cubic crystals, probably of calcium oxalate, are randomly scattered predominantly in pith region of stem and in leaf mesophyll.

Conclusion: Some of anatomical features of *P. indica* are quite common but it also has some specific performances, especially in roots, what will be discussed. Considering the ability to withstand high-temperature and low-temperature stress, additional physiological studies are also required. Acknowledgements: The paper is a result of research within the Agreement No: 451-03-9 / 2021-14 / 200116.

Figure 1: Transverse sections of leaf blade (a, b) leaf petiole (c. d) and stolon (e, f). Glandular trichrome (b), vascular bundle (d) and sclerenchyma in the pericycle (f) in detail.

Figure 2: Transverse sections of rhizome (a, b, c) with detail of external part (b) and crystals in pith cells (c) (arrowed). Transverse section of roots in earlier (d) and later phase of secondary growth (e) with detail showing initiation of secondary lateral meristem (f).

Figure 1

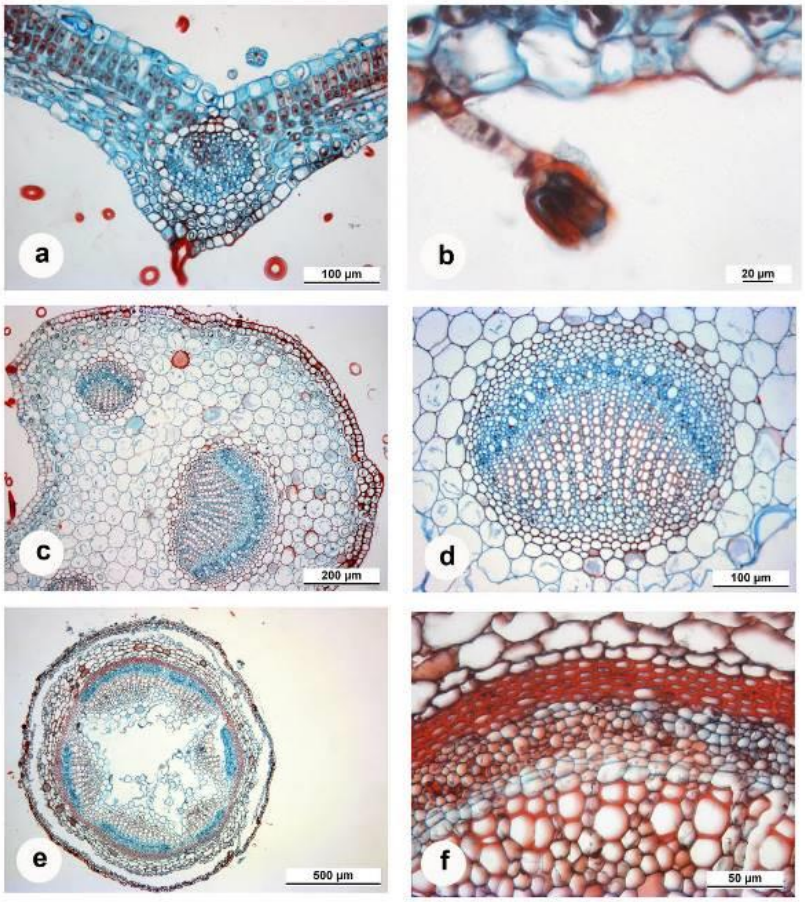

Figure 2

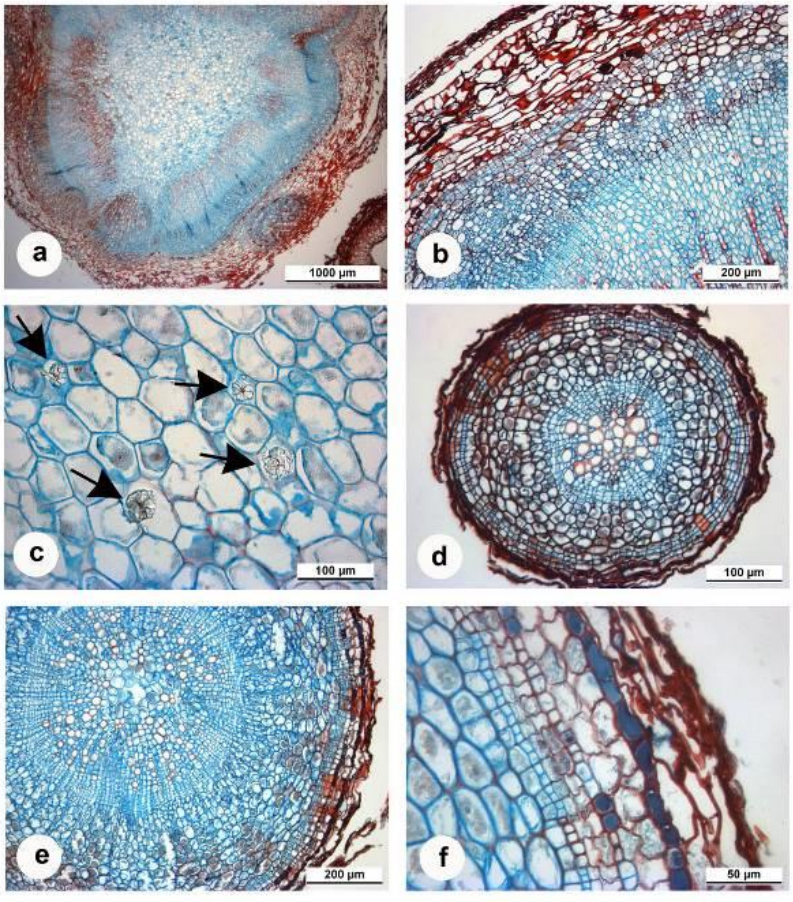

LS2.P006
Pollen morphology of endemic species *Pimpinella serbica* (family Apiaceae)

M. Mačukanović-Jocić[1], D. Rančić[1], S. Kilibarda[1], B. Bekić[1]

[1]Faculty of Agriculture University of Belgrade, Agrobotany, Belgrade, Serbia

Introduction: *Pimpinella serbica* (Vis.) Benth. & Hook**.,** belonging to the Apiaceae, is native to the central and western parts of Balkans (Bosnia and Herzegovina, Montenegro, North Macedonia, Serbia) and Albania. It prefers limestone habitat at an average altitude of about 1300 m forming plant communities with other mountainous species, such as spruce and Greek maple (Pancicii-Aceri heldreichii-Piceetum). In Serbia it inhabits mountains such as Kopaonik, Stara planina, Zlatar, Javor, etc.

Objective: The pollen morphology of *P. serbica,* Balkan endemic species distributed in Serbia, were examined by scanning electron microscopy (SEM) in order to contribute the morphological, taxonomic and melissopalynological studies.

Materials & methods: The umbels were collected from wild plant populations at full flowering stage. A set of three mounted and labelled voucher specimens were processed in standardized way and deposited in the herbarium collection of the Faculty of Agriculture, University of Belgrade.

For SEM study the pollen grains were covered with gold (in BAL-TEC SCD 005 Sputter Coater, 100 seconds in 30 mA) and observed using JEOL JSM- 6390 LV electron microscope at an acceleration voltage of 20 kV. Pollen grains were imaged in polar and equatorial view, and observations and measurements were done on a sample of 30 grains for each morphological character. The following taxonomically significant features describing pollen grains were examined: size, shape, exine sculpture, apertures, polarity, symmetry, equatorial (E) and polar (P) axes length, and apocolpium index.

Results: The pollen grains of *P. serbica* are isopolar, radially symmetrical and small-sized (Figure 1a). The ratio between the polar axis length (P = 21.5 ± 0.8 µm) and the equatorial diameter (E = 12.9 ± 0.9 µm) of 1.7 ± 0.2 indicates prolate shape (Figure 1b). The grains are slightly equatorially expanded with obtuse polar caps, and triangular in polar view with interangular furrows (Fig 1c). The grains have tricolporate apertures with three straight sunken ectocolpi arranged regularly meridionally, of mean length 17.7±0.9 µm, each one with endopore positioned in the indentations between the mesocolpial lobes. Mesocolpial width is 7.3±1.8 µm. Apocolpium index amounts 0.39±0.04. The exine was found to have rugulate sculpture (Figure 1d).

Conclusion: Polen grains of *P. serbica have typical form for Apiaceae family, but some fine details provided by the current study could help in intrageneric differentiation contributing to taxonomic research. The analyzed palynomorphological characteristics may be of special importance for estimating geographical origin of honey, considering this species limited distribution area. The results revealed that exine ornamentation could be a diagnostic trait taxonomically significant and useful for identification to species level.*

Acknowledgements: This is a result of research within the agreement No: 451-03-9 / 2021-14 / 200116.

Figure 1: SEM of pollen grains of *P. serbica (a) in equatorial (b) and* polar view (c) and detail of exine surface showing rugulate sculpturing pattern (d)

Figure 1

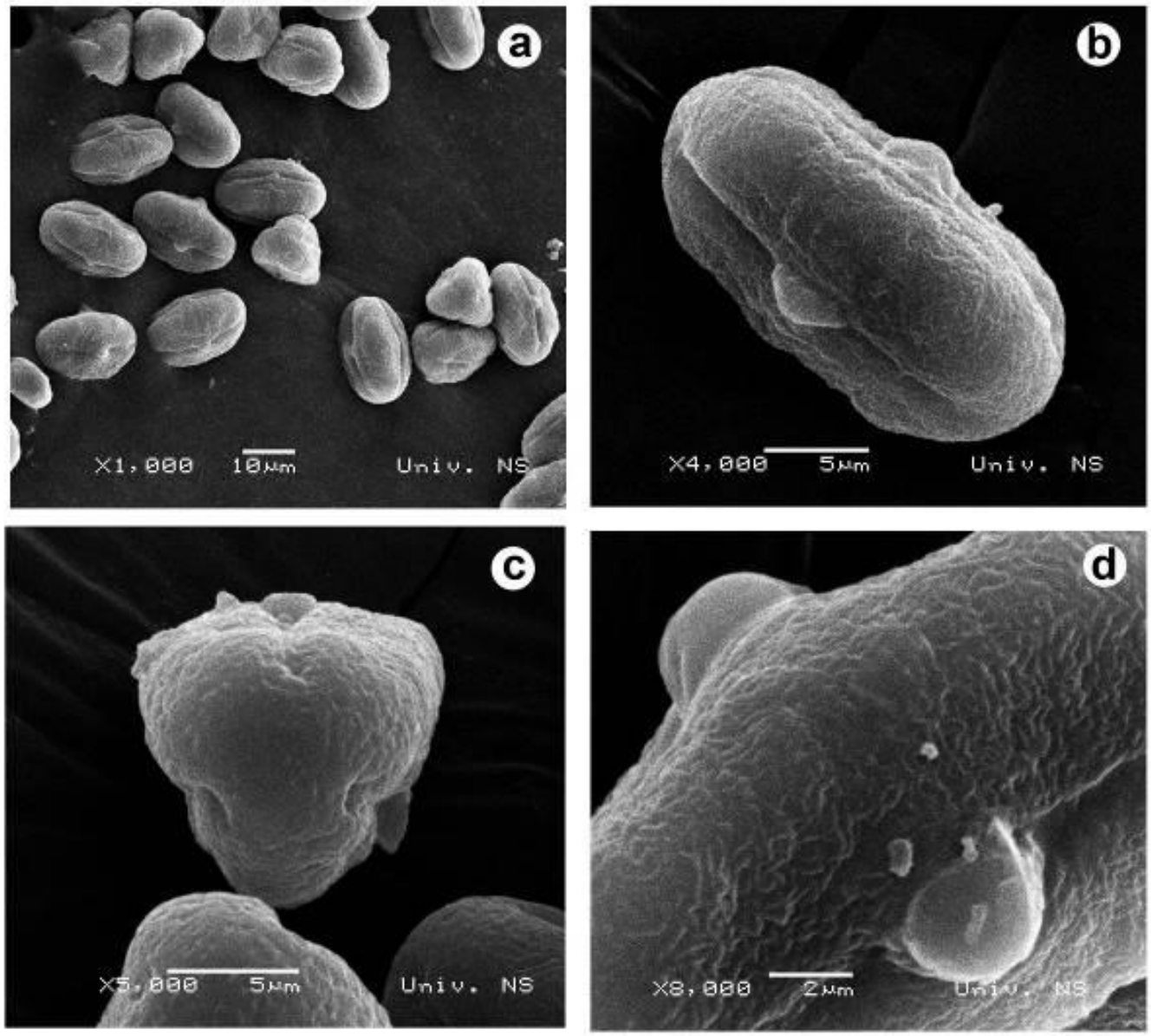

LS2.P007
Ultrastructural features of *Polyonchobothrium clarias* from *Clarias gariepinus* and its role as bio-indicator in the aquatic environment

F. Abdel-Ghaffar[1], S. Al Quraishy[1], M. Dkhil[1], R. Abdel-Gaber[1]

[1]Faculty of Science, Cairo University, Cairo, Egypt

There is a profound and inverse relationship between environmental quality and disease status of fish. Parasites are one of the most serious limiting factors in aquaculture. Therefore, the present investigation was carried to determine parasite infections in the African sharptooth catfish *Clarias gariepinus*, relative to the capability of these parasites to accumulate heavy metals. Up to 100 catfish were infected with cestode *Polyonchobothrium clarias*. The morphology of this parasite species, based on light and scanning electron microscopy, revealed that the adult worm was characterized by a rectangular scolex with a flat to slightly raised rostellum armed with a crown with two semicircles each bearing 13–15 hooks, followed by a number of proglottids. A single set of genitalia was observed clearly in mature proglottid with medullary testes, a bi-lobed ovary was situated near the posterior margin of the proglottid and extending laterally up to the longitudinal excretory canals, tubular uterus arose anteriorly from ootype, and cortical vitelline follicles. The greater portion of the gravid proglottid was occupied by a uterus filled with unoperculate and embryonated eggs. Chemical analysis confirmed that higher accumulation of heavy metals (Zn, Cu, Mn, Cd, Ni, and Pb) in P. clarias than those found in fish tissues and values recommended by FAO/WHO. This supports the hypothesis that cestodes of fish can be regarded as useful bioindicators when evaluating the environmental pollution of aquatic ecosystems by heavy metals.

LS2.P008
Anatomical comparison of hippocampal HS and OLM interneurons using SEM array tomography

Á. Orosz[1], Z. Bardóczi[1], A. Major[1], V. T. Takács[1], P. Papp[1], K. E. Sos[1], M. I. Mayer[1], Z. Hajós[1], T. F. Freund[1], G. Nyiri[1]

[1]Institute of Experimental Medicine, Cerebral Cortex Research Group, Budapest, Hungary

The hippocampal formation of the mammalian brain is essential in learning and memory processes. Its main output neurons are the pyramidal cells, which are innervated by different types of GABAergic neurons, including the somatostatin-positive hippocampo-septal (HS) and oriens-lacunosum moleculare (OLM) interneurons, which regulate the input of the pyramidal cells by dendritic inhibition. To fully understand how the hippocampus, more precisely the dendritic inhibition, works we need precise interneuron models, for which we need their physically and morphologically accurate dendritic parameters. Electrical conductance of neuronal processes depend on several factors, e.g. the surface area of dendritic segments, the local volume of cytosol of dendritic segments, the latter of which is strongly affected by the local volume of their mitochondria. The density and number of excitatory/inhibitory inputs on the different types of dendrites of these neurons are also important, because they control the computational ability of these dendritic segments and the neuron as a whole. We investigated, whether synaptic coverage is different in different regions, like on somata, on different types of dendrites along the dendritic tree, and on the branching points. Using array tomography with scanning electron microscopy (SEM), we reconstructed two different types of GABAergic somatostatin-positive neurons labeled using viral and retrograde BDA tracing: the HS and the OLM interneurons. After the precise calibration of tissue shrinkage/dilatation during tissue processing, we measured the above mentioned real-life parameters along the dendritic tree and the soma. Using double immunolabeling, we also revealed the densities and sizes of inhibitory and excitatory synapses. Our results show highly variable parameters along the dendritic tree that need to be incorporated into precise models of the hippocampal network.

LS2.P009
Pre-processing steps for segmenting 3D SEM images of neurons

S. Radulovic[1], L. Chalet[2], B. Gottschalk[1], S. Wernitznig[1], A. Zankel[3], G. Leitinger[1]

[1]Medical University of Graz, Graz, Austria
[2]University of Franche Comté, Besançon, France
[3]NAWI, Graz, Austria

Introduction and objectives: 3D reconstruction from stacks of electron micrographs of identified neurons, and localization of synaptic connections provide us with valuable information about the way that neuronal circuits work. The most time-consuming part of the procedure is the segmentation process: cell outlines of neurons are drawn manually on software such as Amira and Microscopy Image Browser (MIB). For this, it is important to keep membrane integrity, whilst reducing noise and keeping the structural features of synapses. Here we introduce a solution, which includes pre-processing of electron micrographs. Pre-processed images are suitable for the use of more advanced, fast selecting tools, which significantly shorten the amount of time needed for segmentation.

Materials and methods: Serial block face scanning electron microscopy was used to produce stacks of serial electron micrographs of identified neurons of the locust, *Locusta migratoria*. (Figure 1A) Several image processing steps were performed sequentially on these stacks, using ImageJ software.

First preprocessing step: A histogram matching algorithm was used to homogenize the initial brightness levels within the stack, followed by a low pass Fourier transform band-filter to isolate small structures like cell-membranes. Further a rolling ball algorithm was used to give the cell membranes a higher contrast and thereby the stack was set up for an automated Otsu threshold. The thresholded stacks were analyzed with the particle analyzer implemented in ImageJ to filter out small irregular components present in the original stack not belonging to the cell membranes. In parallel, the particle analyzer was used once more with settings that enabled keeping the large particles such as mitochondria. The result was subtracted from the result of the first round with the particle analyzer.

Second preprocessing step: mitochondria, representing an obstacle during and after segmentation, were the target. For this purpose the histogram-matched stacks were filtered with a median filter after a contrasting step. Finally a Huang´s auto threshold was used to get a binary image (that contained the mitochondria) which was subtracted from the first preprocessing step.

Results: The first step successfully removed many structures inside the cells, but mitochondria attached to the membranes were still visible, compromising the results of the following segmenting steps. This can slow down fast selection tools subsequently used for segmentation (such as "Blow" in Amira). (Figure 1B)

During the second preprocessing step most of the structures inside the cells were deleted. However, at certain locations the membranes appeared discontinuous. Nevertheless combining both steps with fast selection tools significantly enhanced segmentation efficiency compared to a traditional manual approach. (Figure 1C)

In summary, pre-processing can improve the accuracy and efficiency of segmenting algorithms.

Conclusion: The current status of the image processing pipeline shows need for improvement and has to be further elaborated. Nevertheless, it resulted in a binary image that enabled a significant improvement over the traditional manual segmentation and it gives a perspective towards completely automated segmentation processes without the need of manual correction.

Figure 1

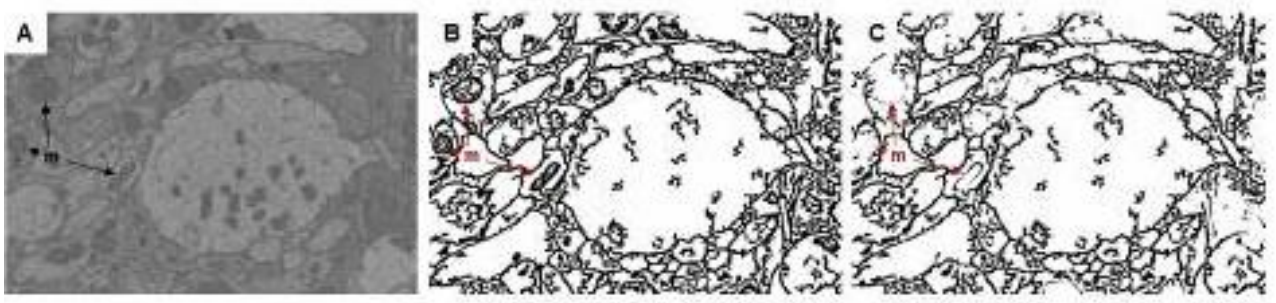

Fig. 1 A: Original micrograph B. First pre-processing step: contrasting membranes and filtering out small irregular components C. Second pre-processing step: removing mitochondria

LS2.P011
Morphological and morphometric characterisation of quadriceps muscles in a murine model of Down syndrome

B. Cisterna[1], P. Bontempi[1], M. Costanzo[1], M. Malatesta[1], C. Zancanaro[1]

[1]University of Verona, Verona, Italy

Introduction: Down syndrome (DS) is a genetically based disease caused by triplication of chromosome 21. Persons with DS exhibit severe muscle weakness associated with muscle hypotonia and deficit in motor coordination, balance and postural control. The Ts65Dn mouse is the most extensively studied murine model of DS sharing with the human condition the DS-like muscle dysfunctions. However, relatively little work has been done in this animal model to investigate the muscle-related deficit and test the efficacy of therapeutic treatments.

Objectives: This study aimed at getting deeper insight into trisomy-associated morphological, quantitative changes in the quadriceps femoris muscle using an innovative combination of light and electron microscopy, immunohistochemistry, and morphometry with magnetic resonance imaging (MRI). The effect of physical exercise was also tested by MRI measuring the same tissue components after four weeks of adapted treadmill training.

Materials & methods: Ts65Dn mice underwent MRI at baseline and after the one-month experimental period. The volume of proximal hindlimb skeletal muscle, intramuscular adipose tissue and subcutaneous adipose tissue as well as the percent proximal hindlimb intramuscular adipose tissue were considered in T2w images.After animal perfusion with a formalin solution, vastus lateralis (VL) and rectus femoris (RF) muscles were removed, further fixed and processed for either ultrastructure (OsO4 post-fixation and embedding in Epon resin) and immunohistochemistry at fluorescence microscopy (embedding in LRWhite resin). For fiber typing, muscle cross sections were incubated with a mouse monoclonal antibody recognizing the heavy chain of skeletal fast fiber myosin. The minimum Feret"s diameter (myofiber size parameter) was measured. Ultrastructural variables (Z line length, number of mitochondria and lipid droplets, mitochondrial area and cristae length) were measured in sections of Epon-embedded muscle.

Results**:** MRI acquisition showed no quantitative changes in tissue composition of the proximal hindlimb muscles, and physical exercise has similar effect in euploid and trisomic mice.A similar percentage of slow fibers was found in both VL and RF from trisomic and euploid mice. Minimum Feret"s diameter was significantly higher in trisomic vs. euploid mice in both muscles. Morphological evaluation at transmission electron microscopy highlighted that the myofibers of both VL and RF contained irregularly arrayed myofibrils with heterogeneous size and pattern, as confirmed by the Z-line length distribution. Large-sized mitochondria rich in cristae were lined between the myofibrils and in the subsarcolemmal region. In the VL muscle of trisomic mice, the sarcoplasmic reticulum was characterized by dilated cisternae and deposits of glycogen surrounding intermyofibrillar mitochondria and sarcoplasmic reticulum. Numerous lipid droplets typically associated with mitochondria were found in the RF muscle of trisomic mice.

Conclusion: The findings consistently demonstrate that, in trisomic mice, the myofibers undergo a form of myofiber hypertrophy associated with myofibrillar atrophy and mitochondrial alterations. Interestingly, the Since MRI did not reveal any quantitative differences in proximal hindlimb muscles in euploid vs. trisomic mice, it is possible that the locomotor deficit in trisomic Ts65Dn mice is also attributable to defective neuromuscular interactions and/or central nervous system damage.

LS2.P012
The 3D structural changes of cristae and mitochondrial respiratory function during the lineage development of goat large luteal cells

Y. F. Jiang[1], P. H. Yu[1], Y. P. Budi[1], C. H. Chiu[2], C. Y. Fu[3]

[1]National Taiwan University, School of Veterinary Medicine, Taipei, Taiwan
[2]National Taiwan University, Animal Science and Technology, Taipei, Taiwan
[3]Academia Sinica, Institute of Cellular and Organismic Biology, Taipei, Taiwan

Question: In mammalians, the reproductive cycles can be defined by the appearance of mature follicles (MF) or corpus luteum (CL) on the ovaries. during the transition between the follicular and luteal phase, the corpus hemorrhagicum (CH) was formed as an intermediate tissue. During the dramatic tissue remodeling in CH, the granulosa cell (GCs) of the follicle proliferated and differentiated into the large luteal cells (LLCs) for later progesterone production in CL. However, the mechanism for the balance between oxygen supply and mitochondrial energy production is still unclear in developing LLCs. Thus the current study was designed to investigate the structural changes of mitochondria during the follicle-luteal transition.

Methods: Ovaries containing mature follicles, corpus hemorrhagicum, and corpus luteum were collected from goats at specific times in the estrous cycle. The enzyme histochemistry of cytochrome C oxidase (COX) was applied to visualize mitochondria at the ultrastructural level. The mitochondrial 3D structures were reconstructed from serial sections with electron tomography. Image-based quantitative analysis on tomograms and immuno-gold labeling was performed to evaluate the respiratory function of mitochondria.

Results: The COX positive mitochondria formed a branched network in granulosa cells. While in LLCs, COX signals appeared in spherical and tubular mitochondria. The LLCs from the CH also showed low enzyme signals and content when compared with GCs or the LLCs from the CL. This result is also consistent with the expression of ATP synthase revealed by immuno-gold labeling on 2D sections.

Conclusion: Our findings suggest that the modulation of mitochondrial morphology and respiratory functions may be related to tissue remodeling during luteal formation.

Figure 1

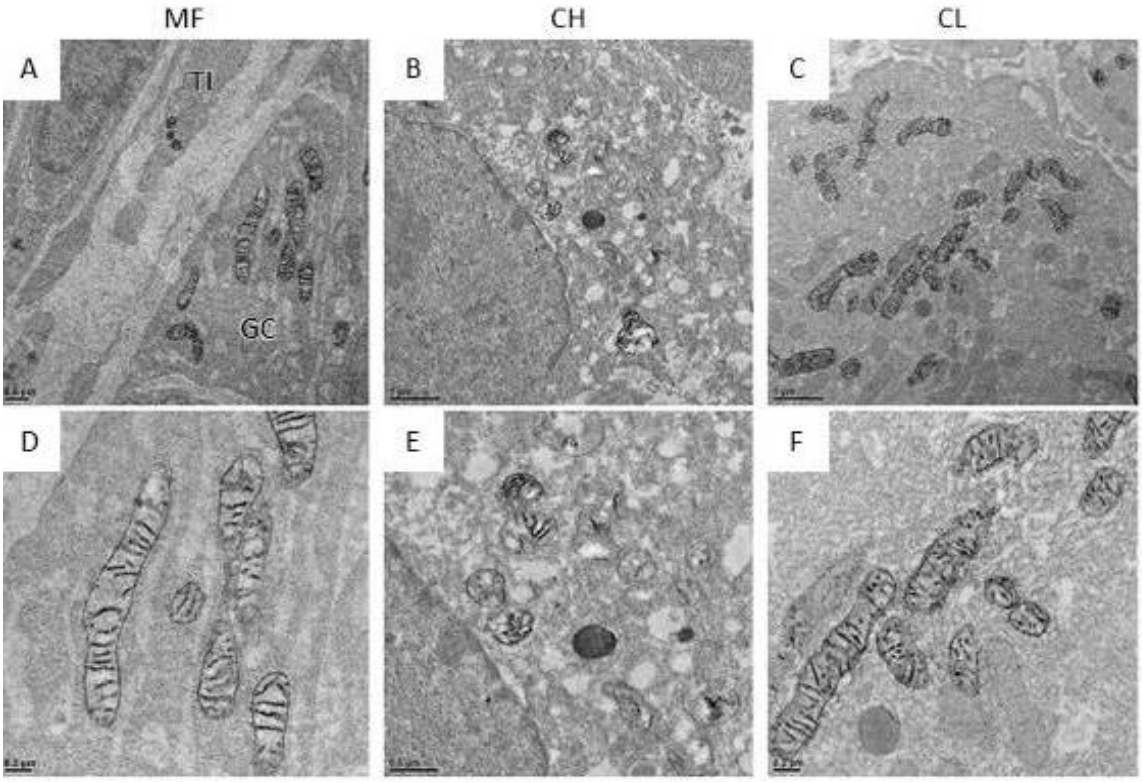

Figure 2

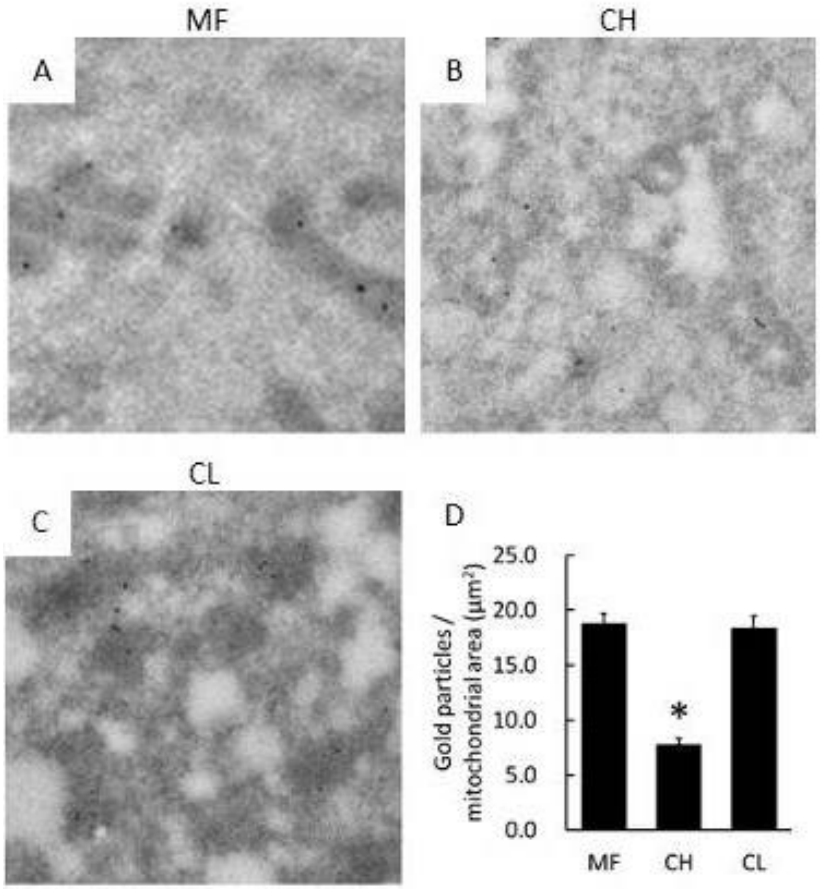

Figure 3

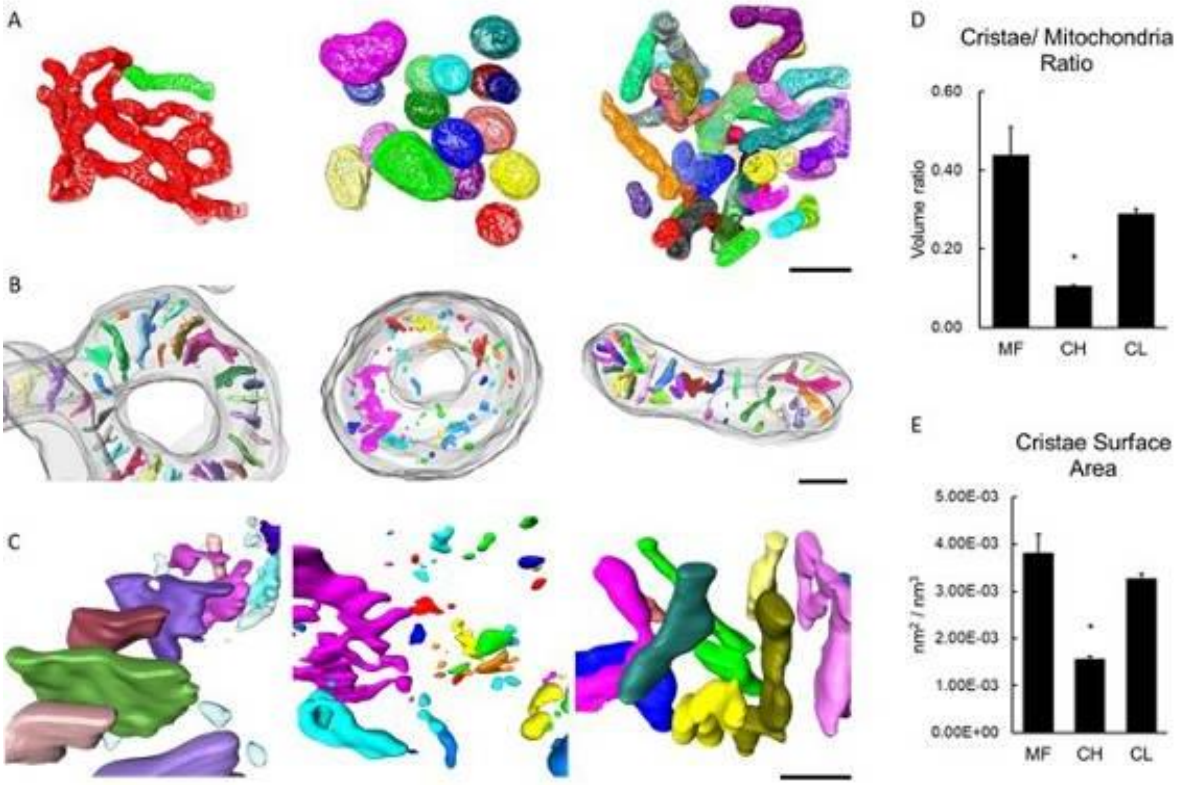

LS2.P013
High content imaging of cell-cell interactions and signaling in 3D breast cancer co-culture model

R. Ali[1], S. Huwaizi[1], A. Alsubait[1], M. Budjelal[1]

[1]King Abdulah International Medical Research Center (KAIMRC), Core Facility, Riyadh, Saudi Arabia

Introduction: The desired effect of cancer therapeutics can only be conceived when applied on complex multicellular structures with different cell types and extracellular matrix (ECM) in three-dimensional (3D) space. 3D cell culture systems have become very popular in the field of drug screening and discovery. There is an immense demand for highly efficient and easy methods to produce 3D spheroids in any cell format. Heterogeneity in size, extended cultivation times, and reproducibility for high throughput assays are limiting factors in the generation of spheroids.

Objectives: This study uses a 3D Breast cancer co-culture system to understand the dynamics of tumor microenvironment in-vitro by integrating cell biology and advanced cellular imaging.

Materials & Methods: Recently we have established a naturally transformed breast cancer cell line, KAIMRC1*1,* from ductal breast carcinoma. We have already characterized these cells grown in monolayers for the biological and molecular markers, induction of MAPK pathways, and their response to different commercially available drugs and compounds.

Results: We have developed a novel and easy method to produce spheroids from KAIMRC1 cells in vitro, which can be used as a 3D model to study proliferation, differentiation, metabolism, cell death, and cells drug response in the tumor microenvironment. We have also developed an in-vitro high content imaging (HCI) based cellular assay using commercially available compound panels to perform initial drug screening in the KAIMRC1 spheroids model (*Figure 2*).

Conclusion: Our approach allows rapid screening of a panel of drugs to assess inhibitory effects on tumor cells' growth in 3D cultures. To mimic a real in-vivo tumor microenvironment, we are now developing a real-time HCI-based assay utilizing 3D KAIMRC1 spheroids co-cultured with patient-derived fibroblast cells (*Figure 1*).

[1] Ali, Rizwan et al. "Isolation and Characterization of a New Naturally Immortalized Human Breast Carcinoma Cell Line, KAIMRC1." BMC Cancer 17 (2017)

Figure 1: (a & b) Monolayer and Spheroids co-culture of KAIMRC1 (Green) and patient-derived fibroblast-like cells (Red), respectively. (c) 3D reconstruction of co-cultured cells.

Figure 2: Schematic representation of HCI assay using breast cancer KAIMRC1 2D monolayer and 3D spheroids culture

Figure 1

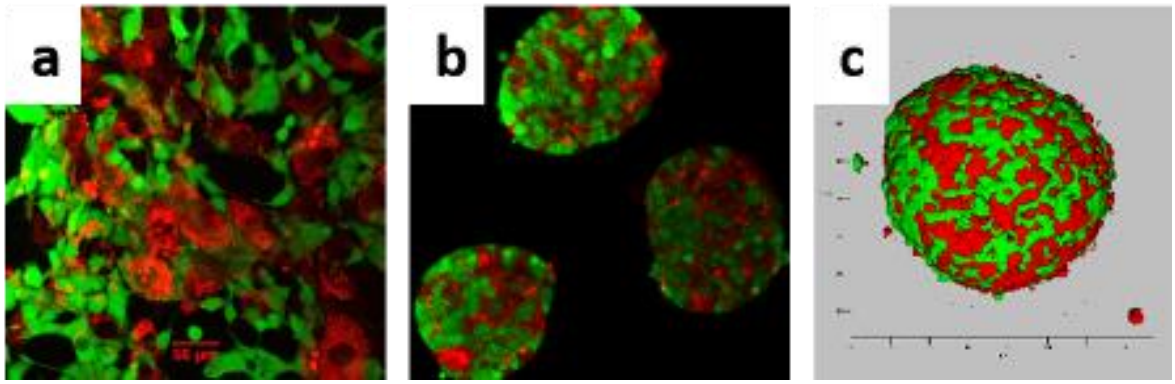

Figure 2

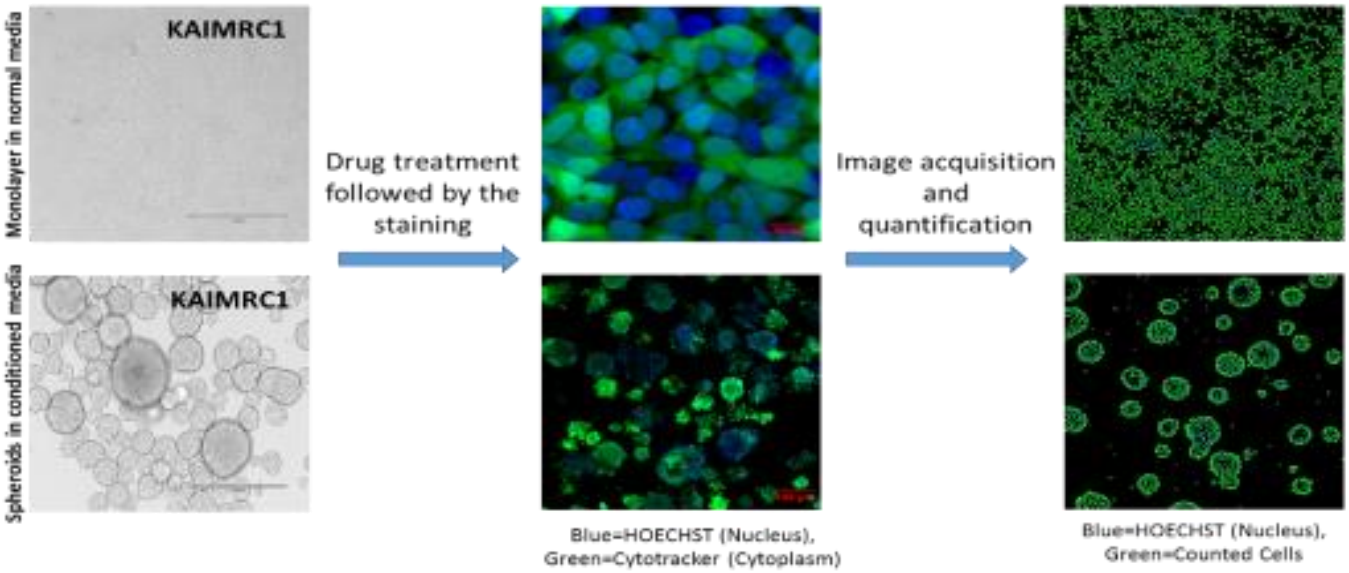

LS2.P014
Ultrastructure of the adhesive system of *Schmidtea mediterranea* (Tricladida, Platyhelminthes)

S. Willi[1], M. Nowakowski[1], D. Stock[2], R. Pjeta[1], P. Ladurner[1], M. W. Hess[3]

[1]University of innsbruck, Zoology, Innsbruck, Austria
[2]University, Department of Material Sciences, Innsbruck, Austria
[3]Medical School Innsbruck, Histology and Embryology, Innsbruck, Austria

Flatworms of the order Tricladida usually describes free-living animals, which are common to many parts of the world, living in both terrestrial and aquatic habitats. Their excellent regenerative ability and a continuously increasing molecular toolbox let them become model organisms for stem cell research since the last century. Interestingly, they also have the capacity to rapidly attach to and detach from many substrates.

We investigated the morphology of the bio-adhesive system of *Schmidtea mediterranea* with light microscopy, scanning- and transmission electron microscopy.

The adhesive system was located ventro-laterally, circumcising the entire animal, the so-called marginal adhesive zone. SEM analysis showed insunk adhesive papillae with gland necks with visible secretory vesicles and elongated microvilli. In TEM sections the adhesive organs were characterized by three types of secretory cells. Gland necks of these cells protruded the epidermis via a modified epithelial cell, called anchor cell. An adhesion related vesicle showed a homogeneous structure with a length of 668 ± 121 nm and a width of 594 ± 110 nm (n=20). Interestingly a second vesicle type showed a striated organization with a length of 777 ± 54 nm and a width of 353 ± 37 nm (n=10). Putative releasing vesicles were also found and had a diameter of 151 ± 30 nm (n=20). High pressure frozen and freeze substituted samples showed the same organization of the adhesive organ but with better preserved ultrastructure. In addition, we took advantage of a transcriptome (Rozanski et al., 2018) and single cell RNA seq data from Fincher et al. (2018) in order to identify potential candidates of adhesion related genes. Gene expression in adhesive organs was confirmed by whole mount *in situ* hybridization. Subsequently we aim to knock-down candidate genes to proof the correct identification of adhesive cells and to test the function of the respective transcript. Our investigations lead to a better understanding of the molecules involved in flatworm bioadhesion, which can pave the way towards developing innovative glues with reversible adhesive properties.

References:
[1] PlanMine 3.0-improvements to a mineable resource of flatworm biology and biodiversity.
[2] Rozanski A, Moon H, Brandl H, Martín-Durán JM, Grohme MA, Hüttner K, Bartscherer K, Henry I, Rink JC. Nucleic Acids Res. 2019 Jan 8;47(D1)
[3] Cell type transcriptome atlas for the planarian **Schmidtea** mediterranea.
[4] Fincher CT, Wurtzel O, de Hoog T, Kravarik KM, Reddien PW. Science. 2018 May 25;360(6391)

LS2.P015
Peroxisomal cooperation with mitochondria and lipid bodies in brown adipocytes of hypothyroid rats

M. Aleksic[1], A. Kalezic[2], B. Korac[2], A. Jankovic[2], A. Korac[1]

[1]University of Belgrade - Faculty of Biology, Center for Electron Microscopy, Belgrade, Serbia
[2]Institute for Biological Research "Siniša Stanković", National Institute of Republic of Serbia, University of Belgrade, Department of Physiology, Belgrade, Serbia

Introduction**:** Due to the presence of uncoupling protein 1, mitochondria are indispensable for thermogenesis (triggered by cold or cafeteria diet) in brown adipocytes. However, peroxisomes and lipid bodies are also important players in this process. Peroxisomes adjust their number, shape, and morphology to contribute to lipid metabolism and maintain cellular homeostasis. It is well known that thyroid hormone deficiency leads to altered lipid metabolism. Bearing this in mind, this study aimed to analyze the peroxisomal population in brown adipocytes in methimazole-induced hypothyroidism.

Methods: Two-month-old male Wistar rats were divided into four groups and fed standard pelleted food ad libitum. Three groups of rats were treated with a 0.04% methimazole solution in drinking water for 7, 15, and 21 days. Animals in the fourth group drank tap water and served as the euthyroid control. Interscapular brown adipose tissue was isolated and routinely processed for either light and electron microscopy analyses or used to isolate light mitochondrial fraction enriched by peroxisomes. Semi-fine tissue sections were used for catalase (CAT) immunohistochemistry, while ultrathin tissue and fraction sections were used for routine electron microscopy analyses and immunogold CAT labeling.

Results: A higher number of CAT immunopositive brown adipocytes were found in hypothyroid groups compared to euthyroid control. The number of peroxisomes, along with the intensity of immunopositivity, increased with the time-course of hypothyroidism. Immunopositive reaction, in the form of fine brown granules, which found in the cytoplasm and around lipid bodies, corresponds to peroxisomes. Immunogold CAT labeling clearly showed that peroxisome positions vary among cells, and that peroxisomal cooperation with mitochondria and lipid bodies was enhanced. Isolated peroxisomes showed two CAT immunoexpression patterns: central, in the matrix, and peripheral, in the submembrane region.

Conclusions: Our results showed that hypothyroidism leads to profound changes in the peroxisomal population of brown adipocytes. Peroxisomes change their number, structure, CAT immunoexpression, and cooperation with mitochondria and lipid bodies to maintain energy balance in altered lipid metabolism.

LS2.P016
Remodeling of septate junctions in invertebrate epithelia during digestive system and integument morphogenesis

N. Žnidaršič[1], U. Bogataj[1], K. Kunčič[1], P. Mrak[1]

[1]University of Ljubljana, Biotechnical Faculty, Department of Biology, Ljubljana, Slovenia

Introduction: Epithelia function as barriers at the external surfaces of the body as well as between different environments in the organism and regulate the transport of materials that cross this barrier. Epithelial cells are connected to each other by different junctions, which are crucial for the integrity of the tissue and for the regulation of the paracellular transport. Tight junctions in vertebrate epithelia and septate junctions (Figure 1A) in invertebrate epithelia are mainly responsible for maintaining selectively permeable seals between cells and thus for the regulation of the apico-basal transport via extracellular space. Remodeling of cell junctions, including tight and septate junctions, is required for adequate function of epithelia subjected to physiological processes that involve tissue stretching, cell-shape changes and differentiation processes during morphogenesis. This issue has gained increasing research interest, but knowledge on invertebrate cell junctions formation and dynamics is very scarce.

Objectives: In this study we aimed to identify ultrastructural modifications of septate junctions in the selected invertebrate epithelia in relation to tissue differentiation during development.

Materials & methods: Ultrastructural characteristics of septate junctions in ectodermal (epidermis, hindgut) and endodermal (digestive glands) epithelia of the arthropod *Porcellio scaber* were determined by transmission electron microscopy in several embryonic and postembryonic developmental stages. The results were evaluated in relation to tissue differentiation during development and to cell-shape changes during molting.

Results: Septate junctions comprising only a few individual septa were revealed in the hindgut and epidermis of the late stage embryo (Figure 1B). A prominent increase in the junction length corresponded to the transition from the embryonic to postembryonic stage (Figure 1C). Septate junctions in the digestive gland epithelium were structurally similar in all examined stages, but their length evidently increased in the mancae released from the female brood pouch to the external environment. In molting postembryonic specimens epidermal cells displayed a substantial shape changes and septate junctions were remodeled into short and discontinuous strings of septa. Similarly, septate junctions in the hindgut were considerably shorter in this stage than in the preceding developmental stages (Figure 1D).

Conclusion: Prominent ultrastructural modifications of septate junctions in the ectodermal gut and integument epithelia corresponded with embryo hatching from the vitelline membrane and with the transition of mancae from the brood pouch to the external environment. Septate junctions of the endodermal digestive gland epithelium were enlarged mainly in the period of release from the brood pouch. In addition, septate junctions of ectodermal epithelia were considerably remodeled during apical extracellular matrix renewal (molting) that is an essential part of integument morphogenesis.

Figure 1: Septate junctions in the hindgut epithelium of *Porcellio scaber*. A) Septate junction in the hindgut of adult animal consists of a long and convoluted string of electron dense septa. B) A short string of septa in late stage embryo. C) Septate junction in early postembryonic stage. D) A short string of septa in molting late stage marsupial manca. SJ – septate junction, AJ – adherens junction, arrowheads – cross sections of microtubules.

Figure 1

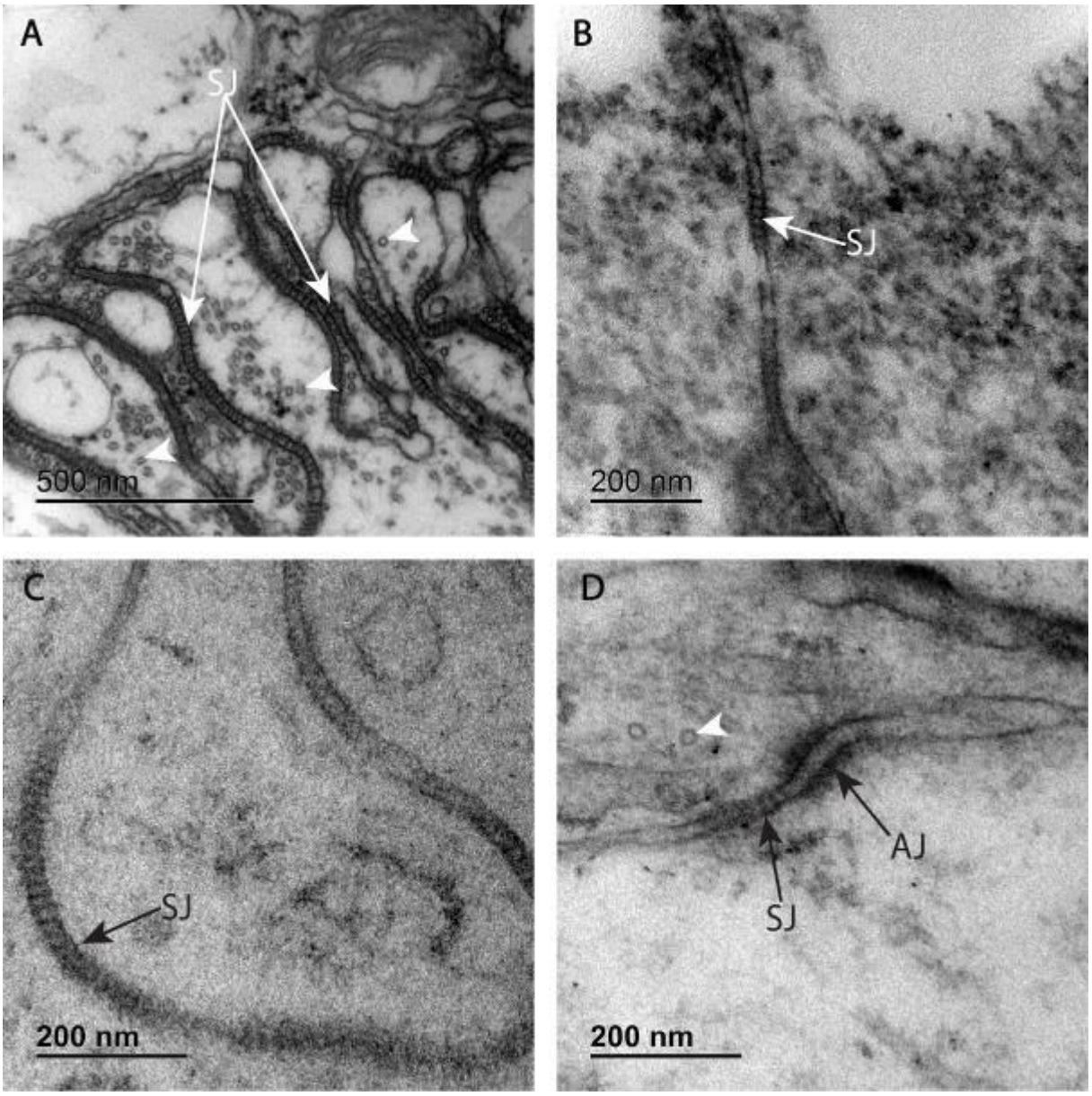

LS2.P017
Important secrets of heart tissue microscopic architectonics revealed by means of "Quantitative Functional Morphology"

T. Ghevondyan[1]

[1]Orbeli Institute of Physiology, National Academy of Science of Armenia, Laboratory of Histochemistry and Electron Microscopy, Yerevan, Armenia

Introduction: Are there any features of the microscopic structure of the myocardium that could be or are of significant importance for a human and knowledge about which may serve human health?

Objectives: To develop a systemic assessing morphological method and, with its help, to reveal the presence of the myocardial architectonic peculiarities and to clarify their functional significance.

Material and methods: Autopsied 140 human whole hearts were investigated. The "system of capillary-myocardial fiber" was investigated in 39 hearts of practically healthy people died from violent reasons (24-87 years) and 20 autopsied heart of patients died from first myocardial infarction (50-89 years). The post-mortem microangiography, organometry, planimetry, histological, morphometrical, stereological methods were used. For integrative assessment of received data a new kind of mathematical modeling: "Quantitative Functional Morphology" (QFM) was developed and used.

Results: QFM is a complex of morphological, morphometric, stereological, mathematical methods that allows "measuring the value of the main function of tissue in a histological slide". This mathematical model allows to measure the "time of the virtual saturation of a unit volume of myocardial fibers with oxygen" - "t").

A significant variation of (t) was found in different 12 parts of the heart left ventricle wall.

A wide variation of the "t" index was found in the hearts of healthy people. In order to exclude the influence of external factors during life on the architectonics of the myocardium, we have created homogeneous groups of cases. Within these groups, a wide variation of the "t" remained. There is also a variation in the value of the "t" index in the hearts of people who died from the myocardial infarction. Despite the variation in the value of the "t" index, the average value of the "t" in hearts with myocardial infarction was significantly and reliably higher than the value of the index for healthy people.

Discussion: Variations in the value of the index "t" in different parts of the left ventricular wall can be explained by differences in contractile loads that different parts experience during systole. The minimization of the possible influence of external factors on remodeling of the myocardium was achieved by composing homogeneous groups. Cases of patients with only the first myocardial infarction were specially selected in order to exclude the influence of postinfarctional cardiac remodeling on parameters of myocardium. The obtained results serve a basis to state that the detected variations are due to innate, possibly hereditary properties of bodies. Perhaps a significant delay of oxygen supply to myocardial fibers can be another explanation for the phenomenon of angina pectoris in rest with relatively intact coronary arteries or moderate stenosis.

Conclusion: A developed QFM method allows revealing the functional state of the myocardium, which objectively has existed, but is invisible in slides. The greater the value of the "t", the worse the lifetime oxygen supply of myocardial fibers, the higher the likelihood of hypoxic and ischemic myocardial injury, suffering or angina pectoris, the early onset of myoacardial infarction.

Therefore, a high value of the "t" index for the capillary-myocardial fiber system should be considered as a risk factor for ischemic heart disease. The lifetime early identification of this risk factor is priority.

LS2.P018
Electron microscopic analysis of the development of multiciliated cells in the respiratory epithelium of the concha nasalis media in the chicken embryo

S. Reinke[1], A. Reinke[1], M. Frank[1,2]

[1]University Medicine Rostock, Medical Biology and Electron Microscopy Centre, Rostock, Germany
[2]University of Rostock, Life, Light & Matter, Rostock, Germany

Introduction: Cilia are highly conserved cell organells which protrude from the cell surface and contain an array of microtubuli that extends from a basal body. While monocilia are present in many cell types, the generation of multiciliated cells is restricted to specialized epithelia. Until now little is known regarding the development of multiciliated cells in the avian respiratory epithelium. In the chicken, the nasal chamber consists of three conchae nasales: the concha nasalis rostralis is lined by squamous epithelium whereas the concha nasalis media is covered with respiratory epithelium bearing multiciliated cells. The concha nasalis caudalis harbours mainly olfactory epithelium.

Objective: Here we have investigated the development and spatial extension of multiciliary cells in the nasal conchae of the embryonic chicken covering developmental stages E12 to E18.

Materials & Methods: Chicken embryos of (var. white leghorn) were collected from eggs after 12 to 18 days of incubation and the ciliated epithelia in the concha nasalis media and adjacent regions were examined on coronary slices using scanning electron microscopy (SEM) as the primary research method. In addition immunohistochemical analysis with antibodies to acetylated tubulin, a well-established ciliary marker, has been used.

Results: At E12 to E13 no elongated cilia have been detected on epithelial cells of the concha nasalis media. Starting at E14 the formation of elongated monocilia on the cell surface is observed. Following E14.5 first multiciliated cells are found alongside many monociliated cells. At E15 this trend continues with an increase in number of multiciliated cells that show growing cilia with different lengths of the ciliary axoneme whereas only a few cells remain with extended monocilia at E16. Regarding E17 such monociliated cells are largely absent and most multiciliated cells have grown a large number of individual cilia to their final length. The epithelial surface starts to show grooves which further increase in depth at E18.

Our analysis of ciliogenesis included adjacent areas as well and we noted that multiciliated cells are much earlier detectable in the nasal septum, at places starting as early as E13. Immunohistochemistry is able to show multiciliated cells and works well to outline the transitions and borders between distinct epithelial areas in a larger region.

Conclusion: In the respiratory epithelium of the conchae nasalis media cells with extended monocilia are present at E14 while first multiciliated cells on the concha nasalis media appear at stage E14.5. The development of the multicilated cells in the respiratory epithelium on the conchae nasalis media is completed in a short time period of approximately three days. The ciliogenesis in the concha nasalis media of the embryonic chicken is similar to the development in the trachea which has been examined previously by our group. However, a distinct earlier onset of ciliogenesis was noted in the nasal septum starting around E13.

Figure 1: SEM pictures of the respiratory epithelium at the concha nasalis media on embryonic stages E14.5 and E18, scale bars are 6µm.

Figure 1

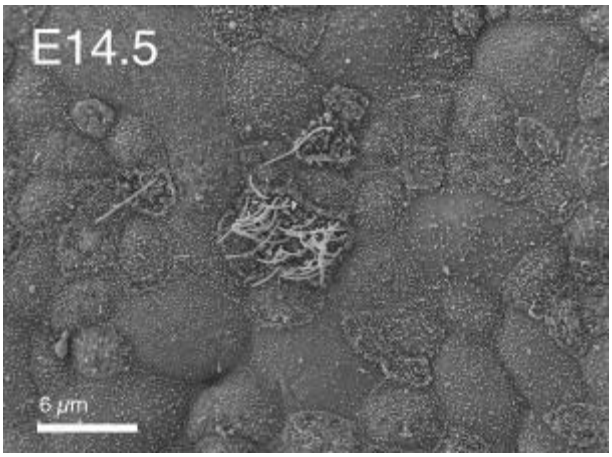

Figure 2

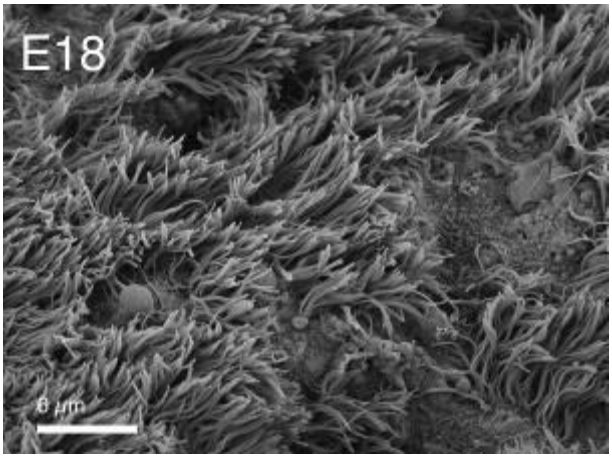

LS3.002-Invited
The coronavirus escape room

G. Wolff[1], R. Limpens[1], D. Agard[2], K. Grünewald[3], A. Koster[1], E. Snijder[1], M. Bárcena[1]

[1]Leiden University Medical Center, Leiden, The Netherlands
[2]University of California San Francisco, San Francisco, United States
[3]Universität Hamburg, Hamburg, Germany

Coronaviruses, like all positive-strand RNA viruses infecting eukaryotes, replicate their genomes in association with intracellular membranes that are transformed by the virus into specialized compartments. These so-called viral replication organelles provide tailored micro-environments that could accumulate relevant factors for the process of viral RNA synthesis while shielding viral replication intermediates from innate immune sensors.

The coronavirus replication organelle is particularly complex and includes several types of interconnected virus-induced double-membrane structures that are derived from the endoplasmic reticulum. Using EM autoradiography, we demonstrated that the process of viral RNA synthesis is specifically associated with characteristic double-membrane vesicles (DMVs) that are derived from the endoplasmic reticulum and accumulate in the perinuclear region. DMVs are not exclusively induced by coronaviruses, but also by other members of the *Nidovirales* order, as well as picornaviruses, hepatitis C virus and noroviruses. Intriguingly, a peculiarity of all the nidovirus-induced DMVs is that they appear in conventional EM as closed structures lacking openings to the cytosol. Therefore, how newly made viral RNA could be exported from these sealed DMVs to the cytosol for translation and packaging into progeny virus particles has long been unclear.

Cellular cryotomography of FIB-milled cryolamella allowed us to analyze coronavirus-induced DMVs in native conditions and in the natural context of the infected cell. Strikingly, our data unveiled a molecular pore spanning the two membranes of the DMVs induced by murine hepatitis virus (MHV). This DMV pore was also detected in cells infected with the severe acute respiratory syndrome coronavirus 2 (SARS-CoV-2), which were chemically fixed prior to cryo-immobilization in compliance with biosafety regulations. Using subtomograms averaging, we determined the structure of the molecular pore in MHV-induced DMVs to ~3 nm resolution. The average reveals an hexameric crown-shaped complex of ~3 MDa assembling around a central channel that connects the DMV lumen with the cytosol. Moreover, using a recombinant virus expressing GFP, we established that six copies of the largest viral transmembrane non-structural protein, nsp3, constitute the core of this molecular pore. Our findings support the notion that this is a conserved coronavirus complex that would serve as an RNA export portal and would therefore have a key role in the viral replication cycle.

We have expanded our investigations to arteriviruses, a distantly-related nidovirus family, and found similar pores in the DMVs induced by these viruses. Our results suggest that double-membrane spanning molecular pores are a general feature of nidovirus replication. Moreover, recent cryo-EM studies have documented viral oligomeric complexes that would control transit to/from the replication organelles of noda- and alphaviruses. Collectively, these results suggest that viral RNA export complexes in replication organelles may well be a common theme across positive-strand RNA viruses. This new class of viral complexes offers novel targets for future antiviral strategies.

LS3.003
In-situ fiducial markers for correlative cryo- FM and FIB-SEM imaging

N. Scher[1], K. Rechav[2], P. Paul-Gilloteaux[3], O. Avinoam[1]

[1]Weizmann Institute of Science, Biomolecular Sciences, Rehovot, Israel
[2]Weizmann Institute of Science, Electron Microscopy Unit, Chemical Research Support, Rehovot, Israel
[3]Université de Nantes, Structure Fédérative de Recherche François Bonamy, INSERM, CNRS, Nantes, France

Imaging of cells and tissues has improved significantly over the last decade. Dual-beam instruments with a focused ion beam mounted on a scanning electron microscope (FIB-SEM), which offer high-resolution 3D imaging of large volumes and fields-of-view are becoming widely used in the life sciences. FIB-SEM has most recently been implemented on fully hydrated, cryo-immobilized, biological samples. However, correlative light and electron microscopy (CLEM) workflows combining cryo- fluorescence microscopy (cryo-FM) and FIB-SEM are not yet commonly available. In our work, we demonstrate that fluorescently labeled lipid droplets can serve as *in-situ* fiducial markers for correlating cryo- FM and FIB-SEM datasets, and that this approach can be used to target the acquisition of large FIB-SEM stacks spanning tens of microns under cryogenic conditions. We also show that cryo-FIB-SEM imaging is particularly informative for questions related to organelle structure and inter-organellar contacts, nuclear organization and mineral deposits in cells.

LS3.004
Comparison of conventional and scanning TEM for biological imagin

M. L. Leidl[1,2], H. L. Robert[1,2], C. Sachse[1,3], K. Müller-Caspary[1,2]

[1]Ernst Ruska-Centre for Microscopy and Spectroscopy with Electrons, Jülich, Germany
[2]RWTH Aachen University, 2nd Institute of Physics, Aachen, Germany
[3]Heinrich-Heine-Universität Düsseldorf, Biology, Düsseldorf, Germany

Cryo-EM methods used in biology employing conventional TEM (CTEM) using plane wave illumination suffer from weak phase contrast. Therefore, CTEM images are typically taken at large defocus to convert phase into amplitude contrast. Consequently, one must deal with contrast reversals by a fast-oscillating coherent transfer function (CTF).

This work first briefly addresses the effects of multiple scattering and propagation in CTEM-based cryo-EM for Apoferritin (PDBe: 7a6a) [1]. Because STEM shows potential for low dose imaging with a high dose-efficiency of contrast [2], we here present a study of the capability of different phase-contrast scanning TEM (STEM) methods to yield contrast at in-focus-conditions.

We perform multislice CTEM and STEM simulations for eight slices and compare it to a single slice (phase approximation). An example is shown in Figure 1. To take into account the low dose, Poisson noise is applied to the simulations and effects such as scattering and propagation in the surrounding amorphous ice are discussed in detail. Comparing the CTEM simulations for a defocus of 100 nm with infinite dose for one and eight slices we found that 10 % of the pixels show a relative deviation larger than 1.8 %. To compare the CTEM image with the potential that was used in the multislice simulation (ground truth), we choose to calculate the Fourier ring correlation (FRC) [3]. The results for an objective aperture radius of 8 mrad equivalent to a resolution of 2.5 Å are shown in Figure 2. The oscillating FRCs are due to the oscillating CTF.

Special attention is drawn to the STEM simulations, for which different signals are calculated with the focus on first moment and differential phase contrast (DPC) [3]. Subsequently the first moment is used to calculate the charge density, which is used to calculate the potential by numerically solving the Poisson"s equation, which can then be compared again to the ground truth. The FSC curves for one and eight slices for a semi-convergence angle of 4 mrad are shown as the red curves in Figure 2. For higher angles, i.e., spatial frequencies, the multislice simulation with eight slices shows a higher correlation. The dip near 0 mrad will be addressed in future studies, for example by evaluating the influence of defocus and the impact of the CTF.

Our results demonstrate that it is promising to perform experimental studies to evaluate the benefits of STEM imaging in the field of cryo-EM in the field of biology. In the future it would be also interesting to investigate the potential of ptychographic methods in this field [2].

Figure 1: Phase of the projected phase grating filtered to frequencies smaller than 8 mrad in a) the potential calculated from the first moment for a semi-convergence angle of 4 mrad in b) and the same simulation binned by a factor of two with a dose of 30 e/Å^2 in c).

Figure 2: Shown are the FSC curves for an objective aperture of 8 mrad and a semi-convergence angle of 4 mrad.

[1] Funding: Helmholtz IVF under contracts VH-NG 1317 (moreSTEM) and ZT-I-0025 (Ptychography 4.0).
[2] L. Zhou et al., "Low-dose phase retrieval of biological specimens using cryo-electron ptychography", nature COMMUNICATIONS, 2020.
[3] M. v. Heel et al., "Fourier shell correlation threshold criteria," Journal of Structural Biology, 2005.
[4] H. Rose, "NONSTANDARD IMAGING METHODS IN ELECTRON MICROSCOPY," Ultramicroscopy, 1977.

Figure 1

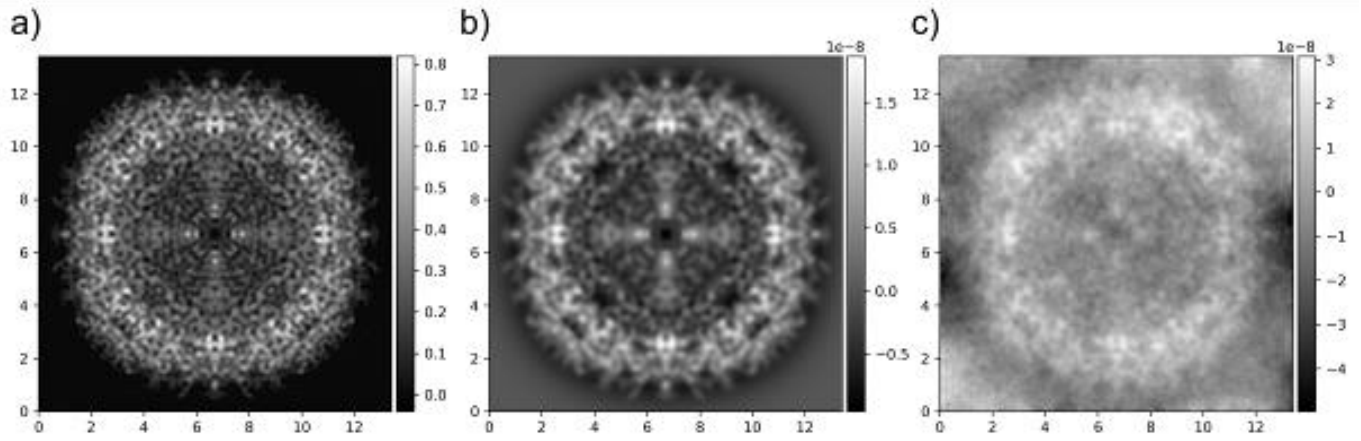

Figure 2

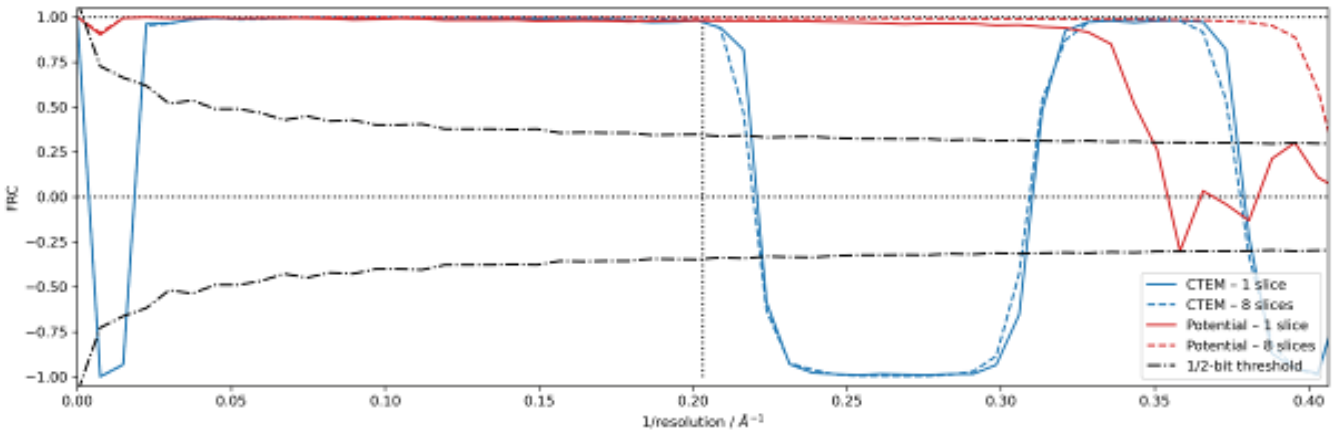

LS3.005
Structural difference of *ex vivo* amyloid fibrils from *in vitro* formed fibrils

M. Schmidt[1], A. Bansal[1], M. Fändrich[1], C. Haupt[1]

[1]University of Ulm, Ulm, Germany

Systemic AA amyloidosis is a world-wide occurring protein misfolding disease of humans and animals. It arises from the formation of amyloid fibrils from serum amyloid A (SAA) protein. Using a SAA mouse model we can study question relevant to amyloid diseases.

Because it is not always easy or possible to obtain ex vivo fibrils, a big question in the field of structural analysis of amyloid fibrils is always how similar are in vitro fibrils from disease relevant fibrils.

Using cryo electron microscopy we could study amyloid fibrils at high resolution which were purified from AA amyloidotic mice and also in vitro formed recombinant SAA fibrils. By comparing both structural models from each reconstruction a structural difference can be shown.

Ex vivo amyloid fibrils consist of fibril proteins that contain more residues within their ordered parts and possess a higher β-sheet content than in vitro fibril proteins. They are also more resistant to proteolysis than their in vitro formed counterparts. These data suggest that pathogenic amyloid fibrils may originate from proteolytic selection, allowing specific fibril morphologies to proliferate and to cause damage to the surrounding tissue.

LS4.001-Invited
Translation of killing based into differentiation based therapy of malignant diseases using nanotechnology: Getting out of the vicious circle.

S. Mijatović[1], A. Korać[2], G. N. Kaluđerović[3], D. Maksimović-Ivanić[1]

[1]Institute for Biological Research “Siniša Stanković”, National Institute of Republic of Serbia, University of Belgrade
[2]University of Belgrade-Faculty of Biology, Center for Electron Microscopy
[3]Department of Engineering and Natural Sciences, University of Applied Sciences, Merseburg

There is growing evidence about tumor promoting features of dying cells in advanced tumor tissue. Crosstalk between dying and surrounding cells often leads to tumor repopulation, local immuno-suppression and metastasis. Consequently, resistance to chemotherapy is rather connected to proliferative response to cell death induced by the therapy than to development of apoptotic resistant phenotype of individual cell. As an alternative approach that will avoid chemotherapy induced tumor repopulation, induction of cell differentiation emerges. Until today, different naturally/synthetic compounds able to convert non/low differentiated malignant cell into less invasive or normal cell like phenotype have been discovered. It was also found that not just the type of the drug, but also dynamic of drug delivery, can define its action and replace cell death induction with non-aggressive tumor suppression.

Objectives: This lecture will give insight into usage of SBA-15 mesoporous silica nanomaterial as a biocompatible drug carrier of metal based chemotherapeutics in terms of improved stability, drug efficacy, and conversion of killing-based to differentiation-inducing property.

Material and methods: Antitumor effect of SBA-15 mesoporous silica nanoparticles loaded with organotin(IV) compound has been evaluated on two melanoma cell lines - less invasive B16 mouse and highly aggressive, anaplastic human melanoma cell line - A375 and singeneic model of melanoma in C57BL6 mice. Cell viability has been determined by MTT and CV. Cell death, proliferation, senescence and production of reactive oxygen/nitrogen species have been estimated by Flow cytometry. Biochemical assays, light microscopy and TEM were used for detection of melanoma cell differentiation. The protein expression relevant for stem maintenance has been assessed by WB.

Results: Melanoma cells internalized drug loaded nanoparticles after 2 h of incubation through passive fluid-phase uptake and macropinocytosis, thus leading to later phenotype changes and loss of malignant potential in both- B16 and A375 cells. In contrast to free immobilized compound induced cell differentiation, an effect previously unknown for metal-based drugs and nanomaterial alone. The strong therapeutic potential was achieved in lower dose range than in the case of the free drug, reflected on morphological, biochemical and ultra-structural features of treated melanoma cells. While anaplastic A375 cells lost stemness and became senescent, B16 cells differentiated into more mature, melanocyte like phenotype. Abolished tumor growth observed in syngeneic model *in vivo* confirmed *in vitro* obtained data, showing that applied treatment was safe and highly efficient.

Conclusion: In opposite to free drug, organotin(IV) compound loaded into mesoporous silica SBA-15 nanocarriers induced melanoma cell reprograming. In this form agent prevented tumor repopulation as a tissue reactive response to cell damage, opening the interest for nanotechnology application in nonaggressive treatments of advanced solid tumors.

LS4.002-Invited
Microscopy analyses in nanomedicine – a new springtime for long-established histochemical techniques

M. Malatesta[1]

[1]University of Verona, Department of Neurosciences, Biomedicine and Movement Sciences, Verona, Italy

Introduction: With the advent of nanomedicine, in the Nineties of the last Century, the knowledge of the interactions of nanomaterials with the biological environment has taken on major importance, in order to set up safe and effective nanoconstructs for diagnostic and therapeutic purposes. The precise and unequivocal detection of nanoconstructs inside cells and tissues is, in fact, essential to investigate their biodistribution, especially with respect to their uptake mechanisms, intracellular trafficking and degradation. This novel experimental demand opened the way to the challenging field of histochemistry applied to nanomedicine.

Objectives: This lecture will give an overview of the histochemical methods used to track nanoparticles in cells and tissues at light and transmission electron microscopy (TEM).

Materials & methods: Tissues and cells treated with organic or inorganic nanoparticles were fixed and submitted to various histochemical protocols aimed at labelling the nanoconstructs with dyes, fluorochromes or antibodies, to make them visible at light (bright field or fluorescence) microscopy and/or TEM.

Results: Incorporation of appropriate fluorophores upon nanoconstruct synthesis is the most commonly used method to label nanoparticles for light microscopy, but this approach may be unsuitable when the sample is characterized by a high autofluorescent signal, or when the nanoconstructs are unable to retain the fluorophore for sufficient time or under certain experimental conditions. In these cases, specific staining procedures may be used. Iron-based nanoparticles have been detected at light microscopy by the classical Prussian Blue staining method. Phosphatidylcholine-based nanoconstructs have been efficiently and stably labelled using dyes usually applied for cell membrane staining. Hyaluronic acid-based nanoparticles have been made visible at bright field microscopy by adapting the critical-electrolyte-concentration Alcian Blue method; since this staining gives rise to an electron dense granular product, these nanoparticles could also be visualized at TEM, which made it possible to analyse in detail their uptake, intracellular interactions and degradation. The application of the histochemical procedure for the photo-oxidation of diaminobenzidine allowed the conversion of the fluorescent signal of fluorochrome-labelled nanoparticles into a stable electron dense, finely granular reaction product visible at the high spatial resolution of TEM. This method proved to be crucial to visualize at the ultrastructural level nanoconstructs made of organic material (such as lipid or polysaccharides) that have a moderate electron density thus being hardly visible inside the cell, in the absence of an appropriate staining. Finally, immunocytochemistry was used to specifically detect molecules loaded into nanocarriers, thus tracking their dynamics inside the biological environment at both light and electron microscopy, according to the type of the antibody marker.

Conclusion: The great development of scientific research in nanomedicine caused the extensive use of microscopy techniques to clearly visualize nanoconstructs in tissues and cells at light and electron microscopy. This resulted in a new springtime for long-established histochemical techniques, which proved to be timeless yet modern in meeting the novel experimental needs of the nanomedical field.

LS4.003
Induction of apoptosis on oral squamous carcinoma cells by electrochemotherapy

M. Condello[1], G. D'Avack[1], E. P. Spugnini[2], R. Vona[3], S. Meschini[1]

[1]Italian National Institute of Health, National Center for Drug Research and Evaluation, Rome, Italy
[2]Regina Elena Cancer Institute, SAFU Department, Rome, Italy
[3]Italian National Institute of Health, Center for Gender-Specific Medicine, Rome, Italy

Question: Electrochemotherapy (ECT) is an innovative strategy to overcome the multidrug resistance (MDR) of various neoplasms. This anticancer treatment combines the administration of chemotherapy with the application of electrical pulses having waveforms capable of increasing the effectiveness of the drug with a non-toxic and well tolerated mechanical system. Its efficacy, as an adjuvant therapy, has already been demonstrated in veterinary patients, in combination with different drugs (1). Our initial data focus on the effect of doxorubicin on human colon cancer MDR cells (LoVo DX) confirming the chemosensitizing effect of ECT through biphasic pulse trains (2).

To investigate the role of electroporation (EP) in combination therapies, we analyzed two squamous carcinoma cell lines, tongue (CAL27) and pharynx (FaDu), using mitomycin C (MMC) as chemotherapeutic drug.

Methods: The main methods used are: cell cultures, flow cytometry, MTT assay, optical and fluorescence microscopy, scanning electron microscopy and Western Blotting.

Results: Tumor cell lines were characterized for MDR transporter expression, as P-glycoprotein (P-gp). Flow cytometric analysis showed that both cell lines did not have P-gp on cell surface, but FaDu cells expressed more intracellular P-gp than Cal 27 cells. MTT assay showed that the single treatments, EP or MMC, did not induce alterations in cell viability compared to the value of the control cells. However, combined treatment (EP + MMC) showed a 30% reduction in cell viability. Optical microscopy observations confirmed the cytotoxic effect induced by combined treatment. Specific experiments aimed at understanding how electroporation carries out its potentiating action demonstrated the induction of apoptosis on both lines. The evaluation of this phenomenon was carried out by flow cytometric Annexin V/propidium iodide assay, by fluorescence microscopic observations of cytochrome c release, and western blotting analysis of pro-apoptotic protein expression change. Finally, scanning electron microscopic observations of FaDu (Figures 1A and 1B) and Cal 27 cells (Figures 1C and 1D) confirmed this effect showing consistent alterations of cell integrity and blebs appearance of different size.

Figure 1: Scanning electron microscopy images of FaDu cells after 24 hours (A), FaDu cells after 48 hours (B), CAL 27 cells after 24 hours (C), CAL 27 cells after 48 hours (D) of combined treatments (EP plus MMC).

Conclusions: A better understanding of drug resistance mechanisms is needed to guide future cancer treatment and achieve better outcomes. In particular, future studies will consider other parameters that could be involved in resistance mechanisms other than the overexpression of transport proteins, such as protective autophagy induced by many chemotherapeutics.

References:
[1] Spugnini EP, Baldi A. Electrochemotherapy in veterinary oncology: state-of-the-art and perspectives. Vet Clin North Am Small Anim Pract. 2019;49(5):967-979.
[2] Meschini S, Condello M, Lista P, Vincenzi B, Baldi A, Citro G, Arancia G, Spugnini EP. Electroporation adopting trains of biphasic pulses enhances in vitro and in vivo the cytotoxic effect of doxorubicin on multidrug resistant colon adenocarcinoma cells (LoVo). Eur. J. Cancer 2012; 48: 2236-43.

Figure 1

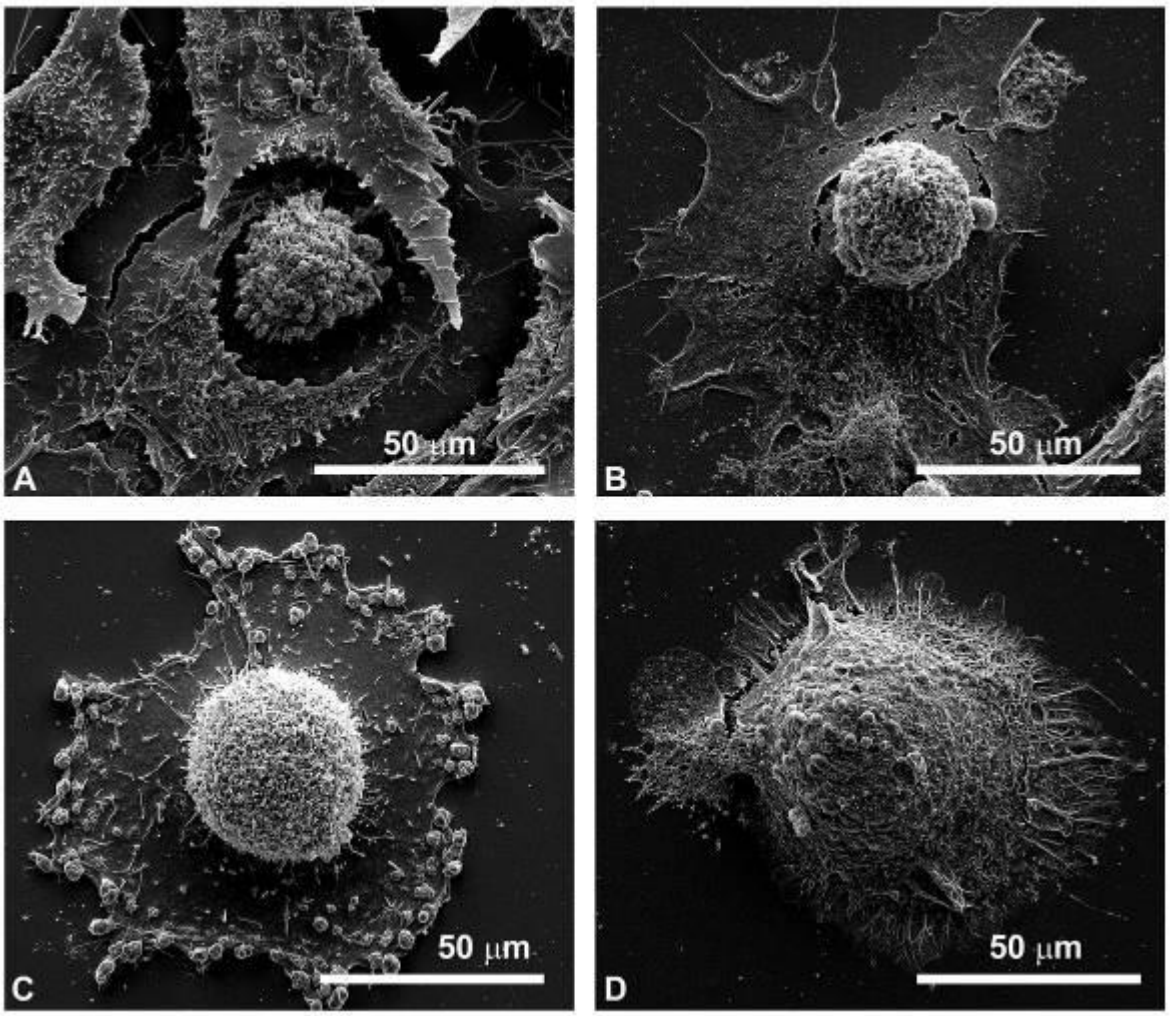

LS4.004
Combined chemical and structural imaging reveals silver and cell fate within 3D hepatic spheroids exposed to silver nanoparticles

Y. Rekik[1,2], V. Tardillo Suàrez[3], V. Raj Sharma[1,2], B. Gallet[4], P. Charbonnier[1], R. Tucoulou[3], M. Chevallet[1]
G. Veronesi[1,3], P. H. Jouneau[2], A. Deniaud[1]

[1]CEA Grenoble/IRIG, Laboratoire de Chimie et Biologie des Métaux (LCBM), Grenoble, France
[2]CEA Grenoble/IRIG, Laboratoire de modélisation et d'exploration des matériaux (MEM), Grenoble, France
[3]The European Synchrotron (ESRF), Grenoble, France
[4]Institut de biologie structurale (IBS), Grenoble, France

Introduction: The liver plays a central role in Human metabolism. It is for instance, involved in the metabolism of xenobiotics including nanodrugs. In order to properly model the fate of these compounds, we developed different types of hepatic spheroids made of hepatocyte cell lines. The cultured spheroids reproduce liver metabolic functions and excretion into the bile canaliculi [1]. In recent years, we have analyzed the fate of silver nanoparticles (AgNPs) in 2D hepatocyte cultures [2, 3]. AgNPs are widely used in consumer goods and medical devices and concerns about their toxicity to humans have been raised [4]. 2D hepatic cultures showed that endocytosed AgNPs release Ag(I) ions throughout the cell. However, AgNP fate under long-term *in vivo* exposure remains puzzling.

Objectives: We used 3D hepatic spheroids to study the fate of silver species upon long-term exposure to AgNPs and a silver salt using a combined chemical and structural analysis via the use of X-ray fluorescence microscopy (XRF) and focused ion beam-scanning electron microscopy (FIB-SEM), respectively. The goal is to study the fate of cell and the transformations of silver species and their trafficking up to excretion in bile canaliculi.

Materials and methods: Hepatic spheroids were exposed to different silver species for up to 7 days: polyvinylpyrrolidone-coated AgNPs (PVP-AgNPs), citrate-coated AgNPs (cit-AgNPs) and $AgNO_3$. After high pressure freezing and resin embedding of the samples, spheroid sections were analyzed by XRF and sample blocks were then imaged by FIB-SEM. After acquisition, cellular organelles were reconstructed in 3D at nanometric resolution.

Results: The combination of XRF and FIB-SEM imaging showed that AgNPs are heavily transformed inside endolysosomes and their excess is stored into vacuoles. Besides, upon transformations, AgNPs release Ag(I) ions that are excreted into bile canaliculi. Interestingly, the exposure to an Ag salt highlighted the formation of Ag-containing particles inside vesicles; a result which would confirm hypothesis made from studies on mice.

Furthermore, the comparative FIB-SEM analysis of the differently-exposed spheroids highlight morphological changes in the mitochondrial network upon exposure to AgNPs, such as mitochondria elongation with PVP-AgNPs for reasons that are not entirely clear at this time.

Figure 1: *XRF and FIB-SEM analysis of AgNPs-exposed spheroids. (A) and (B) XRF maps of a spheroid section. (C) Electron micrograph of a spheroid. (D) and (E) 3D reconstructions from FIB-SEM images. Mitochondria are shown in green, nuclei in pink, Ag-containing vesicles in blue and AgNPs in black.*

Conclusion: In conclusion, the complementary XRF and FIB-SEM analysis of hepatic spheroids exposed to different silver species revealed pioneer results in the understanding of AgNP fate in the liver. In addition, this study emphasized the relevance of spheroids to recapitulate *in vivo* events.

References:
[1] V. R. Sharma, et al., *Biomater. Sci.*, 2019, 8, 485–496.
[2] G. Veronesi, et al., *Nanoscale,* 2016, 8, 17012-21.
[3] V. Tardillo Suàrez, et al., *Environ. Sci. Nano*, 2020, 7, 1373–1387.
[4] S. Chernousova, and M. Epple, *Angewandte Chemie*, 2013, 52, 1636-1653.

Figure 1

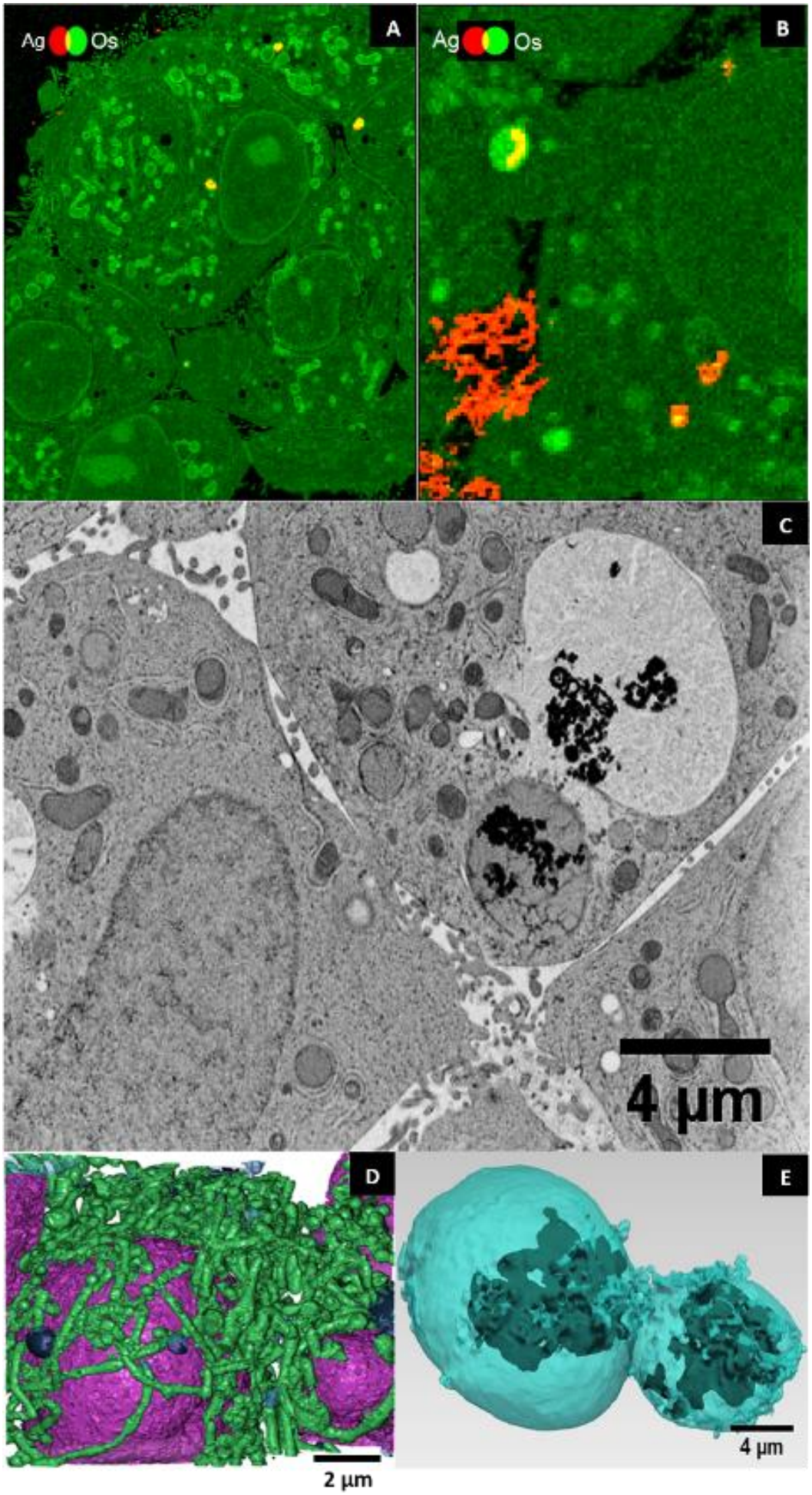

LS4.005
Pentamidine-loaded hyaluronic acid nanocarriers reduce nuclear foci accumulation in a myotonic dystrophy type 1 cell model

M. Repellin[1,2], F. Carton[1,3], M. Galiè[1], G. Lollo[2], M. Malatesta[1]

[1]University of Verona, Department of Neurosciences, Biomedicine and Movement Sciences, Anatomy and Histology Section, Verona, Italy
[2]University of Lyon, Université Claude Bernard Lyon 1, CNRS, LAGEPP UMR 5007, Villeurbanne, France
[3]University of Eastern Piedmont, Department of Health Sciences, Novara, Italy

Introduction: Myotonic Dystrophies (DMs) are the most common adult neuromuscular diseases, involving multiple organs and particularly skeletal muscles. The molecular causes rely on the abnormal expansion of repeated nucleotide sequences located in specific genes. These mutant sequences are then transcribed into expanded RNAs sequences that sequester splicing factors such as Muscleblind-like (MBNL) proteins, forming typical hairpin structures called nuclear foci. Currently, treatments are aimed only at mitigating symptoms but not at treating the molecular causes. Pentamidine (PTM), an FDA-antiparasitic drug, proved to reverse the splicing defects in a DM type 1 (DM1) mouse model; however, the benefits were impaired by substantial toxicity. To overcome this issue, we encapsulated PTM into hyaluronic acid nanocarriers (HA-NPs) to safely deliver the drug to skeletal muscle cells and reverse the splicing defects. The aim of the present investigations was to assess the therapeutic efficacy of PTM-loaded HA-NPs to disrupt nuclear foci into C2C12 transfected cells as a DM1 in vitro model.

Materials and methods: PTM-loaded HA-NPs were prepared by ionic gelation technique. Murine C2C12 myoblasts were cultured in Dulbecco"s modified Eagle medium at 37°C in a 5% CO2 humidified atmosphere. DM1 cell model was established by transfecting C2C12 cells with human genomic segments carrying 0 or 960 interrupted CTG repeats. For cytotoxicity assays, MTT viability tests were performed on C2C12 cells at 2, 24 and 48h after administration of PTM as-in or loaded into HA-NPs. Efficacy assays were performed on the DM1 cell model treated with 10 and 30 µM of PTM as-in or loaded into HA-NPs after 24 and 48h. At each time point, cells were fixed with 4% paraformaldehyde and labelled with anti-MBNL1 antibody; DNA was counterstained with Hoechst 33342. For each sample, the number of nuclear foci per nucleus was assessed manually in 500 DM1 cells.

Results: PTM-loaded HA-NPs showed a size around 200nm, low PdI, negative zeta potential and a PTM encapsulation efficiency of 80%. Cytotoxicity of PTM-loaded NPs was significantly higher compared to PTM due to a higher rate of cell internalization. Transfected C2C12 cells with 960 nucleotide sequences (C2C12-960) demonstrated MBNL1 accumulation in nuclear foci, whereas cells with 0 nucleotide repeats showed a diffuse nuclear MBNL1 distribution. After 24h, untreated C2C12-960 samples showed a majority of cells containing 1-2 foci per nucleus. C2C12-960 cells treated with PTM as-in demonstrate an overall reduction of foci to about 1 per nucleus, while C2C12-960 cells treated with PTM-loaded HA-NPs showed a reduction of foci even more evident, with most of cells devoid of foci. No statistical difference in the number of foci was observed between cells treated with 10 µM of PTM as-in and PTM-loaded NPs. Conversely, the reduction of foci was significantly higher in cells treated with 30 µM of PTM-loaded NPs compared to PTM as-in. After 48h, results were generally similar, but the reduction of foci was significantly higher in cells treated with both concentrations of PTM-loaded NPs compared to PTM as-in.

Conclusion: PTM-loaded HA-NPs are able to reduce significantly the number of nuclear foci in the C2C12 DM1 cell model, opening promising perspectives for their application to reverse the pathological traits in DM1 skeletal muscle.

Acknowledgments: This work received funding from the INVITE project EU Horizon 2020 GA No 754345.

LS4.006
Fluorescent nanodiamonds – a novel tool for all-optical magnetic resonance-based detection of free radical production in live cells

A. Sigaeva[1], F. Perona[2], N. Mougios[3], M. Chipaux[4], R. Schirhagl[1]

[1]University Medical Center Groningen, Biomedical Engineering, Groningen, Netherlands
[2]Ferdinand-Braun-Institut, Joint Lab Diamond Nano Photonics, Berlin, Germany
[3]Center for Biostructural Imaging of Neurodegeneration, OpazoLab, Göttingen, Germany
[4]Swiss Federal Institute of Technology Lausanne (EPFL), Laboratory of Advanced Semiconductors for Photonics and Electronics, Lausanne, Switzerland

Introduction: Over the last years, there has been a growing interest in using nanodiamonds with fluorescent defects of crystal structure (FNDs) as intracellular nanoscale sensors [1]. Fluorescence of a certain type of defects - nitrogen vacancy (NV) centers - strongly and reversibly depends on their immediate environment, particularly on its magnetic properties. Free radicals, by definition containing unpaired electrons, constitute one of the major sources of magnetic signal in live cells. While these molecules are usually considered to be deleterious, certain types of free radicals, such as nitric oxide (NO*), perform important signaling functions in live systems. One of the major challenges in understanding the role of free radicals in health and disease is their high reactivity, which makes it hard to detect these molecules with desired spatial and temporal resolution. Moreover, the majority of methods of free radical detection rely on the reaction between the radical and the probe, thus interfering with the natural effects of the radicals [2].

However, NV centers of FNDs allow for direct quantum sensing of the magnetic signal coming from the radicals. This imaging technique - so-called nanoMRI – does not require external electromagnetic fields, is implemented in a confocal system with a single green pulsing laser, and has an all-optical readout, allowing to record T1 relaxation constant. As FNDs are biocompatible and can be internalized by live cells [3], this method can be used for *in situ* detection of free radicals on single-cell and even subcellular level. Our group has recently shown that NV centers of FNDs can be used for direct optical quantum-based sensing of such magnetic signal – both in cell-free environment [4] and inside the live yeast cells [5].

Objectives: The goal of current project was to further explore the potential of all-optical nanodiamond nanoMRI to detect free radicals and record the dynamic changes in their concentrations on a single-cell level.

Materials and methods: In this study, we performed T1 relaxation measurements in live J774 murine macrophage-like cells, using commercially available FNDs. During the acquisition, the cells were exposed to iNOS inhibitor, L-NAME. The changes in intracellular NO levels were confirmed with the conventional fluorescent assay (DAF-2 DA) by the means of microplate reader and confocal microscopy.

Results: We have for the first time recorded T1 relaxation curves from FNDs internalized by live macrophages. As the NO* production in the system was abolished by L-NAME, we were able to observe the lengthening of T1 constant of FNDs internalized by the cells. Slower relaxation of NV centers reflects lower levels of background "magnetic noise", indicating reduced free radical load in the cells.

Conclusion**:** Our study shows the potential of nanodiamond-based nanoMRI for the direct all-optical monitoring of free radical production on a single-cell level. High spatial and temporal resolution, as well as the technical simplicity, make this approach promising for biomedical imaging applications.

References:
[1] *Small* 2018, 14, 1704263. DOI: 10.1002/smll.201704263
[2] *Acc Chem Res.* 2019 Jul 16; 52(7): 1739–1749. DOI: 10.1021/acs.accounts.9b00102
[3] *Sensors (Basel).* 2018 Feb; 18(2): 355. DOI: 10.3390/s18020355
[4] *ACS Sens.* 2020, 5, 12, 3862–3869. DOI: 10.1021/acssensors.0c01037
[5] *ArXiv:2007.16130*

LS4.P001
Effect of alendronate, hop-extract and their combination on the number and average surface of astrocytes in the brain of ovariectomised female Wistar rats

E. Rođak[1], S. Viland[2], M. Zjalić[3], N. Bijelić[1], M. Heffer[3], D. Odeh[4], N. Oršolić[4]

[1]Faculty of Medicine Osijek, Department of Histology and Embryology, Osijek, Croatia
[2]Faculty of Medicine Osijek, University Graduate Study of Medical Laboratory Diagnostics, Osijek, Croatia
[3]Faculty of Medicine Osijek, Department of Medical Biology and Genetics, Osijek, Croatia
[4]Faculty of Science, University of Zagreb, Department of Biology, Zagreb, Croatia

Introduction: Reduced production of estrogen during menopause is related to development of osteoporosis. Recent research shows it might also be connected to higher risk of degenerative diseases of central nervous system, and researchers believe estrogen has a neuroprotective effect. One of the most frequently used medicinal products for treatment of osteoporosis is alendronate, which passes the blood-brain barrier. Hop extract contains phytoestrogens, especially xanthohumol and 8-prenylnaringenin. Phytoestrogens are sometimes used to alleviate the symptoms of menopause. It is unclear if and how alendronate, phytoestrogens and their combination affect the cells involved in inflammation and neuroprotection in the brain.

Objectives: The objective was to examine the effect of alendronate, hop extract and their combination on the expression of glial fibrillary acidic protein (GFAP), an astrocyte marker, in different regions of the brain of ovariectomized rats.

Materials & methods: The study was performed on brain tissue of 50 female Wistar rats. Animals were divided into 5 groups: a control group (underwent sham operation), and 4 ovariectomized groups (untreated, treated with alendronate, hop extract or their combination). Expression of GFAP was evaluated using immunohistochemical staining and subsequent analysis with the help of ImageJ software package, which was used to determine astrocyte number and average surface.

Results: In most of the examined brain areas, treatment with alendronate, hop extract or their combination affected astrocyte number or their average surface. Group treated with hop extract had significantly larger astrocyte number in periventricular nucleus, periventricular posterior nucleus and medial posteroventral amygdaloid nucleus. Average astrocyte surface was significantly larger in several examined areas of brain in hop extract group and in alendronate group. Groups receiving combination of alendronate and hop extract had average astrocyte surface comparable to control or untreated group in most of the examined areas.

Conclusion: Treatment with alendronate, hop extract or a combination of the two affect the modulation of inflammation and neuroplasticity of brain tissue by changing the number of astrocytes and their surface.

Keywords: Alendronate; Brain; Hop, extract; Inflammation; Ovariectomy; Phytoestrogen.

LS4.P002
Uptake and intracellular fate of ethosomes and transethosomes in epithelial, connective and muscle cell lines

M. Costanzo[1], M. Sguizzato[2], M. A. Lacavalla[1], R. Cortesi[2], E. Esposito[2], M. Malatesta[1]

[1]University of Verona, Department of Neurosciences, Biomedicine and Movement Sciences, Verona, Italy
[2]University of Ferrara, Department of Chemical and Pharmaceutical Sciences, Ferrara, Italy

Introduction: The possibility to deliver drugs through the skin represents an important pharmaceutical goal. Indeed the topical administration of drugs offers the possibility to treat many disorders affecting the skin and the lower tissues. At this regard, different micro- and nano-systems have been proposed for transdermal drug delivery. For instance ethosomes (ET) represent an interesting strategy. These vesicular systems, constituted of phospholipids, ethanol and water, are able to encapsulate poor soluble molecules. The presence of ethanol and phospholipids promotes drug passage through the skin since ethanol can disorganize the stratum corneum barrier, opening spaces for ET crossing, while the affinity between phospholipid and skin lipid allows ET permeation. On this matter, some studies have demonstrated the presence of intact vesicles in the skin strata, suggesting that ET can overcome the stratum corneum, allowing deep drug permeation. Recently, some authors have formulated transethosomes, characterized by the presence of surfactants in the ET composition, acting as edge activators, possibly affecting the vesicles interaction with the skin. Notably, the transdermal potential of transethosomes containing polysorbate 80 (ETw) in comparison to ET deserves to be thoroughly investigated.

Objectives: This work aims at investigating the biocompatibility and intracellular fate of ET and ETw in three cell types, representative of the main cytological components of the skin, at light (LM) and transmission electron microscopy (TEM).

Materials & methods: Keratinocyte, fibroblast and myoblast cell lines were grown in appropriate media at 37°C in a 5% CO2 humidified atmosphere. Cells were treated with different concentrations of ET and ETw and analyzed for biocompatibility by the MTT assay. Cells were then seeded on glass coverslips and incubated for 2h and 24h with ET or ETw at the concentration found to be safe. For fluorescence microscopy, the cells were fixed with paraformaldehyde and the nanocarriers were made visible by using the dye PKH67, the cytoplasm was counterstained with Trypan blue and DNA with Hoechst 33352. Red Oil O staining revealed lipid droplets at bright field microscopy. For TEM, the cells were fixed with aldehydes and OsO4, and embedded in Epon resin.

Results: MTT assay demonstrated that both ET and ETw were safe for all cell lines up to the concentration of 86.6µg/mL. LM showed that the nanocarriers occurred inside all cell types already after 2h and accumulated in large amounts in the cytoplasm after 24h. Oil Red O staining revealed lipid droplet accumulations in all cells treated with ETw. TEM demonstrated that both ET and ETw undergo rapid and massive cell internalization, and persist free in the cytoplasm, likely used as a source of lipids by the enzymes resident in the smooth endoplasmic reticulum. TEM confirmed the presence of large amounts of lipid droplets in cells treated with ETw. No subcellular damage was ever observed, although some stress signs were found in the presence of huge lipid droplet accumulation.

Conclusion: Based on the results obtained with these cell models, Et and ETw proved to be suitably biocompatible and may be envisaged as very efficient tools for transdermal drug delivery. However, caution must be exercised in the choice of the appropriate concentration, especially for ETw, whose heavy uptake may induce an intracellular overload of lipids.

LS4.P003
Ultrastructural evidence of age-related alterations of RNA pathways in myonuclei – a contribution to sarcopenia?

M. A. Lacavalla[1], B. Cisterna[1], C. Zancanaro[1], M. Malatesta[1]

[1]University of Verona, Neuroscience, Biomedicine and Movement, Verona, Italy

Introduction: During aging, skeletal muscle is affected by sarcopenia *i.e*., a progressive loss of muscle mass, strength and endurance. Cell nucleus dysfunctions have been proposed as factors contributing to sarcopenia since impairments in mRNA and rRNA transcription/maturation machinery have been reported in different cell types, including muscle cells, during aging.

Objectives: This study aimed at getting deeper insight into the nuclear pathways involved in the synthesis, transport and degradation of RNAs in skeletal muscle nuclei during aging. Ultrastructural immunocytochemistry was used to reveal the distribution and density of actin (a motor protein and regulator of RNA transcription), 5-methyl cytosine (an epigenetic regulator of gene transcription) and ribonuclease (RNase) A (an RNA degrading enzyme) in defined myonuclear domains of rectus femoris muscles from old and late adult mice.

Materials and methods: Balb-c mice aged 19 months (late adult, n=3) and 28 months (old, n=3) were used (experimental protocol ref.: 538/2015-PR). After animal perfusion with a formalin solution, rectus femoris muscles were removed, further fixed, dehydrated and embedded in LR White resin. Ultrathin sections were incubated with antibodies directed against: the active phosphorylated form of RNA polymerase II (Abcam), nuclear actin (Sigma-Aldrich), 5-methyl cytosine (GeneTex), and RNase A (Abcam). Sections were stained with Uranyl Less EM stain, followed by lead citrate to reduce chromatin contrast and reveal the ribonucleoprotein nuclear constituents. A double immunolabeling was performed with antibodies directed against RNA polymerase II and RNase A, and the sections were stained with terbium citrate to specifically visualize RNA. For actin, 5-mC and RNAse A, a semiquantitative assessment of the immunolabeling was carried out by estimating the gold grain density on the following nuclear compartments: condensed chromatin, nucleolus and interchromatin space. Data for each variable were pooled according to the age group and presented as mean ± standard error of the mean. Statistical group-group comparison was performed with the Mann-Whitney test setting statistical significance at alpha ≤ 0.05.

Results**:** The myonuclei of old mice showed different densities of the investigated molecular factors in comparison to late adult animals. Briefly, the significant decrease of actin in all the considered nuclear compartments of myonuclei from old mice suggests impairment of mRNA transcription and nucleus-to-cytoplasm transport of both mRNA and ribosomal subunits. The significant decrease of 5-mC and RNase A in nucleoli of old *vs.* late adult mice suggests an age-dependent loss of rRNA genes. The co-presence of RNA polymerase II and RNase A in RNA fibrils suggests that RNA degradation is a co-transcriptional process.

Conclusion: The fine immunocytochemical analysis carried out in this study provides novel information on aging-associated changes of nuclear factors involved in chromatin stability as well as in transcription, processing and transport of RNAs in myonuclei of old mice. The alteration of these nuclear pathways may affect protein synthesis and impair the anabolism-catabolism balance essential for muscle mass maintenance, thus contributing to the progression of sarcopenia.

LS4.P004
Calcium phosphate formation on TiO_2 nanomaterials – finding a suitable biomimetic route of nanocomposites preparation

I. Erceg[1], A. Selmani[1], I. Panžić[2], A. Gajović[2], M. Ćurlin[3], N. Maltar Strmečki[1], M. Dutour Sikirić[1]

[1]Ruđer Bošković Institute, Division of Physical Chemistry, Zagreb, Croatia
[2]Ruđer Bošković Institute, Division of Materials Physics, Zagreb, Croatia
[3]School of Medicine, University of Zagreb, Department of Histology and Embryology, Zagreb, Croatia

Among different materials for bone engineering, calcium phosphates (CaPs) attract special attention because the main inorganic component of bones is poorly crystalline, non-stoichiometric, calcium deficient, Na-, Mg- and carbonate hydroxyapatite [1]. Despite their excellent bioactivity and osteoconductivity, CaPs" applications are limited to non-stress bearing applications due to their poor mechanical properties [2]. In recent years, the addition of inorganic nanomaterials (NMs) in CaPs based ceramics, cements and coatings is proposed as a solution to this problem [2].

TiO_2 nanomaterials (TiNMs) attract attention due to their favorable properties for biomedical applications [3], and the possibility to prepare TiNMs of different morphologies, structure and composition. In order to rationalize the design of CaP/TiNM composites, the influence of TiNMs" surface structure and charge density on CaPs formation should be investigated. Until now, most of the studies were performed with TiO_2 (TiNPs) nanoparticles and arrays of nanotubes (TiNTs) in simulated body fluid [6,7].

In order to contribute to the understanding of CaPs formation on TiNMs of different dimensionality, in this research the formation of CaPs in the presence of TiNPs and TiNTs was investigated in two sets of experiments [8]. The ability of TiNMs to induce CaPs formation was tested in corrected simulated body fluid, while the influence of TiNMs on kinetics of formation and properties of formed CaPs was investigated in spontaneously precipitating system.

The influence of TiNMs on CaPs precipitation has been investigated by potentiometric measurements, powder X-ray diffraction (PXRD), electron paramagnetic resonance spectroscopy (EPR), scanning (SEM) and transmission (TEM) electron microscopy, dynamic (DLS) and electrophoretic light scattering (ELS).

Both TiNMs showeded poor ability to promote CaPs formation in c-SBF which can be attributed to their low absolute zeta-potential value. However, during spontaneous precipitation they exhibited unusual dual influence on precipitation kinetics, i.e. inhibition of initially formed amorphous calcium phosphate (ACP) transformation at lower and promotion at higher concentrations. After 1 hour reaction time, in presence of both TiNMs, calcium deficient hydroxyapatite was formed (CaDHA). Morphology of the CaDHA depended on type and concentration of TiNMs. However, PXRD and EPR characterization confirmed that there is no significant difference between CaDHA formed in the presence of different TiNMs.

Obtained results confirm importance of surface structure and charge in CaPs – TiNMs interactions and point to versatile method for biomimetic synthesis of novel biocomposites.

Acknowledgements: This work has been fully supported by Croatian Science Foundationunder the project HRZZ- IP-2018-01-1493.

References:
[1] S.V. Dorozhkin, Calcium Orthophosphates: Applications in Nature, Biology, and Medicine, Pan Stanford, Singapore, 2012.
[2] C. Canal et a., J. Mech. Beh. Biomed. Mater. 4 (2011) 1658.
[3] B.D. Ratner, ed., Biomaterials science: an introduction to materials in medicine, 2nd ed, Elsevier Academic Press, Amsterdam, Boston, 2004.
[4] X. Wang et al., Chem. Rev. 114 (2014) 9346.
[5] D. Fattakhova-Rohlfing et al., Chem. Rev. 114 (2014) 9487.
[6] J.M. Ruso et al., Langmuir. 29 (2013) 2350.
[7] K. Vasilev et al., Biomater. 31 (2010) 532.
[8] I. Erceg et al., Colloids Surf. A Physicochem. Eng. Asp., 593 (2020) 124615.

LS5.003
The megapinosome complex – a mega membrane storage

A. Bauer[1], G. Frascaroli[2], P. Walther[1]

[1]University of Ulm, Center for Electron Microscopy, Ulm, Germany
[2]Leibniz Institute for Experimental Virology, Heinrich-Pette-Institute, Hamburg, Germany

The megapinosome is an endocytic cell organel that we observed in human macrophages with electron microscopy[1,2]. Megapinocytosis shows clear differences to the already known canonical endocytic structures and differs significantly from the classical pinocytosis, which leads to early endosomes and macropinosomes[3]. Megapinosomes are filled with a dense trabecular meshwork consisting of membrane surrounded structures, in contrast to macropinosomes that are described as fluid filled endocytic vacuoles[4,5]. In addition, megapinosomes are, on average, much larger than macropinosomes[1].

The objective is to highlight the differences between the canonical endosomal pathway and the megapinosomal pathway, and to better understand the physiological meaning of the large membrane stock of a megapinosome.

To identify endocytotic structures, we incubated M2 macrophages with BSA gold (10 nm, 5 min) as an endocytotic liquid phase tracer. Samples were high pressure frozen without prefixation, freeze substituted, and embedded in epon[6]. Semi thin sections (600 nm) were imaged with STEM tomography[7]. Structures were identified as endocytotic when they contained BSA gold, and were divided into endocytotic or megapinosomal. Megapinosomes were identified by the presence of a trabecular network. All structures connected to the megapinosomes are classified as part of the megapinosome complex.

The structures of the megapinosome complex are the trabecular meshwork consisting of small, well defined cytosolic bridges and knots, tubules and cisterns. All finely structured components of the megapinosome complex are surrounded by a large, continuous membrane. Therefore, the surface/volume ratio of the megapinosome complex is very high compared to macropinosomes (Table 1). The high influence of the geometrical shape of a cell or a cell compartment to the surface/volume ratio has already been pointed out[8]. By exploring the membrane reservoir of the highly structured surface of macrophages it was found that these can be used for buffering membrane tension[9]. Taking these two findings together, we postulate that one function of the megapinosome complex is to serve as an internal membrane buffer to compensate for surface shape changes.

[1] 1 Bauer et al. 2016, Histochem Cell Biol. 145, 617–627
[2] 2 Bauer et al. 2020, J Struct Biol. 210,107505
[3] 3 Lewis, 1931, Hosp. Bull. 49, 17-27
[4] 4 Swanson, 2008, Nat Rev Mol Cell Biol. 9, 639â649
[5] 5 Swanson and King, 2018, Phil. Trans. R. Soc. B 374
[6] 6 Walther and Ziegler, 2002, J. Microscopy 208, 3–10
[7] 7 Walther et al., 2018, Histochem Cell Biol. 150, 545–556.
[8] 8 Fawcett 1966, ISBN 0-7216-3584-9
[9] 9 Raucher and Sheetz, 1999, Biophys J. 77, 1992-2002

Figure: Part of a megapinosome complex. (A) is one virtual section of the reconstructed tomogram. The trabecular meshwork is topologically equivalent to the cytosol and it is separated by a membrane from the luminal part which is connected with the lumen of the tubules and cisternae. (B) The luminal part of the megapinosome complex is segmented in blue, the endosomes in brown and the clathrin coated pits in green.

Table: The surface and the volume of the megapinosome complex and the endosomes of eight tomograms and of a macropinosome were measured and the surface-to-volume (S/V) ratio was calculated. The S/V ratio of the components of the megapinosome complex are similar to the S/V ratio of endosomes and about an order of magnitude higher than the values of a macropinosome with 1.2 µm diameter.

Figure 1

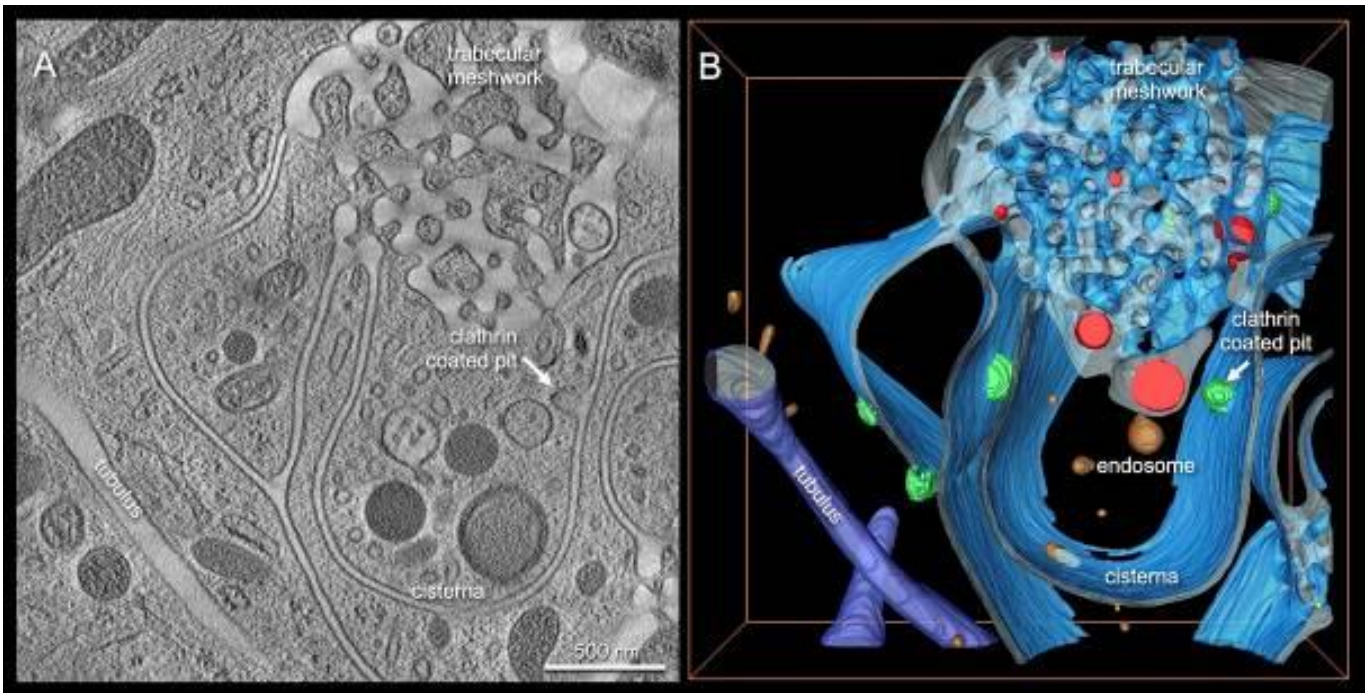

Figure 2

	Surface [μm^2]	Volume [μm^3]	S/V ratio [μm^{-1}]
Megapinosome complex	107.70	2.20	**49**
Endosomes	12.01	0.27	**44**
Macropinosome with about 1.2 µm diameter	4.95	0.82	**6**
Perfect sphere with 1.2 µm diameter (calculated)	4.52	0.90	5

LS5.004
Characterization and enumeration of platelet microvesicles in human platelet concentrates by using transmission electron microscopy including electron tomography

J. Neumüller[1,2], C. Jungbauer[2]

[1]Medical University of Vienna, Center for Anatomy and Cell Biology, Vienna, Austria
[2]Blood Donation Center of the Austrian Red Cross for Vienna, Lower Austria and Burgenland, Vienna, Austria

Objective: Platelet microvesicles (PMV) are delivered from platelets by budding (ectosomes, (∅100-1000 nm) or by exocytosis of α-granules (exosomes, ∅ 50-150 nm; 1). They communicate with particular target cells via surface receptors and their content of nucleic acids, transcription factors, caspases, enzymes, cyto- and chemokines, growth factors and lipid mediators (2) The presence of in transfused platelet concentrates (PC) can cause transfusion reactions such as lung injury and blood vessel damage. PC can be prepared by apheresis or as pooled samples.The goal of our studies was the characterisation and enumeration of PMV in PC by transmission electron microscopy (TEM).

Material & Methods: PMV were prepared by negative contrasting using uranyl- or tulium acetate on carbon/formvar-filmed grids in modification to (3). For enumeration, 15 nm gold particles were added to a pre-dialyzed platelet-free PMV suspension. 0.5 µl of the sample were applied to the filmed grids and allowed to dry. In TEM, micrographs from 4 aspects of the dried layer (about 8700 x 8700 nm) were analysed by morphometry in respect to PMV distribution in terms of area and Feret perimeter.

Electron tomography (ET): Platelet-free PC-samples were ultracentrifuged, embedded in alginate, routinely fixed with aldehyde and osmium tetroxide, dehydrated and embedded in Epon. ET of 300 nm semithin sections was performed using a Tecnai G2 TEM, equipped with a eucentric goniometer and the Xplore 3D software FEI, Eindhoven, The Netherlands). Tilt series from -65° - +65° at an increment of 1° were acquired using an Eagle 4k CCD camera (FEI). Stack files were aligned and reconstructed using the IMOD software (Boulder Lab., Colorado, USA) 3D models and movies were generated by the Amira 5.3 software (Mercury Computer Systems, Merignac, Cedex, France).

Results: PMV numbers varied between 8.75 x 10^7 and 1.02 x 10^9 per µl of the PC samples. There was no significant difference between pooled PC and apheresis PC. Larger particles (ectosomes) were composed of up to 5 smaller vesicles as shown by negative contrast (Figure a) and visualized in 3D by ET (Figure c). The majority of PMV were single exosomes Figure b). During storage over a time period of 8 days, a significant decay of PMV could be demonstrated, above all in apheresis PC.

Conclusion: Enumeration and analysis of PMV in PC can be appropriately carried out using TEM by negative contrast and ET in order to evaluate the quality of PC used for platelet transfusion and to optimize the quality of PC, produced by different manufacturing methods using different apheresis machines.

References:
[1] Boilard E, Duchez AC, Brisson A. Curr Opin Hematol 2015;**22**: 437-44.2. Melki I et al.: Platelets. 2017 May; 28(3):214-221.
[3] Hacker C et al.: Sci Rep. 2016; 6: 25275.

Figure 1

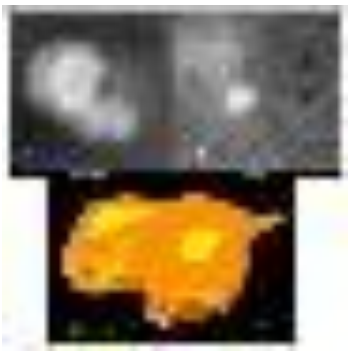

LS5.005
A novel function of the RasGAP protein IqgC in cell adhesion

L. Mijanović[1], D. Putar[1], V. Filić[1], I. Weber[1]

[1]Ruđer Bošković Institute, Division of Molecular Biology, Zagreb, Croatia

Proper cell adhesion is crucial for many cellular processes, such as cell migration, phagocytosis and differentiation[1]. In the migrating *Dictyostelium discoideum* cells, transient stationary adhesion foci form on the ventral cell surface underneath the cell body and the pseudopods[2]. These adhesion foci can be discerned from the F-actin-containing puncta presumably involved in transmitting the traction forces to the substratum[3,4]. The adhesion foci contain a number of proteins homologous to those involved in adhesion in higher eukaryotes, such as talin, paxillin, Rap1, and others[2,4,5]. IqgC is a RasGAP protein, which inactivates small GTPase RasG in *D. discoideum* by stimulating the hydrolysis of GTP bound to its active form. We recently showed that IqgC plays an important role in the regulation of large-scale endocytosis[6].

During cultivation in cell-culture dishes, we noticed that IqgC-null cells easily detach from the plastic surface, indicating that IqgC might be involved in the regulation of cell adhesion to the underlying substrata. We therefore proceeded to investigate the involvement of IqgC and its potential interactors in this process, using biochemical and microscopy approaches.

Using the shaking assay, where cells were mechanically detached from the dish by rotational agitation, we confirmed that cells lacking IqgC are defective in the cell-substratum adhesion, an effect which could be rescued by expressing recombinant IqgC in IqgC-null cells. Cell tracking experiments showed that less adhesive IqgC-null cells migrate faster than wild-type. Somewhat surprisingly, reflection interference contrast microscopy showed slightly larger attachment area in IqgC-null than in wild-type cells. This effect might, however, be explained by our earlier finding that IqgC-null cells have a mild cytokinesis defect, leading to bigger, multinucleate cells[6]. Total internal reflection fluorescence microscopy of cells expressing fluorescently labeled IqgC together with paxillin B or a probe for F-actin demonstrated that IqgC localizes to the paxillin B-containing adhesion foci. The pathways involved in the regulation of cell adhesion in *D. discoideum* are not yet fully elucidated, but it is hypothesized that the small GTPase Rap1 is one of the key regulatory proteins[5,7,8]. Indeed, Rap1 was identified in the IqgC interactome as a potential IqgC binding partner and we confirmed a direct interaction between IqgC and Rap1 using yeast-two-hybrid, pull-down, and bimolecular fluorescence complementation assays.

Here we show that IqgC protein is a positive regulator of the cell adhesion to the underlying substratum in *Dictyostelium discoideum*. Based on the presented results, we hypothesize that IqgC regulates adhesion via binding to small GTPase Rap1.

Figure 1: A) Strength of the cell-substratum adhesion was assessed using the mechanical detachement of cells from the petri dish by rotational agitation. The percentage of *iqgC* null cells detached from the substratum after an hour of shaking is significantly higher that in the wild type cells. wt = 23.98 % ± 1.647; iqgC null = 45.64 % ± 4.65; rescue = 22.01 % ± 2.13 (avg ± SEM); p (wt and KO) = 0.000872727; p (wt and rsc) > 0.5 (two-tailed t-test). **B)** Random cell migration assay showed that the velocity (v) of *iqgC* null cells is slightly larger than the velocity of wild-type AX2 cells. v(wt) = 3.910 ± 0.1 µm/min, n = 134; v(iqgC-) = 4.620 ± 0.13 µm/min, n = 137 (mean ± SEM); p < 5×10-5 (two-tailed t-test).

Figure 2: Microscopic examination of the protein localization to the foci on the ventral surface of the moving cell using TIRF. Colocalization of YFP-IqgC and mRFP-PaxB can be seen in randomly moving vegetative cells. Scale bar is 5 µm.

[1] Khalili AA, Ahmad MR. *Int J Mol Sci*. 2015;16(8):18149-18184.
[2] Kreitmeier M, Gerisch G, Heizer C, Müller-Taubenberger A. *J Cell Biol*. 1995;129(1):179-188.
[3] Uchida KSK, Yumura S. *J Cell Sci*. 2004;117(8):1443-1455.
[4] Bukharova T, Weijer G, Bosgraaf L, Dormann D, van Haastert PJ, Weijer CJ. *J Cell Sci*. 2005;118(18):4295-4310.
[5] Kortholt A, Rehmann H, Kae H, et al. *J Biol Chem*. 2006;281(33):23367-23376.
[6] Marinovic M, Mijanovic L, Sotar M, et al. *Proc Natl Acad Sci U S A*. 2019;116(4):1289-1298.
[7] Jeon TJ, Lee DJ, Merlot S, Weeks G, Firtel RA. *J Cell Biol*. 2007;176(7):1021-1033.
[8] Plak K, Pots H, Van Haastert PJM, Kortholt A. *BMC Cell Biol*. 2016;17(1):1-8.

Figure 1

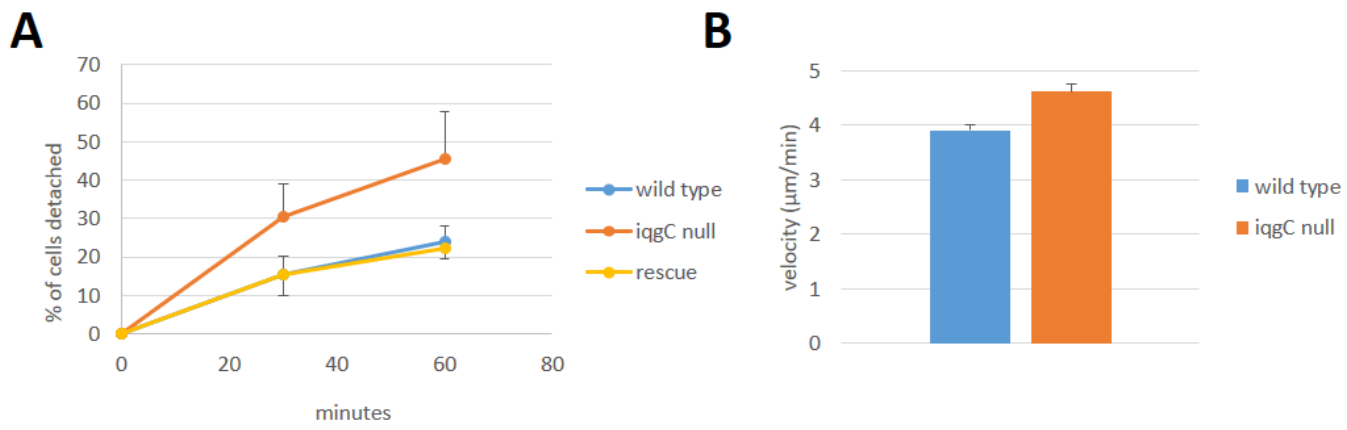

Figure 2

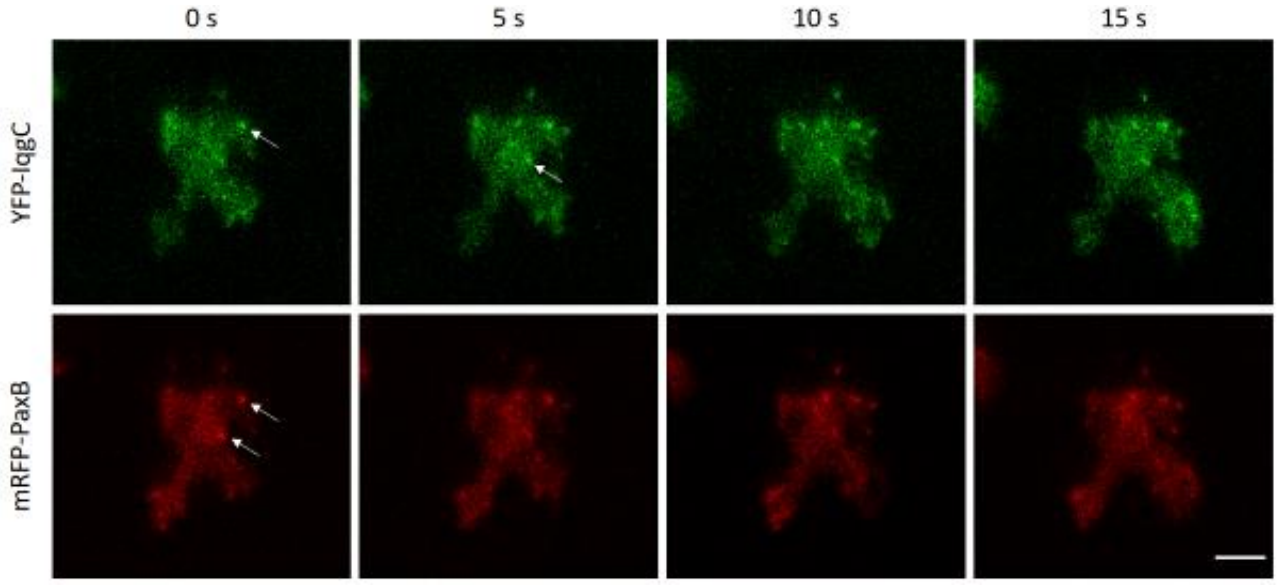

LS5.006
Isolation and characterisation of Tangerin-derived extracellular vesicles

S. Raimondo[1], M. A. Di Bella[1], N. Ganji[1], O. Urzì[1], R. Alessandro[1]

[1]University of Palermo, Biomedicina, Neuroscienze e Diagnostica avanzata, Palermo, Italy

Introduction: Extracellular vesicles (EVs) are membrane-bound lipoproteic structures released by both eukaryotic and prokaryotic cells, with different sizes [1]. The EVs, because of their heterogeneous and complex composition in proteins, lipids and nucleic acids, have been extensively studied in the animal kingdom and they are considered messengers of cell-cell communication, in physiological and pathological conditions [2]. Growing studies have shown their presence also in the plant kingdom; in particular EV-like structures have been purified from lemon juice, grape, grapefruit, orange, tomato and others [3]. The interest in plant EVs originates from the study of their biological properties including their anti-inflammatory and anti-tumor actions in *in vitro* and *in vivo* models [4].

Methods: In this study, we have successfully isolated EVs from tangerin juice by differential centrifugation, filtration steps and ultracentrifugation. The vesicles were characterized by dimensional (Nanosight), biochemical (Western Blot) and morphological analyses. To check the purity of EVs we used negative staining method and examined samples with Transmission electron microscopy.

Results: Nanosight analyses show that the isolated sample has most of structures ranging in size from 150 to 200 nm; larger vesicles, up to 500 nm, are also found in the sample. TEM analyses also show structures smaller than 100 nm in diameter. Western blot analyses show that EVs from mandarin contain Heat Shock Protein 70, a protein described as a marker of both animal and plant EVs.

Conclusions: The data obtained from these preliminary investigations confirm that it is possible to purify EVs from tangerin; furthermore future metabolomics analyses, through HPLC-ESI-Q-ToF-MS, will allow us to define the content of these vesicles and to subsequently study their biological properties in *in vitro* and *in vivo* models.

Figure 1: Representative image of negatively stained EVs isolated from tangerine juice. The electron microscopic view shows the typical round-shaped morphology of the vesicles and their heterogeneity in size with diameter ranging from 60 nm to about 150 nm. Bar = 500nm

[1] G. van Niel, G. D'Angelo, and G. Raposo, Nat Rev Mol Cell Biol, 19(4) (2018)
[2] P.D. Sthal, G.Raposo, Essays Biochem, 62(2), (2018)
[3] C. Yang, M. Zhang, D. Merlin, J Mater Chem B, 6, (2018)
[4] B. Wang, X. Zhuang, Z.B. deng et al., Mol Ther, 22 (2014)

Figure 1

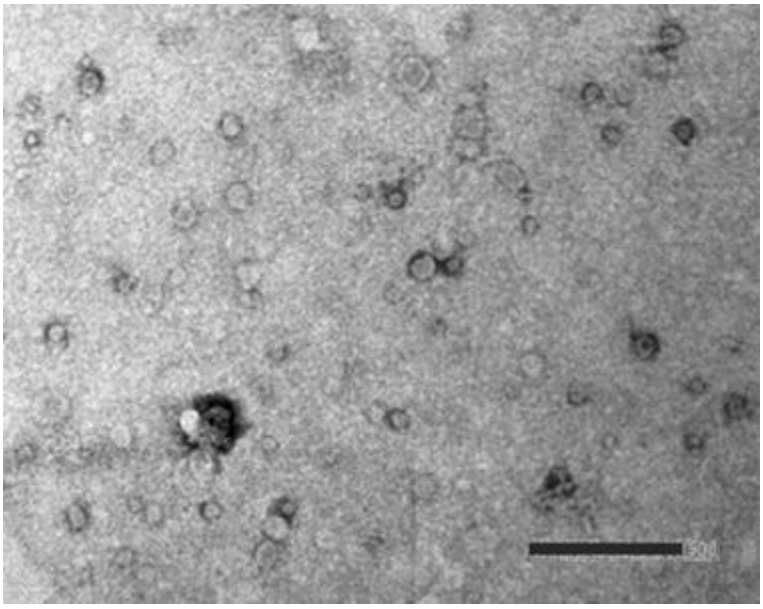

LS5.P001
Requirements for IqgC protein recruitment to macropinosomes in amoeba *Dictyostelium discoideum*

D. Putar[1], L. Mijanović[1], I. Weber[1], V. Filić[1]

[1]Ruđer Bošković Institute, Division of Molecular Biology, Zagreb, Croatia

Large-scale endocytosis is an evolutionary conserved, Ras/PI3K (phosphoinositide 3-kinases) regulated pathway that encompasses nonselective uptake of extracellular fluid or macropinocytosis and particle uptake or phagocytosis[1]. *Dictyostelium discoideum* IQGAP-related protein IqgC is a RasGAP (Ras *GTPase activating protein*) specific for the small GTPase RasG and negatively regulates large-scale endocytosis. IqgC strongly localizes to nascent macropinosome where it colocalizes with active Ras during macropinosome formation[2]. However, IqgC remains on the internalized macropinosome after Ras dissociated from the vesicle. Such dynamics suggests that IqgC has a role in early macropinosome maturation, independent of its interaction with RasG.

Our goal is to elucidate the mechanism of IqgC recruitment to macropinosomes. We will clarify: 1) which IqgC domains are required for its recruitment to the membrane during macropinosome formation and early maturation; 2) whether RasG is required for membrane recruitment of IqgC and 3) which phospholipid interactors mediate strong localization of IqgC to maturing macropinosomes.

To investigate which IqgC domains are important for its localization, we constructed four different fluorescent fusion proteins containing: 1) IqgC RasGAP domain; 2) RasGAP domain and N-terminal region of IqgC; 3) IqgC RasGAP_C-terminal (RGCT) domain and 4) RGCT and C-terminal end of IqgC. Localizations of these truncated proteins during macropinocytosis were assessed in the *iqgC* null cells using confocal microscopy. To investigate the role of RasG in membrane recruitment of IqgC, we examined the localization of IqgC fused with fluorescent protein in the *rasG* null cells. We also mutated the conserved arginine finger in IqgC and examined the localization of this catalitically inactive RasGAP in the *iqgC* null cells. To analyze the lipid-binding specificity of IqgC, we performed a protein-lipid overlay assay using purified IqgC protein and cell lysates containing full-length or truncated versions of IqgC.

Confocal microscopy results showed that RasGAP and RGCT domains alone do not localise to macropinosomes. Furthermore, we showed loss of localization of IqgC to macropinosomes in *rasG* null strain. The same was found for the mutant that has no GAP activity for Ras. Protein-lipid overlay assay showed that IqgC interacts with phosphoinositides, with strongest binding affinity to phosphatidylinositol 3-phosphate (PI(3)P) and PI-bisphosphates PI(4,5)P2, PI(3,5)P2 and PI(3,4)P2.

Neither the RasGAP and RGCT domains alone, nor with adjacent N- and C- terminal end respectively, are sufficient for the recruitment of IqgC to macropinosomes, which suggests that full-length IqgC or a combination of regions are required for its recruitment to macropinosomes. RasG is required for the recruitment of IqgC to the membrane during macropinosome formation, but it is dispensable for its retention during early macropinosome maturation. The latter is probably mediated by phosphoinositides to which IqgC preferentially binds and which are known to be involved in macropinosome formation and early maturation[3].

[1] J. S. King, R. R. Kay, *Philos. Trans. R. Soc. B Biol. Sci.* 374 (2019) 20180158.
[2] M. Marinović, L. Mijanović, M. Šoštar, M. Vizovišek, A. Junemann, M. Fonović, B. Turk, I. Weber, J. Faix, V. Filić, *Proc. Natl. Acad. Sci. U.S.A.* 116 (2019) 1289-1298.
[3] R. Levin, S. Grinstein, D. Schlama, *Biochim. Biophys. Acta - Mol. Cell Biol. Lipids* 1851 (2015) 805-823.

LS5.P002
The role of Miro proteins in intercellular transport of mitochondria via tunnelling nanotubes

J. Novák[1,2], Z. Nahácka[1], Z. Lánský[1], V. Henrichs[1], J. Neužil[1,3]

[1]Czech Academy of Sciences, Institute of Biotechnology, Vestec, Czech Republic
[2]Charles University in Prague , Faculty of Science, Prague, Czech Republic
[3]Griffith University, School of Medical Science, Sydney, Australia

The movement of organelles within and in between cells plays a crucial role in cellular and organismal (patho)physiology. Transport of mitochondria, key organelles of cell metabolism, is a striking example of such a phenomenon, presenting an emerging mechanism utilized by tumour cells to enhance their proliferation and survival. Tumour cells with damaged mitochondria replace malfunction organelles via the import of whole healthy mitochondria from stromal cells, most probably via direct physical connections known as tunnelling nanotubes (TNTs). TNTs are transient membrane structures transiently connecting the cytoplasm of two (or more) cells, enabling transport of a variety of cargo from small signalling molecules to whole organelles. Mitochondria are transported via TNTs with the assistance of motor and adaptor proteins binding them to and dragging along microtubules localized inside the nanotubes. The aim of this work is to investigate the role of Miro1 and Miro2, adaptor proteins of the outer mitochondrial membrane involved in organelles movement within the cell. However, the precise role of Miro proteins in mitochondrial transport between cells via TNTs remains to be elucidated.

With the length from tens to hundreds of microns and width from 50 to 1500 nanometres, TNTs are structures requiring multi-modal microscopy approaches for their investigation. Moreover, dynamic processes like transport of cargo via TNTs require time-lapse low-phototoxicity imaging, with resolution sufficient for tracking of sub-micrometre (e.g. organelle) structures. To investigate the role of Miro proteins in the movement of mitochondria along microtubules, we have been utilizing a reconstituted system of microtubules, motors and adaptors in combination with mitochondria with or without Miro proteins. Imaging by total internal reflection (TIRF) or interference reflectance microscopy (IRM) and subsequent analysis allow us to quantify aspects of mitochondrial movement (velocity, number of associated mitochondria or time of interaction). For investigation of TNTs and movement of mitochondria within these structures, we are establishing co-cultures of mesenchymal stem cells (MSCs, likely donors of mitochondria) with cancer cell lines with or without Miro. Advanced co-culture systems with spatial discrimination of co-cultivated cell populations will allow us to localize and subsequently analyze TNTs with multiple imaging modalities ranging from TIRF/HiLo live-cell imaging to super-resolution and in the near future correlative light-electron microscopy for detailed description of the inter-tubular organization.

LS6.003
Oxygen PFIB/SEM tomography of biological samples

D. Slamková[1]

[1]Thermo Fisher Scientific, R&D, Brno, Czech Republic

Over the past years, the Focused Ion Beam Scanning Electron Microscopy (FIB/SEM) system has been established as a key technology in life science and has become a common method for 3D analysis of biological samples at high isotropic resolution.

A limiting aspect of this technique is the consideration of suitable sample preparation and resin type. Currently, conventional FIB/SEM sample preparation requires enhanced contrasting and embedding in epoxide resins like Epon or Durcupan. These hydrophobic resins are commonly employed for ultrastructural studies, as they are less prone to milling artifacts in gallium-based FIB/SEM systems. In contrast, Acrylic resins (LR White, Lowicryl) tend to generate severe milling artifacts and have low stability under the galium FIB milling (Figure 1A). As a result, the use of these resins for FIB/SEM tomography is very limited, although a range of life science studies will benefit from the possibility to use Acrylic resins for adequate preservation of the cellular structure, as well as the preservation of a fluorescent signal.

Here, we present a PFIB-SEM system that can address some of these limitations. Helios™ 5 Hydra DualBeam is a system featuring Inductively Coupled Plasma (ICP) with four ion species (Xe, Ar, O, N) as an ion source. Special focus is given on the oxygen beam, which provides enhanced sputter rates and extends the FIB-SEM 3D volume acquisition to samples embedded in acrylic resin (Figure 1C). In contrast to gallium FIB, oxygen PFIB displays superior resin compatibility with most resins used in life science and produces a smooth block face without beam-induced damage (Figure 1B) resulting in an improved SEM contrast. We demonstrate that PFIB technology allows for more flexible sample preparation and enables researchers to choose the preparation method that serves best the scientific question.

Next to extending compatibility with multiple resins commonly used in biology the Helios Hydra PFIB also offers new opportunities for exploring 3D visualization and accessing large volumes. The Spin Mill technique is a method for polishing horizontal planes of the sample surface and thus can provide a Serial Block-face Electron Microscopy (SBEM) approach using the capability of the focused ion beam. This technique is based on removing a thin layer from the resin-embedded sample at a glancing angle (typically 4° to the sample surface, Figure 2A) using the PFIB ion beam (for biological resin-embedded samples typically oxygen) and subsequent imaging of the newly created sample surface by the electron beam. Very thin slices in the nm range can be automatically milled from a large region (up to 1 mm2) and imaged repetitively. The Spin Mill technique allows for multiple sites of image acquisition in one experiment, generating a high-resolution 2D image stack for subsequent 3D visualization of features of interest at nanoscale resolution (Figure 2).

The availability of oxygen PFIB/SEM system represented by Helios™ 5 Hydra DualBeam extends the potential of FIB/SEM tomography applications in life-science research. It is a powerful instrument for imaging a wide range of biological samples at a nanoscale resolution. In addition, the capability of delivering an order of magnitude higher currents (up to 2.5 µA) enhances the acquisition speed of PFIB-SEM resulting in increased throughput and reliable reconstruction of the sample volume in three dimensions.

Figure 1

Figure 1. Mouse brain tissue embedded in LR White resin, chemically fixed, milled with (A) Gallium FIB: 30 kV, 65 nA. (B) Oxygen PFIB: 30 kV, 45 nA, pixel width is 9 nm, HFW is 28 um.(C) 3D reconstruction of a mouse brain tissue embedded in acrylic resin. Milling parameters: oxygen: 0,61 nA; 30 kV. Volume is (X x Y x Z) 23,4 µm x 18,2 µm x 20 µm. Slice thickness is 10 nm. Total number of slices is 2000

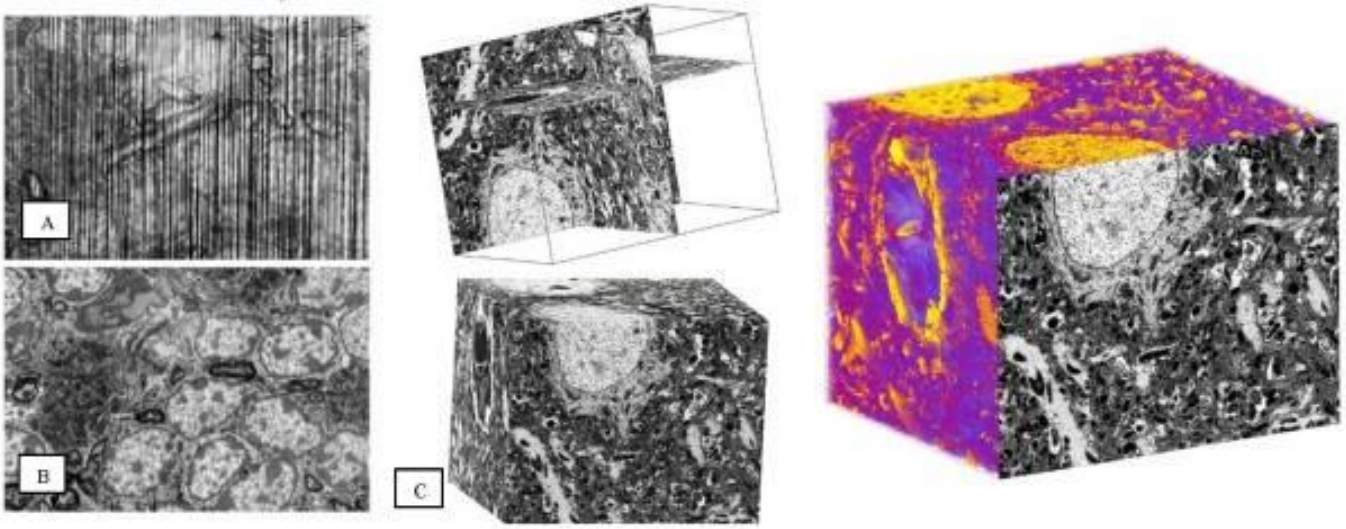

Figure 2

Figure 2. Spin Mill technique. (A) The stage is tilted to the glancing angle 4° to the PFIB beam and continuously rotated by a defined number of steps, at which is the sample surface exposed to PFIB. After milling process, the stage is automatically tilted, so that the electron beam is perpendicular to the sample surface from which SEM images are taken. (B) Perpendicular electron view of the sample, the whole top-face (189 x 187 um) is milled during Spin Mill procedure. (C) First imaging area, HFW is 147 um. (D) Second imaging area, detail of a neuron cell, HFW is 54 um. (E) Third imaging area, subcellular detail, HFW is 8 um.

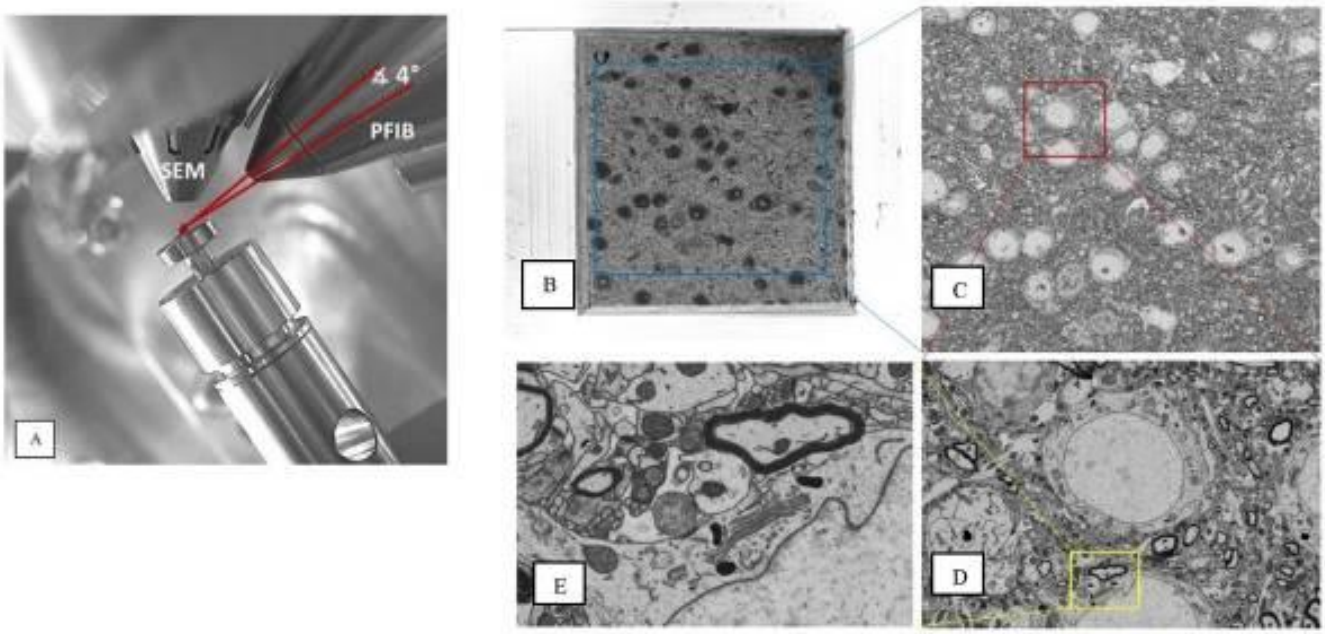

LS6.004
Suitability of organotypic culture to study the iron metabolism in neurodegenerative diseases in the human central nervous system

S. Sunkara[1], V. Etschmaier[2], S. Radulovic[1], S. Patz[2], G. Von Campe[2], P. Steigler[3], G. Leitinger[1]

[1]Medical University of Graz, Cell biology, histology, and embryology, Graz, Austria
[2]Medical University of Graz, Department of Neurosurgery, Graz, Austria
[3]Medical University of Graz, Clinical Department for Transplant Surgery, Graz, Austria

Introduction: Iron deposition in AD is correlated with free radical damage, oxidative stress, amyloid-beta plaques (Aβ) and neurofibrillary tangles (5,6). Though much is known about iron homeostasis in the human body, the knowledge of maintaining this important trace element in the CNS is still a topic of discussion, especially in pathological conditions like AD. The unexplained accumulation of iron could be due to an imbalance of the influx, efflux and storage proteins involved in iron homeostasis (7). The major proteins involved in maintaining iron homeostasis are Ferroportin – iron exporter (Fpn), Transferrin receptor – iron import (TfR) and Ferritin – iron storage (Fn) (8–10). For this study, we opted for organotypic brain slice cultures as a model system to preserve the sample as close to an in-vivo model system as possible. To understand the interaction between iron and AD, we plan to induce artificial Alzheimer"s condition in the brain using Aβ1-42 peptides. We manipulate the iron levels in the cultures using iron overfeed and iron chelators. Following this, we will score the said proteins that are crucial to maintain iron homeostasis in AD condition using double immunogold labelling and image the specimen, using an electron microscope.

Materials and methods: Brain specimen was obtained immediately after surgery from patients with brain tumours and maintained for 12 days. The specimen was sectioned into 300 µm thickness using a McIlwain tissue chopper. The slices were immediately shifted onto a porous membrane over OTC media and maintained for several days. The spinal cord is obtained from the organ transplant donors, sectioned into Aβ1-42 thickness using Leica Vibratome, and cultured for three to four days.

To induce artificial AD condition in the culture ex-vivo, the cultures are maintained on the membrane over serum-free neurobasal media containing exogenous Aβ1-42 peptides. Following this, sections were processed accordingly for IHC staining, TAAB resin embedding, and EFTEM.

Results: We observed that the organotypic brain slice culture maintained up to 6 days in culture were healthy with the absence of dark spots and contamination. The light microscopic images of semi-thin sections showed that the neuropil and cell density is high in cultures from day 0 to day 06 but started to reduce in density with further maintenance. Huge voids in the neuropil and swollen glial cells were observed starting from day 09. Towards the end of the culture, many lipofuscin granules were observed in the cytoplasm covering almost 90% of the cell body. Organotypic cultures maintained up to a week were able to preserve the iron household as was tested by staining against TfR and Fpn. Iron present in the Ferritin core was imaged using Energy Filter Transmission Electron Microscope (EFTEM). Iron was preserved in the cultures and was observed to be concentrated more in the oligodendrocytes and myelin sheath. Electron micrographs generated using TEM showed the preservation of cytoarchitecture, neuronal connectivity and synapses that resemble the in-vivo model animal.

Conclusion: Organotypic culture systems have been a long-standing tool in neuroscience. However, in neuropathological conditions like AD, most of the studies opt for transgenic mice models to study the disease. We believe this ex-vivo model system of AD from human CNS may serve as an excellent alternative to study the AD pathological condition.

Figure 1

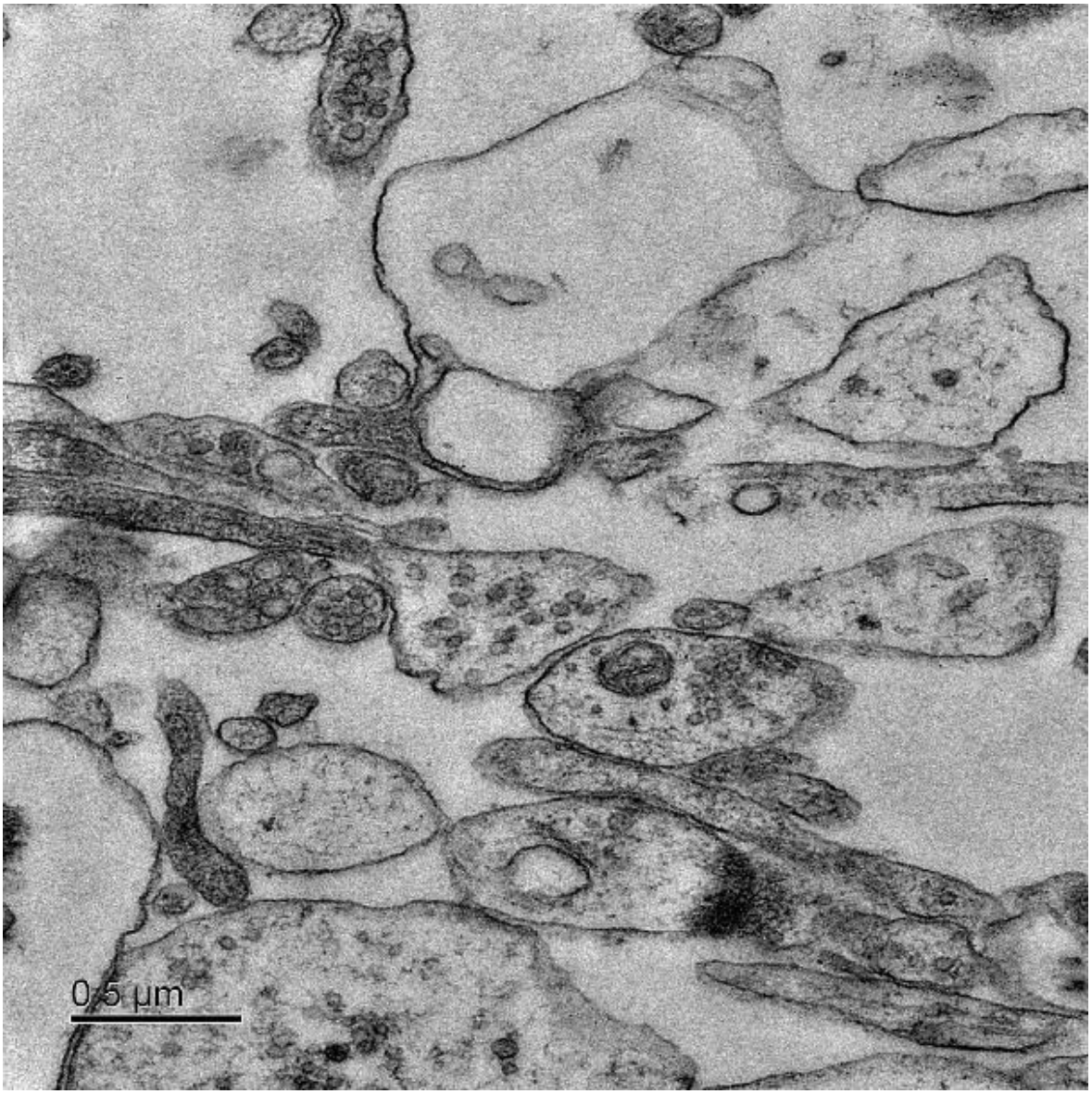

Figure 2

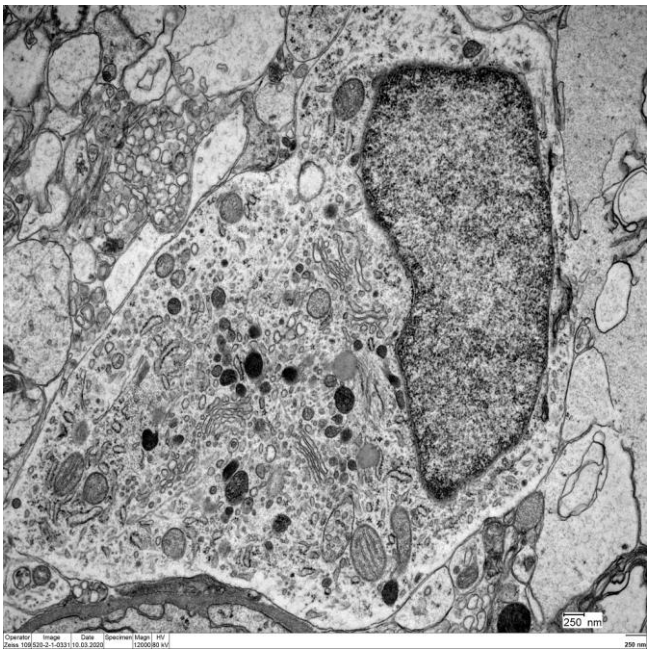

LS6.005
Massive accumulation of trace elements in diplonemid protists

J. Pilátová[1,2,3], D. Tashyreva[3], J. Týč[3], M. Vancová[4,3], B. S. N. Hussain[5], R. Skoupý[6], M. Klementová[7], H. Küpper[5], P. Mojzeš[2], J. Lukeš[4,3]

[1]Charles University in Prague , Faculty of Science, Prague, Czech Republic
[2]Charles University in Prague , Faculty of Mathematics and Physics, Prague, Czech Republic
[3]Czech Academy of Sciences, Biology Centre, Institute of Parasitology, České Budějovice, Czech Republic
[4]University of South Bohemia in Ceske Budejovice, Faculty of Sciences, České Budějovice, Czech Republic
[5]Czech Academy of Sciences, Biology Centre, Institute of Plant Molecular Biology, České Budějovice, Czech Republic
[6]Czech Academy of Sciences, Institute of Scientific Instruments, Brno, Czech Republic
[7]Czech Academy of Sciences, Institute of Physics, Prague, Czech Republic

Introduction: Some organisms have a remarkable capacity to concentrate certain elements from their environment. While this is a well-known feature of multicellular organisms, we know much less about such behavior in unicellular eukaryotes (= protists), which constitute the majority of eukaryotic diversity.

Objectives: Despite being trace elements in most environments, we found strontium (Sr) and barium (Ba) to be massively accumulated in form of crystalline inclusions of celestine ($SrSO_4$) with admixtures of barite ($BaSO_4$) enclosed in intracellular vacuoles of marine protists belonging to the excavate group Diplonemidae. These heterotrophic flagellates have been only recently recognized as belonging to the most diverse and abundant eukaryotes in the world oceans.

Materials and methods: The biogenically formed orthorhombic (bipyramidal and prismatic) microcrystals were unequivocally identified by Raman microspectroscopy. Their crystal structures, elemental composition and 3D-spatial organization were analyzed by electron diffraction, energy-dispersive X-ray spectroscopy with both transmission and cryo-scanning electron microscopy (TEM or SEM EDX) and serial block-face scanning electron microscopy (SBF SEM) (Figure 1).

Results: Our electron diffraction data of crystalline inclusions of diplonemids match the celestine structure (isostructural with barite) with space group Pnma and lattice parameters a = 8.3 Å, b = 5.3 Å, c = 6.8 Å in *Lacrimia* sp. Larger lattice parameters were observed in *Namystinia karyoxenos* a = 8.7 Å, b = 5.5 Å, c = 7.1 Å, which could be explained by the substitution of larger Ba in the crystal structure of celestine. The microanalyses were complemented by consecutive quantification *via* inductively coupled plasma mass spectrometry (ICP-MS). Furthermore, holographic microscopy provided supplementary information on cell dry weights that were otherwise impossible to reach due to inevitable cell lysis during processing. Analysis of elemental composition by ICP-MS confirmed substantial and widely varied Sr content reaching up to 170 mg/g in *Lacrimia* sp. and 3 500 mg/g in *Namystinia karyoxenos*.

Conclusions: Our results bring new insights into the biological roles of trace elements with direct consequences for our understanding of the biogeochemical cycling of Sr and Ba in marine environment and their occurrence in marine sediments.

Figure 1: Microanalytical approaches towards uncovering the chemical nature of crystalline inclusions in diplonemids**.** (a) Raman maps and spectra of celestine in *Lacrimia* sp. with celestine marked in blue and other cytoplasmic contents including lipid bodies, cytochromes and other crystalline structures in white, alongside with the corresponding Raman spectra of biogenic celestine crystals. (b) Cryo-SEM-EDX images of *Lacrimia* sp. complemented with EDX elemental spectra (c) obtained from the area marked by arrows; scale bar 5 µm. (d) The orthorhombic celetine crystals (prismatic or bipyramidal), visible in TEM as electron-dense inclusions in the semi-thin resin sections of *Namystinia karyoxenos.* (e) The representation of h0l oriented sections through three-dimensional electron diffraction datasets (celestine unit cell is displayed as a yellow rectangle). (f) 3D reconstruction of *Lacrimia* sp. based on SBF SEM – cytoplasm in yellow, vacuole in orange and celestine crystals in blue.

Figure 1

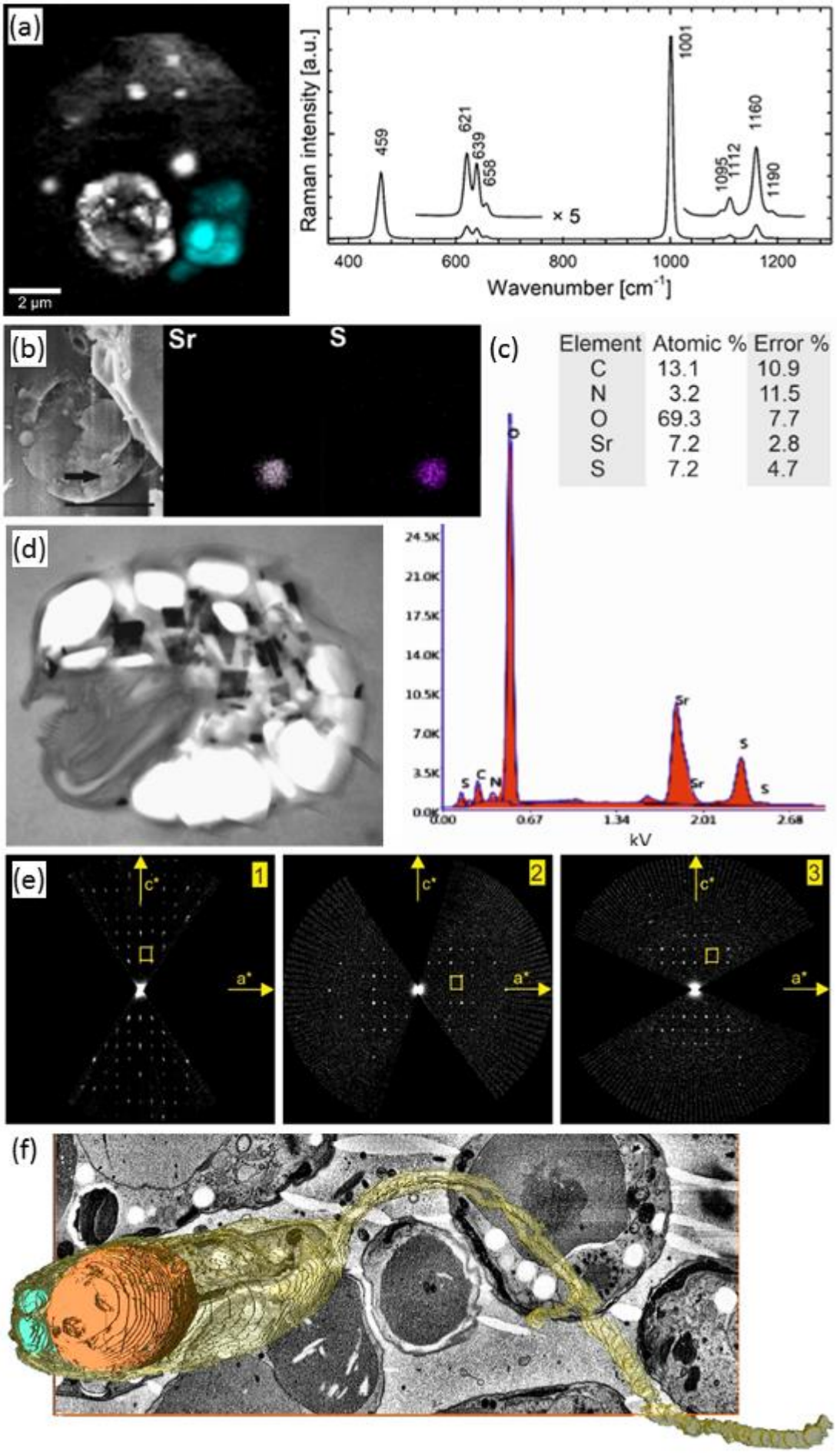
(a)
2 µm
Raman intensity [a.u.]
459
621
639
658
× 5
1001
1095
1112
1160
1190
400
600
800
1000
1200
Wavenumber [cm-1]
(b)
Sr
S
(c)
Element Atomic % Error %
C 13.1 10.9
N 3.2 11.5
O 69.3 7.7
Sr 7.2 2.8
S 7.2 4.7
O
Sr
S
C
N
kV
(d)
(e)
1
2
3
c*
a*
(f)

LS6.006
Electron and light microscopical evaluation of inactive SARS-CoV-2 vaccinated Balb/c mouse kidneys

E. Kervancioglu Demirci[1], E. A. Önen[2], H. S. Mutlu[1], G. Kervancioglu[3], S. Solakoglu[1]

[1]Istanbul University, Istanbul Faculty of Medicine, Histology and Embryology, Istanbul, Turkey
[2]Kocak Farma, Vaccine Biotechnology R&D, Tekirdağ, Turkey
[3]Istanbul Aydin University, Faculty of Medicine, Histology and Embryology, Istanbul, Turkey

Introduction: Vaccine against SARS-CoV-2 development and application is an ongoing process due to pandemics in 2021. Humoral and cellular immunity is mostly the main concern in all of the studies. On the other hand, the virus can cause multiple organ damage. Kidneys are one of the most affected organs. We compared the effect of the active virus, inactive virus, and active virus after vaccination on kidney ultrastructure.

Materials & methods: Isolated virus was replicated in Vero cells, inactivated for vaccine development, purified, concentrated, and controlled with a transmission electron microscope (TEM), quantitative ELISA, and western blotting. Different concentrations of the inactive virus were given intraperitoneally to Balb/c mice of a vaccine development study and antibody production was checked with a neutralized antibody test. The inactive virus concentration for this study was chosen of the highest antibody production. Four groups of mouse (n=5); inhaled active virus after vaccination with the inactive virus (AV), inhaled virus (V), vaccinated (A), and control (C) were sacrificed and their kidneys were removed. The tissues were prepared for light microscopical and TEM evaluation. Formalin-fixed and paraffin-embedded tissues were sectioned 4um thick and stained with hematoxylin and eosin, Masson"s trichrome, and PAS stains and evaluated with light microscopy. Glutaraldehyde fixed and epon embedded tissues were sectioned 500 nm thick and stained with methylene blue and evaluated with light microscopy. Ultrathin sections of 90 nm were stained with uranyl acetate and lead citrate and evaluated with TEM.

Results: TEM and light microscopical findings correlated. Intraglomerular and interstitial capillaries were obstructed with red blood cells in group V. Extracapillary proliferation of parietal epithelium was seen in some glomeruli and some others were collapsed. Both distal and proximal tubules were damaged and some were obstructed, and autophagic vacuoles were visible in epithelial cells. Tubular desquamation, destruction of brush border, and loss in mitochondrial cristae in proximal tubule cells were prominent. Morphology of distal tubules was better in AV than in the V group and also capillaries were more open. In group A, the parietal layer of the Bowman capsule was proliferated and some tubules were lightly reactive.

Discussion: The kidney damage after injection of active virus compares with the literature consisting of human autopsies. The damage in tubules, glomerules, and capillaries in the active virus group attenuated if before vaccinated. The inactive virus caused slight damage, but this should be revised after a period of time if morphologic changes are reversed. In conclusion, the acute phase of infestation after active and inactive viruses can affect kidneys, and vaccine studies should be done cautiously in patients with kidney diseases.

LS6.P001
Ultrastructural analysis of callitrichid hepatitis in captive marmosets and tamarins

S. Richter[1], E. Sós[2], A. Auer[3], Z. Bagó[4]

[1]AGES-Inst. for Veterinary Disease Control Mödling, Pathology Center East - Electron microscopy, Mödling, Austria
[2]Budapest Zoo and Botanical Garden, Budapest, Hungary
[3]University of Veterinary Medicine, Institute of Virology, Vienna, Austria
[4]AGES-Inst. for Veterinary Disease Control Mödling, Pathology Center East, Vienna, Austria

Introduction**:** Lymphocytic choriomeningitis virus (LCMV), a zoonotic Old World arenavirus (Radoshitzky et al. 2015), is widely distributed throughout Europe and America in the common house mouse (*Mus musculus*). Confirmatory evidence of LCMV in other parts of the world is lacking (ECDC). Wild house mice are considered to be the primary reservoir for human and animal infections. LCMV infection of callitrichidae, indicated as callitrichid hepatitis, was already published in the 1980/1990s (Lucke & Bennett, 1982; Stephensen et al., 1991; Montali et al., 1993). Until now, ultrastructural investigations comprise infection studies of marmoset liver cell cultures (Stephensen et al., 1991) and of laboratory mouse (Murphy & Whitfield, 1975).

Material and Method: In 2019, several cases of sudden unexplained deaths were reported in captive callitrichids in the Budapest zoo. Four dead marmosets (*Mico sp.)* and two red-handed tamarins (*Saguinus midas)*, were sent for pathomorphological investigation to the AGES-Institute for Veterinary Disease Control to clarify the source of the disease. Fast negative staining technique (staining with 0,5% UA and 0,5% PTA) and ultrathin sectioning of EPON embedded tissue was chosen for subsequent ultrastructural analysis. Liver, lung, spleen, brain, and faecal samples of the dead monkeys were investigated with a Zeiss TEM 906.

Results and Discussion: The most striking pathomorphological finding was a severe acute necrotising hepatitis with intracytoplasmatic inclusion bodies. Periportal infiltrates of lymphocytes and macrophages extended into the liver lobules. Electron microscopically, LCMV particles were detected in lung and liver of all monkeys. The virus particles had the typical structure of arenaviruses. They were enveloped, pleomorphic, 80 to 150 nm in diameter with a lipid bilayer envelope of approximately 10 to 15nm. Electron-dense internal ribosomal structures, typical for arenaviruses, were inside the virions (Figure 2). Prominent inclusion bodies consisting of condensed ribosome-matrix masses persisted in lung cell as well as in liver cell cytoplasm. Arenaviruses were also detected in faecal samples (Figure 1). The pathomorphological and ultrastructural analyses of callitrichid hepatitis were confirmed by PCR.

Lymphocytic choriomeningitis viruses can be transmitted to monkeys and humans by contact with faeces or urine from infected rodents or with dust containing infective particles. Viremic mice within the enclosures were suggested to be the most likely source of LCM-infection of the investigated callitrichids. The potential exposure of many caretakers and zoo visitors to LCMV-infected tamarins and marmosets makes it particularly important to diagnose the infection with LCMV quickly.

Figure 1: Lymphocytic choriomeningitis virus (LCMV) found in the faecal samples of *Mico sp.* and *Saguinus midas,* negative staining

Figure 2: Utrathin section of arenavirus infected liver tissue, LCMV (arrow)

References:
[1] V.M. Lucke, A.M. Bennett (1982), Lab. Animals 16:73-77.
[2] R.J. Montali et al. (1993), J. Infect. Dis. 167(4):946-950.
[3] F.A. Murphy, S.G. Whitfield (1975), Bull World Health Organ. 52: 409-418
[4] S.R. Radoshitzky et al. (2015), Arch. Virol. 160(7):1851-1874.
[5] Ch.B. Stephensen et al. (1991), J. Virol. 65(8): 3995-4000.

Figure 1

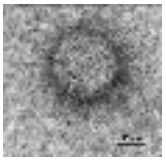

Figure 2

LS6.P002
Ultrastructural and imunohistochemical features of the epidermal cells in amphioxus *branchiostoma lanceolatum*

N. Kević[1], I. Restović[2], I. Bočina[1]

[1]Faculty of Science, University of Split, Ruđera Boškovića 33, Split, Croatia
[2]Faculty of Humanities and Social Sciences, University of Split, Poljička cesta 35, Split, Croatia

Introduction: Epidermis is a surface organ which protects animal from the environmental effects and from the pathogens. In vertebrate family, the epidermis of terrestrial animals is keratinized while in aquatic forms and amphibians can produce mucus. Amphioxus, a cephalochordate, is an important animal model in the study of vertebrate (chordate) phylogeny.

Objectives**:** Epidermal cells of amphioxus (*Branchiostoma lanceolatum* L.) were investigated morphologically by transmission electron microscopy (TEM) and using immunohistochemistry and immunofluorescence for detection of a major cytoskeletal and extracellular matrix proteins.

Materials & methods: The study was done on ten adult amphioxus specimens fresh-caught in the Adriatic Sea. After fixation, dehydration and embedding in paraffin blocks, paraffin sections of 6 µm thick were mounted on glass slides. For immunohistochemistry and immunofluorescence, slides were deparaffinized and rehydrated, then heated in a citrate buffer. Protein blocking buffer was used to exclude unspecific staining. The sections were incubated with primary antibodies according to their own protocols. For immunohistochemistry, DAB staining was used, and for immunofluorescence the sections were incubated with suitable secondary antibodies for one hour. For transmission electron microscopy, small pieces of tissue were fixed in 3.5% paraformaldehyde during 24 hours on 4 °C, and afterwards in 3% glutaraldehyde for 2 hours. The post fixation was done in 2% osmium tetroxide and tissue was embedded in Epoxy resin and cut transversally. Ultrathin sections, stained with uranyl acetate and lead citrate, were observed under Zeiss EM 10A electron microscope.

Results: Epidermis of the amphioxus consisted of one-layered columnar epithelium. These epithelial cells were characterized by voluminous nucleus, a well-developed supranuclear Golgi apparatus, abundant vesicles and apical secretory vesicles surrounded by cytokeratin filaments. A single row of smaller vesicles also appeared close to the basal cell membrane. Short microvilli were seen on the apical domain of the epidermal cells. The plasma membrane of adjacent cells strongly intertwined on its lateral domains in the form of finger-like protrusions. Positive immunolocalization of hyaluronic acid and collagen type I was observed in apical domain of plasma membrane of amphioxus, respectively. This positive signal probably refers to the secretory granules in the apical domain of the epidermal cell shown on the TEM.

Immunolocalization of aggrecan was seen around the cell nucleus, deep below the apical domain, suggesting that aggrecan is not located in secretory granules. A strong signal to cytokeratin 10 was present throughout the cytoplasm of the epidermal cells.

Conclusion: Due to its morphology and histochemical composition, epidermal cells of amphioxus may contribute to course surface protection and the mucous layer in amphioxus may serve as a physical barrier between the body and its environment.

Figure 1: Transmission electron micrograph of amphioxus epidermal cells. A: x12500, B: x20000. GA – golgi apparatus; V – vesicles; f – filaments; mv – microvilli; sv – secretory vesicles; n – nucleus; bl – basal lamina.

Figure 2: Positive immunolocalization (arrows) of aggrecan, collagen type I and hyaluronic acid in amphioxus epidermal cells.

Figure 1

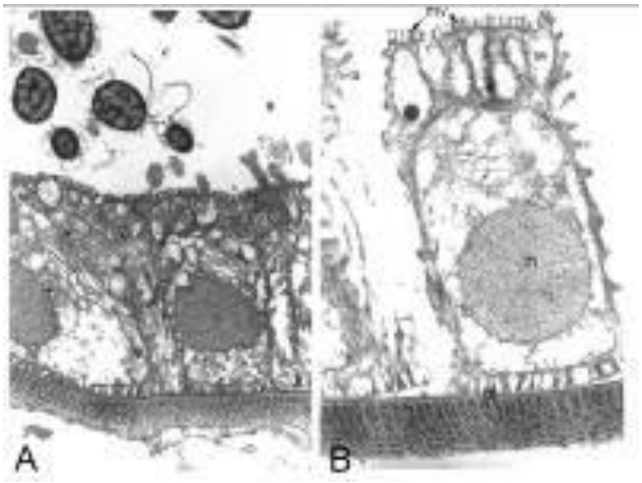

Figure 2

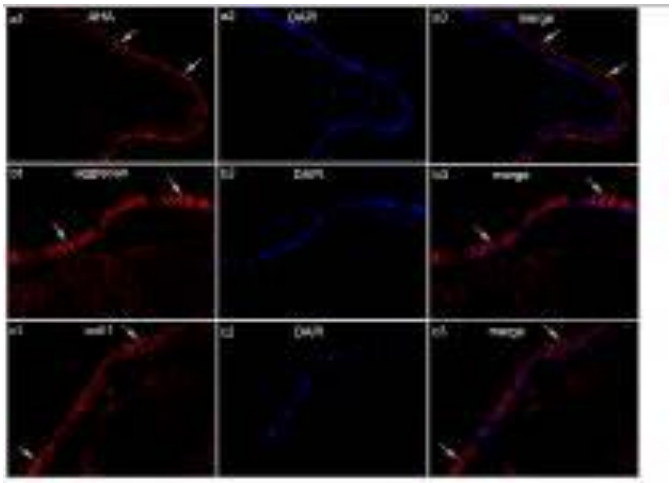

LS6.P003
NEWS from JEOL Lab – Elucidating novel crystalline structures with electron and NMR crystallography

E. Barbet-Massin[1], Y. Nishiyama[2]

[1]JEOL (Germany) GmbH, Freising, Germany
[2]JEOL Ltd., Tokyo, Japan

Intro: The position of hydrogen atoms in nano- and micro-crystals is a valuable information in material science, but also for pharmaceutical research and biology. Unfortunately, understanding hydrogen-bonding networks in such crystals which are too small for X-ray diffractometry (XRD) remains a challenge. In cases of nanocrystals, electron diffraction (ED) or electron 3D crystallography are great alternatives, but may lead to ambiguities when it comes to the position of hydrogen atoms. It often confounds atoms with similar atomic numbers such as carbon, nitrogen, and oxygen. This can be problematic for nanocrystals of organic molecules such as in the case of pharmaceutical tablets. Solid-state nuclear magnetic resonance (SSNMR) is very helpful, since it cannot only measure internuclear distances (including protons) but also assign all atoms in organic molecules.

Objectives: We present the novel development from Riken-JEOL Collaboration Center and Kyoto University iCeMS (Material-Cell Integrated System Center) to determine the molecular structures of low-molecular weight pharmaceutical compounds including the position of hydrogen atoms. This approach integrates ED for global structure analysis, SSNMR for local structure analysis and first-principles quantum chemical calculations, to study microcrystals of 0.1 to 1µm.

Material and Methods: The ED patterns are measured using a JEM-2200FS TEM (JEOL Ltd., Japan) operating at 200 kV with continuous rotation of the sample, and the SSNMR data acquired on a JNM-ECZ600R spectrometer (JEOL RESONANCE Inc., Japan) using 3.2mm and 1mm double-resonance MAS probes (JEOL).

Results: Using this integrated electron and NMR crystallography technique, the structure of the model compound L-Histidine could be confirmed and the previously unknown structure of cimetidine crystal form B could be elucidated (1). In this approach, the initial molecular structures of the compounds were solved from the ED patterns collected by continuously rotating the microcrystal around a single axis under electron irradiation. Relying on ED patterns only, these structures contained misassigned carbon, nitrogen and oxygen atoms, and lacked most hydrogen atom positions. The non-hydrogen elements can be corrected using the SHELXL software (2), and the hydrogen atoms added. In this step, SSNMR plays a key role, both in determining to which heteroatoms the hydrogen are bound (in case of ambiguities, e.g. in heterocycles such as imidazole ring) and measuring the proper X-H bond lengths. These can vary depending on the hydrogen bonding state of each atom. Once all the atomic positions are refined combining ED and SSNMR, several models can still describe the overall supramolecular arrangement of the molecules. To discriminate between those, GIPAW (3) calculations are used in a final step to determine which candidate is the most energetically favorable and calculated SSNMR chemical shifts are compared with experimental ones to conclude on the correct structure.

Conclusion: A combined approach joining the strengths of ED and SSNMR circumvents the challenges of XRD alone for the crystal structure determination of low molecular weight active pharmaceutical ingredients, for which hydrogen-bonding networks play a key role in conformation and crystal packing.

References:
[1] C.Guzmán-Afonso, Y.-l.Hong, Y.Nishiyama, Nat. Commun. 10 (2019) 3537
[2] Hubschle *et al., J. Appl. Cryst.* 44, 1281–1284 (2011)
[3] Pickard & Mauri, *Phys. Rev. B* 63, 245101 (2001)

LS6.P004
The role of lupeol against pesticides induced oxidative liver damage

M. Çöremen[1], İ. B. Türkyılmaz[1], H. US[1], A. Sezen US[1], Ö. Bulan Karabulut[1], R. Yanardağ[1]

[1]İstanbul University, Biology, Istanbul, Turkey

Introduction**:** Pesticides are chemicals used to control of harmful organisms such as some insects and fungi. Pesticides are used widely in agricultural fields and this causes majority of exposed of pesticide in people through unclean vegetable and fruit. Additionally, many researchers believes that pesticides can cause various disorders in human such as cancer, neurodegenerative disease and reproductive disorder (1).

Objectives: Our study aims that to determine the effect of lupeol on pesticides induced oxidative stress and histopathological changes in liver of rats. Also, we want to draw attention to protection from this condition that may impair human health. Oxidative stress parameters increase in case of exposure the pesticides and the antioxidant defense system remains insufficient.

Materials & methods: Sixty-three male Wistar rats into divided nine groups. Control groups were given saline, 50 mg kg -1 corn oil, and 20 mg kg -1 lupeol. Pesticide groups respectively were given 50 mg/kg malathion, 10 mg/kg chlorpyrifos, and 50 mg/kg tebuconazole daily. The antioxidant combination pesticide groups were given the same doses of pesticide and 20 mg/kg lupeol. All reagents were applied via gavage for ten days. Liver tissues were stained H&E and Masson's trichrome and histopathological damage were examined under the light microscope. Proliferating cell nuclear antigen (PCNA) positive cell numbers were determined by immunohistochemical methods. AChE enzyme activity, antioxidant enzymes and oxidative damage parameters were measured by using spectrophotometric and Enzyme Linked Immuno Sorbent Assay methods.

Results: Our study showed that lupeol administration reduced degenerative changes and PCNA levels in the liver, significantly. Lupeol also decreased oxidative stress parameters in liver tissue and ameliorated antioxidant enzymes activity. In addition, lupeol significantly increased AChE enzyme activity.

Conclusion: This study concludes, lupeol has an important protective role against oxidative damage in rat liver exposed to various pesticides according to histopathological, immunohistochemical and biochemical.results.

Keywords: Pesticide, lupeol, oxidative stress, liver

References:

[1] Sabarwal, A., Kumar, K., & Singh, R. P. (2018). Hazardous effects of chemical pesticides on human health–Cancer and other associated disorders. Environmental toxicology and pharmacology, 63, 103-114.

LS6.P005
Multimodal imaging for high resolution nanoanalytics in biological systems

A. Biesemeier[1], T. Taubitz[1], O. De Castro[1], J. N. Audinot[1], T. Wirtz[1]

[1]Luxembourg Institute of Science and Technology, Materials Research and Technology Department, Belvaux, Luxembourg

Metallic nanomaterials become more and more important in our every day"s life, they are used in many fields, e.g. food industry, biomedical research or nanotoxicology. Different highly specialised laboratory instruments must be used in order to investigate respective samples metrologically as well as chemically. Our group develops instruments based on focused ions beams for correlative multimodal imaging addressing the key characteristics needed, i.e. high spatial resolution, chemical sensitivity, dynamic range (for the detection and mapping of elemental concentrations varying over several orders of magnitude) and isotopic selectivity [1].

Here, the npSCOPE instrument [2] will be described in more detail. It is based on a Gas Field Ion Source as also used in a Helium Ion microscope (Zeiss NanoFab ®,[3]), providing finely focussed He^+ and Ne^+ ion beams. The npSCOPE incorporates a combination of three characterisation techniques in one single platform: (1) Secondary Electron (SE) imaging**,** providing morphological and topographical information (lateral resolution of ^{He}SE 0.5 nm). (2) Secondary Ion Mass Spectrometry (SIMS, lateral resolution < 20 nm)**,** providing high-sensitivity surface chemical information using a compact high-performance double-focussing magnetic sector mass spectrometer equipped with a focal plane detector, allowing a full mass spectrum to be recorded for each single pixel. (3) Scanning Transmission Helium Ion Microscopy (STHIM), providing bright and dark field imaging [4]. The npSCOPE is furthermore equipped for the analysis of frozen-hydrated samples.

Several examples on how our instruments can be used, e.g. for the nanotoxicological investigation of incorporated nanoparticles, but also subcellular mapping of structural or metabolic marker ions will be presented.

The use of focused ions beams allows the investigation of samples with high spatial resolution and chemical sensitivity. Using the npSCOPE, also thin biological tissue sections, as they are typically used for TEM investigations, but not suitable for SE imaging, can be properly investigated morphologically using the STHIM detector. In contrast to routine SIMS instrumentation, where a small number of masses of interest have to be chosen prior to analysis, the novel focal plane detector SIMS system allows the post-hoc analysis of all secondary ion species within the selected mass range. This permits also the identification and localisation of secondary ion species that were not expected during experiment design. This is especially important for nanotoxicological investigations of field samples. The integration of multiple imaging and analysis modalities within one single instrument reduces experiment time and avoids artefacts resulting from differing sample preparations and transfer between instruments. Pixel by pixel correlation of the different datasets is directly obtained by image fusion methods.

References:
[1] T. Wirtz, O. De Castro, J.-N. Audinot, P. Philipp, Ann. Rev. Anal. Chem. 12 (2019).
[2] This project has received funding from the European Union"s Horizon 2020 Research and Innovation Programme under grant agreement No. 720964.
[3] T. Wirtz, D. Dowsett, P. Philipp, Helium Ion Microscopy, ed. by G. Hlawacek, A. Gölzhäuser, Springer, 2017.
[4] E. Serralta, N. Klingner, O. De Castro, M. Mousley, S. Eswara, S. Duarte Pinto, T. Wirtz, G. Hlawacek, Beilstein J. Nanotechnol. 11 (2020).

LS6.P007
Wound healing of the earthworm body wall is mainly mediated by dedifferentiation, migration and redifferentiation of tissue cells

A. Erdélyi[1], L. Molnár[1]

[1]University of Pécs, Pécs, Hungary

Introduction: The model animal *Eisenia andrei* (Annelida, Oligochaeta, Lumbricidae) has both extreme regeneration and wound healing capacity. The formation of the scar tissue during the wound healing is a quick process in earthworms (about six hours). However, there is no information about the origin of the scare tissue cells from which distinct tissue cells are differentiated.

Aims: To reveal those cell lineages which contribute to the formation of distinct tissue layers of the body wall.

Material and methods: A standardized dorsal surgical intervention on the anteriormost segments (from first to sixth one) of the model animal was applied in all experiments. The kinetic and histological, cytological characteristics of the wound healing were observed by conventional light- and electron microscopy, histochemical methods (collagen and carbohydrate histochemistry). The intensity of the cell proliferation in distinct tissue layers of the body wall was determined by the calculation of the mitotic index in both normal wound healing and in those ones blocked by mitotic inhibitors (colchicine, demecholcine).

Results: The perfect closure of the body wall wound of *E. andrei* was carried out on the sixth postoperative hour of the surgical intervention. Cell dedifferentiation was identified in both epithelial and muscle layers of the body wall but no cell division was seen them. The wound healing was not inhibited by the application of the mitotic inhibitors.

Discussion: The presented results suggest that the wound healing of the earthworm body wall is mainly carried out by dedifferentiation, migration and probably redifferentiation of distinct tissue cells. Based on these findings we can propose that this is a morphallactic process in earthworms.

LS6.P008
Why do Schwann cells like spider silk? Exploring the structural, mechanical, morphological, and chemical reasons for the acceptance of spider silk by Schwann cells

L. Ploszczanski[1], K. Peter[1], G. Sinn[1], A. Naghilou[2], C. Radtke[2], H. Lichtenegger[1]

[1]University of Natural Resources and Life Sciences, Institute of Physics and Materials Science, Vienna, Austria
[2]MedUni Vienna/Vienna General Hospital, Plastic and Reconstructive Surgery, Vienna, Austria

Spider silk (SPSI) has been established as one of nature's most fascinating materials due to its unique properties. A remarkable application of the SPSI is its use in reconstructive medicine as nerve guidance structure/filament for nerve regeneration. The Schwann cells (SCs), which are a crucial part of the nerve regeneration process adhere to SPSI and migrate along it to support axonal elongation. SPSI degrades without inflammatory response or physiological pH changes. However, the interaction between the SCs and the silk and by that the SPSI properties, that promote SC adhesion are still unclear. The aim of this project is to elucidate material properties of SPSI, that are crucial for its unique performance in nerve regeneration. Not all spider silks show the same medical success, and we believe that properties such as composition, ultrastructure, and mechanical behavior have a pronounced influence on the acceptance of SPSI by SCs. Therefore, by combining experiments consisting of in vitro studies and the material characterization of various SPSIs, the properties, which are responsible for the advanced success of SPSI in nerve regeneration, will be clarified.

Objectives:
1) A systematic characterization of the SPSI from various species in wet and dry conditions with respect to mechanical, morphological, chemical, and structural properties
2) Monitoring the cell adhesion, distribution, motility, and proliferation on various SPSIs to assess the applicability of each silk type for supporting nerve regeneration
3) Establish the properties that make SPSI suitable in nerve regeneration applications based on finding a correlation between objectives 1 and 2

Ultrastructure investigations: The SPSI used in this experiment were: *Nephila edulis* and *Avicularia avicularia* MAG native and treated with ethanol, UV light and autoclaved.

For the tensile tests, one fibre of the major ampullate gland silk of the spider was extracted and mounted with nailpolish on a 3D printed sample holder. Spiders were fixated and sedated to ensure a homogeneous sample collection under forced spinning conditions. Prior to the tensile strength tests, the length of the spider silk has been recorded with a lightmicroscope (Keyence VHX 5000).

For the measurement the thin side supports of the sample carrier are removed with a soldering iron, so that only the thread is under tension.

The spidersilk was pulled with a speed of 25µm/s until terminal rupture on an ASMEC Unat nanoindenter in tensile mode. The collected rawdata was processed with numpy and pandas in python and the resulting graphs normalized.

The morphology and the size of SPSI were observed after the tensile test with scanning electron microscopy (FEI Quanta 250 FEG ESEM). A 10 nm thin gold layer was coated on the SPSI with an Edwards Scancoat 6 sputter coater. The micrographs were obtained by using the ETD. For determining the diameters of the mounted SPSI, five points were evaluated on two fibers from each silk type, leading to the average diameter from ten measurements.

We plan to go beyond the experiments in the SEM with additional spidersilk variants and perform following experiments:

in-situ tensile tests on single fibers. For understanding of the spider silks crystal structure, SAXS and XRD measurements will be conducted while straining the single fibers and fiber bundles in-situ on the adapted tensile stage.

Figure 1

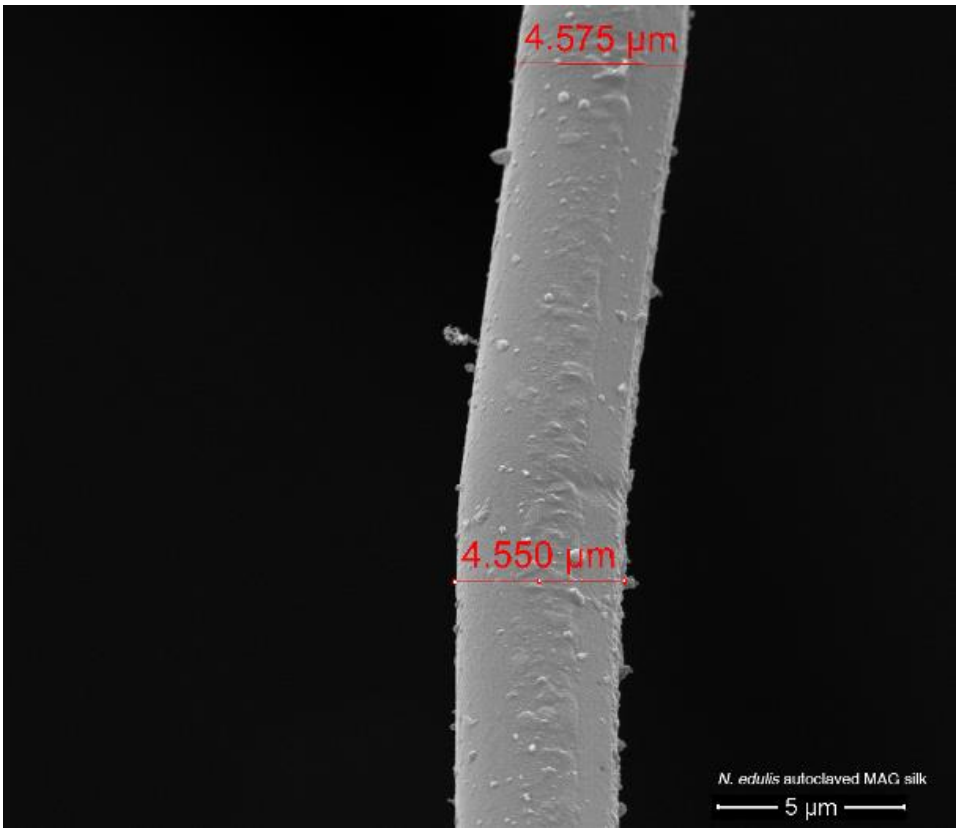

Figure 2

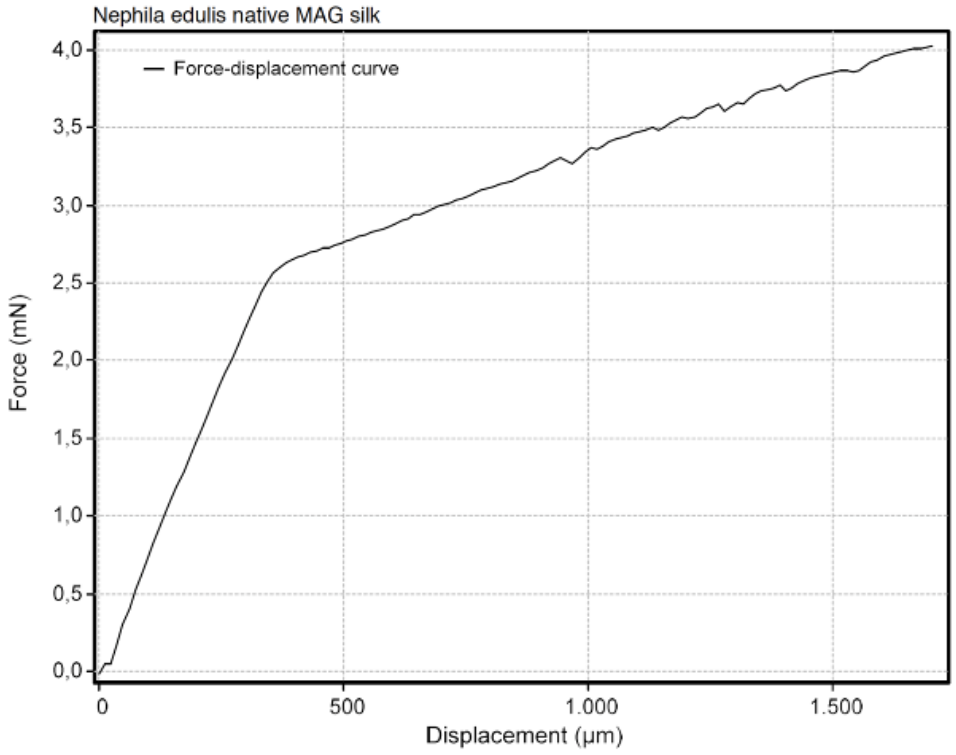

Figure 3

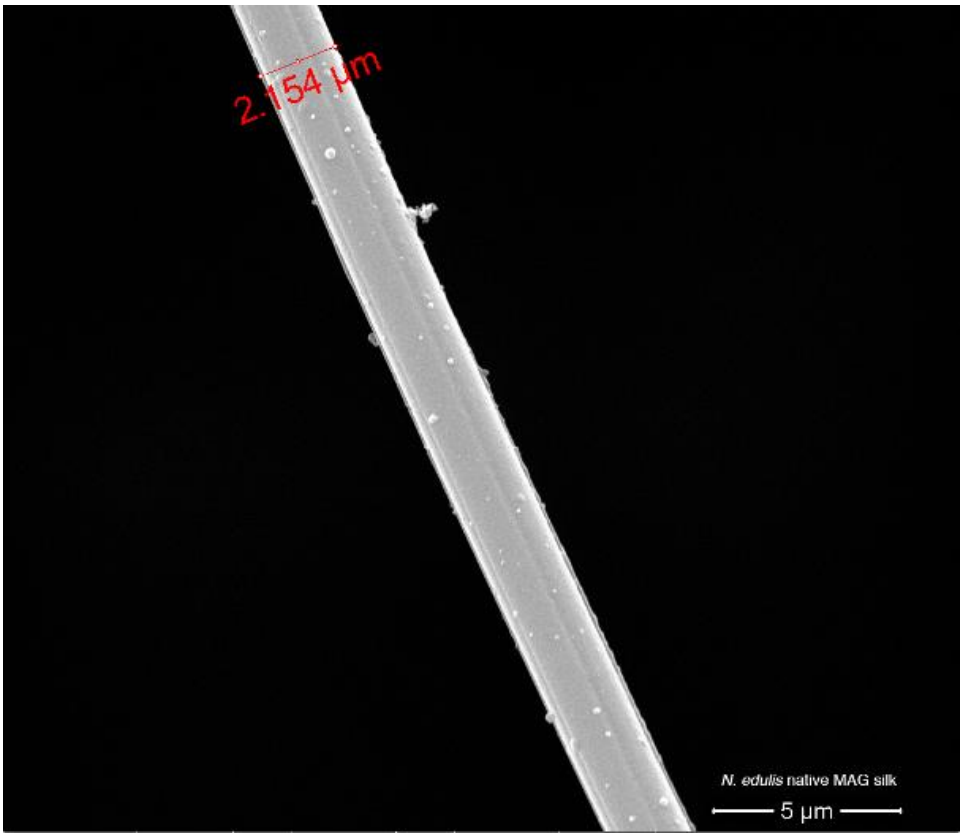

Figure 4

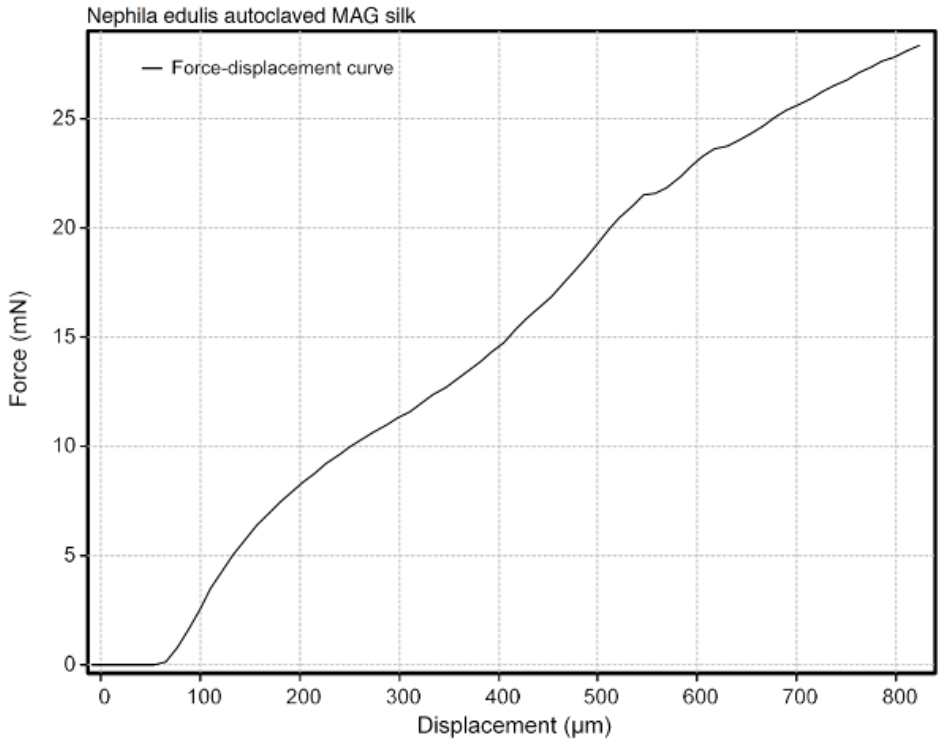

LS6.P009
Raman spectroscopy coupled with multivariate analysis of homemade and commercial honey

I. Pećinar[1], D. Rančić[1], S. Lević[1], S. Kilibarda[1], M. Mačukanović-Jocić[1]

[1]Faculty of Agriculture, Department of Agrobotany, Belgrade, Serbia

Introduction: Raman spectroscopy, as a powerful diagnostic technique for molecular analysis of food samples, was used as a rapid and reliable method for the discrimination of honey according to their source, as well as for faster detection of honey counterfeits. Since honey contains different proportions of sugars as the dominant components, the certain characteristic vibrational mode is useful to differentiate structural-based changes in these carbohydrates.

Objective: In order to contribute to a comprehensive database of Raman bands obtained from food samples, the present study aimed to detect and confirm differences in chemical composition between homemade and commercial honey using Raman spectroscopy as a fast tool combined with multivariate analysis (PCA).

Materials & methods: Raman scattering was excited by a laser at a wavelength of 532 nm equipped with 1200 lines/mm grating. The spectra preprocessing was realized using Spectragryph software, version 1.2.13. Principal component analysis (PCA) was performed using PAST software. Multivariate analysis, based on PCA, was applied in order to detect a possible difference in the chemical composition of honey samples.

Results: Raman spectra of honey show bands at 334, 420, 517, 624, 702, 816, 863, 915, 1070 and 1123 cm-1, which can be attributed to the sugars expected to occur in honey (glucose, fructose and sucrose). Glucose and fructose have dominant vibrational modes of C–C–C, C–C–O, C–O and C–C reported in the range of 200–500 cm-1. The higher intensity band at ~417 cm-1 and its shoulder at 448 cm-1 are probably attributed to the C–C–O vibration of α- and β- glucose, respectively. The glucose band at 417 cm-1 and band at 420 cm-1 of fructose band overlap, while 624 cm-1 is related to ring deformation of fructose. The band at 517 cm-1 could be assigned to the skeletal vibration of glucose. The medium intensity bands in the range from 816 to 975 cm-1 are related to vibrations of glucose and fructose. The band at 1123 cm-1 is assigned to the C-OH deformation of the glucose and sucrose, while a lower intensity band at 1370 cm-1 is assigned to the CH and OH bending mode of sucrose.

The minor contribution of other carbohydrates, proteins, amino acids and organic acids were confirmed by Raman spectroscopy by the bands at 334, 1077, 1266 cm-1 and 1460 cm-1.

The PCA analysis was performed using about forty Raman spectra. The score plot of PC1 versus PC2 shows a reasonably good separation between the samples, where the first and second principal components described 86.21% of data variance. The score plot suggests the clear existence of separation between traditional and commercial honey samples along PC1 axis. The loading plot shows that the variables with the highest positive contribution along PC1 axis corresponded to the signals at 284, 392, 682, 795, 890, 1118 and 1198 cm-1, while signals at 436 and 1026 cm-1 have the highest negative effects. Traditional honey comparing with commercial differs in a higher amount in β-glucose and fructose (assigned to pyranoid ring) content.

Conclusion: This study confirmed that Raman spectroscopy can be applied for the determination of chemical composition and combined with chemometric methods could confirm the differentiation of honey samples. Spectroscopic methods, comparing with standard analytical tools, are especially suitable for this kind of evaluation since they are fast, non-destructive and require a small amount of sample for analysis.

LS6.P010
Effect of antimicrobial peptides on bacterial ultrastructure – a scanning and transmission electron microscopical study

M. Acikel Elmas[1], O. Can[2], T. Kocagoz[3], S. Arbak[4]

[1]Acıbadem University, Histology and Embryology, Istanbul, Turkey
[2]Acıbadem University, Medical Engineering, Istanbul, Turkey
[3]Acıbadem University, Medical Microbiology, Istanbul, Turkey
[4]Acıbadem University, Histology and Embryology, Istanbul, Turkey

Introduction: Many living organisms produce antimicrobial peptides (AMPs) as a part of their innate immune system against bacteria, viruses, and fungi. These peptides are cationic and amphipathic. Because of the ability to interact with bacterial membranes, negatively charged lipids lead to destabilization and permeabilization of the cell membrane. Regarding increased resistance of pathogenic bacteria to traditional antibiotics and medications, AMPs are a promising alternative to treat infections.

Objectives: The aim of the present study is to investigate ultrastructural changes in the bacteria triggered by antimicrobial peptides (AMPs) by scanning electron microscopy (SEM) and transmission electron microscopy (TEM).
Materials & methods: As a gram-negative strain, *Escherichia coli* and gram-positive strain Staphylococcus aureus were exposed to the AMPs and untreated controls were used to compare morphological changes with SEM (Thermo Fisher Scientific- Quattro S SEM) and TEM (Thermo Fisher Scientific- Talos L120C) analysis. For the SEM analysis dialysis membrane was used to capture bacterial cells. Then, routine SEM preparation techniques were used. For the TEM analysis, both strains were firstly fixed with 2,5% glutaraldehyde solution. and following the fixation liquid samples were embedded in agar. At the end of this procedure evenly distributed specimens were treated like easily handled tissue blocks. Then, these tissue blocks were processed for epoxy resin embedding. Thin sections of 600 angstroms were stained with 2% uranyl acetate.

Results: SEM analysis of untreated E.coli and S.aureus cells revealed a smooth cell surface morphology. Different shapes of blisters and numerous small bubbles were obviously seen in AMPs treated cells. TEM analysis showed that the morphology of the bacterial cells treated with AMPs was altered dramatically. The cell membranes, which had an intact ultrastructure in untreated cells, were severely damaged to cause a discharge of cellular contents outside of the cells in the AMPs treated group.

Conclusion: Comprehensive EM analysis revealed that AMPs cause multiple stresses on the membranes of *E. Coli and S.aureus.* So, these results suggest that AMPs play an antibacterial role by destroying the integrity of the cell membranes. This molecule could be suggested to have a promising role to develop a potent antimicrobial agent.

Acknowledgments: This study was financed by The Scientific and Technological Research Council of Turkey (TUBITAK).- project number 217S060

Keywords: AMPs, SEM, TEM, Morphology

References
(Alkotaini et al., 2015; Han et al., 2017; Hartmann et al., 2010)
[1] Alkotaini, B., N. Anuar, and A.A.H. Kadhum. 2015. Evaluation of morphological changes of Staphylococcus aureus an d Escherichia coli induced with the antimicrobial peptide AN5-1. *Appl Biochem Biotechnol*. 175:1868-1878.
[2] Han, J., S. Zhao, Z. Ma, L. Gao, H. Liu, U. Muhammad, Z. Lu, F. Lv, and X. Bie. 2017. The antibacterial activity and modes of LI-F type antimicrobial peptides against Bacillus cereus in vitro. *J Appl Microbiol*. 123:602-614.
[3] Hartmann, M., M. Berditsch, J. Hawecker, M.F. Ardakani, D. Gerthsen, and A.S. Ulrich. 2010. Damage of the bacterial cell envelope by antimicrobial peptides gramicidin S and PGLa as revealed by transmission and scanning electron microscopy. *Antimicrob Agents Chemother*. 54:3132-3142.

LS6.P011
A sample preparation method for observing biological samples by digital holographic microscope

K. Umemura[1], K. Hirayama[1], Y. Ide[1], Y. Matsukawa[1], M. Takemura[1], S. Mayama[2]

[1]Tokyo University of Science, Shinjuku, Japan
[2]Tokyo Diatomology Laboratory, Koganei, Japan

Introduction: The digital holographic microscope (DHM) is becoming a powerful tool to observe three-dimensional structures of microorganisms without any pretreatment. The DHM data involve optical properties of the observed objects, therefore, distinguishment of two objects which composed with different materials is available even though the morphology of the two objects is completely similar. On the other hand, establishments of optimal sample preparation methods for DHM observation is expected to apply the DHM techniques to various biological samples.

Objectives: In order to obtain stable images of micron size objects, we proposed the use of agar gel to stabilize position of the objects during DHM observation.

Materials & methods: A commercially available DHM (HT2, Tomocube Inc., Korea) was used as a DHM equipment. Suspension of microbeads made of silica (SI) or polystyrene (PS). Diameters were 5 and 6 microns for SI and PS, respectively. We mixed the two beads and observed the mixture using a standard TomoDish (Tomocube Inc., Korea). As biological samples, living *cylindrotheca* sp. diatom cells and *HeLa* cells were also observed.

Results: SI and PS were well distinguished by analysis of reflective index (RI) although the two types beads had similar shapes. When the beads were observed in water, some beads were migrated during the observation. It induced obscure results although the DHM can capture movies of the migration. When the beads were immobilized by adding agar gel, stable DHM images were obtained with high reproducibility. In the observation of a diatom cell, protoplasm, vacuole, and chloroplast of the cell were well resolved without any staining and other pretreatment. In the case of HeLa cells, dynamic deformation of the cells induced by addition of enzymes were observed.

Conclusion: We demonstrated several biological samples and microbeads by DHM in liquid with a proposal a sample preparation method using agar gel. Our work provided a helpful information to establish DHM techniques for biological samples.

LS6.P012
Cathodoluminescence imaging of live-stained cell organelles observed using the cryo-scanning electron microscope

M. Vancová[1], R. Skoupý[2], V. Krzyžánek[2], T. Bílý[1], J. Nebesářová[1]

[1]Biology Centre, Czech Academy of Sciences, Institute of Parasitology, České Budějovice, Czech Republic
[2]Institute of Scientific Instruments, Czech Academy of Sciences, Brno, Czech Republic

Cathodoluminescence (CL) is the emission of photons from a material in response to excitation by accelerated electrons. CL imaging of biological specimens has limited usage because of low CL signal intensity and rapid fading under the electron beam. However, new labels (rare-earth element-doped nanocrystals, nanodiamonds, etc.) of nanometer size with high resistance against electron beam excitation, plus recent technological advances, enable the use of CL imaging to identify specific biological structures under the electron beam. Luminescent transition metal complexes are novel probes suited for staining live samples because they display high resistance to photobleaching, capacity for multicolor/multiple probe imaging, and, most importantly, low toxicity. Here, we present their usage for the first time to identify specific cellular compartments using the CL in the cryo-SEM. In vivo stained VERO or Saccharomyces cerevisiae cells were washed in HEPES, imaged with a fluorescence microscope, and high pressure frozen. Frozen cells were transferred to CryoALTO (Gatan) preparative chamber cooled at -135 °C, fractured, etched, and sputter-coated with Au (~2nm). Cells were observed by JEOL SEM 7401F equipped with CRYTUR CL detector at 4 kV using CL and ETD detectors. Independently, the CL imaging was performed by Magellan 400L (FEI) equipped MonoCL4+ detector (Gatan) at -140 °C. In this case, the cells were Au/Pd coated (3 nm). At low magnification, the CL signal helps find cells' positions in the fractured area and identify labeled organelles in high magnification. Parameters for CL detection using CRYTUR CL detector were: 2-7 keV (optimally 4 kV), probe current 30 pA-0.6 nA, dwell time 30-60 µs, pixel size 42.5 nm; dose 3.11-124.4 e^-/nm^2. At low magnification, the CL signal was evident in three consecutive scans at these parameters. Luminescent transition metal complexes are promising probes for observing biological specimens using correlative imaging techniques, including live-cell fluorescence imaging, cryo-fluorescence, and CL imaging at cryo-SEM at low magnification.

This work was supported by TACR (TE01000008) and MEYS CR (Czech BioImaging LM2018129).

LS6.P014
SEM-EDS elemental characterisation of asbestos fibres – An insight into the precision of substrate-free fibre composition assessed by Monte Carlo simulations

E. Arias[1], C. M. Garzón[2], J. W. Sandino[2], A. I. Rodríguez[1]

[1]Universidad Nacional de Colombia, Toxicología, Bogotá, Colombia
[2]Universidad Nacional de Colombia, Física, Bogotá, Colombia

Worldwide, prevalence of structural components with asbestos containing materials (ACMs) needing some intervention (repairing, demolition, substitution, etc.) is a major concern. While analytical transmission electron microscopy (A-TEM) is the first option for ACM characterization (because this could provide an unambiguous fiber characterization), scanning electron microscopy (SEM) allows an affordable and straightforward fiber morphology characterization. However, SEM-EDS (energy dispersive spectroscopy) characterization of asbestos fibers is barely used due to the unacceptable uncertainty in the fiber elemental composition. This impaired accuracy is a straightforward consequence of the non-negligible influence of the substrate in the overall EDS spectrum. In this contribution, we present a straightforward methodology for characterization of fibers in ACMs by SEM-EDS. This methodology is based on the theoretical deconvolution of the individual contributions of the substrate and the fiber to the overall experimental EDS spectrum. Using the freeware Casino software, a theoretical spectrum of the characteristic X-ray emissions is simulated and compared with the experimental one (after Bremsstrahlung radiation correction). As fitting parameters of the modeling, they are set the fiber elemental composition and thickness. We present an experimental analysis on both (i) three different batches of chrysotile reference fibers provided by the National Institute of Standards (NIST), which were supported on mixed cellulose ester (MEC) filters and (ii) debris of a bulk chrysotile rock provided by a local mineral mine. Elemental compositions obtained in experiments carried out at both 10 kV and 30 kV are compared. Although a higher influence of the substrate is obviously obtained in experiments at 30 KV, they did not lead to intrinsically impaired elemental characterizations, while they allow indeed analysis which are time cost-effective. Density of both, asbestos fiber, and MEC-filter, are unknows (nominal values were used in the simulations). We have observed that variations of those densities in around 50% regarding the nominal reference play a minor role in the fiber elemental composition assessed. We observed that the main obstacle for accurate elemental composition of the fiber is the actual chemical composition of the substrate. MEC filters are hygroscopic materials which concentration of oxygen and nitrogen greatly vary between different batches, as well as inside a single filter, where that variations are time dependent. Because both the asbestos fiber and the MEC-filter are rich in oxygen, the methodology we propose is not enough accurate for resolving the exact stoichiometric concentrations in the oxides composing the asbestos fiber, however this methodology gives elemental concentrations which are accurate enough for general screening of the fibers in ACMs. We also present an insight into the role that the following parameters exert on the accuracy of the assessed fiber elemental composition: relative fiber to electron beam drift, utilization of conductive materials for best connecting the MEC-filter and the SEM sample holder, heterogeneities in the fiber chemical composition and thickness, fiber contamination, and fiber morphology, as well as the preparation of the samples analyzed, which are referred to as reference material.

Figure 1

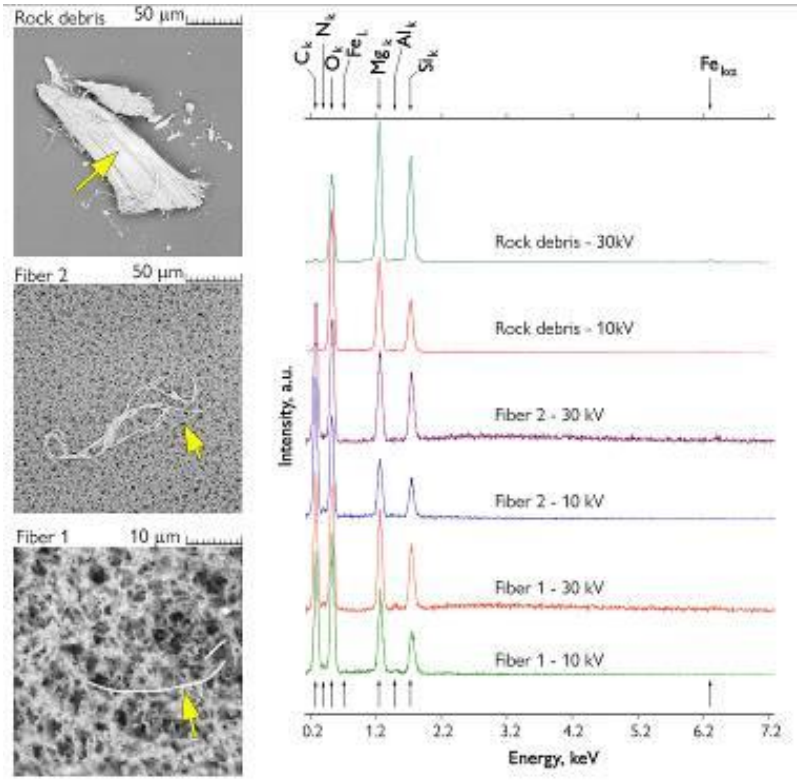

Figure 1 – SEM micrographs of two selected fibers and rock debris (left) and the concomitant EDS spectra (right). Micrographs were registered with Backscattered electrons and 10 kV.

Figure 2

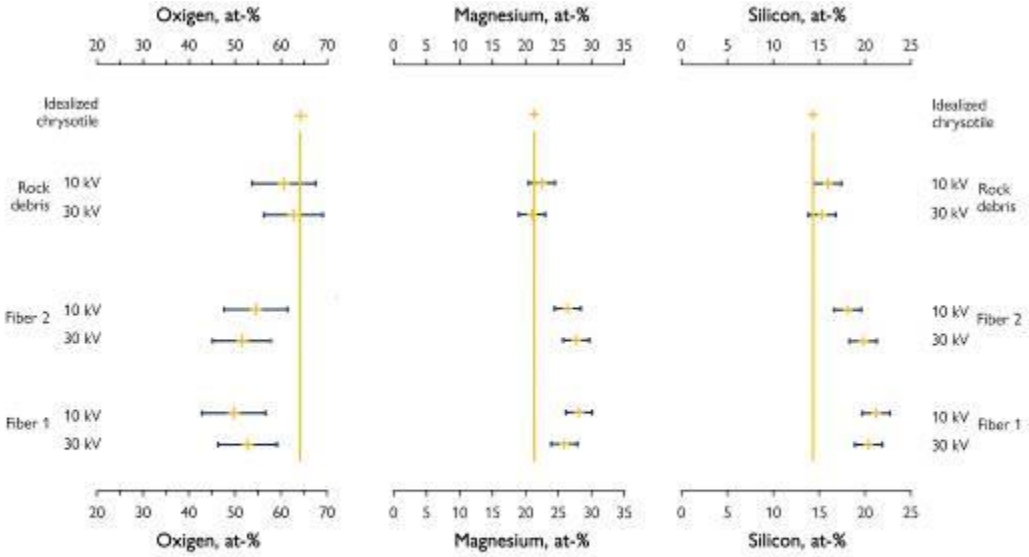

Figure 2 – Concentration of main elements (namely O, Mg and Si) for two selected fibers and rock debris previously shown in Figure 1. Elemental concentration of an idealized chrysotile is superimposed for comparison. In that idealized chrysotile, namely $Mg_3(Si_2O_5)(OH)_4$, we have neglected the H atoms, obtaining the following formulae for reference in this contribution, $Mg_3O_9Si_2$.

LS6.P015
The effects of every-other-day feeding on hippocampal parvalbumin- and calbindin-expressing neurons in 5XFAD mouse model of Alzheimer´s disease

N. Nestorović[1], K. Prpa[2], J. Ćirić[2], D. Milanović[2], M. Manojlović-Stojanoski[1], M. Perović[2]

[1]Institute for Biological Research "Siniša Stanković", National Institute of Republic of Serbia, University of Belgrade, Department of Cytology, Belgrade, Serbia
[2]Institute for Biological Research "Siniša Stanković", National Institute of Republic of Serbia, University of Belgrade, Laboratory for Molecular Neurobiology, Department of Neurobiology, Belgrade, Serbia

Neuronal degeneration associated with Alzheimer's disease (AD) correlates with impaired calcium homeostasis and changes in calcium-binding proteins such as parvalbumin (PV) and calbindin (CB). One of the first brain areas affected by AD is the hippocampus.

The present study aimed to examine the effects of food restriction as a preventive intermittent, every-other-day (EOD) feeding regimen in the brain of 5XFAD mice, a commonly used transgenic animal model of AD, particularly on PV- and CB-expressing neurons in the dorsal hippocampus.

A total of 41 female mice were included in the study: 5XFAD transgenic mice (Tg), n=21 and their non-transgenic littermate controls (non-Tg), n=20. They were provided with food *ad libitum* (AL) until 2 months of age when the development of amyloid deposits and neuroinflammation in the hippocampus and cortex starts. Then 5XFAD mice were assigned to 2 groups: 5XFAD-AL (Tg-AL) group continued to receive food AL (n=12), while the 5XFAD-EOD (Tg-EOD) group was fed EOD (n=9). The non-Tg mice were used as controls and divided the same way: AL group (non-Tg-AL; n=12) and EOD (non-Tg-EOD; n=8). All animals were sacrificed at 6 months of age when the deficits in hippocampal memory start to develop. The left hemispheres of isolated brains were fixed in 4% PFA, cryoprotected, and sectioned (coronal sections, 30µm) at the levels approximately -1.656 to -2.255 from the bregma. For immunofluorescence (IF) detection of PV- and CB-positive neurons in the hippocampus, a monoclonal mouse anti-PV (PARV-19) and rabbit anti-CB D-28K primary antibodies were used, respectively. For visualization of PV and CB, anti-mouse Alexa fluor 568 and anti-rabbit Alexa fluor 488 secondary antibodies were used, respectively. The relative intensity of fluorescence (RIF), as a measure of the expression of PV and CB in C1 and C3 hippocampal subregions, was determined on images obtained using a confocal laser scanning microscope (Leica TCS SP5 II Basic). For each animal, layers from 18 to 4 in Z-stacks for C1 and C3 hippocampal subregions were analyzed.

Distinct distribution of PV- and CB-IF was observed in all hippocampal subregions analyzed and was most obvious in CA3 hippocampal region, with PV-IF present in the pyramidal cell layer and the CB-IF dominantly present in the area consisting mostly of mossy fibers (Figure 1). RIF of both PV and CB in Tg-AL animals was not significantly different when compared to non-Tg animals indicating that mutations had no effects on PV and CB expression in the hippocampus. However, higher signal intensity was observed in both non-Tg and Tg animals after EOD. In particular, 2-way ANOVA revealed a significant effect of EOD on PV-IF in the CA1 region of non-Tg and Tg mice (Fig 2). The effect of EOD was also noted in the CA3 region, where a significant increase by 40% in non-Tg and by 250% in Tg mice was observed (Fig 2). Also, total signal intensity was more prominent in CA1 compared to CA3 region of all animals. Significant changes in CB-IF after EOD were observed in CA1 region of non-Tg mice, as well as in the CA3 region of Tg mice (Figure 2). In CA1 region of Tg mice, and CA3 region of non-Tg mice no effects of EOD were detected.

The present study shows that EOD affects calcium-binding proteins in the hippocampus of 5xFAD mice. EOD induced increase in PV and CB points to specific alteration in network excitability and thus could be of therapeutical importance.

Figure 1

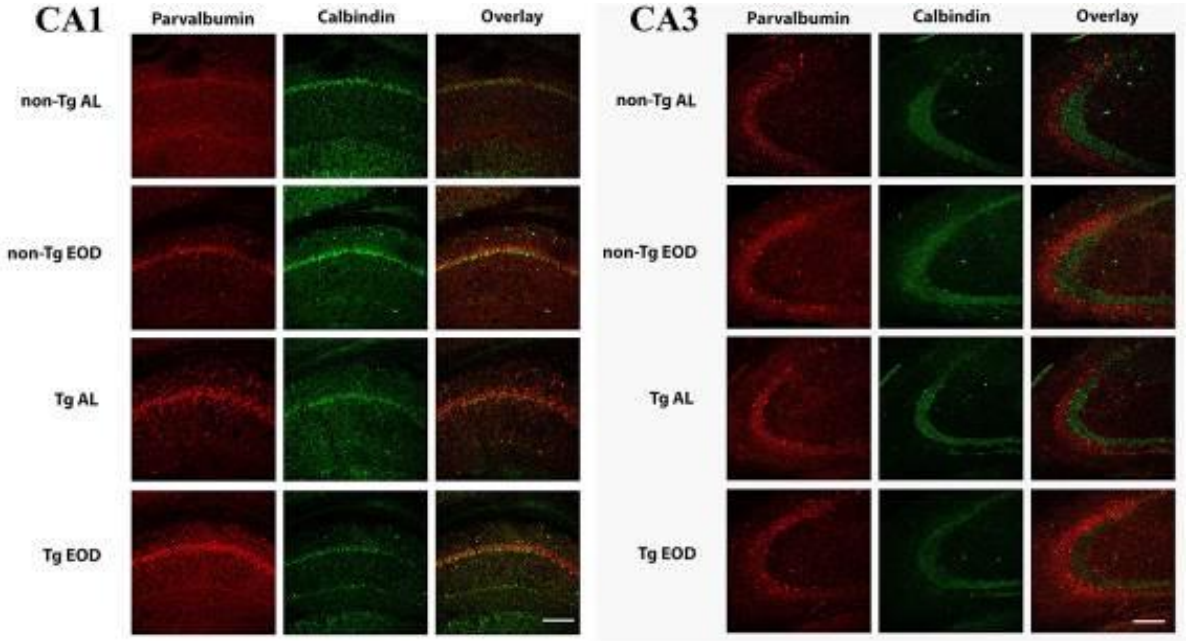

Figure 2

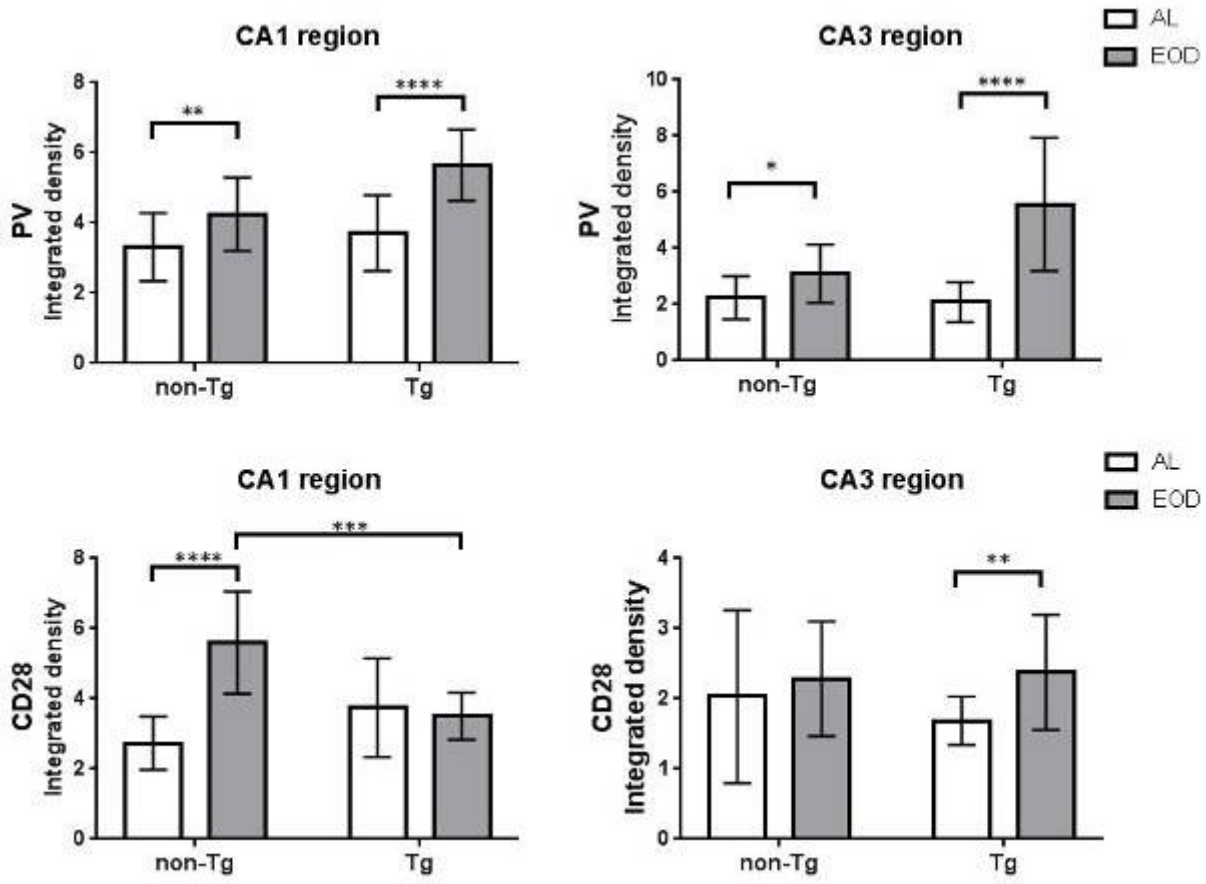

LS6.P017
Expression of Kisspeptin system on oviduct in rats fed with the high-fat diet

L. Kilinc[1], M. Dogan[1], O. Sinen[2], M. Bulbul[2], G. Akkoyunlu[1]

[1]Akdeniz University, Histology and Embryology, Antalya, Turkey
[2]Akdeniz University, Department of Physiology, Antalya, Turkey

Introduction: Mammalian fertilization is a complex process in which a spermatozoon meets and fuses with an oocyte within an oviduct. Oviducts offer a complex environment that contains specific signals from oviductal and follicular fluids that promote sperm capacitation (Lee, Sugimura et al. 1976, Hunter 2005).

High dietary fat intake can cause metabolic and reproductive impairment, even without the obese phenotype. Therefore, it is important to note that exposure to HFD alone can cause impaired fertility, even in frail individuals (Hohos and Skaznik-Wikiel 2017).

Kisspeptins were originally identified as products of the metastasis suppressor gene Kiss1 (Kotani, Detheux et al. 2001). Kisspeptins and the kisspeptin receptor KISS1R play key roles in mammalian reproduction by regulating gonadotropin-releasing hormone (GnRH) secretion from the hypothalamus (de Roux, Genin et al. 2003). Previous studies showed that kisspeptin / KISS1R systems are expressed in epithelial cells lining the lumen of the uterus and ovarian canal and are therefore constantly present in the female reproductive tract (Cejudo Roman, Pinto et al. 2012).

Objectives: To investigate the changes of expression of kisspeptin / KISS1 receptor (KISS1R) proteins along the oviduct of rats fed a high-fat diet.

Material & Methods**:** 4-week-old female rats obtained from Akdeniz University Experimental Animals Unit. Animals were kept in standard conditions; fed with control diet consisting of standard laboratory food (13.5% of total energy from oil) or HFD (60% of total energy from oil) for 8 weeks. Experimental procedures were performed at the age of 12 weeks (250-275 g live weight). Live weights and food consumption of the animals in both groups were calculated weekly and recorded during the experiment.

At the end of the experimental period, the animals were sacrificed and tissues were obtained. Sections were taken from paraffin-embedded tissues. Immunohistochemical staining for KISS1 and GPR54 were performed in both groups' oviduct.

Results: There was a significant increase in body weights of the HFD group during the experiment period compared to the control group.

As a result of immunohistochemical staining, strong kisspeptin immunolabeling indicated the presence of in the ciliated oviduct epithelium surface both the control group and experimental group.

KISS1R expression was located in the cytoplasm of the oviduct epithelium. HFD group also expressed the KISS1R in the oviduct epithelium with increasing intensity.

Conclusion: Kisspeptin/KissR are normally present in the rat oviduct. HFD caused upregulated the kisspeptin/KissR expression. Our findings are compatible with a potential modulatory role of kisspeptin/KissR for peripheral reproductive tissues.

LS6.P018
The protective effects of resveratrol and vitamin D on liver fibrosis and apoptosis in fructose-fed diet and streptozotocin induced T2DM model

M. Anapali[1], A. S. Akdemir[2], F. Kaya Dagistanli[2], M. Öztürk[2], T. Ulutin[2]

[1]Atatürk University, Faculty of Medicine, Medical Biology Department, Erzurum, Turkey
[2]Istanbul University-Cerrahpasa, Cerrahpasa Medicine Faculty, Medical Biology Department, Istanbul, Turkey

Introduction: Type 2 diabetes mellitus (T2DM) is associated with risk for severe liver disease. As a potent antioxidant, resveratrol is a natural compound that possesses anti-inflammatory and anti-diabetogenic properties. It has been reported that insulin resistance and a low level of vitamin D (vitD) may have a higher risk of developing type 2 diabetes [1-3].

Objective: In this study, we researched the effect of resveratrol, vitD or resveratrol+vitD combined treatment on liver cell mass, liver fibrosis and apoptosis in modified version of a new model of T2DM [4] induced by high fructose diet and low-dose streptozotocin (STZ).

Methods: In this study, 8-week-old male Sprague-Dawley rats were randomly subdivided into 8 groups of 7 animals in each group. In diabetic groups, a single dose of 40 mg/kg STZ injected after 10% fructose diet *ad libitum* for 2 weeks, then continued the 10% fructose diet *ad libitum* for 3 weeks. At the end of the 5th week, we started treatment. At the end of 5 weeks, rats were treated with resveratrol (1 mg/kg/day bw), vitD (oral 170/IU/week) or resveratrol (1 mg/kg/day bw) and vitD (oral 170/IU/week) for 4 weeks. At the end of 9 weeks, rats were sacrificed and liver tissues were taken under anaesthesia. Blood glucose (BG) levels of all rats were measured. The liver tissue sections were immunostained with PCNA and active caspase-3 antibodies. TUNEL assay was used for detection of apoptosis. Sirius-Red assay was used for detection of liver fibrosis. All values were analyzed with statistical methods.

Results: BG levels (Figure1-A) were significantly increased in the diabetic control group compared with the other group. The BG levels of the diabetic control group were significantly elevated compared to other groups ($p<0.001$). We found that resveratrol and vitD treatments reduced fasting BG levels, but resveratrol+vitD combination therapy reduced fasting blood glucose levels almost the same as the healthy control group. Collagen accumulation was observed around liver central vein in the diabetic group by Sirius-Red staining. PCNA positive cell number significantly decreased in the diabetic group compared to other groups ($p<0.0001$). In the diabetic group, active-caspase-3 immunopositive cells and apoptotic cells were higher than other groups ($p<0,001$) (Figure1-B). In rats treated with both resveratrol and vitD, fibrosis and apoptotic cells decreased. They exhibited liver morphology characteristics similar to the control group.

Figure 1: (A) The blood glucose levels of all groups. (B) Immunolocalization of PCNA, active caspase-3 and TUNEL in the liver for Diabetic (a,b,c) and Diabetic+Resveratrol+VitD (d,e,f) groups. Immunostaining: Streptavidin-biotin peroxidase (a,b,d,e) and TUNEL method (c,f). Magnifications: 200x.

Conclusion: We found that resveratrol and vitD are effective in preventing liver fibrosis and apoptosis, also resveratrol increases the effectiveness of vitD in the combine therapy. The combination of resveratrol and vitD may be a potential therapeutic approaches for liver diseases depend on T2DM.

References:
[1] Tanriverdi G, Kaya-Dagistanli F, Ayla S, et al. Histol Histopathol 31 (2016)
[2] Wang S, Cai B, Han X, et al. Medicine 99 (2020)
[3] Udomsinprasert W and Jittikoon J. Biomed Pharmacother 109 (2019)
[4] Wilson RD and Islam MS. Pharmacol Rep 64 (2012)

This presented work was supported by the Research Fund of Istanbul University. Project No.TYL-2017-26139

Figure 1

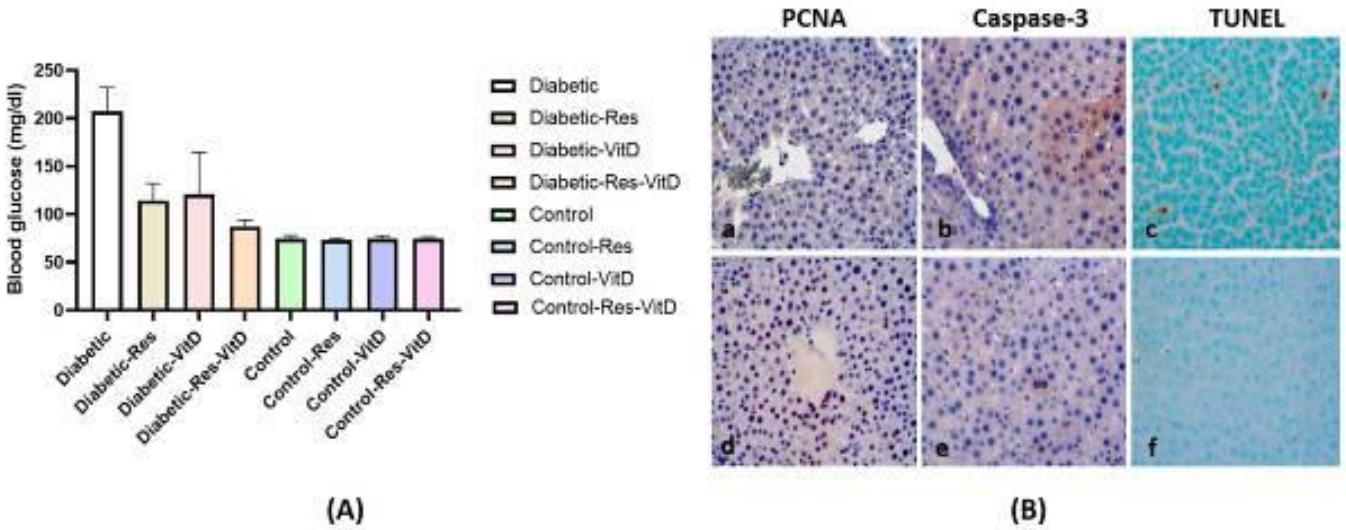
Blood glucose (mg/dl)
250
200
150
100
50
0
Diabetic
Diabetic-Res
Diabetic-VitD
Diabetic-Res-VitD
Control
Control-Res
Control-VitD
Control-Res-VitD
PCNA
Caspase-3
TUNEL
a
b
c
d
e
f
(A)
(B)

LS6.P019
Effects of combined resveratrol and vitamin D treatment on islets cells functions in fructose-fed diet/streptozotocin-induced T2DM rats

F. Kaya Dagistanli[1], A. S. Akdemir[1], M. Anapali[2], D. Aydemir[3], N. N. Ulusu[3], T. Ulutin[1], M. Öztürk[1]

[1]Istanbul University-Cerrahpasa, Cerrahpasa Faculty of Medicine, Department of Medical Biology, Istanbul, Turkey
[2]Atatürk University, Faculty of Medicine, Medical Biology Department, Erzurum, Turkey
[3]Koc University, School of Medicine, Medical Biochemistry Department, Istanbul, Turkey

Introduction: Diabetes mellitus is characterized by hyperglycemia and impaired insulin secretion and associated with metabolic abnormalities which cause serious complications. Resveratrol treatment improves insulin sensitivity, glycemic control of diabetic rats and patients with type 2 diabetes mellitus (T2DM) [1]. Vitamin D (vitD) promotes pancreatic beta cell function and regulates hyperglycemia and hyperinsulinemia [2].

Objectives: The aim was to investigate the effects of combined resveratrol and vitD treatment on pancreatic islet cells activation and β-cell regeneration in fructose-fed diet/streptozotocin(STZ)-induced T2DM rats.

Materials & methods: In this study, 8-week-old male Sprague-Dawley rats were randomly subdivided into 8 groups. In diabetic groups, a single dose of 40 mg/kg STZ injected after 10% fructose diet *ad libitum* for 2-weeks, then continued 10% fructose diet *ad libitum* for 3-weeks. At the end of 5-weeks, rats were treated with resveratrol (1mg/kg/day bw), vitD (oral 170/IU/week), combined resveratrol (1mg/kg/day bw) and vitD (oral 170/IU/week) for 4-weeks. Blood glucose (BG) levels of all rats were measured. The pancreas tissue sections were immunostained with insulin, glucagon, somatostatin and PCNA antibodies. Insulin, glucagon and GLP-1 levels were measured in the rat serum samples by Magpix Luminex Multiplex device.

Results: BG levels were significantly increased in the diabetic group compared with the other groups. Serum insulin levels increased significantly in all diabetic groups because of the development of insulin resistance compared to non-diabetic control groups. However, in the combined resveratrol+vitD diabetes group, serum insulin levels were similar to the control group, this was consistent with increased β-cell mass. Combined treatment increased GLP-1 levels whereas decreased glucagon levels in the non-diabetic controls, unlike diabetic groups. In the combined group, markedly enhanced β-cell mass due to increased islets size and β-cell clusters scattered in the exocrine tissue as well as around the ducts were observed compared to the diabetics (Fig 1). PCNA positive cells were increased especially in the big size islets of the combined group compared to the diabetics. Hypertrophic and centrally located somatostatin cells in the diabetic group were seen a similar order and appearance to the control group in the diabetic combined group (Fig 1). Glucagon cell occupied area significantly decreased in the islets of the combined group, consistent with the decreased serum GLP-1 and increased glucagon levels compared to the diabetics (Fig 1).

Figure 1: Immunolocalization of insulin, glucagon and somatostatin in the pancreas of the control, diabetic and combined resveratrol+vitD diabetic groups. Immunostaining: Streptavidin-biotin peroxidase method. Magnifications: 200x.

Conclusion: We found that resveratrol and vitD when used in combination, rather than being used alone, contributed to the improvement of islet morphology and regeneration of β-cell as well as the regulation of glucose and insulin homeostasis in this diabetes model. Therefore, we considered that the combined resveratrol+vitD usage might be beneficial in T2DM.

References:
[1] Szkudelski T, Szkudelska K. Biochim Biophys Acta. 1852 (2015)
[2] Harinarayan CV. Hormones (Athens) 13 (2014)

The study was supported by the Research Fund of Istanbul University-Cerrahpasa, Istanbul, Turkey Project No. TSA-2019-32274

Figure 1

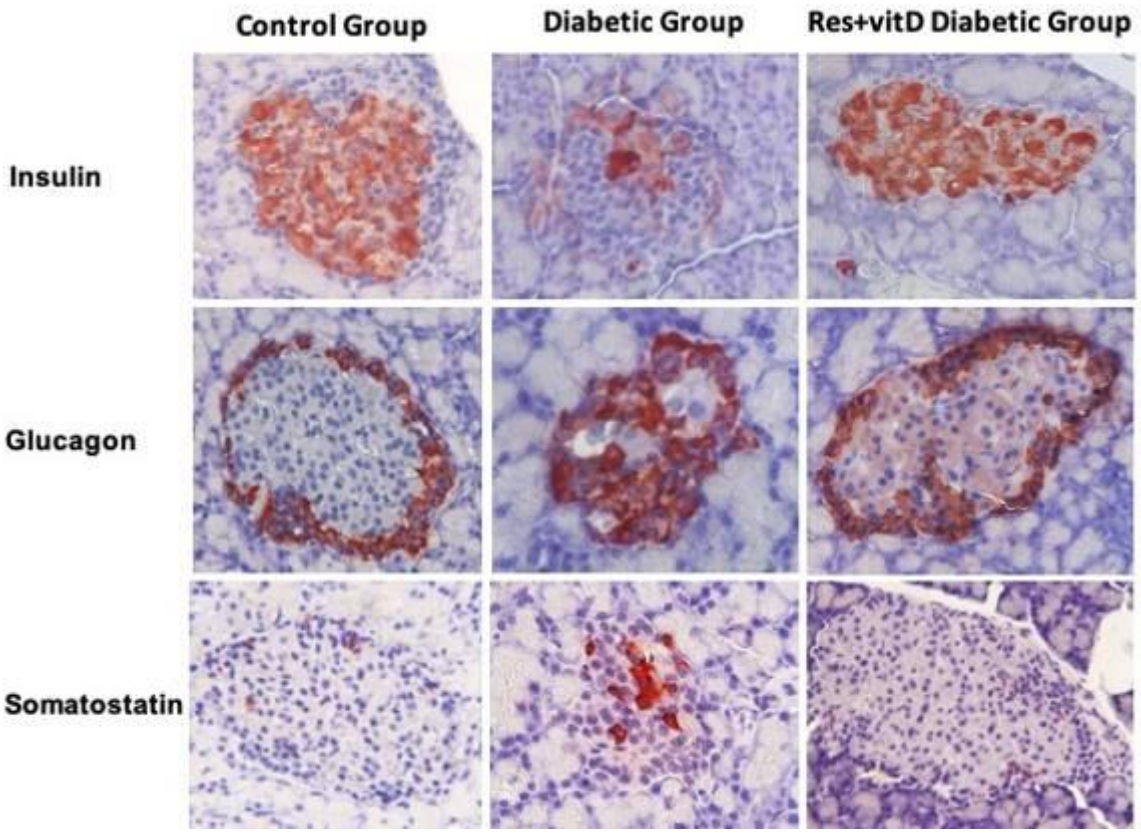
Control Group
Diabetic Group
Res+vitD Diabetic Group
Insulin
Glucagon
Somatostatin

LS7.002-Invited
Creating biomimetic bioactive environments for tumour engineering based on alginate hydrogels and perfusion bioreactors

B. Obradovic[1], J. Stojkovska[1,2], D. Veljovic[1], M. Milivojevic[3], M. Stevanovic[3,4,5], M. Dragoj[6], T. Stankovic[6], M. Pesic[6]

[1]Faculty of Technology and Metallurgy, University of Belgrade, Belgrade, Serbia
[2]Innovation Center of the Faculty of Technology and Metallurgy, Belgrade, Belgrade, Serbia
[3]Institute of Molecular Genetics and Genetic Engineering, University of Belgrade, Belgrade, Serbia
[4]Faculty of Biology, University of Belgrade, Belgrade, Serbia
[5]Serbian Academy of Sciences and Arts, Belgrade, Serbia
[6]Institute for Biological Research "Siniša Stanković", National Institute of Republic of Serbia, University of Belgrade, Belgrade, Serbia

Introduction: Tumor engineering uses certain strategies of tissue engineering to create 3-dimensional (3D) environments for cultures of cancer cells in order to attain specific aspects of tumor architecture and function that are absent in traditional 2D monolayer cultures. One of such approaches is to use biomaterials as cell carriers that mimic the native extracellualr matrix, in conjunction with bioreactors that provide efficient supply of biochemical and biophysical signals. In the present work, we use perfusion bioreactors and two immobilized cell systems: glioma cells in alginate microfibers and osteosarcoma cells in composite scaffolds based on alginate and β-tricalcium phosphate (β-TCP).

Materials and Methods: Rat glioma cells C6 (ATCC® CCL-107™) and human glioblastoma cells U-87 MG (ATCC® HTB-14™) were immobilized each, in alginate microfibers by simple extrusion of cell suspensions (1-8x10^6 cell/ml) in 1.5-2.8 % Na-alginate solutions (A3249, AppliChem, Germany) into $CaCl_2$ solutions. Macroporous alginate scaffolds were produced by controlled gellation by Ca^{2+} of 1 wt% Na-alginate mixtures containing 1 wt% of hydrothermally synthesized β-TCP particles followed by freeze-drying and rehydration. Murine K7M2-wt osteosarcoma cells (ATCC® CRL-2836™) were seeded and perfused into the obtained scaffolds. Perfusion bioreactors were filled either with microfibers or scaffolds and continuously perfused at superficial velocities ranging from 40 – 100 μm/s. Static cultures served as controls. Cell proliferation was determined by cell counting, cell viability by the MTT test and live/dead staining using confocal microscopy, while the composite scaffold structure was analyzed by field emission scanning electron microscopy (FE-SEM).

Results and Discussion: Cells were successfully immobilized in Ca-alginate hydrogel microfibers with at least 2x10^6 cell/ml needed for the cell survival. By comparing static and perfusion bioreactor cultures, it was shown that the optimal culture conditions are greatly determined by the cell type. Cultures of U-87 glioblastoma cells were highly affected by hydrodynamic shear stresses so that the cells immobilized in alginate microfibers (4x10^6 cell/ml) over 28 days of static culture stayed viable, proliferated, formed cell aggregates and retained their normal morphology while perfusion at the superficial velocity of 80 mm/s induced cell death despite the protection by the alginate matrix. On the other hand, rat glioma C6 cells immobilized in alginate microfibers (1.5x10^6 cell/ml) stayed viable over 14 days under both static and the same perfusion conditions, while only in the latter case proliferated up to 5-fold. Macroporous scaffolds based on Ca-alginate and β-TCP were shown to be bioactive in the culture medium as confirmed by formed hydroxyapatite crystals throughout the scaffolds, revealed by FE-SEM. Preliminary studies of osteosarcoma cells immobilized in these scaffolds have shown positive effects of the 3D bioactive environment, while perfusion conditions still have to be optimized to enhance cell proliferation.

Conclusion: Use of biomaterials and biomimetic bioreactors shows high potentials for establishment of physiologically relevant 3D cancer cell culture systems capturing some of the key features of the *in vivo* tumor microenvironment. Still, efforts have to be made to select and optimize the proper combination of biomaterial properties and bioreactor operating conditions for each cancer cell type.

LS7.003
Interaction of viral transduction enhancing EF-C peptide nanofibrils with cells studied by SEM and correlative FRET-based light and 3D electron microscopy (FRET-3D CLEM)

D. Schütz[1], B. Glocker[2], S. Rode[2,1], J. A. Müller[1], K. M. Sparrer[1], O. Fackler[3,4], J. Münch[1,5], P. Walther[2], C. Read (Villinger)[2,6]

[1]Ulm University Medical Center, Institute of Molecular Virology, Ulm, Germany
[2]University of Ulm, Center for Electron Microscopy, Ulm, Germany
[3]University Hospital Heidelberg, Center for Integrative Infectious Disease Research, Integrative Virology, Heidelberg, Germany
[4]Partner Site Heidelberg, German Center for Infection Research (DZIF), Heidelberg, Germany
[5]Ulm University Medical Center, Core Facility Functional Peptidomics, Ulm, Germany
[6]Ulm University Medical Center, Institute of Virology, Ulm, Germany

Introduction: Self-assembling peptide nanofibrils (PNFs) are gaining increasing attention as versatile molecules in material science and biomedicine. One important application of PNFs is to enhance retroviral gene transfer, a technology central for gene therapy approaches.

The best-investigated and commercially available PNF is derived from a 12-mer peptide termed EF-C. Boosting virion fusion rates with the cell depends on the polycationic surface of EF-C PNF, which bind to the negatively charged membranes of viruses and cells, thereby overcoming electrostatic repulsion.

Objectives: Interaction of EF-C PNF with the cell surface and uptake into cells were studied to better understand the mechanism of transduction enhancement. Furthermore, prior to application of EF-C fibrils in gene therapy, a better understanding of the fate of EF-C PNF after uptake into cells is required.

Materials and Methods**:** To this end, we performed scanning electron microscopy (SEM) after PNF-treatment of different cell types. Furthermore, we developed a FRET-based assay to monitor putative degradation of intact fibrils into peptide subunits after uptake into cells. For ultrastructural validation of this assay we conducted correlative light and electron microscopy (CLEM). For this, we localized the respective fluorescence signal prior to EM sample preparation and then analyzed these positions by transmission electron microscopy (TEM) or scanning transmission electron microscopy (STEM) tomography. We refer to the correlation of FRET-fluorescence microscopy with 3D EM as FRET-3D CLEM.

Results: SEM indicated active capture of fibrils by cellular protrusions such as filopodia (Figure 1A). This was corroborated by live-cell imaging. After uptake into cells the FRET signal switched from red to green fluorescence, indicating degradation of the PNF. TEM and STEM of cells revealed correlation of the red fluorescence signal with prominent electron dense structures. Most of these structures were found extracellularly or close to the cell surface (Figure 1B). In contrast, a green fluorescence signal correlated with indistinct less electron dense structures. These degraded fibrils accumulated exclusively inside intracellular vesicles, suggesting lysosomal degradation of EF-C fibrils after uptake into cells.

Conclusion: The mechanism of PNF-mediated viral transduction enhancement involves active capture of virus-loaded fibrils by cellular protrusions. Furthermore, we show that fibrils are degraded after uptake into cells which is a pre-requisite for their application in gene therapy.

Figure 1: (A) SEM of EF-C protein nanofibrils (PNF) on Hela cells. (B) FRET-3D CLEM of FRET labelled EF-C PNF after 24h on Hela cells. The same cell is imaged with fluorescence microscopy and STEM. Nu: nucleus, ex: extracellular. FRET: Red fluorescence originates from putatively intact fibrils and green fluorescence from putatively degraded fibrils. STEM: Bright-field STEM image of a 800 nm thick EM section showing different grey values corresponding to red and green fluorescence. (3) Virtual section of a STEM tomogram. The ultrastructure of "red" and "green" fibrils differs.

Figure 1

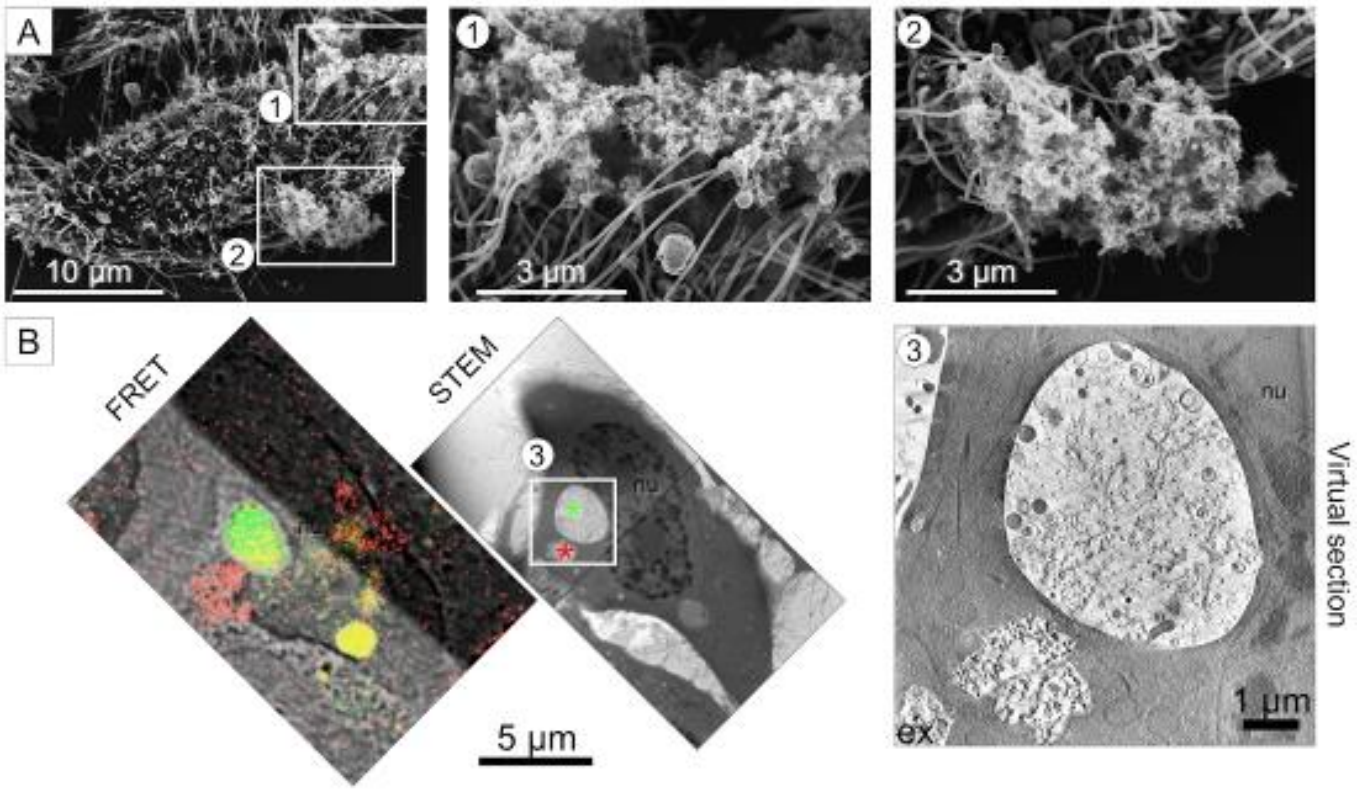
A
1
2
10 µm
1
3 µm
2
3 µm
B
FRET
STEM
3
nu
*
5 µm
3
nu
1 µm
ex
Virtual section

LS7.004
Quantitative 3D visualisation of interactions between artificial scaffolds and live cells using optical microscopy

D. Chorvát[1], A. Mateasik[1], T. Teplicky[2], B. Cunderlikova[1,2]

[1]Slovak Centre of Scientific and Technical Information, International Laser Centre, Bratislava, Slovakia
[2]Comenius University in Bratislava, Faculty of Medicine, Bratislava, Slovakia

The advances in microfabrication techniques are opening the new frontiers in a preparation of 3D cell culture models. An example of such techniques is two-photon photo-polymerization lithography that has capability to fabricate scaffold structures with optimal dimensions and well-defined chemical and physical properties that can provide an environment that supports the growth of living cells [1]. Optical microscopy is routinely used for the visualization and characterization of cell behavior in such environments.

In this study, we present the quantitative computational approach that allowed visualization of the interactions between the living cells (esophageal cancer cell line, Kyse 450) and the fabricated scaffolds prepared by 3D two-photo-polymerization lithography. The various fluorescent dyes were used to concurrently label the cell membranes, cell nuclei and the scaffold structures. Fluorescent samples were scanned with confocal microscope as a 3D stack of planar multichannel images through a volume of samples. The image channels were selected according to the emission characteristics of used fluorescent dyes to achieve the best possible separation of fluorescence signals from the dyes.

To accomplish quantitative characterization of data, the individual imaged objects were localized in volumetric data by 3D unsupervised segmentation. The segmentation algorithm was based on concurrent processing of channels of volumetric data, which contain signals from cell nuclei and cell membranes. Pixel level classifiers using gradient diffusion approach were applied to delineate individual cell nuclei in corresponding image channel. From the known positions of cell nuclei, the voxels with signals from cell membranes were subsequently determined by nuclei-seeded watershed on remaining channels. All voxels unclassified in the previous step were treated by adaptive thresholding segmentation to identify voxels belonging to scaffolds. A surface regression was applied on the extracted classified voxels to achieve a complete reconstruction of boundary surfaces of cells and scaffolds. This approach resulted in high resolution polygonal models that can be further utilized for various quantitative visualizations and measurements.

The research leading to these results has received funding from LASERLAB-EUROPE (Horizon 2020 programme, Grant agreement no. 871124) and by project VEGA 1/0119/19.

References:
[1] Teplicky T., Mateasik A., Kosnac D., Chorvat D., Cunderlikova B., Fabrication of 3D fibre scaffolds for tumor-immune system interactions by two photon polymerisation, Proceedings Volume 11271, Laser 3D Manufacturing VII; 1127111 (2020).

Figure 1: 3D geometrical representation of cell clusters prepared from Kyse 450 cell line grown on the scaffold structure after six days. Scaffold structure was fabricated from OrmoComp by 2-photon photopolymerization process. The cells were stained with acridine orange to visualize intracellular organelles, namely cytoplasm and nucleoli (green) and acidic organelles (yelow). Visualization of scaffold was possible due to OrmoComp inherent autofluorescence. *Left*: Representative image from 3D data stack recorded by confocal microscope, *right:* reconstructed 3D geometry,

Figure 1

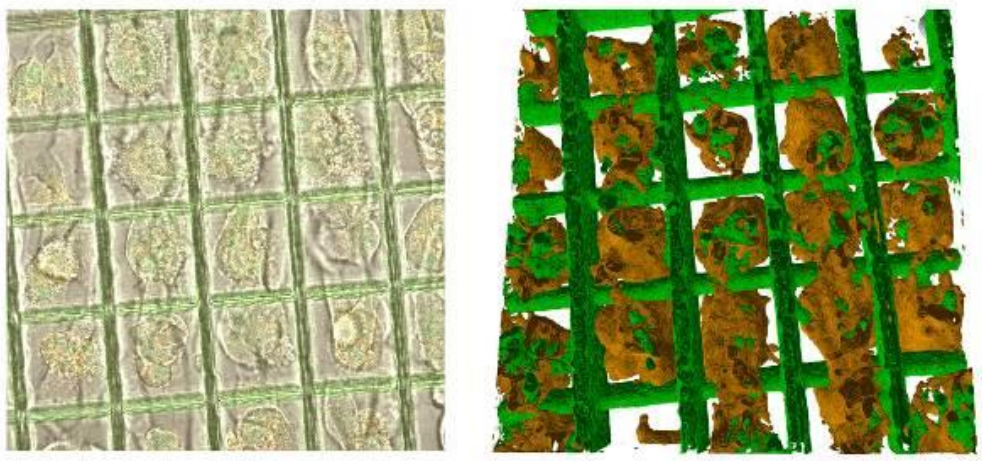

LS7.005
Electron microscopy contributions to producing an effective germicide photocatalyst

R. Herring[1], S. Pazdernik[1], Z. Hadisi[1], M. Akbari[1], V. Moradi[1]

[1]University of Victoria, Victoria, Canada

The information obtained from Scanning Electron Microscopy (SEM) and High Resolution Transmission Electron Microscopy (HRTEM) of a Fe doped TiO2 photocatalytic crystals played a significant role to enable their efficient activation using safe, visible light and to verify their germicide mechanism against bacteria now being tested against COVID-19 virus. When activated using visible light, these crystals produce hydroxyl radicals, OH:, one of the strongest oxidants, able to kill bacteria effectively and efficiently upon contact. Prior to this work, ultraviolet (UV) was necessary to activate the TiO2 crystals severely limiting their disinfecting applications as UV is carcinogenic and doesn"t pass through water nor glass. Resolving and understanding this problem, as we show here, paved the way towards applying them to keep surfaces germ free, theoretically forever since the crystals are a catalyst, and using the crystals to clean water reducing our environmental impact on rivers, lakes and oceans, helping to prevent red tides and reduce the acidification of our waters.

HREM imaging of freshly made Fe doped TiO2 crystals revealed the existence of a thin amorphous contamination layer on their surfaces (Figure 1) sometimes just a couple atoms thick. Cleaning the surface of the Fe doped TiO2 nanoparticles using HCl acid removed the surface contamination resulting in the atomic planes of the Fe doped TiO2 crystals to extend to the surface. The surface cleaning significantly improved the transport of the electrons and positive holes to the surface where they create hydroxyl radicals and super oxygen radicals from water improving the disinfecting ability and degradation efficiency of the water cleaning process [1, 2].

Crystals applied to surfaces kept them germ free (Figure 2a) lasting for several weeks. Afterwards, reactivation of the crystals on soiled surfaces continued upon cleaning the surface of spilt food and drink. Mixing the crystals with E-coli in solution and exposing them to ambient light reduced cell survival to zero after 4 hours (Figure 2b). The mechanism by which the crystals killed E-coli was revealed by SEM showing lysed cell membranes at points of contact with the crystals (Figure 2c). The degradation process is indescriminant, cleaning all germs on surfaces as wells eliminating al contaminants in wastewater including the ammonia necessary to reduce red tides. Tests against the COVID-19 virus on many types of surfaces are now being conducted.

[1] V. Moradi, M.B.G. Jun, A. Blackburn, R.A. Herring, Applied Surface Science **427** (2018) 791.
[2] V. Moradi, M.B.G. Jun, A. Blackburn, R.A. Herring, Journal Environmental Sciences **83** (2019) 183.

Grants from NSERC Discovery and Engage, CFI and BCKDF are greatly appreciated.

Figure 1

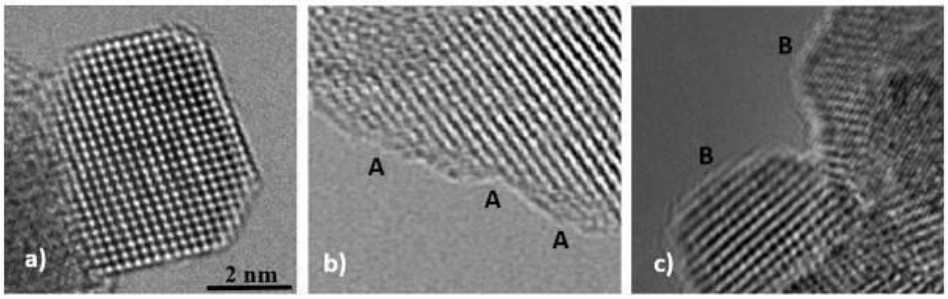

Figure 2

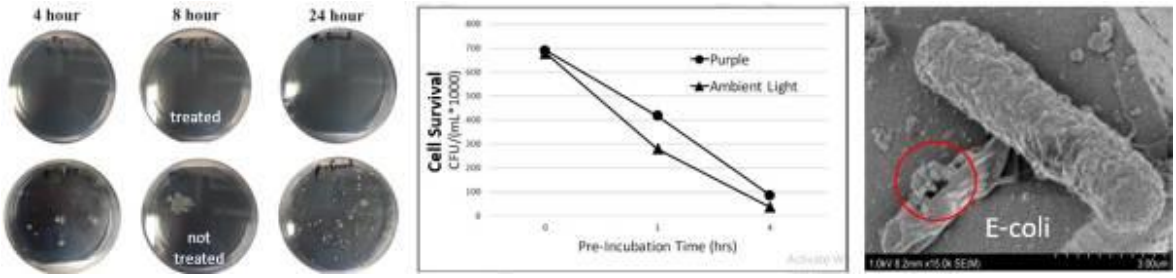

LS7.006
Magnetic resonance microscopy for the non-destructive analysis of polymer micro structures produced using additive manufacturing

A. Berg[1,2], B. Koch[3], A. Hochwallner[3], J. Stampfl[3], C. Grasl[1,4], F. Moscato[1,4,5]

[1]Medical University of Vienna, Center for Medical Physics and Biomedical Engineering, Vienna, Austria
[2]Medical University of Vienna, High-field MR-Center, Vienna, Austria
[3]Technical University of Vienna, Institute of Material Science and Technology, Vienna, Austria
[4]Ludwig Boltzmann Institute for Cardiovascular Research, Vienna, Austria
[5]Austrian Cluster for Tissue Regeneration, Vienna, Austria

Introduction: Magnetic Resonance Imaging (MRI) on humans is known for its non-destructive character using radiowaves (rf) at high magnetic fields. However polymer/resin materials usually cannot be visualized using MRI due to the very short signal decay characterized by the transverse relaxation time T2. Moreover the spatial resolution in MRI on human scanners is restricted to smallest voxel sizes of typically $(400\mu m)^3$ even at high field (7T).

Objectives: Our contribution will shortly explain the main differences between optical and MR-microscopy (MRM) in spatial encoding. We will demonstrate how to overcome the problems in the detection of polymer material and achieve microscopic spatial resolution on a human high field MR-scanner. Two examples for the application of these two methodological approaches will be shown:

a) the imaging of microscopic polymer structures from additive micro-manufacturing technology: 2-photon Direct Laser Writing (DLW),

b) the imaging of a microscopic polymer layer substructure.

Materials and Methods**:** 3.1 MR-microscopy

The spatial encoding in MRI is obtained via slice selective excitation, phase- and frequency encoding of the sample signal. The extraordinary high microscopic spatial resolution on a human MR-scanner is achieved using a prototype strong magnetic field gradient insert along with sensitive rf-detectors and optimized measurement protocols. The hollow structure of sample 1 (3-Dimensional (3D) cubes, figure1) could be visualized using the contrast between the low T2 of the polymer material against the high T2 of a surrounding added organic liquid.

3.2 Polymer-samples

The first polymer sample is manufactured using a high-resolution 3D printing system, based on 2-photon polymerization (NanoOne, UpNano GmbH Vienna/A). The set of cubes features a 3D-periodic grid structure (period a_1 = 512 µm, a_2 = 256 µm, a_8 = 4 µm) with cavity spacings (figure 1a). The cube set design covers volumes differing by 6 orders of magnitude ($V1/V8>10^6$) and is excellently suited both for checking the quality of the micro-manufacturing process and for evaluating the spatial resolution available with the relevant microscopic visualization method.

The second polymer sample (figure 1b) results from a hybrid 3D-printing process which allows for the manufacturing of multi-material structures with periodic soft and hard acrylate/methacrylate double layer structures down to th ≅ 29µm thickness.

Results: An MR-microscopic slice originating from a 3D MR data set is shown in figure 1. 3D printing structures and possible printing errors at dimension ≥60 µm inside the objects could be visualized.It is worth noticing that the available 3D Multi-slice images with isotropic voxels offer information about the inner structure of the 3D-printing performance in arbitrary slice selection due to the rf-signal penetration through the polymer material without significant absorption in MRI, whilst SEM or optical methods are restricted mainly to the surface,

Conclusion: Though MR-microscopy -by far- cannot achieve the high spatial resolution of optical microscopy, advanced MR-technology based on prototype insert hardware on high field human scanners is capable of the non-destructive visualization of the inner structure even in polymer objects of microscopic size produced with additive micro-manufacturing. Features and evtl. 3D-printing errors at sizes ≥60 µm can in principle be located within the object in the context of quality control.

Figure 1

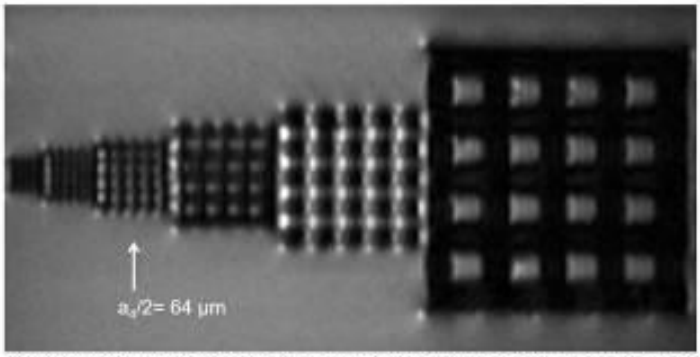

***Fig. 1a (left)**: MR-microscopic slice located in the centre of the set of 3D-cubes (voxel size: 39 x 39 x 40 µm³). The grid structure within the cube with a/2 = 64 µm bar width still can be visualized. The shown slice is located inside of the 3D-cubes avoiding limitation to surface areas. The tiny artefacts at the edges of the cube originate from tiny differences in magnetic susceptibility.*

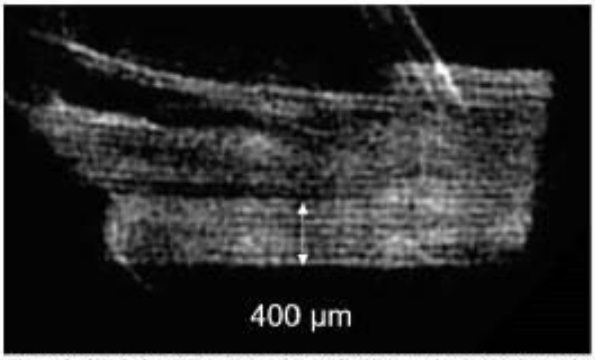

***Fig. 1b (right)**: MR-microscopy of the acrylate-methacrylate double layer structures in the polymer material. The slice (th = 520 µm) orientation within the 3D MR-data set is chosen such, that it is oriented rectangular to the double layers. One polymer layer features a thickness of about 29 µm (7 double layer periods range 400 µm).*

LS7.P001
Soft X-ray analysis for high resolution spectroscopy at low voltages – biomedical application

S. Matveev[1], G. Raggl[1]

[1]JEOL (Germany) GmbH, Freising, Germany

Introduction: Investigating and analyzing materials - especially comprising light elements - at both high spatial and spectral resolution has always been a challenge requiring sophisticated equipment such as UHV Auger microprobe systems or transmission electron microscopes equipped with an electron energy loss spectrometer. Moreover, these methods need advanced sample preparation techniques and are only suitable to analyze extremely thin layers. In order to pave the way for easily accessible high-end spectroscopy of even bulk materials, JEOL has developed a new type of wavelength dispersive spectrometer (WDS) that can be mounted on common scanning electron microscopes (SEM) or electron microprobes (EPMA). It utilizes a variable line spacing diffraction grating, allowing the efficient and parallel collection of very low-energy X-rays (so called "soft" X-rays). This new Soft X-ray Emission Spectrometer (SXES) exhibits high spectral resolution (0.3eV), which allows to measure chemical state of carbon in diamond-like coatings (DLC, Figure 1), and thus SXES can be efficiently used for biomedical application.

Objectives: We have tested performance of an electron microprobe equipped with SXES to quantitatively and qualitatively characterize thin DLC coatings doped with various metals as well as to determine chemical state of C in such coatings. Various metals were added in order to change sp2/sp3 bonding ratio and thus hardness and elasticity of the films widely used as hard protection of various medical devices including orthopaedic and cardiovascular.

Materials & methods: Silicon wafers were coated with DLC layers doped with H, Si, W, Ag, and Cu. The coatings were analyzed using WDS, EDS and SXES detectors mounted on JEOL JXA-iHP200F field emission gun probe microanalyzer. Chemical state of C was measured using JEOL SS-94000SXES with JS200N diffraction grating.

Results: Here we present results of SXES spectroscopy of thin amorphous carbon coatings applied to Si wafers by sputter coating method using carbon and metal targets. Fine structure of CKa(2) reflects differences in sp2/sp3 ratios in DLC layers doped with different metals (Figure 1). X-ray elemental maps (Figure 2) along with secondary and backscattered electron micrographs allow to test films for homogeneity and possible damage or contamination on the micron level. EPMA was used to quantitatively analyze composition of thin films thus allowing to control amount of doping material as well as Ar concentration.

Conclusion: We demonstrate that EPMA equipped with SXES spectrometer provides integrated solution for further development and quality control of the DLC coatings. Such instrument can be used to provide information about composition of the hard coating, its homogeneity and surface defects at micron level. It can also provide information about sp3/sp2 ratio of the DLC-X structure.

Figure 1: SXES spectra showing fine structure of CKa(2) X-ray emission line in DLC coatings doped with various metals

Figure 2: WDS elemental maps illustrating chemical homogeneity of the films.

Figure 1

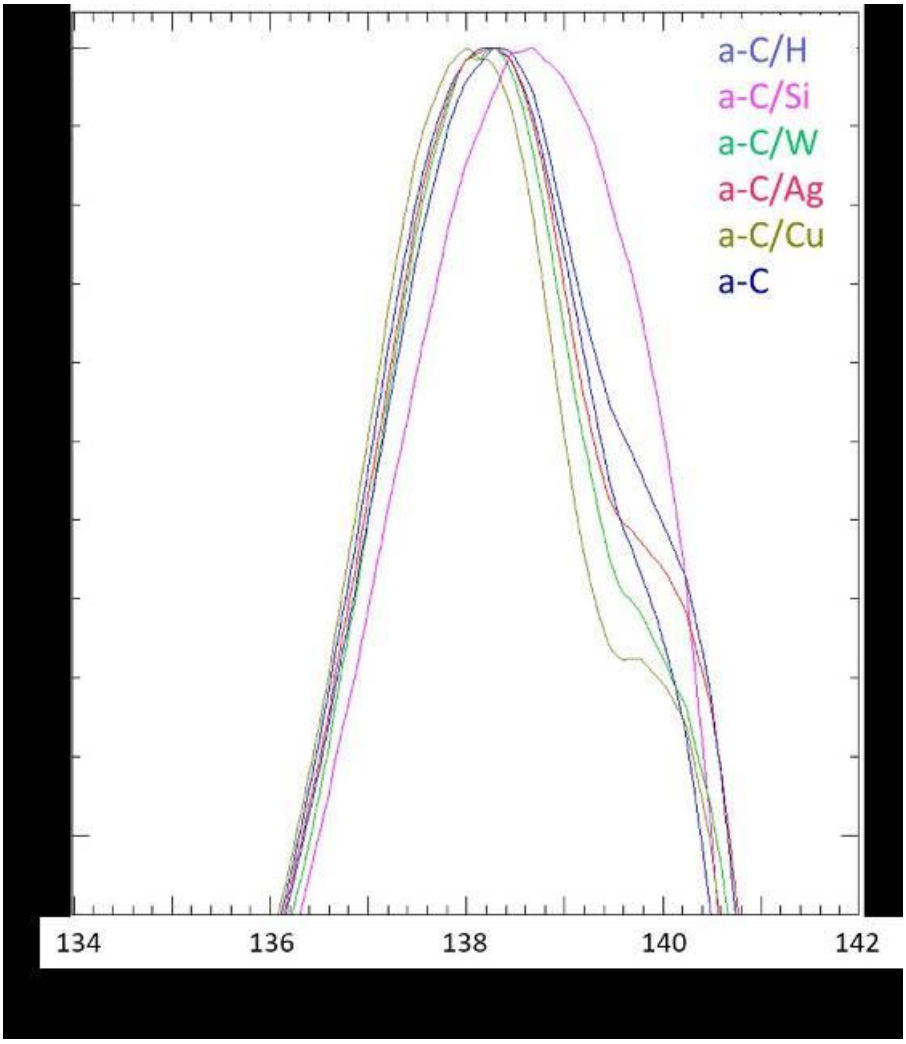

Figure 2

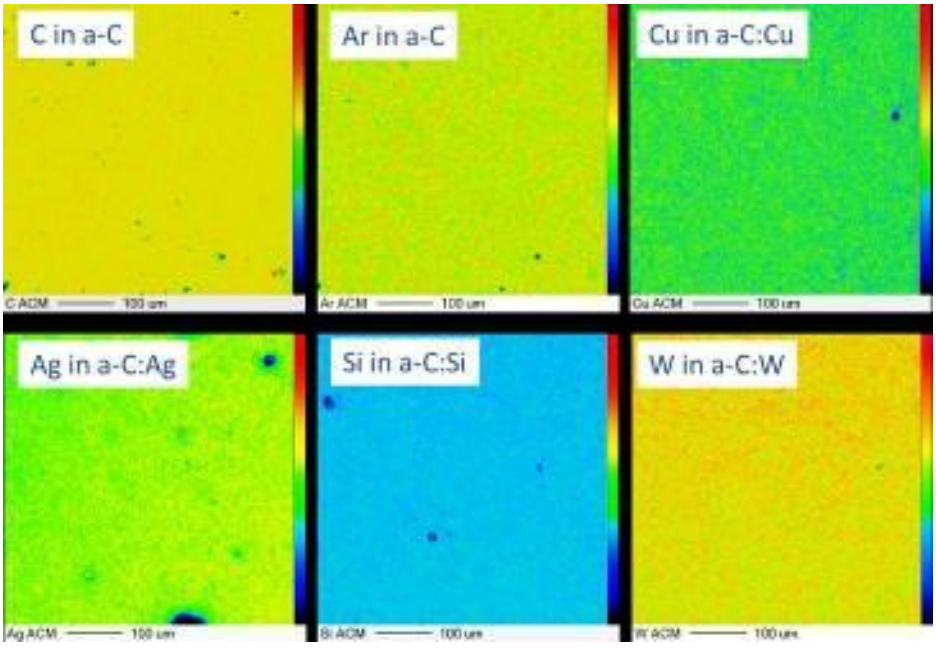

LS7.P002
Effects of antiviral agents on SARS-CoV-2 virions studied via electron microscopy

T. Bergner[1], C. Read (Villinger)[1], T. Weil[2], C. Conzelmann[2], P. Rebmann[3], A. Kirupakaran[3], M. H. Le[3], T. Schrader[3], P. Walther[1], J. Münch[2]

[1]University of Ulm, Center for Electron Microscopy, Ulm, Germany
[2]Ulm University Medical Center, Institute of Molecular Virology, Ulm, Germany
[3]University of Duisburg-Essen, Faculty of Chemistry, Essen, Germany

Introduction: The severe acute respiratory syndrome coronavirus 2 (SARS-CoV-2), the causative virus of the COVID-19 pandemic, is a highly pathogenic beta-coronavirus that can cause severe infections of the lower respiratory tract (1). Up to this day, over 100 million people have contracted the virus and there have been 2 million fatal cases worldwide. This shows the importance for understanding SARS-CoV-2 morphology and morphogenesis on an ultrastructural level aiding development of antiviral agents. As a potential broad-spectrum antiviral agent, molecular tweezers like CLR01 (2) and novel tweezer variants are a promising tool, since they have a destabilizing effect on membranes of enveloped viruses.

Objectives: To understand how the molecular tweezer CLR01 and four of its derivatives affect SARS-CoV-2 virions, we used negative staining transmission electron microscopy (TEM). To reveal which of the tweezer variants is most potent, quantitative EM was applied.

Materials and Methods: SARS-CoV-2 supernatants were treated either with molecular tweezers at 250 µM and 50 µM concentration or PBS for 30 min at 37°C and then inactivated by 2% paraformaldehyd. Negative staining TEM was performed as described in (3). In brief, 10 µL of the treated virus supernatants was placed directly onto freshly glow-discharged 300 mesh copper grids which were coated with a carbon reinforced formvar film. After 10 min adsorption at room temperature, grids were washed three times with double-distilled water and negatively stained with 0.5% uranyl acetate in water. Virions were imaged with a JEOL 1400 operated at 120 kV. The virions were assigned to intact or defective virions and their ratio was calculated. In a second part of the project, we examined the morphology of SARS-CoV-2 via different electron microscopic techniques.

Results: Treatment of SARS-CoV-2 with 250 µM CLR01 and the novel tweezer variants resulted in defective virions (Figure1 A). This effect was dose-dependent for all tweezers (Fig 1 B). The quantitative negative stain procedure revealed differences regarding the potency of the tweezer variants whereas all new tweezers were more potent than CLR01. CP024, the most potent molecular tweezer, damaged nearly all virions at 250 µM and still more than 80% of the virions at 50 µM concentration.

Conclusion: We show that SARS-CoV-2 virions are damaged by molecular tweezers and most efficiently by the new tweezer derivatives. This is paving the way for their application as antiviral agents. The present work demonstrates that electron microscopy is an essential technique for visualization of pathogenic viruses such as SARS-CoV-2 and research on antiviral strategies.

Figure 1: A) Negative staining TEM of intact (top) and damaged (bottom) SARS-CoV2 virions after treatment with PBS or tweezer for 30 min at 37°C. Scalebar is 100 nm. B) Percentage of intact virions in PBS treated supernatants compared with supernatants treated with 50 and 250 µM CLR01 or indicated tweezer derivatives.

[1] Klein et al (2020) *Nature Communications*
[2] Münch et al (2020) *Journal of the American Chemical Society*
[3] Laue (2010) *Methods Cell Biology*

Figure 1

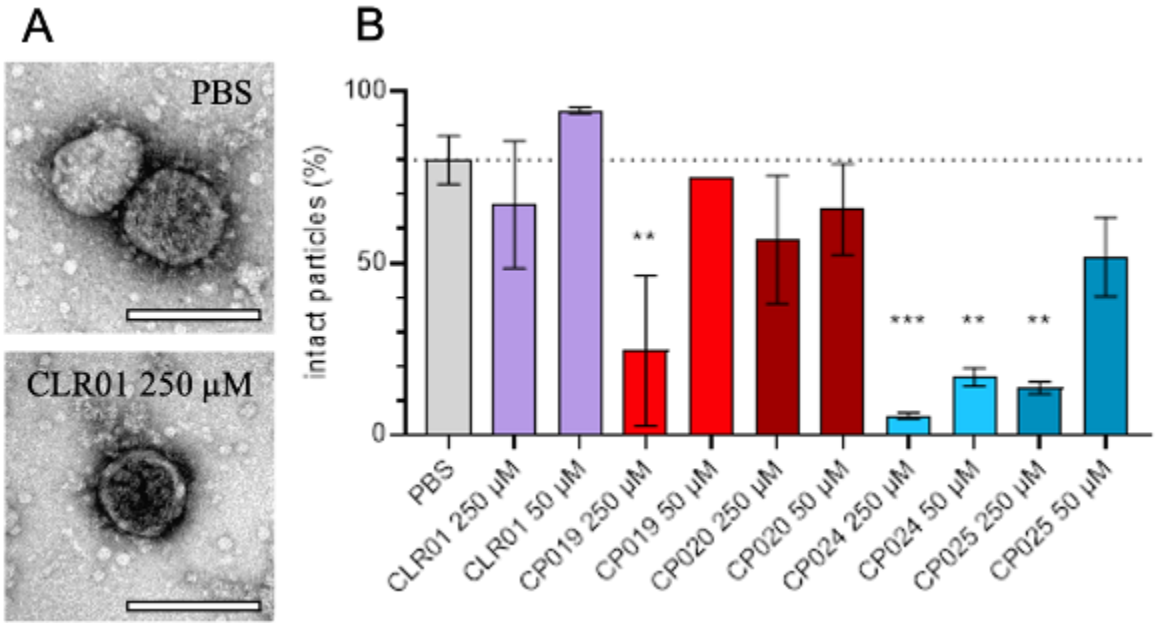
A
PBS
CLR01 250 µM
B
intact particles (%)
100
50
0
**
***
**
**
PBS
CLR01 250 µM
CLR01 50 µM
CP019 250 µM
CP019 50 µM
CP020 250 µM
CP020 50 µM
CP024 250 µM
CP024 50 µM
CP025 250 µM
CP025 50 µM

LS7.P003
Optoelectronic neurostimulation effects on an ultrastructural level

M. Nowakowska[1], A. L. Schachner-Nedherer[2], R. Reimer[2], M. Üçal[1], S. Patz[1], N. Shrestha[2], S. Scheruebel[2], T. Rienmüller[3], S. Stoppacher[3], T. Schmidt[2], D. Ziesel[3], S. Langthaler[3], R. Schindl[2], E. Głowacki[4], R. Prassl[2], D. Kolb[5,6], G. Leitinger[5], K. Kornmueller[2]

[1]Medical University of Graz, Department of Neurosurgery, Graz, Austria
[2]Medical University of Graz, Gottfried Schatz Research Center for Cell Signaling, Metabolism and Aging, Biophysics Department, Graz, Austria
[3]Graz University of Technology, Institute of Health Care Engineering with European Testing Center of Medical Devices, Graz, Austria
[4]Linköping University, Laboratory of Organic Electronics, Linköping, Sweden
[5]Medical University of Graz, Gottfried Schatz Research Center for Cell Signaling, Metabolism and Aging, Division of Cell Biology, Histology and Embryology, Graz, Austria
[6]Medical University of Graz, Core Facility Ultrastructure Analysis, Center for Medical Research, Graz, Austria

Introduction: Despite tremendous progress within the last years, treatment options for many neurological disorders are still limited. Promoting the remyelination process of axons is a key therapeutic target. Remyelination restores function and has a significant role in neuroprotection. We here propose an optoelectronic approach to stimulate neurons. An organic electrolytic photocapacitor, in short a photocap, is a soft and flexible device that can transduce light pulses into transient electrical potentials. The currents are strong enough to trigger action potentials in excitable cells.

Objectives: Our objective is to establish an electric interface between photocaps and neuronal cells. We aim to stimulate neuronal cells and to observe an enhanced migration of oligodendrocyte precursor cells (OPCs) to dorsal root ganglia (DRG) cells upon stimulation. This should lead to an enhanced myelination effect, which we aim to visualize and quantify on an ultrastructural level by electron microscopy (EM).

Materials & Methods: Photocaps were kindly provided by Eric Głowackis lab from Linköping University/Sweden. Rat dorsal root ganglia were dissected, dissociated by enzymatic digestion and cultured on pretreated (Matrigel or Poly-D-Lysine) photocaps until DIV21. In parallel a culture of cerebral mixed glial cells from postnatal rat brains was prepared and cultured until DIV12, followed by separation of OPCs at DIV13 and cultivation of purified OPCs until DIV21. OPCs were then added to the DRG cells and co-cultured until DIV38. OPCs matured into oligodendrocytes and myelin formation was followed by immunostaining techniques. Simultaneously, a culture of purified cortical neurons from postnatal cells continued until DIV 17. Cells were chemically fixed and samples for TEM, STEM and SEM were prepared according to standardized procedures. Electron micrographs were recorded on a Zeiss EM900 transmission electron microscope (80 kV), Fei Tecnai G² 20 transmission electron microscope (120 kV), or a Zeiss Sigma500 VP scanning electron microscope. EM studies were complemented with electrophysiological recordings and Ca2+-imaging.

Results: We established a stable co-culture of DRGs and OPCs on photocaps, testing factors that affect cell adhesion, cell viability and signal propagation capabilities. Myelin-formation on DRG cells was followed in the electron microscope at various time points. The thickness of myelin sheaths was directly measured from the EM images. The ability to trigger action potentials after light-stimulation was demonstrated on cortical neurons and measured by electrophysiological methods.

Conclusion: Optoelectronic neurostimulation is a promising approach and an elegant way to resolve many unmet challenges in the treatment of neurological disabilities. Studying cell-photocap-interactions requires a highly interdisciplinary approach, and EM techniques contribute as an excellent tool to study the effects of stimulation with unprecedented resolution.

IM1.003
Advances in preparing cross-sectional TEM specimen of quantum nanostructures

H. Wang[1], V. Srot[1], B. Fenk[1], G. Laskin[1], J. Mannhart[1], P. A. Van Aken[1]

[1]Max Planck Institute for Solid State Research, Stuttgart, Germany

Introduction: Quantum nanostructures have triggered much research attention due to their fascinating physical properties and emerging applications like quantum computing and sensing [1]. For understanding the underlying physical mechanisms, detailed microscopic investigations using TEM are rather demanding. As TEM has become increasingly powerful, TEM specimens suitable for atomic-level observation are often the main bottleneck in materials characterization. In particular, the small size of engineered nanostructures makes cross-sectional TEM specimen preparation exceptionally challenging.

Objectives: In this work, we aim to develop an optimized pathway for making high-quality cross-sectional TEM specimens of quantum nanostructures.

Materials & methods: Here, a challenging system consisting of the $SrRuO_3$ (SRO) quantum-dot (QD) arrays deposited on a $SrTiO_3$ (STO) substrate has been selected as the model material [2,3]. We demonstrate that a combination of ion-beam-milling techniques can produce higher-quality specimens of quantum nanostructures compared to TEM specimens prepared by a combination of tripod polishing followed by Ar^+ ion milling.

Results: Figure 1(a) shows the top view of a 30 nm SRO QD periodic array. In the proposed method, the TEM lamella in cross-sectional orientation was firstly prepared using a focused ion beam (FIB) (Zeiss CrossBeam XB 1540). Simultaneous imaging in the FIB device enables accurate positioning of the QD regions and assures the presence of dots in the thin lamella by cutting the sample inclined by 5◦ relative to the dots array. Furthermore, the preparation of TEM lamellae with several large electron-transparent regions that are separated by thicker walls effectively reduces the bending of the specimen and offers broad thin areas (Figure 1(b)). Each electron-transparent area was thinned by FIB to different thicknesses (Figure 1(c)). Final thinning and polishing of the targeted regions to remove amorphized material, implanted Ga ions, or redeposited material was performed using a NanoMill system (Fischione Model 1040).

Figure 2 shows the STEM results on the cross-section of a single SRO QD. The high-angle annular dark-field (HAADF) image in Figure 2(a) depicts a clear contrast between SRO and STO with a sharp interface. The homogeneous signal intensities in SRO and STO indicate a uniform thickness in the respective areas. Figure 2(b) is an energy-dispersive X-ray spectroscopy (EDS) map of Figure 2(a), displaying the elemental distribution of Ru and Ti. The HAADF and annular bright-field (ABF) images of the interfacial zone are presented in Figure 2(c) and Figure 2(d), showing that mismatched SRO and STO lattices are patched up in high quality with a clean and coherent interface. The vertically averaged intensity profiles in the inset of Figure 2(c) and Figure 2(d) depict the signal intensity variations of Sr, Ru, Ti, and O at the interface region.

Conclusion: We trust that our optimization of the combined methods (FIB & NanoMill) has significant implications not only for preparing TEM specimens of quantum dots, but also for other emerging quantum nanostructures.

References:
[1] J Mannhart et al., Rep. Prog. Phys. 79 (2016), p. 084508.
[2] H. Wang et al., Micron 140 (2021), p. 102979
[3] G. Laskin, H. Wang, et al., Nano Lett. 19 (2019), p.1131
[4] This project has received funding from the European Union"s Horizon 2020 research and innovation programme under grant agreement No. 823717 – ESTEEM3.

Figure 1: (a) An SEM image of the top-view of a patterned QD array. (b) Backscattered electron image of the final FIB lamella. (c) Thickness map of the lamella based on the backscattered electron signal.

Figure 2: (a) and (b) correspond to an HAADF image and an EDS map of a single SRO QD. (c) and (d) are the HAADF and ABF images around the interface region. The insets are the vertical-averaged signal-intensity profiles.

Figure 1

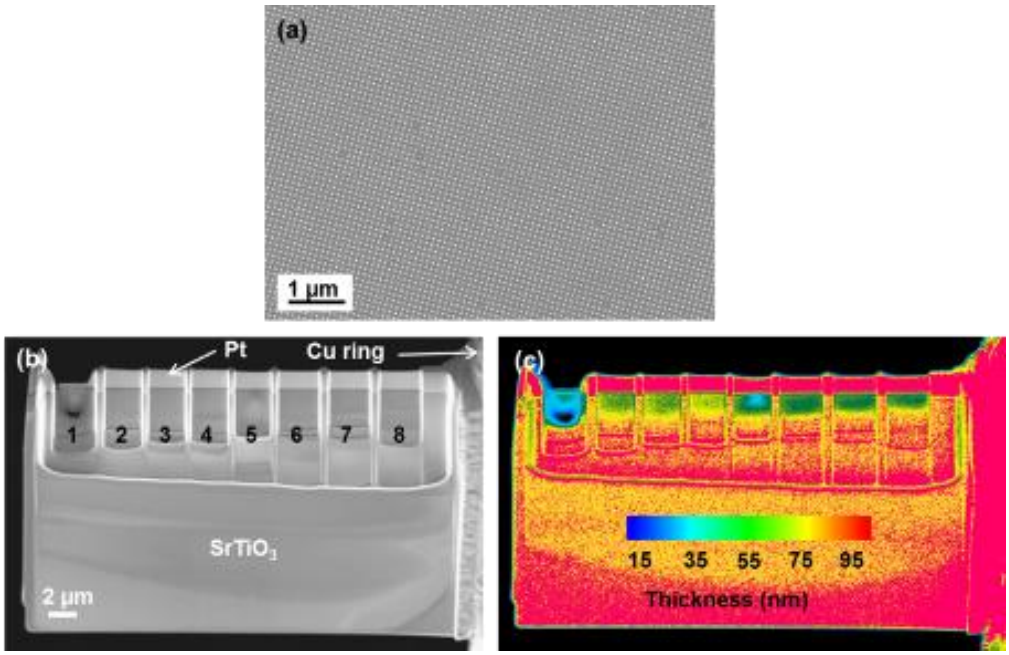

Figure 2

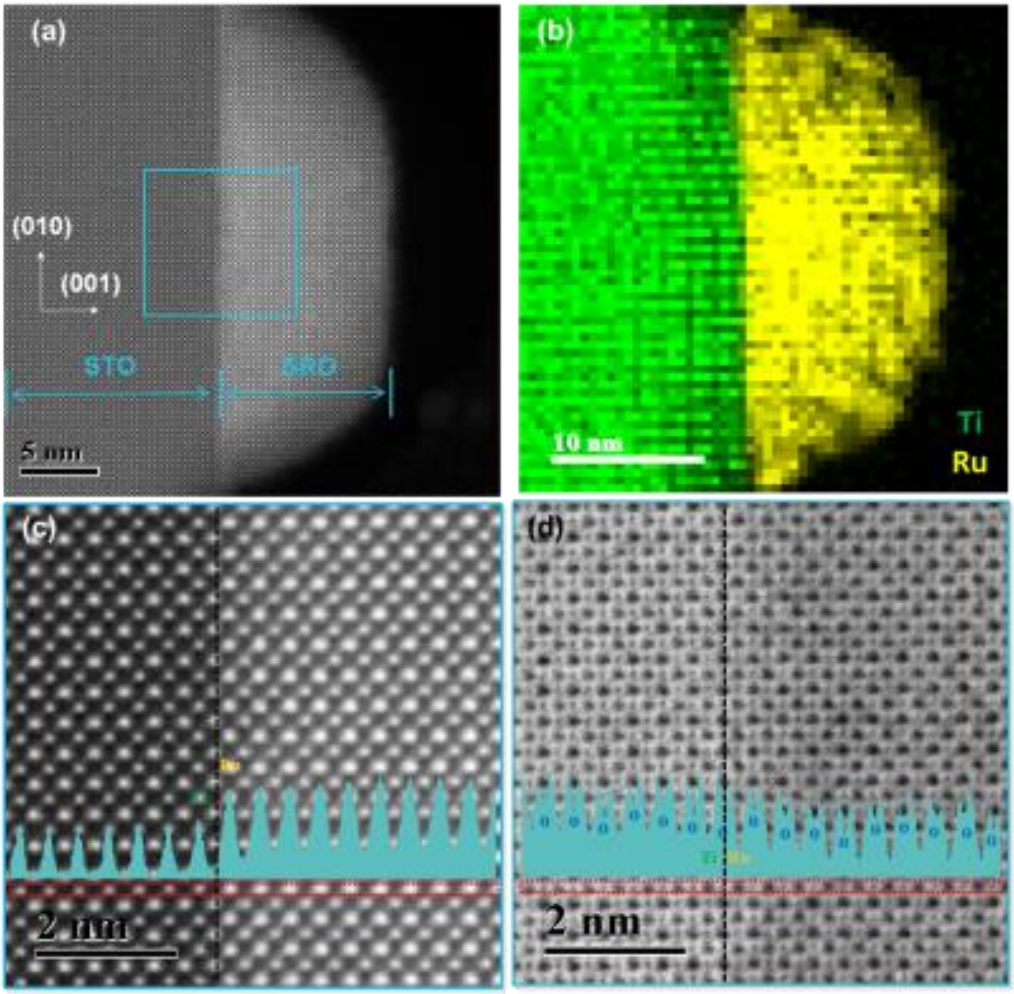

IM1.004
Optimisation of the SBEM protocol for sample preparation of different animal tissues

J. Nebesářová[1,2], E. Ďurinová[1,3], R. Skoupý[4], J. Týč[1], M. Vancová[1,3]

[1]Biology Centre, Czech Academy of Sciences, Laboratory of Electron Microscopy, České Budějovice, Czech Republic
[2]Charles University in Prague, Faculty of Science, Prague, Czech Republic
[3]University of South Bohemia in Ceske Budejovice, Faculty of Science, České Budějovice, Czech Republic
[4]Institute of Scientific Instruments, Czech Academy of Sciences, Electron Microscopy, Brno, Czech Republic

Serial block-face scanning electron microscopy (SBEM) is a suitable method for studying the ultrastructure of biological specimen up to mm3 volume scope. Ultrathin sections are cut off from the sample using an ultramicrotome inside the microscope, and back-scattered electron imaging is used to visualise the area of interest on the newly exposed sample surface. The biggest challenges we face in SBEM are sample preparation, finding the region of interest (ROI) within the sample, sample charging during the imaging and data processing and storage. Insufficient contrast in specimen often seriously limits the sample imaging. Therefore the sample preparation represents the crucial step in the SBEM analysis.

At present, we use for SBEM specimen preparation procedures established for transmission electron microscopy. Usually, it starts with chemical fixation followed by dehydration, including en bloc staining, and the procedure is finished by sample embedding in a hard epoxy resin. Several protocols have been developed by modifying the chemicals used, incubation times or temperatures (Deerinck, Hua, Genaud, Katsumoto). The aim of our study was to compare samples of different animal tissues prepared according to these protocols and evaluate their quality of ultrastructure preservation, image contrast and charging in SEM.

The thickness of a layer on sample surface containing heavy metals was measured by optical microscopy on semi-thin sections. The distribution of individual elements was measured by EDX analysis on blocks, as well as image contrast and tendency to charging which were evaluated directly at SBEM analysis.

We confirmed that the use of different protocols affects the penetration of heavy metals into the sample and consequently the level of charging during electron irradiation and the image contrast in BSE imaging. We showed that the most used protocol (Deerinck) results in incompletely contrasted sample leaving only outer regions approx. up to 200 nm from the surface to be stained appropriately. Based on these results we suggested modifications of the SBEM specimen preparation protocol directed to the most problematic steps - contrasting and embedding.

This work was supported by TACR (TE 01000008), and MEYS CR (Czech BioImaging LM2015062).

References:

[1] Deerinck, T. J. et al.: Microscopy, 6–8 (2010).
[2] Hua, Y. et al.: *Nature Communications*, *6*(1), 7923 (2015) https://doi.org/10.1038/ncomms8923
[3] Katsumoto T. et al.: *J. Electron Microscopy*, *30*(3), 177-182 (1981) https://doi.org/10.1093/oxfordjournals.jmicro.a05030
[4] Genoud, C. et al.: *Frontiers in Neuroanatomy*, *12*(September), 1–8 (2018) https://doi.org/10.3389/fnana.2018.00076

Figure 1: The distribution of heavy atoms in the mouse brain tissue prepared for SBF-SEM according to Hua et all. protocol. Fe (orange), Os (brown), Pb (beige), U(yellow)

Figure 1

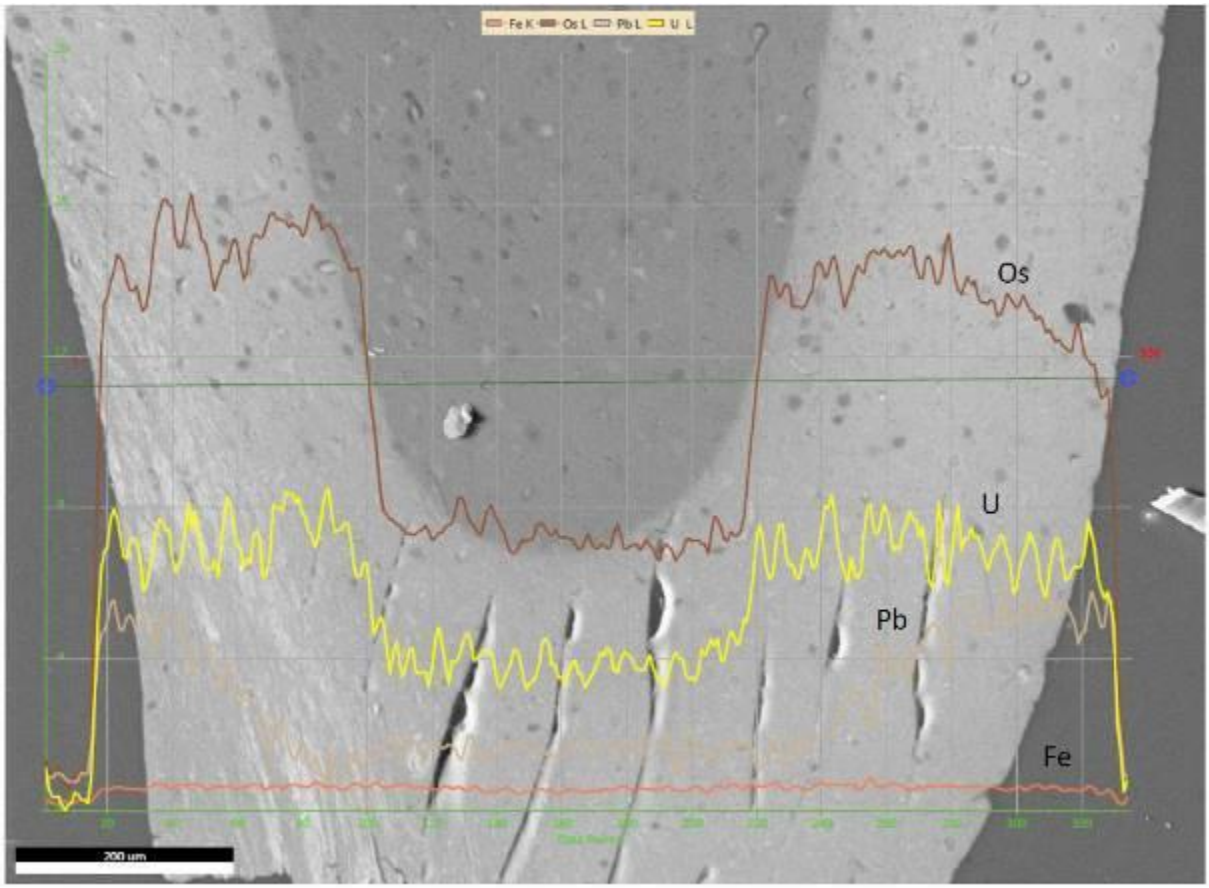

IM1.005
In-situ electrical biasing study of Pb(Zr,Ti)O3 thin films on MEMS chips by HAADF and DPC STEM imaging

A. Vogel[1,2], M. Sarott[2], M. Fiebig[2], M. Trassin[2], M. Campanini[1], M. Rossell[1]

[1]Empa–Swiss Federal Laboratories for Materials Science and Technology , Electron Microscopy Center, Dübendorf, Switzerland
[2]ETH Zurich, D-MATL, Zurich, Switzerland

Introduction: Since their discovery in 1920, ferroelectrics found a large number of applications in modern life. Their auxiliary properties, such as piezoelectricity and pyroelectricity, have led to the development of actuators, sensors and dielectric capacitors based on ferroelectric materials. In data storage applications, ferroelectricity presents a unique alternative to ferromagnetism as it allows for more energy efficient and faster devices. However, the commercialization of ferroelectric memory devices has been hindered by major reliability issues [1, 2] such as retention loss [3], imprint [4], and fatigue [5]. At present, a lack of dynamical data on the atomic scale impedes further knowledge of the microscopic processes involved in ferroelectric systems. Therefore, it is essential to understand the role of structural and charged defects in the context of domain wall motion and domain nucleation.

Objectives: In-situ scanning transmission electron microscopy (STEM) studies of the ferroelectric response to electrical biasing have mostly been conducted using specialized holders that allow contacting the film using a micromanipulator needle. While this approach has undoubtedly helped advance our understanding of ferroelectrics [6,7], some of its disadvantages include the inhomogeneous electric fields underneath the needle-like tip and piezoelectric responses of the ferroelectric film induced by the force of the tip during contact. We have developed a workflow to prepare ferroelectric thin film specimens on commercially available MEMS chips manufactured by Protochips enabling more accessible in-situ electrical biasing experiments in the TEM.

Materials & Methods: In particular, $Pb(Zr,Ti)O_3$ (PZT) thin films grown on Nb-doped $SrTiO_3$ (STO) by pulsed laser deposition (PLD) are prepared in a capacitor-like geometry using a FEI Helios 660 SEM/FIB equipped with an EasyLift Nanomanipulator. To allow for electrical biasing of the films, the specimen are deposited on a MEMS-chip with premanufactured platinum electrodes and a contact is established using ion-beam assisted chemical vapor deposition of Pt. The response of the films to the electrical biasing is then investigated in-situ by differential phase contrast (DPC) STEM and conventional high-angle annular dark field (HAADF) STEM imaging using a FEI Titan Themis microscope equipped with a probe CEOS DCOR spherical aberration corrector operated at 300 kV.

Results: We show that electrical biasing in this geometry is feasible and test the limits of the possible applied voltages before specimen breakdown. From HAADF time series, we extract atomic resolution polarization maps and characterize the domain state before and after electrical biasing. During electrical biasing, low-magnification DPC imaging reveals the nucleation and growth of 180° domains in the PZT film. Moreover, it discloses that the presence of structural defects and needle-like a-domains causes non-uniform growth of the switched domain front.

[1] O. Auciello, J. F. Scott, and R. Ramesh, Physics Today 51 (1998), p. 22-27.
[2] W. L. Warren, D. Dimos, and R. M. Waser, MRS Bulletin 21 (1996), p. 40-45.
[3] A. Gruverman and M. Tanaka, Journal of Applied Physics 89 (2001), p. 1836.
[4] A. K. Tagantsev et al., Journal of Applied Physics 96 (2004), p. 6616-6623.
[5] A. K. Tagantsev et al., Journal of Applied Physics 90 (2001), p. 1387-1402.
[6] P. Gao et al., Nature Communications 2, 591 (2011).
[7] M.-G. Han et al., Nature Communications 5, 4693 (2014).

IM1.006
PharmacoSTORM – a powerful approach for super-resolution imaging

S. Prokop[1], P. Ábrányi-Balogh[2], B. Barti[1], M. Vámosi[1], L. Barna[1], G. Urbán[1], A. Tóth[3], B. Dudok[1], A. Egyed[2], H. Deng[4] M. Zöldi[1], G. M. Leggio[1,5], L. Hunyady[3], M. Van Der Stelt[4], G. M. Keserű[2], I. Katona[1]

[1]Institute of Experimental Medicine, Budapest, Hungary
[2]Research Centre for Natural Sciences, Budapest, Hungary
[3]Semmelweis University, Department of Physiology, Budapest, Hungary
[4]Leiden University & Oncode Institute, Department of Molecular Physiology, Leiden, Netherlands
[5]University of Catania, Department of Biomedical and Biotechnological Sciences, Catania, Italy

Introduction: A major challenge for contemporary biomedical research is to uncover the nanoscale molecular changes underlying human diseases. Super-resolution imaging techniques, such as Stochastic Optical Reconstruction Microscopy (STORM) enable the visualization of nanoscale protein distribution. The most widely used technique for fluorescent protein labeling is immunostaining, which however suffers from major limitations. The size of an antibody is comparable to the spatial resolution of super-resolution imaging methods, and the poor penetration of large-size probes results in their uneven distribution in thick tissue samples. The amplification steps during the staining process further complicate the quantification of the final images. Another major drawback is the lack of sensitive and specific antibodies for many proteins, including important pharmaceutical targets.

Objectives: Our goal was to develop novel fluorescent small-molecules, that can selectively identify proteins in cell-cultures and tissue and are suitable for single-molecule localization microscopy. We have focused our attention to the synthesis of ligand-based probes, that are able to bind important pharmacological targets, including ones that are lacking selective antibodies.

Materials & methods: We have developed a workflow to generate novel probes. As a first step, we perform *in silico* analysis of the protein structure of the target and its available ligands. Next, we use molecular docking simulations to design fluorescent analogues that preserve their high affinity. We synthesize the novel probes by attaching photoswitchable fluorescent dyes and characterize the new compounds via high-throughput *in vitro* pharmacological assay. High-affinity probes are further tested with conventional diffraction-limited fluorescent microscopy and finally with STORM super-resolution imaging.

Results: We designed and characterized new labeling probes for members of different protein families: a G protein-coupled receptor, an enzyme, and an ion channel, and successfully applied them in single-molecule imaging studies. We show that the selectivity of our probes can be easily tested by competitive ligand-binding STORM experiments, without the need for genetic knock-out controls. In addition, we developed a fluorescent analogue of a novel antipsychotic drug, that can selectively label its main pharmacological targets in cell culture and tissue as well. We were able to detect the binding of single fluorescent antipsychotic molecules even at subnanomolar concentration by STORM. We exploited the high localization accuracy of our approach by imaging ligand binding in a cell-type and compartment-specific manner.

Conclusions: PharmacoSTORM is an efficient technique for the nanoscale localization of versatile proteins. The high detection sensitivity of single-molecule localization microscopy enables the specific visualization of receptor-ligand interactions even at low ligand concentrations. Moreover, PharmacoSTORM can address important questions of translational pharmacology by providing a way to directly visualize the interactions of clinically used drugs with nanometer precision.

IM1.P001
Direct Synthesis of ZIF-8 on Transmission Electron Microscopy Grids Allows Insights into the Growth Process.

M. Hugenschmidt[1,2], K. Kutonova[2,3], E. P. Valadez Sánchez[4], S. Moulai[4], H. Gliemann[4], S. Bräse[2,3,5], C. Wöll[2,3]
D. Gerthsen[1,2]

[1]Karlsruhe Institute of Technology (KIT), Laboratory for Electron Microscopy, Karlsruhe, Germany
[2]Karlsruhe Institute of Technology (KIT), 23DMM2O – Cluster for Excellence (EXC-2082/1 – 390761711), Karlsruhe, Germany
[3]Karlsruhe Institute of Technology (KIT), Institute of Organic Chemistry (IOC), Karlsruhe, Germany
[4]Karlsruhe Institute of Technology (KIT), Institute of Functional Interfaces (IFG), Karlsruhe, Germany
[5]Karlsruhe Institute of Technology (KIT), Material Research Center for Energy Systems (MZE), Karlsruhe, Germany

Introduction: Metal-organic frameworks (MOFs) have received increased attention in recent years due to their exceptional properties and versatility [1]. MOFs consist of metal nodes connected by organic linkers. Particularly interesting are surface-anchored films (SURMOFs), which are grown on bulk substrates [2]. Transmission electron microscopy (TEM) is a key technique for the analysis of the structural and chemical properties of SURMOFs on the nanoscale. For TEM sample preparation, however, the SURMOF film must be detached from the bulk substrate and transferred to an electron-transparent support. This detachment process is a severe source of damage for the SURMOF film. The preparation of SURMOFs for TEM studies is thus an obstacle that has not yet been solved satisfactorily.

Objectives: In our study, we focus on ZIF-8 that belongs to the class of zeolitic imidazolate frameworks (ZIFs) [3]. As a new approach for TEM sample preparation, we deposit ZIF-8 directly on a thin amorphous carbon (aC) film supported by a TEM grid. This allows us to study the pristine material and to completely avoid preparation-induced artifacts.

Materials & Methods: We employ a dipping procedure **(**Figure 1) for layer-by-layer growth of ZIF-8 on the support film. The amount of deposited material can be controlled by the number of deposition cycles. Samples were grown with 10 up to 100 deposition cycles to analyze the growth mechanism.

Results: The morphology of the deposited ZIF-8 is examined by scanning electron microscopy (SEM). We find the typical shape development of particles with increasing size of particles on the support film as described by Cravillon et al. [4]. The shape development starts with cubes after 39 deposition cycles (Figure 2a) that develop into rhombic dodecahedra (RDs) after 50 cycles (Figure 2b**).** Further investigations show that the support film is fully covered by coalesced particles after 100 deposition cycles. HRTEM analysis confirms the ZIF-8 crystal structure of the particles from Fourier-transformed high-resolution (HR)TEM images (Figure 2c, d). Scanning TEM tomography was applied to analyze the interface structure between ZIF-8 particles and the aC film.

Conclusion: Direct synthesis of SURMOFs on TEM grids is a promising approach for TEM studies of SURMOFs because artifacts induced by the preparation are completely avoided. The technique was tested for ZIF-8 but is also promising for other MOFs and nanoscaled materials produced by additive manufacturing techniques.

References:
[1] Heinke and Wöll, Adv. Mater. 31, 1806324 (2019)
[2] Shekhah and Eddaoudi, Chem. Commun., 49, 10079 (2013)
[3] Park et al., PNAS 103, 10186 (2006)
[4] Cravillon et al., CrystEngComm 14, 492 (2012)
[5] Hugenschmidt et al., Part. Part. Syst. Charact. 37, 2000209 (2020)
[6] We acknowledge funding by the Deutsche Forschungsgemeinschaft (DFG, German Research Foundation) under Germany"s Excellence Strategy – 2082/1 – 390761711 and thank the Carl Zeiss Foundation for financial support.

Figure 1: Scheme of ZIF-8 synthesis on an aC film supported by a TEM grid.

Figure 2: Growth of ZIF-8 on a thin aC film. 5 keV secondary-electron SEM images **a)** after 39 deposition cycles showing particles with cubic shape and **b)** after 50 deposition cycles: particles with predominantly RD shape and low-index projections as indicated (from [5])**. c)** Average-background-filtered HRTEM image of ZIF-8 crystal and **d)** Fourier transform of the image in (c), confirming the ZIF-8 crystal structure in [110] direction [3].

Figure 1

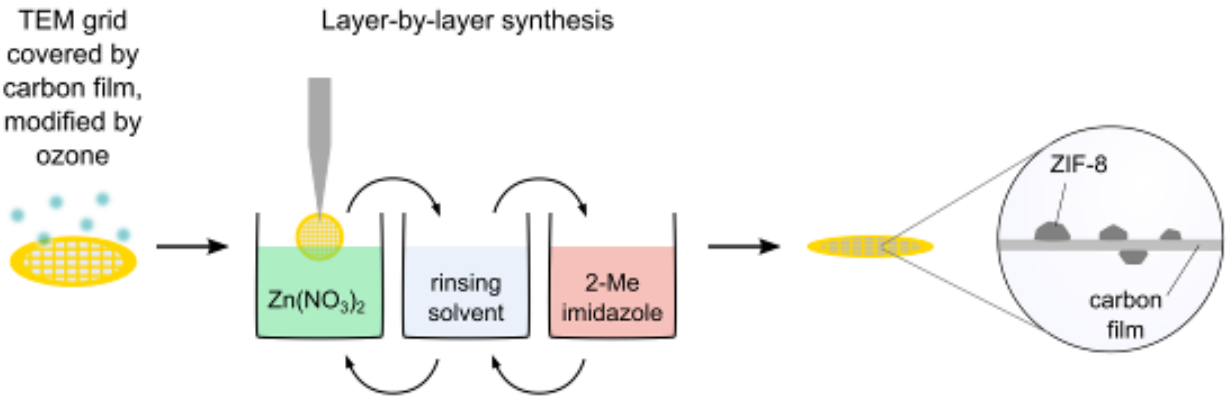

Figure 2

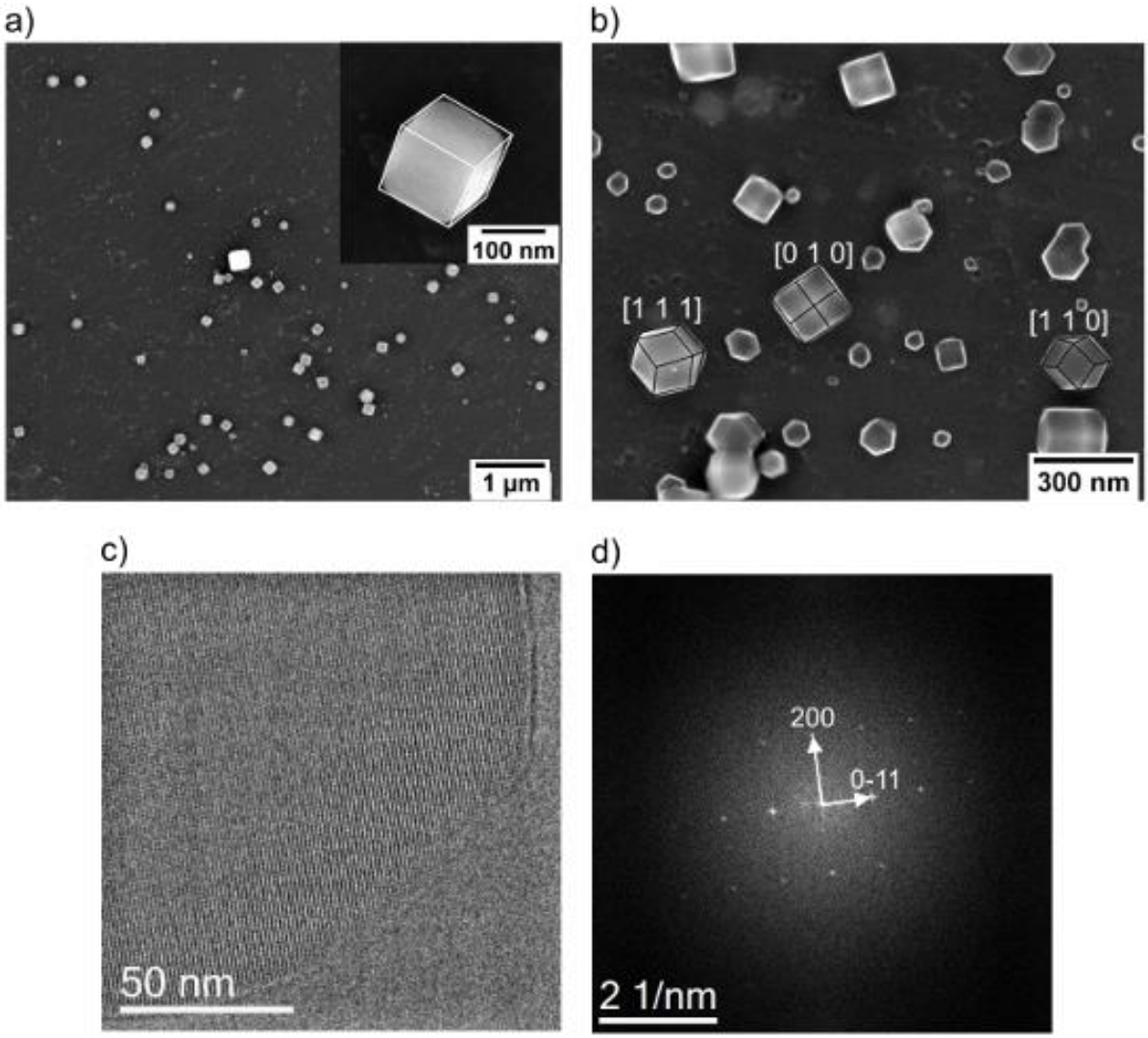

IM1.P002
Alternative contrasting approaches for serial block-face scanning electron microscopy

F. Kitzberger[1,2], E. Ďurinová[1,2], J. Týč[1], J. Nebesářová[1,2]

[1]Institute of Parasitology, Biological Centre, Czech Academy of Sciences, Ceske Budejovice, Laboratory of Electron Microscopy, České Budějovice, Czech Republic
[2]University of South Bohemia in Ceske Budejovice, Faculty of Science, České Budějovice, Czech Republic

The majority of biological samples for electron microscopy is nowadays contrasted with uranyl acetate. However, the fact that it is a radioactive and toxic compound and recent strict regulations of the usage of radioactive material, even for purely scientific purposes, makes its usage very complicated. Therefore, non-radioactive and contrasting alternatives had to be developed to replace the uranyl acetate. These alternatives, such as samarium triacetate, neodymium acetate, or platinum-blue, were successfully applied in the transmission electron microscopy as negative contrasting agents. (Hosogi et al., 2015; Inaga et al., 2007; Kuipers & Giepmans, 2020) We aimed to apply these approaches during the preparation of samples for SBF-SEM and compare them with the traditional uranyl acetate, to find, whether they could be a suitable alternative. The experiment was done with three types of samples, a suspension of parasitic protozoa, brain tissue, and tobacco leaf and was recorded on Thermo Scientific™ VolumeScope™ scanning electron microscope (SEM). The experiments had shown, that Pt-Blue provides sufficient contrast and ultrastructural preservation. According to the results, Pt-Blue would be an effective substituent for the UA, in case the UA is not available.

Acknowledgment: This work was supported by TACR (TN 01000008) and *Czech-BioImaging* (*LM2018129)*.
[1] Hosogi, N., Nishioka, H., & Nakakoshi, M. (2015). *Microscopy*, *64*(6), 429–435. https://doi.org/10.1093/jmicro/dfv054
[2] Inaga, S., Katsumoto, T., Tanaka, K., Kameie, T., Nakane, H., & Naguro, T. (2007). *Archives of Histology and Cytology*, *70*(1), 43–49. https://doi.org/10.1679/aohc.70.43
[3] Kuipers, J., & Giepmans, B. N. G. (2020).. *Histochemistry and Cell Biology*, *153*(4), 271–277. https://doi.org/10.1007/s00418-020-01846-0

IM1.P003
Use of neodymium salt as staining medium for EM samples points out new perspectives

N. Cyran[1], D. Gruber[1], S. Reipert[1]

[1]University of Vienna, Cell Imaging and Ultrastructure Research, Vienna, Austria

Since several years ago restriction for the use of uranyl salt containing staining media was announced, alternative solutions for a sufficient staining result will be examined by EM (Electron Microscope) users. In contrast to uranyl acetate which reliably and satisfactorily stains almost every type of sample (animals, plants, fungi or microorganisms), experiences with lanthanoids as samarium, gadolinium or ytterbium lead to assorted and partly unpredictable results. Frequently, several attempts are necessary to select an appropriate staining medium for a particular sample type. Therefore, the search for a reliable and versatile staining medium for a wide range of samples is ongoing.

Recently, neodymium (III) acetate has been discovered as a promising medium usable for positive as well as for negative staining (Kuipers & Giepmans, 2020). Beside good staining results, neodymium is not toxic, not radioactive and straightforward to handle.

For our comparative studies we used ultrathin sections of different sample types on copper grids, that were stained with 2.5% gadolinium (III) acetate or 4% neodymium (III) acetate, both followed by 3% lead citrate. Staining results were compared.

For all tested histological sections, we obtained stronger contrast and thus crispier images with neodymium then with gadolinium (Figure 1). In particular, lipid membranes, ribosomes and filaments of any kind become more obvious. Moreover, due to the automatized contrast adjustment of the CCD camera, the comparably weakly stained Gadolinium-treated sections display the knife marks much clearer, which are not visible with the neodymium staining.

Conclusively, the neodymium (III) acetate staining results seem to illustrate a potential substitute for the controversial uranyl acetate staining for both positive and negative staining for future applications.

Figure 1: Comparison of the contrast achieved with gadolinium (A, C) and neodymium (B, D) staining solution. (A, B): Nauplii of *Artemia franciscana*, both mitochondrial structures and ribosomes are substantially clearer displayed by using neodymium. (C, D): Similar results with clear advantages for neodymium could be attained on samples of human fibroblast cell cultures. Scale bars: 500 nm.

References:
[1] Jeroen Kuipers, Ben N. G. Giepmans: Neodymium as an alternative contrast for uranium in electron microscopy. Histochemistry and Cell Biology (2020) 153:271–277. https://doi.org/10.1007/s00418-020-01846-0

Figure 1

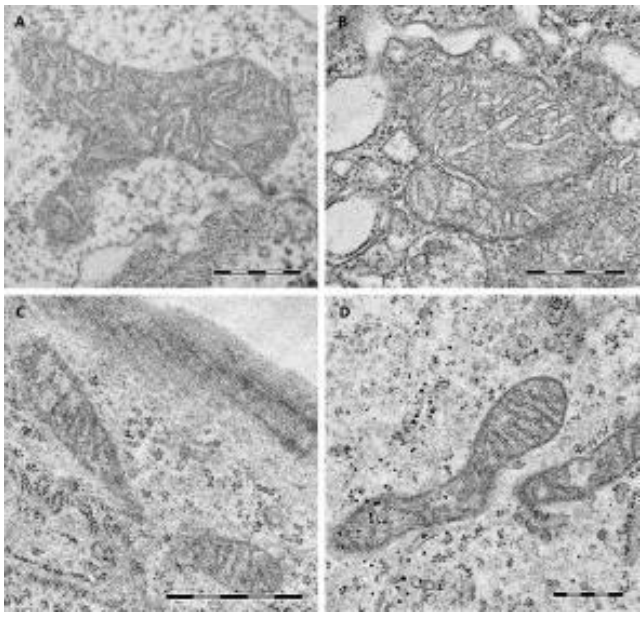

IM1.P004
Towards Atomic Defect Engineering for Fundamental Building Blocks of Quantum Electronics

M. Quincke[1], T. Lehnert[1,2], I. Keren[3], H. Steinberg[3], U. Kaiser[1]

[1]University of Ulm, Electron Microscopy Group of Materials Science, Ulm, Germany
[2]University of Ulm, Institute for Quantum Optics, Ulm, Germany
[3]The Hebrew University of Jerusalem, The Racah Institute of Physics, Jerusalem, Israel

Introduction: Quantum dots (QDs) are regions where electron states can be isolated in space, and electronic transport takes place through single-electron processes. Since in QDs the electron quantum states can be manipulated coherently, they considered as promising platforms for quantum information storage [1].

Objectives: Transport measurements performed with devices based on layered van-der-Waals tunnel junctions can reveal the electronic properties of QDs associated with defects in the barrier, but are not providing any information about the structure [2]. Therefore, a link between different characterization methods such as high-resolution Transmission electron microscopy (TEM), atomic force microscopy (AFM) as well as transport measurements needs to be developed to investigate defect based QDs.

Materials & methods: We exfoliate transition metal dichalcogenides (TMDs) on polyvinyl alcohol (PVA) coated SiO_2 and characterize the TMD-flakes with AFM. Afterwards, we use the chromatic and spherical aberration-corrected Sub-Angstrom Low-Voltage Electron Microscope (SALVE), for engineering and simultaneously imaging of defects [3]. Using the TEM, the exact atomic coordinates can be identified and density functional theory calculations can be used to determine theoretically the properties of a defect, which can be correlated with transport measurements.

Results: We show a newly developed method to transfer the TMD flake from the TEM grid back again to SiO_2 or polymer substrates to analyse the surface and the defects with AFM, and to show differences between pre- and post-electron-beam-irradiation. Ultimately, we intend for transport measurements to be performed on the TMDs with well characterized atomic defects.

Conclusion: To sum up we show a preparation technique, which serves as a common platform for TEM and transport measurements. This allows us to gain insights into the atomic structure of devices built up from 2D materials.

[1] J. M. Elzerman et al.: "Single-shot read-out of an individual electron spin in a quantum dot", *Nature* 430, p. 431–435 (2004)
[2] T. Dvir et al.: "Zeeman Tunability of Andreev Bound States in van der Waals Tunnel Barriers", *Phys. Rev. Lett.* 123, 217003 (2019)
[3] X. Zhao et al.: "Engineering and modifying two-dimensional materials by electron beams", *MRS Bulletin* 42, p. 667–676 (2017)

IM1.P005
Freeze and thaw – not necessarily a mission impossible for electron microscopy!

D. Kolb[1], M. Galhuber[2], N. Kupper[2], G. Dohr[2], A. Prokesch[2], G. Leitinger[2], M. Gauster[2], D. Kratky[2], G. Kwapiszewska[3], K. Jandl[3], M. Schweiger[4], A. Olschewski[3,4], E. Gschwandtner[3,4,5], D. Kolb[1,2]

[1]Center for Medical Research, Core Facility Ultrastructure Analysis, Graz, Austria
[2]Division of Cell Biology, Gottfried Schatz Research Center for Cell Signaling, Metabolism and Aging, Graz, Austria
[3]Division of Physiology, LBI for Lung Vascular Research, Otto Loewi Research Center for Vascular Biology, Immunology and Inflammation, Graz, Austria
[4]Institute of Molecular Biosciences, Biochemistry, Graz, Austria
[5]Medical University of Vienna, Division of Thoracic Surgery, Department of Surgery, Vienna, Austria

Introduction: To preserve the ultrastructure of biological samples for electron microscopy is a challenging task that can be reached through a standard chemical fixation procedure or with special freezing and thawing procedures employing cryoprotectants and/or specialized devices. Increasing efforts in cryo-storage of samples from clinical ("biobanking") and preclinical samples render accurate analyses on cryo-stored samples, that were not specifically prepared for ultrastructural analyses but simply immersed in liquid nitrogen, imperative.

Objectives: We present a simple, rapid, and effective method for preparing frozen, biobanked bulk tissues for electron microscopy that does not require any specific instrumentation.

Material & Methods: This procedure consists of dry ice-cooled pre-trimming of frozen tissue, aldehyde fixation for three hours at 37°C followed by standard embedding steps. Herein investigated tissues comprised human term placentae, clinical lung samples from patients suffering from chronic obstructive pulmonary disease, and different mouse tissues. All frozen samples were compared to electron micrographs prepared directly from fresh tissue samples.

Results: Our protocol results in highly conserved ultrastructural features and tissue-specific details (Galhuber et al 2021). Additionally, our method showed that morphometric analysis of lipid droplets and mitochondria in livers of fasted mice can be made (Galhuber et al 2021).

Summing up, we provide a protocol for ultrastructural and statistical analyses of cryo-stored bulk tissue.

[1] Galhuber M.
[2] Kupper N.
[3] Dohr G.
[4] Gauster M.
[5] Kwapiszewska G.
[6] Olschewski A.
[7] Jandl K.
[8] Gschwandtner E.
[9] Schweiger M.
[10] Kratky D.
[11] Leitinger G.
[12] Prokesch A.
[13] Kolb D.

Histochem Cell Biol. 2021| Simple method of thawing cryo-stored samples preserves ultrastructural features in electron microscopy.

IM1.P006
Opportunities and challenges in coordinated metadata for EM

O. Mannix[1], M. Wollgarten[2], V. Hoffmann[3], B. Port[4], M. Nolden[4]

[1]Helmholtz-Zentrum Berlin für Materialien und Energie GmbH, HMC Hub Matter, Berlin, Germany
[2]Helmholtz-Zentrum Berlin für Materialien und Energie GmbH, Institute Solar Fuels, Berlin, Germany
[3]Research Center Jülich, HMC Hub Information, Jülich, Germany
[4]Deutsches Krebsforschungszentrum, HMC Hub Health, Heidelberg, Germany

The challenge: Up to 80% of published data can be inaccessible after 20 years (http://dx.doi.org/10.1016/j.cub.2013.11.014). Storing data and metadata in repositories can solve the problem; but is often met with reluctance. This is despite funding agencies and publishers increasingly requesting that data be stored in repositories. Metadata, information about data itself are critical for long-term storage. They are essential when finding, understanding and re-using research data.

The importance of metadata was seen when the COVID-19 pandemic suddenly restricted laboratory access. Paper writing increased; but few scientists studied their "old" data. This is a direct consequence of research data lacking the metadata required to contextualise research data, making data-analysis (even by the owner) difficult, even impossible.

The opportunity: You, your group, and your (current and future) collaborators can reuse your own data! This saves time and money. Secondly, data in openly accessible repositories can be cited in standard journal publications. In this way you get credit for your work and increase your scientific visibility. In addition, data with high quality metadata adhering to a community standard means an end to file conversions - you need conventions to end conversions. Conventions open the possibility of creating data which is interoperable between microscopy techniques, for example between electron and x-ray microscopy. These examples follows the ideas found in the FAIR principles: findable, accessible, interoperable, and reusable (http://dx.doi.org/10.1038/sdata.2016.18).

Help and support from HMC: The Helmholtz Metadata Collaboration (HMC) is a platform to support scientists in developing strategies and tools to automate and improve metadata collection. We provide training to the scientific community on subjects linked to metadata and FAIR. The HMC works across all disciplines represented in the Helmholtz Association and we have a mandate to link to wider initiatives including NFDI (Nationale Forshungsdateninfrastruktur) consortia and the EOSC (European Open Science Cloud). In addition, metadata projects are supported technically and financially through our annual project calls.

HMC and electron microscopy**:** Electron microscopy is used by scientists from diverse disciplines. We represent this diversity as we come from the materials, information and life sciences respectively. Metadata is necessarily an interdisciplinary topic and we aim to bring the diverse stakeholders in electron microscopy, including those from other initiatives, together to identify and bridge gaps. In particular we would like to:

- work with you to ensure our efforts are relevant to the community

- support you in establishing metadata standards for electron microscopy ensuring interoperability between the various disciplines using the technique

- work with you to engage with manufacturers on improving metadata collection from instruments

- train you on how to maintain and benefit from these standards

Get involved: Interested in joining our efforts? Come to our poster and discuss with us!

Figure 1


HMC
HELMHOLTZ
METADATA
COLLABORATION
GEOMAR
Helmholtz-Zentrum
Geesthacht
Zentrum für Material- und Küstenforschung
AWI
HZB
Helmholtz
Zentrum Berlin
GFZ
UFZ
HELMHOLTZ
Zentrum für Umweltforschung
JÜLICH
Forschungszentrum
DLR
HZDR
dkfz.
DEUTSCHES
KREBSFORSCHUNGSZENTRUM
IN DER HELMHOLTZ-GEMEINSCHAFT
KIT
Karlsruher Institut für Technologie

IM1.P007
Large field-of-view site specific plan view TEM lamella preparation preserving as prepared surfaces

T. Westphal[1], T. Meyer[1,2], B. Kressdorf[2], U. Ross[2], C. Jooss[2], M. Seibt[1]

[1]University of Göttingen, 4th Institute of Physics - Solids and Nanostructures, Göttingen, Germany
[2]University of Göttingen, Institute of Materials Physics, Göttingen, Germany

Introduction: Preparation of high-quality lamellae is a pre-requisite and challenging task for state-of-the art studies of materials by various methods of transmission electron microscopy (TEM). While preparation of high-quality site-specific lamellae in cross-section geometry has become a standard procedure, preparation in plan-view geometry is still an equally important and demanding task. Published procedures can be roughly divided into two categories, (i) techniques based on a mechanical treatment e.g. tripod polishing [1], and (ii) FIB based approaches directly extracting a block of material from the frontside using a protection layer in order to avoid strong contamination due to redeposition [2]. The former method lacks site specificity and the latter suffers from a limited field-of-view in addition to a plethora of problems related to the required removal of the protection leading to damaged or contaminated surfaces.

Objectives: The goal of this work is to present a novel strategy of site-specific plan-view lamella preparation with a large field of view without a protection layer and without contaminating the surface. This can be reached by combining a mechanical pre-preparation followed by a backside lift-out in the FIB.

Materials & methods: We demonstrate the preparation for two material systems. One material system is a $Pr_{0.66}Ca_{0.34}MnO_3$ (PCMO) film deposited on a $SrTi_{0.998}Nb_{0.002}O_3$ (STNO) substrate as it has been described in [3]. The other material system is single crystalline silicon.

The mechanical treatment consists of a single grinding step. Therefore, the sample is glued upside down on a stub and is ground to a thickness of approximately 20 µm. FIB treatment begins with milling two markers from the backside through the sample near the site of interest. Changing to the frontside and by using the electron beam, the distances of the two markers from the site of interest are measured. Flipping to the backside the position of the site of interest is localised. By a backside lift-out the lamella is extracted and subsequently thinned. The resulting lamella is analysed in the TEM to assess the quality of the surface.

Results: The steps from the site of interest on the surface to the final lamella are shown in Figure 1. In Figure 1(a) an SEM image shows the annular feature that was prepared for this demonstration by the ion beam. The markers are shown from the back- and frontside in Figure 1(b) and (c). In Figure 1(d) the final lamella with the feature in the middle is shown, proving site-specificity.

In order to show that the preparation results in a clean surface, a lamella from PCMO-STNO is prepared. Figure 2 shows a SAED pattern and an HRSTEM image of an area with a lamella thickness of about 20 nm.

Conclusion: By combining a mechanical grinding with a backside lift-out in the FIB we have demonstrated a novel strategy of site-specific plan-view lamella preparation without contaminating the surface.

Figure 1: SEM images of Si sample. (a) Annular feature milled by ion beam. Backside (b) and frontside (c) of the markers milled for feature localisation. (d) Final lamella with the feature in the middle.

Figure 2: SAED pattern (a) and ADF-STEM image (b) from a thin region of the PCMO-STNO lamella showing high crystalline quality and no significant signal of contamination.

References:
[1] R. Anderson et al., MRS Proc. **480** (1997)
[2] M. Jublot et al., Micron (Oxford, England: 1993) **56**, 63 (2014)
[3] B. Ifland et al., New J. Phys. **19**, 63046 (2017)

Figure 1

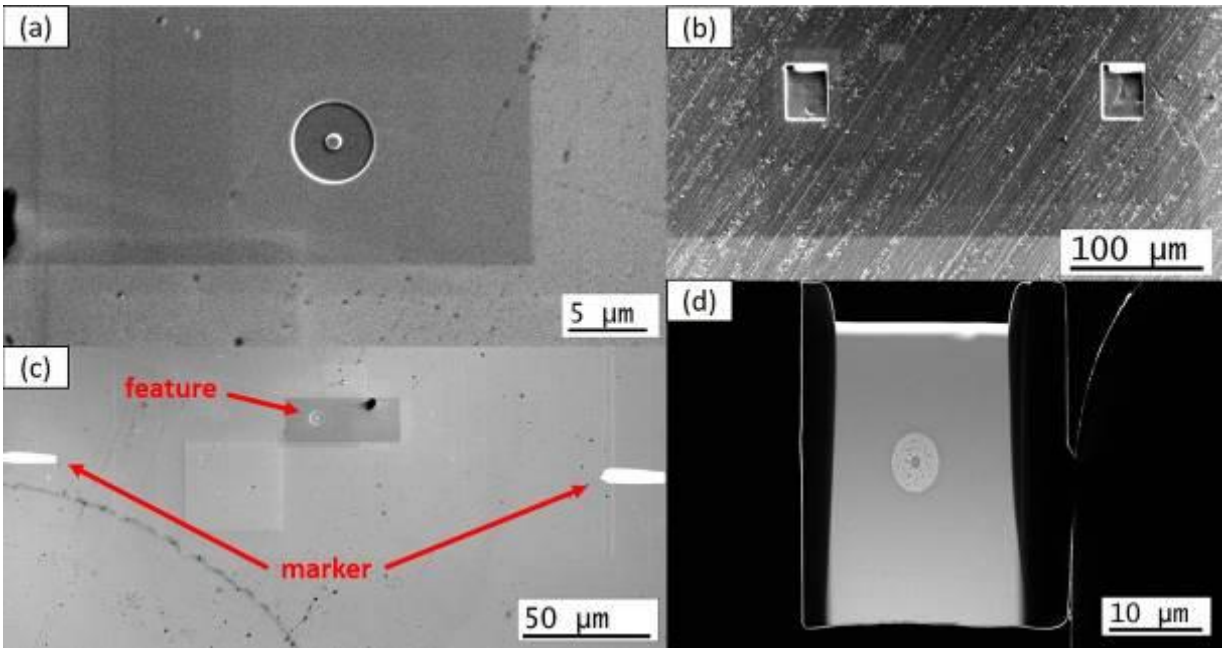

Figure 2

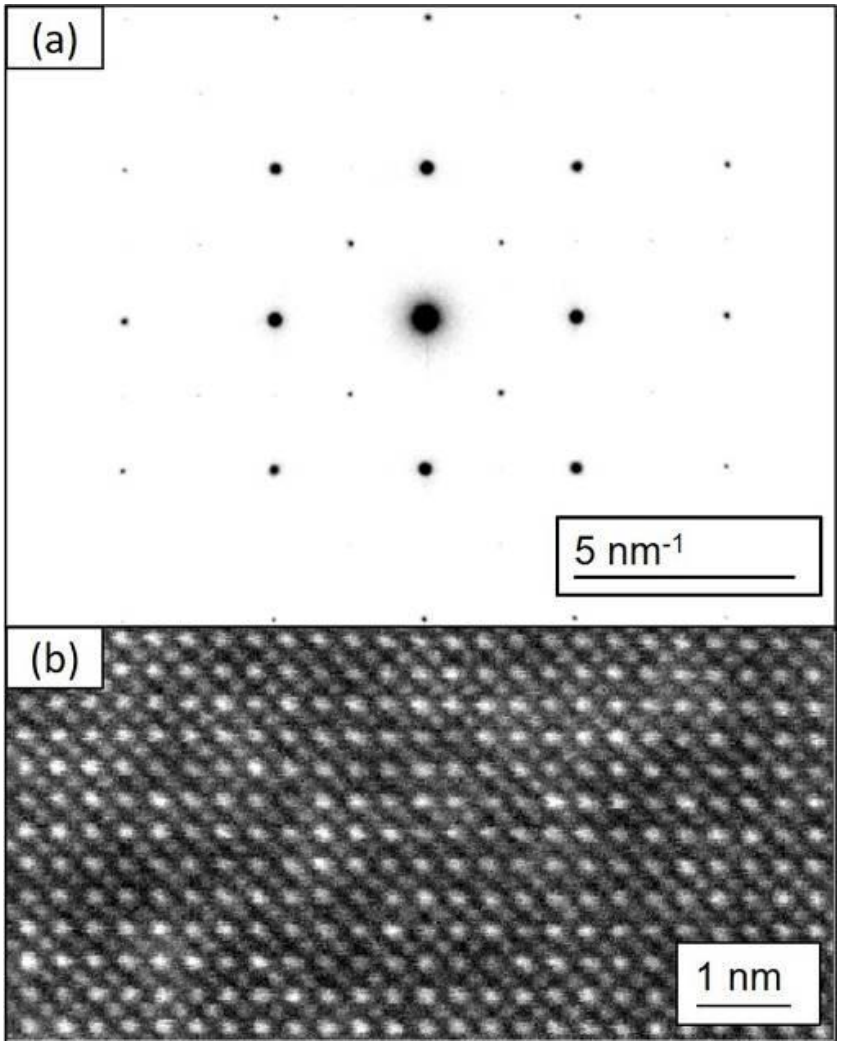

IM1.P008
Chemical investigation of carbonaceous contaminants in transmission electron microscopy

J. Menten[1,2], T. Lunkenbein[2], S. Kujawa[3], A. Bordet[1], R. Schlögl[1,2], W. Hetaba[1,2]

[1]Max Planck Institute for Chemical Energy Conversion, Mülheim an der Ruhr, Germany
[2]Fritz Haber Institute of the Max Planck Society, Berlin, Germany
[3]Thermo Fisher Scientific, Eindhoven, Netherlands

Abstract: In transmission electron microscopy (TEM), sample investigations are often affected by carbon contamination deposited on the specimen surface. In order to perform experiments that deliver data with the desired image quality and spectroscopy resolution, several methods have been utilized in order to improve these measurements [1]. A better understanding of the chemical composition and origin of these contaminants is necessary in order to improve the quality of the obtained data by reducing the amount of carbon deposition.

By utilizing proton-transfer-reaction mass spectrometry (PTR-MS), we are able to gain insight in the chemical composition of the contaminants that may influence TEM measurements and to establish sample-specific cleaning strategies considering the efficiency of cleaning procedures such as plasma cleaning [2].

Objectives: Studying catalyst samples that consist of nanoparticles stabilized by supported ionic liquid phase and are stored in organic solvents is challenging for several reasons: These samples are prone to decomposition in the electron beam, while at the same time the high carbon content of the nanoparticle surroundings requires thoughtful measurement parameters in order to limit the accumulation of carbonaceous material on the specimen surface during TEM investigations.

Our research focuses on the chemical investigation of these contaminants and quantitative evaluation of cleaning procedures for improving TEM experiments.

Material/Methods: For our experiments, we used a Thermo Fisher environmental cell TEM octagon as a model chamber for studying the contaminants contributing to carbon deposition within a TEM. These organic compounds were analyzed by a Ionicon PTR-TOF 1000 mass spectrometer.

Results: Figure 1 shows the concentrations of C_4H_6 and $C_3H_6O_2$ after employing plasma cleaning with air and Argon, respectively. The analyzed contamination was accumulated during TEM operation in the octagon.

When investigating the C_4H_6 concentration, a constant decrease was observed, while for $C_3H_6O_2$, a concentration maximum was observed after 4h of cleaning with air plasma due to previous oxidation of other contaminants. Only cleaning for an extended period lead to a reduced concentration.

The subsequent application of Argon plasma resulted in an increased contaminant concentration, demonstrating the different cleaning properties of air and Argon plasma.

The analysis of contamination in the octagon can also be applied to the aforementioned catalyst samples, leading to the establishment of a sample-specific preparation based on outgassing rates of the different components included in the sample itself.

Conclusion: Our experiments open a door to a general improvement of the cleanliness in the microscope and its associated equipment. Based on the chemical characteristics of contaminants, different cleaning protocols can be established. TEM investigations of these samples can be performed in a better way by applying a knowledge-based approach when choosing suitable preparation methods and customizing the cleaning procedures based on the analysis of the chemical composition of the contaminants.

[1] C.M. McGilvery et al., Micron 43 (2012), p. 450-455
[2] T.C. Isabell et al., Microscopy and Microanalysis 5 (1999), p. 126-135

Figure 1: PTR-MS signals for characteristic contaminant fragments $(C_4H_6)H^+$ (m/z=55.0548, left) and $(C_3H_6O_2)H^+$ (m/z=75.0446, right) after application of different plasma treatments.

Figure 1

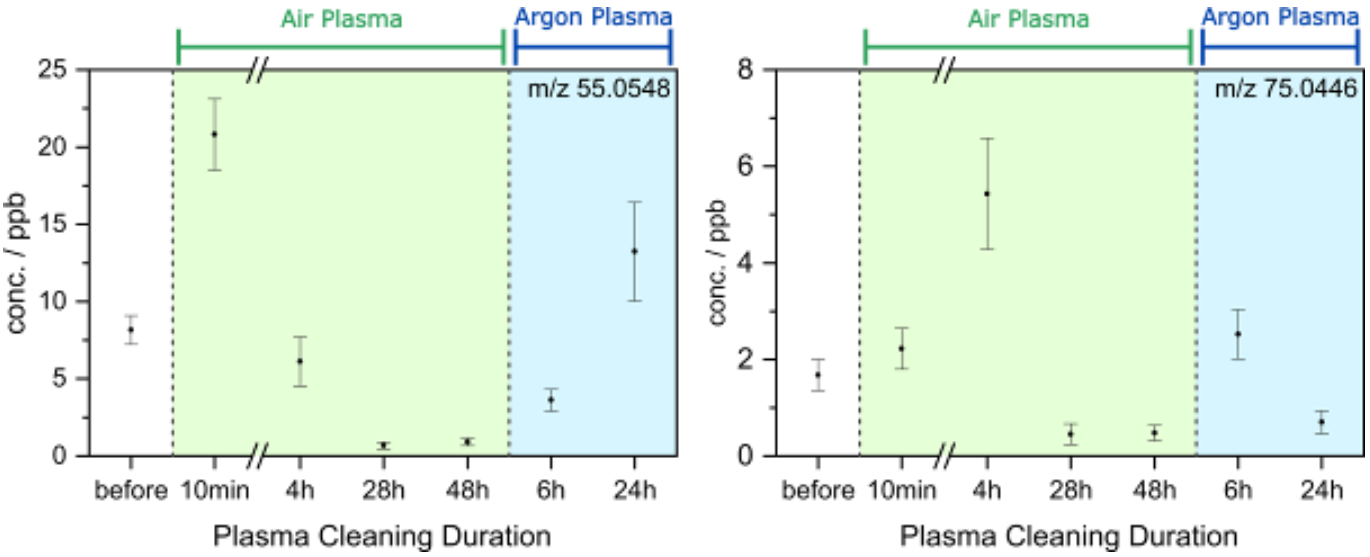

IM1.P009
Correlative characterization of catalysts

C. Neidiger[1]

[1]Karlsruhe Institute of Technology (KIT), Institut für Nanomaterialien, Eggenstein-Leopoldshafen, Germany

Introduction: The characterization of materials at different length scales and with several methods can lead to further insight into the morphology and the properties of a material. However, the various results need to be combined to extract the maximum information. To achieve correlation between images and spectra of increasing magnification, markers or features of the sample are tracked and cross-correlated to ensure a precise overlay. Heterogeneous catalysts are an example for a system that would benefit from correlative characterization. Due to the heterogeneity of the catalyst, several regions of interest may be very different in morphology and thus activity. Previous bulk characterization only yielded results that average over the whole sample. Position-accurate results are useful to understand the mechanisms behind the activity and reaction pathways on the catalyst. The change and degradation of morphology needs to be understood for the manufacturing of more stable and better catalysts.

Objectives: Image registration is key to accurately identify features across images taken with various instruments. However, different contrast modes, magnifications and translation between the images make cross-correlation a challenging task. The objective is to compile and develop a set of tools for accurate image registration from multisensory input images. This is the prerequisite for identifying local structures of interest in a material along all length scales from micro to nanometer and atomic resolution. Ultimately, a workflow will be established that enables identification of regions of interest, precise positioning and repeatable imaging throughout multiple instruments.

Materials and methods: The catalyst material investigated with X-ray µCT, visual light microscopy (VLM), FIB-SEM and TEM, is FeMoOx in form of pellets, industrially used in the Formox process. An initial overview of the sample is gained under a visual light microscope and a broad first region of interest selected. The pellet is prepared with laser cutting to a suitable size for optimum µCt resolution. Markers are added by FIB milling on the sample to allow navigation on the sample and positioning relative to the coordinates in the various instruments. The X-ray µCT is used to record an overview tomogram of the specimen and a tomogram of a ROI at higher resolution. In the FIB-SEM the ROI is further characterized by serial sectioning. Finally, a lamella is cut from the sample to be investigated in TEM. Here the selected regions of interest are investigated up to atomic scale.

Results: Pillars of about 450 µm diameter have been prepared by laser cutting and the depth of the damaged material is 10-20 µm. This enables µCT images with good resolution. Markers of 15 by 30 µm can be identified in VLM and SEM and will help with alignment in the reconstruction of tomograms. Repositioning and localization of ROI between VLM and SEM has been established by means of a commercial holder system. Catalyst pellets that were reacted for varying amounts of time display distinct variation in the structure, with a gradient from reacted material to pristine bulk material across the diameter of the pellet.

Conclusion: The correlation of images and spectra gained by several instruments requires precise localization and registration of signals. As a result, information that is more complex can be extracted that gives insight into the influence of structure on catalyst material performance.

IM1.P010
Advanced EBSD sample preparation solutions by broad ion beam milling

L. Palasse[1], P. Nowakowski[2]

[1]Bruker Nano Analytics, Berlin, Germany
[2]E.A. Fischione Instruments, Inc., Export, PA, United States

Successful electron backscatter diffraction (EBSD) material analysis cannot be achieved without good sample surface preparation. Since EBSD signal comes from the top few nanometers of the specimen, it requires a surface free from crystal lattice damage, plastic deformation, contamination and oxidation. In this presentation, we review the pros and cons of the different EBSD polishing techniques and demonstrate the advantages of Broad Ion Beam (BIB) milling.

The widely used mechanical polishing technique is limited to coarse-grained materials with phases of similar hardness. Polyphase sample comprising soft and hard materials cannot be prepared because hard particles removed during the first (coarse) polishing step act as a grinding medium which tears the soft phase.

Electrochemical polishing is fast and can be automated, but its application is limited to conductive and monophase materials with homogenous surfaces. It can be hazardous because it uses highly acidic and corrosive solutions. Focused Ion Beam (FIB) milling is also applicable for EBSD sample preparation, but it is limited to preparation area below 250 µm2 and can cause material damage that must be removed prior to EBSD measurement [1].

The alternative preparation technique for mono- to multiphase materials is BIB milling. Without requiring chemicals, BIB milling removes residual artifacts incurred during mechanical polishing. It achieves high-quality polished surfaces on almost any material, even multi-layers specimen of phases with different hardness and milling rates. It can prepare areas of up to centimeter scale [2] [Model 1062 TrionMill, Fischione Instruments] and prevents preparation-induced phase transformation of metastable phases, like the austenite-to-martensite dynamic transformation in steels [3]. Another benefit is the use of a cryo stage to allow BIB milling of beam-sensitive materials, like Zn or low temperature solder junctions (Figure 1).

We review EBSD results acquired with *e*-Flash^{FS} EBSD detector [Bruker Nano Analytics] on large areas of alloys and solder bumps polished by mechanical and BIB milling techniques. EBSD results demonstrate that surface topography produced by BIB milling has no correlation with the distribution of crystallographic orientations and misorientations (Figure 2 & 3). This confirms that BIB milling is an excellent surface preparation technique for high quality EBSD measurements.

[1] Saowadee, N., Agersted, K., & Bowen, J. (2012). Effects of focused ion beam Milling on electron backscatter diffraction patterns in strontium titanate and stabilized zirconia. *Journal of Microscopy*, 246(3),279-286 https://doi.org/10.1111/j.1365-2818.2012.03616.x
[2] Nowakowski, P., Wiezorek, J., Spinelli, I., Ray, M., & Fischione, P. (2019). Elastic and plastic strain measurement using electron backscatter diffraction technique: The influence of sample preparation. *Microscopy and Microanalysis*, 25(S2), 534-535 https://doi.org/10.1017/s1431927619003404
[3] Giannuzzi, L., & Michael, J. (2020). Ion-induced transformation of metastable phases. *Microscopy and Microanalysis*, 26(S2),792-793 https://doi.org/10.1017/s1431927620015858

Figure 1: EBSD phase map of a Sn-Cu solder bump prepared under cryogenic conditions

Figure 2: ARGUS™ color-coded orientation contrast image [Bruker Nano Analytics] of a bulk specimen of Zr alloy

Figure 3: corresponding kernel average misorientation (KAM) distribution in false color with pattern quality as background

Figure 1

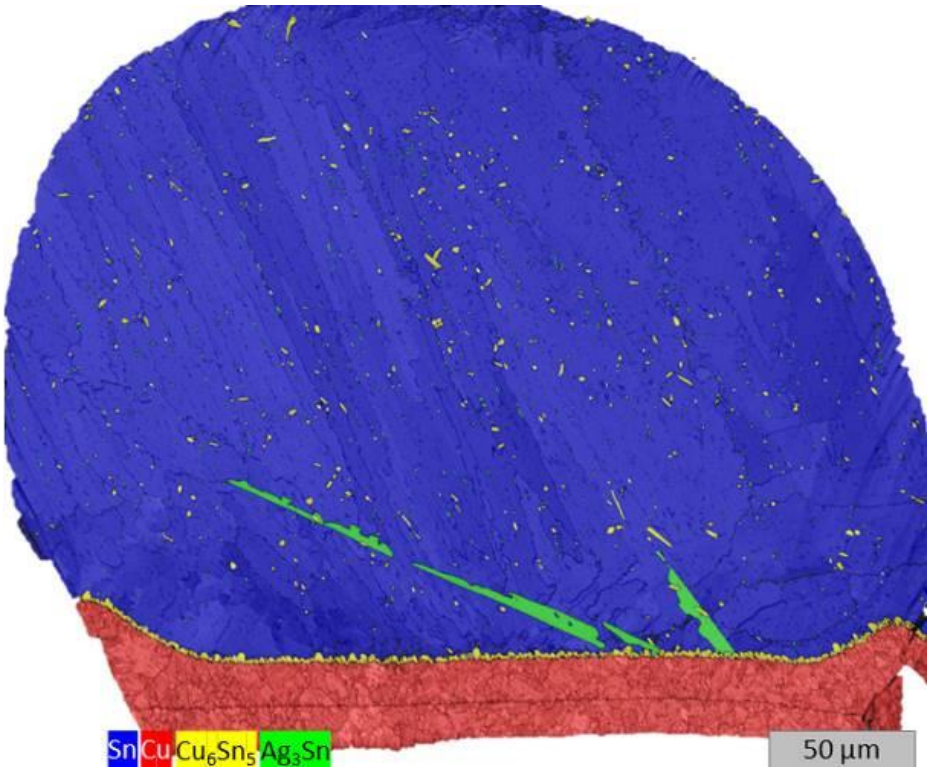

Figure 2

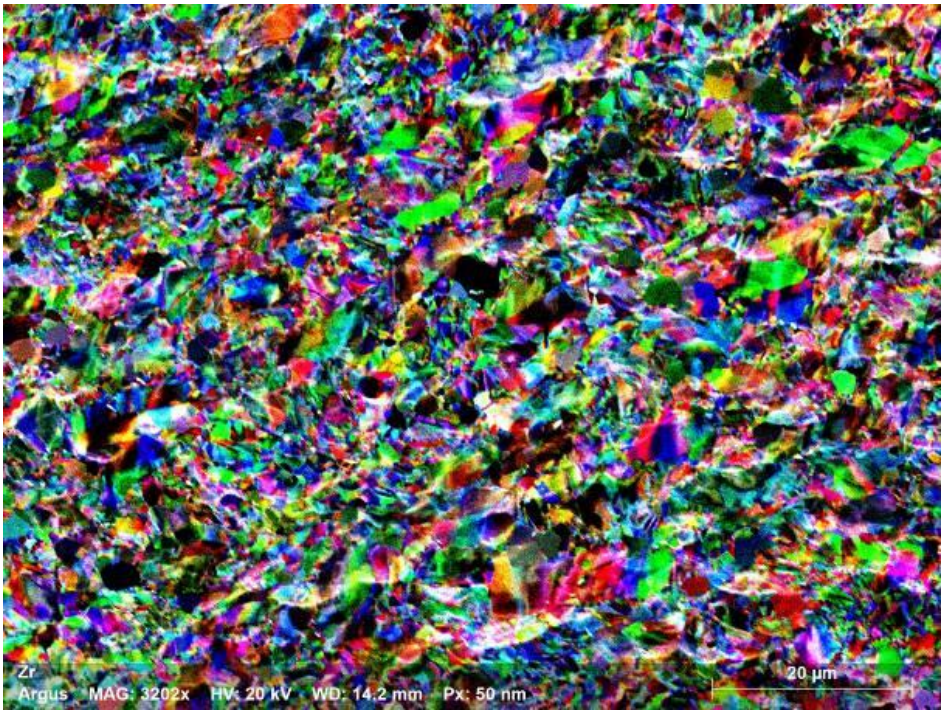

Figure 3

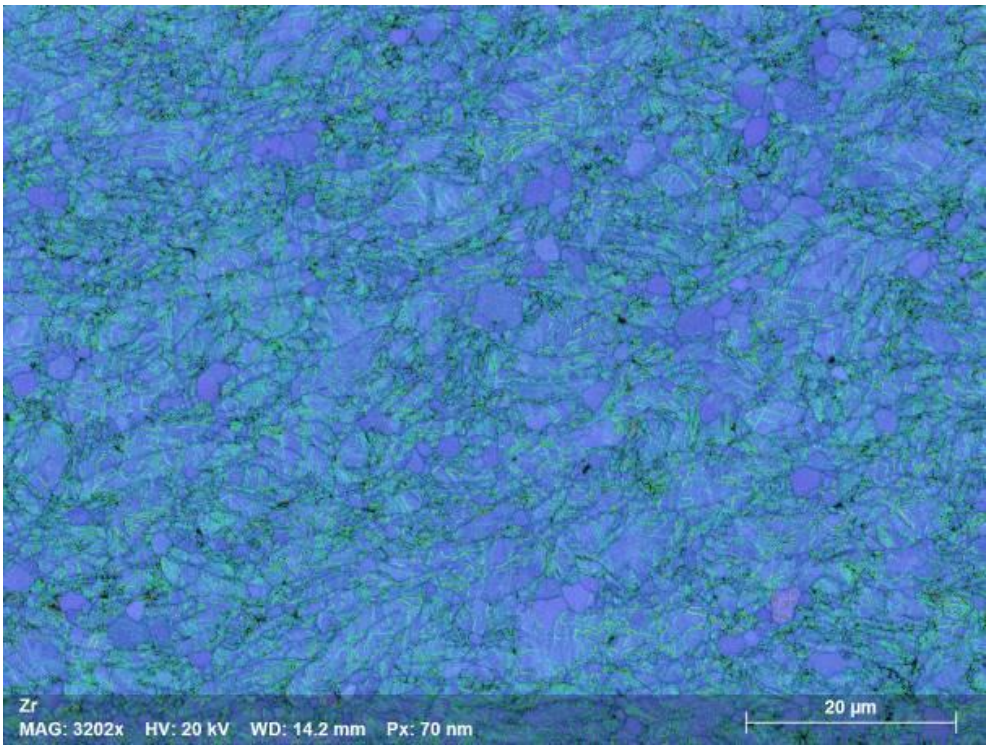

IM1.P011
Fs-laser sample preparation for microstructure analysis of ceramic materials

T. Volkenandt[1], F. Pérez-Willard[1], T. Schubert[2], B. Tordoff[1]

[1]Carl Zeiss Microscopy GmbH, Oberkochen, Germany
[2]Aalen University, Materials Research Institute Aalen, Aalen, Germany

Ceramics play an import role in engineering and materials sciences because of their various beneficial properties. Technical ceramics offer for example great hardness and insulating properties, resistance to heat, wear, and chemicals. These properties make them ideal candidates for a wide range of applications. As for most materials, their properties are governed by the microstructure resulting from production and processing. Therefore, in-depth understanding of the microstructure is needed to improve and foster the development of new ceramics with tailored properties.

Analyzing the microstructure of ceramics, however, can be challenging because of those very same mechanical and electrical properties. Their brittleness complicates sample preparation and their non-conductivity hinders analysis and structuring with electron or ion beams.

To address these challenges, we explored the application of fs-laser milling for sample preparation of ceramic materials using a LaserFIB. LaserFIB is a new class of instruments that has recently been introduced and consists of a fs-laser system integrated into a focused ion beam scanning electron microscope (FIB-SEM) [1]. This combination offers on the one hand massive material removal by laser ablation and on the other hand high-resolution imaging and ion patterning capabilities in one single instrument. To protect sensitive FIB-SEM components from debris and contamination, all laser work is done in a separated chamber extending the airlock. Correlative sample transfer between the chambers is fast and easy, while at the same time ensuring longevity and performance of the whole system.

The sample preparation capabilities of the LaserFIB were tested using a variety of technical ceramic materials including Zirconia (ZrO_2), Silicon Nitride (Si_3N_4), Forsterite ($Mg_2[SiO_4]$), Lead Zirconate Titanate ($Pb[Zr_xTi_{1-x}]O_3$ ($0 \leq x \leq 1$)) and a compound of SiC-ZrB_2. A laser milling recipe was developed to cross-section these materials and laser ablation rates were determined. It could be shown that all tested ceramics can be machined by the fs-laser in a fast and precise manner enabling large-scale sample preparation. As an example, for Forsterite it was possible to achieve ablation rates up to 26 mm^3/h. Figure 1 shows an SEM image of a laser-cut cross-section in SiC-ZrB_2 illustrating the resulting preparation quality without any FIB post-polishing. Pores and the individual phases of the compound can nicely be distinguished and analyzed. Previous studies showed that the surface quality of laser-cut cross-sections is even suitable for EBSD analysis [2].

In this contribution we will summarize our results about using a fs-laser for sample preparation of ceramic materials. Details about the developed laser milling recipe will be presented as well as multiple application examples. We will also comment on possible preparation artefacts and application of the technique to other material systems like metals or composite materials.

Figure 1: SEM image of laser-cut cross-section in SiC-ZrB2 compound.

References:
[1] B. Tordoff et al., The LaserFIB: new application opportunities combining a high-performance FIB-SEM with femtosecond laser processing in an integrated second chamber. Appl. Microsc. 50, 24 (2020). https://doi.org/10.1186/s42649-020-00044-5
[2] T. Schubert et al., Rapid Sample Preparation for EBSD-Analysis Enabled by the LaserFIB, ZEISS Application Note (2020), available online.

Figure 1

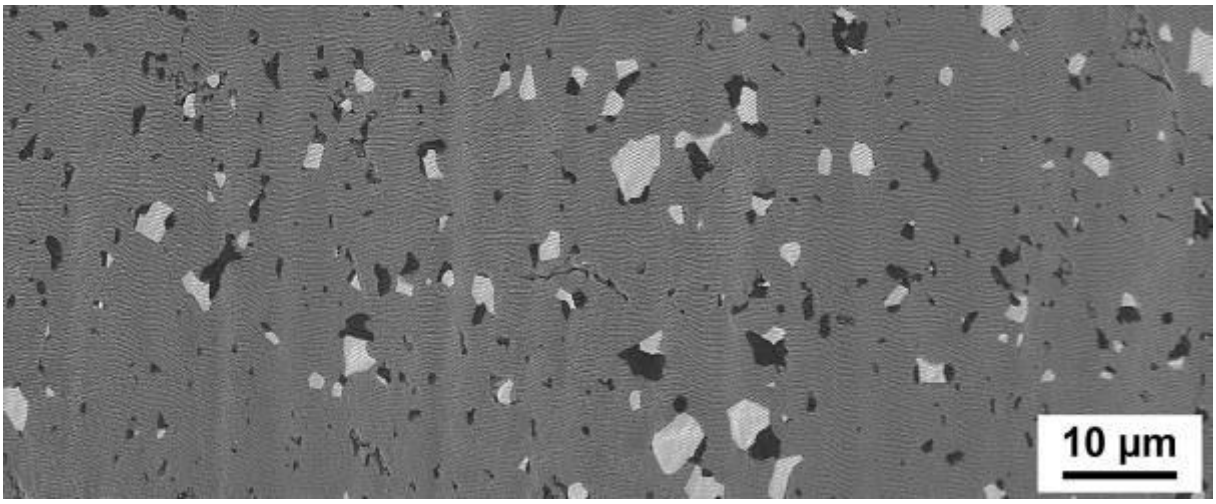

IM2.001-Invited
Towards atomic-scale quantitative energy dispersive X-ray spectroscopy

K. E. MacArthur[1]*, A. B. Yankovich[2], A. Béché[3], M. Luysberg[1], H. G. Brown[4], S. D. Findlay[5], M. Heggen[1], L. J. Allen[6]

[1]The Ernst Ruska Centre for Microscopy and Spectroscopy with Electrons and the Peter Grünberg Institute Forschungszentrum Jülich, 52425 Jülich, Germany
[2]Department of Physics, Chalmers University of Technology, SE-412 96 Gothenburg, Sweden
[3]Electron Microscopy for Materials Science (EMAT), University of Antwerp, 2020 Antwerp, Belgium
[4]Ian Holmes Imaging Center, Bio21 Molecular Science and Biotechnology Institute, University of Melbourne, Parkville, Victoria 3052, Australia
[5]School of Physics and Astronomy, Monash University, Clayton, Victoria 3800, Australia
[6]School of Physics, University of Melbourne, Parkville, Victoria 3010, Australia

Thanks to silicon drift detectors (SDDs) and aberration correction in the scanning transmission electron microscope (STEM), we can now routinely achieve beautiful EDX maps which reveal atomic-scale features within our materials. However, it still remains to understand exactly where the X-ray signals come from within the specimen and how accurately they can be quantified at these length scales.

When a crystal is aligned along a low-order zone-axis (necessary for atomic resolution imaging) electron channelling occurs. Electron channelling aligned columns of atoms provide an additional focusing effect on the electron beam, increasing the electron density close to the atomic nuclei resulting in a higher number of scattering and ionization events [1, 2]. For longer columns we get the oscillations of the probe electron density down the length of the column which complicates the evaluation of composition because atomic ordering within a column significantly affects the results.

Excellent quantitative agreement between calibrated experiments and multi-slice simulations using MuSTEM has been demonstrated [3, 4]. However, the challenge we are often faced with is most materials science applications the atomic-structure is unknown. Therefore, we need an approach that allows us to suppress the channelling and create a first guess of the materials structure using simple linear-based EDX quantification methods. Using SrTiO3-DyScO3 multilayers as an example, we will discuss the combined effect of sample tilt [4] and spatial integration for ameliorating the effects of channelling and improving the accuracy of EDX quantification. Figure 1 shows the effect of sample tilt on an integrated line profile of Ti-K from both simulations and experiment. In suppressing channelling the total number of X-ray counts drops off however this brings the absolute values closer to the linear approximation [4]. There is a balance to be found between beautiful atomic-scale but only qualitative maps and improving the quantification at a cost of some loss of resolution. Finally, we will also look at the effects of scattering and beam broadening and how this affects our ability to measure the accurate composition profile across an interface. The remaining limitations and the challenges will be discussed. [5]

References

[1] K.E. MacArthur et al. Ultramic. 156 (2015), p. 1-8
[2] K.E. MacArthur et al. Ultramic. 182 (2016), p. 264-275
[3] Z. Chen et al. Ultramic. 168, (2016), p. 7-16
[4] N.R. Lugg et al. Ultramic. 151 (2015), p.150-159

[5] The authors acknowledge financial support from the DFG (grant number HE 7192/1-2), the Discovery Projects funding scheme of the Australian Research Council (Projects DP140102538 and FT190100619) and the European Union's Horizon 2020 No. 823717 – ESTEEM3.

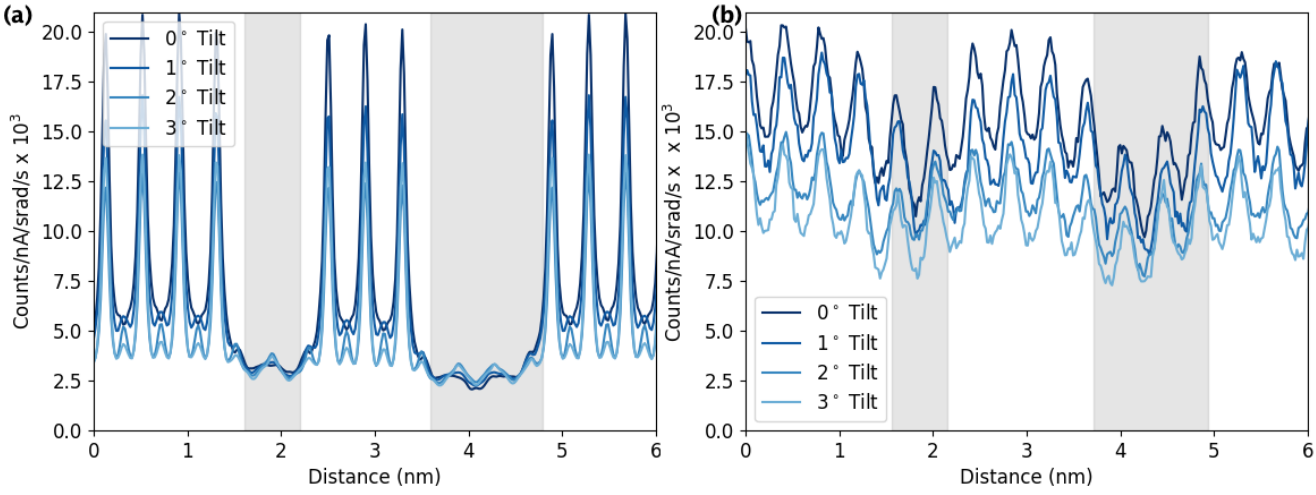

Figure 1: Comparison of quantified X-ray line profiles for Ti-K in a SrTiO3-DyScO3 multilayer oxide from simulation (a) and experiment (b) at different sample tilts, the grey regions indicate the approximate location of the DyScO3 layers. (a) is simulated with a perfectly abrupt interface. Although the match between experiment and simulation is close in average value there is still a significant resolution different which needs to be understood. (b) There is also no clear distinction between the layers in (b) although this is in part due to beam broadening and scattering occurring.

IM2.002-Invited
Probing structural defects in oxide films at atomic resolution

M. D. Rossell

Empa, Swiss Federal Laboratories for Materials Science and Technology, Überlandstrasse 129, CH-8600, Dübendorf

Transition-metal oxides (TMOs) display a wide diversity of properties, such as ferroelectricity, ferromagnetism, ion conduction, colossal magnetoresistance, superconductivity and catalytic activity, *which are essentially determined* by the electronic states of the partially occupied TM d-orbitals. In addition, the local coordination environment of the TM can change around structural defects and dramatically modify the functional properties of TMOs, and hence the performance of the devices made therefrom. Thus, a comprehensive understanding and precise control of defects is critical to obtain unprecedented functional properties and efficiently move forward in the field of defect engineering.

Thanks to advancements in thin film epitaxy and characterization techniques, and theoretical modeling, it is nowadays known that structural defects can be either detrimental or beneficial, depending on the targeted application. A first step in assessing the impact of a particular defect on the material properties is to investigate its exact atomic configuration. For this purpose, we use aberration-corrected scanning transmission electron microscopy (STEM) in combination with energy dispersive x-ray (EDX) spectroscopy and electron energy-loss spectroscopy (EELS). Thus, direct chemical and electronic information of the individual atomic species is collected. A correlation with the electronic properties of the defect is then achieved by the aid of theoretical modeling. Models of the defects, based on the experimental data, are constructed and ab initio methods are used to calculate their electronic properties.

In this contribution, I will address two different systems, namely BiFeO3 [1] and SrFeO3-δ [2] thin films.
Firstly, the influence of edge misfit dislocations on the local electronic properties of BiFeO3 thin films will be discussed. By using a combined experimental and theoretical strategy based on STEM, EDX, EELS, off-axis holography and atomistic simulations we explore the chemical properties and the bonding characteristics of the atoms located at and near the dislocation cores. We find that small amounts of Fe atoms are present at the BiFeO3 dislocations cores, which result in uncompensated Fe spins along the dislocations giving rise to a magnetic signal. This suggests the possibility of exploiting misfit dislocations in antiferromagnetic thin films to achieve ferromagnetic properties beyond those of the corresponding perfect BiFeO3 structure [1].
Secondly, we demonstrate that extended planar defects found in epitaxially grown SrFeO3-δ thin films consist of Fe2O2+α double layers of FeO5 polyhedra alternating with SrO and FeO2 perovskite-type layers in an ordered arrangement, analogous to the Sr4Fe6O12+δ crystal structure. Our experimental and theoretical EELS data, combined with projected density of states calculations, reveal peak width changes and energies shifts, which suggest an increased electron doping of the Fe 3deg band in the Fe2O2+α layers as compared to the SrFeO3−δ film. Thus, we show that the presence of Fe2O2+α planar defects intersecting orthogonally in an extraordinary labyrinth network can effectively modify the electron-hole conductivity in SrFeO3-δ films [2].

[1] P. Agrawal, M. Campanini, A. Rappe, S. Liu, V. Grillo, C. Hébert, R. Erni, D. Passerone, M. D. Rossell, Phys. Rev. Materials 3, 034410 (2019).
[2] M. D. Rossell, P. Agrawal, M. Campanini, D. Passerone, R. Erni, Phys. Rev. Materials 4, 075001 (2020).

IM2.004
Unscrambling mixed elements atom-by-atom by combining HAADF STEM and EDX

A. De Backer[1,2], E. Bladt[1,2], Z. Zhang[1,2,3], K. H. W. Van Den Bos[1,2], S. Bals[1,2], S. Van Aert[1,2]

[1]EMAT, University of Antwerp, Antwerp, Belgium
[2]NANOlab Center of Excellence, University of Antwerp, Antwerp, Belgium
[3]Department of Materials, University of Oxford, Oxford, United Kingdom

The unique electronic, optical, or catalytic properties of nanocrystals are largely controlled by the exact arrangement of the atoms. Therefore, quantitative structure determination is essential for the development of new nanocrystals. For homogeneous nanoparticles, the number of atoms can be counted from high resolution annular dark field scanning transmission electron microscopy (HAADF STEM) images [1] where intensities scale with number of atoms and the atomic number Z. For mixed columns, all types of elements will contribute differently to the image intensities thus significantly complicating the quantitative interpretation of the image intensities [2]. To overcome this limitation, we propose combining HAADF STEM images and elemental maps acquired by energy dispersive X-ray (EDX) spectroscopy [3] enabling atom-counting for heterogeneous nanostructures, even when the difference in atomic number is only one.

The so-called scattering cross-section (SCS), corresponding to the total intensity of electrons scattered by a single atomic column, has been shown to be a successful performance measure for atom-counting and composition determination in HAADF STEM [1,4-6]. Similarly, EDX STEM SCSs can be defined from elemental maps. Since both HAADF STEM and EDX imaging are incoherent techniques, a linear relation between the EDX and HAADF STEM SCSs is assumed. In order to confirm the linear relation, experimental STEM images and EDX maps of a CeO2 nanoparticle have been acquired. The SCSs are represented in a scatter plot indeed suggesting a linear relationship (Figure 1).

As a proof of concept, the combination of EDX and HAADF STEM images is used to count the number of atoms for a Ag-coated Au nanorod. Figure 2(a) shows a times series for both the STEM images and the Ag and Au EDX maps. Using an iterative weighted least squares minimization, the averaged experimental SCSs have been matched to simulated values by estimating normalization constants for the EDX SCSs, assuming a linear scaling between the STEM and EDX SCSs. The resulting number of Ag and Au atoms for each atomic column are shown in Figure 2(b). This methodology opens up new possibilities for the characterization of heterogeneous nanostructures with adjacent atomic numbers at the atomic scale [7].

References:
[1] S. Van Aert et al., Physical Review B 87 (2013), p. 064107.
[2] K.H.W. van den Bos et al., Physical Review Letters 116 (2016), p. 246101.
[3] A.J. D"Alfonso et al., Physical Review B 81 (2010), p. 100101.
[4] S. Van Aert et al., Ultramicroscopy 109 (2009), p. 1236.
[5] H. E et al., Ultramicroscopy 133 (2013), p. 109.
[6] G.T. Martinez et al., Ultramicroscopy 187 (2018), p. 84.
[7] This work was supported by the European Research Council (Grant 770887 PICOMETRICS to SVA and Grant 815128 REALNANO to SB, Grant 823717 ESTEEM3). The authors acknowledge financial support from the Research Foundation Flanders (FWO, Belgium) through project fundings and postdoctoral grants to ADB and EB.

Figure 1: (a) Experimental HAADF STEM image of a Ce nanoparticle. (b) Experimental atomic resolution EDX elemental map for the Ce L shell. (c) The EDX SCSs as a function of the HAADF STEM SCSs. The grey line highlights the linear relation between the SCSs of both techniques.

Figure 2: (a) Experimental HAADF STEM images and EDX elemental maps for Ag and Au. (b) The total number of atoms and the number of Au and Ag atoms.

Figure 1

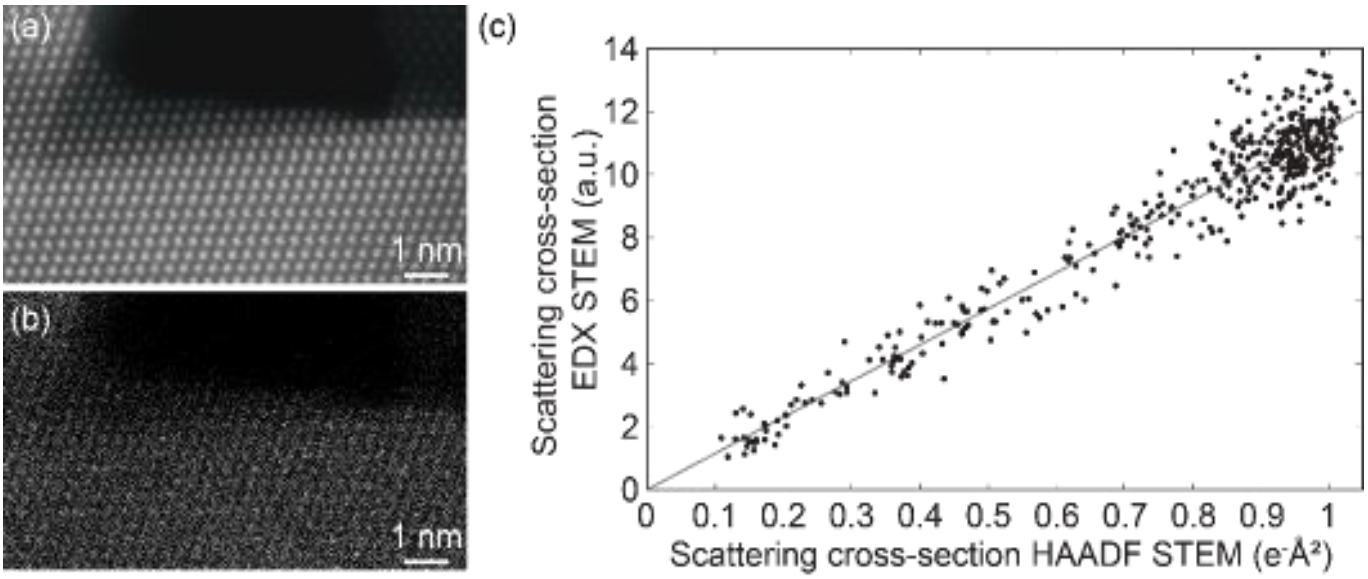

Figure 2

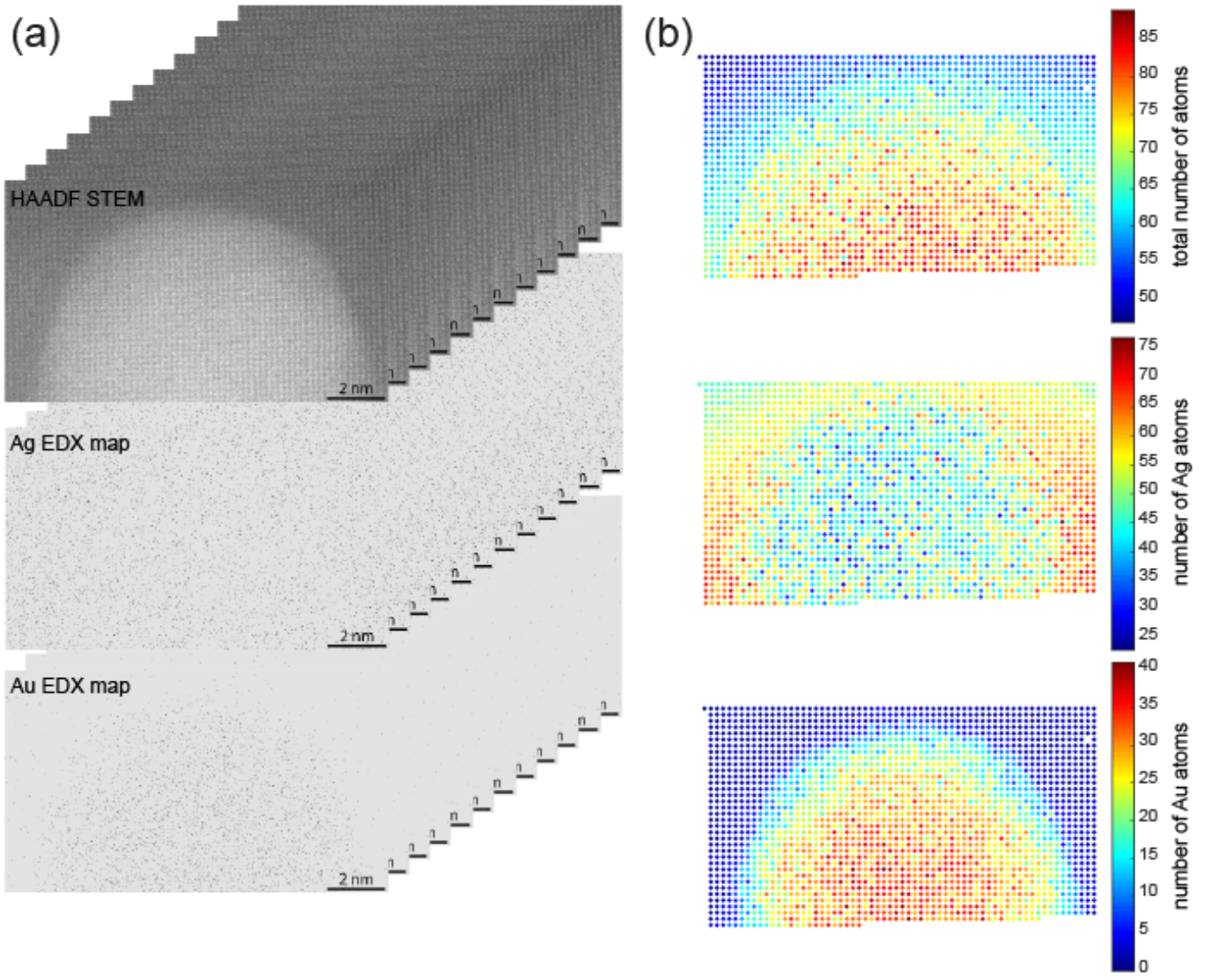

IM2.005
Obstacles for atomic-resolution elemental mapping by EFTEM

M. J. Mohn[1], J. Biskupek[1], Z. Lee[1], H. Rose[1], U. Kaiser[1]

[1]University of Ulm, Materialwissenschaftliche Elektronenmikroskopie, Ulm, Germany

Being the standard technique for elemental mapping in conventional TEM, energy-filtered TEM (EFTEM) is expected to localize ionization-edge signals across large fields of view. In microscopes equipped with a corrector for both the spherical and chromatic aberration (C_s & C_c), these EFTEM images can even show atomic resolution if large energy windows are used [1]. However, especially for thick samples, preservation of elastic contrast is observed in the EFTEM images, hampering the direct interpretation as elemental maps on the atomic scale [2]. Only very thin samples are expected to enable a direct interpretation, as the usual conceptions for the preservation of elastic contrast rely on multiple scattering.

Here we report on C_c/C_s-corrected EFTEM of graphene, a single layer of weakly scattering carbon atoms. We demonstrate that even for the thinnest possible TEM samples, there are severe drawbacks for a direct interpretation of EFTEM signals as elemental maps.

Our EFTEM experiments were performed in the C_c/C_s-corrected SALVE low-voltage TEM at 80 kV [3], tuned for sufficiently small C_c, and a positive C_s of a few µm. Using a 20 eV large energy window in the GIF Quantum energy filter, we were able to resolve the graphene lattice using the carbon K-edge signal at around 300 eV. In post-processing, our EFTEM images were averaged over multiple unit cells to enhance the signal-to-noise ratio. Eventually, this procedure allows us to directly analyze the contrast in the C-K-edge images (Figure 1). Instead of the expected bright-atom contrast of a carbon elemental map, we observe both bright-atom and dark-atom contrast. As demonstrated by the focus series in Figure 2, this is due to a behavior similar to the phase contrast in high-resolution TEM, where either bright-atom or dark-atom contrast can be obtained by changing the defocus. [4]

Possible reasons for these unexpected findings will be discussed by comparison with EFTEM image simulations for the C-K-edge signals by means of the mutual coherence function (MCF) method, which includes both elastic and inelastic scattering. Furthermore, we will compare the C-K-edge images with plasmon-loss images that show only preserved elastic contrast. Eventually, we will also present simulated EFTEM signals for individual carbon atoms in order to clarify the origin of the unexpected dark-atom contrast in the C-K-edge images of graphene. These simulations demonstrate that the interpretation of the C-K-edge images is hampered by contrast inversions, apart from the preservation of elastic contrast.

We acknowledge the financial support of the German Research Foundation (DFG) with project grant no. 424798828.

[1] K.W. Urban et al., PRL 110 (2013), 185507.
[2] B. D. Forbes et al., Ultramicroscopy 147 (2014), 98–105.
[3] M. Linck et al., PRL 117 (2016), 076101.
[4] M. J. Mohn et al., Ultramicroscopy 219 (2020), 113119.

Figure 1: C_c/C_s-corrected 80 kV EFTEM images from the zero loss (ZL) and C-K edge of graphene (290–310 eV window): Different experiments show the graphene lattice with either bright-atom contrast (a,b) or dark-atom contrast (c,d). All images were averaged over more than 100 unit cells to improve the signal-to-noise ratio.

Figure 2: C_c/C_s-corrected 80 kV EFTEM focus series with the C-K-edge signal of graphene (20 eV window centered at 300 eV energy loss). Defocus offsets of ± 8 nm around the optimum focus $C_{1,opt}$ show inversions from dark-atom contrast to bright-atom contrast and vice versa.

Figure 1

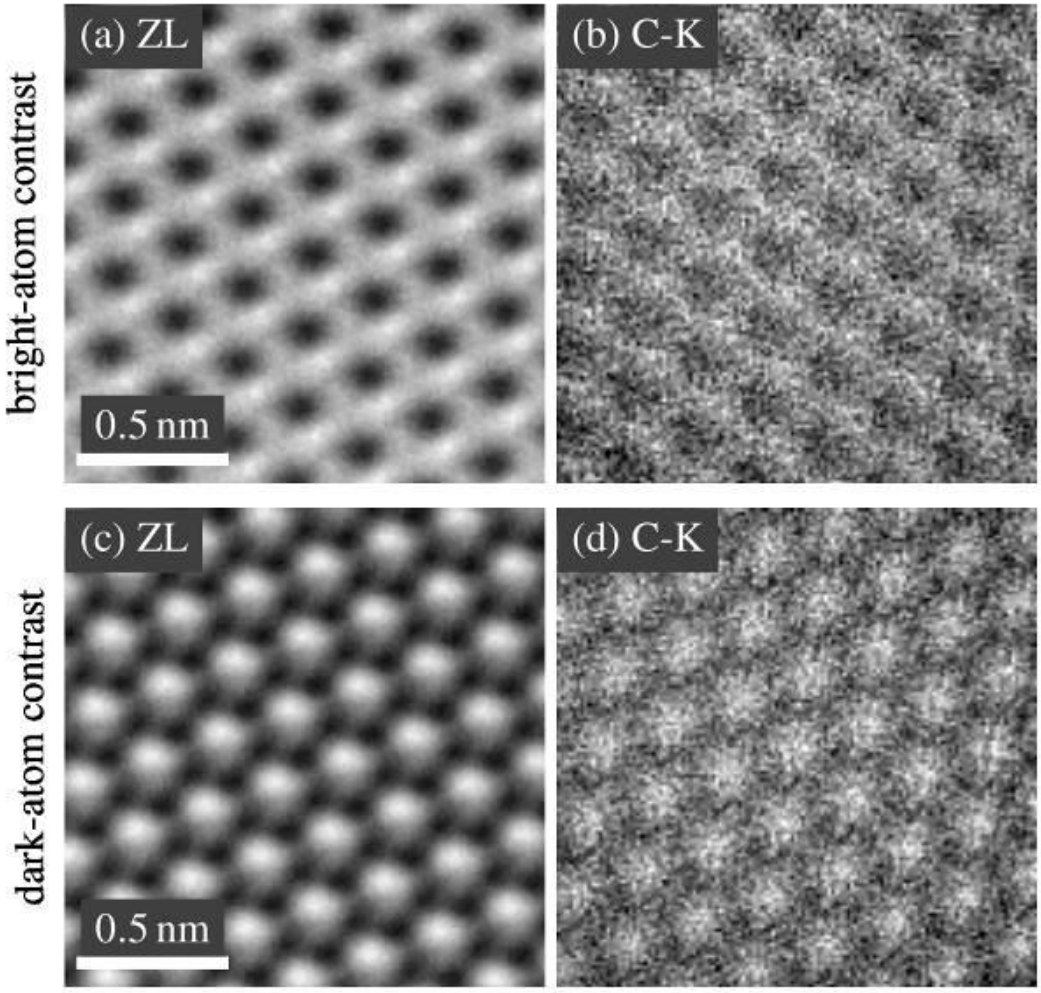

Figure 2

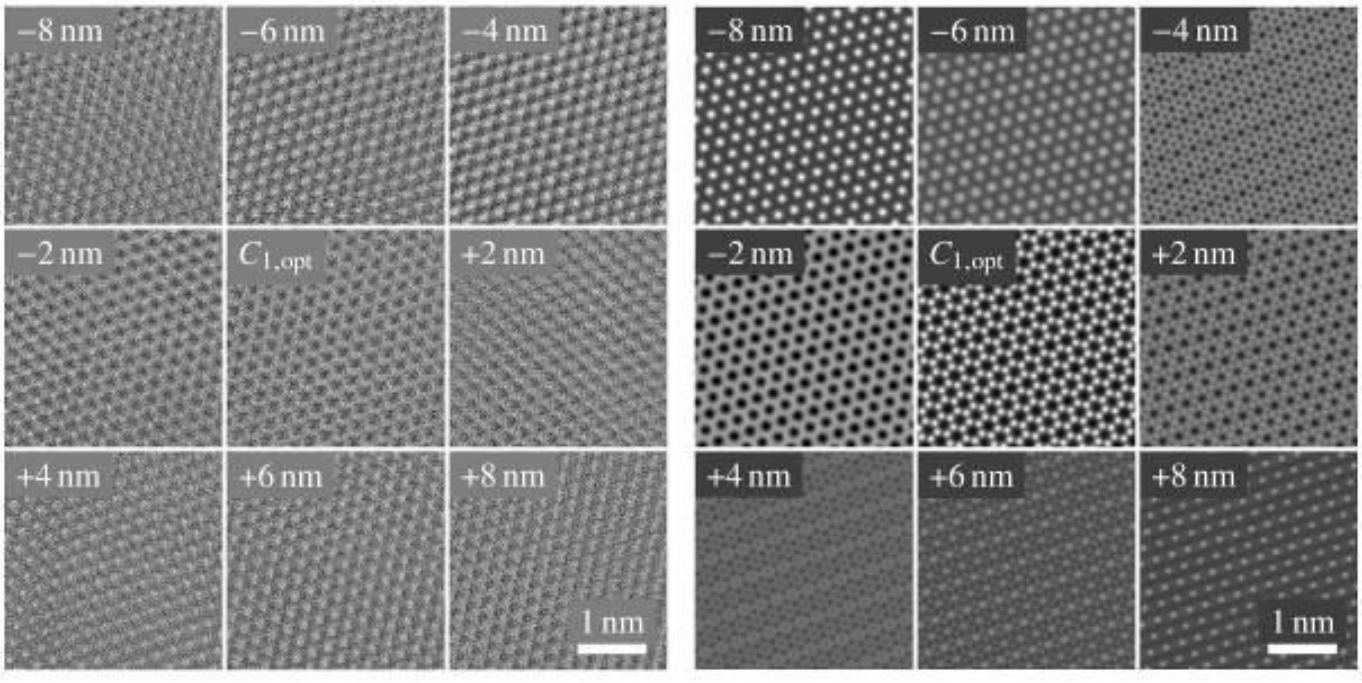

(a) Experiment: C-K edge, 290–310 eV

(b) Simulation: C-K edge, 290–310 eV

IM2.P001
Parameter optimisation in orbital mapping

M. Ederer[1], S. Löffler[1,2]

[1]TU Vienna, USTEM, Vienna, Austria
[2]TU Vienna, Institute of Solid State Physics, Vienna, Austria

Despite the recent advances in instrumentation, directly mapping electronic states in real space with the electron microscope remains a challenge owing to the extreme demands on stability, resolution and intensity. Here, we study the real-space mapping of core transitions with the use of electron energy-loss spectrometry (EELS). Up to now knowledge about electronic orbitals in materials has been mostly based on theory or indirect experimental measurements. Only recently has it been shown that the direct spatial mapping of electron transitions using scanning transmission electron microscopy (STEM) and EELS is possible [1, 2]. However, the low signal to noise ratio (SNR) makes the experimental realization extremely challenging. Thus, finding the optimal conditions for the experiment including sample preparation is crucial. Here we investigate the effect of different parameters on the resulting real-space image by means of numerical simulations. With the use of optimization metrics we gauge this effect and aim to find the perfect parameter set with focus on optimizing the material thickness. As an example, Figure 1(a) shows the energy-filtered map of rutile at the oxygen K-edge for three sample thicknesses. We consider multiple methods in order to evaluate the impact of a certain parameter set on the image and compare them in their ability to measure the image fidelity. The first method consists of calculating the normalized difference of two handpicked points of interest in the orbital map [Figure 1(b)]. This normalized difference describes how well the orbitals can be distinguished from elastic scattering effects like channeling. The second image fidelity criterion considered in this work is the structural similarity (SSIM) index [3] [Figure 1(c)]. It takes the whole image into account and is thus robust against changes in image brightness and small translations. Both metrics show an oscillatory behaviour in this system and outline the complex dependence of the orbital map on the sample thickness.

Figure 1: (a) Orbital maps of rutile in the [001] crystallographic direction with a sample thickness of 0.3 nm, 15 nm, and 30 nm. The images are extracted for an energy loss of 535.9 eV corresponding to the K-edge of oxygen, with an acceleration voltage of 100 kV. The scalebars indicate 0.5 nm. The blue and green dots mark the points used for the difference in (b). Bottom row: Image fidelity of rutile orbital maps using the modified contrast metric (b) and the SSIM index (c).

These methods can be applied to a variety of systems including interfaces between materials. Due to the experimental challenges it is vital to determine the optimal sample conditions to maximize contrast and SNR. This paves the way for the broad applicability of orbital mapping in the future. [4]

[1] S. Löffler et al. Real-space mapping of electronic orbitals. Ultramicroscopy 177, 26 (2017).
[2] M. Bugnet et al. In preparation.
[3] Zhou Wang et al. Image quality assessment: from error visibility to structural similarity. IEEE Transactions on Image Processing 13, 600 (2004).
[4] The authors gratefully acknowledge financial support by the Austrian Science Fund FWF (grant nr. I4309-N36).

Figure 1

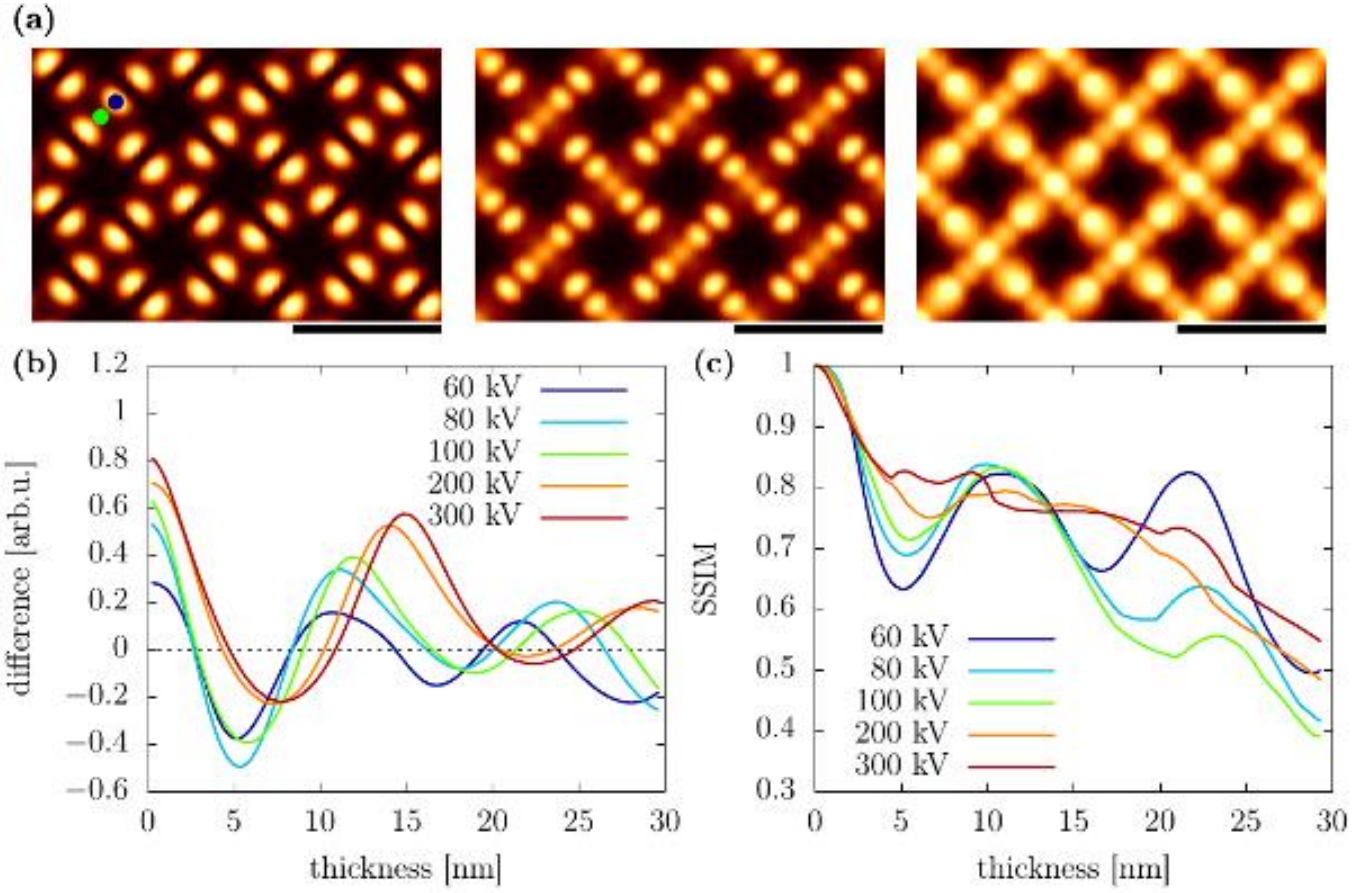
(a)
(b)
difference [arb.u.]
thickness [nm]
60 kV
80 kV
100 kV
200 kV
300 kV
(c)
SSIM
thickness [nm]
60 kV
80 kV
100 kV
200 kV
300 kV

IM2.P002
Orbital mapping – beyond the dipole approximation

M. Ederer[1], S. Löffler[1,2]

[1]TU Vienna, USTEM, Vienna, Austria
[2]TU Vienna, Institute of Solid State Physics, Vienna, Austria

With the current generation of Cs-corrected electron microscopes, mapping electronic states in real space has come within reach [1]. Nonetheless, there are still several hurdles to overcome due to the extremely demanding experimental conditions. Thus, it is important to theoretically determine beforehand if the structure of the material allows the detection of electronic state properties, like shape and orientation of the orbitals, at all. In this work we use the point group symmetry of the sample material to achieve this goal.

For core-loss processes, the transition to an unoccupied electonic state in the conduction band allows the extraction of information about neighbouring atoms and the crystal field, provided that a specific transition can be singled out. This is the case when the resulting two-dimensional map is not rotationally symmetric, which can be determined by the group symmetry of the transition matrix element [2]. Thus, the order of expansion in calculating the matrix element plays an equally important role as the point group symmetry of the material. In order to verify the symmetry predictions we simulate the energy-filtered mapping process of the TEM together with EELS.

As an example, we have studied molybdenum disulfite (MoS_2). This model system explicitly showcases the impact the point group symmetry and the order of the transition matrix have on the orbital map. The energy-filtered map is taken at the L_3-edge of Mo and Figure 1 shows the spatial distribution of the transition to a final orbital with d_{xz}- and d_{yz}-character. In the direction perpendicular to the atomic planes, the three-fold rotational symmetry makes it impossible to extract any directional information at all. We find completely circular shapes for both the dipole approximation [Figure 1(a)] and non-dipole approximation [Figure 1(b)]. For the [010] crystallographic direction (Figure 1, bottom row), the strongly reduced symmetry leads to spatial distributions heavily directed perpendicular to the atomic planes. Moreover, it becomes apparent that the dipole approximation is insufficient to simulate the mapped orbitals and higher orders are needed to fully capture the shape of the final d-orbital.

Figure 1: Orbital maps of MoS_2 extracted at the L_3-edge, with an acceleration voltage of 80 kV and a sample thickness of one unitcell. The scalebars indicate 0.5 nm. Top row: [001] crystallographic direction. Bottom row: [010] crystallographic direction. Green: calculated within the dipole approximation. Blue: calculated with higher order terms included in the transition element.

These symmetry based methods can be applied to a variety of systems including interfaces between materials. While not completely replacing the need for more extensive simulations, they can help prescreen materials not suited for orbital mapping. This lays the groundwork for the broad applicability of orbital mapping in the future. [3]

[1] S. Löffler et al. Real-space mapping of electronic orbitals. Ultramicroscopy 177, 26 (2017).
[2] Löffler et al. In preparation.
[3] The authors gratefully acknowledge financial support by the Austrian Science Fund FWF (grant nr. I4309-N36).

Figure 1

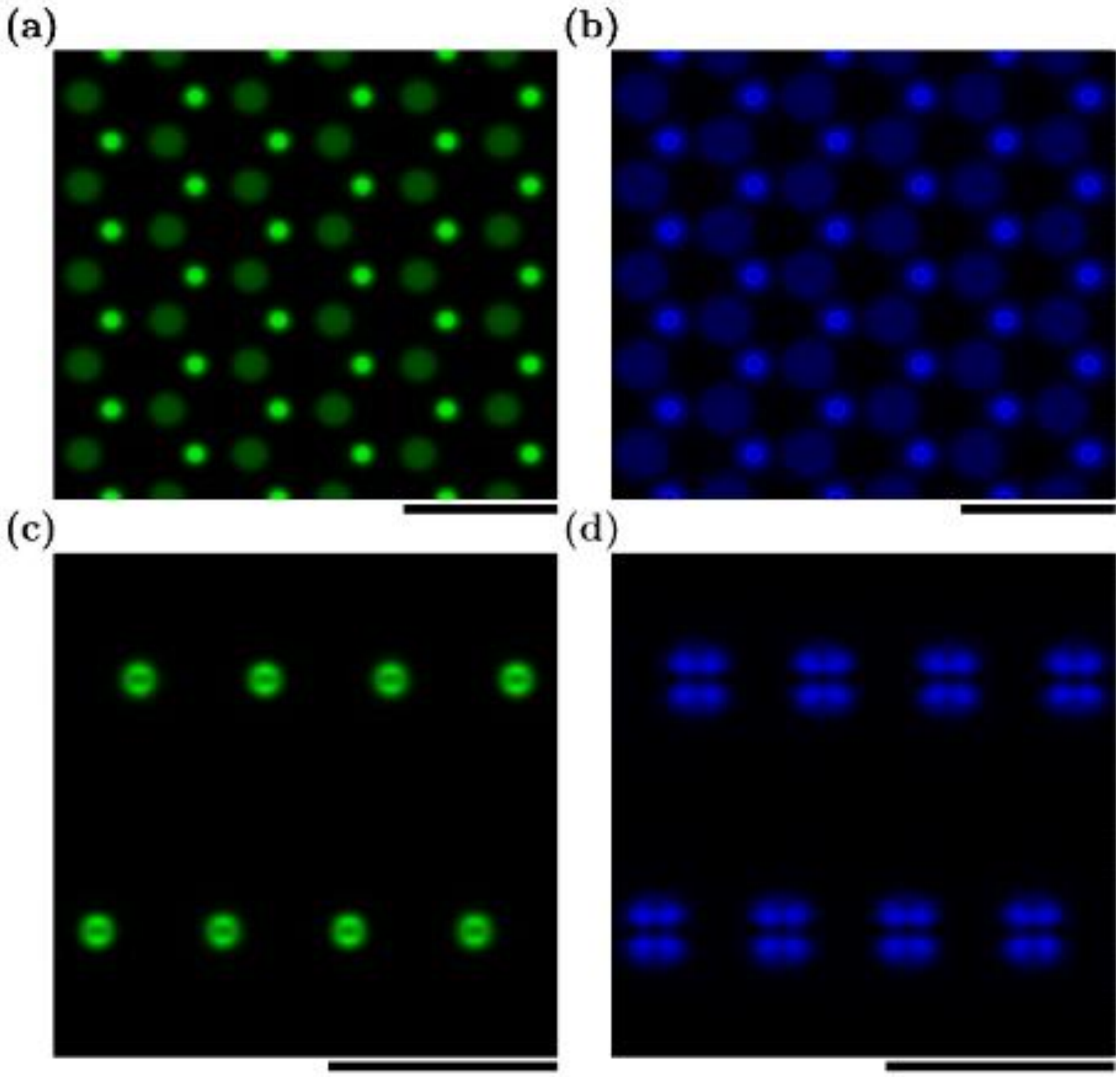

IM2.P003
EMCD on antiferromagnets

S. Löffler[1], F. Spies[2], M. Stöger-Pollach[1]

[1]TU Wien, USTEM, Vienna, Austria
[2]TU Wien, Institute of Solid State Physics, Vienna, Austria

Energy-loss magnetic chiral dichroism (EMCD) is a versatile method to study magnetism down to the atomic scale using TEM and EELS [1]. At its core, it is based on the fact that inelastic scattering in spin-polarized materials favors a specific orbital angular momentum transfer from the probe beam to the sample's atoms. The resulting scattered beam therefore features the peculiar phase structure known also from electron vortex beams [2]. Thus, the goal of EMCD is to determine how prominent this peculiar phase structure is. In the conventional setup that does not require the addition of vortex creation or filtering devices, this goal is achieved by an interference experiment. Using an incident plane wave and measuring close to the Thales circle, interference effects can be observed between the the transmitted beam and a diffracted beam, which was phase shifted due to elastic scattering. As a consequence, EMCD strongly depends on elastic scattering. In particular, this setup makes it impossible to measure any magnetic information in antiferromagnets. This can be understood from the fact that if elastic scattering is identical for the spin-up and spin-down atoms, one always measures the sum of a positive and a negative signal of equal magnitude.

To overcome this issue, we use convergent beam EMCD [3]. Using a convergent beam breaks the translational symmetry of the plane wave and allows to probe the signal from spin-up and spin-down atomic planes separately. Figure 1 shows the simulated EMCD signal strength for the Ni L edge for a 20 nm thick NiO crystal tilted into systematic row condition including the (1 1 -1) diffraction spot with a beam energy of 200 keV. As expected, the EMCD signal vanishes for small convergence semi angles, but a sizable effect of around 15 % can be obtained for $\alpha > 5$ mrad.

The approach presented in this work paves the way for the efficient investigation of antiferromagnets on the atomic scale. This is not only of interest from a fundamental physics point of view, but can lead to important advances in applications such as spin valves, magnetic sensors, hard disks, or magnetoresistive random-access memory. [4]

[1] P. Schattschneider et al., Nature 441 (2006) 486
[2] Verbeeck et al., Nature 467 (2010) 301
[3] S. Löffler & W. Hetaba, Microscopy 67 (2018) i60
[4] SL acknowledges financial support by the Austrian Science Fund (FWF) under grant nr. I4309-N36.

Figure 1: EMCD signal strength as a function of the convergence semi-angle α and the beam position in a 20 nm NiO crystal tilted into systematic row condition including the (1 1 -1) spot with detector positions as in [3]. Ni1 refers to spin-up atomic planes, Ni2 refers to spin-down atomic planes. The distance between Ni1 and Ni2 is approx. 0.24 nm. An acceleration voltage of 200 kV and ideal lenses were used in the calculation.

Figure 1

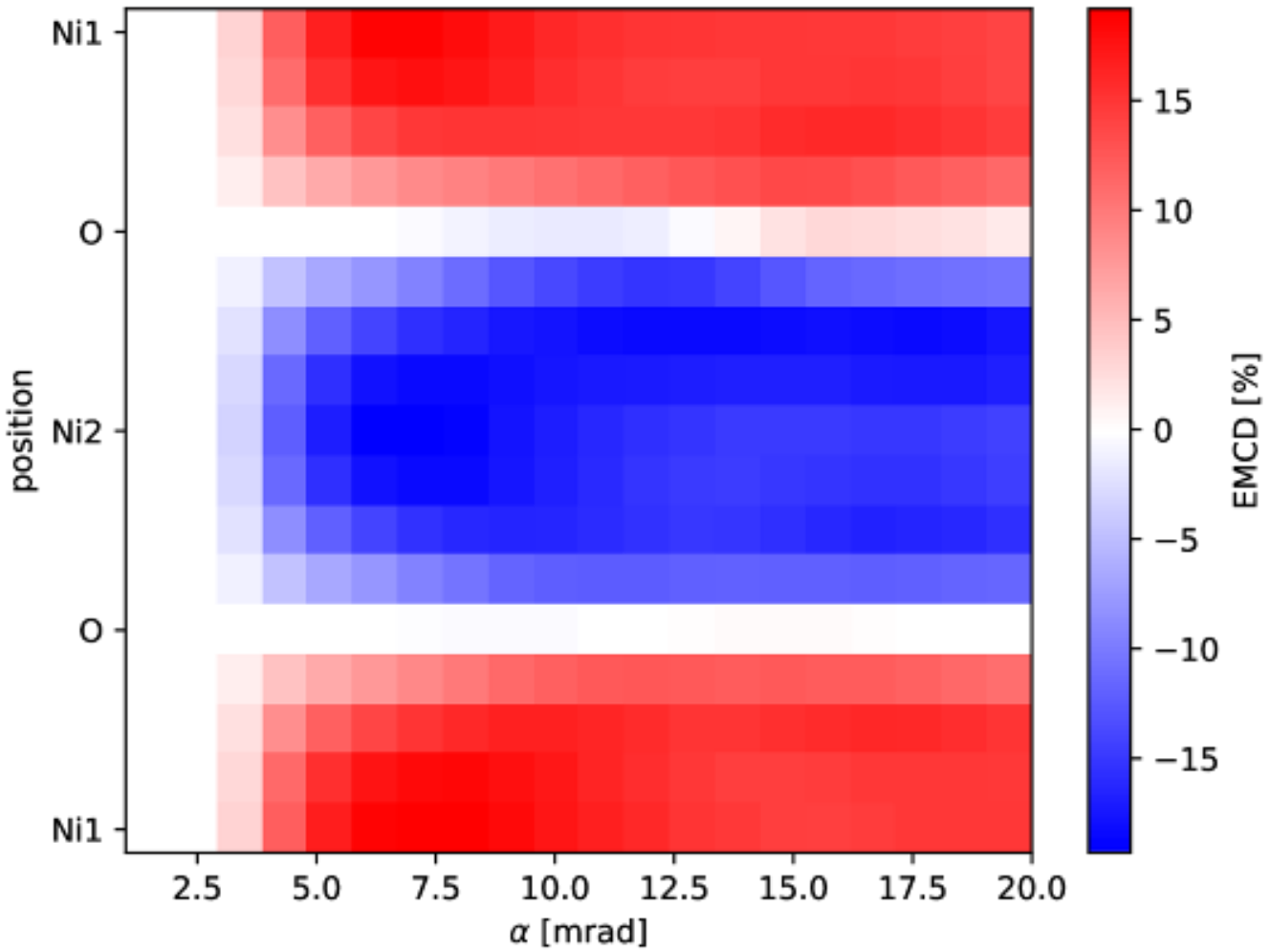
Ni1
O
Ni2
O
Ni1
position
2.5
5.0
7.5
10.0
12.5
15.0
17.5
20.0
α [mrad]
15
10
5
0
−5
−10
−15
EMCD [%]

IM2.P004
Post-processing procedure for orbital mapping of rutile by STEM-EELS

M. Oberaigner[1], D. Knez[1], G. Kothleitner[1,2], S. Löffler[3]

[1]Institute of Electron Microscopy and Nanoanalysis, Graz University of Technology, Graz, Austria
[2]Graz Centre for Electron Microscopy (ZFE), Graz, Austria
[3]University Service Centre for Transmission Electron Microscopy, Vienna University of Technology, Vienna, Austria

Recently, it was shown that scanning transmission electron microscopy (STEM) in combination with electron energy loss spectroscopy (EELS) allows for a real-space mapping of atomic orbitals [1]. Although state of the art electron microscopes offer the required spatial- and energy resolution, the inherently poor signal-to-noise ratio (SNR) for such experiments imposes a major challenge.

The poor SNR necessitates the development and application of advanced post-processing procedures. For mapping atomic orbitals, the procedure has to maintain the high spatial resolution as well as all details of the EELS fine structure.

In this work, we use a rutile sample. Due to the different bond lengths between titanium and oxygen, rutile exhibits orbitals which are rotated 90° to each other when viewed along the [001]-direction (Figure 1). The specimen is prepared by wedge polishing and focused ion milling. The measurements are performed with the FEI Titan³ G2 equipped with a monochromator and Cs-corrector. The EELS signal is recorded by a direct detection camera, which offers higher SNR through its much-improved detective quantum efficiency.

Figure 1: EELS signal at $L_{2,3}$-edges of titanium in rutile with the contribution of each state. The marked energy range is used to map the eg-states, which are rotated 90° to each other in rutile [001].

Although using a direct detection camera, the SNR is still not good enough to map orbitals from the unprocessed spectrum image. To overcome problems with low SNR EELS data, multivariate analysis techniques such as principal component analysis (PCA) are often used. For high noise, however, PCA introduces artifacts or even removes faint fine structures [2], which prevents mapping orbital signatures directly from the raw data. As a remedy, reference dark field images can be recorded simultaneously with the EELS signal. Containing high-spatial resolution information, these references can be used to precisely stack and re-align multiple cells and to average the corresponding electron energy-loss spectra to a signal level sufficient for PCA denoising. The noise of a direct detection camera is mostly governed by the shot noise contribution (Poisson noise), which enables the application of weighted PCA optimized to such Poisson noise dominated data [3].

The proposed post-processing procedure was capable to image the e_g-state of titanium in rutile [001], which agrees with STEM-EELS simulations (Figure 2).

Figure 2: Schematic post-processing procedure of rutile [001], mapping the e_g-like-states of titanium.

Due to the inherently poor SNR, PCA cannot be applied directly on the raw data without altering the EELS fine structure. Therefore, the SNR is increased first by averaging the EELS signal according to the dark field image. Afterwards, the EELS signal is denoised via PCA to map atomic orbitals.

[1] S. Löffler et al, Ultramicroscopy, 177 (2017)
[2] S. Lichtert et al, *Ultramicroscopy*, 125 (2013)
[3] Keenan et al, In Surf. Interface Anal., 36 (3) (2004)
The authors acknowledge financial support by the Austrian Science Fund (FWF) under grant nr. I4309-N36

Figure 1

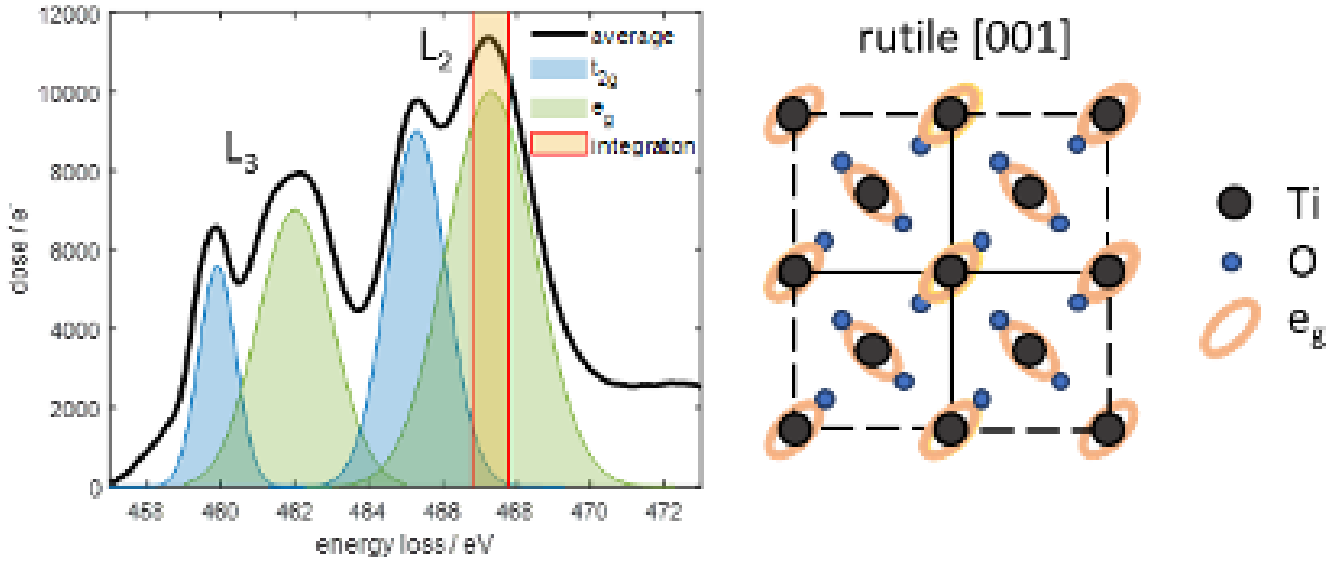

Figure 2

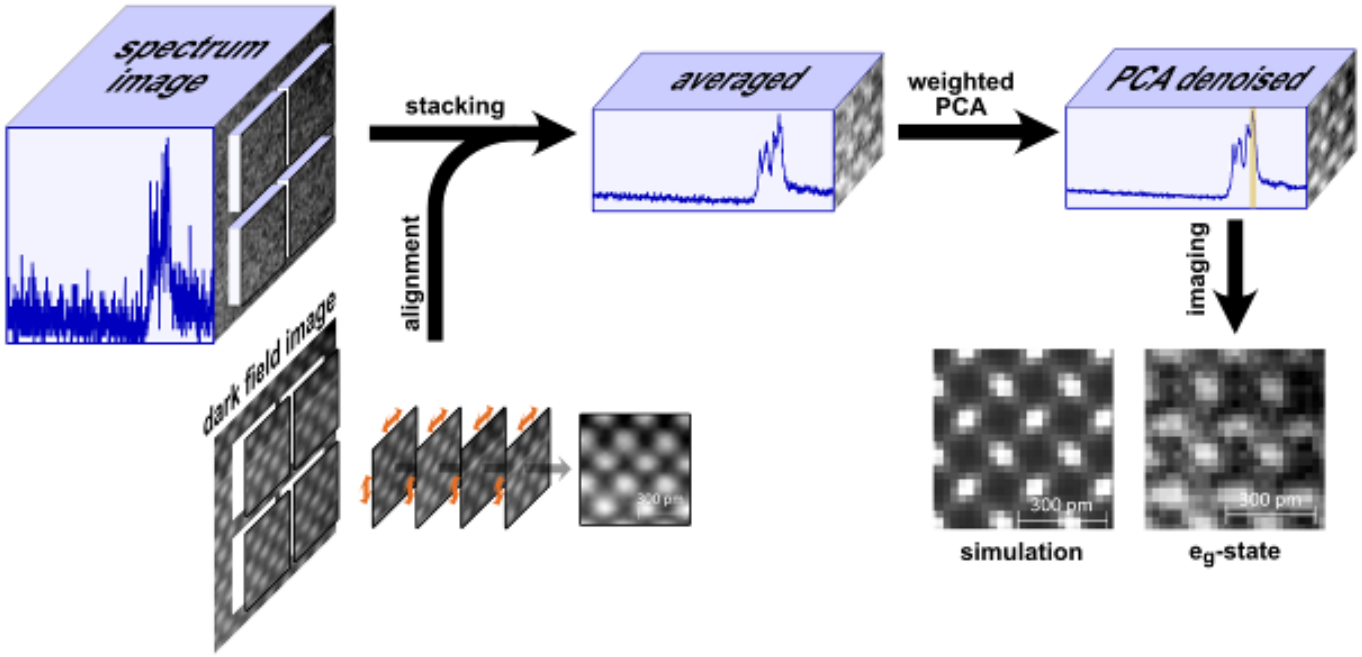

IM2.P005
Developing a new analytic equation for assessing film thickness by electron-excited EDS – an experimental insight into TiN films deposited on diverse substrates

J. P. N. Cruz[1], C. M. Garzón[1], A. A. C. Recco[2]

[1]Universidad Nacional de Colombia, Física, Bogotá, Colombia
[2]Universidade do Estado de Santa Catarina, Física, Joinville, Brazil

Thickness of coatings and films significantly affects in-service performance of covered parts. Energy dispersive spectroscopy (EDS) in the analytical scanning electron microscope (SEM) allows a fast and reliable simultaneous assessment of film thickness and elemental composition. In addition, simultaneous data on crystallographic and morphological properties of covered materials can be obtained. EDS film thickness assessment is nondestructive and could be developed for thickness mapping over a scanned area, it with lateral resolution of the magnitude order of 1.0 µm.

This contribution reports on a methodology for assessing coating thickness from both the experimental EDS spectrum and theoretical Monte Carlo simulations of the dispersion of electrons inside the covered samples (and the concomitant emission of characteristic X-ray photons). An in-depth insight into the accuracy and precision of film thickness assessment for TiN films grown onto three different substrates (i.e. stainless steel, glass, and silicon) is presented. In addition, the development of a new analytic equation for assessing film thickness from both the microscope accelerating voltage (V_0) and the EDS peak intensity-ratio, I_r, (I_r: the ratio in the EDS spectrum between the strongest peak coming from the substrate and the Ti_k peak from the coating) is presented. The performance of three freeware graphical user interfaces for carrying out the Monte Carlo simulations was compared among them, namely Casino, MC-Xray and DTSA.

Monte Carlo predictions on the coating thickness were compared with reference thicknesses independently assessed by cross-sectional micrographs obtained in the SEM. Percent discrepancy between reference and predicted thicknesses was lower than 30 %, where the lower the V_0 the less accurate the predicted thickness. In general, none of the three software's compared outperformed the others, although predicted thicknesses significantly varied between them.

Monte Carlo simulations let stating a new analytic equation which allows assessing film thickness (th) as follows:

$$th = th_{cr} \cdot \exp[-\beta(I_r)^{1/n}] \qquad \text{(Eq. 1)}$$

where th_{cr} (critical thickness) is the largest film thickness which is assessable at a fixed V_0, β is a multiplication factor and n is an exponent. A continuous fitted interpolation of discrete Monte Carlo simulations for film thicknesses as a function of both V_0 and I_r was carried out using equation 1 (Figure 1). The percent discrepancy between the discrete simulations and the continuous fitted curve was lower than the intrinsic relative standard deviation of the Monte Carlo simulations themselves (Figure 1). An in-depth insight into the precision and the sensibility of predictions formulated using equation 1 is presented.

Figure 1

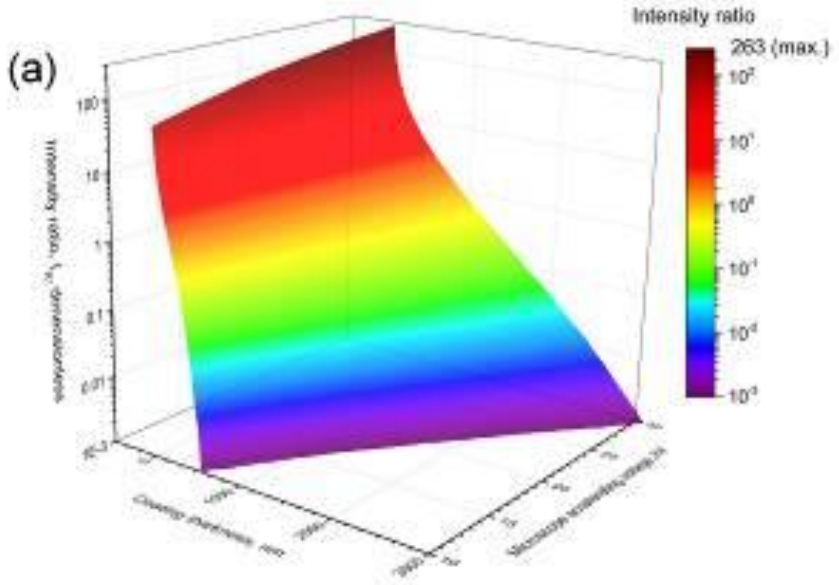

(b)

$$th = th_{cr} \cdot e^{-\beta(I_r)^{1/n}}$$

where,

th: coating thickness,

th_{cr}: critical thickness (it is the largest film thickness which is assessable at a fixed microscope accelerating voltage),

β: multiplication factor,

n: exponent,

where th_{cr}, β and n are assessable from the microscope accelerating voltage V_0 and substrate type.

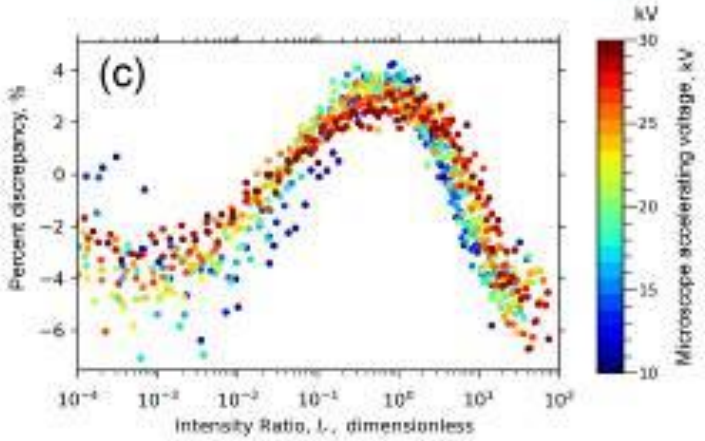

Figure 1 – (a) Monte Carlo simulated surface for the relationship between coating thickness, Intensity-ratio (Ir), and microscope accelerating voltage (V_0) (around 1200 discrete data points were simulated). (b) The analytic equation which depicts the relationship above mentioned (c) The percent discrepancy between discrete data points simulated with Monte Carlo and the continuous curve fitted with the equation in the inset (b).
TiN coatings onto silicon substrate.

IM2.P006
Dual-EMCD – a simple and robust technique for magnetic spectroscopy

D. Pohl[1], S. Schneider[1], B. Rellinghaus[1]

[1]TU Dresden (DCN), Dresden, Germany

Introduction: Electron magnetic circular dichroism (EMCD) [1], allows for the element specific measurement of the spin and orbital magnetic moments with up to nanometer resolution. Despite being in development for more than a decade, the method has not yet reached widespread employment. One of the reasons is the experimental difficulty to acquire at least two subsequent sets of electron energy loss spectra (EELS) obtained under opposite scattering angles from identical and unaltered sample positions that are required for the calculation of the dichroic signal. The fact that during the time between these subsequent measurements the sample may have experienced some drift and/or or the sample area may have been contaminated during the acquisition of the first spectrum frequently impedes the determination of the usually small EMCD signals.

Objectives: We make use of the ultrafast electrostatic deflector implemented in our Gatan Continuum spectrometer to acquire two EEL spectra at opposite scattering angles virtually simultaneously. In the Dual-EELS mode [2], the deflector is used to collect the low-loss and high-loss EEL spectra on two spatially separated areas of the spectrometer camera. In our present approach, this technique is modified to read out the two dichroic signals needed for EMCD evaluation.

Materials & methods: The magnetic contribution to the EELS under two-beam conditions is maximal at two distinct positions of the diffraction pattern (Fig1-left). In spectroscopy mode of the spectrometer, the incoming diffraction pattern is focused and energy dispersed in qx direction. In Dual-EELS mode, the fast deflector shifts the 2D (E-q) spectrum to two separate readout areas. Adjusting the deflector strength enables the acquisition of the two "halfs" 2D spectrum (Figure1-central).

Results & Conclusion: A proof-of-principle experiment is performed on a thin Fe layer epitaxially grown on MgO (Figure 2), magnetized in by the field of the objective lens and tilted into 2-beam condition (prerequisites for measuring EMCD). Figure 2 shows a STEM ADF image of the Fe sample (left) and the background-subtracted and normalized EEL spectra (right). Comparing the upper and lower spectra shows a difference on L and L edges of Fe, which is the fingerprint of EMCD. These successful first measurements pave the way to faster and more robust EMCD measurements specificially of more complex magnetic structures. Details of the technique and technical limitations will be discussed.

[1] P. Schattschneider et al., *Nature* 441 (2006), p. 486.
[2] J. Scott, J. et al., *Ultramicroscopy* 108 (2008) 1586.

We gratefully acknowledge the support by Peter Stiegler (Ametek GmbH – Business Unit Gatan).

Figure 1: Dual-EMCD scheme. *Left*: The magnetic contributions in the two-beam diffraction pattern are localized on both sides of the (000)-(110) line. In spectroscopy mode, the diffraction pattern is focused and energy dispersed along qx. *Mid*: Using the fast deflector, the 2D (E-q) spectrum is shifted to two opposite areas on the camera. By means of the deflector strength the read-out areas (dashed) are chosen such that they cover just the area with maximal magnetic contribution of the 2D spectra, resulting in two 1D spectra to be analyzed for the presence of EMCD signals (*right*).

Figure 2: *Left*: ADF-STEM image of a thin Fe layer on MgO. *Right*: Background-subtracted, normalized Dual-EMCD spectra (of the area highlighted in the STEM image) revealing the signature of EMCD.

Figure 1

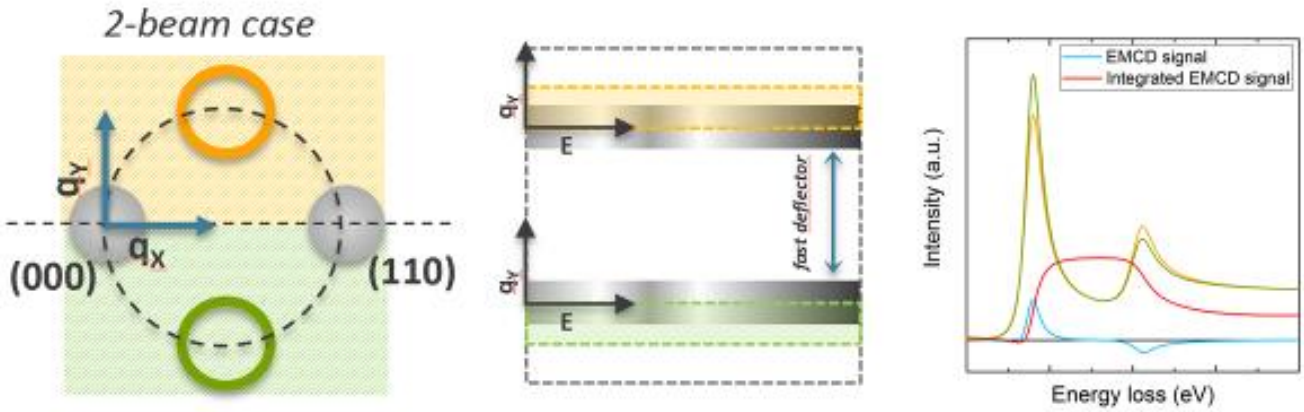

Figure 2

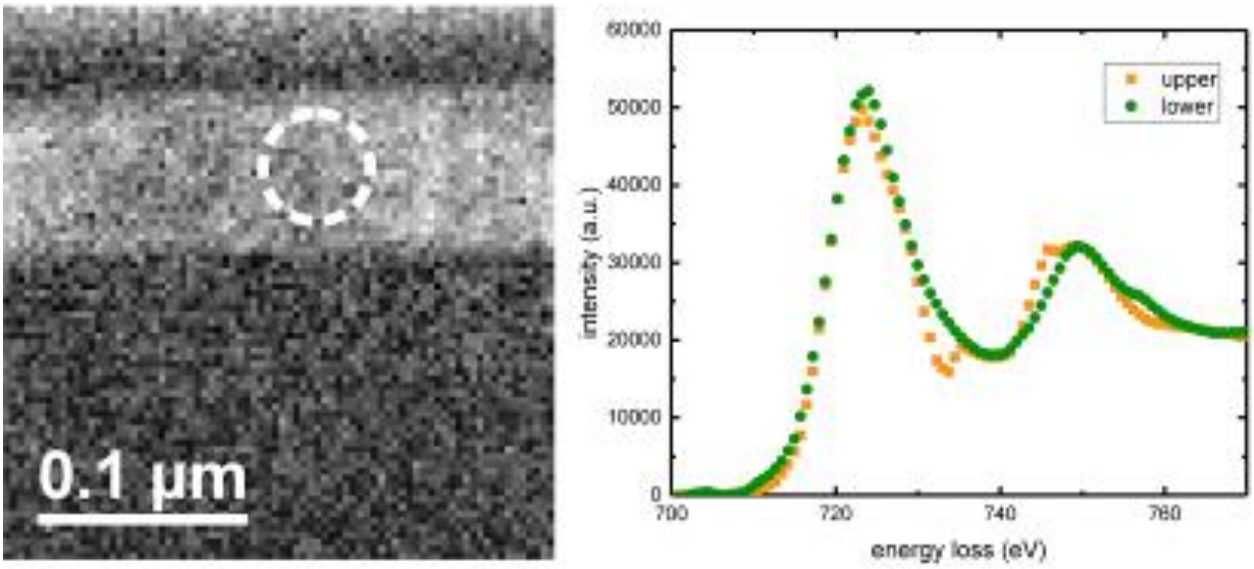

IM2.P007
Constrained Poisson matrix factorisation for EDXS hyperspectral unmixing

A. Teurtrie[1], T. Holvoet[2], N. Perraudin[3], H. Chen[1], D. T. L. Alexander[1], G. Obozinski[4], C. Hébert[1]

[1]Swiss Federal Institute of Technology Lausanne (EPFL), Electron Spectrometry and Microscopy Laboratory, Lausanne, Switzerland
[2]Ghent university, Ghent, Belgium
[3]ETH Zurich, Swiss Data Science Center, Zurich, Switzerland
[4]Swiss Federal Institute of Technology Lausanne (EPFL), Swiss Data Science Center, Lausanne, Switzerland

In scanning transmission electron microscopy, spectroscopic maps can be acquired using Energy-Dispersive X-ray Spectroscopy (EDXS). Sometimes, a direct analysis of the data leads to an accurate chemical quantification. However, the samples often contain a mixture of several overlapping phases with similar chemical compositions which complicates the quantification. Several methods have been developed to unmix the spectral signatures of EDXS data, such as independent component analysis [1], vertex component analysis [2] or Non-negative Matrix Factorization (NMF) [3]. These techniques tend to induce artefacts in the analysis of phases with overlapping spectral signatures and are not suitable for quantification.

To tackle this problem, we leverage machine learning techniques to propose innovative spectrum image decomposition. Our approach is based on a physically informed factorization model which imposes structural constraints on the learned matrices. The Poisson distribution of the data is considered by using a Poisson likelihood. We further constrain the unmixed spectra by physically modelling them. The characteristic X-rays are modeled using theoretical databases [4,5]. The continuum X-rays consist of the bremsstrahlung modified by the detector efficiency and absorption effects [6,7].

With these physical models, we design synthetic datasets for the characterization and validation of our algorithm. The parameters for the simulation of the datasets are based on artificial lower mantle samples containing a mixture of bridgmanite (Brg, (Mg,Fe)SiO3), ferropericlase (Fp, (Mg,Fe)O) and Ca-rich perovskite (Ca-pv, CaSiO3) [8]. These phases share certain elements, which induces spectral mixing, and they also overlap spatially. The complexity of these systems makes them a challenging test case for our approach.

To include physical prior knowledge in the factorization model, the data are decomposed into three matrices. One matrix corresponds to the characteristic X-rays of the elements of each phase while another matrix corresponds to their continuum X-rays. The third matrix represents the abundances of each learned phases. As for the NMF, the different matrices are constrained to take non-negative values. Moreover, the column vectors of the abundance matrix are constrained to sum to 1. To solve this non-convex optimization problem, the algorithm performs multiplicative updates [9].

The synthetic spectrum images were simulated to mimic ferropericlase and Ca-perovskite particles (Fig 1 (c) and (b)) embedded in Brg (Fig 1 (a)). The concentration of the particles never reaches 1, in order to account for the absence of pure Fp or Ca-pv pixels as in experimental spectrum images.

Our algorithm was applied to the synthetic dataset and its results are displayed in Figure 1. The three phases are correctly identified and the reconstructed spectra show only a few discrepancies with the ground truth. The angles between the determined endmembers and the true spectra are 7.7° for Brg, 7.2° for both Fp and Ca-pv. For comparison, NMF applied on the same dataset yield 7.8° for Brg, 15.0° for Fp and 9.1° for Ca-pv.

Figure 1: (a), (b) and (c) reconstructed and true abundances of the simulated Brg, Ca-pv and Fp, respectively. (d), (e) and (f) reconstructed and true spectra of the simulated Brg, Ca-pv and Fp, respectively.de la Peña, F. *et al. Ultramicroscopy* 111, 2011

[1] Dobigeon, N. & Brun, N. *Ultramicroscopy* 120, 2012
[2] Shiga, M. *et al. Ultramicroscopy* 170, 2016
[3] Shoonjans, T. *et al. Spectrochimica Acta Part B: Atomic Spectroscopy* 66, 2011
[4] Bote D. *et al. Physical Review A* 77, 2008
[5] Chapman *et al. Journal of Microscopy*, 136, 1984
[6] G.W. Lorimer, *Mineralogical Magazine*, 51, 1987
[7] Hirose, K. *et al. Science* 358, 2017
[8] Lee, D. & Seung, S. *Advances in neural information processing systems,* 13, 2001

Figure 1

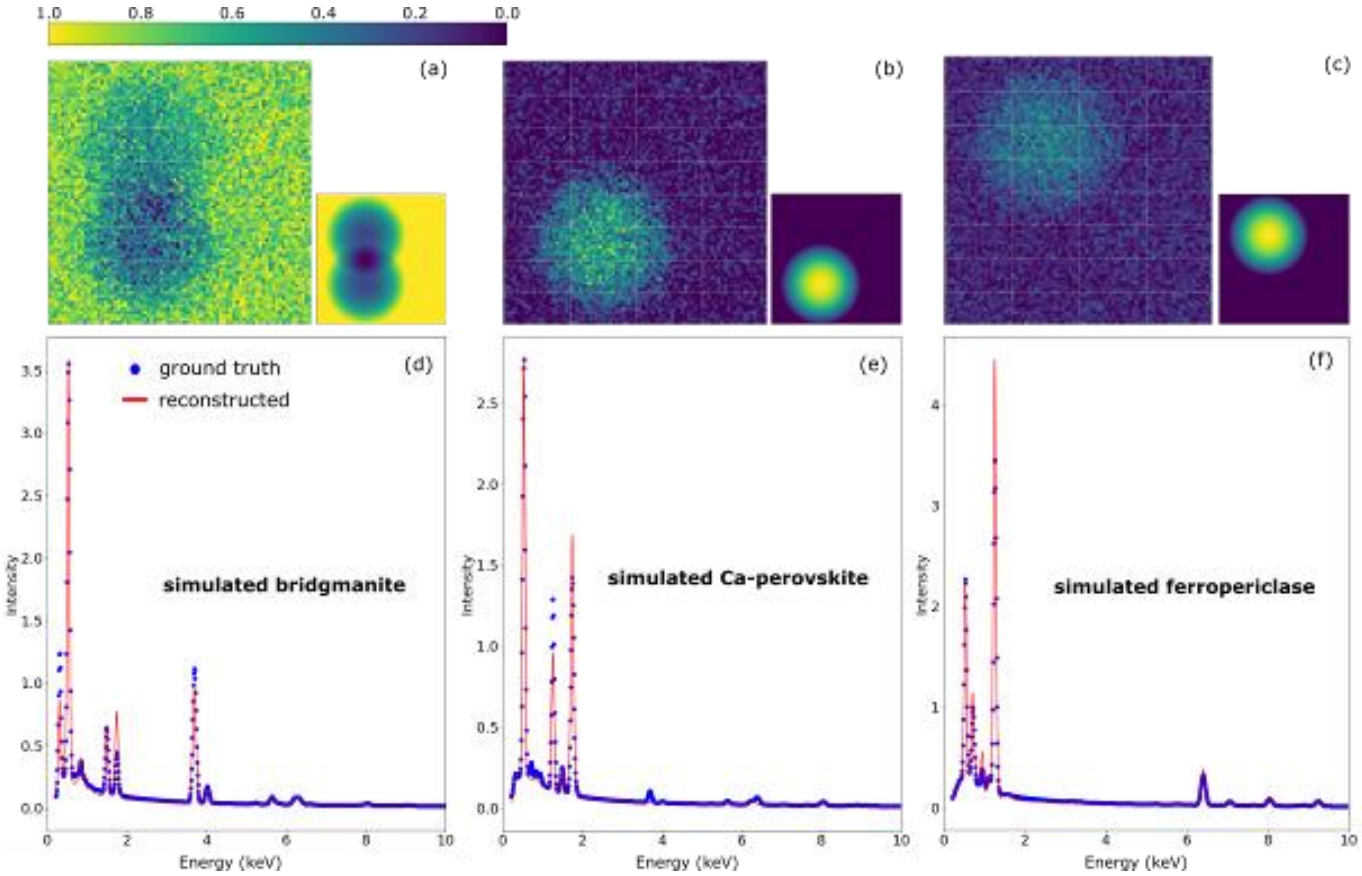
1.0
0.8
0.6
0.4
0.2
0.0
(a)
(b)
(c)
(d)
(e)
(f)
ground truth
reconstructed
simulated bridgmanite
simulated Ca-perovskite
simulated ferropericlase
Intensity
Energy (keV)

IM2.P008
Quantitative EDS compared to WDS analysis using microanalytical standards and interlaboratorial test sample

K. Balzuweit[1,2], I. Chagas dos Santos[1], G. De Gouvea Almada[1], M. De Almeida Flores[2], L. A.R. Garcia[2], B. Barbosa Moreira[2], W. Tito Soares[2], R. Aranda[2], M. Cruz Costa de Souza[2], R. Costa Ribeiro[2]

[1]Universidade Federal de Minas Gerais, Physics, Belo Horizonte, Brazil
[2]Universidade Federal de Minas Gerais, Center of Microscopy, Belo Horizonte, Brazil

Microanalysis has been an increasing need as analytical characterization, performed in several types of equipment by the most diverse areas, from traditionally metallurgy, geology and chemistry into forensic science, environmental sciences, cultural heritage and many others. In electron microscopy, historically microprobe analysis (EPMA) has been used for quantitative analysis. Scanning Electron Microscopes (SEM) were always more a visualization tool where low current, of the order of pA are key for high resolution imaging, but unfit for reliable quantification. However, the last decades have seen an astonishing evolution of the electron microscopes: at the same time they are much more versatile, more stable, easier to use, with higher resolution and magnification, more sensitive detectors and a much better signal to noise relation. The stability of the current SEM"s plus the Silicon Drift Detectors Electron Dispersive X-ray Spectrometer (SDD-EDS) is slowly turning them into both visualization and real analytical tools as there is a growing need for better, faster and higher magnification quantitative analytical data combined with imaging, on heterogeneous samples.

The present work compares results of several microanalytical standards and interlaboratorial test samples in order to asses the use of EDS-SDD as a reliable analytical tool as long as good practices are followed.

A Jeol 8900 microprobe with 4 WDS spectrometers, a Quanta200FEG SEM with a Bruker SDD-EDS and a Quanta3D FEG dual SEM-FIB with a Bruker SDD-EDS were used to analyze metallic, minerals and oxide samples. Care about good practices on sample preparation, correct alignment of the microscopes, spectrometer calibration, enough count rate, use of matrix correction routines (ZAF) and calibration standards were fundamental to guarantee the reliability of the results.

Several microanalytical standards and interlaboratorial test samples and some of the results are presented. Table 1 shows the result of a metallic sample with quite a good agreement between EPMA and SEM results, even for trace elements as silicon and vanadium. Figure 1 and 2 show respectively results of an oxide and a platinum palladium sulfide. The lines represent the EPMA data and the points with the error bars the SDD-EDS SEM data, showing again a very reasonable agreement even for overlapping peaks as for platinum and palladium. However, samples as monazites where rare earth elements overlap heavily is still a problem for SDD-EDS quantification, as can be seen in figure 3.

Summarizing, quantitative results for several types of materials performed with SDD-EDS SEM are in quite good agreement with WDS-EPMA analysis considering a precision of about 10 times less. However some samples with many overlapping peaks as monazites are still a challenge for quantification.

Acknowledgments: all measurements were performed at Centro de Microscopia da UFMG, and we acknowledge our funding agencies FINEP, FAPEMIG and CNPq.

Figure 1

Element	Iron	Chromium	Nickel	Manganese	Molybdenum	Silicon	Vanadium
SEM	52 (1)	20,2 (0,5)	16,3 (0,4)	7,5 (0,2)	2,8 (0,1)	0,39 (0,04)	0,17 (0,03)
Microprobe	52,96 (0,01)	20,85 (0,64)	15,90 (0,10)	7,87 (0,10)	2,66 (0,30)	0,38 (0,01)	0,17 (0,02)

Figure 2

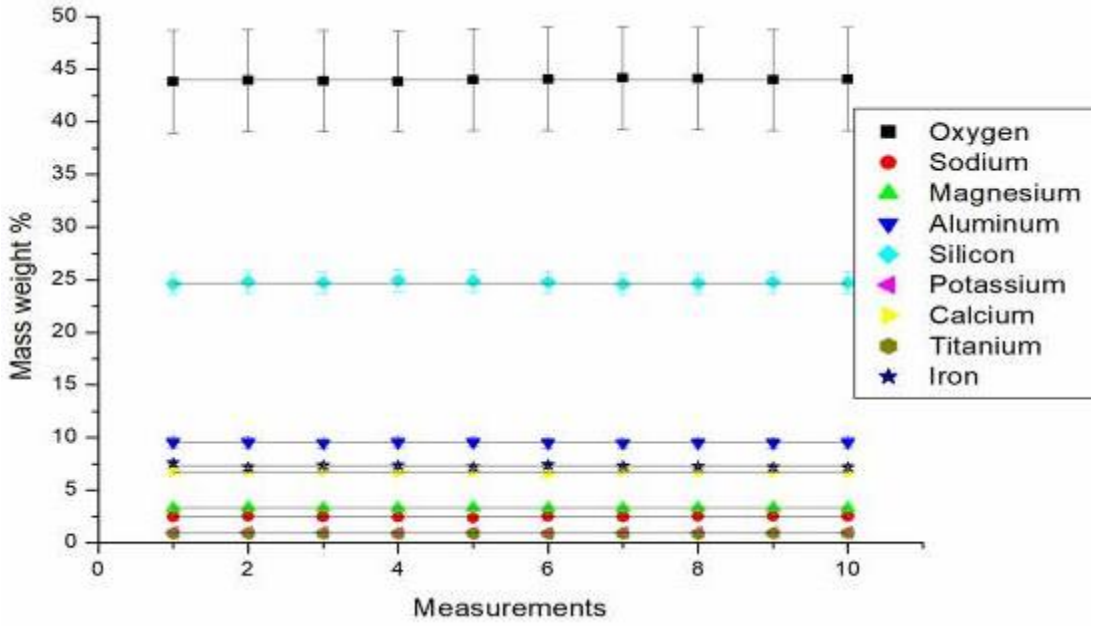

Figure 3

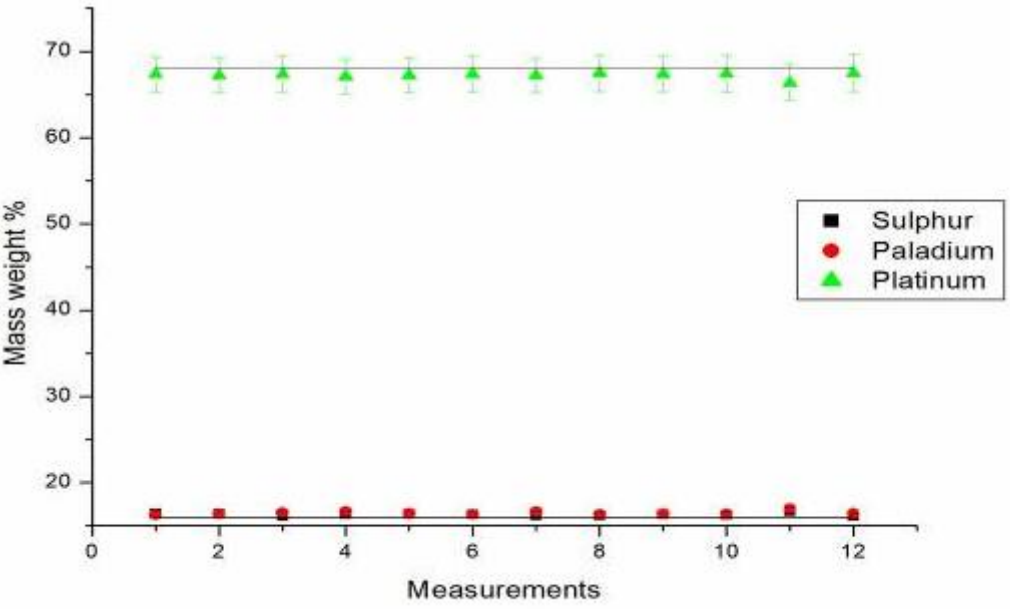

Figure 4

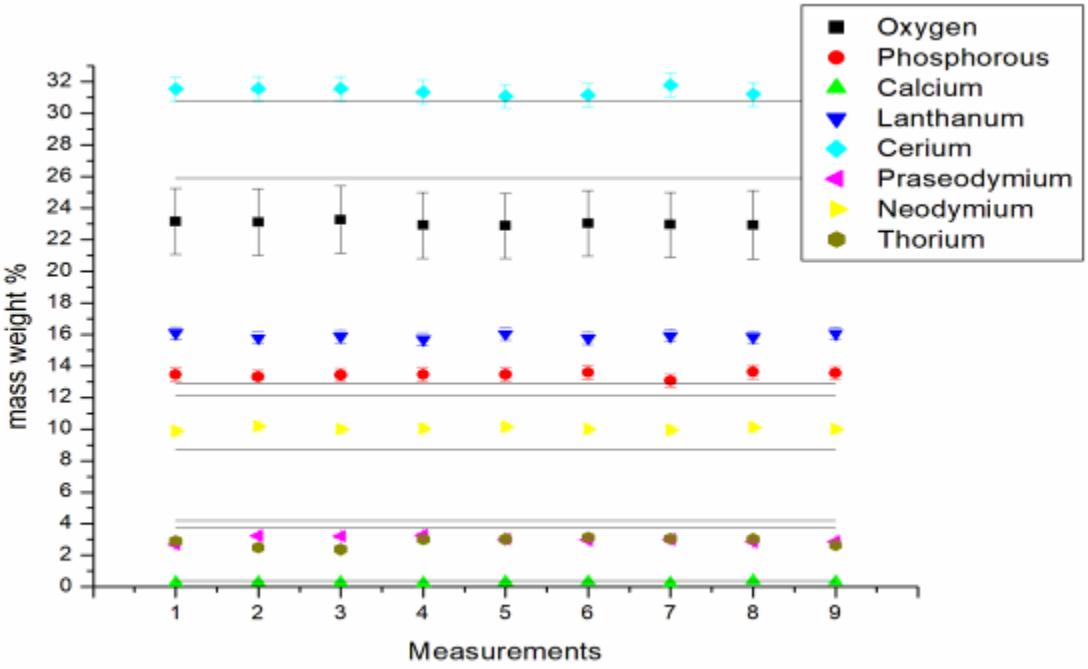
Oxygen
Phosphorous
Calcium
Lanthanum
Cerium
Praseodymium
Neodymium
Thorium
mass weight %
Measurements
0
2
4
6
8
10
12
14
16
18
20
22
24
26
28
30
32
1
2
3
4
5
6
7
8
9

IM2.P009
Application of SEM-WDS with a redesigned grazing incidence optic for X-ray elemental analysis

M. Abratis[1], J. Silbermann[1], S. Boehm[1]

[1]Bruker Nano GmbH, Berlin, Germany

Microanalysis using energy-dispersive X-ray spectrometry on scanning electron microscopes (SEM-EDS) is widespread in material sciences and life sciences. Due to its versatility, robustness and speed SEM-EDS is very popular and appropriate for the majority of analytical applications. For more demanding tasks however, requiring higher spectral resolution, light element sensitivity or trace element detection capabilities beyond the limits of EDS, wavelength-dispersive X-ray spectrometry on scanning electron microscopes (SEM-WDS) is the ideal technique for gaining even more accurate and precise data during microanalysis.

For the present study we applied Bruker"s parallel beam WD spectrometer XSense equipped with a grazing incidence collimating optics, six different dispersing elements and a pressure-controlled flow proportional counter. The present spectrometer is equipped with a redesigned 3-cone mirror optic that shows extremely low residual beam divergence. The improvement compared to the conventional optic is 75-100 % more count rate and 20-30% better resolution. A 3-axis optic positioning unit and a powerful alignment software algorithm ensure precise alignment of the optic relative to the excitation spot on the sample. This unique combination of the new grazing incidence optic with the auto-optic alignment capability results in highest possible resolution of a parallel beam WD spectrometer. Excellent stability and reproducibility are enabled by a pressure-controlled P-10 flow proportional counter and negligible thermal drift of the optic positioning stage.

Samples investigated for this presentation include glass, ceramics, metals and minerals. The results show that SEM-WDS with a grazing incidence optic is a powerful tool for qualitative and quantitative analyses and element distribution mappings.

Figure 1: Comparison of WDS and EDS spectra acquired on tantalum-silicide.

Figure 1

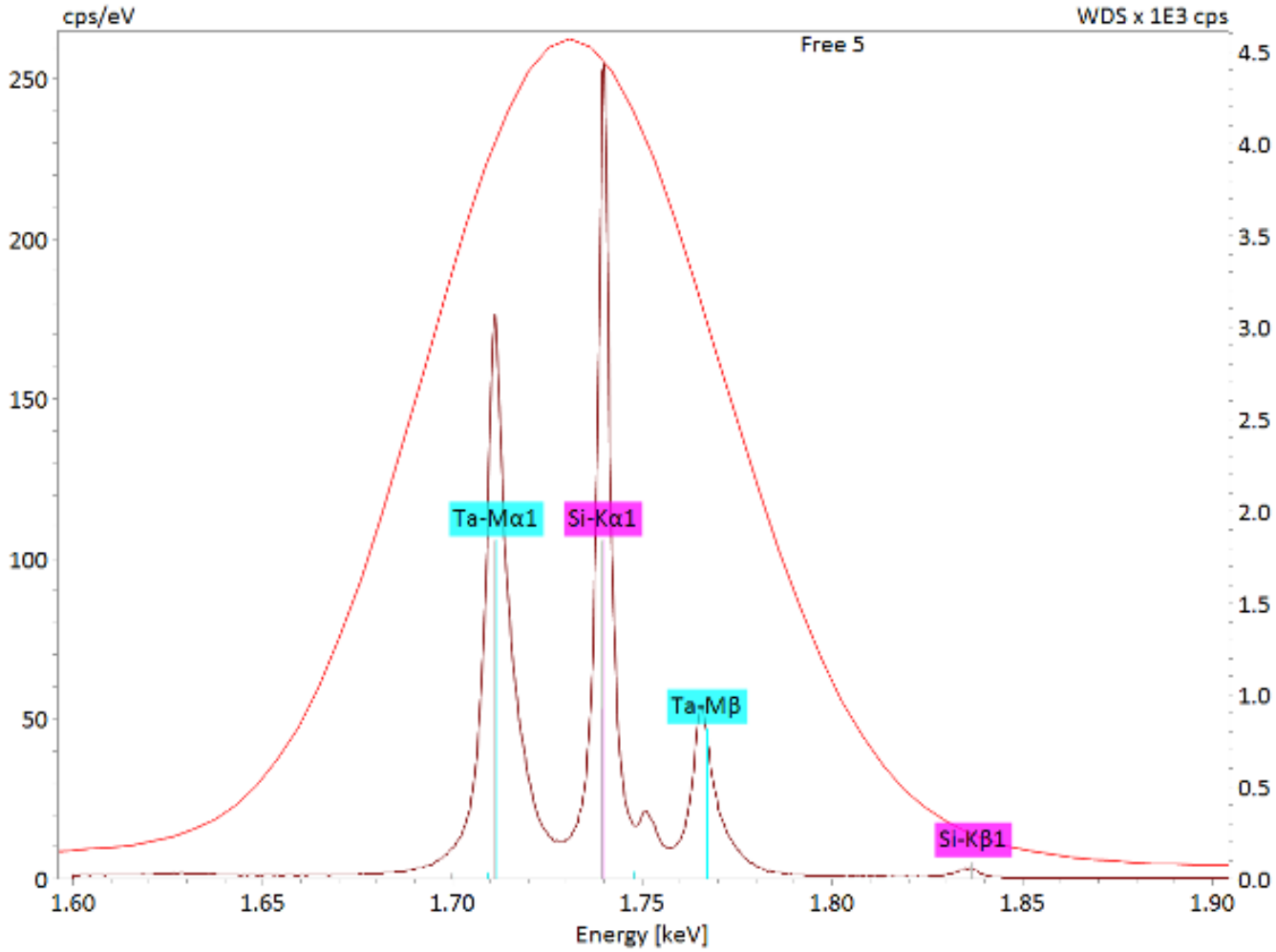
cps/eV
WDS x 1E3 cps
Free 5
250
200
150
100
50
0
4.5
4.0
3.5
3.0
2.5
2.0
1.5
1.0
0.5
0.0
Ta-Mα1
Si-Kα1
Ta-Mβ
Si-Kβ1
1.60
1.65
1.70
1.75
1.80
1.85
1.90
Energy [keV]

IM2.P010
Ultramicrotomy of polymers at its best – ultra sonic

C. Mayrhofer[1], H. Plank[1,2], I. Letofsky-Papst[1,2], H. Gnägi[3]

[1]Graz Centre for Electron Microscopy (ZFE), Graz, Austria
[2]Institute of Electron Microscopy and Nanoanalysis, Graz, Austria
[3]Diatome Ltd, Nidau, Switzerland

Introduction: Sample preparation is a very important and crucial step for several microscopic methods such as light microscopy (LM), transmission electron microscopy (TEM), scanning electron microscopy (SEM) or atomic force microscopy (AFM). Microtomy allows for the sample preparation of many materials and the characterization of inner structures, facilitating well-defined specimen sectioning for either ultra-smooth surfaces (block-faces), or ultrathin sections [1]. Typical applications are the generation of 1) smooth surfaces for reflection-LM, AFM, infrared or Raman spectroscopy; 2) the production of semithin sections with typical thicknesses of about 2 microns for conventional LM; and 3) ultrathin cuts with thicknesses of 100 nm and less for TEM. Depending on the application and material, ultramicrotomy can often comprise pre-preparative steps like hardening, embedding, staining for contrast enhancement or cooling down below room temperature [2].

Besides the professional equipment needed for all this, the demands and challenges for high-quality samples require skilled personal, long-time experience and the employment of a few tricks. In this work we present a small selection of special methods and techniques to highlight some of the outstanding possibilities with ultramicrotomy.

Materials & methods: New demands for the block-face smoothness have led to the development of an ultrasonic oscillating knife (Diatome, Switzerland) [3]. It offers the advantage to section materials at room temperature, which normally require cryo temperatures. The ultra sonic knife allows the cutting of ultrathin sections free of compression as well as absolutely flat block-faces. Also, the elimination of cyclic compression and relaxation during slicing results in much more homogeneous block-face surfaces for AFM, as well as in thinner sections for TEM investigations (slice thickness

Results: Excellent results are achieved with rigid polymers such as PS, PMMA, ABS, HIPS, modified PP and blends of various kind at room temperature; for soft polymers outstanding results in TEM and AFM analyses were achieved by using the cryo sonic knife that is currently being developed by Diatome.

Felmi-ZFE designed optimal holders to measure samples in the microscopes without reclamping the sample after microtomy.

Literature
[1] G.H. Michler: Electron Microscopy of Polymers, Springer Verlag Berlin 2008.
[2] L.C. Sawyer, D.T.Grubb, G.F.Meyers: Polymer Microscopy, Springer Verlag Berlin 2008.
[3] Studer, D., Gnaegi, H.: Minimal compression of ultrathin sections with use of an oscillating diamond knife. Journal of Microscopy, 197 (2000) 94-100
[4] Mayrhofer, C.: Tips and Tricks in Ultramicotomy, MC 2013, Regensburg

Figure 1: Left: Room temperature: Comparison HIPS without (A) and with oscillation (B); Right: Cryo: Comparison vulcanizates histo cryo (C) and cryo sonic (D)

Figure 1

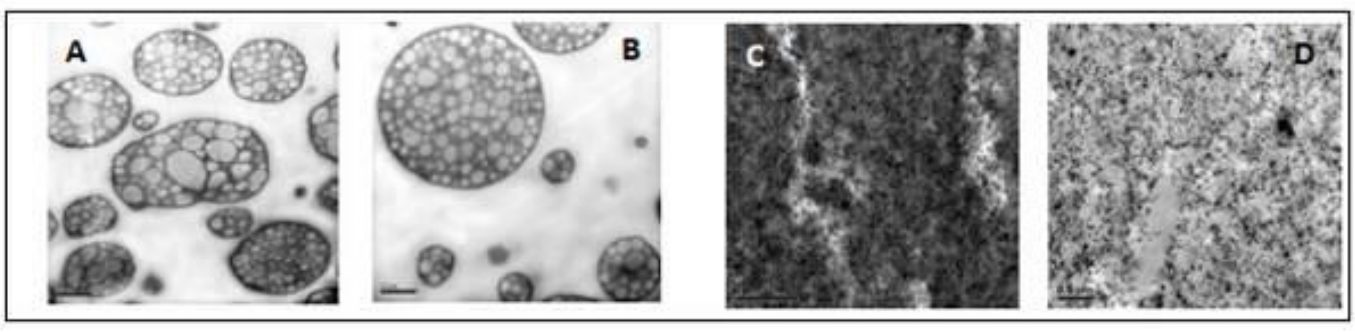

IM3.001-Invited
The optics for a multi-beam scanning electron microscope with transmission detection

P. Kruit[1], W. Zuidema[2], J. Fermie[2], A. M. Gheidari[3], J. Stopka[4], B. Seda[4]

[1]Delft University of Technology, Dept Imaging Physics, Delft, The Netherlands
[2]DELMIC, Kanaalweg 4, 2628 EB Delft, The Netherlands
[3]Thermo Fisher Scientific, De Schakel 2, 5651 GG Eindhoven, The Netherlands
[4]Thermo Fisher Scientific, Vlastimila Pecha 1282/12, 627 00 Brno-Černovice, Czechia

The multi-beam Scanning Electron Microscope (MBSEM) described here is aimed at fast imaging of large biological tissues, either for volume imaging or large area mapping. It has been developed in a collaboration between Delmic, TU Delft, Thermo Fisher Scientific and Technolution and is based on the 20 years of multi-beam experience at Delft University[1]. The goal of the design is to have the maximum current for a system that can deliver a resolution of about 5 nm at electron energies that yield the highest signal-to-noise and contrast-to-noise, which we estimate is 3-8 keV[2].

Clearly, a single beam system is current-limited by the aberrations of the objective lens. In a multi-beam system that uses a common objective lens, it turns out that the maximum current is determined by the stochastic Coulonb interactions between the beam electrons[3]. Once this limit is established, the minimum number of beams can be determined, given the brightness of the source and the aberrations of the objective lens. We settled for an 8x8 square array of electron beamlets with a current of 400 pA – 1nA per beamlet. At the highest beam current, the resolution is compromised by the Coulomb interactions. The optics of the source follows the well-established principles of splitting the beam from a Schottky source with a single aperture plate that also acts as an array of miniature lenses[4]. These lenses focus the beamlets inside the collimator lens so that this lens will not cause energy dispersion in the beam focus, see figure 1.

The 64 beamlets are scanned over the sample simultaneously, so that every beamlet scans an area of 3.2x3.2 µm. Thus, one scan covers a field of 25.6x25.6 µm. Signal detection is achieved through an optical detection pathway, where electrons transmitted through a sample produce light in a scintillator substrate. Since light intensity depends on the number and energy of electrons hitting the scintillator plate, fluctuations in the light intensity are a metric for the electron density of the sample. As a detector, a rapid multi-pixel photon counter array is used, enabling fast scan rates.

The distance between the electron beams is coupled to the distance between the detectors in the detector array, so that can, once designed, not easily be changed. Thus, the only optical function of the SEM column is to image the plane of the collimator lens onto the sample with a minimum of aberrations and Coulomb interaction. Since the magnification is determined by the distance between the beams, the correct ratio between spot size and pitch must already be set in the multi-beam source.

Field curvature in the sample plane is set to zero by the field curvature corrector in the multi-beam source. It turns out that individual focusing and stigmation of the beamlets is not required. Common astigmatism, introduced by non-roundness of the objective lens, is corrected by the regular common stigmator of the SEM column. We found that this introduces a distortion of the square beam pattern, which can be corrected by a second stigmator at a different position in the column.

Using the transmission detector, high quality images can be acquired of biological material (figure 2). With stage movement routines, controlled by an interferometer, these fields can be rapidly tiled to form ‘megafields’, comprising of many multi-beam fields.

[1] Ren, Y. & Kruit, P. Transmission electron imaging in the Delft multibeam scanning electron microscope 1. *J. Vac. Sci. Technol. B Nanotechnol. Microelectron.* 34, (2016).
[2] Zuidema, W. & Kruit, P. Transmission imaging on a scintillator in a scanning electron microscope. *Ultramicroscopy* 218, 113055 (2020).
[3] Stopka, J., Zuidema, W. & Kruit, P. Trajectory displacement in a multi beam scanning electron microscope. *Ultramicroscopy* 223, 113223 (2021).
[4] Zhang, Y. & Kruit, P. High brightness 100-electron-beam source for high-resolution applications. *J. Vac. Sci. Technol. B Microelectron. Nanom. Struct.* 25, (2007).

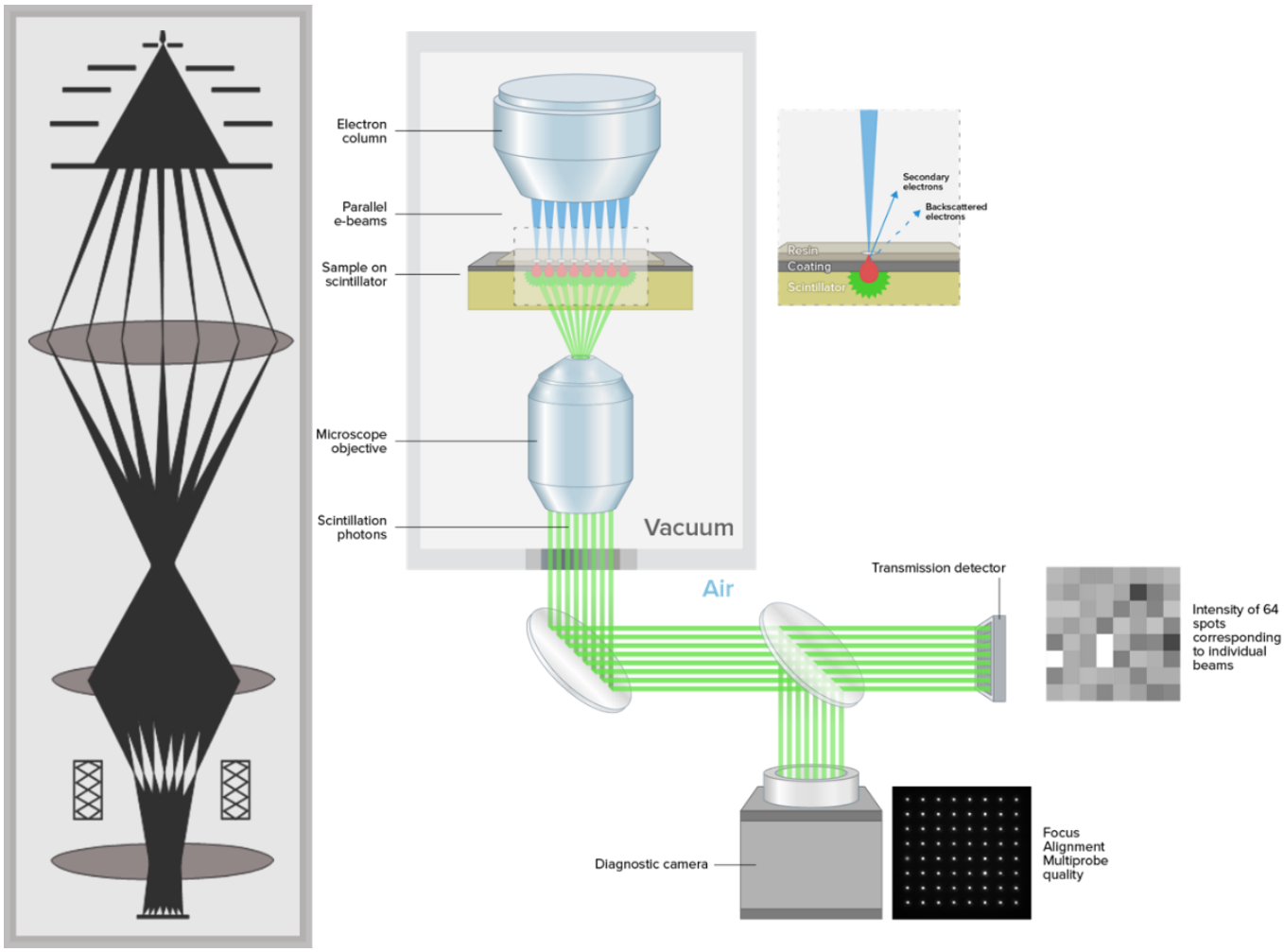

Figure 1: System design of the multibeam SEM. (A) Schematic of the electron column (B) Schematic of the detection system

LS2

Figure 2: Rat pancreas: OTO staining, EPON embedding, 80 nm sections. 4 nm pixel size, 3 µs dwell. Sample courtesy of Ben Giepmans (UMCG, NL), imaging by Job Fermie of Delmic.

IM3.003
The resolvability of features at low voltage and low dose imaging

F. Quigley[1,2], P. McBean[1,2], P. O'Donovan[1], L. Jones[1,2]

[1]Trinity College Dublin, School of Physics, Dublin, Ireland
[2]Trinity College Dublin, CRANN- Centre for Research on Adaptive Nanostructures and Nanodevices, Dublin, Ireland

Low voltage transmission electron microscopy (≤80kV) has many applications in imaging 2D materials, which would be damaged at higher voltages (Klie, 2009). Once spherical aberration has been corrected for in a Transmission Electron Microscope (TEM), chromatic aberration may dominate and limit the ultimate resolution of the microscope. The chromatic (defocus) blur can be reduced by decreasing the energy spread of the impeding electrons. Options for reducing energy spread can include using a low energy spread electron source, such as a cold field-emission source, or installing an electron monochromator after the gun. However, while the installation of a monochromator produces the lowest energy spread, it results in a dramatic decrease in current of up to 97% for a FWHM of 25meV (Hachtel et al., 2018), which can reduce the signal to noise ratio of the image. The objective of our work was to assess this trade-off between energy spread and beam current on the resolvability of features in images.

Recent additions by our group to the Prismatic software (Ophus, 2017) allow the effect of chromatic aberration to be included while simulating TEM images. This is done by approximating the chromatic aberration with a defocus spread (Aarholt et al., 2020). Finite electron beam source size was simultaneously implemented in Prismatic, along with the addition of Poisson noise. Using Prismatic, we examine how low electron energy spreads and low electron dose affect the image quality of a 2D material for a spherical aberration corrected TEM. This will demonstrate the trade-off between energy spread and beam current on image quality. It also showcases the developments in Prismatic in simulating chromatic aberration, finite source size, and Poisson noise in TEM images.

[1] Aarholt, T., Frodason, Y. K., & Prytz, Ø. (2020). Imaging defect complexes in scanning transmission electron microscopy: Impact of depth, structural relaxation, and temperature investigated by simulations. *Ultramicroscopy*, *209*(October 2019), 112884. https://doi.org/10.1016/j.ultramic.2019.112884
[2] Hachtel, J. A., Lupini, A. R., & Idrobo, J. C. (2018). Exploring the capabilities of monochromated electron energy loss spectroscopy in the infrared regime. *Scientific Reports*, *8*(1), 1–10. https://doi.org/10.1038/s41598-018-23805-5
[3] Klie, R. (2009). Reaching a new resolution standard with electron microscopy. *Physics*, *2*, 155425. https://doi.org/10.1103/physics.2.85
[4] Ophus, C. (2017). A fast image simulation algorithm for scanning transmission electron microscopy. *Advanced Structural and Chemical Imaging*, *3*(1), 1–11. https://doi.org/10.1186/s40679-017-0046-1

Acknowledgments**:** This project was supported through funding from the Provost Project Award, Advanced Microscopy Laboratory, Centre for Research on Adaptive Nanostructures and Nanodevices (CRANN), AMBER (Advanced Materials and BioEngineering Research), Science Foundation Ireland and the Royal Society.

IM3.004
Continuous-wave photonic chip-based temporal phase plates for electron microscopy

A. Feist[1,2], A. S. Raja[3], J. W. Henke[1], J. Liu[3], G. Arend[1], G. Huang[3], F. J. Kappert[1], R. N. Wang[3], J. Pan[3], O. Kfir[1,2]
T. Kippenberg[3], C. Ropers[1,2]

[1]University of Göttingen, IV. Physical Institute, Göttingen, Germany
[2]Max Planck Institute for Biophysical Chemistry, Göttingen, Germany
[3]Swiss Federal Institute of Technology Lausanne (EPFL), Institute of Physics, Lausanne, Switzerland

The active optical shaping of free-electron beams enables a broad range of applications, from efficient free-space acceleration [1] and attosecond bunching of electrons [2] to the implementation of laser-driven phase plates [3,4] and beam splitters [5]. Recent experiments on inelastic electron-light scattering (IELS) [6,7] have demonstrated the potential of using resonant field enhancement for increasing the interaction between electrons and photons [8,9]. However, bringing IELS-enabled beam shaping to state-of-the-art continuous-beam electron microscopes is challenging, due to low optical transition probabilities, thus typically requiring the use of femtosecond high-intensity laser pulses.

In this work, we demonstrate IELS on a CW-pumped Si_3N_4 microresonator with a *Q*-factor of $>10^6$, achieving an unprecedented high coupling to a continuous electron beam. The interaction strength between the electrons and the evanescent cavity field is spatially mapped and we discuss the potential application as a versatile temporal phase plate for electrons.

In an ultrafast transmission electron microscope (UTEM) [10], a continuous electron beam passes by a CW pumped Si_3N_4 microresonator (see Figure 1.a)), which is installed in a custom-designed TEM sample holder. The air-cladded microresonator chips (Figure 1.b)) are fabricated using the photonic Damascene process [11] and exhibit a linewidth of ~70 MHz), as well as a free spectral range of ~1 THz for the quasi-TM fundamental mode. The electron beam interacts with the whispering gallery mode, confined in the fiber-coupled photonic chip. When the CW laser is tuned to a resonance of the cavity, the initially narrow energy distribution is significantly broadened up to about 50 eV, indicating a strong temporal phase modulation (Figure 1.c)).

We envision a new class of active electron-optical elements for TEM based on IELS, that combine these capabilities with the flexibility of state-of-the-art integrated photonics, e.g. for laser-based electron beam splitters and programmable phase plates.

[1] J. England *et al.*, Rev. Mod. Phys. 86**,** 1337–1389 (2014).
[2] E. Priebe *et al.*, Nat. Photonics 11, 793 (2017).
[3] Schwartz *et al.* Nat. Methods 16, 1016–1020 (2019).
[4] M. Vanacore *et al.*, Nat. Mater. 18, 573–579 (2019).
[5] Feist *et al.*, Phys. Rev. Research 2, 043227 (2020).
[6] Barwick, D. J. Flannigan, and A. H. Zewail, Nature 462, 902 (2009).
[7] J. García de Abajo, *et al.*, Rev. Mod. Phys. 82, 0034–6861 (2010).
[8] Kfir *et al.*, Nature 582, 46–49 (2020).
[9] Wang *et al.*, Nature 582, 50–54 (2020).
[10] Feist *et al.*, Ultramicroscopy 176, 63 (2017).
[11] Liu *et al.*, Optica 5**,** 1347–1353 (2018).

Figure 1: a) Inside of a transmission electron microscope (TEM), an electron beam passes close to a CW-pumped integrated Si_3N_4 microresonator in aloof geometry. b) SEM image if the microresonator chips (side view, electron beam indicated in green) c) Electron energy distribution of the transmitted beam recorded with a magnetic-prism spectrometer. For resonant excitation of the cavity mode, a spectral broadening of up to ~50 eV is observed.

Figure 1

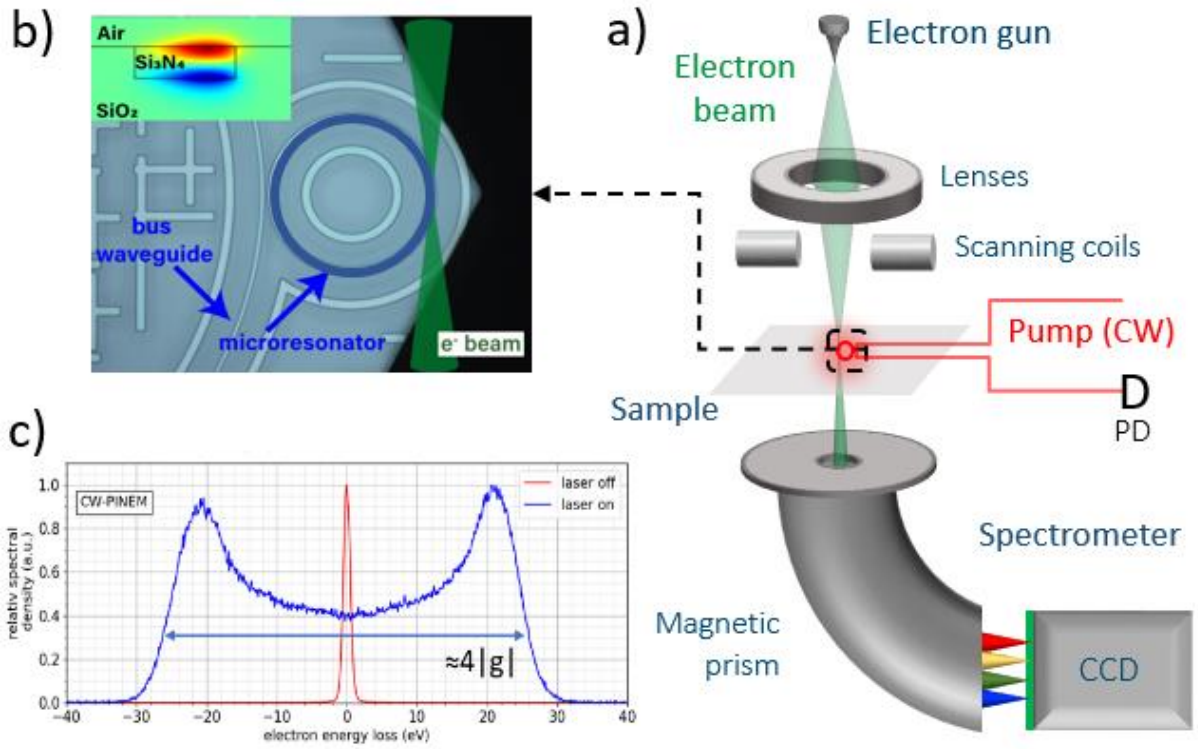
b)
Air
Si3N4
SiO2
bus waveguide
microresonator
e⁻ beam
a)
Electron gun
Electron beam
Lenses
Scanning coils
Pump (CW)
D
PD
Sample
Spectrometer
Magnetic prism
CCD
c)
CW-PINEM
laser off
laser on
relativ spectral density (a.u.)
≈4|g|
electron energy loss (eV)

IM3.005
Early results from the Argonne XPAD detector for the Analytical Electron Microscope

N. Zaluzec[1]

[1]Argonne National Laboratory, Photon Science Directorate, Lemont, IL, United States

Since 2004, Argonne has been working on designs of linear arrays of Silicon Drift Detectors (SDD's) for x-ray energy dispersive spectroscopy (XEDS) in the Analytical Electron Microscope (AEM). The goal to maximize the solid angle, sensitivity as well as mitigate artifacts. Evolving the our π steradian detector solution [1], the X-ray Perimeter Array Detector (XPAD) combined with a custom electron optical pole piece (ZTwin) has improved upon the π steradian detector performance and is operating on the prototype 30-300 kV PicoProbe AEM instrument which is located in the Materials Design Laboratory at Argonne.

Using a 60 mm^2 detector as a reference base (1x), our experimental measurements have shown that the XPAD collection efficiency (solid angle) is greater than 20 times the 60 mm^2 SDD system and exceeds the performance metrics of the original π steradian detector, reaching Argonne's design target. A comparison of the normalized performance of the XPAD is illustrated in Figure 1. [2]

Figure 1: Normalized performance of XEDS Collection for Ge Kα (Integrated Counts/nA-sec) from a 20nm thick ultra-nanocrystalline Ge film on SiNx for Single, Quad and XPAD XEDS systems

Due to the increased collection efficiency of the XPAD, there is also a corresponding improvement in the minimum detectable mass fraction. An improvement of an order of magnitude, from ~ 2 $x10^{-3}$ to ~ 2 $x10^{-4}$ (Figure 2), has been realized as was predicted previously[3]. In addition, the functional dependence of the x-ray signal as well as the peak to background with incident beam energy from 30 to 300 keV, as discussed in that earlier work has also been verified.

Additional work is in progress to further delineate the PicoProbe and XPAD performance metrics [4].

Figure 2: Improvement of MMF of Au nanoparticles on SiNx at 80 kV. Solid line Quad 30 mm2 SDD, Dashed line XPAD

References:
[1] Argonne National Laboratory. (2010). High collection efficiency X-ray spectrometer system with integrated electron beam stop, electron detector and X-ray detector for use on electron-optical beam lines and microscopes, US Patent 8,314,386
[2] Zaluzec, N.J. Microscopy & Microanalysis Meeting Pittsburgh PA, USA. August 2021, in press
[3] Zaluzec N.J. (2019) "Improving the sensitivity of X-ray microanalysis in the analytical electron Microscope" *Ultramicroscopy V203 163*
[4] Acknowledgements; This work was supported by the Photon Science Directorate and Laboratory Directed Research and Development (LDRD) funding from Argonne National Laboratory, provided by the Director, as well as the Office of Science, of the U.S. Department of Energy under Contract No. DE-AC02-06CH11357. It was also supported in part by CRADA #01300701 between Argonne National Laboratory and ThermoFisher Scientific Instruments.

Figure 1

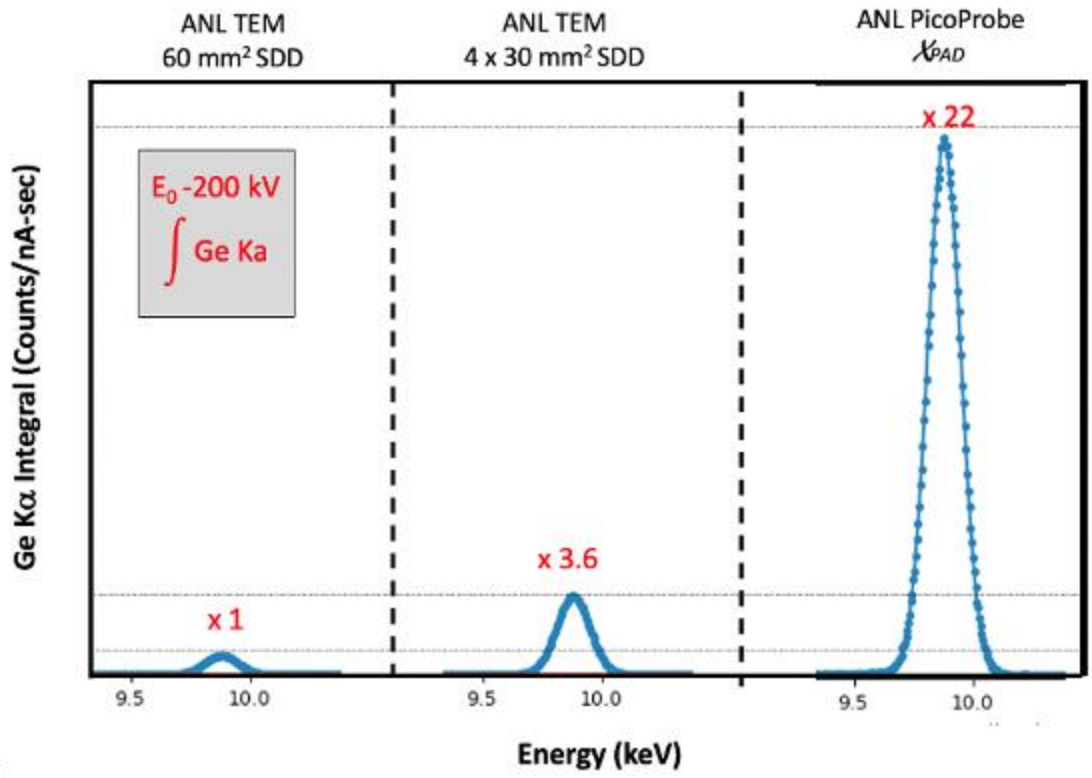

Figure 2

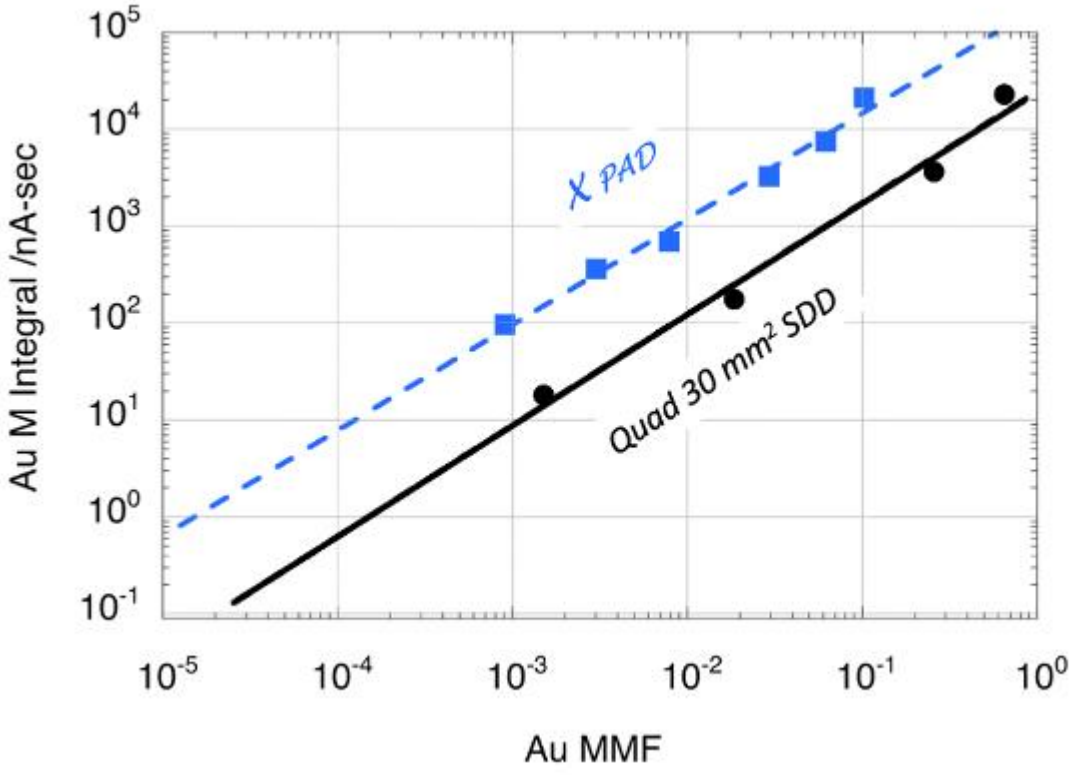

IM3.006
Vortex mode stability in mode conversion experiments and a possible practical manifestation of free-electron Landau states

T. Schachinger[1,2], P. Hartel[3], P. H. Lu[4], R. E. Dunin-Borkowski[4], P. Schattschneider[1,2]

[1]TU Wien, USTEM, Vienna, Austria
[2]TU Wien, Institute of Solid State Physics, Vienna, Austria
[3]CEOS GmbH, Heidelberg, Germany
[4]Research Center Jülich, Ernst Ruska-Centre for Microscopy and Spectroscopy with Electrons and Peter Grünberg Institute, Jülich, Germany

Recent progress in transferring the astigmatic mode conversion (MC) principle from light optics [1] to electron optics has provided an interesting alternative for the production of high-brightness and high-purity electron vortex beams (EVBs) [2]. EVBs carry quantized orbital angular momentum (OAM) $m\hbar$ and have already been applied in a multitude of experiments [3], with potential applications in nanoscale magnetic measurements using the electron magnetic circular dichroism technique [4,5].

The mode stability, *i.e.*, its transverse dispersion along the electron trajectory, is the basis for reliable and controllable experiments.

For a single quadrupole (QP) MC setup [6] (Figure 1(a)), image simulations (Figure 1(b)) show that a dual QP setup (Figure 1(c)) results in enhanced vortex mode stability up to one Rayleigh range z_R (Figure 1(d)), when compared to a single QP MC setup.

However, experiments on the dual QP MC setup reveal several unexpected observations: (i) For defocus (*df*) values larger than z_R, the vortex mode begins to disperse (Figure 2 lower right panel), in contrast to predictions based on wave optical simulations (Figure 2, inset in the lower right panel); (ii) When switching the polarity of the EVB by a π/2 QP rotation, the observation planes are apparently interchanged, *i.e.*, the far-field pattern appears in the front-focal plane, whereas the focused EVB appears in the back-focal plane and *vice versa* for the opposite vortex mode (Figure 2).

In order to shed some light on these anomalies, ray tracing simulations have been performed using realistic magnetic field distributions. The MC optics are optimized for non-vortex beams (black lines), yielding a well-focused stigmatic beam at the MC output (Figure 3(a) inset). By assigning OAM to the electrons, the $m\neq0$ beams are no longer mode-matched/stigmatic (Figure 3(a) inset).

Analysis of the azimuthal rotation of the electrons shows a slight angular dispersion of ~1.5° between $m=\pm1$ electrons after passing the adapter lens (ADL). The influence of such a slight angular misalignment has been tested (Figure 3(b)). The focal planes of $m=\pm1$ electrons are now separated from one another (Figure 3(b) inset), possibly explaining the observation (Figure 2).

The beam waist inside the ADL is comparable to the magnetic length parameter in the ADL field [7]. The angular dispersion could therefore be caused by peculiar Landau state rotations inside the ADL. This would be the first practical implication of free-electron Landau states. These findings could also help to provide optimized experimental parameters to enhance vortex mode stability in electron optical MC experiments.

Acknowledgements: The Austrian Science Fund (FWF) (P29687-N36, I4309-N36) is gratefully acknowledged. The authors are grateful to M. Obermair, M. Dries and D. Gerthsen for HPP production and J. Zach for providing realistic field distributions. CEOS GmbH acknowledges the EU Horizon 2020 research and innovation program (grant No. 823717 ESTEEM3). PHL and REDB acknowledge the EU Horizon 2020 Research and Innovation Programme (Grant Nos 856538 3D MAGiC, 823717 ESTEEM3 and 766970 Q-SORT).

References:
[1] Beijersbergen et al., OptCom, 96**,** 123-132 (1993)
[2] Schachinger et al., UM, submitted, arxiv.org/abs/2103.10899
[3] Bliokh et al., PhysRep, 690, 1-70 (2017)
[4] Schachinger et al., UM, 179, 15 (2017)
[5] Pohl et al., SciRep**,** 7, 934 (2017)
[6] Schattschneider et al., PRL, **109**, 084801 (2012)
[7] Schattschneider et al., NatCom, **5**, 4586 (2014)

Figure 1

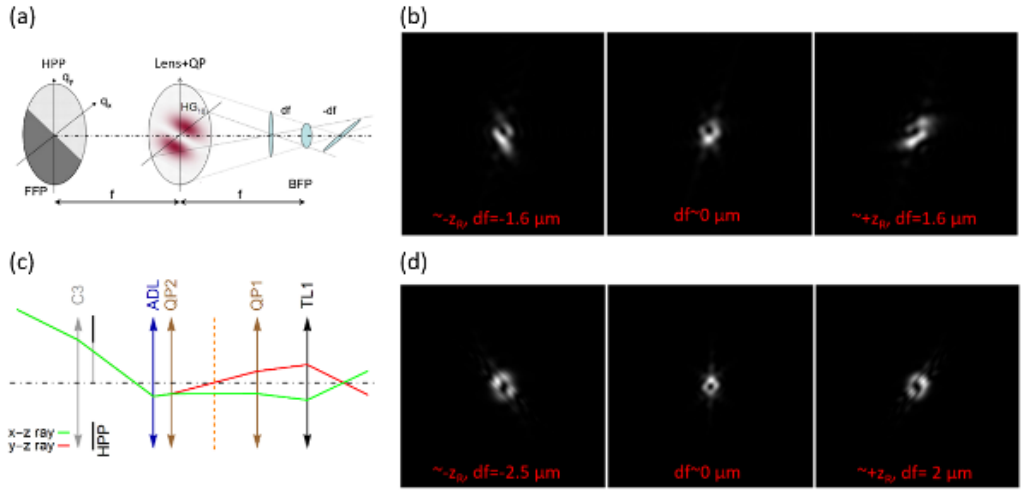

Fig. 1: (a) Experimental setup for single QP mode conversion (MC), adopted from [6]. (c) Ray path diagram for the dual QP MC setup. A Hilbert-phase-plate (HPP) produces a Hermite-Gaussian (HG) mode, which is converted to a vortex mode and stabilized inside the QP doublet QP1 and QP2. (b,d) Wave optical simulation results comparing the vortex mode stability of the two methods. In (b) the single QP MC ansatz resembling the experiment in [6] and in (d) the dual MC approach realized in a Cs-corrector [2] were simulated within the defocus range of plus/minus one Rayleigh range ($\pm z_R$). The closed donut like EVB structure is better conserved in the latter case.

Figure 2

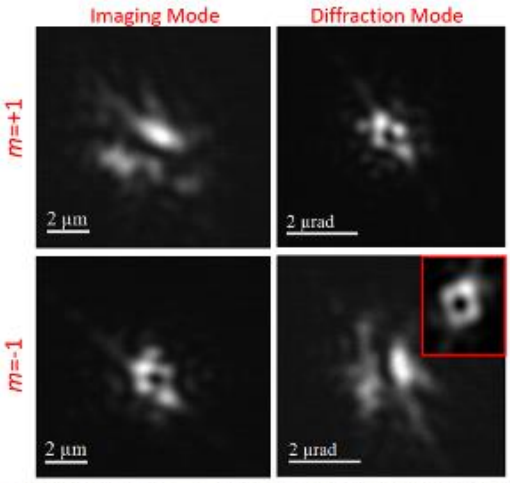

Fig. 2: Vortex mode instability for df>>z_R and vortex mode switching anomaly in the dual QP setup. The far-field pattern (df>>z_R) of the EVB in the lower right panel is strongly dispersed when compared to simulations (inset in the lower right panel). By switching the modes' polarity, the observation planes are seemingly interchanged.

Figure 3

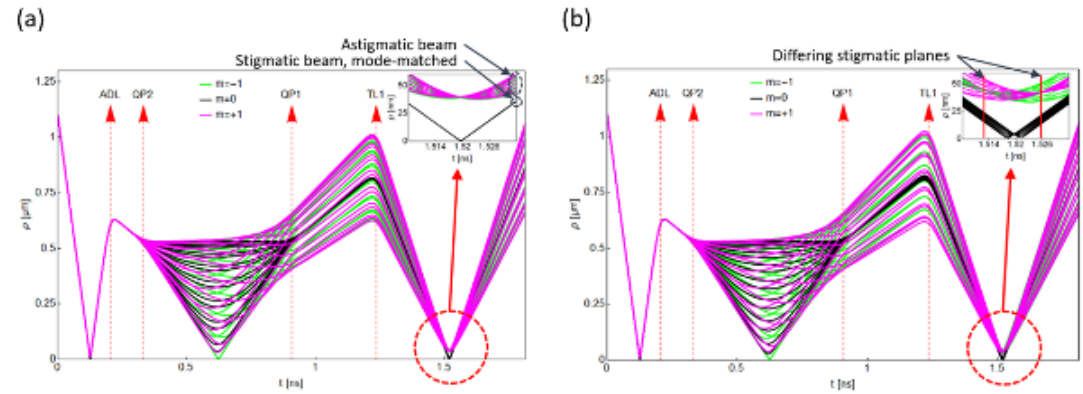

Fig. 3: (a,b) Ray tracing simulations of the dual MC setup, showing bundles of 200 kV electron rays, providing a possible explanation for the observed vortex mode instability by the introduction of OAM and for the axial separation of stigmatic planes by slightly adjusting the QP2 azimuthal rotation angle to compensate for a Landau-level-induced angular shift of vortex electrons.

IM3.P001
Strong exciton-photon interactions in WSe2 slabs using Cathodoluminescence Spectroscopy

M. Taleb[1], F. Davoodi[1], F. Diekmann[1], K. Rossnagel[1,2], N. Talebi[1]

[1]Christian-Albrechts-Universität zu Kiel, Kiel, Germany
[2]Ruprecht Haensel Laboratory, Hamburg, Germany

Introduction: Semiconducting transition metal dichalcogenides (TMDC) combined with photonic cavities, exhibit strong light-matter coupling, leading to emergence of new quasi particles [1], namely exciton-polaritons (EP). EPs have been extensively studied using near-field techniques such as SNOM and EELS for their fundamental properties [2]. These methods convey subwavelength features where EP propagations were directly imaged at monochromatic photon energies. Here, we apply cathodoluminescence (CL) spectroscopy for the first time to probe EPs and stemming spatial correlations in atomically-flat TMDCs such as Wse_2 [3]. Being based on spontaneous interactions, the resolved spatial interference maps are the direct proof of the spontaneous coherences associated with propagating exciton polaritons.

Objectives: In this work, we use an electron-based probe (Figure 1a) to excite optical modes of WSe_2 flakes and investigate their spontaneous coherences by means of CL. We demonstrate that the transversal one-dimensional optical confinement within the thin film and the propagation of the optical waves along the longitudinal orientation, allow for strong exciton-photon couplings leading to an energy split. Experimental results fallowed by numerical simulations, provide deep inside into the electron-photon interaction mechanisms inside the specimen.

Material and Methods: WSe_2 single-crystalline structures in 2H phase was grown by the standard chemical vapor transport method and were further exfoliated to obtain thin nanosheets of WSe_2. Optical characterizations were investigated using a Zeiss-SIGMA field-emission scanning electron microscope equipped with an off-axis aluminum parabolic mirror and CL detectors/spectrometers. Mathematical simulations were performed using both FDTD method and the COMSOL Multiphysics software to gain an insight into the temporal distribution of the electron-induced radiation and exciton-photon interactions.

Results: CL radiation collected from thin WSe_2 flakes demonstrated a wavelength splitting on the order of 100 nm, comparable to the predicted spectral and spatial maps. A deep at the A exciton wavelength of 751 nm and broad peaks associated with lower and upper polariton branches were observed, respectively; below and above the A exciton. Numerous interference fringes in the wavelength-distance CL map are clear signature of the spontaneous coherence caused by the excitation of EPs. Spatial interference fringes up to several orders confined along the edges revealed the excitation of edge exciton polaritons (Figure1b). In addition to the omnipresent deep at the position of A exciton, additional oscillations were observed in the range of the LP branch associated with photon-mediated interactions between A and B excitons.

Conclusion: We demonstrated strong coupling between excitons and photonic modes of freestanding thin WSe_2 flakes. CL results show anti-crossing of upper and lower polariton branches and long-range propagation of EPs. Our results demonstrate that CL spectroscopy can be used to probe coherent optical modes of semiconducting van der Waals materials.

Figure 1: (a) Propagation mechanisms of the surface excitations (b) distance-wavelength CL map along the flake edge.

References:
[1] Nature Photonics 10, 216–226 (2016)
[2] *Nature Photonics* 11, 356-360 (2017)
[3] M. Taleb, et al., Charting the Exciton-Polariton Landscape in WSe2 Thin Flakes by Cathodoluminescence Spectroscopy, Submittend, *arXiv:2101.01465*

Figure 1

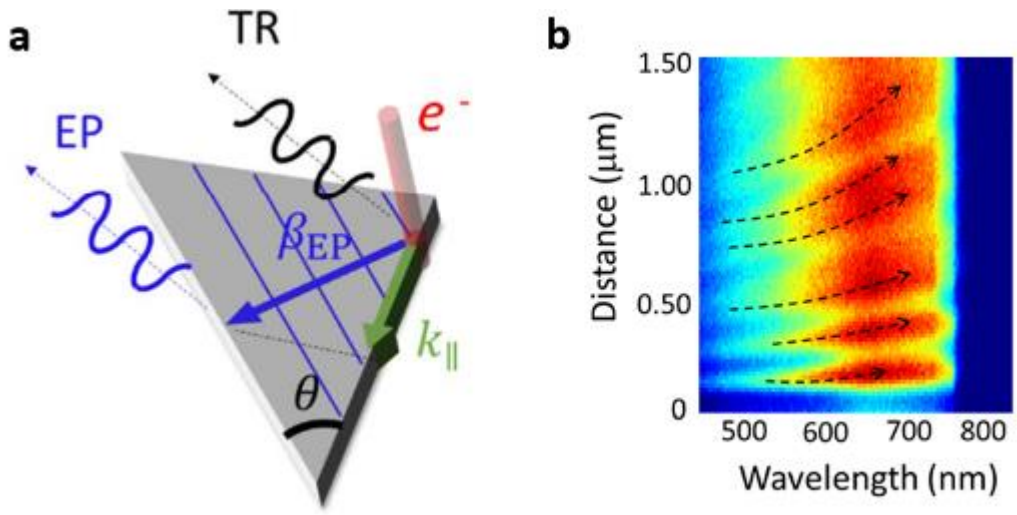
a
TR
EP
e⁻
β_{EP}
$k_{\parallel}$
θ
b
Distance (μm)
1.50
1.00
0.50
0
500
600
700
800
Wavelength (nm)

IM3.P002
The JSM-IT800 series – The next level of Intelligence Technology in FE-SEM combining ultrahigh resolution and unprecedented ease of use

T. Harzer[1]

[1]JEOL (Germany) GmbH, Freising, Germany

Intro: JEOL is a world leading manufacturer of electron- and ion-optical systems. The company"s portfolio includes lithography tools using both electron and ion beams as well as characterization systems like Scanning Electron Microscopes (SEM) and Transmission Electron Microscopes (TEM).

Challenges: Advances in materials and life sciences necessitate an increasing performance of the imaging and analytical capabilities of modern Field Emission Scanning Electron Microscopy (FE-SEM) systems. The new JSM-IT800 FE-SEM series is a highly stable yet flexible platform to encounter a variety of applications ranging from morphological and chemical studies to the crystallographic analysis of a wide variety of materials. In addition to the brand new easy to use "SEM Center" user interface, the high-performance electron emitter ensures a fast and easy sample characterization.

Advantages: The JSM-IT800 series comes with a patented JEOL In-Lens Schottky Plus Field Emission Electron Gun, a state of the art electron optical control system called "Neo Engine" and a JEOL EDS system which is fully integrated into the "SEM Center" user interface. The In-Lens Schottky Plus Emitter allows the user to conduct high resolution imaging, high speed elemental mapping and EBSD and Soft X-ray analysis by providing high probe currents at low accelerating voltages (e.g. 100 nA @ 5 kV). The systems ease of use is acomplished by JEOL`s new electron optical engine (Neo Engine) providing both, stable observation conditions and enhanced auto-functions. In addition, the JSM-IT800 series offers two objective lens types to satisfy the individual user requirements. The Hybrid Lens (HL) system is tailored for general purpose applications whereas the Super Hybrid Lens (SHL) version is used for observation and analysis at ultra low accelerating voltages at highest resolution. Moreover, the JSM-IT800SHL introduces the Upper Hybrid Detector (UHD) as the newly integrated standard In-Lens detector of the system which enables the user to obtain images with significantly enhanced Signal to Noise ratio allowing for an easy observation with high image fidelity.

Besides the standard Everhart-Thornley and UHD detector, a variety of new backscatter electron detectors can be incorporated into the JSM-IT800 systems. The Scintillator Backscattered Electron Detector (SBED) enables material contrast imaging at low accelerating voltages due to its excellent sensetivity whereas the multi-segment Versatile Backscatter Electron Detector (VBED) allows for additional 3D-topographical imaging.

Figure 1: Schematic of the detector setup of the JSM-IT800SHL Field Emission Scanning Electron Microscope.

Figure 2: High resolution images of alumina particles acquired @ 500 V acceleration voltage using JEOL`s new Upper Hybrid Detector.

Figure 1

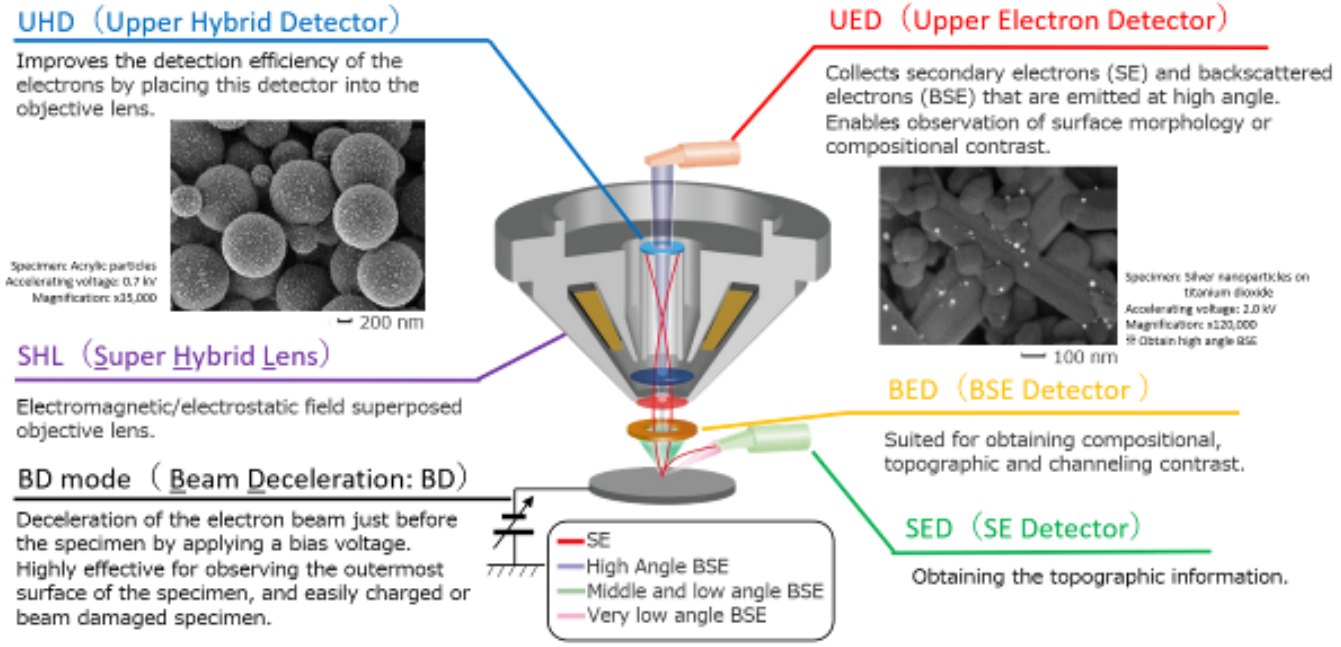

Figure 2

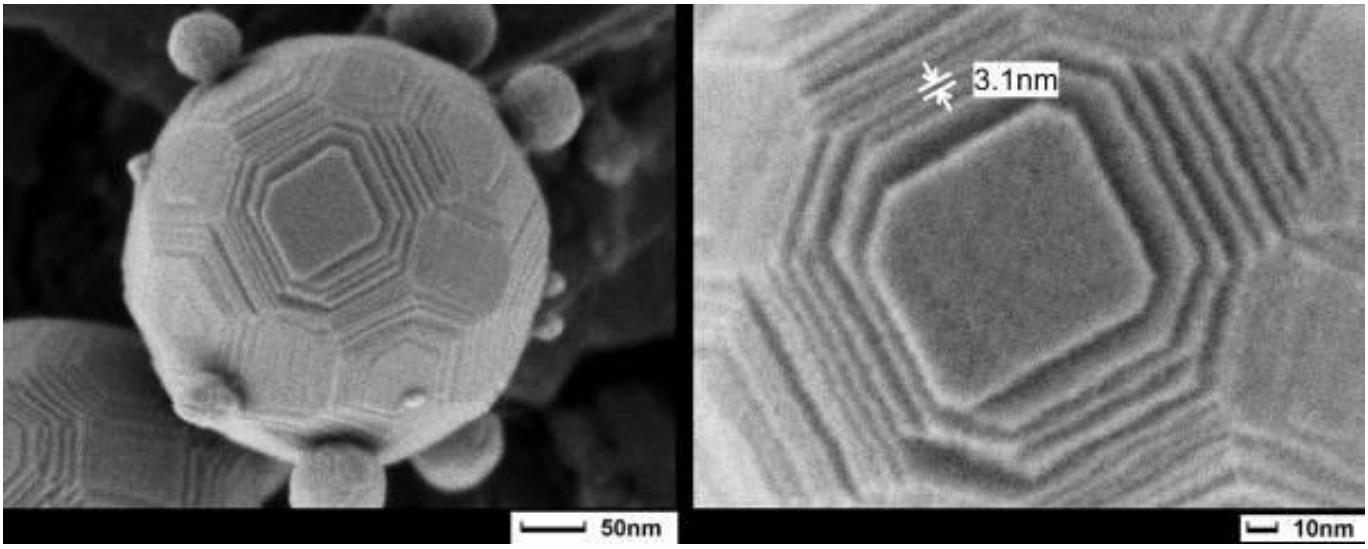

IM3.P003
Correlative Raman Imaging and Scanning Electron Microscopy (RISE) combined with Energy-Dispersive X-Ray Spectroscopy (EDXS) for the investigations of polymer materials

R. Schmidt[1], H. Fitzek[2], A. Zankel[1,2], M. Nachtnebel[2], C. Mayrhofer[2], H. Schröttner[1,2], M. Dienstleder[2], S. Mertschnigg[1,2], M. Poteser[3], H. P. Hutter[3], W. Eppel[4]

[1]Graz University of Technology, Institute of Electronmicroscopy, Graz, Austria
[2]Austrian Centre for Electron Microscopy, Graz, Germany
[3]Medical University of Vienna, Centre for Public Health, Vienna, Austria
[4]Medical University of Vienna, Department of Obstetrics and Gynecology, Vienna, Germany

The aim of this contribution is to demonstrate the power of the new system RISE (Raman Imaging and Scanning Electron microscopy), which provides high resolution imaging by the scanning electron microscope Zeiss Sigma 300 VP (Zeiss, Oberkochen, Germany) and chemical analysis, using an integrated confocal Raman microscope from WITec (Ulm, Germany) .[1, 2, 3]

In combination with an EDXS (energy-dispersive X-ray spectroscopy) system from Oxford Instruments (Abingdon, England), sample characterization in the same region of interest (ROI) can afford complementary information about the surface of a specimen.

Therefor different specimens were investigated: At the cross-section of a commercially available coffee cup, which was embedded in resin and cut by an ultramicrotome, a Raman mapping of the different polymer layers and individual Raman spectra of the different components, respectively, could be ascertained by the new system (Figure 1). [4]

Figure 1: Left: Correlative Raman map - SEM image of a paper coffee cup cross-section. **Right:** Raman spectra and component identification. [4]

At the investigation of a packing foil results show additionally to a layered structure, additives in one layer, which could be identified as rutile particles by Raman spectroscopy. These particles were further analysed by automated particle analysis, which enables the differentiation between diverse single particles. [2]

The possibilities of detecting nanoparticles with the RISE system in the range of a couple of 100 nm is demonstrated in different environments, ranging from ideal (distilled water) to challenging (sea salt solution and amniotic fluid). Promising results could be achieved in this field. [3]

References:
[1] C. Cardell, I. Guerra, An overview of emerging hyphenated SEM-EDX and Raman spectroscopy systems: Applications in life, environmental and materials sciences, Trends in Analytical Chemistry Volume 77, March 2016, 156-166
[2] R. Schmidt, H. Fitzek, M. Nachtnebel, C. Mayrhofer, H. Schroettner, A. Zankel, The combination of electron microscopy, Raman microscopy and energy dispersive X-ray spectroscopy for the investigation of polymeric materials, Macromolecular Symposia, Vol. 384, 1, 2019
[3] R. Schmidt, M. Nachtnebel, M. Dienstleder, S. Mertschnigg, H. Schroettner, A. Zankel, M. Poteser, H.-P. Hutter, W. Eppel, H. Fitzek, Correlative SEM-Raman microscopy to reveal nanoplastics in complex environments, Micron (accepted)
[4] Zankel, A., Fitzek, H.: Seminar on Electron Microscopy and Nanoanalysis 2: (Raman + EDX) @ Zeiss Sigma 300 VP - Correlative Microscopy and Spectroscopy

Figure 1

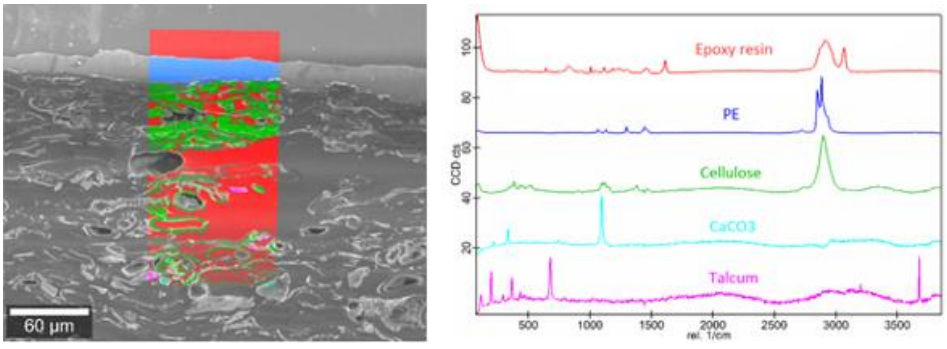

IM3.P004
In situ TEM applications of sample drive lasers and fast-switching deflectors

J. Persson[1]

[1]JEOL (Germany) GmbH, Freising, Germany

Introduction: In situ TEM is a powerful tool for revealing fundamental nanoscale processes in physics, biology, and materials science. Thanks to advances in both instrumentation and technique, this is true now more than ever. This talk will explore the possibilities for studying laser-driven processes with the help of electrostatic deflection systems that can switch states on the nanosecond scale. To set the stage, we will review recent results showing laser-driven sintering, dewetting, and coarsening in nanostructured gold at kHz frame rates. These results will serve both as examples of current capabilities and as motivation for the core of the talk: new developments involving electrostatic beam blankers, programmable high-speed timing systems, and advanced automation and data analysis.

Objectives: We wish to examine and elucidate the synergy of using high speed beam blanking in conjunction with laser illumination of the specimen for in situ studies of nanomaterial dynamics. We demonstrate the use of post specimen sub-framing systems to achieve extremely high frame rates during observation of laser driven material processes.

Materials & Methods: A recently developed laser module, "Luminary Micro" (JEOL/IDES), facilitates direct focused laser-sample interaction. This has previously successfully been used to show dewetting of gold on a surface, sintering of nanoparticles and more [1], and has now been developed into a mature product [2]. Two electrostatic optical systems have been developed that can be precisely synchronized with the laser. The first of these, a pre specimen electrostatic dose modulator (EDM), works with a timing control system, "Synchrony" (JEOL/IDES), to enable nanosecond precision definition of electron beam temporal profiles. The second, a post specimen camera subframing system, "Relativity", (JEOL/IDES) has previously been shown to provide kHz scale fame rates with similarly precise timing control [3]. Particles were produced using standard techniques.

Results: It is shown that the high-speed timing system in coordination with the advanced data analysis system give a benefit to in situ experiments. The methodology is validated through the demonstrated ability to record high-frame-rate details of well understood material processes, thus paving the way for future experiments on material systems and processes with completely unknown dynamics.

Conclusion: Together the systems described here, a compact sample laser, a pre-specimen EDM, a post specimen camera subframing deflector, and a precision timing controller enable users to craft scriptable experiment definitions to control all timing aspects of a laser driven in situ experiment. From dose rate to heating profiles to camera frame rate, users can decide how their experimental conditions will evolve with nanosecond precision.

References:
[1] B. W. Reed, A. A. Moghadam, R. S. Bloom, S. T. Park, A. M. Monterrosa, P. M. Price, C. M. Barr, S. A. Briggs, K. Hattar, J. McKeown, and D. J. Masiel, *Struct. Dyn.* 6, 054303 (2019)
[2] https://www.jeol.co.jp/en/products/detail/LuminaryMicro.html
[3] B. W. Reed, S. T. Park, R. S. Bloom, and D. J. Masiel, *Microsc. Microanal.* 23 (Suppl 1), 84 (2017)

IM3.P005
Ernst Abbe´s research program leading i.a. to the apochromate objectives (1886)

H. Kubbinga[1]

[1]University of Groningen, retired, Groningen, Netherlands

In the history of microscopy [1], or more generally optics, Ernst Abbe (1840-1905) occupies a special position. As chief-physicist of Carl Zeiss (1816-1888), in Jena (1866-), he launched a research program far ahead of the time. First and foremost was his convincing the glass specialist Otto Schott (1851-1935) to settle in Jena and found a glass works. New glasses of all kinds were the result (1881-). Abbe took care to have all relevant constants measured with the utmost precision, i.a. refraction indexes at well-defined wave lengths, the various dispersions, and density. Most of the data remained unpublished, naturally, though new optical systems were taken into production. The first novelty concerned the so-called "apochromate" objectives, in which the chromatic aberration was further minimized (1886-). In my paper I would like to discuss Abbe"s approach on the base of a surviving construction drawing of such an objective.

[1] See my papers in the successive *Yearbooks* of the European Microscopy Society: "Early microscopes. 17th century" (2015); "Microscopes in the 18th century" (2016); and "Microscopes in the 19th century-part I (1800-ca.1860)" (2017).

IM3.P006
Expanding performance and usability of high-speed / low-dose STEM scanning

T. Mullarkey[1,2], J. J.P. Peters[1], C. Downing[3], L. Jones[1,3]

[1]Trinity College Dublin, School of Physics, Dublin, Ireland
[2]Centre for Doctoral Training in the Advanced Characterisation of Materials, Dublin, Ireland
[3]Advanced Microscopy Laboratory, Centre for Research on Adaptive Nanostructures and Nanodevides (CRANN), Dublin, Ireland

Modern advances in scanning transmission electron microscopy (STEM), such as aberration correction, have meant that for many technologically relevant samples it is no longer our instrument that limits our resolution, but instead sample damage caused by the electron beam [1,2]. Reducing both the electron dose and the dose-rate by lowering the beam current and pixel dwell-time are key avenues to combat this which are available to all microscope operators.

However, when imaging under these conditions, we find that artefacts such as signal streaking and detector afterglow begin to dominate our images [3]. Even in the absence of these artefacts the signal level in a single image frame is too low for the precision required in many studies, whilst navigating and focusing the image become near impossible. The problems then are severalfold; finding a way to eliminate these imaging artefacts, enabling navigating under ultra-low-dose conditions, and producing final data of a suitably high signal level.

Here we present a strategy for software and hardware retrofitting of the Gatan Digiscan to solve these issues in the following ways:

- Using a refinement of our previous work [4], we pulse count electrons with a FPGA to create digital images live within Digital Micrograph to eliminate the previously described artefacts.
- Implementation of a live rolling live-average, such as those seen in SEMs, into Digital Micrograph to aid in navigating under low-dose conditions.
- Enabling the ability to capture a continuous buffer of image frames, allowing live playback of data, including those from before the operator began recording.

The combination of the above approaches natively into Digital Micrograph creates a powerful tool where the image acquisition capabilities of the STEM are pushed to their limits. Every electron is counted in the digital signal, and with the image buffer no data is wasted. These benefits are exemplified when imaging fragile specimens as the rolling live-average eliminates the need to go to higher electron doses to find a region of interest within the sample, and live playback of frames means we may be able to capture crucial dynamic events, if not rewind to before a point where a sample becomes too damaged. These benefits will be demonstrated through comparisons of analogue and digital data, and examples where the data buffer was used to find otherwise irretrievable data.

References:
[1] R. F. Egerton, P. Li, and M. Malac, *Micron* **35**, 399 (2004).
[2] A. De Backer, G. T. Martinez, K. E. MacArthur, L. Jones, A. Béché, P. D. Nellist, and S. Van Aert, *Ultramicroscopy* 151, 56 (2015).
[3] J. P. Buban, Q. Ramasse, B. Gipson, N. D. Browning, and H. Stahlberg, *J. Electron Microsc. (Tokyo).* 59, 103 (2010).
[4] T. Mullarkey, C. Downing, and L. Jones, *Microsc. Microanal.* 26**,** 2964 (2020).

IM3.P007
Increasing the usable frame-rate of your existing STEM

J. Peters[1,2], T. Mullarkey[1,2], C. Downing[2], L. Jones[1,2]

[1]Trinity College Dublin, School of Physics, Dublin, Ireland
[2]Centre for Research on Adaptive Nanostructures and Nanodevices, Advanced Microscopy Laboratory, Dublin, Ireland

Scanning transmission electron microscopy has increasingly become the preferred imaging mode in TEM due to its intuitive interpretation and ability to collect multiple signals simultaneously. However, the serial nature of STEM gives rise to several limitations that must be considered in any experiment. STEM is vulnerable to sample drift effects, presenting as non-rigid distortions in an image [1], and the high local beam current density and the resulting electron dose rate is capable of damaging many technologically interesting specimens. Recent developments in in-situ microscopy have led to the desire to capture dynamic events at high frame rates. Current scanning speeds attainable in typical STEMs are on the order of seconds for a 512x512 image, leading to a high probability of distorted images of beam damaged samples with low temporal resolution.

All of these problems can be mitigated by increasing the scan speed when imaging. The acquisition time of a single STEM image results from several variables: the pixel count, the pixel dwell time and the line flyback time. Decreasing the pixel count is an easy way to increase STEM frame rates, but often comes with an unacceptable penalty to resolution and/or field of view. Minimum usable pixel dwell times are typically limited by detector afterglow and the control electronics, with values on the order of 1 µs typically achievable [2]. Flyback waiting time is to account for the hysteresis in the scan coils arising from induction effects in the scan coils [3]. The Flyback time is typically on the order of 500 µs, and can account for a significant proportion of the image acquisition time. While is it possible to use improved hardware to reduce flyback hysteresis or dwell times, this presents a price hurdle and potentially disrupts integration into existing hardware and/or software [4].

Here we present a methodology to increase the achievable framerates of a Gatan Digiscan II controlling a Nion UltraSTEM. Through a careful, one-time calibration of the hysteresis behaviour of the scan system, we are able to correct for this in real time at the microscope. We show that our high framerate acquisition does not present any loss of precision through distortion analyses. Finally, we discuss the remaining limitations on STEM frame rates and strategies for future improvement.

[1] L. Jones, H. Yang, T. J. Pennycook, M. S. J. Marshall, S. Van Aert, N. D. Browning, M. R. Castell, and P. D. Nellist, Adv. Struct. Chem. Imaging **1**, 8 (2015).
[2] T. Mullarkey, C. Downing, and L. Jones, Microsc. Microanal. **27**, 99 (2020).
[3] J. P. Buban, Q. Ramasse, B. Gipson, N. D. Browning, and H. Stahlberg, J. Electron Microsc. **59**, 103 (2010).
[4] R. Ishikawa, Y. Jimbo, M. Terao, M. Nishikawa, Y. Ueno, S. Morishita, M. Mukai, N. Shibata, and Y. Ikuhara, Microscopy **69**, 240 (2020).

IM3.P008
Introducing the term "probe high tension" and extreme x-ray collection efficiency on Spectra Ultra S/TEM

D. Stroppa[1]

[1]Thermo Fisher Scientific, Eindhoven, Netherlands

Besides being the first commercial platform with corrector(s), first generation Titan TEM was capable of high tension range from 300 kV down to 80 kV. For improved optical and specimen stability, bifilar coil design was introduced in the objective lens unit [1], enabling fast mode switches for any given high tension. Overnight high tension switches have become the norm, and since then, market expectations have moved forward that current S/TEMs have a high tension range down to 30 kV with stability achieved over a couple of hours. This timescale can be considered too long in some cases, for instance, S/TEMs shared by several multi-disciplinary research groups.

Research community has also driven the market in terms of x-ray collection efficiency and output count rate maximization in elemental studies. Lithium doped silicon (Si(Li)) EDS detectors were replaced with silicon drift detectors (SDDs) and Super-X became the first EDS detection system with multiple SDDs on a S/TEM [2]. Growing beam sensitive materials research field and time to data considerations have brought solid angles to around 2 sr and output count rates to 1 million cps.

Recent advances in R&D allow us to introduce a new platform within the Spectra portolio, which will address the above mentioned market demands in full. This new member, Spectra Ultra S/TEM, is equipped with an EDS detection system allowing unshadowed solid angle of above 4 sr without any compromise in terms of spatial resolution (i.e. larger pole piece). Moreover, Spectra Ultra S/TEM can stabilize within minutes after a high tension switch, whereby introducing the term "probe high tension" to the TEM community. In this way, one can now use high tension as an experiment variable similar to changing probe current or convergence angle in microscope operation.

We believe that Spectra Ultra S/TEM will further accelerate research in beam sensitive materials. Thanks to the unprecedented x-ray collection efficiency, extreme low doses can now be used to generate high quality elemental maps. Furthermore, depending on the specimen behavior under the electron beam, probe high tension can be tuned as often as needed for experiment optimization within one TEM session.

Keywords: EDS solid angle, beam sensitive specimens, low dose imaging, high tension flexibility

References:
[1] van der Stam, M. et al. Microsc. Microanal., 2005, 19, 9-11.
[2] Schlossmacher, P. et al. Microsc. Microanal., 2010, 24, S5-S8.

IM3.P009
RAFA lens for enhanced far focused probes, imaging and analytical resolutions

M. Rafa[1], R. Herring[1]

[1]University of Victoria, Victoria, Canada

Since the beginning of optics whether focusing a beam by a refractive lens or reflective lens, the intensity at and close to the optic axis has not been able to be focused to a distant, tight, three-dimensional (3D) probe due to the absence of or shallow convergence angle afforded by beam. This limitation has resulted in the formation of an elongated, eliptical intensity profile along the optic axis with reduced intensity limiting the resolution of both 3D optical imaging and 3D analytical analyses of specimens in the direction along the optic axis of the microscope. These focusing problems have been solved with the RAFA lens (reflective advanced focusing aperture lens) accomplished using a 3D shaped cone reflector having a surface that is very slightly curved like a lens to focus a plane wave to the distant 3D spot (Figure 1). After the plane wave reflects off the surface of the cone reflector, it then reflects off of a flat mirror to form the high-intensity, far focused spot now able to be used as a probe for lasers and acoustic beams (Figure 2).

The reflective RAFA lens obeys Snell"s law, which enables all wavelengths to be focused to the same focused probe position. Thus a laser beam is focused to the same spot as an acoustic beam. Multiple beams of different wavelengths can be simultaneously focused to the same position. Additionally, since the focused probe position lies on the optic axis and the focusing is strictly dependent on the cone"s curved surface, the aberrations such as spherical aberration, chromatic aberration and coma can be fully corrected enabling the size of the focused probe to be determined by the planarity of the beam and its associated wavelength. Shifting the cone reflector forward or backwards along the optic axis shifts the focused probe position along the optic axis enabling limited focusing of the specimen during imaging and analytical analyses. Application of the RAFA lens to electron and ion beams is possible by applying a repulsive potential on its surfaces, i.e., the cone reflector and reflecting mirror. Increasing or decreasing the repulsive potential on the reflecting mirror will also shift the focused spot enabling movement of the beam on and off the optic axis. Off-axis circular motion of the beam can occur by using several electrostatic plates for the reflecting mirror, which is circular, having different charge potentials on each plate rotating 360 degrees.

Grants from NSERC Discovery, CFI and BCKDF are greatly appreciated.

Figure 1: Configuration of the RAFA lens showing two plane wave emitters, which could have different wavelengths, each focused to the same focused probe position by reflecting off the cone lens and then off a reflecting mirror surface. All of the intensity is focused to the far probe position having an enhanced 3D intensity profile enabling higher resolution imaging and analytical analyses than current lens designs.

Figure 2: a) Ray path simulations showing the beam"s intensity reflecting off the cone lens and the side mirror to form the far focused probe.

Figure 3 a): a constructed RAFA lens for acoustic beams and lasers, and b) its visible demonstration focusing a HeNe red laser to a high-intensity, tight focused probe spot located 10 cm from the RAFA lens.

Figure 1

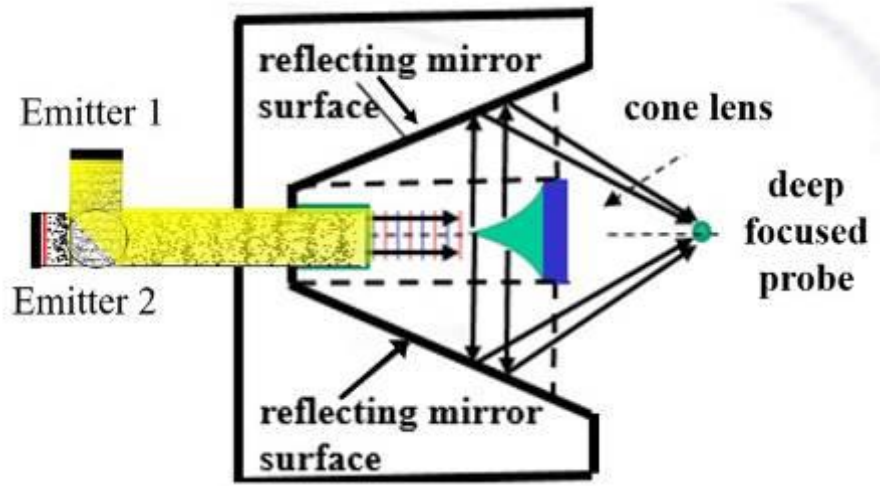

Figure 2

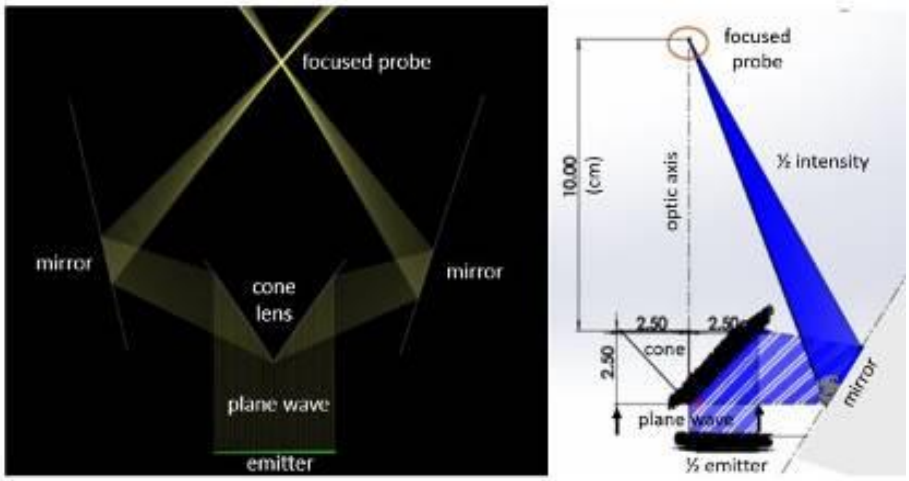

Figure 3

IM4.001-Invited
Imaging of electric and magnetic near fields of plasmonic antennas by EELS

M. Horák[1], V. Křápek[1,2], A. Konečná[1,3], M. Hrtoň[1], T. Šikola[1,2]

[1]Brno University of Technology, CEITEC, Brno, Czech Republic
[2]Brno University of Technology, Institute of Physical Engineering, Brno, Czech Republic
[3]Materials Physics Center CSIC-UPV/EHU, San Sebastian, Spain

Localized surface plasmon resonances are self-sustained collective oscillations of free electrons in metallic nanostructures. Mapping of localized surface plasmon modes with high spatial and energy resolution is necessary to understand their nature and spatio-spectral characteristics. This can be done by scanning transmission electron microscopy (STEM) combined with electron energy loss spectroscopy (EELS) which measures the energy transferred from electrons to the LSP. Importantly, EELS is sensitive to the electric near field component of localized surface plasmon modes parallel with the electron beam and cannot be directly associated with the magnetic near field.

In our contribution, we use the Babinet's principle to facilitate characterization of both the electric and the magnetic near field of plasmonic antennas. Babinet's principle relates the properties of a planar plasmonic antenna (particle) and a complementary plasmonic antenna (aperture) in a thin metal film of the same size and shape. In particular, the energies of LSPR in both types of antennas shall be identical and the magnetic near-field distribution of the particle antenna shall correspond to the electric near field distribution of the complementary aperture antenna. The spatially-resolved EELS mapping of the aperture antennas can thus help to deduce the magnetic near fields associated with the localized surface plasmon resonances in particle antennas and vice versa [1]. We demonstrate such use of Babinet's principle in a combined experimental and theoretical study for disc-shaped antennas/apertures [2] and plasmonic bow-tie (see Figure 1) and diabolo antennas/apertures with electric/magnetic hot spots [3,4]. Moreover, we will also discuss optimal experimental conditions in STEM-EELS for achieving the best signal-to-background ratio (see Figure 2) [5] as well as suitable techniques for fabrication of high-quality plasmonic nanostructures [6,7].

References:
[1] M. Horák et al., *Microsc. Microanal.* 26(S2) (2020) 2628-2630.
[2] M. Horák et al., *Sci. Rep.* 9 (2019) 4004.
[3] V. Křápek et al., *Nanophotonics* 9 (2020) 623-632.
[4] M. Hrtoň et al., *Phys. Rev. Appl.* 13 (2020) 054045.
[5] M. Horák, T. Šikola, *Ultramicroscopy* 216 (2020) 113044.
[6] M. Horák et al., *Sci. Rep.* 8 (2018) 9640.
[7] L. Kejík et al., *Opt. Express* 28 (2020) 34960-34972.

Figure 1: Transverse dipolar mode [peak 1 in (a,b)] in a bow-tie antenna. EEL spectra of bow-tie (a) and inverted bow-tie (b) antenna. Schematic representation the transverse dipolar mode (c), calculated surface charge (d), electric (e) and magnetic (f) out-of-plane near-field distributions. STEM micrographs and EELS maps of the bow-tie (g) and inverted bow-tie (h) antenna. Note that the spatial distribution of EELS map of particle in (g) corresponds well to calculated electric out-of-plane near-field distribution in (e) and the spatial distribution of EELS map of aperture in (h) corresponds well to calculated magnetic out-of-plane near-field distribution in (f).

Figure 2: EEL spectra of the same rod at different beam energies: (a) measured raw EEL spectra and extracted signal; (b-d) STEM ADF images of the rod with marked area for integration of EEL spectra in (a) recorded during STEM-EELS mapping at 300 keV (b), 120 keV (c), and 60 keV (d); (e) signal to background ratio at different beam energies.

Figure 1

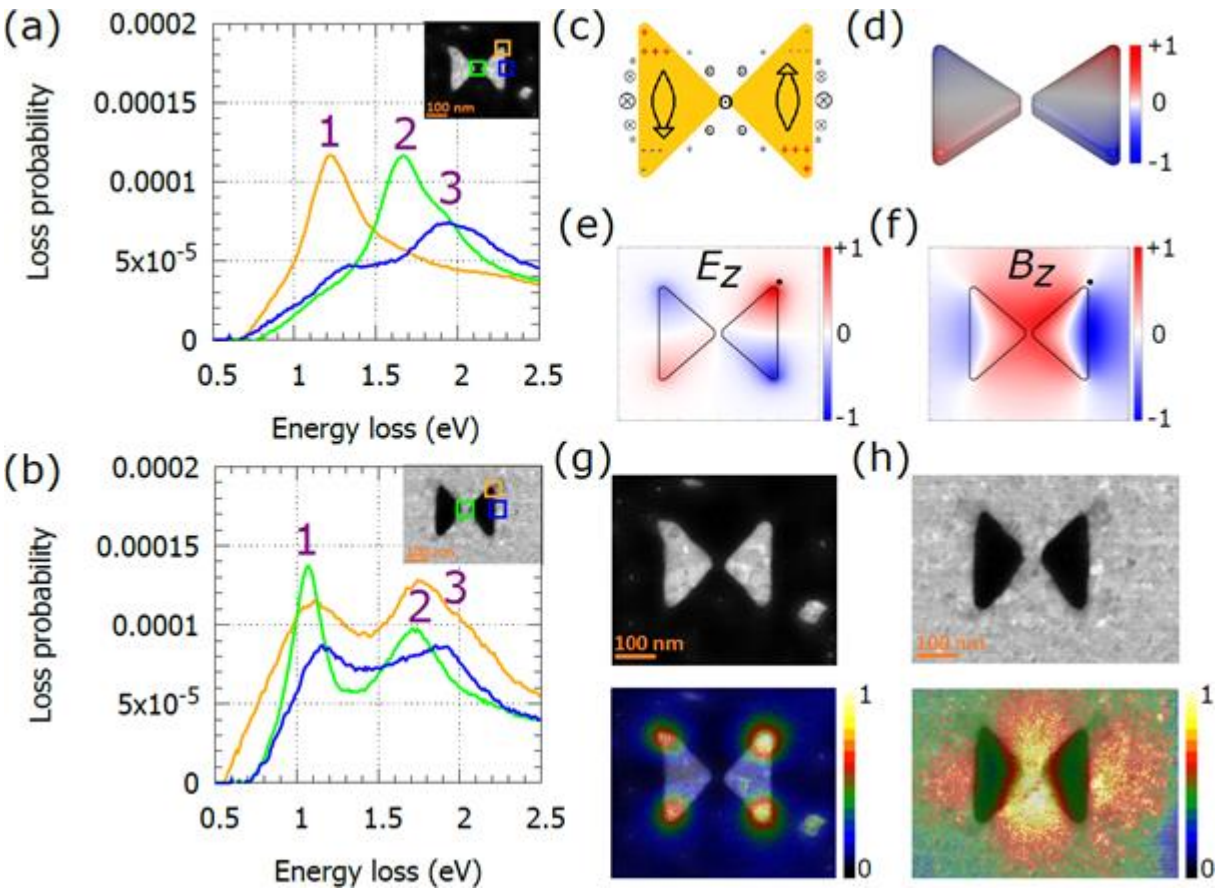

Figure 2

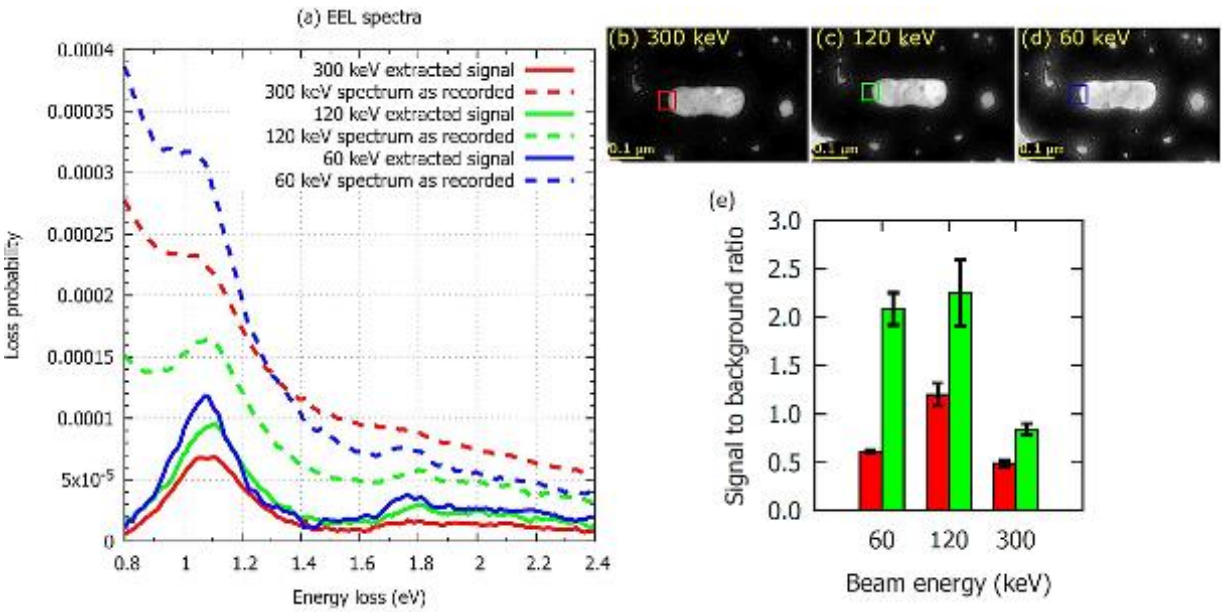

IM4.002
Including inelastic plasmon scattering in multislice simulations for quantitative STEM – challenges and solutions

F. F. Krause[1], T. Grieb[1], M. Schowalter[1], A. Beyer-Leser[2], S. S. Firoozabadi[2], P. Kükelhan[2], H. L. Robert[3], K. Müller-Caspary[3], K. Volz[2], A. Rosenauer[1]

[1]Universität Bremen, IFP, Bremen, Germany
[2]Universität Marburg, Marburg, Germany
[3]Research Center Jülich, Jülich, Germany

The use of multislice simulations of the electron beam propagating through the specimen as reference data to evaluate experimental STEM images is a well-established technique for quantitative evaluation. Using the frozen phonon method to include inelastic phonon scattering, the simulations include thermal diffuse scattering (TDS) and Bloch diffraction, the two major scattering mechanisms. Especially for micrographs acquired from HAADF scattering such simulations have been proven to allow accurate precise evaluation of thickness or composition at atomic resolution.

The transfer of these successes into the medium- and low-angle regime however, has been difficult: The measured intensity at low scattering angles is found to be higher than expected from frozen phonon simulations. A primary suspect for causing this elevation is plasmon scattering. Indeed, energy filtered, angle resolved experiments presented here confirm that plasmon loss diffraction patterns show an elevated intensity between semi-convergence angle and ~40 mrad.

The inclusion of plasmon scattering into multislice simulations is hence of high interest to restore the possibility for accurate evaluations in the low-angle regime. This work presents the implementation of the inelastic plasmon scattering events by inclusion of transition-potentials into the multislice routine, which allow for transition of intensity to inelastic channels, in which further elastic propagation is simulated.

Because the energy loss due to a plasmon excitation is more than four magnitudes smaller than the probe electron energy, the characteristic scattering angle that mainly determines the shape of the transition potentials is only of few µrad. Simultaneously it is necessary to have a reciprocal space extent of several hundred mrad to accurately model TDS. As computational limitations limit the numerical grid size to few thousands of pixels in each direction, the plasmon transition potential is usually undersampled. This can cause a severe overestimation of lowest-angle scattering resulting in an underestimation of the influence of plasmons in the simulation. An integration scheme is proposed to mend this for the simulation of diffraction intensities.

Beyond the characteristic angle, the Lorentzian-shaped transition potential drops quickly to very small values, which has led other authors to the proposal of introducing a critical cuttoff angle, which has been shown to work accurately for conventional energy filtered TEM simulations. In the present work it is shown, that plasmon scattering from the central beam to angles up to ~45 mrad even though improbable is the main contribution to the difference between simulations with and without the inclusion of plasmons. This is due to the very large intensity disparity between central beam and the outer diffraction pattern. It is thus of utmost importance to fully model the transition potentials without a cutoff to high angles, where they are dominated by a term derived from the plasmon dispersion relation.

The simulation results including plasmon effects are compared to energy filtered experimental diffraction patterns of silicon. Figure 1 shows the ratio of zero and plasmon loss intensities: The presented simulations are able to generally reproduce the amount and angle distribution of the plasmon scattering. There are admittedly discrepancies, as the experimental plasmon scattering seems to be weaker than predicted. This can be partly attributed to other effects as is discussed.

Figure 1

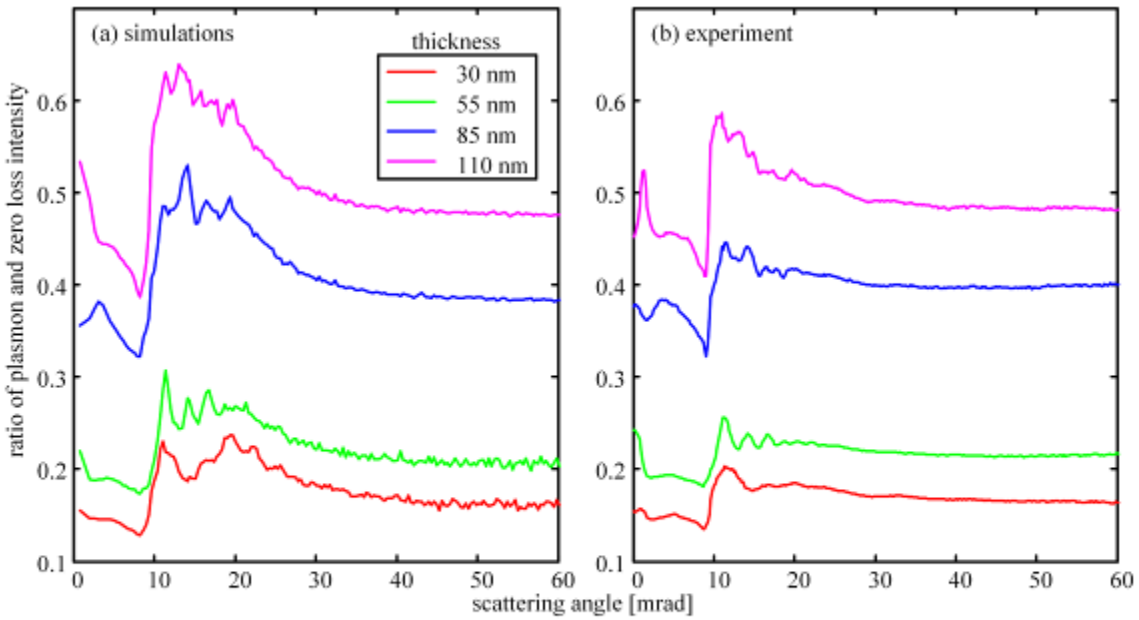

Figure 1: Ratios of the intensities of plasmon loss and zero loss filtered diffraction patterns of silicon in [100] direction for different thicknesses as a function of scattering angle. The acceleration voltage was 300 kV at a semiconvergence angle of 9 mrad. (a) shows the simulation results according to the described method, (b) shows experimental results using a GIF imaging filter. Despite some discrepancies, the amount and angle distribution of the plasmon scattering is in fair agreement with the experiment and decidedly better than for simulations without plasmon scattering.

IM4.003
Mode-selective imaging and control of nano-plasmonic near-fields

H. Lourenço-Martins[1,2], M. Sivis[1,2], A. Geese[1], T. R. Harvey[1], T. Danz[1], R. M. Sarhan[3], M. Bargheer[3], A. Feist[1], C. Ropers[1,2]

[1]University of Göttingen, IV. Physical Institute, Göttingen, Germany
[2]Max Plank Institute for Biophysical Chemistry, Göttingen, Germany
[3]Universität Potsdam, Institut für Physik und Astronomie, Potsdam, Germany

Electron energy-loss spectroscopy (EELS) in a transmission electron microscope (TEM) is a powerful technique to probe optical and electronic excitations with a sub-nanometer spatial resolution [1, 2]. However, probing spontaneous losses, this technique does not provide time-domain access to ultrafast processes and is restricted in its spectral resolution even for the most advanced electron sources available (10-100 meV).

Here, recent developments in the field of ultrafast transmission electron microscopy (UTEM) promise to overcome these limitations by probing laser-excited optical modes with femtosecond electron pulses. Specifically, in a stroboscopic laser-pump/electron probe scheme, an optically excited sample is measured with photo-emitted ultrashort electron wave-packets [3] and scanning their relative time delay gives access the involved ultrafast dynamics. Such an instrument thus combines the spatial resolution of a conventional TEM (nm) with the unrivaled spectral and temporal resolutions provided by ultrafast lasers (resp. sub-meV and hundreds of femtoseconds), and therefore offers unique capabilities to probe optical fields at the nanoscale.

In this talk, I will demonstrate how this technique – usually referred to as photon-induced near-field electron microscopy (PINEM) – can be used to analyse the modal structure of the optical response of individual plasmonic nano-resonators (gold and silver nano-triangles) directly at the nanoscale. We will present our boundary element method (BEM)-based data analysis which enable us to extract from optical near-field maps, the magnitude and relative phase of each plasmonic modes excited by a femtosecond pump laser, as illustrated on figure 1. Thanks to this method, we will analyse the influence of the laser polarization, wavelength and incidence angle on the population of each modes. Particularly, we will show that the total optical near-field excited by the laser, result from the interference pattern of a large number of plasmonic modes which can be controlled by tuning the laser properties. Finally, we will theoretically and experimentally demonstrate that the plasmonic optical near-field can be coherently manipulated by pumping the system with two phase-locked optical pulses of different wavelength, which enables to create a complex beating pattern between two different plasmonic modes in the same single nano-resonator.

Figure 1: Illustration of the BEM mode analysis approach developed in this work. **a.** A nanometer resolved map of the optical near field associated to the plasmons pumped by a femtosecond laser is recorded by EELS. **b.** The associated TEM image is processed to extract the 3D geometry of the nanostructure. **c.** The model is used to compute the plasmonic eigenmode of the structures. **d.** Based on a L1-L2 optimization procedure, the magnitude and relative phase of each modes is reconstructed from the near-field map.

References:
[1] J. Nelayah et al., " Mapping surface plasmons on a single metallic nanoparticle", Nat. Phys. 3, 348–353 (2007)
[2] H. Lourenço-Martins et al., " Self-hybridization within non-Hermitian localized plasmonic systems", Nat. Phys. 14, 360–364 (2018)
[3] A.Feist et al., " Quantum coherent optical phase modulation in an ultrafast transmission electron microscope" Nature 521, 200–203 (2015)

Figure 1

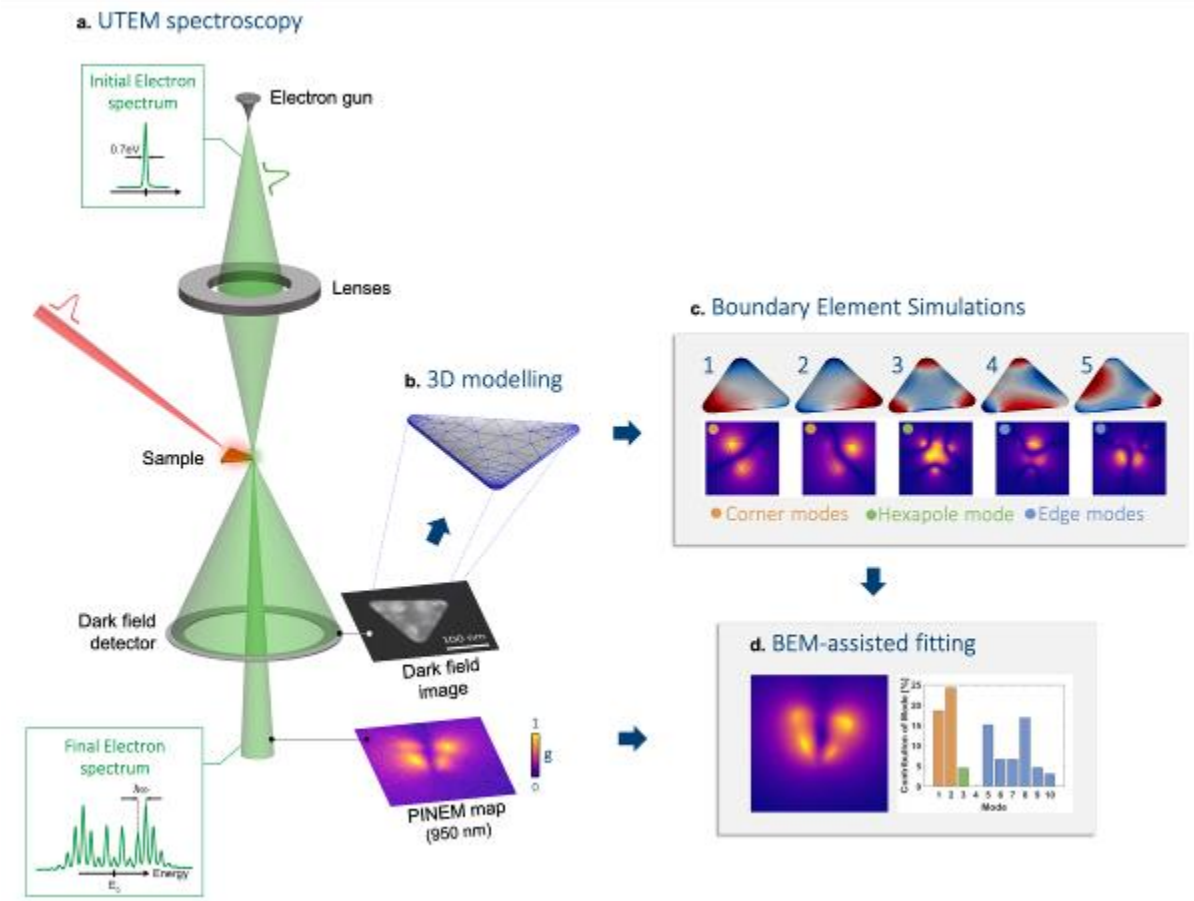
a. UTEM spectroscopy
Initial Electron spectrum
0.7eV
Electron gun
Lenses
Sample
Dark field detector
Dark field image
Final Electron spectrum
Energy
PINEM map (950 nm)
b. 3D modelling
c. Boundary Element Simulations
1
2
3
4
5
Corner modes
Hexapole mode
Edge modes
d. BEM-assisted fitting
Mode

IM4.004
Revealing nanoscale semiconductor carrier dynamics with ultrafast scanning electron microscopy

M. Garming[1], P. Kruit[1], J. P. Hoogenboom[1]

[1]Delft University of Technology, Imaging Physics, Delft, Netherlands

Observing the dynamics of photo-excited electrons and holes is essential to optimizing semiconductor nanodevices functionality. Ultrafast scanning electron microscopy (USEM) has been developed to image semiconductor carrier dynamics at sub-optical resolution using a scheme in which carriers are photo-excited with a fs laser, and subsequently probed with a pulsed electron beam while recording the carrier induced change in SE yield [1]. USEM has been demonstrated on a wide range of materials, but further improvements in USEM instrumentation, e.g. improving sensitivity to reveal surface-mediated dynamics, bridging the optical pump and electron probe spatial scales, or facilitating electron pulse generation, have received less attention.

We present novel implementations for USEM that address current limitations. Lock-in detection allows to disentangle surface-mediated dynamics from bulk recombination, a high numerical aperture objective lens enables diffraction-limited optical pumping, and electron pulses are generated with a beam blanker.

Our USEM setup (Figure 1) is implemented in a FEI Quanta scanning electron microscope, modified to accommodate a fs-laser (25 fs, 95 MHz) and an integrated inverted microscope [2] for optical excitation from above or through an objective lens below the sample. We use a standard beam blanker to pulse the electron beam (90 ps) [3] without modification of the SEM source unit. Lock-in detection is implemented by chopping the pump laser allowing us to directly distinguish the laser induced portion of the SE signal.

We demonstrate that lock-in USEM is capable of discriminating differences in surface-mediated carrier dynamics resulting from only a single atomic layer using Ga- and As-terminated GaAs (Figure 2) [4]. We explain the differences through interface dependent carrier trapping leading to a few hundred mV surface photo voltage on the GaAs, modulating the SE collection efficiency around the photo-excited area [5], and confirm this with particle tracing simulations. We further show, with high-resolution optical pumping through the objective lens, that similar effects can be observed on MoS2 on sub-micron length scales.

In conclusion, we have constructed a beam blanker based USEM setup with lock-in SE detection that can be used to study dynamics of photo-excited charge carriers in semiconductors. Lock-in detection reveals the occurrence of localized surface photo voltages resulting from carrier trapping, which vary greatly with GaAs surface termination. Our lock-in USEM implementations open the door to high-resolution studies of photo-excited carrier dynamics in and around semiconductor nanostructures.

[1] Cho et al., PNAS 111 (2014), 2094
[2] Zonnevylle et al., J. Microscopy 252 (2013), 58
[3] Moerland et al., Optics Express 24 (2016), 24760
[4] Garming et al, J. Phys. Chem. Letters 11 (2020), 8880
[5] Zani et al., Micron 121 (2019), 53

Figure 1: The SEM based setup has a pulsed electron beam (90 ps, 50 nm) and incorporates a fs-laser. In USEM measurements, the pulsed electron beam is scanned around the fs laser spot. Lock-in detection enhances signal.

Figure 2: Laser induced SE yield for different laser pump electron probe delays for different GaAs surfaces. Both samples show a decrease in SE yield at t = 0 ns with ns scale recovery. The signal recovers to reveal the slow dynamics, with different patterns manifesting the different surface terminations; we explain these through local surface photo voltages.

Figure 1

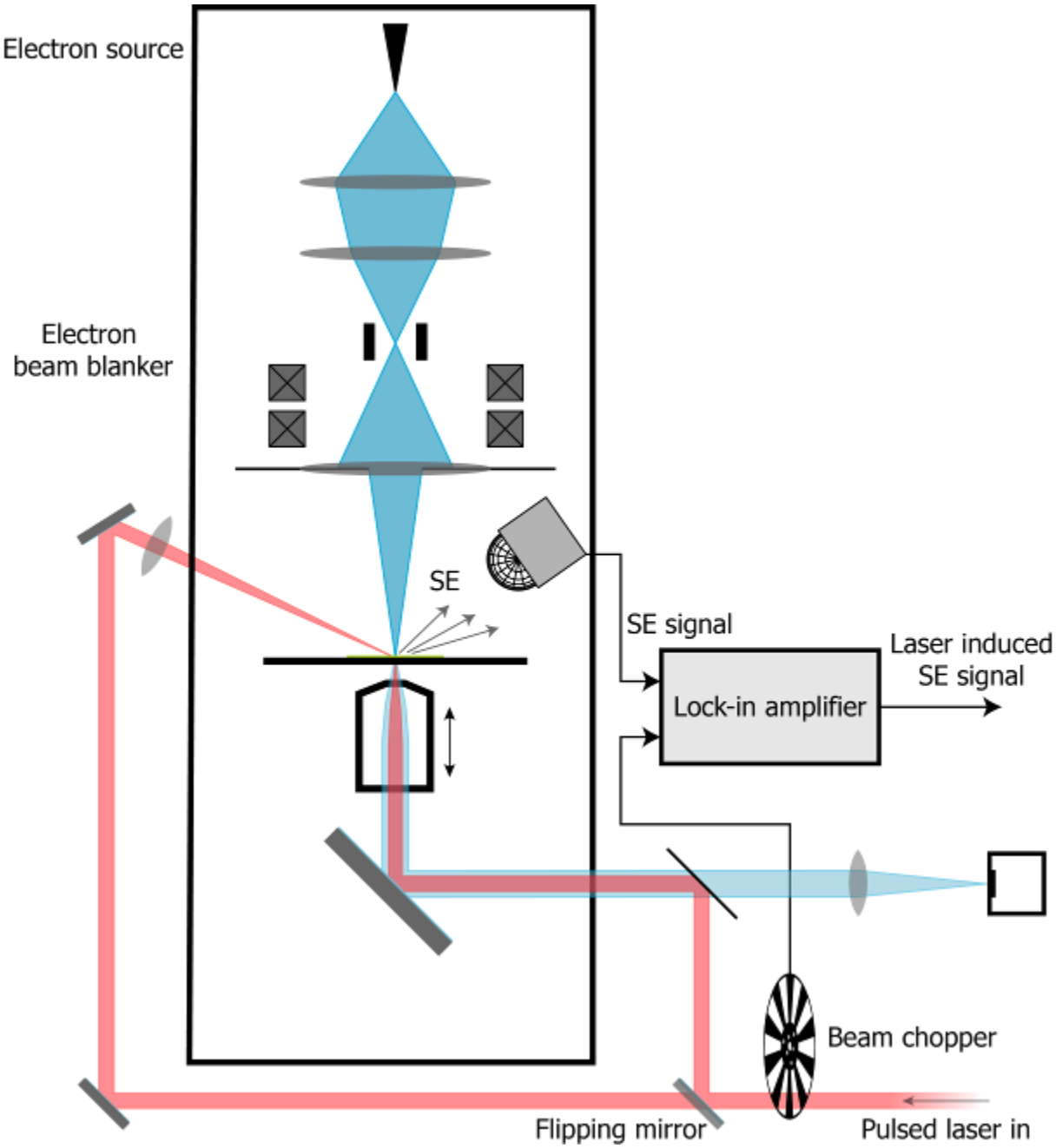

Figure 2

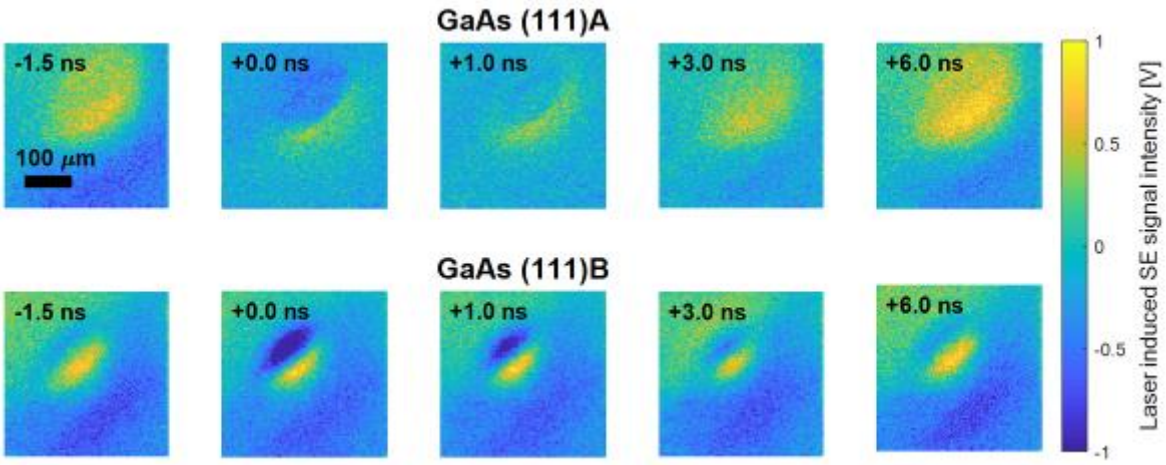

IM4.005
The frequency resolved frozen phonon method for vibrational (STEM-)EELS and applications to plane wave illumination simulations

P. Zeiger[1], J. Rusz[1]

[1]Uppsala University, Department of Physics and Astronomy, Uppsala, Sweden

Introduction: We have recently introduced the "frequency-resolved frozen phonon multislice method" (FRFPMS) as a versatile and efficient model for vibrational (STEM-)EELS [1]. The method relies on a combination of Molecular Dynamics (MD) and elastic multislice simulations. A colored-noise thermostat based on the generalized Langevin equation is used to excite a non-equilibrium distribution of velocities in the MD simulations to generate snapshots of the atomic positions [2,3,4]. Similar to how classical frozen phonon multislice method calculations are performed [5], these snapshots are fed into elastic multislice calculations. The thermal diffuse scattering (TDS) is then extracted from coherent and incoherent intensities similar to the process described in Reference [6]. Within the FRFPMS method, the TDS intensity is identified as the vibrational EELS signal at the energy loss corresponding to the frequency excited in the MD simulation. The FRFPMS method does not require explicit knowledge of the phonon modes of the specimen and is therefore well suited for simulations of large systems containing tens or hundreds of thousands of atoms.

Objective: We shed light on some of the properties of the FRFPMS method. We show, how difficulties in the interpretability of spectra can arise from the very narrow width of the δ-thermostat [2] used in our earlier work [1]. We remedy this issue by a so-called hotspot thermostat [4]. Furthermore, we show data of the distribution of the FRFPMS vibrational signal in the diffraction plane for an incident plane wave beam and discuss its agreement with other recent results [7,8].

Methods: We use the software packages LAMMPS, DrProbe, phonopy and phonolammps in addition to in-house codes. All data is simulated for a hexagonal boron nitride model and a plane wave beam.

Results: We show in Figure 1 and example of how the TDS intensity in energy-bin resolved diffraction patterns reproduces a projection of the 3-d phonon dispersion. Such diffraction patterns visualize nicely how the signal is distributed in the diffraction plane as a function of energy bin. We show the directional dependence of spectra in Figure 2 at selected positions in the diffraction plane. Note how the spectra at symmetrically equivalent positions differ due to different relative orientations of momentum transfer and individual polarization vectors of phonon modes.

Conclusion: The FRFPMS method is an efficient and versatile model for large-scale vibrational STEM-EELS simulations and captures spectral details well in the diffraction plane.

References:
[1] P. M. Zeiger, J. Rusz, Physical Review Letters 124, 025501 (2020)
[2] M. Ceriotti, G. Bussi, M. Parrinello, Journal of Chemical Theory and Computation 6, 1170 (2010)
[3] M. Ceriotti, M. Parrinello, Procedia Computer Science 1, 1607 (2010)
[4] R. Dettori, M. Ceriotti, J. Hunger, C. Melis, L. Colombo, D. Donadio, Journal of Chemical Theory and Computation 13, 1284 (2017)
[5] R. F. Loane, P. Xu, J. Silcox, Acta Crystallographica Section A: Foundations of Crystallography 47, 267
[6] B. D. Forbes, A. V. Martin, S.D. Findlay, A. J. D'Alfonso, L. J. Allen, Phys. Rev. B 82, 104103 (2010)
[7] R. Senga, K. Suenaga, P. Barone, S. Morishita, F. Mauri, T. Pichler, Nature 573, 247 (2019)
[8] B. Plotkin-Swing, G. J. Corbin, S. De Carlo, N. Dellby, C. Hoermann, M.V. Hoffman, T. C. Lovejoy, C. E. Meyer, A. Mittelberger, R. Pantelic, L. Piazza, O. L. Krivanek, Ultramicroscopy 217, 113067 (2020)

Figure 1

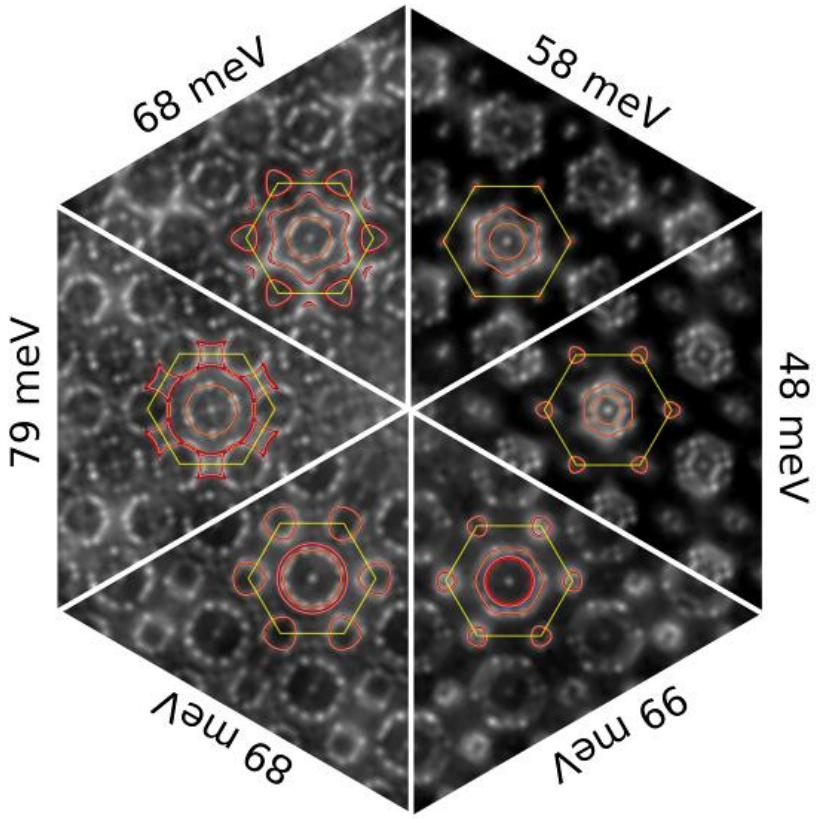

Figure 2

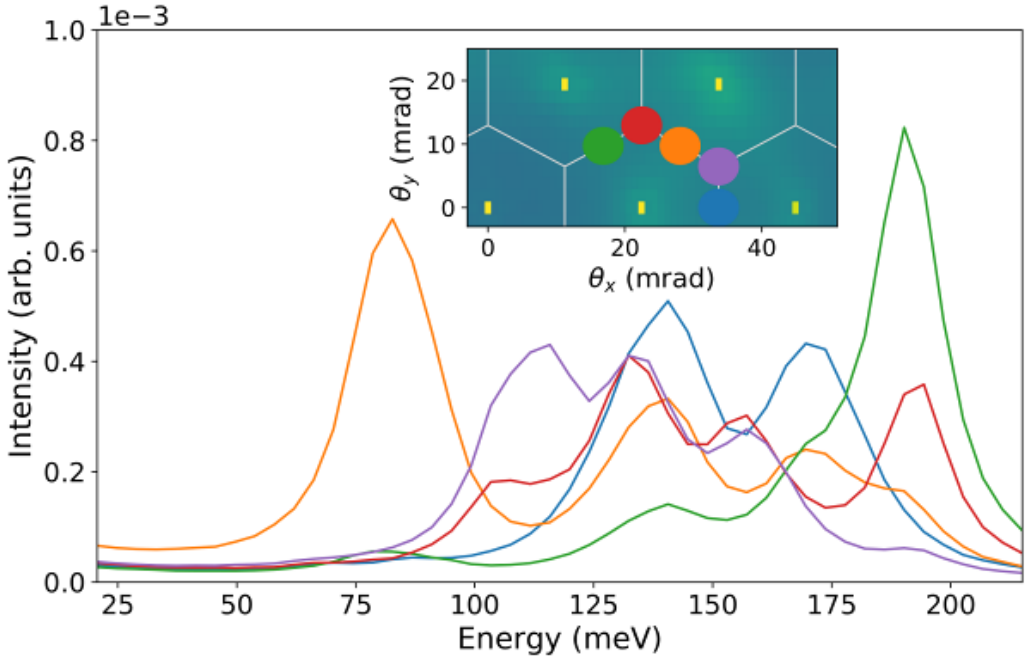

IM4.006
ADMM image processing techniques adapted to STEM-EELS Maps

C. Zietlow[1], J. K. Lindner[1]

[1]Paderborn University, Physics, Paderborn, Germany

Introduction: STEM-EELS and especially STEM-EELS maps are inherently subject to huge amounts of noise disguising the signal and thus the information to be extracted from it. Often, iterative denoising and deconvolution techniques are needed to recover part of the information hidden within the noise. Since many years Richardson-Lucy deconvolution algorithms (RLA) and Wiener filtering (WF) are the standard procedure for data treatment in EELS. However, since the RLA is suited to pure Poisson and WF to pure Gaussian noise, both lack the ability to fully adapt to the Gauss-Poisson mixed noise statistics faced in real measurements, limiting the success of such strategies.

Objectives: To better adapt to the problem and thus improve the data treatment, it is reasonable to overthink the use of these algorithms. Indeed, there are better suited techniques available for EELS. The aim of this work is to implement a technique capable of reducing the whole noise statistics and to determine the performance in retrieving the original information in low-energy EELS maps.

Methods: A modern class of algorithms rely on the principles of solving the `augmented Lagrangian", which is adaptable to a large variety of problems concerning image optimization. One of the methods to solve these kinds of ill-posed problems is the `Alternating Direction Method of Multipliers" (ADMM) algorithm [1], which has gained a lot of interest concerning image denoising and deconvolution in general within the last decade [2].

Simulated EEL spectra generated using the MNPBEM MATLAB toolbox [3] can be used to evaluate the algorithms. By resembling experimental conditions by blurring with a ZLP and treating the signal with both Poisson and Gaussian type noise, data close to reality can be recreated, but with the important difference, that the original input signal, or `ground truth", is known. In a next step, the reconstructed signal can then be compared to the original by the relative-squared-error (RSE), in order to quantify the quality of the respective algorithm.

Results: The acquisition process of STEM-EELS maps adds different layers of Gaussian and Poisson noise to the data, that need to be addressed independently to reveal the underlying signals.

A way is shown, how to quickly estimate the quantities of different noises and how to implement the ADMM routines in order to optimally deal with the different noise types. Further, to show the applicability to real experimental data, the success of ADMM algorithms is demonstrated by denoising and deconvolving STEM-EELS maps of surface plasmons in a metallic nanoparticle (Figure 1).

Conclusion: For the first time, an ADMM algorithm is used to denoise and deconvolve theoretical and experimental EELS maps and the superior performance of this technique is demonstrated.

References:
[1] S. Boyd et al., Found. Trends Mach. Learn Vol. **3**, No. 1, 1–122 (2010)
[2] Ikoma et al., Sci. Rep. 8, 11489 (2018)
[3] U. Hohenester et al., Comp. Phys. Commun. 183, 370 (2012)

Figure 1: Center: STEM-ADF image of a triangular gold nanoparticle with corresponding EEL spectrum, recorded at the tip of the triangle. Superimposed are the normalized spectrum as acquired (black), after ADMM treatment (pink) and simulated (blue dot), exhibiting three plasmon peaks. To the left/right: STEM-EELS plasmon maps at the corresponding energies are displayed, with the untreated data in the upper, ADMM treated maps in the middle and simulated maps in the lower row.

Figure 1

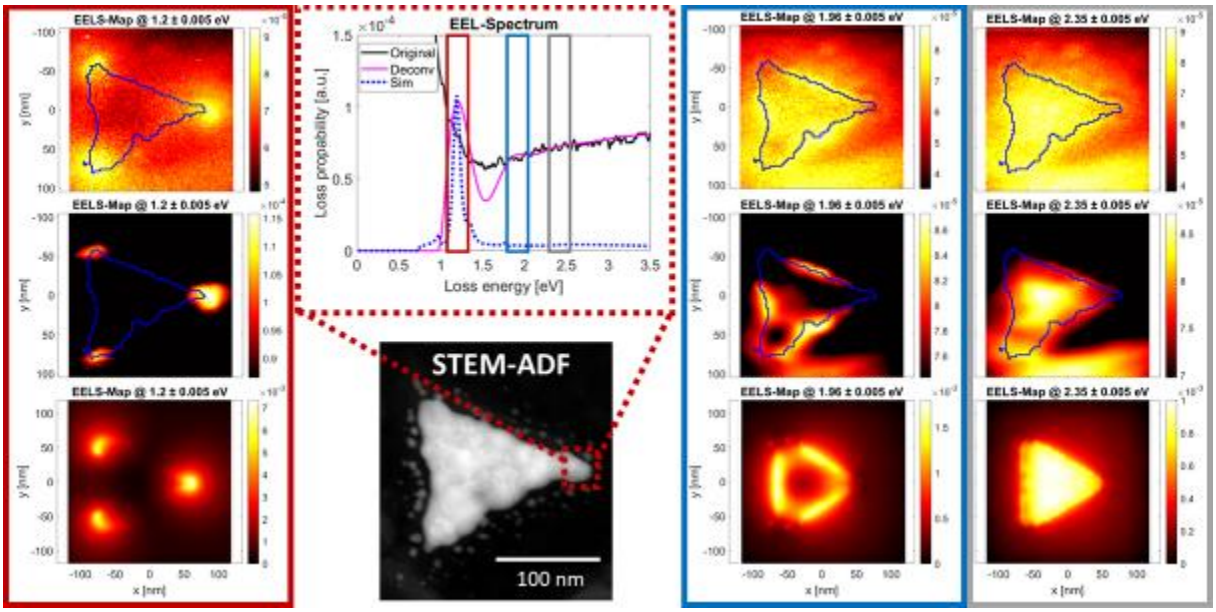
EELS-Map @ 1.2 ± 0.005 eV
EELS-Map @ 1.2 ± 0.005 eV
EELS-Map @ 1.2 ± 0.005 eV
y [nm]
x [nm]
EEL-Spectrum
Original
Deconv
Sim
Loss propability [a.u.]
Loss energy [eV]
STEM-ADF
100 nm
EELS-Map @ 1.96 ± 0.005 eV
EELS-Map @ 1.96 ± 0.005 eV
EELS-Map @ 1.96 ± 0.005 eV
EELS-Map @ 2.35 ± 0.005 eV
EELS-Map @ 2.35 ± 0.005 eV
EELS-Map @ 2.35 ± 0.005 eV

IM4.007
STEM-EELS imaging of resonant eigenmodes in dielectric silicon nanocavities

D. T. L. Alexander[1], V. Flauraud[2], F. Demming-Janssen[3]

[1]Swiss Federal Institute of Technology Lausanne (EPFL), Electron Spectrometry and Microscopy Laboratory (LSME), Institute of Physics (IPHYS), Lausanne, Switzerland
[2]Swiss Federal Institute of Technology Lausanne (EPFL), Microsystems Laboratory (LMIS1), Microengineering Institute (IMT), Lausanne, Switzerland
[3]SIMUSERV GmbH, Würzburg, Germany

While plasmonic materials receive much attention for manipulating light at the sub-wavelength scale, dielectric nanocavities have been proposed as alternatives for use as optical nanoantennas [1]. They benefit from lower absorption losses, owing to their resonances being driven by displacement currents within the volume, rather than the actual currents of surface charge for plasmonics [2]. Further, by supporting both electric and magnetic resonances, dielectrics have an extra degree of freedom for tailoring light scattering.

High energy resolution low-loss electron energy-loss spectroscopy (EELS) allied to scanning transmission electron microscopy (STEM) is now a key tool for the near-field probing of plasmonic resonances [3]. Here, we extend the method to the study of resonances excited in optical dielectric nanocavities. By implicating symmetry arguments for the stimulus–response [4], backed up by dipole excitation simulations, we assign EELS signatures to corresponding resonant eigenmodes, achieving ± 0.01 eV agreement between experiment and simulation for certain modes.

The STEM-EELS data are acquired on planar dielectric nanostructures using a FEI Titan Themis 60-300 with Gatan GIF Quantum ERS spectrometer. The samples are made from 100 nm thick amorphous Si on 35 nm thick Si-N membranes, using nanolithography to etch nanocavities in the forms of discs, ellipses, triangle, squares and rectangles. To improve EELS signal-to-noise within the projected nanocavity volume, a high energy 300 keV electron beam is applied, monochromated to give an energy spread of ~110 meV. Simulations are made using CST Studio Suite 3D EM analysis software.

The results analysis paints a complex picture. When the incident probe impacts near the edge of a disc, low energy dipole eigenmodes are excited. In smaller discs of $\lesssim$ 250 nm diameter they are magnetic in nature, while in larger discs they correspond to low-Q factor electric modes with broad EELS peaks, superposed by in-plane toroidal eigenmodes. By breaking degeneracy, the elliptical form allows the latter two modes to be discriminated in the STEM-EELS data. Higher order edge-excited modes are also resolved in larger discs. When the incident probe is placed within the volume, other eigenmodes are excited, having vertically-oriented current loops. An out-of-plane toroidal dipole is excited at cavity centres. In contrast, as shown in Figure 1, the MD_2 mode [5] with three counter-rotating current loops is excited off-centre, giving two lobes of intensity in the EELS maps of the ellipse and rectangle.

The study demonstrates the potential of STEM-EELS for the near-field imaging of resonant eigenmodes in dielectric nanocavities. Compared to plasmonic excitations, the volume-based excitations lead to some key differences in the data. Finally, the eigenmode analysis allows the results to be related to the light-optical response.

[1] M. Decker and I. Staude, J. Opt. 18 103001 (2016)
[2] J. van de Groep and A. Polman, Opt. Express 21 26285 (2013)
[3] A. Polman et al., Nat. Mater. 18 1158 (2019)
[4] G. D. Bernasconi et al., ACS Photonics 4 156 (2017)
[5] Y. Yang et al., Phys. Rev. B 95 165426 (2017)

Figure 1: EEL spectra, from regions shown on the STEM images, and intensity maps for the MD_2 eigenmode in a 450 nm disc, and 450 x 300 nm ellipse and rectangle, with plan-view simulations of their electric field resonances. The purple EEL spectrum from the disc edge is shown for comparison. Scale bars: 100 nm.

Figure 1

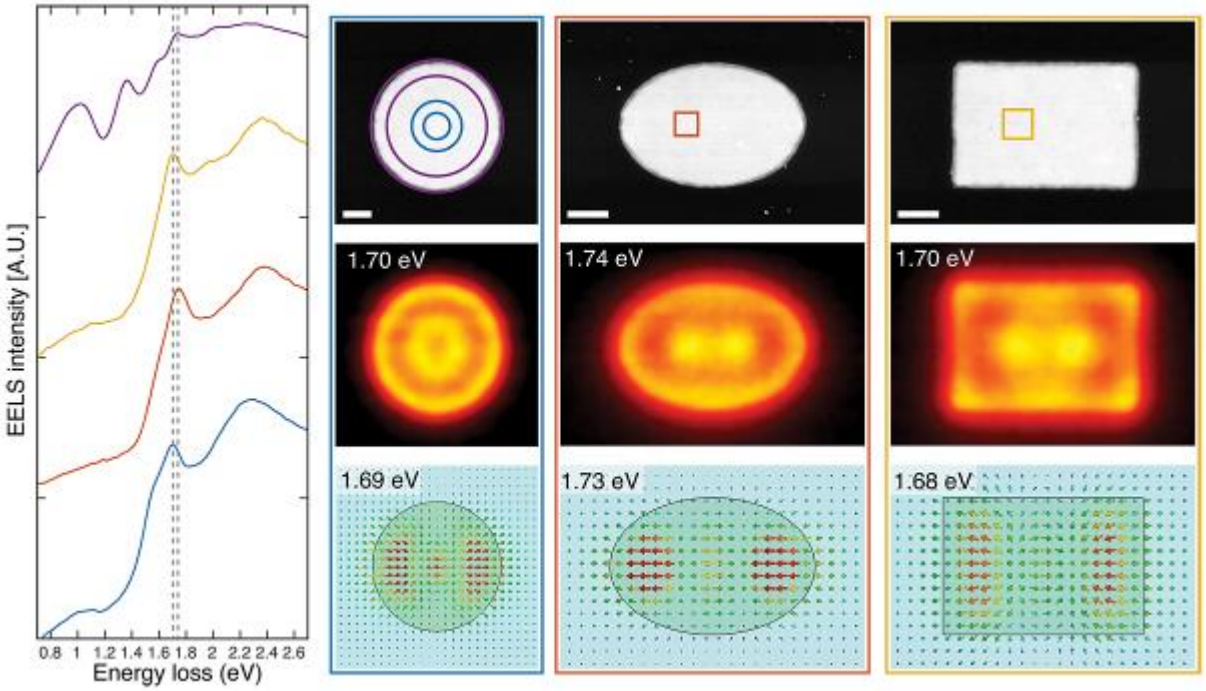
EELS intensity [A.U.]
0.8 1 1.2 1.4 1.6 1.8 2 2.2 2.4 2.6
Energy loss (eV)
1.70 eV
1.74 eV
1.70 eV
1.69 eV
1.73 eV
1.68 eV

IM4.008
High-resolution EELS at atomic resolution using a recently developed aberration corrected transmission electron microscope equipped with a double Wien-filter type monochromator

P. Wachsmuth[1], M. Mukai[1]

[1]JEOL (Germany) GmbH, Freising, Germany

Objectives: Here we report on the performance and application of a recently developed analytical electron microscope equipped with a high-order aberration corrector and a double Wien filter type monochromator [1]. This microscope is aimed at the study of the electronic structure of various materials at high spatial resolution and a wide range of acceleration voltages.

Effects and Advantages: The high-order aberration corrector corrects aberration up to six-fold astigmatism extending the flat area of the Ronchigram up to 60mrad [2,3] even at acceleration voltages as low as 30kV. The effect due to chromatic aberration is minimized by the monochromated electron probe. The energy spread can be adjusted independently of the probe size on the sample plane using differently sized slits located the two Wien filters. As shown in Figure 1 an energy resolution of down to 14meV can be achieved [4].

This instrument provides a high spatial and energy resolution at voltages as low as 30kV, allowing the for-example investigation electronic structure of beam sensitive and 2D materials. In addition, the high energy resolution of down to 14meV gives access to information on vibrational modes of the sample.

Here we give applications examples on high resolution electron energy-loss spectra of the vibrational spectrum of different materials such as Boron Nitride (Figure2) and iconic liquid C2mim-TFSI (Figure3).

Figure 1: Zero-loss peak spectrum at 30 kV showing an energy resolution of 14 meV.

Figure 2: Low-loss EELS map of a hexagonal boron nitride (h-BN) with a monochromatic probe using a 0.1 µm slit. probe size = 1 nm, probe current = 10 pA, acquisition time for each pixel = 0.3 seconds. (a) shows the ADF-STEM image the mapping area. (b) shows the extracted low-loss spectrum from the edge of the specimen indicated with the framed yellow square in Figure (a). This spectrum, measured with ΔE = 22 meV, showed a peak corresponding to an optical phonon at 170 meV. (c) shows the EELS map at the phonon energy. The phonon intensity was delocalized at the vacuum area > 100 nm beyond the sample edge due to the delocalization of inelastical scattering of electrons.

Figure 3: (a) Structure of ionic liquid C2mim-TFSI, which is composed of [C2mim+] cation and [TFSI-] anion. (b) The EEL spectra, calculated and experimental IR spectra with energy scale.

EELS magnified by ×1, ×10 and ×250 spectra are shown. In the ×250 magnified EEL spectrum, a broad peak, indicated by an arrow, appears at -0.4 eV,. This low-energy peak was confirmed to match the vibrational peaks in the IR spectrum (~3000cm-1) and was attributed to the C-H stretching vibrations of the [C2mim+] cations using theoretical calculations. Sample courtesy of Dr. Mizoguchi, The University of Tokyo [5]

References:
[1] M. Mukai, et al.: Ultramicroscopy 140 (2014)
[2] H. Mueller, et al.: Microsc. Microanal., 12 (2006), 442-455.
[3] T. Ishikawa, et al.: Microsc. Microanal., 13 (supple.3), (2015) 1599-1600
[4] M. Mukai, et. al.: Microsc. Microanal., 21 (suppl3), 2015 [5] T. Miyata, et al.: Microscopy. 63, 5, (377). 1, 2014

Figure 1

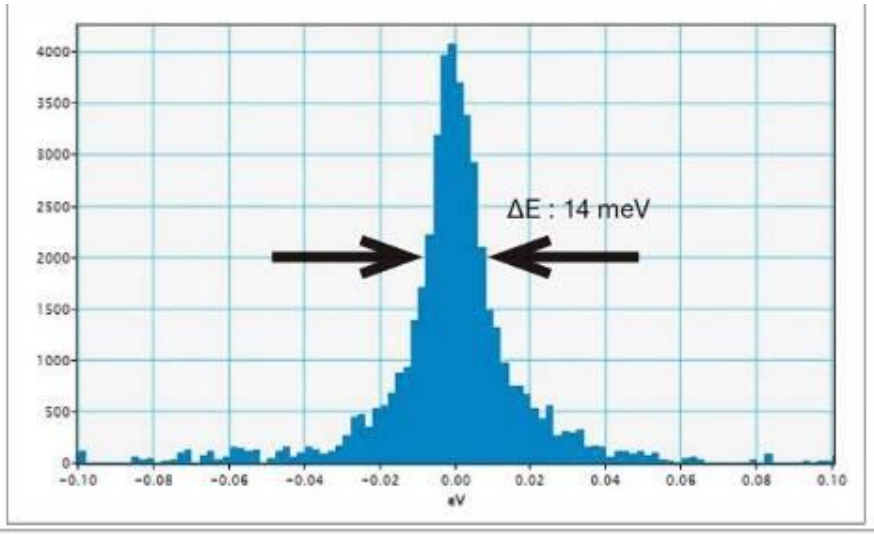

Fig.1.

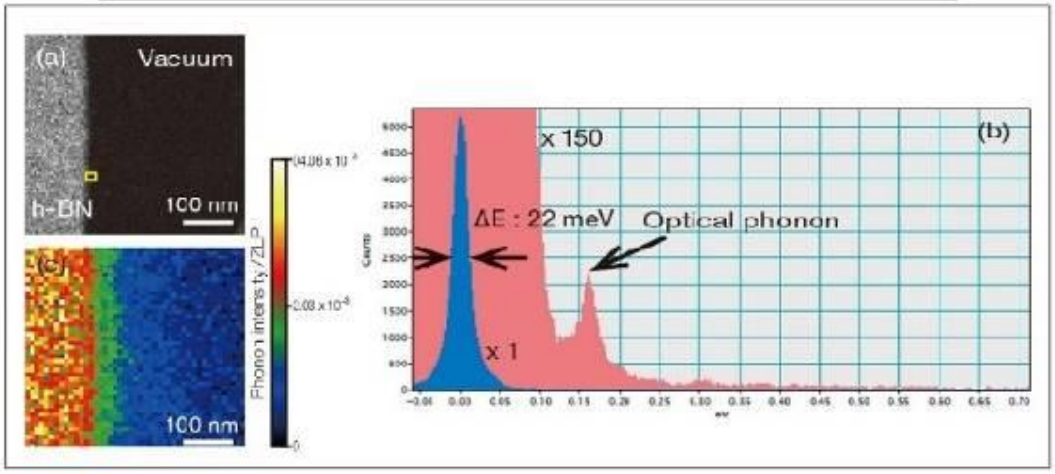

Fig.2.

Figure 2

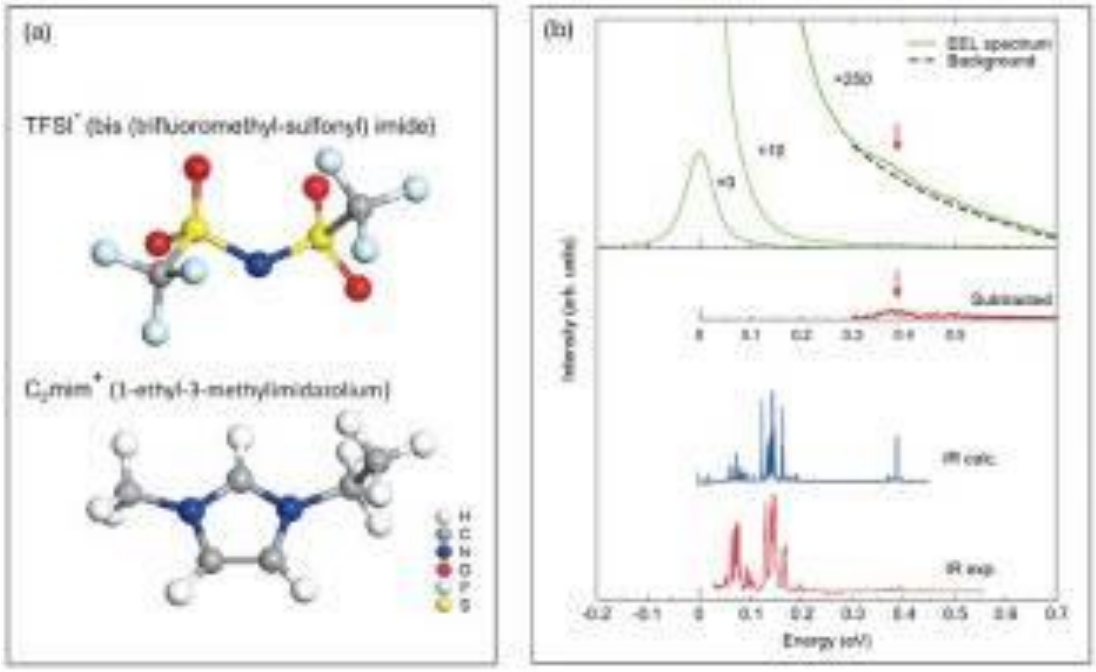

IM4.P001
Coherent light emission of GaAs in a scanning (transmission) electron microscope

M. Stöger-Pollach[1], C. Pichler[1], O. Eibl[1], K. Bukvišová[2]

[1]TU Wien, Vienna, Austria
[2]CEITEC BUT, Brno, Czech Republic

For most materials science oriented applications, incoherent cathodoluminescence (CL) is of main interest, where the recombination of electron-hole pairs yields the emission of light. However, the incoherent signal is superimposed by coherently excited photons, similar to the situation in Energy-Dispersive X-ray Analysis (EDX). In EDX two very different processes superimpose in each spectrum: Bremsstrahlung and characteristic X-ray radiation. Both processes yield X-rays, however, the origin is substantially different. Therefore, in the present CL-study we focus on the coherent emission of light, in particular Čerenkov radiation. We use a 200 µm thick GaAs sample, not electron transparent and therefore not acting as a light guide, and investigate the radiation emitted from the top surface of the sample generated by back-scattered electrons on their way out of the specimen.

Coherent light emission under electron irradiation is caused by the excitation of Čerenkov photons (CP) and by the excitation of Transition radiation. Whereas the latter is a non-relativistic effect, the prior appears as soon as the speed of a charged particle (electron) $ve-$ exceeds the phase velocity of light inside the medium cn.

In Figure 1a a CL-spectrum is shown of the 200 µm thick GaAs sample recorded with an electron dose rate of 8050 e− nm2·s and a beam energy of 120 keV. We can identify three main regions, whereof the peak at 892 nm is the most prominent one. This peak is related to the electron transitions between the conduction band and the valence band referred "main interband transition" (MIBT) peak. It can be fitted by a Gaussian function. The second most prominent part of the spectrum is a background at beyond 900 nm wavelength. This part of the spectrum is called "Čerenkov photons" (CP). The third fraction of the spectrum can be found at shorter wavelengths and is related to defect states [1]. These intensities can be explained in terms of non-radiative recombination processes which are coupled to Gallium vacancies and EL-2 defects [2] – which are understood as arsenic anti-site defects. Therefore, we call this part of the spectrum further-on "defect states related photons". For any further analysis, all recorded spectra are decomposed into these three contributions, where only the main interband transition peak is fitted by using a Gaussian function.

We investigate the position and full width at half maximum (FWHM) of the MITB as well as the intensity of the CP and the defect related photons. The varying parameters are electron dose rate, electron dose, temperature, and beam energy. We find that at elevated beam energies CP have a strong influence on the overall spectrum, because back scattered electrons on their way out of the specimen are exciting the detected signal, which is in general only scattered in forward direction.

Figure1: a) CL spectrum of GaAs decomposed into MITB, CP and defect related states, b) simulated CL spectrum dependent on the beam energy, c) intensities of CP and MITB with respect to the beam energy, d-f) temperature dependence of the CL spectrum showing the position and FWHM of the MITB, g) dependence of the intensities of the whole CL spectrum and the CP on the electron dose rate, h) electron dose dependent behavior of the MITB intensity and its FWHM.

[1] B. G. Yacobi, D. B. Holt, J. Appl. Phys. 59 (1986) R1
[2] G. Koschek, H. Lakner, E. Kubalek, Phys. Stat. Sol. A 106 (1988) 651–658.

Figure 1

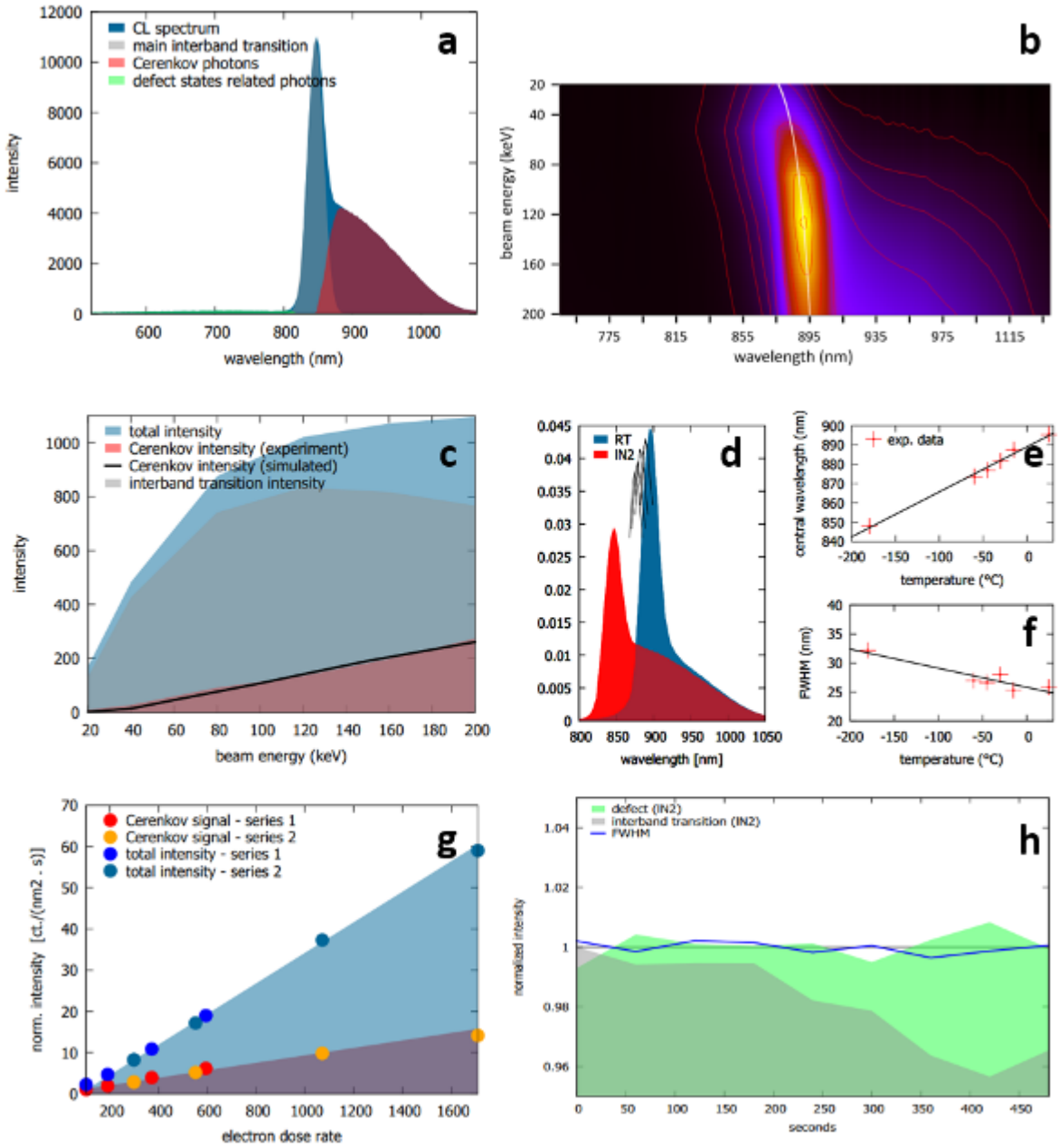
a
CL spectrum
main interband transition
Cerenkov photons
defect states related photons
intensity
wavelength (nm)
b
beam energy (keV)
wavelength (nm)
c
total intensity
Cerenkov intensity (experiment)
Cerenkov intensity (simulated)
interband transition intensity
intensity
beam energy (keV)
d
RT
IN2
wavelength [nm]
e
exp. data
central wavelength (nm)
temperature (°C)
f
FWHM (nm)
temperature (°C)
g
Cerenkov signal - series 1
Cerenkov signal - series 2
total intensity - series 1
total intensity - series 2
norm. intensity [ct./(nm2 . s)]
electron dose rate
h
defect (IN2)
interband transition (IN2)
FWHM
normalized intensity
seconds

IM4.P002
Relativistic Kramers-Kronig analysis using high energy resolution EELS

A. Eljarrat[1], W. Aggoune[1], M. Zupancic[2], Z. Galazka[2], M. Albrecht[2], C. Draxl[1,3], C. T. Koch[1]

[1]Humboldt University of Berlin, Department of Physics, Berlin, Germany
[2]Leibniz-Institut für Kristallzüchtung, Berlin, Germany
[3]European Theoretical Spectroscopic Facility (ETSF), n/a, Germany

Kramers-Kronig analysis (KKA) obtains from low-loss electron energy-loss spectroscopy (EELS) the underlying dielectric function. Conventional KKA has a limited range of application as relativistic effects such as Cerenkov loss are not included and the result implicitly relies on our ability to subtract the zero-loss peak (ZLP) tails and suppress plural-scattering effects.

Following our recent development of a relativistic KKA (rKKA) algorithm [1], we present a new version that processes the full raw spectrum as a whole at each iteration. This is achieved by including the effect of ZLP and plural-scattering using Fourier-logarithmic deconvolution and its forward analogue, Fourier-exponential convolution operations. As in the previous version, the Kroeger formulation of the surface and bulk full-relativistic double differential cross section (DDCS) is employed.

In this contribution, we report on the application of this formalism for stand-alone measurement of the dielectric function and opto-electronic properties from low-loss EELS obtained in homogeneous regions of thin film samples. This new relativistic algorithm is based on a forward model of the recorded low-loss EELS signal. Hence, it has been designed and thoroughly tested using model-based realistic synthetic data, including; bulk and surface relativistic effects in thin film samples; the effect of ZLP tails and plural scattering; and detector issues such as noise or gain intensity offset.

Relativistic KKA has also been applied on experimental data from a variety of semiconductor materials. In particular, we present STEM-EELS data from relevant semiconductor materials obtained using the Nion HERMES instrument at HU-Berlin.

As portrayed in Figure 1, we investigate the opto-electronic properties of BaSnO3 single crystal grown from the melt [2] using the electron beam to reveal the indirect band gap of this material, at around 3 eV. In order to perform this measurements, relativistic loss needs to be considered as it could affect the result. By acquiring the EELS data at a lower voltage (60 kV) we can reduce the impact of bulk relativistic loss. At the same time, using our rKKA, the dielectric function retrieved from EELS measurements shows excellent agreement with simulations performed using the Bethe-Salpeter equation (BSE) formalism.

Figure 2 is showing experimental EELS from a crystalline Silicon (211) sample with a resolution of 30 meV. In this example, the ZLP deconvolution and relativistic correction obtained using the new version of rKKA reveals the indirect band gap onset at around 1.1 eV. Our analysis indicates that the native oxide layer has a strong impact on the retrieved dielectric properties. We currently focus our efforts in obtaining an ultraclean c-Si sample. For this analysis it is also imperative to obtain spectra at high energy resolution and reducing the ZLP tails. Our instrumental set-up is especially adequate for this task, since it combines a monochromated cold-FEG electron beam and a Dectris hybrid pixel direct-detection camera. Such experimental set-up allows to acquire EELS spectra with energy resolution below 10 meV.

[1] A. Eljarrat and C.T. Koch Ultramicroscopy 206, 112825, 2019.
[2] Z. Galazka et al. J. Phys.: Condens. Matter. 29 (2017) 075701.

Figure 1: dielectric function of BaSnO3 obtained from EELS measurement and BSE simulation.

Figure 2: Valence EELS of c-Si 211 specimen. The energy-loss function (ELF) is obtained after applying ZLP deconvolution to obtain a single scattering distribution (SSD) and relativistic correction (Scor). The SSD reveals the position of the band structure excitations, where the expected position of the indirect band gap indicated with a dashed line corresponds very well with the observed onset.

Figure 1

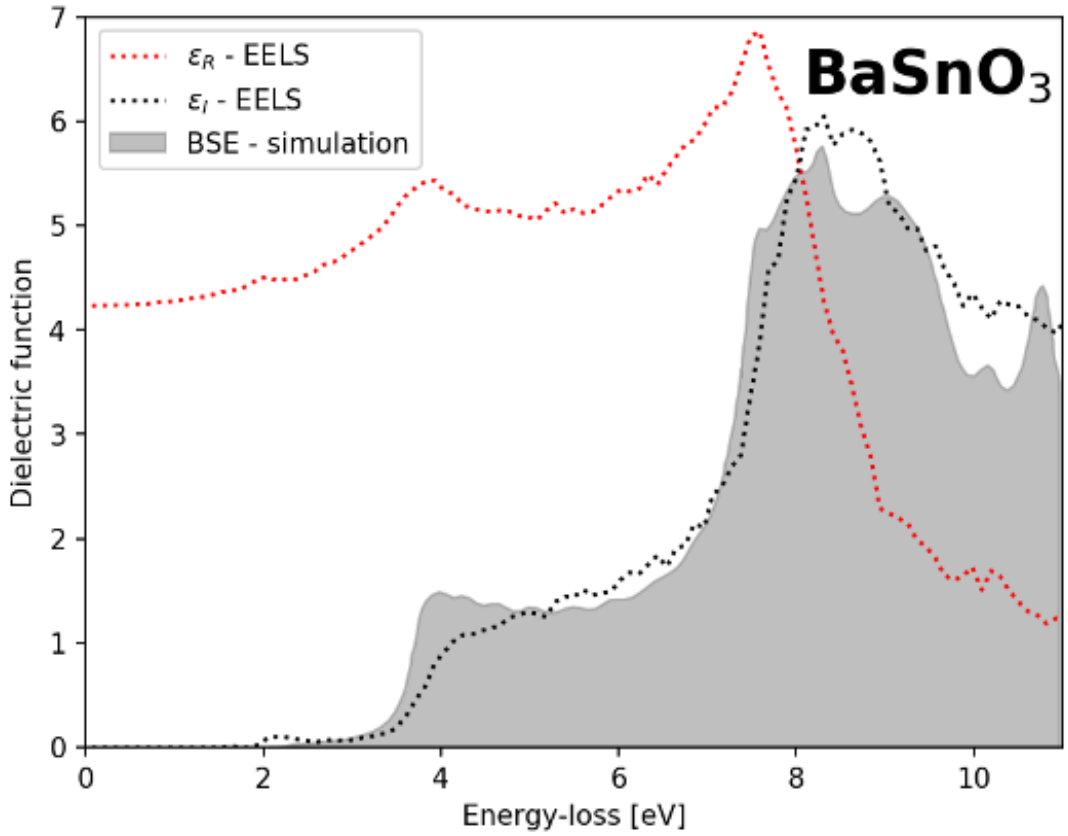

Figure 2

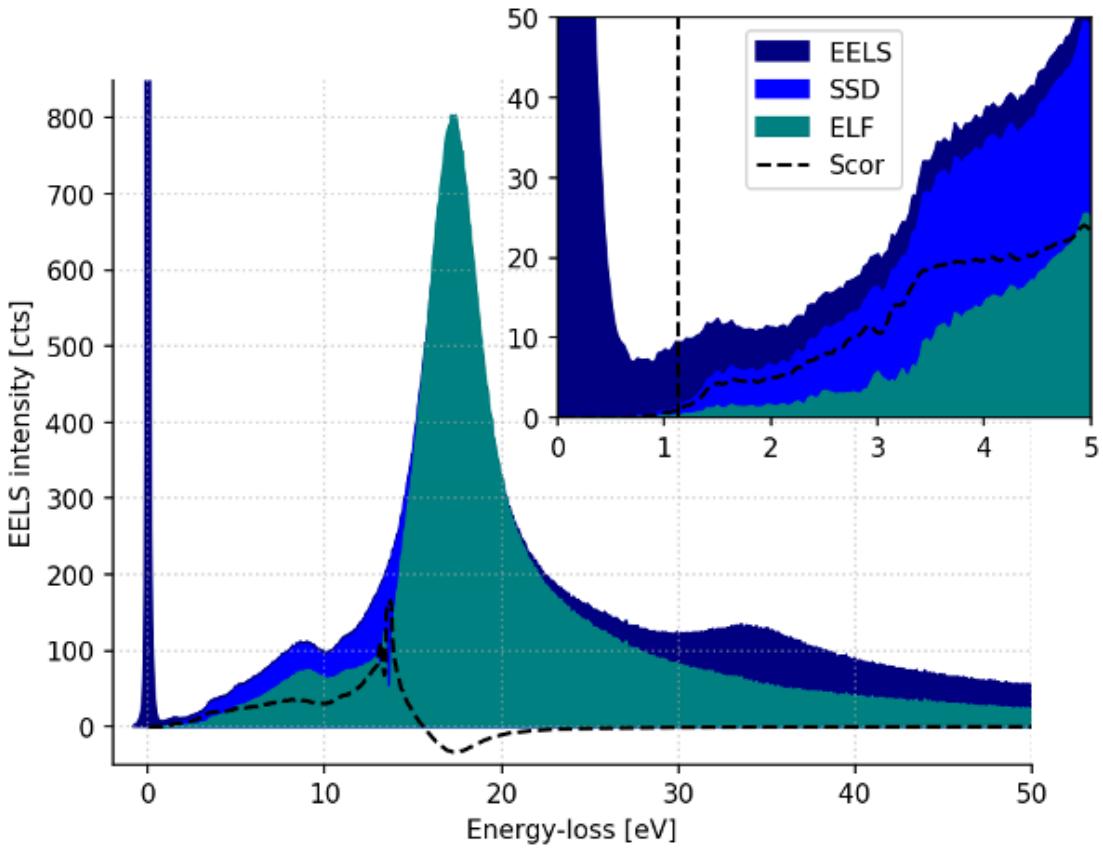

IM4.P004
Low-energy excitations in transition-metal oxides by STEM-EELS spectromicroscopy

C. P. Su[1], X. Li[1], K. Ruotsalainen[2], O. Stéphan[1], A. Nicolaou[3], A. Gloter[1]

[1]Laboratoire de Physique des Solides, Université Paris-Saclay, Orsay, France
[2]Helmholtz-Zentrum Berlin für Materialien und Energie GmbH, Hahn-Meitner-Platz 1, Berlin, Germany
[3]Synchrotron SOLEIL, L'Orme des Merisiers Saint-Aubin, Gif-sur-Yvette, France

The transition metal oxides exhibit a variety of interesting properties, such as ferroelectricity, magnetism, superconductivity, etc. The atomic structural degrees of freedom and the electron"s degrees of freedom (charge and spin) lead to various phenomena through phase transitions. More additional properties emerge from the coupling of these orders. All these orders can be studied through collective excitations (phonon, plasmon, magnon).

By scanning transmission electron microscopy (STEM) with monochromator, the energy resolution can go as low as 5meV [1], and such low-energy excitations can thus be investigated by electron energy-loss spectrum (EELS). We focus on the low-energy excitations, *id est*, the plasmon, the metal-metal (d-d) and charge-transfer (p-d) excitations on the transition-metal oxides. Combining the spatial images and the low-energy excitations is able to understand the coupling between structures and electronic excitations [2, 3].

In this work, we discussed about the d-d transitions on transition metal oxides, such as NiO and $SrVO_3$. The observations of d-d excitations by EELS are shown in Figure 1. The behaviors of these two samples are very different, an atomic type d-d excitation on NiO (no dipolar contribution, weak surface delocalization in aloof beam) and a plasmonic type d-d excitation on $SrVO_3$ (dipolar contribution, strong surface delocalization in aloof beam). Afterwards, how about these behaviors on the nanostructures? Figure 2 shows that the nanostructures of $SrVO_3$ exhibit the Fabry-Perot type d-d based surface plasmon modes. The surface plasmons modes at different energies are visible for several rod-type geometries, at the half-rod; at the slit that is a complementary system with a rod according to Babinet"s principle [4]. The relationship between the geometry of the nanostructures and the measured EELS low-energy excitations offers a way to retrieve meaningful physical parameters for the transition metal oxide. With the possibility of keeping some spatial resolution, it can contribute to a more complete understanding of transition-metal oxides physic, in complement to more traditional core loss excitations (transition-metal $L_{2,3}$, O-K edges).

Figure 1: (a) Disperson curve and (b) bulk/aloof measurements of NiO and $SrVO_3$.

Figure 2: The Fabry-Perot type d-d based surface plasmon modes in $SrVO_3$ of (a) half-rod with q-dispersion measurements and (b) slit nanostructures.

Refences:
[1] L. Krivanek et al., Vibrational spectroscopy in the electron microscope, *Nature* 514, 209 (2014).
[2] Gloter et al., Probing non-dipole allowed excitations in highly correlated materials with nanoscale resolution, *Ultramicroscopy* 109, 1333 (2009).
[3] Mkhitaryan et al., Can copper nanostructures sustain high-quality plasmons, *Nano letters,* (2021).
[4] B. Ögüt et al., Hybridized metal slit eigenmodes as an illustration of Babinet"s principle, *ACS Nano* 5, 6701 (2011).

Figure 1

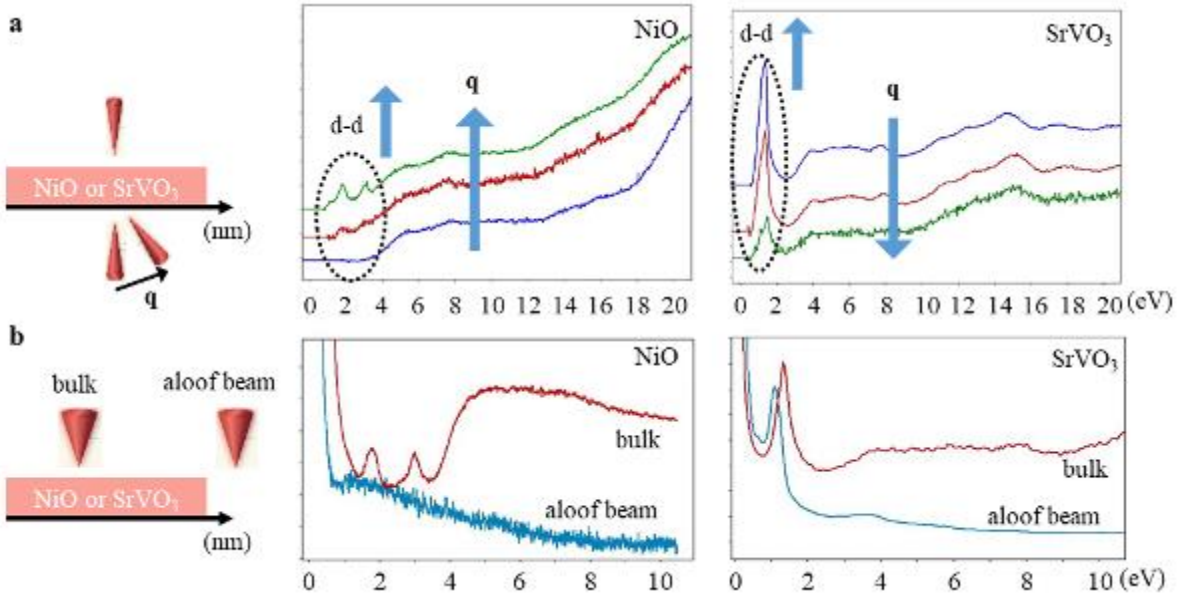

Figure 2

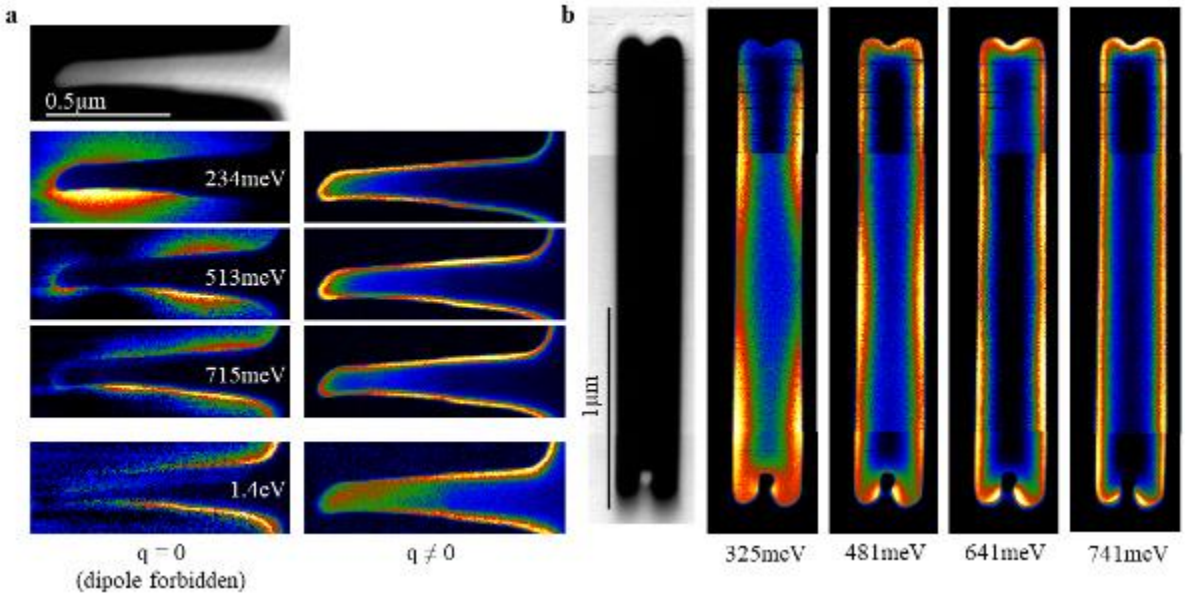

IM5.003
SPED and SNBED investigations on dominant kinks in GaP nanowires grown in an *in situ* (S)TEM gas cell holder

D. P. Krug[1], M. Widemann[1], S. Ahmed[1], F. Gruber[1], A. Beyer-Leser[1], K. Volz[1]

[1]Philipps-University Marburg, Structure and Technology Research Laboratory, Marburg, Germany

Nanowires (NW), especially those consisting of III/V semiconductor materials, are used for many technical applications, like photonic devices, e.g. LEDs, photodetectors, lasers, and solar cells [1]. A detailed understanding of the growth behavior such as growth rate, growth direction, or kinking mechanisms is required to develop such devices. A widely used fabrication process for these materials is metal-organic vapor phase epitaxy (MOVPE). *In-situ* (scanning) transmission electron microscopy ((S)TEM) allows the investigation of dynamic processes, which occur during growth. Gas environmental cells and heating holders enable the supply of gases while heating the sample, making conditions comparable to MOVPE-process realizable in any TEM [2]. To this end, a commercially available Protochips Inc. *in-situ* system has been modified. To allow the usage of toxic and pyrophoric gases, like the precursor gases used in MOVPE growth, gas mixing, appropriate gas monitoring, and gas scrubbing systems have been added [3]. A double Cs-corrected JEOL JEM 2200FS operating at 200 kV was used for the TEM observations. Samples were prepared by depositing Au nanoparticles (NP) from a suspension droplet onto a micro electro mechanical system (MEMS) chip. Growth took place through vapor-liquid-solid (VLS) growth mechanism [4], catalyzed by the Au NP. Precursors used for GaP NW VLS growth were tertiarybutylphosphine and trimethylgallium at partial pressures between 10-1 and 10-2 hPa and a V/III ratio of around 10. Growth was performed at a temperature of 450 °C. A JEOL JIB- 4601F SEM was used to measure kink angles which can occur in GaP NW. Growth in gas environmental cells comes with several challenges, like the gas cell holder's single tilt capability, the diffuse signals from the SiN windows, and a gas volume in the cell with elevated pressure. This technical framework often makes it challenging to achieve proper images of the sample during growth and post-growth investigations. Because of that, a special holder, capable for a single MEMS chip, was designed and fabricated in-house for SPED (scanning precession electron diffraction) and SNBED (scanning nanobeam electron diffraction) investigations of the kinked NW. These investigations were conducted using NanoMegas's ASTAR system [5] installed at a JEOL JEM 3010 operating at 300 kV.

Our results show that straight growing NW change their growth directions after random distances by incorporating kinks as it is shown by a TEM image in [Figure1 (a)]. Statistics of kink angles show the different predominance of distinct angles related to corresponding formation mechanisms of NW kinks, as shown as a histogram in [Figure2]. SPED and NBED investigations give insights into the kinking mechanisms of the NW by mapping lattice orientation changes in growth direction as it is shown in [Figure1 (b)]. We present the developed MEMS chip holder and the mechanism of kinking, investigated by SPED and SNBED.

Figure 1: TEM image of a kinked GaP-NW a) and corresponding SNBED orientation map b)

Figure 2: Histogram of the angular distribution of kinks in GaP-NW

References:
[1] R. Yan, et al., Nature Photonics 3 (2009), pp. 569-576.
[2] L. F. Allard, et al., Microscopy and Microanalysis 18.4 (2012), pp. 656-666.
[3] R. Straubinger, et al., Microscopy and Microanalysis 23.4 (2017), pp. 751-757.
[4] R. S. Wagner, W. C. Ellis, Applied Physics Letters 4 (1964), pp. 89.
[5] E. Rauch, et al., Z. Kristallogr. 225 (2010) pp. 103-109.

Figure 1

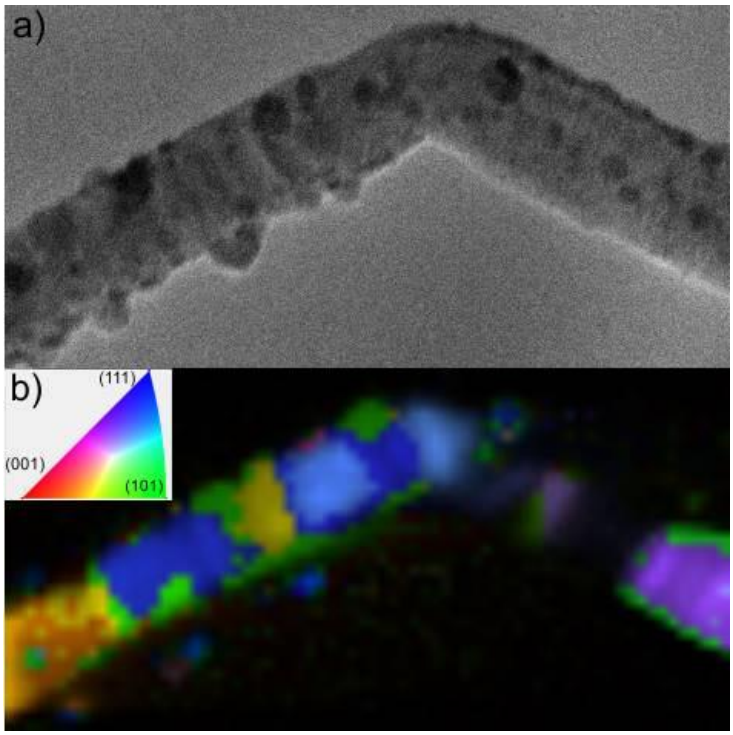

Figure 2

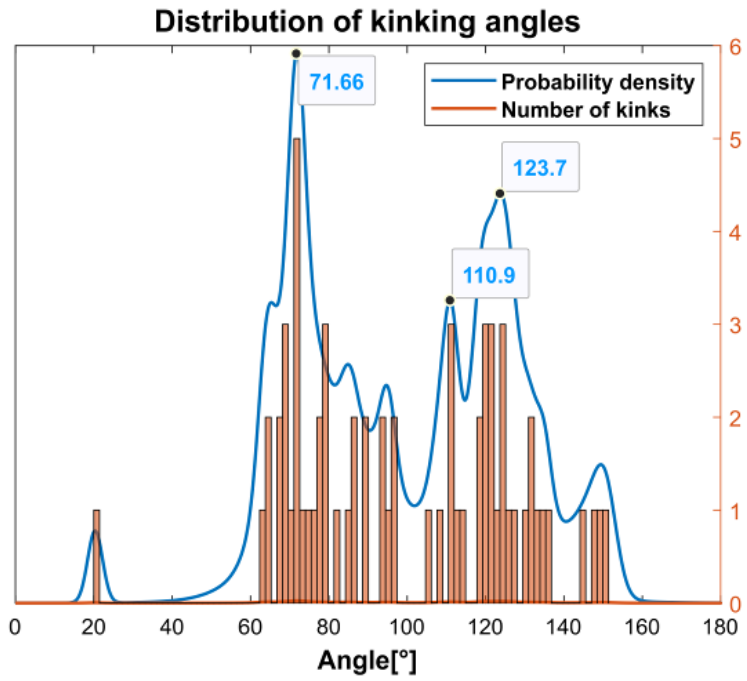

IM5.004
In situ nanoscale characterisation of electrical and magnetic properties of 3D nanostructures by combination of AFM, SEM and FIB

C. Schwalb[1], J. Hütner[1,2], H. Frerichs[1], M. Wolff[1,2], R. Winkler[3], G. Fantner[4], H. Plank[3]

[1]Quantum Design Microscopy GmbH, Darmstadt, Germany
[2]GETec Microscopy GmbH, Vienna, Austria
[3]Graz University, Institue for Electron Micrsocopy and Nanoanalysis, Graz, Austria
[4]Swiss Federal Institute of Technology Lausanne (EPFL), Lausanne, Switzerland

Combining different analytical methods into one instrument is of great importance for the simultaneous acquisition of complementary information. Especially the in-situ combination of scanning electron microscopy (SEM) and atomic force microscopy (AFM) enables completely new insights in the micro and nano-world. In this work, we present the unique in-situ combination of scanning electron and ion microscopy (SEM/FIB) and atomic force microscopy (AFM) for nanoscale characterization [1-3].

We will present a variety of case studies to highlight the advantages of interactive correlative in-situ nanoscale characterization for different materials and nanostructures. We show results for *in-situ* electrical characterization by conductive AFM for 2D materials (Figure 1) as well as electrostatic force microscopy (EFM) of piezoceramic films.

In addition, we will present first results for the in-situ characterization of magnetic nanostructures by combination of SEM and high-vacuum magnetic force microscopy (MFM). SEM enables to identify grain boundaries in, e.g., duplex steel samples, where the magnetic properties at the grain boundaries can be directly analyzed via MFM to characterize the magnetic properties with nanometer resolution and distinguish between ferromagnetic and paramagnetic domains (see Figure 2).

In a further step, we demonstrate how in-situ correlative analysis with the AFSEM in an SEM can be extended into the third dimension to measure nanomechanical properties of soft material. To achieve this, FIB slicing and mapping of nanomechanical properties using the AFSEM is performed in repetitive steps to build up a 3-dimensional elasticity map.

Based on the broad variety of applications regarding the nanoscale characterization of different materials and devices we anticipate that correlative analysis by combination of in-situ AFM and SEM/FIB will be one of the driving characterization tools in the future.

[1] D. Yablon *et al.*, Microscopy and Analysis 31(2) 14-18 (2017)
[2] J. Kreith *et al.*, Rev. Sci. Instr**.** 88 053704 (2017)
[3] S.H. Andany *et al.*, Beilstein J. Nanotechnol**.** 11**,** 1272-1279 (2020)

Figure 1

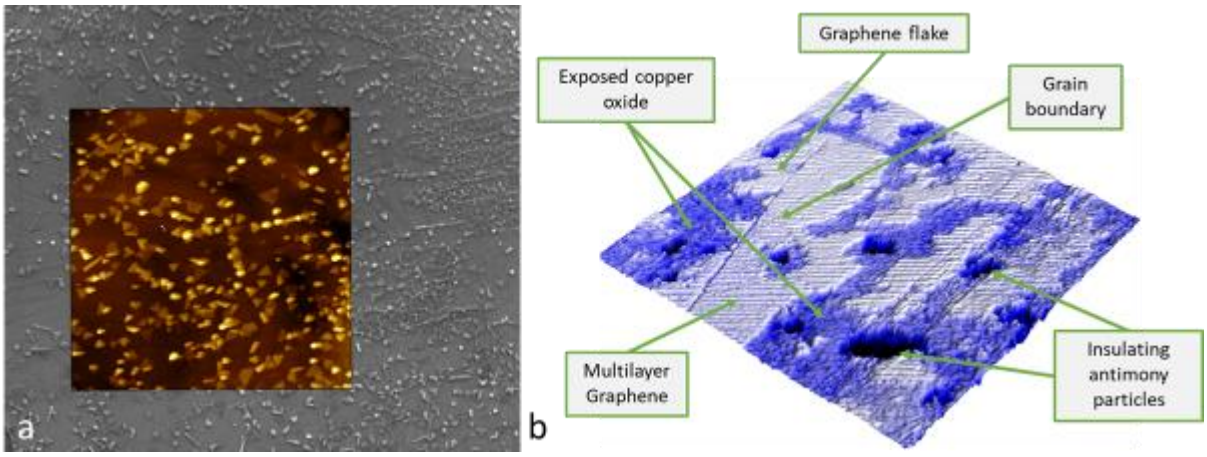

Figure 2

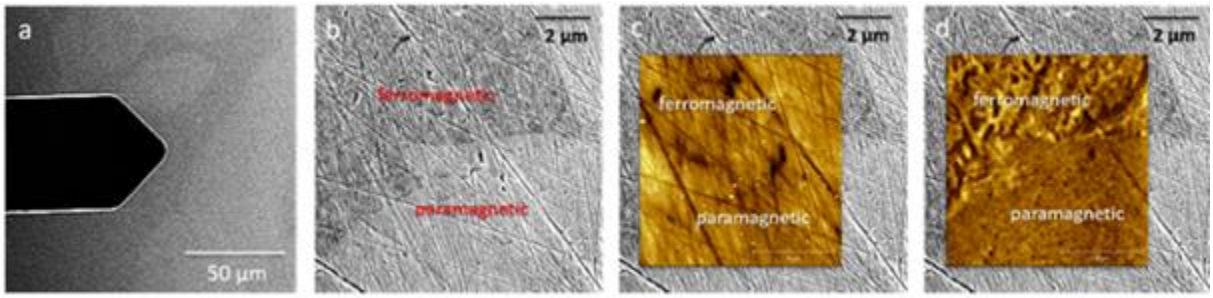

Figure 3

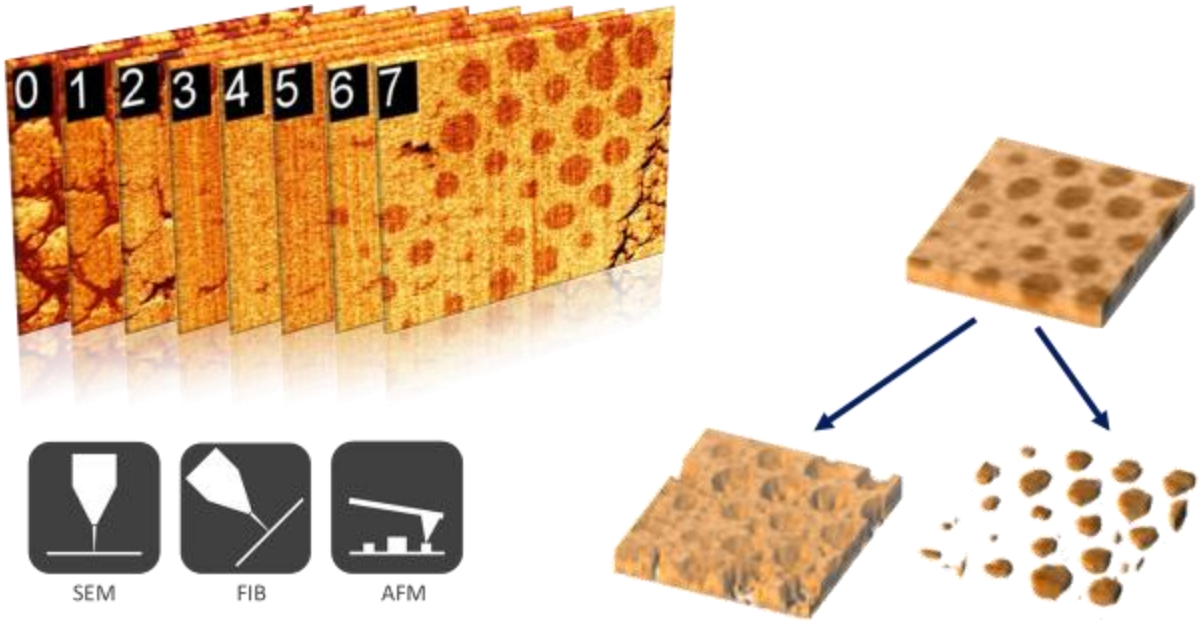

IM5.005
First cryo-electron microscopy facility in Slovenia enables cutting-edge research in the wider region

M. Kisovec[1], M. Podobnik[1]

[1]National Institute of Chemistry, Department of Molecular Biology and Nanobiotechnology, Ljubljana, Slovenia

Introduction: The field of cryo-electron microscopy (cryo-EM) has seen rapid development and significant technical improvements over the past decade. Perhaps the most important have been advances in sample preparation, direct electron detectors, data processing and data analysis, for which the Nobel Prize in Chemistry was awarded in 2017. Cryo-EM has become an important tool to gain structural insights into cells, organelles, protein complexes, proteins, and more recently peptides and small crystalline molecules. At atomic or near- atomic resolution cryo-EM offers a unique combination of features. In this talk, I will mostly focus on our experience with Micro Electron Diffraction (MicroED) method.

Objectives: A local cryo-electron microscope is essential to remain competitive in the field of structural research. In order for cutting-edge research to flourish in Slovenia and the wider region, the acquisition of such equipment was of paramount importance. Through the collaboration of several partners, the first cryo-EM microscope was acquired in late 2019 and is now installed at National Institute of Chemistry in Slovenia. The automated 200 kV cryo-EM microscope will enable researchers in Slovenia and also in the wider south-eastern EU region to accelerate their research and become more competitive in the international environment.

Materials & methods: Glacios™ from Thermo Fisher Scientific, a 200 kV microscope with the Direct Electron Detector (DED), which enables Single Particle Analysis (SPA), tomography (cryo-ET) and MicroED, was selected. This particular microscope has the distinction of being one of the first cryo-EM microscopes in the region to offer the capability of electron diffraction on microcrystals. This cryo-EM allows researchers to test and screen various samples (isolated proteins, (synthetic) protein complexes, biological membranes, viruses and virus-like particles, nanoparticles, etc.) as well as perform sample optimization for final data collection, which can be performed either at this microscope or at other cryo-EM facilities that provide access to the state-of-the-art 300 kV machines.

The facility is also equipped with everything needed for grid and sample preparation (e.g. Glow Discharge machine and a Vitrobot vitrification robot). Local IT infrastructure has also been set up to enable data processing, and access to remote (Slovenian) HPC resources enables even faster and more thorough data analysis.

Results: This cryo-EM facility enables the determination of three-dimensional structures of (macro)molecules and their complexes at atomic resolution, and also serves as a stepping stone to apply for data acquisition at the 300 kV microscopes abroad. The facility is operated by the facility manager and a group of trained researchers using all three methodological approaches (SPA, cryo-ET, MicroED) and is in operation around the clock. The facility also successfully collaborates with the industrial partners.

Conclusion: The fully functional cryo-EM facility at the National Institute of Chemistry, Ljubljana, Slovenia, enables the determination of three-dimensional structures of biological (macro)molecules and their complexes at atomic resolution, as well as samples from materials science. The research projects are mainly basic (academic) in nature, but the collaboration with industry is fruitful. Interest in the use of the Glacios microscope comes not only from Slovenia, but from the entire region.

IM5.006
Optimising a workflow for cryo-TEM tomography – fabrication and transfer of frozen hydrated lamella

D. Pinkas[1], S. Zachej[2], J. Havrankova[2], H. Raabova[1], E. Vlčák[1], S. Mimietz-Oeckler[3], R. Kirmse[3], P. Hozák[4]
V. Filimonenko[1,4]

[1]Institute of Molecular Genetics of the Czech Academy of Sciences, Core Facility for Electron Micrtoscopy, Prague, Czech Republic
[2]TESCAN ORSAY HOLDING, a.s., Prague, Czech Republic
[3]Leica Mikrosysteme GmbH, Vienna, Austria
[4]Institute of Molecular Genetics of the Czech Academy of Sciences, Laboratory of Biology of the Cell Nucleus, Prague, Czech Republic

Electron microscopy provides unique insight into the ultrastructure of cells and tissues. Preservation of sensitive biological samples in close-to-native state is crucial for obtaining quality data. Vitrification with subsequent observation in cryo conditions in an electron microscope is a valuable approach. Cryo-electron tomography is a method of choice to gain volume information about the object. A serious technical limitation is the thickness of the object. While small objects, like bacteria, viruses, isolated cellular organelles, or thin areas of cytoplasm at the edge of a eukaryotic cell can be imaged directly, bigger parts of cells or tissues need to be thinned before observation. Fabrication of a thin FIB-milled lamellae from a frozen hydrated sample with subsequent cryo-transfer and tilt series acquisition in cryoTEM is currently the best workflow introducing minimal artefacts into the sample compared to other available techniques. The workflow is technically challenging and needs significant skills and optimization of all steps to produce homogeneously thin lamella and to avoid heat damage, mechanical damage, and surface contamination of the lamella.

We demonstrate optimization of the semi-automated cryo TEM lamella preparation workflow on yeast, mammalian and plant samples using TESCAN FIB-SEM Cryo AMBER system equipped with the Leica VCT500 cryo transfer stage for operation in cryogenic conditions. The use of a side-entry TEM cryoholder makes the workflow more universal and accessible for a broader range of microscopy workplaces, compared to autoloader-equipped systems that are currently used in most cases.

Acknowledgements: This project is supported by MEYS CR (LRI Czech-BioImaging LM2018129, COST Inter-excellence internship LTC19048), OPVVV (CZ.02.1.01/0.0/16_013/0001775), IMG grant (RVO: 68378050).

IM5.P001
Assembly for correlation analysis of samples using cryogenics scanning electron microscopy (cryo-SEM) and Raman micro-spectroscopy

T. Laznicka[1], K. Hrubanova[1], J. Jezek[1], S. Bernatova[1], K. Mrazova[1], S. Obruca[2], P. Zemanek[1], V. Krzyžánek[1]

[1]The Czech Academy of Sciences, Institute of Scientific Instruments, Brno, Czech Republic
[2]Brno University of Technology, Faculty of Chemistry, Brno, Czech Republic

In this project, our main motivation was to establish an assembly that allows handling and an attachment of commercial holders used for the observation of deep-frozen samples by cryogenic scanning electron microscopy (cryo-SEM) and their analysis at low temperature using the Raman micro-spectrometer. Our assembly allows movement of the sample using a sliding mechanism and measuring the liquid cryogen level. The LabVIEW software environment was used to determine the cryogen level and sample displacement. Besides, we present a possibility of correlative measurement using these two techniques for various biotechnological applications.

The assembly was specifically designed for the analysis of deep-frozen samples using a Raman micro-spectrometer InVia (Renishaw) at low temperatures with the possibility of specifying the area of interest. Moreover, it allows the attachment of various commercial sample holders. As a result, it meets its compatibility with the most commercially available cryo-SEM systems.

Our assembly is consisting of a main Dewar vessel, which contains cryogenic fluids (LN2). The stage was made by 3D printing and enables 3 positions for different types of sample holders used in cryogenic sample preparation systems (Leica microsystems, Gatan and Quorum technologies). The stage is located in the Dewar vessel below the liquid level. This Dewar is connected to a piezoelectric stage allowing *XY* movement. The stage is placed in the groove of the Raman spectrometer table, which is connected to a linear translation providing displacement in the *Z* direction. To minimize contamination caused by condensation of the air humidity, the Dewar is covered with transparent Plexiglas (Figure 1a). A Capton foil is placed on the spectrometer objective to reduce additional moisture contamination.

Our home-made system is used primarily in biotechnological applications. It allows a more efficient correlation between individual analyses of microorganisms containing biopolymer particles. For example, several representatives of soil microorganisms, such as bacteria *Cupriavidus necator* H16, are able to produce polyhydroxyalkanoates (PHA) [1]. PHAs are polyesters of hydroxyalkanoic acids which serve as carbon and energy storage. Moreover, PHAs attract attention as an ecological alternative to petrochemical plastics which can be biotechnologically produced from waste streams of various industrial processes.

It was proved that the combination of Raman spectroscopy with the cryo-SEM technique can provide a deeper insight into the chemical and mechanical properties of intracellular polymeric granules inside the bacterial cells [2]. We believe that this study will be of significant assistance to the research groups being involved in bacterial strains which accumulate PHA. Presented results are convincing enough to warrant more extensive investigations with larger sets of bacterial strains to evaluate the combination of described techniques.

References:
[1] Obruca, S. at al, PLoS ONE, 2016, 11(6), e0157778
[2] Kucera, D. at al, Applied Microbiology and Biotechnology, 2016, 100(3), pp. 1365–1376

The research was supported by the Technology Agency of the Czech Republic (TN01000008) and the Czech Academy of Sciences (MSM100652102).

Figure 1: a) Cross-section of the cryo assembly for Raman spectrometer, b) Testing of the experimental set-up, c) Spectral analysis of the *C. necator* H16 containing PHAs granules measured by cryo-Raman micro-spectrometer.

Figure 1

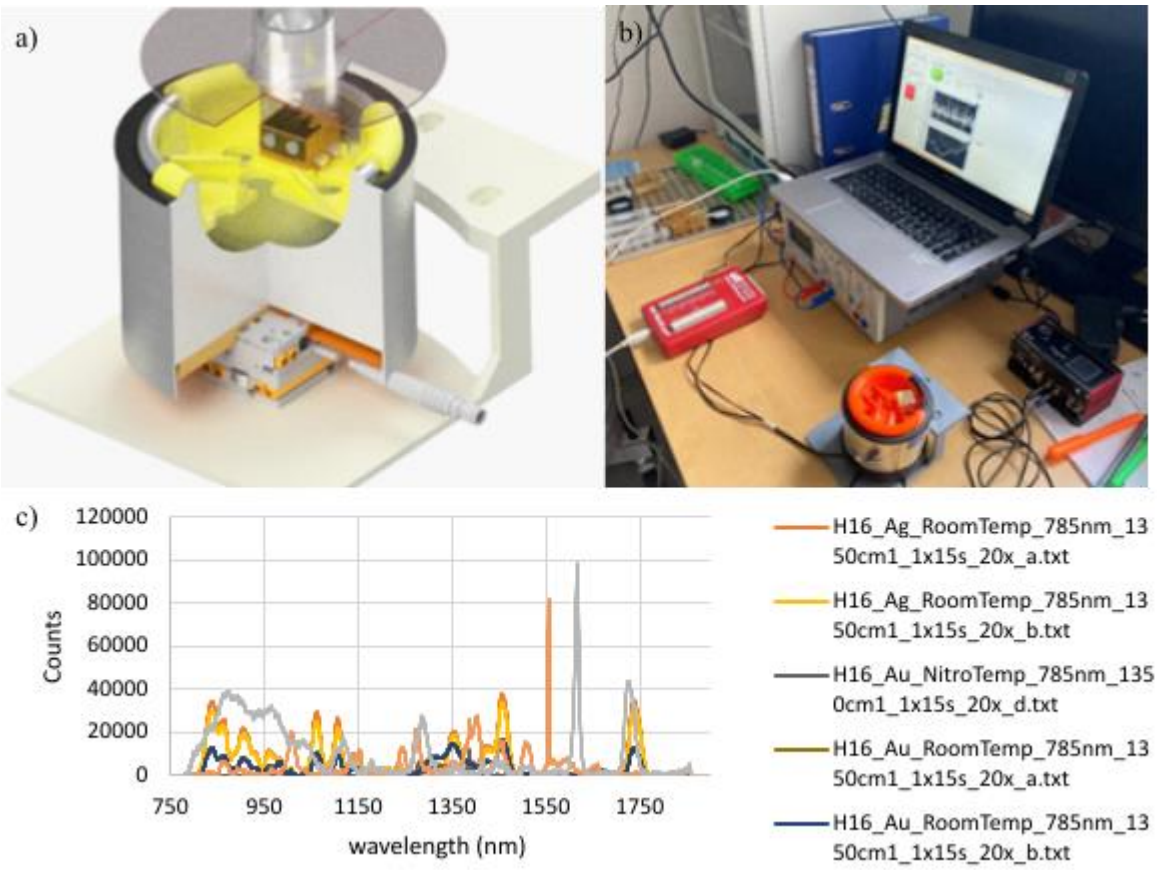
a)
b)
c)
120000
100000
80000
60000
40000
20000
0
Counts
750
950
1150
1350
1550
1750
wavelength (nm)
H16_Ag_RoomTemp_785nm_1350cm1_1x15s_20x_a.txt
H16_Ag_RoomTemp_785nm_1350cm1_1x15s_20x_b.txt
H16_Au_NitroTemp_785nm_1350cm1_1x15s_20x_d.txt
H16_Au_RoomTemp_785nm_1350cm1_1x15s_20x_a.txt
H16_Au_RoomTemp_785nm_1350cm1_1x15s_20x_b.txt

IM5.P002
Usability of lanthanide salts as alternatives to uranyl acetate for negative stain single particle analysis

E. Ďurinová[1,2], Z. Gardian[1,2]

[1]Biology Centre, Czech Academy of Sciences, Institute of Parasitology, České Budějovice, Czech Republic
[2]University of South Bohemia in Ceske Budejovice, Faculty of Science, České Budějovice, Czech Republic

Negative stain single particle analysis is a useful screening technique for cryo-EM. Uranyl acetate (UAc) is the most common staining agent providing reliable contrast and stability. However, the usage of UAc brings certain difficulties. Firstly, UAc is a super toxic chemical and regular exposure especially to the solid state is a health risk. Consequently, the usage of UAc is being restricted worldwide due to its toxic and radioactive properties. In this study, we focus on evaluation of different lanthanide salts as safer alternatives to UAs in RT single particle analysis.

We chose three widely available compounds showing reliable results in standard ultrathin section preparation – samarium, neodymium, and europium acetates. These staining agents were used to visualize two different macromolecules – symmetrical water soluble helicase P4 (~6 nm size) and an asymmetric membrane protein PSI-LHCI (~ 16 nm size). The 2D classification was compared to that obtained from a standard UAc staining. We evaluated contrast and overall usability.

We provide detailed comparison of the obtained contrast and discuss the stain stability upon electron exposure and required adjustments in staining procedure. However, all three tested lanthanide stains show promising usability on both sample macromolecules.

This project was supported by projects:
Czech-BioImaging *LM2018129 and cz.02.1.01/0.0/0.0/13_013/0001775* funded by MEYS CR and ERDF.

Figure 1: A) Crystal structure of P4 protein of bacteriophage PHI8 (resolution 2.79 Å)[1], B) 2D class obtained from single particle analysis of the P4 protein stained with uranyl acetate, C) 2D class of the P4 protein stained with neodymium acetate

[1] El Omari K, Meier C, Kainov D, Sutton G, Grimes JM, Poranen MM, Bamford DH, Tuma R, Stuart DI, Mancini EJ. Tracking in atomic detail the functional specializations in viral RecA helicases that occur during evolution. Nucleic Acids Res. 2013 Nov;41(20):9396-410. doi: 10.1093/nar/gkt713. Epub 2013 Aug 11. PMID: 23939620; PMCID: PMC3814363.

Figure 1

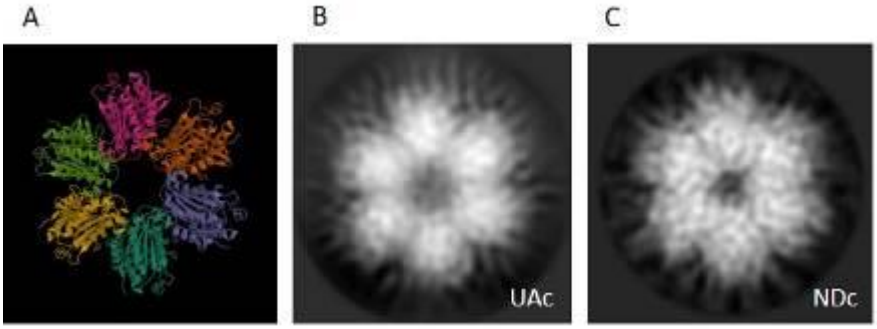

IM5.P003
The combined use of SEM, EPMA and FIB for the characterisation of novel biomaterials for bone regeneration

M. Essani[1], H. Moussi[2], B. Charbonnier[2], J. Le Bideau[1], P. Weiss[2], P. Abellan[1]

[1]Université de Nantes, CNRS, Institut des Matériaux Jean Rouxel (IMN), Nantes, France
[2]Université de Nantes, INSERM U1229, Regenerative Medicine and skeleton Research Lab (RMES), Pays de loire, Nantes, France

Bone has the innate ability to spontaneously heal without scarring through complex physiological processes [1]. Unfortunately, this regenerative ability is limited, and surgical interventions including the filling of bone defect are often required to achieve healing [2]. One of the therapeutic strategies used for bone regeneration consists on the injection of biomaterials embedded with bone marrow mesenchymal stem cells onto bone defect. Most widely used biomaterials include calcium phosphate (CaP) injectable bone substitutes (IBS). Despite significant advantages over other bone substitutes, IBS still lacks of suitable biodegradation rate and bioactivity which is partly due to the absence of an appropriate macroporous interconnected network and the presence of sintered CaP particles. Recent developments at RMES laboratory allowed for the elaboration of macroporous IBS based on reactive CaP powders and hydrogel matrix [2]. Biological *in vivo* evaluation showed that the IBS biodegradation and the regeneration of a critical-sized defect depended on the nature and macroarchitecture of both the hydrogel and the inorganic phase of the implanted IBS. Correlating the biological response to the chemical and structural parameters of the biomaterial would allow for unveiling new prospects for the design of clinically relevant biomaterials. On the other hand, the characterization of the biomaterial-stem cells interactions (or host-biomaterial) will provide insight into parameters impacting the biomaterial"s biological performances.

Among advanced tools that were reported as efficient for chemical and structural analysis of materials exhibiting complex structures include the use of focused ion beam (FIB) and scanning electron microscopy (SEM) [3]. The analysis consists on serial sectioning using FIB and imaging with SEM which enables obtaining a 3D representation of the material microstructure [3]. Other studies showed the advantages of combining FIB, SEM and electron probe microanalysis (EPMA) for morphological and chemical characterization of samples [4]. These techniques can be substantially used to characterize both the hierarchical structure and chemical properties of IBS. Nevertheless, attention must be paid when applying such techniques to beam sensitive samples such as biomaterials.

In this work, we present our latest results of analysis with FIB, SEM and EPMA on reference biomaterials. A first analysis was performed on a CaP - IBS mixed with gelatin, showing a highly porous structure (Fig 1). Serial sectioning of the region of interest in the sample was further performed with FIB along with imaging by SEM and energy dispersive spectroscopy (EDS) mapping. This enables obtaining a 3D representation of both microstructure and elemental distribution inside the mixture (Fig 2) which can provide a clear view on 3D pore morphology, pores connectivity inside the sample as well as internal diffusion of all elements.

Analyses will be performed in cryogenic condition, which, in addition of protecting the biological samples, may allow for the observation of cell-biomaterial interactions.

References:
[1] A. Oryana, et al. (2015). Biomed Environ Sci, Vol 28, pp. 57-71.
[2] I. Lodoso-Torrecilla et al. (2021). Acta Biomaterialia, 119, pp 1-12.
[3] M.A. Groeber et al. (2006). Materials Characterization, 57, pp. 259-273.
[4] M. Taheri et al (2012), Corros. Sci., 59, pp. 222-228.

Figure 1

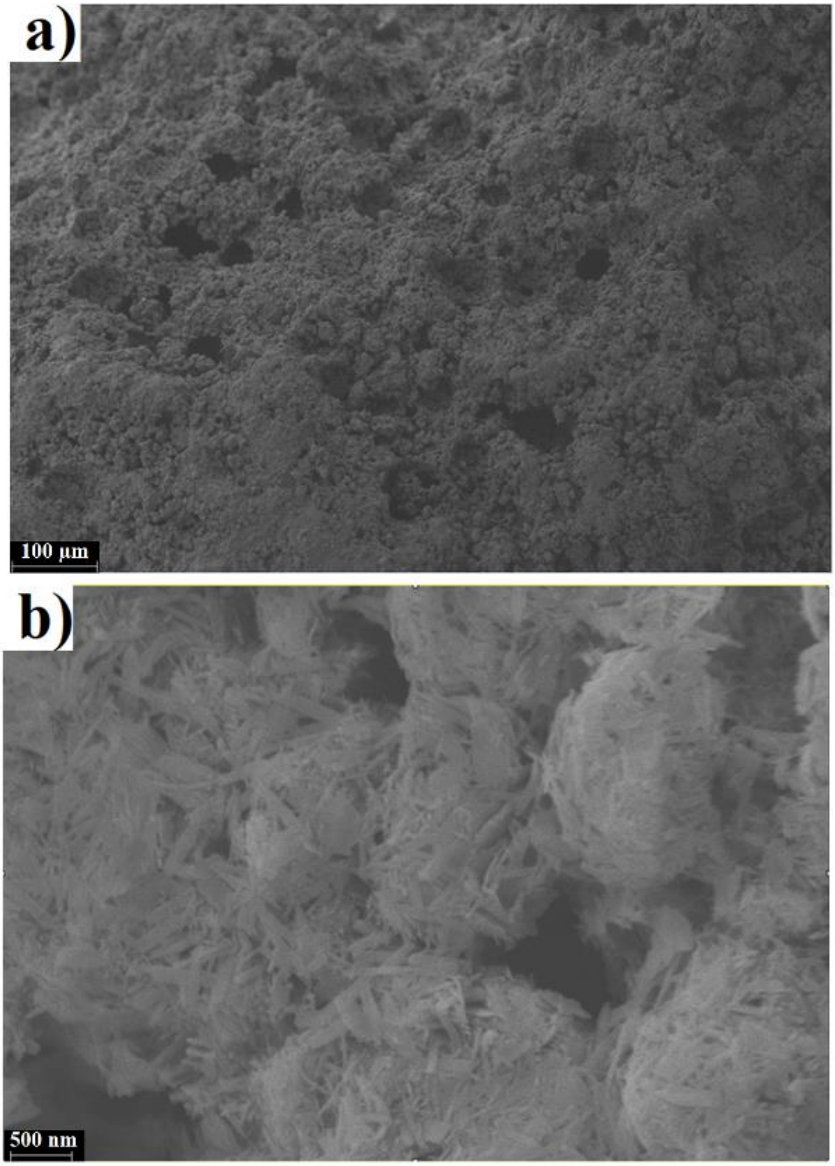

Figure 1. SEM images of cement/ gelatin mixture exhibiting highly porous complex structure with a) pores having a size of hundreds of micrometers and b) pores with a size ranging from tens to hundreds of nanometers.

Figure 2

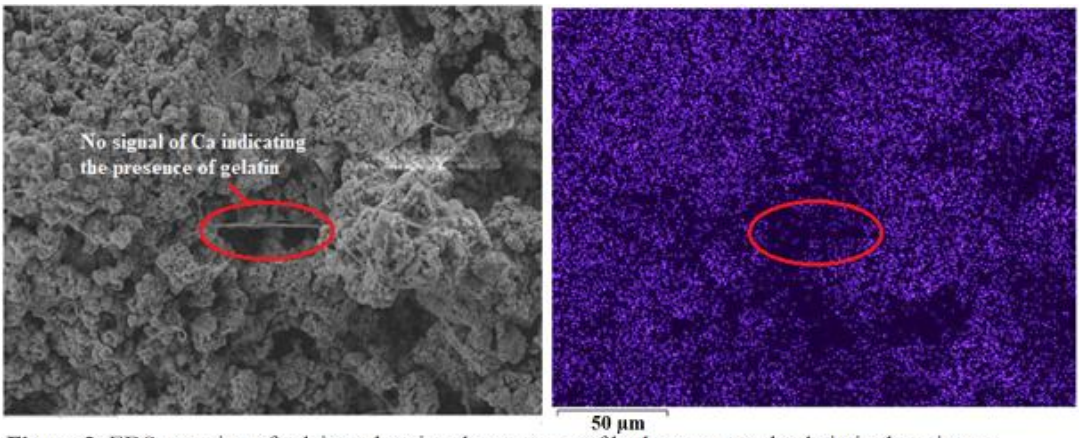

Figure 2. EDS mapping of calcium showing the presence of both cement and gelatin in the mixture.

IM5.P004
Structural investigation of all-solid-state battery NCM-cathode-LLZO-electrolyte composites using (cryo) STEM and PED

T. Demuth[1], T. Fuchs[2], A. Pokle[1], A. Beyer-Leser[1], J. Janek[2], K. Volz[1]

[1]Philipps-University Marburg, Materials Science Center (WZMW) and Department of Physics, Marburg, Germany
[2]Justus-Liebig-University, Institute of Physical Chemistry & Center for Materials Research, Giessen, Germany

All-solid-state batteries (ASBs) offer higher energy density, longer cycle life and better safety than conventional lithium-ion batteries and thus promise to be the next generation of energy storage devices[1]. However, the electrode–electrolyte interphase impedance is one of the main limiting factors prolonging the breakthrough of ASBs[2]. It is known that layered oxides like $LiNi_{0.5}Co_{0.2}Mn_{0.3}O_2$ (NCM 523) suffer from capacity fade during cycling due to the formation of spinel- or rocksalt-like phases at the particles" surface[3]. In the case of $Li_{1.2}Ni_{0.2}Mn_{0.6}O_2$ such surface modifications even occur during cathode synthesis[4].

We investigate the influence of the sintering temperature of electrode-electrolyte composite samples consisting of NCM 662 and Al-doped cubic $Li_{6.25}Al_{0.25}La_3Zr_2O_{12}$ (LLZO) on the formation of surface modification layers using multiple transmission electron microscopy techniques.

Different samples (only isostatically pressed and not sintered, sintered at 500°C and sintered at 600°C) are prepared using a focused ion beam approach. With these materials a more elaborate preparation procedure is undertaken as the LLZO and NCM secondary particles are loosely attached to each other. In order to prevent the lamellae from breaking apart, we apply an all-around deposition layer to create a framework that supports the particles during the subsequent thinning steps.

(High angle) annular darkfield (HAADF) scanning transmission electron microscopy (STEM) is used to examine the atomic structure of the samples. For the investigation of LLZO grains low beam dose techniques including cryo STEM are applied due to the high beam sensitivity of the material. Furthermore, we use precession electron diffraction (PED) to determine the phases of the primary grains, especially at the NCM-LLZO interface on a large scale. Using this technique, an area of the sample is scanned and diffraction patterns are recorded for each scan point. These diffraction patterns are quasi kinematical in nature due to the precession of the electron beam, facilitating phase determination.

For the sample sintered at 500°C we observe a phase transition from the layered phase in the bulk to a spinel-like phase at the NCM primary grains" surfaces along the lithium diffusion channels. While most particles in the bulk consist of the layered phase, NCM primary grains at the interface to LLZO tend to be composed of rocksalt-like structure. This phenomenon is also observed for a sample sintered at 600°C. In this case, however, much more NCM primary grains, even in the bulk, are composed of the rock-salt like structure than in the sample sintered at 500°C. For LLZO grains the formation of a core-shell-like structure independent from the sintering temperature can be reported.

Combining the structural information obtained by the highly precise and local analysis by STEM with the phase information of a large area of the sample derived from PED datasets is a powerful method to investigate possible phase transformations at the electrode-electrolyte interface.

References:
[1] Nanda, J., Wang, C., & Liu, P. *MRS Bulletin* 2018 *43*(10), 740-745.
[2] Wang, Z., *et al*. *Nano Letters* 2016 *16* (6), 3760-3767.
[3] Jung, S.-K., *et al*. *Adv. Energy Mater*. 2014, *4*, 1300787.
[4] Gu, M., *et. al. Nano Letters* 2012 *12*, 5186-5191.

IM5.P005
Applications of vaporiser in atmospheric gas and heating TEM

D. Zhou[1], R. G. Spruit[1], H. P. Garza[1], Z. Su[2], C. Lu[2], X. Zhang[3], F. Zhang[3], W. Liu[3]

[1]DENSsolutions B.V., Delft, Netherlands
[2]Xi'an Jiaotong University, Department of Nuclear Science and Technology, School of Energy and Power Engineering, Xi'an, China
[3]Dalian Institute of Chemical Physics (DICP), Chinese Academy of Sciences, Dalian National Laboratory for Clean Energy, Dalian, China

Introduction: Water"s negative effects on metal corrosion1 and catalyst deactivation2 are well known and under study for decades. On the positive side, water can act as reactants in hydrogen production reactions, like water-gas shift reaction3 (water is also a product in reverse water-gas shift reaction (RWGS)). With the introduction of aberration correctors, in-situ and operando gas and heating TEM can reveal structure and composition down to atomic resolution in their working status. However, the investigations on water"s influence to gas-solid reactions at atmospheric environment inside a TEM are limited due to limited control over the water vapor flow and fear of potential leak to contaminate the TEM columns. In this work, we will present two application examples of our recently developed vaporizer for MEMS-based gas and heating TEM. One is the FeCrAl alloy corrosion and the other is water"s influence on NiAu nanoparticles for RWGS.

Material and Methods: DENSsolutions" Climate G+ system, including 3 feeds GSS, TEM sample holder, vaporizer componnets between GSS and TEM holder, gas and heating nano-reactor and Impulse software, DENSsolutions gas analyzer, and a FEI Titan (TEM) operated at 300 kV were used in this work. FeCrAl alloy was firstly cut and thinned by focused ion beam and then transferred to Climate nano-reactor. NiAu nanoparticles were firstly dissoved in ethanol and then transferred to the Climate nano-reactor by drop-casting.

Results**:** Figure 1 shows that the FeCrAl alloy changed from pure bending contrast (a) to with bubble contrast (b), and then to planar defects (c) under about 90% humidity level at 300 oC, 400 oC and 700 oC respectively. These three were picked from thousands of in-situ TEM images acquired during temperature increase from room temperature to 1200 oC, which will be presented dynamically on-site.

For NiAu nanoparticles, we firstly investigated three extreme situations, i.e. reduction condition without vapor (H2 & He), reduction condition with highest humidity vapor (H2, H2O & He) and only vapor at highest humidity level (H2O & He), as shown in Figure 2. The particle retained in a structure of Ni core and Au shell in H2 & He. Loose NiO structure formed outside the particle upon introduction of high humidity vapor (H2, H2O & He), and then condensed upon disappearance of H2 in the inlet gas (H2O & He).Then we varies humidity level from 0 to ~50% with H2 and without H2. We found an interesting oscillative transition between loose and condensed NiO layer formation, whose periodicity influenced by humidity level. More experimental details and their interpretations will be presented on-site.

Conclusion**:** Development and application of such vaporizer are expected to help design more sustainable metal materials and catalysts from fundamental failure mechanism studies.

References:
[1] Stefan Ritter, Nuclear Corrosion, Woodhead Publishing, 2020
[2] Goguet et.al., Deactivation Mechanism of a Au/CeZrO4 Catalyst During a Low-Temperature Water Gas Shift Reaction, J. Phys. Chem. C 2007, 111, 45, 16927-16933
[3] Ebrahimi et.al., A review of recent advances in water-gas shift catalysis for hydrogen production, Emergent Materials 2020, 3, 881-917

Figure 1

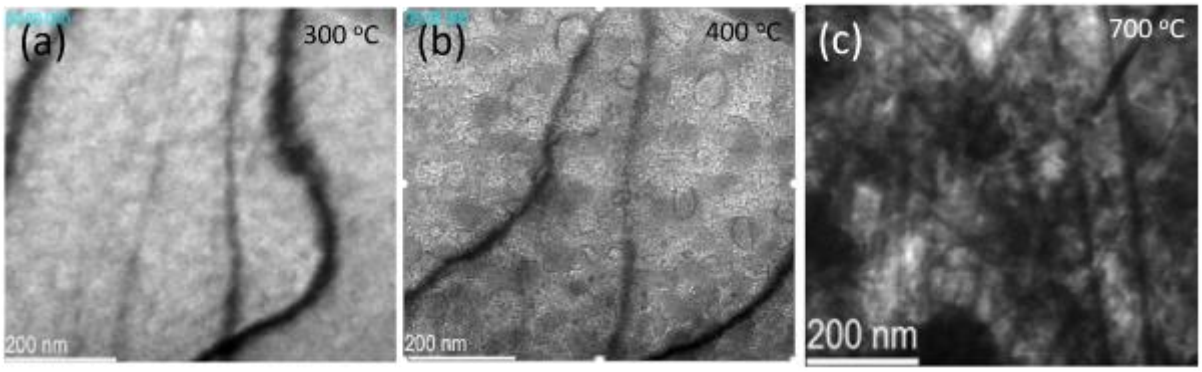

Figure 2

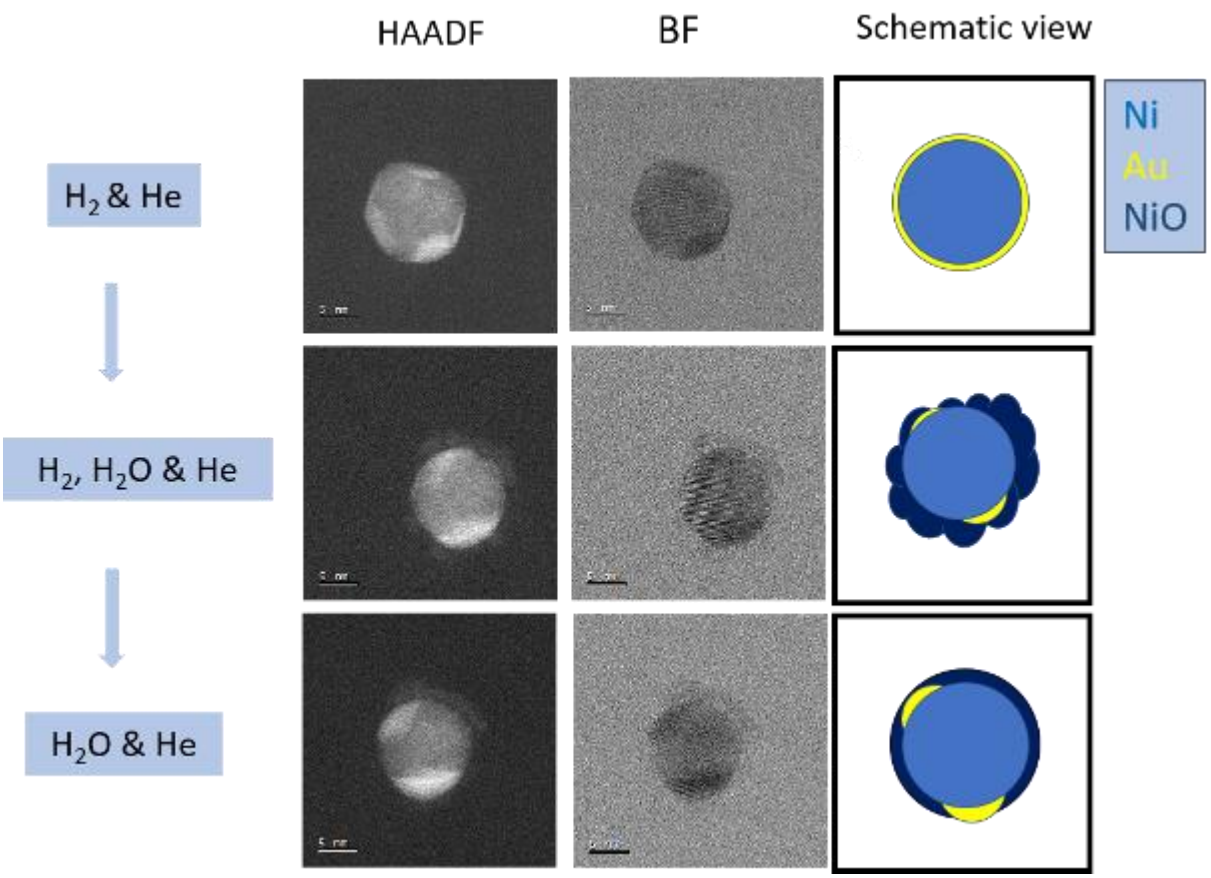

IM5.P006
In situ ESEM method for observation of ice grain boundary morphology

M. Olbert[1], K. Závacká[1], V. Neděla[1]

[1]Institute of Scientific Instruments, Czech Academy of Sciences, Brno, Czech Republic

When the aqueous solution freezes, the dissolved ions and molecules are expelled from ice and are concentrated into the freeze concentrated solution (FCS). By further decrease of temperature they may be trapped at the grain boundaries (veins) [1]. The inappropriate freezing procedures can cause a major loss of active pharmaceutical ingredients (APIs) and can have bad influence on the long-term stability of the product [2]. At present, the latest innovations of the ESEM are available for the research. The microscope equipped with high efficiency detectors [3], self-developed cooling stage (Peltier stage) and 2nd generation of hydration system, is the perfect tool for low-dose observation with higher resolution of static and dynamic *in-situ* processes in the delicate frozen sample.

ESEM is a very beneficial tool for the research, since it offers an exclusive opportunity to observe the exact structure of micro-sized grain boundaries of frozen solutions and dynamical *in-situ* processes. We intent to show how different types of cooling can change the morphology of frozen aqueous solution and structure of the frozen grain boundaries. The knowledge from this field would be beneficial for exact approach in the sample preparation. Thus, the contribution in pharmaceutical industry would be raised to maximum.

We observed 0.5 M NaCl samples, which were frozen upon two types of cooling. Fast cooling (immersing the liquid aqueous sample into liquid nitrogen at the temperature of - 196 °C) resembled to the freezing of biological and pharmaceutical samples. The freezing of seawater in oceans and on the poles was simulated by the slow cooling (putting the sample into, precooled bath at - 50 °C). Non-commercial ESEM AQUASEM II equipped with a new Combined System for high-efficiency detection of Secondary and Backscattered Electrons (CSSBE) and self-designed cooling stage optimised for ice investigation was used. Samples were observed at the air pressure 300 Pa and temperature - 50 °C.

Figure 1A: shows revealing grain boundaries (bright grey) after the sublimation of hexagonal ice (dark grey). In the case of fast cooling, ice formed long parallel lamellae. After sublimation of ice the frozen FCS made of hydrohalite crystals formed thin long boundaries. During slow cooling, the ice formed its crystals in the shape of grains (Figure 1B). Again, after ice sublimation the boundaries made of crystallised salt remain in their unharmed structure. These boundaries are made of walls and triple junctions (place where 3 walls meet) which are more prevalent in this type of cooling. We assume this could be places where chemical properties of the FCS can change upon cooling.

Using our custom-modified ESEM equipped with latest technological innovations gives us the unique opportunity to show the detailed 3D structure of the frozen aqueous solution without any conductive coating, which helps us to trustworthy interpret the influence of the cooling rates on the structure of the sample. [4]

References:
[1] V. F. Petrenko, R. W. Whitworth, "Physics of ice" (Oxford University Press, New York) p.149
[2] M. T. Cicerone, M. J. Pikal and K. K. Qian, Adv. Drug Deliv. Rev., vol. 93 (2015) p. 14–24.
[3] V. Nedela et al, Ultramicroscopy, vol. 184 (2017), p. 1-11.
[4] The project was supported by the Grant Agency of Czech Republic GA 19-08239S and GA 19-03909.

Figure 1

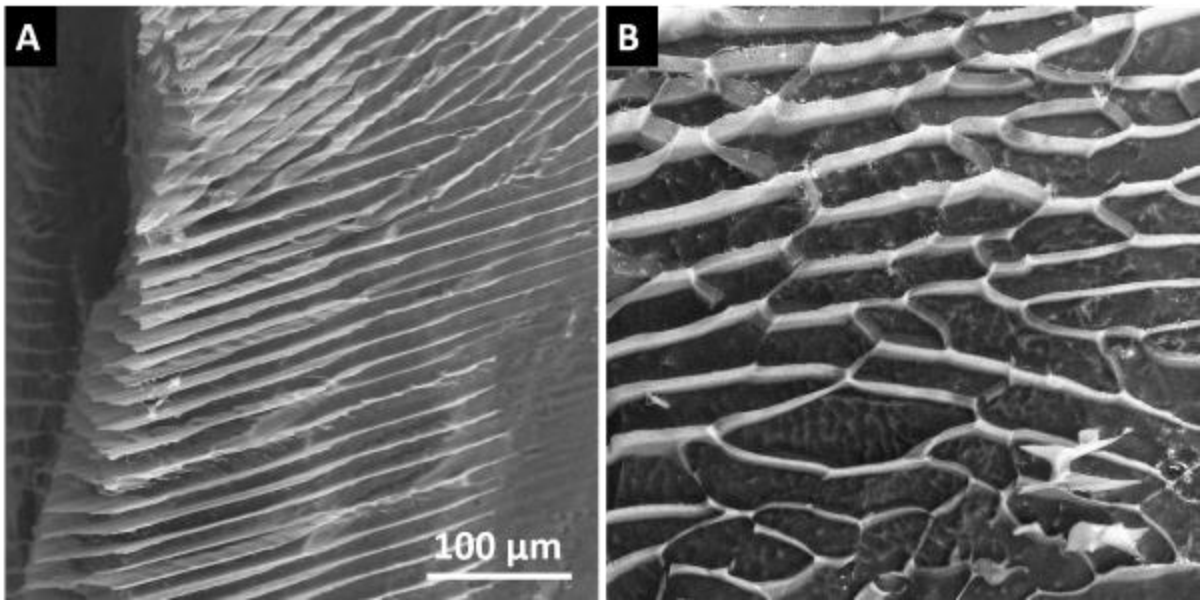

IM5.P007
Enhancing SEMs' and FIB/SEMs' capabilities through the addition of specialised manipulation and positioning tools

A. J. Smith[1], K. Schock[1], A. Rummel[1], S. Kleindiek[1]

[1]Kleindiek Nanotechnik, Reutlingen, Germany

Introduction: This work will aim to provide an overview of the applications that can be addressed by adding a set of micromanipulators - optionally equipped with specialized end effectors - to an SEM or FIB/SEM. In addition, a number of positioning platforms for dedicated tasks will be introduced that provide enhanced functionality to the SEM or FIB/SEM yielding improved performance and/or access to novel in situ applications.

Materials & Methods: The systems employed in this work were a Zeiss Supra40 SEM, an FEI 200 Quanta 3D FIBSEM, in combination with a range of micromanipulators and plug-in tools as well as substages manufactured by Kleindiek Nanotechnik.

Experimental procedure: It is more or less the default for FIB/SEMs to be equipped with at least a single micromanipulator for the purpose of tranferring TEM lamella from the bulk to appropriate holders. Beyond this every-day task, micromanipulators can be used for a host of other applications, ranging from electrical and mechanical characterization of various types of materials to more advanced "pick & place" tasks where e.g. nanowires or CNTs need to be arranged in certain manner. Utilizing micromanipulators equipped with needles, grippers, force sensors, or other tools is key to performing these tasks. On the other hand, adding enhanced functionality e.g. in the form of environmental control, AFM imaging capability, or unique and/or extremely precise positioning performance can also be essential in achieving desired outcomes.

To this end, a range of micromanipulation tools including various endeffectors will be introduced. Beyond that compact, easy to install and remove platforms for in situ AFM imaging, sample heating and cooling, as well as a number of other specific tasks will be described including application examples demonstrating the tools' relevance.

For example, a novel tilting sub-stage which provides a second, eucentric axis of tilt that can be oriented perpendicularly to the microscope's own tilt axis is used to mitigate so-called curtaining effects when FIB milling cross sections on inhomogeneous materials.

Another example is a miniature Gas Injection System (GIS) that can be used with custom precursors or to inject inert gases or oxygen will be discussed.

Conclusion: Incorporating micromanipulators and/or dedicated substages to an SEM or FIB/SEM tool can open up novel and exciting pathways for experimentation in a wide array of research fields. These include electrically and mechanically characterizing nanowires and nanoparticles, testing material properties in combination with other alanysis methods (such as EBSD, EDX, etc.), elucidating the electrical behavior of novel semi-conductor materials, transferring cryogenically frozen TEM lamella, preparing smooth cross sections for further investigation on difficult to mill materials, and many more.

Figure 1

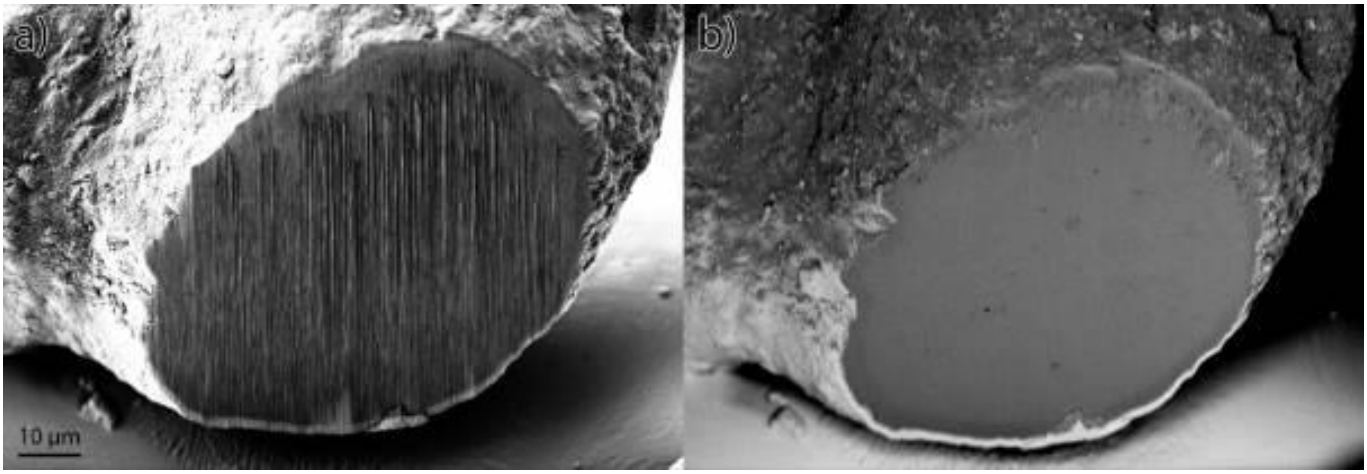

Figure 2

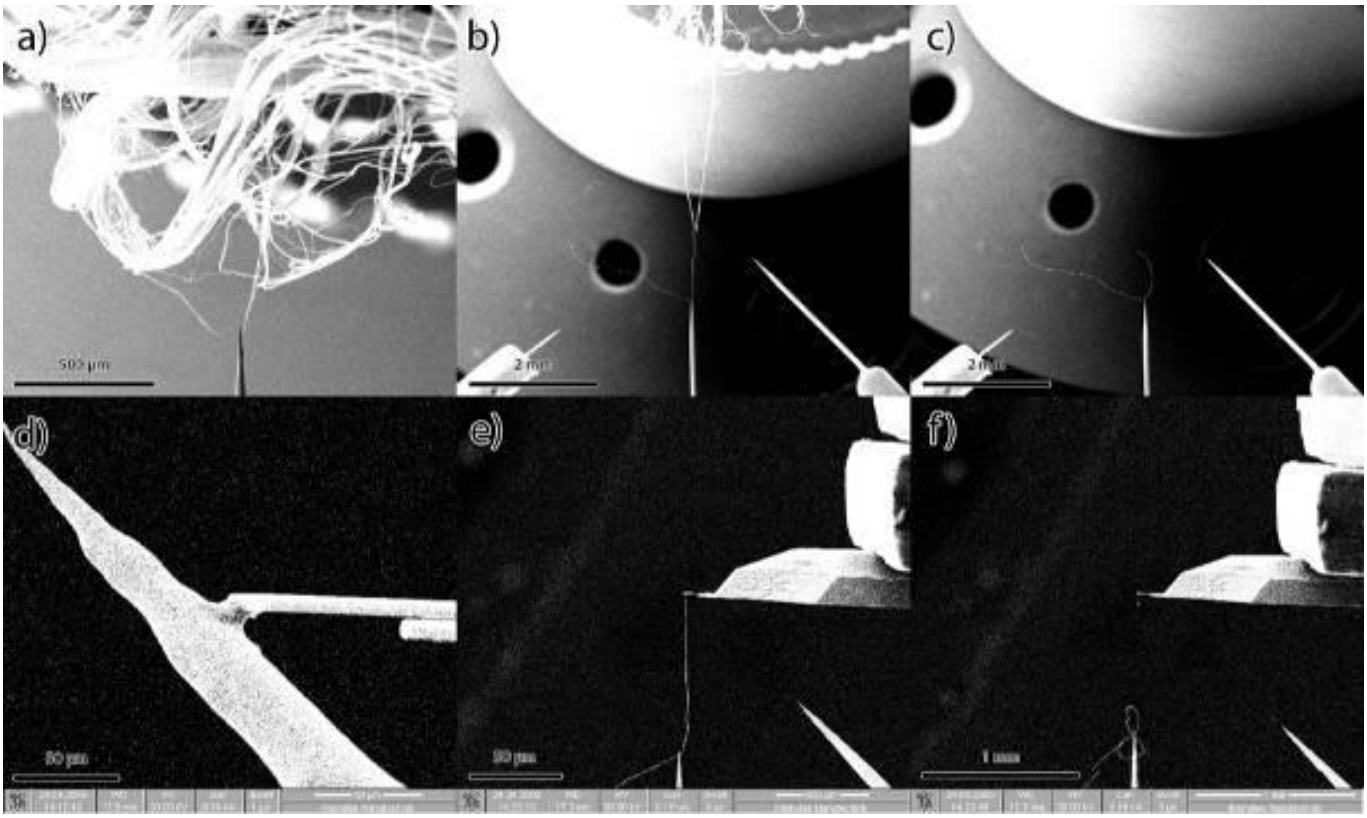

IM6.002-Invited
Large-scale electron tomographic reconstruction of mitotic spindles

T. Botzenhart [1], G. Fabig[1], R. Kiewisz[1], D. Baum[2]

[1]Technische Universität Dresden, Medizinische Fakultät Carl Gustav Carus, Dresden, Germany
[2]Zuse Institute Berlin, Berlin, Germany

The mitotic spindle has been described over 100 years ago, but our ultrastructural understanding of this fundamental dynamic process is still somehow limited. Here we introduce a refined workflow that allows for screening and selection of mitotic spindles. This workflow further involves the stitching of serial semi-thick sections for 3D reconstruction by electron tomography and a detailed automated analysis of microtubule organization in the staged spindles.

In more detail, we have improved several steps of specimen preparation to efficiently enrich mammalian cells, such as HeLa, U2OS and RPE-1 cells, and attach them to sapphire discs. We perform high-pressure freezing, followed by freeze substitution and sample embedding in epoxy resin. Moreover, we apply a protocol that uses a histological dye to stain the DNA/the chromosomes. This staining procedure allows for staging and selection of rare events within plastic-embedded cells before performing further processing for electron tomography. Afterwards, the selected cells are subject to serial sectioning, and these serial sections are then used for tomographic data acquisition. After automated reconstruction (using IMOD Batch processing), semi-automated microtubule segmentation and stitching of the single tomograms (using ZIB Amira), complete volumes of selected spindles at single-microtubule resolution are obtained.

We also developed software for automated data analysis. Our custom-made software allows us to investigate the ultrastructure of mitotic spindles with a precision that could not be achieved so far. Last not least, we developed a web-based platform for the visualization of annotated and analyzed mitotic spindles, allowing multiple users to investigate our 3D models interactively.

IM6.004
Development of a 3D liquid-phase STEM method to study cell-biomaterials interactions

A. Bekel[1], L. M. Lebas[1], B. Lesaint[1], C. Gaillard[1,2], L. Roiban[1], K. Masenelli-Varlot[1]

[1]INSA-Lyon, MATEIS UMR 5510, Villeurbanne, France
[2]Université Lyon 1, Pharmacie, Lyon, France

The successful development of new implants relies on a better understanding of the interactions between cells and biomaterials [1]. Cell adhesion onto the biomaterial is a key step to predict the future of an implant in the human body. Cell adhesion is involved in many cellular processes such as proliferation, migration and differentiation [2]. Recent studies have shown that the substrate on which the cell is cultured can lead to different cell morphologies, which is linked to the expression of specific genes [3, 4]. Cell adhesion is widely studied through focal adhesion labelling in confocal microscopy. The morphological analysis is mostly done in 2D using high vacuum scanning electron microscopy, a label-free technique requiring heavy sample preparation including dehydration. To reduce the changes during the sample preparation, a solution may be the use of liquid-phase SEM (LPSEM) analysis.

A home-made scanning transmission electron microscopy (STEM) tomography device, specific to LPSEM, has previously been developed to study aqueous suspensions in 3D [5]. In this work, we further develop the device and propose a 3D analysis method to study whole cells in 3D close to their native state.

3T3 cells were cultured onto a gold TEM grid covered with a fibronectin coated carbon film, for 24 h at 37°C, 5% of CO2 in humid astmosphere. Cells were rinsed with PBS twice, then cells were fixed with 4% glutaraldehyde for 30 minutes. Cells were stored in PBS at +4°C until images acquisition.

Images were recorded in transmission using a FEI QuattroS environmental SEM (ESEM) operated at 15 keV. Humidity was maintained at or above 70 % and the temperature around the sample at 4°C in order to insure a continuous hydration of the sample. Bright field (BF) and High Angle Annular Dark Filed (HAADF) were recorded at different tilt angles. The tilt images were aligned using Imod software, the volumes were computed using the TomoJ plugin of ImageJ. Data segmentation and the 3D model were performed using ImageJ and 3d Slicer.

We will show that Liquid-Phase electron tomography in ESEM enables the 3D analysis of whole hydrated cells without any heavy sample preparation. We will first present the technical settings used for image acquisition on hydrated biological objects. Then, we will show complementary volumes reconstructed from BF and HAADF tilt image series (see figure 1 A et B). Morphological parameters describing cell parts, such as the filopodia, will be extracted.

The limits of the technique will be explored in terms of culture medium, cell thickness, spatial resolution and electron dose received by the sample. Complementary results obtained by collecting secondary electrons on cells/thick substrates will also be analyzed.

Figure 1: Orthogonal cross-sections of the reconstructed 3T3 cell volume from images collected at different tilt angles in BF A) or HAADF B) mode.

Such development opens the way towards the 3D analysis of intact cells in environments mimicking their native environment. Another targeted application is the 3D study of the morphological interactions between cells and biomaterials.

[1] H. Zhou et al., *Cells Mater.*, 3, 2, 141–150, 1993.
[2] G. D. Rosen and D. S. Dube, *Encycl. Respir. Med. Four-Volume Set*, 41–47, 2006.
[3] C. Y. Yang et al., *Eur. Cells Mater.*, 20, 1, 415–430, 2010.
[4] M. F. A. Cutiongco et al., *Nat. Commun.*, 11, 1, 1–13, 2020.
[5] K. Masenelli-Varlot *et al.*, *Microsc. Microanal.*, 20, 2, 366–375, 2014.

Figure 1

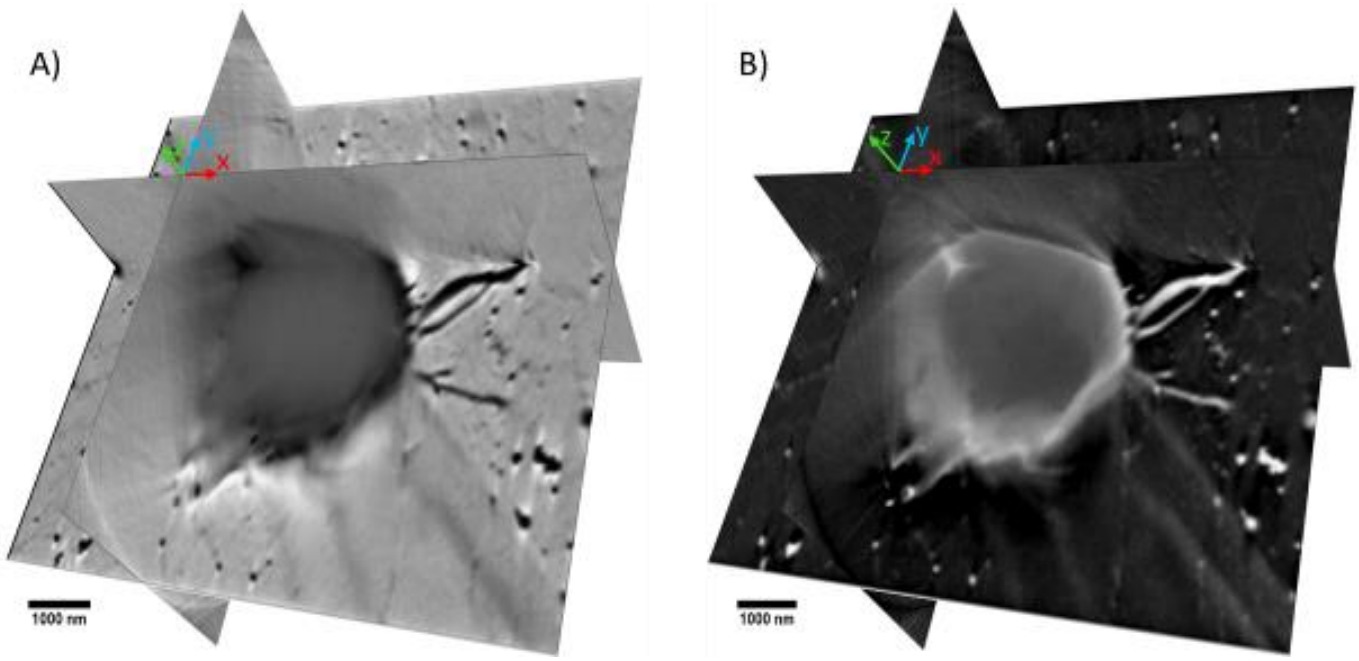

IM6.005
3D investigations on ciliogenesis in hRPE cells

R. Rachel[1], K. Buerger[2], K. Schmidt[2], R. Witzgall[2]

[1]University of Regensburg, Center for Electron Microscopy, Regensburg, Germany
[2]University of Regensburg, Molecular and Cellular Anatomy, Regensburg, Germany

Introduction: Human retinal pigment epithelial (hRPE1) cells can be serum starved under laboratory conditions in order to induce the formation of primary cilia as sensory organelles. In hRPE1 cells, the formation of the cilium follows the so-called intracellular pathway. Several proteins are recruited to the mother centriole / basal body in order to organize this process.

Objectives: In this study, we aimed at investigating the recruitment of one key protein, the small GTPase RAB8A, to the forming cilium. In addition, we wanted to visualize 3D snapshots of the forming ciliary vesicle to analyze membrane remodeling processes at this stage.

Materials & methods: hRPE1 cells stably expressing versions of CENTRIN1 and RAB8A tagged with different fluorescent proteins were serum starved to induce cilia formation for a given period of time. Cells were fixed by adding formaldehyde and the subcellular distribution of fusion proteins was recorded by fluorescence light microscopy (focal stacks). In order to analyze early ciliogenesis we specifically selected cells with RAB8A localizing to one of the two centrioles as a dot and thus as a vesicular structure. Samples were prepared for electron microscopy (fixation with glutaraldehyde; staining with OsO4 and UAc; dehydration, resin embedding). On sections with a nominal thickness of 600 (or more) nm, we reidentified the respective area within a cell containing the fluorescent markers and therefore the centrosome with the developing cilium. At these areas, STEM tomograms [1] were recorded. The software eC-CLEM [2] was used to correlate the position of the fluorescent signals with ultrastructural features [3].

Results: The thickness of the STEM tomograms enabled us to visualize the ultrastructural localization of RAB8A to the stage when preciliary vesicles fuse into one larger ciliary vesicle. In addition, we were able to capture the complete volume of various stages of ciliogenesis in 3D, showing that ciliary vesicle formation is highly dynamic and undergoes complex structural changes.

Conclusion: Using the approach described, we are able to show that mCherry-RAB8A is recruited at the basal body of the forming cilium at distinct, early time points. STEM tomograms are ideally suited in order to visualize the full 3D structure of subcellular organelles like the forming primary cilium.

References:
[1] Rachel et al. 2020 J Struct Biol 211: 107551
[2] Paul-Gilloteaux, et al. 2017 Nature Methods 14: 102–103
[3] Buerger et al. 2021 Meth Cell Biol 162: 171-203

Figure 1: image row shows three slices/*xy* planes (each with a thickness of 2.7 nm; 67 nm apart from each other) of a STEM tomogram after reconstruction using the simultaneous iterative reconstruction technique algorithm (IMOD software package). The slices were cropped to the region of the basal body of the cell. Bar, 200 nm.

Figure 1

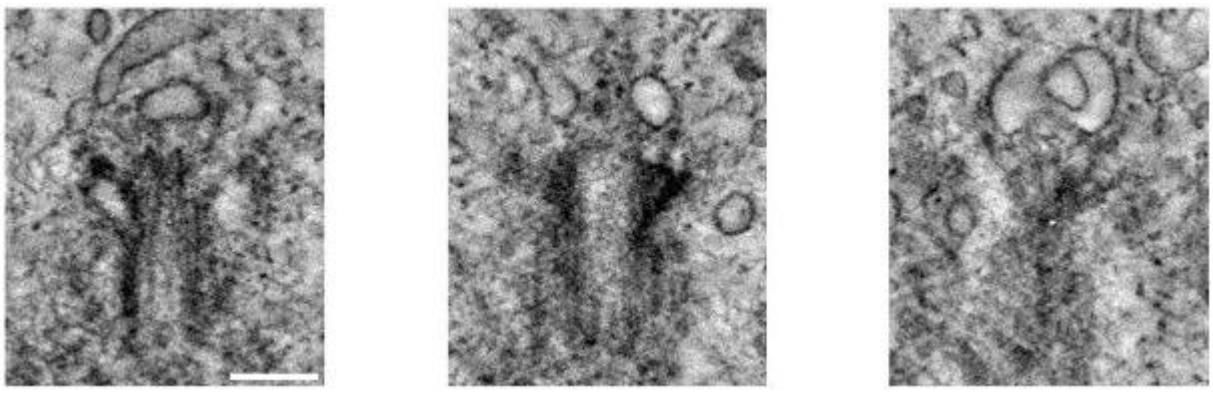

IM6.P001
Large volume 3D EDS mapping of *Paramecium*

Y. Yamaguchi[1], T. Haruta[1], Y. Moriya[1], J. Gilbert[2], S. Asahina[1]

[1]JEOL Ltd., Tokyo, Japan
[2]Bruker Nano GmbH, Berlin, Germany

Array Tomography (AT) is a powerful technique which enables us to observe three-dimensional (3D) structures of large volumes of biological specimens by using Scanning Electron Microscopy (SEM) [1]. Furthermore, AT has the opportunity to acquire 3D information on elements in the specimens by the combination of AT and Energy Dispersive X-ray Spectroscopy (EDS). Recently, we have reported 3D EDS mapping by using AT-EDS [2]. We have tried to obtain a 3D EDS map of biological tissues with silver nanoparticles. In addition, we have tried to obtain 3D EDS maps of *Paramecium* with preserving several kinds of nanoparticles in phagosomes. In this study, we report the novel method of large volume 3D EDS mapping of *Paramecium* by AT-EDS.

Objective is to reveal the whole 3D structures of *Paramecium* by using AT and the 3D EDS maps of a phagosome with Gold, Silver and Silica nanoparticles by using AT-EDS.

Paramecium was cultured in water with gold nanoparticles (size 40 nm), then in water with silver nanoparticles (size 40 nm), and finally in water with silica nanoparticles (size 50 nm) for 1 hour each. The *Paramecium* was fixed with glutaraldehyde and OsO_4 and then block stained with Uranium. Ultra thin sections totaling 283 slices with a thickness of 200 nm were prepared by an ultramicrotome, and after being embedded with resin, they were mounted on a carbon substrate (Ultra Flat Carbon: UFC, JEOL Ltd.). The ultra thin sections on UFC were stained with small amounts of Uranium and Lead for enhancing the contrast of backscattered electrons (BSE). The 3D volume imaging was carried out by FE-SEM (JSM-7900F, JEOL Ltd.). Serial two-dimensional (2D) images of each section were acquired automatically at an incident voltage of 7 kV. A 3D image of the whole structure of *Paramecium* was reconstructed by stacking the 2D images. 3D elemental mapping was carried out by EDS (XFlash®5060FlatQUAD, Bruker) installed on the JSM-7900F (JEOL Ltd). This EDS has a solid angle of 1.0 sr. This is about 50 times larger than the conventional EDS. Thus, it is possible to acquire an elemental map in a shorter time even from ultra thin section samples. A 2D elemental map (Au-Mα line, Ag-Lα line and Si-Kα line) of each section of a phagosome was acquired for about 1 minute at an incident voltage of 7 kV. The 3D elemental map was constructed by stacking the serial 2D elemental maps.

A 3D image of *Paramecium* was obtained with a volume of 226 µm x 90 µm x 56 µm. Several phagosomes were contained in this 3D structure. A slice image of a phagosome in the XY plane at a height of 32 µm in the Z direction is shown in Figure 1. A 3D elemental map of this phagosome was obtained with 17 µm x 8 µm x 10 µm volume (Figure 2). As a result, a large number of Gold nanoparticles and a few Silicon nano particles were detected in the phagosome. However, Silver nanoparticle was not detected at all.

The 3D image of the whole structure of *Paramecium* can indicate the position of phagosomes. And then, 3D EDS mapping by using AT-EDS revealed the distribution and amount of Gold, Silver and Silica nanoparticles in *Paramecium*. The difference in amount of Gold, Silver and Silica in the phagosome may be due to the selectivity in ingestion of these elements by *Paramecium,* or the order of adoption of each element ingested by *Paramecium*.

References:
[1] K.D.Micheva and S.J. Smith, Neuron 55(1) (2007), p.25
[2] Yamaguchi Y. et al, Microsc. Microanal. 25 (Suppl 2) (2019), p.1092

Figure 1

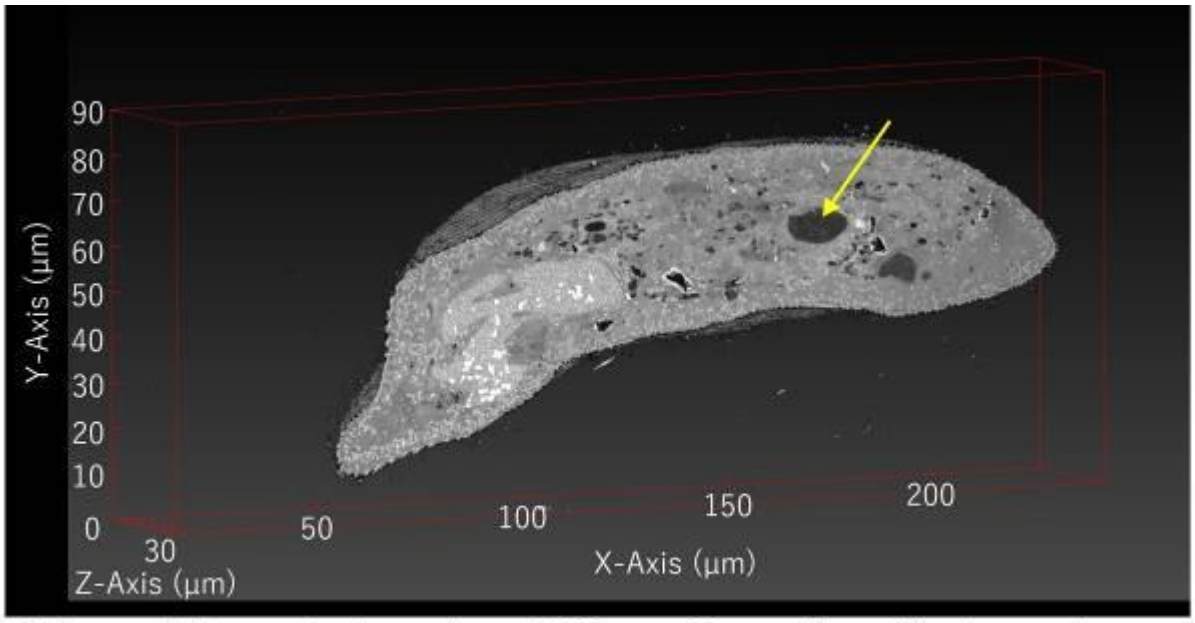

3D image of *Paramecium* in a volume of 226 µm x 90 µm x 56 µm. Slice image of a phagosome at a height of 32 µm in the Z direction. Yellow arrow indicates a phagosome.

Figure 2

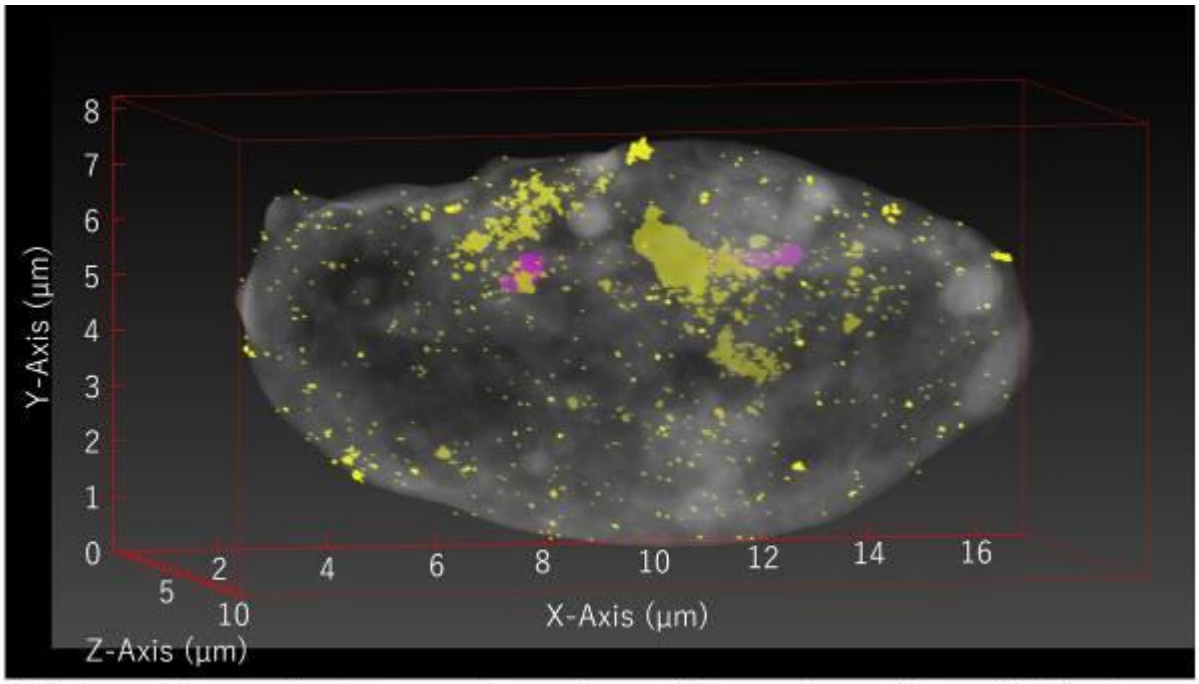

3D elemental map of a phagosome in a volume of 17 µm x 8 µm x 10 µm. Gold is shown in yellow and silicon is shown in magenta. Overlayed with 3D SEM image.

IM6.P002
Shape and structure of archaeal cells, analysed by STEM tomography

R. Rachel[1], L. Dengler[2], A. Bellack[2], H. Huber[2], V. Heinz[3], R. Reichelt[2]

[1]University of Regensburg, Center for Electron Microscopy, Regensburg, Germany
[2]University of Regensburg, Microbiology and Archaea Centre, Regensburg, Germany
[3]University of Regensburg, Biophysics II, Regensburg, Germany

Introduction: In our laboratory, we cultivate numerous prokaryotic cells which serve as model systems for studying the cell biology of Archaea. One of our previous studies focused on the archaeon *Ignicoccus hospitalis*, a prokaryotic cell with a highly unusual mode of compartmentalisation [1]. Using electron cryo-tomography and sub-tomogram averaging, we analysed *Pyrococcos furious*, a motile cell expressing numerous archaella, and presented a model of the its archaeallar motor in 3D [2]. Other archaea studied in our lab include *Methanocaldococcus villosus*, a hyperthermophilic methanogen with exceptional motility, and novel isolates collected from various biotopes in Costa Rica. For these cells, a detailed ultrastructural analysis is lacking which may serve as basis for an understanding of their cell biology, e.g. understanding their compartmentalization.

Objectives: Using STEM tomography of thick sections, we visualize and analyse prokaryotic cells, their subcellular compartments, and cell appendages in 3D in a rather undisturbed state.

Materials & methods: Cells are analysed by electron tomographic methods [3, 4]. In our on-going studies, cells are gently concentrated on ultrafiltration membranes, then cryo-immobilized by high-pressure freezing, followed by freeze-substitution and resin embedding. Sections up to 900 nm thick are analysed by STEM tomography, in some cases, combined with dual-axis tilting. This technique eliminates the focus gradient at high tilt, by increasing the depth of focus. At the same time, we can image and analyse rather large volumes of the samples, sometimes even close to a full cell. We extend our studies towards naturally occurring lab mutants.

Results In the STEM tomography datasets of *P. furiosus* (Figure1), we can visualize the cells with minimal distortion, as a result of the cryo-fixation based sample preparation protocol. The natural shape and ultrastructure of the cells is trapped in an undisturbed way, at a resolution of about 5 nm. We can trace the extracellular appendages, and we unravel yet undescribed features, like kinks and sharp bends in the archaeal cell wall, pointing to novel types of cytoskeleton and to unique mechanisms of cell shape determination.

Conclusion Combined ultrastructural and biochemical analyses are necessary in order to fully understand the complexity of coccoid archaeal cells. We will complement our studies using electron cryo-tomography [2], in the near future.

References:
[1] Heimerl et al, 2017: Front Microbiol 8: 1072
[2] Daum et al, 2017: eLife 6: 27470
[3] Rachel et al, 2010: Meth Cell Biol 96: 47-69;
[4] Rachel et al, 2020: J Struct Biol 211(3):107551

Figure 1: IMOD screenshot of a 3D reconstruction of a ca. 600 nm thick section of a cell of *Pyrococcus furiosus*, obtained by STEM tomography. A, XZ plane; B, XY plane; C, YZ plane. The marked areas point to cell compartments in which the archaella are anchored. Black arrow: archaella (diameter: 11 nm). Bar: 200 nm

Figure 1

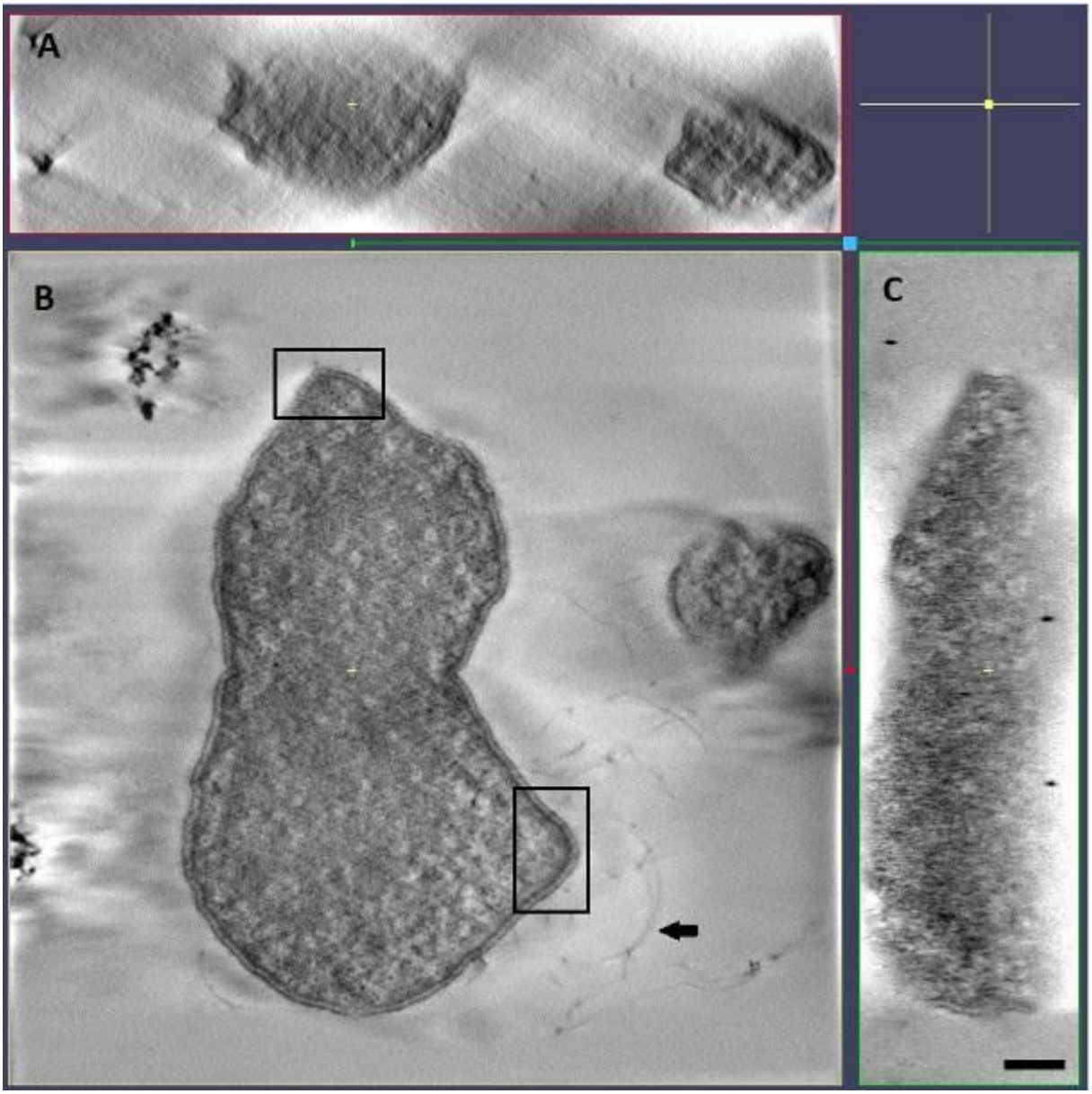

IM7.004
3D atomic resolution tomography from iDPC-STEM images using multiple atom model prior

S. Hosseinnejad[1], E. G. T. Bosch[2], H. Kohr[2], I. Lazić[2], V. Zharinov[1], E. Franken[2], J. Sijbers[1], J. De Beenhouwer[1]

[1]imec - Vision Lab, University of Antwerp, Antwerp, Belgium
[2]Thermo Fisher Scientific, Eindhoven, Netherlands

3D reconstruction at the atomic scale for specimens consisting of both heavy and light elements is challenging with common scanning transmission electron microscopy (STEM) methods. Integrated differential phase-contrast (iDPC) STEM is a state-of-the-art imaging method with the capability of imaging heavy and light elements simultaneously, which is not possible with annular dark field (ADF) STEM [1, 2]. By acquiring iDPC-STEM projections at different tilt angles, 3D images of compound structures consisting of different elements can be reconstructed using tomographic reconstruction algorithms.

In [3], an atomic resolution reconstruction method for HAADF-STEM tilt series was introduced in which atoms are iteratively detected and replaced by a prior model of the atom potential. In this work, a similar reconstruction method is applied to simulated iDPC-STEM data for the first time by using separate atomic models for different elements. Since no prior knowledge about the structure of the materials is enforced, an unbiased reconstruction of both crystalline and amorphous structures is possible.

iDPC-STEM projections of a platinum nanodecahedron with 4021 atoms [4] on an amorphous carbon substrate with 53598 atoms [5] were simulated using the multislice method [2, 6, 7]. In this work, 181 simulated projections with 1-degree tilt increments were used for the reconstruction. Figure 1 shows a 3D rendering of the sample together with one of the iDPC-STEM and ADF-STEM projection images showing that iDPC-STEM image shows the platinum atoms as well as the carbon atoms which are almost invisible for ADF-STEM.

We aim at 3D reconstruction of both platinum crystal structure and amorphous substrate. Although the detection of the carbon atoms is more challenging due to their amorphous structure and the weaker contrast associated with them, the tomographic reconstruction of the simulated iDPC-STEM projections of the platinum nanodecahedron on the carbon substrate in Figure 2 reveals the heavy element (Pt) of the crystal as well as the light element (C) of the amorphous substrate which can not be done with ADF-STEM. In conclusion, 3D image of both heavy and light atoms is reconstructed by using a multi atom model prior and iDPC-STEM projection.

Figure 1: a) Model of a Pt (red) nanodecahedron particle on a substrate consisting of amorphous carbon (blue); b) One of the simulated iDPC-STEM projection images; c) A simulated ADF-STEM projection image with the same tilt angle. The field of view is 8x8 nm2. The beam energy used is 80 keV and the beam convergence (semi) angle is 20 mrad.

Figure 2: Reconstruction of simulated platinum nanodecahedron on an amorphous carbon substrate. A slice through the 3D reconstruction is shown for the SIRT reconstruction (a), the final reconstruction consisting of platinum and carbon atoms by using the atom model prior (b)

References:
[1] Lazić I, Bosch EGT, Lazar S, Ultramicroscopy, 2016;160:265-280.
[2] Lazić I, Bosch EGT, Advances in Imaging and Electron Physics, 2017;199:75-184.
[3] Goris B, De Beenhouwer J, et al., Nano Lett., 2015;15(10):6996-7001.
[4] Chen CC, Zhu C, et al. Nature. 2013;496(7443):74-7.
[5] Ricolleau C, Le Bouar Y, et al., J. Appl. Phys., 2013;213504.
[6] Kirkland EJ, Advanced Computing in Electron Microscopy, Springer S + B Media LLC, 2010.
[7] Bosch EGT, Lazić I, Ultramicroscopy, 2015;156:59-72.

Figure 1

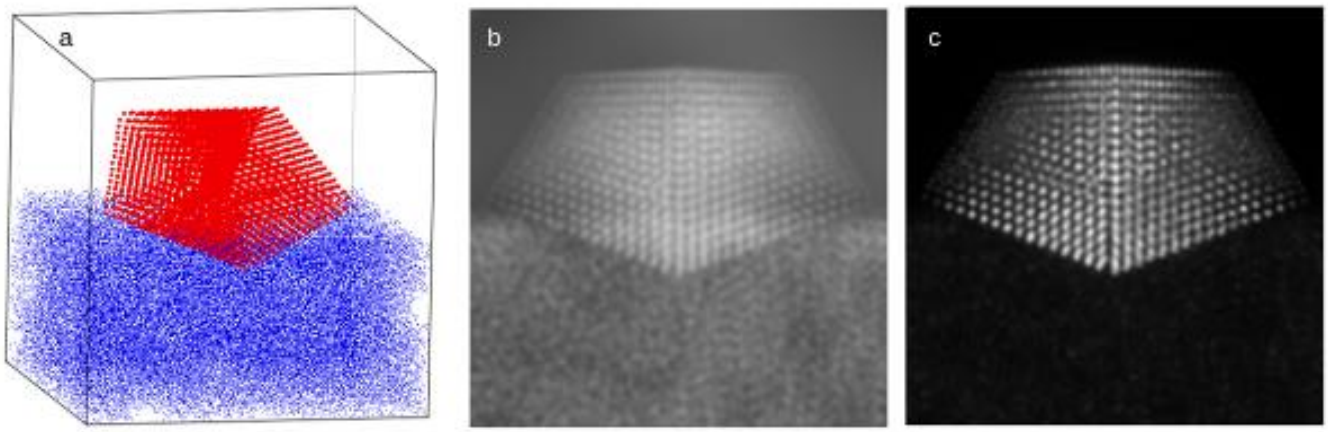

Figure 2

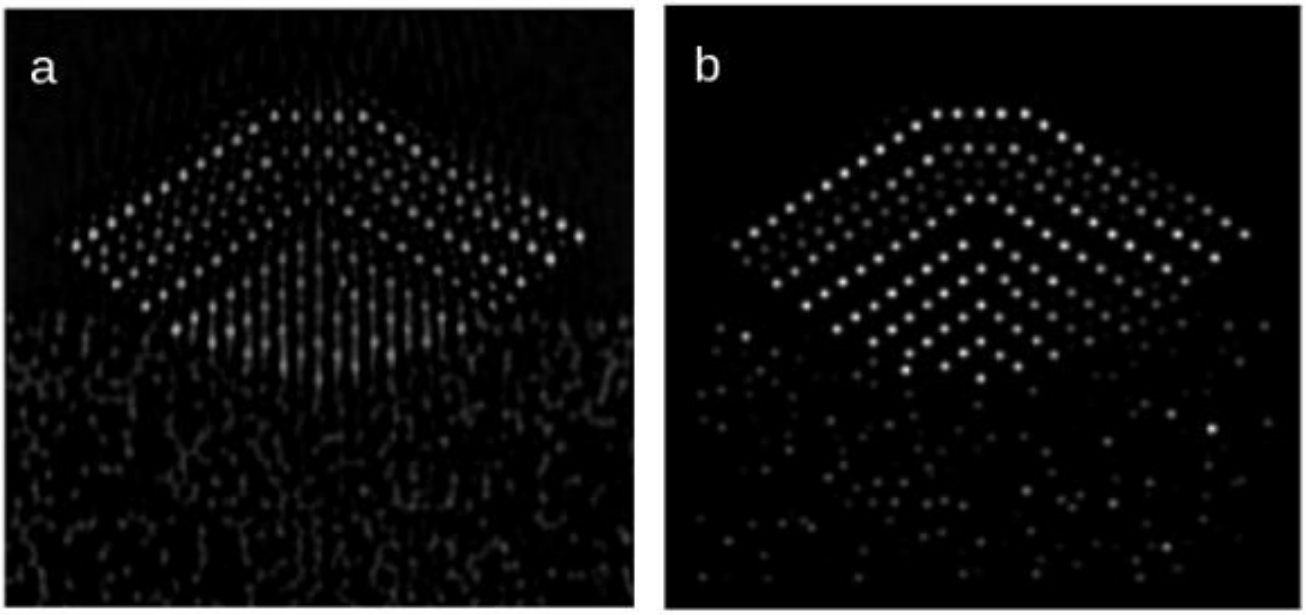

IM7.005
Multimodal and multicolour microscopy to identify biomolecules in large-scale electron microscopy

P. De Boer[1], A. Srinivasa Raja[1], J. P. Hoogenboom[1], B. N. G. Giepmans[1]

[1]University Medical Center Groningen, Biomedical Sciencs of Cells and Systems, Groningen, Netherlands

Electron microscopy (EM) is a powerful tool for imaging biomolecules at near-molecular resolution in cells and tissue, which is essential to understand the regulation of life and disease. However, restricted fields of view (FOVs) at high resolution hamper the quantitative power of EM. We routinely perform large-scale 2D EM on complete cells and tissue sections to maintain both large FOVs and high resolution, called nanotomy for nano-anatomy (www.nanotomy.org). Disease and tissue specific databases are being created as a resource for biomedical EM data for researchers worldwide, such as our recent repository for the study of human type 1 diabetes with datasets from over fifty donors [1]. However, identifying specific molecules in these large grey-scaled datasets is troublesome. Therefore we optimized and routinely apply energy dispersive X-ray analysis (EDX) for nanometer resolution elemental fingerprinting on bio-samples [2]. EDX-based "colorEM" allows identification of elemental enriched probes as well as endogenously present elements (figure 1). Furthermore, with correlated light and electron microscopy (CLEM) multimodal fluorescent and EM labels show specific biomolecules in a high resolution context [3]. Though, targeting, spectral variety, and registration are often limited. Therefore, to better identify proteins of interest, we now develop a super-resolution fluorescence technique for integrated CLEM called electron beam-induced super resolution microscopy (eSRM): fluorescence signals are recorded during scanning of the focused electron beam, local modifications of the signal by the electron beam allow localization of fluorescence molecules with improved resolution (figure 2). Fluorescent proteins are optimized for high fluorescence yield in vacuum, either stability or lability under electron irradiation, and compatibility with EM sample preparation. This resulted in several candidate probes with both an increase in vacuum quantum yield and fluorescence maintained during EM sample preparation. Thus, the quantitative power of EM is improved by nanotomy in combination with analytical EM and optimized CLEM methods.

References:
[1] de Boer et al., *Nature Communications,* 11, 2020
[2] Scotuzzi et al., *Scientific Reports*, 7,7:45970, 2017
[3] de Boer et al., *Nature Methods*, 12(6):503-13, 2015

Figure 1: EDX defines cell-types and subcellular structures in nanotomy maps. (a) nanotomy overview of a rat islet of Langerhans. (b) Area of interest (indicated in a; cyan dot) shows four cells with different granules based on grey levels and morphology. (c-f) Elemental content in the ROI for nitrogen (N), phosphorus (P), sulfur (S), and osmium (Os). (g) Overlay of N (red), P (green), and S (blue) allows identification of cells and granules. (h) Overlay of back scatter ICD image (BSD, grey) over the color-image of g. Bars: 50 µm (a) and 2 µm (b-h). The figure is adapted from [2].

Figure 2: Electron beam-induced super resolution microscopy (eSRM). (a) Post-embedding immunolabeling of insulin on an ultrathin rat pancreas section using alexa fluor 594 (orange), with the region of interest (ROI) depicted. (b) Widefield fluorescence image of ROI. (c) SEM image of the ultrastructure of the ROI revealing single insulin granules (black cores). (d) Image after the eSRM protocol, showing the bleached ROI. (e) The same ROI as in b after the eSRM protocol. (f) The eSRM image from e overlaid on the SEM image of c. Bars: 10 µm (a, d) and 1 µm (b-c, e-f).

Figure 1

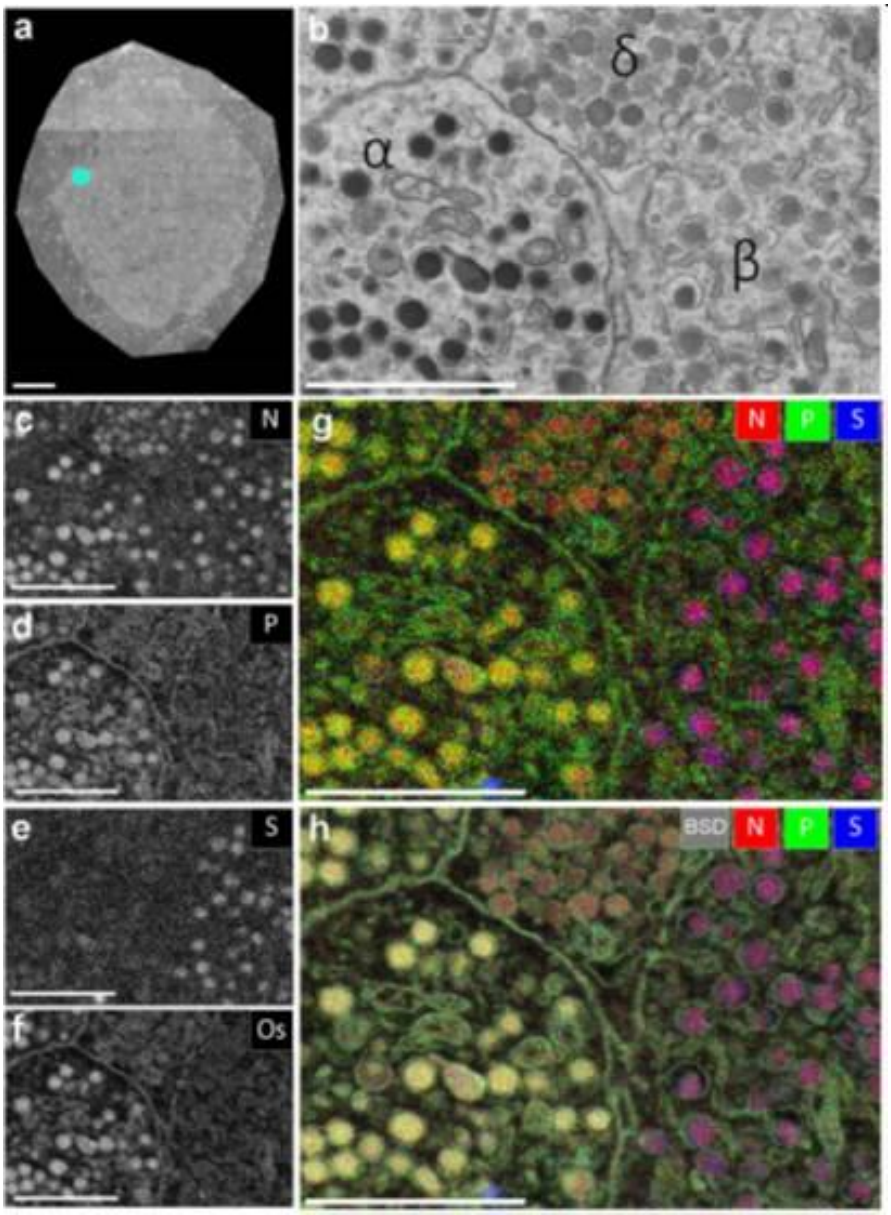

Figure 2

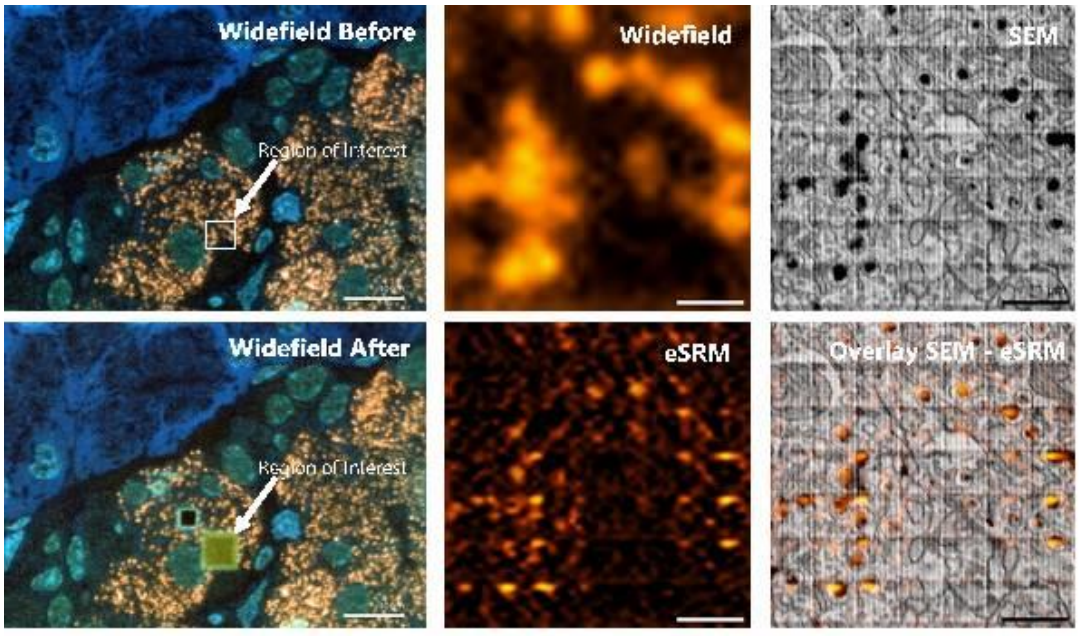

IM7.P001
Correlation of FluidFM® technology and fluorescence microscopy for the visualisation of ceular detachment steps

F. Weigl[1], A. Sancho[1,2], J. Groll[1]

[1]University of Würzburg, Department for Functional Materials in Medicine and Dentistry and Bavarian Polymer Institute (BPI), Pleicherwall 2, Würzburg, Germany
[2]University of the Basque Country UPV/EHU, Department of Automatic Control and Systems Engineering, Plaza de Europa 1, Donostia, Spain

Introduction: Mechanobiology is a rapidly growing field of research that focuses on the role of physical forces in cellular functions and processes. On a cellular level, adhesion forces occur between cells and their surrounding extracellular matrix as well as between adjacent cells. To obtain a better understanding of these biological functions, the correlation of different microscopical techniques has become more and more important within the last years. Especially, Atomic Force Microscopy (AFM) as one of the most commonly used techniques for the analysis of cell adhesion, was combined with a variety of optical microscopy techniques. Since AFM is limited to the investigation of early phase adhesion, Fluidic Force Microscopy (FluidFM®) that allows the quantification of mature adhesion forces was developed.[1,2] Although FluidFM® has brought new advances in the study of mechanobiological events[3,4], there is still the need of qualitative analysis of cellular detachment forces. Here, we present a new system correlating Fluorescence Microscopy and FluidFM® (FL-FluidFM®), which enables the simultaneous visualization and quantification of cell substrate forces.

Methods: The correlated investigation of cell-substrate adhesion was performed by Single-Cell Force Spectroscopy (SCFS) using FluidFM® and Fluorescence Microscopy in one system. Therefore, adherent rat embryonic fibroblasts (REF52) were immobilized at the cantilever tip by applying a negative pressure, followed by cellular detachment. During this process, the detachment forces were quantified by force-distance curves and, at the same time, visualized by optical tracking of fluorescently labelled cells. Afterwards, the detachment steps were characterized by distinguishing between different types of biomechanical events.

Results: With the integration of Fluorescence Microscopy into the FluidFM® technology, we were able to show an optical tracking of cell components during the cell detachment. At the same time, the detachment process, as well as its force-distance curves, were not negatively affected by the laser excitation. Furthermore, first results also indicated that the emerging detachment steps within a force-distance curve could be classified into initial rupture events followed by membrane tether arising at the end of a cellular detachment.

Conclusion: The establishment of FL-FluidFM® as a novel correlated device, paves the way for a new type of characterization of cellular detachment forces. Not only the maximum force of mature cell contacts can be investigated but rather the correlation between force steps and corresponding biomechanics within a detached cell. Therefore, combined FluidFM® and Fluorescence Microscopy has the potential to reveal new insights into the mechanobiology of cell adhesion.

References:
[1] Helenius, J. *et al*., *J Cell Sci* 121**,** 1785-1791 (2008).
[2] Meister, A. *et al*., *Nano Lett* 9, 2501-2507 (2009).
[3] Sancho, A. *et al.*, *Sci Rep* 7*,* 46152 (2017).
[4] Wysotzki, P. *et al.*, *Colloid Surface B* 190, 110894 (2020).

IM7.P002
The novel approach to correlative microscopy using AFM-in-SEM and CPEM technology

J. Horak[1], V. Hegrova[1], Z. Novacek[1], M. Pavera[1], J. Neuman[1]

[1]NenoVision s.r.o., Brno, Czech Republic

Scanning electron microscopy (SEM) and atomic force microscopy (AFM) are two of the most used, complementary techniques for surface analysis at the nanoscale. Thus, combining them by integrating a compact AFM into SEM brings novel possibilities for true correlative microscopy and advanced multi-modal sample characterization that would be often unfeasible using each imaging modality separately.

LiteScope 2.0 (Figure 1a) produced by the NenoVision company represents a compact AFM, which is designed to be integrated into a large variety of SEMs. In general, the strength of the resulting AFM-in-SEM hybrid system lies in combining the AFM modes (3D topography, electrical, mechanical, and magnetic measurements) with SEM capabilities (fast imaging with wide resolution range, chemical analysis, surface modification, etc.). Further advantages include fast region of interest localization and AFM tip navigation by SEM, and complete sample measurement in in-situ conditions, which dramatically facilitates analysis of sensitive samples. Uniquely, LiteScope design enables simultaneous acquisition and correlation of AFM and SEM data by a technique called Correlative Probe and Electron Microscopy (CPEM).

CPEM technology anbles to keep constant offset between electron beam and AFM probe during the image acquisition (Figure 1b), since the scanning movement is conducted by a piezo scanner that carries the sample. This ensures simultaneous data collection in the same coordinate system and with identical pixel size. The resulting 3D CPEM view can combine multiple channels, both from AFM and SEM (Figure 1c), enabling thorough analysis for specific applications.

Above mentioned advantages are demonstrated in Figure 2, showing structural analysis of multilayered WSe2 flakes on Si nanopillars, where a certain shape of the WSe2 monolayer over the nanopillars creates a single-photon emitter. The AFM-in-SEM system enabled to quickly localize the structure of interest on a complex sample. The correlated CPEM image combines AFM topography with SEM material contrast and provides unmistakable data interpretation.

In conclusion, the AFM-in-SEM strategy benefits from the complementarity of both techniques alongside significant savings both in time and resources. Also, it opens completely new possibilities for advanced data correlation and measurements, e.g. in the field of surface modification, semiconductor or spectroscopy.

Figure 1: (a) AFM LiteScope 2.0, (b) CPEM principle and (c) 3D CPEM view of tungsten alloy consisting of multiple channels (AFM, AFM + SEM SE and AFM + SEM BSE).

Figure 2: Exfoliated WSe2 flakes on Si nanopillars: SEM overview of the sample and fast AFM probe navigation. The signal from secondary electrons detector (SE), AFM topography with height profile, and resulting 3D CPEM view of merged AFM topography and SE signal.

Figure 1

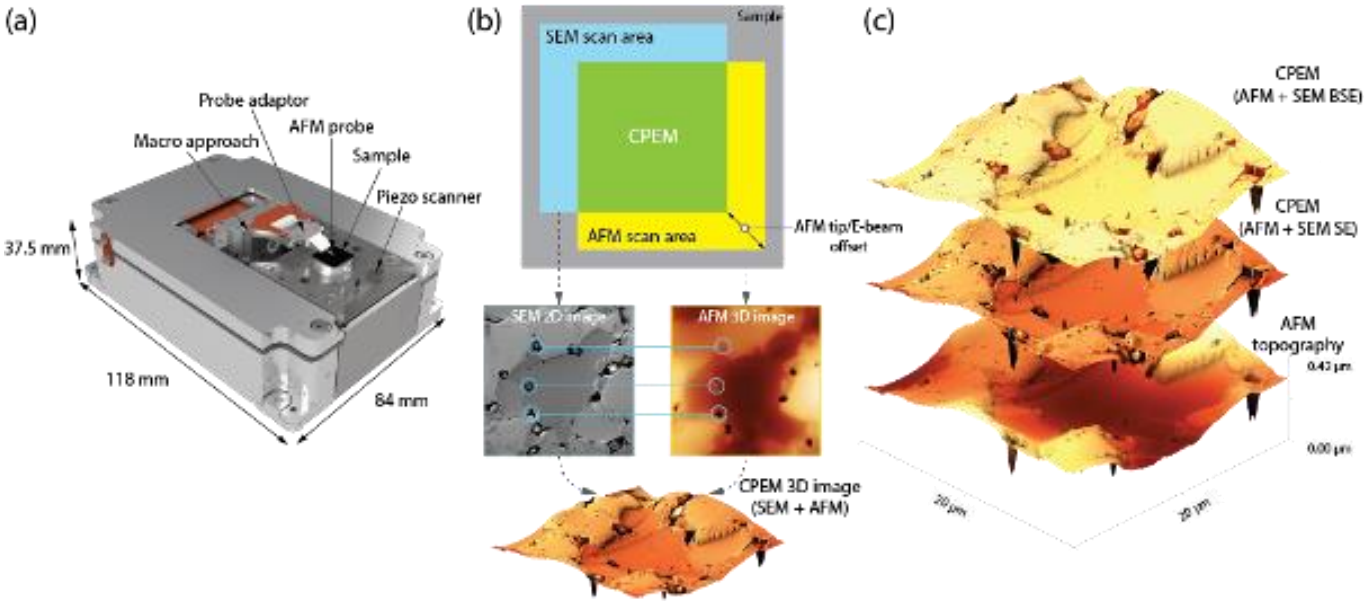

Figure 2

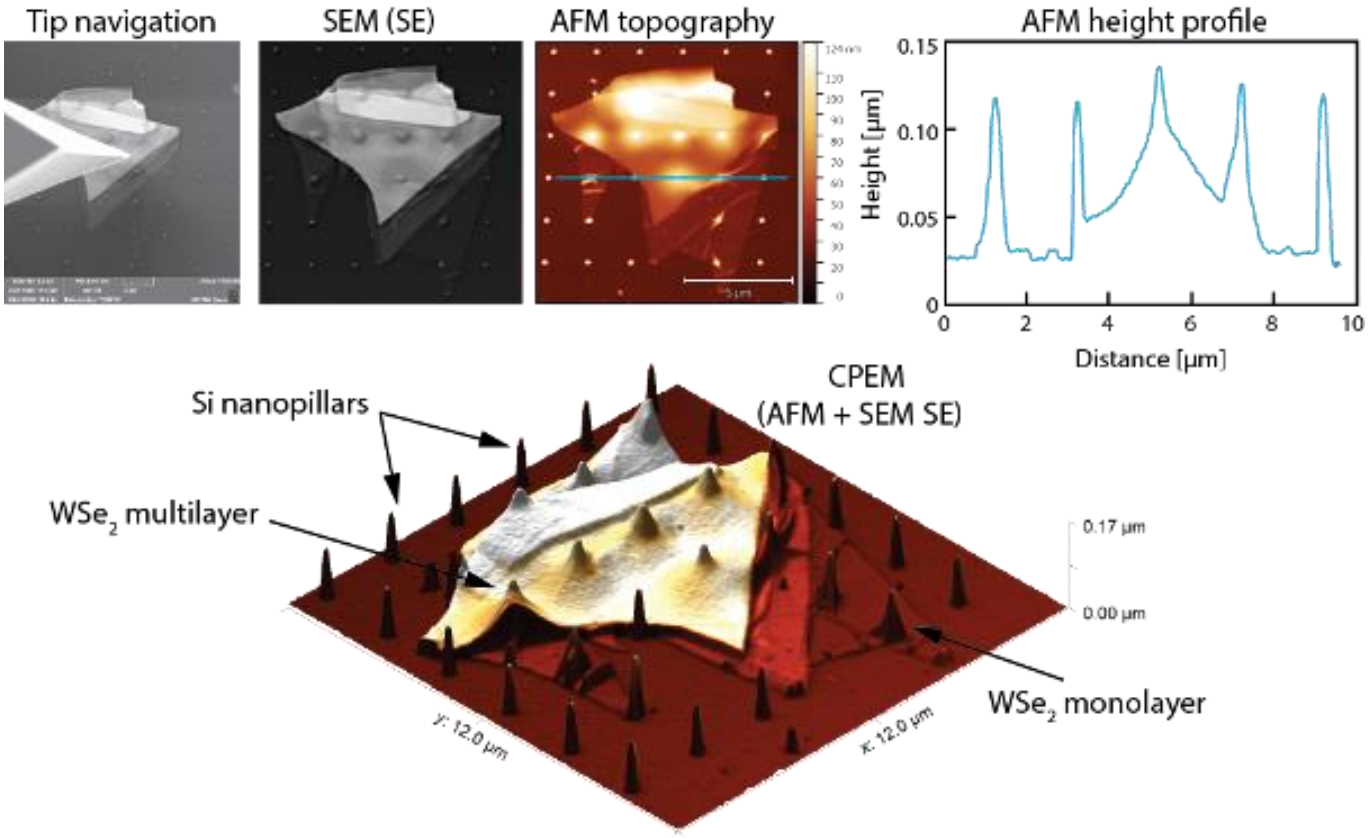

IM7.P003
Combining AFM with super-resolution optical imaging towards multiparametric correlative microscopy

A. Koernig[1], D. Stamov[1], T. Neumann[1], A. Kraus[1], H. Haschke[1]

[1]Bruker Nano GmbH, Berlin, Germany

Question: The last three decades have established atomic force microscopy (AFM) as an indispensable tool for high-resolution structural analysis of specimens ranging from single molecules to complex biological systems. AFM currently offers premium spatial resolution of the analysed samples while simultaneously being able to correlate topography and mechanics at near native/physiological imaging conditions. Recording the stimulated emission depletion (STED) microscopy fluorescence delivers a multi-colour image with a spatial resolution 6-10 times enhanced relative to conventional optical methods and, therefore, reach the same order of magnitude as the spatial resolution of the AFM.

We have developed a new AFM technology which enables the high-speed study of the time-resolved dynamics associated with single molecule and cellular processes on the millisecond scale. The scanner technology further allows full integration of AFM into advanced commercially available light microscopy techniques. We will further introduce a dual scanner technology, allowing the simultaneous control of two Z piezos, namely high-speed feedback control, and larger Z-motion control and tracking of corrugated samples.

Methods: To reach the objectives, we have applied a tip-scanning AFM setup (JPK NanoWizard AFM, Bruker), which will be demonstrated in combination with a Stedycon compact line STED (Abberior Instruments).

Results: We will present examples of how we are able to resolve the nanoscale structure and thermodynamic fluctuations of individual DNA biomolecules at high-speed scan rates (up to 10 frames per second), follow the dynamic reorganization of the membrane-associated cytoskeleton of living cells at high-temporal and high-spatial resolution, and automatically map the topography and mechanical properties of cell cultures across the entire area of the microscope stage. We will demonstrate how AFM imaging and super-resolution 2color easy3D STED measurements can be combined and show results on the co-localized imaging and sample manipulation with a precision far below the diffraction limit. This will be applied for comprehensive investigation of biological samples and immunological assignment of the high-resolution cytoskeletal filaments in living fibroblasts. The mechanical stimulation of microtubules and actin filaments with AFM in living cells while performing STED experiments will be presented. We will also show examples of the accuracy of registering/overlay the AFM and optical images on commercially available DNA origami structures with dimensions below the diffraction limit.

Conclusions: The demonstrated high-speed AFM and optical integration allows the study of millisecond scale dynamic processes, while leveraging the advantages of immunolabelling techniques, and quantification of mechanical properties, for truly correlative microscopy.

IM7.P004
Fast determination of the thickness of electron-transparent specimens using quantitative STEM-in-SEM and Monte-Carlo simulations

K. Adrion[1], M. Hugenschmidt[1,2], E. Müller[1], D. Gerthsen[1,2]

[1]Karlsruhe Institute of Technology (KIT), Laboratory of Electron Microscopy, Karlsruhe, Germany
[2]Karlsruhe Institute of Technology (KIT), 23DMM2O – Cluster for Excellence (EXC-2082/1 – 390761711), Karlsruhe, Germany

Accurate values for the thickness of electron-transparent specimens in electron microscopy are of general interest, e.g. as a parameter for quantitative simulations and calculations in the field of transmission electron microscopy (TEM). Several thickness-determination techniques exist, e.g. based on plasmon losses in electron energy loss spectra [1,2], convergent-beam electron diffraction [3], or exploitation of thickness contours in images acquired under two-beam diffraction conditions. However, the accuracy, precision, and time consumption differs significantly and often yields thickness values only for a small sample region. We will show in this work that scanning transmission electron microscopy (STEM) in a scanning electron microscope (STEM-in-SEM) is well suited for thickness determination with rather satisfying accuracy (error within a few percent). This technique has been further elaborated by us after previous initial work [4,5]. We will give an in-depth instruction and discussion of the technique so that users can avoid pitfalls. For the experimental work, a dual-beam FEI Strata 400S was used. The instrument is equipped with a multi-segmented STEM detector with a bright-field (BF) segment in the center and several ring-shaped annular dark-field (ADF) and a high-angle (HA) ADF segments (**Figure 1**). The inner and outer physical radii of the active segments determine the investigated scattering-angle range. The experimental STEM intensity I_{exp} is normalized with respect to the intensity of the primary electron beam I_0 and the back-level intensity I_{bl} to facilitate comparison of experimental and simulated STEM intensities:

$$I=(I_{exp}-I_{bl})/(c\cdot I_0-I_{bl}) \quad (1)$$

I_0 is obtained by directly scanning the activated segments of the STEM detector (**Figure 1**). Inactive segments of the detector (here the central segments) yield I_{bl}. Less sensitive regions of the activated segments, e.g. contact lines, are taken into account by the factor c. The final step is to compare the intensities I with calculated normalized intensities from Monte-Carlo simulations (NISTMonte1.2 [6] modified by us), which are performed as a function of the sample thickness and thus relate normalized STEM intensities to the thickness. **Figure 2** shows as an example a FIB-milled silicon specimen with wedge-shaped geometry. The color-coded inset is a thickness map obtained with the presented method. Further applications will be presented.

STEM-in-SEM is a versatile method for the determination of the sample thickness. With known material parameters, the local thickness can be determined quickly and precisely.

References:
[1] Malis et al., Microsc. Tech. 8, 193 (1988)
[2] Zhang et al., Micron 43, 8 (2012)
[3] Rozeveld and Howe, Ultramicroscopy 50, 41 (1993)
[4] Volkenandt et al., Microsc. Microanal. 16, 604 (2010)
[5] Čalkovský et al., Ultramicroscopy 207, 112843 (2019)
[6] Ritchie, Surf. Interface Anal., 37, 1006 (2005)
[7] Hugenschmidt et al., J. Microsc. 274, 150 (2019)

Figure 1: 30 keV STEM image obtained by directly scanning the STEM detector. The outer part of the HAADF segment is covered by the objective lens pole piece (adapted from [7]). The average intensities of the marked areas give I_0 and I_{bl}.

Figure 2: Side perspective of a Si wedge imaged at 30 keV with the activated HAADF and ADF segments. The color-coded inset displays the thickness according to the legend. The white line shows a qualitative line profile of the thickness map, revealing the wedge edge has an offset of ~70 nm.

Figure 1

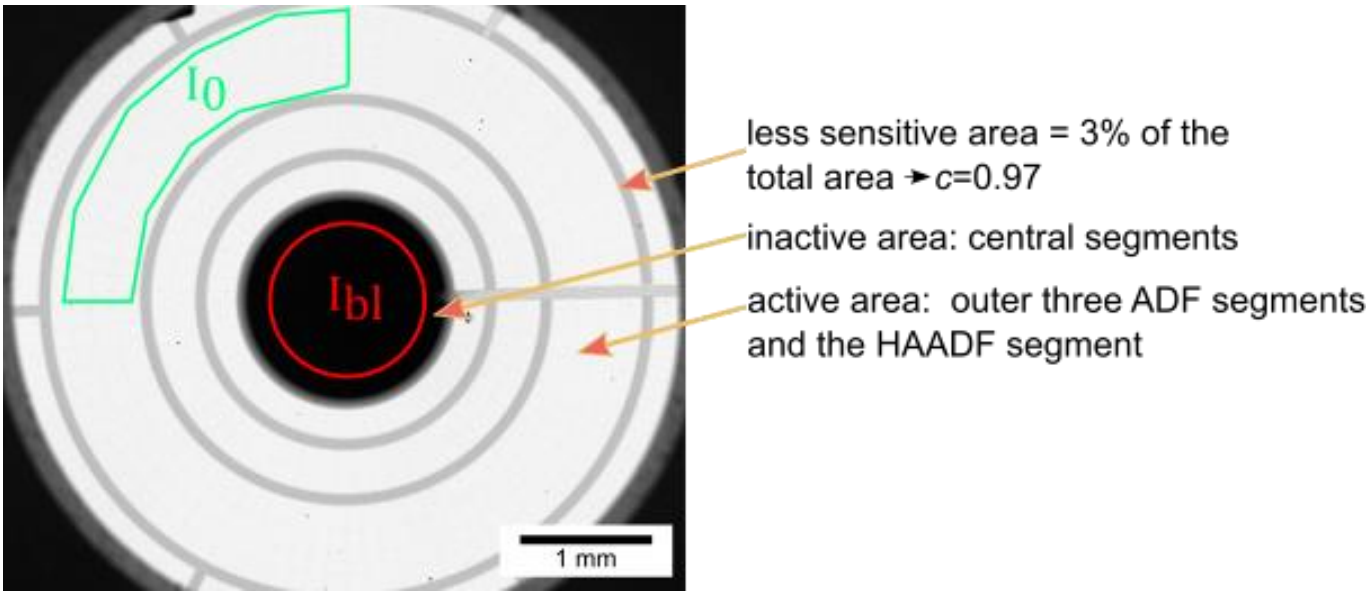

Figure 2

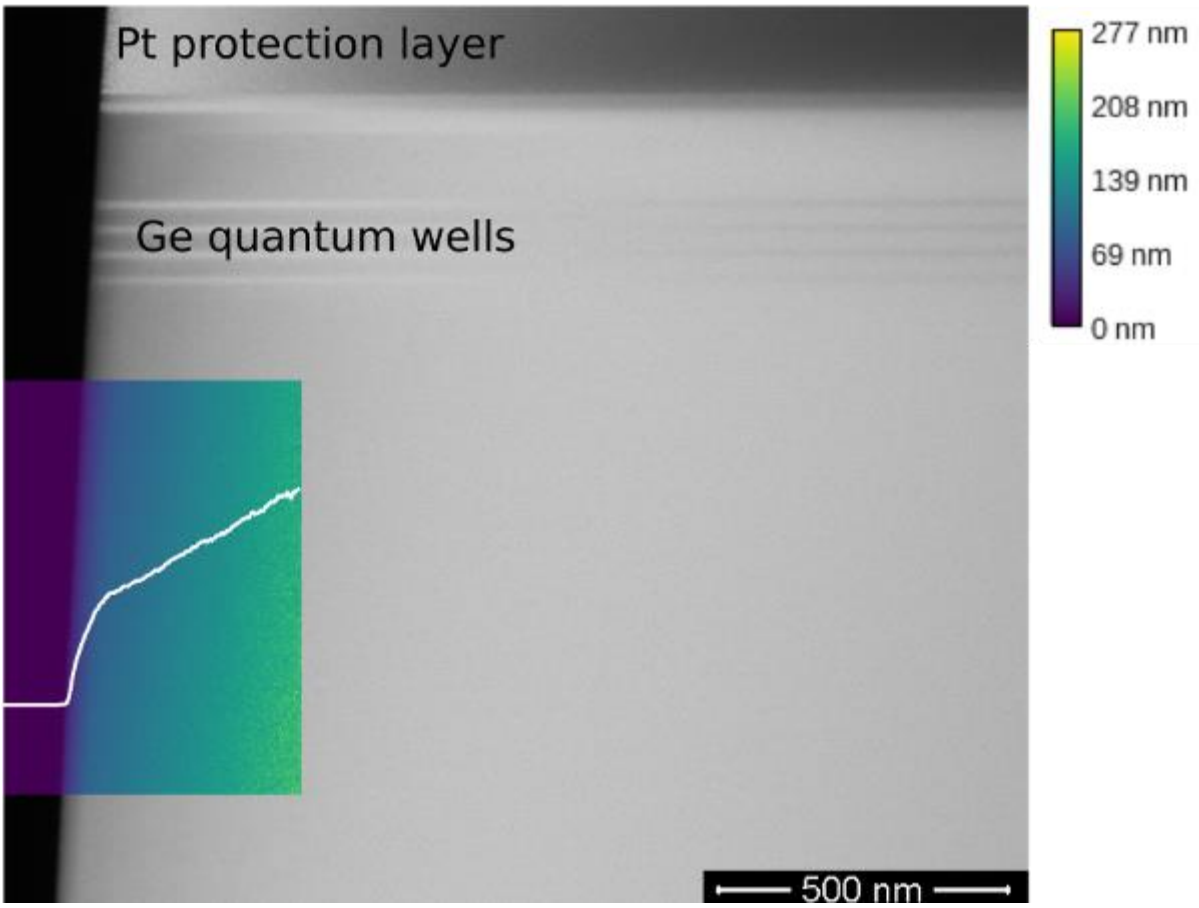

IM7.P005
A novel method for improving resolution and image contrast in integrated differential phase-contrast (IDPC)-STEM

Z. Li[1], J. Biskupek[1], U. Kaiser[1], H. Rose[1]

[1]University of Ulm, Ulm, Germany

Techniques for obtaining efficient phase contrast in the scanning transmission electron microscope (STEM) imaging were proposed in the 1970s [1-3]. One of the techniques is the integrated differential phase-contrast (IDPC). In the IDPC mode, the differential phase contrast (DPC) images are first acquired by subtracting the signals collected by opposite segments of a quadrant detector [3,4] or an annular quadrant detector [5]. The IDPC image is subsequently obtained by integrating the difference signals along the two symmetric axes of the segments. This method has demonstrated experimentally its advantage by showing the images of heavy and light atoms simultaneously and by suppressing high-frequency noise [4,5].

The current IDPC methods have limitations – they can be only applied to thin samples. For a thick sample which suffers dynamical scattering, a large defocus might be required to focus the probe at the inner structure of the sample. In this case, the anisotropy of the CTF increases, which makes it difficult to interpret the image contrast. With the help of simulations, we found that by increasing the number of detector segments, it is possible to apply the IDPC method also to thick samples.

The example structure for this simulation is a polyoxometalate (POM) particle stuffed in a single-wall carbon nanotube, shown in Figure 1. IDPC image simulation is performed at 80kV by using different detector geometries. As the probe focuses at different thickness of the sample, the image contrast and resolution improve when the number of detector segments increases. Experimental realisation for the proposed IDPC-STEM imaging requires an aberration-corrected STEM equipped with a pixelated detector. A set of Ronchigrams corresponding to each scanning position have then to be collected, and numerical detectors are applied posteriorly.

Figure 1: Simulations of IDPC-STEM images using different numbers of detector segments for a Cc/Cs-corrected STEM operating at 80kV. The sample is a polyoxometalate (POM) particle stuffed in a SWNT and the illumination is parallel to the SWNT. The length of the SWNT is 6nm. The images in each row are simulated for a given location of the probe focus. Scale bar: 0.5nm.

Aknowledgement

We acknowledge the finanical support of the German Research Foundation (DFG) within the project 456681676.

[1] H Rose. Optik 39 (1974) 416–436.
[2] N. Dekkers and H De Lang. Optik 41.4 (1974) 452–456.
[3] H Rose. Ultramicroscopy 2 (1977) 251-267.
[4] I. Lazić, E. G. Bosch, and S. Lazar. Ultramicroscopy 160 (2016) 265–280.
[5] E. Yücelen, I. Lazić, and E. G. Bosch. Scientific reports 8 (2018) 1–10.

Figure 1

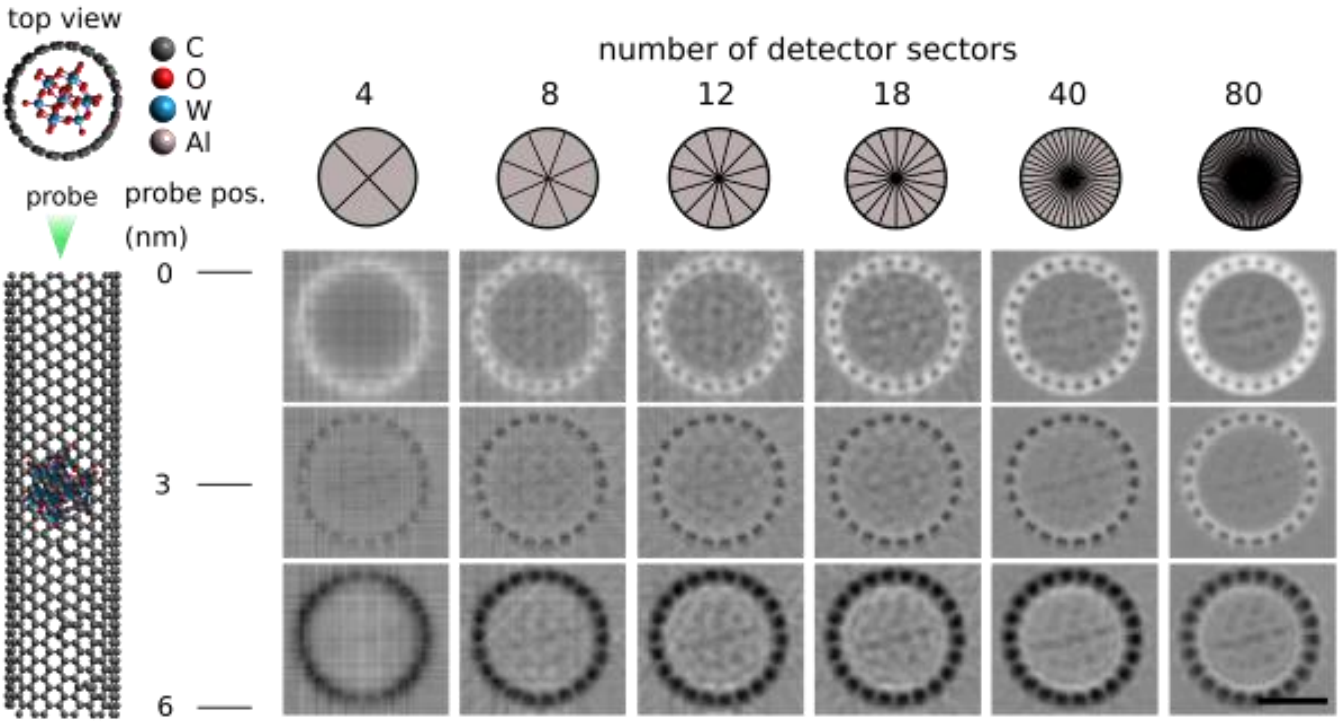
top view
C
O
W
Al
probe
probe pos.
(nm)
0
3
6
number of detector sectors
4
8
12
18
40
80

IM7.P006
Machine-learning approach for resolution enhancement of low-dose STEM data

L. Gambini[1], S. Sanvito[1], L. Jones[1], T. Mullarkey[1]

[1]Trinity College Dublin, Physics, Dublin, Ireland

Electron microscopy allows academic and industrial users to resolve the structure of materials at the atomic level. Specifically, a scanning transmission electron microscope (STEM) enables the recording of images with resolutions below 0.1 nm. However, this result is achievable only when a high electron dose is employed, a practice that may cause damage to the analyzed specimen and affect the observation. This aspect sets some limitations on the range of applications of high-resolution electron microscopy.

My work proposes a strategy, based on machine-learning techniques, which enable a significant improvement in the quality of STEM images generated at low electron dose. These are strongly affected by Poisson noise, an effect related to the quantised nature of the electron beam, which cannot be corrected at the instrumentation level. The neural network employed in this work presents a symmetric architecture known as autoencoder, a model extensively used in image processing. The training of the model was conducted on a dataset made of simulated STEM images including different materials and a large range of doses. The variety of the dataset determined the ability of the algorithm to generalize and perform well on previously unobserved data. The algorithm was validated with tests conducted on simulated and experimental images, obtained at various levels of electron dose and for different types of specimen.

The results show a significant improvement in the image quality and the possibility to extract information with more precision from the processed data compared to the original ones. The application of the proposed algorithm allows the microscope user to reduce the electron dose during the acquisition process and therefore enables the analysis of fragile materials with satisfactory resolution.

IM7.P007
Project "Pattern" – an open access online tool for spatial analysis of immunolabeling in electron microscopy

D. Pinkas[1], E. Vlčák[1], V. Filimonenko[1,2], J. Janáček[3], J. Novák[4], M. Jiřina[4], P. Hozák[2]

[1]Institute of Molecular Genetics of the ASCR, v. v. i., Electron Microscopy Core Facility, Prague, Czech Republic
[2]Institute of Molecular Genetics of the ASCR, v. v. i., Department of Biology of the Cell Nucleus, Prague, Czech Republic
[3]Institute of Physiology ASCR v.v.i., Department of Biomathematics, Prague, Czech Republic
[4]Czech Technical University in Prague, Faculty of Information technology, Department of applied mathematics, Prague, Czech Republic

On-section immunolabelling in electron microscopy, while sharing labeling principles with immunofluorescence, provides precise localization of selected antigens within the context of cellular ultrastructure. However, evaluation of such images often lacks unbiased quantitative approach and relies on subjective impressions. We have developed an easy-to-use online tool for semi-automatic multi-stage analysis of immunolabeling on EM images spanning particle detection and classification, mathematical and statistical evaluation and visualization of results. This builds on previous work of A. Philimonenko et al. [1], C. Schofer et al. [2] and V. Philimonenko et al. [3]. The tool detects basic particles ("big" and "small" spheres) automatically and enables use of custom particles of different shapes; results of detection and identification can be manually reviewed and edited. The tool uses pair correlation and pair cross-correlation functions for clustering and colocalization evaluation with results presented both numerically and graphically. Labelled structures are visualised via mapping and their spatial relations to other structures or particles are further evaluated. Apart from usual planar 2D evaluation, the tool can also evaluate spatial relations in volume and along linear structures. Statistical significance of detected patterns is calculated and presented in a comprehensive way without the need for deep insight into statistical analysis. All results and respective settings can be exported. Particle coordinates can be kept on the server for prolonged periods of time to be compared to new datasets. Projects can be shared with colleagues. For routine analysis, useful results can be available in just a few clicks.

The tool is provided to the broad scientific community in open access mode by the Institute of Molecular Genetics of the Czech Academy of Sciences within the Czech-BioImaging research infrastructure at pattern.img.cas.cz. The tool emphasizes convenience and understandability of the interface. The platform is modular and can be expanded with more capabilities in the future.

This project is supported by MEYS CR (LM2018129), OPVVV (CZ.02.1.01/0.0/16_013/0001775), IMG grant (RVO: 68378050) and TACR (TE01020118) grants.

References:
[1] Philimonenko, A. A., Janáček J. and Hozák P. "Statistical evaluation of colocalization patterns in immunogold labeling experiments." Journal of structural biology 132.3 (2000): 201-210.
[2] Schöfer, C., Janáček, J., Weipoltshammer, K., Pourani, J., & Hozák, P. (2004). Mapping of cellular compartments based on ultrastructural immunogold labeling. Journal of structural biology, 147(2), 128-135.
[3] Philimonenko, V. V., Philimonenko, A. A., Šloufová, I., Hrubý, M., Novotný, F., Halbhuber, Z., ... & Hozák, P. (2014). Simultaneous detection of multiple targets for ultrastructural immunocytochemistry. Histochemistry and cell biology, 141(3), 229-239

IM8.001-Invited
Impact of defocus in high-resolution momentum-resolved STEM

H. L. Robert[1,2], F. Winkler[1], I. Lobato[3], S. Van Aert[3], F. J. Lyu[4], Q. Chen[4], K. Müller-Caspary[1,2]

[1]Research Center Jülich, Ernst Ruska-Centre for Microscopy and Spectroscopy with Electrons (ER-C), Jülich, Germany
[2]RWTH Aachen University, 2nd Institute of Physics, Aachen, Germany
[3]University of Antwerp, Electron Microscopy for Materials Science (EMAT), Antwerp, Belgium
[4]Peking University, Department of Electronics, Beijing, China

Recently, the recording of a detailed diffraction pattern at each scan position was enabled in scanning transmission electron microscopy (STEM), by using a fast electron camera, thus elevating the number of measurement dimensions to four. In this work, we increase it further by implementing the automated acquisition of focal series momentum-resolved (MR) STEM [1]. In particular, we report the individual defocus-dependence [2,3] of conventional STEM signals, and 4D STEM-specific signals such as the diffraction patterns" first and second moments. Comprehensive simulations are employed to interprete our results.

Experiments are done on an α-In2Se3 specimen, using an aberration-corrected FEI Titan 80-300 STEM instrument equipped with a Medipix camera, running with a frame rate higher than 2 kHz [4]. Results are given in figure 1, where various STEM signals are plotted against probe defocus. Using a dedicated Fishione detector, a high-angle annular dark field (HAADF) signal is obtained alongside the signals extracted from the diffraction patterns. Those include the first moment (M1) of each diffraction frame, which displays sensitivity to the local electric field in thin specimens [5], as well as the second moment (M2). The bright field (BF) and the annular bright field (ABF) signals are extracted through the application of virtual detectors. As verified in the experiment, the signals all display a unique dependence to defocus. In particular, it is observed that both the ABF and the M2 signals reach a contrast maximum for two distinct foci.

In figure 2.b and 2.c, simulated HAADF and M2 images of the α-In2Se3 crystal are plotted against specimen thickness and defocus. Through this simulation, with the thickness estimation depicted in figure 2.a, it is found that the two foci closely (within 1.5 nm) coincide with the vertical positions the specimen"s interfaces with vacuum. The smooth contrast decay of the HAADF signal is observed both in the simulation and the experiment.

Our study"s outcome is two-fold. First, a limit to considering MR STEM as a universal acquisition mode is put to light, as common STEM signals, such as HAADF and first moment, should be recorded at different foci. Second, it is showed that the foci of signals such as e.g., the second moment, can yield geometrical information including the vertical positions of the specimens" entrance and exit surfaces. Findings will be discussed with respect to perturbations by mistilt, amorphous carbon contamination and possible applications in materials science.

Figure 1: Signals extracted from the experimental data. The M1 and M2 signals are calculated using a cut-off angle of 27 mrad. The two bright field signals, BF and BFr, are obtained by summing intensity respectively within the full primary beam, up to 23 mrad, and within a reduced diffraction region, up to 17 mrad. The ABF is obtained by summing intensity between 17 and 23 mrad. Images corresponding to local contrast maxima are highlighted in red. The size of the scan window is 2 nm and the step between two defoci is 1.5 nm. The zero-position of the defocus axis is arbitrary.

Figure 2: a) The thickness is measured to 13.45 nm by comparison between experimental (top) and simulated (bottom) position-averaged convergent electron diffraction (PACBED) patterns. The mistilt is estimated to 1.7 mrad and is included in the simulation. Simulated b) HAADF and c) M2 images are plotted against defocus and thickness. The specimen"s surfaces are indicated.

[1] Funding from the Initiative and Network Fund of the Helmholtz Association under contract VH-NG-1317 is gratefully acknowledged
[2] Bürger et. al.; Ultram. 219, 113118 (2020)
[3] C. Addiego et. al.; Ultram. 208, 112850 (2020)
[4] R. Plackett et. al.; J. instr. 8, C01038 (2013)
[5] K. Müller-Caspary et. al.; Nat. comm. 5, 5653 (2014)

Figure 1

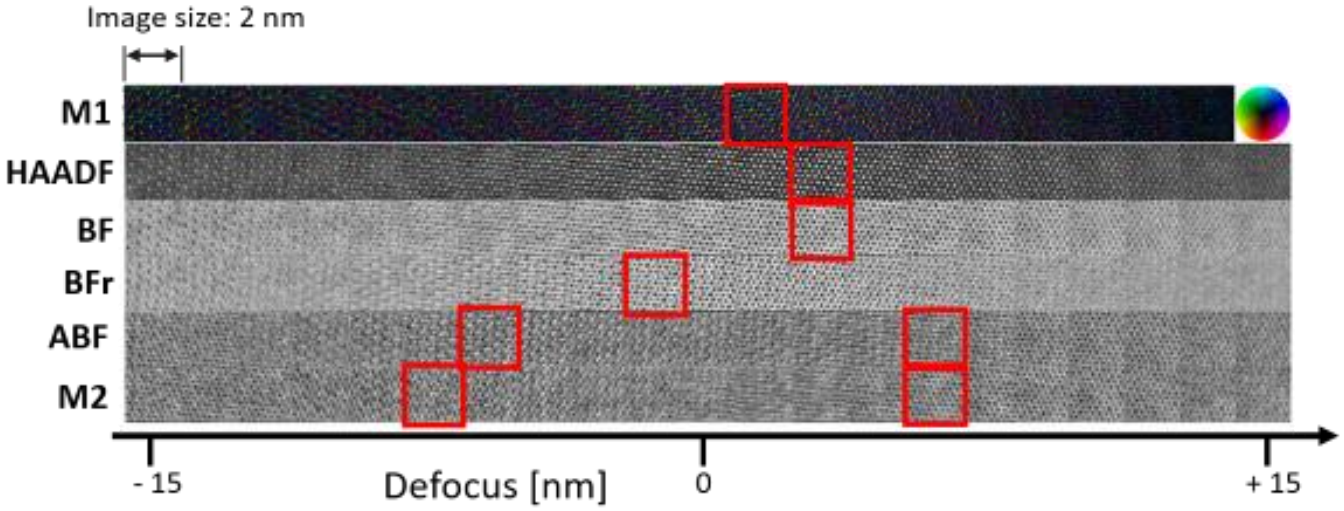

Figure 2

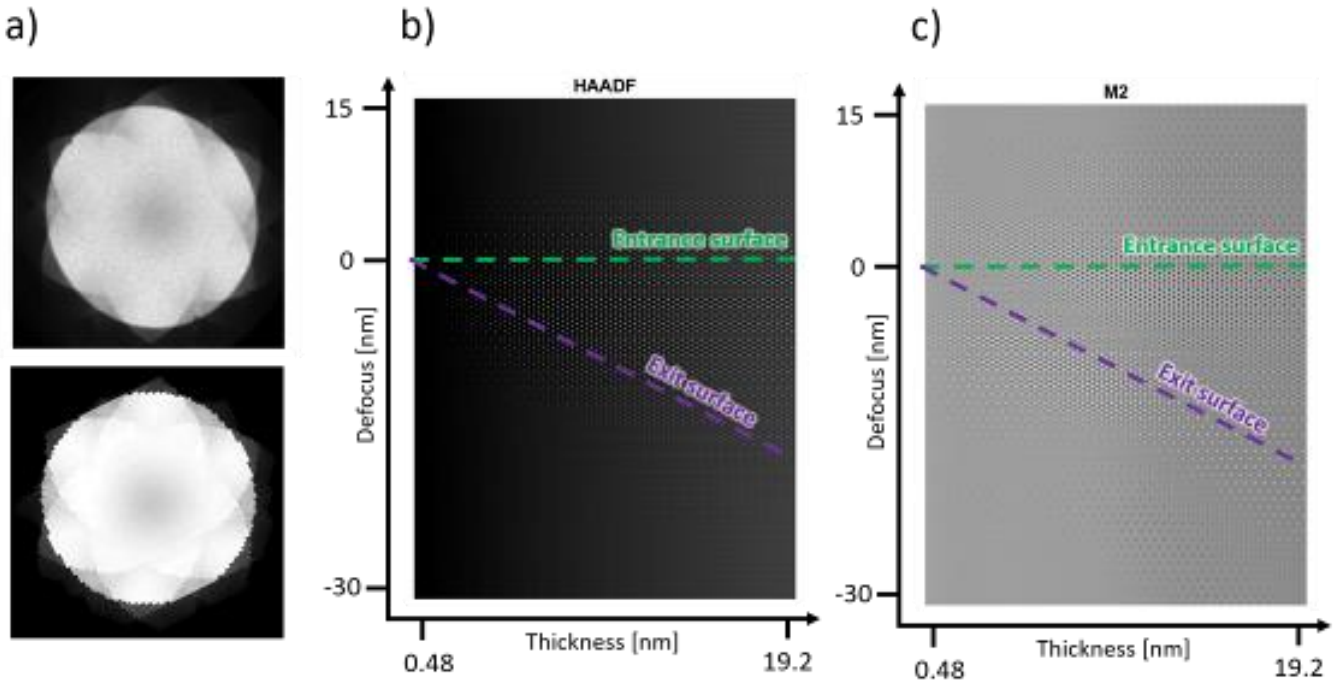

IM8.002-Invited
Magnetism and atomic vibrations in transmission electron microscopy

J. Rusz[1], P. Zeiger[1], K. Lyon[1], A. Edström[2], A. Lubk[3], A. Bergman[1]

[1]Uppsala University, Department of Physics and Astronomy, Uppsala, Sweden
[2]KTH Royal Institute of Technology, Stockholm, Sweden
[3]IFW Dresden, Dresden, Germany

Recent dramatic improvements in the instrumentation have allowed to detect scattered electrons with energy resolutions well below 10 meV [1] while maintaining atomic spatial resolution [2]. Improved detectors [3] are approaching noise levels close to purely shot noise, allowing to analyse more and more subtle effects, such as detailed phonon bandstructures. As of today, monochromated electron energy loss spectroscopy (EELS) has allowed to distinguish isotope compositions and vibrational signatures of individual defects, such as impurity atoms [4] or stacking faults [5].

These significant achievements call for development of theoretical methods, versatile enough to take into account the experimental geometry, such as electron beam shape and direction, electron beam propagation effects, capable to treat 2-dimensional as well as bulk samples with arbitrary atomic structures. Such methods should be also efficient enough that large structure models containing tens of thousands of atoms, allowing to describe scattering on interfaces, various types of defects or even isotope compositions.

We have developed a method having an ambition to satisfy these demands [6]. Non-equilibrium molecular dynamics calculations offer a route to avoid explicit calculation of individual phonon modes, which can be prohibitively expensive for large structure models. Thus, an evolution of the frozen phonon model leads to a frequency-resolved frozen phonon multislice method, a method largely preserving the flexibility and efficiency of frozen phonon multislice calculations, while offering the spectroscopic dimension in addition. We will present examples of vibrational EELS simulations of systems with defects at both nanometer and atomic scale.

Another frontier opened up by the improved instrumentation is magnetism. Interaction of electron beam with magnetic fields inside the sample is inherently weaker than the corresponding interaction with electric fields. Experiment of Loudon [7] has revealed a minuscule magnetic Bragg peak in an antiferromagnetic NiO under the Neel temperature. While this experiment was challenging, increased sensitivity of instruments will make such experiments more easily accessible.

To describe the propagation of electron beam through a magnetic sample it is needed to extend the classical multislice method. Recently developed Pauli multislice method [8] builds such formalism starting from Pauli equation instead of Schrödinger equation. Using this method we have studied interaction of magnetism in samples with electron beams [8] and described an extension of the atomic scale differential phase contrast (DPC) method to magnetic materials [9].

References:
[1] O. Krivanek et al., Nature 514, 209 (2014).
[2] F. Hage et al., Phys. Rev. Lett. 122, 016103 (2019)
[3] B. Plotkin-Swing et al., Ultramic. 217, 113067 (2020).
[4] F. Hage et al., Science 367, 1124 (2020).
[5] X. Yan et al., Nature 589, 65 (2021).
[6] P. Zeiger and J. Rusz, Phys. Rev. Lett. 124, 025501 (2020).
[7] J. C. Loudon, Phys. Rev. Lett. 109, 267204 (2012).
[8] A. Edström, A. Lubk, J. Rusz, Phys. Rev. Lett. 116, 127203 (2016).
[9] A. Edström, A. Lubk, J. Rusz, Phys. Rev. B 99, 174428 (2019).

IM8.003
Phase object reconstruction from 4D STEM dataset with neural network

C. P. Yu[1], T. Friedrich[1], T. Pennycook[1], J. Verbeeck[1], S. Van Aert[1]

[1]University of Antwerp, Department of Physics, Antwerp, Belgium

We present a computational imaging method for 4D-electron microscopy data, which retrieves an exit wave from Convergent Beam Electron Diffraction Patterns (CBED) using a deep learning approach. Subsequently, the object image is reconstructed using the phase object approximation. The trained Neural Network (NN) reads a group of 3 by 3 adjacent CBEDs and predicts the amplitude and phase of the exit wave at the center (Fig 1). The retrieved wave function is then used to reconstruct patches of the object, they are then added to a common array to form a full object, which is a full-scale phase image of the scanned region.

Figure 1: Schematic representation of the reconstruction process.

To train the NN, simulations were used with a variety of condition to generate synthetic datasets (>300.000 samples). In combination with augmenting the data with Poisson noise, we avoid overfitting issues. The U-NET based architecture of the NN is adapted to the task and performs well while maintaining a small size and fast performance.

Figure 2: Comparison of imaging modes: annular dark field (ADF), our Neural Network based approach (NN) and single side band phase reconstruction (SSB) for a focal- and dose series of a simulated graphene sample with an electron beam of 60 keV and convergence angle of 25 mrad.

The approach was validated on real and synthetic datasets. To show the power of the method in a real microscopy experiment, the reconstruction is performed on a simulated dataset of different defocus and dose values as shown in figure 2. For comparison, three methods, including annular dark field imaging (ADF), the proposed method with NN, and single side band (SSB) [1], are used to generate the object image. While ADF is capable of real time construction of the image, it shows poor image quality under low dose, which is worsened with larger defocus. On the other hand, SSB has better dose efficiency, preserving atomic feature at larger defocus, but only allows post-experiment reconstruction. The result from our NN shows superior resolution over the other two and good robustness against low dose noise even with some defocus. Furthermore, since the reconstruction can be performed in near real time, microscopists can use the result from our NN to search for the region of interest with better tolerance of defocus and low dose.

A new reconstruction method is proposed that is capable of reconstructing high quality images and aids searching for regions of interest and proper experimental conditions. Help as such can be essential when dealing with materials sensitive to beam damage [2].

References:
[1] Pennycook, T. J., Lupini, A. R., Yang, H., Murfitt, M. F., Jones, L., & Nellist, P. D. (2015). Efficient phase contrast imaging in STEM using a pixelated detector. Part 1: Experimental demonstration at atomic resolution. *Ultramicroscopy*, *151*, 160-167.
[2] Liu, L., Wang, N., Zhu, C., Liu, X., Zhu, Y., Guo, P., ... & Han, Y. (2020). Direct imaging of atomically dispersed molybdenum that enables location of aluminum in the framework of zeolite ZSM-5. *Angewandte Chemie*, *132*(2), 829-835.
[3] This work was supported by the European Research Council (Grant 770887 PICOMETRICS to SVA and Grant 823717 ESTEEM3). J.V. and S.V.A acknowledge funding from the University of Antwerp through a TOP BOF project. We also acknowledge funding from the European Research Council under the European Union"s Horizon 2020 research and innovation programme via 802123-HDEM.

Figure 1

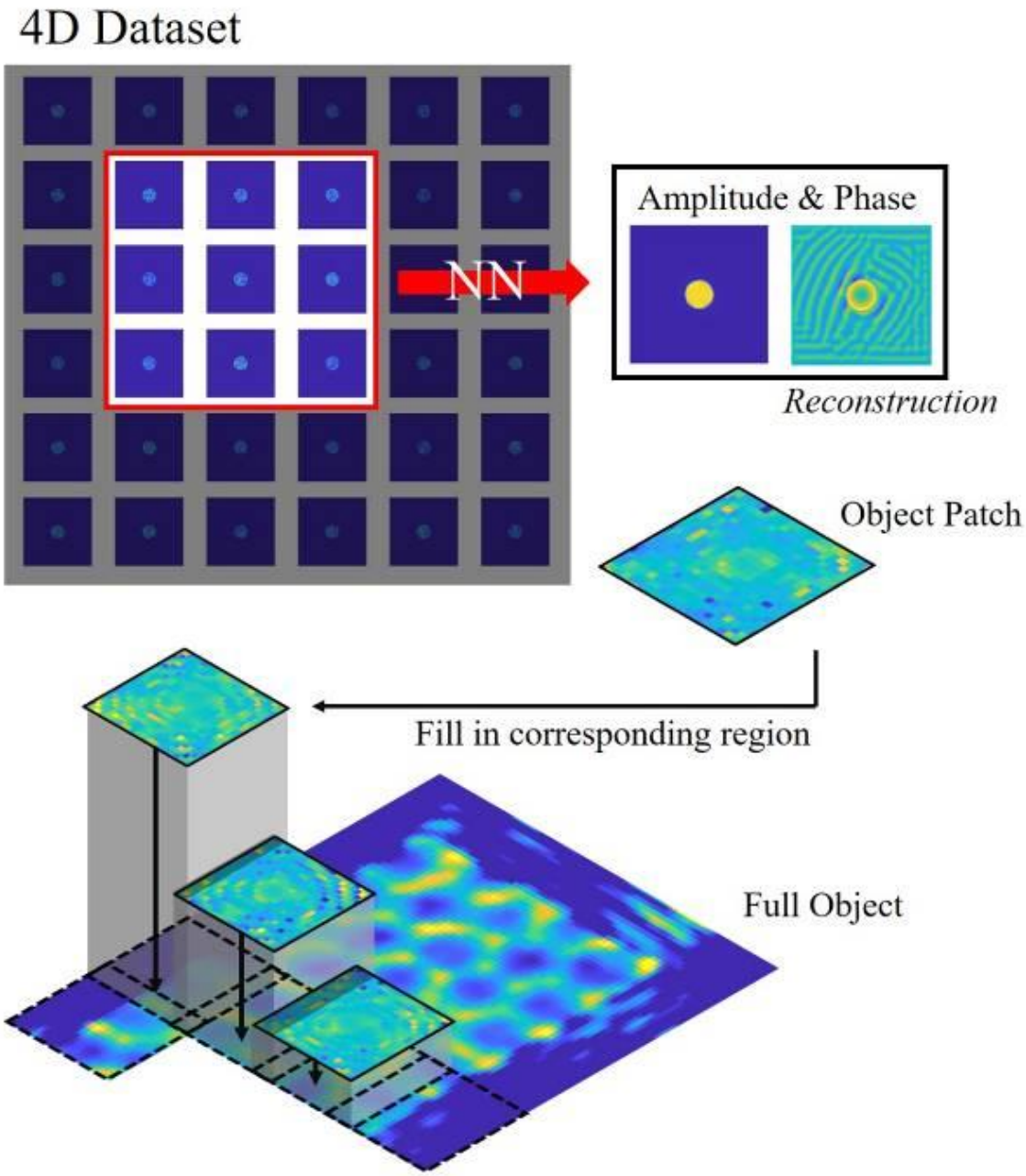

Figure 2

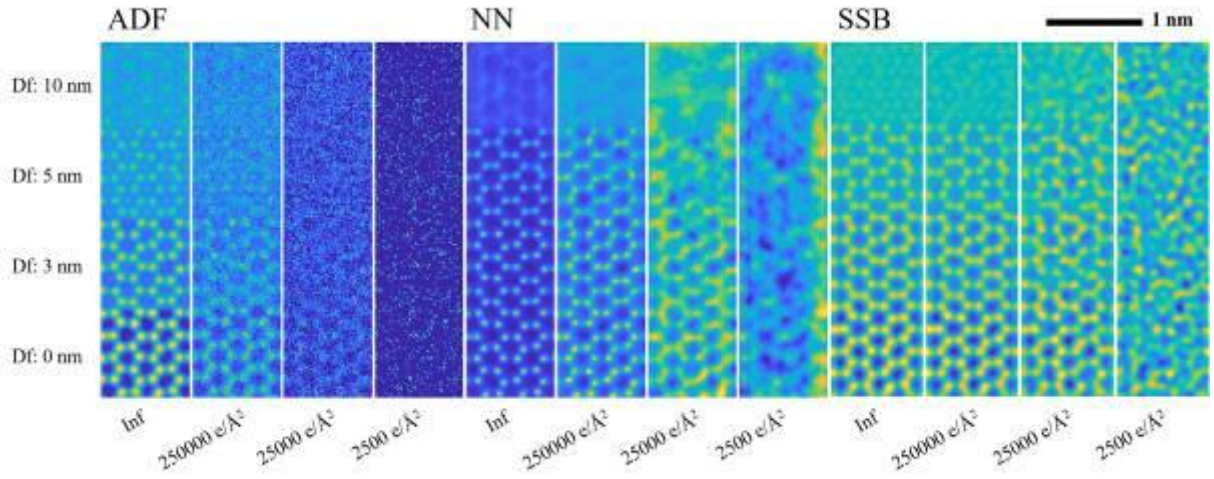

IM8.004
4D-STEM in the SEMs and FIB/SEMs: Design of two different transmission diffraction sub-stages and applications

J. Müller[1], J. Schmehr[2], J. Cao[2], C. Mirek[1], B. Haas[1], S. Shabih[1], W. Van Den Broek[1], J. Becker[2], C. T. Koch[2]

[1]Humboldt University of Berlin, Department of Physics, Berlin, Germany
[2]X-Spectrum GmbH, Hamburg, Germany

Introduction: A wide range of diffraction-based techniques have recently been developed for 4D-STEM [1], many of these techniques can also be employed in conventional SEMs and FIB/SEMs by inserting a fast camera below the electron-transparent sample. We built two different diffraction sub-stages for SEMs and FIB/SEMs, which can acquire transmission electron diffraction patterns at high speed and synchronized with the positioning of the electron beam. Compared to dedicated transmission electron microscopes, using SEMs as a base platform allows for simpler, more easily customizable, and more economical systems. In addition, the lower acceleration voltage of 0.5kV to 30kV results in stronger scattering as well as reduced knock-on damage. We will present two plug and play sub-stages and show a summary of applications spanning from nm to mm scale.

Objectives: Our goal is to develop and apply dose-efficient low voltage electron diffraction techniques to investigate hybrid inorganic/organic systems, thin bulk materials, as well as low dimensional systems. Combining existing detectors like EDX, CL, SE, and various back-scatter signals available for the SEM platform, with 4D-STEM and multi-axis sample control offers a wide range of tools for the investigation of local material parameters. This combination is a handy addition to labs that synthesize thin samples and have access to a SEM or FIB/SEM, but don"t want to invest in a dedicated TEM, yet prefer to investigate their materials in-house.

Material & Methods: We implemented two different transmission diffraction sub-stages within our Zeiss GeminiSEM 500. The first setup consists of a Medipix 3 direct electron detector with a thin entrance window (X-Spectrum GmbH) [2] and a sample holder mounted above it, achieving 2000fps with 256x256 pixels per frame in 12bit mode. The second setup consists of a compact 2.5x2.5x1.1cm³ scintillator-based CMOS camera, a hexapod sub-stage holding the sample (e.g. a TEM grid) on its controllable platform and a linear positioner to move the camera. This camera consists of a fiber-coupled scintillator, achieving 160fps at 1200x1200 pixels or up to 2000fps at 64x64 pixels. The camera length can be varied from 5 to 40mm by physically moving the camera with a software controlled linear stage - there are no post-specimen lenses. Convergence angle and beam current are controlled via the SEM, allowing for the acquisition of spot patterns, CBED patterns, Ronchigrams and shadow images.

Results: We applied our SEM diffraction setups to map material properties like layer thickness, crystal orientations, strain, electric fields, magnetic fields, unit cell parameters, crystallinity and other crystallographic information.

Conclusion: Fast transmission electron diffraction mapping in SEMs is a feasible and well-working tool to investigate thin bulk materials and low-dimensional materials. Direct electron detectors with their fast acquisition speed, high dynamic range and single electron sensitivity are a perfect addition to this field.

References:
[1] C. Ophus, Microscopy and Microanalysis, Volume 25, Issue 3, June 2019, pp. 563-582
[2] https://x-spectrum.de

We acknowledge financial support by the German Research Foundation (DFG grant nrs. KO 2911/12-1, KO 2911/13-1, BR 5095/2-1 and Projektnummer 182087777 - SFB951).
We thank Harald Niebel, Björn Gamm, Markus Boese from Carl Zeiss Microscopy GmbH for help with controlling the SEM.

Figure 1

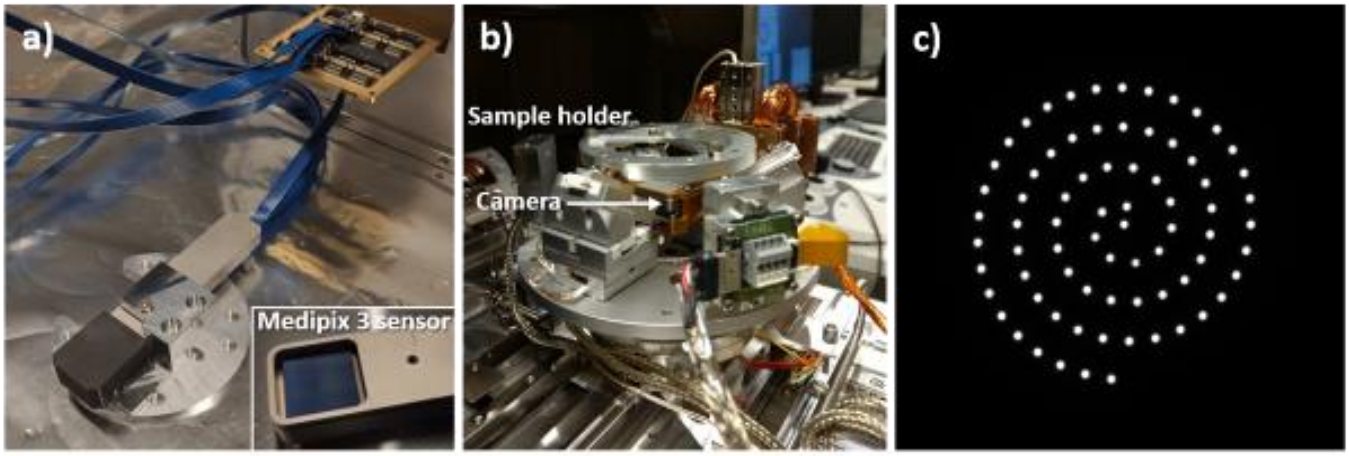

a) First setup (preliminary) using a Medipix 3 sensor from X-Spectrum GmbH. b) Second setup mounted on the dovetail mount of the SEM stage. c) Spiral scan pattern acquired with the second setup using our in-house scan generator.

Figure 2

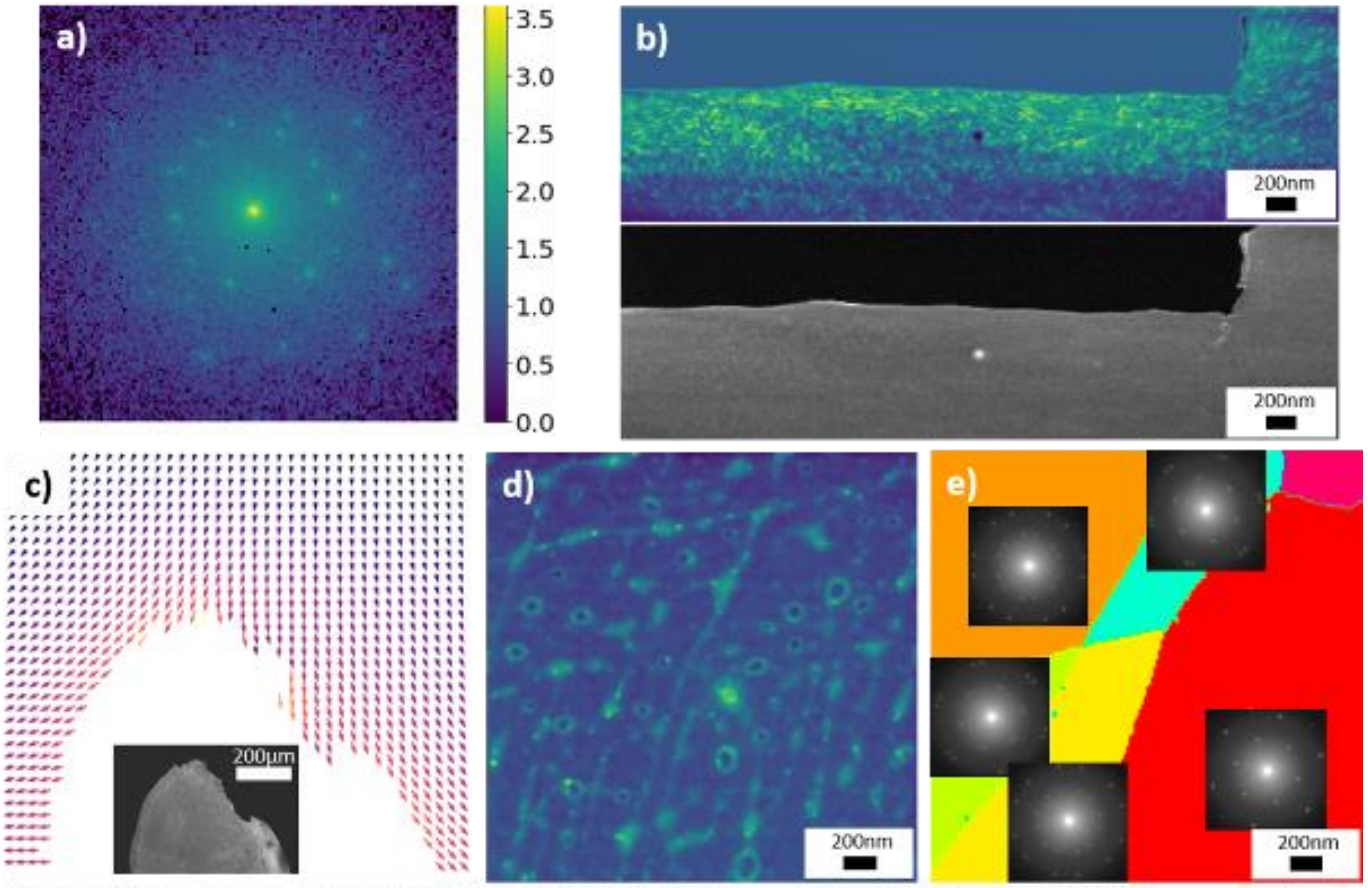

a) Diffraction pattern (log scale) of graphite acquired with the first setup using the Medipix 3 sensor (20keV electron energy, 1ms exposure time). Second setup: b) 4D-STEM dataset (20keV electron energy) of a human tooth prepared with a Jeol IB-09060CIS Cyro Ion Slicer, top: Fluctuation EM analysis with LiberTEM showing crystallites, bottom: simultaneously acquired SEM inlens signal. c) Beam deflection of a +80V biased metal tip surrounded by a grounded circular aperture (maximum beam deflection is 13.1mrad at 6.5keV electron energy. d)/e) 4D-STEM dataset (15keV electron energy) of a bilayer graphene sample from Graphenea, Inc. d) virtual dark field image using LiberTEM and e) clustering using LiberTEM with diffraction patterns corresponding to the highlighted areas.

IM8.005
Atomically-resolved quantification of light elements using energy-filtered scanning transmission electron microscopy

S. S. Firoozabadi[1], A. Beyer-Leser[1], P. Kükelhan[1], D. Heimes[1], J. Lehr[1], W. Stolz[1], K. Volz[1]

[1]Philipps-University Marburg, Materials Sciences Centre and Faculty of Physics, Marburg, Germany

Quantification of light elements, e.g., nitrogen or lithium, are in high demand due to their large variety of applications in the field of electronics, optoelectronics, and batteries. One of the widespread methods for structural characterization of semiconductors is quantitative scanning transmission electron microscopy (STEM). It is achievable by comparing image simulations and experiments at high scattering angles where mainly Rutherford scattered electrons are expected [1]. It shows a good agreement to other methods, e.g. high-resolution x-ray diffraction (HRXRD), but superior lateral resolution. Nevertheless, due to their low amount of protons, light elements do not scatter efficiently into the scattering angles employed in the high angle annular dark-field (HAADF) STEM method. Accordingly, lower detection angles are favorable. However, there is a significant discrepancy between experiments and complementary image simulations at these angles. It is shown that there are sources of error influencing the image intensity at low angle regimes including inelastic scattering (plasmon excitations) as a predominant source [2, 3].

Here, we propose a method for chemical mapping of light elements on an atomic scale. As an interesting candidate in the field of optoelectronics, GaNAs is chosen as a model system due to its low energy bandgap. The nitrogen concentration is determined by comparing energy-filtered annular dark-field STEM images and multislice image simulations [4]. Relatively low angles are chosen to be sensitive to the nitrogen content. We address the sources of discrepancies at the low angular regime as follows. The static atomic displacements are considered in the image simulations by relaxing the supercell in advance. The discrepancy introduced by neglecting the plasmon excitations is addressed by energy filtering. Besides, by utilizing a fast pixelated detector, which allows us to record the whole convergent beam electron diffraction pattern (CBED) for every probe position, we are flexible in choosing the optimum angular range to minimize other sources of error.

An electron transparent sample consisting of GaNAs quantum wells in [010] direction is prepared by focused ion beam (FIB) (JEOL JIB-4601F, JEOL Ltd.) and polished by low voltage Ar ions using a NanoMill® (Model 1040, E. A. Fischione Instruments). A double aberration-corrected STEM JEOL JEM2200FS (JEOL Ltd.) operated at 200 kV and equipped with an in-column Omega energy filter above a pixelated detector (pnCCD (S)TEM Camera, PNDetector) allows obtaining energy-filtered (-6 to 6 eV) CBEDs for every probe position. Multislice image simulations are applied with the STEMsalabim software package [4]. Simulations are carried out for varying compositions of nitrogen in GaNAs. Every created supercell is relaxed by the valance force field model. Thermal diffuse scattering and chromatic aberration are also taken into account.

Quantitative STEM of light elements is facilitated by doing energy-filtered STEM in the optimal angular range. The determined thickness in the barrier area is in good agreement with the thickness measured by the well-known HAADF-STEM method. Also, the resulting nitrogen concentration agrees with the complementary HRXRD measurements.

[1] LeBeau, J. M., Physical Review Letters 100 (2008), 206101
[2] Beyer, A., Scientific Reports 10, no. 1 (2020): 1-15
[3] Grieb, T., Ultramicroscopy 221 (2021): 113175
[4] Oelerich, J. O., Ultramicroscopy 177 (2017): 91-96

IM8.006
Dose and signal to noise in 4D STEM imaging of beam-sensitive materials

C. O'Leary[1], A. I. Kirkland[1,2,3], P. D. Nellist[1]

[1]University of Oxford, Department of Materials, Oxford, United Kingdom
[2]Diamond Light Source, ePSIC, Didcot, United States
[3]Rosalind Franklin Institute, Didcot, United Kingdom

The development of fast pixelated detectors, particularly direct electron detectors, has allowed the acquisition of 4D scanning transmission electron microscope (STEM) data in reasonable timescales, with detector frame times faster than 1 ms now possible. Because the entirety of the detector plane is recorded, imaging methods based on the 4D STEM data set make much more efficient use of the transmitted electrons compared to conventional STEM imaging modes such as annular dark-field and phase contrast using a bright-field detector.

A range of imaging methods making use of the 4D STEM data set have emerged, including differential phase contrast (DPC), first moment or centre of mass, integrated DPC and ptychography. Each has a different transfer function associated with it (for example Figure 1), but because the final image is being reconstructed using an *in-silico* algorithm rather than by optics, the transfer function is controlled by the algorithm and does necessarily indicate the strength of the signal relative to the noise transfer. Furthermore, some methods also filter the noise.

Here, calculations and experimental results will be used to illustrate the transfer functions associated with the different 4D STEM approaches. The extent to which noise is transferred will also be discussed, and it will be proposed that the spectral signal to noise forms a good metric to compare methods [1]. Applications to beam-sensitive samples including organic materials will be highlighted. [2]

[1] O"Leary et al., *Ultramicroscopy* 221 (2021) 113189. DOI: 10.1016/j.ultramic.2020.113189
[2] The authors acknowledge use of characterization facilities within the David Cockayne Centre for Electron Microscopy, Department of Materials, University of Oxford and in particular the EPSRC (EP/K040375/1 with further support from Grant No. EP/M010708/1) and additional instrument provision from the Henry Royce Institute (Grant reference EP/R010145/1). Further support was received from JEOL UK Ltd. COL and PDN are grateful to PNDetector for their support in using the JEOL 4DCanvas pixelated detector.

Figure 1: Azimuthally averaged Fourier transform of the ptychographically reconstructed phase of amorphous carbon vs (a) the image spatial frequency and (b) for α = 7.5 mrad (solid lines) and α = 14.4 mrad (dashed lines).

Figure 1

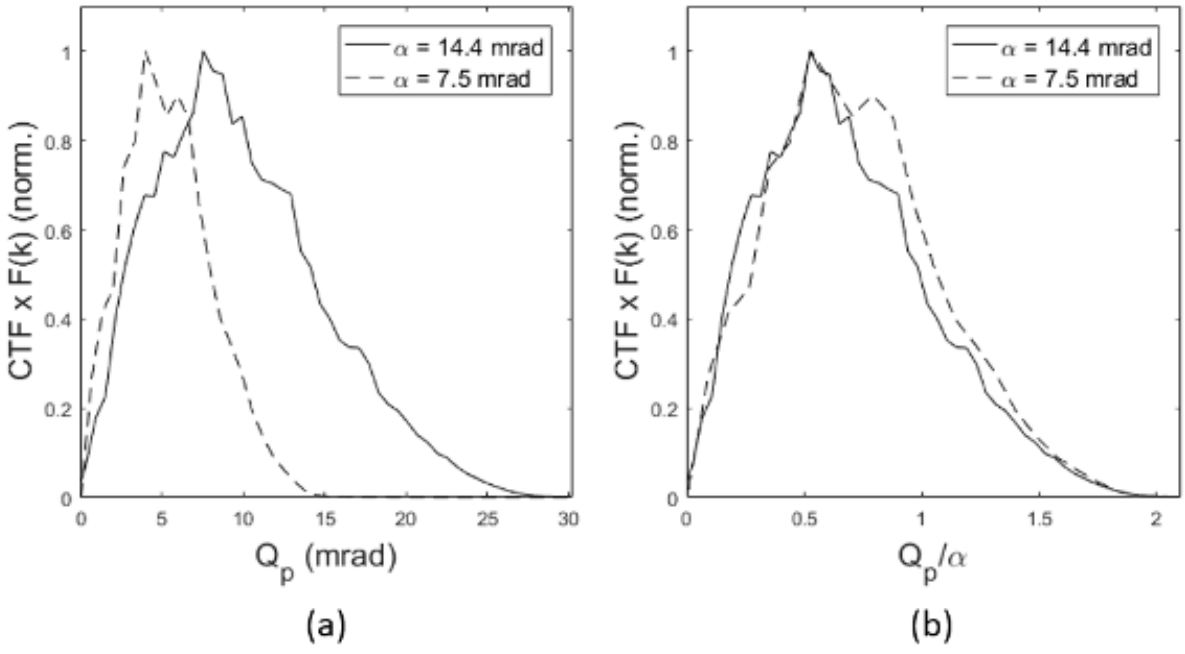

IM8.P001
Higher moments in DPC

S. Löffler[1], D. Boya[2], M. Stöger-Pollach[1]

[1]TU Wien, USTEM, Vienna, Austria
[2]TU Wien, Institute of Solid State Physics, Vienna, Austria

Differential phase contrast (DPC) is a versatile method for characterizing electromagnetic fields down to the atomic scale by measuring the effects they have on the electron beam"s momentum distribution [1]. There is a caveat, however: quantum mechanics and Ehrenfest"s theorem [2] dictate that only the average field strength integrated over the beam profile is experimentally accessible. Hence, resolution and accuracy can suffer when the field varies on a length scale similar to or smaller than the one of the beam.

However, there is a wealth of information readily available experimentally that is currently not used for DPC. Conventionally, atomic fields are determined from the expectation value of the momentum operator $\langle p_i \rangle$, i.e., the center-of-gravity of the diffraction pattern. Mathematically, this corresponds to the first moment (or mean value) of the momentum distribution. In addition to that, there are higher moments such as the variance that characterize the momentum distribution in more detail. These can easily be derived experimentally from expectation values of the form $\langle p_i p_j \rangle$, etc.

Here, we investigate on quantum-mechanical grounds what information about atomic electric fields can be derived from these higher moments. In particular, we show that the second moment $\langle pipj \rangle$ is related to the outer product of the electric field with itself. From this, information about the (averaged) second derivative can be inferred, thus paving the way for improved resolution and accuracy, especially close to high-symmetry points (where the first moment data averages out).

Figure 1 shows an illustrative example of a single atomic column comprised of 4 Si atoms. When the beam is positioned on the atomic column, no change in $\langle p_i \rangle$ is observed due to symmetry. However, the momentum distribution has notable tails, which do change $\langle p_i p_j \rangle$ and lead to a significantly improved approximation of the potential (and hence the electric field). The approximation could be improved further by using a narrower beam and higher order approximations as can be derived from $\langle p_i p_j p_k \rangle$, etc. A similar picture can also be seen when positioning the beam next to the atomic column, where $\langle p_i \rangle$ does not vanish.

Using higher moments of the momentum distribution for DPC comes at no additional effort when fast pixelated detectors are used and is primarily limited by noise. As such, it is easy to implement and promises great improvements to the determination of the electrostatic potential. [3]

[1] K. Müller, F.F. Krause et al., Nat. Comm. 5 (2014) 5653
[2] P. Ehrenfest, Z. f. Physik, 45 (1927) 455
[3] SL acknowledges financial support by the Austrian Science Fund (FWF) under grant nr. I4309-N36.

Figure 1: Simulations for a single atomic column with 4 Si atoms using 300 keV electrons with a convergence semi-angle of 30 mrad. Left: vacuum, middle: beam on the atomic column, right: beam close to the atomic column. Top: diffraction patterns, bottom: line profiles through the electrostatic potential, the real-space intensity distribution of the incident wave function ψ_0, the linear approximation to the potential derived from $\langle p_i \rangle$, and the quadratic approximation derived from $\langle p_i \rangle$ and $\langle p_i p_j \rangle$.

Figure 1

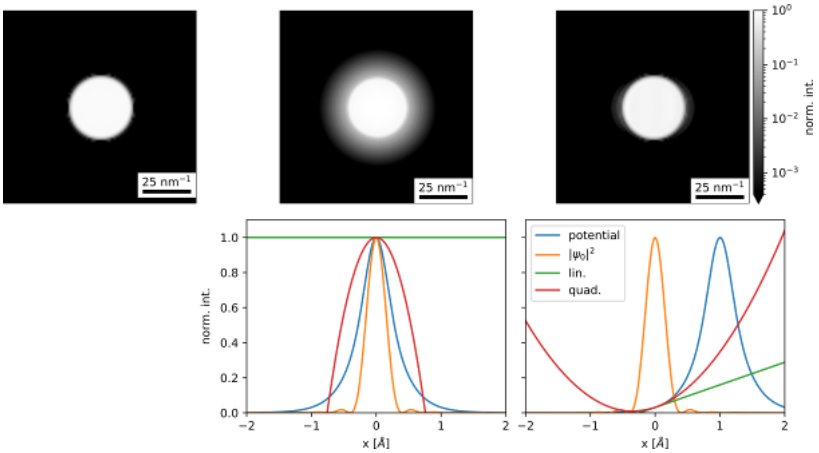

IM8.P002
Automatic dislocation density measurement using Scanning Electron Microscopy

J. Gallet[1], S. Cazottes[1], T. Chaise[1], C. Langlois[1], M. Perez[1]

[1]INSA-Lyon, MATEIS, Lyon, France

Introduction: Mechanical properties of metallic material can be predicted as a function of their microstructure by constitutive laws [1]. One of the key microstructural parameters, which is often difficult to precisely characterize, is the dislocation density.

For the metallurgical community, there is a need for more representative measurements in order to better describe the mechanical behavior of such materials.

The main objective of this project is to develop a method for characterizing dislocation densities using a clustering approach based on the difference of intensity that exists between the dislocations and the matrix.

Materials & Methods: Dislocations can be observed in a SEM using ECCI (Electron Channeling Contrast Imaging), when the sample is correctly oriented in a condition to generate a contrast between the matrix and the dislocations. However, the precise orientation of the sample is difficult due to the SEM set-up. R-ECCI (Rotational-ECCI) method [2-3], consists in acquiring a series of rotating back scattered electron images. From this image serie, an intensity profile of the different dislocations and of the matrix can be extracted. The dislocation density can then be automatically determined by applying a clustering algorithm on the intensity profiles.

All tests were carried out on a rolled duplex steel deformed by a uni-axial tensile test to achieve different deformation rates.

Results: The lowest and highest dislocation density measurable was determined to be between 1012 and 1014m-2.

Figure 1: (a'') and (b''): Images of dislocation clustering (in green) obtained from a series of BSE images (a) and (b): BSE images on a duplex steel sample which gives a dislocation density of approximately 4.1012 m-2 (a') and 5.1014 m-2 (b').

Moreover, a quantitative comparison between the results obtained using this method and traditional measurement techniques such as TEM, XRD and EBSD was achieved.

References:
[1] J. Blaizot et al. / International Journal of Plasticity xxx (2015).
[2] L"hôte, G. et al. Rotational-Electron Channeling Contrast Imaging analysis of dislocation structure in fatigued copper single crystal. Scripta Materialia162, 103–107 (2019).
[3] Cazottes Rotational-Electron Channeling Contrast Imaging analysis of dislocation structure in fatigued copper single crystal. Scripta Materialia162, 103–107 (2019).

Keywords: SEM, R-ECCI, dislocation, deformation, clustering

Figure 1

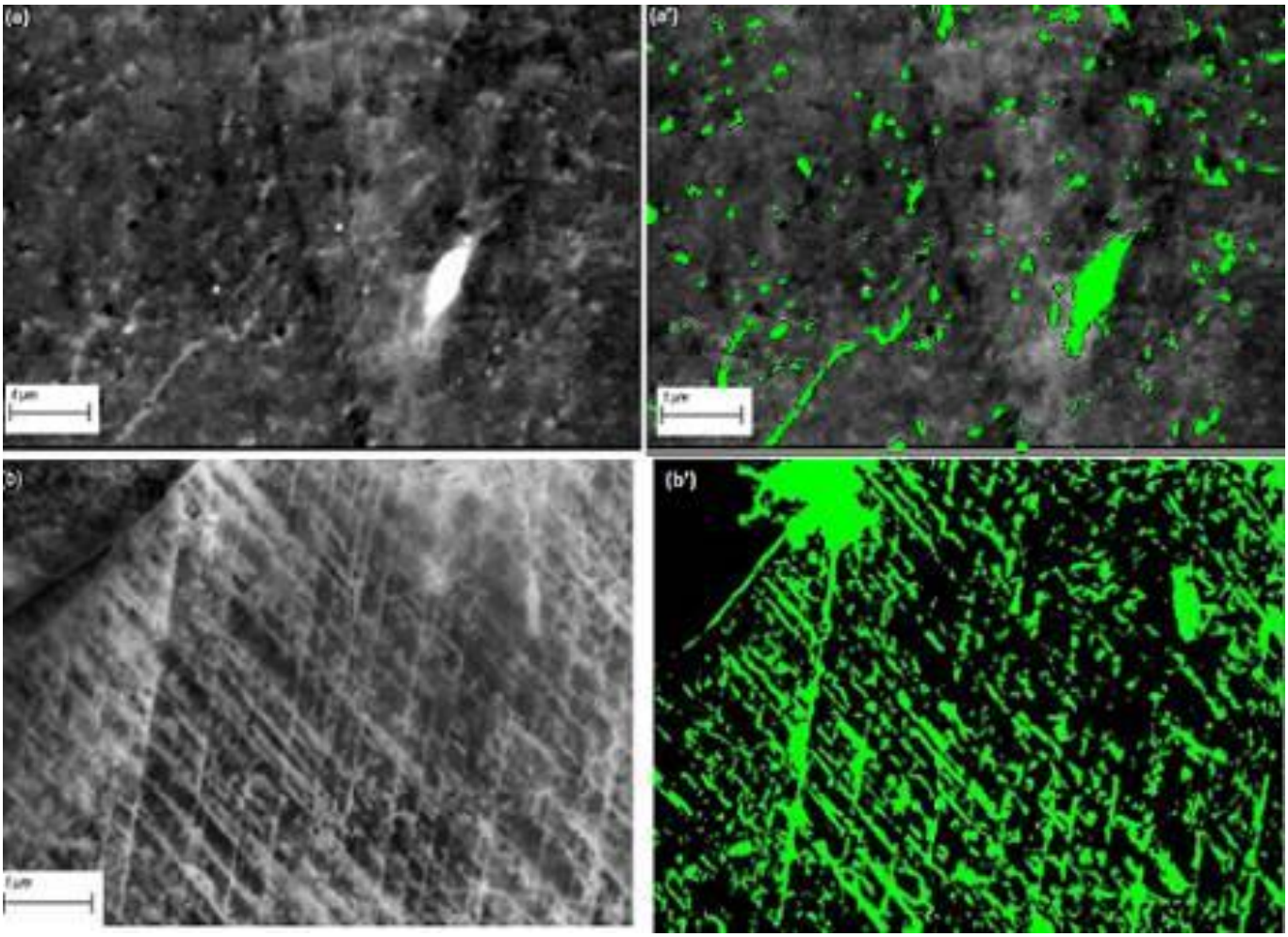

IM8.P003
Investigation of the kinetics of the structural evolution of materials based on photometric analysis of the results of *in situ* experiments

V. Ermishkin[1], N. Minina[2], S. Kulagin[1], J. Solovyeva[1], A. Tomenko[1]

[1]Baikov Institute of Metallurgy and Material Sciences, High voltage electron microscopy group, Moscow, Russian Federation
[2]Baikov Institute of Metallurgy and Material Sciences, Department of physical methods of materials research, Moscow, Russian Federation

When studying structural transformations in metals and alloys, stimulated by an external energy effect of various physical nature, the value of the information received about their kinetics, driving forces, qualitative diversity, and the staging of processes essentially depend on the experimental technique and methods of analyzing their data. The experience of the conducted research has shown that the greatest opportunities for achieving their scientific efficiency are the combination of in situ experimental technique with photometric analysis of video recording of observations of the structural evolution of the materials under study, carried out synchronously with the influencing factors. Carrying out research under such conditions makes it possible to establish a one-to-one correspondence between the intensity of influencing factors (mechanical, temperature, electromagnetic, corrosion, radiation, etc.), to find the threshold values of these factors corresponding to a qualitative change in the mechanisms of structural transformations, their kinetic characteristics and the values of thermal activation parameters of the processes that control them. A frame-by-frame analysis of structural observations recorded by a video camera makes it possible to quantitatively analyze the kinetics of the evolution of defect, phase, and grain structures, as well as the size distributions of their elements over the surface under study. The possibilities offered by photometric analysis of structural images (PHASI) and the degree of its detail do not depend on the method of visualization of the structural features of the materials under study and are successfully implemented at different scale levels in light, scanning electron microscopy and transmission electron microscopy. The PHASI method is based on a differential scheme for comparing fragments of the same place on the surface of the object under study, of which one is the reference one, usually corresponds to the initial state, that is, to the moment before the start of the effect of the factor under study, and the second to its state at a given time after the start of the effect. Apart from the images of the selected fragments, the brightness spectra of the reflection of visible light from them are displayed on the monitor screen in the coordinates "spectral density - intensity". Spectral density is understood as the ratio of the number of pixels with an intensity value in a certain range ΔI to the total number of pixels into which the studied image is divided. The work was carried out on aluminium alloy B95 in order to determine the effect of cryo-mechanical loading on the redistribution of alloying elements over the thickness of a sheet subjected to compression loading at the boiling point of liquid nitrogen. It is shown that in the direction of the punch pressure, the concentration of alloying elements decreases from the maximum on the upper surface of the sheet to the minimum on its supporting surface. This type of redistribution of alloying elements of the alloy leads to a corresponding change in its defective structure and mechanical properties in the direction normal to the surface of the sheet.

IM8.P004
3D electron diffraction/micro-ED for structural characterisation of beam sensitive loratadine and linagliptin APIs using pixelated detectors

P. Das[1], A. Galanis[1], A. Gomez-Perez[1], S. Nicolopoulos[1]

[1]NanoMEGAS SPRL, Brussels, Belgium

In recent years, the scientific community has shown a renewed interest in use of 3D Electron Diffraction (3D-ED) for characterization of pharmaceutical compounds. For many API"s (active pharmaceutical ingredient), it is always challenging to grow bigger crystals suitable for single crystal X-ray diffraction (SCXRD). In those cases, 3D-ED in Transmission Electron Microscope (TEM) could be a useful alternative tool, for structural studies as crystals as small as 50 nm can be studied.

The principle of acquiring 3D-ED data for pharmaceuticals, consists of focusing the electron beam on a nm size crystal in TEM/STEM mode and sampling the reciprocal space in small steps (usually 1 degree tilt or less) using beam precession or using continuous rotation (Micro-ED with or without beam precession) of the crystal [1]. As organic crystals are often very beam sensitive, data collection can be done either at room temperature and/or at cryo-conditions using pixelated detectors at low dose conditions (< 0.01e/Å2/sec) [2]. The acquired 3D-ED data can be processed to determine *ab-initio* unit cell, space group, atomic positions and Hydrogen atom positions can also be determined.

Recently, we have reported determination of the crystal structure of the metastable form II of Loratadine API using a combination of low resolution 3D-ED data and density functional theory (DFT). The limited resolution of the ED data (>1 Å), combined with the complexity of configurational disorder resulted that the structure could not be obtained using *ab-initio* direct methods. Instead, using simulated annealing based on the ED data, two possible starting models emerged. DFT energy minimization helped to confirm the correct model (Figure 1), where the experimental structural solution has been validated in agreement with SCXRD studies [3].

Recently, a further study of an industrial important API, Linagliptin has also been performed by our group. The compound presents over 30 polymorphs reported in the literature, where only 2 of them have crystal structure data available. We have used 3D-ED techniques to solve *ab-initio* the structure of a new Linagliptin polymorphic form (commercial reagent) using Pixelated detector (Medipix III, Amsterdam Scientific Instruments, Netherlands). This structure is one of the largest structures ever solved by 3D-ED data.

Our results show that 3D-ED/Micro-ED techniques in combination with Direct Detection cameras can be used as a powerful tool for phase identification and structural characterization for nm size (50-500 nm) beam sensitive pharmaceutical materials.

Figure 1: Lortadine Form II structure solved using 3D-ED data.

Figure 1

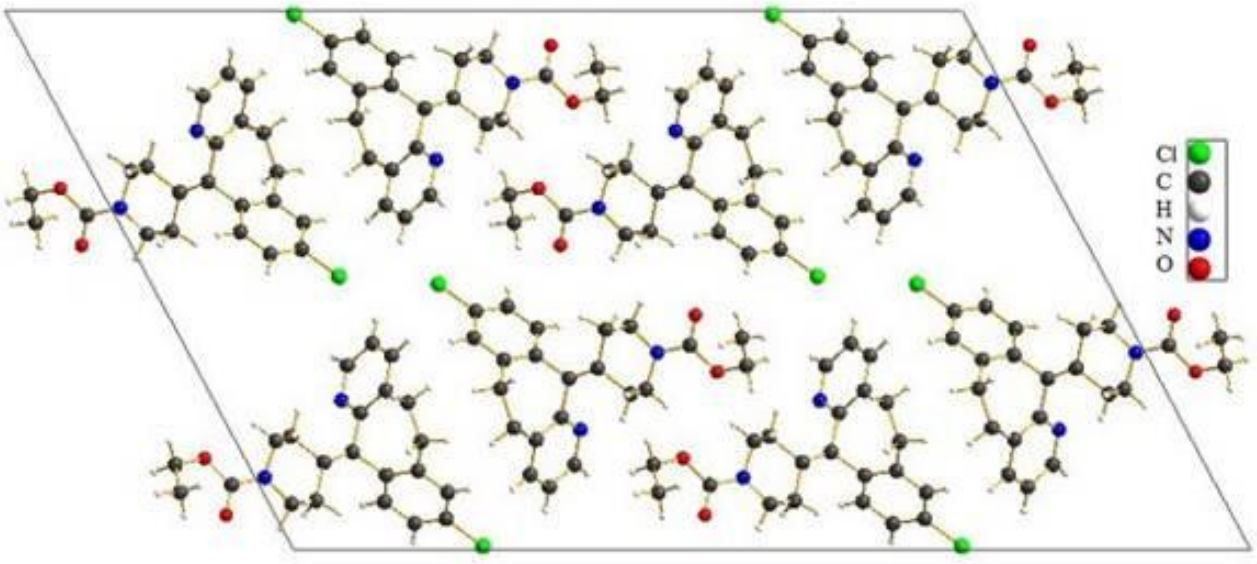

IM8.P005
Towards measurement of polarisation-induced electric fields in ferroelectrics by momentum-resolved STEM – Impact of systematic errors

A. Strauch[1,2], J. Ye[1,2], A. Sokolov[3], E. Tsymbal[3], A. Rosenauer[4], M. Beleggia[5], T. Denneulin[1], K. Müller-Caspary[1,2]

[1]Research Center Jülich, Ernst Ruska-Centre, Jülich, Germany
[2]RWTH Aachen University, Aachen, Germany
[3]University of Nebraska-Lincoln, Lincoln, United States
[4]Universität Bremen, IFP, Bremen, Germany
[5]Technical University of Denmark, Lyngby, Germany

Ferroelectric tunnel junctions are a focus of next-generation memories where polarisation represents a logical bit. However, devices with $BaTiO_3$ (BTO) tunnel junctions cannot be reversibly polarised at ferroelectric layer thicknesses of a few nanometres [1]. Therefore, (S)TEM methods that allow for quantitative mapping of polarisation-induced electric fields are desirable.

The advent of ultrafast cameras in STEM allows for high momentum and spatial resolution in aberration-corrected STEM. Especially, momentum-resolved STEM (MR-STEM) has enabled first moment-based imaging of subatomic electric fields in thin specimens [2,3], and electron ptychography [4]. Recently, polarisation-induced fields in semiconductors were mapped by unit-cell averaged MR-STEM [5]. The method assumes that long-range components of the electric field are dominant over atomic ones when averaging first moments over unit cells. The validity of this assumption depends on crystal symmetry and experimental parameters such as specimen thickness or tilt. This leads to a systematic error δ which we address here for polarisation mapping in perovskite ferroelectrics in both experiment and simulation.

Experimental MR-STEM data from BTO and $PbZr_{0.2}Ti_{0.8}O_3$ (PZT) has been evaluated with different methods and compared to comprehensive simulations. Using an isolated atom model with periodic boundary conditions in STEMsim [6], all non-zero first moments in unit-cell averages arise from dynamical scattering and contribute to δ, hence being caused by symmetry breaking due to atom displacements (Figure 1a). A mistilt of 2mrad in direction of the polarisation axis can double δ compared to the untilted case (Figure 1b). A tilt around the polarisation axis introduces a systematic error of a similar magnitude, but perpendicular to the polarisation axis.

The formally calculated atomic electric fields in Figure 2a cannot be related to the electric field directly due to dynamical scattering, but the atom positions can be resolved. In the unit cell average, the 45° domain boundaries as expected from [7] can be seen. This matches the result of the structure evaluation in Figure 2b. A single domain seems to have an electric field around 90MV/cm. The systematic error is below 40MV/cm taking mistilt of up to 2mrad into account. This and further experimental results are critically examined by comprehensive simulations addressing mistilts, thickness dependencies and ionicity obtained by DFT.

Figure 1: Systematic error δ in PZT depending on thickness for a) displacement d of the atoms relative to literature values and b) sample tilt. X- and y-tilt refers to a tilt around and perpendicular to the polarisation axis, respectively.

Figure 2: Experimental results from PZT recorded with an aberration-corrected Titan at 300kV. The sample thickness is around 10nm by comparing PACBED with simulations. a) Colour-coded (apparent) projected electric field from first moments (Medipix recording) with the unit-cell averages (white vectors). b) HAADF signal with displacement of the centre atom (vectors).

[1] Garcia et al., Nat. Commun. 5 (2014)
[2] Müller et al., Nat. Commun. 5 (2014)
[3] Müller-Caspary et al., Ultramicroscopy 178 (2017)
[4] Jiang et al., Nature 559 (2018)
[5] Müller-Caspary et al., Phys. Rev. Lett. 122 (2019)
[6] Rosenauer et al., Microsc. Semic. Mat. 120 (2007)
[7] Denneulin et al., J. Phys. Condens. Matter 30 (2018)
[8] Funding: Initiative and Network Fund (Helmholtz), contract VH-NG-1317

Figure 1

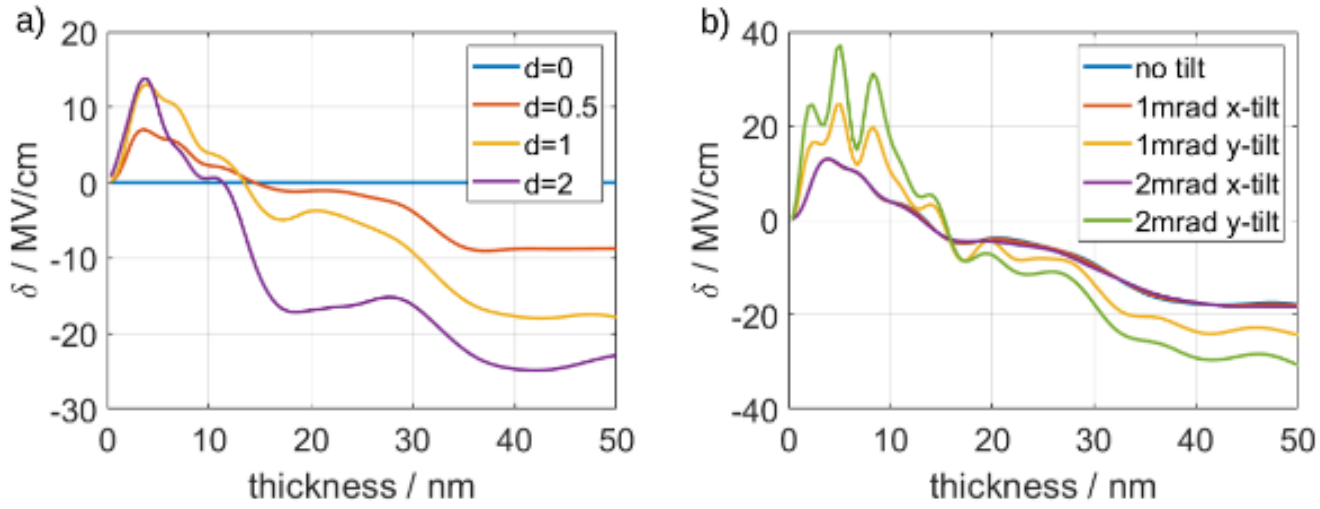

Figure 2

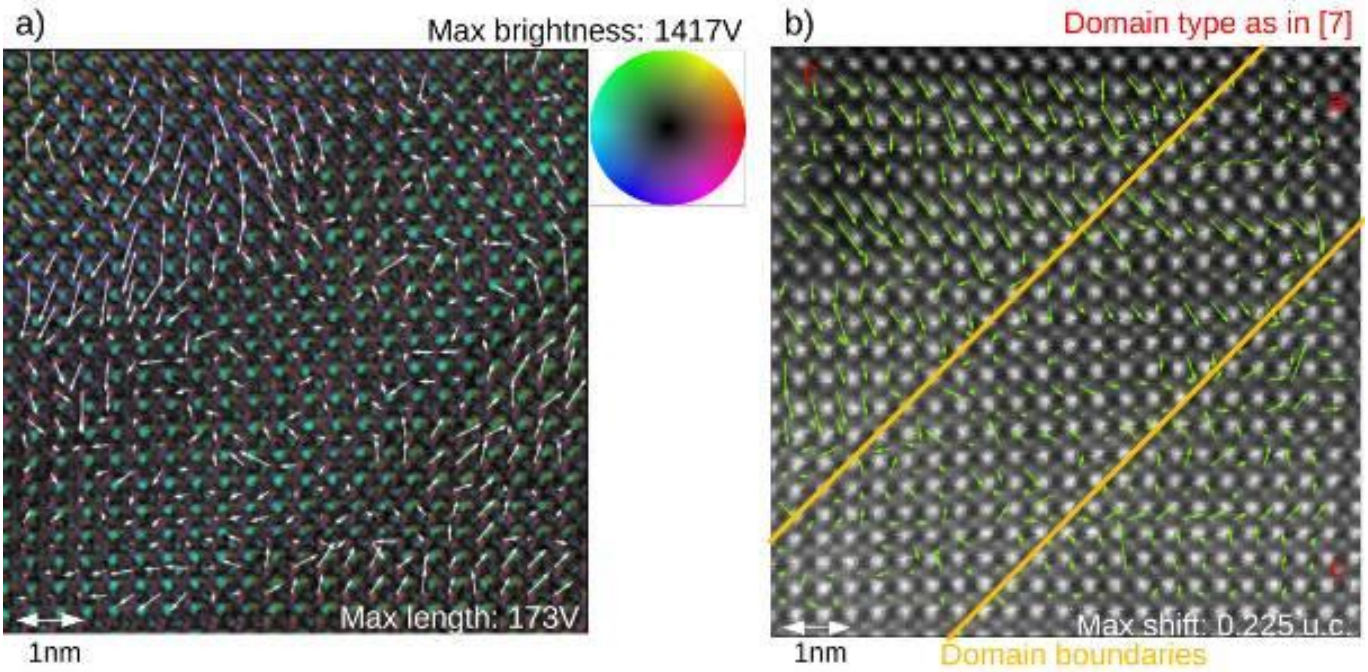

IM8.P006
eCHORD an original approach for multiscale characterisation of aluminium alloys

R. Facchinetti[1], C. Langlois[1], S. Cazottes[1], J. Chevy[2], C. Maurice[3], T. Douillard[1], C. Nardin[2]

[1]INSA-Lyon, MATEIS, Villeurbanne, France
[2]Constellium, Voreppe, France
[3]Mines Saint-Etienne, Saint-Etienne, France

An aluminium alloy might be composed of precipitates of wide size range. Therefore, several characterization techniques are usually necessary to have a complete view of a microstructure.

One promising approach for multiscale microstructure characterization with the SEM (Scanning Electron Microscope) as a single tool is the eCHORD method [1**]**, which provides crystalline orientations maps from millimetric to nanometric region of interest.

This method is based on electron channelling contrast and has the advantage that the sample tilt is only about 10°, and that the accelerating voltage can be lowered to a few kV, resulting in an improved spatial resolution in comparison to EBSD (Electron Backscattered Diffraction). A series of BSE images is recorded during the rotation of the sample around its tilted normal direction, from which the intensity profiles of each pixel can be extracted as a function of the rotation angle. By comparing the obtained intensity profiles with the one calculated from ECP (Electron Channelling Patterns) simulations, the orientation of each pixel can be determined. The angular resolution achieved on Aluminium alloys is about 0.1°.

On the one hand the improvement of spatial resolution facilitates the observation of the nanoscale structure. It can be used for the observation of dislocations [2] or to discriminate precipitates. On the other hand, for the millimeterscale a correction of the effect of the beam"s deviation is detailed in [3], in order to obtain large scale orientation maps.

We present here an original method to obtain orientations maps from millimetric to nanometric region of interest with the SEM as a single tool.

References:
[1] C.Lafond, T.Douillard, S.Cazottes, P.Steyer, and C.Langlois. Electron CHanneling Orientation Determination (eCHORD): An original approach to crystalline orientation mapping. *Ultramicroscopy*, 186 :146–149, March 2018.
[2] G. L"hôte, C. Lafond, P. Steyer, S. Deschanel, T. Douillard, C. Langlois, and S. Cazottes. Rotational-Electron Channeling Contrast Imaging analysis of dislocation structure in fatigued copper single crystal. *Scripta Materialia*, 162 :103–107, March 2019.
[3] C. Lafond, T. Douillard, S. Cazottes, M. De Graef, P. Steyer, and C. Langlois. Towards large scale orientation mapping using the eCHORD method. Ultramicroscopy, 208 :112854, January 2020.

Figure: *IPF cartography on z of an aluminum sample with its colour code. The orientations are obtained with eCHORD*

Figure 1

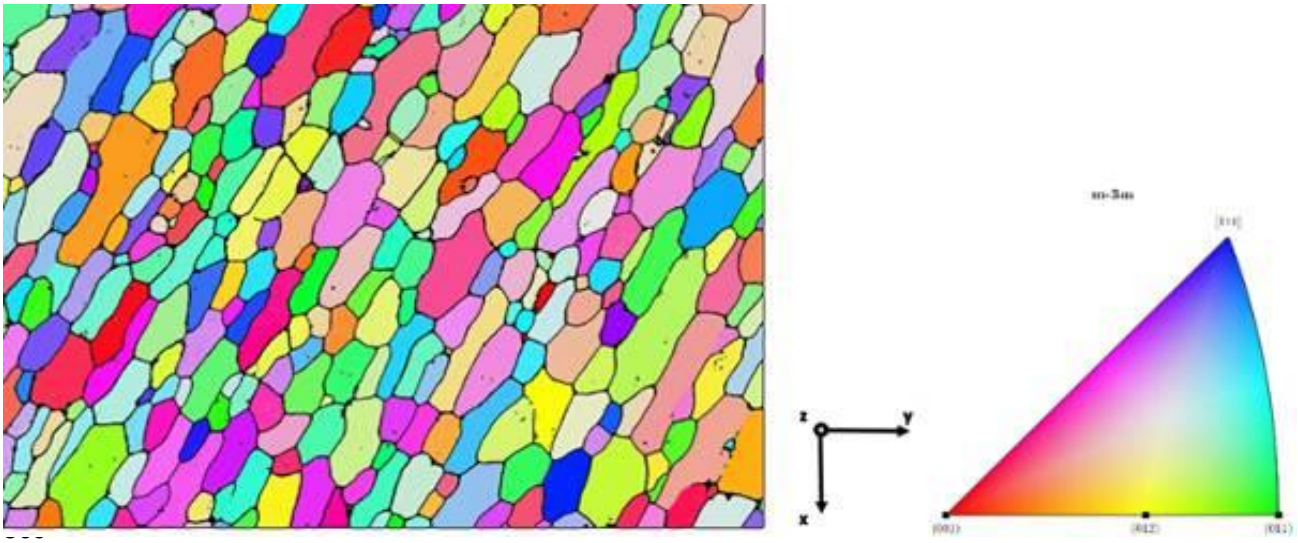

IM8.P007
Live scanning ptychography with the LiberTEM software framework

D. Weber[1], A. Strauch[1,2], A. Clausen[1], A. Bangun[1,2], A. Lesnichaia[1,2], K. Müller-Caspary[1,2]

[1]Research Center Jülich, Ernst Ruska-Centre, Jülich, Germany
[2]RWTH Aachen University, Aachen, Germany

Introduction: The development of ultrafast cameras for transmission electron microscopy (TEM) with frame rates of up to several kHz enabled the collection of the full diffraction space at each scan point in scanning TEM (STEM). This technology paved the way for momentum-resolved STEM techniques with high samplings in both real and diffraction space (4D STEM). An interpretable image of the specimen is generated by computational means, which can include electron ptychography [1], among many others. Practical use of these techniques requires suitable software infrastructure and implementations.

Objectives: Up to now, computationally intensive processing such as ptychography were usually applied offline after transferring data to a processing workstation or cluster. In this work, we demonstrate live scanning ptychography.

The implementation of a method should be disentangled from data logistics. That means that such methods can be applied in different scenarios independent of instrumental modalities, and in turn that the same data processing infrastructure allows to implement a wide range of non-trivial data processing routines. That requires an open, versatile and user-friendly application programming interface (API).

Materials & methods: The LiberTEM software framework is designed for MapReduce-like computation on large-scale array data with a user-defined function (UDF) API that allows live processing and results display.

The "single side band" (SSB) ptychography [2] reconstruction is a linear function of the input data. This property allowed to rearrange the underlying mathematical equation to make it suitable for MapReduce-like incremental processing.

The data stream of a Quantum Detectors Merlin camera running at 1000 fps was passed into the LiberTEM UDF engine, which was running several analyses simultaneously, including SSB ptychography. SrTiO3 (STO) along the (100) zone axis and In2Se3 were used as specimens.

Results: The ptychography result was displayed side-by-side with virtual detectors and first moment analysis while scanning continuously. SSB showed qualitative phase contrast on the oxygen columns in STO also for thicker specimens and while moving or changing magnification. Figures 1 and 2 show screenshots for illustration. The reconstruction was also verified against simulations.

Conclusion: We demonstrate that this SSB implementation is suitable for live display and provides practical, robust phase contrast where conventional STEM only gives a weak signal. Furthermore, we show how LiberTEM UDFs cleanly separate the implementation of the computational method from the back-end implementation, which allows to swap between different execution engines.

LiberTEM and the SSB implementation are available on GitHub:

*https://github.com/LiberTEM/LiberTEM/
*https://github.com/Ptychography-4-0/ptychography (beta)

Acknowledgments:
Helmholtz society: VH-NG1317 and ZT-I-0025
Horizon 2020: grant agreements No 780487 and 823717.

Figure 1: Screenshot from live 4D STEM acquisition with ptychography (left) and annular dark field (right) on STO along the (100) axis. Note the phase contrast on the oxygen columns for ptychography.

Figure 2: Screenshot from live 4D STEM acquisition with ptychography, bright field, annular dark field and first moment analysis on In2Se3.

References:
[1] Rodenburg et al, Ultramicroscopy, 1993, 48, 304-314
[2] Pennycook et al., Ultramicroscopy, 2015, 151:160 – 167

Figure 1

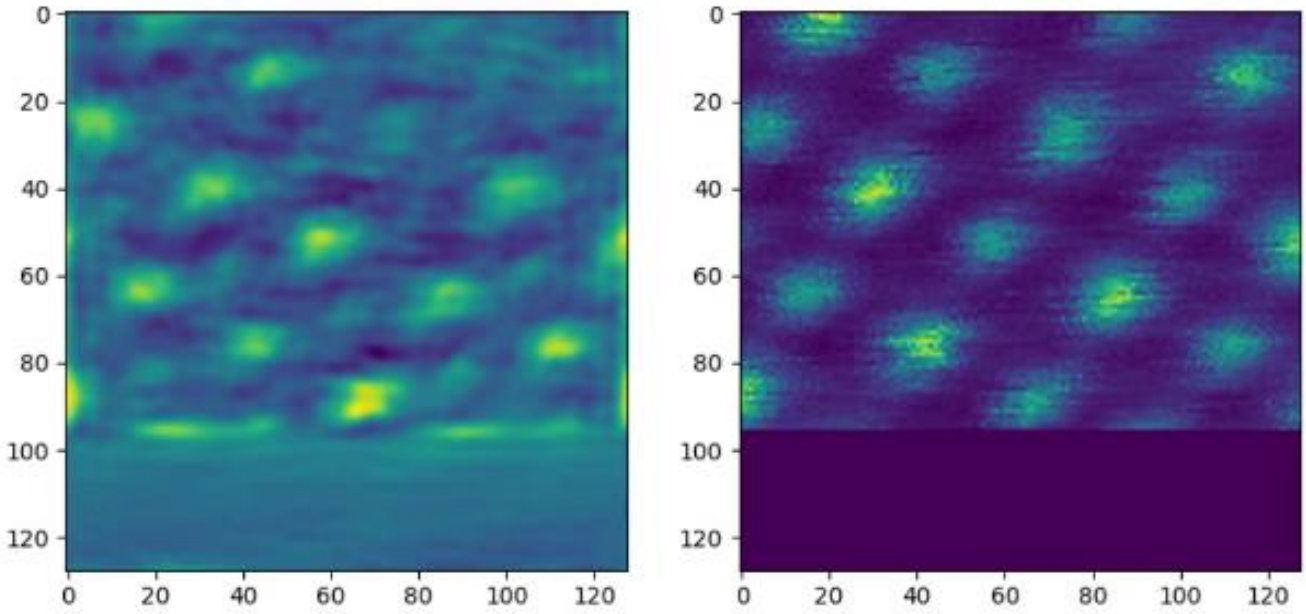

Figure 2

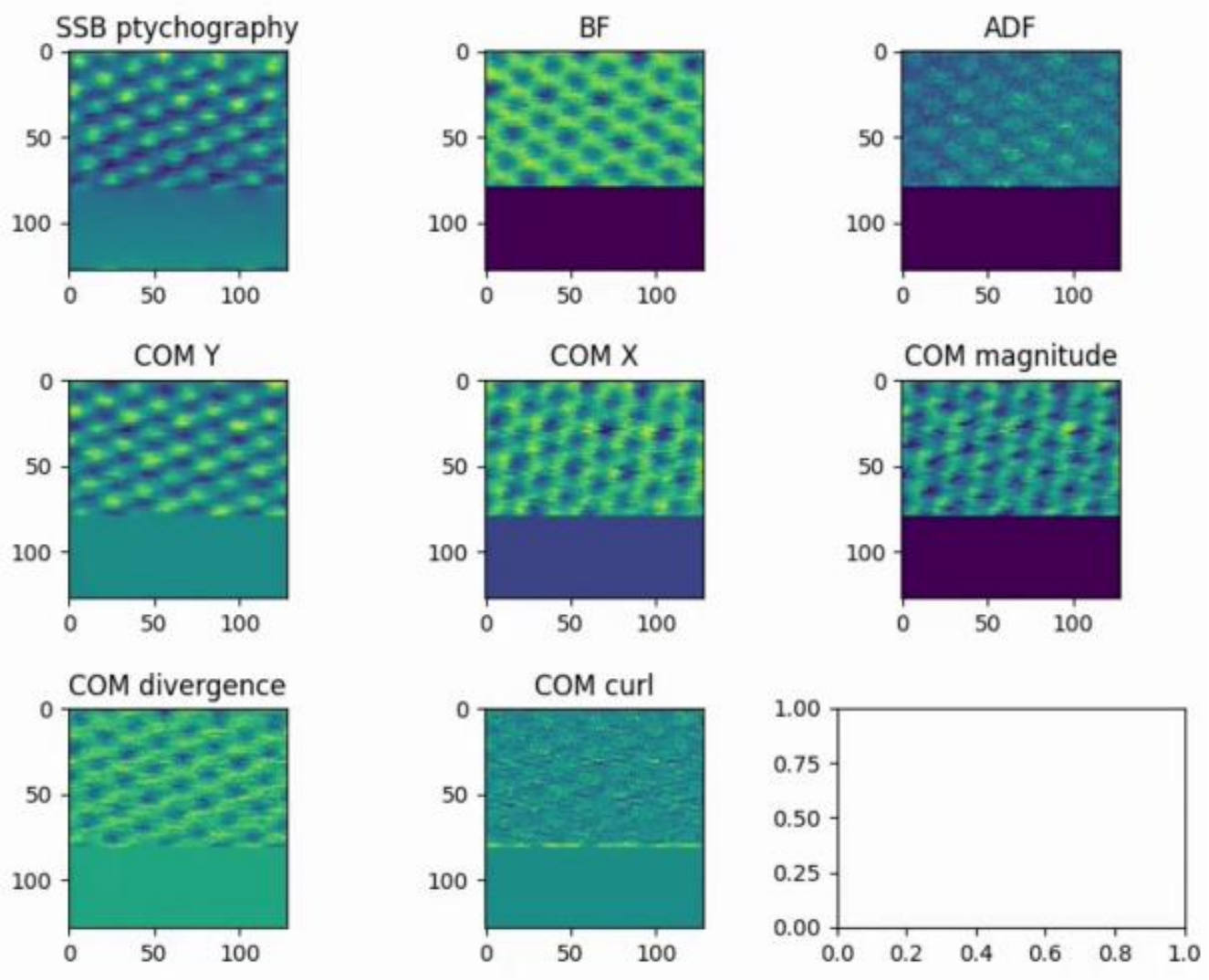

IM8.P008
Influence of inelastic scattering on high-resolution momentum-resolved STEM of bulk platinum

H. L. Robert[1,2], F. F. Krause[3], A. Beyer-Leser[4], T. Grieb[3], S. S. Firoozabadi[4], P. Kükelhan[4], M. Schowalter[3], A. Rosenauer[3], K. Volz[4], K. Müller-Caspary[1,2]

[1]Research Center Jülich, Ernst Ruska-Centre for Microscopy and Spectroscopy with Electrons (ER-C), Jülich, Germany
[2]RWTH Aachen University, 2nd Institute of Physics, Aachen, Germany
[3]Universität Bremen, Institut für Festkörperphysik, Bremen, Germany
[4]Philipps-University Marburg, Marburg, Germany

Aside from thermal diffuse scattering, simulation-based scanning transmission electron microscopy (STEM) approaches rarely include the influence of energy-loss on an electron diffraction pattern. This is because the inelastically scattered electrons are usually thought to follow an identical angle-dependence to the elastically scattered ones. Recent experiments, however, pointed out inelastic scattering as a possible contribution to a mismatch between simulation and experiment, observed in the low-angle region (<40 mrad) of diffraction space [1].

To evaluate the influence of energy-loss on the scattering distribution, especially plasmon excitation, a momentum-resolved (MR) STEM experiment was performed [2,3], using a double-aberration-corrected Jeol JEM-2200FS instrument equipped with a pnCCD camera [4] and an omega filter. Spatially resolved diffraction patterns were recorded from a Pt bulk crystal in [110] zone axis, using a 10 eV-wide energy window, centred on the zero-loss peak, and a 30 eV-wide one, centred on the first plasmon peak (22.6 eV). Data treatments include a restriction of the scan positions to an interval of thickness common to both datasets, determined using an unfiltered high-angle annular dark field (HAADF) signal recorded in parallel to the 4D data, as illustrated in figure 1.

For the acceleration voltage of 200 kV and a thickness of 51 nm, the total contribution of plasmon-scattered electrons is found to reach 31% of all detected intensity, and to display an angle-dependence significantly different from the elastic contribution. Simulations are thus performed with an updated interaction model, using the STEMsim software [2,5]. As depicted in figure 2, the simulated ratio of plasmon-loss over zero-loss electrons is plotted against scattering angle and compared with experimental results. Common features include a valley ranging from the centre of the primary beam up to the semi-convergence angle (15.1 mrad), with a bump at 11.5 mrad. High values are observed from there up to 30 mrad. For higher scattering angles (>50 mrad), the ratio reaches a plateau, which indicates a convergence of both contributions to a common dependence. In the simulation, the elastic contribution is nevertheless increased by an additional factor.

Our results demonstrate the need for plasmon scattering to be included in simulation-based methods such as quantitative angle-resolved and MR STEM, where the low-angle intensity is an important source of information for thickness and composition measurement [1,6]. It is also observed that, even with the inclusion of plasmon scattering, a discrepancy between simulation and experiment remains and will be a focus of future work.

Figure 1: a) Unfiltered HAADF images recorded in parallel to the zero-loss (ZL) and the plasmon-loss (PL) data. b) Voronoi segmentation. c) The average intensity in each cell, being a linear function of thickness, is used to find a common intensity interval. Further work is then done by only including the scan positions in the cells whose average unfiltered HAADF intensity is within this interval. d) Schematics of the instrument.

Figure 2: Ratio of plasmon-loss over zero-loss intensity plotted as a function of scattering angle, both for experiment and simulation.

[1] K. Müller-Caspary et al.; Sci. rep. 6, 37146 (2016)
[2] A. Beyer et. al.; Sci. rep. 10, 17890 (2020)
[3] Fundings from the Initiative and Network Fund of the Helmholtz Association under contract VH-NG-1317 and from the Deutsche Forschungsgemeinschaft under project DFG SFB 1083 "Structure and Dynamics of Internal Interfaces" are gratefully acknowledged.
[4] H. Ryll; J. instr. 11, P04006 (2016)
[5] A. Rosenauer et. Al.; Springer Proc. Phys. 120, 169-172 (2007)
[6] T. Grieb et. al.; Ultram. 221, 113175 (2021)

Figure 1

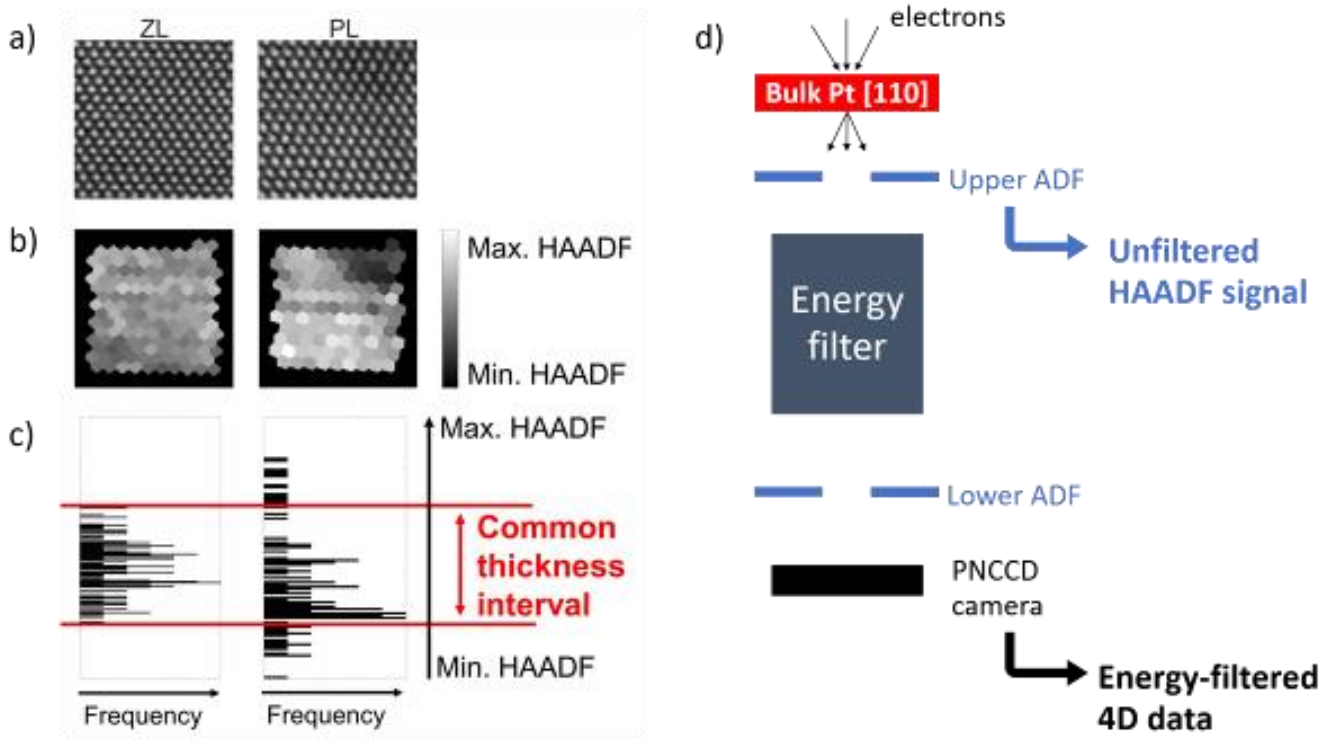

Figure 2

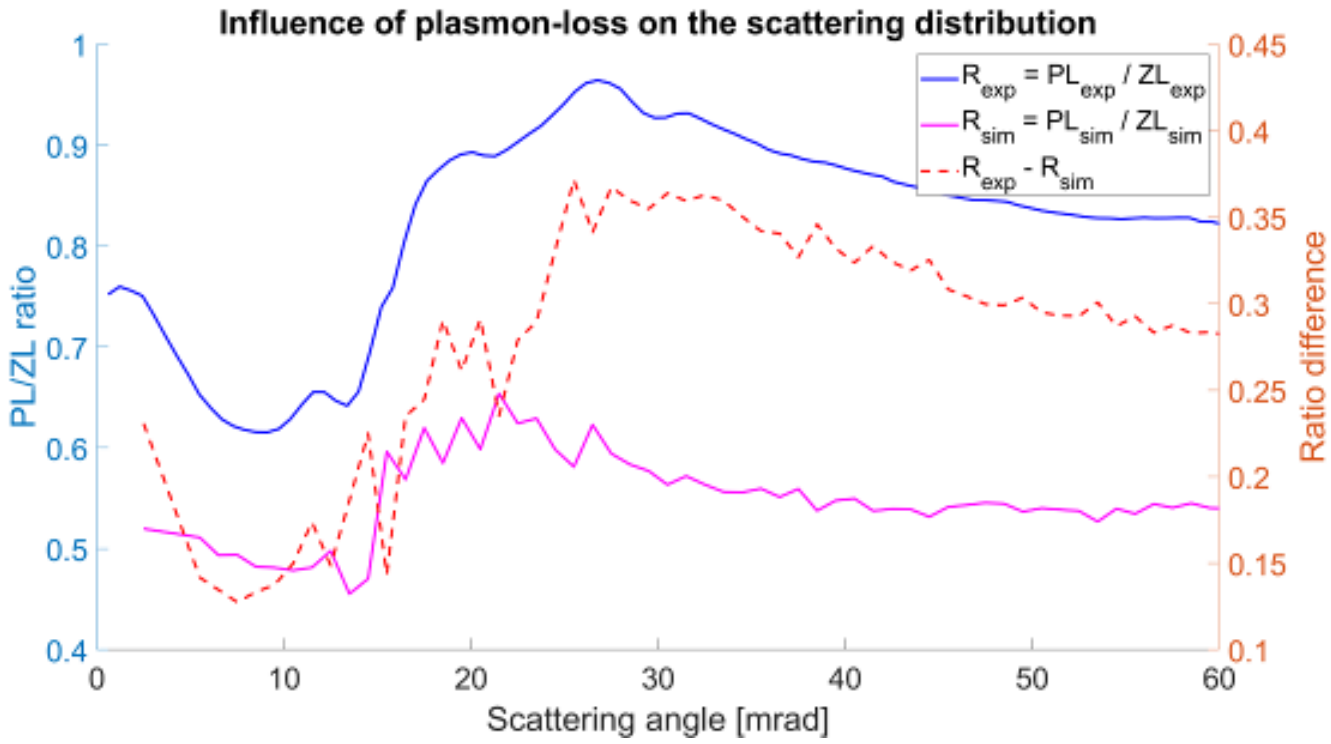

IM8.P009
Reference based atom counting from Voronoi averaged STEM intensities with inclusion of column crosstalk

F. F. Krause[1], M. Schowalter[1], A. Rosenauer[1]

[1]Universität Bremen, IFP, Bremen, Germany

For the investigation and characterisation of nanoscopic structures, scanning transmission electron microscopy has proven to be a very important tool. With its capability of atomic resolution, it can give very precise and accurate projections of such structures. However, in many cases, the full geometry has to be determined. For this, it is of high value to know the height of each projected atomic column with the highest possible precision, ideally with single-atom precision. Methods, which have this capability, are referred to as "atom counting" and have been of high interest in the past years.

To this end, two types of methods have been developed: Statistical approaches and techniques that are based on the comparison of measured STEM images to simulations [1]. Former can constitute a challenge in their computational demands due to a necessary model fit in a high-dimensional parameter space. However, these fits inherently include possible crosstalk between neighbouring atomic columns. Latter, on the other hand, are relatively simple to apply, because they only require a lookup in the simulation references [2]. The crosstalk that can occur due to scattering or channelling effects of heavy columns is usually neglected.

This contribution will present a method to determine the crosstalk between columns from simulations and subsequently take this crosstalk into account in the evaluation of measured experimental images in an evaluation based on the average STEM intensity in each column"s Voronoi cell in the image. For this purpose, frozen phonon multislice simulations of supercells with roughened surfaces are created, which as a result consist of columns of different height. These simulated images are evaluated using Voronoi cells and, using the known column heights, the crosstalk between each two columns can be precisely quantified as a function of both their distance and height as well as their composition. It will be shown that the function representing the crosstalk is relatively smooth, monotonically decreasing and positive definite due to the incoherent character of high-angle STEM imaging. The dependency of the crosstalk on microscope parameters such as coherent and incoherent aberrations will be analysed.

Once the crosstalk can be described with a function, its effects can be removed from experimental data. If the crosstalk mainly depends on the column distances, which are known from the images, this crosstalk removal can be applied by a simple matrix inversion without noticeable computational effort. This is the case for single-atomic crystals with a limited thickness variation. The dependence of the crosstalk on further quantities such as the column height and height differences was investigated and will be discussed. The result of the crosstalk correction on the evaluation of atom counting will be shown for simulated STEM images. Figure 1 exemplarily shows the improvement for atom counting for a very thin gold sample. Fig 2. shows a comparison of the counting error for different specimen thicknesses.

[1] A. De Backer *et al.*, Ultramicroscopy 134 (2013), p. 23
[2] J. LeBeau *et al.*, Nano Letters 10 (2010), p. 4405

Figure 1

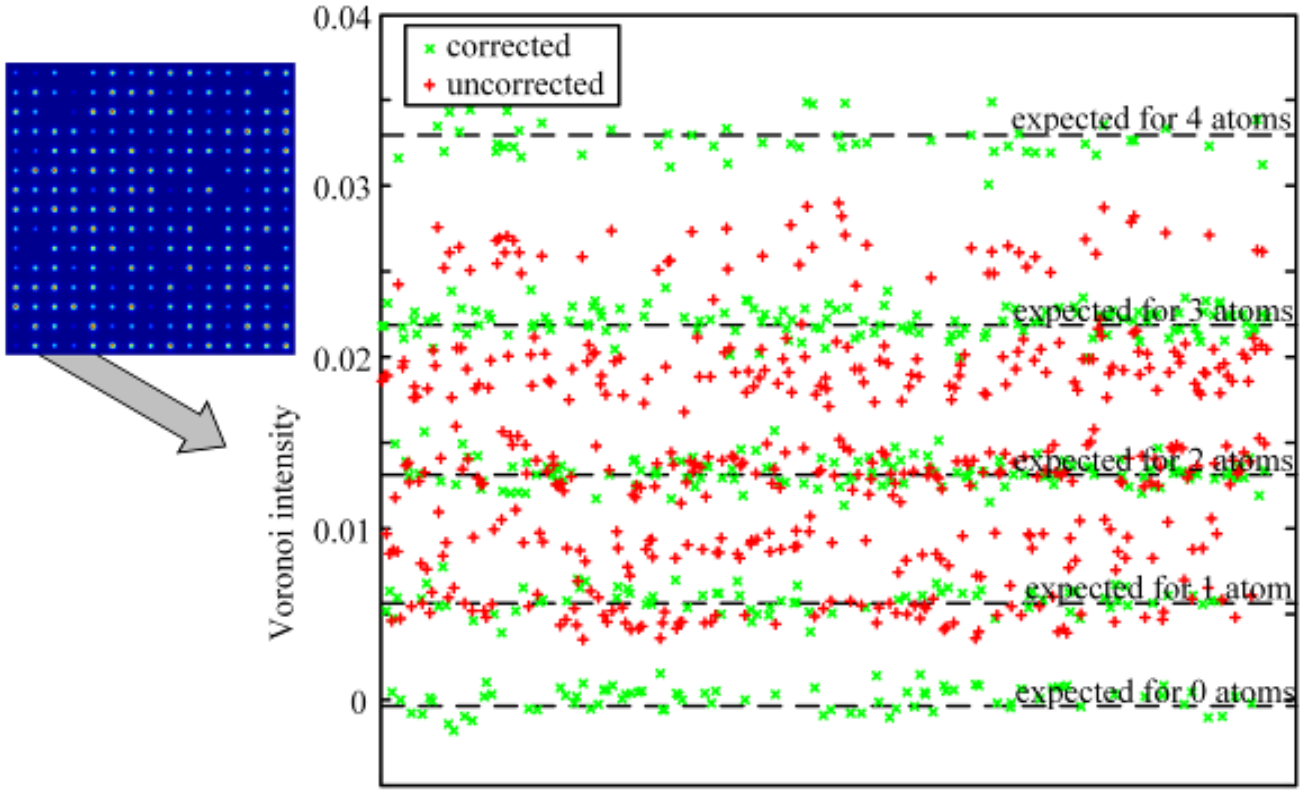

Figure 1: Effect of the correction scheme: The Voronoi evaluation of a STEM image of thin gold yields the plotted red intensity values, which scatter quite far from the expected values (black dashed). The correction strongly reduces this spread and allows for accurate thickness determination (green).

Figure 2

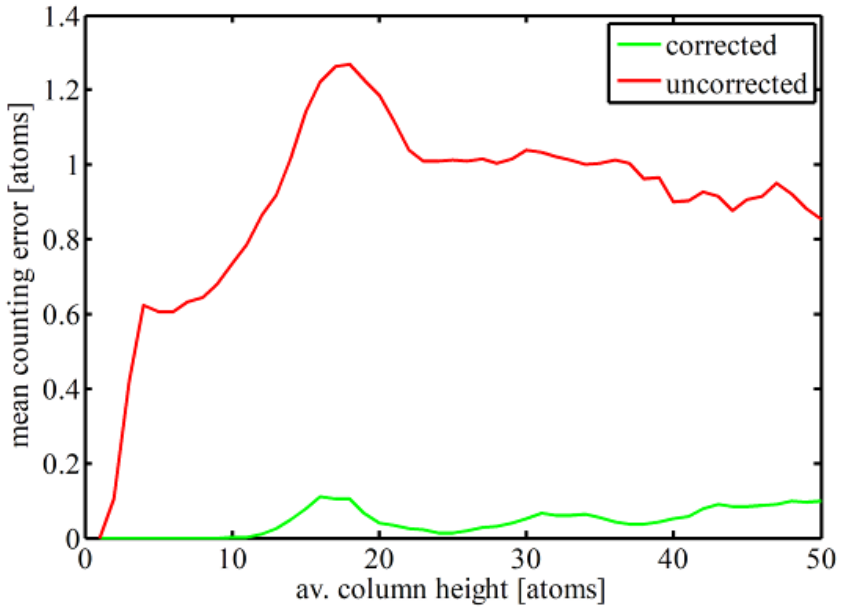

Figure 2: Voronoi atom counting error with and without the presented correction scheme: With the correction, the error suffices for single atom precision while without it, errors of more than an atom occur.

IM8.P010
Optimal experiment design for counting atoms of different chemical nature using 4D scanning transmission electron microscopy

D. G. Sentürk[1,2], A. De Backer[1,2], S. Van Aert[1,2]

[1]EMAT, University of Antwerp, Antwerp, Belgium
[2]NANOlab Center of Excellence, University of Antwerp, Antwerp, Belgium

Aberration-corrected ADF STEM has become a powerful tool for materials characterisation. To predict the optimal angles of the annular detector to solve a specific materials research question, the probability of error (Pe) was introduced using statistical detection theory [1,2]. This enabled us to find the optimal inner and outer angle to count the number of atoms from monotype nanosystems. When investigating heteronanostructures, the use of pixelated detectors is advantageous since it allows us to create multiple 2D STEM images simultaneously [3] or ultimately to use the full 4D STEM dataset.

Here, we extend the concept of the Pe to investigate the potential benefit of analysing multiple 2D STEM images when counting atoms of different types. This problem is formulated as a statistical hypothesis test, where each hypothesis corresponds to a specific number of atoms in an atomic column. The Pe corresponds to the probability to choose the wrong hypothesis. To compute the Pe, realistic 4D STEM simulations are performed from which multiple 2D STEM images are generated with different inner and outer detector angles. From these 2D images scattering cross-sections (SCS) are computed corresponding to the total scattered intensity for each atomic column. These SCSs are an optimal criterion for atom-counting [2]. Furthermore, electron counting noise is taken into account when computing the Pe. To illustrate the concept, the Pe to distinguish between pure Ag and Au columns up to 60 atoms thick was calculated for SCSs for an incident electron dose of 10^4 $e^-/Å^2$ as a function of detector angles (Figure 1a). The result shows that the optimal Pe equals 50% when using a single ADF detector whereas it can be reduced to 29% for two non-overlapping detectors. In Figure 1b, the Pe is evaluated as a function of the electron dose under the optimal detector settings for a single ADF detector, for two optimal independent detectors and for the full dark field region of the 4D STEM dataset. This shows that for an incident electron dose of 10^4 $e^-/Å^2$, the Pe can be further reduced to almost zero when exploring the 4D STEM dataset. Moreover, to reach a Pe as low as 30%, the required electron dose can be reduced to only $5 \cdot 10^2$ $e^-/Å^2$.

In summary, the Pe is used to find optimal strategies to count atoms from 4D STEM. In particular, the method will be generalised to create multiple 2D STEM images providing independent information concerning thickness, composition and ordering of the atoms along the viewing direction [4].

[1] J. Gonnissen et al., Appl. Phys. Lett. 105 (2014) 063116
[2] A. De Backer et al., Ultramicroscopy 151 (2015) 46
[3] N. Shibata et al., J. Electron Microsc. 59 (2010) 473
[4] This work was supported by the European Research Council (Grant 770887 PICOMETRICS to SVA and Grant 823717 ESTEEM3). The authors acknowledge financial support from the Research Foundation Flanders (FWO Belgium) through project fundings and a postdoctoral grant to ADB.

Figure 1: Pe to distinguish between pure Ag and Au columns **(a)** as a function of the outer angle of a single ADF detector with fixed inner angle (red), the inner angle of a single ADF detector with fixed outer angle (blue), and the common angle x for two independent detectors (yellow) **(b)** Pe as a function of the incident electron dose calculated for a single ADF detector (blue), two independent ADF detectors (yellow), and for the full dark field region of the 4D STEM dataset (green).

Figure 1

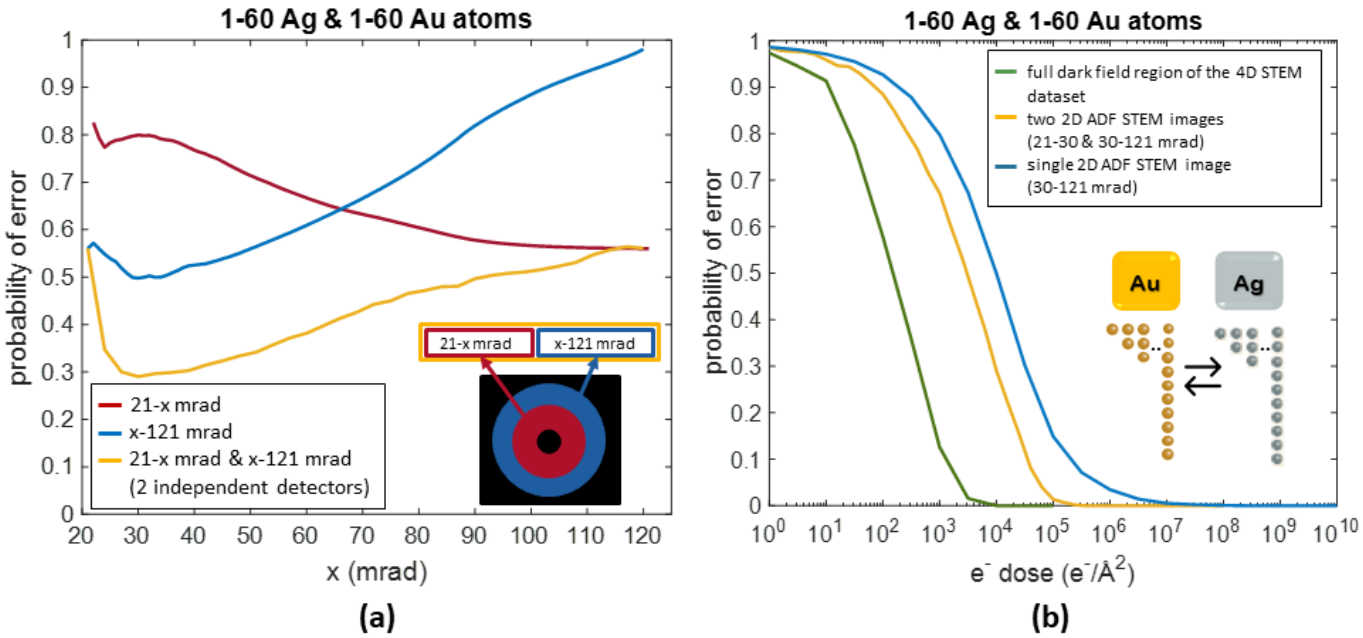
1-60 Ag & 1-60 Au atoms
probability of error
x (mrad)
21-x mrad
x-121 mrad
21-x mrad & x-121 mrad
(2 independent detectors)
(a)
1-60 Ag & 1-60 Au atoms
full dark field region of the 4D STEM dataset
two 2D ADF STEM images (21-30 & 30-121 mrad)
single 2D ADF STEM image (30-121 mrad)
Au
Ag
e⁻ dose (e⁻/Å²)
(b)

IM8.P011
Self-supervised denoising for scanning transmission electron microscopy images

F. Wang[1], T. R. Henninen[1], D. Keller[1], R. Erni[1]

[1]EMPA, Dübendorf, Switzerland

Introduction: Modern scanning transmission electron microscopy (STEM) can provide sub-ångström imaging resolution, but their recorded images usually contain more noises than signals and are difficult to interpret. The field of image denoising is currently dominated by supervised deep learning models that are trained on pairs of the noisy-clean image sets. However, due to the complex experimental configurations and mathematical models behind the experiments, simulating ground-truth and noisy image pairs are very difficult, and it is challenging or even impossible for unsupervised denoising models. Recent self-supervised models such as Noise2Self[1], Noise2Void[2] can restore images only using noisy images, but their performance is not good when interpreting STEM images[3].

Objective: The success of the current self-supervised models comes at a price of the blind pixel(s), i.e., loss of information, either in the encoder before the first residual connection, or in the decoding layer after the last residual connection. However, ignoring a pixel in the noisy input or dropping out values in the middle of the network gives away some useful information, and intentionally leads to degraded performance. As our approach is matching the noisy images to themselves, we cannot use residual connections in our network. We thus turn our focus to autoencoder, which has provided a general framework for lossy compression and then followed by decompression of the data to solve the identical mapping problem.

Results: We test our model on various experimental STEM images recorded using an electron dose ranging from 10^4 eÅ^{−2} to 10^6eÅ^{−2}. The samples are prepared with typical pixel sizes of the recorded images are 6.3-12.6 pm acquired at 1-20 frames per second (fps) and resolutions from 512×512 pixels to 2048×2048 pixels. Each dataset includes thousands of images, and it takes about 5 hours to train our model for 100 epochs in the dataset with 1000 × 512 × 512 pixels. We show the living view of an isolated atom gets absorbed in Figure 1, and show the interpretation of atoms and huge clusters in Figure 2.

Conclusion: We have demonstrated a general framework for image denoising, which only uses the noisy images as input and has no prerequisite on the training set nor the prior information. Our approach is dedicated to restoring heavily noisy images for the ballooning dataset produced by STEM recent detectors. Instead of applying the popular dropout/masking pixel(s) tricks, we adopt a compressive autoencoder architecture to reserve all the information from the training data and using MCNN technique for fast convergence. We hope our framework will find a lot of applications in a wide range of fields, especially in places where there is abundant measurement data available but is heavily noisy as the detector radiation power is strictly limited.

[1] Batson, Joshua, and Loic Royer. "Noise2self: Blind denoising by self-supervision." International Conference on Machine Learning. PMLR, 2019.
[2] Krull, Alexander, Tim-Oliver Buchholz, and Florian Jug. "Noise2void-Learning Denoising from Single Noisy Images." CVPR, 2129–37, 2019.
[3] Wang, Feng, Trond R. Henninen, Debora Keller, and Rolf Erni. "Noise2Atom: Unsupervised Denoising for Scanning Transmission Electron Microscopy Images." Applied Microscopy 50, no. 1: 23.

Figure 1

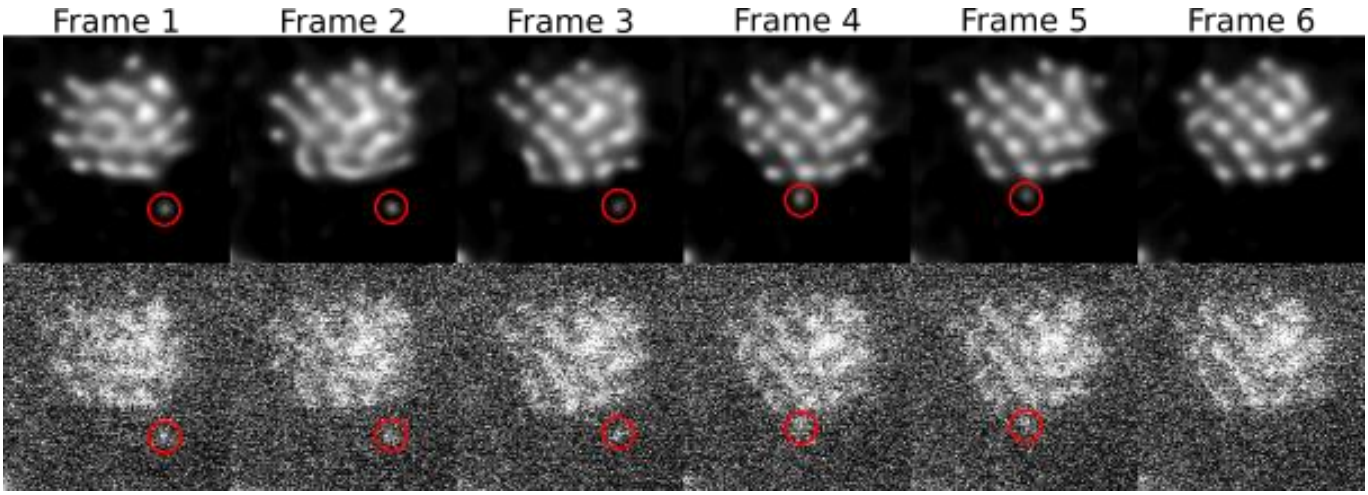

Figure 2

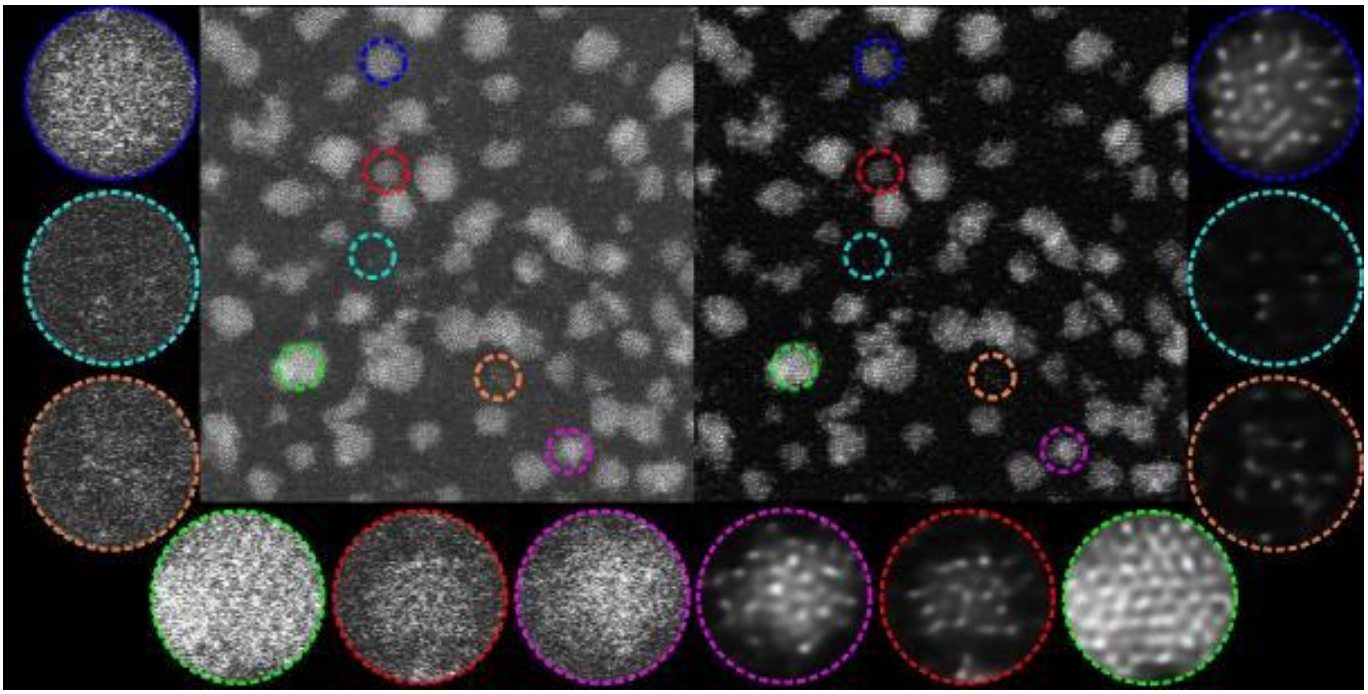

IM8.P012
Dynamic diffraction lattice phase imaging using DBI

R. Herring[1]

[1]University of Victoria, Victoria, Canada

A method using diffracted beam interferometry (DBI) [1] to obtain two-dimensional atomic lattice phase images is described showing two examples using crystals of aluminum and gold. These lattice phase images most likely form due to the residual phase contribution of dynamic diffraction within the interfering beams. Dynamic diffraction is complex and the bane of high resolution imaging especially in strongly electron scattering specimens. Being able to measure its contribution to the overall phase image would help to produce better high resolution electron microscopy (HRTEM) lattice images by providing a means for its removal.

The method involves interfering two symmetrical Bragg diffracted beams on the optic axis using an electron biprism (Figure 1a). Kinematically, they should 100% cancel their phase when interfered on the optic axis to produce a flat phase image. This is not the case. Instead, a residual lattice phase image is produced (Figure 1b,c and Figure 2). The most likely candidate for this residual lattice phase is dynamic diffraction having been picked up by the interfering Bragg diffracted beams during their passage through the crystal specimen.

The phase contributions for a perfect crystal to the interference of the two symmetrically diffracted Bragg beams, , on the optic axis is simply given as,

Interestingly, the dynamic lattice phase contributions, do not cancel, possibly due to crystal misalignments, long range crystal strain, point defects or some other phase object(s). Dynamic diffraction has complex contributions to lattice images as there are many possibilities for producing it, especially for strong phase objects like gold and heavy metals.

In this report, aluminum and gold crystals representing weak and strong phase objects, respectively, were used for the two-beam DBI experiments. The residual lattice phase images produced by Al were relatively simple compared to the more complex, residual lattice phase images for Au (Figure 1 and Figure 2).

In these experiments the interference of two symmetrically Bragg diffracted beams on the optic axis revealed residual phase at the crystal"s atomic lattice sites producing a lattice phase image. This residual lattice phase measurement offers possibilities to help understand dynamic diffraction"s contribution to HREM lattice images with the goal of being able to determine the number and types of atoms.

R.A. Herring, G. Pozzi, T. Tanji, A. Tonomura, Ultramicroscopy 60 (1995) 153. R.A. Herring, "Phase Imaging Dislocations using Diffracted Beam Interferometry" Microscopy (2020) MICRO-2020-00047.

3. S. Penkova, R.A. Herring, Microsc. Microanal. 25 (Suppl 2), 2019 104. doi:10.1017/S1431927619001259

Grants from NSERC Discovery, CFI and BCKDF are greatly appreciated.

Figure 1: a) Electron optical configuration interfering two symmetrical Bragg diffracting beams on the optic axis by means of an electron biprism, b) DBI interferogram of Al, and c) its reconstructed phase image revealing residual lattice phase.

Figure 2: a) DBI phase image of the interference of symmetrical Bragg diffracted beams of Au showing an amorphous C (a-C) deposit with its phase spectrum passing through the line in the upper right corner, a dislocation network, D (see [2], [3]), and the residual phase, R, in the perfect crystal magnified in b) and its phase lattice structure along the line shown in c) the phase spectrum clearly revealing the complex phase shift"s periodicity.

Figure 1

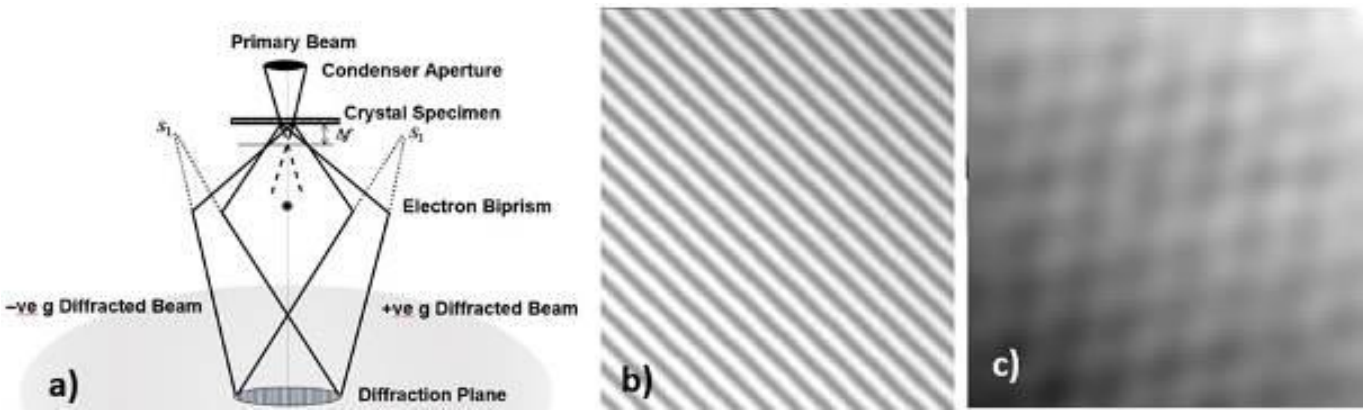

Figure 2

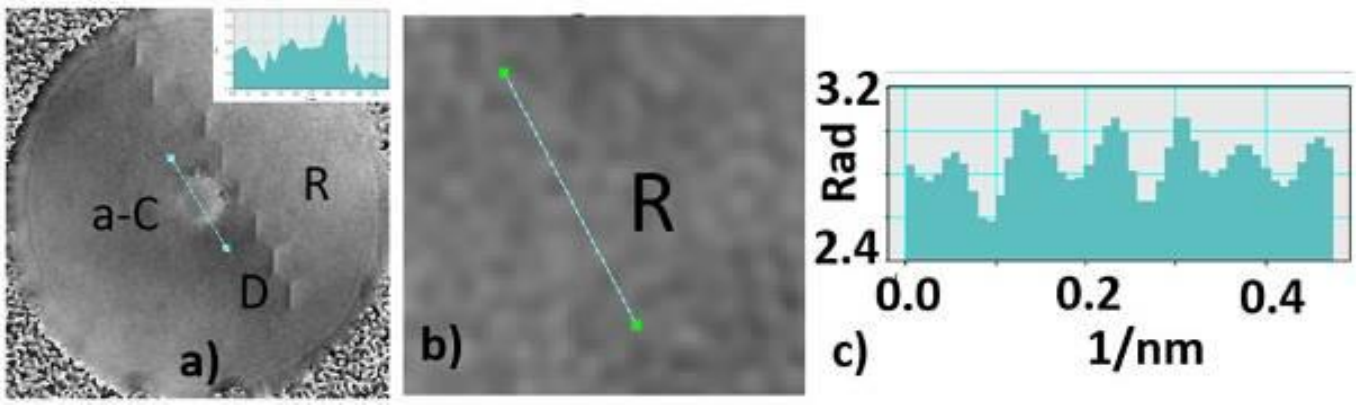

Figure 3

The phase contributions for a perfect crystal to the interference of the two symmetrically diffracted Bragg beams, $\phi_{g_{hkl}}, \phi_{g_{\bar{h}\bar{k}\bar{l}}}$, on the optic axis is simply given as,

$$\Delta\phi = \phi_{g_{hkl}} - \phi_{g_{\bar{h}\bar{k}\bar{l}}} + \sum\phi_{g_{hkl}} - \sum\phi_{g_{\bar{h}\bar{k}\bar{l}}} = \sum\phi_{g_{hkl}} - \sum\phi_{g_{\bar{h}\bar{k}\bar{l}}} \qquad 1)$$

Interestingly, the dynamic lattice phase contributions, $\sum\phi_{g_{hkl}} \neq \sum\phi_{g_{\bar{h}\bar{k}\bar{l}}}$ do not cancel, possibly due to crystal misalignments, long range crystal strain, point defects or some other phase object(s). Dynamic diffraction has complex contributions to lattice images as there are many possibilities for producing it, especially for strong phase objects like gold and heavy metals.

IM8.P013
4D-STEM live-processing at 15'000 detector images per second for efficient series acquisition

B. Haas[1], A. Mittelberger[2], C. Meyer[2], B. Plotkin-Swing[2], N. Dellby[2], O. Krivanek[2], T. Lovejoy[2], C. T. Koch[1]

[1]Humboldt University of Berlin, Department of Physics & IRIS Adlershof, Berlin, Germany
[2]Nion Co., Kirkland, WA, United States

4D-STEM acquisition using fast pixelated detectors is an intensely researched field in electron microscopy [1]. It has recently been shown that acquiring and registering series of 4D maps can substantially improve the quality [2]. However, this produces massive amounts of data and its quality can only be judged after processing.

To efficiently acquire 4D-STEM data, it is therefore advantageous to have live feedback to judge the quality of incoming data on the fly. Ideally, the utilized detector has a sufficiently high frame rate that live-processed data allows to evaluate the region of interest close to the speed of traditional STEM imaging.

Using a Nion HERMES microscope with IRIS spectrometer (operated at 60kV with a 36mrad and 75pA probe), we combine a Dectris ELA direct detector [3] with novel live-processing capabilities of the Nion Swift software [4] to achieve virtual detector feedback on the fly while acquiring 4D-STEM data. As a demonstration sample we use SrTiO3 and a twisted bilayer graphene flake. The ELA detector combines the readout noise-free characteristics of hybrid-pixel detectors with a relatively large number of pixels (1030x514) and very high frame rates (up to 18"000 fps for 1030x130 pixel readout). The Python-based Nion Swift software now allows to define customizable virtual detectors via masks and applies them to the data while it is streaming in. This live-processing runs smoothly on a standard workstation computer.

We present live-processing results of 15"000 frames per second of a Dectris ELA detector via Nion Swift. A screenshot of the software interface displaying the output of virtual detectors during data acquisition is shown in Figure 1. The high frame rate allows this data set with 512x512 scan points to be acquired within 17s. As the detector is mounted behind the spectrometer, inelastic scattering (larger than a few eV) can be (and was) filtered out. A customizable amount of 4D data sets is cached in the background on hard drive(s) and only the data chosen by the operator based on the live data processing is permanently stored, the other dynamically drops out. Figure 2 shows data acquired from a bilayer graphene sample and registered in post-processing using SmartAlign [5]. Here, only the live-processing output was stored, allowing to acquire data sets that would be larger than disk space.

The live-processing in Swift using a Dectris ELA detector allows to efficiently acquire high-quality 4D-STEM data sets approaching the speed of normal STEM imaging, which renders the acquisition of 4D-STEM series routine work.

[1] C. Ophus, Microsc. Microanal. 25, 563 (2019)
[2] B. Haas et al., Microscop. Microanal. 26 (Suppl 2), 1898 (2020), arxiv.org/abs/2103.03202
[3] B. Plotkin-Swing et al., Ultramicroscopy 217, 113067 (2020)
[4] C. Meyer et al., Microscop. Microanal. 25 (Suppl 2), 122 (2019), https://github.com/nion-software/nionswift
[5] L. Jones *et al.*, Adv. Struct. Chem. Imag. 1, 8 (2015)
[6] Acknowledgements: We thank Tobias Schulz from Institute for Crystal Growth (IKZ) in Berlin for providing the SrTiO3 sample.

Figure 1: Nion Swift interface while acquiring and live processing data using a Dectris ELA detector at 15'000 detector frames per second (SrTiO3 sample).

Figure 2: A non-rigidly registered 4D-STEM series of a twisted bilayer graphene sample (bottom) in comparison to a single data set (top). The maps were acquired at 15'000 detector frames per second using the live processing mode.

Figure 1

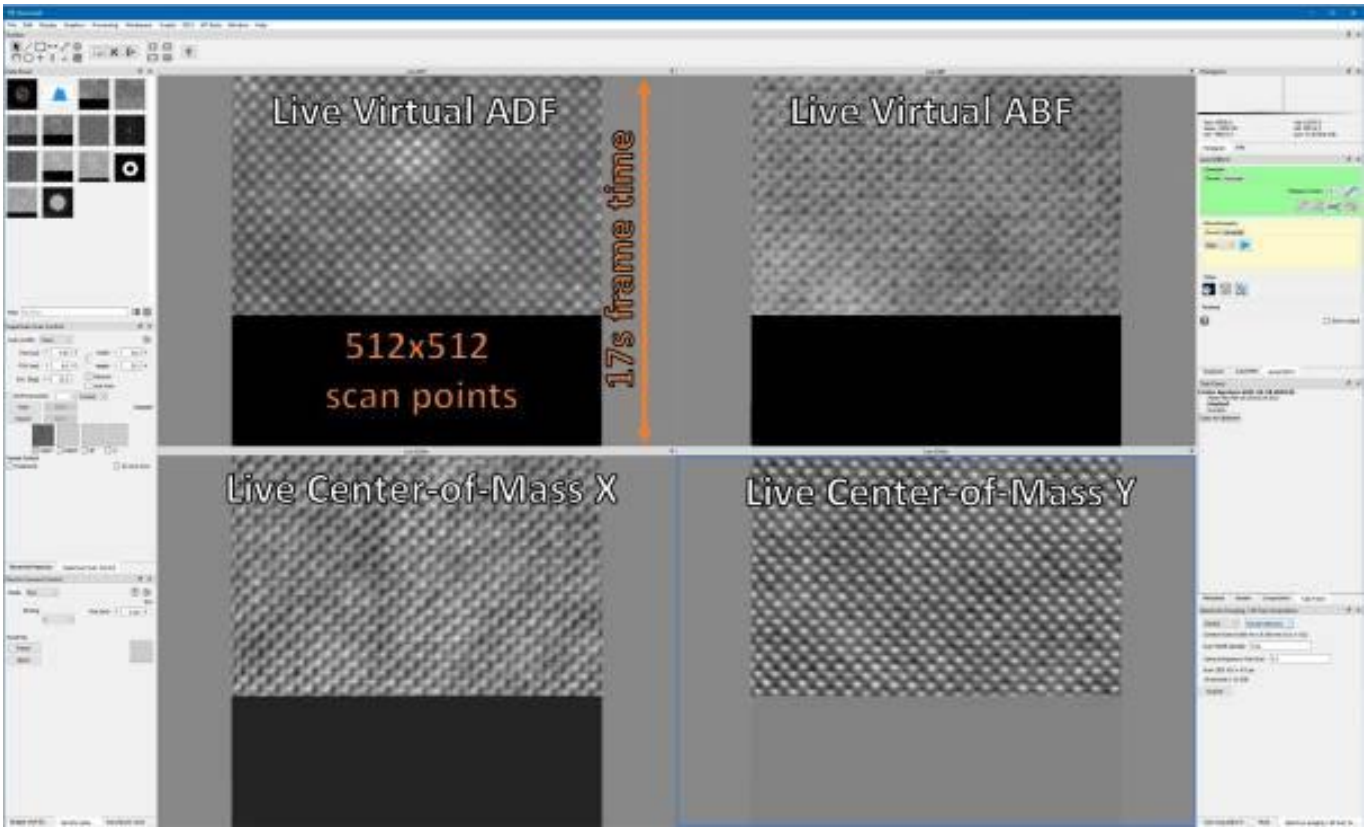

Figure 2

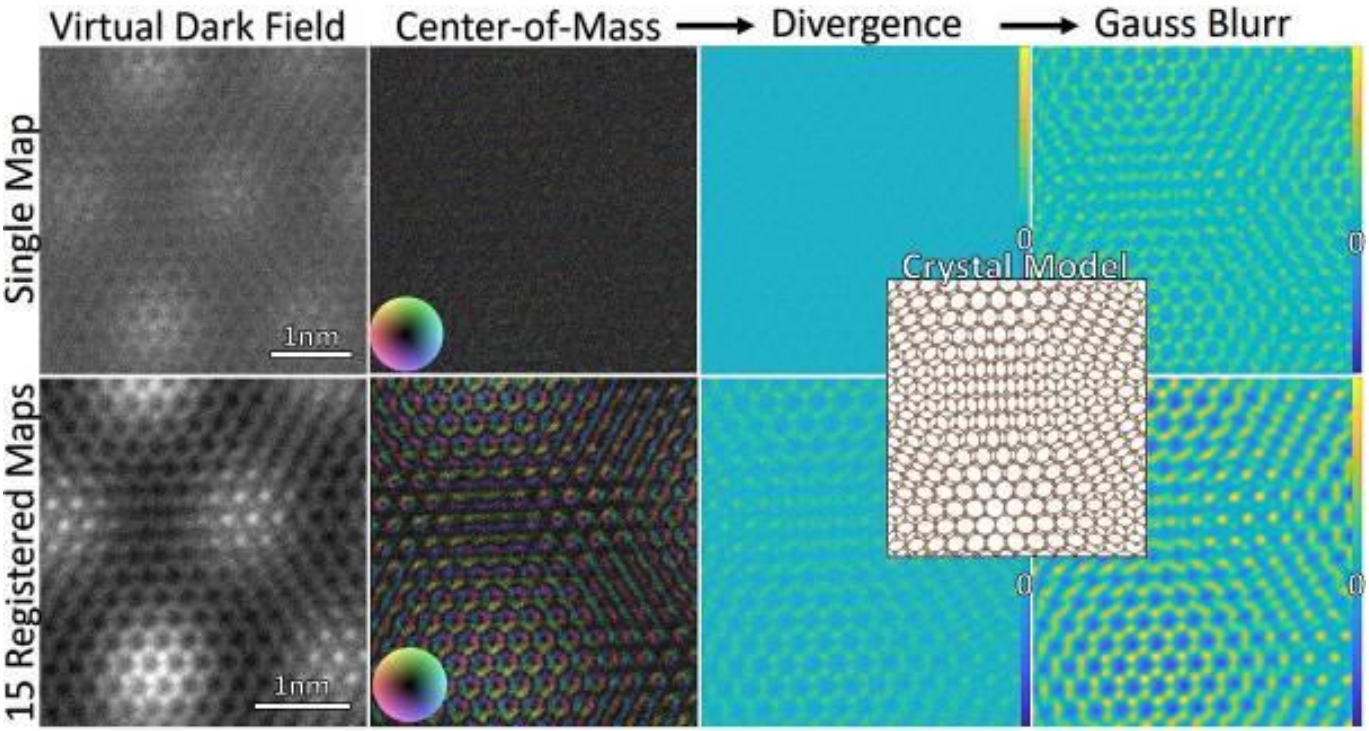

IM8.P014
Investigating the orientation relationship of nano-sized precipitates using 4D-STEM

N. Cautaerts[1], E. Rauch[2], J. Jeong[1], G. Dehm[1], C. H. Liebscher[1]

[1]Max Planck Institute for Iron Research, Düsseldorf, Düsseldorf, Germany
[2]University of Grenoble, Grenoble, France

Understanding the formation mechanisms of secondary phases and the structure of their interface with the primary phase are important for understanding material behavior. A key component to achieve this understanding is deducing the orientation relationship of the phase with the parent phase. When secondary phase domains are small, as is the case for nano-sized precipitates, directly measuring the orientation relationship with classical TEM techniques can be very tricky, especially if the orientation relationship has multiple variants.

The aim of this work was to deduce the orientation relationships of small particles using 4D-STEM template-based orientation mapping. Typically this type of work is done using the ASTAR system (NanoMegas). However, we show that the signal to noise ratio of the data was insufficient to resolve the reflections from the small particles. Instead we used a 4K CMOS camera which has a significantly improved signal to noise ratio. The system we investigated were radiation induced G-phase precipitates 10-20 nm in diameter in austenite, for which the orientation relationship was not yet reported. Using a two-stage template matching procedure, we were able to deduce the orientation relationship of individual particles in the field of view. We showed that G-phase forms in austenite with orientation relationships characteristic of the FCC to BCC transformation.

Figure 1

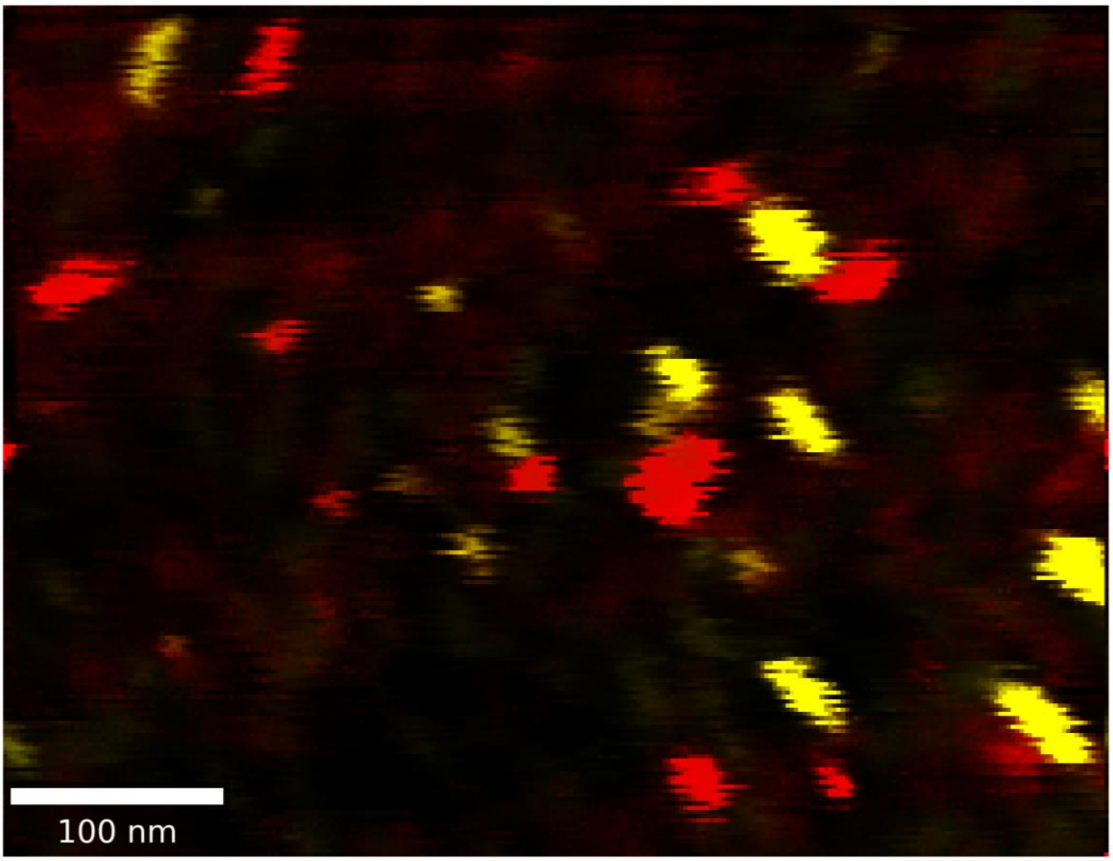

IM8.P015
Automated mapping of the crystallographic sample orientation from diffraction patterns in momentum-resolved STEM

M. Cattaneo[1,2], K. Müller-Caspary[1,2], J. Barthel[1], K. MacArthur[1], M. Lipińska-Chwałek[1]

[1]Research Center Jülich, Jülich, Germany
[2]RWTH Aachen University, Aachen, Germany

In scanning transmission electron microscopy (STEM), sample tilt is a parameter that we need to control for optimum imaging conditions. However, residual tilt cannot always be eliminated because of the limited precision of the tilt stage and because it is partly due to the sample geometry at interfaces or bent specimens. In this study, we present an automated method for measuring local crystal orientation from convergent beam electron diffraction patterns. Using ultrafast cameras that record a diffraction pattern at each scan position (4D STEM), mapping of crystal orientation over a field of view becomes possible. The availability of tilt mapping has the potential to improve strain measurements [1], spectroscopy at interfaces [2], and quantitative studies of bent samples that require local sample tilt as input to simulations.

Central to our method is the detection of Kikuchi band crossings in diffraction patterns. The location of the Kikuchi band crossing with respect to the central beam is a measure of out-of-plane inclination while a mutual change of azimuthal orientation of all bands around a crossing indicates in-plane rotation. Band positions are determined from peaks in azimuthal scans of an annular region at large scattering angles (Figure 1). This procedure has been implemented in a fast computer program and can be automatically applied to a series of patterns as recorded in a 4D STEM experiment. Achievable accuracy and precision were investigated by simulations. For realistic parameters related to the detector and electron dose used, the method was found to be accurate within 0.1 mrad for the out-of-plane orientation and 5 mrad for the in-plane orientation for diffraction patterns averaged over a unit cell. The spatial resolution of this approach is limited by the lateral extent of probe propagation in the crystal. In case of e.g. [110] Fe, the probe extends laterally over 5 unit cells at 40nm sample thickness. The method is applied to 4D STEM data from a twin boundary in steel using an Electron Microscope Pixel Array Detector (EMPAD) in a probe-corrected FEI Titan microscope operated at an accelerating voltage of 200 kV. The analysis provides a map of position-dependent local crystal orientation with unit cell sampling and reproduces the expected in-plane rotation of 70.53° between the twins (Figure 2). Such an analysis is possible within minutes and provides immediate insight into the presence of sample bending, strain fields, and stacking faults.

Figure1: Measuring orientation by Kikuchi bands. (a) CBED pattern with renormalized high-angle annular area. The green cross marks the central beam, the red dot marks the band intersection. (b) Azimuthal scan in the selected dark-field area. The six peaks correspond to the three brightest Kikuchi bands.

Figure2: Orientation mapping over a twin boundary in steel. (a) Synthetic high-resolution HAADF image showing a horizontal twin boundary. (b) Map of local out-of-plane crystal tilt indicating sample bending of a few milliradians over the field of view.

[1] T. Grieb et al., Ultramic. 190 (2018)
[2] K.E. MacArthur et al., Microsc. & Microanal. Accepted
[3] Funding: Jülich Melbourne Postgraduate Academy (JUMPA, M.C.), Helmholtz Contract VH-NG-1317 (K. M-C.), DFG HE 7192/1-2 (K. M.). EMPAD data has been recorded within a cooperation with Thermo Fisher Scientific, Inc.

Figure 1

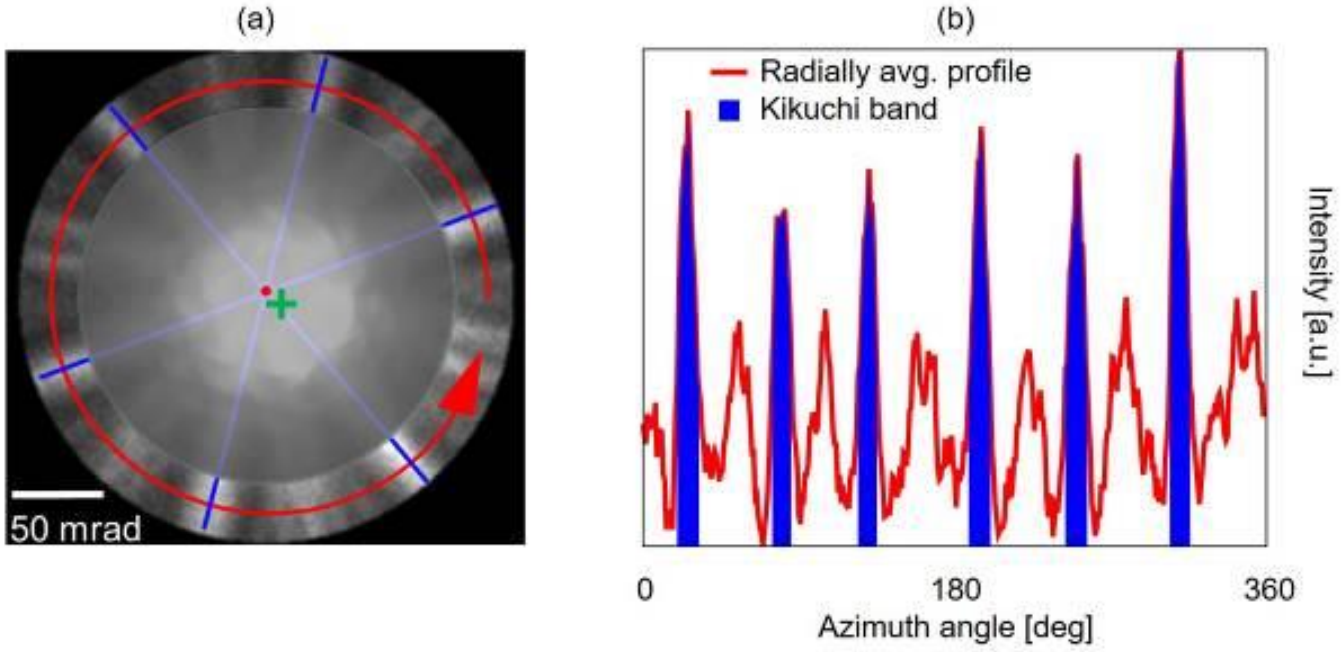

Figure 2

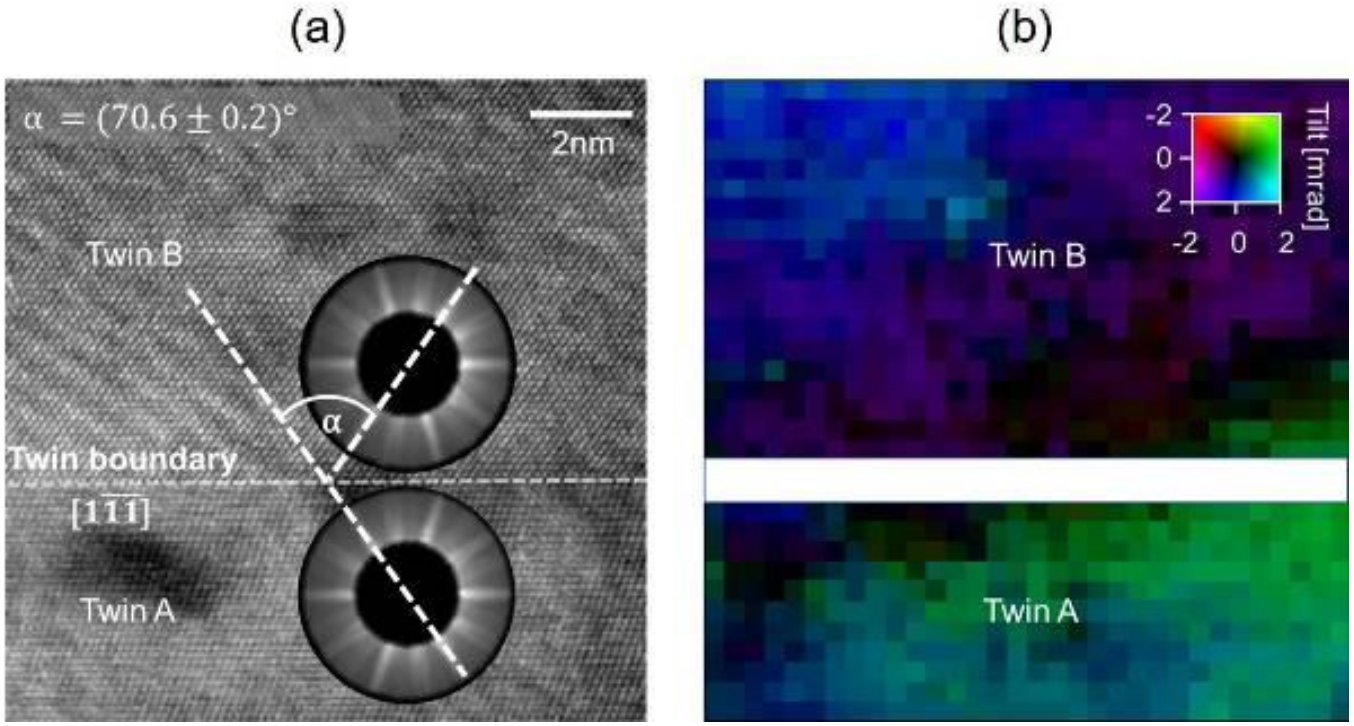

IM8.P016
Towards quantitative elemental mapping across interfaces by combining momentum-resolved STEM and EDX

M. Cattaneo[1,2], K. MacArthur[1], J. Barthel[1], K. Müller-Caspary[1,2]

[1]Research Center Jülich, Jülich, Germany
[2]RWTH Aachen University, Aachen, Germany

The introduction of fast cameras to scanning transmission electron microscopy (STEM) allows for the recording of full diffraction patterns at each scan position (4D STEM). In energy dispersive X-ray (EDX) spectroscopy, silicon drift detectors and aberration correction have increased detection efficiency and available current density. The resulting higher counts in EDX data allow for atomic-scale maps on beam resilient samples. Combining 4D STEM and EDX is desirable to uniquely quantify elemental composition across interfaces.

Here we face two major challenges. Electron channelling causes the EDX signal to depend on both composition and atomic ordering [1 ,2], and beam scattering makes an interface appear more diffuse than it actually is [3]. Sample tilt can ameliorate channelling effects, but the effects of beam broadening persist. Using simulations in direct comparison to experimental data, it is possible to separate structure information including chemical composition from beam-broadening effects. This approach requires accurate sample information as input to simulations, including atomic structure, sample tilt, and thickness. Since these quantities potentially change across interfaces, we propose to perform momentum-resolved STEM in combination with EDX elemental mapping, producing a 5D data set.

5D STEM of a DyScO3-SrTiO3 (DSO-STO) multilayer sample is demonstrated with a probe-corrected Thermo Fisher Titan electron microscope operated at an accelerating voltage of 200 kV. The microscope is equipped with a four quadrant Super-X EDX detector and an electron microscope pixel array detector. An HAADF STEM image of the multilayer is shown in Figure 1 together with colour-coded elemental maps, both revealing atomic layer contrast under large sample tilt. Position averaged convergent beam electron diffraction patterns (PACBEDs) were extracted from the 4D STEM data by averaging patterns from the centres of each DSO and STO layer (Figure 2). A sample thickness of approximately 20 nm was estimated by comparing the bright features of the PACBEDs to simulations, whereas the Kikuchi bands reveal the local sample tilt.

From a first attempt to apply these additional parameters in an EDX STEM simulation [4] for an abrupt interface (inset Figure 1b), less delocalization of EDX signal would have been expected compared to the experiment. In conclusion, some degree of intermixing at the interfaces needs to be considered in the structure model.

Figure 1: (a) STEM HAADF image and (b) elemental mapping of a DSO-STO multilayer sample under large sample tilt parallel to the layers. PACBED patterns shown in Figure 2 were generated from the areas marked in (a). Atomic plane contrast in the composed elemental map has been enhanced by noise filtering for demonstration purpose. A simulated map for an atomically sharp interface is shown as inset.

Figure 2: PACBEDs for layers of (a, c) DSO and (b, d) STO as marked in Figure 1a. No significant change of sample tilt is found between the four regions. The bright parts of the patterns also show no strong difference between layers of the same structure, indicating constant sample thickness.

[1] N.R. Lugg et al., Ultramic. 151 (2015)
[2] K.E. MacArthur et al., Ultramic. 182 (2017)
[3] S.R. Spurgeon et al., Microsc. & Microanal. 23 (2017)
[4] L.J. Allen et al., Ultramic. 151 (2015)
[5] Funding: Jülich Melbourne Postgraduate Academy (JUMPA, M.C.), DFG HE 7192/1-2 (K. M.). and Helmholtz Contract No. VH-NG-1317 (K. M-C.)

Figure 1

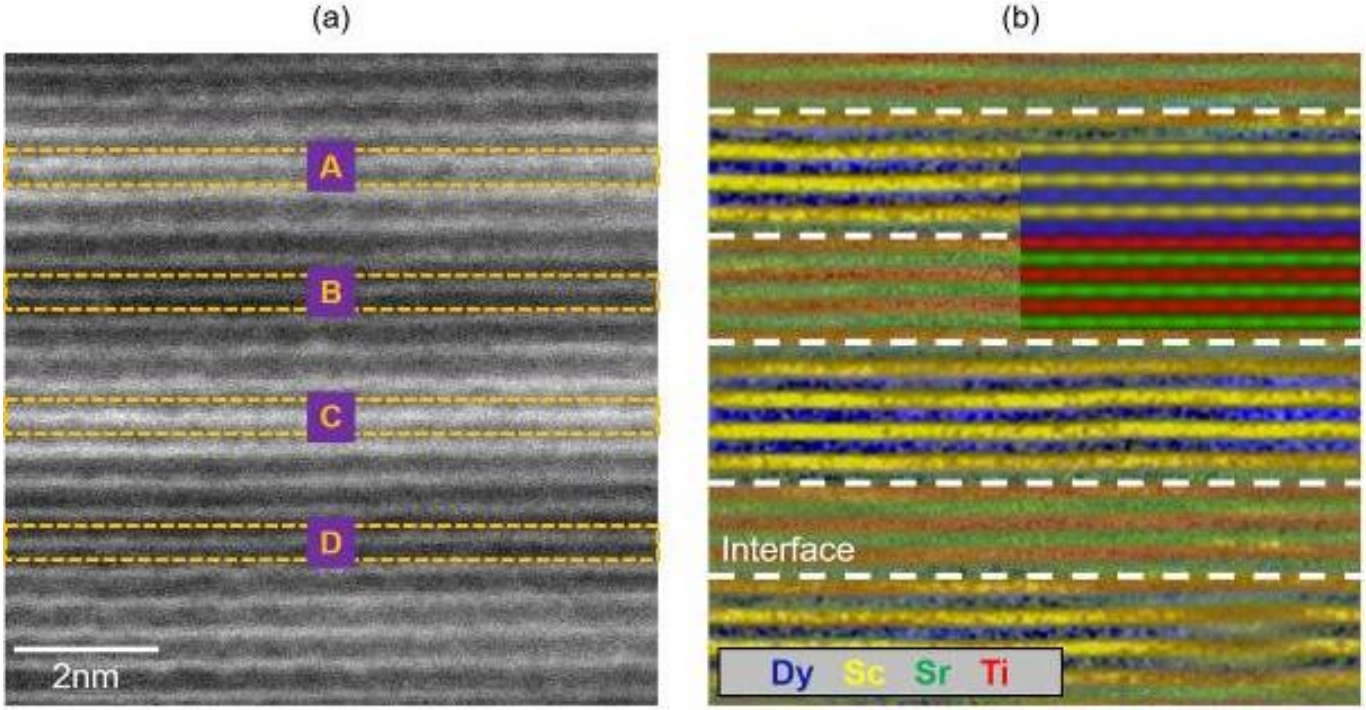

Figure 2

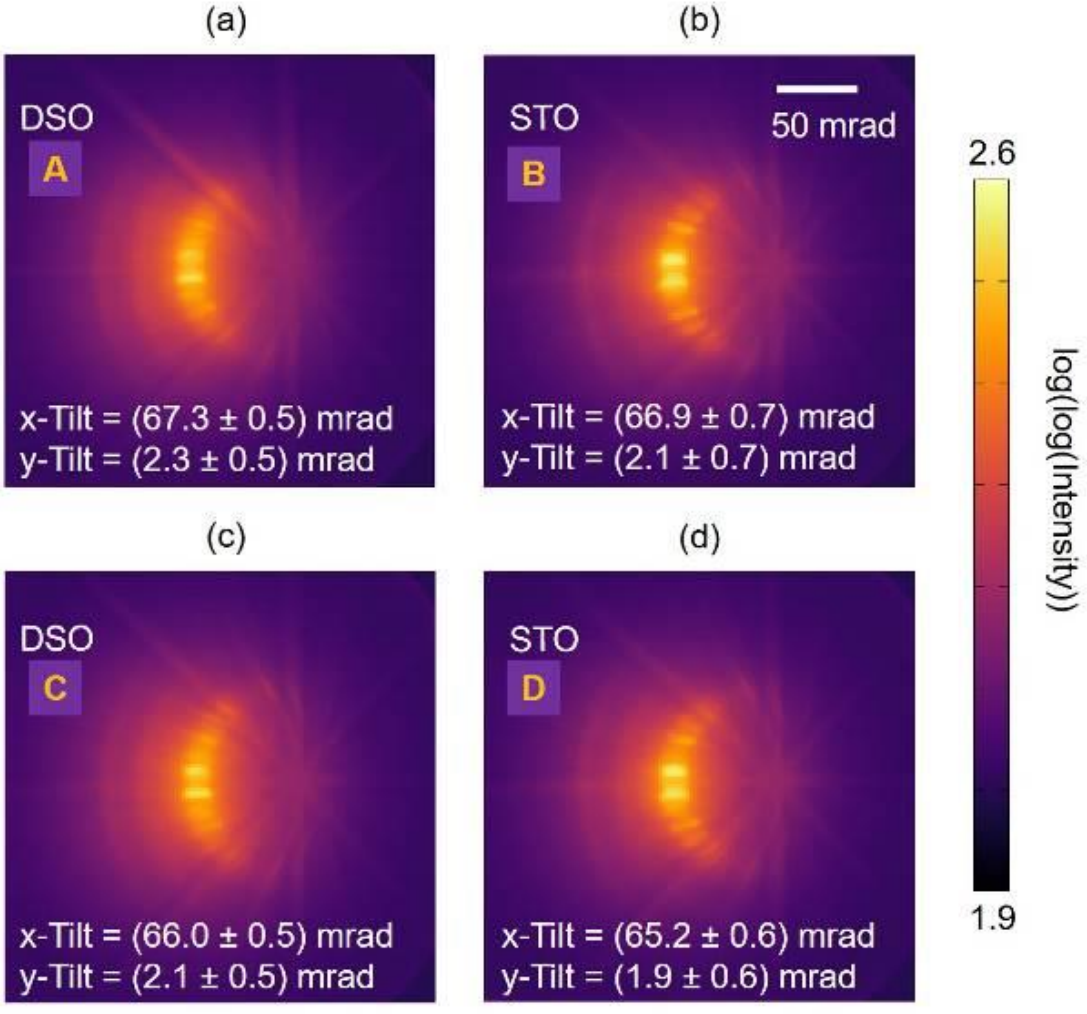

IM8.P017
Interaction-free measurements and quantitative phase imaging with a flexible electron interferometer

A. Turner[1], C. Johnson[1], B. McMorran[1]

[1]University of Oregon, Physics, Eugene, United States

Quantum protocols, such as interaction-free measurements (IFMs),[1] have been proposed for low-dose, high-resolution imaging of beam-sensitive materials.[2,3] However, the realization of electron interaction-free imaging requires the development of a scanning, path-separated electron interferometer. Here we construct a two-grating Mach-Zehnder interferometer (2GMZI) in a conventional transmission electron microscope (TEM) and use it to demonstrate (1) efficient electron IFMs of an opaque sample[4] and (2) quantitative phase imaging.

The interferometer involves two nanofabricated diffraction gratings installed in a field-emission TEM. The input grating splits the beam into two main paths which focus to narrow probes at the sample. One path interacts with the sample while the other is held as a reference. The two paths recombine at the second grating, interfere and co-propagate to the detector. The relative position of the two gratings can be aligned such that the output destructively interferes, creating a dark port. The intensity depends on the phase and amplitude of the sample.

When inserting an opaque sample into one of the interferometer paths, we see an increase in dark port events: the signature of IFMs. The IFM efficiency?, for this 2GMZI is ?=20.7±2.3% (ideally $?_o$=33%). However, the probability that we errantly detect the presence of the sample is P_E=8.7±0.7%.

We also use the 2GMZI for direct phase imaging. We image a 50 nm latex nanoparticle with a phase resolution of ?ph=200 mrad. Current work is focused on decoupling the phase and amplitude loss, improving the spatial and phase resolution, and refining the gratings to achieve stable IFM alignment while scanning.

The 2GMZI is particularly effective due to the tunable path separation, adjustable alignment, accessibility of interferometer paths, scanning capabilities for imaging, and real time phase information. Furthermore, all of the above are achieved while using conventional bright field and CCD detectors. As shown, the 2GMZI is capable of IFMs with electrons and quantitative phase imaging. When achieved simultaneously, interaction-free imaging will advance low-dose, high-resolution imaging of radiation-sensitive samples.

Figure 1: Schematic of optical IFM experiment with the sample (a) removed and (b) inserted. The 2GMZI output with the sample removed (c) and inserted (d). The graph shows the normalized dark port (DP), bright port (BP) and total (Tot) currents.

Figure 2: (a) Schematic of the 2GMZI with the dark port (DP) focused on the bright field (BF) detector. (b) The normalized interferometer output as a function of the relative grating shift, shown in terms of the position of the second grating over the input grating pitch, $?x_2/p_1$. (c) Simulated and experimental HAADF and 2GMZI images aligned at the maximum and minimum. Scalebars represent 10 nm. (d) The phase reconstruction from the intensity cross-section.

References:
[1] Elitzur, A. C. & Vaidman, L. Quantum mechanical interaction-free measurements. *Found Phys* 23, 987–997 (1993).
[2] Putnam, W. P. & Yanik, M. F. Noninvasive electron microscopy with interaction-free quantum measurements. *Phys. Rev. A* 80, 040902 (2009).
[3] Kruit, P. *et al.* Designs for a quantum electron microscope. *Ultramicroscopy* 164, 31–45 (2016).
[4] Turner, A. E., Johnson, C. W., Kruit, P. & McMorran, B. J. Interaction-free measurement with electrons. *Under Review* (2021).

Figure 1

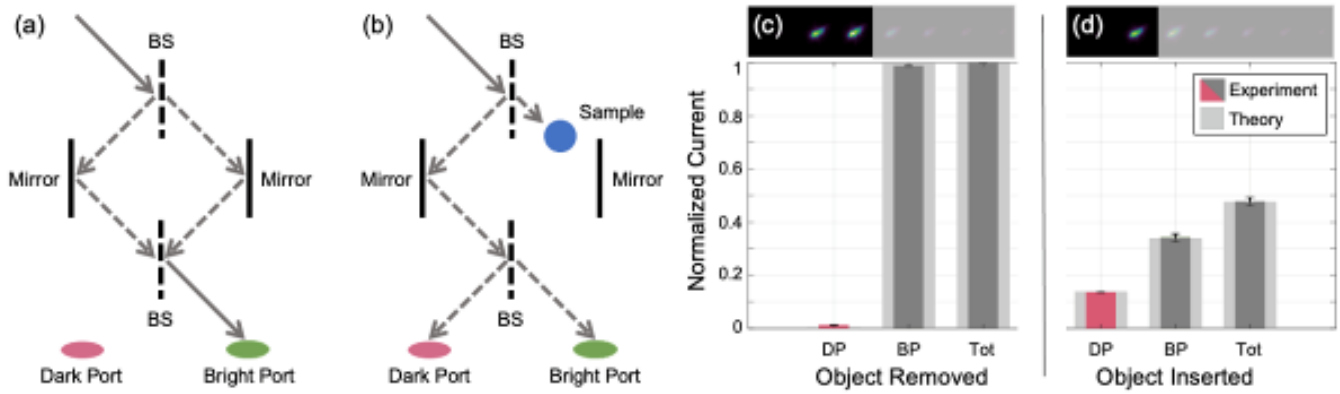

Figure 2

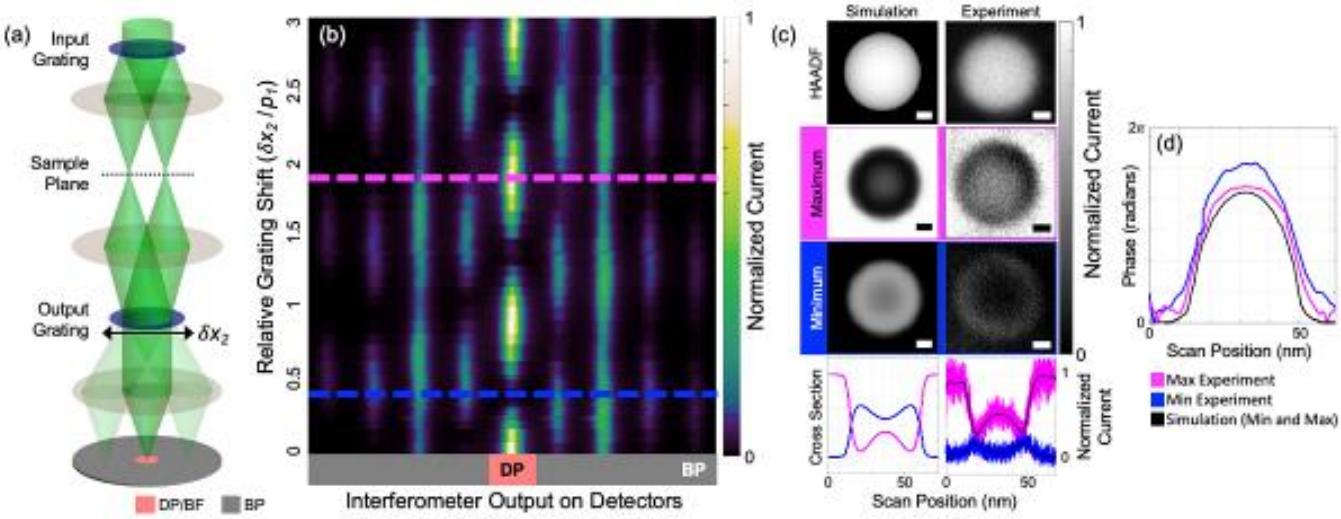

IM8.P019
The correlation between ptychographic phase and ADF intensity – a new approach for quantitative STEM

A. Mostaed[1], A. I. Kirkland[1,2,3], P. D. Nellist[1]

[1]University of Oxford, Department of Materials, Oxford, United Kingdom
[2]electron Physical Science Imaging Centre (ePSIC), Diamond Light Source, Didcot, United Kingdom
[3]The Rosalind Franklin Institute, Harwell Campus, Didcot, United Kingdom

Introduction*:* Ptychography offers the highest phase contrast and signal to noise ratio among phase contrast imaging techniques in TEM [1]. This technique can be used to revel the position of light atoms in the structure of materials containing both light and heavy atoms. In this technique, the reconstructed phase from an atomic column contains information about the number of atoms in that column. For instance, Figure 1(a) shows that the contrast, i.e. the reconstructed single side band (SSB) phase, of a Si column increases by increasing the number of its atoms. This shows that the ptychographic phase can be used to reveal the number of atoms in an atomic column. However, as displayed in Figs. 1(b) and 1(c), the increment in the phase does not happen when the sample thickness is larger than ~5nm (i.e. the thickness for 9 Si atoms along [001]). In fact, when the number of Si atoms in a column is more than 9 atoms, phase wrapping happens and the phase decays with further increasing the number of Si atoms (Figure 1(c)). Here, we are proposing a method by which it is possible to push the limitations of the ptychographic phase quantification.

Figure 1: Reconstructed ptychographic phase (SSB) for an atomic column containing 1,3,5,7 and 9 Si atoms. Line profiles across the reconstructed phase of Si columns containing (b) 1 to 9 atoms and (c) 10 to 23 atoms. The data presented here were simulated by µSTEM[2].

Results: We know that atomic columns appear with ***roughly*** a Gaussian***-like*** shape in both reconstructed phase and ADF images. Fig 2 shows an ADF image and reconstructed SSB-phase obtained from an atom column containing nine Si atoms. In a simple case, when the standard deviations of the fitted Gaussian to both images are similar (which is the case in Figs. 2(a) and 2(b)), the relation between the phase and ADF intensity at each pixel, as shown in Figure 2(c), would be linear (i.e. $\varphi_{i,j} = aI_{i,j} + b$; where a and b are constants). Figure 2(d) shows the fitted lines to the phase vs. ADF intensity curves obtained from Si columns containing various number of atoms from 1 atom to 23 atoms. This figure shows that atom columns containing different atoms can be distinguished from each other by considering their reconstructed phase and ADF intensity as described before. By considering only the phase (Figure 1), it is possible to measure the number of Si atoms in a column when there are up to 4 or 5 atoms in that column. However, using the proposed method, we increased that number to more than 20 atoms.

Figure 2: (a) Reconstructed ptychographic phase (SSB) of an atomic column containing 9 Si atoms. (b) ADF image from the Si column shown in (a). (c) Phase vs. ADF intensity of i^{th},j^{th} pixels for the images shown in (a) and (b). (d) Fitted lines to the phase vs. ADF intensity curves obtained from Si columns containing various number of atoms from 1 atom to 23 atoms. The data presented here were simulated by µSTEM[2].

Conclusions: The reconstructed ptychographic phase is quantifiable when the sample thickness is less than few nanometers (e.g. ~3nm for Si along [001]). In this work, however, we showed that it is possible to obtain quantitative information from samples with larger thicknesses by correlating the ADF intensity with ptychographic phase. Using this technique we showed that atom columns containing up to 23 Si atoms (~12nm) can be distinguished from each other. We expect this approach to be applicable for quantitative analysis of atom columns in any other materials.

Acknowledgements: The authors acknowledge funding from the EPSRC (Grant No. EP/M010708/1) and EU Horizon 2020 Enabling Science and Technology through European Electron Microscopy (823717 ESTEEM3).

References:
[1] T. Seki, Y. Ikuhara, N. Shibata, *Ultramicroscopy* 193 (2018) 118–125.
[2] L.J. Allen, A.J. D'Alfonso, S.D. Findlay, *Ultramicroscopy* 151 (2015) 11–22.

Figure 1

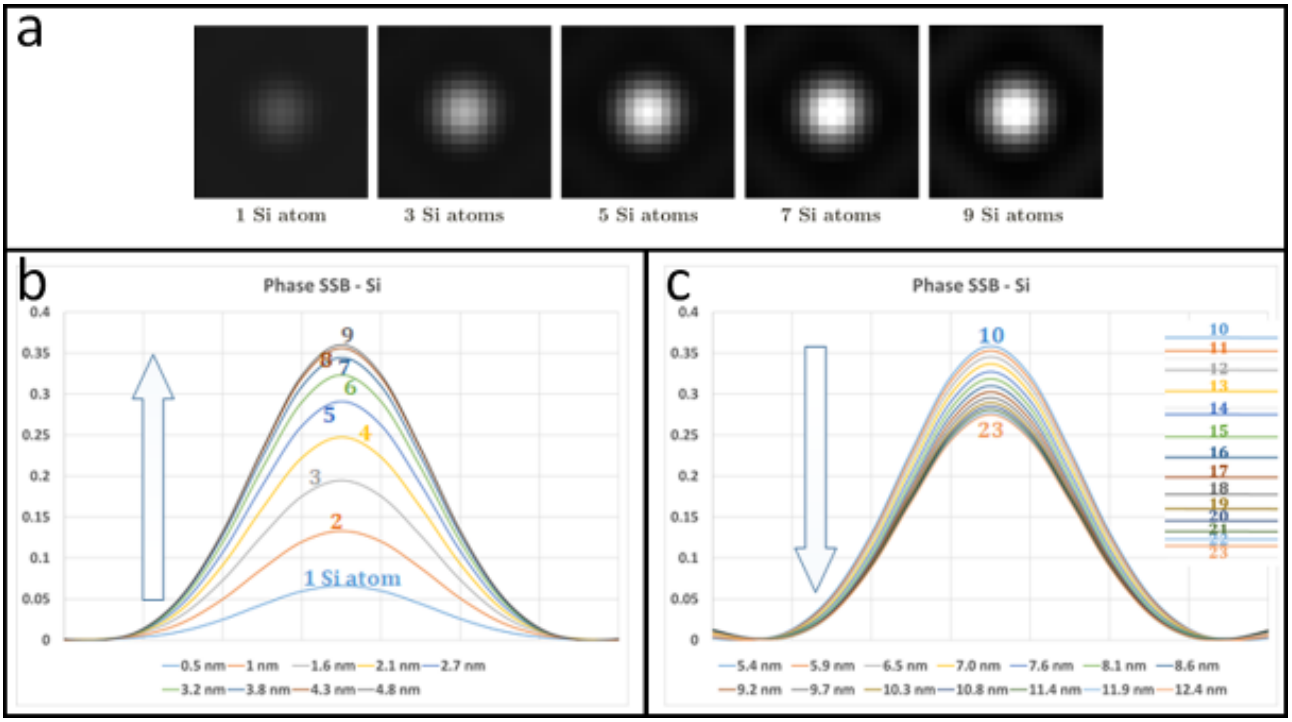

Figure 2

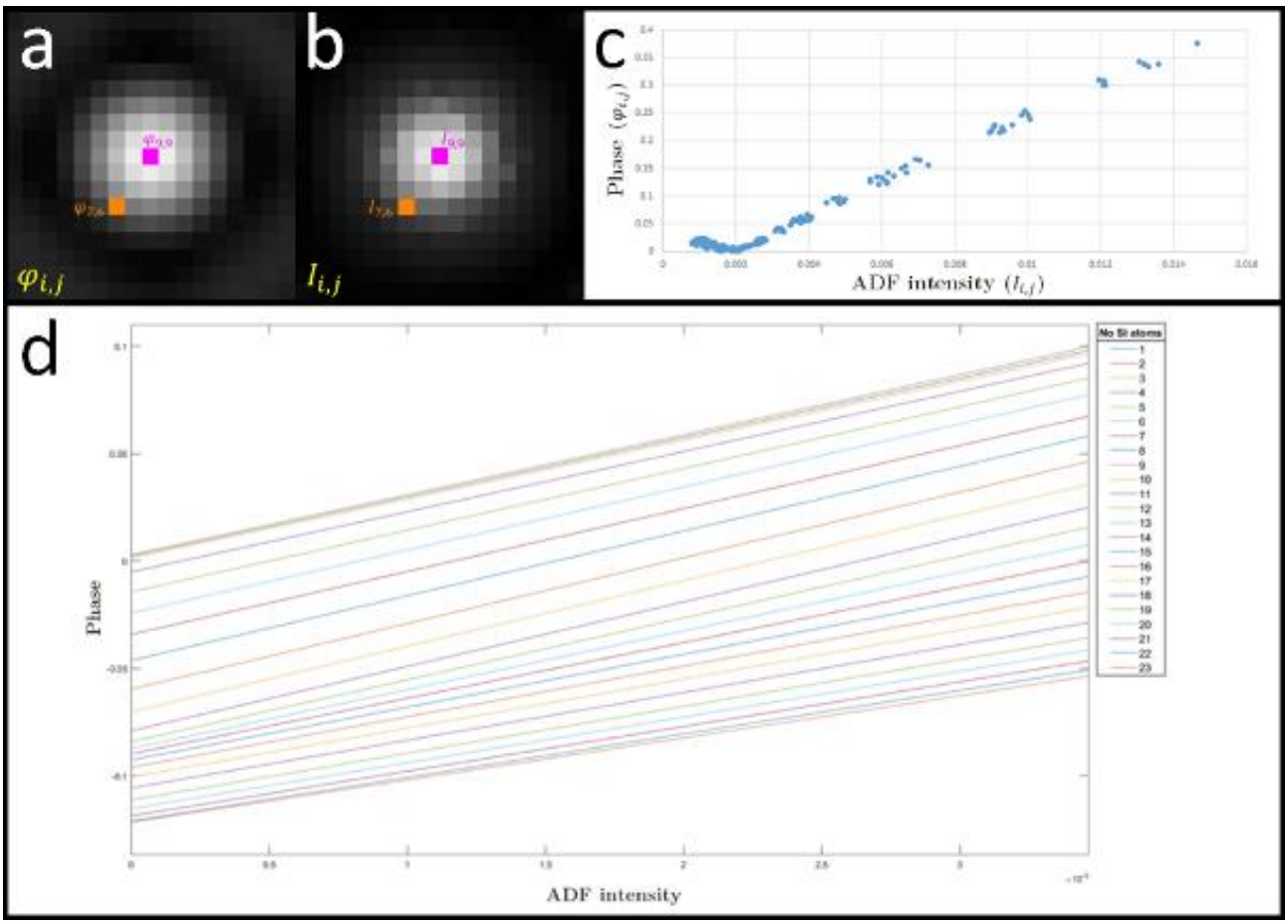

IM8.P020
Quantitative characterisation of nanometer scale electric fields via momentum-resolved STEM

A. Beyer-Leser[1], S. S. Firoozabadi[1], D. Heimes[1], T. Grieb[2], A. Rosenauer[2], K. Müller-Caspary[3,4], K. Volz[1]

[1]Philipps-University Marburg, Materials Science Centre and Department of Physics, Marburg, Germany
[2]Universität Bremen, Institut für Festkörperphysik, Bremen, Germany
[3]RWTH Aachen University, II. Institute of Physics, Aachen, Germany
[4]Research Center Jülich, Ernst Ruska-Center for Microscopy and Spectroscopy with Electrons, Jülich, Germany

Many of today´s nano-scale devices such as transistors, solar cells and batteries rely on built-in electric fields. These fields can have strengths of several MV/cm and an extension of several tens of nanometers. Moreover, parasitic fields in the same order of magnitude can lead to a device´s failure. Therefore, the visualization and quantification of such fields are highly desired.

A suitable high spatial resolution for this task is provided by scanning transmission electron microscopy (STEM). Recently, fast pixelated detectors allow for four-dimensional STEM (4DSTEM) measurements. Especially momentum-resolved STEM (MRSTEM) has been shown to be capable of measuring electric fields within a sample by mapping the shift of the center-of-mass (COM) of the diffracted intensity. This shift is directly proportional to the strength of the electric field present (Müller-Caspary et al., 2017). Up to now, MRSTEM has been applied mainly to address the fields introduced by the atomic columns of the sample atoms, which requires very thon TEM specimen (Ophus, 2019). In contrast to that, in this contribution we address longer-range fields present in actual devices. Since they are several orders of magnitude smaller than atomic electric fields, much higher TEM-sample thicknesses are required to introduce a notable shift to the COM.

As model system, we use two GaAs-based pn junctions with different, well-defined electric fields determined by the dopant concentrations on both sides of a junction. To create a TEM lamella with defined thickness steps, advanced focused ion beam (FIB) preparation was carried out in a JEOL JIB 4601 resulting in seven steps between 150 and 350 nm. Additional low energy Argon ion milling was performed in a Fischione Nanomill to reduce the presence of inactive, amorphous layers on the sample"s surface. The 4DSTEM measurements were carried out in double aberration-corrected JEOL JEM 2200FS operating at 200 kV. A pixelated pnCCD detector was used to capture a diffraction pattern at each scanning point with full-frame mode at 1000 frames per second. Complementary simulation of the 4D data was carried out using the STEMsalabim code (Oelerich et al., 2017). Home-written Matlab scripts were used for post-processing of the acquired data and retrieving the electric fields.

The key properties of the two pn junctions, such as the polarity of the junction (i.e., pn or np), the width of the depletion width, the doping levels on each side of the junctions, as well as the field strengths and the built-in voltages were derived quantitatively from the experimental data (Beyer et al., 2021). The doping levels derived are in very good agreement with supplementary, non-TEM-based methods, i.e. Hall and electrochemical capacitance-voltage (ECV) measurements.

This contribution shows how MRSTEM can be used to detect and quantify electric fields present in actual devices.

IM8.P021
Measurement of aberrations in STEM by artificial intelligence

B. Diederichs[1,2], A. Bangun[1], I. Lobato[3], S. Van Aert[3], F. Filbir[3,2], K. Müller-Caspary[1,4]

[1]Research Center Jülich, Ernst Ruska-Centre, Jülich, Germany
[2]Helmholtz Center Munich, Department of Scientific Computing, Munich, Germany
[3]Universiteit Antwerpen, EMAT, Antwerp, Belgium
[4]RWTH Aachen University, Aachen, Germany

The measurement and correction of aberrations in both conventional and scanning TEM (STEM) is a major research focus since many decades, particularly resulting in aberration-correcting hardware [1] that nowadays enables the view inside atoms. A widespread method for aberration measurement employs tilt-tableaus recorded at different foci in STEM during the experiment, whereas a posteriori methods involve ptychographic approaches [2] for thin specimen. In fact, contrast features in Ronchigrams of amorphous foils are fingerprints of aberrations. However, they are rather used for the manual correction of low orders than being employed directly in an automated manner. On the other hand, machine learning has taken over large part of image processing. With the introduction of trainable deep architectures and advances in processing power utilizing GPUs, deep neural networks are best in class in a wide range of imaging applications. It is therefore worthwhile to investigate the performance of deep learning techniques in direct aberration estimation from Ronchigrams in STEM which we report here. The capabilities of different neural network architectures to estimate aberration coefficients from one or multiple CBED images are studied. We start by recognizing defocus, 2-fold astigmatism and coma and address the question whether a single Ronchigram suffices or if larger samples are necessary. For the latter, we assume that focus can be varied by known steps in the range of 10nm. The method is developed using multislice simulations using aberrated probes interacting with an amorphous carbon foil with a realistic radial distribution function. We then train multiple CNNs for regression using architectures close to AlexNet, ResNet, and also own ones which include additional skip connections from the lower filters to the final regression layer to emphasize lower order features. As loss we use the mean absolute value, which proved more stable than mean squared loss in training. Poisson noise is accounted for in the data augmentation pipeline, meaning that during training in each epoch we reroll the Poisson noise. If only defocus is present, most networks perform well, given an average error of less than 3nm, using a single Ronchigram. However, two Ronchigrams taken 10nm apart are necessary to distinguish between over- and underfocus. To this end, we use a two-channel input for our neural network. Next, we introduced 2-fold astigmatism up to 50nm and coma up to 1000nm. The error of the defocus deteriorates to approximately 5nm. The A1 coefficient can also be estimated with an error of 5nm. We show some examples in Figure 1 (true/predicted values). Although these results yield precisions within the range of existing techniques, the CNN capability to achieve this from A SINGLE (assuming only overfocus) Ronchigram with noise is encouraging. In that respect, we plan to investigate further strategies to enhance CNN performance by using larger ensembles of Ronchigrams. The results favor the architectures with additional skip connections, but the differences are minor and could be mere coincidence. Whereas our study demonstrate the capability of CNN for aberration detection in principle, necessary optimizations to the network architecture and electron-optical settings will be discussed in order to achieve higher precisions and address higher-order aberrations.

[1] Haider et al., Nature 392, 768-769 (1998)
[2] Yang et al., Nat. Comm. 7, 12532 (2016)

Figure 1

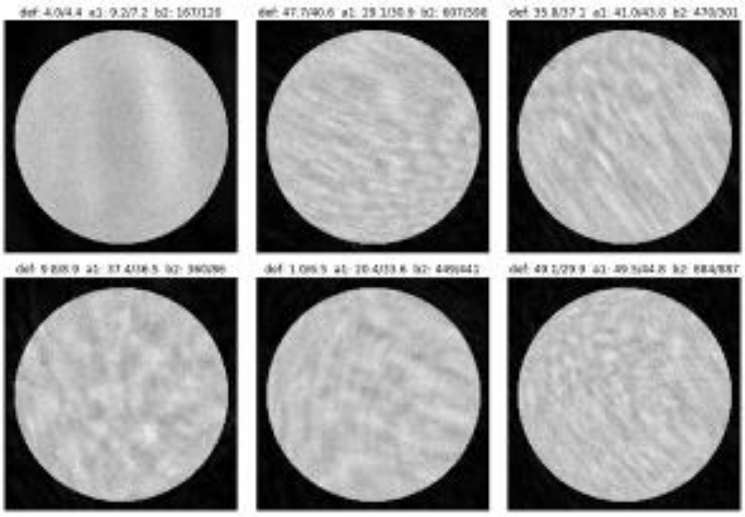

IM8.P022
Combining 4DSTEM and multislice simulations to quantify long-range electric fields

D. Heimes[1], A. Beyer-Leser[1], S. S. Firoozabadi[1], J. Belz[1], K. Volz[1]

[1]Philipps-University Marburg, Faculty of Physics and Materials Sciences Center, Marburg, Germany

Many of today"s electronic devices, e.g., solar cells, transistors, and batteries, have built-in nano-scale electric fields, whose quantitative characterization is desired. Scanning transmission electron microscopy (STEM) utilizing fast pixelated detectors (4DSTEM) facilitates measuring those fields [1, 2]. This is done by determining the diffraction pattern"s shift in center of mass (COM) which is proportional to the electric field for thin specimens [3]. The general challenge in this is that the existence of a COM shift does not automatically prove the existence of a field, because of the COM"s sensitivity to other factors. The special challenge for measuring the built-in fields in electronic devices is the COM"s strong thickness dependence combined with the occasional necessity of having specimens which are several hundreds of nanometers thick [1].

Quantifying the COM-influencing factors in order to measure built-in electric fields via 4DSTEM and predicting optimal experimental parameters is the objective of this study. To achieve this, STEM multislice simulations [4, 5] including nano-scale electric fields will be applied. This approach is well suited for the analysis of individual parameters and their isolated effect on the COM.

In a first case study, a GaAs p-n junction is investigated, at whose characteristic depletion region an electric field forms [6] (cf. Figure 1). To include the interaction of electrons with the built-in electric field, the corresponding voltage is included in the scattering potentials of the STEM multislice simulations.

Simulation series for three different cases are carried out:

- only the atomic scattering using the isolated atoms approach [5]

- only the built-in voltage as the scattering potential

- combination of both

From the simulated COM then the electric field and the electric potential are calculated.

Figure 2 depicts exemplary results for a GaAs p-n junction of 100 nm thickness for a simulation in which only the built-in voltage served as scattering potential. Shown is the electric field which was calculated from the simulated COM, together with the potential which was derived from the field via integration. The field"s shape is as expected for a p-n junction (cf. Figure 1). Also, the potential shows a good quantitative agreement with the input potential which is shown as dashed line in Figure 2.

These results reveal the capability of this method to correctly include the deflection of electrons due to the field of a p-n junction and to reproduce the input voltage for the case that atomic scattering is neglected.

Further results reveal the dependence of the measured voltage on the specimen thickness, the convergence angle, and other factors.

This study is a promising approach for improving the quantitative measurement of nano-scale electric fields via 4DSTEM and shows the necessity to carry out complex image simulation studies.

References:
[1] Beyer, A., et al., "Quantitative characterization of nanometer-scale electric fields via momentum-resolved STEM", Nano Letters (accepted 2021-02-19).
[2] Gao, W., et al., Nature 575.7783 (2019): 480-484.
[3] Müller, K., et al., Nature communications 5.1 (2014): 1-8.
[4] Oelerich, J. O., et al., Ultramicroscopy 177 (2017): 91-96.
[5] Kirkland, E. J., Advanced computing in electron microscopy. Springer Science & Business Media, 2010.
[6] Neudeck, G. W., The PN junction diode. No. 2. Addison Wesley Publishing Company, 1983.

Figure 1

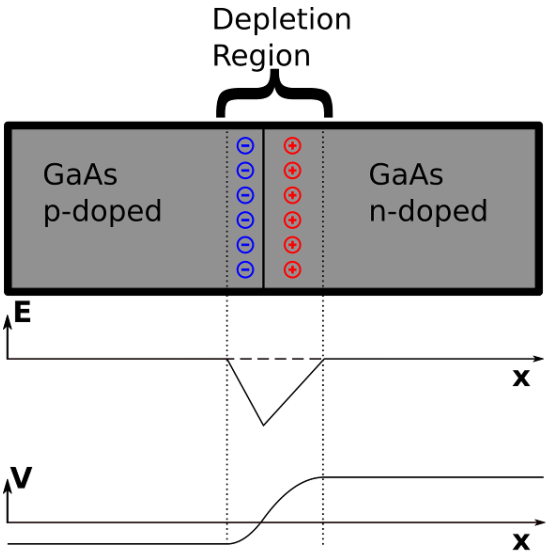

Figure 1: GaAs p-n junction at equilibrium condition with its built-in field and voltage. Shown are the conditions for the same carrier concentrations as used for the simulation shown in Figure 2.

Figure 2

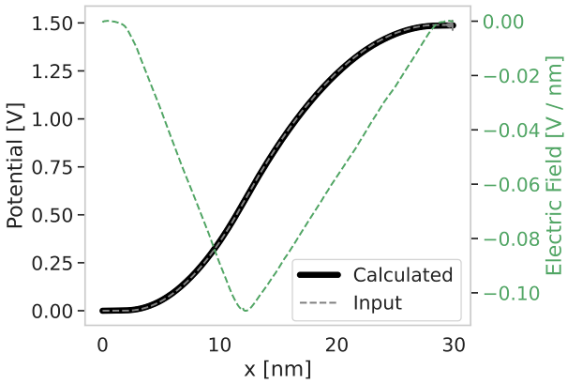

Figure 2:

The electric field which was calculated from the simulated COM, together with the potential which was derived from the field via integration.

Also shown is the input p-n junction voltage which was used as scattering potential.

IM8.P023
Low-dose 4D-STEM imaging of Li-ion battery materials to understand structural changes during cycling

E. Hedley[1], W. Song[1,2], E. Liberti[3], P. G. Bruce[1,2,4,5], P. D. Nellist[1]

[1]University of Oxford, Department of Materials, Oxford, United Kingdom
[2]The Faraday Institution, Didcot, Oxford, United Kingdom
[3]The Rosiland Franklin Institute, Didcot, Oxford, United Kingdom
[4]University of Oxford, Department of Chemistry, Oxford, United Kingdom
[5]The Henry Royce Institute, Oxford, United Kingdom

4D STEM has flourished in recent years as hardware developments in fast-pixelated detectors have caught up with the theory. This has opened up new areas of materials science to 4D STEM imaging through low dose techniques. Lithium-ion batteries are important for energy storage applications. However, performance is limited by the energy density and lifetime particularly of the cathode component [1]. The challenge for electron microscopy lies in the low electron scattering strength of the Li and O species, and the electron beam sensitivity of the materials.

This project aims to answer outstanding questions surrounding the migration of transition metals and the resulting formation of molecular oxygen in layered cathodes and to investigate emerging cathode materials such as disordered rocksalts. The high sensitivity and fast readout-speed of modern pixelated detectors means that very low dose imaging can be performed, combined with the high dose efficiency 4D STEM techniques such as ptychography this allows us to understand structural changes due to cycling at the atomic scale.

High energy density cathodes experience structural changes during cycling which degrade performance they also contain a combination of heavy transition metals and light elements. It is possible to collect ADF information simultaneously to the 4D dataset [2], for example figure 1. Ptychography allows us to locate the lighter atoms while Z-contrast can be obtained from the ADF images. It has also previously been demonstrated that ADF data can be used to abstract quantitative information [3].

Recently, in order to attempt to overcome the structural changes, significant interest has emerged in disordered rocksalt cathodes. Nanobeam electron diffraction (NBED) has been carried out on pristine LiMnO2. Fluctuation electron microscopy analysis involves investigating the variance in a 4D dataset as a function of spatial frequency. This can reveal information relating the medium range ordering, which has been shown to be related to the Li transport properties.

Initial results of our investigation into applying 4D STEM techniques to Li ion battery materials will be discussed. Combining this quantitative information from ADF with phase images allows us to understand more about the nature of the structural changes. Additionally, NBED experiments have shown promising preliminary results in understanding ordering. Advances in detector technology have allowed 4D STEM to become a viable method to image beam sensitive materials. We harness this low dose capability to understand structural changes in cathodes materials which result in performance degradation.

1. Tarascon, J. M. & Armand, M. *Nature* 414, 359–367 (2001).
2. Yang, H. *et al. Nat. Commun.* 7, 1–8 (2016).
3. De Backer, A., Martinez, G. T., Rosenauer, A. & Van Aert, S. *Ultramicroscopy* 134, 23–33 (2013).

The authors acknowledge use of characterization facilities within the David Cockayne Centre for Electron Microscopy, Department of Materials, University of Oxford and in particular the Faraday Institution (FIRG007, FIRG008), the EPSRC (EP/K040375/1 "South of England Analytical Electron Microscope") and additional instrument provision from the Henry Royce Institute (Grant reference EP/R010145/1).

Figure 1: a) Simultaneous ADF acquired alongside 4D-STEM data used to form b) synthetic dark field image by virtual imaging and c) to reconstruct the phase using the single-side band method. Images acquired on JOEL ARM200Fat 200kV using pn-ccd.

Figure 1

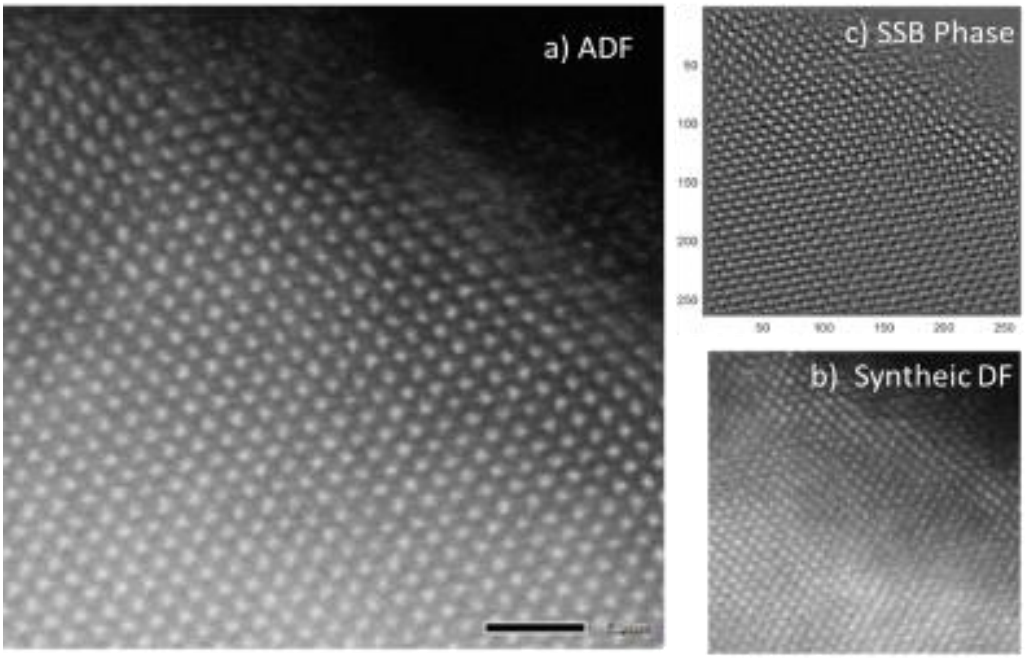

IM8.P024
Imaging of light elements in LiNiO2 using 4D-STEM

S. Ahmed[1], A. Pokle[1], J. Belz[1], M. Bianchini[2], A. Beyer-Leser[1], J. Janek[3], K. Volz[1]

[1]Structure and Technology Research Laboratory (STRL), University of Marburg, Physics, Marburg, Germany
[2]BASF, Ludwigshafen, Germany
[3]Institute of Physical Chemistry, Justus-Liebig-Universität Giessen, Giessen, Germany

Atomic-level understanding is the key to understand the degradation mechanisms in energy storage materials. Cathode-active materials (CAM), specifically layered Nickel, Cobalt, and Manganese (NCM) containing CAMs, are of supreme importance when it comes to either conventional or all-solid-state Lithium-ion batteries (LIBs). Significant challenges lie in imaging light elements like Li and O, especially when such elements are present in the vicinity of heavier elements like Ni, Mn, and Co. Furthermore, the industrial-grade CAMs come in the form of secondary particles containing densely packed primary particles. First, it is difficult to thin down the sample considerably, and secondly, it is not every time possible to find desired zone axes conditions. Electron microscopy (EM) based techniques like TEM focus-series reconstruction[1] and four-dimensional (4D) STEM ptychography,[2] have strict sample thickness requirements and are computationally exhausting. Image simulations have shown that ABF (bright annular field) imaging in STEM can image Li in different compounds.[3] We showed that –ABF, with an inner detector angle of 8 mrad and outer detector angle of 16 mrad, it is possible to image Li-ions in [100] zone axis at 200 kV acceleration voltage using 15.07 mrad convergence semi-angle (α).[4] We further showed that contrast from light elements could be enhanced by subtracting bright-field (BF) image from the ABF image.[4,5] The [210] zone axis is the next most prominent zone axis after the [100] zone axis in the layered NCM CAMs. However, it is impossible to image all elements simultaneously in this zones axis with ABF by a conventional selection of inner and outer detector angles of α/2 and α, respectively. It is because of a considerable increase in the atomic columns' interatomic distances and a significant reduction of spatial atomic distances in the STEM image plane.

We did STEM contrast simulations for LiNiO2 in [210] zone axis up to 50 nm specimen thickness at 200 kV acceleration voltage and having α from 9 mrad to 30 mrad. Our simulations suggest the optimum α value that gives good contrast and adequate resolution in the ABF regime. Decreasing α from the optimum value decreases the resolution whereas increasing the value improves the resolution at the expense of contrast from all elements. The optimum inner and outer detector angles required to achieve the best contrast from light elements in the ABF regime are also found. Finally, a TEM sample has been prepared using a focused ion beam and low energy ion milling from a realistic LiNiO2 secondary particle, and 4D data sets have been taken using a pixelated (pnCCD) detector while applying the optimum parameters (suggested by the simulations). We experimentally show that it is possible to simultaneously image all elements in the [210] zone axis by optimizing the ABF image parameters. We achieved further contrast enhancement from Li- and O-ions by subtracting the BF image from the optimized ABF image to make the *optimized* eABF image. We believe that this method can be successfully applied to other materials systems that contain elements of different atomic numbers in the close vicinity.

References:
[1] Y. Shao-Horn et al., *Nat. Mater.* **2003**, *2*, 464.
[2] J. G. Lozano et al., *Nano Lett.* 2018.
[3] S. D. Findlay et al., *Ultramicroscopy* 2011, *111*, 1144.
[4] S. Ahmed et al., *Adv. Energy Mater.* 2020, *10*, 2001026.
[5] S. D. Findlay et al., *Ultramicroscopy* 2014, *136*, 31.

IM8.P025
Comparison of phase retrieval algorithms applied to electron ptychography

B. März[1], A. Bangun[1], O. Melnyk[2], A. Clausen[1], D. Weber[1], R. E. Dunin-Borkowski[1], F. Frank[2], K. Müller-Caspary[1,3]

[1]Ernst Ruska-Centre for Microscopy and Spectroscopy with Electrons, Jülich, Germany
[2]Helmholtz Center Munich, Mathematical Imaging and Data Analysis, Munich, Germany
[3]RWTH Aachen University, Aachen, Germany

One of the limitations in established scanning transmission electron microscopy (STEM) is that the integrated signals recorded on conventional dark- or bright field detectors do not allow for the recovery of the phase of the object transmission function. Nowadays, the availability of 4D STEM data that combine real- and diffraction space information at high samplings and resolutions in both spaces, allows for the application of numerous phase-retrieval techniques.

Ptychography addresses the phase problem by overlapping the probe's illuminations and relying on reconstruction algorithms to obtain the complex object transfer function [1]. Recent years have seen an increase in research efforts to establish reconstruction algorithms, beginning from the classical alternating projection methods such as Gerchberg-Saxton (GS) [2], Difference Map [3] and ePIE [4], to a direct method such as Wigner Distribution Deconvolution (WDD) [5], and eventually in the area of optimization theory, which is called the Amplitude Flow (AF) [6]. Despite the vast development of phase retrieval algorithms, it is still unclear whether those algorithms can be adapted for arbitrary specimen thicknesses, or if the reconstructions obtained with different algorithms are consistent with each other and whether they differ in terms of, e.g., their robustness against noise, starting conditions, sensitivity to being trapped in local minima or dynamical scattering.

In this work, we evaluate those algorithms using the data generated by a multi-slice method. We also modify those algorithms to estimate both the object (specimen) and the illumination (electron probe). Figure 1 demonstrates the reconstruction of the object"s phase, where (a-c) is the reconstruction of the alternating projection method, i.e., GS, ePIE, DM, (d) AF, (e) WDD, and the ground truth (f). With a random initialization, the convergence is achieved after 100 iterations for 4-layer WSe2 with a thickness of 2.2781 nm. For all numerical simulations, the Airy function is used as the initial probe and is updated by utilizing the reconstruction from the object and the convergence is observed at 100 iterations, as depicted in Figure 2.

Figure 1: Reconstruction of the object"s phase from different algorithms

Figure 2: Reconstruction of the probe"s amplitude from different algorithms

Acknowledgement: Funding: Helmholtz IVF under contracts VH-NG 1317 (moreSTEM)
and ZT-I-0025 (Ptychography 4.0)

[1] R. Hegerl, W. Hoppe. Phys. Chem. 74(11), 1148–1154 (1970)
[2] R.W. Gerchberg, W. Saxton, Optik 34(3), 275 (1971)
[3] V. Elser: Phase retrieval by iterated projections, J. Opt. Soc. Am. A 20, 40 (2003)
[4] A.M. Maiden, J.M. Rodenburg, Ultramicroscopy 109(10), 1256–1262 (2009)
[5] J. Rodenburg, R. Bates, Philos. Trans. R. Soc. A 339(1655), 521–553 (1992)
[6] Gang Wang; Georgios B. Giannakis; Yonina C. Eldar, IEEE Trans. IT (Vol: 64,.2018)

Figure 1

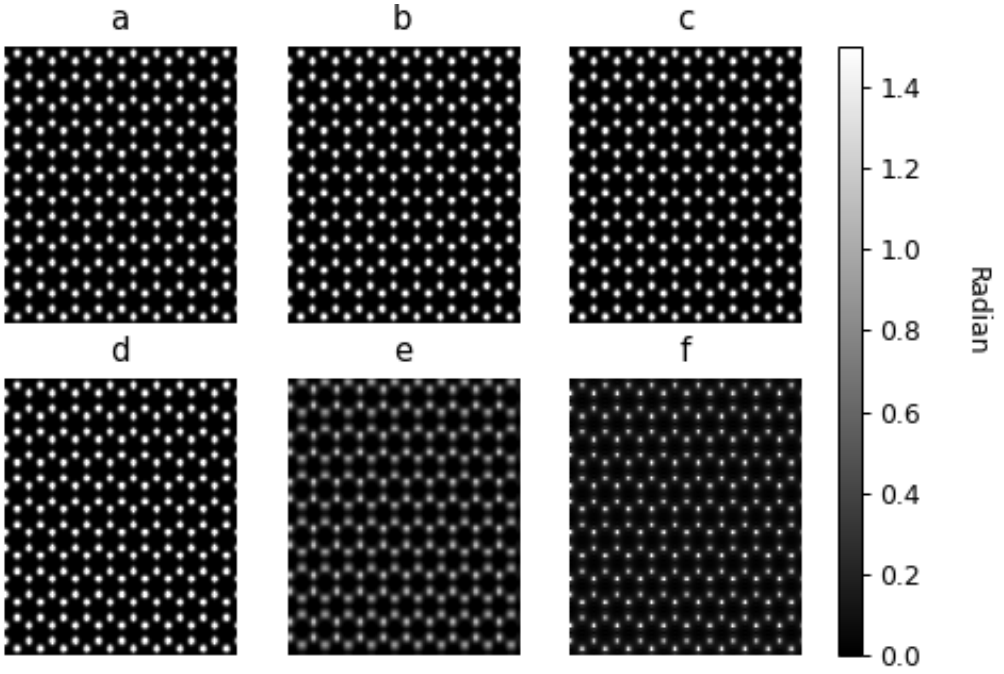

Figure 2

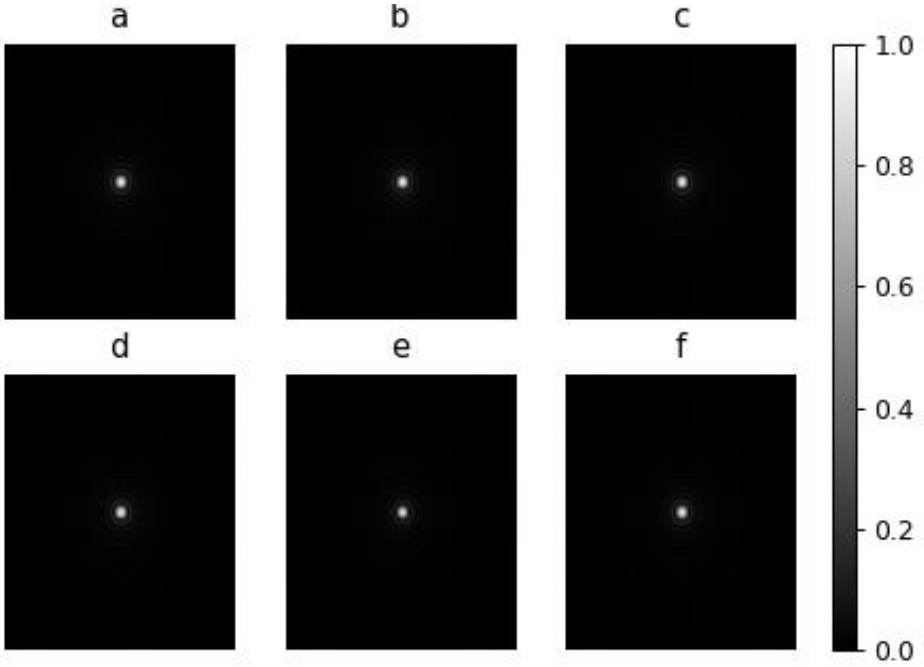

IM8.P026
On software tools which assist electron microscopists with sharing metadata and numerical results in accordance with the FAIR data stewardship principles

M. Kühbach[1,2], S. Shabih[2], A. Vaid[1], C. T. Koch[2]

[1]Fritz Haber Institute of the Max Planck Society, The NOMAD Laboratory, Berlin, Germany
[2]Humboldt University of Berlin, Institut für Physik & IRIS Adlershof, Berlin, Germany

Microscopy experiments and associated computational and theoretical analyses of microscopy data are the resources of laboratory and data-processing workflows that yield numerical data and contextualization through metadata. The purpose of microscopy experiments is ideally accurate and precise delivery of quantitative evidence in support of or against a formulated set of research hypotheses.

A large variety of hardware and software tools is routinely used by microscopists in the life and the material science communities. Faced in addition with individually larger and faster acquirable data, makes a comprehensive documentation of data and numerical processing steps with contextualizing metadata a challenging task. These challenges have consequences for how findable, accessible, interoperable, and how reproducible microscopy research is at present; and thus how efficiently such data can be exchanged between microscopists. Termed under the acronym FAIR and the associated data stewardship principles [1], the processes of measuring, collecting, managing, and sharing of electron microscopy experiments requires to take action [2, 3].

Software tools can support the microscopists with further automating of research data management tasks and can help with distilling a completely documented representation of an experiment. Tools for performing particular data analyses exist but are at best incomplete when it comes to how these document metadata in an open and organized manner. Sharing of image processing and artificial intelligence methods as well as the data itself has proven significant promise for scientific progress [4].

With this motivation, we will report the status of our efforts on the development of software tools for the building of a research data infrastructure to assist microscopists with measuring, collecting, managing and sharing their metadata in a FAIR-ready manner. We will report specific examples of how the tools enable to collect metadata in use cases from scanning and transmission electron microscopy experiments. Specifically, we will detail how we implemented the idea of using a common metadata schema, which is community-specific yet particular-method-agnostic. We report on the role and value of parsers as tools within automated protocols for filling in the metadata schema. Furthermore, we will detail how an electronic lab notebook solution, like eLabFTW [5], can be equipped with tools to assist users with automating the metadata collection process.

Our results support that it is possible to find a common schema to store detailed microscopy (meta)data for making such data not only supplementary material but repurposable resources to be placed in an open research database [2]. We expect that collecting FAIR-ready microscopy data has the potential to substantially support the development and the verification of improved data analyses or artificial intelligence methods for the microscopy community.

References:
[1] M. D. Wilkinson et al. In: Sci. Data 3 (2016). DOI: 10.1038/sdata.2016.18.
[2] C. Draxl and M. Scheffler. In: Handbook of Materials Modeling. Ed. by S. Yip and W. Andreoni. Springer, Cham, 2020. DOI: 10.1007/978-3-319-42913-7.
[3] J. Bonevich et al. Tech. rep. Natl. Inst. Stand. Technol. Spec. Publ. 1217. 2017. DOI: 10.6028/NIST.SP.1217.
[4] EMBL-EBI. (Accessed March 05, 2021). URL: https://www.ebi.ac.uk/pdbe/emdb.
[5] N. Carpi et al. In: J. Open Source Softw (2017). DOI: 10.21105/joss.00146.

IM8.P028
Application of stela hybrid pixel electron detector for 4D STEM characterisation of 2D materials at low energies

A. Pakzad[1], R. Dos Reis[2]

[1]Gatan Inc., Pleasanton, CA, United States
[2]Northwestern University, Evanston, United States

Two-dimensional (2D) materials are an emerging class of materials that have generated great interest in the fields of fundamental research and device applications in the recent years. The most familiar example is graphene, which is a sheet of single layer of carbon atoms, but some other 2D structures such as isolating hexagonal BN_2 and semiconducting MoS_2 have also been intensively studied in the past decade, and new structures continue to be discovered.

Small dimension of 2D materials makes an electron microscope and specifically scanning transmission electron microscopy (STEM) a valuable tool for their characterization, but this comes with its challenges. During a STEM experiment, performed at common accelerating voltages (80 to 300 kV), electron energy absorbed by thin 2D specimens results in unwanted changes in the material properties [1]. This is known as electron irradiation damage, and in the case of 2D materials is mainly found to be knock-on damage, where an atom is ejected from its lattice site forming a lattice vacancy. This kind of damage can be minimized and, in many cases, eliminated if the primary electron energy is reduced to below 80 kV [2].

Operating the STEM at <80 kV requires an electron detector designed for low energies. Additionally, STEM spatial resolution is reduced as the electron energy is reduced to prevent radiation damage. Use of highly stable geometrical aberration correctors in combination with a monochromatic electron beam helps in this case, but in turn limits the electron dose available, dictating both a dose efficient STEM method, and an electron counting detector.

To address these issues, here we have used Gatan's Stela detector and four-dimensional (4D) STEM ptychography to characterize several types of 2D structures at <80 kV. Stela is a hybrid pixel electron detector designed for low-energy (<80 kV) and high-speed (>16000 fps) diffraction applications, and is fully integrated in Gatan's Digital Micrograph software. We applied STEM-ptychography, a dose efficient phase retrieval method, to process 4D STEM datasets and reconstruct the object function using the entire bright field region of the diffraction pattern. Ptychography shows a superior performance for extremely low electron doses in comparison to traditional STEM image modalities (ADF, ABF).

[1] Egerton, R. F. Control of Radiation Damage in the TEM. Ultramicroscopy 127 (2013): 100.
[2] Komsa, H.-P., et al. Two-Dimensional Transition Metal Dichalcogenides under Electron Irradiation: Defect Production and Doping. Phys. Rev. Lett. 109 (3) (2021): 035503.
[3] RdR acknowledges the support of the EPIC facility of Northwestern University"s NUANCE Center, which has received support from the SHyNE Resource (NSF ECCS-2025633), the IIN, and Northwestern's MRSEC program (NSF DMR-1720139). This research was supported in part through the computational resources and staff contributions provided for the Quest high performance computing facility at Northwestern University which is jointly supported by the Office of the Provost, the Office for Research, and Northwestern University Information Technology.

IM8.P029
Structure-aware multi-view 3D reconstruction of dislocations in TEM with message passing neural networks

O. Altingövde[1], A. Mishchuk[2], G. Ganeeva[3], E. Oveisi[4], C. Hébert[3], P. Fua[1]

[1]Swiss Federal Institute of Technology Lausanne (EPFL), CVLAB, Lausanne, Switzerland
[2]Swiss Federal Institute of Technology Lausanne (EPFL), CVLAB, LSME, Lausanne, Switzerland
[3]Swiss Federal Institute of Technology Lausanne (EPFL), LSME, Lausanne, Switzerland
[4]Swiss Federal Institute of Technology Lausanne (EPFL), CIME, Lausanne, Switzerland

Efficient analysis of the three-dimensional (3D) shape and distribution of curvilinear crystal defects, namely dislocations, is an open research topic in material science and computer vision. In order to determine the structural and opto-electrical characteristics of the material, accurate 3D reconstructions of dislocations are required. In its current state, an established way to obtain 3D information of dislocations is electron tomography which relies on acquiring dozens of images from tilted sample for wide range of angles. Although tomography yields sufficient results in many cases, it is manually demanding to acquire, register and process dozens of images. In previous works [1, 2], it is shown that a classical stereo reconstruction approach may be applied as an alternative in order to increase reconstruction throughput while providing good performance. A later work [3] employing modern data-driven computer vision models showed that this stereo approach can be largely automatized and be used in various imaging conditions.

In this work, we further improve the performance and memory consumption of previous convolutional neural network (CNN) based stereo reconstruction approach and extend it to be applicable in cases where more than two images are available. Our proposed multi-view approach directly incorporates the structural prior of dislocations to the model"s architecture and estimates 3D line segments approximating 3D shape of dislocations.

In its core, our method has two stages which are structural connectivity estimation and depth estimation. In first stage, we employ a CNN to estimate affinity of sampled image locations on dislocation cores. This affinity information is used in the later depth estimation stage to eliminate the depth discontinuities on dislocations (Figure1). Unlike previous deep data-driven method, our new approach uses structural knowledge to separate depth estimations of different dislocation segments and yields more accurate reconstructions. In Figure 2, an example affinity estimation is shown for 4 different image locations on the same dislocation. It may be seen that dislocation points that are connected by dislocation segment in 3D results in higher affinity. This information is crucial to connect 3D point estimations and obtain linear structures in 3D.

Figure1: (a) Stereo-pair of bright-field STEM images, (b) sampled image locations and estimated connectivity i.e affinity between image locations, (c) and final 3D reconstruction estimation.

Figure2: (a) Sampled locations are shown on bright-field STEM image, (b) pixel value changes on search axis on the second image with respect to depth for each location (c) estimated connectivity information of sampled locations from the profiles on the search axis. Bright colors represent higher affinity between image locations hence stronger connection.

[1] E. Oveisi, A. Letouzey, D. Alexander, Q. Jeangros, R. Schaublin, G. Lucas, P. Fua, C. Hebert, Tilt-Less 3D Electron Imaging and Reconstruction of Complex Curvilinear Structures, Nature Scientific Reports 7.
[2] E. Oveisi, A. Letouzey, S. D. Zanet, G. Lucas., M. Antoni, P. Fua, C. Hebert, Stereo-Vision Three-Dimensional Reconstruction of Curvilinear Structures Imaged with a TEM, Ultramicroscopy (2018).
[3] O. Altingovde, A. Mishchuk, G. Ganeeva, E. Oveisi, C. Herbert, P. Fua, 3D Reconstruction of Curvilinear Structures with Stereo Matching Deep Convolutional Neural Networks, Ultramicroscopy, (In peer review).

Figure 1

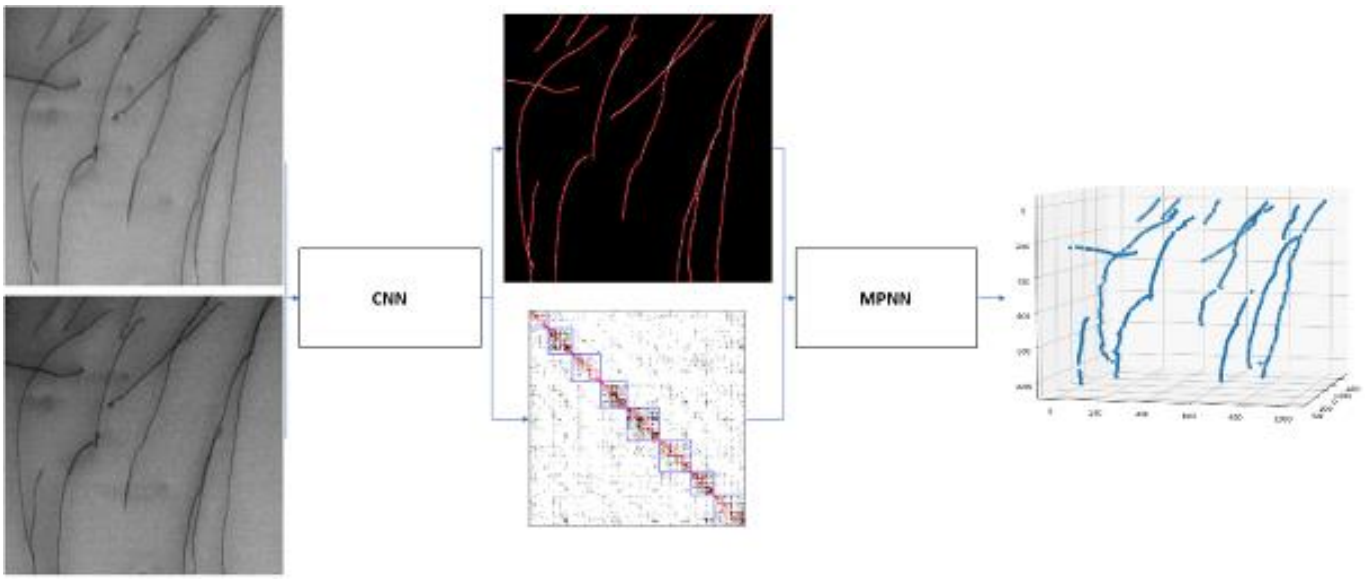

Figure 2

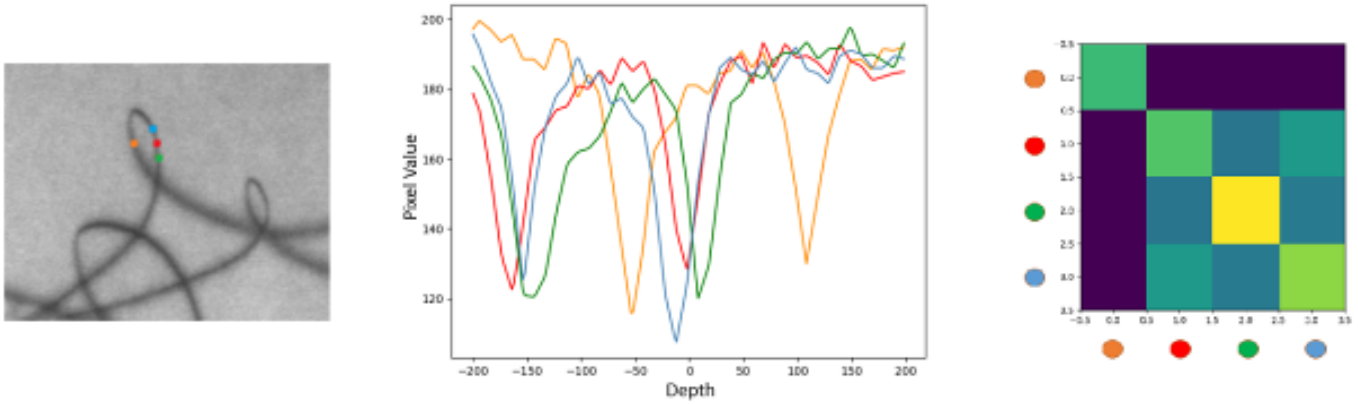

IM8.P030
Ab initio description of bonding for transmission electron microscopy

J. Madsen[1], T. Susi[1]

[1]University of Vienna, Faculty of Physics, Vienna, Austria

Transmission electron microscopy (TEM) is one of the most versatile and powerful experimental tools for the imaging and diffraction of materials at the atomic scale. In TEM, the sample structure is encoded in the scattering of the electron waves by the specimen electrostatic potential. This potential includes the contribution of the screened nuclear cores and the valence electron density, and since valence electrons are responsible for all chemistry, studying them is of significant scientific interest [1].

The modern electron microscope could be an ideal tool for the high-resolution imaging of charge redistribution caused by chemical bonding. However, these measurements are a challenge because only a tiny fraction of the total electrons in a material participate in bonding and because the dense cores dominate the scattering signal. As improvements in instrumentation and techniques continue rapidly, this is changing, as evidenced by the surging popularity of techniques such as four-dimensional scanning transmission electron microscopy (4D-STEM) combined with ptychography in materials science and cryogenic microcrystal electron diffraction in structural biology [2, 3].

The simulation of TEM images or diffraction patterns is often required to interpret their contrast and extract specimen features [1]. The scattering potential used in simulations is typically described by the independent atom model [4]. This approximation is fast and relatively accurate, especially for scanning TEM (STEM) annular dark-field contrast, but it completely neglects valence bonding.

In the first part of this presentation, we review recent advances in electron microscopy, arguing that charge transfer effects are measurable and a key to a deeper understanding of materials [5-7]. In the second part, we introduce a new software tool for simulating electron scattering from first-principles that does not neglect valence bonding.

Our code, abTEM, was created to make it easy to integrate accurate simulations of materials with image simulations [8]. Additionally, abTEM is written purely in Python and designed for easy modification and extension, allowing domain experts to extend abTEM to meet their specific needs.

[1] Madsen J, Pennycook TJ, Susi T, Ultramicroscopy, 113253 (2021)
[2] Lazíc I, Bosch EGT, Lazar S, Ultramicroscopy 160, 265– 280 (2016)
[3] Nannenga BL, Gonen T, Nat Methods 16, 369–379 (2019)
[4] Kirkland EJ, Advanced Computing in Electron Microscopy, Springer US, 2nd ed. (2010)
[5] Meyer JC, Kurasch S, Park HJ, Skakalova V, Künzel D, Groß A, Chuvilin A, Algara-Siller G, Roth S, Iwasaki T, Starke U, Smet JH, Kaiser U, Nature Mater 10, 209–215 (2011)
[6] Winkler F, Barthel J, Tavabi AH, Borghardt S, Kardynal BE, Dunin Borkowski RE, Phys. Rev. Lett. 120, 156101 (2018)
[7] Susi T, Madsen J, Ludacka U, Mortensen JJ, Timothy TJ, Lee Z, Kotakoski J, Kaiser U, Meyer JC, Ultramicroscopy 197, 16–22 (2019)
[8] Madsen J and Susi T, Open Res Europe, 1:24 (2021)

IM8.P031
Sub 50nm Transmission Kikuchi Diffraction (TKD) of a TiAlNb TEM lamella using a modern Schottky FE-SEM and EBSD system

R. Schmidt[1], D. Zimmer[2], H. Gabrisch[3]

[1]Hitachi High-Tech Europe GmbH, Nano-Technology Solution Business, Krefeld, Germany
[2]Oxford Instruments GmbH NanoAnalysis, Wiesbaden, Germany
[3]Helmholtz-Zentrum Geesthacht, Metal Physics / Institute of Materials Research, Geesthacht, Germany

Introduction: The determination of unknown phases and their orientation in crystalline materials can be quite time consuming in a conventional Transmission Electron Microscope (TEM). First an EDX mapping must be acquired, then the diffraction pattern of representative grains must be found and evaluated manually or by a software support.

Objective: In this presentation a standard TEM lamella was used in a High Resolution Field Emission SEM (Hitachi SU7000) to record simultaneously the EDX and EBSD mappings in Transmission mode (TKD) from a TiAlNb alloy. Thus the advantage of a better spatial resolution through a minimized interaction volume by the thin lamella and the speedy access to the profound diffraction library of the EBSD system were combined.

Materials & method: The material, a Ti-42Al-8.5Nb (in at.-%) alloy, was prepared by hot-isostatic pressing of pre-alloyed powder under 200Pa at 1250°C. It was prepared conventionally to a 3mm disc, followed by electropolishing with a solution of perchloric acid in methanol and buthanol at -39°C. The method of Transmission Kikuchi Diffraction in the SEM is shortly explained and compared with other diffraction based methods in the SEM, Electron Channeling Contrast Imaging (ECCI) and Electron Channeling Patterning (ECP). The novel concept of the SU7000 is given by the feature that all 6 SEM signals, the Upper SE, the Lower SE, the BSE(Compo), the BSE(Topo), the Middle detector and the CL detector, plus EDX and the EBSD patterns can be recorded at a working distance of 6mm (Figure 1). This allows to use the SEM for High Resolution imaging with in-lens SE at 30kV and at the same time for High Resolution EDX and EBSD, whereas the forward scattered detectors of the EBSD camera act as a kind of "partial" annular dark field (ADF) detector. A high speed EBSD camera (Oxford symmetry, generation1) with a top acquisition speed of 3000 patterns per second and a commercial TKD sample holder were used in the measurements.

Results: The Ti-42Al-8.5Nb-TEM lamella was imaged with the SEM signals, where surface information, such as contamination, were visualized using the Upper SE detector, while the lamella structure of the alloy with less than 44nm lamella spacings was clearly visible in the BSE signal (Figure 2). A 30min simultaneously recorded EDX/EBSD mapping in TKD mode outlines the distribution of a γ-phase with a $L1_0$ structure, space group P 4/m mm, and a hexagonal α_2 phase, space group P 6_3/m m, with a sub 50nm resolution (Figure3).

Conclusion: The combination of an Ultra High Resolution Schottky FE-SEM with modern, high speed EBSD systems can be used for a quick phase analysis of crystals. Even if the sample is prepared for diffraction analysis in the TEM, it may be possible to use it straightforward in the SEM and achieve a lateral EDX/EBSD resolution of less than 50nm.

Figure 1

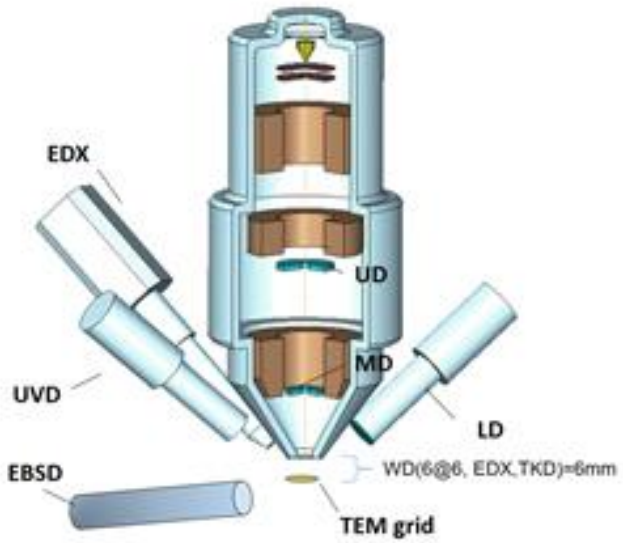

Figure 2

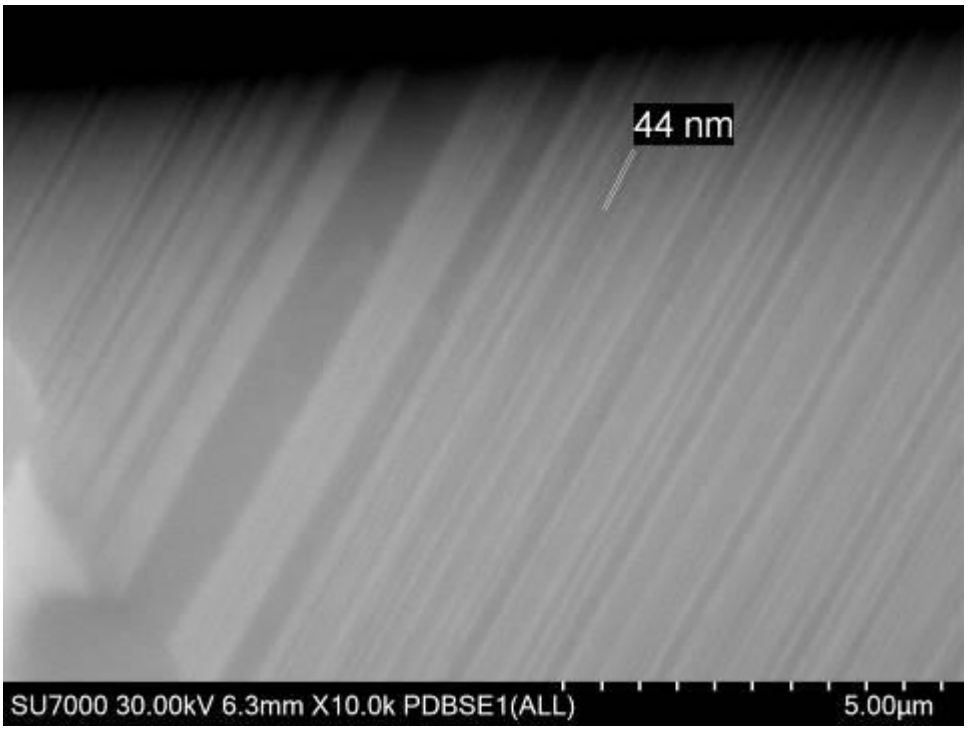

Figure 3

IM8.P032
STEM-PDF – Open source software for STEM pair distribution function mapping

S. Kang[1], L. Chen[1], D. Wang[1,2], X. Mu[1], C. Kübel[1,2,3]

[1]Karlsruhe Institute of Technology (KIT), Institute of Nanotechnology (INT), Eggenstein-Leopoldshafen, Germany
[2]Karlsruhe Nano Micro Facility (KNMF), Eggenstein-Leopoldshafen, Germany
[3]Technical University of Darmstadt, Joint Research Laboratory Nanomaterials, Darmstadt, Germany

Four Dimensional-Scanning Transmission Electron Microscope (4D-STEM) is a powerful tool to investigate the nanostructure of complex materials. By combining Pair Distribution Function (PDF) analysis with 4D-STEM as illustrated in figure 1, STEM PDF enables local structure analysis and phase mapping for nanocomposite materials containing amorphous phases [1]. The power of this technique to answer structural questions has been demonstrated, e.g. analyzing the bond changes during cycling of batteries [2], the structure of metallic nanoglasses [3] and phase distribution of heterojunction organic solar cell [4]. However, 4D-STEM datasets are usually big and in high dimensions; dealing with the data demands high-level programming skills and a deep understanding of optics. Here, we developed STEM-PDF; an open-source software written in Python, providing easy access to process the STEM PDF data.

In this presentation, we introduce examples of STEM PDF analysis with our software; (1) amorphous NiNb and *(2)* amorphous Cu50Zr50/nanocrystalline Cu multilayer. We observed the intrinsic heterogeneous nature of the amorphous alloys and local structure change with shear banding on a nanometer scale. As shown in figure 2, the software performs PDF calculation for both single and batch processing of electron diffraction array acquired in 4D-STEM, as well as, a tool for calculating the PDFs from a given structure model. We believe this software will benefit the material research communities, improving the capability of local structural analysis of amorphous nanophases.

Keywords: 4D-STEM, Spatially Resolved-Pair Distribution Function (SR-PDF), Amorphous materials

[1] X. Mu, *Ultramicroscopy* 168 (2016) 1-6.
[2] Z. Li et al., Nat. Commun. 9 (2018) 5115.
[3] Y. Ivanisenko et al., Adv. Eng. Mater. 1800404 (2018) 1–16.
[4] X. Mu et al., Microscopy. 68 (2019) 301–309.

Figure 1: (a) Configuration of 4D SED experimental set up. (b) STEM PDF data acquisition and processing and (c) an example of structural map and local structure analysis.

Figure 2: Demonstration of the STEM PDF software. (a) The 4D SED data viewer. (b) PDF processing panel where the diffraction data is picked up from the 4D SED data viewer. (c) The PDF data cube viewer. (d) The simulation panel for simulate PDF according to a given structure.

Figure 1

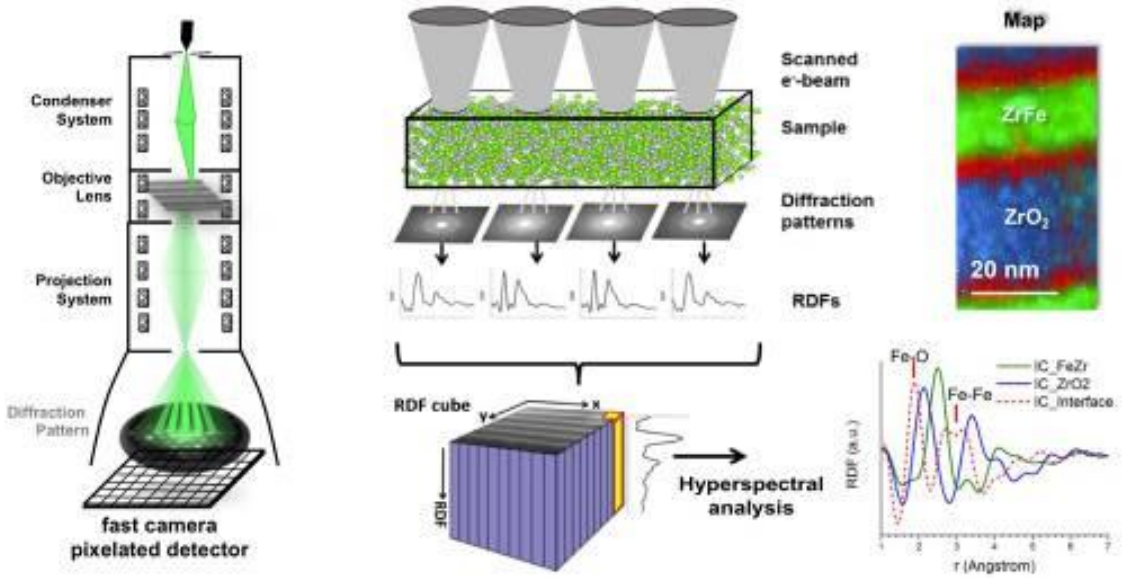

Figure 2

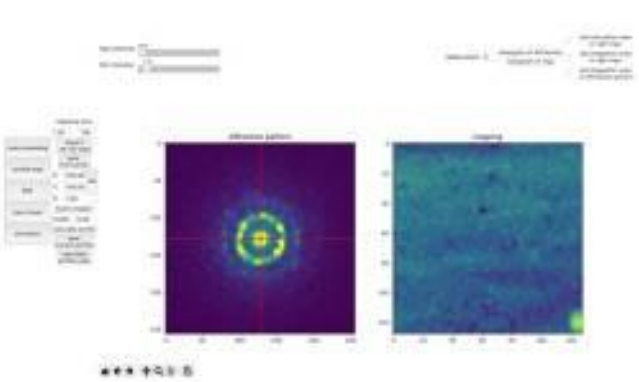

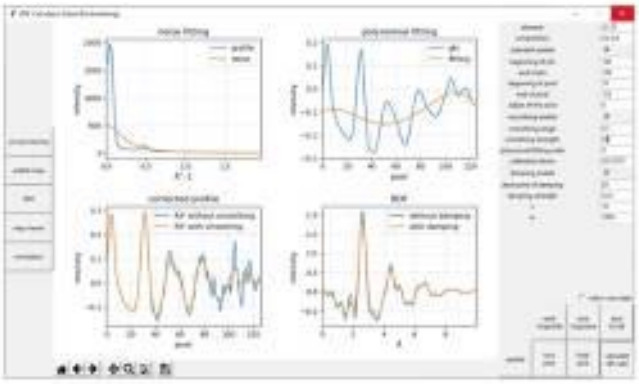

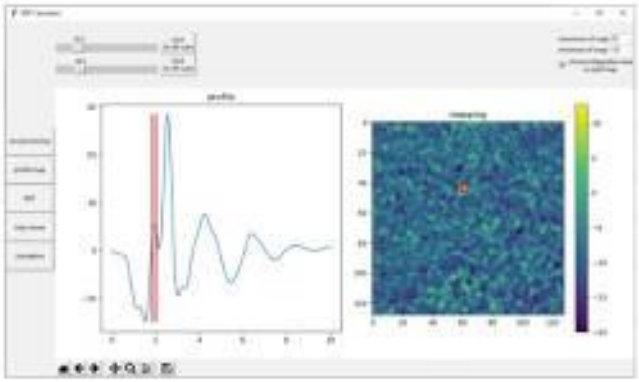

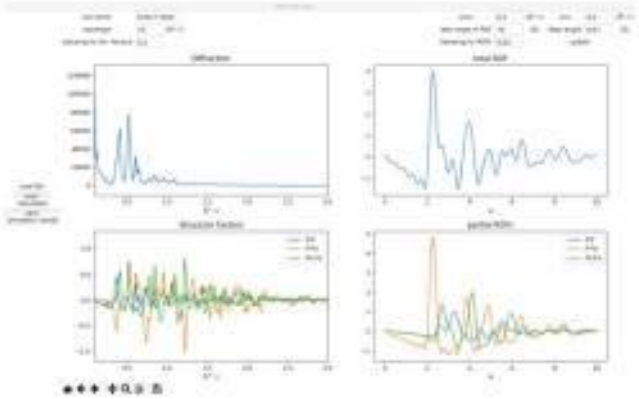

IM8.P033
Improvements towards the inclusion of magnetic effects in large-scale multislice calculations of elastic electron scattering

K. Lyon[1], J. Rusz[1]

[1]Uppsala University, Department of Physics and Astronomy, Uppsala, Sweden

Question: At the theoretical heart of many TEM approaches, including electron holography and Lorentz microscopy, lies the multislice method [1], which simulates the propagation of the incident electron wavefunction through a crystal. While this method is well-established in the literature, the inclusion of magnetic effects poses novel challenges to both the efficiency and implementation of the multislice method for larger systems. This abstract presents our recent efforts to face these challenges.

Methods: First, by working with the paraxial Pauli equation where the non-periodic magnetic vector potential plays a role [2], the 2D Fourier transform utilized in conventional multislice calculations to speed things up considerably can no longer be applied as before [1]. We introduce a formulation for the real space magnetic multislice that takes advantage of this speedup by including non-periodic magnetic contributions perturbatively. Second, as magnetic multislice calculations over large crystals require knowledge of the full magnetic fields with an accuracy near the level afforded by DFT calculations [2], we formulate a parameterization of magnetic fields analogous to electron form factors for a variety of magnetic elements, allowing for the quick calculation of magnetic fields at any point in a crystal system.

We make use of the Pauli multislice framework presented in [2]. For the calculation of magnetic fields, DFT calculations are done in GPAW, from which the spin density can be used via the Poisson equation to obtain the magnetic field and vector potential [2]. DFT calculations are done for individual atoms with magnetic moments, and the magnetic fields and vector potentials are fit to quasi-dipole like expressions that satisfy symmetry relations and physical constraints on the field components over all space while avoiding the divergent behaviour near atom centres expected from a simplistic dipole approximation.

Results: While real space multislice methods require an iterative procedure until a certain convergence criterion is reached that often requires up to ten iterations, our perturbative Pauli multislice implementation can be run without the use of any such iterative procedure, much like the conventional multislice.

The parameterization of magnetic fields via our quasi-dipole approach can be accomplished with as few as nine parameters across many magnetic atoms yielding fits with extremely low errors. These parameterized magnetic fields from atomic systems can then be summed together for multiatomic systems. One such example of A_x on an 84Å × 84Å slice of bcc Fe model generated with atomistic spin dynamics code UppASD [3] constructed via the parameterized values is attached.

Conclusion: In conclusion, the development of a perturbative approach to magnetic multislice simulations along with parameterization of magnetic fields and vector potentials in a way analogous to parametrization of atomic form factors allows for far more efficient calculation of elastic electron scattering in systems where magnetic effects are expected to play an important role.

[1] E. J. Kirkland, Advanced Computing in Electron Microscopy (2nd edition), Springer, 2010.
[2] A. Edström, A. Lubk, J. Rusz, Phys. Rev. B94, 174414, 2016.
[3] O. Eriksson, A. Bergman, L. Bergqvist, and J. Hellsvik, Atomistic Spin Dynamics - Foundations and Applications, Oxford University Press, Oxford, 1st edition, 2017.

Figure 1

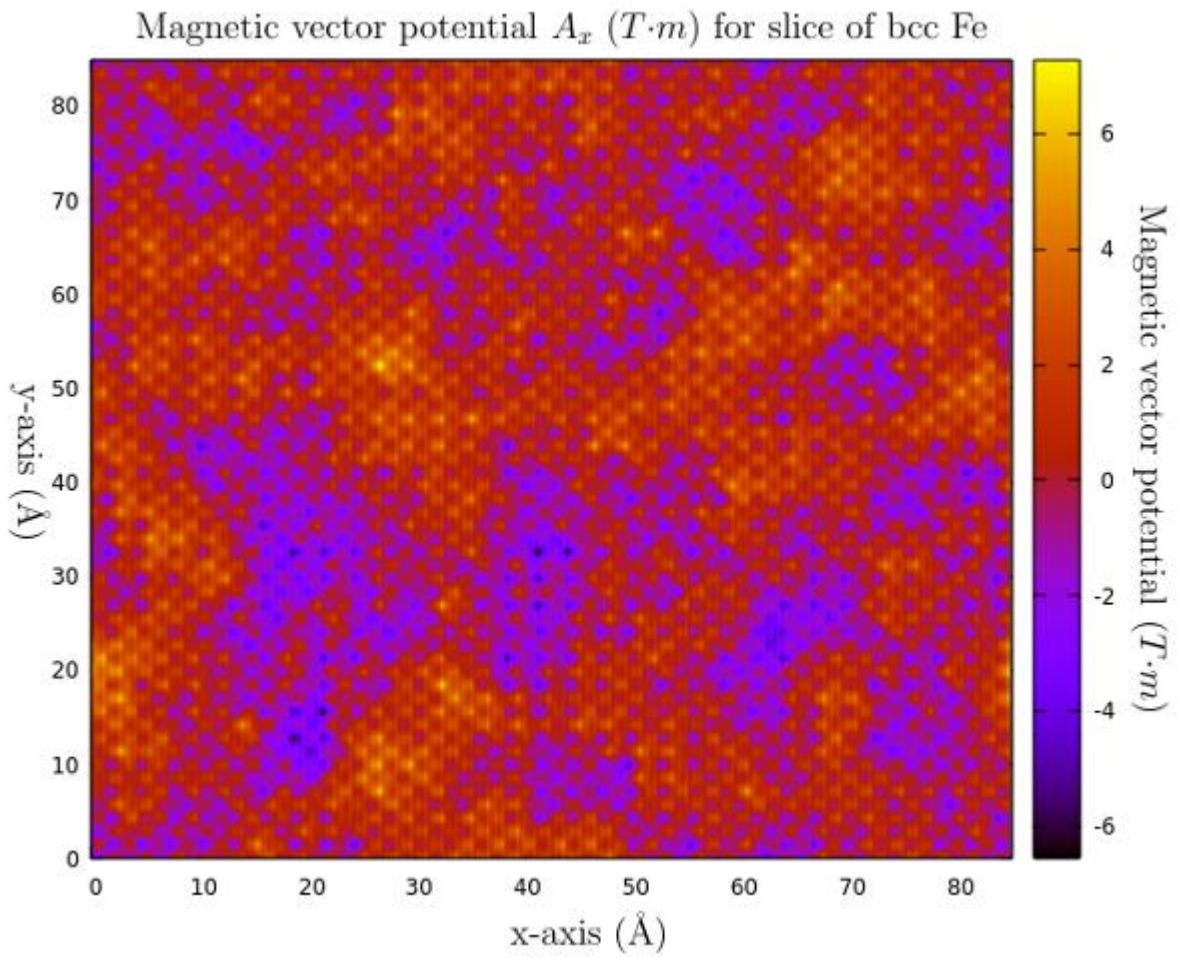
Magnetic vector potential A_x $(T{\cdot}m)$ for slice of bcc Fe
y-axis (Å)
x-axis (Å)
Magnetic vector potential $(T{\cdot}m)$
0
10
20
30
40
50
60
70
80
-6
-4
-2
0
2
4
6

OT2.001
Electron irradiation of two-dimensional MoS_2 – Insights into the influence of electronic excitations on defect production from first-principles calculations

S. Kretschmer[1], T. Lehnert[2], U. Kaiser[2], A. V. Krasheninnikov[1,3]

[1]Helmholtz-Zentrum Dresden-Rossendorf e.V. (HZDR), Dresden, Germany
[2]University of Ulm, Center for Electron Microscopy, Ulm, Germany
[3]Aalto University, Aalto, Finland

Introduction: Two-dimensional (2D) materials are routinely characterized nowadays in the transmission electron microscope (TEM). The high-energy electron beam in TEM can create defects in the target, and as the influence of defects on materials properties is expected to be stronger in systems with reduced dimensionalities, understanding defect production in 2D materials is of particular importance. Irradiation-induced defects can appear through three mechanisms, namely ballistic or knock-on damage (1), ionization and electronic excitations (2) and beam-induced chemical etching (3). Only the first channel is well understood, while numerous observations of defects formation in 2D transition metal dichalcogenides below the knock-on threshold point out that other mechanism should be important.

Objectives & Methods: Here we investigate the role of electronic excitations in defect production by using advanced first-principles simulation techniques based on the Ehrenfest dynamics combined with time-dependent density-functional theory and demonstrate that a combination of excitations and knock-on damage in 2D MoS_2 under electron beam can give rise to the formation of vacancies and explain the experimental observations of defects production far below the knock-on threshold.

Results: As our first-principles calculations show, electronic excitations will quickly delocalize in an otherwise unperturbed periodic structure. The situation changes dramatically then the translational symmetry is broken, as is the case for the displacement of one target atom upon momentum transfer from an impinging electron.

Conclusions: We propose a possible mechanism for the observed sub-knock-on threshold damage which involves the localization of the excitation at an emergent vacancy site. According to our calculations, this localized electronic excitation then gives rise to a decrease in the displacement threshold as anti-bonding states are occupied at the emergent defect site. Consequently, beam damage may be expected for voltages below the knock-on threshold as observed by the Sub Angstrom Low Voltage Electron (SALVE) microscope operated by our collaborators at Ulm University.

Figure caption:
(a) Sketch of the initial simulation ED setup with a delocalized excitation, which localizes at the incipient vacancy when the recoil S atom is displaced.
(b) Evolution of the excitation in MoS_2 sheet, side and top views, which localizes at the emerging vacancy

Figure 1

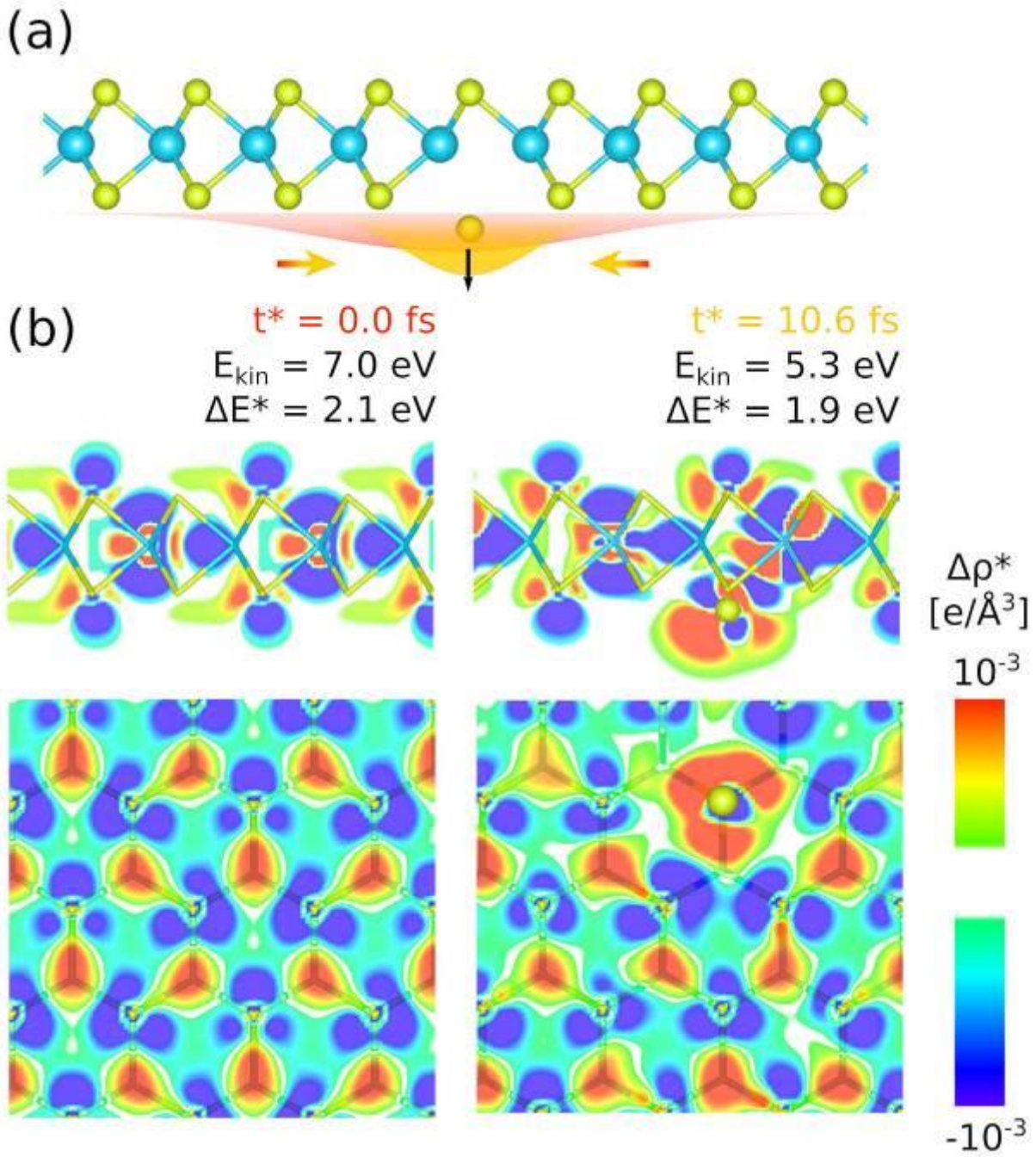
(a)
(b)
t* = 0.0 fs
E_kin = 7.0 eV
ΔE* = 2.1 eV
t* = 10.6 fs
E_kin = 5.3 eV
ΔE* = 1.9 eV
Δρ*
[e/Å³]
10^-3
-10^-3

OT2.002
Determination of key parameters for carbon contamination – quantitative measurement of contamination thickness and comparison with theory

A. Marx[1], M. Hugenschmidt[1,2], K. Adrion[1], E. Müller[1], D. Gerthsen[1,2]

[1]Karlsruhe Institute of Technology (KIT), Laboratory for Electron Microscopy, Karlsruhe, Germany
[2]Karlsruhe Institute of Technology (KIT), 23DMM2O – Cluster for Excellence (EXC-2082/1 – 390761711), Karlsruhe, Germany

Electron-beam-induced carbon contamination is formed by the interaction of the electron beam with volatile precursor molecules (contaminants) in electron microscopy. Polymerization by the beam transforms contaminants into carbon-rich solid contamination, which is an undesirable side effect and impedes the investigation of samples by covering structures of interest. The goal of our work is to measure, understand and prevent the growth of electron-beam-induced carbon contamination. Contamination growth depends on many parameters and requires systematic experimental studies to determine the parameters that mainly influence it. Moreover, discrete values for many parameters are not well known. A differential equation for the density of contaminants n on the sample surface was established by Müller [1]. It can be solved under stationary conditions ($dn/dt=0$) to obtain the contamination thickness t_c as a function of time T $t_c(T)=(m_c\sigma_j/\rho_c e)\cdot n(x)\cdot T$ (1) with the distance x from the center of irradiation, current density j, charge e, mean mass of cross-linked molecules m_c, contamination density ρ_c , and the cracking and cross-linking cross-section of the adsorbed molecules [2]. We compare calculated t_c values with contamination thicknesses that are measured using scanning transmission electron microscopy in a scanning electron microscope (STEM-in-SEM) where a stationary defocused beam adequately mimics the conditions in Müller's approach [1]. A FEI Strata 400S dual-beam microscope was used to grow contamination test patterns on thin amorphous carbon films (~10 nm). The test pattern consists of 3x3 circular patches with an area of 1 µm² (**Figure 1a**). Different illumination times between 5 s and 10 min were chosen. The beam is defocused to obtain circular patches and homogeneous irradiation. High-angle annular dark-field (HAADF-)STEM images are taken after the contamination growth. The contamination thickness is quantified by comparing experimental HAADF-STEM intensities, normalized with the intensity of the incident electron beam, and Monte-Carlo simulations performed as a function of the thickness. The thickness map of a contamination pattern is shown in **Figure 1b** (support-film thickness subtracted). Line profiles through circular contamination patches give t_c as a function of the distance x from the center (cf. **Figure 2** for the patch in **Figure 1b** marked by a red arrow). Experimental t_c values are compared with results of **Eq. (1)** for exemplary parameters from the literature and hydrocarbon molecules (e.g. for C_3H_8). For unknown parameters, we analyze the influence of parameter changes on the calculated t_c, which allows making reasonable assumptions. With this strategy, experimental t_c values can be well described by calculated t_c. This is shown in **Figure 2** where we have assumed a surface diffusion coefficient of 10^{-6} cm²/s. In sum, we systematically study contamination growth to determine relevant parameters by comparing measured and calculated contamination thicknesses.

References:
[1] Müller, Optik 33 (1971), p. 296
[2] Hirsch et al., Scanning 16 (1993), p. 101
[3] We acknowledge funding by the Deutsche Forschungsgemeinschaft (DFG, German Research Foundation) under Germany's Excellence Strategy – 2082/1 – 390761711.

Figure 1: a) Scheme of the electron-beam pattern. b) Thickness map of a contamination test pattern.

Figure 2: Contamination thickness: Theoretical values (black line, Eq. 1), and measured thickness profile (orange, see red arrow in Figure 1b).

Figure 1

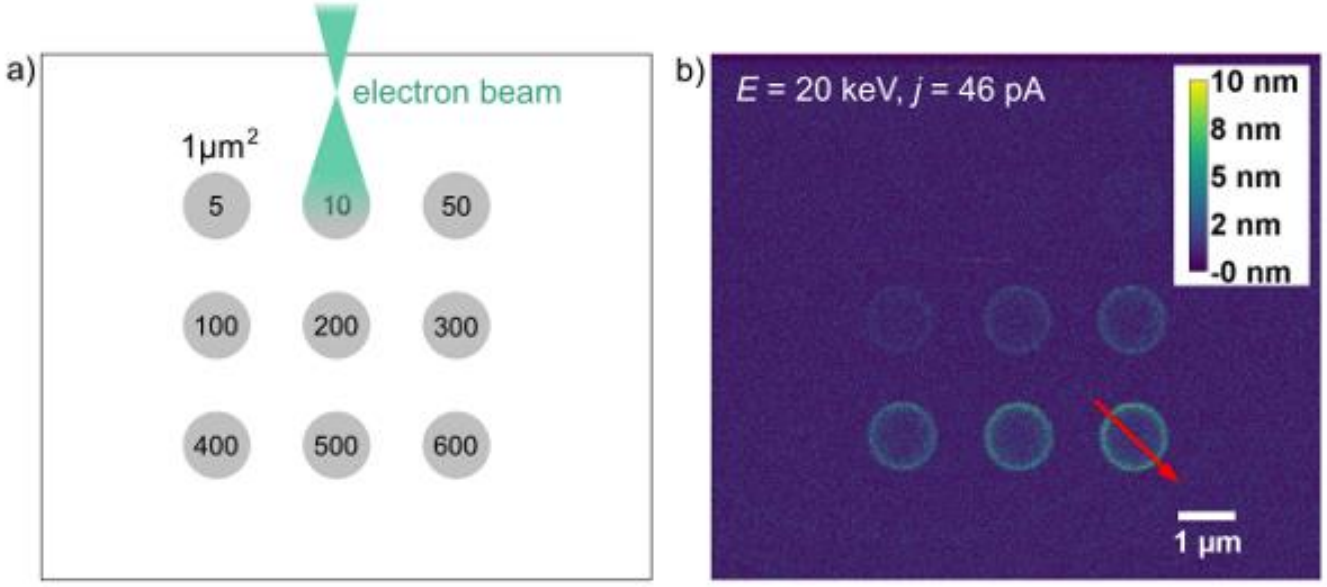

Figure 2

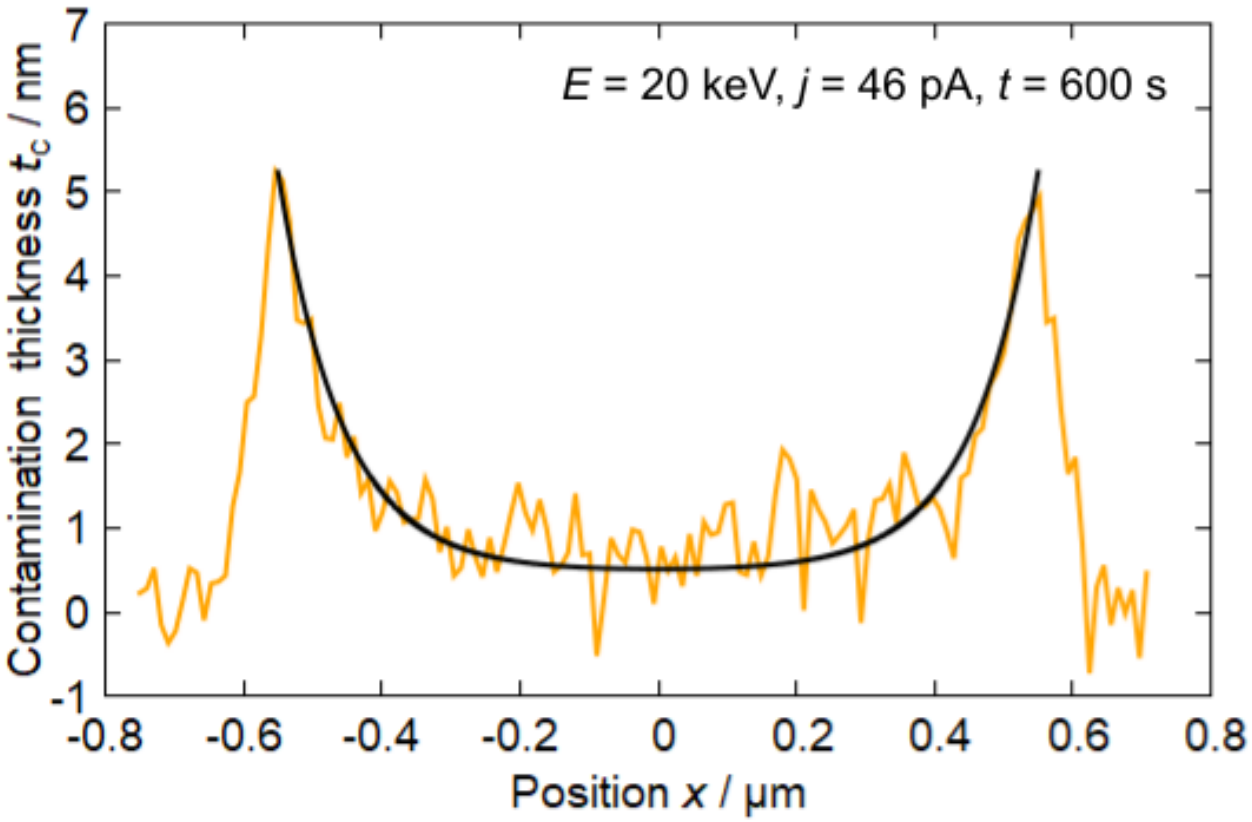

OT2.003
Sub-2 Å resolution HRTEM imaging of beam-sensitive 2D polymers at 120 kV

B. Liang[1], C. Leist[1], T. E. Gorelik[1], H. Qi[1,2,3], U. Kaiser[1]

[1]University of Ulm, Electron Microscopy Group of Materials Science, Ulm, Germany
[2]Technische Universität Dresden, Faculty of Chemistry and Food Chemistry, Dresden, Germany
[3]Technische Universität Dresden, Center for Advancing Electronics Dresden (cfaed), Dresden, Germany

Two-dimensional polymers (2DPs) and COFs (2DCOFs) have attracted many research interests in the last years. However, due to their extreme electron beam sensitivity, the direct structural study of 2DPs and 2DCOFs with aberration-corrected HRTEM remains a challenging task.

Many efforts have been devoted to improving the resolution HRTEM characterization of the 2DPs and 2DCOFs towards the instrumentational limit. One of the most crucial factors determining specimen stability is the acceleration voltage. To quantify the dependence of damage and image contrast as a function of acceleration voltage, the information coefficient has been introduced, which represents the highest amount of information available when one unit of damage is produced[1].

Here we apply a systematic analysis of the information coefficient of 2DPs and 2DCOFs for different acceleration voltages of 80, 120, 200, and 300 kV. The results demonstrate that 120 kV is superior to the traditionally applied high acceleration voltage of 300 kV. Approximately 5-7 % higher information gain can be achieved at 120 kV, while an electron beam energy of 80 kV destroys the material within the dose of 45-60 e/Å^2. Imaging with a 120 kV beam and applying the low-dose technique[2], we have successfully imaged different 2DPs and 2DCOFs with sub-2 Å resolution (see as an example Figure 1). This imaging set-up provides sufficient resolution to image the linker components in different frameworks. The enhanced image contrast due to lower acceleration voltage allowed for image acquisition with defocus values of a few tens of nanometers, greatly facilitating direct imaging interpretation. This avoids confusion due to delocalization under high defocus, which is important for elucidating non-periodic features such as defects and grain boundaries.

Determination of the optimized electron acceleration voltage and the critical dose is crucial for further improving atomically-resolved imaging of 2D organic materials.

Figure 1: AC-HRTEM characterization of 2D COF-bph. Image a shows an HRTEM image of 2D COF-bph with 1.9 Å resolution, the FFT is the inset at the upper-right corner. In the FFT the large orange circle marks the special resolution of 2 Å, and the small red circles mark the reflections beyond 2 Å, and some reach up to 1.9 Å. In b, the schematic structure of 2D COF-bph is shown, the lattice parameter is 3 nm. Image c is the enlarged image of a, the scale bar is 2 nm, the overlay is a structural scheme of 2D COF-bph.

[1] Peet, M. J., Henderson, R. & Russo, C. J. The energy dependence of contrast and damage in electron cryomicroscopy of biological molecules. *Ultramicroscopy* 203, 125–131 (2019).
[2] Egerton, R. F. Control of radiation damage in the TEM. *Ultramicroscopy* 127, 100–108 (2013).

Figure 1

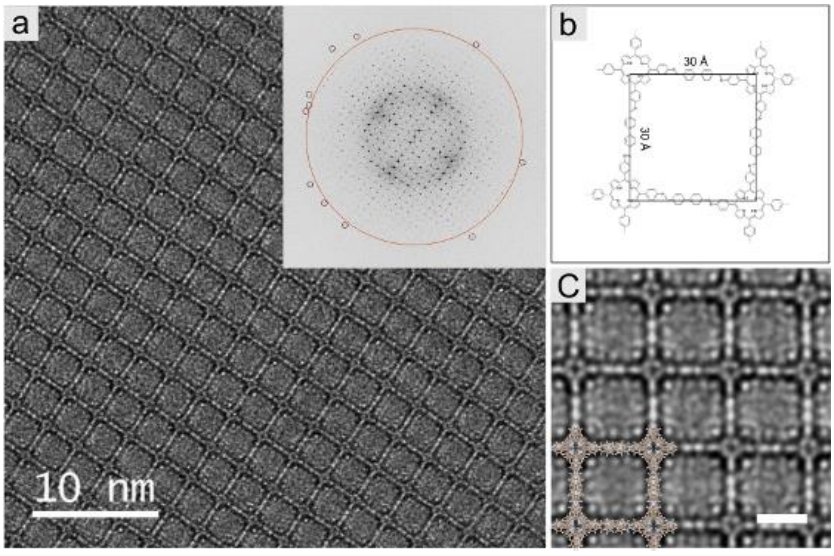

OT2.004
Core structure and mobility of Shockley partial dislocations in GaN by aberration-corrected HRTEM

I. G. Vasileiadis[1], I. Belabbas[2], J. Moneta[3], J. Smalc-Koziorowska[3], G. P. Dimitrakopulos[1]

[1]Aristotle University of Thessaloniki, Department of Physics, Thessaloniki, Greece
[2]Université de Bejaia, Equipe de Cristallographie et de Simulation des Matériaux, Laboratoire de Physico-Chimie des Matériaux et Catalyse, Faculté des Sciences Exactes, Bejaia, Algeria
[3]Institute of High Pressure Physics, Polish Academy of Sciences, Warsaw, Poland

Elucidation of dislocation core structure and behavior in III-nitride heterostructures is crucial for understanding their influence on device performance. The dissociation of **a**-type screw dislocations on the basal plane into two Shockley partials separated by an I_2 stacking fault (SF) is related to deformation caused by stress during or after growth.[1] A combination of aberration-corrected high resolution transmission electron microscopy (AC-HRTEM), geometrical phase analysis (GPA) with the dislocation density tensor, image simulations, and density functional theory (DFT) calculations was employed to study the core structures of such partials, as well as their mobility under e-beam irradiation.

In this work, emphasis was placed on 30° Shockley partial dislocation pairs arising from the decomposition of **a**-type screw dislocations in GaN. The elucidation of the dislocations´ core structures and their interactions in atomic scale can contribute to understanding their introduction mechanisms, their impact on various material properties and their behavior under irradiation and stress. A stringent AC-HRTEM analysis in conjunction with DFT calculations can effectively distinguish the atomic configurations of the cores.

The partials were observed under optimized imaging conditions along the <2-1-10> zone axis. The exact location of dislocation cores was determined experimentally by GPA using the dislocation density tensor. Equilibrium core structures were obtained by DFT calculations.

Relaxed core structures were employed as input for HRTEM image simulations. The core configurations were directly determined under imaging conditions allowing for imaging Ga-N dumbbells with bright contrast. The elucidation of the stable cores was performed by direct comparison between experimental and simulated HRTEM images. Figure 1 illustrates the models, the simulated and experimental images of the partials in the glide configuration that were observed and match to low-energy models.[1] Their mobility was also investigated under *in-situ* e-beam irradiation. A shrinking of the I_2 SF was observed leading to the re-formation of the initial screw dislocation. Sequentially aligned HRTEM images revealed that the partial with N-polarity was the mobile one. DFT calculations showed that point defects at the dislocation's core can modify its local electronic structure making its motion compatible with recombination enhanced dislocation glide (REDG).

AC-HRTEM analysis was conducted on pairs of 30° Shockley partials delimiting I_2 SFs. Based on image simulations, the core structures were identified using appropriate imaging conditions and comparison to relaxed models. The shrinking of the I_2 SF and re-formation of the lattice dislocation through partial dislocation glide under *in situ* e-beam irradiation was attributed to the activation of the REDG effect.

Figure 1: (a) and (b) Schematic illustrations showing respectively the relaxed glide models of the N-polarity single-period (SP) and the Ga-polarity double-period (DP) cores. (c) and (d) HRTEM image simulations of the (a) and (b) cores respectively. (e) and (f) Experimental HRTEM images revealing directly the structure of (a) and (b) models respectively.

[1] I. Belabbas, et al., J. Appl. Phys. 126, 165702 (2019)

Supported by the IKY project "Strengthening Human Resources Research Potential via Doctorate Research" (MIS-5000432) and the project HARMONIA UMO-2016/22/M/ST5/00298.

Figure 1

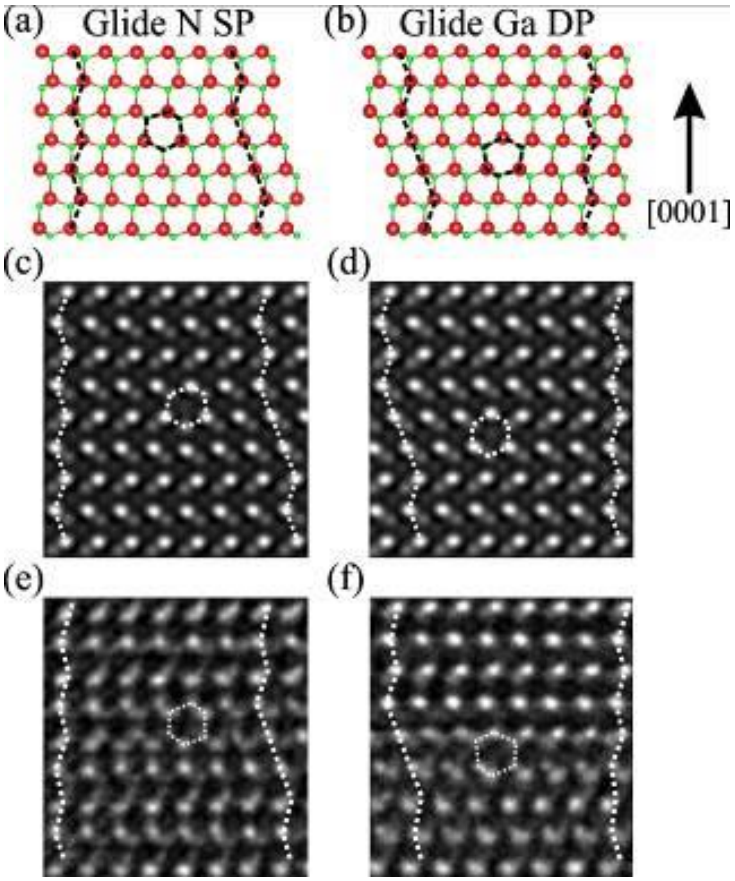

OT2.005-Invited
Devices with "Zero D" holes for basic science and applications

M. Drndic[1]

[1]University of Pennsylvania, Physics and Astronomy, Philadelphia, PA, United States

Atom-size holes in 2D materials can change the material's properties, for example the bandgap, as in antidot lattices and transistors. Atom vacancies can make the 2D membranes permeable to particles in liquids or gases, allowing basic physics transport studies at the atomic scale. These holes are comparable in size to several fundamental length scales. Angstrom-size holes can allow the passage of water but can block the salt ions and can effectively desalinate water. Raman peak shifts combined with aberration-corrected transmission electron microscopy, provide a comprehensive approach to characterize the holes. When molecules are driven through holes in a conducting liquid, they perturb the current flow through the hole, from which molecule"s physical and chemical properties can be inferred. DNA, proteins and other biomolecules can be detected in this way. Thanks to new materials, device designs and custom electronics, 2D membrane devices are advancing steadily from academic labs to a wide range of applications benefiting society in the near future. Of course, electron microscopy is central in research.

Figure 1

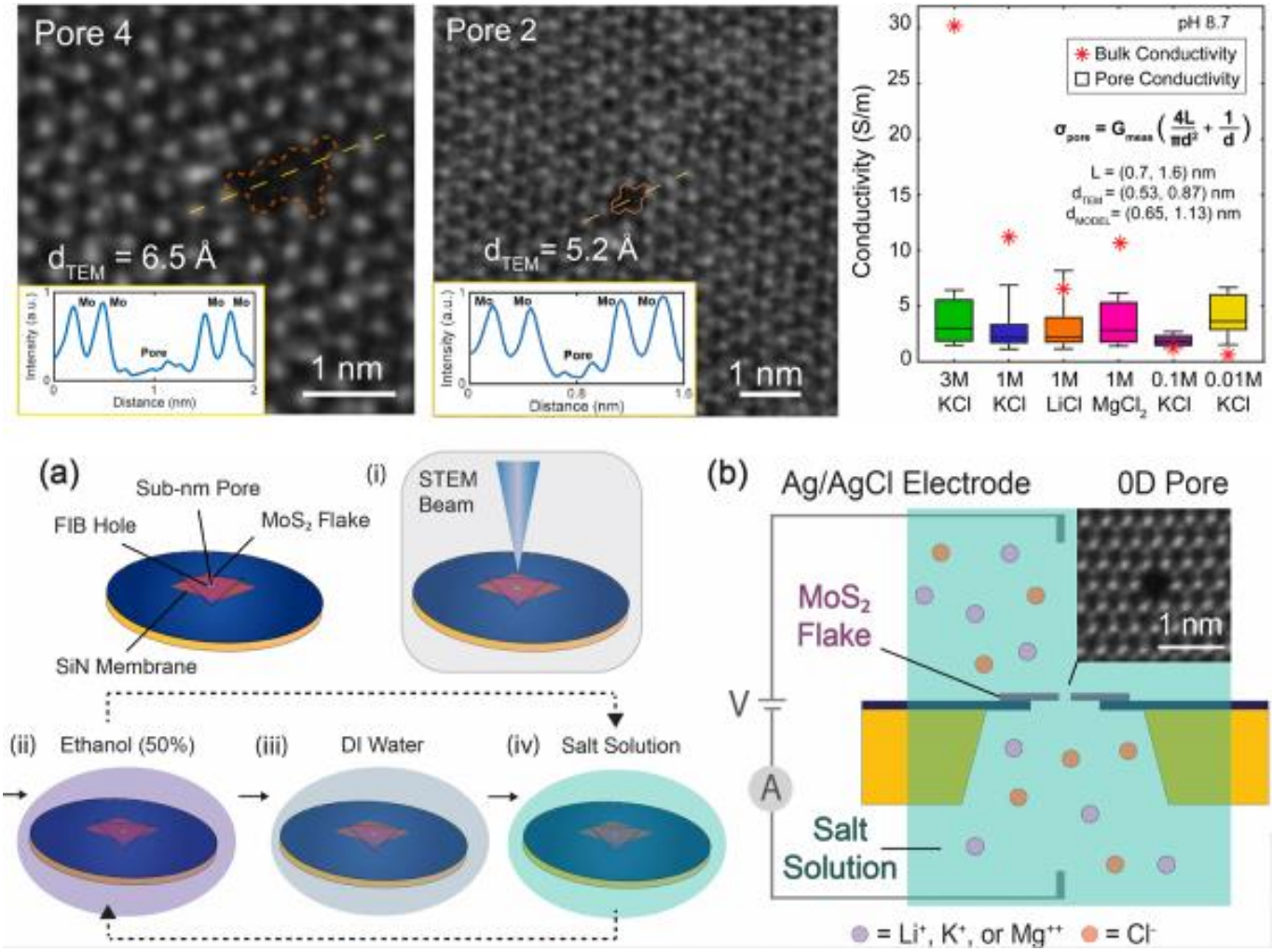

OT2.P001
Video recording *in situ* of the crystal growth at electron-beam irradiation of thin amorphous films

A. Bagmut[1]

[1]National Technical University “Kharkiv Polytechnic Institute”, Department of Physics, Kharkiv, Ukraine

Substance in a non-crystalline solid state can crystallize spontaneously or under the influence of the physical action, i.e. to pass from a metastable non-crystalline solid state to a stable crystalline state. In general, crystallization of stoichiometric films occurs according to one of the following schemes [1]: layer polymorphous crystallization (LPC), island polymorphous crystallization (IPC) and dendrite polymorphous crystallization (DPC). The purpose of this work is the electron microscope study with in situ video recording of crystal growth in amorphous films and the systematization of crystallization reactions according to structural and morphological features.

Amorphous films were obtained by thermal evaporation of substance in vacuum, by pulsed laser sputtering targets in oxygen atmosphere and by ion-plasma deposition of metal in argon - oxygen mixture. Phase transformations and structural analysis were performed by the methods of TEM, using microscopes EM-100L and PEM-100-01, operating at the accelerating voltage of 100 kV. The process of crystallization of the films was recorded from the screen of the electron microscope with Canon Power Shot G15 camera in the video recording mode with the frame rate of 30 s-1.

In the case of LPC (V2O3, Fe2O3, Sb2S3, Cr2O3 and others) under the action of the electron beam, the crystals with different morphology (disco-shaped, sickle-shaped and needle-shaped crystals) can be formed in the amorphous film, and each film has its own kinetics of evolution. At the fixed density of the electron beam going through the film, the disk-shaped crystals grow at the constant rate and invariable morphology, for which time dependence of crystal fraction $x(t) \sim t2$. Steps and crystalline layers, moving at different speed into the depth of the amorphous matrix, may accompany the LPC of amorphous films [2] (Fig 1).

In the case of IPC (Al2O3, ZrO2, Yb2O2S, Ni, Re and others) the polycrystalline layer is formed. The average crystal diameter $\langle D \rangle \sim t$, and $x(t)$ is described by the the Johnson-Mail-Avrami-Kolmogorov (JMAK) formula $x = 1\text{-}\exp(-ntk)$, where k is the Avrami coefficient (reaction order) and n is an effective rate constant, describing both nucleation and growth.

In the case of DPC (films of HfO2, Fe-C) single crystals in the form of dendrite branches of the first order are the site of formation of branches of the second and third order. The branches are formed from the series of randomly oriented crystals in the process of geometric selection.

Figure 1: Film shots of layer crystallization of amorphous film of Cr2O3. Photomicrographs correspond to the periods of time t, that passed after the video recording had started: (a) t = 0 s; (b) t = 0.83 s; (c) t = 1.67 s. 1 - amorphous phase. S1 is the crystallization front, moving with the velocity $v1_T$. S2 is the crystallization front, moving with the velocity $v2_T$. S2 - crystallization front after the merger of S1 and S2

[1] A.G. Bagmut, Classification of the Amorphous Film Crystallization Types with Respect to Structure and Morphology Features, Tech. Phys. Lett. 38 (2012) 488-491.
[2] A.G. Bagmut, I.A. Bagmut, Kinetics of autoepitaxial crystal growth in amorphous films of Cr2O3, J. Cryst. Growth. 517 (2019) 68-71.

Figure 1

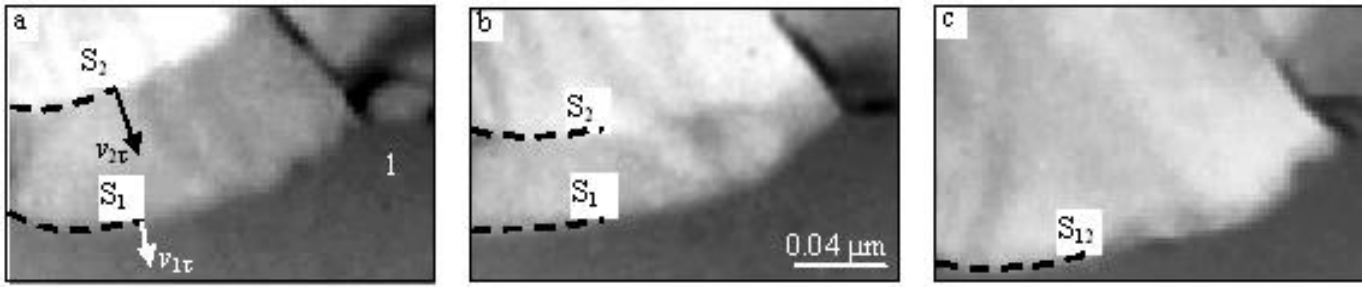

OT2.P002
Visualising electron-beam induced plasma characteristics in an ETEM

U. Ross[1], J. Lindner[1], V. Roddatis[2], T. Meyer[1], C. Jooss[1]

[1]University of Göttingen, Institut für Materialphysik, Göttingen, Germany
[2]GFZ German Research Centre for Geosciences, Interface Geochemistry, Potsdam, Germany

Real-time study of the interactions of materials with chemically active environments such as gases or liquids provides the opportunity to elucidate the underlying mechanisms of the chemical reactions involved. In this context, determining the influence of the electron beam illumination on gases in an environmental TEM (ETEM) experiment is essential. The beam-gas interaction creates an electrolyte through the production of several ionic species and free electrons in the gas, which may alter reaction pathways under ambient conditions. Depending on the experimental parameters and the gas composition the ionization can lead to a dilute plasma state.

The particular properties of this ionized gas under in-situ conditions must be determined so as to estimate the role of possible plasma-assisted catalysis effects. The electric field distribution plays a key role and its measurement could strongly assist in the model development of such reactions. The electric field distribution around biased electrodes in an ETEM is modified by the presence of the plasma and its local composition. The plasma sheath around a biased conductor, which forms due to space-charge redistribution effects, is sensitive to the lens magnetic field which shifts the local ion density around the sample.

Plasma parameters in the ETEM are determined from pA IV curves measured in-situ by use of a modified TEM holder that is used as a Langmuir plasma probe. The plasma states of helium and argon are characterized in dependence of beam current and nominal pressure. The projected plasma sheath shape is determined on a nanometer scale for a two electrode setup by application of 4D-STEM field mapping around a small gap between two FIB-fabricated tungsten tips, with respect to different magnetic field strength at the sample plane. In-situ IV curves are simultaneously recorded in order to qualitatively verify the influence of the magnetic plasma drift.

Detailed plasma probe analysis using orbital motion limited theory (OML) was used to determine ion-densities, free electron temperatures and the resulting electron Debye shielding lengths (Figure1). Center-of-mass evaluation of the 4D-STEM field mappings confirms the shielding effect of the plasma generation, as well as the sheath quenching through the plasma drift in presence of crossed electric and magnetic fields in the microscope (Figure2). This is in accordance with conventional plasma experiments, despite the locally confined generation volume around the electron beam at the sample plane.

The existence of the beam induced plasma state in ETEM with ambient gases has to be considered when structural changes of active materials are linked to chemical reactions by in-situ methods. Our results lead us to a more detailed understanding of the plasma properties and the resulting altered electric field distribution in ETEM. The determined plasma parameters offer the opportunity for plasma simulations and the adaption of further plasma measurement techniques.

Figure 1: Langmuir probe IV series for Argon and Helium demonstrating plasma characteristics at constant beam current (top) and gas pressure (bottom).

Figure 2: Projected electrostatic field modulus from 4DSTEM, in vacuum (top left) and at variable objective lens excitation, resulting plasma shielding (top right) as well as magnetic sheath deformation (bottom row).

Figure 1

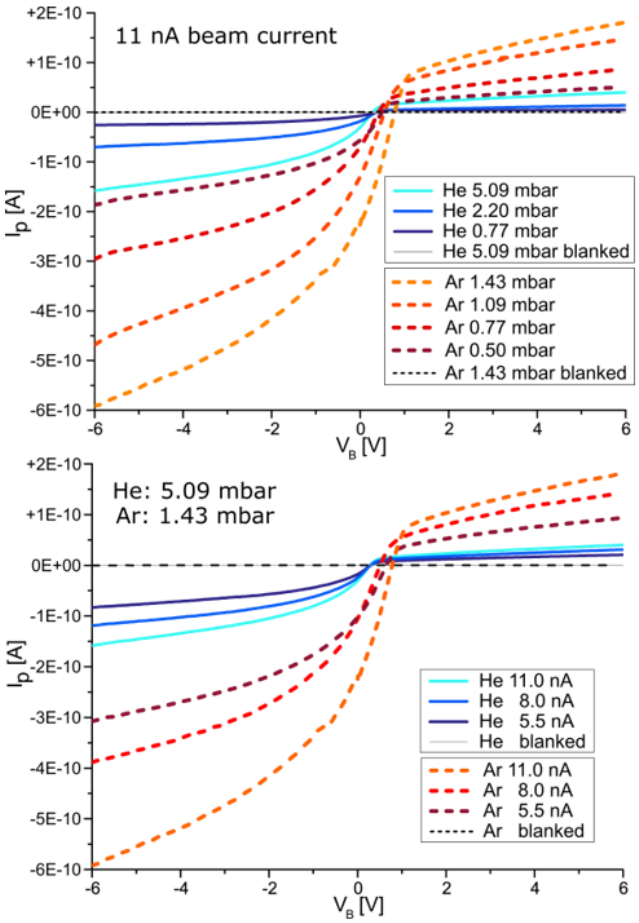

Figure 2

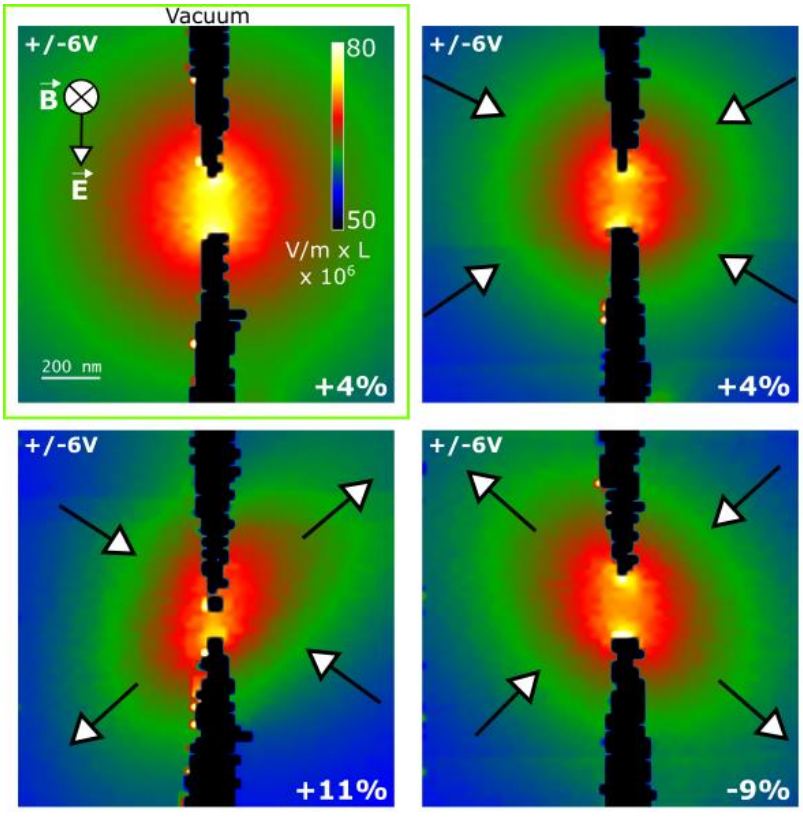

OT2.P003
Distinction of microplastics by serial electron pair distribution function (ePDF) analysis

C. Rohner[1], R. Schlögl[1], T. Lunkenbein[1]

[1]Fritz Haber Institute of the Max Planck Society , Department of Inorganic Chemistry, Berlin, Germany

ePDF allows the analysis of the average local structure of an amorphous or semicrystalline material.(1) Applied to the class of microplastics (MP) it could serve as a means for the distinction of polymer types in mixtures of (sub)micron particles. In this size regime, contemporary methods of polymer quantification such as Raman microscopy are limited by spatial resolution.

Polyethylene (PE), polypropylene (PP), and polyethylene terephthalate (PET) MP were examined by TEM and ED under low dose, non-cryo conditions using Gatan Orius and Tietz TVIPS cameras. Reduced pair density functions (RDF) were calculated from the processed and background subtracted ED data and compared to simulated RDF. Beam induced effects were determined by serial electron diffraction (ED) at different beam dose rates and analysis of the time dependent ED.

High quality serial ED suitable for PDF analysis was recorded from different MP (e.g. Figure *1*). The ePDF method yields a qualitative agreement of experimentally determined and simulated RDFs for PE, PP and PET (Figure *2*). The RDFs of the examined polymers allow a distinction of the materials, granted that the differences between PE and PP are small. In the short distance region (1-5 Å) all experimental peaks can be assigned to C-H, C-C or C-O bond lengths or remote pair distances by comparison to the model RDFs. The beam induced effects on the structures are visible in the temporal evolution of the RDFs. The change in structure depends on the polymer type and the total dose/dose rate. The observed changes in the RDFs can be rationalized by considering the chemical structures of the materials. In the cases of PE and PP, first C-C-bond scission dominates, leading to a loss of medium range (5-10 Å) order, then C-H bond scission becomes more prevalent and graphitization occurs. In contrast, the RDFs of PET show little change with beam exposure. This can be rationalized by a lack of initial medium range order in the glassy material, and by the presence of the extended π-electron system which provides more resilience to the beam effects compared to the single bonded PE and PP.

We show that detailed structural information can be gained on highly beam sensitive polymer materials by following a low dose ePDF approach without cryo or staining techniques. The approach should be extendable to 4D STEM methods and thus allow for automated handling of environmental samples if combined with computational techniques.

Figure 1: A TEM image acquired after the ED measurement. The red circle indicates the approximate position of the SA aperture. **B** First frame of the processed and background subtracted serial ED. **C** Azimuthally integrated scattered intensity. The colour code indicates the total exposure time at the end of acquisition of a frame.

Figure 2: RDFs derived from serial ED measured on cryo ball milled PE, PP, and PET microplastic particles, respectively. **A** Results of measurements taken with a dose rate of ≈ 45 e/(nm2s), and **B** a dose rate of ≈ 160 e/(nm2s). Each graph in **A** and **B** shows the experimental time series of RDFs, G(r) (coloured lines), the calculated RDF of a model structure, G(r) model (grey lines), and the elemental pair distribution function of the model (stacked bar charts). The colour scale indicates the total exposure time at the end of acquisition of an ED frame. **C** 3D model structures

[1] Gorelik TE et al. Acta Cryst. 2019;75:532–49.

Figure 1

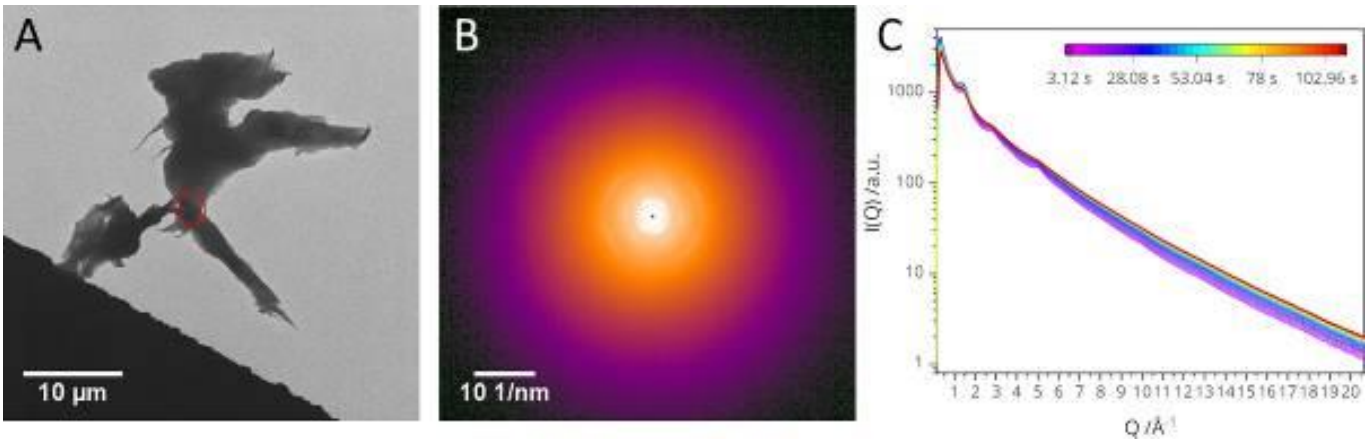

Figure 2

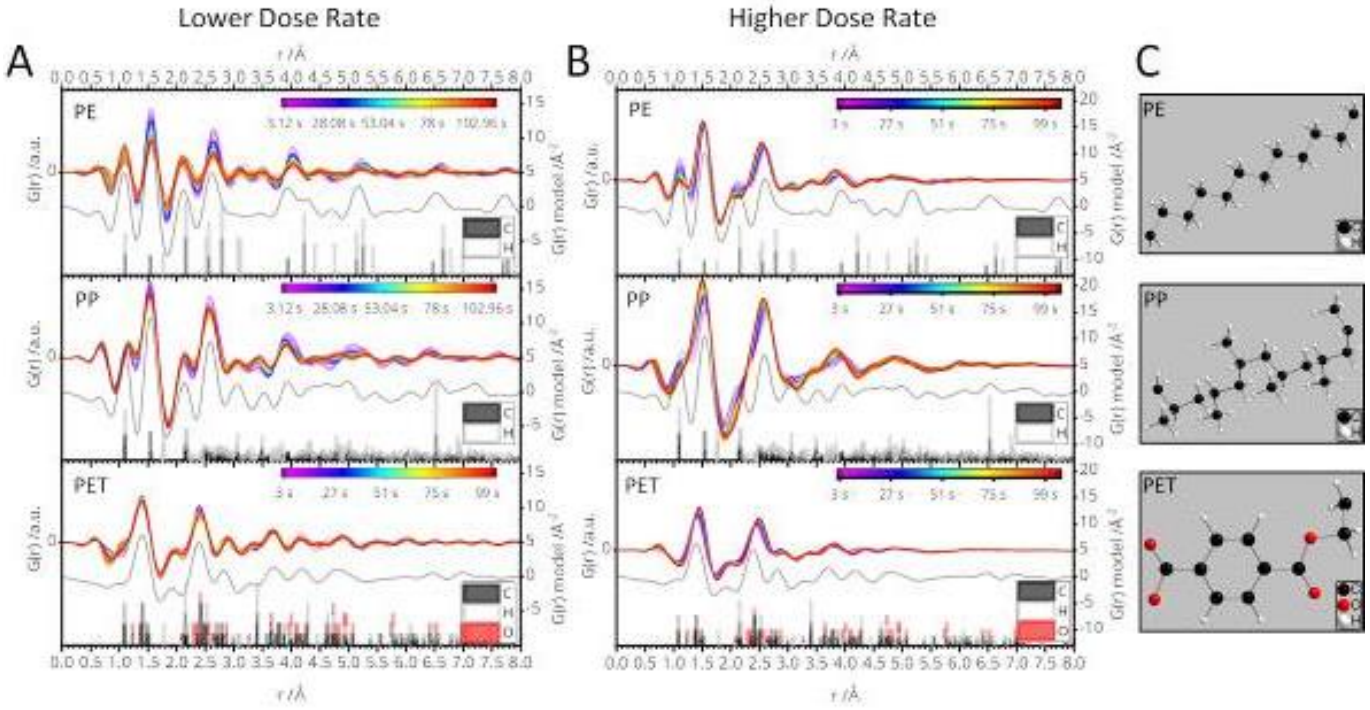

OT2.P004
In situ TEM investigation of graphene-encapsulated 2D NaCl crystal decomposition

T. Lehnert[1,2], S. Kretschmer[3], F. Bräuer[1], A. V. Krasheninnikov[3,4], U. Kaiser[1]

[1]University of Ulm, Electron Microscopy Group of Materials Science, Ulm, Germany
[2]University of Ulm, Instiute for Quantum Optics, Ulm, Germany
[3]Helmholtz-Zentrum Dresden-Rossendorf e.V. (HZDR), Institute of Ion Beam Physics and Materials Research, Dresden, Germany
[4]Aalto University, Department of Applied Physics, Aalto, Finland

Transmission Electron Microscopy (TEM) combined with graphene encapsulations allow high-resolution analysis of radiation sensitive materials because graphene increases the resistance of the encapsulated material against the electron beam [1, 2]. Moreover, due to strong van-der-Waals forces, an enclosed environment between the graphene sheets is produced, which allows in-situ TEM experiments in, for example, so-called graphene liquid cells [3]. Most studies with graphene encapsulations in a TEM are related to in-situ experiments but the effect of the electron beam interaction with the whole system during imaging is not fully understood yet.

Here, we report about the decomposition process of graphene encapsulated quasi-two-dimensional (2D) sodium chloride (NaCl) crystals, which were prepared via supersaturation from a saline solution within a graphene liquid cell. We used aberration-corrected high-resolution transmission electron microscopy (AC-HRTEM) for systematic in-situ studies of electron-beam-induced decomposition processes of the quasi-2D NaCl crystals. After an initial stability, we have observed an abrupt decomposition, which follows a logistic decay function. We explain the decomposition behavior of the NaCl crystals with the structural integrity of the encapsulating graphene. We show that already one, during observation created point defect in the encapsulating graphene is sufficient to initiate abrupt NaCl decomposition. In addition, we combine our experimental results with density functional theory (DFT) calculations to understand the underlying mechanisms of the decomposition, based on displacement with respect to the Coulomb interaction between Na+ and Cl- ions. Our studies reveal the importance of defect-free graphene for optimal protection and give also a deeper insight of electron-beam-induced decomposition processes in ionic crystals.

[1] T. Lehnert et al., Appl. Phys. Lett. 110, 033106 (2017)
[2] G. Algara-Siller et al., Appl. Phys. Lett. 103, 203107 (2013)
[3] T. Lehnert et al., ACS Nano 11, 7967-7973 (2017)

LBN.P002
3D electron diffraction: a dedicated device for structural elucidation of nanocrystalline particles

E. Hovestreydt[1], G. Santiso-Quinones[1], A. Lanza[1], G. Steinfeld[1]

[1]ELDICO Scientific AG, Mgt, Villigen, Switzerland

In the recent years, many achievements using electron diffraction techniques (3D ED) have been made. Such experiments are currently done in a (modified) transmission electron microscope. A strong need has emerged for instrumentation specifically dedicated to 3D ED experiments.

Here we present an electron diffractometer: a new device developed and optimized exclusively for 3D ED which allows a time-effective, automated and standardized experimental workflow along with user-friendly operability. Furthermore, the electron diffractometer is conceived to make use exclusively of well-established crystallographic approaches and to interact seamlessly with readily available crystallographic software.

Experimental examples of different kind of materials measured with this device will be showcased.

[1] Gruene, T., Wennmacher, J. T. C., Zaubitzer, C., Holstein, J. J., Heidler, J., Fecteau-Lefebvre, A., De Carlo, S., Müller, E., Goldie, K. N., Regeni, I., Li, T., Santiso-Quinones, G., Steinfeld, G., Handschin, S., van Genderen, E., van Bokhoven, J. A., Clever, G. H. & Pantelic, R. (2018) A*ngew. Chem. Int. Ed.* **57**, 16313.

Keywords: 3D ED; electron diffraction; nano-crystallography; electron diffractometer

Fig. 1

LBN.P003
New additively enhanced interface for multi-material orthodontic brackets – analysis after one-year *in-vitro* simulated aging

U. Botzenhart[1], H. Meissner[1,2], P. Risthaus[3], C. Wagner[3], F. Marquardt[4], E. López[4], F. Brückner[4]

[1]Faculty of Medicine, Carl Gustav Carus, TU Dresden, Department of Orthodontics, Dresden, Germany
[2]Faculty of Medicine, Carl Gustav Carus, TU Dresden, Department of Prosthetic Dentistry, Dresden, Germany
[3]Forestadent, Bernhardt Förster GmbH, Pforzheim, Germany
[4]Fraunhofer Institute for Material and Beam Technology IWS, Dresden, Germany

Questions: Multi-material compositions, especially for dental applications, are critical due to the oral environment, which can alter the properties of combined materials and affect their bond. Micro-topologies can improve the interface for resin injection molding around metallic inserts by undercuts and surface-enlargements, thus improving the adhesion between the different materials. The aim of the present study was to analyze the structure and biocompatibility of multi-material brackets of different metal-plastic combinations for oral/dental application, characterized by an additively manufactured interface generated by Laser Metal Deposition (LMD).

Methods: Simplified bracket bodies (n= 51) formed by injection molding (P.A.N.A.C.E.A.) were delivered to LMD-process for additively forming pin shaped structures (316L,<200µm) to improve composite-material interface. For injection molding around metallic inserts with PEEK (polyether ether ketone;n=25) and polyamide (n=26), respectively, giving the bracket the final shape, the build-up strategy with the best pull-off force results out of four former tested (different geometry and process parameters) was selected. Additionally, brackets out of metallic inserts without additively enhanced surface were also produced and were serving as control groups (PEEK n=25;polyamide n=25). All test brackets were analyzed by stereomicroscopy for insert molding defects and after one year simulated oral thermal (Thermocycler SD, Mechatronik GmbH, Feldkirchen-Westerham, Germany) and mechanical aging (Toothbrush simulator, Willitec GmbH, Munich, Germany), and surface roughness of compound brackets was also measured, as well. Statistics were performed by descriptive analysis and paired t-test (significance level:$p \leq 0.05$).

Results: Regardless of interface, stereomicroscopy analysis of infiltrated brackets revealed numerous filling-defects in PEEK (n=13/36%) compared to polyamide samples, where no filling-defects could be detected. However, PEEK infiltration was much better at additively enhanced surfaces (n=8/32% vs. n=5/45% defects in the test compared to the control group, respectively), whereas n=14 (56%) samples in the control group had to be excluded from the outset and were not taken further into account, since no compound could be reached. In none of the samples still under consideration (test groups: PEEK n=17, polyamide n=26;control groups: PEEK n=6, polyamide n=25) a detachment of the compound could be found after simulation of one year thermal and mechanical aging and an exposure of the interface could only be detected in the test groups with one sample each. Independently of the interface, surface roughness of both plastic materials significantly decreased with aging (0.2-0.3µm vs. 0.5-0.6µm beforehand;$p<0.0001$). While PEEK initially had somewhat lower Ra values compared to polyamide samples ($p=0.01$), this reversed for materials after aging ($p<0.0001$).

Conclusions: Additive manufacturing is a favorable technique to modify interface of complex geometries and enhance composite material properties for oral clinical use. The material compound was not compromised by one year simulated oral thermal and mechanical aging, but surface roughness significantly decreased with aging and substance abrasion was critical with exposure of micro-topologies in some, but clinical negligible cases, so that the weak point was not the interface but laid in the material properties of the resins used for final bracket shaping.

LBN.P004
Gaussian Processes for Structure Factor Retrieval from Large-Angle-Rocking-Beam Electron Diffraction

S. Fairman[1], B. Haas[1], N. Dellby[2], S. Shabih[1], C. Koch[1]

[1]Humboldt-Universität zu Berlin, Physik, Berlin, Germany
[2]Nion Company, Kirkland, United States

In recent years electron crystallography has developed into a viable tool for structure determination. Electron crystallography does not suffer from overlapping reflections observed in X-ray diffraction of powders or the need for large single crystals required for single-crystal X-Ray crystallography. Averaging over dynamical diffraction signals, structures are now routinely solved using direct methods [1] or 3DED [2]. When preserving the variation of diffraction intensity with incident beam direction, D-LACBED and comparable data serves well for crystal structure refinement [3]. Large-Angle Rocking-Beam Electron Diffraction (LARBED) accesses the same information available in convergent beam electron diffraction (CBED) but for "convergence" angles up to 100mrad, independent of the size of the unit cell [4].

Results from simulations are presented in Fig.1 from a Gaussian Processes (GP) based algorithm called TuRBO [6] which is more adaptable to high dimensional problems than traditional GP. The algorithm directly fits the structure factors (U(g)) to the LARBED pattern while also retrieving thickness and tilt offset, where fitting the tilt means there is no need to align exactly to zone axis.

Although no U(g) have been fitted to experimental data yet, a SrTiO3(100) sample was investigated at 60kV in a Nion HERMES microscope equipped with a Dectris ELA direct electron detector (1030 x 514 pixels). The detector counts electron arrivals that deposit energy greater than an adjustable threshold, and is able to record incident intensities spanning 7 orders of magnitude with a detective quantum efficiency (DQE) ≥0.8 [5]. It registers essentially no dark signal other than rare cosmic rays, which allows long exposure times with virtually no added noise, as shown in Fig.2. It is also able to record up to 2250 whole frames per second, without any penalty of increased read-out noise. This not only decreases the time of the data collection but also reduces the impact of stage drift and damage for beam sensitive specimens. These benefits combined with the simulation data are promising for experimental LARBED.

References:
[1] Palatinus et al., Science 355, 166-169 (2017)
[2] Z. Huang et al., Chem. Sci. 12, 1206-1219 (2021)
[3] R. Beanland et al, Acta Cryst. A77, 196-207 (2021)
[4] C. T. Koch, Ultramicroscopy, vol. 111, no. 7, pp. 828–840 (2011)
[5] B. Plotkin-Swing et al., Ultramicroscopy 217, 113067 (2020)
[6] D. Eriksson et al., Advances in Neural Information Processing Systems 32 (NeurIPS 2019)

Acknowledgements**:** DFG (KO 2911/12-1[BerlinEM] & SFB951[HIOS])

Figure1: (A) A simulated SrTiO3(001) LARBED pattern including 25 diffraction spots. (B) The LARBED pattern using U(g) fitted by TuRBO. (C) The absolute value of the electrostatic potential with one unit cell drawn in white, the left corresponding to (A) and the right to (B). The retrieved thickness 30nm and tilt offset 10mrad were fitted correctly. (D) Thresholding shows the unit cell from the background.

Figure 2: Spot diffraction patterns of SrTiO3 are shown at similar tilt angles with a convergence angle of 0.8mrad (A) A line scan on the Dectris detector showing the low noise at short exposure time ~50ms and (B), an exposure time of 1s and a beam current of ~24pA, showing that sequentially counting with long exposure improves the signal to noise ratio.

Figure 3: Mean diffraction pattern of Si(211) tilt series of 441 tilts collected at 60kV with a tilt range of 38mrad on the Dectris ELA.

Figure 1:

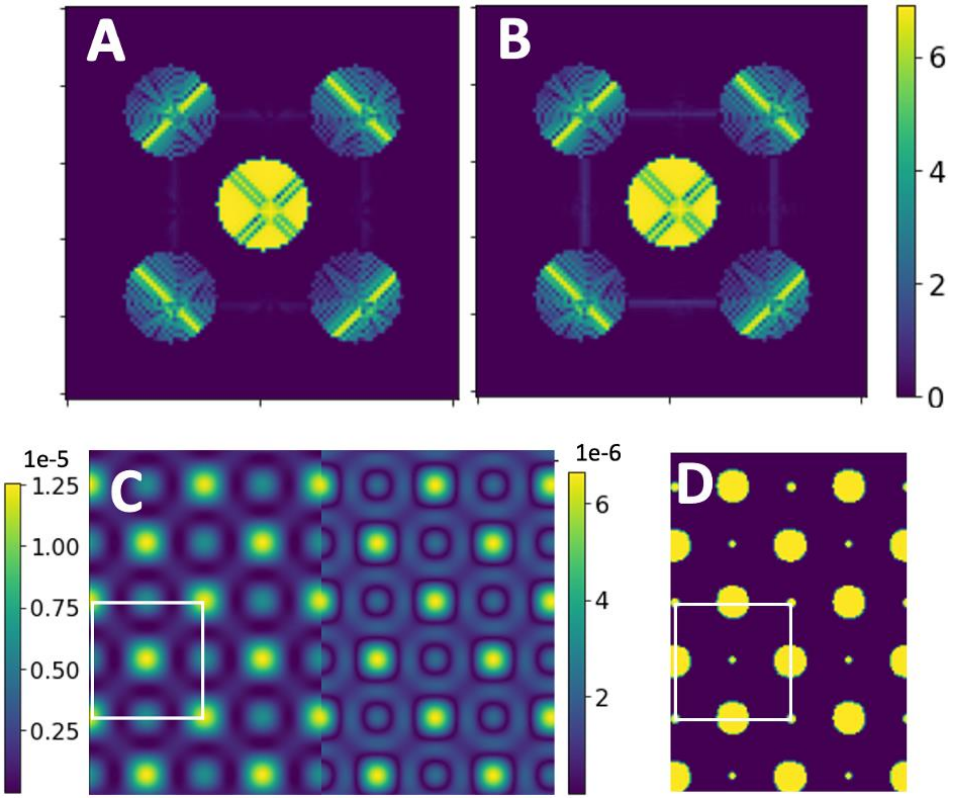

Fig. 2

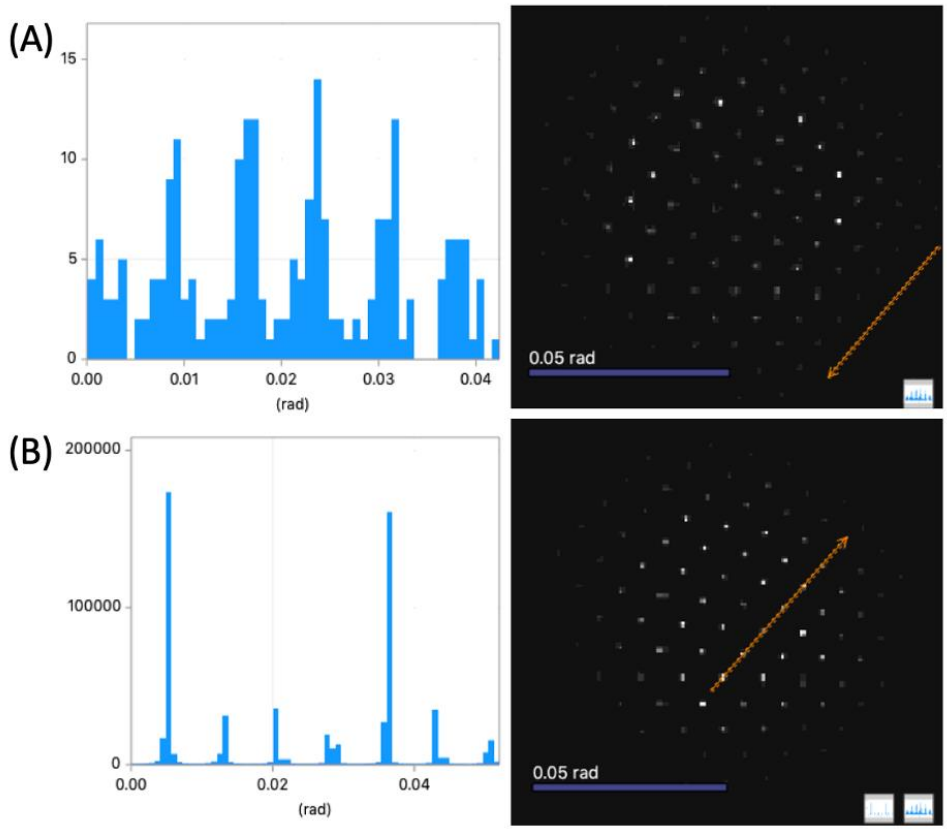

Fig. 3

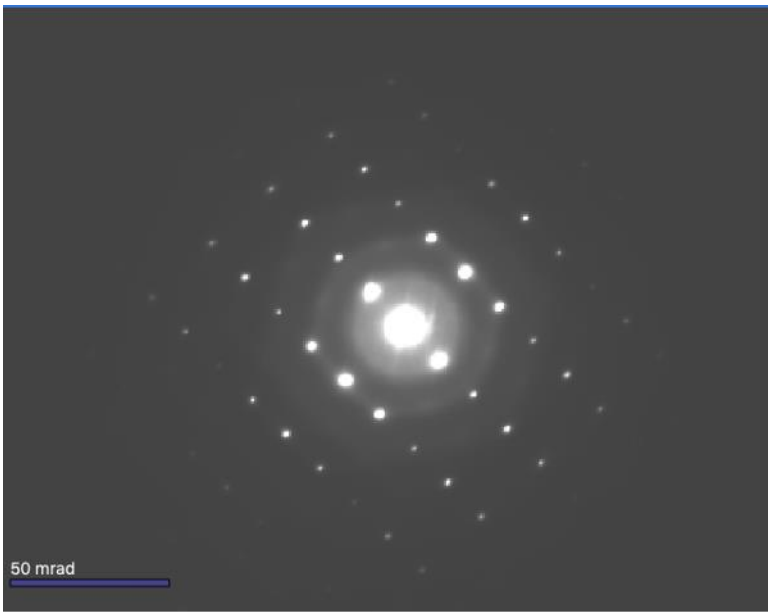

LBN.P005
Autophagy in pancreatic acinar cells of rats fed by sucrose-rich diet

M. Ukropina[1], R. Glišić[2], M. Čakić-Milošević[1]

[1]University of Belgrade, Faculty of Biology, Belgrade, Serbia
[2]University of Kragujevac, Faculty of Science, Kragujevac, Serbia

Introduction: Pancreas is an accessory organ of the gastrointestinal tract, with acinar cells being the dominant cell type in exocrine and β-cell in endocrine portion of the gland. Although generally considered as mononuclear (1N), 50-60% of acinar cells in adult rats are in fact binuclear (2N) [1]. Some of them were previously showed to differently express PDX1 transcription factor in rats fed by sucrose-rich diet, namely one nucleus was PDX1-positive, in contrast to the other one [2]. Since PDX1 is normally expressed only in insulin-producing β-cells, emergence of this factor in acinar cells suggests the potential of 2N exocrine cells to transdifferentiate.

Objectives: The goal of this study was to establish whether there is a change in ultrastructural features in 2N acinar cells, especially regarding the fate of the nuclei and zymogen granules (ZG), after chronic sucrose ingestion.

Materials & methods: Fourteen young adult Wistar rats fed with commercial rodent chow, were divided in two groups. Control (C) group had access to tap water, and sucrose (S) group to 10% sucrose solution in tap water, both ad lib. After three weeks, pancreas was fixed and processed for electron microscopy. Morphometric measurements were taken regarding number of ZG in acinar cells.

Results: The number of ZG was signifficantly decreased in 2N acinar cells in S group, relative to both 1N cells of S group as well as 1N and 2N cells of C group. Also, large autophagic vacuole filled with ZG and unidentified debris, was observed in 2N cell at the position previously occuppied by one of the nuclei, corresponding to it by size.

Conclusion: Since it is known that acinar cells can survive the autophagy of one nucleus [3], we propose that specific population of 2N acinar cells with only one nucleus positive to PDX1 is capable of autophagy of PDX1-negative nucleus and ZG, during the process of transdifferentiation. It could be concluded that sucrose-rich diet has a potential to induce cell reprogramming of 2N acinar cells in vivo toward typical 1N insulin-producing β-like cells.

[1] PS Oates & RG Morgan, Am J Anat. 1986, 177:547-54.
[2] M Ukropina, V Petković, M Čakić-Milošević, MC 2013 Regensburg, Proceedings pp. 135-136.
[3] 3. Haschek and Rousseaux"s Handbook of Toxicologic Pathology. 3rd Edition. Academic Press Imprint (Elsevier): London, UK; 2013:3064pp.

LBN.P006
3D cell culture model for investigation of the role of estradiol in the human endocervical cells

M. Curlin[1], N. Bradaric[2]

[1]University of Zagreb School of Medicine, Center for Electron Microscopy, Zagreb, Croatia
[2]University of Zagreb Faculty of Science, Department of Biology, Zagreb, Croatia

Introduction: The secretory epithelium of the human endocervix secretes mucus whose biochemical, biophysical and functional properties change during the menstrual cycle and, at the time of ovulation, gains properties that allow sperm survival and fertilization. The mechanism behind the role of estradiol in the regulation of these changes is still unknown. There are also limited data concerning the inflammatory role of estradiol in the cervical tissue. Many studies have shown that estradiol inhibits generation of proinflammatory factors, suggesting an anti-inflammatory role of estrogen. In the uterine cervix, the expression of estrogen receptor α was significantly higher in cervical carcinomas and chronic cervicitis compared to that in the healthy cervix. On the other hand, it is assumed that estrogen supports cancerogenesis in the breast tissue, ovaries and cervix by its crosstalk to inflammatory cytokines and pathways. Since there are many unanswered questions and gaps in our knowledge regarding the role of estrogen in the cervix, more studies of the regulatory and inflammatory roles of estrogen are needed. In order to investigate endocervical tissue under controlled conditions and using an experimental model that highly resembles the *in vivo* conditions, it is required to develop a 3D cell culture of highly differentiated and functional endocervical cells with clearly defined polarity, intercellular junctions, and mucin secretion ability which is not possible with the traditional cell culture model.

Objectives: The goal of this pilot study was to establish and assess the morphology and functionality of the hystotypic 3D cell culture model of human endocervical tissue by using a human endocervical epithelial cell line, extracellular matrix (ECM) and transwell insert as a scaffold that allows cells growth at the "medium - air" interface and to assess the influence of estradiol to cell morphology and secretory activity of the differentiated cells.

Materials & methods: Human endocervical epithelial cells End1/E6E7 were seeded on pre-coated ECM transwell inserts and cultivated in different time periods at which cells achieved complete differentiation, and exposed to ß-estradiol at different incubation times. Cell growth, differentiation and secretory activity were assessed by cytological, cytochemical, immunocytochemical methods and light and electron microscopy.

Results: The first signs of differentiation appeared on the sixth day of cultivation, but the full differentiation and functionality in the sense of mucin production was achieved by the 18th day. The uniformity of mucin production in the cells between days 18 and 24 enabled the application of the established 3D culture in the experiment of cell exposure to estradiol. The cells exposed to estradiol showed enhanced formation of tight and adherent junctions between the cells, but the reduced accumulation of mucin within the cells.

Conclusion: In this study, a functional experimental model comprising a 3D culture of human epithelial endocervical cells and a set of assessment methods has been established. The ability of the cultured cells to show the morphological and functional changes after exposure to estradiol, makes this model a useful tool for investigation of the role of estradiol in the endocervical cells.

Figure 1: Workflow of the 3D cell cultivation and assessment by cytological, cytochemical, immunocytochemical methods and light microscopy.

Figure 1

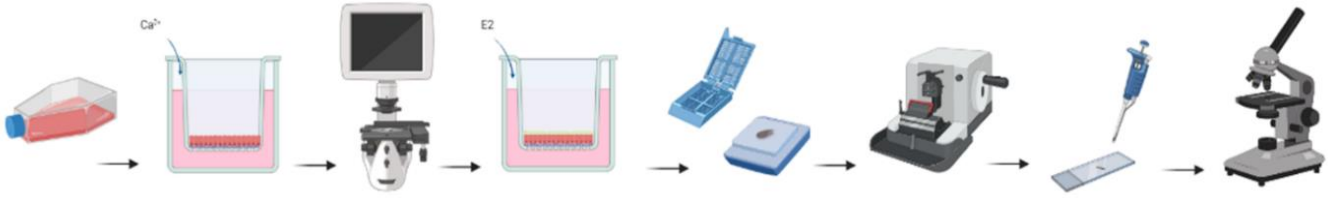

LBN.P007
Morphological and ultrastructural investigations of zygospores of the streptophytic green algae *Mougeotia* and *Spirogyra*

C. Permann[1], A. Andosch[2], K. Herburger[3], S. Obwegeser[1], A. Holzinger[1]

[1]University of Innsbruck, Innsbruck, Austria
[2]University of Salzburg, Salzburg, Austria
[3]University of Copenhagen, Frederiksberg, Denmark

The streptophytic green algae class Zygnematophyceae is the immediate sister lineage to embryophytes. Investigations on their physiology and biology, especially their resistance, are essential in expanding our knowledge on the evolution of land plants. Many studies conclude a high tolerance against abiotic stresses, like high irradiation, freezing events or desiccation. However, as most investigations concern streptophytic green algae in a vegetative state, less is known about the role of sexual reproduction. Conjugation, a special from of sexual reproduction found in Zygnematophyceae might represent a key adaptation to terrestrial habitats. This process is not neccesarily dependent on the availability of water and the formed zygospores are characterized by a multilayered thick cell wall, leading to a protective structure. In the present study we collected field samples from the Austrian alps, containing conjugating stages and/ or zygospores of the genera *Mougeotia* and *Spirogyra*. In *Mougeotia* we were able to demonstrate all stages of an extragametangial anisogamous scalariform conjugation. A 4-month maturation process led to an increase of storage compounds, mainly lipids in the cell lumen, while the chloroplasts seemed to undergo a process of reduction. Scanning electron microscopy revealed the different surface structures of the two *Mougeotia* species, crucial for species assignment. Transmission electron micrographs of high-pressure frozen or chemically fixed material showed an electron dense mesospore in both genera, while it was thicker in *Mougeotia*. This middel layer also seemed to be the surface structure defining part of the zygospores. The exo- and endospore had a distinct orientation of the microfibrils in *Spirogyra,* which was not observed in *Mougeotia*. Pectins (homogalacturonan (HG)), hemicelluloses (xyloglucans/ xylans), extensins and arabinogalactan proteins (AGPs) were detected by glycan microarray analysis, all representing major land plant cell wall components. Overall, our multitechnical approach suggests a major reorganization of the cell wall during maturation in the zygospores of Zygnematophyceae. This process most likely is the basic fundament of their high resistance.

LBN.P008
Histological organization of the endocrine pancreas in adult Balkan crested newt *Triturus ivanbureschi* (Amphibia, Caudata, Salamandridae)

M. Ukropina[1], M. Čakić-Milošević[1]

[1]University of Belgrade, Faculty of Biology, Belgrade, Serbia

Introduction: Amphibians are at the moment the most endangered vertebrates worldwide. One of the important factors contributing to their endangerment is pollution. Although it is well known that histological organization of various organs is often affected by pollution, that aspect is relatively understudied. At the same time, there is a paucity of data concerning the histology of non-mammalian vertebrates overall, in particular of tailed amphibians. Hence, further studies are needed regarding the baseline histological organization in this group of animals.

Objectives: This study was conducted in order to describe the histological organization of the endocrine pancreas in so far uninvestigated species *Triturus ivanbureschi*.

Materials & methods: Two adult individuals of *T. ivanbureschi*, one of each sex, were collected from the pond on mountain Dukat, Serbia. The pancreas was routinely prepared for both light and electron microscopy. Hematoxylin & eosin, as well as Giemsa staining were employed.

Results: Light microscopy revealed individual as well as groups of endocrine cells scattered among exocrine acini. When in larger groups, endocrine cells are organized in aggregations of irregular shape, forming anastomosing 1-2 cell wide cords along the blood vessels. Electron microscopy showed the presence of three different types of endocrine cells. Two types are characterized by oval shape, sometimes with processes, of which one type has electron-dense granules with translucent halo, and the other one has lightly contrasted granules without a halo. Cells of the third type are elongated with electron-dense granules, also without a halo.

Conclusion: Histological organization of the endocrine pancreas described earlier in some other newt species resembles mammalian pancreatic islets, with a core of B cells surrounded by a mantle of A cells [1]. In contrast, clusters of endocrine cells in the pancreas of *T. ivanbureschi* are rather similar to chord-like islets described for Italian cave salamander *Hydromantes ambrosii* [2]. Morphological data obtained in the present study are not in line with those previously published by others, so they are not alone sufficient to identify cell types and hormones contained in their granules. For example, B cells in Japanese newt *Cynopus pyrrhogaster* are described as oval or elliptical and granules of B cells were without the halo [3], while in B cells of *T. carnifex* granules have clear halo [1]. In *T. ivanbureschi*, however, granules with halo are evident in irregularly shaped cells. Thus, specific identification of granules content is needed to precisely determine endocrine cell types in the pancreas of *T. ivanbureschi*.

[1] S Buono & R Putti, Ital J Zool, 2004, 71: S2, 85-88.
[2] G Faraldi et al., Cell Mol Biol (Noisy-le-grand), 1993, 39(3):269-78.
[3] T Oikawa et al., Jikken Dobutsu. 1992, 41(4):505-14.

LBN.P009
Microscopic study of ferroptotic death of β-cells in diabetogenic conditions in vitro

M. Markelić[1], A. Stančić[2], T. Saksida[2], M. Vučetić[3], I. Grigorov[2], V. Martinović[2], K. Veličković[1], V. Otašević[2]

[1]University of Belgrade-Faculty of Biology, Department of Cell and Tissue Biology, Belgrade, Serbia
[2]Institute for Biological Research, Department of Molecular Biology, Belgrade, Serbia
[3]Centre Scientifique de Monaco, Medical Biology Department, Monaco, Monaco

Feroptosis is a recently described, programmed form of cell death. It is iron-dependant and characterized by the accumulation of lipid peroxides and reactive species. The main pathological hallmark of diabetes is β-cell loss, and so far, several types of β-cell death have been described. However, involvement of ferroptosis in β-cell loss induced by diabetogenic factors is still unexplored.

The aim of this study was to investigate potential involvement of ferroptosis in the regulation of β-cell loss in diabetes. For that purpose Rin-5F pancreatic β-cells were treated with well-known diabetes-mimicking agents: high glucose (HG; 25 mM), hydrogen peroxide (H_2O_2; 75 μM) and streptozotocin (STZ; 10 mM)) for 12h in the absence or presence of ferrostosis inhibitor, ferrostatin-1 (Fer-1, 1.5 μM). As a positive control, an inducer of ferroptosis RSL3 (3 μM) was used. Cells were prepared for flow citometry (death cell assay – propidium iodide (PI) staining; dihydrorhodamine 123 (DHR) reactive oxygen species (ROS) detection) and microscopic analyses (phase contrast analysis of cells viability, morphology and cell confluence; Sudan III detection of neutral lipids and lipofuscin; Prussian blue detection of intracellular iron accumulation; C11-BODIPY detection of lipid peroxides and immunofluorescence detection of phospho-NFE2-related factor 2 (pNrf2)).

Our results demonstrated that mimicking diabetic microenvironment by HG, STZ and H2O2 induced ferroptosis of β-cells *in vitro* (Fig. 1), since observed alterations were similar to those induced by RSL3. As we observed microscopically, total cell number decreased, percentage of dead PI+ cells increased and cell changed their morphology from typical to spherical and detached. In addition, increased accumulation of lipid peroxides, ROS, lipids and/or lipofuscin and iron were observed after these treatments. Fer-1 rescued cells from death after all treatments, along with abolishing the effects of those treatments on ROS, lipid peroxides and iron content. Further, Fer-1-induced activation of Nrf2, which is well known as an antioxidant transcriptional factor that regulates level of many of the ferroptosis-related molecules including those involved in metabolism of GSH, iron and lipids. Taken together, our results demonstrated ferroptosis involvement in the β-cell loss under diabetogenic conditions, thus proposing it as a new potential target in the diabetes therapy approach.

Figure 1. Demonstration of ferroptotic-related alterations of Rin-5F pancreatic β-cells treated with ferroptosis inducer RSL3, high glucose (HG), hydrogen peroxide (H_2O_2) or streptozotocin (STZ) in the absence or presence of ferrostosis inhibitor, ferrostatin-1 (Fer-1)

Figure 1

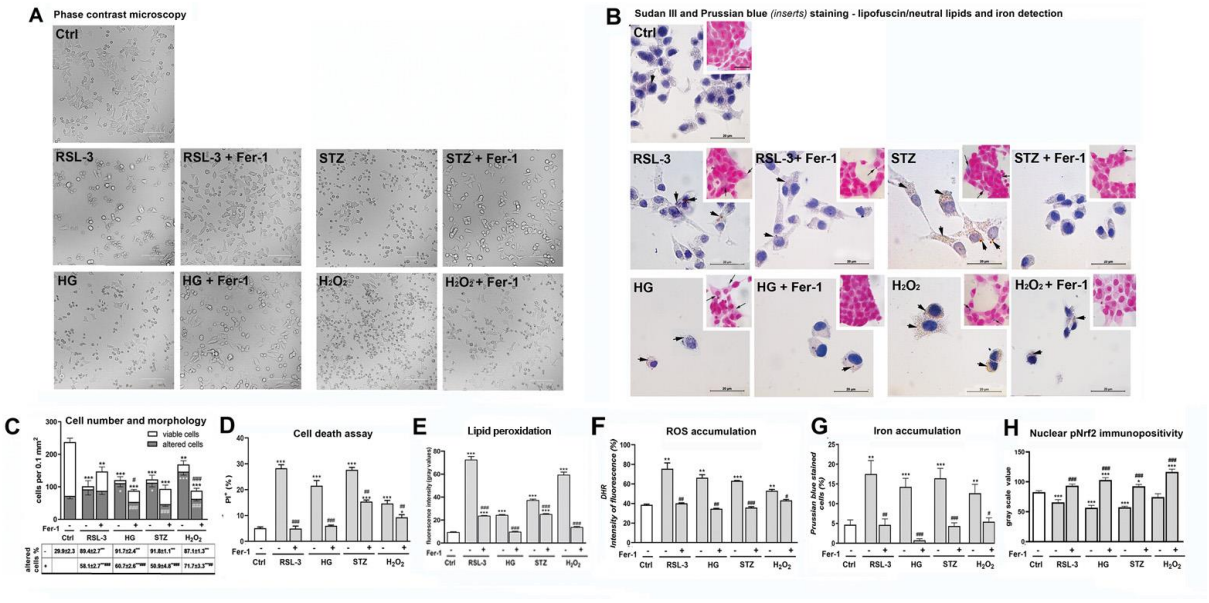

LBN.P010
Feeding apparatus of microscopic animals: new approach to study tardigrades with confocal laser microscopy.

E. Massa[1], L. Rebecchi[1], R. Guidetti[1]

[1]University of Modena and Reggio Emilia, Life Sciences, Modena, Italy

Introduction: Tardigrades (aka waterbears, Fig. 1A-B) are translucent eight-legged animals smaller than 1 mm distributed all over the word. They have been discovered only after the microscope invention and their taxonomically relevant anatomical structures are few due to their size, e.g. the cuticle ornamentation, claws, and feeding apparatus (FA, Fig. 1B-D). These are constituted by autofluorescent molecules (excitation λ 488 nm, emission λ 509-614 nm) historically reported as α-chitin bound with proteins.

Objectives: The morphological comparison of the FA in different lineages of Tardigrada is here explored to increase the number of structures useful for systematic purposes and to better understand the molecular nature and the functioning of this vital apparatus.

Materials & methods: seven species of tardigrades (at least 5 animals/species), from both Heterotardigrada and Eutardigrada classes, have been analysed via confocal laser scanning microscope (CLSM, Leica TCS SP8). Alive animals were singularly mounted on slide with distilled water (dH2O) after their staining with the chitin bonding stain Calcofluor White (CFW, 1:50 in dH2O for 1h; excitation λ 405 nm, emission λ 425-470 nm). The imaging was performed with both the autofluorescent molecules and the fluorescence of chitin bound with CFW, the curves of emission were tested with λ2 mapping analysis.

Results: In all the CFW stained specimens the chitin fluoresced. This finding confirms the chitinous composition of the cuticle and the presence of a chitinous lining in the foregut (Fig. 2A) and in the hindgut of the animals. The FA fluoresced if excited with both the 405 and 488 laser lines (Fig. 2A-B). Autofluorescent areas (Fig. 2B) never overlapped the areas stained with CFW (Fig. 2A) and their emission signals were distinguishable. Autofluorescent areas perfectly overlapped all the structures of the FA, but the aragonite stylets, visible in bright field microscopy. Besides, CFW revealed chitinous structures that have been rarely observed before and usually too thin to be appreciable in light microscopy. Most of the structures of the FA are composed of an autofluorescence unidentified substance that is lined in the outside (e.g. stylet furcae, Fig. 1C-D, 2C) and/or the inside (e.g. the placoids; Fig. 1C-D, 2C) with chitin.

Conclusion: Some structures of the FA identified with the CFW staining are morphologically specific of different lineages and hence suitable for systematic purposes. The position of the autofluorescent areas (Fig. 2B) suggests that their molecules are harder than chitin and could support the attach of the musclesand/or oppose resistance to the sucking force and to continuous movements of the furcae during the feeding. As historically stated, the autofluorescent substance could be chitin bound with protein that, whilst stiffing the chitin, hides the bonds β1-4 in the polysaccharide, i.e. the substrate of the CFW. The chitinous structures (Fig. 2A) are instead localized where higher flexibility is required, e.g., in the stylet"s envelopes (Fig. 1C-D).

Figure 1: Tardigrade (Macrobiotidae): A. Whole specimen, lateral view, scanning electron microscope; B. Whole specimen, dorsal view, light microscope; C-D. Schematic drawn of the feeding apparatus (C. dorsal view, D. lateral view). Bar 100 µm.

Figure 2: Feeding apparatus of a Macrobiotidae species, CLSM maximum projection, example: A. Calcofluor White; B. Autofluorescence; C. Overlay of A and B. Bars 10 µm.

Figure 1

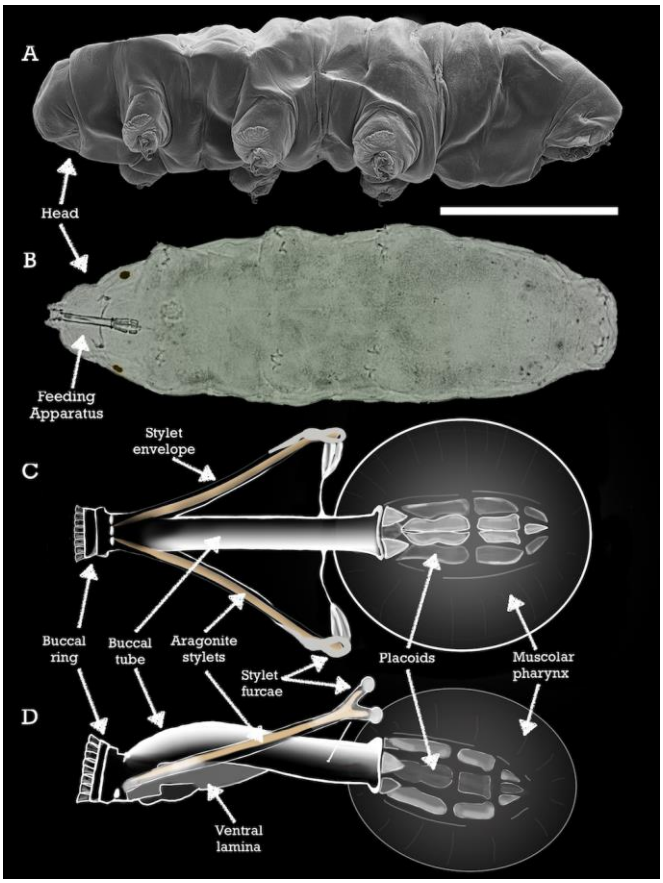

Figure 2

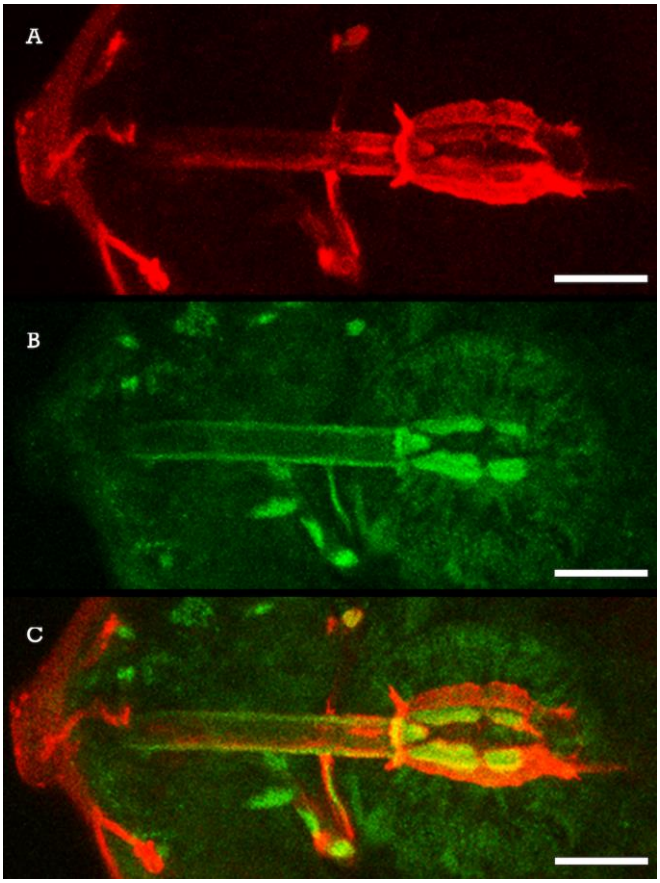

LBN.P011
Effect of short-term fasting on distribution of activated insulin receptor in somatotrophs during diestrus and proestrus

T. Dakić[1], M. Markelić[2], I. Lakić[1], T. Jevdjović[1], K. Veličković[2], A. Ružičić[1], N. Jasnić[1], S. Djurašević[1], J. Djordjević[1] P. Vujović[1]

[1]University of Belgrade-Faculty of Biology, Department of Comparative Animal Physiology and Ecophysiology, Belgrade, Serbia
[2]University of Belgrade-Faculty of Biology, Department of Cell and Tissue Biology, Belgrade, Serbia

Although initially recognized as a peripherally secreted and acting hormone, insulin is now known to be involved in various processes in central nervous system (CNS) such as regulation of energy homeostasis. Our previous results suggest short-term fasting promotes hypothalamic insulin synthesis. As previously demonstrated, insulin suppressed synthesis and secretion of growth hormone (GH) in pituitary somatotroph (GH^+) cells, acting both directly on them via its receptor (IR) or indirectly via hypothalamus. GH has been well known for its anabolic, antilipogenic and prolipolytic effects, and as previously shown, its serum levels increased during fasting. The main goal of this study was to elucidate whether insulin affects GH and IR levels in GH^+ cells during the short-term fasting in female rats. Animals in proestrus and diestrus were used to determine whether the estrous cycle plays a role in fasting-induced response of the pituitary gland (PG) in terms of the examined parameters.

Two-month-old female rats were divided in four groups (n=9) according to feeding status and estrous cycle phase: i) diestrus-fed, ii) diestrus-fasting, iii) proestrus-fed, and iv) proestrus-fasting group. Food deprivation started at 6 p.m. and lasted for 6h. After sacrifice, serum and cerebrospinal fluid (CSF) were collected, while pituitary glands were removed and prepared for western blot (IR, IRp, GH) or immunofluorescence analyses (GH and phospho-Tyr1361 IR - pIR).

Serum insulin levels decreased significantly in both fasting groups. However, insulin CSF levels remained unaltered when compared to fed animals. Our results demonstrated decreased GH content in PGs during fasting in comparison to fed animals, especially during diestrus. To examine insulin action in PGs, total IR and IRp levels were analyzed. No significant changes were noted in pituitary IR expression nor activation (ratio of IRp/IR) among the analysed groups of animals. However, immunofluorescence analysis uncovered a different pattern of IRp localization in GH^+ cells of fed and fasted animals. In addition to membranes and cytoplasm, activated IR was also detected in the nuclei of these cells. However, while increased membranous and cytoplasmic IRp immunopositivity were detected after the short-term fasting, nuclear translocation was less frequently noticeable in fasting animals, especially those in proestrus.

The absence of significant IR dephosphorylation during short-term fasting suggests the importance of insulin effects in GH synthesis/release, even when peripheral level of insulin is decreased. Canonically, insulin exerts its effects by binding to its receptor on the cell surface, thus activating the downstream signaling cascades. Insulin-IR complex is rapidly internalized in order to be either recycled back to the membrane or to be degraded in lysosomes. However, a growing body of evidence shows that IR also translocates to the nucleus, where it acts as a transcriptional factor. To our best knowledge this study is the first one to report IRp translocation to nuclei of somatotrophs. Since correlation between GH levels and nuclear pIR translocation was noted in GH^+ cells, it is possible that nuclear IRp is involved in GH synthesis. Future studies are needed to elucidate mechanisms of nuclear IRp action in GH^+ cells and its adaptive significance.

LBN.P012
Effects of prolonged oral intake of cadmium on goblet cells in the rat small intestine and possible protection by probiotic bacteria

M. Čakić-Milošević[1], R. Glišić[2], M. Ukropina[1]

[1]University of Belgrade, Faculty of Biology, Belgrade, Serbia
[2]University of Kragujevac, Faculty of Science, Kragujevac, Serbia

Introduction: Cadmium (Cd) is a toxic heavy metal present in the atmosphere, water and soil. Ingestion of contaminated food and water is the most common route of its entry into the human body. Upon intestinal absorption, a substantial amount of orally ingested Cd accumulates in the intestinal mucosa. Although remains shortly therein, Cd can cause mucosal injury, which further increases its uptake and potentiates systemic toxicity [1]. Intestinal goblet cells (GC) synthesize and secrete mucus which is an integral part of the enteric defence against various harmful agents. The composition and amount of mucus can be modified in response to different physiological and pathological conditions and through interaction with intestinal microbiota [2].

Objectives: The purpose of this study was to investigate whether prolonged Cd intake adversely affects enteric GC and if it does, to assess possible protective effects of simultaneous administration of PB.

Materials and methods: Male Wistar rats (n=24) kept under standard laboratory conditions were used for this study. Animals were divided into 4 equal groups and treated as follows: control group - tap water (TW) and commercial pelleted food (CF), ad lib; PB group - TW, CF supplemented with probiotic (PROBIOTIC®, Ivancic i sinovi, d.o.o.); Cd group - TW with dissolved cadmium-chloride (Fisher Scientific, 70 ppm) and CF; PB+Cd group - TW with dissolved cadmium-chloride and CF supplemented with probiotic. After 5 weeks of treatment, animals were sacrificed and the proximal part of the jejunum was dissected and routinely processed for light microscopy. Five µm thick paraffin sections stained with alcian blue/nuclear fast red were analyzed and photographed (Leica DMLB light microscope, Leica Microsystems, Wetzlar, Germany). Morphometry was performed using a freely available ImageJ analysis software. Statistical analysis was performed by a two-tailed Student"s t-test, with data reported as means ± s.e.m. and statistical significance set at $P<0.05$.

Results: Representative micrographs from control and treatment groups are shown in Fig. 1. GC are least common in the Cd group (Fig. 1C) while they are the most prominent in the PB+Cd group (Fig. 1D).

Figure 1: Intestinal mucosa of rats from control (A), PB (B), Cd (C) and PB+Cd (D) group. GC - blue.

Results of the morphometric analysis are summarized in Table 1. No treatment affected the number of GC inside crypts. In villi, Cd intake decreased the number of GC in comparison to control, while after combined treatment the number of GC increased in comparison to PB group.

Table 1. GC in villi and crypts (number per 1000 µm of subepithelial lamina length).

Conclusion: Probiotic bacteria may protect the intestinal epithelium from injury caused by prolonged oral intake of Cd. Obtained results suggest that protective effects of PB, besides already known sequestration of Cd [3], could be achieved through regulation of number and activity of GC.

[1] R Świergosz-Kowalewska, Microsc Res Tech, 2001, 55:208-222.
[2] K Gillois et al., Microorganisms, 2018, 6:53.
[3] Q Zhai et al., AEM, 2013, 79:1508-1515.

Figure 1

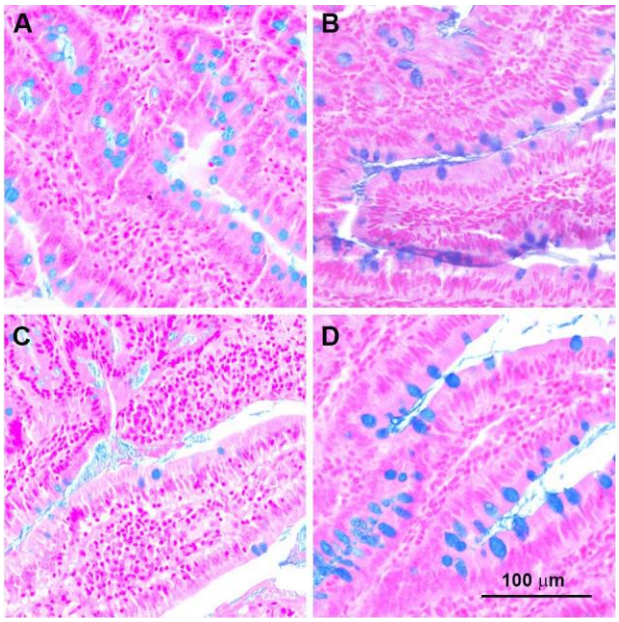

Figure 2

Group	Villi	Crypts
Control	32.9±2.27	19.0±2.19*
PB	29.1±2.32	22.2±2.68
Cd	18.8±1.53#	17.3±1.73
PB+Cd	38.8±2.09†	23.0±2.78*

* in comparison to villi
# in comparison to control
† in comparison to PB

LBN.P013
A pilot microscopic study on bacteriophages using TEM and cryo-TEM

K. Hrubanova[1], T. Heuser[2], Z. Kaźmierczak[3,4], K. Dabrowska[3,4], M. Drab[3], V. Krzyzanek[1]

[1]Czech Academy of Sciences, Institute of Scientific Instruments, Electron Microscopy, Brno, Czech Republic
[2]Vienna BioCenter Core Facilities, Electron Microscopy Facility, Vienna, Austria
[3]Polish Academy of Sciences, Hirszfeld Institute of Immunology and Experimental Therapy, Wroclaw, Poland
[4]Regional Specialist Hospital, Research and Development Center, Wroclaw, Poland

Bacteriophages are one of the most diverse group of biological entities in Earth"s biosphere. Phages are perfectly capable of distinguishing bacterial cells from mammalian cell. Even more, phage are highly host-specific, typically infect and kill an individual species [1]. Therefore, the most rewarding application of bacteriophages is based on their potential to supersede antibiotics. In the institute of the Polish partner (HIIET) for over 40 years they utilize this differential power of phage to safely cure human patients infected with antibiotic-resistant bacterial pathogens (phage therapy). Previously, it has been shown the ability of bacteriophage T4 and its sub-strain HAP1 to bind to cancer cells and to reveal antimetastatic activity in a mouse B16 melanoma model. This effect was significantly stronger for HAP1 compared to the parental strain [2]. In this pilot study we have focused on structural characterization of T4 phage and HAP1 phage using transmission electron microscopy. Our main aim was to optimize protocols in sample preparation and microscopical measurements for our follow-up research.

T4 phage was purchased from ATCC (Rockville, MD, USA) and HAP1 phage from IIET (Wroclaw, Poland). Both were cultured on an *Escherichia coli* B host (IIET) in medium LB-Broth high salt for 10 h at 37 °C. Phage lysates were purified by filtration through polysulfone membrane filters. Phage lysate was tested for phage concentration by determination of phage titer after serial dilution with PBS.

The morphology of the isolated phage was observed by two different methods TEM (Morgagni, FEI) on negative stained samples and cryo-TEM (Glacios, Thermo Fisher Scientific) of phages vitrified by plunge freezing. For TEM analysis 5 µl phage suspension was placed onto a copper grid containing a thin layer of carbon. After one minute incubation, the droplet was carefully removed with a piece of filter paper and subsequently negative stained by adding a 2% uranyl acetate staining solution (5 µl, 1 min). After the grids dried, they were analyzed by TEM. For cryo-TEM experiments 4µl droplet of the phage suspension were applied to a Quantifoil grid (Cu 200 mesh R1.2/1.3) and vitrified by immersion freezing into liquid ethane using a plunge freezer (EM GP, Leica) and observed at temperatures below -160°C [3].

We compared two microscopic techniques TEM and cryo-TEM that we used for morphological analysis of two types of bacteriophages T4 and HAP (Fig 1, Fig 2). In the Fig. 2 different contrast of capsids was detected – the phage at the top contains complete DNA inside a head and uncontracted tail; the phage below has contracted sheat and no DNA inside a head. TEM can be considered as a very efficient tool for direct morphological analysis of single phages. Our experiments represent pilot study to optimize sample preparation and technical setting. We believe that this study will be of significant assistance in our further research in the field of phage therapy.

Figure 1: Representative TEM micrograph of negative stained bacteriophages HAP1.

Figure 2: High-resolution micrograph of deep frozen bacteriophages T4 obtained by cryo-TEM.

[1] Majevska J. et al: *Viruses* 7 (2015), 4783-4799
[2] Dabrowska K. et al: *Anticancer Research* 24 (2004), 3991-3996
[3] Pany A. et al: *Int J Cosmet Sci* 43 (2021), 263-268
[4] The research was supported by the Czech Academy of Sciences (project MSM100652102), National Science Centre in Poland, grant UMO-2015/19/N/NZ4/03609

Figure 1

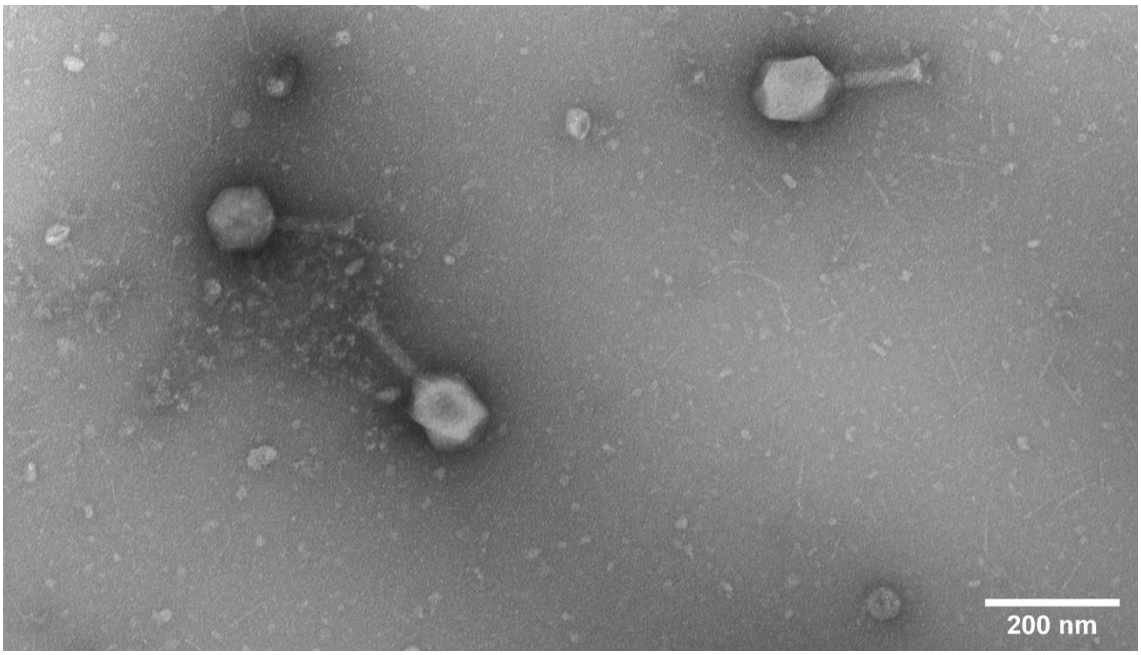

Figure 2

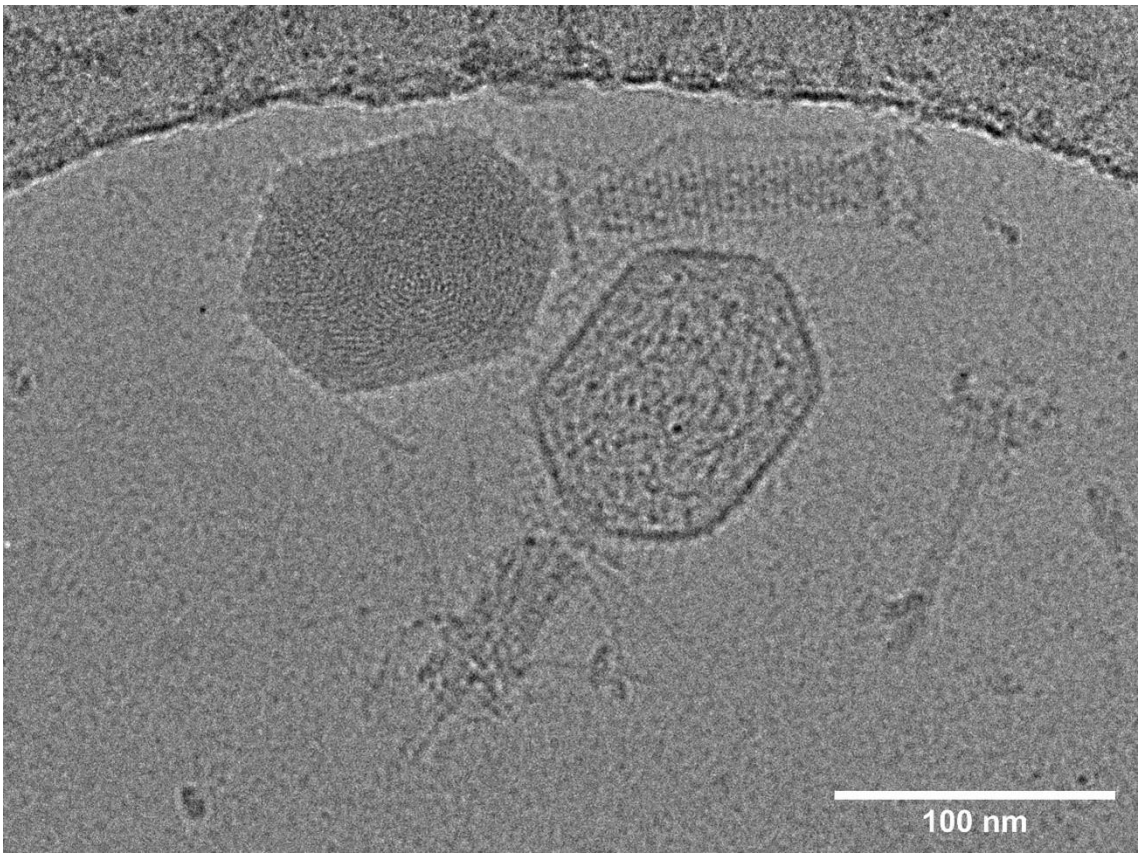

LBN.P014
Imaging *in vitro* microtubules treated by nanosecond pulsed electric field

T. Zakar[1], D. G. Blanco-Campoy[1], M. Cifra[1]

[1]IPE, Bioelectrodynamics, Prague, Czech Republic

Microtubules (MTs) are cylindrical cytoskeletal polymers indispensable for numerous vital cellular activities such as maintenance of cell shape, division, migration and ordered vesicle transport powered by motor proteins. One of the core strategies used in cancer pharmacology is to disrupt the integrity of MTs in the mitotic spindle thus blocking and/or restraining mitotic division. It has been shown recently that MTs can be disrupted with nanosecond electric pulses (nsEPs) in the cell. However, the direct effects of nsEPs on isolated, *in vitro* microtubules are yet unknown. Analysis of MT morphology and dynamics is dependent on the quality of MT imaging. Nanoscopic thickness of MTs presents a challenge regarding their microscopic imaging with a resolution high enough to identify individual MTs. In our current work we attempted to follow the morphological changes of MTs after nsEP treatment at different levels of resolution by several imaging techniques such as: phase contrast microscopy, differential interference contrast microscopy, holographic microscopy and atomic force microscopy.

LBN.P016
Characterisation of the multi-layered microstructure of *Patella caerulea* shell using Electron Backscatter Diffraction (EBSD)

K. Berent[1], A. Checa[2,3]

[1]AGH University of Science and Technology, Academic Centre for Materials and Nanotechnology, Krakow, Poland
[2]Universidad de Granada, Departamento de Estratigrafía y Paleontología, Granada, Spain
[3]CSIC-Universidad de Granada, Instituto Andaluz de Ciencias de la Tierra, Armilla, Spain

Calcified biomaterials produced by invertebrates are used as a source of inspiration for the biomimetics of novel materials. This is particularly the case of molluscs, which are the masters among metazoans in the production of both calcitic and aragonitic microstructures. The composition of shells is 95% to 99% CaCO3 and 1-5% organic macromolecules including proteins, polysaccharides and lipids. The mineral fraction gives the shell stiffness, strength and hardness, whereas the organic fraction provides ductility so that the final product has strength and toughness properties well above those of the individual components. Despite the few studies on limpets, it is clear that they secrete a variety of calcitic microstructures unparalleled by any other molluscan group. Specimens of the limpet *Patella caerulea* consists of three external calcitic layers. The very margin is made of a granular microstructure (G). The inner layers form irregular cross foliated (ICF) herringbone and concentric cross foliated microstructure (CCF). Internal to the calcitic layers, there is a thin aragonitic crossed-lamellar (CL) layer traversed by the myostracum.

The electron backscatter diffraction (EBSD) technique was performed to determine the microstructure and crystallographic orientations of the different shell layers. The samples were examined with an FEI Versa 3D FEG scanning electron microscope equipped with an EDAX Hikari CCD camera. Post-processing of the obtained data was done using TSL OIM v.7 analysis software. A cross-section of specimens was first mounted in epoxy resin, then ground to 4000 grit using SiC papers, polished using 1 and 0.25 µm diamond solutions and finally finished with 5 minutes of colloidal silica polishing. The experiments were done under a low vacuum atmosphere (40 Pa of H_2O) at an accelerating voltage of 15 kV. The present study for the shell structure of a limpet has obtained several new results including the crystallographic aspects. The crystalline units in the ICF layer gradually change their growth orientations from radial to commarginal. Moving toward the inner shell surface, there is a change in the crystallographic orientation and formed a CCF layer, composed of two sets. The average c-axis orientation is different for the two sets by about 90-110°.

Acknowledgements: This work was financed by the Polish National Agency for Academic Exchange (grant no PPI/APM/2018/1/00049/U/001).

LBN.P017
SEM analysis of soot particles collected by means of cascade impaction

P. Kozikowski[1], P. Sobiech[1]

[1]Central Institute for Labour Protection, Department of Chemical, Biological and Aerosol Hazards, Warsaw, Poland

There are many techniques for measuring nanoobjects, their agglomerates and aggregates (NOAA), during workplace testing. However, there are few methods for collecting the nanoobjects themselves from the air at workstations with the ability to simultaneously assess worker exposure to NOAA emissions. The most commonly used airborne particle sampling heads are limited to large fractions i.e. PM10, PM2.5, PM1 inhalable, thoracic and respirable fractions.

Electron microscopy is currently one of the fundamental techniques for the observation and analysis of nano-objects. Due to its easy preparation, very high resolving power (1 nm) and ability to perform chemical composition analysis, it has quickly become an indispensable research tool in many scientific and industrial fields.

Electron microscopy has many advantages that typical airborne particle concentration meters do not have. It enables identification of nano-objects together with accurate stereological description, making it complementary and supplementary.

The biggest obstacle of electron microscopy is its subjectivity, local character of analysis and lack of standardisation regarding recommended magnifications, number of examined fields and counting methods. Additionally, it is difficult to compare the obtained results with the parameters determined in real time.

The aim of the research work was to use a cascade impactor as a method for collecting the nanometre sized fraction – excluding the micrometer-sized one – for microscopic analysis. Cascade impactors do not require knowledge of the density or shape of the particles to determine their aerodynamic diameter, since it depends mainly on the design of the device and the measurement conditions. However, such a description is not always sufficient for risk assessment of nanoobjects. Observation of the deposited nanoparticles under an electron microscope is a complementary technique to the gravimetric methods and real-time counters as it enables nanoobjects identification together with a precise stereological description and chemical composition analysis.

SEM method improves the resolution capability of cascade impactors, which depends on the number of cascades. It also shows differences in particle morphology and chemical composition of the deposits. However, one should be mindful of the measurement parameters in order to avoid partial or complete overlapping of particles and agglomeration of nanoparticles, which may prevent stereological analysis.

Electron microscopy (SEM or TEM) combined with EDS single particle chemical analysis is not the standard for routine workplace assessments due to the high requirement of working hours. Nevertheless, the use of single particle analysis is currently the only approach to confirm the presence of nanomaterials. Wider adoption of the SEM technique, however, requires some automation of image acquisition as well as data analysis.

Figure 1

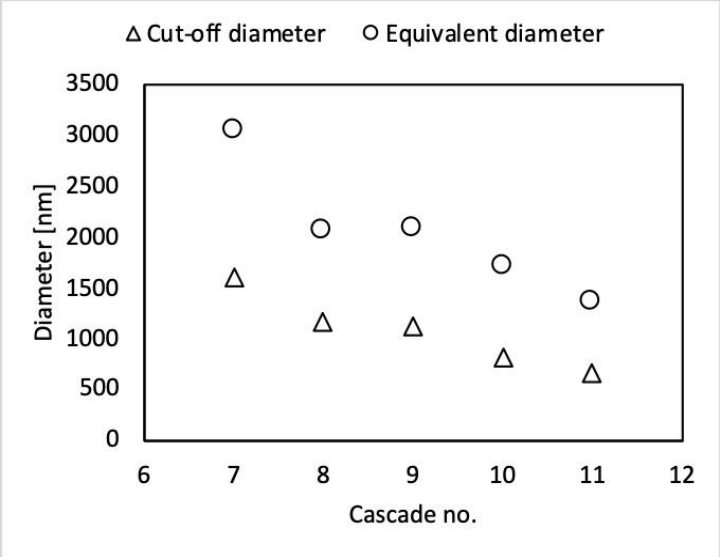

Figure 2

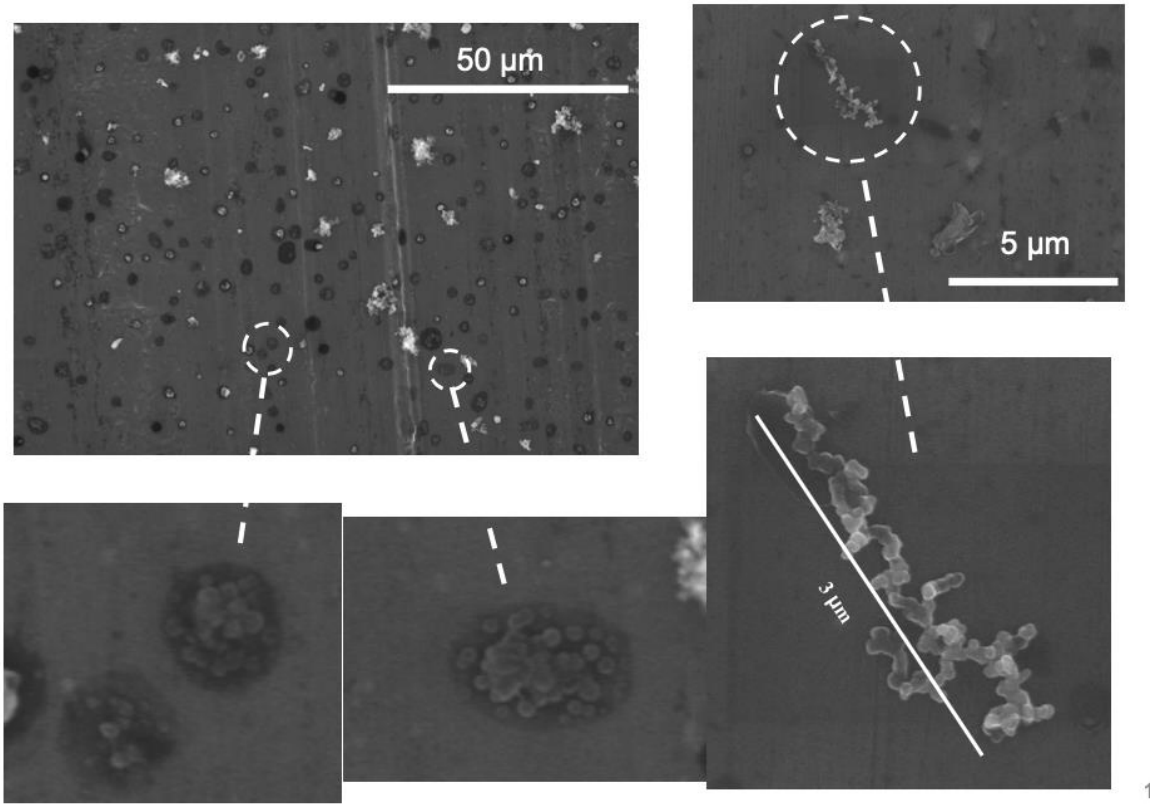

LBN.P018
Quantitative mapping of lithium in the scanning electron microscope using composition by difference method

D. Stowe[1], J. Osterreicher[2], S. Gneiger[2], C. Simson[2], A. Grossalber[2], S. Mu[3], J. Lee[1]

[1]Gatan Inc, PLEASANTON, United States
[2]Austrian Institute of Technology, LKR Light Metals Technologies, Ranshofen, Austria
[3]EDAX LLC, Mahwah, United States

Lithium-containing compounds and alloys are critical to technologies of the twenty-first century. Progress in Li-ion batteries lightweight structural alloy technologies has been remarkable given the lack of a method to determine lithium content at the microscale. Energy dispersive X-ray spectroscopy (EDS) in the scanning electron microscope (SEM) is commonly employed for microanalysis, however, this has is not suitable for elements with atomic number (Z) < 4 as the characteristic X-rays are easily attenuated by the sample or contamination and require specialized detectors. Even so, a limit of detection of ~20 wt. % Li and inability to perform quantitative analysis are significant issues [1]. However, quantification of Li in the SEM was demonstrated recently using a composition by difference method based on EDS and quantitative backscattered electron imaging (qBEI) [2]. EDS was used to quantify elements Z = 4 – 94, whilst qBEI was used to determine the mean atomic mass (the qBEI signal being a function of atomic number for Z = 1 – 94). The fraction of light elements (Z = 1 – 3) was calculated enabling detection of <5 wt. % Li in a MgLi alloy.

We extend the composition by difference method to generate quantitative, spatially resolved elemental maps of a Mg-Li-Al alloy. The sample was cast with nominal composition of Mg52.6-Li18.3-Al29.1 wt. % and prepared by argon milling using an Ilion™ polisher (Gatan Inc.). EDS and qBEI maps were recorded at 3 and 5 kV, respectively, selected to reveal the sample microstructure whilst also ensuring comparable sampling depths of the signals. Quantified EDS maps were captured using an Octane Elite EDS System and APEX software (EDAX LLC) and qBEI was performed using an OnPoint™ backscattered electron detector (Gatan Inc.). Image analysis was performed using DigitalMicrograph® software (Gatan Inc.).

Microanalysis revealed a eutectic microstructure (61:39 area) of Mg-rich matrix and Al-rich secondary phase. Magnesium, aluminum and, for the first time, lithium elemental maps were calculated using the composition by difference method of [2]. The matrix was determined to be Mg90.6-Li9.4 wt. % with little spatial variation; however, the second phase exhibited wide compositional variation from Mg26-Li11-Al63 to Mg10-Li43-Al-47 (mean Li content of 35.5 wt. %). These results agree well with thermodynamic calculations using Thermo-Calc software predicting a Mg-rich matrix with BCC Li configuration and an FCC AlLi secondary intermetallic phase capable of accommodating broad ranges of Mg-content. Despite care in sample handling some evidence of reaction with atmosphere was observed consequently, these regions were excluded from the calculated elemental maps.

The results demonstrate that single-digit mass percentages of Li can be mapped quantitatively in the SEM using the composition by difference method. Limitations are known to include surface topography as well as by the presence of unknown quantities of H, He or voids. Nevertheless, the method offers distinct advantages compared specialized "Li" EDS detectors.

References:
[1] P. Hovington *et al*., Scanning 38 (2016) p571–578
[2] JA. Österreicher *et al*., Scripta Materialia 194 (2021) 113664

Figure 1: a) Secondary and b) backscattered electron images and c) EDS map of MgLiAl alloy

Figure 2: Secondary electron image and elemental metal fraction maps; white pixels excluded from the analysis due to topographic influence (arrowed in the secondary electron image).

Figure 1

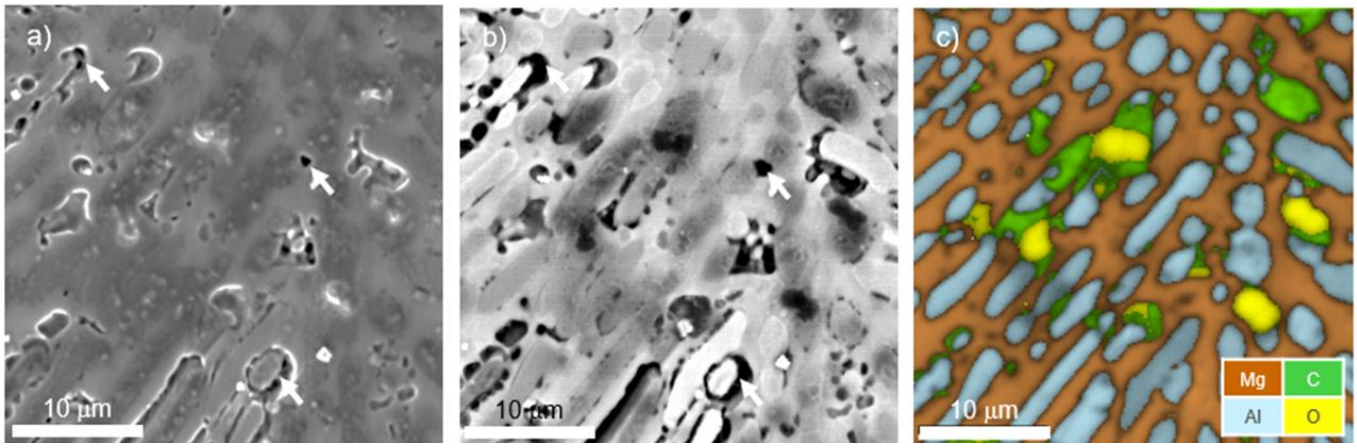

Figure 2

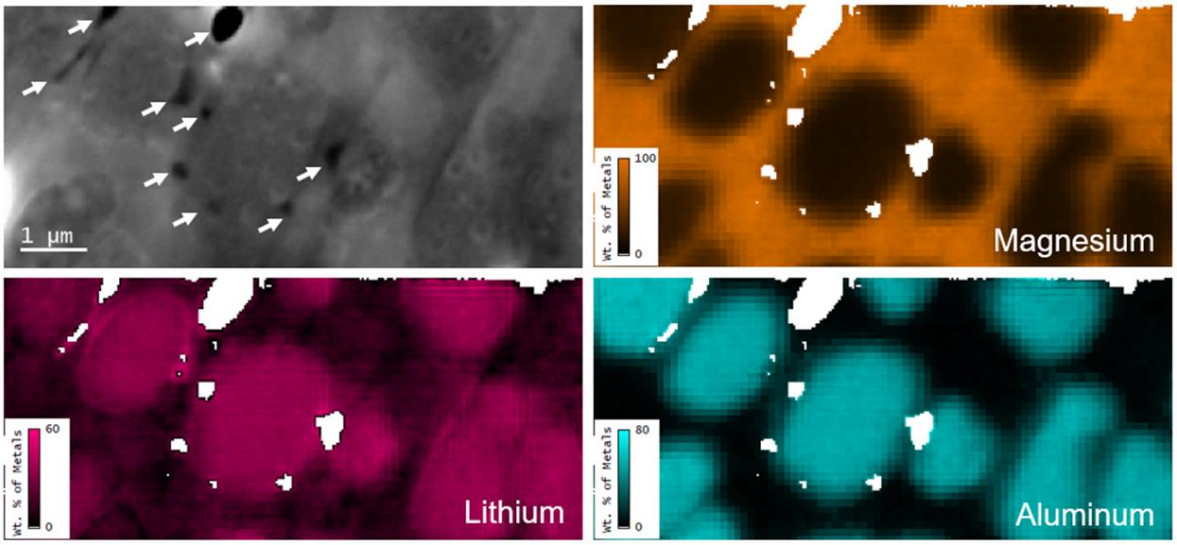

LBN.P019
LSPR evolution of copper nanoparticles during oxidation studied with environmental transmission electron microscopy and theoretical modeling

A. ziashahabi[1], S. Kadkhodazadeh[1]

[1]DTU, nanolab, lyngby, Denmark

Copper nanoparticles (NPs) have been intensively applied in different areas including catalysis, optoelectronics, plasmonics, and photovoltaics. However, the chemical instability of copper and its tendency to oxidize has hindered some of its applications, particularly in nanoplasmonics. Copper undergoes the Kirkendall oxidation process[1], leading to the formation of void(s) inside the metallic nanoparticle. In this respect, environmental Transmission Electron Microscopy (ETEM) provides a promising in-situ method to study in detail the changes occurring during the oxidation process.

In this work, we used ETEM to monitor the oxidation of copper NPs and study the localized surface plasmon resonance (LSPR) changes during this process. Annular dark-field scanning TEM (ADF STEM) microscopy was employed to investigate the formation of hollow oxide NPs. The LSPR evolution of the NPs was studied by electron energy-loss spectroscopy (EELS). The EELS spectra of the NPs were also simulated using the boundary element method (BEM) calculations and compared with the experimental results.

ADF STEM images and EELS spectra were obtained at 300 kV using an FEI TITAN ETEM instrument. The electron probe convergence semi-angle was set to 10 mrad, the ADF collection semi-angle to 28 mrad and the electron probe size was approximately 0.5 nm. The EELS spectra were recorded with an energy resolution of 0.15 eV, a dispersion per channel of 0.01 eV, and an acquisition time of ~ 50 ms. BEM calculations were performed to calculate the EELS spectra with MNPBEM toolbox[2]. The dielectric function of Cu and the optical constants of Cu2O were taken from the Palik[3] and Ribbing and Roos[4] databases, respectively. In the simulations, the position of the electron probe, beamwidth, and kinetic energy of the electrons was set according to the experimental values.

Figure 1 shows a series of ADF STEM images of a Cu NP oxidized under an O_2 atmosphere with 3 mbar pressure and temperature 150 ˚C. The EEL spectra of the NP obtained at different times during the oxidation are presented in Figure 2a. The simulated EELS spectra of the corresponding NP are depicted in figure 2b. For EELS simulations, the beam was placed at 2 nm out of the boundary of the particle in the X, and Y directions. From figure 2 one can conclude that both theoretical and experimental results show the redshift of the LSPR peak energy followed by broadening and damping during oxidation. In the EELS simulations, the spherical shape was assumed for the generated voids with the corresponding volume ratio for each NP.

In-situ STEM imaging of Cu NPs during oxidation reveals the Kirkendall oxidation mechanism, which is in agreement with theoretical simulations. These results imply the morphology and composition dependence of the LSPR energy.

Figure 1: ADF STEM images of a copper nanoparticle during the oxidation process at 150 ˚C.

Figure 2: a) experimental and b) simulated EELS spectra of the copper NP during the oxidation.

References:
[1] Susman, M. D., Vaskevich, A. & Rubinstein, I. *J. Phys. Chem. C* 120, 16140–16152 (2016).
[2] Hohenester, U. & Trügler, A. MNPBEM. *Comput. Phys. Commun.* 183, 370–381 (2012).
[3] *Handbook of optical constants of solids II*. (Academic Press, 1991).
[4] Ribbing, Carl G., and Arne Roos. "Copper Oxides (Cu2O, CuO)." *Handbook of optical constants of solids*. Academic Press, 1997. 875-882.

Figure 1

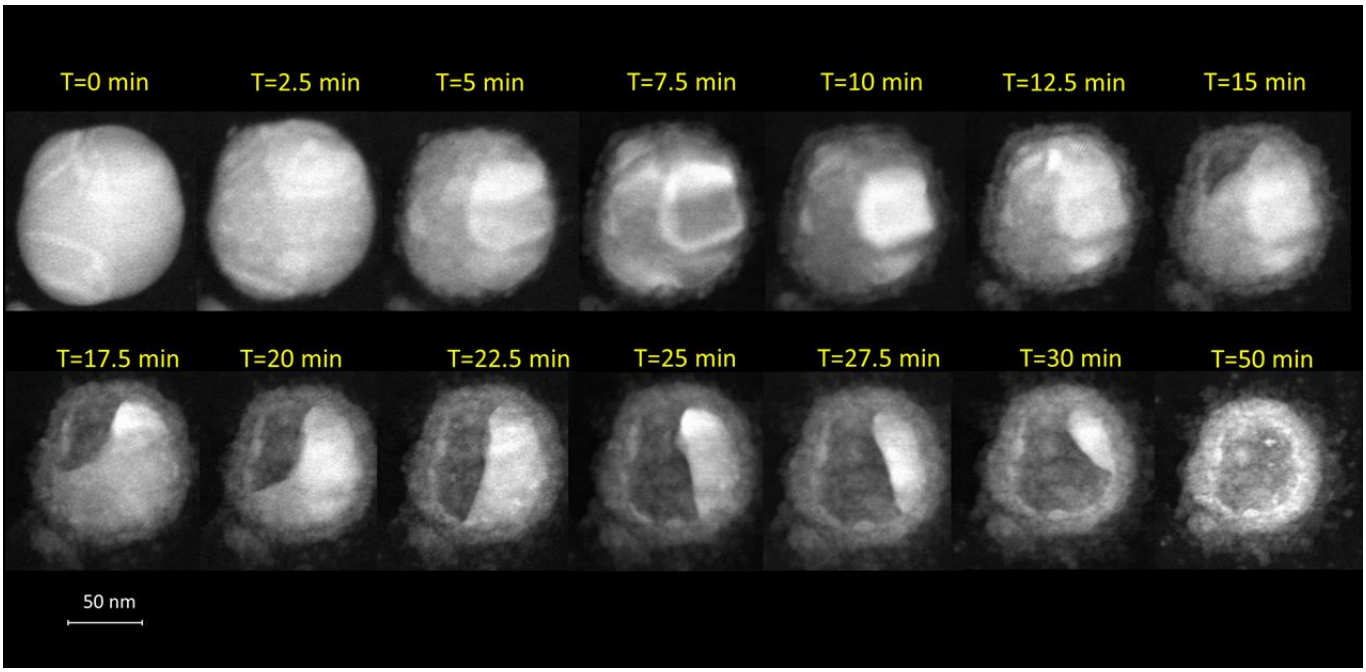

Figure 2

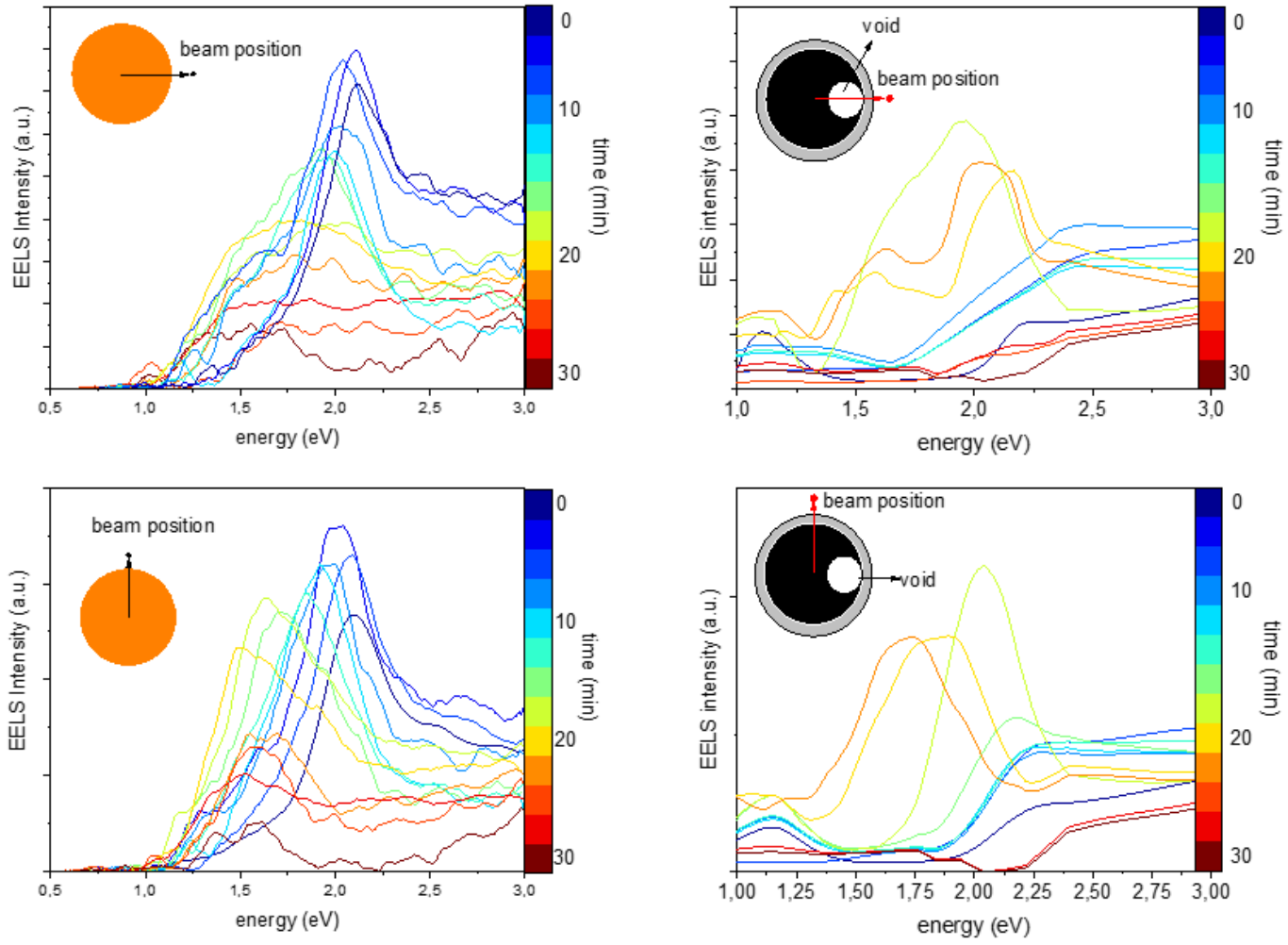

LBN.P020
Transmission electron microscopy study of rapidly solidified intermetallic alloys

A. Zięba[1], K. Stan-Głowińska[1], Ł. Rogal[1], L. Lityńska-Dobrzyńska[1]

[1]Institute of Metallurgy and Materials Science Polish Academy of Sciences, KRAKÓW, Poland

Production of intermetallic alloys for industrial applications requires the development of inexpensive and easy procedures. Problems are related to the high difference in melting point of constituent elements and phases accumulation in a narrow range of composition. Part of these inconveniences can be avoided by the melt-spinning method. Rapid solidification conditions enable limitation of diffusion and obtaining desired structure in a simple and fast process. Products are obtained in the form of fragmented brittle ribbons that can be pulverized and successfully applied in areas where a high specific surface is required (e.g. catalysis).

In this study, the characterization of aluminum intermetallic alloys from Al-Co and Al-Fe systems were presented. Materials with compositions related to selected intermetallic phases were induction melted from pure elements and then remelted and cast in the melt spinning process. The microstructure of obtained materials were examined by transmission electron microscopy using bright field, diffraction and high-resolution mode.

The Al-Co phase diagram in the vicinity of 23.5 at.% cobalt content shows many phases of similar chemical composition, but with different crystallographic structure, temperature range and stability [1]. These phases are structurally related and the transformations between them are found [2]. The melt spinning process produces a multiphase structure including metastable phases and a decagonal quasicrystal. The Al13Co4 alloy contains monoclinic Al13Co4, monoclinic Al9Co2 and a decagonal quasicrystalline phase. A crystallographic relationship between the monoclinic Al13Co4 and the decagonal quasicrystalline phase was observed in the high-resolution images. The Al5Co2 alloy contained a decagonal quasicrystalline phase in its entire volume.

Bases on the Al-Fe phase diagram [3], the Al13Fe4 and Al5Fe2 phases structurally related to the Al13Co4 and Al5Co2 were selected for the study. The Al13Fe+ rapidly solidified ribbon consists of monoclinic Al13Fe4 grains and aluminum solid solution, while the Al5Fe2 alloy showed a single-phase structure. Selected area electron diffraction patterns of this material showed superlattice reflections suggesting the presence of phases with a higher degree of ordering [4].

Obtained ribbons from Al-Co and Al-Fe systems were tested as catalysts. All examined materials revealed catalytic activity, but the best properties achieved single-phase materials. The structural investigation was necessary to establish factors determining catalytic activity and show the further direction of research.

Acknowledgments: This work was financially supported by the National Science Centre (NCN) Poland within project No. 2017/25/B/ST8/02804.

References:
[1] Priputen, P., Kusý, M., Drienovský, M., Janičkovič, D., Čička, R., Černičková, I., & Janovec, J., Experimental reinvestigation of Al-Co phase diagram in vicinity of Al13Co4 family of phases, J. Alloys Compd. 647 (2015) 486–497.
[2] Ma, X.L., & Kuo, K.H., Crystallographic characteristics of the Al-Co decagonal quasicrystal and its monoclinic approximant τ2-AI13Co4, Metall. Mater. Trans. A 25 (1994) 47–56.
[3] Zienert, T., & Fabrichnaya, O., Experimental investigation and thermodynamic assessment of the Al-Fe system, J. Alloys Compd. 743 (2018) 795–811.
[4] Hamada, T., Higashi, M., Niitsu, K., & Inui, H., Phase equilibria among η-Fe2Al5 and its higher-ordered phases, Sci. Technol. Adv. Mater. 22 (2021) 373–385.

LBN.P021
Challenges and solutions for EDS of semiconductor nanostructure

M. Falke[1], I. Nemeth[1], P. Soni[1]

[1]Bruker Nano GmbH, Product Management and Applications, Berlin, Germany

Energy dispersive X-ray analysis for identification and quantification of element distributions in semiconductor nanostructures is a well established and often routinely used technique. However, some overlaps of characteristic X-ray lines of specific elements used, such as Hf, Si, Ta and W, or Cu and Ta and their deconvolution from system peaks still pose a challenge. Furthermore, the new materials and their combinations, which are under investigation aiming at even further miniaturization present new questions in EDS analysis as well.

We present hardware and software approaches to better tackle these challenges. EDS data acquired using single side entry small and larger collection angle detectors in STEM as well as an annular high solid angle arrangement in SEM for semiconductor analysis are discussed. Suitable approaches to deconvolute overlapping lines and to identify and exclude spurious peaks caused by material outside the region of interest are shown.

One of the examples discusses data acquired at 0.4sr collection angle with a 100mm^2 racterack-shaped silicon drift detector in an aberration corrected FEG-STEM. The first figure shows the successful deconvolution of typical elements of a FinFET structure using a physical TEM background model, and the intensity ratios within one line series known from a comprehensive atomic data base. The spectrum used for deconvolution is the sum spectrum of the region of interest (data courtesy: ACE LLC.).

Another example shows data from a semiconductor structure acquired in SEM using an annular X-ray detector with only 60mm^2 active area placed between the pole piece and a TEM specimen, and thus achieving a collection angle of 1sr. Here we show in the second and third figure, how the Ga and Pt deposited during FIB-lamellae preparation can be distinguished from Ta, which is actually part of the structure of interest (specimen courtesy: Global Foundries Inc.).

In summary, we show detailed analysis approaches demonstrating, how new and challenging questions in elemental analysis of semiconducting nanostructures can be answered.

Figure 1

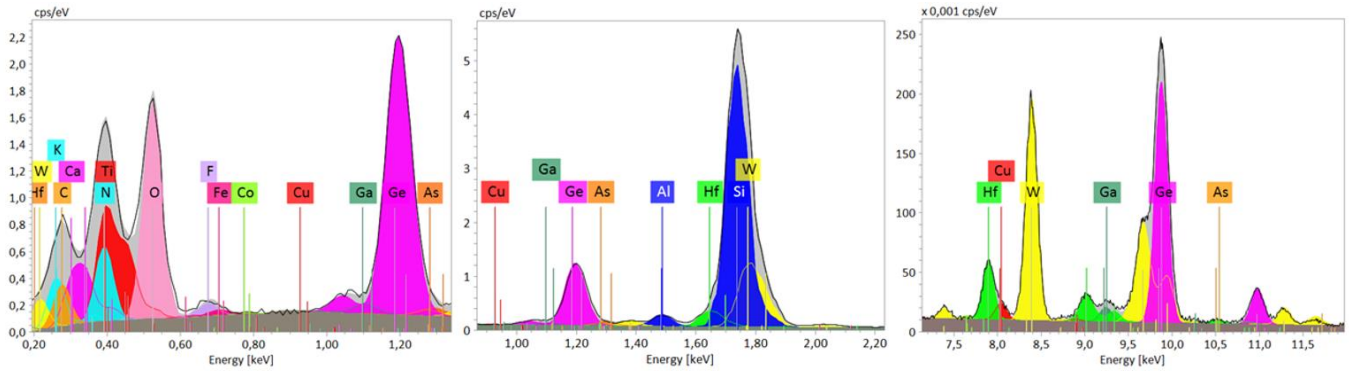

Figure 2

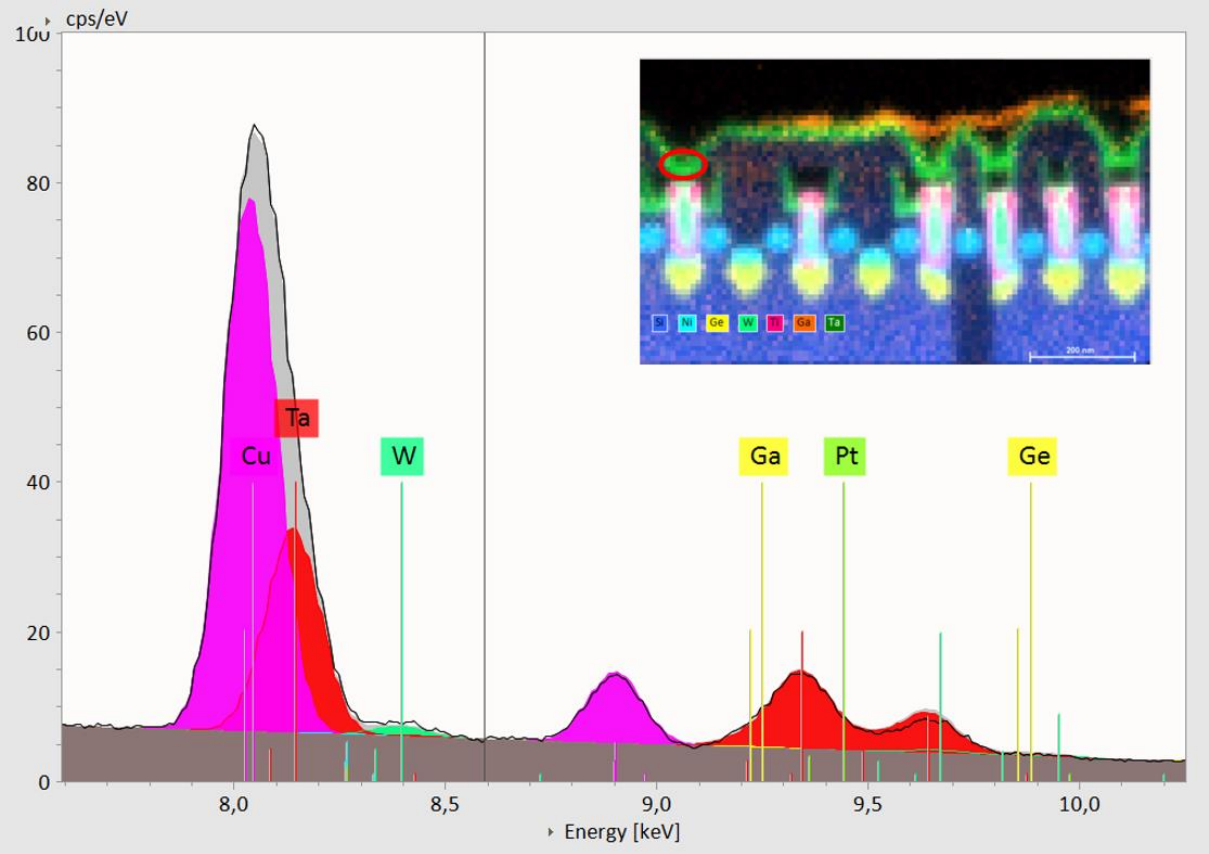

Figure 3

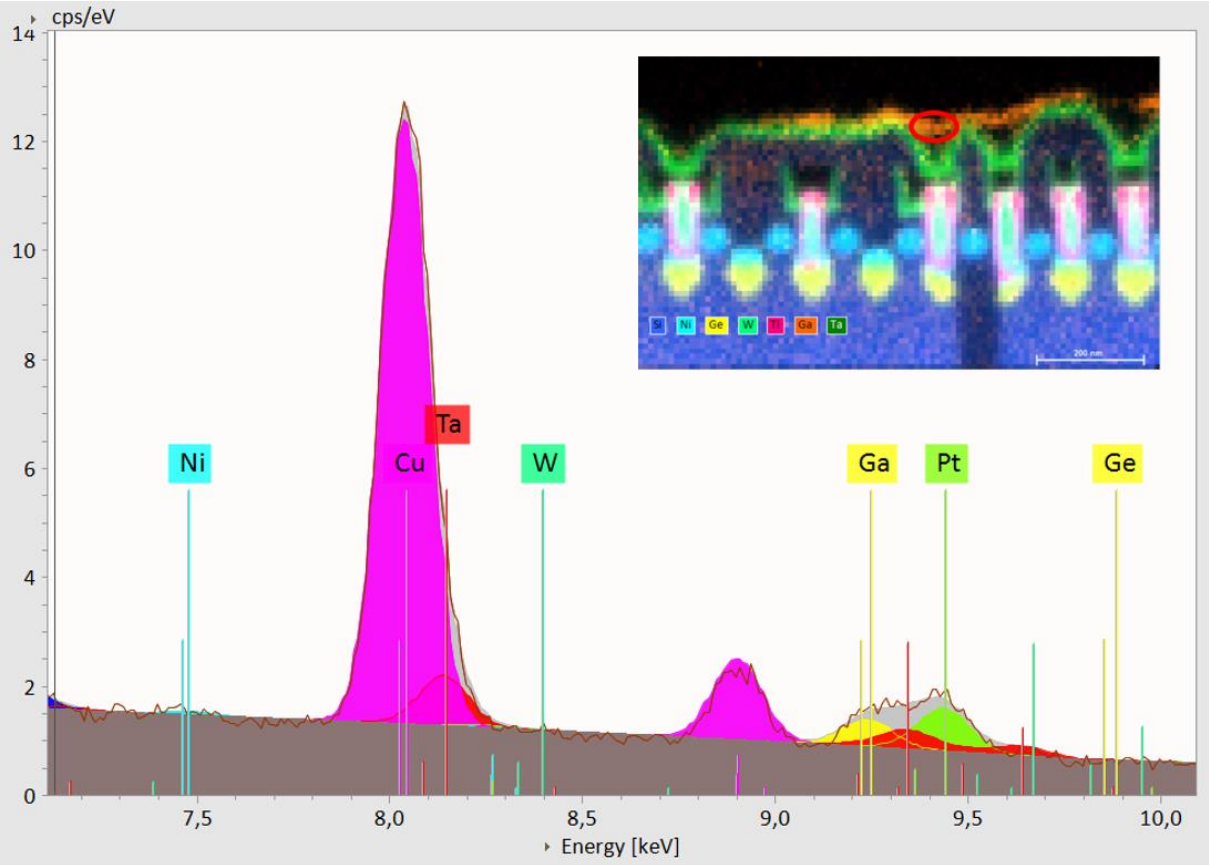

LBN.P022
Ferritin Crystallization – A Non-Classical Mechanism Resolved Molecularly in 3D

H. Weissman[1], L. Houben[1], S. G. Wolf[1], B. Rybtchinski[1]

[1]Weizmann Institute of Science, Molecular Chemistry and Material Science, Rehovot, Israel

Protein crystallization is important in structural biology, disease control, and pharmaceuticals. It has been recently recognized that non-classical crystallization, involving initial formation of amorphous precursor phase, often occurs in protein, organic, and inorganic crystallization processes. Consequently, two-step nucleation theory was put forward: it postulates initial formation of low density solvated amorphous aggregates that subsequently densify leading to nucleation. This view differs substantially from classical nucleation theory, which implies that crystalline nuclei forming in solution have the same density and structure as the final crystalline state. However, a molecular mechanism of non-classical protein crystallization has not been elucidated, posing the following fundamental questions: What is the nature of the amorphous precursors? Does crystallization take place within them? If so, how does order develop at the molecular level? In order to adequately answer these questions, three-dimensional (3D) molecular-level imaging of a crystallization process is required. Herein we present a study of ferritin crystallization using cryo-STEM tomography with quantitative order analysis, providing a 3D picture of crystallization with molecular resolution. The crystallization is associated with amorphous aggregates that densify and develop crystalline order. The evolution of crystalline order and density are parallel and gradual. Our study provides an insight into non-classical protein crystallization and reveals a paradigm of continuous evolution of crystalline order.[1]

[1] Houben, H. Weissman, S. G. Wolf, B. Rybtchinski, *Nature* 2020, *579*, 540–543.

Figure 1

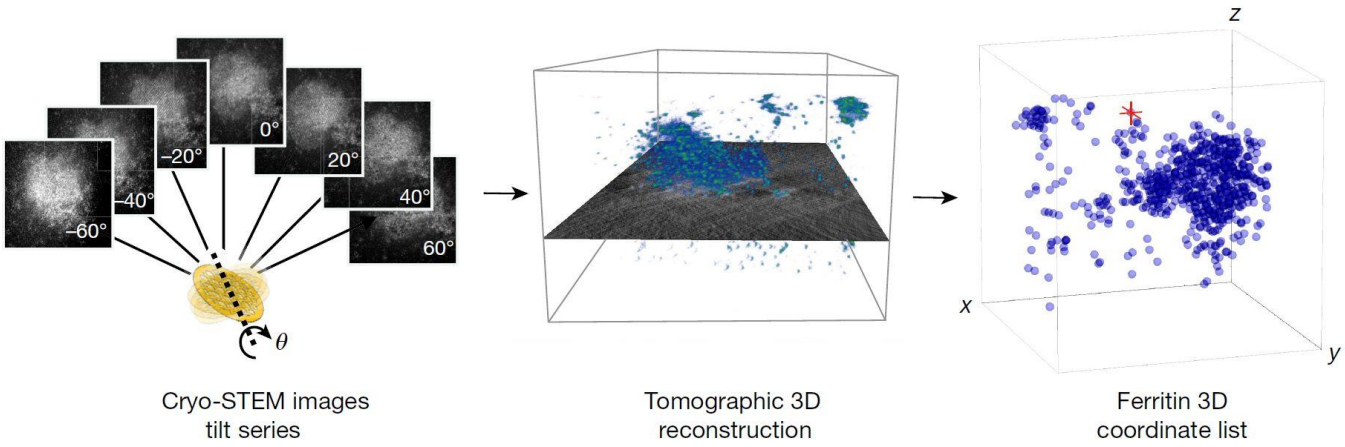

LBN.P023
Three-dimensional digital reconstruction of nickel cermet microstructure of solid oxide fuel cell anode using FIB-SEM tomography

K. Berent[1], T. Prokop[2], J. Szmyd[2], G. Brus[2]

[1]AGH University of Science and Technology, Academic Centre for Materials and Nanotechnology, Krakow, Poland
[2]AGH University of Science and Technology, Fundamental Research in Energy Engineering, Krakow, Poland

Solid Oxide Fuel Cells are highly efficient energy conversion devices capable of converting chemical energy directly into electrical energy [1]. Focused Ion Beam/Scanning Electron Microscopy (FIB/SEM) tomography is a novel powerful approach for three-dimensional (3D) imaging that opens new possibilities to expand morphological context description and analysis into the third dimension. The advantage of this technique is the large spatial resolution and the possibility of using a large stripping pitch (from several to several tens nm). In this research, we investigate the performance of the Ni-YSZ anodes from the SOFC stack before and after a prolonged period of operation. The analysis of the spatial distribution of different phases and porosity in SOFC anode provides an understanding of the structural influence on the transport properties. Afterwards, a detailed three-dimensional (3D) image analysis enables the comprehensive quantitative evaluation of the morphological parameters such as average grain size, phase volume fraction, phase tortuosity factor and the triple phase boundary (TPB).

In this study, FIB/SEM tomography was carried out on an FEI Versa 3D SEM. The sample was repeatedly milled with focused gallium (Ga) ions and each newly produced block face is imaged using an Everhart-Thornley detector (ETD) in combination with Auto Slice&View (ASV) software. The first step in the optimization of the imaging conditions was the determination of the optimal signal. The interaction volume decreases with the electron acceleration voltage. The phase contrast of a conventional Ni/yttria-stabilized zirconia anode was possible at low-kV due to the smaller interaction volume [2]. For this reason, observation was conducted under a beam voltage in the range of 0.7–1kV. Avizo software was used to stack and segment the SE images yielding a three-dimensional reconstruction and to quantify the microstructure. 3D datasets were collected from the reference anode and from anode after long-term operation. The phase volume fraction was measured by counting the number of voxels corresponding to Ni, YSZ and pores (Fig. 1). The sample average TPB length was calculated using the volume expansion method, as implemented by Iwai, et al. [3]. The use of the FIB / SEM technique for the analysis of the SOFC anode microstructure allowed us to obtain significant insight into the estimation of transport properties resulting from changes in the microstructural parameters occurring after the ageing experiment.

Figure 1: Cross-sectional FIB-SEM tomography images of the reference anode after FIB milling (a), and the corresponding segmented image (b). Three dimensional reconstruction of reference sample (c).

Aknowledgments: This work was supported by Polish National Research Center under the SONATA-10 program, grant no. UMO-2015/19/D/ST8/00839.

[1] T. Prokop, K. Berent, H. Iwai, J. Szmyd, G. Brus; International Journal of Hydrogen Energy (**2018**), DOI: https:// http://conapps.intern/timemanager/mitarbeiter/phone/list.org/10.1016/j.ijhydene.2018.04.023
[2] K. Thydén, Y.L. Liu, J.B. Bilde-Sørensenb; Solid State Ionics (2008), 1984–1989
[3] H. Iwai, N. Shikazono, T. Matsui, H. Teshima, M. Kishimoto, R. Kishida, D. Hayashi, K. Matsuzaki, D. Kanno, M. Saito, H. Muroyama, K. Eguchi, N. Kasagi, H. Yoshida; Journal of Power Sources 195 (2010), 955–961

Figure 1

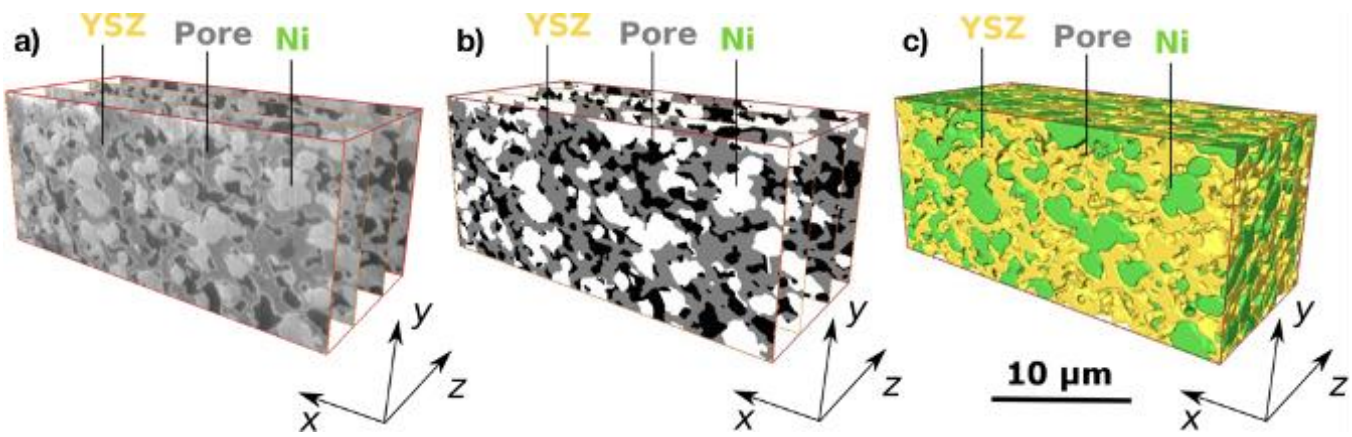

WS1.001-Invited
Selective effects of ionophores targeting the Golgi apparatus in the epithelial-to-mesenchymal transition

M. Kralj[1], M. Marjanović[1], A. M. Mikecin Dražić[1], M. Mioč[1], F. Kliček[2], M. Novokmet[2], G. Lauc[2]

[1]Ruđer Bošković Institute, Division of Molecular Medicine, Zagreb, Croatia
[2]GENOS, Glycoscience Research Laboratory, Zagreb, Croatia

Introduction**:** The epithelial-to-mesenchymal transition (EMT) is implicated in cancer metastasis, drug resistance and could give rise to cells with properties similar to cancer stem cells (CSCs). Targeting the EMT program to selectively eliminate CSCs is a promising strategy to improve cancer therapy. A recent study using an in vitro model that recapitulates EMT in human prostate cancer identified a monovalent ionophore and GA disturbing agent monensin (Mon) as an effective anticancer drug that is selective against EMT-like cells. Another K^+/H^+ ionophore salinomycin (Sal) was previously identified as a selective inhibitor of CSC-like cells, but the mechanism of its action is still not fully understood. Given that Mon and Sal are both monovalent cation ionophores and show potent anticancer effects, here we consider the possibility that both of them mediate their inhibitory effects on EMT and CSC by disrupting GA.

Objectives**:** To elucidate the effects of Sal and Mon on GA and test the possibility that the disruption of Golgi architecture and function mediates their effects on EMT and CSC.

Materials & methods: We used a breast CSC model, established by experimental induction of EMT in immortalized human mammary epithelial cells (HMLE). We performed global gene expression profiling by RNA-Seq, western blotting, flow cytometry and confocal microscopy, as well as analysed the N-Glycome on secreted proteins.

Results: We demonstrated that both Sal and Mon showed selective cytotoxic effects against cells exhibiting EMT phenotypes. Sal induced expression of Golgi-related genes and, similarly to Mon, lead to marked changes in Golgi morphology, particularly in EMT cells. Both ionophores affected protein post-translational modifications including protein processing and glycosylation that take place inside GA.

Conclusions**:** Our study demonstrates, for the first time, that Sal is a GA disturbing agent and identifies an increased sensitivity to GA disruption as a novel vulnerability of EMT cells. Based on our results, we propose that targeting GA could be a novel therapeutic approach for metastatic cancer patients. However, further studies are needed to gain better insight into the links between GA morphology and function and EMT that could be specifically targeted in cancer.

WS2.002-Invited
Enabling Science Through European Electron Microscopy – ESTEEM: A European Success Story
Achievements and importance of the ESTEEM initiatives – ESTEEM (2006-2011), ESTEEM2 (2012-2016) and ESTEEM3 (2019-2023)

The three successive ESTEEM (Enabling Science and Technology through European Electron Microscopy) projects bring together in a sustainable network, since the 6th Framework Programme of the European Commission and up until now, the leading European Laboratories equipped with the most advanced transmission electron microscopy (TEM) installations offering the best expertise in all different TEM fields.

This advanced consortium is now established as the primary European portal for industrial and academic scientists, who need access to latest generation TEM instrumentation, methodology or tools combined with the most cutting-edge TEM expertise for solving complex materials problems in various fields of science such as physics, materials science, engineering, chemistry or even life and earth sciences.

The core of ESTEEM has been the provision of Transnational Access (TA) to front-line instrumentation located in the partner laboratories. As a demonstration of the ESTEEM capabilities to meet the users' needs, since the beginning of ESTEEM and until the first 30 months of ESTEEM3, a total of about 10.000 transnational access days were offered to more than 600 scientists coming from more than 40 countries. These figures show a real demand from the academic and industrial communities and an urgent need for a strong European infrastructure network to be maintained in the field of TEM. In addition, between ESTEEM and ESTEEM3, the focus has strongly evolved towards mainly TA activities
The Networking Activities (NA) of the ESTEEM projects firstly aimed at disseminating the outputs to both academic and industrial users and the wider media. ESTEEM has recently implemented a wide variety of activities aiming at improving the dissemination of outputs, such as Open Access publications in high-ranked journals, lectures at selected conferences and setting up of an educational hub. An important component of these activities has been the organisation of a series of schools, workshops and webinars offering training by specialists in advanced techniques. ESTEEM has also put a focus on communication towards industrial engagement to attract more companies with the support of six SMEs, which are partners of the project. These networking activities have developed the core tools required to offer a stable and sustainable pan-European user facility across multiple laboratories, where ESTEEM, ESTEEM2 and ESTEEM3 provided excellent results.

The Joint Research Activities (JRA) of the ESTEEM projects focus on the development of advanced TEM methods required for the solution of key problems in materials and nanoscience, in which key issues such as specimen preparation, data interpretation, treatment and automation through theory and simulation, and standardization of protocols and methodologies were addressed. These JRA have strengthened TA capabilities within the ESTEEM3 consortium by providing a higher level of overall service to all TA users for the benefit of European scientists and industry.

In terms of impact: The ESTEEM consortium has contributed to the establishment of a strategic leadership in electron microscopy (i) to guide future developments and promote advanced electron microscopy to the wider research community, (ii) to provide transnational access for the academic and industrial research communities to the most powerful characterisation techniques available at the nanoscale, (iii) to train in innovative methods in electron microscopy, and (iv) to be a forum for discussing emerging cutting-edge electron microscopy techniques.